Solid Mechanics and Its Applications

Earl H. Dowell *Editor*

A Modern Course in Aeroelasticity

Sixth Edition

Springer

Solid Mechanics and Its Applications

Founding Editor

G. M. L. Gladwell

Volume 264

The fundamental questions arising in mechanics are: Why?, How?, and How much? The aim of this series is to provide lucid accounts written by authoritative researchers giving vision and insight in answering these questions on the subject of mechanics as it relates to solids. The scope of the series covers the entire spectrum of solid mechanics. Thus it includes the foundation of mechanics; variational formulations; computational mechanics; statics, kinematics and dynamics of rigid and elastic bodies; vibrations of solids and structures; dynamical systems and chaos; the theories of elasticity, plasticity and viscoelasticity; composite materials; rods, beams, shells and membranes; structural control and stability; soils, rocks and geomechanics; fracture; tribology; experimental mechanics; biomechanics and machine design. The median level of presentation is the first year graduate student. Some texts are monographs defining the current state of the field; others are accessible to final year undergraduates; but essentially the emphasis is on readability and clarity.

Springer and Professors Barber and Klarbring welcome book ideas from authors. Potential authors who wish to submit a book proposal should contact Dr. Mayra Castro, Senior Editor, Springer Heidelberg, Germany, email: mayra.castro@springer.com

Indexed by SCOPUS, Ei Compendex, EBSCO Discovery Service, OCLC, ProQuest Summon, Google Scholar and SpringerLink.

More information about this series at http://www.springer.com/series/6557

Earl H. Dowell
Editor

A Modern Course in Aeroelasticity

Sixth Edition

Springer

Editor
Earl H. Dowell
Department of Mechanical Engineering
and Materials Science
Duke University
Durham, NC, USA

ISSN 0925-0042 ISSN 2214-7764 (electronic)
Solid Mechanics and Its Applications
ISBN 978-3-030-74235-5 ISBN 978-3-030-74236-2 (eBook)
https://doi.org/10.1007/978-3-030-74236-2

This Springer imprint is published by the registered company Springer Nature Switzerland AG
The registered company address is: Gewerbestrasse 11, 6330 Cham, Switzerland

Preface to the Sixth Edition

For the last several years, the lectures in the course on Aeroelasticity at Duke University have been recorded and those are available to readers of this book upon request.

At the end of the 2020 spring semester, each of my then Ph.D. students, Dani Levin, Kevin McHugh, Maxim Freydin, Michael Lee, and also my faculty colleague, Jeff Thomas, presented lectures on their current research interests. I know you will enjoy their presentations as I did on the (1) the use of the ZERO computer code for aeroelastic analysis, (2) hypersonic fluid-structure interaction, (3) the construction of Reduced Order Models for the Navier–Stokes equations and (4) the use of harmonic balance methods for nonlinear aeroelastic analysis. My own lectures largely covered the first four chapters of the book, "A Modern Course in Aeroelasticity", using the fifth edition. For this sixth edition, the first twelve chapters of the latest edition are largely unchanged except for the correction of most, if not all, of the typos that appear in the fifth edition. The first homework assignment for the aeroelasticity course last spring was to find the typos in the chapter Static Aeroelasticity. Subsequent homework covered the chapters Dynamic Aeroelasticity and Nonsteady Aerodynamics of Lifting and Non-lifting Surfaces and a summer reading course with one of the Ph.D. students in the course, Richard Hollenbach, led to typos in the later chapters Stall Flutter–Some Recent Advances in Nonlinear Aeroelasticity, being identified and corrected. Also, the chapters Modern Analysis for Complex and Nonlinear Unsteady Flows in Turbomachinery and Some Recent Advances in Nonlinear Aeroelasticity have been modestly revised.

The experimental videos that appear on the Aeroelasticity website at Duke University are discussed extensively in the chapter Aeroelastic Models Design/Experiment and Correlation with New Theory, a new chapter of the sixth edition, and represent about 20 years of aeroelasticity experiments conducted on a range of nonlinear aeroelastic models at Duke University. Much of this work was led by Dr. Deman Tang. The chapter Aeroelastic Models Design/Experiment and Correlation with New Theory complements the chapter Experimental Aeroelasticity which provides an introduction to experimental methods that have traditionally been used

based upon the concepts of linear aeroelastic models. Also, in the sixth edition of the book, a chapter on hypersonic aeroelasticity or fluid structural thermal dynamics interaction(FSTDI), the chapter Fluid/Structural/Thermal/Dynamics Interaction (FSTDI) in Hypersonic Flow, is included with contributions from Kevin McHugh and Maxim Freydin. Currently, hypersonic aeroelasticity or FSTDI is a particularly active area of research and development including a number of fascinating experimental programs at several universities and governmental laboratories. An overview of these current and prospective programs is given including an assessment of the state of the art and the identification of outstanding challenges.

The Duke University Aeroelasticity Team hopes that you will enjoy all of this old and new material. Special acknowledgement and appreciation are extended to Dr. Deman Tang and Dr. Dani Levin for their contributions to the new edition of the book and to the Aeroelasticity website, respectively.

Durham, USA Earl H. Dowell

Preface to the Fifth Edition

In this fifth edition, a new chapter is added, Chap. 14, Some Recent Advances in Nonlinear Aeroelasticity: Fluid-Structure Interaction in the Twenty-First Century, with a discussion of some of the most recent research results that have been obtained in the last decade. Also, a new author and distinguished colleague, Dr. Deman Tang, has joined us. And the opportunity has been taken to correct all the typographical errors that we and our readers have found.

With this edition, the first author is making available upon request video/audio recordings of his semester-long lectures that cover Chaps. 1-4 as well as selected lectures on current research topics. It is planned to continually update these video/audio lectures and these updates will also be made available to those to purchase the new edition. Also available are lecture notes and additional homework problems and their solutions augmenting those already included in the text.

Earl H. Dowell

Preface to the Fourth Edition

In this edition, several new chapters have been added and others substantially revised and edited. Chapter 6 on Aeroelasticity in Civil Engineering originally authored by Robert Scanlan has been substantially revised by his close colleague, Emil Simiu. Chapter 9 on Modeling of Fluid-Structure Interaction by Earl Dowell and Kenneth Hall is entirely new and discusses modern methods for treating linear and nonlinear unsteady aerodynamics based upon computational fluid dynamics models and their solutions. Chapter 11 by Earl Dowell, John Edwards and Thomas Strganac on Nonlinear Aeroelasticity is also new and provides a review of recent results. Chapter 12 by Robert Clark and David Cox on Aeroelastic Control is also new and provides an authoritative account of recent developments. Finally, Chapter 13 by Kenneth Hall on Modern Analysis for Complex and Nonlinear Unsteady Flows in Turbomachinery is also new and provides an insightful and unique account of this important topic. Many other chapters have been edited for greater clarity as well and author and subject indices are also provided.

Dr. Deman Tang has provided invaluable contributions to the production of the text and all of the authors would like to acknowledge his efforts with great appreciation.

Earl H. Dowell

Preface to the Third Edition

The authors would like to thank all those readers of the first and second editions who have written with comments and suggestions. In the third edition, the opportunity has been taken to revise and update Chapters 1 to 9. Also, three new chapters have been added, i.e., Chapter 10, Experimental Aeroelasticity; Chapter 11, Nonlinear Aeroelasticity and Chapter 12, Aeroelastic Control. Chapter 10 is a brief introduction to a vast subject; Chapter 11 is an overview of a frontier of research and Chapter 12 is the first connected, authoritative account of the feedback control of aeroelastic systems. Chapter 12 meets a significant need in the literature. The authors of the first and second editions welcome two new authors, David Peters who has provided a valuable revision of Chapter 7 on rotorcraft and Edward Crawley who has provided Chapter 12 on aeroelastic control. It is a privilege and a pleasure to have them as members of the team. The author of Chapter 10 would also like to acknowledge the great help he has received over the year from his distinguished colleague, Wilmer H. "Bill" Reed, III, in the study of experimental aeroelasticity. Mr. Reed kindly provided the figures for Chapter 10. The author of Chapter 12 would like to acknowledge the significant scholarly contribution of Charrissa Lin and Ken Kazarus in preparing the chapter on aeroelastic control. Finally, the readers of the first and second editions will note that the authors and subject indices have been omitted from this edition. If any reader finds this an inconvenience, please contact the editor and we will reconsider the matter for the next edition.

Earl H. Dowell

Preface to the Second Edition

The authors would like to thank all those readers who have written with comments and errata for the First Edition. Many of these have been incorporated into the Second Edition. They would like to thank Professor Holt Ashley of Stanford University who has been most helpful in identifying and correcting various errata.

Also, the opportunity has been taken in the Second Edition to bring up-to-date several of the chapters as well as add a chapter on unsteady transonic aerodynamics and aeroelasticity. Chapters 2, 5, 6 and 8 have been substantially revised. These cover the topics of Static Aeroelasticity, Stall Flutter, Aeroelastic Problems of Civil Engineering Structures and Aeroelasticity in Turbomachines, respectively. Chapter 9, Unsteady Transonic Aerodynamics and Aeroelasticity, is new and covers this rapidly developing subject in more breadth and depth than the First Edition. Again, the emphasis is on fundamental concepts rather than, for example, computer code development per se. Unfortunately due to the press of other commitments, it has not been possible to revise Chapter 7, Aeroelastic Problems of Rotorcraft. However, the Short Bibliography has been expanded for this subject as well as for others. It is hoped that the readers of the First Edition and also new readers will find the Second Edition worthy of their study.

Earl H. Dowell

Preface to the First Edition

A reader who achieves a substantial command of the material contained in this book should be able to read with understanding most of the literature in the field. Possible exceptions may be certain special aspects of the subject such as the aeroelasticity of plates and shells or the use of electronic feedback control to modify aeroelastic behavior. The first author has considered the former topic in a separate volume. The latter topic is also deserving of a separate volume.

In the first portion of the book, the basic physical phenomena of divergence, control surface effectiveness, flutter and gust response of aeronautical vehicles are treated. As an indication of the expanding scope of the field, representative examples are also drawn from the non-aeronautical literature. To aid the student who is encountering these phenomena for the first time, each is introduced in the context of a simple physical model and then reconsidered systematically in more complicated models using more sophisticated mathematics.

Beyond the introductory portion of the book, there are several special features of the text. One is the treatment of unsteady aerodynamics. This crucial part of aeroelasticity is usually the most difficult for the experienced practitioner as well as the student. The discussion is developed from the fundamental theory underlying numerical lifting surface analysis. Not only the well-known results for subsonic and supersonic flow are covered but also some of the recent developments for transonic flow, which hold the promise of bringing effective solution techniques to this important regime.

Professor Sisto's chapter on Stall Flutter is an authoritative account of this important topic. A difficult and still incompletely understood phenomenon, stall flutter, is discussed in terms of its fundamental aspects as well as its significance in applications. The reader will find this chapter particularly helpful as an introduction to this complex subject.

Another special feature is a series of chapters on three areas of advanced application of the fundamentals of aeroelasticity. The first of these is a discussion of Aeroelastic Problems of Civil Engineering Structures by Professor Scanlan. The next is a discussion on the Aeroelasticity of Helicopters and V/STOL aircraft by Professor Curtiss. The final chapter in this series treats Aeroelasticity in

Turbomachines and is written by Professor Sisto. This series of chapters is unique in the aeroelasticity literature and the first author feels particularly fortunate to have the contributions of these eminent experts.

The emphasis in this book is on fundamentals because no single volume can hope to be comprehensive in terms of applications. However, the above three chapters should give the reader an appreciation for the relationship between theory and practice. One of the continual fascinations of aeroelasticity is this close interplay between fundamentals and applications. If one is to deal successfully with applications, a solid grounding in the fundamentals is essential.

For the beginning student, the first course in aeroelasticity could cover Chapters 1-3 and selected portions of Chapter 4. For a second course and the advanced student or research worker, the remaining chapters would be appropriate. In the latter portions of the book, more comprehensive literature citations are given to permit ready access to the current literature.

The reader familiar with the standard texts by Scanlan and Rosenbaum, Fung, Bisplinghoff, Ashley and Halfman and Bisplinghoff and Ashley will appreciate readily the debt the authors owe to them. Recent books by Petre (*Theory of Aeroelasticity. Vol. I Statics, Vol. II Dynamics.* In Romanian Publishing House of the Academy of the Socialist Republic of Romania, Bucharest, 1966) and Forsching (*Fundamentals of Aeroelasticity*. In German. Springer-Verlag, Berlin, 1974) should also be mentioned though these are less accessible to an English-speaking audience. It is hoped the reader will find this volume a worthy successor.

Earl H. Dowell

Contents

Contributors

Robert Clark Mechanical Engineering and Materials Science Duke University, Durham, NC, USA

Earl H. Dowell Mechanical Engineering and Materials Science, Duke University, Durham, NC, USA

Kenneth Hall Mechanical Engineering and Materials Science Duke University, Durham, NC, USA

David A. Peters Mechanical Engineering, Washington University, St. Louis, MO, USA

Emil Simiu National Institute for Standards and Technology, Gaithersburg, MD, USA

Fernando Sisto Mechanical Engineering, Stevens Institute of Technology, Hoboken, NJ, USA

Deman Tang Mechanical Engineering and Materials Science Duke University, Durham, NC, USA

Short Bibliography

Books

1. Bolotin, V. V. (1963) Nonconservative Problems of the Elastic Theory of Stability, Pergamon Press
2. Bisplinghoff, R. L., Ashley, H. and Halfman, R. L. (1955) Aeroelasticity, Addison-Wesley Publishing Company, Cambridge, Mass., (BAH)
3. Bisplinghoff, R. L., and Ashley, H. (1962) Principles of Aeroelasticity, John Wiley and Sons, Inc., New York, N.Y., Also available in Dover Edition. (BA)
4. Fung, Y. C. (1955) An Introduction to the Theory of Aeroelasticity, John Wiley and Sons, Inc., New York, N.Y., Also available in Dover Edition
5. Scanlan, R. H. and Rosenbaum, R. (1951) Introduction to the Study of Aircraft Vibration and Flutter, The Macmillan Company, New York, N.Y., Also available in Dover Edition
6. AGARD Manual on Aeroelasticity, Vols. I-VII, Beginning 1959 with continual updating. (AGARD)
7. Ashley, H., Dugundji, J. and Rainey, A. G. (1969) Notebook for Aeroelasticity, AIAA Professional Seminar Series
8. Dowell, E. H. (1975) Aeroelasticity of Plates and Shells, Noordhoff International Publishing, Leyden
9. Simiu, E., and Scanlan, R. H.(1996) Wind Effects on Structures - An Introduction to Wind Engineering, John Wiley and Sons
10. Johnson, W., Helicopter Theory, Princeton University Press
11. Dowell, E. H., and Ilgamov, M. (1988) Studies in Nonlinear Aeroelasticity, Springer - Verlag
12. Paidoussis, M. P.(1988) Fluid - Structure Interactions: Slender Structures and Axial Flow, Volume 1, Academic Press

In parentheses, abbreviations for the above books are indicated which are used in the text.

Survey articles

1. Garrick, I. E.(1976) Aeroelasticity - Frontiers and Beyond, 13th Von Karman Lecture, J. of Aircraft, Vol. 13, No. 9, pp. 641–657.
2. Several Authors (1976) Unsteady Aerodynamics. Contribution of the Structures and Materials Panel to the Fluid Dynamics Panel Round Table Discussion on Unsteady Aerodynamics, Goettingen, May, AGARD Report R-645, March 1976.
3. Rodden, W. P.(1976) A Comparison of Methods Used in Interfering Lifting Surface Theory, AGARD Report R-643, March 1976.
4. Ashley, H. (1970) Aeroelasticity, Applied Mechanics Reviews, February
5. Abramson, H. N. (1969) Hydroelasticity: A Review of Hydrofoil Flutter, Applied Mechanics Reviews, February
6. Many Authors (1969) Aeroelastic Effects From a Flight Mechanics Standpoint, AGARD, Conference Proceedings No. 46
7. Landhal, M. T., and Stark, V. J. E. (1968) Numerical Lifting Surface Theory - Problems and Progress, AIAA Journal, 6(11), November, pp. 2049–2060.
8. Many Authors (1967) Symposium on Fluid - Solid Interactions ASME Annual Winter Meeting, November
9. Kaza, K. R. V.(1988) Development of Aeroelastic Analysis Methods for Turborotors and Propfans - Including Mistuning, In: Lewis Structure Technology, Vol. 1, Proceedings, NASA Lewis Research Center
10. Ericsson, L. E. and Reading, J. P. (1988) Fluid Mechanics of Dynamic Stall, Part I, Unsteady Flow Concepts, and Part II, Prediction of Full Scale Characteristics, J. Fluids and Structures, Vol. 2, No. 1 and 2, pp. 1–33 and 113–143
11. Mabey, D. G. (1998) Some Aspects of Aircraft Dynamic Loads Due to Flow Separation, AGARD-R-750, February
12. Yates, E. C.,Jr. and Whitlow W.,Jr. (1987) Development of Computational Methods for Unsteady Aerodynamics at the NASA Langley Research Center, in AGARD-R-749, Future Research on Transonic Unsteady Aerodynamics and its Aeroelastic Applications, August
13. Gad-el-Hak, M. (1987) Unsteady Separation on Lifting Surfaces, Applied Mechanics Reviews, Vol. 40, No. 4, pp. 441–453
14. Hajela P(ed) (1987) Recent Trends in Aeroelasticity, Structures and Structural Dynamics, University of Florida Press, Gainesville
15. Jameson, A. (1983) The Evolution of Computational Methods in Aerodynamics, J. Applied Mechanics, Vol. 50, No. 4, pp. 1052–1070.
16. Seebass, R. (1984) Advances in the Understanding and Computation of Unsteady Transonic Flows, In: Krothapalli A., Smith C.(eds) Recent Advances on Aerodynamics, Smith, Springer - Verlag
17. McCroskey, W. J. (1982) Unsteady Airfoils, In: Annual Reviews of Fluid Mechanics, Vol. 14, pp. 285–311
18. Tijdeman, H. and Seebass, R. (1980) Transonic Flow Past Oscillating Airfoils, In: Annual Reviews of Fluid Mechanics, Vol. 12, pp. 181–222

19. Ormiston, R., Warmbrodt, W., Hodges, D., and Peters, D. (1988) Survey of Army/NASA Rotocraft Aeroelastic Stability Research, NASA TM 101026 and USAASCOM TR 88-A-005
20. Dowell, E.H. and Hall, K.C. (2001) Modeling of Fluid-Structure Interaction, Annual Reviews of Fluid Mechanics, Vol.33, pp.445–490
21. Eastep, Franklin E.(ed) (2003) Flight Vehicle Aeroelasticity, a series of invited articles by several authors in the Journal of Aircraft, Vol.40, No.5, pp.809–874

Journals

AHS Journal
AIAA Journal
ASCE Transactions, Engineering Mechanics Division
ASME Transaction, Journal of Applied Mechanics
International Journal of Solids and Structures
Journal of Aircraft
Journal of Fluids and Structures
Journal of Sound and Vibration

Other journals will have aeroelasticity articles, of course, but these are among those with the most consistent coverage.

The impact of aeroelasticity on design is not discussed in any detail in this book. For insight into this important area, the reader may consult the following volumes prepared by the National Aeronautics and Space Administration in its series on SPACE VEHICLE DESIGN CRITERIA. Although these documents focus on space vehicle application, much of the material is relevant to aircraft as well. The depth and breadth of coverage vary considerably from one volume to the next, but each contains at least a brief State-of-the-Art review of its topics as well as a discussion of Recommended Design Practices. Further, some important topics are included which have not been treated at all in the present book. These include the following as already mentioned in the Preface.

Aeroelasticity of plates and shells (panel flutter) (NASA SP-8004) and Aeroelastic effects on control systems dynamics (NASA SP-8016, NASA SP-8036 NASA SP-8079) as well as Structural response to time-dependent separated fluid flows (buffeting) (NASA SP-8001), Fluid motions inside elastic containers (fuel sloshing) (NASA SP-8009, NASA SP-8031) and Coupled structural propulsion instability (POGO) (NASA SP-8055).

It was intended to revise these volumes periodically to keep them up-to-date. Unfortunately, this has not yet been done.

1. NASA SP-8001 1970
   Buffeting During Atmospheric Ascent
2. NASA SP-8002 1964
   Flight Loads Measurements During Launch and Exit

3. NASA SP-8003 1964
Flutter, Buzz and Divergence
4. NASA SP-8004 1972
Panel Flutter
5. NASA SP-8006 1965
Local Steady Aerodynamic Loads During Launch and Exit
6. NASA SP-8008 1965
Prelaunch Ground Wind Loads
7. NASA SP-8012 1968
Natural Vibration Wind Analysis
8. NASA SP-8016 1969
Effect of Structural Flexibility on Spacecraft Control System
9. NASA SP-8009 1968
Propellant Slosh Loads
10. NASA SP-8031 1969
Slosh Suppression
11. NASA SP-8035 1970
Wind Loads During Ascent
12. NASA SP-8036 1970
Effect of Structural Flexibility on Launch Vehicle Control System
13. NASA SP-8050 1970
Structural Vibration Prediction
14. NASA SP-8055 1970
Prevention of Coupled Structure-Propulsion Instability (POGO)
15. NASA SP-8079 1971
Structural Interaction with Control Systems.

Introduction

Earl H. Dowell

Abstract This brief chapter touches on the basic questions to be addressed in the book and provides some historical context for the development of the field of aeroelasticity.

Several years ago, Collar suggested that aeroelasticity could be usefully visualized as forming a triangle of disciplines, dynamics, solid mechanics and (unsteady) aerodynamics (Fig. 1).

Aeroelasticity is concerned with those physical phenomena which involve significant mutual interaction among inertial, elastic and aerodynamic forces. Other important technical fields can be identified by pairing the several points of the triangle. For example,

- Stability and control (flight mechanics) = dynamics + aerodynamics
- Structural vibrations = dynamics + solid mechanics
- *Static* aeroelasticity = steady flow aerodynamics + solid mechanics

Conceptually, each of these technical fields may be thought of as a special aspect of aeroelasticity. For historical reasons only the last topic, static aeroelasticity, is normally so considered. However, the impact of aeroelasticity on stability and control (flight mechanics) has increased substantially in recent years.

In modern aerospace vehicles, the relevant physical phenomena may be even more complicated. For example, stresses induced by high temperature environments can be important in aeroelastic problems, hence the term

aerothermoelasticity

In other applications, the dynamics of the guidance and control system may significantly affect aeroelastic problems, or vice versa, hence the term

E. H. Dowell (✉)
Mechanical Engineering and Materials Science Duke University, Durham, NC, USA
e-mail: earl.dowell@duke.edu

E. H. Dowell (ed.), *A Modern Course in Aeroelasticity*, Solid Mechanics and Its Applications 264, https://doi.org/10.1007/978-3-030-74236-2_1

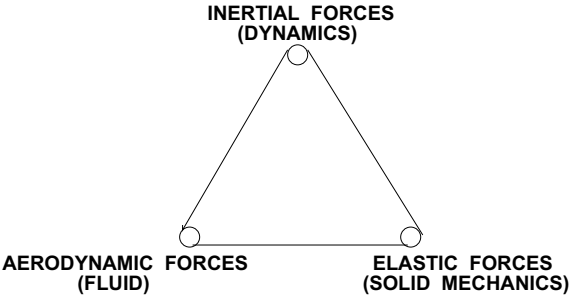

Fig. 1 Collar diagram

aeroservoelasticity

For a historical discussion of aeroelasticity including its impact on aerospace vehicle design, consult in this chapter of Bisplinghoff and Ashley [2] and AGARD CP No.46, "Aeroelastic Effects from a Flight Mechanics Standpoint" [6].

We shall first concentrate on the dynamics and solid mechanics aspects of aeroelasticity with the aerodynamic forces taken as given. Subsequently, the aerodynamic aspects of aeroelasticity shall be treated from first principles. Theoretical methods will be emphasized, although these will be related to experimental methods and results where this will add to our understanding of the theory and its limitations. For simplicity, we shall begin with the special case of static aeroelasticity.

Although the technological cutting edge of the field of aeroelasticity has centered in the past on aeronautical applications, applications are found at an increasing rate in civil engineering, e.g., flows about bridges and tall buildings; mechanical engineering, e.g., flows around turbomachinery blades and fluid flows in flexible pipes; and nuclear engineering; e.g., flows about fuel elements and heat exchanger vanes. It may well be that such applications will increase in both absolute and relative number as the technology in these areas demands lighter weight structures under more severe flow conditions. Much of the fundamental theoretical and experimental developments can be applied to these areas as well and indeed it is hoped that a common language can be used in these several areas of technology. To further this hope we shall discuss subsequently in some detail several examples in these other fields, even though our principal focus shall be on aeronautical problems. Separate chapters on civil engineering, turbomachinery and helicopter (rotor systems) applications will introduce the reader to the fascinating phenomena which arise in these fields.

Since most aeroelastic phenomena are of an undesirable character, leading to loss of design effectiveness or even sometimes spectacular structural failure as in the case of aircraft wing flutter or the Tacoma Narrows Bridge disaster, the spreading importance of aeroelastic effects will not be warmly welcomed by most design engineers. However, the mastery of the material to be discussed here will permit these effects to be better understood and dealt with if not completely overcome. Moreover

in recent years, the beneficial effects of aeroelasticity have received greater attention. For example, the promise of new aerospace systems such as uninhabited air vehicles (UAVs) and morphing aircraft will undoubtedly be more fully realized by exploiting the benefits of aeroelasticity while mitigating the risks.

Static Aeroelasticity

Earl H. Dowell

Abstract The basics of static aeroelasticty, in contrast to dynamic aeroelasticity, are reviewed and some classic subjects such as divergence and control surface reversal are treated. The discussion starts with simple mathematical and physical models and progresses to more complex models and solution methods. Most of these models and methods prove to be useful in dynamic aeroelasticity as well.

1 Typical Section Model of an Airfoil

We shall find a simple, somewhat contrived, physical system useful for introducing several aeroelastic problems. This is the so-called 'typical section' which is a popular pedagogical device.[1] This simplified aeroelastic system consists of a rigid, flat, plate airfoil mounted on a torsional spring attached to a wind tunnel wall. See Fig. 1; the airflow over the airfoil is from left to right.

The principal interest in this model for the aeroelastician is the rotation of the plate (and consequent twisting of the spring), α, as a function of airspeed. If the spring were very stiff or airspeed were very slow, the rotation would be rather small; however, for flexible springs or high flow velocities the rotation may twist the spring beyond its ultimate strength and lead to structural failure. A typical plot of elastic twist, α_e, versus airspeed, U, is given in Fig. 2. The airspeed at which the elastic twist increases rapidly to the point of failure is called the 'divergence airspeed', U_D. A major aim of any theoretical model is to accurately predict U_D. It should be emphasized that the above curve is representative not only of our typical section model but also of real aircraft wings. Indeed the primary difference is not in the basic physical phenomenon of divergence, but rather in the elaborateness of the theoretical analysis required to predict accurately U_D for an aircraft wing versus that required for our simple typical section model.

[1] See chapter 'Aeroelasticity in Civil Engineering', BA, especially pp. 189–200.

E. H. Dowell (✉)
Mechanical Engineering and Materials Science Duke University, Durham, NC, USA
e-mail: earl.dowell@duke.edu

E. H. Dowell (ed.), *A Modern Course in Aeroelasticity*, Solid Mechanics and Its Applications 264, https://doi.org/10.1007/978-3-030-74236-2_2

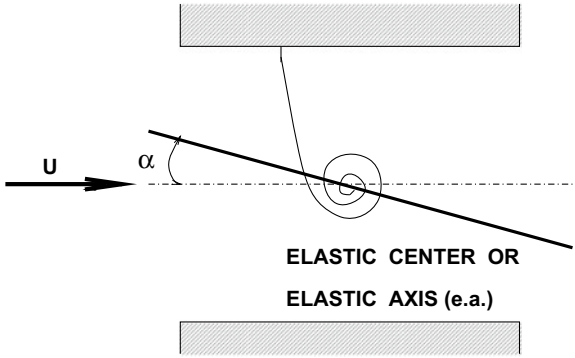

Fig. 1 Geometry of typical section airfoil

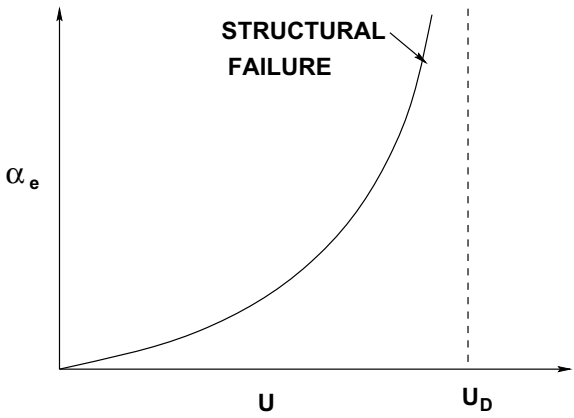

Fig. 2 Elastic twist versus airspeed

To determine U_D theoretically we proceed as follows. The equation of static equilibrium simply states that the sum of aerodynamic plus elastic moments about any point on the airfoil is zero. By convention, we take the point about which moments are summed as the point of spring attachment, the so-called 'elastic center' or 'elastic axis' of the airfoil.

The total aerodynamic angle of attack, α, is taken as the sum of some initial angle of attack, α_0 (with the spring untwisted), plus an additional increment due to elastic twist of the spring, α_e.

$$\alpha = \alpha_0 + \alpha_e \tag{1.1}$$

In addition, we define a point on the airfoil known as the 'aerodynamic center'.[2] This is the point on the airfoil about which the aerodynamic moment is independent of angle of attack, α. Thus, we may write the moment about the elastic axis as

[2] For two dimensional, incompressible flow this is at the airfoil quarter-chord; for supersonic flow it moves back to the half-chord. See Ashley and Landahl [1]. References are given at the end of each chapter.

$$M_y = M_{AC} + Le \tag{1.2}$$

where

M_y moment about elastic axis or center
M_{AC} moment about aerodynamic center, both moments are positive nose up
L lift, net vertical force positive up
e distance from aerodynamic center to elastic axis, positive aft.

From aerodynamic theory [1] (or experiment plus dimensional analysis) one has

$$L = C_L q S \tag{1.3a}$$

$$M_{AC} = C_{MAC} q S_c$$

where

$$C_L = C_{L_0} + \frac{\partial C_L}{\partial \alpha}\alpha, \quad \text{lift coefficient} \tag{1.3b}$$

$C_{MAC} = C_{MAC_0}$, a constant, aerodynamic center moment coefficient in which

$$q = \frac{\rho U^2}{2}, \text{ dynamic pressure and}$$

ρ air density
U air velocity
c airfoil chord
l airfoil span
S airfoil area, c $\times$ 1

Equation (1.3a) defines C_L and C_{MAC} (1.3b) is a Taylor Series expansion of C_L for small α. C_{L_0} is the lift coefficient at $\alpha \equiv 0$. From (1.2), (1.3a) and (1.3b), we see the moment is also expanded in a Taylor series. The above forms are traditional in the aerodynamic literature. They are not necessarily those a nonaerodynamicist would choose.

Note that C_{L_0}, $\partial C_L/\partial\alpha$, C_{MAC_0} are nondimensional functions of airfoil shape, planform and Mach number. For a flat plate in two-dimensional incompressible flow [1]

$$\frac{\partial C_L}{\partial \alpha} = 2\pi, \qquad C_{MAC_0} = 0 = C_{L_0}$$

In what follows, we shall take $C_{L_0} \equiv 0$ for convenience and without any essential loss of information.

From (1.2), (1.3a) and (1.3b)

$$M_y = eqS\left[\frac{\partial C_L}{\partial \alpha}(\alpha_0 + \alpha_e)\right] + qScC_{MAC_0} \tag{1.4}$$

Now consider the elastic moment. If the spring has linear moment-twist characteristics then the elastic moment (positive nose up) is $-K_\alpha \alpha_e$ where K_α is the elastic spring constant and has units of moment (torque) per angle of twist. Hence, summing moments we have

$$eqS\left[\frac{\partial C_L}{\partial \alpha}(\alpha_0 + \alpha_e)\right] + qScC_{MAC_0} - K_\alpha \alpha_e = 0 \tag{1.5}$$

which is the equation of static equilibrium for our 'typical section' airfoil.

Solving for the elastic twist (assuming $C_{MAC_0} = 0$ for simplicity) one obtains

$$\alpha_e = \frac{qS}{K_\alpha}\frac{e\frac{\partial C_L}{\partial \alpha}\alpha_o}{1 - q\frac{Se}{K_\alpha}\frac{\partial C_L}{\partial \alpha}} \tag{1.6}$$

This solution has several interesting properties. Perhaps most important is the fact that at a particular dynamic pressure the elastic twist becomes infinitely large. This is, when the denominator of the right-hand side of (1.6) vanishes

$$1 - q\frac{Se}{K_\alpha}\frac{\partial C_L}{\partial \alpha} = 0 \tag{1.7}$$

at which point $\alpha_e \to \infty$.

Equation (1.7) represents what is termed the 'divergence condition' and the corresponding dynamic pressure which may be obtained by solving (1.7) is termed the 'divergence dynamic pressure',

$$q_D \equiv \frac{K_\alpha}{Se(\partial C_L/\partial \alpha)} \tag{1.8}$$

Since only the positive dynamic pressures are physically meaningful, note that only for $e > 0$ will divergence occur, i.e., when the aerodynamic center is ahead of the elastic axis. Using (1.8), (1.6) may be rewritten in a more concise form as

$$\alpha_e = \frac{(q/q_D)\alpha_0}{1 - q/q_D} \tag{1.9}$$

Of course, the elastic twist does not become infinitely large for any real airfoil; because this would require an infinitely large aerodynamic moment. Moreover, the linear relation between the elastic twist and the aerodynamic moment would be violated long before that. However, the elastic twist can become so large as to cause structural failure. For this reason, all aircraft are designed to fly below the divergence

dynamic pressure of all airfoil or lifting surfaces, e.g., wings, fins, control surfaces. Now let us examine Eqs. (1.5) and (1.9) for additional insight into our problem, again assuming $C_{MAC_0} = 0$ for simplicity. Two special cases will be informative. First, consider $\alpha_0 \equiv 0$. Then (1.5) may be written

$$\alpha_e \left[qS \frac{\partial C_L}{\partial \alpha} e - K_\alpha \right] = 0 \tag{1.5a}$$

Excluding the trivial case $\alpha_e = 0$ we conclude from (1.5a) that

$$qS \frac{\partial C_L}{\partial \alpha} e - K_\alpha = 0 \tag{1.7a}$$

which is the 'divergence condition'. This will be recognized as an eigenvalue problem, the vanishing of the coefficient of α_e in (1.5a) being the condition for nontrivial solutions of the unknown, α_e.[3] Hence, 'divergence' requires only a consideration of elastic deformations.

Secondly, let us consider another special case of a somewhat different type, $\alpha_0 \neq 0$, but $\alpha_e \ll \alpha_0$. Then (1.5) may be written approximately as

$$eqS \frac{\partial C_L}{\partial \alpha} \alpha_0 - K_\alpha \alpha_e = 0 \tag{1.10}$$

Solving

$$\alpha_e = \frac{qSe(\partial C_L/\partial \alpha)\alpha_0}{K_\alpha} \tag{1.11}$$

Note this solution agrees with (1.6) if the denominator of (1.6) can be approximated by

$$1 - q \frac{Se}{K_\alpha} \frac{\partial C_L}{\partial \alpha} = 1 - \frac{q}{q_D} \approx 1$$

Hence, this approximation is equivalent to assuming that the dynamic pressure is much smaller than its divergence value. Note that the term neglected in (1.5) is the aerodynamic moment due to the elastic twist. This term can be usefully thought of as the 'aeroelastic feedback'.[4] Without this term, solution (1.11) is valid only when $q/q_D \ll 1$; and it cannot predict divergence. A feedback diagram of Eq. (1.5) is given in Fig. 3. Thus, when the forward loop gain,G, exceeds unity, $G \equiv qeS(\partial C_L/\partial \alpha)/K_\alpha > 1$, the system is statically unstable, see Eq. (1.8). Hence, aeroelasticity can also be thought of as the study of aerodynamic + elastic feed-

[3] Here in static aeroelasticity q plays the role of the eigenvalue; in dynamic aeroelasticity q will be a parameter and the (complex) frequency will be the eigenvalue. This is a source of confusion for some students when they first study the subject.

[4] For the reader with some knowledge of feedback theory as in, for example, Savant [2].

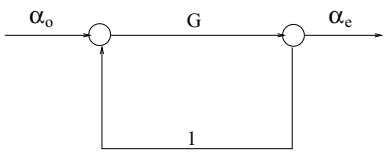

Fig. 3 Feedback representation of aeroelastic divergence

back systems. One might also note the similarity of this divergence problem to conventional 'buckling' of structures.[5] Having exhausted the interpretations of this problem, we will quickly pass on to some slightly more complicated problems, but whose physical content is similar.

1.1 Typical Section Model with Control Surface

We shall add a control surface to our typical section of Fig. 1, as indicated in Fig. 4. For simplicity, we take $\alpha_0 = C_{MAC_0} = 0$; hence, $\alpha = \alpha_e$. The aerodynamic lift is given by

$$L = qSC_L = qS\left(\frac{\partial C_L}{\partial \alpha}\alpha + \frac{\partial C_L}{\partial \delta}\delta\right) \quad \text{positive up} \tag{1.12}$$

and the moment by

$$M_{AC} = qScC_{MAC} = qSc\frac{\partial C_{MAC}}{\partial \delta}\delta \quad \text{positive nose up} \tag{1.13}$$

and the moment about the hinge line of the control surface by

$$H = qS_H c_H C_H = qS_H c_H\left(\frac{\partial C_H}{\partial \alpha}\alpha + \frac{\partial C_H}{\partial \delta}\delta\right) \quad \text{positive tail down} \tag{1.14}$$

where S_H is the area of control surface, c_H the chord of the control surface and C_H the (nondimensional) aerodynamic hinge moment coefficient. As before, $\frac{\partial C_L}{\partial \alpha}$, $\frac{\partial C_L}{\partial \delta}$, $\frac{\partial C_{MAC}}{\partial \delta}$, $\frac{\partial C_H}{\partial \alpha}$, $\frac{\partial C_H}{\partial \delta}$ are aerodynamic constants which vary with Mach and airfoil geometry. Note $\frac{\partial C_H}{\partial \delta}$ is typically negative.

The basic purpose of a control surface is to change the lift (or moment) on the main lifting surface. It is interesting to examine aeroelastic effects on this lift.

To write the equations of equilibrium, we need the elastic moments about the elastic axis of the main lifting surface and about the hinge line of the control surface. These are $-K_\alpha\alpha$ (positive nose up), $-K_\delta(\delta - \delta_0)$ (positive tail down), and $\delta_e \equiv \delta - \delta_0$, where δ_e is the elastic twist of control surface in which δ_0 is the difference

[5] Timoshenko and Gere [3].

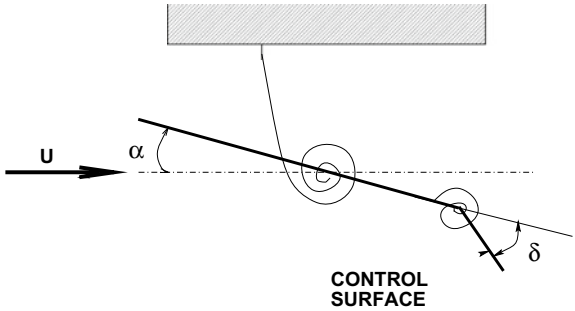

Fig. 4 Typical section with control surface

between the angle of zero aerodynamic control deflection and zero twist of the control surface spring.

The two equations of static moment equilibrium are

$$eqS\left(\frac{\partial C_L}{\partial \alpha}\alpha + \frac{\partial C_L}{\partial \delta}\delta\right) + qSc\frac{\partial C_{MAC}}{\partial \delta}\delta - K_\alpha \alpha = 0 \tag{1.15}$$

$$qS_H c_H\left(\frac{\partial C_H}{\partial \alpha}\alpha + \frac{\partial C_H}{\partial \delta}\delta\right) - K_\delta(\delta - \delta_0) = 0 \tag{1.16}$$

The above are two algebraic equations in two unknowns, α and δ, which can be solved by standard methods. For example, Cramer's rule gives

$$\alpha = \frac{\begin{vmatrix} 0 & eqS\frac{\partial C_L}{\partial \delta} + qSc\frac{\partial C_{MAC}}{\partial \delta} \\ -K_\delta\delta_0 & qS_HC_H\frac{\partial C_H}{\partial \delta} - K_\delta \end{vmatrix}}{\begin{vmatrix} eqS\frac{\partial C_L}{\partial \alpha} - K_\alpha & eqS\frac{\partial C_L}{\partial \delta} + qSc\frac{\partial C_{MAC}}{\partial \delta} \\ qS_HC_H\frac{\partial C_H}{\partial \alpha} & qS_HC_H\frac{\partial C_H}{\partial \delta} - K_\delta \end{vmatrix}} \tag{1.17}$$

and a similar equation for δ. To consider divergence we again set the denominator to zero. This gives a quadratic equation in the dynamic pressure q. Hence, there are two values of divergence dynamic pressure. Only the lower positive value of the two is physically significant.

In addition to the somewhat more complicated form of the divergence condition, there is a *new physical phenomenon* associated with the control surface called 'control surface reversal'. If the two springs were rigid, i.e.,$K_\alpha \to \infty$ and $K_\delta \to \infty$, then $\alpha = 0$, $\delta = \delta_0$, and

$$L_r = qS\frac{\partial C_L}{\partial \delta}\delta_0 \tag{1.18}$$

With flexible springs, however,

$$L = qS\left(\frac{\partial C_L}{\partial \alpha}\alpha + \frac{\partial C_L}{\partial \delta}\delta\right) \tag{1.19}$$

where α, δ are determined by solving the equilibrium Eqs. (1.15), and (1.16). In general, the latter value of the lift will be smaller than the rigid value of lift. Indeed, the lift may actually become zero or even negative due to aeroelastic effects. Such an occurrence is called 'control surface reversal'. To simplify matters and show the essential character of control surface reversal, we will assume $K_\delta \to \infty$ and hence, $\delta \to \delta_0$ from the equilibrium condition (1.16). Solving the equilibrium Eq. (1.15), we obtain

$$\alpha = \delta_0 \frac{\frac{\partial C_L}{\partial \delta} + \frac{c}{e}\frac{\partial C_{MAC}}{\partial \delta}}{\frac{K_\alpha}{qSe} - \frac{\partial C_L}{\partial \alpha}} \tag{1.20}$$

But

$$\begin{aligned} L &= qS\left(\frac{\partial C_L}{\partial \delta}\delta_0 + \frac{\partial C_L}{\partial \alpha}\alpha\right) \\ &= qS\left(\frac{\partial C_L}{\partial \delta} + \frac{\partial C_L}{\partial \alpha}\frac{\alpha}{\delta_0}\right)\delta_0 \end{aligned} \tag{1.21}$$

so that, introducing (1.20) into (1.21) and normalizing by L_r, we obtain

$$\frac{L}{L_r} = \frac{1 + q\frac{Sc}{K_\alpha}\frac{\partial C_{MAC}}{\partial \delta}\left(\frac{\partial C_L}{\partial \alpha}/\frac{\partial C_L}{\partial \delta}\right)}{1 - q\frac{Se}{K_\alpha}\frac{\partial C_L}{\partial \alpha}} \tag{1.22}$$

Control surface reversal occurs when $L/L_r = 0$

$$1 + q_R \frac{Sc}{K_\alpha}\frac{\partial C_{MAC}}{\partial \delta}\left(\frac{\partial C_L}{\partial \alpha}/\frac{\partial C_L}{\partial \delta}\right) = 0 \tag{1.23}$$

where q_R is the dynamic pressure at reversal, or

$$q_R \equiv \frac{\frac{-K_\alpha}{Sc}\left(\frac{\partial C_L}{\partial \delta}/\frac{\partial C_L}{\partial \alpha}\right)}{\frac{\partial C_{MAC}}{\partial \delta}} \tag{1.24}$$

Typically, $\partial C_{MAC}/\partial \delta$ is negative, i.e., the aerodynamic moment for positive control surface rotation is nose down. Finally, (1.22) may be written

$$\frac{L}{L_r} = \frac{1 - q/q_R}{1 - q/q_D} \tag{1.25}$$

where q_R is given by (1.24) and q_D by (1.8). It is very interesting to note that when K_δ is finite, the reversal dynamic pressure is still given by (1.24). However, q_D is now the lowest root of the denominator of (1.17). Can you reason physically why this is so?[6]

[6] See, [3], pp. 197–200.

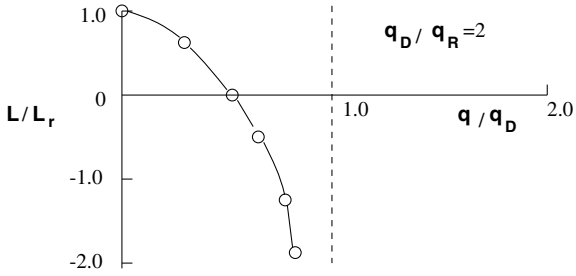

Fig. 5 Lift versus dynamic pressure

A graphical depiction of (1.25) is given in the Fig. 5 where the two cases, $q_D > q_R$ and $q_D < q_R$, are distinguished. In the former case L/L_r, decreases with increasing q and in the latter the opposite is true. Although the graphs are shown for $q > q_D$, our analysis is no longer valid when the divergence condition is exceeded without taking into account nonlinear effects. It is interesting to note that the q_R given by (1.24) is still the correct answer even for finite K_δ. Consider (1.15). For reversal or zero lift, $L = 0$, (1.15) simplifies to

$$q_R S_c \frac{\partial C_{MAC}}{\partial \delta}\delta - K_\alpha \alpha = 0 \tag{1.15\_R}$$

and (1.12) becomes

$$\frac{\partial C_L}{\partial \alpha}\alpha + \frac{\partial C_L}{\partial \delta}\delta = 0 \tag{1.12\_R}$$

Eliminating α, δ from these two equations (or setting the determinant to zero for nontrivial solutions) gives

$$K_\alpha \frac{\partial C_L}{\partial \delta} + \frac{\partial C_L}{\partial \alpha} q_R Sc \frac{\partial C_{MAC}}{\partial \delta} = 0 \tag{1.26}$$

Solving (1.26) for q_R gives (1.24). Note that by this approach an eigenvalue problem has been created. Also note the moment equilibrium about the control surface hinge line does not enter into this calculation. See Appendix B, Chapter 2 for a more conceptually straightforward, but algebraically more tedious approach.

At the generalized reversal condition, when $\alpha_0 \neq 0$, $C_{MAC_0} \neq 0$, the lift due to a *change* in δ is zero, by definition. In mathematical language,

$$\frac{dL}{d\delta} = 0 \ \text{ at } \ q = q_R \tag{1.27}$$

To see how this generalized definition relates to our earlier definition of the reversal condition, consider again the equation for lift and also the equation for overall moment equilibrium of the main wing plus control surface, viz.

$$L = qS\left[\frac{\partial C_L}{\partial \alpha}\alpha + \frac{\partial C_L}{\partial \delta}\delta\right] \tag{1.19}$$

and

$$qScC_{MAC_0} + qSc\frac{\partial C_{MAC}}{\partial \delta}\delta + eqS\left[\frac{\partial C_L}{\partial \alpha}\alpha + \frac{\partial C_L}{\partial \delta}\delta\right] - K_\alpha(\alpha - \alpha_0) = 0 \tag{1.28}$$

From (1.19)

$$\frac{dL}{d\delta} = qS\left[\frac{\partial C_L}{\partial \alpha}\frac{d\alpha}{d\delta} + \frac{\partial C_L}{\partial \delta}\right] \tag{1.29}$$

where $\frac{d\alpha}{d\delta}$ may be calculated from (1.29) as

$$\frac{d\alpha}{d\delta} = \frac{-\left[qSc\frac{\partial C_{MAC}}{\partial \delta} + qSe\frac{\partial C_L}{\partial \delta}\right]}{eqS\frac{\partial C_L}{\partial \delta} - K_\alpha} \tag{1.30}$$

Note that neither C_{MAC_0} nor α_0 appear in (1.30). Moreover when (1.30) is substituted into (1.29) and $dL/d\delta$ is set to zero, the same expression for q_R is obtained as before, (1.24), when reversal was defined as $L = 0$ (for $\alpha_0 = C_{MAC_0} = 0$).

This result may be given a further physical interpretation. Consider a Taylor series expansion for L in terms of δ about the reference condition, $\delta \equiv 0$. Note that $\delta \equiv 0$ corresponds to a wing without any control surface deflection relative to the main wing. Hence the condition $\delta \equiv 0$, may be thought of as a wing *without* any control surface.

The lift at any δ may then be expressed as

$$L(\delta) = L(\delta = 0) + \frac{\partial L}{\partial \delta}\Big|_{\delta=0}\delta + \cdots \tag{1.31}$$

Because a linear model is used, it is clear that higher order terms in this expansion vanish. Moreover, it is clear that $dL/d\delta$ is that same for any δ, cf. (1.29) and (1.30).

Now consider $L(\delta = 0)$. From (1.19)

$$L(\delta = 0) = qS\frac{\partial C_L}{\partial \alpha}\alpha(\delta = 0) \tag{1.32}$$

But from (1.28)

$$\alpha(\delta = 0) = \frac{K_\alpha \alpha_0 + qS_cC_{MAC_0}}{K_\alpha - eqS\frac{\partial C_L}{\partial \alpha}} \tag{1.33}$$

Note that $\alpha(\delta = 0) = 0$ for $\alpha_0 = C_{MAC_0} = 0$. Thus, in this special case, $L(\delta = 0) = 0$, and

$$L(\delta) = \frac{dL}{d\delta}\Big|_{\delta=0}\delta = \frac{dL}{d\delta}\Big|_{any\,\delta}\delta \tag{1.34}$$

and hence

$$L(\delta) = 0 \text{ or } \left.\frac{dL}{d\delta}\right|_{any\delta} \delta = 0 \tag{1.35}$$

are equivalent statements when $\alpha_0 = C_{MAC_0} = 0$.

For $\alpha_0 \neq 0$ and/or $C_{MAC_0} \neq 0$, however, the reversal condition is more meaningfully defined as the condition when the lift due to $\delta \neq 0$ is zero, i.e.

$$\frac{dL}{d\delta} = 0 \text{ at } q = q_R \tag{1.27}$$

In this case, at the reversal condition from (1.32) and (1.33),

$$L(\delta)|_{\text{at reversal}} = L(\delta = 0)|_{\text{at reversal}} = qS\frac{\partial C_L}{\partial \alpha}\left[\frac{\alpha_0 + \frac{qSc}{K_\alpha} C_{MAC_0}}{1 - \frac{eqS\frac{\partial C_L}{\partial \alpha}}{K_\alpha}}\right] \tag{1.36}$$

and hence the lift at reversal per se is indeed not zero in general unless $\alpha_0 = C_{MAC_0} = 0$.

1.2 Typical Section Model—Nonlinear Effects

For sufficiently large twist angles, the assumption of elastic and/or aerodynamic moments proportional to twist angle becomes invalid. Typically the elastic spring becomes stiffer at larger twist angles; for example the elastic moment-twist relation might be

$$M_E = -K_\alpha \alpha_e - K_{\alpha_3} \alpha_e^3$$

where $K_\alpha > 0$, $K_{\alpha_3 > 0}$. The lift angle of attack relation might be

$$L = qS[(\partial C_L/\partial \alpha)\alpha - (\partial C_L/\partial \alpha)_3 \alpha^3]$$

where $\partial C_L/\partial \alpha$ and $(\partial C_L/\partial \alpha)_3$ are positive quantities. Note the lift decreases for a large α due to flow separation from the airfoil. Combining the above in a moment equation of equilibrium and assuming for simplicity that $\alpha_0 = C_{MAC} = 0$, we obtain (recall (1.5))

$$eqS[(\partial C_L/\partial \alpha)\alpha_e - (\partial C_L/\partial \alpha)_3 \alpha_e^3] - [K_\alpha \alpha_e + K_{\alpha_3} \alpha_e^3] = 0$$

Rearranging,

$$\alpha_e[eqS(\partial C_L/\partial \alpha) - K_\alpha] - \alpha_e^3[eqS(\partial C_L/\partial \alpha)_3 + K_{\alpha_3}] = 0$$

Solving, we obtain the trivial solution $\alpha_e \equiv 0$, as well as

$$\alpha_e^2 = \frac{\left[eqS\frac{\partial C_L}{\partial \alpha} - K_\alpha\right]}{\left[eqS(\frac{\partial C_L}{\partial \alpha})_3 + K_{\alpha_3}\right]}$$

To be physically meaningful α_e must be a real number; hence the right hand side of the above equation must be a positive number for the nontrivial solution $\alpha_e \neq 0$ to be possible.

For simplicity let us first assume that $e > 0$. Then we see that only for $q > q_D$ (i.e., for $eqS(\partial C_L/\partial\alpha) > K_\alpha$) are nontrivial solutions possible. See Fig. 6. For $q < q_D$, $\alpha_e \equiv 0$ as a consequence of setting $\alpha_0 \equiv C_{MAC} \equiv 0$. Clearly for $e > 0$, $\alpha_e \neq 0$ when $q > q_D$ where

$$q_D \equiv \frac{K_\alpha}{eS\partial C_L/\partial\alpha}$$

Note that two (symmetrical) equilibrium solutions are possible for $q > q_D$. The actual choice of equilibrium position would depend upon how the airfoil is disturbed (by gusts for example) or possibly upon imperfections in the spring or airfoil geometry. α_0 may be thought of as an initial imperfection and its sign would determine which

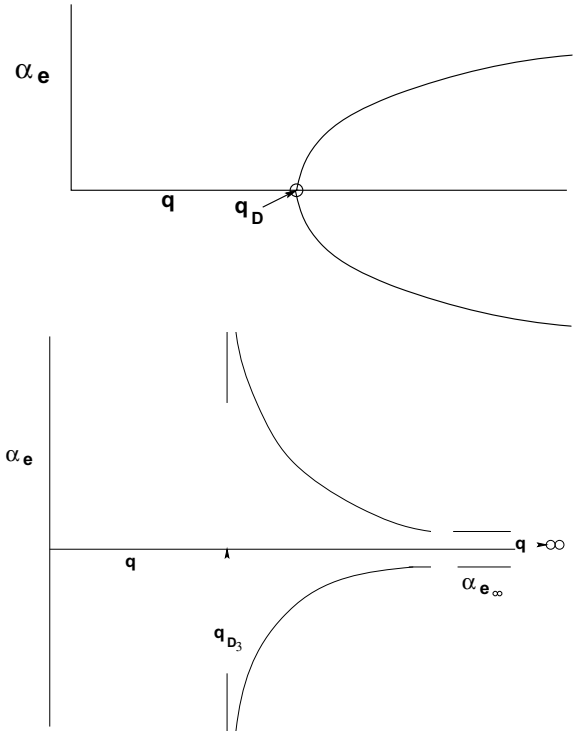

Fig. 6 (Nonlinear) equilibria for elastic twist: $e > 0$. (top) $e < 0$. (bottom)

of the two equilibria positions occurs. Note that for the nonlinear model α_e remains finite for any finite q. For $e < 0$, the equilibrium configurations would be as shown in the Fig. 6 where

$$q_{D_3} = -K_{\alpha_3}/[eS(\partial C_L/\partial\alpha)_3]$$

and

$$\alpha^2_{e_\infty} = \partial C_L/\partial\alpha/(\partial C_L/\partial\alpha)_3$$

As far as the author is aware, the behavior indicated in Fig. 6 has never been observed experimentally. Presumably structural failure would occur for $q > q_D$, even though α_{e_∞} is finite. It would be most interesting to try to achieve the above equilibrium diagram experimentally.

The above discussion does not exhaust the possible types of nonlinear behavior for the typical section model. Perhaps one of the most important nonlinearities in practice is that associated with the control surface spring and the elastic restraint of the control surface connection to the main lifting surface.[7]

2 One Dimensional Aeroelastic Model of Airfoils

2.1 Beam-Rod Representation of Large Aspect Ratio Wing

We shall now turn to a more sophisticated, but more realistic beam-rod model which contains the same basic physical ingredients as the typical section.[8] A beam-rod is here defined as a flat plate with rigid chordwise sections whose span, l, is substantially larger than its chord, c. See Fig. 7. The airflow is in the x direction. The equation of static moment equilibrium for a beam-rod is

$$\frac{d}{dy}\left(GJ\frac{d\alpha_e}{dy}\right) + M_y = 0 \tag{2.1}$$

$\alpha_e(y)$ nose up twist about the elastic axis, e.s., at station y
M_y nose up aerodynamic moment about e.a., per unit distance in the spanwise, y, direction
G shear modulus
J polar moment of inertia ($= ch^3/3$ for a rectangular cross-section of thickness, $h, h \ll c$)
GJ torsional stiffness

[7] Woodcock [4].

[8] See chapter 'Aeroelastic Response of Rotorcraft', BA, pp. 280–295, especially pp. 288–295.

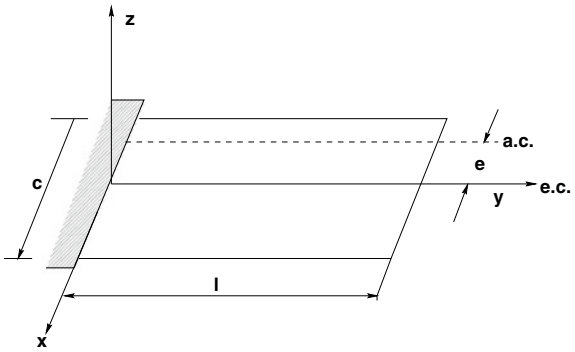

Fig. 7 Beam-rod representation of wing

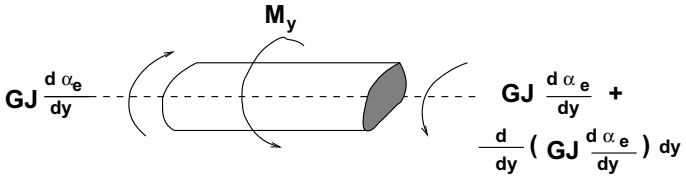

Fig. 8 Differential element of beam-rod

Equation (2.1) can be derived by considering a differential element dy (see Fig. 8) The internal elastic moment is GJ from the theory of elasticity.[9] Note for $d\alpha_e/dy > 0$, $GJ(d\alpha_e/dy)$ is positive nose down. Summing moments on the differential element, we have

$$-GJ\frac{d\alpha_e}{dy} + GJ\frac{d\alpha_e}{dy} + \frac{d}{dy}\left(GJ\frac{d\alpha_e}{dy}\right)dy + H.O.T. + M_y dy = 0$$

In[10] the limit, as $dy \to 0$,

$$\frac{d}{dy}\left(GJ\frac{d\alpha_e}{dy}\right) + M_y = 0 \tag{2.1}$$

Equation (2.1) is a second order differential equation in y. Associated with it are two boundary conditions. The airfoil is fixed at its root and free at its tip, so that the boundary conditions are

$$\alpha_e = 0 \ \text{ at } \ y = 0 \quad GJ\frac{d\alpha_e}{dy} = 0 \ \text{ at } \ y = l \tag{2.2}$$

[9] Housner, and Vreeland [5].

[10] Higher Order Terms.

Turning now to the aerodynamic theory, we shall use the 'strip theory' approximation. That is, *we shall assume that the aerodynamic lift and moment at station y depends only on the angle of attack at station y* (and is independent of the angle of attack at other spanwise locations.) Thus moments and lift per unit span are, as before,

$$M_y = M_{AC} + Le \tag{2.3a}$$

$$L \equiv qcC_L \tag{2.3b}$$

where now the lift and moment coefficients are[11] given by

$$C_L(y) = \frac{\partial C_L}{\partial \alpha}[\alpha_0(y) + \alpha_e(y)] \tag{2.3c}$$

$$M_{AC} = qc^2 c_{MAC} \tag{2.3d}$$

Equations (2.3b) and (2.3d) define C_L and C_{MAC} respectively.

Using (2.3) in (2.1) and nondimensionalizing (assuming for simplicity, constant wing properties)

$$\tilde{y} \equiv \frac{y}{l}$$

$$\lambda^2 \equiv \frac{qcl^2}{GJ}\frac{\partial C_L}{\partial \alpha}e$$

$$K \equiv -\frac{qcl^2}{GJ}\left(e\frac{\partial C_L}{\partial \alpha}\alpha_0 + C_{MAC_0}c\right)$$

Equation (2.1) becomes

$$\frac{d^2\alpha_e}{d\tilde{y}^2} + \lambda^2\alpha_e = K \tag{2.4}$$

which is subject to boundary conditions (2.2). These boundary conditions have the nondimensional form

$$\alpha = 0 \quad \text{at} \quad \tilde{y} = 0 \tag{2.5}$$

[11] A more complete aerodynamic model would allow for the effect of an angle of attack at one spanwise location, say η, on (nondimentional) lift at another, say y. This relation would then be replaced by $C_L(y) = \int A(y-\eta)[\alpha_0(\eta) + \alpha_e(\eta)]d\eta$ where A is an aerodynamic influence function which must be measured or calculated from an appropriate theory. More will be said about this later.

$$\frac{d\alpha_e}{d\tilde{y}} = 0 \quad \text{at} \quad \tilde{y} = 1$$

The general solution to (2.4) is

$$\alpha_e = A \sin \lambda\tilde{y} + B \cos \lambda\tilde{y} + \frac{K}{\lambda^2} \tag{2.6}$$

Applying boundary conditions (2.5), we obtain

$$B + \frac{K}{\lambda^2} = 0, \qquad \lambda[A \cos \lambda - B \sin \lambda] = 0 \tag{2.7}$$

Solving equation (2.7), $A = -(K/\lambda^2) \tan \lambda$, $B = -K/\lambda^2$, so that

$$\alpha_e = \frac{K}{\lambda^2}[1 - \tan \lambda \sin \lambda\tilde{y} - \cos \lambda\tilde{y}] \tag{2.8}$$

Divergence occurs when $\alpha_e \to \infty$, i.e., $\tan \lambda \to \infty$, or $\cos \lambda \to 0$.[12] Thus, for $\lambda = \lambda_m = (2m-1)\frac{\pi}{2} (m = 1, 2, 3, \ldots)$, $\alpha_e \to \infty$. The lowest of these, $\lambda_1 = \frac{\pi}{2}$ is physically significant. Using the definition of λ preceding Eq. (2.4), the divergence dynamic pressure is

$$q = (\pi/2)^2 \frac{GJ}{l} / lce(\partial C_L/\partial\alpha) \tag{2.9}$$

Recognizing that $S = lc$, we see that (2.9) is equivalent to the typical section value, (1.8), with

$$K_\alpha = \left(\frac{\pi}{2}\right)^2 \frac{GJ}{l} \tag{2.10}$$

Consider again (2.8). A further physical interpretation of this result may be helpful. For simplicity, consider the case when $C_{MAC_0} = 0$ and thus $K = -\lambda^2\alpha_0$. Then the expression for α_e, (2.8), may be written as

$$\alpha_e = \alpha_0[-1 + \tan \lambda \sin \lambda\tilde{y} + \cos \lambda\tilde{y}] \tag{2.8a}$$

The tip of twist of $\tilde{y} = 1$ may be used to characterize the variation of α_e with λ, i.e,

$$\alpha_e(\tilde{y} = 1) = \alpha_0 \left[\frac{1}{\cos \lambda} - 1\right] \tag{2.8b}$$

and thus

$$\alpha = \alpha_0 + \alpha_e = \alpha_0/\cos \lambda \tag{2.8c}$$

[12] Note $\lambda \equiv 0$ is not a divergence condition! Expanding (2.8) for $\lambda \ll 1$, we obtain $\alpha_e = \frac{K}{\lambda^2}[1 - \lambda^2\tilde{y} - (1 - \frac{\lambda^2\tilde{y}^2}{2}) + \cdots] \to K[\frac{\tilde{y}^2}{2} - \tilde{y}]$ as $\lambda \to 0$.

From $(2.8)_c$, we see that for low flow speeds or dynamic pressure, $\lambda \to 0$, $\alpha = \alpha_0$. As $\lambda \to \pi/2$, α monotonically increases and $\alpha \to \infty$ as $\lambda \to \pi/2$. For a given wing design, a certain twist might be allowable. From $(2.8)_c$, or its counterpart for more complex physical and mathematical models, the corresponding allowable or design λ may be determined.

Another design allowable might be the allowable structural moment, $T \equiv GJd\alpha_e/dy$. Using (2.8) and the definition of T, for a given allowable T the corresponding allowable λ or q may be determined.

2.2 Eigenvalue and Eigenfunction Approach

One could have treated divergence from the point of view of an eigenvalue problem. Neglecting those terms which do *not* depend on the elastic twist, i.e., setting $\alpha_0 = C_{MAC_0} = 0$, we have $K = 0$ and hence

$$\frac{d^2\alpha}{d\tilde{y}^2} + \lambda^2\alpha = 0 \tag{2.11}$$

with

$$\alpha = 0 \quad \text{at} \quad y = 0$$

$$\frac{d\alpha}{d\tilde{y}} = 0 \quad \text{at} \quad y = 1 \tag{2.12}$$

The general solution is

$$\alpha = A \sin \lambda\tilde{y} + B \cos \lambda\tilde{y} \tag{2.13}$$

Using (2.12) and (2.13)

$$B = 0$$

$$\lambda[A \cos \lambda - B \sin \lambda]$$

we conclude that

$$A = 0$$

or

$$\lambda \cos \lambda = 0 \text{ and } A \neq 0 \tag{2.14}$$

The latter condition, of course, is 'divergence'. Can you show that $\lambda = 0$, does not lead to divergence? What does (2.13) say? For each eigenvalue, $\lambda = \lambda_m = (2m - 1)\frac{\pi}{2}$ there is an eigenfunction,

$$\alpha_m \sim \sin \lambda_m \tilde{y} = \sin (2m-1)\frac{\pi}{2}\tilde{y} \tag{2.15}$$

These eigenfunctions are of interest for a number of reasons:

1. They give us the twist distribution at the divergence dynamic pressure as seen above in (2.15).
2. They may be used to obtain a series expansion of the solution for any dynamic pressure.
3. They are useful for developing an approximate solution for variable property wings.

Let us consider further the second of these. Now we let $\alpha_0 \neq 0$, $C_{MAC_0} \neq 0$ and begin with (2.4)

$$\frac{d^2\alpha_e}{d\tilde{y}} + \lambda^2 \alpha_e = K \tag{2.4}$$

Assume a series solution of the form

$$\alpha_e = \sum_n a_n \alpha_n(\tilde{y}) \tag{2.16}$$

$$K = \sum_n A_n \alpha_n(\tilde{y}) \tag{2.17}$$

where a_n, A_n are to be determined. Now it can be shown that

$$\begin{aligned} \int_0^1 \alpha_n(\tilde{y})\alpha_m(\tilde{y})d\tilde{y} &= \frac{1}{2} \quad \text{for} \quad m = n \\ &= 0 \quad \text{for} \quad m \neg n \end{aligned} \tag{2.18}$$

This is the so-called 'orthogonality condition'. We shall make use of it in what follows. First, let us determine A_n. Multiply (2.17) by α_m and $\int_0^1 \cdots d\tilde{y}$.

$$\int_0^1 K\alpha_m(\tilde{y})d\tilde{y} = \sum_n A_n \int_0^1 \alpha_n(\tilde{y})\alpha_m(\tilde{y})d\tilde{y} = A_m \frac{1}{2}$$

using (2.18). Solving for A_m,

$$A_m = 2\int_0^1 K\alpha_m(\tilde{y})d\tilde{y} \tag{2.19}$$

Now let us determine a_n. Substitute (2.16) and (2.17) into (2.4) to obtain

$$\sum_n \left[a_n \frac{d^2\alpha_n}{d\tilde{y}^2} + \lambda^2 a_n \alpha_n \right] = \sum_n A_n \alpha_n \tag{2.20}$$

Now each eigenfunction, α_n, satisfies (2.11)

$$\frac{d^2\alpha_n}{d\tilde{y}^2} + \lambda_n^2 \alpha_n = 0 \tag{2.11}$$

Therefore, (2.20) may be written

$$\sum_n a_n[-\lambda_n^2 + \lambda^2]\alpha_n = \sum A_n \alpha_n \tag{2.21}$$

Multiplying (2.21) by α_m and $\int_0^1 \cdots d\tilde{y}$,

$$[\lambda^2 - \lambda_m^2] a_m \frac{1}{2} = A_m \frac{1}{2} \qquad \text{(multiplication)}$$

Solving for a_m,

$$a_m = \frac{A_m}{\left[\lambda^2 - \lambda_m^2\right]} \tag{2.22}$$

Thus,

$$\alpha_e = \sum a_n \alpha_n = \sum_n \frac{A_n}{\left[\lambda^2 - \lambda_m^2\right]} \alpha_n(\tilde{y}) \tag{2.23}$$

where A_n is given by (2.19).[13]

Similar calculations can be carried out for airfoils whose stiffness, chord, etc., are *not* constants but vary with spanwise location. One way to do this is to first determine the eigenfunction expansion *for the variable property wing* as done above for the constant property wing. The determination of such eigenfunctions may itself be fairly complicated, however. An alternative procedure can be employed which expands the solution for *the variable property* wing in terms of the eigenfunctions of the *constant property wing*. This is the last of the reasons previously cited for examining the eigenfunctions.

[13] For a more detailed mathematical discussion of the above, see Hildebrand [6], pp. 224–234. This problem is one of a type known as 'Sturm-Liouville Problems'.

2.3 Galerkin's Method

The equation of equilibrium for a *variable* property wing may be obtained by substituting (2.3) into (2.1). In dimensional terms

$$\frac{d}{dy}\left(GJ\frac{d}{dy}\alpha_e\right) + eqc\frac{\partial C_L}{\partial \alpha}\alpha_e = -eqc\frac{\partial C_L}{\partial \alpha}\alpha_0 - qc^2 C_{MAC_0} \tag{2.24}$$

In nondimensional terms

$$\frac{d}{dy}\left(\gamma\frac{d\alpha_e}{d\tilde{y}}\right) + \lambda^2\alpha_e\beta = K \tag{2.25}$$

where

$$\gamma \equiv \frac{GJ}{(GJ)_{ref}} \qquad K = -\frac{qcl^2}{(GJ)_{ref}}\left[e\frac{\partial C_L}{\partial \alpha}\alpha_0 + cC_{MAC_0}\right]$$

$$\lambda^2 \equiv \frac{ql^2 c_{ref}}{(GJ)_{ref}}\left(\frac{\partial C_L}{\partial \alpha}\right)_{ref} e_{ref} \qquad \beta = \frac{c}{c_{ref}}\frac{e}{e_{ref}}\frac{\left(\frac{\partial C_L}{\partial \alpha}\right)}{\left(\frac{\partial C_L}{\partial \alpha}\right)_{ref}}$$

Let

$$\alpha_e = \sum_n a_n \alpha_n(\tilde{y})$$

$$K = \sum_n A_n \alpha_n(\tilde{y})$$

As before. Substituting the series expansions into (2.25), multiplying by α_m and $\int_0^1 \cdots d\tilde{y}$,

$$\sum a_n \left\{\int_0^1 \frac{d}{d\tilde{y}}\left(\gamma\frac{d\alpha_n}{d\tilde{y}}\right)\alpha_m\, d\tilde{y} + \lambda^2\int_0^1 \beta\alpha_n\alpha_m\, d\tilde{y}\right\} =$$
$$\sum_n A_n \int_0^1 \alpha_n\alpha_m\, d\tilde{y} = \frac{A_m}{2} \tag{2.26}$$

The first and second terms cannot be simplified further unless the eigenfunctions or 'modes' employed are eigenfunctions for the variable property wing. Hence, a_n is not as simply related to A_n as in the constant property wing example. Equation (2.26) represents a system of equations for the a_n. In matrix notation

$$[C_{mn}]\{a_n\} = \{A_m\}\frac{1}{2} \tag{2.27}$$

where

$$C_{mn} \equiv \int_0^1 \frac{d}{d\tilde{y}}\left(\gamma\frac{d\alpha_n}{d\tilde{y}}\right)\alpha_m d\tilde{y} + \lambda^2\int_0^1 \beta\alpha_n\alpha_m\, d\tilde{y}$$

By truncating the series to a finite number of terms, we may formally solve for the a_n,

$$\{a_n\} = \frac{1}{2}[C_{mn}]^{-1}\{A_m\} \tag{2.28}$$

The divergence condition is simply that the determinant of C_{mn} vanish (and hence $a_n \to \infty$)

$$|C_{mn}| = 0 \tag{2.29}$$

which is a polynomial in λ^2. It should be emphasized that for an 'exact' solution, (2.27), (2.28) etc., are infinite systems of equations (in an infinite number of unknowns). In practice, some large but finite number of equations is used to obtain an accurate approximation. By systematically increasing the terms in the series, the convergence of the method can be assessed. This procedure is usually referred to as Galerkin's method or as a 'modal' method.[14] The modes, α_n, used are called 'primitive modes' to distinguish them from eigenfunctions, i.e., they are 'primitive functions' for a variable property wing even though they are eigenfunctions for a constant property wing.

3 Rolling of a Straight Wing

We shall now consider a more complex physical and mathematical variation on our earlier static aeroelastic lifting surface (wing) studies. For variety, we treat a new physical situation, the rolling of a wing (rotation about the root axis). Nevertheless, we shall meet again our old friends, 'divergence' and 'control surface effectiveness' or 'reversal'.

The present analysis differs from the previous one as follows:

a integral equation formulation versus differential equation formulation
b aerodynamic induction effects versus 'strip' theory
c 'lumped element' method of solution versus modal (or eigenfunction) solution.

The geometry of the problem is shown in Fig. 9.

[14] Duncan [7].

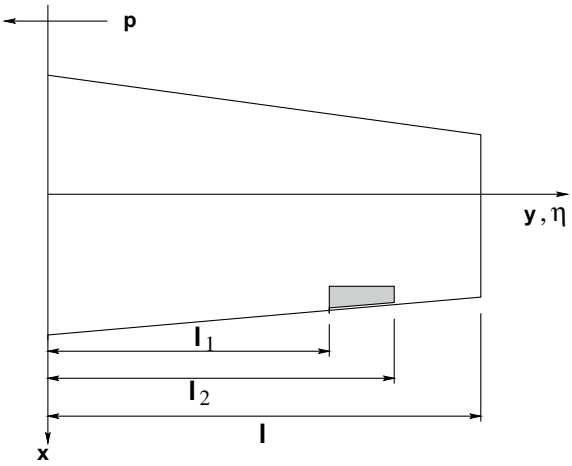

Fig. 9 Rolling of a straight wing

3.1 Integral Equation of Equilibrium

The integral equation of equilibrium is

$$\alpha(y) = \int_0^1 C^{\alpha\alpha}(y, \eta) M_y(\eta) d\eta \tag{3.1}$$

Before[15] deriving the above equation, let us first consider the physical interpretation of $C^{\alpha\alpha}$:

Apply a unit point moment at some point, say $y = \gamma$, i.e.,

$$M_y(\eta) = \delta(\eta - \gamma)$$

Then (3.1) becomes

$$\alpha(y) = \int_0^1 C^{\alpha\alpha}(y, \eta)\delta(\eta - \gamma) d\eta = C^{\alpha\alpha}(y, \gamma) \tag{3.2}$$

Thus $C^{\alpha\alpha}(y, \gamma)$ is the twist a y due to a unit moment at γ, or alternatively, $C^{\alpha\alpha}(y, \eta)$ is the twist at y due to a unit moment at η. $C^{\alpha\alpha}$ is called a *structural influence function*.

Also note that (3.1) states that to obtain the total twist, one multiplies the actual distributed torque, M_y, by $C^{\alpha\alpha}$ and sums (integrates) over the span. This is physically plausible.

[15] For simplicity, $\alpha_0 \equiv 0$ in what follows.

$C^{\alpha\alpha}$ plays a central role in the integral equation formulation.[16] The physical interpretation of $C^{\alpha\alpha}$ suggests a convenient means of measuring $C^{\alpha\alpha}$ in a laboratory experiment. By successively placing unit couples at various locations along the wing and measuring the twists of all such stations for each loading position we can determine $C^{\alpha\alpha}$. This capability for measuring $C^{\alpha\alpha}$ gives the integral equation a preferred place in aeroelastic analysis where $C^{\alpha\alpha}$ and/or GJ are not always easily determinable from purely theoretical considerations.

3.2 Derivation of Equation of Equilibrium

Now consider a derivation of (3.1) taking as our starting point the differential equation of equilibrium. We have, you may recall,

$$\frac{d}{dy}\left(GJ\frac{d\alpha}{dy}\right) = -M_y \tag{3.3}$$

with

$$\alpha(0) = 0 \quad \text{and} \quad \frac{d\alpha}{dy}(l) = 0 \tag{3.4}$$

as boundary conditions.

As a special case of (3.3) and (3.4) we have for a unit torque applied at $y = \eta$,

$$\frac{d}{dy}GJ\frac{dC^{\alpha\alpha}}{dy} = -\delta(y-\eta) \tag{3.5}$$

with

$$C^{\alpha\alpha}(0,\eta) = 0 \quad \text{and} \quad \frac{dC^{\alpha\alpha}}{dy}(l,\eta) = 0 \tag{3.6}$$

Multiply (3.5) by $\alpha(y)$ and integrate over the span,

$$\int_0^1 \alpha(y)\frac{d}{dy}\left(GJ\frac{dC^{\alpha,\alpha}}{dy}\right)dy = -\int_0^1 \delta(y-\eta)\alpha(y)dy = -\alpha(\eta) \tag{3.7}$$

Integrate LHS of (3.7) by parts,

$$\alpha GJ\frac{dC^{\alpha\alpha}}{dy}\Big|_0^1 - GJ\frac{d\alpha}{dy}C^{\alpha\alpha}\Big|_0^1 + \int_0^1 C^{\alpha\alpha}\frac{d}{dy}\left(GJ\frac{d\alpha}{dy}\right)dy = -\alpha(\eta) \tag{3.8}$$

[16] For additional discussion, see the following selected references: Hildebeand [6] pp. 388–394 and BAH, pp. 39–44.

Using boundary conditions (3.4) and (3.6), the first two terms of LHS of (3.8) vanish. Using (3.3) the integral term may be simplified and we obtain,

$$\alpha(\eta) = \int_0^1 C^{\alpha\alpha}(y, \eta) M_y(y) dy \tag{3.9}$$

Interchanging y and η,

$$\alpha(y) = \int_0^1 C^{\alpha\alpha}(\eta, y) M_y(\eta) d\eta \tag{3.10}$$

Equation (3.10) is identical to (1), *if*

$$C^{\alpha\alpha}(\eta, y) = C^{\alpha\alpha}(y, \eta) \tag{3.11}$$

We shall prove (3.11) subsequently.

3.3 Calculation of $C^{\alpha\alpha}$

We shall calculate $C^{\alpha\alpha}$ from (3.5) using (3.6). Integrating (3.5) with respect to y from 0 to y_1,

$$\begin{aligned} GJ(y_1)\frac{dC^{\alpha\alpha}}{dy}(y_1, \eta) - GJ(0)\frac{dC^{\alpha\alpha}}{dy}(0, \eta) \\ = -1 \quad \text{if} \quad y_1 > \eta \\ = 0 \quad \text{if} \quad y_1 < \eta \equiv S(y_1, \eta) \end{aligned} \tag{3.12}$$

3.4 Sketch of Function $S(y_1, \eta)$

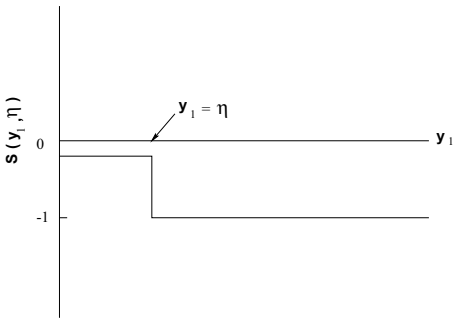

Dividing (3.12) by $GJ\ (y_1)$ and integrating with respect to y_1 from 0 to y_2,

$$C^{\alpha\alpha}(y_2,\ \eta) - C^{\alpha\alpha}(0,\eta) - GJ(0)\frac{dC^{\alpha\alpha}}{dy}(0,\eta)\int_0^{y_2}\frac{1}{GJ}dy_1$$
$$= \int_0^{y_2}\frac{S(y_1,\eta)}{GJ(y_1)}dy_1 = -\int_\eta^{y_2}\frac{1}{GJ(y_1)}dy_1 \quad \text{for} \quad y_2 > \eta$$
$$= 0 \qquad \text{for} \qquad y_2 < \eta \tag{3.13}$$

From boundary conditions, (3.6),

$$\text{(a)} \quad C^{\alpha\alpha}(0,\eta) = 0$$

$$\text{(b)} \quad \frac{dC^{\alpha\alpha}}{dy}(l,\eta) = 0$$

These may be used to evaluate the unknown terms in (3.12) and (3.13). Evaluating (3.12) at $y_1 = l$

$$\text{(c)}\ GJ(l)\underbrace{\frac{dC^{\alpha\alpha}}{dy}}_{\to 0}(l,\eta) - GJ\frac{dC^{\alpha\alpha}}{dy}(0,\eta) = -1$$

Using (a) and (c), (3.13) may be written,

$$C^{\alpha\alpha}(y_2,\eta) = \int_0^{y_2}\frac{1}{GJ}dy_1 - \int_\eta^{y_2}\frac{1}{GJ}dy_1$$

$$= \int_0^{\eta}\frac{1}{GJ}dy_1 \qquad \text{for} \qquad y_2 > \eta$$

$$= \int_0^{y_2}\frac{1}{GJ}dy_1 \qquad \text{for} \qquad y_2 < \eta$$

One may drop the dummy subscript on y_2, of course. Thus

$$C^{\alpha\alpha}\ (y,\eta) = \int_0^{y}\frac{1}{GJ}dy_1 \quad \text{for} \quad y < \eta$$

$$= \int_0^{\eta}\frac{1}{GJ}dy_1 \quad \text{for} \quad y > \eta \tag{3.14}$$

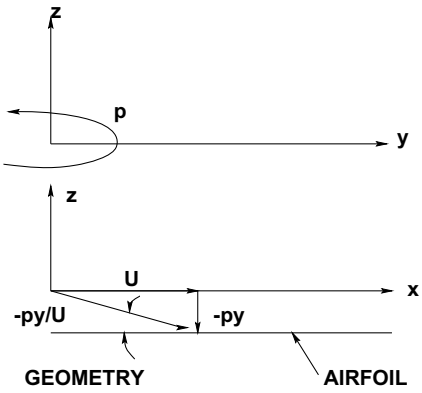

Fig. 10 Coordinate system and velocity diagram

Note from the above result we may conclude by interchanging y and η that

$$C^{\alpha\alpha}(y,\eta) = C^{\alpha\alpha}(\eta, y)$$

This is a particular example of a more general principle known as Maxwell's Reciprocity Theorem[17] which says that all structural influence functions for linear elastic bodies are symmetric in their arguments. In the case of $C^{\alpha\alpha}$ these are y and η, of course.

3.5 Aerodynamic Forces (Including Spanwise Induction)

First, let us identify the aerodynamic angle of attack; i.e., the angle between the airfoil chord and relative airflow. See Fig. 10. Hence, the total angle of attack due to twisting and rolling is

$$\alpha_{Total} = \alpha(y) - \frac{py}{U}$$

The control surface will be assumed rigid and its rotation is given by

$$\delta(y) = \delta_R \quad \text{for} \quad l_1 < y < l_2 = 0 \quad \text{otherwise}$$

From aerodynamic theory or experiment

$$C_L \equiv \frac{L}{qc} = \int_0^1 A^{L\alpha}(y,\eta)\alpha_T(\eta)\frac{d\eta}{l} + \int_0^1 A^{L\delta}(y,\eta)\delta(\eta)\frac{d\eta}{l} \tag{3.15}$$

[17] Bisplinghoff, Mar, and Pian [8], p. 247.

Here $A^{L\alpha}$, $A^{L\delta}$ are aerodynamic influence functions; as written, they are nondimensional. Thus, $A^{L\delta}$ is nondimensional lift at y due to unit angle of attack at η. Substituting for α_T and δ, (3.15) becomes,

$$C_L = \int_0^1 A^{L\alpha}\alpha\frac{d\eta}{l} - \frac{pl}{U}\int_0^1 A^{L\alpha}\frac{\eta}{l}\frac{d\eta}{l} + \delta_R\int_{l_1}^{l_2} A^{L\delta}\frac{d\eta}{l}$$

$$C_L = \int_0^1 A^{L\alpha}\alpha\frac{d\eta}{l} + \frac{pl}{U}\frac{\partial C_L}{\partial\left(\frac{pl}{U}\right)} + \delta_R\frac{\partial C_L}{\partial\delta_R} \tag{3.16}$$

where

$$\frac{\partial C_L}{\partial\left(\frac{pl}{U}\right)}(y) \equiv -\int_0^1 A^{L\alpha}\frac{\eta}{l}\frac{d\eta}{l}$$

and

$$\frac{\partial C_L}{\partial\delta_R}(y) \equiv \int_{l_1}^{l_2} A^{L\delta}\frac{d\eta}{l}$$

Physical Interpretation of $A^{L\alpha}$ and $A^{L\delta}$:$A^{L\alpha}$ is the lift coefficient at y due to unit angle of attack at n. $A^{L\delta}$ is the lift coefficient at y due to unit rotation of control surface at η.

Physical Interpretation of $\partial C_L/\partial\ (pl/U)$ and $\partial C_L/\partial\delta_R$:$\partial C_L/\partial\ (pl/U)$ is the lift coefficient at y due to unit rolling velocity, pl/U. $\partial C_L/\partial\delta_R$ is the lift coefficient at y due to unit control surface rotation, δ_R.

As usual

$$C_{MAC} \equiv \frac{M_{AC}}{qc^2} = \frac{\partial C_{MAC}}{\partial\delta_R}\delta_R \tag{3.17}$$

is the aerodynamic coefficient moment (about a.c.) at y due to control surface rotation. Note

$$\partial C_{MAC}/\partial\alpha_T \equiv 0$$

by definition of the aerodynamic center. Finally the total moment loading about the elastic axis is

$$M_y = M_{AC} + Le = qc[C_{MAC}c + C_L e] \tag{3.18}$$

Using (3.16) and (3.17), the above becomes

$$M_y = qc\left[c\frac{\partial C_{MAC}}{\partial \delta_R}\delta_R + e\left\{\int_0^1 A^{L\delta}\alpha\frac{d\eta}{l} + \frac{\partial C_L}{\partial\left(\frac{pl}{l}\right)}\left(\frac{pl}{U}\right) + \frac{\partial C_L}{\partial \delta_R}\delta_R\right\}\right] \tag{3.19}$$

Note that $A^{L\alpha}$, $A^{L\delta}$ are more difficult to measure than their structural counterpart, $C^{\alpha\alpha}$. One requires an experimental model to which one can apply unit angles of attack at various discrete points along the span of the wing. This requires a rather sophisticated model and also introduces experimental difficulties in establishing and maintaining a smooth flow over the airfoil. Conversely

$$\frac{\partial C_L}{\partial \frac{pl}{U}}, \frac{\partial C_L}{\partial \delta_R} \quad \text{and} \quad \frac{\partial C_{MAC}}{\partial \delta_R}$$

are relatively easy to measure since they only require a rolling or control surface rotation of a *rigid wing with the same geometry* as the flexible airfoil of interest.

3.6 Aeroelastic Equations of Equilibrium and Lumped Element Solution Method

The key relations are (3.1) and (3.19). The former describes the twist due to an aerodynamic moment load, the latter the aerodynamic moment due to twist as well as rolling and control surface rotation.

By substituting (3.19) into (3.1), one could obtain a single equation for α. However, this equation is not easily solved analytically except for some simple cases, which are more readily handled by the differential equation approach. Hence, we seek an approximate solution technique. Perhaps the most obvious and convenient method is to approximate the integrals in (3.1) and (3.19) by sums, i.e., the wing is broken into various spanwise segments or 'lumped elements'. For example, (3.1) would be approximated as:

$$\alpha\,(y_i) \cong \sum_{i=1}^{N} C^{\alpha\alpha}\,(y_i, \eta_j) M_y\,(\eta_j)\Delta\eta \quad i = 1, \ldots, N \tag{3.20}$$

where $\Delta\eta$ is the segment width and N the total number of segments. Similarly, (3.19) may be written

$$M_y(y_i) \cong qc\left\{\left[c\frac{\partial C_{MAC}}{\partial \delta_R} + e\frac{\partial C_L}{\partial \frac{pl}{U}}\frac{pl}{U} + e\frac{\partial C_L}{\partial \delta_R}\delta_R\right] + e\sum_{j=1}^{N} A^{L\alpha}(y_i, \eta_j)\alpha(\eta_j)\frac{\Delta\eta}{l}\right\} \quad i = 1, \ldots, N \tag{3.21}$$

To further manipulate (3.20) and (3.21), it is convenient to use matrix notation. That is,

$$\{\alpha\} = \Delta\eta[C^{\alpha\alpha}]\{M_y\} \tag{3.20}$$

and

$$\{M_y\} = q\begin{bmatrix}\backslash\\ c^2\\ \backslash\end{bmatrix}\left\{\frac{\partial C_M AC}{\partial\delta_R}\right\}\delta_R + q\begin{bmatrix}\backslash\\ ce\\ \backslash\end{bmatrix}\left\{\frac{\partial C_L}{\partial\frac{pl}{U}}\right\}\frac{pl}{U}$$

$$+ q\begin{bmatrix}\backslash\\ ce\\ \backslash\end{bmatrix}\left\{\frac{\partial C_L}{\partial\delta_R}\right\}\delta_R + q\begin{bmatrix}\backslash\\ ce\\ \backslash\end{bmatrix}[A^{L\alpha}]\{\alpha\}\frac{\Delta\eta}{l} \tag{3.21a}$$

All full matrices are of order $N \times N$ and row or column matrices of order N.. Substituting (3.21) into (3.20), and rearranging terms gives,

$$\left[\begin{bmatrix}\backslash\\ 1\\ \backslash\end{bmatrix} - q\frac{(\Delta\eta)^2}{l}[E][A^{L\alpha}]\right]\{\alpha\} = \{f\} \tag{3.23}$$

where the following definitions apply

$$\{f\} \equiv q[E]\left[\left\{\frac{\partial C_L}{\partial\delta_R}\right\}\delta_R + \left\{\frac{\partial C_L}{\partial\left(\frac{pl}{U}\right)}\right\}\frac{pl}{U}\right]\Delta\eta$$

$$+q[F]\left\{\frac{\partial C_{MAC}}{\partial\delta_R}\right\}\delta_R\ \Delta\eta$$

$$[E] \equiv [C^{\alpha\,\alpha}]\begin{bmatrix}\backslash\\ ce\\ \backslash\end{bmatrix}$$

$$[F] \equiv [C^{\alpha\,\alpha}]\begin{bmatrix}\backslash\\ c^2\\ \backslash\end{bmatrix}$$

Further defining

$$[D] \equiv \begin{bmatrix}\backslash\\ 1\\ \backslash\end{bmatrix} - q\frac{(\Delta\eta)^2}{l}[E][A^{L\alpha}]$$

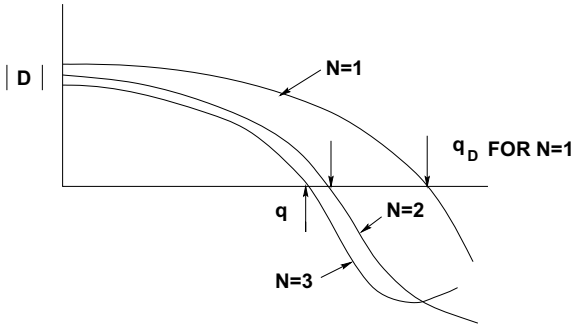

Fig. 11 Characteristic determinant versus dynamic pressure

we may formally solve (3.23) as

$$\{\alpha\} = [D]^{-1}\{f\} \tag{3.24}$$

Now let us interpret this solution.

3.7 Divergence

Recall that the inverse does not exist if

$$| D | = 0 \tag{3.25}$$

and hence,

$$\{\alpha\} \rightarrow \{\infty\}$$

Equation (3.25) gives rise to an eigenvalue problem for the divergence dynamic pressure, q_D. Note (3.25) is a polynomial in q.

The lowest possible root (eigenvalue) of (3.25) gives the q of physical interest, i.e.,$q_{\text{Divergence}}$. Rather than seeking the roots of the polynomial we might more simply plot $|D|$ versus q to determine the values of dynamic pressure for which the determinant is zero. A schematic of such results for various choices of N is shown below in Fig. 11. From the above results we may plot q_D (the lowest positive q for which $|D| = 0$) versus N as shown below in Fig. 12. The 'exact' value of q_D is obtained at $N \rightarrow \infty$. Usually reasonably accurate results can be obtained for small values of N, say 10 or so. The divergence speed calculated above does not depend upon the rolling of the wing, i.e.,p is considered prescribed, e.g., $p = 0$.

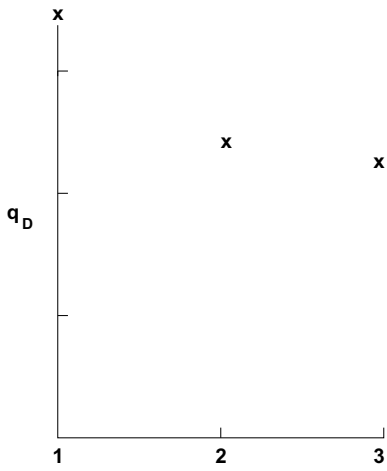

Fig. 12 Convergence of divergence dynamic pressure with modal number

3.8 Reversal and Rolling Effectiveness

In the above we have taken pl/U as known; however,in reality it is a function of δ_R and the problem parameters through the requirement that the wing be in static rolling equilibrium, i.e., it is an additional degree of freedom. For rolling equilibrium at a steady roll rate, p, the rolling moment about the x-axis is zero.

$$M_{\text{Rolling}} \equiv 2\int_0^1 Ly dy = 0 \tag{3.26}$$

Approximating (3.26),

$$\sum_i L_i y_i \Delta y = 0 \tag{3.27}$$

or, in matrix notation,

$$2\lfloor y \rfloor \{L\} \Delta y = 0 \tag{3.28}$$

or

$$2q\lfloor cy \rfloor \{C_L\} \Delta y = 0$$

From (3.16), using the 'lumped element' approximation and matrix notation,

$$\{C_L\} = \frac{\Delta\eta}{l}[A^{L\alpha}]\{\alpha\} + \left\{\frac{\partial C_L}{\partial \delta_R}\right\}\delta_R + \left\{\frac{\partial C_L}{\partial\left(\frac{pl}{U}\right)}\right\}\frac{pl}{U} \tag{3.16}$$

Substitution of (3.16) into (3.28) gives

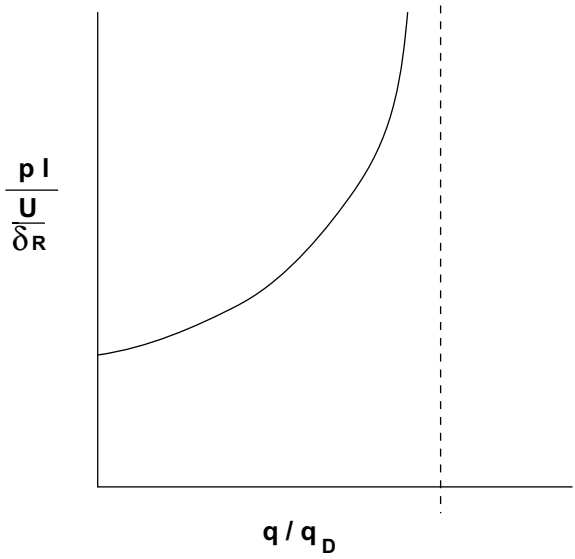

Fig. 13 Roll rate versus dynamic pressure

$$\lfloor cy \rfloor \left\{ \frac{\Delta\eta}{l}[A^{L\alpha}]\{\alpha\} + \left\{\frac{\partial C_L}{\partial \delta_R}\right\}\delta_R + \left\{\frac{\partial C_L}{\partial\left(\frac{pl}{U}\right)}\right\}\frac{pl}{U}\right\} = 0 \tag{3.29}$$

Note that (3.29) is a single algebraic equation. Equation (3.29) plus (3.20) and (3.21) are $2N + 1$ linear algebraic equations in the $N(\alpha)$ plus $N(M_y)$ plus $1(p)$ unknowns. As before $\{M_y\}$ is normally eliminated using (3.21) in (3.20) to obtain N, Eq. (3.22), plus 1, Eq. (3.29), equations in $N(\alpha)$ plus $1(p)$ unknowns. In either case the divergence condition my be determined by setting the determinant of coefficients to zero and determining the smallest positive eigenvalue, $q = q_D$.

For $q < q_D$, pl/U (and α) may be determined from (3.23) and (3.29). Since our mathematical model is linear

$$pl/U \sim \delta_R$$

and hence a convenient plot of the results is as shown in Fig. 13. As

$$q \to q_D, \frac{pl}{U}(\text{and}\{\alpha\}) \to \infty$$

Another qualitatively different type of result may sometimes occur. See Fig. 14. If

$$\frac{pl}{U/\delta_R} \to 0 \quad \text{for} \quad q \to q_R < q_D$$

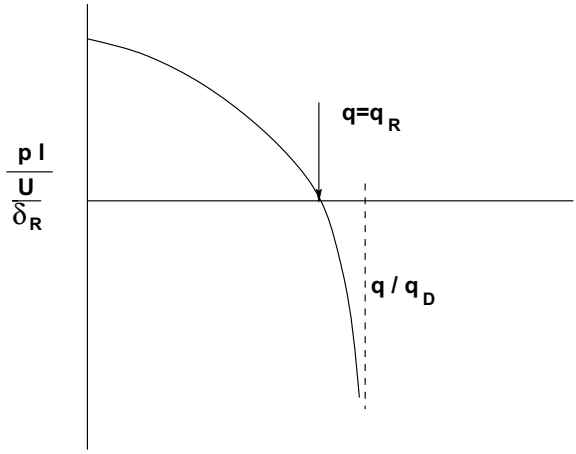

Fig. 14 Roll rate versus dynamic pressure

then 'rolling reversal' is said to have occurred and the corresponding $q = q_R$ is called the 'reversal dynamic pressure'. The basic phenomenon is the same as that encountered previously as 'control surface reversal'. Figures 13 and 14 should be compared to Fig. 5a, b.

It is worth emphasizing that the divergence condition obtained above by permitting p to be determined by (static) rolling equilibrium will be different from that obtained previously by assuming $p = 0$. The latter physically corresponds to an aircraft constrained not to roll, as might be the case for some wind tunnel models. The former corresponds to a model or aircraft completely free to roll.[18]

The above analysis has introduced the simple yet powerful idea of structural and aerodynamic influence functions. While the utility of the concept has been illustrated for a one-dimensional aeroelastic model, not the least advantage of such an approach is the conceptual ease with which the basic notion can be extended to two-dimensional models, e.g., plate-like structures, or even three-dimensional ones (though the latter is rarely needed for aeroelastic problems).

In a subsequent section we briefly outline the generalization to two-dimensional models. Later this subject will be considered in more depth in the context of dynamic aeroelasticity.

3.9 Integral Equation Eigenvalue Problem and the Experimental Determination of Influence Functions

For the special case of a constant section wing with 'strip theory' aerodynamics one may formulate a standard integral equation eigenvalue problem for the determination

[18] This distinction between the two ways in which the aircraft may be restrained received renewed emphasis in the context of the oblique wing concept. Weisshaar and Ashley [9].

of divergence. In itself this problem is of little interest. However, it does lead to some interesting results with respect to the determination of the structural and aerodynamic influence functions by experimental means.

For such a wing,

$$M_y = Le + M_{AC} = eqc\frac{\partial C_L}{\partial \alpha}\alpha + \cdots$$

where the omitted terms are independent of twist and may therefore be ignored for the divergence (eigenvalue) problem. Also the coefficients of α may be taken as constants for a constant section wing. Substituting the above expression into the integral equation of structural equilibrium we have

$$\alpha(y) = eqc\frac{\partial C_L}{\partial \alpha}\int_0^1 C^{\alpha\alpha}(y,\eta)\alpha(\eta)d\eta$$

This is an eigenvalue problem in integral form where the eigenvalue is

$$\lambda \equiv eqc\frac{\partial C_L}{\partial \alpha}$$

One may solve this problem for the corresponding eigenvalues and eigenfunctions which satisfy the equation

$$\alpha_n(y) = \lambda_n \int_0^1 C^{\alpha\alpha}(y,\eta)\alpha_n(\eta)d\eta$$

Incidentally, the restriction to a constant section wing was unnecessary and with a moderate amount of effort one could even use a more sophisticated aerodynamic model. Such complications are not warranted here.

These eigenfunctions or similar functions may be usefully employed to determine by experimental means the structural, $C^{\alpha\alpha}$, and aerodynamic, $A^{l\alpha}$, influence functions. The former is not as attractive as the use of point unit structural loads as we shall see; however, the procedure outlined below for the determination of $A^{L\alpha}$ probably deserves more attention than it has previously received.

Assume the structural influence function can be expanded in terms of the eigenfunctions

$$C^{\alpha\alpha}(y,\eta) = \sum_n C_n(y)\alpha_n(\eta) \tag{3.30}$$

where the C_n are to be determined. Also recall that

$$\alpha_n(y) = \lambda_n \int_0^1 C^{\alpha\alpha}(y,\eta)\alpha_n(\eta)d\eta \tag{3.31}$$

and the α_n are the eigenfunctions and λ_n the eigenvalues of $C^{\alpha\alpha}$ satisfying (3.31) and an orthogonality condition

$$\int \alpha_n \alpha_m dy = 0 \quad \text{for} \quad m \neq \eta$$

Then multiply (3.30) by $\alpha_m(\eta)$ and integrate over the span of the wing; the result is

$$C_m(y) = \frac{\int_0^1 C^{\alpha\alpha}(y,\eta)\alpha_m(\eta)d\eta}{\int_0^1 \alpha_m^2(\eta)d\eta}$$

and from (3.31)

$$C_m cyl = \frac{\alpha_m(y)}{\lambda_m \int_0^1 \alpha_m^2(\eta)d\eta} \tag{3.32}$$

Hence (3.32) in (3.30) gives

$$C^{\alpha\alpha}(y,\eta) = \sum_n \frac{\alpha_n(y)\alpha_n(\eta)}{\lambda_n \int_0^1 \alpha_n^2(\eta)d\eta} \tag{3.33}$$

Thus if the eigenfunctions are known then the Green's function is readily determined from (3.33). Normally this holds no special advantage since the determination of the α_n, theoretically or experimentally, is at least as difficult as determining the Green's function, $C^{\alpha\alpha}$, directly. Indeed as discussed previously if we apply unit moments at various points along the span the resulting twist distribution is a direct measure of $C^{\alpha\alpha}$. A somewhat less direct way of measuring $C^{\alpha\alpha}$ is also possible which makes use of the expansion of the Green's (influence) function. Again using (3.30)

$$C^{\alpha\alpha}(y,\eta) = \sum_n C_n \alpha_n(\eta) \tag{3.29}$$

and assuming the α_n are orthogonal (although not necessarily eigenfunctions of the problem at hand) we have

$$C_n(y) = \frac{\int_0^1 C^{\alpha\alpha}(y,\eta)\alpha_n(\eta)d\eta}{\int_0^1 \alpha_n^2(\eta)d\eta} \tag{3.34}$$

Now we have the relation between twist and moment

$$\alpha(y) = \int_0^1 C^{\alpha\alpha}(y,\eta)M_y(\eta)d\eta \tag{3.35}$$

Clearly if we use a moment distribution

$$M_y(\eta) = \alpha_n(\eta)$$

the resulting twist distribution will be (from (3.34))

$$\alpha(y) = C_n(y) \int_0^1 \alpha_n^2(\eta) d\eta \tag{3.36}$$

Hence we may determine the expansion of the Green's function by successively applying moment distribution in the form of the expansion functions and measuring the resultant twist distribution. For the structural influence function this offers no advantage in practice since it is easier to apply point moments rather than moment distributions.

However, for the aerodynamic Green's functions the situation is different. In the latter case we are applying a certain twist to the wing and measuring the resulting aerodynamic moment distribution. It is generally desirable to maintain a smooth (if twisted) aerodynamic surface to avoid complications of flow separation and roughness and hence the application of a point twist distribution is less desirable than a distributed one. We quickly summarize the key relations for determining the aerodynamic influence function. Assume

$$A^{L\alpha}(y, \eta) = \sum_n A_n^{L\alpha}(y) \alpha_n(\eta) \tag{3.37}$$

We know that

$$C_L(y) = \int_0^1 A^{L\alpha}(y, \eta) \alpha(\eta) d\eta \tag{3.38}$$

For orthogonal functions, α_n we determine from (3.37) that

$$A_n^{L\alpha}(y) = \frac{\int_0^1 A^{L\alpha}(y, \eta) \alpha_n d\eta}{\int_0^1 \alpha_n^2(\eta) d\eta} \tag{3.39}$$

Applying the twist distribution $\alpha = \alpha_n(\eta)$ to the wing, we see from (3.38) and (3.39) that the resulting lift distribution is

$$C_L(y) = A_n^{L\alpha}(y) \int_0^1 \alpha_n^2(\eta) d\eta \tag{3.40}$$

Hence by measuring the lift distributions on 'warped wings' with twist distributions $\alpha_n(\eta)$ we may completely determine the aerodynamic influence function in terms of its expansion (3.37). This technique or a similar one has been used occasionally,[19] but not as frequently as one might expect, possibly because of the cost and expense of testing the number of wings sufficient to establish the convergence of the series.

[19] Covert [10].

In this regard, if one uses the α_n for a Galerkin or modal expansion solution for the complete aeroelastic problem one can show that the number of C_n, $A_n^{L\alpha}$ required is equal to the number of modes, α_n, employed in the twist expansion.

4 Two Dimensional Aeroelastic Model of Lifting Surfaces

We consider in turn, structural modeling, aerodynamic modeling, the combining of the two into an aeroelastic model, and its solution.

4.1 Two Dimensional Structures—Integral Representation

The two dimensional or plate analog to the one-dimensional or beam-rod model is

$$w(x, y) = \iint C^{wp}(x, y; \xi, \eta) p(\xi, \eta) d\xi \, d\eta \tag{4.1}$$

where

w vertical deflection at a point, x, y, on plate
p force/area (pressure) at point ξ, η on plate
C^{wp} deflection at x, y due to unit pressure at ξ, η

Note that w and p are taken as positive in the same direction. For the special case where

$$w(x, y) = h(y) + x\alpha(y) \tag{4.2}$$

and

$$C^{wp}(x, y; \xi, \eta) = C^{hF}(y, \eta) + xC^{\alpha F}(y, \eta) + \xi C^{hM}(y, \eta) + x\xi C^{\alpha M}(y, \eta) \tag{4.3}$$

with the definitions

C^{hF} is the deflection of y axis at y due to unit force F
$C^{\alpha F}$ is the twist about the y axis at y due to unit force F, etc.,

we may retrieve our beam-rod result. Note that (4.2) and (4.3) may be thought of as polynomial (Taylor Series) expansions of deflections.

Substituting (4.2), (4.3) into (4.1), we have

$$h(y) + x\alpha(y) = \left[\int C^{hF} \left(\int p(\xi, \eta) d\xi \right) d\eta + \int C^{hM} \left(\int \xi p(\xi, \eta) d\xi \right) d\eta \right]$$

$$+x\left[\int C^{\alpha F}\left(\int p(\xi,\eta)d\xi\right)d\eta + \int C^{\alpha M}\left(\int \xi p(\xi,\eta)d\xi\right)d\eta\right] \tag{4.4}$$

If y, η lie along an elastic axis, then $C^{hM} = C^{\alpha F} = 0$. Equating coefficients of like powers of x, we obtain

$$h(y) = \int C^{hF}(y,\eta)F(\eta)\,d\eta \tag{4.5}$$

$$\alpha(y) = \int C^{\alpha M}(y,\eta)M(\eta)\,d\eta \tag{4.6}$$

where

$$F \equiv \int p\,d\xi, \quad M \equiv \int p\xi\,d\xi$$

Equation (4.6) is our previous result. Since for static aeroelastic problems, M is only a function of α (and not of h), (4.6) may be solved independently of (4.5). Subsequently (4.6) may be solved to determine h if desired. Equation (4.5) has no effect on divergence or control surface reversal, of course, and hence we were justified in neglecting it in our previous discussion.

4.2 Two Dimensional Aerodynamic Surfaces—Integral Representation

In a similar manner (for simplicity we only include deformation dependent aerodynamic forces to illustrate the method),

$$\frac{p(x,y)}{q} = \iint A^{pw_x}(x,y;\xi,\eta)\frac{\partial w}{\partial \xi}(\xi,\eta)\frac{d\xi}{c_r}\frac{d\eta}{l} \tag{4.7}$$

where

A^{pw_x} nondimensional aerodynamic pressure at x, y due to unit $\partial w/\partial\xi$ at point ξ, n
c_r reference chord, l reference span

For the special case

$$w = h + x\alpha$$

and, hence,

$$\frac{\partial w}{\partial x} = \alpha$$

we may retrieve our beam-rod aerodynamic result.

For example, we may compute the lift as

$$L \equiv \int p dx = q c_r \int_0^1 A^{L\alpha}(y, \eta)\alpha(\eta)\frac{d\eta}{l} \tag{4.8}$$

where

$$A^{L\alpha} \equiv \iint A^{pw_x}(x, y; \xi, \eta)\frac{d\xi}{c_R}\frac{dx}{c_r}$$

4.3 Solution by Matrix-Lumped Element Approach

Approximating the integrals by sums and using matrix notation, (4.1) becomes

$$\{w\} = \Delta\xi\Delta\eta[C^{wp}]\{p\} \tag{4.9}$$

and (4.7) becomes

$$\{p\} = q\frac{\Delta\xi}{c_r}\frac{\Delta\eta}{l}[A^{pw_x}]\left(\frac{\partial w}{\partial \xi}\right) \tag{4.10}$$

Now

$$\left(\frac{\partial w}{\partial \xi}\right) \cong \frac{w_{i-1} - w_{i-1}}{2\Delta\xi}$$

is a difference representation of the surface slope. Hence

$$\left(\frac{\partial w}{\partial \xi}\right) = \frac{1}{2\Delta\xi}[W]\{w\} = \frac{1}{2\Delta\xi}\begin{bmatrix} [W] & [0] & [0] & [0] \\ & [W] & [0] & [0] \\ & & [W] & [0] \\ & & & [W] \end{bmatrix}\{w\} \tag{4.11}$$

is the[20] result shown for *four* spanwise locations, where

[20] For definiteness consider a rectangular wing divided up into small (rectangular) finite difference boxes. The weighting matrix[(W)] is for a given spanwise location and various chordwise boxes. The elements in the matrices, $\{\partial w/\partial\xi\}$ and $\{w\}$, are ordered according to fixed spanwise location and then over all chordwise locations. This numerical scheme is only illustrative and not necessarily that which one might choose to use in practice.

$$[W] = \underbrace{\begin{bmatrix} 0 & 1 & 0 & 0 & \cdot \\ -1 & 0 & 1 & 0 & \cdot \\ 0 & -1 & 0 & 1 & \cdot \\ & & \cdots & & \\ \cdots & 0 & 0 & -1 & 0 \end{bmatrix}}_{number\ of\ chordwise\ location} \tag{4.12}$$

is a numerical weighting matrix. From (4.9), (4.10), (4.11), we obtain an equation for w,

$$[D]\{w\} \equiv \left[\begin{bmatrix} \backslash \\ 1 \\ \backslash \end{bmatrix} - q \frac{(\Delta\xi)^2}{c_r} \frac{(\Delta\eta)^2}{l} \frac{1}{2\Delta\xi} [C^{wp}][A^{pw_x}][W] \right] \{w\} = \{0\} \tag{4.13}$$

For divergence

$$|D| = 0$$

which permits the determination of q_D.

5 Other Physical Phenomena

5.1 *Fluid Flow Through A Flexible Pipe*

Another static aeroelastic configuration exhibiting divergence is a long slender pipe with a flowing fluid.[21] See Fig. 15. We shall assume the fluid is incompressible and has no significant variation across the cross-section of the pipe. Thus, the aerodynamic loading per unit length along the pipe is (invoking the concept of an equivalent fluid added mass moving with the pipe and including the effect of convection velocity[22] U),

$$-L = \rho A \left[\frac{\partial}{\partial t} + U \frac{\partial}{\partial x} \right]^2 w = \rho A \left[\frac{\partial^2 w}{\partial t^2} + 2U \frac{\partial^2 w}{\partial x \partial t} + U^2 \frac{\partial^2 w}{\partial x^2} \right] \tag{5.1}$$

where

$A \equiv \pi R^2$ open area for circular pipe
ρ, U fluid density, axial velocity
w transverse deflection of the pipe

[21] Housner [11].
[22] See Sect. 4.

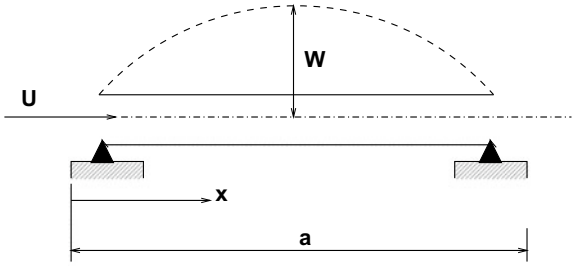

Fig. 15 Fluid flow through a flexible pipe

x axial coordinate
t time

The equation of motion for the beam-like slender pipe is

$$EI\frac{\partial^4 w}{\partial x^4} + m_p\frac{\partial^2 w}{\partial t^2} = L \tag{5.2}$$

where

$m_p \equiv \rho_p 2\pi Rh$ for a thin hollow circular pipe of thickness h, mass per unit length
EI beam bending stiffness

Both static and dynamic aeroelastic phenomena are possible for this physical model but for the moment we shall only consider the former. Further we shall consider for simplicity simply supported or pinned boundary conditions, i.e.,

$$w = 0$$

and

$$M \equiv EI\frac{\partial^2 w}{\partial x^2} = 0 \quad \text{at} \quad x = 0, a \tag{5.3}$$

where M is the elastic bending moment and a, the pipe length.

Substituting (5.1) into (5.2) and dropping the time derivatives consistent with limiting our concern to static phenomena, we have

$$EI\frac{\partial^4 w}{\partial x^4} + \rho AU^2\frac{\partial^2 w}{\partial x^2} = 0 \tag{5.4}$$

subject to boundary conditions

$$w = \frac{\partial^2 w}{\partial x^2} = 0 \quad \text{at} \quad x = 0, a \tag{5.5}$$

The above equations can be recognized as the same as those governing the buckling of a beam under a compressive load of magnitude,[23] P. The equivalence is

$$P = \rho U^2 A$$

Formally we may compute the buckling or divergence dynamic pressure by assuming[24]

$$w = \sum_{i=1}^{4} A_i e^{p_i x}$$

where the p_i are the four roots of the characteristic equation associated with (5.4),

$$EIp^4 + \rho U^2 A p^2 = 0$$

Thus

$$p_{1,2} = 0$$

$$p_3,\, p_4 = \pm i \left(\frac{\rho U^2 A}{EI} \right)^{\frac{1}{2}}$$

and

$$w = A_1 + A_2 x + A_3 \sin \frac{\lambda x}{a} + A_4 \cos \frac{\lambda x}{a} \tag{5.6}$$

where

$$\lambda^2 \equiv \left(\frac{\rho U^2 A}{EI} \right) a^2$$

Using the boundary conditions (5.5) with (5.6) we may determine that

$$A_1 = A_2 = A_4 = 0$$

and either $A_3 = 0$ or $\sin \lambda = 0$

For nontrivial solutions

$$A_3 \neq 0$$

[23] Timoshenko and Gere [3].

[24] Alternatively one could use Galerkin's method for (5.4) and (5.5) or convert them into an integral equation to be solved by the 'lumped element' method.

and

$$\sin \lambda = 0$$

or

$$\lambda = \pi, 2\pi, 3\pi, etc. \tag{5.7}$$

Note that $\lambda = 0$ is a trivial solution, e.g., $w \equiv 0$.

Of the several eigenvalue solutions the smallest nontrivial one is of the greatest physical interest, i.e.,

$$\lambda = \pi$$

The corresponding divergence or buckling dynamic pressure is

$$\rho U^2 = \frac{EI}{Aa^2}\pi^2 \tag{5.8}$$

Note that λ^2 is a nondimensional ratio of aerodynamic to elastic stiffness; we shall call it and similar numbers we shall encounter an 'aeroelastic stiffness number'. It is as basic to aeroelasticity as Mach number and Reynolds number are to fluid mechanics. Recall that in our typical section study we also encountered an 'aeroelastic stiffness number', namely,

$$\frac{qs\frac{\partial C_L}{\partial \alpha}}{K_\alpha}e$$

as well as in the (uniform) beam-rod wing model,

$$\frac{q(lc)e\frac{\partial C_L}{\partial}\alpha}{\frac{GJ}{l}}$$

5.2 (Low Speed) Fluid Flow Over A Flexible Wall

A mathematically similar problem arises when a flexible plate is embedded in an otherwise rigid surface. See Fig. 16. This is a simplified model of a physical situation which arises in nuclear reactor heat exchangers, for example. Aeronautical applications may be found in the local skin deformations on aircraft and missiles. Early airships may have encountered aeroelastic skin buckling.[25]

For a one dimensional (beam) structural representation of the wall, the equation of equilibrium is, as in our previous example,

[25] Shute [12], p. 95.

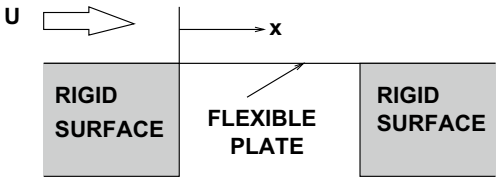

Fig. 16 Fluid flow over a flexible wall

$$EI\frac{\partial^4 w}{\partial x^4} = L$$

Also, as a rough approximation, it has been shown that the aerodynamic loading may be written as[26]

$$L \sim \rho U^2 \frac{\partial^2 w}{\partial x^2}$$

Hence using this aerodynamic model, there is a formal mathematical analogy to the previous example and the aeroelastic calculation is the same. For more details and a more accurate aerodynamic model, the cited references should be consulted.

6 Sweptwing Divergence

A swept wing, one whose elastic axis is at an oblique angle to an oncoming fluid stream, offers an interesting variation on the divergence phenomenon. Consider Fig. 17. The angle of sweep is that between the axis perpendicular to the oncoming stream (y axis) and the elastic axis ($\bar{y}$ axis). It is assumed that the wing can be modeled by the bending-torsion deformation of a beam-rod. Thus the two structural equations of equilibrium are

Bending equilibrium of a beam-rod

$$\frac{d^2}{d\bar{y}^2}\left(EL\frac{d^2h}{d\bar{y}^2}\right) = -\bar{L} \tag{6.1}$$

Torsional equilibrium of a beam-rod

$$\frac{d^2}{d\bar{y}^2}\left(GJ\frac{d\alpha_e}{d\bar{y}}\right) + \bar{M}_y = 0 \tag{6.2}$$

Here h is the bending displacement of the elastic axis and is assumed positive downward. α_e, the elastic twist about the $\bar{y}$ axis, is positive nose up.

[26] Dowell [13], p. 19, Kornecki [14], Kornecki, Dowell and O'Brien [15].

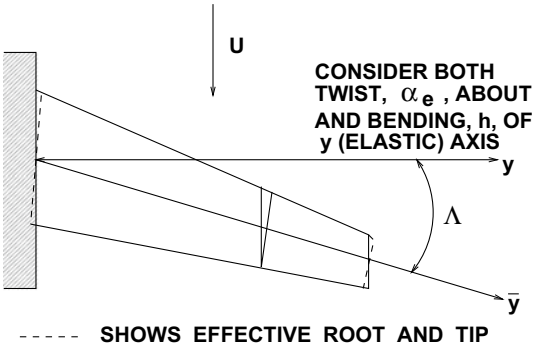

Fig. 17 Sweptwing geometry

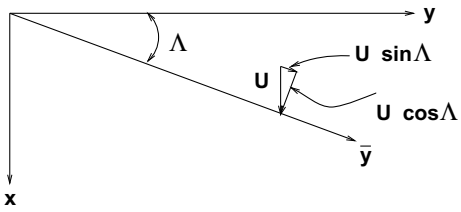

Fig. 18 Velocity diagram in the x, $y(\bar{x}, \bar{y})$ plane

Now consider the aerodynamic model. Consider the velocity diagram, Fig. 18. A strip theory aerodynamic model will be invoked with respect to chords perpendicular to the $\overline{y}$ axis. Thus the lift and aerodynamic moment per unit span are given by

$$\bar{L} = \bar{C}_L c \bar{q} \tag{6.3}$$

and

$$\begin{aligned} \bar{M}_y =& \bar{L}\bar{e} + \bar{M}_{AC} \\ =& \bar{C}_L c \bar{q} e + \bar{C}_{MAC} \bar{c}^2 \bar{q} \end{aligned} \tag{6.4}$$

where $\bar{q} = \frac{1}{2}\rho(U \cos \Lambda)^2 = q \cos^2 \Lambda$. Also $\bar{C}_L$ is related to the (total) angle of attack, α_T, by

$$\bar{C}_L(\bar{y}) = \frac{\partial \bar{C}_L}{\partial \alpha} \alpha_T(\bar{y}) \tag{6.5}$$

where

$$\alpha_T = \alpha_e + \frac{dh}{d\bar{y}} \tan \Lambda \tag{6.6}$$

To understand the basis of the second term in (6.6), consider the velocity diagram of Fig. 19. From this figure we see the fluid velocity normal to the wing is $U \sin \Lambda dh/d\bar{y}$ and thus the effective angle of attack due to bending of a swept wing is

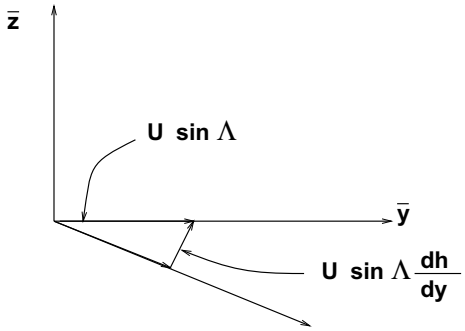

Fig. 19 Velocity diagram in $\bar{y}, \bar{z}$ plane

$$U \sin \Lambda \frac{dh}{d\bar{y}} / U \cos \Lambda = U \frac{dh}{d\bar{y}} \tan \Lambda \tag{6.7}$$

From (6.1) to (6.6), the following form of the equations of equilibrium is obtained.

$$\frac{d^2}{d\bar{y}^2}\left(EI\frac{d^2h}{d\bar{y}^2}\right) = -\frac{\partial \bar{C}_L}{\partial \alpha}\left[\alpha_e + \frac{dh}{d\bar{y}} \tan \Lambda\right] \bar{c} q \cos^2 \Lambda \tag{6.7}$$

$$\frac{d}{d\bar{y}}\left(GJ\frac{d\alpha_e}{d\bar{y}}\right) + \frac{\partial \bar{C}_L}{\partial \alpha}\left[\alpha_e + \frac{dh}{d\bar{y}} \tan \Lambda\right] \bar{c} q \cos^2 \Lambda \bar{e} + \bar{C}_{MAC} \bar{c}^2 q \cos^2 \Lambda = 0 \tag{6.8}$$

SPECIAL CASES;

- If the beam is very stiff in bending, $EI \to \infty$, then from (6.7), $h \to 0$. Equation (6.8) then is very similar to the torsional equation for an unswept wing with slightly modified coefficients.
- If the beam-rod is very stiff in torsion, $GJ \to \infty$, then from (6.8), $\alpha \to 0$. Equation (6.7) then reduces to

$$\frac{d^2}{d\bar{y}^2}\left(EI\frac{d^2h}{d\bar{y}^2}\right) + \frac{\partial \bar{C}_L}{\partial \alpha} \sin \Lambda \cos \Lambda \bar{c} q \frac{dh}{d\bar{y}} = 0 \tag{6.9}$$

As we shall see, divergence in bending alone is possible even for a swept wing which is very stiff in torsion. This is not possible for an unswept wing.

To illustrate this, consider a further special case, namely a beam with constant spanwise properties. Introducing appropriate non-dimensionalization then (6.9) becomes

$$\frac{d^4h}{d\tilde{y}^4} + \lambda \frac{dh}{d\tilde{y}} = 0 \tag{6.10}$$

where $\tilde{y} \equiv \bar{y}/l$ and

$$\lambda = \frac{\frac{\partial \bar{C}_L}{\partial \alpha} q \bar{c} \bar{l}^3}{EI} \sin \Lambda \cos \Lambda$$

The boundary conditions associated with this differential equation are zero deflection and slope at the root:

$$h = \frac{dh}{d\tilde{y}} = 0 \quad @ \quad \tilde{y} = 0 \tag{6.11}$$

and zero bending moment and shear force at the tip

$$EI \frac{d^2 h}{d\tilde{y}^2} = EI \frac{d^3 h}{d\tilde{y}^3} = 0 \quad @ \quad \tilde{y} = 1 \tag{6.12}$$

Equations (6.10)–(6.12) constitute an eigenvalue problem. The eigenvalues of λ are all negative and the lowest of these provides the divergence condition.

$$\lambda_D = -6.33 = \frac{\partial \bar{C}_L}{\partial \alpha} \frac{\sin \Lambda \cos \Lambda \bar{c} \bar{l}^3 q}{EI} \tag{6.13}$$

The only way the right hand side of (6.13) can be less than zero is if $\sin \Lambda < 0$ or $\Lambda < 0$.

Thus only swept forward wings can diverge in bending without torsional deformation. This suggests that swept forward wings are more susceptible to divergence than swept back wings. This proves to be the case when both bending and torsion are present as well.

For many years, the divergence tendency of swept forward wings precluded their use. In recent years composite materials provide a mechanism for favorable bending-torsion coupling which alleviates this divergence. For a modern treatment of these issues including the effects of composite structures two reports by Weisshaar [16, 17] are recommended reading.

A final word on how the eigenvalues are calculated. For (6.10)–(6.12), classical techniques for constant coefficient differential equations may be employed. See BAH, pp. 479–489. Even when both bending and torsion are included (6.7), (6.8), if the wing properties are independent of spanwise location, then classical techniques may be applied. Although the calculation does become more tedious. Finally, for a variable spanwise properties Galerkin's method may be invoked, in a similar though more elaborate manner to that used for unswept wing divergence.

References

1. Ashley H, Landahl M (1965) Aerodynamics of wing and Bodies. Addison-Wesley, Boston
2. Savant CJ Jr (1958) Basic feedback control system design. McGraw-Hill, New York
3. Timoshenko SP, Gere J (1961) Theory of elastic stability. McGraw-Hill, New York

4. Woodcock DL (1959) Structural non-linearities, vol. I, chap 6, AGARD Manual on Aeroelasticity
5. Housner GW, Vreeland T Jr (1966) The analysis of stress and deformation. The MacMillan Co., New York
6. Hildebrand FB (1961) Advance calculus for engineers. Prentice-Hall, New Jersey
7. Duncan WJ (1937) Galerkin's methods in mechanics and differential equations. Aeronaut Res Comm, Reports and memoranda, No 1798
8. Bisplinghoff RL, Mar JW, Pian THH (1965) Statics of deformable solids. Addison-Wesly, New York
9. Weisshaar TA, Ashley H (1974) Static aeroelasticity and the flying wing, revisited. J. Aircraft 11:718–720
10. Covert EE (1961) The aerodynamics of distorted surfaces. In: Proceedings of symposium on aerothermoelasticity. ASD TR 61-645, pp 369-398
11. Housner GW (1952) Bending vibrations of a pipe line containing flowing fluid. J Appl Mech 19:205
12. Shute N (1954) Slide rule. Wm. Morrow & CO., Inc., New York, p 10016
13. Dowell EH (1974) Aeroelasticity of plates and shells. Noordhoff International Publishing
14. Kornecki A (1974) Static and dynamic instability of panels and cylindrical shells in subsonic potential flow. J. Sound Vibr 32:251–263
15. Kornecki A, Dowell EH, O'Brien J (1976) On the aeroelastic instability of two-dimensional panels in uniform incompressible flow. J. Sound Vibr 47:163–178
16. Weisshaar TA (1978) Aeroelastic stability and performance characteristics of aircraft with advanced composite sweptforward wing structures, AFFDL TR-78-116
17. Weisshaar TA (1979) Forward swept wing static aeroelasticity, AFFDL TR-79-3087

Dynamic Aeroelasticity

Earl H. Dowell

Abstract Dynamic aeroelasticty is considered and the dynamic stability (Flutter) of linear aeroelastic systems is considered as well as the response to external disturbances including atmospheric turbulence (Gusts). The discussion proceeds from simpler physical models and mathematical methods to more complex ones. An introduction to the modeling of aerodynamics forces is also provided to prepare the reader for the material in chapter 'Nonsteady Aerodynamics of Lifting and Non-lifting Surfaces'.

In static aeroelasticity we have considered various mathematical models of aeroelastic systems. In all of these, however, the fundamental physical content consisted of two distinct phenomena, 'divergence' or static instability, and loss of aerodynamic effectiveness as typified by 'Control surface reversal'. Turning to dynamic aeroelasticity we shall again be concerned with only a few distinct fundamental physical phenomena. However, they will appear in various theoretical models of increasing sophistication. The principal phenomena of interest are (1) 'flutter' or dynamic instability and (2) response to various dynamic loadings as modified by aeroelastic effects. In the latter category primary attention will be devoted to (external) aerodynamic loadings such as atmospheric turbulence or 'gusts'. These loadings are essentially random in nature and must be treated accordingly. Other loadings of interest may be impulsive or discrete in nature such as the sudden loading due to maneuvering of a flight vehicle as a result of control surface rotation.

To discuss these phenomena we must first develop the dynamic theoretical models. This naturally leads us to a discussion of how one obtains the equations of motion for a given aeroelastic system including the requisite aerodynamic forces. Our initial discussion of aerodynamic forces will be conceptual rather than detailed. Later, in chapter 'Nonsteady Aerodynamics of Lifting and Non-lifting Surfaces', these forces are developed from the fundamentals of fluid mechanics. We shall begin by using the 'typical section' as a pedagogical device for illustrating the physical content of dynamic aeroelasticity. Subsequently using the concepts of structural and

E. H. Dowell (✉)
Mechanical Engineering and Materials Science Duke University, Durham, NC, USA
e-mail: earl.dowell@duke.edu

E. H. Dowell (ed.), *A Modern Course in Aeroelasticity*, Solid Mechanics and Its Applications 264, https://doi.org/10.1007/978-3-030-74236-2_3

aerodynamic influence and impulse functions, we shall discuss a rather general model of an aeroelastic system. The solution techniques for our aeroelastic models are for the most part standard for the modern treatment of the dynamics of linear systems and again we use the typical section to introduce these methods.

We now turn to a discussion of energy and work methods which have proven very useful for the development of structural equations of motion. In principle, one may use Newton's Second Law (plus Hooke's Law) to obtain the Equations of motion for any elastic body. However, normally an alternative procedure based on Hamilton's Principle or Lagrange's Equations is used.[1] For systems with many degrees of freedom, the latter are more economical and systematic.

We shall briefly review these methods here by first deriving them from Newton's Second Law for a single particle and then generalizing them for many particles and/or a continuous body. One of the major advantages over the Newtonian formulation is that we will deal with work and energy (scalars) as contrasted with accelerations and forces (vectors).

1 Hamilton's Principle

1.1 Single Particle

Newton's Law states

$$\vec{F} = m\frac{d^2\vec{r}}{dt^2} \tag{1.1}$$

where $\bar{F}$ is the force vector and $\vec{r}$ is the displacement vector, representing the actual path of particle. m is the particle mass.

Consider an adjacent path, $\vec{r} + \delta\vec{r}$, where $\vec{r}$ is a 'virtual displacement' which is small in some appropriate sense. If the time interval of interest is $t = t_1 \rightarrow t_2$ then we shall require that

$$\delta\vec{r} = 0 \quad \text{at} \quad t = t_1, t_2$$

although this can be generalized. Thus, the actual and adjacent paths coincide at $t = t_1$, or t_2

Now form the dot product of (1.1) with $\delta\vec{r}$ and $\int_{t_1}^{t_2} \cdots dt$. The result is

$$\int_{t_1}^{t_2} \left(m\frac{d^2\vec{r}}{dt^2} \cdot \delta\vec{r} - \vec{F} \cdot \delta\vec{r} \right) dt = 0 \tag{1.2}$$

The second term in brackets can be identified as work or more precisely the 'virtual work'. The 'virtual work' is defined as the work done by the actual forces being moved

[1] See, for example, Meirovitvh [1].

through the virtual displacement. We assume that the force remains fixed during the virtual displacement or, equivalently, the virtual displacement occurs instantaneously, i.e., $\delta t = 0$.

It follows that the first term must also have the dimensions of work (or energy). To see this more explicitly, we manipulate the first term by an integration by parts as follows:

$$\begin{aligned} m\int_{t_1}^{t_2} \frac{d^2\vec{r}}{dt^2}\cdot\delta\vec{r}\,dt &= m\frac{d\vec{r}}{dt}\cdot\delta\vec{r}\,\Big|_{t_1}^{t_2} \\ &\quad - m\int_{t_1}^{t_2}\frac{d\vec{r}}{dt}\cdot\frac{d}{dt}(\delta\vec{r})dt \\ &= -m\int_{t_1}^{t_2}\frac{d\vec{r}}{dt}\cdot\delta\frac{d\vec{r}}{dt}dt \\ &= -\frac{m}{2}\int_{t_1}^{t_2}\delta\left(\frac{d\vec{r}}{dt}\cdot\frac{d\vec{r}}{dt}\right)dt \end{aligned} \tag{1.3}$$

Hence (1.2) becomes

$$\int_{t_1}^{t_2}\left[\frac{1}{2}m\delta\left(\frac{d\vec{r}}{dt}\cdot\frac{d\vec{r}}{dt}\right)+F\cdot\delta\vec{r}\right]dt = 0$$

or

$$\int_{t_1}^{t_2}\delta[T+W]dt = 0 \tag{1.4}$$

where

$$\delta T \equiv \delta\frac{1}{2}m\frac{d\vec{r}}{dt}\cdot\frac{d\vec{r}}{dt} \tag{1.5}$$

is defined as the 'virtual kinetic energy' and

$$\delta W \equiv \vec{F}\cdot\delta\vec{r} \tag{1.6}$$

is the 'virtual work'. Hence, the problem is cast in the form of scalar quantities, work and energy. Equation (1.4) is Hamilton's Principle. It is equivalent to Newton's Law.

Before proceeding further it is desirable to pause to consider whether we can reverse our procedure, i.e., starting from (1.4), can we proceed to (1.1)? It is not immediately obvious that this is possible. After all, Hamilton's Principle represents an integrated statement over the time interval of interest while Newton's Second Law holds at every instant in time. By formally reversing our mathematical steps however, we may proceed from (1.4) to (1.2). To take the final step from (1.2) to (1.1) we must recognize that our choice of $\delta\vec{r}$ is arbitrary. Hence, if (1.2) is to hold for any possible choice of $\delta\vec{r}$, (1.2) must follow. To demonstrate this we note that, if $\delta\vec{r}$ is arbitrary and (1.1) were not true, then it would be possible select $\delta\vec{r}$ such that (1.2) would not be true. Hence (1.2) implies (1.1) if $\delta\vec{r}$ is arbitrary.

1.2 Many Particles

The previous development is readily generalized to many particles. Indeed, the basic principle remains the same and only the work and energy expressions are changed as follows:

$$\delta T = \sum_i \frac{m_1}{2} \delta \left(\frac{d\vec{r}_i}{dt} \cdot \frac{d\vec{r}_i}{dt} \right) \tag{1.7}$$

$$\delta W = \sum_i \vec{F}_i \cdot \delta \vec{r}_i \tag{1.8}$$

where

$$\begin{aligned} m_i &\text{ is the mass of } i\text{th particle,} \\ \vec{r}_i &\text{ is the displacement of } i\text{th particle, and} \\ \vec{F}_i &\text{ is the force acting on } i\text{th particle.} \end{aligned} \tag{1.9}$$

1.3 Continuous Body

For a continuous body (1.7) and (1.8) are replaced by (1.10) and (1.11)

$$\delta T = \iiint_{\text{volume}} \frac{\rho}{2} \delta \frac{d\vec{r}}{dt} \cdot \frac{d\vec{r}}{dt} dV \tag{1.10}$$

where ρ is the density (mass per unit volume), V is the volume, and δW is the virtual work done by external applied forces and internal elastic forces. For example, if $\vec{f}$ is the vector body force per unit volume and $\vec{p}$ the surface force per unit area then

$$\delta W = \iiint_{\text{volume}} \vec{f} \cdot \delta \vec{r} dV + \iint_{\text{surface area}} \vec{p} \cdot \delta \vec{r} dA \tag{1.11}$$

1.4 Potential Energy

In a course of elasticity[2] it would be shown that the work done by internal elastic forces is the negative of the virtual elastic potential energy. The simplest example is that of an elastic spring. See sketch below.

[2] Bisplinghoff, Mar, and pian [2], Timoshenko and Goodier [3].

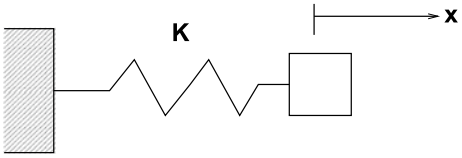

The force in the spring is

$$-Kx$$

where the minus sign arises from the fact that the force of the spring on the mass opposes the displacement, x. The virtual work is

$$\begin{aligned}\delta W &= -Kx\delta x \\ &= -\delta\frac{Kx^2}{2}\end{aligned}$$

The virtual change in potential energy is

$$\begin{aligned}\delta U &\equiv -\delta W \\ &= \delta\frac{Kx^2}{2} = \delta\left(\frac{Fx}{2}\right)\end{aligned} \tag{1.12}$$

Considering the other extreme, the most complete description of the potential energy of an elastic body which satisfies Hooke's Law is (see Bisplinghoff, Mar and Pian [2])

$$U = \frac{1}{2}\iiint_{\mathrm{V}} [\sigma_{xx}\epsilon_{xx} + \sigma_{xy}\epsilon_{xy} + \sigma_{xy}\epsilon_{xy} + \cdots]dV \tag{1.13}$$

where σ_{xx} is the stress component (analogous to F) and ϵ_{xx} is the strain component (analogous to x), etc.

From this general expression for potential (strain) energy of an elastic body we may derive some useful results for the bending and twisting of beams and plates. For the bending of a beam, the usual assumption of plane sections over the beam cross-section remaining plane leads to a strain-displacement relation of the form

$$\epsilon_{yy} = -z\frac{\partial^2 w}{\partial y^2}$$

where z is the vertical coordinate through the beam and w is the vertical displacement of the beam. Hooke's Law reads,

$$\sigma_{yy} = E\epsilon_{yy} = -Ez\frac{\partial^2 w}{\partial y^2}$$

and we assume all other stresses are negligible

$$\sigma_{yz} = \sigma_{xy} = \sigma_{xz} = \sigma_{xx} = \sigma_{zz} = 0$$

If we further assume $w(x, y, z) = h(y)$ where y is the lengthwise coordinate axis of the beam, then

$$U = \frac{1}{2} \int EI \left(\frac{\partial^2 h}{\partial y^2} \right)^2 dy$$

where

$$I \equiv \int z^2 dz \int dx$$

For the twisting of a thin beam , analogous reasoning leads to similar results. Assume $w = \alpha x$ and α is the angle of twist about the y axis. Then

$$\epsilon_{xy} = -z \frac{\partial^2 w}{\partial x \partial y}$$

$$\sigma_{xy} = \frac{E}{(1+v)} \epsilon_{xy} = \frac{E}{(1+v)} z \frac{\partial^2 w}{\partial x \partial y}$$

Thus

$$U = \frac{1}{2} \int GJ \left(\frac{\partial \alpha}{\partial y} \right)^2 dy$$

where

$$G \equiv \frac{E}{2(1+v)}, \qquad J \equiv 4 \int z^2 dz \int dx$$

The above can be generalized to the bending of a plate in two dimensions.

$$\epsilon_{yy} = -z \frac{\partial^2 w}{\partial y^2}$$

$$\epsilon_{xx} = -z \frac{\partial^2 w}{\partial x^2}$$

$$\epsilon_{xy} = -z \frac{\partial^2 w}{\partial x \partial} y$$

$$\sigma_{xx} = \frac{E}{(1-v^2)} [\epsilon_{xx} + v \epsilon_{yy}]$$

$$\sigma_{yy} = \frac{E}{(1-v^2)} [\epsilon_{yy} + v \epsilon_{xx}]$$

$$\sigma_{xy} = \frac{E}{(1+v)}\epsilon_{xy}$$

and

$$U = \frac{1}{2}\iint D\left[\left(\frac{\partial^2 w}{\partial x^2}\right)^2 + \left(\frac{\partial^2 w}{\partial y^2}\right)^2 + 2v\frac{\partial^2 w}{\partial x^2}\frac{\partial^2 w}{\partial y^2} + 2(1-v)\left(\frac{\partial^2 w}{\partial x \partial y}\right)^2\right] dx\, dy$$

where

$$D \equiv \frac{E}{(1-v^2)}\int_{-h/2}^{+h/2} z^2 dy, \quad \text{plate bending stiffness}$$

and

$$w = w(x, y)$$

1.5 Nonpotential Forces

Now, if one divides the virtual work into potential and nonpotential contributions, one has Hamilton's Principle in the form

$$\int [(\delta T - \delta U) + \underbrace{\vec{F_{NC}} \cdot \vec{\delta r}}_{\delta W_{NC}}] dt = 0 \tag{1.14}$$

where F_{NC} includes only the nonpotential (or nonconservative) forces.

In our aeroelastic problems the nonconservative virtual work is a result of aerodynamic loading. For example, the virtual work due to the aerodynamic pressure (force per unit area) on a two-dimensional plate is clearly

$$\delta W_{NC} = \iint p\, \delta w\, dx\, dy$$

Note that if the deflection is taken to be a consequence of a chordwise rigid rotation about and bending of a spanwise elastic axis located at, say $x = 0$, then

$$w = -h(y) - x\alpha(y)$$

and hence

$$\delta W = \int \left[-\int p dx\right] \delta h\, dy + \int \left[-\int px\, dx\right] \delta\alpha\, dy$$

where

$L = \int p\, dx$ net vertical force/per unit span
$M_y \equiv -\int px\, dx$ net moment about y axis per unit span

Thus, for this special case,

$$\delta W = \int -L\,\delta h\,dy + \int M_y \delta\alpha dy$$

Can you derive equations for T and U in terms of h and α?

2 Lagrange's Equations

Lagrange's equations may be obtained by reversing the process by which we obtained Hamilton's Principle. However to obtain a more general result than simply a retrieval of Newton's Second Law we introduce the notion of 'generalized' coordinates. A 'generalized' coordinate is one which is arbitrary and independent (of other coordinates). A set of 'generalized' coordinates is sufficient[3] to describe the motion of a dynamical system. That is, the displacement of a particle or point in a continuous body may be written

$$\vec{r} = \vec{r}(q_1, qq_2, q_3, \ldots, t) \tag{2.1}$$

where q_i is the ith generalized coordinate. From (2.1) it follows that

$$T = T(\dot{q}_i, q_i, t) \tag{2.2}$$

$$U = U(\dot{q}_i, q_i, t)$$

Thus Hamilton's Principle may be written

$$\int_{t_1}^{t_2} [\delta(T - U) + \delta W_{NC}]dt = 0 \tag{1.14}$$

Using (2.2) in (1.14)

$$\sum_i \int_{t_1}^{t_2} \left[\frac{\partial(T-U)}{\partial \dot{q}_i}\delta\dot{q}_i + \frac{\partial(T-U)}{\partial q_i}\delta q_i + Q_i \delta q_i \right] dt = 0 \tag{2.3}$$

where the Generalized forces, Q_i, are known from

$$\delta W_{NC} \equiv \sum_i Q_i \delta q_i \tag{2.4}$$

As we will see (2.4) *defines* the Q_i as coefficients of δq_i in an expression for δW_{NC} which must be obtained independently of (2.4). Integrating the first term of (2.3) by

[3] And necessary, i.e., they are independent.

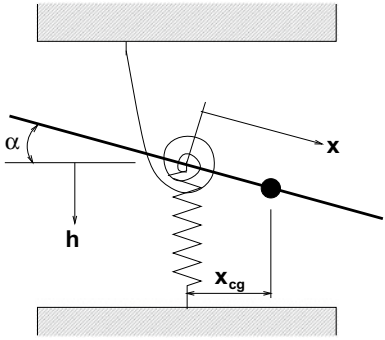

Fig. 1 Geometry of typical section airfoil

parts (noting that $\delta q_i = 0\ t = t_i, t_2$) we have

$$\sum_i \cancel{\frac{\partial(T-U)}{\partial q_i}}\delta q_i|_{t_1}^{t_2} + \int_{t_1}^{t_2}\Big[-\frac{d}{dt}\frac{\partial(T-U)}{\partial \dot{q}_i}\delta q_i + \frac{\partial(T-U)}{\partial q_i}\delta q_i + Q_i\delta q_i\Big]dt = 0 \tag{2.5}$$

Collecting terms

$$\sum_i \int_{t_1}^{t_2}\left[-\frac{d}{dt}\frac{\partial(T-U)}{\delta \dot{q}_i} + \frac{\partial(T-U)}{\partial q_i} + Q_i\right]\delta q_i dt = 0 \tag{2.6}$$

Since the δq_i are independent and arbitrary it follows that each bracketed quantity must be zero, i.e.,

$$-\frac{d}{dt}\frac{\partial(T-U)}{\delta \dot{q}_i} + \frac{\partial(T-U)}{\partial q_i} + Q_i = 0 \quad i = 1, 2, \ldots \tag{2.7}$$

These are Lagrange's equations (Fig. 1).

2.1 Example—Typical Section Equations of Motion

x is measured along chord from e.a.; note that x is *not* a generalized coordinate, e.g., it cannot undergo a virtual change.

$$\text{generalized coordinates} \quad \{q_1 = h,\ q_2 = \alpha\}$$

The displacement of any point on the airfoil is

$$\vec{r} = u\vec{i} + w\vec{k} \tag{2.8}$$

where u is the horizontal displacement component, w is the vertical displacement component, and $\vec{i}, \vec{k}$ are the unit, cartesian vectors.

From geometry

$$\left.\begin{aligned} u &= x[\cos\alpha - 1] \simeq 0 \\ w &= -h - x\sin\alpha \cong -h - x\alpha \end{aligned}\right\} \text{ for } \alpha \ll 1 \tag{2.9}$$

Hence,

$$\begin{aligned} T &= \frac{1}{2}\int\left[\left(\frac{dw}{dt}\right)^2 + \left(\frac{du}{dt}\right)^2\right]\rho dx \\ &\simeq \frac{1}{2}\int\left(\frac{dw}{dt}\right)^2\rho dx \\ &= \frac{1}{2}\int(-\dot{h} - \dot{\alpha}x)^2\rho dx \\ &= \frac{1}{2}\dot{h}^2\int\rho dx + \frac{1}{2}2\dot{h}\dot{\alpha}\int x\rho dx + \frac{1}{2}\dot{\alpha}^2\int x^2\rho dx \\ &= \frac{1}{2}\dot{h}^2 m + \frac{1}{2}2\dot{h}\dot{\alpha}S_\alpha + \frac{1}{2}\dot{\alpha}^2 I_\alpha \end{aligned} \tag{2.10}$$

where $m \equiv \int \rho\, dx$ total mass

$S_\alpha \equiv \int \rho x dx \equiv x_{c.g.} m$ mass unbalance

$I_\alpha \equiv \int \rho x^2 dx$ moment of intertia

$\rho \equiv$ mass per unit chord length

The potential energy is

$$U = \frac{1}{2}K_h h^2 + \frac{1}{2}K_\alpha \alpha^2 \tag{2.11}$$

where K_n and K_α are the spring stiffnesses For our system, Lagrange's equations are

$$\begin{aligned} -\frac{d}{dt}\left(\frac{\partial(T-U)}{\partial\dot{h}}\right) + \frac{\partial(T-U)}{\partial h} + Q_h = 0 \\ -\frac{d}{dt}\left(\frac{\partial(T-U)}{\partial\dot{\alpha}}\right) + \frac{\partial(T-U)}{\partial\alpha} + Q_\alpha = 0 \end{aligned} \tag{2.12}$$

where

$$\delta W_{NC} = Q_h\delta h + Q_\alpha\delta\alpha \tag{2.13}$$

Now let us evaluate the terms in (2.12) and (2.13). Except for Q_h these are readily obtained by using (2.10) and (2.11) in (2.12). Hence, let us first consider the determination of Q_h, Q_α. To do this we calculate *independently* the work done by the aerodynamic forces.

$$\begin{aligned}\delta W_{NC} &= \int p\delta w dx \\ &= \int p(-\delta h - x\delta\alpha)dx \\ &= \delta\left(-\int p dx\right) + \delta\alpha\left(-\int p x dx\right) \\ &= \delta h(-L) + \delta\alpha(M_y)\end{aligned} \tag{2.14}$$

where we identify from (2.13) and (2.14)

$$\begin{aligned}L &\equiv \int p dx = Q_h \\ M_y &\equiv -\int p x dx = Q_\alpha\end{aligned}$$

Note the sign convention is that p is positive up, L is positive up and M_y is positive nose up. Putting it all together, noting that

$$\frac{\partial(T-U)}{\partial h} = -K_h h \quad \text{etc.}$$

we have from Lagrange's equations

$$\begin{aligned}-\frac{d}{dt}(m\dot{m} + S_\alpha\dot{\alpha}) - K_h h - L = 0 \\ -\frac{d}{dt}(S_\alpha\dot{h} + I_\alpha\dot{\alpha}) - K_\alpha\alpha + M_y = 0\end{aligned} \tag{2.15}$$

These are the equations of motion for the 'typical section' in terms of the particular coordinates h and α.

Other choices of generalized coordinates are possible; indeed, one of the principal advantages of Lagrange's equations is this freedom to make various choices of generalized coordinates. The choice used above simplifies the potential energy but not the kinetic energy. If the generalized coordinates were chosen to be the translation of an rotation about the center of mass the kinetic energy would be simplified, viz.

$$T = \frac{m}{2}\dot{h}_{cm}^2 + \frac{I_{cm}}{2}\dot{\alpha}_{cm}^2$$

but the potential energy would be more complicated. Also the relevant aerodynamic moment would be that about the center of mass axis rather than that about the elastic axis (spring attachment point).

Another choice might be the translation of and rotation about the aerodynamic center axis though this choice is much less often used than those discussed above.

Finally we note that there is a particular choice of coordinates which leads to a maximum simplification of the inertial and elastic terms (though not necessarily the aerodynamic terms). These may be determined by making some arbitrary initial choice of coordinates, e.g., h and α, and then determining the 'normal modes' of the system in terms of of these.[4] These 'normal modes' provide us with a coordinate transformation from the initial coordinates, h and α, to the coordinates of maximum simplicity. We shall consider this matter further subsequently.

3 Dynamics of the Typical Section Model of An Airfoil

To study the dynamics of aeroelastic systems, we shall use the 'typical section'[5] as a device for exploring mathematical tools and the physical content associated with such systems. To simplify matters, we begin by assuming the aerodynamic forces *are given* where $p(x, t)$ is the aerodynamic pressure, L, the resultant (lift) force and M_y the resultant moment about the elastic axis. See Fig. 2. The equations of motion are

$$m\ddot{h} + K_h h + S_\alpha \ddot{\alpha} = -L \tag{3.1}$$

$$S_\alpha \ddot{h} + I_\alpha \ddot{\alpha} + K_\alpha \alpha = M_y \tag{3.2}$$

where

$$L \equiv \int p\, dx$$

$$M_y \equiv \int px\, dx$$

We will find it convenient also to define the 'uncoupled natural frequencies',

$$\omega_h^2 \equiv K_h/m, \quad \omega_\alpha^2 \equiv K_\alpha/I_\alpha \tag{3.3}$$

These are 'natural frequencies' of the system for $S_\alpha \equiv 0$ as we shall see in a moment.

[4] Meirvovitch [4].

[5] BA, pp. 201–246.

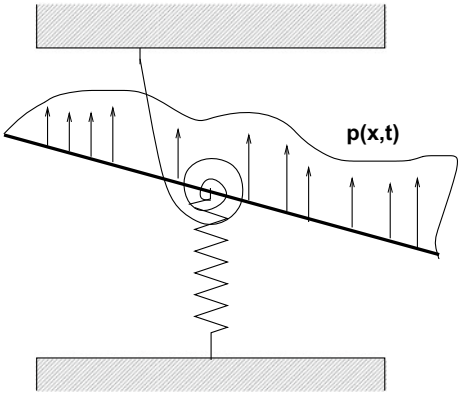

Fig. 2 Typical section geometry

3.1 Sinusoidal Motion

This is the simplest type of motion; however, as we shall see, we can exploit it systematically to study more complicated motions.

Let

$$\begin{aligned} L &= \bar{L}e^{i\omega t}, & M_y &= \bar{M}_y e^{i\omega t} \\ h &= \bar{h}e^{i\omega t}, & \alpha &= \bar{\alpha}e^{i\omega t} \end{aligned} \tag{3.4}$$

Substituting (3.4) and (3.3) into (3.2) we have in matrix notation

$$\begin{bmatrix} m(-\omega^2+\omega_h^2) & -S_\alpha\omega^2 \\ -S_\alpha\omega^2 & I_\alpha(-\omega^2+\omega_\alpha^2) \end{bmatrix} \begin{Bmatrix} \bar{h} \\ \bar{\alpha} \end{Bmatrix} = \begin{Bmatrix} -\bar{L} \\ \bar{M}_y \end{Bmatrix} \tag{3.5}$$

Solving for $\bar{h},\ \bar{\alpha}$ we have the transfer function, H_{hL}

$$\begin{aligned} \frac{\bar{h}}{\bar{L}} &= \frac{-[1-(\omega/\omega_\alpha)^2] + d/b\frac{x_\alpha}{r_\alpha^2}\left(\frac{\omega}{\omega_\alpha}\right)^2}{K_h\left\{[1-(\omega/\omega_\alpha)^2][1-(\omega/\omega_h)^2] - \frac{x_\alpha^2}{r_\alpha^2}\left(\frac{\omega}{\omega_\alpha}\right)^2\left(\frac{\omega}{\omega_h}\right)^2\right\}} \\ &\equiv H_{hL}\left(\omega/\omega_\alpha;\ \frac{\omega_h}{\omega_\alpha}, d/b, x_\alpha, r_\alpha\right) \end{aligned} \tag{3.6}$$

where

$$d \equiv \bar{M}_y/\bar{L}$$

and b is the reference length (usually selected as half-chord by tradition),

$$x_\alpha \equiv \frac{S_\alpha}{mb} = \frac{x_{c.g.}}{b}$$

Fig. 3 Transfer function

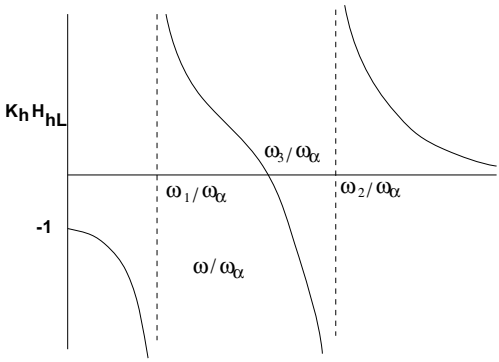

and

$$r_\alpha^2 \equiv \frac{I_\alpha}{mb^2}$$

A plot of H_{hL} is shown below in Fig. 3. $\frac{\omega_1}{\omega_\alpha}$, $\frac{\omega_2}{\omega_\alpha}$ are the roots of the denominator, the system 'natural frequencies'.

$$\frac{\omega_1^2}{\omega_h \omega \alpha}, \frac{\omega_2^2}{\omega_h \omega_\alpha} = \frac{\left[\frac{\omega_h}{\omega_\alpha} + \frac{\omega_\alpha}{\omega_h}\right] \pm \left\{\left[\frac{\omega_h}{\omega_\alpha} + \frac{\omega_\alpha}{\omega_h}\right]^2 - 4\left[1 - \frac{x_\alpha^2}{r_\alpha^2}\right]\right\}^{\frac{1}{2}}}{2[1 - x_\alpha^2/r_\alpha^2]} \tag{3.7}$$

A similar equation may be derived for

$$\frac{\bar{\alpha}}{\bar{L}} \equiv H_{\alpha L}\left(\omega/\omega_\alpha; \frac{\omega_h}{\omega_\alpha}, d/b, x_\alpha, r_\alpha\right) \tag{3.8}$$

ω_1 and ω_2 are again the natural frequencies. H_{hF}, $H_{\alpha F}$ are so-called 'transfer functions'; they are 'mechanical' or 'structural transfer functions' as they describe the motion of the structural system under specified loading. Later on we shall have occasion to consider 'aerodynamic transfer functions' and also 'aeroelastic transfer functions'. ω_3/ω_α is the root of the numerator of H_{hL} (but not in general of $H_{\alpha L}$ which will vanish at a different frequency),

$$\left(\frac{\omega_3}{\omega_\alpha}\right)^2 = \frac{1}{1 + (d/b)x_\alpha/r_\alpha^2} \tag{3.9}$$

Note that infinite response occurs at the natural frequencies, ω_1 and ω_2, for both H_{hL} and $H_{\alpha L}$. This is not an instability; it is a 'resonance' with the infinite response due to the absence of any damping in the system. Had structural or aerodynamic damping been included as will be done in later examples, then the transfer functions would become complex numbers which is a mathematical complication. However,

the magnitude of the transfer functions would remain finite though large at $\omega = \omega_1$, ω_2 which is an improvement in the realism of the physical model. With L and M assumed given, which admittedly is somewhat artificial, the question of instability does not arise. We will elaborate on this point later when we discuss the notion of instability in a more precise way.

From sinusoidal motion we may proceed to periodic (but not necessarily sinusoidal) motion.

3.2 Periodic Motion

The above analysis can be generalized to any periodic motion by expanding the motion into a Fourier (sinusoidal) series. Define:

$$T_0 \equiv \text{ basic period}$$

$$\omega_0 \equiv 2\pi/T_0, \quad \text{fundamental frequency}$$

Then a periodic force, $L(t)$, may be written as

$$L(t) = \sum_{n=-\infty}^{\infty} L_n e^{+in\omega_0 t} \tag{3.10}$$

where

$$L_n = \frac{1}{T_0} \int_{-T_0/2}^{T_0/2} L(t) e^{-in\omega_0 t} dt \tag{3.11}$$

Using (3.10) and (3.6)

$$h(t) = \sum_n H_{hL}\left(\frac{\omega_0 n}{\omega_\alpha}\right) L_n e^{in\omega_0 t} \tag{3.12}$$

From periodic motion we may proceed to arbitrary time dependent motion.

3.3 Arbitrary Motion

By taking the limit as the basic period becomes infinitely long, $T_0 \to \infty$, we obtain results for non-periodic motion.

Define

$\omega \equiv n\omega_0$

$\Delta\omega \equiv \Delta n\omega_0$[6]$=\omega_0 = 2\pi/T_0$ frequency increment
$L^*(\omega) \equiv \frac{L_n}{\Delta\omega} = \frac{L_n T_0}{2\pi}$ force per frequency increment

Then (3.10) becomes

$$L(t) = \int_{-\infty}^{\infty} L^*(\omega) e^{+i\omega t} d\omega \tag{3.10}$$

Equation (3.11) becomes

$$L^*(\omega) = \frac{1}{2\pi} \int_{-\infty}^{\infty} L(t) e^{-i\omega t} dt \tag{3.11}$$

Equation (3.12) becomes

$$h(t) = \int_{-\infty}^{\infty} H_{hL}(\omega/\omega_\alpha) L^*(\omega) e^{i\omega t} d\omega \tag{3.12}$$

An interesting alternate form of (3.12) can be obtained by substituting (3.11) into (3.12). Using a dummy time variable, τ, in (3.11) and interchanging order of integration in (3.12), gives

$$h(t) = \int_{-\infty}^{\infty} I_{hL}(t-\tau) L(\tau) d\tau \tag{3.13}$$

where

$$I_{hL}(t) \equiv \frac{1}{2\pi} \int_{-\infty}^{\infty} H_{hL}(\omega/\omega_\alpha) e^{i\omega t} d\omega \tag{3.14}$$

Comparing (3.12) and (3.14), note that I_{hL} is the response to $L^*(\omega) = \frac{1}{2\pi}$ or from (3.10) and (3.11), $L(t) = \delta(t)$. Hence, I is the response to an impulse force and is thus called the impulse function.

Equations (3.10)–(3.11) are a pair of Fourier transform relations and (3.13) is a so-called convolution integral.

Note (3.13) is suitable for treating transient motion; however, a special case of the Fourier transform is often used for transient motion. This is the Laplace transform.

Laplace transform. Consider

$$L(\tau) = 0 \quad \text{for} \quad \tau < 0$$

also

$$I_{hL}(t-\tau) = 0 \quad \text{for} \quad t - \tau < 0$$

The latter will be true for any physically realizable system since the system cannot respond before the force is applied.

[6] Note $\Delta n = 1$ since any n is an integer.

Define

$$p \equiv i\omega; \quad \text{thus} \quad \omega = -ip$$

and

$$L^{\dagger} \equiv 2\pi L^{*}(-ip)$$

then (3.10) becomes

$$L(t) = \frac{1}{2\pi i} \int_{-i\infty}^{i\infty} L^{\dagger} e^{pt} dp$$

Equation (3.11) becomes

$$L^{\dagger} = \int_{0}^{\infty} L(t) e^{-pt} dt \tag{3.15}$$

Equation (3.13) becomes

$$h(t) = \int_{0}^{t} I_{hL}(t-\tau) L(\tau) d\tau$$

where

$$I_{hL}(t) = \frac{1}{2\pi i} \int_{-i\infty}^{i\infty} H_{hL}\left(\frac{-ip}{\omega_{\alpha}}\right) e^{pt} dp$$

Utilization of Transform Integral Approach for Arbitrary Motion. There are several complementary approaches in practice. In one the transfer function, H_{hL}, is first determined through consideration of simple sinusoidal motion. Then the impulse function is evaluated from

$$I_{hL}(t) = \frac{1}{2\pi} \int_{\infty}^{\infty} H_{hL}(\omega) e^{i\omega t} d\omega \tag{3.14}$$

and the response is obtained from

$$h(t) = \int_{0}^{t} I_{hL}(t-\tau) L(\tau) d\tau \tag{3.13}$$

Alternatively, knowing the transfer function, $H_{hL}(\omega)$, the transform of the input force is determined from

$$L^{*}(\omega) = \frac{1}{2\pi} \int_{-\infty}^{\infty} L(t) e^{i\omega t} d\omega \tag{3.11}$$

and the response is calculated from

$$h(t) = \int_{-\infty}^{\infty} H_{hL}(\omega) L^{*}(\omega) e^{i\omega t} d\omega \tag{3.12}$$

Both approaches give the same result, of course.

As a simple example we consider the translation of our typical section for $S_\alpha \equiv 0$, i.e., the center of mass coincides with the elastic axis or spring attachment point. This uncouples the rotation from translation and we need only consider

$$m\ddot{h} + K_h h = -L \tag{3.1}$$

We assume a force of the form

$$\begin{aligned} L &= e^{-at} \quad \text{for} \quad t > 0 \\ &= 0 \quad \text{for} \quad t < 0 \end{aligned} \tag{3.16}$$

From our equation of motion (or (3.6) for $S_\alpha = x_\alpha = 0$) we determine the transfer function as

$$H_{hL}(\omega) = \frac{-1}{m[\omega_h^2 - \omega^2]}, \qquad \omega_h^2 \equiv K_h/m \tag{3.6}$$

From (3.14), using the above and evaluating the integral, we have

$$\begin{aligned} I_{hL}(t) &= \frac{1}{m\omega_h} \sin \omega_h t \quad \text{for} \quad t > 0 \\ &= 0 \quad \text{for} \quad t < 0 \end{aligned} \tag{3.17}$$

From (3.13), using above (3.17) for I_{hL} and given L, we obtain

$$h(t) = -\frac{1}{m\omega_h} \left\{ \frac{\omega_h e^{-at} - \omega_h \cos \omega_h t + a \sin \omega_h t}{a^2 + \omega_h^2} \right\} \tag{3.18}$$

We can obtain the same result using our alternative method. Calculating L^* from (3.11) for our given L, we have

$$L = \frac{1}{2\pi} \frac{1}{a + i\omega}$$

Using above and the previously obtained transfer function in (3.12) we obtain the response. The result is, of course, the same as that determined before. Note that in accordance with our assumption of a system initially at rest, $h = \dot{h} = 0$ at $t = 0$. Examining our solution, (3.18), for large time we see that

$$h \to -\frac{1}{m\omega_h} \left\{ \frac{-\omega_h \cos \omega_h t + a \sin \omega_h t}{a^2 + \omega_h^2} \right\} \quad \text{as} \quad t \to \infty$$

This indicates that the system continues to respond even though the force L approaches zero for large time! This result is quite unrealistic physically and is a consequence of our ignoring structural damping in our model. Had we included this

effect in our equation of motion using a conventional analytical damping model[7]

$$m[\ddot{h} + 2\zeta_n \omega_h \dot{h}] + K_h h = -L \tag{3.1}$$

the response would have been

$$h = \frac{1}{m\omega_h} \left\{ \frac{\omega_h e^{-at} + [-\omega_h \cos \omega_h t + a \sin \omega_h t] e^{-\zeta_h \omega_h t}}{a^2 + \omega_h^2} \right\} \tag{3.19}$$

for small damping, $\zeta_h \ll 1$, which is the usual situation. *Now* $h \to 0$, for $t \to \infty$. Furthermore, if the force persists for a long time, i.e., $a \to 0$, then

$$h(t) \to -\frac{1}{m\omega_h} \left\{ \frac{\omega_h}{\omega_h^2} \right\} = -\frac{1}{K_h}$$

which is the usual static or steady state response to a force of unit amplitude. The terms which approach zero for a large time due to structural damping are usually termed the transient part of the solution. If

$$a \ll \zeta_h \omega_h$$

the transient solution dies out rapidly compared to the force and we usually are interested in the steady state response. If

$$a \gg \zeta_h \omega_h$$

the 'impulsive' force dies out rapidly and we are normally interested in the transient response. Frequently the maximum response is of greatest interest. A well known result is that the peak Dynamic response is approximately twice the static response if the force persists for a long time and the damping is small. That is, if

$$\zeta_h \ll 1$$

$$a \ll \omega_h$$

then h_{max} occurs when (see (3.19))

$$\cos \omega_n t \cong -1 \quad \text{or} \quad t = \frac{\pi}{\omega_h}$$
$$\sin \omega_n t \cong 0$$

and

[7] Meirovicth [4].

$$h_{\max} = -\frac{1}{m\omega_h}\frac{\omega_h}{\omega_h^2}[1-(-1)]$$
$$= -\frac{2}{K_h}$$

The reader may wish to consider other special combinations of the relative sizes of

a force time constant
ω_h system natural time constant
$\zeta_h\omega_h$ damping time constant

A great deal of insight into the dynamics of linear systems can be gained thereby.

The question arises which of the two approaches is to be preferred. The answer depends upon a number of factors, including the computational efficiency and physical insight desired. Roughly speaking the second approach, which is essentially a frequency domain approach, is to be preferred when analytical solutions are to be attempted or physical insight based on the degree of frequency 'matching' or 'mismatching' of H_{hL} and L^* is desired. Clearly a larger response will be obtained if the maxima of H and L^* occur near the same frequencies, i.e., they are 'matched', and a lesser response will be obtained otherwise, i.e., the maxima are 'mismatched'. The first approach, which is essentially a time domain approach, is generally to be preferred when numerical methods are attempted and quantitative accuracy is of prime importance.

Other variations on these methods are possible. For example the transfer function, H_{hL}, and the impulse function, I_{hL}, may be determined experimentally. Also the impulse function may be determined directly from the equation of motion, bypassing any consideration of the transfer function. To illustrate this latter remark, consider our simple example

$$m\ddot{h} + K_h h = -L \tag{3.1}$$

The impulse function is the response for h due to $L(t) = \delta(t)$. Hence, it must satisfy

$$m\ddot{I}_{hl} + K_h I_{hl} = -\delta(t) \tag{3.20}$$

Let us integrate the above from $t = 0$ to ϵ.

$$\int_0^\epsilon [m\ddot{I}_{hl} + K_h I_{hl}]dt = -\int_0^\epsilon \delta(t)dt$$

or

$$m\dot{I}_{hl}|_0^\epsilon + K_h \int_0^\epsilon I_{hl}dt = -1$$

In the limit as $\epsilon \to 0^+$, we obtain the 'initial condition',

$$\dot{I}_{hl}(0^+) = -\frac{1}{m} \tag{3.21}$$

and also

$$\dot{I}_{hl}(0^+) = 0$$

Hence, solving (3.20) and using the initial velocity condition, (3.21), we obtain

$$I_{hl} = -\frac{1}{m\omega_h} \sin \omega_h t \quad \text{for} \quad t > 0 \tag{3.17}$$

which is the same result obtained previously.

Finally, all of these ideas can be generalized to many degrees of freedom. In particular using the concept of 'normal modes' any multi-degree-of-freedom system can be reduced to a system of uncoupled single-degree-of-freedom systems.[8] As will become clear, when aerodynamic forces are present the concept of normal modes which decouple the various degrees of freedom is not as easily applied and one must usually deal with all the degrees of freedom which are of interest simultaneously.

3.4 Random Motion

A random motion is by definition one whose response is neither repeatable nor whose details are of great interest. Hence attention is focused on certain averages, usually the mean value and also the mean square value. The mean value may be treated as a static loading and response problem and hence we shall concentrate on the mean square relations which are the simplest characterization of *random*, *dynamic* response.

Relationship between mean values. To see the equivalence between mean value Dynamic response and static response, consider

$$h(t) = \int_{-\infty}^{\infty} I_{hl}(t - \tau) L(\tau) d\tau \tag{3.13}$$

and take the mean of both sides (here a bar above the quantity denotes its mean, which should not be confused with that symbol's previous use in our discussion of sinusoidal motion). By definition

$$\bar{h} \equiv \lim \frac{1}{2T} \int_{-T}^{T} h(t) dt \quad \text{and thus}$$

$$\bar{h} = \lim \frac{1}{2T} \int_{-T}^{T} \int_{-\infty}^{\infty} I_{hl}(t - \tau) L(\tau) d\tau dt$$

Interchanging the order of integration and making a change of variables, the right hand side becomes

[8] Meirovitch [4].

$$\begin{aligned}\bar{h} &= \int_{-\infty}^{\infty} \{\lim \frac{1}{2T} \int_{-T}^{T} L(t-\tau)dt\} I_{hL}(\tau)d\tau \\ &= \bar{L} \int_{-\infty}^{\infty} I_{hl}(\tau)d\tau \\ &= \bar{L} H_{hl}(\omega = 0) \\ &= -\frac{\bar{L}}{K_h}\end{aligned}$$

which is just the usual static relationship between h and L. Unfortunately, no such simple relation exists between the *mean square* values. Instead all frequency components of the transfer function, H_{hl}, contribute. Because of this it proves useful to generalize the definition of a square mean.

Relationship between mean square values. A more general and informative quantity than the mean square, the correlation function, ϕ, can be defined as

$$\phi_{LL}(\tau) \equiv \lim \frac{1}{2T} \int_{-T}^{T} L(t)L(t+\tau)dt \tag{3.22}$$

The mean square of L, $\bar{L^2}$, is given by

$$\bar{L^2} = \phi_{LL}(\tau = 0) \tag{3.23}$$

As $\tau \to \infty$, $\phi_{LL} \to 0$ if L is truly a random function since $L(t)$ and $L(t+\tau)$ will be 'uncorrelated'. Indeed, a useful check on the randomness of L is to examine ϕ for large τ. Analogous to (3.22), we may define

$$\begin{aligned}\phi_{hh}(\tau) &\equiv \lim \frac{1}{2T} \int_{-T}^{T} h(t)h(t+\tau)dt \\ \phi_{hL}(\tau) &\equiv \lim \frac{1}{2T} \int_{-T}^{T} h(t)L(t+\tau)dt\end{aligned} \tag{3.24}$$

ϕ_{hL} is the 'cross-correlation' between h and L. ϕ_{hh} and ϕ_{LL} are 'autocorrelations'. The Fourier transform of the correlation function is also a quantity of considerable interest, the 'power spectra',

$$\Phi_{LL}(\omega) \equiv \frac{1}{\pi} \int_{-\infty}^{\infty} \phi_{LL}(\tau)e^{i\omega\tau}d\tau \tag{3.25}$$

(Note that a factor of two difference exists in (3.25) from the usual Fourier transform definition. This is by tradition.) From (3.25), we have

$$\begin{aligned}\phi_{LL}(\tau) &= \frac{1}{2}\int_{-\infty}^{\infty} \Phi_{LL}(\omega) e^{i\omega t} d\omega \\ &= \int_0^{\infty} \Phi_{LL}(\omega)\cos\omega\tau d\omega\end{aligned} \tag{3.26}$$

The latter follows since $\Phi_{LL}(\omega)$ is a real even function of ω. Note

$$\bar{L^2} = \phi_{LL}(0) = \int_0^{\infty} \Phi_{LL}(\omega) d\omega \tag{3.27}$$

Hence a knowledge of Φ_{LL} is sufficient to determine the mean square. It turns out to be most convenient to relate the power spectra of L to that of h and use (3.27) or its counterpart for h to determine the mean square values.

To relate the power spectra, it is useful to start with a substitution of (3.13) into the first of (3.24).

$$\begin{aligned}\phi_{hh}(\tau) = \lim \frac{1}{2T}\int_{-T}^{T} &\left\{\int_{-\infty}^{\infty} L(\tau_1) I_{hL}(t-\tau_1) d\tau_1\right\} \\ &\times \left\{\int_{-\infty}^{\infty} L(\tau_2) I_{hL}(t+\tau-\tau_2) d\tau_2\right\} dt\end{aligned}$$

Interchanging order of integrations and using a change of integration variables

$$\begin{aligned} t' &\equiv t - \tau_1; \qquad \tau_1 = t - t' \\ t'' &\equiv t + \tau - \tau_2; \qquad \tau_2 = t + \tau - t''\end{aligned}$$

we have

$$\phi_{hh} = \int_{-\infty}^{\infty}\int_{-\infty}^{\infty} I_{hL}(t') I_{hL}(t'') \phi_{LL}(\tau + t' - t'') dt' dt'' \tag{3.28}$$

Once could determine $\bar{h^2}$ from (3.28)

$$\bar{h^2} = \phi_{hh}(\tau = 0) = \int_{-\infty}^{\infty}\int_{-\infty}^{+\infty} I_{hL}(t') I_{hL}(t'') \phi_{LL}(t' - t'') dt' dt'' \tag{3.29}$$

However we shall proceed by taking the Fourier transform of (3.28).

$$\begin{aligned}\Phi_{hh} \equiv &\frac{1}{\pi}\int_{-\infty}^{\infty} \phi_{hh}(\tau) e^{-i\omega t} d\tau \\ = &\frac{1}{\pi}\iiint I_{hL}(t') I_{hL}(t'') \phi_{LL}(\tau + t' - t'') e^{-i\omega t} dt' dt'' d\tau \\ = &\frac{1}{\pi}\iiint I_{hL}(t') e^{+i\omega t'} I_{hL}(t'') e^{-i\omega t''} \\ &\times \phi_{LL}(\tau + t' - t'') \exp -i\omega(\tau + t' - t'') dt' dt'' d\tau\end{aligned}$$

Defining a new variable

$$\tau' \equiv \tau + t' - t''$$
$$d\tau' = d\tau$$

we see that

$$\boxed{\Phi_{hh}(\omega) = H_{hl}(\omega)H_{hl}(-\omega)\Phi_{LL}(\omega)} \tag{3.30}$$

One can also determine that

$$\begin{aligned} \Phi_{hL}(\omega) &= H_{hL}(-\omega)\Phi_{LL}(\omega) \\ \Phi_{hh}(\omega) &= H_{hL}(-\omega)\Phi_{hL}(\omega) \end{aligned} \tag{3.31}$$

Equation (3.30) is a powerful and well-known relation.[9] The basic procedure is to determine Φ_{LL} by analysis or measurement, compute Φ_{hh} from (3.30) and $\bar{h^2}$ from an equation analogous to (3.26)

$$\bar{h^2} = \int_0^\infty \Phi_{hh}(\omega)d\omega = \int_0^\infty |H_{hL}(\omega)|^2 \Phi_{LL}(\omega)d\omega \tag{3.32}$$

Let us illustrate the utility of the foregoing discussion by an example.

Example *Airfoil response to a gust.* Again for simplicity consider translation only.

$$m\ddot{h} + K_h h = -L \tag{3.1}$$

Also for simplicity assume quasi-steady aerodynamics.[10]

$$L = qS\frac{\partial C_L}{\partial \alpha}\left[\frac{\dot{h}}{U} + \frac{w_G}{U}\right] \tag{3.33}$$

w_G taken as positive up, is a vertical fluid 'gust' velocity, which varies randomly with time but is assumed here to be uniformly distributed spatially over the airfoil chord. Various transfer functions may be defined and calculated. For example

$$\frac{\bar{h}}{\bar{L}} \equiv H_{hL} = \frac{-1}{m[-\omega^2 + \omega_h^2]}, \qquad \omega_h^2 \equiv K_/m \tag{3.34}$$

is the structural transfer function[11] (motion due to lift) (cf. (3.6))

$$\frac{\bar{L}}{\bar{h}} \equiv H_{Lh} = qS\frac{\partial_C L}{\partial \alpha}\frac{i\omega}{U} \tag{3.35}$$

[9] Crandall and Mark [5].

[10] $\frac{\dot{h}}{U} + \frac{\omega_G}{U}$ is an effective angle of attack, α.

[11] Here we choose to use a dimensional rather than a dimensionless transfer function.

is the aerodynamic transfer function (lift due to motion)

$$\frac{\bar{L}}{\bar{w}_G} \equiv H_{Lw_G} = qS\frac{\partial_C L}{\partial\alpha}\frac{1}{U} \tag{3.36}$$

is the aerodynamic transfer function[12] (lift due to gust velocity field) and

$$H_{hw_G} \equiv \frac{\bar{h}}{\bar{w}_G} = \frac{-H_{Lw_G}}{\left[-\frac{1}{H_{hL}} + H_{Lh}\right]} \tag{3.37}$$

is the aeroelastic transfer function (motion due to gust velocity field).

The most general of these is the aeroelastic transfer function which may be expressed in terms of the structural and aerodynamic transfer functions, (3.37). Using our random force-response relations, we have from (3.32)

$$\begin{aligned}\bar{h^2} &= \int_0^\infty |H_{hw_G}|^2 \Phi_{w_G w_G} d\omega \\ &= \int_0^\infty \frac{\left[qS\frac{\partial C_L}{\partial\alpha}\frac{1}{U}\right]^2}{[-m\omega^2 + K_h]^2 + \left[qS\frac{\partial C_L}{\partial\alpha}\frac{\omega}{U}\right]^2}\Phi_{W_G W_G} d\omega\end{aligned}$$

Define an effective damping constant as

$$\zeta \equiv \frac{qS\frac{\partial C_L}{\partial\alpha}\frac{1}{U}}{2\sqrt{mK_h}} \tag{3.38}$$

then

$$\bar{h^2} = \frac{\left[qS\frac{\partial C_L}{\partial\alpha}\frac{1}{U}\right]^2}{m^2}\int_0^\infty \frac{\Phi_{w_G w_G} d\omega}{[-\omega^2 + \omega_h^2]^2 + 4\zeta^2\omega_h^2\omega^2}$$

which, for small ζ may be evaluate as[13]

$$\bar{h^2} \cong \frac{qS\frac{\partial C_L}{\partial\alpha}\pi}{2K_h}\frac{\Phi_{w_G w_G}(\omega = \omega_h)}{U} \tag{3.39}$$

Typically,[14]

---

[12] We ignore a subtlety here in the interest of brevity. For a 'frozen gust', we must take $\omega_G = \bar{\omega}_G \exp i\omega(t - x/U_\infty)$ in determining this transfer function. See later discussion in Sects. 6, 2 and 3.

[13] Crandell and Mark; the essence of the approximation is that for small ζ, $\Phi_{w_G w_G}(\omega) \cong \Phi w_G w_G(\omega_h)$ and maybe taken outside the integral. See the subsequent discussion of a graphical analysis.

[14] Houbolt, Steiner and Pratt [6]. Also see later discussion in Sect. 6.

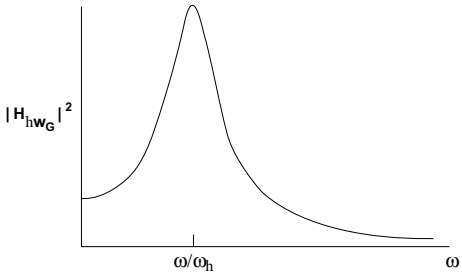

Fig. 4 Aeroelastic transfer function

$$\Phi_{w_G w_G}(\omega) = \bar{w}_G^2 \frac{L_G}{\pi U} \frac{1 + 3\left(\frac{\omega L_G}{U}\right)^2}{\left[1 + \left(\frac{\omega L_G}{U}\right)^2\right]^2} \tag{3.40}$$

as determined from experiment or considerations of the statistical theory of atmospheric turbulence. Here, L_G is the 'scale length of turbulence'; which is not to be confused with the lift force. Nondimensionalizing and using (3.39) and (3.40), we obtain

$$\frac{\bar{h}^2/b^2}{\bar{w}_G^2/U^2} = \frac{qS}{2} \frac{\frac{\partial C_L}{\partial \alpha}}{K_h b} \frac{\frac{\omega_h L_G}{U}}{\frac{\omega_h b}{U}} \left\{ \frac{1 + 3\left(\frac{\omega_h L_G}{U}\right)^2}{\left[1 + \left(\frac{\omega_h L_G}{U}\right)^2\right]^2} \right\} \tag{3.41}$$

Note as $\frac{\omega_h L_G}{U} \to 0$ or $\infty, \bar{h}^2/b^2 \to 0$. Recall L_G is the characteristic length associated with the random gustfield. Hence, for very large or very small characteristic lengths the airfoil is unresponsive to the gust. For what $\frac{\omega_h L_G}{U}$ does the largest response occur?

As an alternative to the above discussion, a correlation function approach could be taken where one uses the time domain and the aeroelastic impulse function.

$$\frac{I_{hw_G}}{b} = -\frac{qS \frac{\partial C_L}{\partial \alpha} \frac{1}{U} e^{-\zeta \omega_h t}}{m b \omega_h^2 \sqrt{1 - \zeta^2}} \sin \sqrt{1 - \zeta^2} \omega_h t \tag{3.42}$$

but we shall not pursue this here. Instead the frequency domain analysis is pursued further.

It is useful to consider the preceding calculation in graphical form for a moment. The (square of the) transfer function is plotted in Fig. 4. and the gust power spectral density in Fig. 5.

We note that the power spectral density is slowly varying with w relative to the square of the transfer function which peaks sharply near $\omega = \omega_h$. Hence one may, to a close approximation, take the power spectral density as a constant with its value determined at $\omega = \omega_h$ in computing the mean square response. This is a simple but powerful idea which carries over to many degrees-of-freedom, and hence many resonances, provided the resonant frequencies of the transfer function are known. For some aeroelastic systems, locating the resonances may prove difficult.

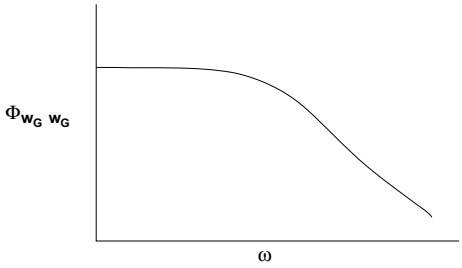

Fig. 5 Gust (auto) power spectral density

There are other difficulties with the approach which should be pointed out. First of all we note that including the (aerodynamic) damping due to motion is necessary to obtain a physically meanful result.Without it the computed response would be infinite! Hence, an accurate evaluation of the effective damping for an aeroelastic system is essential in random response studies. It is known that in general the available aerodynamic theories are less reliable for evaluating the (out-of-phase with displacement) damping forces than those forces in-phase with displacement.[15] Another difficulty may arise if instead of evaluating the mean square displacement response we instead seek to determine the mean square of acceleration. The latter quantity is frequently of greater interest from the standpoint of design. The relevant transfer function is given by

$$H_{\ddot{h}w_G} = (i\omega)^2 H_{hw_G} \tag{3.43}$$

and the mean square is therefore

$$\ddot{h}^2 = \frac{\int_0^\infty \omega^4 \left[qS\frac{\partial C_L}{\partial \alpha}\frac{1}{U}\right]^2 \Phi_{w_G w_G} d\omega}{[-m\omega^2 + K_n]^2 + \left[qS\frac{\partial C_L}{\partial \alpha}\frac{\omega}{U}\right]^2} \tag{3.44}$$

If we make the same approximation as before that $\Phi_{w_G w_G}$ is a constant, we are in difficulty because $|H_{\ddot{h}w_G}|^2$ does not approach zero as $\omega \to \infty$ and hence the integral formally diverges. This means greater care must be exercised in evaluating the integral and in particular considering the high frequency behavior of the gust power spectral density. Also, one may need to use a more elaborate aerodynamic theory. In the present example we have used a quasi-steady aerodynamic theory which is reasonably accurate for low frequencies;[16] however, to evaluate the acceleration response it will frequently be necessary to use a full unsteady aerodynamic theory in order to obtain accurate results a high frequencies in (3.44).

Measurement of power spectra. We briefly digress to consider an important application of (3.27) to the experimental determination of power spectra. For definiteness consider the measurement of gust power spectra. Analogous to (3.27) we have

[15] Acum [7].

[16] Acum [7].

$$\bar{w}_G^2 = \int_0^\infty \Phi_{w_G w_G}(\omega) d\omega \tag{3.45}$$

It is assumed that a device is available to measure w_G over a useful range of frequencies. The electronic signal from this device is then sent to an electronic 'filter'. The latter, in its most ideal form, has a transfer function given by

$$\begin{aligned} H_{Fw_G} &= 1 \quad \text{for} \quad \omega_c - \frac{\Delta\omega}{2}\omega < \omega_c + \frac{\Delta\omega}{2} \\ &= 0 \ \text{ otherwise} \\ \text{where } \omega_c &\equiv \omega_c \text{center frequency of the filter} \\ \Delta\omega &\equiv \ \text{frequency bandwidth of the filter} \end{aligned} \tag{3.46}$$

Now if we assume that the power spectrum varies slowly with w and we choose a filter with $\Delta\omega \ll \omega_c$, then (3.45) may be approximated by taking $\Phi_{w_G w_G}(\omega) \cong \Phi_{w_G w_G}(\omega_c)$ and moving it outside the integral. The result is

$$\bar{w}_G^2 \cong \Phi_{w_G w_G}(\omega_c)\Delta\omega$$

Solving for the power spectrum,

$$\Phi_{w_G w_G}(\omega_c) = \frac{\bar{w}_G^2}{\Delta\omega} \tag{3.47}$$

By systematically changing the filter center frequency, the power spectrum may be determined over the desired range of frequency. The frequency bandwidth, $\Delta\omega$, and the time length over which $\bar{w}_G^2$ is calculated must be chosen with care. For a discussion of these matters, the reader may consult Crandall and Mark [5], and references cited therein.

For a more extensive discussion of random motion of two-dimensional plate-like structures with many degrees of freedom, see Appendix I, 'A Primer for Structural Response to Random Pressure Fluctuations'.

3.5 *Flutter—An Introduction to Dynamic Aeroelastic Instability*

The most dramatic physical phenomenon in the field of aeroelasticity is flutter, a dynamic instability which often leads to catastrophic structural failure. One of the difficulties in studying this phenomenon is that it is not one but many. Here we shall introduce one type of flutter using the typical section structural model and a *steady flow* aerodynamic model. The latter is a highly simplifying assumption whose accuracy we shall discuss in more detail later. From (3.1) and with a steady

aerodynamic model, $L = qS\frac{\partial C_L}{\partial \alpha}\alpha$, $M_y = eL$, the equations of motion are

$$\begin{aligned} m\ddot{h} + S_\alpha \ddot{\alpha} + K_h h + qS\frac{\partial C_L}{\partial \alpha}\alpha = 0 \\ I_\alpha \ddot{\alpha} + S_\alpha \ddot{h} + K_\alpha \alpha - qSe\frac{\partial C_L}{\partial \alpha}\alpha = 0 \end{aligned} \tag{3.48}$$

To investigate the stability of this system we assume solutions of the form

$$\begin{aligned} h &= \bar{h}e^{pt} \\ \alpha &= \bar{\alpha}e^{pt} \end{aligned} \tag{3.49}$$

and determine the possible values of p, which are in general complex numbers. If the real part of any value of p is positive, then the motion diverges exponentially with time, (cf. (3.49)), and the typical section is unstable.

To determine p, substitute (3.49) into (3.48) and use matrix notation to obtain

$$\begin{bmatrix} [mp^2 + K_h] & S_\alpha p^2 + qS\frac{\partial C_L}{\partial \alpha} \\ S_\alpha p^2 & I_\alpha p^2 + K_\alpha - qSe\frac{\partial C_L}{\partial \alpha} \end{bmatrix} \begin{Bmatrix} \bar{h}e^{pt} \\ \bar{\alpha}e^{pt} \end{Bmatrix} = \begin{Bmatrix} 0 \\ 0 \end{Bmatrix} \tag{3.50}$$

For nontrivial solutions the determinant of coefficients is set to zero which determines p, viz.

$$Ap^4 + Bp^2 + C = 0 \tag{3.51}$$

where

$$\begin{aligned} A &\equiv mI_\alpha - S_\alpha^2 \\ B &\equiv m\left[K_\alpha - qSe\frac{\partial C_L}{\partial \alpha}\right] + K_h I_\alpha - S_\alpha qS\frac{\partial C_L}{\partial \alpha} \\ C &\equiv K_h\left[K_\alpha - qSe\frac{\partial C_L}{\partial \alpha}\right] \end{aligned}$$

Solving (3.51)

$$p^2 = \frac{-B \pm [B^2 - 4AC]^{\frac{1}{2}}}{2A} \tag{3.52}$$

and taking the square root of (3.52) determines p.

The signs of A, B and C determine the nature of the solution. A is always positive for any distribution of mass; C is positive as long as q is less than its divergence value, i.e.

$$\left[K_\alpha - qSe\frac{\partial C_L}{\partial \alpha}\right] > 0$$

which is the only case of interest as far as flutter is concerned. B may be either positive or negative; re-writing

$$B + mK_\alpha + K_h I_\alpha - [me + S_\alpha] q Se \frac{\partial C_L}{\partial \alpha} \tag{3.53}$$

If $[me + S_\alpha] < 0$ then $B > 0$ for all q. Otherwise $B < 0$ when

$$K_\alpha + \frac{K_h I_\alpha}{m} - \left[1 + \frac{S_\alpha}{me}\right] q Se \frac{\partial C_L}{\partial \alpha} < 0$$

Consider in turn two possibilities, $B > 0$ and $B < 0$.
$B > 0$: Then the values of p^2 from (3.52) are real and negative provided

$$B^2 - 4AC > 0$$

and hence the values of p are purely imaginary, representing neutrally stable oscillations. On the other hand if

$$B^2 - 4AC < 0$$

the values of p^2 are complex and hence at least one value of p will have a positive real part indicating an unstable motion. Thus

$$B^2 - 4AC = 0 \tag{3.54}$$

gives the boundary between neutrally stable and unstable motion. From (3.54) one may compute an explicit value of q at which the dynamic stability, 'flutter', occurs, i.e.,

$$Dq_F^2 + Eq_F + F = 0$$

$$\text{or} \qquad q_F = \frac{-E \pm [E^2 - 4DF]^{\frac{1}{2}}}{2D} \tag{3.55}$$

where

$$D \equiv \left\{[me + S_\alpha] S \frac{\partial C_L}{\partial \alpha}\right\}^2$$

$$E \equiv \{-2[me + S_\alpha][mK_\alpha + K_h I_\alpha] + 4[mI_\alpha - S_\alpha^2] eK_h\} S \frac{\partial C_L}{\partial \alpha}$$

$$F = [mK_\alpha + K_h I_\alpha]^2 - 4[mI_\alpha - S_\alpha^2] K_h K_\alpha$$

In order for flutter to occur at least one of the q_F determined by (3.55) must be real and positive. If both are, the smaller of the two is the more critical; if neither are, flutter does not occur. Pines[17] has studied this example in some detail and derived a number of interesting results. Perhaps the most important of these is that for

[17] Pines [8].

$$S_\alpha \leq 0$$

i.e., the center of gravity is ahead of the elastic axis, no flutter occurs. Conversely as S_α increases in a positive sense the dynamic pressure at which flutter occurs q_F is decreased. In practice, mass is often added to a flutter prone structure so as to decrease S_α and raise q_F. Such a structure is said to have been 'mass balanced'. Now consider the other possibility for B.

$B < 0$: B is positive for $q \equiv 0$ (cf. (3.51) et. seq.) and will only become negative for sufficiently large q. However, the condition

$$B^2 - 4AC = 0$$

will occur before

$$B = 0$$

since $A > 0$, $C > 0$. Hence, to determine when flutter occurs, only $B > 0$ need be considered.

In concluding this discussion, let us study the effect of S_α in more detail following Pines.

Consider the first special case $S_\alpha = 0$. Then

$$D = \left[meS \frac{\partial C_L}{\partial \alpha} \right]^2$$

$$E = 2me\{I_\alpha K_h - mK_\alpha\} S \frac{\partial C_L}{\partial \alpha}$$

$$F = \{mK_\alpha - K_h I_\alpha\}^2$$

and one may show that

$$E^2 - 4DF = 0$$

Using this result and also (3.55) and (2.18), it is determined that

$$q_F/q_D = 1 - \omega_h^2/\omega_\alpha^2 \tag{3.56}$$

Thus if $q_d < 0$ and $\omega_h/\omega_\alpha < 1$, $q_F < 0$, i.e., no flutter will occur. Conversely if $q_D > 0$ and $\omega_h/\omega_\alpha > 1$, then $q_F < 0$ and again no flutter will occur.

Now consider the general case, $S_\alpha \neq 0$. Note that $D > 0$ and $F > 0$ for all parameter values. Thus from (3.55), $q_F < 0$ if $E > 0$ and no flutter will occur. After some rearrangement of the expression for E, it is found that (in non-dimensional form)

$$\bar{E} \equiv E/\left(2m^2 I_\alpha \omega_\alpha^2 S \frac{\partial C_L}{\partial \alpha}\right) = e\left[-1 + (\omega_h/\omega_\alpha)^2 - 2\frac{x_{cg}^2}{r_{cg}^2}(\omega_h/\omega_\alpha)^2\right] - x_{cg}\left[1 + (\omega_h/\omega_\alpha)^2\right] \tag{3.57}$$

From this equation, the condition for no flutter, $E > 0$ or $\bar{E} > 0$, gives the following results.

- If $x_{cg} = 0$, then no flutter occurs for $e > 0$ and $\omega_h/\omega_\alpha > 1$ or for $e < 0$ and $\omega_h/\omega_\alpha < 1$.
- If $e = 0$, then no flutter occurs for $x_{cg} < 0$ and any ω_h/ω_α.
- For small x_{cg}, i.e., if

$$x_{cg}^2/r_{cg}^2 \ll 1$$

then $\bar{E} > 0$ implies

$$e\frac{[-1 + (\omega_h/\omega_\alpha)^2]}{[1 + (\omega_h/\omega_\alpha)^2]} - x_{cg} > 0$$

For ω_h/ω_α small (the usual case), this implies

$$-e - x_{cg} > 0$$

while for w_h/w_α large, this implies

$$e - x_{cg} > 0$$

as the conditions for no flutter.

3.6 Quasi-Steady, Aerodynamic Theory

Often it is necessary to determine p by numerical methods as a function of q in order to evaluate flutter. For example, if one uses the slightly more complex 'quasi-steady' aerodynamic theory which includes the effective angle of attack contribution, $\dot{h}/U$, so that

$$qS\frac{\partial C_L}{\partial \alpha}\alpha$$

becomes

$$qS\frac{\partial C_L}{\partial \alpha}\left[\alpha + \frac{\dot{h}}{U}\right] = \rho\frac{US}{2}\frac{\partial C_L}{\partial \alpha}[U\alpha + \dot{h}]$$

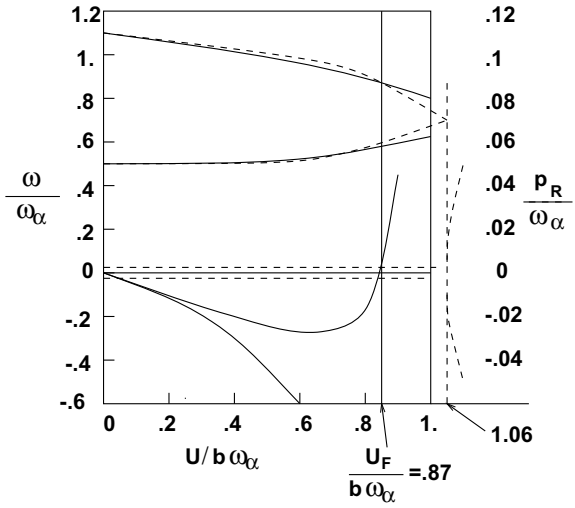

Fig. 6 Dimensionless frequency ω/ω_α and damping p_R/ω_α of the aeroelastic modes of the typical section, estimated using steady-state aerodynamic operators and plotted versus reduced airspeed $U/b\omega_\alpha$. System parameters are $x_\alpha = 0.2,\ r_\alpha = 0.5,\ \omega_h/\omega_\alpha = 0.5,\ (2m/\pi\rho_\infty bS) = 10,\ e/b = 0.4,\ \frac{\partial C_L}{\partial\alpha} = 2\pi$. Solid curves − with aerodynamic damping. Dashed curves—without aerodynamic damping

then (3.51) will contain terms proportional to p and p^3 and the values of p must be determined numerically. An example of such a calculation is given in Fig. 30 of B.A. which is reproduced below as Fig. 6.

Denote

$$p = p_R + i\omega$$
$$\omega_h^2 \equiv K_h/m,\ \omega_\alpha^2 \equiv K_\alpha/I_\alpha$$
$$x_\alpha \equiv S_\alpha/mb,\ r_\alpha^2 \equiv I_\alpha/mb^2$$
$$b = \text{a reference length}$$

Since the values of p are complex conjugates only half of them are shown. The solid lines are for the $\dot{h}/U$ or aerodynamic damping effect included and the dash lines for it omitted. There are several interesting points to be made.

(1) With aerodynamic damping omitted the typical section model is neutrally stable until $U = U_F$. For $U = U_F$ the bending and torsion frequencies merge and for $U > U_F$ the system is unstable.
(2) With aerodynamic damping included, for small U all values of p are stable and flutter occurs at sufficiently large U where p_R changes sign from negative to positive. There is a tendency for the frequencies to merge but complete merging does not occur.
(3) *In this example for this approximate aerodynamic theory*, the addition of aerodynamic damping reduces the flutter velocity U_F. This last result has been a source of consternation (and research papers). Whether it occurs in the real physical problem or whether it is a consequence of our simplified theoretical model is not known. No experiment has yet been performed where the aerodynamic (or structural) damping has been systematically varied to verify or refute this result.

Finally we mention one further general complication which commonly occurs in analysis. When even more elaborate, fully unsteady aerodynamic theories are employed, the aerodynamic forces are usually only conveniently known for neutrally stable motion, i.e.,

$$p = i\omega, \qquad p_R \equiv 0$$

Hence, indirect or iterative methods are usually required to effect a solution for $U = U_F$ and often no information is obtained for $U < U_F$ or $U > U_F$. We shall return to this issue later.

4 Aerodynamic Forces for Airfoils-An Introduction and Summary

Having developed the mathematical tools for treating the dynamics of our aeroelastic system, we now turn to a topic previously deferred, the determination of the aerodynamic forces. Usually, we wish to relate the aerodynamic lift and moment to the motion of the airfoil. In order not to break unduly the continuity of our discussion of aeroelastic phenomena, we give a brief summary of known results here and defer a discussion of the aerodynamic theory from first principles until chapter 'Nonsteady Aerodynamics of Lifting and Non-lifting Surfaces'.

From aerodynamic theory we know that the motion appears in the aerodynamic force relation through the 'downwash', w_a i.e.,

$$w_\alpha \equiv \frac{\partial z_a}{\partial t} + U_\infty \frac{\partial z_a}{\partial x} \tag{4.1}$$

where z_a is vertical displacement of airfoil at point x, y at time t. We shall not give a formal derivation of (4.1) here but shall indicate the physical basis from which it follows. For an inviscid fluid the boundary condition at a fluid-solid interface, e.g., at the surface of an airfoil, requires that the fluid velocity component normal to the surface be equal to the normal velocity of the surface on the instantaneous position of the surface. (If we have a nearly planar solid surface undergoing small motions relative to its own dimensions we may apply the boundary condition on some average position of the body, say $z = 0$, rather than on the instantaneous position of the surface, $z = z_a$.) In a coordinate system fixed with respect to the fluid the boundary condition would read

$$w_a = \frac{\partial z_a}{\partial t}$$

where w_a is the normal fluid velocity component, the so-called 'downwash', and $\frac{\partial z_a}{\partial t}$ is the normal velocity of the body surface. In a coordinate system fixed with respect to the body there is an additional convection term as given in (4.1). This may be derived by a formal transformation from fixed fluid to fixed body axes.

Finally if in addition to the mean flow velocity, U_∞, we also have a vertical gust velocity, w_G, then the boundary condition is that the total normal fluid velocity at the body surface be equal to the normal body velocity, i.e.,

$$w_{\text{total}} \equiv w_a + w_G = \frac{\partial z_a}{\partial t} + U_\infty \frac{\partial z_a}{\partial x}$$

where w_a is the additional fluid downwash due to the presence of the airfoil beyond that given by the prescribed gust downwash w_G. The pressure loading on the airfoil is

$$p + p_G$$

where p is the pressure due to

$$w_a = -w_G(x,t) + \frac{\partial z_a}{\partial t} + U_\infty \frac{\partial z_a}{\partial x}$$

and p_G is the prescribed pressure corresponding to the given w_G. Note, however, that p_G is continuous through $z = 0$ and hence gives no net pressure loading on the airfoil. Thus, only the pressure p due to downwash w_a is of interest in most applications.

For the typical section airfoil example,

$$z_a = -h - \alpha x \tag{4.2}$$

and

$$w_a = \underbrace{-w_G - \dot{h} - \dot{\alpha} x - U_\alpha}\, \alpha$$

From the first and last terms we note that $\frac{w_G}{U_\infty}$ is in some sense equivalent to an angle of attack, although it is an angle of attack which varies with position along the airfoil, $w_G = w_G(x,t)$!

Using the concept of aerodynamic impulse functions, we may now relate lift and moment to h, α and w_G. For simplicity let us neglect w_G for the present.

The aerodynamic force and moment can be written

$$\begin{aligned} L(t) \sim & \int_{-\infty}^{\infty} I_{L\dot{h}}(t-\tau)[\dot{h}(\tau) + U_\infty \alpha(\tau)]d\tau \\ & + \int_{-\infty}^{\infty} I_{L\dot{\alpha}}(t-\tau)\dot{\alpha}(\tau)d\tau \end{aligned} \tag{4.3}$$

Equation (4.3) is the aerodynamic analog to (3.13). Note that $\dot{h} + U_\infty \alpha$ always appear in the same combination in w_a from (4.2). It is conventional to express (4.3) in nondimensional form. Thus,

$$\frac{L}{qb} = \int_{-\infty}^{\infty} I_{L\dot{h}}(s-\sigma)\left[\frac{d\frac{h}{b}(\sigma)}{d\sigma} + \alpha(\sigma)\right]d\sigma + \int_{-\infty}^{\infty} I_{L\dot{\alpha}}(s-\sigma)\left[\frac{d\alpha(\sigma)}{d\sigma}\right]d\sigma \tag{4.4}$$

and

$$\frac{M_y}{qb^2} = \int_{-\infty}^{\infty} I_{M\dot{h}}(s-\sigma)\left[\frac{d\frac{h}{b}(\sigma)}{d\sigma} + \alpha(\sigma)\right]d\sigma + \int_{-\infty}^{\infty} I_{M\dot{\alpha}}(s-\sigma)\left[\frac{d\alpha(\sigma)}{d\sigma}\right]d\sigma$$

where

$$s \equiv \frac{tU_\infty}{b}, \qquad \sigma \equiv \frac{\tau U_\infty}{b}$$

For the typical section, the 'aerodynamic impulse functions', $I_{L|doth}$, etc., depend also upon Mach number. More generally, for a wing they vary with wing platform geometry as well, e.g., aspect ratio.

Equation (4.4) may be used to develop relations for sinusoidal motion by reversing the mathematical process which led to (3.13). Taking the Fourier transform of (4.4),

$$\frac{\bar{L}(k)}{qb} \equiv \int_{-\infty}^{\infty} \frac{L(s)}{qb} e^{-iks} ds = \int_{-\infty}^{\infty}\int_{-\infty}^{\infty} I_{L\dot{h}}(s-\sigma)\left[\frac{d\frac{h}{b}}{d\sigma} + \alpha\right] e^{-iks} d\sigma ds + \cdots \tag{4.5}$$

where the *reduced frequency* is given by

$$k \equiv \frac{\omega b}{U_\infty}$$

Defining

$$\gamma \equiv s - \sigma, \qquad d\gamma = ds$$

$$\frac{\bar{L}(k)}{qb} = \int_{-\infty}^{\infty}\int_{-\infty}^{\infty} I_{L\dot{h}}(\gamma)\left[\frac{d\frac{h}{b}}{d\sigma} + \alpha\right] e^{-ik\gamma} e^{ik\sigma} d\sigma\, d\gamma + \cdots = H_{L\dot{h}}(k)\left[ik\frac{\bar{h}}{b} + \bar{\alpha}\right] + \cdots \tag{4.6}$$

where

$$H_{L\dot{h}}(k) \equiv \int_{-\infty}^{\infty} I_{L\dot{h}}(\gamma) e^{-ik\gamma} d\gamma$$
$$\frac{\bar{h}}{b} \equiv \int_{-\infty}^{\infty} \frac{h(\sigma)}{b} e^{-ik\sigma} d\sigma$$
$$\bar{\alpha} \equiv \int_{-\infty}^{\infty} \alpha(\sigma) e^{-ik\sigma} d\sigma$$

$H_{L\dot{h}}$ etc., are 'aerodynamic transfer functions'. From (4.4), (4.6) we may write

$$\begin{aligned} \frac{\bar{L}}{qb} &= H_{L\dot{h}} \left[ik\frac{\bar{h}}{b} + \bar{\alpha} \right] + H_{L\dot{\alpha}} ik\bar{\alpha} \\ \frac{\bar{M}_y}{qb^2} &= H_{M\dot{h}} \left[ik\frac{\bar{h}}{b} + \bar{\alpha} \right] + H_{M\dot{\alpha}} ik\bar{\alpha} \end{aligned} \tag{4.7}$$

Remember that 'transfer functions', aerodynamic or otherwise, may be determined from a consideration of sinusoidal motion only. Also note that (4.2), (4.3) and (4.7) are written for pitching about an axis $x = 0$. That is, the origin of the coordinate system is taken as the pitch axis. By convention, in aerodynamic analysis the origin of the coordinate system is usually taken at mid-chord. Hence

$$z_a = -h - \alpha(x - x_{e.a.}) \tag{4.2}$$
$$w_a = -\dot{h} - \dot{\alpha}(x - x_{e.a.}) - U_\infty \alpha$$
$$= (-\dot{h} - U_\infty \alpha) - \dot{\alpha}(x - x_{e.a.})$$
$$= (\dot{h} - U_\alpha \alpha + \dot{\alpha} x_{e.a.}) - \dot{\alpha} x$$

where

$x_{e.a.}$ = distance form mid-chord to e.a.

Equation (4.4) and (4.7) should be modified accordingly, i.e.

$$\frac{d\frac{h}{b}}{d\sigma} + \alpha$$

is replaced by

$$\frac{d\frac{h}{b}}{d\sigma} + \alpha - \dot{\alpha} a \quad \text{where} \quad a \equiv \frac{x_{e.a.}}{b}$$

In the following table we summarize the state-of-the-art for the aerodynamic theories normally used in industrial practice in terms of Mach number range and geometry. All of these assume inviscid, small perturbation potential flow models. The transonic range, $M \approx 1$, is a currently active area of research.

4.1 Aerodynamic Theories Available

Mach number	Two dimensional	Geometry three dimensional
$M \ll 1$	Available	Rather elaborate numerical methods available for determining transfer functions
$M \approx 1$	Available but of limited utility because of inherent three dimensionality of flow	Rather elaborate numerical methods available for determining (linear, inviscid) transfer functions; nonlinear and/or viscous effects may be important, however.
$M \gg 1$	Available and simple because of weak memory effect.	Available and simple because of weak three dimensional effects.

The results for high speed ($M \gg 1$) flow are particularly simple. In the limit of large Mach number the (perturbation) pressure loading on an airfoil is given by

$$p = \rho \frac{U_\infty^2}{M} \left[\frac{\frac{\partial z_a}{\partial t} + U_\infty \frac{\partial z_a}{\partial x}}{U_\infty} \right]$$

or

$$p = \rho a_\infty \left[\frac{\partial z_a}{\partial t} + U_\infty \frac{\partial z_a}{\partial x} \right]$$

This is a local, zero memory relation in that the pressure at position x, y at time t depends only on the motion at the same position and time and does *not* depend upon the motion at other positions (local effect) or at previous times (zero memory effect). This is sometimes referred to as aerodynamic 'piston theory'[18] since the pressure is that on a piston in a tube with velocity

$$w_a = \frac{\partial z_a}{\partial t} + U_\infty \frac{\partial z_a}{\partial x}$$

This pressure-velocity relation has been widely used in recent years in aeroelasticity and is also well known in one-dimensional plane wave acoustic theory. Impulse and transfer functions are readily derivable using aerodynamic 'piston theory'.

The 'aerodynamic impulse functions' and 'aerodynamic transfer functions' for two-dimensional, incompressible flow, although not as simple as those for $M \gg 1$,

[18] Ashley, and Zartarian [9]. Also see chapter 'Nonsteady Aerodynamics of Lifting and Non-lifting Surfaces'.

are especially well-known.[19] They were the first available historically and provided a major impetus to aeroelastic investigations. The forms normally employed are somewhat different from the notation of (4.4) and (4.7). For example, the lift due to transient motion is normally written

$$\begin{aligned}\frac{L}{qb} &= 2\pi\left[\frac{d^2\frac{h}{b}}{ds^2}+\frac{d\alpha}{ds}-a\frac{d^2\alpha}{ds^2}\right]\\ &\quad+4\pi\left\{\phi(0)\left[\frac{d\frac{h}{b}}{ds}+\alpha+\left(\frac{1}{2}-a\right)\frac{d\alpha}{ds}\right]\right.\\ &\quad\left.+\int_0^s\left(\frac{d\frac{h}{b}}{d\sigma}+\alpha+\left(\frac{1}{2}-a\right)\frac{d\alpha}{d\sigma}\right)\dot{\phi}(s-\sigma)d\sigma\right\}\end{aligned} \tag{4.8}$$

One can put (4.8) into the form of (4.4) where

$$\begin{aligned}I_{Lh} &= 2\pi D+4\pi\dot{\phi}+4\pi\phi(0)\delta\\ I_{L\dot{\alpha}} &= 4\pi\left(\frac{1}{2}-a\right)\dot{\phi}+4\pi\left(\frac{1}{2}-a\right)\phi(0)\delta-2\pi aD\end{aligned} \tag{4.9}$$

Here δ is the delta function and D the doublet function, the latter being the derivative of a delta function. In practice, one would use (4.8) rather than (4.4) since delta and doublet functions are not suitable for numerical integration, etc. However, (4.8) and (4.4) are formally equivalent using (4.9) Note that (4.8) is more amenable to physical interpretation also. The terms outside the integral involving $\ddot{h}$ and $\ddot{\alpha}$ may be identified as inertial terms, sometimes called 'virtual mass' terms. These are usually negligible compared to the inertial terms of the airfoil itself if the fluid is air.[20] The quantity

$$-\left[\frac{d\frac{h}{b}}{ds}+\alpha+\left(\frac{1}{2}-a\right)\frac{d\alpha}{ds}\right]$$

may be identified as the downwash at the $\frac{3}{4}$ chord. Hence, the $\frac{3}{4}$ chord has been given a special place for two-dimensional, incompressible flow. Finally, note that the 'aerodynamic impulse functions', I_{Lh}, I_{Li}, can be expressed entirely in terms of a single function ϕ, the so-called Wagner function.[21] This function is given below in Fig. 7. A useful approximate formulae is

$$\phi(s) = 1-0.165e^{-0.0455s}-0.335e^{0.3s} \tag{4.10}$$

[19] See chapter 'Nonsteady Aerodynamics of Lifting and Non-lifting Surfaces'.

[20] For light bodies or heavy fluids, e.g., lighter-than-airships or submarines, they may be important.

[21] For a clear, concise discussion of transient, two-dimensional, incompressible aerodynamics, see Sears [10], and the discussion of Sears' work in BAH, pp. 288–293.

Fig. 7 Wagner function

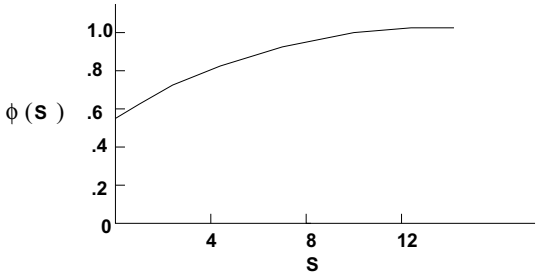

Fig. 8 Kussner function

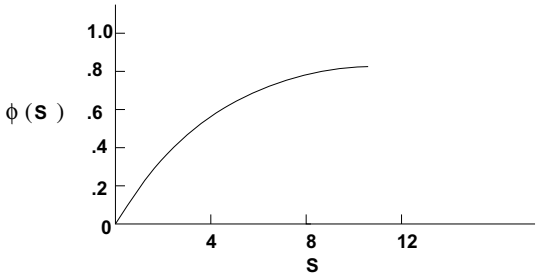

For Mach numbers greater than zero, the compressibility of the flow smooths out the delta and doublet functions of (4.9) and no such simple form as (4.8) exists. Hence, only for incompressible flow is the form, (4.8), particularly useful. Finally, we should mention that analogous impulse functions exist for gust loading due to gust vertical velocity, w_G.

$$\begin{aligned} \frac{L_G}{qb} &= \oint_{-\infty}^{\infty} I_{LG}(s-\sigma)\frac{w_G(\sigma)}{U}d\sigma \\ \frac{M_{yG}}{qb^2} &= \int_{-\infty}^{\infty} I_{MG}(s-\sigma)\frac{w_G(\sigma)}{U}d\sigma \end{aligned} \tag{4.11}$$

For incompressible flow

$$I_{LG} = 4\pi\dot{\psi}$$

$$I_{MG} = I_{LG}\left(\frac{1}{2}+a\right)$$

where ψ, the Kussner function, can be approximated by (See Fig. 8)

$$\psi(s) = 1 - 0.5e^{-0.13s} - 0.5e^{-s} \tag{4.12}$$

The Wagner and Kussner functions have been widely employed for transient aerodynamic loading of airfoils. Even for compressible, subsonic flow they are frequently used with empirical corrections for Mach number effects. Relatively simple, exact

formulae exist for two-dimensional, supersonic flow also.[22] However, for subsonic and/or three-dimensional flow the aerodynamic impulse functions must be determined by fairly elaborate numerical means. Finally we note that (4.11) may be written in the frequency domain as

$$\begin{aligned} \frac{\bar{L}_G}{qb} &= H_{LG}(\omega)\frac{\bar{w}_G}{U} \\ \frac{\bar{M}_y}{qb^2} &= H_{MG}(\omega)\frac{\bar{w}_G}{U} \end{aligned} \tag{4.13}$$

Equations (4.7) and (4.13) will be useful when we treat the gust problem as a random process and make use of power spectral techniques. For further discussion of gust aerodynamics, see Sects. 2 and 3.

4.2 General Approximations

Frequently simplifying assumptions are made with respect to the spatial or temporal dependence of the aerodynamic forces. Here we discuss three widely used approximations.

4.2.1 'Strip Theory' Approximation

In this approximation, one employs the known results for two-dimensional flow (infinite span airfoil) to calculate the aerodynamic forces on a lifting surface of finite span. The essence of the approximation is to consider each spanwise station as though it were a portion of an infinite span wing with uniform spanwise properties. Therefore the lift (or, more generally, chordwise pressure distribution) at any spanwise station is assumed to depend only on the downwash at that station as given by two-dimensional aerodynamic theory and to be independent of the downwash at any other spanwise station.

4.2.2 'Quasisteady' Approximation

The strip theory approximation discussed above is unambiguous and its meaning is generally accepted. Unfortunately, this is not true for the quasi-steady approximation. Its qualitative meaning is generally accepted, i.e., one ignores the temporal memory effect in the aerodynamic model and assumes the aerodynamic forces at any time depend only on the motion of the airfoil at that same time and are independent of

[22] See BAH, pp. 367–375, for a traditional approach and chapter 'Nonsteady Aerodynamics of Lifting and Non-lifting Surfaces' for an approach via Laplace and Fourier Transforms.

the motion at earlier times. That is, the history of the motion is neglected as far as determining aerodynamic forces. For example, the piston theory aerodynamic approximation is inherently a quasi-steady approximation.

As an example of the ambiguity that can develop in constructing a quasi-steady approximation, consider the aerodynamic forces for two-dimensional, incompressible flow, e.g., see (4.8). One such approximation which is sometimes used is to approximate the Wagner function by

$$\phi = 1$$

and hence

$$\phi(0) = 1, \quad \dot{\phi} = 0$$

This is clearly a quasi-steady model since the convolution integral in (4.8) may now be evaluated in terms of the airfoil motion at the present time, $s \equiv \frac{tU_\infty}{b}$, and thus the aerodynamic forces are independent of the history of the airfoil motion.

An alternate quasi-steady approximation which is used on occasion is to first obtain the aerodynamic forces for steady motion, e.g., only those terms which involve α in (4.8)and then to define an equivalent unsteady angle of attack.

$$\alpha + \frac{dh}{dt}\frac{1}{U_\infty}$$

to replace α everywhere in the steady aerodynamic theory. Clearly this second quasi-steady approximation is different from the first. (An interesting and relatively short exercise for the reader is to work out and compare these two approximations in detail using (4.8).) However, both are used in practice and the reader should be careful to determine exactly what a given author means by 'quasi-steady approximation'.

The ambiguity could be removed if there were general agreement that what is meant by the quasi-steady approximation is an expansion in reduced frequency for sinusoidal airfoil motion. However, even then, there would have to be agreement as to the number of terms to be retained in the expansion. (Recall that powers of frequency formally correspond to time derivatives.)

4.3 Slender Body or Slender (Low Aspect Ratio) Wing Approximation

Another approximation based upon spatial considerations is possible when the lifting surface is of low aspect ratio or one is dealing with a slender body. In such cases the chordwise spatial rates of change (derivatives) may be neglected compared to spanwise rates of change and hence the chordwise coordinate effectively becomes a parameter rather than an independent coordinate. This approach is gen-

erally attributed to R. T. Jones.[23] It is useful as an asymptotic check on numerical methods for slender bodies and low aspect ratio wings. However it is useful for quantitative predictions for only a modest range of practical lifting surfaces.

A particulary interesting result is available for the external flow about a slender body when the body has rigid cross-sections and deforms only in the direction, i.e.,

$$z_a(x, y, t) = z_a(x, t)$$

The lift force per unit chordwise distance is given by[24]

$$\begin{aligned} L = &- \rho_\infty \frac{dS}{dx} U \left[U \frac{\partial z_a}{\partial x} + \frac{\partial z_a}{\partial t} \right] \\ &- \rho_\infty S \left[U^2 \frac{\partial^2 z_a}{\partial x^2} + 2U \frac{\partial^2 z_a}{\partial x \partial t} + \frac{\partial^2 z_a}{\partial t^2} \right] \end{aligned} \tag{4.14}$$

Equation (4.14) may be more compactly and insightfully written as

$$L = -\rho_\infty \left[\frac{\partial}{\partial t} + U \frac{\partial}{\partial x} \right] \left\{ S \left[\frac{\partial z_a}{\partial t} + U \frac{\partial z_a}{\partial x} \right] \right\} \tag{4.14}$$

For a cylinder of constant, circular cross-section

$$S = \pi R^2, \quad \frac{dS}{dx} = 0$$

and (4.14) becomes

$$L = -\rho_\infty S \left[U^2 \frac{\partial^2 z_a}{\partial x^2} + 2U \frac{\partial^2 z_a}{\partial x \partial t} + \frac{\partial^2 z_a}{\partial z^2} \right] \tag{4.15}$$

It is interesting to note that (4.15) is the form of the lift force used by Paidoussis and other for *internal* flows. Recall Sect. 5, Eq. (5.2). Dowell and Widnall, among others, have shown under what circumstances (4.15) is a rational approximation for external and internal flows.[25]

5 Solutions to the Aeroelastic Equations of Motion

With the development of the aerodynamic relations, we may now turn to the question of solving the aeroelastic equations of motion. Substituting (4.4) into (3.1) and (3.2), these equations become:

---

[23] Jones [11].

[24] BAH, p. 418.

[25] Dowell and Widnall [12], Widnall and Dowell [13], Dowell [14].

$$m\ddot{h} + S_\alpha \ddot{\alpha} + K_h h = -L = \Big\{ - \int_0^s I_{L\dot{h}}(s-\sigma)\left[\frac{d\frac{h}{b}}{d\sigma} + \alpha\right] d\sigma - \int_0^s I_{L\dot{\alpha}}(s-\sigma)\frac{d\alpha}{d\sigma} d\sigma - \int_0^s I_{LG}(s-\sigma)\frac{w_G}{U} d\sigma \Big\} qb$$

and

$$\begin{aligned} I_\alpha \ddot{\alpha} + S_\alpha \ddot{h} + K_\alpha \alpha = & M_y \\ = & \Big\{ \int_0^s I_{M\dot{h}}(s-\sigma)\left[\frac{d\frac{h}{b}}{d\sigma} + \alpha\right] d\sigma \\ & + \int_0^s I_{M\dot{\alpha}}(s-\sigma)\frac{d\alpha}{d\sigma} d\sigma \\ & + \int_0^s I_{MG}(s-\sigma)\frac{w_G}{U} d\sigma \Big\} qb^2 \end{aligned} \tag{5.1}$$

where

$$s \equiv \frac{tU_\infty}{b}$$

and $I_{L\dot{h}}$, etc. are nondimensional impulse functions. Equation (5.1) are linear, differential-integral equations for h and α. They may be solved in several ways, all of which involve a moderate amount of numerical work. Basically, we may distinguish between those methods which treat the problem in time domain and those which work in the frequency domain. The possibilities are numerous and we shall discuss representative examples of solution techniques rather than attempt to be exhaustive.

5.1 Time Domain Solutions

In this day and (computer) age, perhaps the most straightforward way of solving (5.1) (and similar equations which arise for more complicated aeroelastic systems) is by numerical time integration using finite differences. Such integration is normally done on a digital computer. A simplified version of the procedure follows:

Basically, we seek a step by step solution for the time history of the motion. In particular, given the motion at some time, t, we wish to be able to obtain the motion at some later time, $t + \Delta t$. In general Δt must be sufficiently small;just how small we will discuss in a moment. In relating the solution at time, $t + \Delta t$, to that at time, t, we use the idea of a Taylor series, i.e.,

$$
\begin{aligned}
h(t+\Delta t) &= h(t) + \frac{dh(t)}{dt}\Delta t + \frac{1}{2}\frac{d^2h(t)}{dt^2}(\Delta t)^2 + \cdots \\
\alpha(t+\Delta t) &= \alpha(t) + \frac{d\alpha(t)}{dt}\Delta t + \frac{1}{2}\frac{d^2\alpha(t)}{dt^2}(\Delta t) + \cdots
\end{aligned}
\tag{5.2}
$$

If we think of starting the solution at the initial instant, $t = 0$, we see that normally $h(0), dh(0)/dt, \alpha(0), d\alpha(0)/dt$, are given as initial conditions since we are dealing with (two) second order equations for h and $alpha$. However, in general, $d^2h(0)/dt^2$, $d^2\alpha(0)/dt^2$ and all higher order derivatives are *not* specified. They can be determined though from equations of motion themselves, (5.1). Equation (5.1) are two *algebraic* equations for d^2h/dt^2, $d^2\alpha/dt^2$, in terms of lower order derivatives. Hence, they may readily be solved for d^2h/dt^2, $d^2\alpha/dt^2$. Moreover, by differentiating (5.1) successively the higher order derivatives may also be determined, e.g., d^3h/dt^3, etc. Hence, by using the equations of motion themselves the terms in the Taylor Series may be evaluated, (5.2), and h at $t = \Delta t$ determined. Repeating this procedure, the time history may be determined at $t = 2\Delta t, 3\Delta t, 4\Delta t$, etc.

The above is the essence of the procedure. However, there are many variations on this basic theme and there are almost as many numerical integration schemes as there are people using them.[26] This is perhaps for two reasons: (1) an efficient scheme is desired (this involves essentially a trade-off between the size of Δt and the number of terms retained in the series, (5.2), or more generally a trade-off between Δt and the complexity of the algorithm relating $h(t + \Delta t)$ to $h(t)$); (2) some schemes including the one outlined above, are numerically unstable (i.e., numerical errors grow exponentially) if Δt is too large. This has led to a stability theory for difference schemes to determine the critical Δt and also the development of difference schemes which are inherently stable for all Δt. Generally speaking, a simple difference scheme such as the one described here will be stable if Δt is small compared to the shortest natural period of the system, say one-tenth or so. A popular method which is inherently stable for all Δt is due to Houbolt.[27]

Finally, analytical solutions or semi-analytical solutions may be obtained under certain special circumstances given sufficient simplification of the system dynamics and aerodynamics. These are usually obtained via a Laplace Transform. Since the Laplace Transform is a special case of the Fourier transform, we defer a discussion of this topic to the following section on frequency domain solutions.

5.2 *Frequency Domain Solutions*

An alternative procedure to the time domain approach is to treat the problem in the frequency domain. This approach is more popular and widely used today than the time domain approach. Perhaps the most important reason for this is the fact that

[26] Hamming [15].

[27] Houbolt [16].

the aerodynamic theory is much more completely developed for simple harmonic motion that for arbitrary time dependent motion. That is, the unsteady aerodynamicist normally provides $H_{L\dot{h}}$, for example, rather than $I_{L\dot{h}}$. Of course, these two quantities form a Fourier transform pair,

$$\begin{aligned} H_{L\dot{h}}(k) &= \int_{-\infty}^{\infty} I_{L\dot{h}}(s) e^{-iks} ds \\ I_{L\dot{h}}(s) &= \frac{1}{2\pi} \int_{-\infty}^{\infty} H_{L\dot{h}}(k) e^{iks} dk \end{aligned} \tag{5.3}$$

where

$$k \equiv \frac{\omega b}{U}, \qquad s \equiv \frac{tU}{b}$$

and, in principle, given $H_{L\dot{h}}$ one can compute $I_{L\dot{h}}(s)$. However, for the more complex (and more accurate) aerodynamic theories $H_{L\dot{h}}$ is a highly oscillatory function which is frequently only known numerically at a relatively small number of frequencies, k. Hence, although there have been attempts to obtain $I_{L\dot{h}}$ by a numerical integration of $H_{L\dot{h}}$ over all frequency, they have not been conspicuously successful. Fortunately, for a determination of the stability characteristics of a system, e.g., flutter speed, one need only consider the frequency characteristics of the system dynamics, per se, and may avoid such integrations.

Another reason for the popularity of the frequency domain method is the powerful power spectral description of random loads such as gust loads, landing loads (over randomly rough surfaces), etc. These require a frequency domain description. Recall (3.25) and (3.40).

The principal disadvantage of the frequency domain approach is that one performs two separate calculations; one, to assess the system stability, 'flutter', and a second, to determine the response to external loads such as gusts, etc. This will become clearer as we discuss the details of the procedures.

Let us now turn to the equations of motion, (5.1), and convert them to the frequency domain by taking the Fourier transform of these equations. The result is

$$\begin{aligned} -\omega^2 m\bar{h} - \omega^2 S_\alpha \bar{\alpha} + K_n \bar{h} &= -\bar{L} \\ &= \left\{ - H_{L\dot{h}}(k) \left[\frac{i\omega \bar{h}}{U} + \bar{\alpha} \right] - H_{L\dot{\alpha}}(k) \frac{i\omega b}{U} \bar{\alpha} \right. \\ &\quad \left. - H_{LG}(k) \frac{\bar{w}_G}{U} \right\} qb \\ -\omega^2 I_\alpha \bar{\alpha} - \omega^2 S_\alpha \bar{b} + K_\alpha \bar{\alpha} &= \bar{M}_y \\ &= \left\{ H_{M\dot{h}}(k) \left[\frac{i\omega \bar{h}}{U} + \bar{\alpha} \right] + H_{m\dot{\alpha}}(k) \frac{i\omega b}{U} \bar{\alpha} \right. \end{aligned} \tag{5.4}$$

$$+H_{MG}\frac{\bar{w}_G}{U}\Big\}qb^2$$

where

$$\bar{h} \equiv \int_{-\infty}^{\infty} h(t)e^{i\omega t}dt, etc.$$

Collecting terms and using matrix notation,

$$\begin{bmatrix} -\omega^2 m + K_h + H_{Lh}\frac{i\omega}{U}qb & -\omega^2 S_\alpha + (H_{L\dot{h}} + H_{L\dot{\alpha}}\frac{i\omega b}{U})qb \\ -\omega^2 S_\alpha - (H_{M\dot{h}}\frac{i\omega}{U})qb^2 & -\omega^2 I_\alpha + K_\alpha - (H_{M\dot{h}} + H_{M\dot{\alpha}}\frac{i\omega b}{U})qb^2 \end{bmatrix}.$$

$$\begin{Bmatrix} \bar{h} \\ \bar{\alpha} \end{Bmatrix} = qb\frac{\bar{w}_G}{U}\left\{-H_{LG}H_{MG}b\right\} \tag{5.5}$$

Formally, we may solve for $\bar{h}$ and $\bar{\alpha}$ by matrix inversion. The result will be

$$\frac{\frac{\bar{h}}{b}}{\frac{\bar{w}_G}{U}} \equiv H_{hG}$$

which is one of the aeroelastic transfer functions to a gust input and

$$\frac{\bar{\alpha}}{\frac{\bar{w}_G}{U}} \equiv H_{\alpha G} \tag{5.6}$$

It is left to the reader to evaluate these transfer functions explicitly from (5.5). Note these are aeroelastic transfer functions as opposed to the purely mechanical or structural transfer functions, H_{hF} and $H_{\alpha F}$, considered previously or the purely aerodynamic transfer functions, $H_{L\bar{h}}$, etc. That is, H_{hG} include not only the effects of structural inertia and stiffness, but also the aerodynamic forces due to structural motion.

With the aeroelastic transfer functions available one may now formally write the solutions in the frequency domain

$$\frac{h(t)}{b} = \frac{1}{2\pi}\int_{-\infty}^{\infty} H_{hG}(\omega)\mathcal{F}\left(\frac{w_G}{U}\right)e^{-i\omega t}d\omega \tag{5.7}$$

where the Fourier transform of the gust velocity is written as

$$\mathcal{F}w_G \equiv \int_{-\infty}^{\infty} w_G(t)e^{i\omega t}dt \tag{5.8}$$

Compare (5.7) with (3.12).

Alternatively, one could write

$$\frac{h(t)}{b} = \int_{-\infty}^{\infty} I_{hG}(t-\tau)\frac{w_G(t)}{U}d\tau \tag{5.9}$$

where

$$I_{hG}(t) \equiv \frac{1}{2\pi}\int_{-\infty}^{\infty} H_{hG}(\omega)e^{i\omega t}d\omega \tag{5.10}$$

Compare (5.9) and (5.10) with (3.13) and (3.14). As mentioned in our discussion of time domain solutions, the integrals over frequency may be difficult to evaluate because of the oscillatory nature of the aerodynamic forces.

Finally, for random gust velocities one may write

$$\Phi_{(h/b)(h/b)} = |H_{hG}(\omega)|^2 \Phi_{(w_g/U)(w_G/U)} \tag{5.11}$$

where $\Phi_{(h/b)(h/b)}$, $\Phi_{(w_g/U)(w_G/U)}$, are the (auto) power spectra of $\frac{h}{b}$ and $\frac{w_g}{U}$, respectively. Thus

$$\left(\frac{\bar{h}}{b}\right)^2 = \int_{-\infty}^{\infty} |H_{hG}|^2 \Phi_{(w_g/U)(w_G/U)}d\omega \tag{5.12}$$

Compare (5.12) with (3.25). Since the transfer function is squared, the integral (5.12) may be somewhat easier to evaluate than (5.7) or (5.10). The gust velocity power spectra is generally a smoothly varying function. Equation (5.12) is commonly used in applications.

To evaluate stability, 'flutter', of the system one need not evaluate any of these integrals over frequency. It suffices to consider the eigenvalues (or poles) of the transfer function. A pole of the transfer function, ω_p, will give rise to an aeroelastic impulse function of the form

$$I_{hG} \sim e^{i\omega_p t} = e^{i(\omega_p)_R t}e^{-(\omega_p)_I t}$$

see (5.10). Hence, the system will be stable if the imaginary part, $(\omega_p)_I$, of all poles is positive. If any one (or more) pole has a negative imaginary part, the system is unstable, i.e., it flutters. The frequency of oscillation is $(\omega_p)_R$, the real part of the pole. Note that the poles are also the eigenvalues of the determinant of coefficients of $\bar{h}$ and $\bar{\alpha}$ in (5.5).

Having developed the mathematical techniques for treating dynamic aeroelastic problems we will now turn to a discussion of results and some of the practical aspects of such calculations.

6 Representative Results and Computational Considerations

We will confine ourselves to two important types of motion, 'flutter' and 'gust response'.

6.1 Time Domain

If we give the typical section (or any aeroelastic system) an initial disturbance due to an impulsive force, the resultant motion may take one of two possible forms as shown in Figs. 9 and 10. 'Flutter' is the more interesting of these two motions, since, if it is present, it will normally lead to catastrophic structural failure which will result in the loss of the flight vehicle. All flight vehicles are carefully analyzed for flutter and frequently the structure is stiffened to prevent flutter inside the flight envelope of the vehicle.

Even if flutter does not occur, however, other motions in response to continuous external forces may be of concern with respect to possible structural failure. An important example is the gust response of the flight vehicle. Consider a vertical gust velocity time history as shown in Fig. 11. The resulting flight vehicle motion will have the form shown in Fig. 12. Note that the time history of the response has a certain well defined average period or frequency with modulated, randomly varying amplitude. The more random input has been 'filtered' by the aeroelastic transfer function and only that portion of the gust velocity signal which has frequencies near the natural frequencies of the flight vehicle will be identifiable in the response. This characteristic is perhaps more readily seen in the frequency domain than in the time domain.

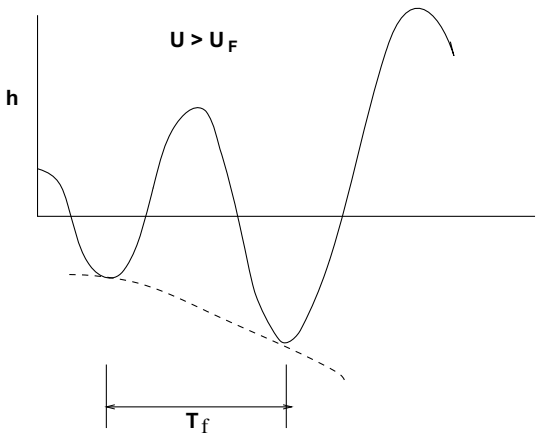

Fig. 9 Time history of unstable motion or "flutter"

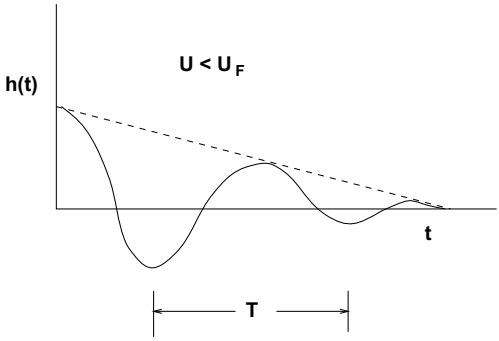

Fig. 10 Time history of stable motion

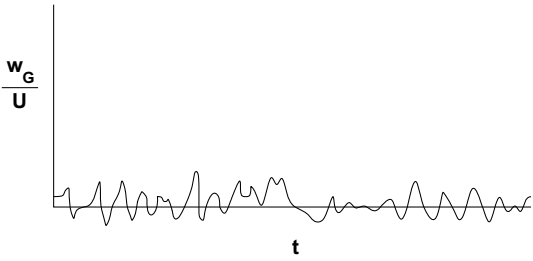

Fig. 11 Time history of gust velocity

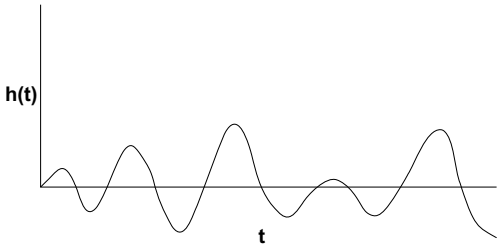

Fig. 12 Time history of motion due to gust velocity

6.2 Frequency Domain

To assess flutter, we need only examine the poles of the transfer function. This is similar to a 'root locus' plot.[28] Typically, the real, w_R, and imaginary, w_I, parts of the complex frequency are plotted versus flight speed. For the typical section there will be two principal poles corresponding to two degrees of freedom and at small flight speed or fluid velocity, these will approach the natural frequencies of the mechanical or structural system.See Fig. 13. Flutter is identified by the lowest airspeed for which one of the w_I becomes negative. Note the coming together or 'merging' of the w_R of the two poles which is typical of some types of flutter . There are many variations on the above plot in practice but we shall defer a more complete discussion until later.

[28] Savant [18].

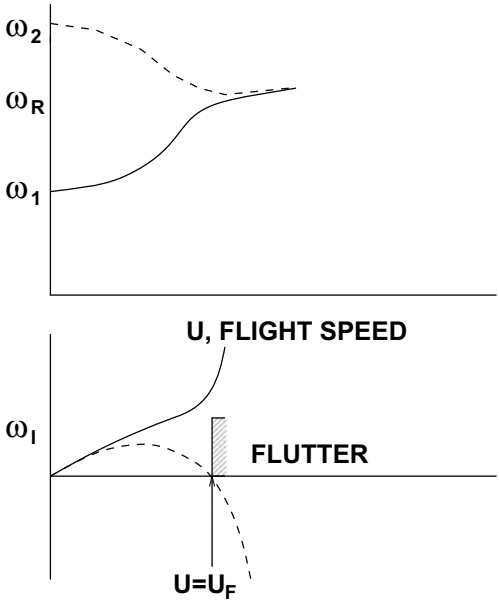

Fig. 13 Real and imaginary components of frequency versus air speed

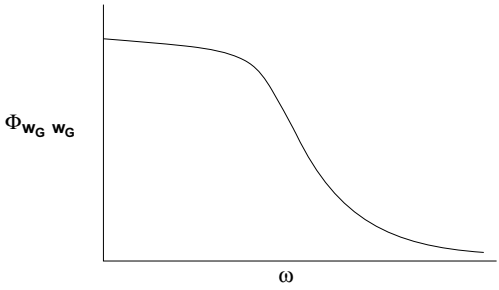

Fig. 14 Gust power spectra

Next, let us turn to the gust problem. A typical gust spectrum would be as in Fig. 14. The transfer function (at some flight speed) would be as shown in Fig. 15. Thus, the resultant response spectrum would appear as in Fig. 16. As U approaches U_F, the resonant peaks of $|H_{hG}|^2$ and Φ_{hh} would approach each other for the system whose poles were sketched previously. For $U = U_F$ the two peaks would essentially collapse into one and the amplitude becomes infinite. For $U > U_F$ the amplitude predicted by the analytical model would become finite again for the power spectral approach and this physically unrealistic result is a possible disadvantage of the method.

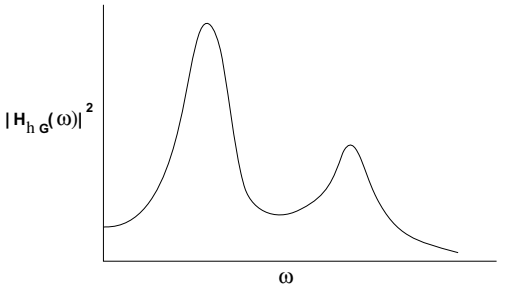

Fig. 15 Transfer function

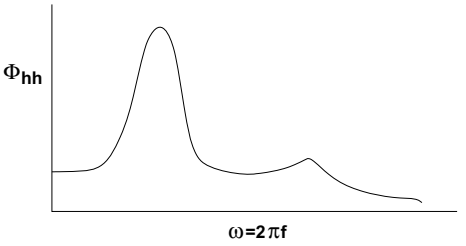

Fig. 16 Power spectra of motion

6.3 Flutter and Gust Response Classification Including Parameter Trends

Here we shall study some of the important parameters which affect flutter and gust response of the typical action as well as more complex flight vehicles.

6.3.1 Flutter

If one nondimensionalizes the typical section equations of motion, one finds that the motion can be expressed formally as

$$\begin{aligned} \frac{h}{b} &= F_1\left(\omega_\alpha t; \frac{S_\alpha}{mb}, \frac{I_\alpha}{mb^2}, \frac{m}{\rho(2b)^2}, \frac{e}{b}, \frac{\omega_h}{\omega_\alpha}, M, \frac{U}{b\omega_\alpha}\right) \\ \alpha &= F_2(w_\alpha t \ldots) \end{aligned} \tag{6.1}$$

where the functions F_1, F_2, symbolize the results of a calculated solution using one of the several methods discussed earlier.

The choice of nondimensional parameters is not unique but a matter of convenience. Some authors prefer a nondimensional dynamic pressure, or 'aeroelastic stiffness number'

$$\lambda \equiv \frac{1}{\mu k_\alpha^2} = \frac{4\rho U^2}{m\omega_\alpha^2}, \qquad \text{(aeroelastic stiffness)}$$

to the use of a nondimensional velocity, $U/b\omega_\alpha$.

The following short-hand notation will be employed:

$$\omega_\alpha t \quad \text{nondimensional time}$$
$$x_\alpha \equiv \frac{S_\alpha}{mb} \quad \text{static unbalance}$$
$$r_\alpha^2 \equiv \frac{I_\alpha}{mb^2} \quad \text{radius of gyration (squared)}$$
$$\mu \equiv \frac{m}{\rho(2b)^2} \quad \text{mass ratio}$$
$$a \equiv \frac{e}{b} \quad \text{location of elastic axis measured from aerodynamic center or mid-chord}$$
$$\frac{\omega_h}{\omega_\alpha} \quad \text{frequency ration}$$
$$M \quad \text{Mach number}$$
$$k_\alpha = \frac{\omega_\alpha b}{U} \quad \text{inverse of refuced velocity}$$

Time is an independent variable which we do not control; however, in some sense we can control the parameters, x_α, r_α, etc., by the design of our airfoil and choice of where and how we fly it. For some combination of parameters the airfoil will be dynamically unstable, i.e., it will 'flutter'.

An alternative parametric representation would be to assume sinusoidal motion

$$h = \bar{h}e^{i\omega t}$$

$$\alpha = \bar{\alpha}e^{i\omega t}$$

and determine the eigenvalues, ω. Formally, recalling $\omega = \omega_R + i\omega_I$,

$$\begin{aligned} \frac{\omega_R}{\omega_\alpha} &= G_R\left(x_\alpha, r_\alpha, \mu, a, \frac{\omega_h}{\omega_\alpha}, M, \frac{U}{b\omega_\alpha}\right) \\ \frac{\omega_I}{\omega_\alpha} &= G_I\left(x_\alpha, r_\alpha, \mu, a, \frac{\omega_h}{\omega_\alpha}, M, \frac{U}{b\omega_\alpha}\right) \end{aligned} \tag{6.2}$$

If for some combination of parameters, $\omega_I < 0$, the system flutters.

Several types of flutter are possible. Perhaps these are most easily distinguished on the basis of the eigenvalues, $\omega_R/\omega_\alpha, \omega_I/\omega_\alpha$ and their variation with airspeed, $U/b\omega_\alpha$. Examples are shown below of the several possibilities with brief discussions of each.

In one type of flutter (called coupled mode or bending-torsion flutter) the distinguishing feature is the coming together of two (or more) frequencies, ω_R, near the flutter condition, $\omega_I \to 0$ and $U \to U_F$. See Fig. 17. For *'Coalescense' or Merging Frequency' Flutter* $U > U_F$ one of ω_I becomes large and positive (stable pole) and

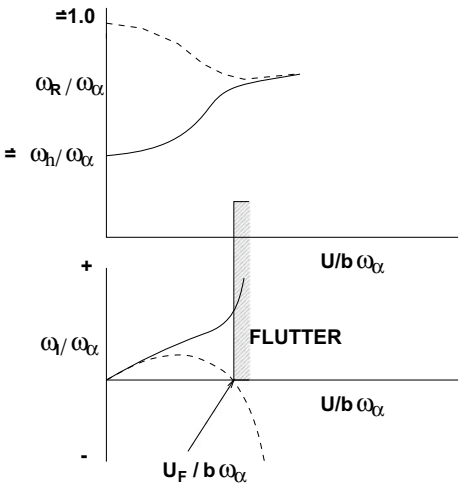

Fig. 17 Real and imaginary components of frequency versus air speed

the other which gives rise to flutter becomes large and negative (unstable pole) while the corresponding ω_R remain nearly the same. Although one usually speaks of the torsion mode as being unstable and the bending mode stable, the airfoil normally is undergoing a flutter oscillation composed of important contributions of both h and α. For this type of flutter the out-of-phase or damping forces of the structure or fluid are not qualitatively important. Often one may neglect structural damping entirely in the model and use a quasi-steady or even a quasi-static aerodynamic assumption. This simplifies the analysis and, perhaps more importantly, leads to generally accurate and reliable results based on theoretical calculations.

'Single-Degree-of-Freedom' Flutter

In another type of flutter, the distinguishing feature is the virtual independence of the frequencies, ω_R, with respect to variations in airspeed, $U/b\omega_\alpha$. See Fig. 18. Moreover the change in the true damping, ω_I, with airspeed is also moderate. However, above some airspeed one of the modes (usually torsion) which has been slightly positively damped becomes slightly negatively damped leading to flutter. This type of flutter is very sensitive to structural and aerodynamic out-of phase or damping forces. Since these forces are less well described by theory than the in-phase forces, the corresponding flutter analysis generally gives less reliable results. One simplification for this type of flutter is the fact that the flutter mode is virtually the same as one of the system natural modes at zero airspeed and thus the flutter mode and frequency (though not flutter speed!) are predicted rather accurately by theory. Airfoil blades in turbomachinery and bridges in a wind often encounter this type of flutter.

There is yet another one-degree-of-freedom type of flutter, but of a very special type. The flutter frequency is zero and hence this represents the *'Divergence' or 'Zero Frequency' Flutter*.

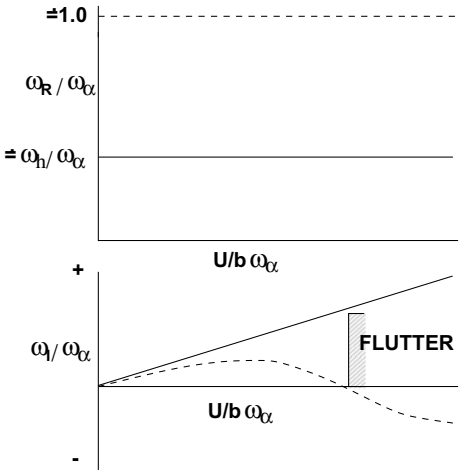

Fig. 18 Real and imaginary components of frequency versus air speed

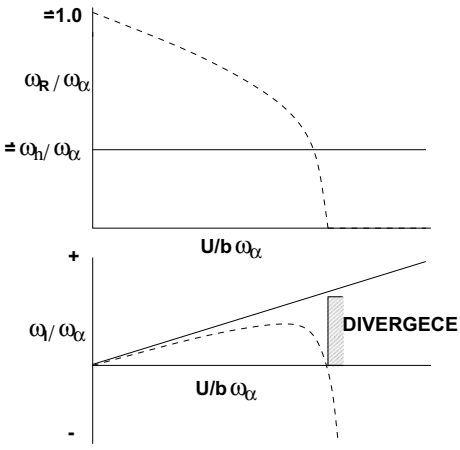

Fig. 19 Real and imaginary components of frequency versus air speed

Static instability which we have previously analyzed in our discussion of static aeroelasticity under the name of 'divergence'. See Fig. 19. Because it is a static type of instability, out-of-phase forces are again unimportant and the theory is generally reliable.

We note that in all of the above we have considered only positive ω_R even though there are negative ω_R as well and these *are* physically meaningful. There are at least two reasons why this practice is usually followed. For those models where the aerodynamic transfer functions can be (approximately) expressed as a polynomial in $p \equiv i\omega$, the negative ω_R plane is (nearly) the mirror image of the positive ω_R plane and the ω_I are identical, i.e., all poles are complex conjugates in p. Secondly, some of the structural damping models employed in flutter analysis are only valid for $\omega_R < 0$; hence, the $\omega_R < 0$ in such cases cannot be interpreted in a physically valid

way. However, there are some types of travelling wave flutter in planes and shells for which a consideration of negative ω_R is essential. In such cases a change in sign of ω_R represents a change in direction of a travelling wave.

Flutter Calculations in Practice

At this point it should be emphasized that, in practice, one or another of several *indirect* methods is often used to compute the flutter velocity, e.g., the so called '$V-g$ method'. In this approach structural damping is introduced by multiplying the structural frequencies squared

$$\omega_h^2, \omega_\alpha^2$$

by $1+ig$ where g is a structural coefficient and pure sinusoidal motion is assumed, i.e., $\omega=\omega_R$ with $\omega_I \equiv 0$. For a given U, the g is that required to sustain pure sinusoidal motion for each aeroelastic mode. The computational advantage of this approach is that the aerodynamic forces only need be determined for real frequencies. The disadvantage is the loss of physical insight. For example, if a system (with no structural damping) is stable at a given airspeed, U, all the values of g so determined will be negative, but these values of g cannot be interpreted directly in terms of ω_I. Moreover, for a given system with some prescribed damping, only at one airspeed $U=U_F$ (where $\omega=\omega_R$ and $\omega_I \equiv 0$) will the mathematical solution be physically meaningful. The limitations of the '$V-g$ method' are fully appreciated by experienced practitioners and it is a measure of the difficulty of determining the aerodynamic forces for other than pure sinusoidal motion, that this method remains very popular. Here we digress from our main discussion to consider this and related methods in some detail.

For sinusoidal motion

$$\begin{aligned} h &= \bar{h}e^{i\omega t} \\ \alpha &= \bar{\alpha}e^{i\omega t} \\ L &= \bar{L}e^{i\omega t} \\ M_y &= \bar{M}_y e^{i\omega t} \end{aligned}$$

The aerodynamic forces (due to motion *only*) can be expressed as

$$\begin{aligned} \bar{L} &= 2\rho_\infty b^2\omega^2(2b)\left\{[L_1+iL_2]\frac{\bar{h}}{b}+[L_3+iL_4]\bar{\alpha}\right\} \\ \bar{M}_y &= -2\rho_\infty b^3\omega^2(2b)\left\{[M_1+iM_2]\frac{\bar{h}}{b}+[M_3+iM_4]\bar{\alpha}\right\} \end{aligned} \tag{6.3}$$

This form of aerodynamic forces is somewhat different from that previously used in this text and is only one of several (equivalent) alternative forms employed in the literature. Here L_1, L_2, L_3, L_4 are (nondimensional) real aerodynamic coefficients

which are functions of reduced frequency and Mach number. L_1, L_2, L_3, L_4 are the forms in which the coefficients are generally tabulated for supersonic flow.[29]

Using the above aerodynamic forms for $\bar{L}$ and $\bar{M}_y$ in (74) and setting the determinant of coefficients of $\bar{h}$ and $\bar{\alpha}$ to zero to determine nontrivial solutions, one obtains

$$\begin{aligned}\Delta(\omega) \equiv & \left\{\frac{m}{2\rho_\infty b(2b)}\left[1+\left(\frac{\omega_\alpha}{i\omega}\right)^2\left(\frac{\omega_h}{\omega_\alpha}\right)^2\right]-[L_1+iL_2]\right\} \\ & \times\left\{\frac{m}{2\rho_\infty b(2b)}r_\alpha^2\left[1+\left(\frac{\omega_\alpha}{i\omega}\right)^2\right]-[M_3+iM_4]\right\} \\ & -\left\{\frac{mx_\alpha}{2\rho_\infty b(2b)}-[L_3+iL_4]\right\}\left\{\frac{mx_\alpha}{2\rho_\infty b(2b)}-[M_1+iM_2]\right\}=0\end{aligned} \tag{6.4}$$

Because L_1, L_2, etc. are complicated, transcendental functions of k (and M) which are usually only known for real values of k (and hence real values of ω), often one does not attempt to determine from (6.4) the complex eigenvalue, $\omega = \omega_R + i\omega_I$. Instead one seeks to determine the conditions of neutral stability when w is purely real. Several alternative procedures are passible; two are described below.

In the first the following parameters are chosen.

$$\frac{\omega_h}{\omega_\alpha}, r_\alpha, x_\alpha, M \quad \text{and (a real value of)} k$$

Equation (6.4) is then a complex equation whose real and imaginary parts may be used independently to determine the two (real) unknowns

$$\left(\frac{\omega}{\omega_\alpha}\right)^2 \quad \text{and} \quad \frac{m}{2\rho_\infty bS}$$

From the imaginary part of (6.4), which is a linear equation in these two unknowns, one may solve for $(\omega/\omega_\alpha)^2$ in terms of $m/2\rho_\infty bS$. Substituting this result into the real part of (6.4) one obtains a quadratic equation in $m/2\rho_\infty b^2$ which may be solved in the usual manner. Of course, only real positive values of $m/2\rho_\infty bS$ are meaningful and if negative or complex values are obtained these are rejected. By choosing various values of the parameters one may determine under what physically meaningful conditions flutter (neutrally stable oscillations) may occur. This procedure is not easily extendable to more than two degrees of freedom and it is more readily applied for determining parameter trends than the flutter boundary of a specific structure. Hence, a different method which is described below is frequently used.

This method has the advantage of computational efficiency, though from a physical point of view it is somewhat artificial. Structural damping is introduced as an additional parameter by multiplying ω_α^2 and ω_h^2 by $1+ig$ where g is the structural damping coefficient. The following parameters are selected $\omega_h/\omega_\alpha, r_\alpha, x_\alpha, M$, (a real

[29] Garrick [19].

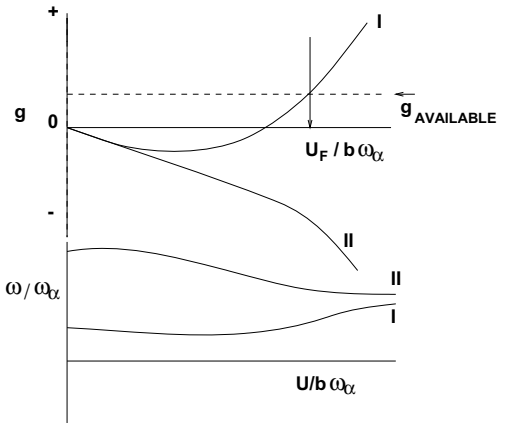

Fig. 20 Structural damping and frequency required for neutrally stable motion versus air speed

value) of k, and $m/2\rho_\infty bS$. Equation (6.4) is then identified as a complex polynomial in the complex unknown

$$\left(\frac{\omega_\alpha}{\omega}\right)^2 (1 + ig)$$

Efficient numerical algorithms have been devised for determining the roots of such polynomials. A complex root determines

$$\frac{\omega_\alpha}{\omega} \quad \text{and} \quad g$$

From ω_α/ω and the previously selected value of $k \equiv \omega b/U_\infty$ one may compute

$$\frac{\omega_\alpha b}{U_\infty} = \frac{\omega_\alpha}{\omega} k$$

One may then plot g versus $U_\infty/b\omega_\alpha$.[30] A typical result is shown in Fig. 20 for two roots (two degrees of freedom). g is the value of structural damping *required* for neutral stability. If the *actual* structural damping is $g_{AVAILABLE}$ then flutter occurs when (see Fig. 20)

$$g = g_{AVAILABLE}$$

It is normally assumed in this method that for $g < g_{AVAILABLE}$ and $U < U_F$ no flutter will occur. Sometimes more complicated velocity-damping or $V - g$ curves are obtained, however. See Fig. 21. Given the uncertainty as to what $g_{AVAILABLE}$ may be for a real physical system, it may then be prudent to define the flutter speed as the minimum value of $U_\infty/b\omega_\alpha$ for any $g > 0$. Here the physical interpretation of the result becomes more difficult, particularly when one recalls that the factor $1 + ig$ is only an approximate representation of damping in a structure. Despite this

[30] (For each complex root of the polynomial.)

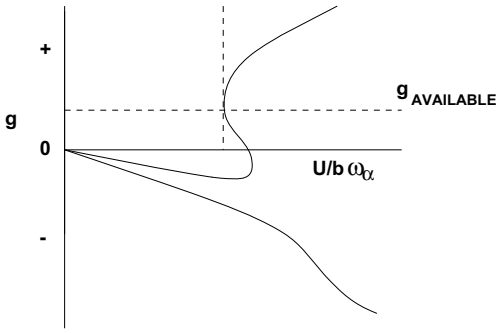

Fig. 21 Structural damping required for flutter versus air speed

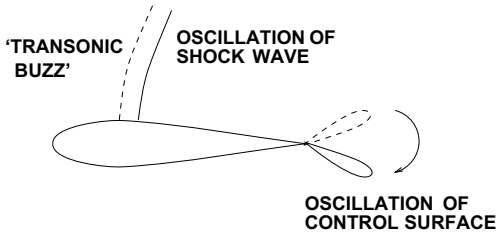

Fig. 22 Schematic of transonic buzz geometry

qualification, the $V - g$ method remains a very popular approach to flutter analysis and is usually only abandoned or improved upon when the physical interpretation of the result becomes questionable.

One alternative to the $V - g$ method is the so-called $p - k$ method.[31] In this approach time dependence of the form $h, \alpha \sim e^{pt}$ is assumed where $p = \sigma + i\omega$. In the aerodynamic terms *only* $ak \equiv \omega b/U$ is *assumed*. The eigenvalues p are computed and the new ω used to compute a new k and the aerodynamic terms re-evaluated. The iteration continues until the process converges. For small σ, i.e., $|\sigma| \ll |\omega|$, the σ so computed may be interpreted as true damping of the system (Fig. 22).

Nonlinear Flutter Behavior

There are two other types of flutter which are of importance, 'transonic buzz' and 'stall flutter'. Both of these involve significant aerodynamic nonlinearities and are, therefore, not describable by our previous models. Indeed, both are poorly understood theoretically compared to classic flutter and recourse to experiment and/or empirical rules-of-thumb is often made. Recent advances in numerical solution of the nonlinear equations of fluid mechanics (computational fluid dynamics) have provided an improved methodology for modeling these types of flutter. See chapters 'Modeling of Fluid-Structure Interaction' and 'Nonlinear Aeroelasticity'.

Typically an oscillating control surface gives rise to an oscillating shock which produces an oscillating pressure field which gives rise to an oscillating control surface which gives rise to an oscillating shock and so on and so forth (Fig. 23).

[31] Hassig [20].

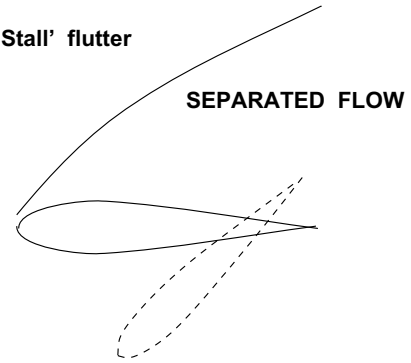

Fig. 23 Schmatic of separated flow geometry

The airfoil profile shape is known to be an important parameter and this fact plus the demonstrated importance of the shock means that any aerodynamic theory which hopes to successfully predict this type of flutter must accurately account for the nonuniform mean steady flow over the airfoil and its effect on the small dynamic motions which are superimposed due to control surface and shock oscillation. An early and insightful theoretical model is that of Eckhaus; also see the discussion by Landahl. Lambourne has given a valuable summary of the early experimental and theoretical evidence.[32] See chapters 'Modeling of Fluid-Structure Interaction' and 'Nonlinear Aeroelasticity' for the most recent literature on this topic. An airfoil oscillating through large angles of attack will create a time lag in the aerodynamic moment which may give rise to *negative* aerodynamic damping in pitch and, hence, flutter, even though for small angles of attack the aerodynamic damping would be positive. This is associated with separation of the flow, an effect of fluid viscosity Compressor, turbine and helicopter blades are particularly prone to this type of flutter, since they routinely operate through large ranges of angle of attack. Chapter 'Stall Flutter' discusses this type of flutter in some detail. Also see chapters 'Modeling of Fluid-Structure Interaction' and 'Nonlinear Aeroelasticity'.

Parameter Trends for Flutter

Coalescence flutter is perhaps most common for airfoils under conventional flow conditions (no shock oscillation and no stall). It is certainly the best understood. Hence, for this type of flutter, let us consider the the variation of (nondimensional) flutter velocity with other important parameters.

Static Unbalance. x_α:
If $x_\alpha < 0$ (i.e., c.g. is ahead of e.a.) frequently no flutter occurs. If $x_\alpha < 0$ the surface is said to be 'mass balanced'.

Frequency Ratio. $\frac{\omega_h}{\omega_\alpha}$:
Not unexpectedly, for coalescence flutter $U_F/b\omega_\alpha$ is a minimum when $\omega_h/\omega_\alpha \simeq 1$. That is, if ω_h and ω_α are closer in value, then the aeroelastic frequencies will coalesce more readily and at a lower flow velocity (Fig. 24).

[32] Eckhaus [21], Landahl [22], Lambourne [23].

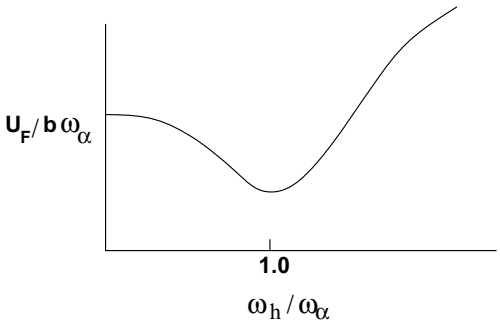

Fig. 24 Flutter airspeed versus frequency ratio

Mach Number. M:
The aerodynamic pressure on an airfoil is normally greatest near Mach number equal to one[33] and hence, the flutter speed (or dynamic pressure) tends to be a minimum there. For $M \gg 1$ the aerodynamic piston theory predicts that the aerodynamic pressure, p, varies as

$$p \sim \rho \frac{U^2}{M}$$

Hence, $U_F \sim M^{\frac{1}{2}}$ for $M \gg 1$ and constant μ. Also

$$\lambda_F \sim (\rho U^2)_F \sim M$$

Compatibility Conditions:
Note that for flight at constant altitude of a specific aircraft ρ (hence, μ) and a_∞ (speed of sound) are fixed. Since

$$U = Ma_\infty$$

$U/b\omega_\alpha$ and M are not independent, but are related by

$$\left(\frac{U}{b\omega_\alpha}\right) = M\left(\frac{a_\infty}{b\omega_\alpha}\right)$$

Thus, a compatibility relation must also be satisfied for physically meaningful in a flight flutter conditions as indicated by dashed line in Fig. 25. By repeating the flutter calculation for various altitudes (various ρ, a_∞ and hence various μ and $a_\infty/b\omega_\alpha$), one may obtain a plot of flutter Mach number versus altitude as given in Fig. 26.

[33] See chapter 'Nonsteady Aerodynamics of Lifting and Non-lifting Surfaces'.

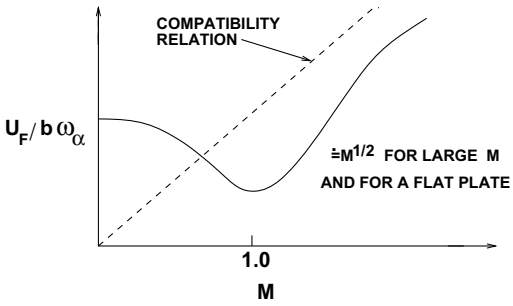

Fig. 25 Flutter airspeed versus mach number

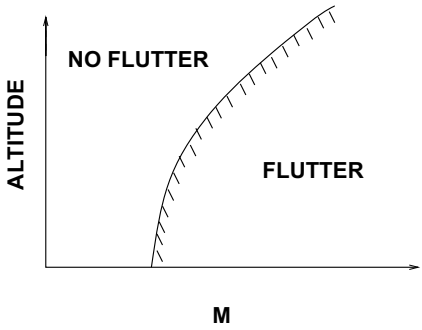

Fig. 26 Altitude versus mach number

There is a counterpart to this compatibility condition for testing of aeroelastic models in a compressible wind tunnel.

Mass ratio. μ:
For large μ the results are essentially those of a constant flutter dynamic pressure; for small μ they are often those of constant flutter velocity as indicated by the dashed line in Fig. 27. However, for $M \equiv 0$ and two-dimensional airfoils theory predicts $U_F \to \infty$ for some small but finite μ (solid line). This is contradicted by the experimental evidence and remains a source of some controversy in the literature.[34] Crisp[35] has suggested that the rigid airfoil chord assumption is untenable for small μ and that by including elastic chordwise bending the discrepancy between theory and experiment may be resolved. See Fig. 27.

Flutter Prevention

After one has ascertained that there is a flutter problem then there is more than a casual curiosity as to how to fix it, i.e., increase U_F, without adding any weight, of course. There is no universal solution, but frequently one or more of the following are tried.

[34] Abramson [24]. Viscous fluid effects are cited as the source of the difficulty.
[35] Crisp [25].

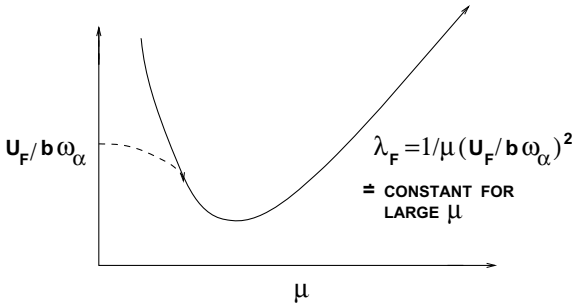

Fig. 27 Flutter air speed versus mass ratio

(1) add mass or redistribute mass so that $x_\alpha < 0$, 'mass balance'
(2) increase torsional stiffness, i.e., increase ω_α
(3) increase (or decrease) $\frac{\omega_h}{\omega_\alpha}$ if it is near one (for fixed ω_α)
(4) add damping to the structure, particularly for single-degree-of-freedom flutter or stall flutter
(5) require the aircraft to be flown below its critical Mach number (normally used as a temporary expedient while one of the above items is studied)

More Complex Structural Models

The above discussion was in the context of the typical section. For more complex aerospace vehicles, additional degrees of freedom, equations of motion and parameters will appear. Basically, these will have the form of additional frequency ratios (stiffness distribution) and inertial constants (mass distribution). Hence, *for example*, we might have $\frac{\omega_h}{\omega_\alpha}$ replaced by $\frac{\omega_1}{\omega_\alpha}$, $\frac{\omega_2}{\omega_\alpha}$, $\frac{\omega_3}{\omega_\alpha}$, etc. and x_α, r_α replaced by

$$\int \rho x\,dx,\ \int \rho x^2 dx,\ \int \rho x^3 dx,\ \text{etc.}$$
$$\int \rho xy\,dx\,dy,\ \int \rho y\,dy,\ \int \rho y^2 dy,\ \text{etc.}$$

We will turn to such issues in Sect. 7.

6.4 Gust Response

To the parameters for flutter we add

$$\frac{w_G}{U}$$

Fig. 28 Sharp edged gust

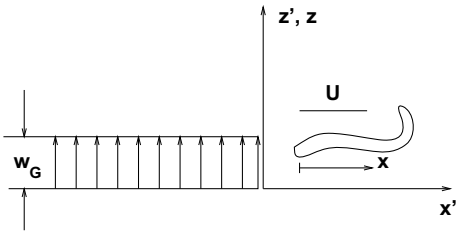

for gust response.[36] Since w_G is a time history (deterministic or random) we actually add a functional as a parameter rather than a constant. Hence, various gust responses will be obtained depending on the nature of the assumed gust time history.

The several approaches to gust response analysis can be categorized by the type of atmospheric turbulence model adopted. The simplest of these is the sharp edged gust; a somewhat more elaborate model is the 1-COSINE gust. Both of these are deterministic; a third gust model is now increasingly used where the gust velocity field is treated as a random process.

Discrete Deterministic Gust:

An example of a useful gust time history is a *sharp edged gust*,

$$w_G = 50\text{ft/s} \quad \text{for} \quad \left.\begin{array}{l} x < Ut \\ \text{or} \quad t > \dfrac{x}{U} \end{array}\right\},\ x' < 0$$

$$= 0 \qquad \text{for} \quad x > Ut, x' > 0$$

x', t' fixed in atmosphere

x, t fixed with aircraft

(Galilean transformation) $x' = xUt$ (if $x' = x = 0$ at $t = t' = 0$)

$t' = t$

In this model w_G is constant with respect to space *and* time in the atmospheric fixed coordinate system for all $x' < 0$. We shall deal with the aerodynamic consequences of this property in the next chapter (Fig. 28).

A somewhat more realistic gust model allows for the spatial scale of the gust field. In this model w_G is independent of time, t', but varies with distance, x', in the atmospheric fixed coordinate system, x', t'. For obvious reasons it is called a 1-COSINE gust i.e.,

[36] Houbolt, Steiner and Pratt [6].

Fig. 29 1-COSINE gust

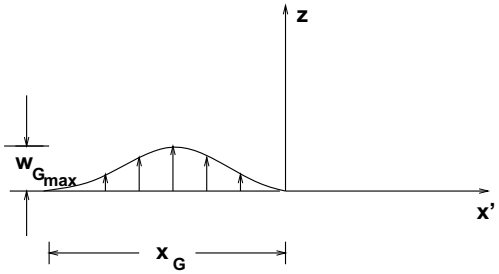

Fig. 30 Response to deterministic gust

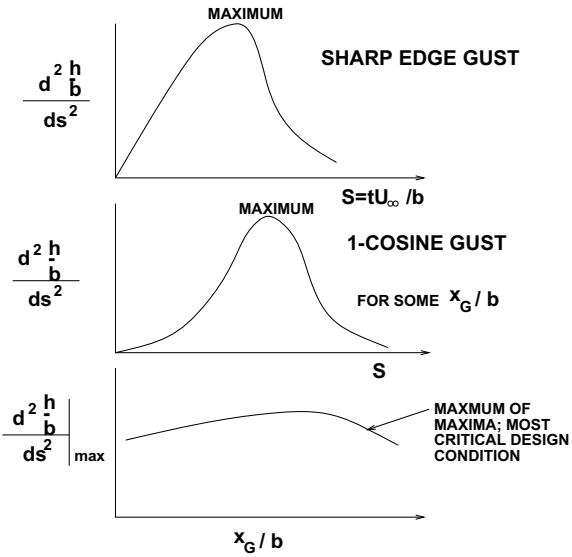

$$w_G = \frac{w_{G_{\max}}}{2}\left[1 - \cos\frac{2\pi x'}{x_G}\right]$$
$$\text{for} \quad t < \frac{x_G}{U}, \quad x' < 0$$
$$= 0 \quad \text{for} \quad t > \frac{x_G}{U}, \quad x' > 0$$

Recall

$$x' = x - U_\infty t$$

x_G is normally varied to obtain the most critical design condition (largest response to the gust excitation) and typically $w_{G_{\max}} \simeq 50$ft/sec. See sketch below. Schematic results for flight vehicle response to these deterministic gust models are shown below (Figs. 29 and 30).

Random Gust:
In a random gust field, we still adopt the assumption that w_G, though now a random variable, varies only with x' and is independent of t'. In the theory of isotropic turbulence this is usually referred to as Taylor's hypothesis[37] or the 'frozen gust' assumption. Thus

$$w_G(x') = w_G(x - U_\infty t)$$

Since x and t only appear in the above combination, we may consider the alternative functional form

$$w_G = w_G\left(t - \frac{x}{U_\infty}\right)$$

The correlation function may then be defined as

$$\phi_{w_G w_G}(\tau) \equiv \lim \frac{1}{2T} \int_{-\infty}^{\infty} w_G\left(t - \frac{x}{U_\infty}\right) w_G\left(t - \frac{x}{U_\infty} + \tau\right) dt$$

and the power spectral density as

$$\Phi_{w_G w_G}(\omega) \equiv \frac{1}{\pi} \int_{-\infty}^{\infty} \phi_{w_G w_G}(\tau) e^{-i\omega t} dt$$

The power spectral density is given in Fig. 31. A useful approximate formula which is in reasonable agreement with measurements is[38]

$$\Phi_{w_G w_G} = \frac{\bar{w_G^2} \pi L_G}{U} \frac{1 + 3\left(\frac{\omega L_G}{U}\right)^2}{\left[1 + \left(\frac{\omega L_G}{U}\right)^2\right]^2}$$

Typically,

$$\bar{w_G^2} \simeq 33 \text{ ft/s}$$
$$L_G \simeq 50{-}500 \text{ ft}; \quad \text{gust scale length}$$

We conclude this discussion with a representative vehicle responses to random gust fields drawn from a variety of sources.[39] The analytical results are from mathematical models similar to those described above, but with more elaborate structural and aerodynamic ingredients as described in succeeding pages in this chapter and chapter 'Nonsteady Aerodynamics of Lifting and Non-lifting Surfaces'.

---

[37] Houbolt, Steiner and Pratt [6]. The basis for the frozen gust assumption is that in the time interval for any part of the gust field to pass over the flight vehicle (the length/U_∞)the gust field does not significantly change its (random) spatial distribution. Clearly this becomes inaccurate as U_∞ becomes small.

[38] Houbolt, Steiner and Pratt [6].

[39] These particular examples were collected and discussed in Ashley, Dugundji and Rainey [24].

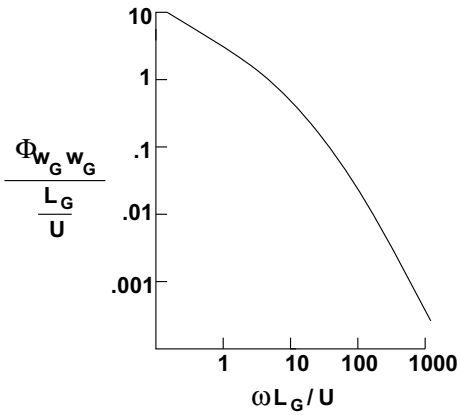

Fig. 31 Gust power spectral density

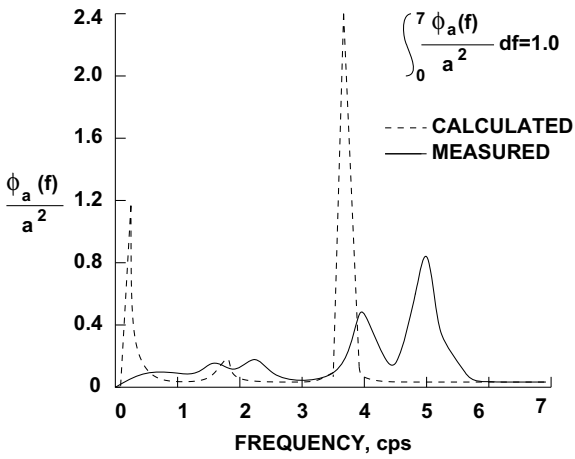

Fig. 32 Acceleration power spectral density. From Stenton [26]

In the Fig. 32, the measured and calculated power spectral densities for acceleration at the pilot station of the XB-70 aircraft are shown. The theoretical structural model allows for rigid body and elastic degrees of freedom using methods such as those described later in this chapter. The aerodynamic theory is similar to those described in chapter 'Nonsteady Aerodynamics of Lifting and Non-lifting Surfaces'. The dramatic conclusion drawn from his figure is that theory and experiment do not necessarily agree closely! If one assumes the peaks in the measured and calculated spectra are associated with resonances at natural frequencies of the (aeroelastic) system, then one concludes the theoretical model is not predicting these adequately. Since the resonances are determined primarily by mass and stiffness (springs), one concludes that for real vehicles even these characteristics may be difficult to model mathematically. This is quite aside from other complications such as structural damping and aerodynamic forces.

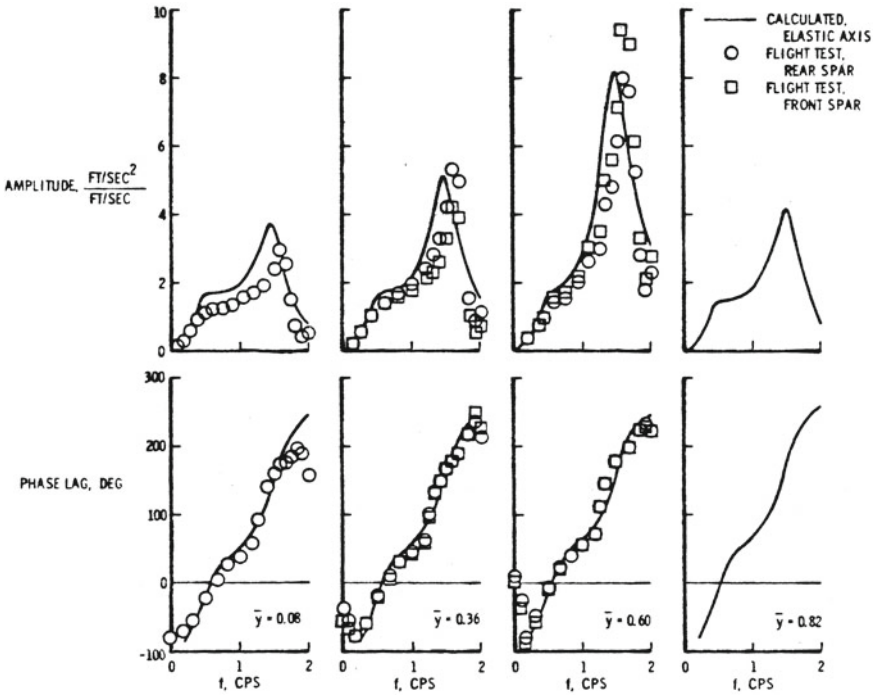

Fig. 33 $\bar{y}$ = nondimensional distance along span. From Houbolt [6]

Usually when one is dealing with a real vehicle, physical small scale models are built and with these (as well as the actual vehicle when it is available) the resonant frequencies are measured (in the absence of any airflow). The results are then used to 'correct' the mathematical model, by one method or another, including a possible direct replacement of calculated resonant frequencies by their measured counterparts in the equations of motion. When this is done the peak frequencies in the measured and calculated spectra will then agree (necessarily so) and the question then becomes one of how well the peak levels agree.

A comparison for another aircraft, the B-47, is shown in Fig. 33. Here the measured and calculated resonant frequencies are in good agreement. Moreover the peak levels and indeed all levels are in good correspondence. The particular comparison shown is for the system transfer function which relates the acceleration at a point on the aircraft to the random gust input. The calculated transfer function has been obtained from an aeroelastic mathematical model. The measured transfer function (from flight test) is inferred from a measurement of gust power spectra and cross-spectra between the vehicle acceleration and gust velocity field using the relation (c.f. e.g. (3.31))

$$H_{\ddot{h}w_G} = \frac{\Phi_{\ddot{h}w_G}}{\Phi w_G w_G}$$

Both the amplitude and phase of the transfer function are shown as a function of frequency for various positions along the wing span ($\bar{y} = 0$ is at the wing root and $\bar{y} = 1$ at the wing tip). Such good agreement between theory and experiment is certainly encouraging. However, clearly there is a major combined theoretical-experimental effort required to determine accurately the response of structures to gust loading. It should be noted that according to [6], Fig. 33 is the bending strain transfer function. 'The dimensions of the ordinates . . . are those for acceleration because the responses of the strain gages were calibrated in terms of the strain per unit normal acceleration experienced during a shallow pull-up maneuver.'

7 Generalized Equations of Motion for Complex Structures

7.1 Lagrange's Equations and Modal Methods (Rayleigh–Ritz)

The most effective method for deriving equations of motion for many complex dynamical systems is to use Lagrange's Equations.[40]

$$\frac{d}{dt}\frac{\partial L}{\partial \dot{q}_i} - \frac{\partial L}{\partial q_i} = Q_i$$

where

$$\begin{aligned} L &\equiv \text{T-U, Lagrangian} \\ T &\equiv \text{kinetic energy} \\ U &\equiv \text{potential energy} \\ Q_i &\equiv \text{generalized forces} \\ q_i &\equiv \text{generalized coordinates} \end{aligned}$$

The essential steps in the method are, first, a suitable choice of q_i and then an evaluation of T, U and Q_i in terms of Q_i and $\dot{q}_i$.

Lagrange's equations have, as one of their principal advantages, the ability to obtain the equations of motion for complex systems with little or no more difficulty than that required for rather simple ones, such as the 'typical section'. Here we shall consider a two-dimensional (planar) representation on a flight vehicle. (See Fig. 34).

We note that this formulation can include 'rigid' body as well as flexible body modes. For example, the following choices of modal functions, z_m, include rigid body vertical translation, pitching (rotation about y axis) and rolling (rotation about x axis), respectively.

[40] Recall Sect. 2.

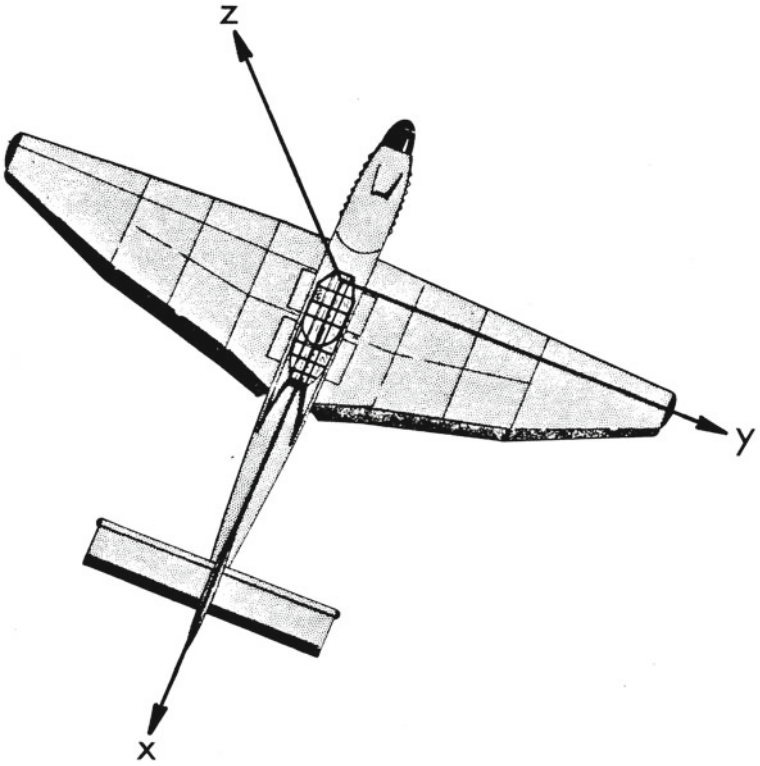

Fig. 34 Two-dimensional (planar) representation of a flight vehicle

$$z_1 = 1 \quad \text{vertical translation}$$
$$z_2 = x \quad \text{pitching}$$
$$z_3 = y \quad \text{rolling}$$

For such modes the potential elastic or strain energy is zero; however, in general, strain energy must be included for the flexible body modes.

The use of Lagrange's equations, while formally compact, does not reveal explicitly all of the complications which may arise in deriving equations of motion for an unrestrained vehicle or structure. These are seen more clearly in the discussion in a later section of integral equations of equilibrium.

7.2 Kinetic Energy

The $x - y$ plane is the plane of the (aircraft) structure. We consider deformations perpendicular to the $x - y$ plane (in the z direction). The normal displacement with

respect to a fixed inertial reference plane we call $z_a(x, y, t)$. We may then express the kinetic energy as

$$T = \frac{1}{2} \iint m(\dot{z})_a^2 dx\, dy \tag{7.1}$$

where m—mass/area and $\dot{z}_a \equiv \frac{\partial z_a}{\partial t}$. If we expand the displacement in a modal series, say

$$z_a = \sum_m q_m(t) z_m(x, y) \tag{7.2}$$

then the kinetic energy may be written as

$$T = \frac{1}{2} \sum_m \sum_n \dot{q}_m \dot{q}_n M_{mn} \tag{7.3}$$

where the *generalized mass* is given by

$$M_{mn} \equiv \iint m z_m z_n dx\, dy$$

For small motions the above integral over the body may be taken as over the undeformed structure.

If the chosen modes, z_m, satisfy an orthogonality condition

$$M_{mn} = M_m \delta_{mn} \qquad \begin{aligned} \delta_{mn} &= 1 \quad \text{for} \quad m = m \\ &= 0 \quad \text{for} \quad m \neq n \end{aligned}$$

Then (7.3) simplifies to

$$T = \frac{1}{2} \sum_m \dot{q}_m^2 M_m \tag{7.4}$$

7.3 Strain (Potential Elastic) Energy

For the strain energy, we may write a similar relation to (7.3).

$$U = \frac{1}{2} \sum_m \sum q_m q_n K_{mn} \tag{7.5}$$

where K_{mn} is a generalized spring constant which is determined from an appropriate structural theory.[41] Indeed if the z_m are the 'natural' or 'normal'modes of the structure, one may show that

[41] Recall Sect. 2.

$$K_{mn} = \omega_m^2 M_m \delta_{mn} \tag{7.6}$$

where ω_m is the mth 'natural frequency'.[42]

Equations (7.3)–(7.6) are the keys to the Lagrangian approach. Before continuing, we pause to consider K_{mn} in more detail.

Alternative Determination of K_{mn}

A stiffness influence function, $K(x, y, \xi, \eta)$, may be defined which is the (static) force/area required at point x, y to give a unit deflection at point ξ, η. Hence

$$p(x, y) = \iint K(x, y; \xi, \eta) z_a(\xi, \eta) d\xi \, d\eta \tag{7.7}$$

A simple spring analog of (7.7) is

$$F = Kd \quad \text{simple spring analog}, \quad d = \quad \text{spring displacement}$$

The potential energy stored in the elastic body is thus

$$\begin{aligned} U &= \frac{1}{2} \iint p(x, y) z_a(x, y) dx \, dy \\ U &= \frac{1}{2} Fd \quad \text{simple spring analog} \end{aligned} \tag{7.8}$$

Using (7.8) in (7.7),

$$U = \frac{1}{2} \iint \iint K(x, y; \xi, \eta) z_a(\xi, \eta) z_a(x, y) d\xi \, d\eta dx \, dy \tag{7.9}$$

$$U = \frac{1}{2} K d^2 \quad \text{simple spring analog}$$

Using our modal expansion

$$z_a(x, y, t) = \sum_m q_m(t) z_m(x, y)$$

in (7.9) we obtain

$$U = \frac{1}{2} \sum_m \sum n K_{mn} q_m q_n$$

where

[42] Meirovitch [4].

$$K_{mn} \equiv \iint \iint K(x, y; \xi, \eta) z_m(\xi, \eta) z_n(x, y) d\xi \, d\eta dx \, dy$$
$$U = \frac{1}{2} K d^2 \quad \text{simple spring analog} \tag{7.10}$$

From Maxwell's Reciprocity Theorem

$$K(x, y; \xi, \eta) = K(\xi, \eta; x, y)$$

and hence

$$K_{mn} = K_{nm} \tag{7.11}$$

$K(x, y; \xi, \eta)$ can be determined by a suitable theoretical analysis or it can be inferred from experiment. For the additional insight to be gained, let us consider the latter alternative. It is a difficult experiment to measure K directly since we must determine a distribution of force/area which gives unit deflection at one point and zero deflection elsewhere. Instead it is much easier to measure the inverse of K, a flexibility influence, $C(x, y; \xi, \eta)$ which is the deflection at x, y due to a unit force/area at ξ, η. For $C(x, y; \xi, \eta)$ we have the following relation (recall Sect. 4)

$$z_a(x, y) = \iint C(x, y; \xi, \eta) p(\xi, \eta) d\xi \, d\eta \tag{7.12}$$

Using (7.7) and (7.12) it can be shown that

$$\iint C(x, y; \xi, \eta) K(\xi, \eta; r, s) d\xi \, d\eta = \delta(r - x, s - y) \tag{7.13}$$

where δ is a Dirac delta function. Equation (7.13) is an integral equation for C or K given the other. However, it is rarely, if ever, used. Instead (7.6) and (7.1) are attacked directly by considering a finite number of loads and deflections over small (finite) areas of size $\Delta x \Delta y = \Delta\xi \Delta\eta$. Hence (7.7) and (7.12) are written

$$p(x_i, y_i) = \sum_i K(x_i, y_i; \xi_j, \eta_j) z_a(\xi_j, \eta_j) \Delta\xi \Delta\eta \tag{7.7}$$

$$z_a(x_j, y_j) = \sum_j C(x_j, y_j; \xi_i, \eta_i) p(\xi_i, \eta_i) \Delta\xi \Delta\eta \tag{7.11}$$

In matrix notation

$$\{p\} = [K]\{z_a\} \Delta\xi \Delta\eta \tag{7.7}$$

$$\{z_a\} = [C]\{p\} \Delta\xi \Delta\eta \tag{7.11}$$

Substitution of (7.12) into (7.7) and solving, gives

$$[K] = [C]^{-1}/(\Delta\xi)^2(\Delta\eta)^2 \tag{7.14}$$

Equation (7.14) is essentially a finite difference solution to (7.13). Hence, *in practice*, if (7.10) is used to compute K_{mn}, one measures C, computes K from (7.14) and then evaluates K_{mn} by numerical integration of (7.10). For a fuller discussion of influence functions, the reader may wish to consult Bisplinghoff, Mar and Pian [2].

There is one further subtlety which we have not discussed as yet. If rigid body motions of the structure are possible, then one may wish to use a C measure with respect to a fixed point. For example it may be convenient to measure C with the center of the mass fixed with respect to translation and rotation. This matter is discussed for fully later in the chapter when integral equations of equilibrium are reviewed.

We now continue the general discussion from which we digressed to consider K_{mn}. Two examples will be considered next.

Examples

(a) Torsional Vibrations of A Rod

To illustrate the key relations (7.3)–(7.6) in a more familiar situation, consider the torsional vibrations of a rod. Here

$$z_a = -x\alpha(y, t) \qquad \text{(cf. 7.2)}$$

and thus (7.1) becomes

$$T = \frac{1}{2}\int I_\alpha \dot{\alpha}^2 dy \tag{7.15}$$

where

$$I_\alpha \equiv \int mx^2 dx$$

$$\alpha \equiv \text{angle of twist}$$

From structural theory [2],

$$U = \frac{1}{2}\int GJ\left(\frac{d\alpha}{dy}\right)^2 dy \tag{7.16}$$

Let

$$\alpha = \sum_{m=1}^{M} q_m^\alpha \alpha_m(y) \tag{7.17}$$

then

$$T = \frac{1}{2} \sum_m \sum_n \dot{q}_m^\alpha \dot{q}_n^\alpha M_{mn} \tag{7.18}$$

where

$$M_{mn} \equiv \int I_\alpha \alpha_m \alpha_n dy \qquad \text{(cf. 7.3)}$$

and

$$U = \frac{1}{2} \sum_m \sum_n q_m^\alpha q_n^\alpha K_{mn} \tag{7.19}$$

where

$$K_{mn} = \iint GJ \frac{d\alpha_m}{dy} \frac{d\alpha_n}{dy} dy \qquad \text{(cf. 7.5)}$$

The specific structural model chosen determines the accuracy with which the generalized and stiffness are determined, but they always exist.

(b) Bending-Torsional Motion of A Beam-Rod

The above is readily generalized to include bending as well as torsional vibration of a beam-rod.

Let

$$z_a(x, y, t) = -x\alpha(y, t) - h(y, t) \qquad \text{(cf. 7.2)}$$

$\alpha \equiv$ twist about elastic axis

$h \equiv$ bending deflection of elastic axis

and thus (7.1) becomes

$$T = \frac{1}{2} \left\{ \int M\dot{h}^2 dy + 2 \int S_\alpha \dot{h}\dot{\alpha} dy + \int I_\alpha \dot{\alpha}^2 dy \right\} \tag{7.20}$$

where

$$M \equiv \int m\, dx, \qquad S_\alpha \equiv \int mx\, dx, \qquad I_\alpha \equiv \int mx^2\, dx$$

Also from structural theory [2],

$$U = \frac{1}{2} \left\{ \int GJ \left(\frac{\partial \alpha}{\partial y} \right)^2 dy + \int EI \left(\frac{\partial^2 h}{\partial y^2} \right)^2 dy \right\} \tag{7.21}$$

Let

$$h = \sum_{r=1}^{R} q_r^h h_r(y)$$
$$\alpha = \sum_{m=1}^{M} q_m^\alpha \alpha_m(y) \tag{7.22}$$

Then

$$T = \frac{1}{2}\sum_m \sum_n \dot{q}_m^\alpha \dot{q}_n^\alpha M_{mn}^{\alpha\alpha} + 2\sum_m \sum_r \dot{q}_m^\alpha \dot{q}_r^h M_{mr}^{\alpha h} + \sum_r \sum_s \dot{q}_r^h \dot{q}_s^h M_{rs}^{hh} \tag{7.23}$$

where

$$M_{mn}^{\alpha\alpha} \equiv \int I_\alpha \alpha_m \alpha_n dy, \quad M_{mr}^{\alpha h} \equiv \int S_\alpha \alpha_m h_r dy, \quad M_{rs}^{hh} \equiv \int mh\, h_s dy \tag{7.24}$$

and

$$U = \frac{1}{2}\left\{\sum_m \sum_n q_m^\alpha q_n^\alpha K_{mn}^{\alpha\alpha} + \sum_r \sum_s q_r^h q_s^h K_{rs}^{hh}\right\} \quad \text{(cf. 7.5)}$$

where

$$K_{mn}^{\alpha\alpha} \equiv \int GJ \frac{d\alpha_m}{dy}\frac{d\alpha_n}{dy}, \qquad K_{rs}^{hh} \equiv \int EI \frac{d^2 h_r}{dy^2}\frac{d^2 h_s}{dy^2} dy \tag{7.25}$$

Off all possible choices of modes, the 'free vibration, natural modes' are often the best choice. These are discussed in more detail in the next section.

7.4 *Natural Frequencies and Modes-Eigenvalues and Eigenvectors*

Continuing with our general discussion, consider Lagrange's equationswith the generalized forces set to zero,

$$\frac{d}{dt}\left(\frac{\partial(T-U)}{\partial \dot{q}_i}\right) + \frac{\partial U}{\partial q_i} = 0 \qquad i = 1, 2, \ldots, M$$

and thus obtain, using (7.3) and (7.5) in the above,

$$\sum M_{mi}\ddot{q}_m + K_{mi} q_m = 0 \qquad i = 1, \ldots, M \tag{7.26}$$

Consider sinusoidal motion

$$q_m = \bar{q}_m e^{iwt} \tag{7.27}$$

then, in matrix motion, (7.26) becomes

$$-\omega^2[M]\{q\} + [K]\{q\} = \{0\} \tag{7.28}$$

This is an eigenvalue problem for the eigenvalues, ω_j, $j = 1, \ldots, J$ and corresponding eigenvalues, $(q)_j$. If the modal functions originally chosen, z_m or α_m and h_r, were 'natural modes' of the system then the M and K matrices will be diagonal and the eigenvalue problem simplifies.

$$-\omega^2 \begin{bmatrix} \backslash & & \\ & M & \\ & & \backslash \end{bmatrix} \{q\} + \begin{bmatrix} \backslash & & \\ & M\omega_j^2 & \\ & & \backslash \end{bmatrix} \{q\} = \{0\} \tag{7.29}$$

and

$$\omega_1^2, \begin{Bmatrix} q_1 \\ 0 \\ 0 \\ 0 \\ 0 \end{Bmatrix}_1$$

$$\omega_2^2, \begin{Bmatrix} 0 \\ q_2 \\ 0 \\ 0 \\ 0 \end{Bmatrix}_2$$

etc.

$$\omega_M^2, \begin{Bmatrix} 0 \\ 0 \\ 0 \\ q_M \end{Bmatrix}_M$$

If this is not so then the eigenvalues may be determined from (7.22) and a linear transformation may be made to diagonalize the M and K matrices. The reader may wish to determine the eigenvalues and eigenvectors of the typical section as in exercise.

For our purposes, the key point is that expression like (7.3)–(7.6) exist. For a more extensive discussion of these matters, the reader may consult Meirovitch [4].

7.5 Evaluation of Generalized Aerodynamic Forces

The Generalized forces s in Lagrange's equations are evaluated from their definition in terms of Virtual work.

$$\delta W_{NC} = \sum_m Q_m \delta q_m \tag{7.24-2}$$

Now the virtual work may be evaluated independently from

$$\delta W_{NC} = \iint p \delta z_\alpha dx\, dy \tag{7.25-2}$$

where p is the net aerodynamic pressure on an element of the structure with (differential) area $dx\, dy$. Using (7.2) in (7.25-2)

$$\delta W_{NC} = \sum_m \delta q_m \iint p z_m dx\, dy \tag{7.26-2}$$

and we may identify from (7.25-2) and (7.24-2)

$$Q_m \equiv \iint p z_m dx\, dy \tag{7.27-2}$$

From aerodynamic theory,[43] one can establish a relationship of the form

$$p(x, y, t) = \iint \int_0^t A(x - \xi, y - \eta, t - \tau) \times \underbrace{\left[\frac{\partial z_a}{\partial \tau}(\xi, \eta, \tau) + U \frac{\partial z_a}{\partial \xi}(\xi, \eta, \tau) \right]}_{\text{'downwash'}} d\xi\, d\eta d\tau \tag{7.28-2}$$

A may be physically interpreted as the pressure at point x, y at times t due to a unit impulse of downwash at point ξ, η at time τ. Using (7.2) and (7.28-2) in (7.27-2) we may evaluate Q_m in more detail,

$$Q_m = \sum_n \int_0^t [\dot{q}_n(\tau) I_{nm\dot{q}}(t - \tau) + q_n(\tau) I_{nmq}(t - \tau)] d\tau \tag{7.29-2}$$

where

[43] See chapter 'Nonsteady Aerodynamics of Lifting and Non-lifting Surfaces', and earlier discussion in Sect. 4.

$$I_{nm\dot{q}}(t-\tau) \equiv \iint \iint A(x-\xi, y-\eta, t-\tau) z_n(\xi,\eta) z_m(x,y) dx\, dy d\xi\, d\eta$$

$$I_{nmq}(t-\tau) \equiv \iint \iint A(x-\xi, y-\eta, t-\tau) \times U \frac{\partial z_n}{\partial \xi}(\xi,\eta) z_m(x,y) dx\, dy d\xi\, d\eta$$

$I_{nm\dot{q}}$, I_{nmq} may be thought of as generalized aerodynamic impulse functions.

7.6 *Equations of Motion and Solution Methods*

Finally applying Lagrange's equations, using 'normal mode' coordinates for simplicity,

$$M_m[\ddot{q}_m + \omega_m^2 q_m] = \sum_{n=1}^{M} \int_0^1 [\dot{q}_n(\tau) I_{nm\dot{q}}(t-\tau) + q_n(\tau) I_{nmq}(t-\tau)] d\tau \qquad m = 1, \ldots, M \tag{7.30}$$

Note the form of (7.30). It is identical, mathematically speaking, to the earlier results for the typical section.[44] Hence similar mathematical solution techniques may be applied.

Time domain solutions. A Taylor Series expansion is

$$q_n(t+\Delta t) = q_n(t) + \dot{q}_n\Big|_t \Delta t + \frac{\ddot{q}_n}{2}\Big|_t (\Delta t)^2$$

One may solve for $\ddot{q}_n$ from (7.30) and hence $q_n(t+\Delta t)$ is determined. $q_n(t)$, $\ddot{q}_n(t)$ are known from initial conditions and

$$\dot{q}_n(t+\Delta t) = \dot{q}_n(t) + \ddot{q}_n(t)\Delta t + \cdots \tag{7.31}$$

Frequency domain solutions. Taking a Fourier transform of (7.30)

$$M_m[-\omega^2 + \omega_m^2]\bar{q}_m = \sum_{n}^{M} [i\omega H_{\mathrm{nm\dot{q}}} + H_{\mathrm{nmq}}]\bar{q}_n$$

where

$$\bar{q}_m \equiv \int_{-\infty}^{\infty} q_m e^{-i\omega t} dt$$

[44] Provided $S_\alpha \equiv 0$ so that h, α are normal mode coordinates for the typical section.

In matrix notation

$$\left[\left[\begin{array}{c} \backslash \\ M_m(-\omega^2+\omega_m^2) \\ \backslash \end{array}\right] - [i\omega H_{nm\dot{q}} + H_{nmq}]\right]\{\bar{q}_n\} = \{0\} \tag{7.32}$$

By examining the condition for nontrivial solutions

$$|[\cdots]| = 0$$

we may find the 'poles' of the aeroelastic transfer functions and assess the stability of the systems.

Response to gust excitation. If we wish to examine the gust response problem then we must return to (7.28) and add the aerodynamic pressure due to the gust loading

$$p_G(x, y, t) = \iiint A(x-\xi, y-\eta, t-\tau) w_G(\xi, \eta, \tau) d\xi\, d\eta d\tau$$

The resulting Generalized forces s are

$$Q_{mG}(t) = \iiiint\!\!\int A(x-\xi, y-\eta, t-\tau) \times w_G(\xi, \eta, \tau) z_m(x, y) d\xi\, d\eta\, dx\, dy\, d\tau \tag{7.33}$$

Adding (7.33) to (7.30) does not change the mathematical technique for the time domain solution. In the frequency domain, the right hand column of (7.32) is now $(\bar{Q}_{mG})$

$$\bar{Q}_{mG} = \int_{-\infty}^{\infty} Q_{mG} e^{-i\omega t} dt$$

Hence by solving (7.32) we may obtain generalized aeroelastic transfer functions

$$\frac{\bar{q}_n}{\bar{Q}_{mG}} \equiv H_{q_n Q_{mG}}(\omega; \cdots) \tag{7.34}$$

and employ the usual techniques of the frequency domain calculus including power spectral methods.

7.7 *Integral Equations of Equilibrium*

As an alternative approach to Lagrange's Equations, we consider an integral equation formulation using the concept of a structure influence (Green's) function. We shall treat a flat (two-dimensional) structure which deforms under (aerodynamic) loading

in an arbitrary way. We shall assume a symmetrical vehicle and take the origin of our coordinate system at the vehicle center of mass with the two axes in the plane of the vehicle as principal axes, x, y. See Fig. 34. Note the motion is assumed sufficiently small so that no distinction is made between the deformed and undeformed axes of the body. For example the inertia and elastic integral properties are evaluated using the (undeformed) axes x, y. The axes x, y are inertial axes, i.e., fixed in space. If we consider small deflections normal to the x, y plane, the x, y axes are approximately the principal axes of the deformed vehicle.

It will be useful to make several definitions.

z_a absolute vertical displacement of a point from x, y plane, positive up
m mass/area
p_E external applied force/area, e.g., aerodynamic forces due to gust, p_G
p_M force/area due to motion, e.g., aerodynamic forces (but not including inertial forces)

$$p_Z = p_E + p_M - m\frac{\partial^2 z_a}{\partial t^2}$$

total force/area, including inertial forces. Let us first consider equilibrium of rigid body motions.

Translation:

$$\iint p_Z dx\, dy = 0 \tag{7.35}$$

Pitch:

$$\iint x p_Z dx\, dy = 0 \tag{7.36}$$

Roll:

$$\iint y p_Z dx\, dy = 0 \tag{7.37}$$

Now consider equilibrium of deformable or elastic motion.

$$\begin{aligned} z_a^{elastic} &\equiv z_a(x, y, t) - z_a(0, 0, t) - x\frac{\partial z_a}{\partial x}(0, 0, t) - y\frac{\partial z_a}{\partial y}(0, 0, t) \\ &= \iint C(x, y; \xi, \eta) p_Z(\xi, \eta t) d\xi\, d\eta \end{aligned} \tag{7.38}$$

where

$z_a^{elastic}$ $\equiv$ deformation (elastic) of a point on vehicle

C $\equiv$ structural influence or Green's function; the (static) elastic deformation a x, y due to unit force/area at ξ, η for a vehicle fixed[45] at the origin, $x = y = 0$.

Since the method of obtaining the subsequent equations of motion involves some rather extensive algebra, we outline the method here.

1 Set $p_E = p_M = 0$.
2 Obtain 'natural frequencies and modes'; prove orthogonality of modes.
3 Expand deformation, z_a for nonzero p_E and p_M in terms of normal modes or natural modes and obtain a set of equation for the (time dependent) coefficients of the expansion. The final result will again be (7.30).

7.8 Natural Frequencies and Modes

Set $p_E = p_M = 0$. Assume sinusoidal motion, i.e.,

$$z_a(x, y, t) = \bar{z}_a(x, y)e^{i\omega t} \tag{7.39}$$

then (7.38) becomes

$$\begin{aligned} \bar{z}_a(x, y) - \bar{z}_a(0, 0) - x\frac{\partial \bar{z}_a}{\partial x}(0, 0) - y\frac{\partial \bar{z}_a}{\partial y}(0, 0) \\ = \omega^2 \iint C(x, y; \xi, \eta) m(\xi, \eta) \bar{z}_a(\xi, \eta) d\xi \, d\eta \end{aligned} \tag{7.40}$$

The frequency ω has the character of eigenvalue. Equation (7.40) can be put into the form of a standard eigenvalue problem by solving for $\overline{z}_a(0, 0)$, $\frac{\partial \bar{z}_a}{\partial x}(0, 0)$, $\frac{\partial \bar{z}_a}{\partial y}(0, 0)$ and substituting into (7.40). For example, consider the determination of $\overline{z}_a(0, 0)$. Multiply (7.40) by m and integrate over the flight vehicle area. The result is:

$$\begin{aligned} \iint m\bar{z}_a dx \, dy - \bar{z}_a(0, 0) \iint m \, dx \, dy \\ - \frac{\partial \bar{z}_a}{\partial x}(0, 0) \iint mx \, dx \, dy - \frac{\partial \bar{z}_a}{\partial y}(0, 0) \iint mx \, dx \, dy \\ = \omega^2 \iint m(x, y) \left[\iint C(x, y; \xi, \eta) \bar{z}_a(\xi\eta) d\xi \, d\eta \right] \cdot dxdy \end{aligned} \tag{7.41}$$

Examining the left hand side of (7.41), the first integral is zero from (7.35), the third and fourth integrals are zero because of our use of center-of-mass as our origin of coordinates. The second integral is identifiable as the total mass of the vehicle.

[45] By fixed we mean 'clamped' in the sense of the structural engineer, i.e., zero displacement and slope. It is sufficient to use a static influence function, since invoking by D'Alambert's Principle the inertial contributions are treated as equivalent forces.

$$M = \iint m\, dx\, dy$$

Hence

$$\begin{aligned}\bar{z}_a(0,0) &= -\frac{\omega^2}{M}\iint m(x,y)\left[\iint C m \bar{z}_a d\xi\, d\eta\right] dx\, dy \\ &= -\frac{\omega^2}{M}\iint m(\xi,\eta)\bar{z}_a(\xi,\eta) \\ &\qquad \times\left[\iint C(x,y;\xi,\eta)m(x,y)dx\, dy\right] d\xi\, d\eta\end{aligned} \tag{7.42}$$

where the second line follows by change of order of integration. In a similar fashion $\frac{\partial \bar{z}_a}{\partial x}(0,0)$, $\frac{\partial \bar{z}_a}{\partial y}(0,0)$ may be determined by multiplying (7.40) by mx and my respectively with integration over the flight vehicle. The results are

$$\begin{aligned}\frac{\partial \bar{z}_a}{\partial x}(0,0) = &-\frac{\omega^2}{I_y}\iint m(\xi,\eta)\bar{z}_a(\xi,\eta)\left[\iint C(x,y;\xi,\eta)x m(x,y)dx\, dy\right] \\ &\cdot d\xi\, d\eta\end{aligned} \tag{7.43}$$

etc. where

$$Iy \equiv \iint x^2 m(x,y)dx\, dy$$

$$Iy \equiv \iint y^2 m(x,y)dx\, dy$$

In (7.42) and (7.43) note that x, y are now dummy integration variables, not to be confused with the x, y which appear in (7.40). Using (7.41), (7.42), (7.43) in (7.40) we have

$$\bar{z}a(x,y) = \omega^2 \iint G(x,y;\xi,\eta)m(\xi,\eta)\bar{z}a(\xi,\eta)d\xi\, d\eta \tag{7.44}$$

where

$$\begin{aligned}G(x,y;\xi,\eta) \equiv\ & C(x,y;\xi,\eta) \\ &- \iint C(r,s;\xi,\eta)\left[\frac{1}{M} + \frac{xr}{I_y} + \frac{ys}{I_x}\right] m(r,s)dr\, ds\end{aligned}$$

Equation (7.44) has the form of a standard eigenvalue problem. In general, there are infinite number of nontrivial solutions (eigenfunctions), ϕ_m with corresponding eigenvalues, w_m, such that

$$\phi_m(x,y) = \omega_m^2 \iint G(x,y;\xi,\eta)m(\xi,\eta)\phi_m(\xi,\eta)d\xi\, d\eta \tag{7.45}$$

These eigenfunctions could be determined in a number of ways; perhaps the most efficient method being the replacement of (7.45) by a system of linear algebraic equations through approximation of the integral in (7.45) by a sum.

$$\phi_m(x_i, y_i) = \omega_m^2 \sum_j G(x_i, y_i; \xi_j, \eta_j) m(\xi_j, \eta_j) \phi_m(\xi_j, \eta_j) \Delta\xi \, \Delta\eta \tag{7.46}$$

In matrix notation,

$$\{\phi\} = \omega^2 [G_{ij} \, \Delta\xi \, \Delta\eta] \begin{bmatrix} \backslash & & \\ & m & \\ & & \backslash \end{bmatrix} \{\phi\}$$

or

$$\left[\begin{bmatrix} \backslash & & \\ & 1 & \\ & & \backslash \end{bmatrix} - \omega^2 [G_{ij} \, \Delta\xi \, \Delta\eta] \begin{bmatrix} \backslash & & \\ & m & \\ & & \backslash \end{bmatrix} \right] \{\phi\} = \{0\} \tag{7.47}$$

Setting the determinant of coefficients to zero, we obtain a polynomial in ω^2 which gives us (approximate) eigenvalues as roots. The related eigenvector of (7.47) is an approximate description of the eigenfunctions of (7.46).

An important and useful property of eigenfunctions is their orthogonality, i.e.,

$$\iint \phi_m(x, y) \phi_n(x, y) dx \, dy = 0 \quad \text{for} \quad m \neq n \tag{7.48}$$

We shall digress briefly to prove (7.48).

7.8.1 Proof of Orthogonality

Consider two different eigenvalues and eigenfunctions .

$$\phi_m(x, y) = \omega_m^2 \iint G m \phi_m d\xi \, d\eta \tag{7.49a}$$

$$\phi_n(x, y) = \omega_n^2 \iint G m \phi_n d\xi \, d\eta \tag{7.49b}$$

Multiply (7.49a) and (7.49b) by $m\phi_n(x, y)$ and $m\phi_m(x, y)$ respectively and $\int\int \cdots dx \, dy$.

$$\frac{1}{\omega_m^2} \iint \phi_n \phi_m m \, dx \, dy = \iint \phi_n m \left[\iint G \phi_m m \, d\xi \, d\eta \right] \cdot dx \, dy \tag{7.49c}$$

$$\frac{1}{\omega_n^2}\iint \phi_m \phi_n m\, dx\, dy = \iint \phi_m m \left[\iint G\phi_n m\, d\xi\, d\eta\right] \cdot dx\, dy \tag{7.49d}$$

Interchanging the order of integration in (7.49c) and interchanging x, y and ξ, η, and vice versa on the right-hand side gives:

$$\begin{aligned}\frac{1}{\omega_m^2}\iint \phi_m \phi_n m\, dx\, dy = \iint \phi_m m[\iint G(\xi, \eta; x, y) \\ \cdot \phi_n(\xi, \eta) m(\xi, \eta) d\xi\, d\eta] dx\, dy\end{aligned} \tag{7.50}$$

If G were symmetric, i.e.,

$$G(\xi, \eta; x, y) = G(x, y; \xi, \eta) \tag{7.51}$$

then the right-hand side of (7.49d) and (7.49c) would be equal and hence one could conclude that

$$\left[\frac{1}{\omega_m^2} - \frac{1}{\omega_n^2}\right]\iint \phi_m \phi_n m\, dx\, dy = 0$$

or

$$\iint \phi_m \phi_n m\, dx\, dy = 0 \quad \text{for} \quad m \neq n \tag{7.52}$$

Unfortunately, the situation is more complicated since G is *not* symmetric. However, from (7.44), et. seq., one can write

$$\begin{aligned}&G(\xi, \eta; x, y) - G(x, y; \xi, \eta) \\ &\quad = \iint C(r, s; \xi, \eta)\left[\frac{1}{M} + \frac{ys}{I_x} + \frac{xr}{I_y}\right] m(r, s) dr\, ds \\ &\qquad - \iint C(r, s; x, y)\left[\frac{1}{M} + \frac{\eta s}{I_x} + \frac{\xi r}{I_y}\right] m(r, s) dr\, ds\end{aligned} \tag{7.53}$$

Using the above to substitute for $G(\xi, \eta; x, y)$ in (7.50) and using (7.35)–(7.37) to simplify the result, one sees that the terms on the right-hand side of (7.53) contribute nothing. Hence, the right-hand sides of (7.49d) and (7.49c) are indeed equal.

The orthogonality result follows. Note that the rigid body modes

$$\begin{aligned}\omega_1 &= 0 \quad & \phi_1 &= 1 \\ \omega_2 &= 0 \quad & \phi_2 &= x \\ \omega_3 &= 0 \quad & \phi_3 &= y\end{aligned} \tag{7.54}$$

are orthogonal as well. One can verify readily that the above satisfy the equations of motion, (7.35)–(7.38), and that the orthogonality conditions follow from (7.35)–(7.37).

7.9 Forced Motion Including Aerodynamic Forces

We will simplify the equations of motion to a system of ordinary integral-differential equations in time by expanding the deformation in terms of normal modes.

$$z_a(x, y, t) = \sum_{m=1}^{\infty} q_m(t)\phi_m(x, y) \tag{7.55}$$

Recall the natural modes, ϕ_m, must satisfy the equations of motion with $p_E = p_M = 0$ and

$$z_a \sim e^{i\omega_m t}$$

Substituting (7.55) in (7.35)–(7.37) and using orthogonality, (7.52), and (7.54),

$$\ddot{q}_1 \iint m\,dx\,dy = \iint [p_E + p_M]dx\,dy \tag{7.56}$$

$$\ddot{q}_2 \iint x^2 m\,dx\,dy = \iint x[p_E + p_M]dx\,dy \tag{7.57}$$

$$\ddot{q}_3 \iint y^2 m\,dx\,dy = \iint y[p_E + p_M]dx\,dy \tag{7.58}$$

The reader should be able to identify readily the physical significance of the several integrals in the above equations. Substituting (7.55) into (7.38) gives

$$\begin{aligned} \sum_{m=1}^{\infty} q_m \Big[\phi_m(x, y) - \phi_m(0, 0) - x\frac{\partial \phi_m}{\partial x}(0, 0) - y\frac{\partial \phi_m}{\partial y}(0, 0)\Big] \\ = \iint C(x, y; \xi, \eta)\left[p_E + p_M - m\sum_{m=1}^{\infty} \ddot{q}_m \phi_m(\xi, \eta)\right] d\xi\,d\eta \end{aligned} \tag{7.59}$$

Now the normal modes, ϕ_m, satisfy

$$\begin{aligned} &\phi_m(x, y) - \phi_m(0, 0) - x\frac{\partial \phi_m}{\partial x}(0, 0) - y\frac{\partial \phi_m}{\partial y}(0, 0) \\ &= \omega_m^2 \iint C(x, y; \xi, \eta) m(\xi, \eta)\phi_m(\xi, \eta) d\xi\,d\eta \quad m = 1, \ldots, \infty \end{aligned} \tag{7.60}$$

Also the left-hand side of (7.59) is identically zero for the rigid body modes, $m = 1, 2, 3$. Further using (7.60)in the right-hand side of (7.59) for $m = 4, 5, \ldots$, gives finally

$$\sum_{m=4}^{\infty}\left(q_m+\frac{\ddot{q}_m}{\omega_m^2}\right)\left[\phi_m(x,y)-\phi_m(0,0)-x\frac{\partial\phi_m}{\partial x}(0,0)-y\frac{\partial\phi_m}{\partial y}(0,0)\right] = \iint C(x,y;\xi,\eta)[p_E+p_M-m\ddot{q}_1-m\xi\ddot{q}_2-m\eta\ddot{q}_3]d\xi\,d\eta \tag{7.61}$$

Multiplying (7.61) by $m(x,y)\phi_n(x,y)$ and $\int\int\cdots dx\,dy$, invoking orthogonality, gives

$$M_n\left(q_n+\frac{\ddot{q}_n}{\omega_n^2}\right)=\iint\phi_n m\Big\{\iint C[p_E+p_M-m\ddot{q}_1-m\xi\ddot{q}_2 - m\eta\ddot{q}_3]d\xi\,d\eta\Big\}dx\,dy \tag{7.62}$$

where the 'generalized mass', M_n, is defined as

$$M_n\equiv\iint\phi_n^2 m\,dx\,dy$$

Now the structural influence function, C, is symmetric, i.e.,

$$C(x,y;\xi,\eta)=C(\xi,\eta;x,y) \tag{7.63}$$

This follows from Maxwell's reciprocity theorem[46] which states that the deflection at x, y due to a unit load at ξ, η is equal to the deflection at ξ, η due to a unit load at x, y.

Using (7.63) and interchanging the order of integration in (7.62), one obtains

$$M_n\left(q_n+\frac{\ddot{q}_n}{\omega_n^2}\right)=\iint[p_E+p_M-m\ddot{q}_1-m\xi\ddot{q}_2-m\eta\ddot{q}_3] \cdot\left\{\iint C(\xi,\eta;x,y)\phi_n(x,y)m(x,y)dx\,dy\right\}\cdot d\xi\,d\eta \tag{7.64}$$

Using (7.60) in (7.64),

$$M_n\left(q_n+\frac{\ddot{q}_n}{\omega_n^2}\right)=\frac{1}{w_n^2}\iint[p_E+p_M-m\ddot{q}_1-m\xi\ddot{q}_2-m\eta\ddot{q}_3] \cdot\left[\phi_n(\xi,\eta)-\phi_n(0,0)-\xi\frac{\partial\phi_n}{\partial\xi}(0,0)-\eta\frac{\partial\phi_n}{\partial\eta}(0,0)\right] \cdot d\xi\,d\eta \tag{7.65}$$

By using orthogonality, (7.52) and the equations of rigid body equilibrium, (7.56)–(7.58), one may show that the right-hand side of (7.65) can be simplified as follows:

[46] Bisplinghoff, Mar and Pian [2].

$$M_n\left(q_n + \frac{\ddot{q}_n}{\omega_n^2}\right) = \frac{1}{\omega_n^2}\iint [p_E + p_M]\phi_n d\xi\, d\eta \tag{7.66}$$

Defining the Generalized forces,

$$Q_n \equiv \iint [p_E + p_M]\phi_n d\xi\, d\eta \qquad \text{(generalized force)}$$

one has

$$M_n[\ddot{q}_n + \omega_n^2 q_n] = Q_n \quad n = 1, 2, 3, 4, \ldots \tag{7.67}$$

Note that there is no inertial or structural coupling in the Eq. (7.67), However p_M generally depends upon $q_1, q_2, \ldots$ and hence the equations are aerodynamically coupled.[47] The lack of inertial and structural coupling is due to our use of natural or normal modes. Finally, note that the rigid body equation of motions, (7.56)–(7.58), also have the form of (7.67). Hence n may run over all integer values.

Examples

(a) Rigid Wing Undergoing Translation Responding to A Gust

One mode only $\phi_1 = 1, q_1$ ($\equiv -h$ was notation used previously in typical section model) and thus

$$M_1\ddot{q}_1 = Q_1^M + Q_1^E \tag{7.68}$$

$$Q_1^M = \iint p_M \phi_1 dx\, dy = \int L_M\, dy \tag{7.69}$$

$$Q_1^E = \iint p_E \phi_1\, dx\, dy = \int L_G\, dy \tag{7.70}$$

where

$$L_M \equiv \int p_M\, dx \quad \text{lift/span} \tag{7.71}$$

$$L_G \equiv \int p_E\, dx \quad \text{lift/span} \tag{7.72}$$

Introducing nondimensional time, $s \equiv tU/b$, (7.68) may be written

$$\frac{U^2}{b^2} M_1 q'' = \int_0^t L_M\, dy + \int_0^t L_G\, dy \tag{7.73}$$

[47] Cf. (7.31).

where

$$' \equiv \frac{d}{ds} \qquad \text{(nondimensional)}$$

Assuming strip-theory, two dimensional, incompressible flow aerodynamics, one has (recall Sect. 4 and see chapter 'Nonsteady Aerodynamics of Lifting and Non-lifting Surfaces')

$$L_M(s) = -\pi\rho U_\infty^2 \left[q''(s) + 2\int_0^s q''(\sigma)\phi(s-\sigma)d\sigma \right] \tag{7.74}$$

Note we have assumed $q_1'(0) = 0$ in the above. Similarly

$$\begin{aligned} L_G &= 2\pi\rho U_\infty b \left[w_G(0)\psi(s) + \int_0^s \frac{dw_G(\sigma)}{d\sigma}\psi(s-\sigma)d\sigma \right] \\ &= 2\pi\rho U^2 b \left[\int_0^s \frac{w_G(\sigma)}{U}\psi'(s-\sigma)d\sigma \right] \end{aligned} \tag{7.75}$$

where

$$\psi'(s) \equiv \frac{d\psi}{ds}$$

Here we have assumed that w_G is independent of y for simplicity. Substituting (7.74) and (7.75) into (7.73) we have

$$\begin{aligned} \frac{U_\infty^2}{b^2} M q_1''(s) = \pi\rho U_\infty^2 (2bl) \Big[&-\frac{q_1''}{2b} - \frac{1}{b}\int_0^s q_1''(\sigma)\phi(s-\sigma)d\sigma \\ &+ \int_0^s \frac{w_G(\sigma)}{U_\infty}\psi'(s-\sigma)d\sigma \Big] \end{aligned} \tag{7.76}$$

$M \equiv \iint m\phi_1\, dx\, dy$, total mass of wing

Note $\int L\, dy = lL$ since we have assumed b is a constant and $l \equiv$ half-span of wing. Equation (7.76) may be solved in several ways which have previously been discussed in the context of the typical section airfoil. Here, we shall pursue the method of Laplace Transforms. Transforming (7.76) (p is the Laplace Transform variable) gives

$$\frac{U^2}{b^2} M p^2 \bar{q}_1(p) = \pi\rho U^2 (2bl) \left[\frac{\bar{w}_G}{U} p\bar{\psi} \frac{p^2\bar{q}_1}{2b} - \frac{p^2\bar{q}_1}{b}\bar{\psi} \right] \tag{7.77}$$

We have taken $q(0) = q'(0) = 0$ while using the convolution theorem, i.e.,

$$\overline{\left\{ \int_0^s w_G(\sigma)\psi'(s-\phi)d\sigma \right\}} = \bar{w}_G p\bar{\phi} \qquad \text{(convolution theorem 1)}$$

$$\overline{\left\{ \int_0^s q_1''(\sigma)\phi'(s-\sigma)d\sigma \right\}} = p^2\bar{q}_1\bar{\phi} \qquad \text{(convolution theorem 2)}$$

and a bar $\bar{()}$ denotes Laplace Transform. Solving (7.77) for $\bar{q}_1$ gives

$$\bar{q}_1(p) = \frac{\frac{b}{2}\frac{\bar{w}_G}{U}\bar{\psi}}{p(\frac{\mu}{2} + \frac{1}{4} + \frac{1}{2}\bar{\phi})} \tag{7.78}$$

where

$$\mu \equiv \frac{M}{\pi(2bl)b\rho}, \quad \text{mass ratio.}$$

To complete the solution we must invert (7.78). To make this inversion tractable, ϕ and ψ are approximated by

$$\begin{aligned} \psi(s) &= 1 - 0.5e^{-0.13s} - 0.5e^{-s} \\ \phi(s) &= 1 - 0.165e^{-0.0455s} - 0.335e^{-0.3s} \end{aligned} \tag{7.79}$$

Thus

$$\begin{aligned} \bar{\psi} &= (0.565p + .013)/p(p + 0.0455)(p + 0.3) \\ \bar{\phi} &= \frac{0.5p^2 + 0.02805p + 0.01365}{p^3 + 0.3455p^2 + 0.01365p} \end{aligned} \tag{7.80}$$

and

$$\bar{q}_1 = \frac{b\frac{\bar{w}_G}{U}0.565(p^3 + 0.575p^2 + 0.093p + 0.003)}{(\mu + 0.5)p(p + 0.13)(p + 1)(p^3 + a_1p^2 + a_2p + a_3)} \tag{7.81}$$

where

$$a_1 \equiv \frac{0.3455\mu + 0.67}{\mu + 0.5}$$

$$a_2 \equiv \frac{0.01365\mu + 0.28}{\mu + 0.5}$$

$$a_3 \equiv \frac{0.01365}{\mu + 0.5}$$

Often one is interested in the acceleration,[48]

$$\begin{aligned} \ddot{q}_1 &= \frac{U^2}{b^2}q_1''\ddot{q}_1 = \frac{U^2}{b^2}\mathcal{L}^1\{p^2\bar{q}_1\} \\ &= \frac{0.565}{\mu + 0.5}\int_0^s \frac{U_\infty}{b}w_G(\sigma)\{A_1e^{-0.13(s-\sigma)} \\ &\quad + A_2e^{-(s-\sigma)} + B_1e^{\gamma_1(s-\sigma)} \\ &\quad + B_2e^{\gamma_2(s-\sigma)} + B_3e^{\gamma_3(s-\sigma)}\}d\sigma \end{aligned} \tag{7.82}$$

[48] For $q_1(0) = \dot{q}(0) = 0$. $\mathcal{L}^1 \equiv$ inverse Laplace Transform.

where

$$A_1 = \frac{N(-0.13)}{D'(.013)}$$

$$A_2 = \frac{N(-1)}{D'(-1)}$$

$$B_{k=1\,2\,3} = \frac{N(\gamma_k)}{D'(\gamma_k)}$$

and

$$\begin{aligned} N(p) &\equiv p(p^3 + 0.5756p^2 + 0.09315p + 0.003141) \\ D(p) &\equiv (p + 0.13)(p + 1)(p^3 + a_1 p + a_3) \\ \gamma_k &\text{ are the roots of } p^3 + a_1 p^2 + a_1 p + a_3 = 0 \end{aligned}$$

Note that bracketed term in (7.82) must be a real quantity though the components thereof may be complex (conjugates). Also, what does it mean physically if the real part of $\gamma 1$, $\gamma 2$ or $\gamma 3$ is positive?

An even simpler theory of gust response is available if one further approximates the aerodynamic forces. Foe example, using a quasi-static aerodynamic theory (recall Section 3.4), one has

$\psi = 1$ and thus $L_G = 2\pi\rho U_\infty^2 b \frac{w_G}{U_\infty}$

and

$\phi = 0$, and thus $L_M = 0$ (ignoring virtual inertia term)
Hence

$$\begin{aligned} M_1 \ddot{q}_1 &= \int L^G \, dy = 2\pi\rho U^2 bl \frac{w_G}{U} \\ \ddot{q}_{1_s} &= \pi \frac{\rho U^2}{M} (2bl) \frac{w_G}{U_\infty} = \frac{U_\infty}{b} \frac{w_G}{\mu} \end{aligned} \tag{7.83}$$

The subscripted quantity, $\ddot{q}_1$, is called the *static approximation to the gust response*. Figure 35 is a schematic of the result from the full theory, (7.82), referenced to the static result, (7.83). Here we have further assumed a sharp-edge gust, i.e., wG= constant. After Fig. 22 BAH. The maxima of the above curves are presented in Fig. 36. As can be seen the static approximation is a good approximation for large mass ratio, μ. For smaller μ the acceleration is less than the static result. Hence the quantity, $\frac{\ddot{q}_{1\max}}{\ddot{q}_{1_s}}$ is sometimes referred to as a 'gust alleviation' factor.

A somewhat more sophisticated aerodynamic approximation is to let (again recall Sect. 4)

$$\begin{aligned} \psi &= 1 \quad \text{and thus} \quad L_G = 2\pi\rho U^2 b \frac{w_G}{U} \\ \phi &= 1 \quad \text{and thus} \quad L_M = -\pi\rho U^2 [q''(s) + 2q'(s)] \end{aligned} \tag{7.84}$$

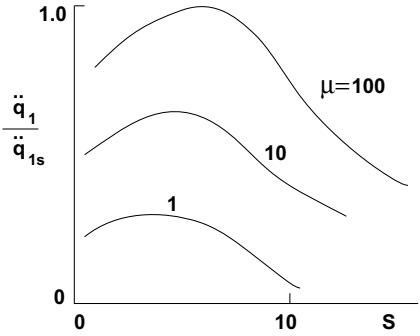

Fig. 35 Acceleration time history

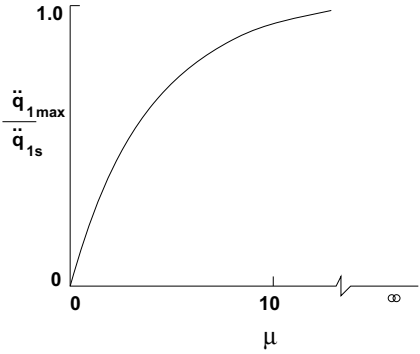

Fig. 36 Maximum acceleration versus mass ratio

assuming $q'(0) = 0$. In the motion induced lift, the L_M first term is a virtual inertial term which is generally negligible compared to the inertia of the flight vehicle. However, the second term is an aerodynamic damping term which provides the only damping in the system and hence may be important. It is this aerodynamic damping, even in the guise of the full (linear)aerodynamic theory, which gives results substantially different from the static approximation. Equation (7.84) is termed a quasi-steady aerodynamic approximation.

Using the approximation (7.84), (7.68) becomes for a constant chord, b, wing of span, l, (in nondimensional form)

$$(\mu + 0.5)q_1''(s) + q_1'(s) = \frac{bw_G(s)}{U_\infty} \tag{7.85}$$

where

$$\mu \equiv \frac{M_1}{\pi\rho(2bl) \cdot b}$$

Taking the Laplace transform of (7.85) with initial conditions

$$q_1'(0) = q(0) = 0, \quad w_G(0) = 0 \qquad \text{(Laplace transform)}$$

we have

$$(\mu+0.5)p^2\bar{q}_1(p)+p\bar{q}_1(s)=\frac{b\bar{w}_G(p)}{U_\infty} \qquad \text{(Laplace with 7.85)}$$

Solving

$$\bar{q}_1(p)=\frac{\frac{b}{U_\infty}\bar{w}_G(p)}{p\{(\mu+0.5)p+1\}}$$

and thus

$$\begin{aligned} q_1''(s) &= \mathcal{L}^{-1}p^2\bar{q}_1(p) \\ &= \frac{1}{(\mu+0.5)}\mathcal{L}^{-1}\frac{b}{U_\infty}\bar{w}_G(p)\cdot\left[1-\frac{\frac{1}{\mu+0.5}}{p+\frac{1}{\mu+0.5}}\right] \\ &= \frac{1}{\mu+0.5}\int_0^s \frac{b}{U_\infty}w_G(\sigma)\cdot\left\{\delta(s-\sigma)-\frac{1}{\mu+0.5}\exp\left(-\frac{s-\sigma}{\mu+0.5}\right)\right\}d\sigma \end{aligned} \tag{7.86}$$

or

$$\begin{aligned} \ddot{q}_1 = \frac{U_\infty^2}{b^2}q_1''(s) &= \frac{1}{\mu+0.5}\int_0^s \frac{U_\infty}{b}w_G(\sigma) \\ &\times\left\{\delta(s-\sigma)-\frac{1}{\mu+0.5}\exp\left(-\frac{s-\sigma}{\mu+0.5}\right)\right\} \end{aligned}$$

Since

$$\begin{aligned} \ddot{q}_{1_s} &= \frac{U_\infty}{b}\frac{w_G(s)}{\mu} \quad \text{(static result)}, \\ \frac{\ddot{q}_1}{\ddot{q}_{1_s}} &= \frac{\mu}{\mu+0.5}\frac{1}{w_G(s)}\int_0^s w_G(\sigma) \\ &\times\left\{\delta(s-\sigma)-\frac{1}{\mu+0.5}\exp\left(-\frac{s-\sigma}{\mu+0.5}\right)\right\}d\sigma \end{aligned} \tag{7.87}$$

For a sharp edge gust

$$\begin{aligned} w_G &= w_0 : \text{const} \quad (s>0), \\ &= 0 \quad (s<0) \end{aligned}$$

Equation (7.87) becomes

$$\frac{\ddot{q}_1}{\ddot{q}_{1_s}}=\frac{\mu}{\mu+0.5}\exp\left(-\frac{s}{\mu+0.5}\right) \tag{7.88}$$

Equation (7.88) is presented graphically in the Fig. 37. From (7.88) one may plot the maxima (which occur at $s=0$ for the quasi-steady aerodynamic theory) vs. μ.

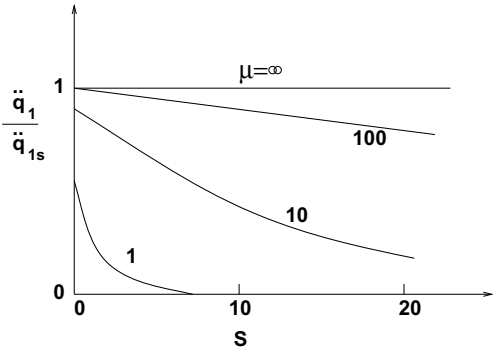

Fig. 37 Acceleration time history: Quasi-steady aerodynamics

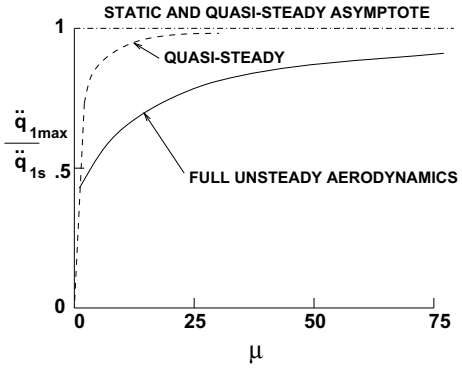

Fig. 38 Maximum acceleration for wing in translation encountering a sharp edge (step function) gust as given by various aerodynamic models versus mass ratio

These are shown in Fig. 38 where the results are compared with those using the full unsteady aerodynamic theory and the static aerodynamic theory. What conclusion do you draw concerning the adequacy of the various aerodynamic theories?

(b) Wing Undergoing Translation and Spanwise Bending

$$M_n\ddot{q}_n + M_n\omega_n^2 q_n = Q_n^M + Q_n^G \quad n = 1, 2, 3, \ldots \tag{7.89}$$

q_1 rigid body mode of translation
$q_2, q_3 \ldots$ beam bending modal amplitudes of wing The mode shapes are denoted by $\phi_n(y)$ and are normalized such that the generalized masses are given by

$$M_n \equiv \iint \phi_n^2 m\, dx\, dy = \int \left[\int m\, dx\right] \phi_n^2 dy = M \tag{7.90}$$

The Generalized forces are given by

$$\begin{aligned} Q_n^M &= \iint P_M \phi_n \, dx \, dy = \int L_M \phi_n \, dy \\ Q_n^G &= \iint P_G \phi_n \, dx \, dy = \int L_G \phi_n \, dy \end{aligned} \tag{7.91}$$

Introduce $s \equiv \frac{Ut}{b_r}$ where b_r is reference half chord. Also let the chord vary spanwise, i.e.,

$$b(y) = b_r g(y) \tag{7.92}$$

where g is given from the wing geometry. Equation (7.89) may be written

$$\frac{U^2}{b_r^2} M q_n'' + M \omega_n^2 q_n = Q_n^M + Q_n^G \tag{7.93}$$

Using two-dimensional aerodynamics in a 'strip theory' approximation and assuming the gust velocity is uniform spanwise, the aerodynamic lift forces are

$$\begin{aligned} L_M(y,s) = &- \pi \rho (b_r g)^2 \frac{U^2}{b_r^2} \sum_m \phi_m q_m'' \\ &- 2\pi \rho U \left(\frac{U}{b_r} \right) (b_r g) \int_0^s \left(\sum_m \phi_m q_m''(\sigma) \right) \phi(s-\sigma) d\sigma \end{aligned}$$

and

$$L_G(y,s) = 2\pi \rho U (b_r g) \int_0^s w_G(\sigma) \psi'(s-\sigma) d\sigma \tag{7.94}$$

Substituting (7.94) into (7.91) and the result into (7.89) gives (when nondimensionalized)

$$\begin{aligned} \mu[q_n'' + \Omega_n^2 q_n] + \sum_{m=1}^{\infty} A_{nm} q_m'' + 2 \sum_m B_{nm} \int_0^s q_m''(\sigma) \phi(s-\sigma) d\sigma \\ = 2 b_r B_{1_n} \int_0^s \frac{w_g(\sigma)}{U} \psi'(s-\sigma) d\sigma \quad n = 1, 2, 3, \ldots \end{aligned} \tag{7.95}$$

where

$$\begin{aligned} \mu &\equiv \frac{M}{\pi \rho S b_r}, \quad \Omega_n \equiv \frac{\omega_n b_r}{U} \\ A_{nm} &\equiv \frac{b_r}{S} \int_{-1/2}^{1/2} g^2 \phi_n \phi_m dy \\ B_{nm} &\equiv \frac{b_r}{S} \int_{-1/2}^{1/2} g \phi_n \phi_m dy \\ S &\equiv \int_{-1/2}^{1/2} 2b \, dy = 2 b_r \int_{-1/2}^{1/2} g \, dy, \quad \text{wing area} \end{aligned} \tag{7.96}$$

Equation (7.95) is a set of integral-differential equations in one variable, time. They are mathematically similar to the typical section equations. If we further restrict ourselves to consideration of translation plus the first wing bending mode, we have two equations in two unknowns. These may be solved as in Examples (a) by Laplace Transformation. Alternatively, Examples (a) and (b) could be handled by numerical integration in the time domain. Yet another option is to work the problem in the frequency domain.

(c) Random Gusts Solution in the Frequency Domain

Pursuing the latter option, we only need replace the Laplace transform variable, p, by iw where w is the Fourier frequency. For simplicity, consider again Example (a). Equation (7.81) may be written

$$\frac{\bar{q}_1}{b} = H_{qG}(\omega)\frac{w_{G_{(\omega)}}}{U} \tag{7.97}$$

where

$$H_{qG}(\omega) \equiv \frac{0.565[(i\omega)^3 + 0.5756(i\omega)^2 + 0.093i\omega + 0.003]}{(\mu + 0.5)(i\omega)[i\omega + 0.13][i\omega + 1][(i\omega)^3 + a_1(i\omega)^2 + a_2(i\omega)a_3]}$$

is a transfer function relating sinusoidal rigid body response to sinusoidal gust velocity. The poles of the transfer function can be examined for stability. The mean square response to a random gust velocity can be written as (cf. Eq. (7.40) in Sect. 3)

$$\left(\frac{\bar{q}_1}{b}\right)^2 = \int_0^\infty |H_{qG}(\omega)|^2 \Phi_{(w_G/U)(w_G/U)} d\omega \tag{7.98}$$

Similar expressions can be obtained for two or more degrees of freedom.

8 Other Fluid-Structural Interaction Phenomena

8.1 Fluid Flow Through a Flexible Pipe: "Firehose" Flutter

This problem has received a good deal of attention in the research literature. It has a number of interesting features, including some analogies to the flutter of plates. Possible technological applications include oil pipelines, hydraulic lines, rocket propellant fuel lines and human lung airways.[49] The equation of motion is given by (Fig. 39)[50]

[49] Weaver and Paidoussis [27] Also see Daidoussis [28].

[50] Note that slender body aerodynamic theory is used.

Fig. 39 Geometry of pipe

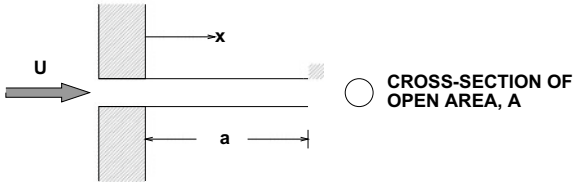

$$EI\frac{\partial^4 w}{\partial x^4} + m\frac{\partial^2 w}{\partial t^2} + \rho A\left[\frac{\partial^2 w}{\partial t^2} + 2U\frac{\partial^2 w}{\partial x\,\partial t} + U^2\frac{\partial^2 w}{\partial x^2}\right] = 0 \tag{8.1}$$

EI	bending stiffness of pipe	A	open area of pipe
m	mass/length of pipe	w	transverse deflection of pipe
ρ	fluid density	a	pipe length
U	fluid velocity		

We consider a cantilevered pipe clamped at one end of and free at the other. Previously we had considered a pipe pinned at both ends and discovered that a static instability occurred.[51] The present boundary conditios lead to a dynamic instability, flutter. We shall consider a classic eigenvalue analysis of this differential equation. Let

$$w = \bar{w}(x)e^{i\omega t} \tag{8.2}$$

where the ω are to be determined by the requirement that nontrivial solutions, $\bar{w}(x) \neq 0$, are sought. Substituting (8.2) into (8.1) we have cancelling out the common factor, $e^{i\omega t}$

$$\left\{EI\frac{d^4\bar{w}}{dx^4} - m\omega^2\bar{w} + \rho A\left[-\omega^2\bar{w} + 2Ui\omega\frac{d\bar{w}}{dx} + U^2\frac{d^2\bar{w}}{dx^2}\right]\right\}\cancel{e^{i\omega t}} = 0 \tag{8.3}$$

This ordinary differential equation may be solved by standard methods. The solution has the form

$$\bar{w}(x) = \sum_{i=1}^{4} C_i e^{p_i x}$$

where $p_1,\ldots,\ p_4$ are the four roots of

$$EIp^4 - m\omega^2 + \rho A[-\omega^2 + 2Ui\omega p + U^2p^2] = 0 \tag{8.4}$$

The four boundary conditions give four equations for $C1,\ldots,C4$. These are

[51] Sections 5.

$$
\begin{aligned}
&w(x=0)=0 \Rightarrow C_1+C_2+C_3+C_4=0\\
&\frac{\partial w}{\partial x}(x=0)=0 \Rightarrow C_1p_1+C_2p_2+C_3p_3+C_4p_4=0\\
&EI\frac{\partial^2 w}{\partial x^2}(x=a)=0 \Rightarrow C_1p_1^2e^{p_2a}+C_2p_2^2e^{p_2a}+C_3p_3^2e^{p_3a}+C_4p_4^2e^{p_4a}=0\\
&EI\frac{\partial^3 w}{\partial x^3}(x=a)=0 \Rightarrow C_1p_1^3e^{p_2a}+C_2p_2^3e^{p_2a}+C_3p_3^3e^{p_3a}+C_4p_4^{37}e^{p_4a}=0
\end{aligned}
\tag{8.5}
$$

Setting the determinant of coefficients of (8.5) equal to zero gives

$$
D\equiv\begin{vmatrix}
1 & 1 & 1 & 1\\
p_1 & p_2 & p_3 & p_4\\
p_1^2e^{p_1a} & p_2^2e^{p_2a} & p_3^2e^{p_3a} & p_4^2e^{p_4a}\\
p_1^3e^{p_1a} & p_2^3e^{p_2a} & p_3^3e^{p_3a} & p_4^3e^{p_4a}
\end{vmatrix}=0 \tag{8.6}
$$

Equation (8.6) is a transcendental equation for ω which has no known analytical solution. Numerical solution are obtained as follows. For a given pipe at a given U one makes a guess for ω (in general a complex number with real and imaginary parts.) The $p_1,\ldots,p_4$ are then evaluated from (8.4). D is evaluated from (8.6); in general it is not zero and one must improve upon the original guess for ω (iterate) until D is zero. A new U is selected and the process repeated. For $U=0$, the ω will be purely real and correspond to the natural frequencies of the pipe including the virtual mass of the fluid. Hence, it is convenient to first set $U=0$ and then systematically increase it. A sketch of ω versus U is shown below in nondimensional form. These results are taken from a paper by Paidoussis who has worked extensively on this problem. When the imaginary part of ω_I becomes negative, flutter occurs. The nondimensional variables used in presenting these results are (we have changed the notation from Paidoussis with respect to frequency)

$$
\begin{aligned}
\beta &\equiv \rho A/(\rho A+m)\\
u &\equiv (\rho\frac{AU^2}{EI})^{\frac{1}{2}}a\\
\Omega &\equiv [(m+\rho A)/EI]^{\frac{1}{2}}\omega a^2
\end{aligned}
$$

Also shown are the results obtained by a Galerkin procedure using the natural modes of a cantilevered beam (Fig. 40).

The stability boundary for this system may be presented in terms of u and β as given in Fig. 41. Also shown is the frequency, Ω_F, of the flutter oscillation. These results have been verified experimentally by Gregory and Paidoussis.[52] For a very readable historical and technical review of this problem, see the paper by Paidoussis and Issid.[53] A similar physical problem arises in nuclear reactor fuel bundles where

[52] Gregory and Paidoussis [29].

[53] Paidoussis and Issid [30].

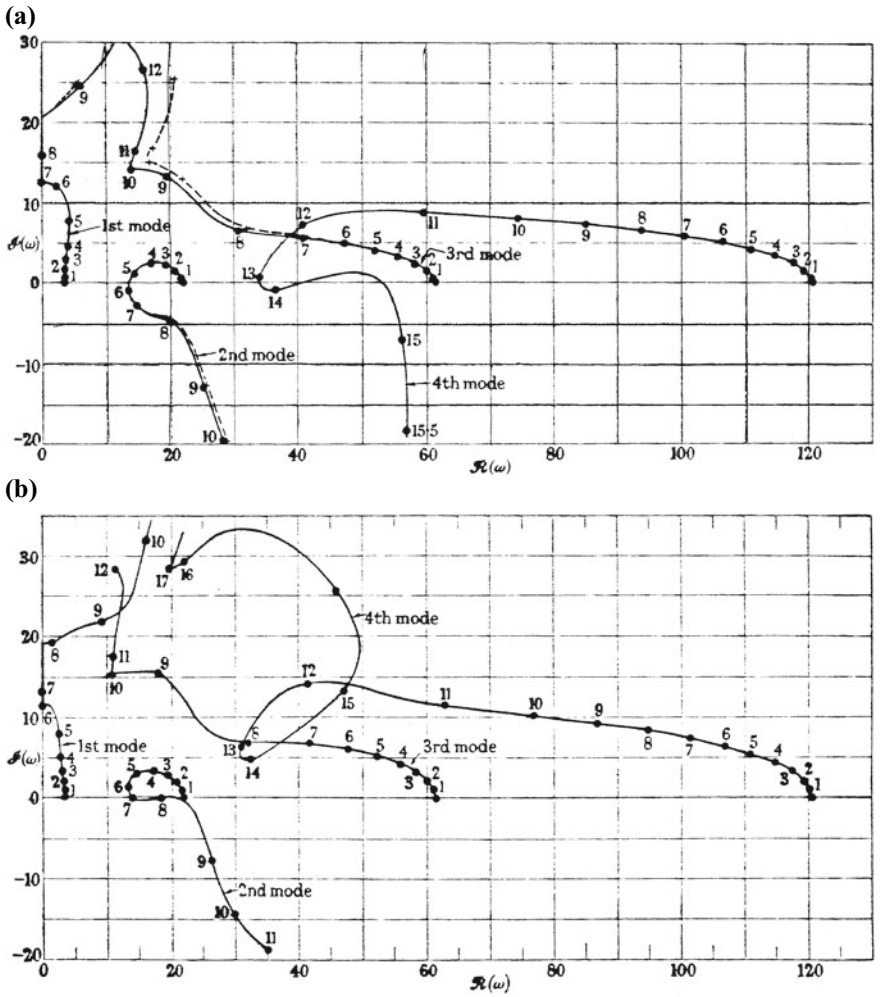

Fig. 40 **a** The dimensionless complex frequency of the four lowest modes off the system as a function of the dimensionless flow velocity for $\beta = 0.200$.—Exact analysis—four-mode approximation (Galerkin). Numbers on graph are values of u. **b** The dimensionless complex frequency of the four lowest modes of the system as a function of the dimensionless flow velocity for $\beta = 0.295$

one has a pipe in an external flow. The work of Chen is particularly noteworthy.[54] For an authoritative discussion of this class of phenomena, see the book by Paidoussis [31].

[54] Chen [31].

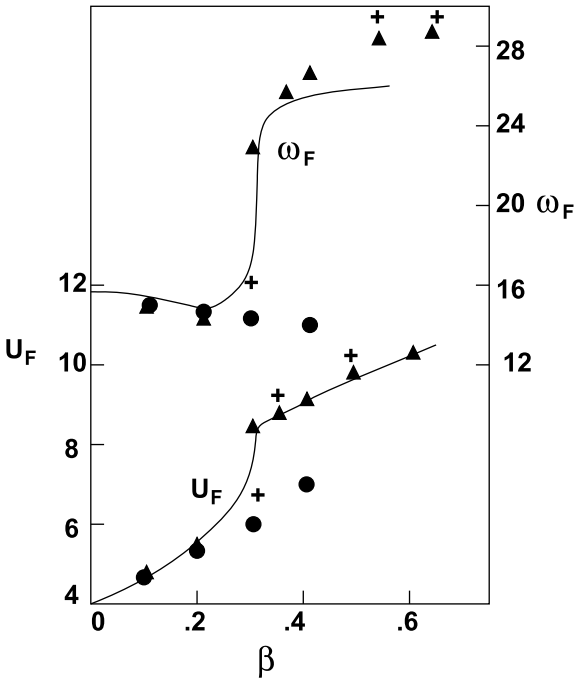

Fig. 41 Flutter boundary for flexible pipe

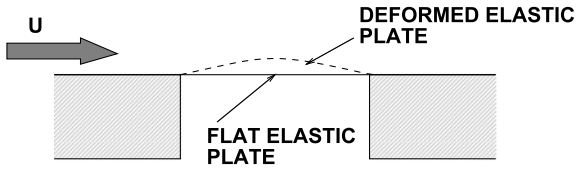

Fig. 42 Geometry of elastic plate

8.2 (High Speed) Fluid Flow Over a Flexible Wall—A Simple Prototype for Plate or Panel Flutter

One type of flutter which becomes of considerable technological interest with the advent of supersonic flight is called 'panel flutter'. Here the concern is with a thin elastic plate or panel supported at its edge. For simplicity consider two dimensional motion. The physical situation is sketched below.

Over the top of the elastic plate, which is mounted flush in an otherwise rigid wall, there is an airflow. The elastic bending of the plate in the direction of the airflow (streamwise) is the essential difference between this type of flutter and classical flutter of an airfoil as exemplified by the typical section. It is not our purpose to probe deeply into this problem here; for a thorough treatment the reader is referred to Dowell.[55] We

[55] Dowell [32]. Also see Bolotin [33].

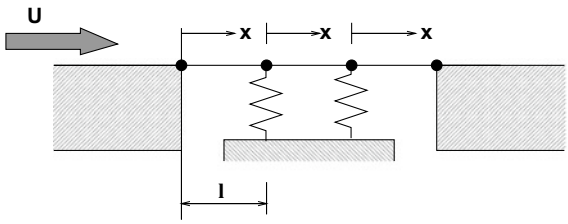

Fig. 43 Geometry of rigid plates with hinges

shall instead be content to consider a highly simplified model (somewhat analogous to the typical section model for airfoil flutter)which will bring out some of the important features of this type of problem. Thus we consider the alternative physical model shown in Fig. 42.[56] Here our model consists of three rigid plates each hinged at both ends. The hinges between the first and second plates and also the second and third plates are supported by springs. The plates have mass per unit length, m, and are of length, l. At high supersonic Mach number, $M >> 1$, the aerodynamic pressure change (perturbation) p, due to plate motion is modelled by (see chapter 'Nonsteady Aerodynamics of Lifting and Non-lifting Surfaces') a quasi-steady or quasi-static form

$$p = \frac{\rho_\infty U_\infty^2}{M_\infty} \frac{\partial w}{\partial x} \tag{8.7}$$

where $w(x, t) \frac{\partial w}{\partial x}$ are deflection and slope of any one of the rigid plates (Fig. 43).

To write the equations of motion for this physical model we must recognize that there are two degrees of freedom. It is convenient to choose as generalized coordinates, q_1, q_2, the vertical deflections of the springs.

The potential energy of the model is then

$$U = \frac{1}{2} k q_1^2 + \frac{1}{2} k q_2^2 \tag{8.8}$$

The kinetic energy requires expression for w in terms of q_1 and q_2 since the mass is distributed. For each plate we have, in turn,

$$\begin{aligned}
&\text{Plate 1:} \quad w = q_1 \frac{x}{l}, \qquad \frac{\partial w}{\partial x} = q_1 / l \\
&\text{Plate 2:} \quad w = q_1 \left[1 - \frac{x}{l}\right] + q_2 x / l, \qquad \frac{\partial w}{\partial x} = \frac{q_2 - q_1}{l} \\
&\text{Plate 3:} \quad w = q_2 \left[1 - \frac{x}{l}\right], \qquad \frac{\partial w}{\partial x} = \frac{-q_2}{l}
\end{aligned} \tag{8.9}$$

[56] This was suggested by Dr. H. M. Voss.

Because the plates are rigid, the slopes are constant within each plate. x is measured from the front (leading) edge of each plate. The kinetic energy is

$$T = \frac{1}{2}\int m\left(\frac{\partial w}{\partial t}\right)^2 dx \tag{8.10}$$

Using (8.9) in (8.10), we obtain after integration

$$T = \frac{1}{2}ml\left[\left(\frac{2}{3}\right)\dot{q}_1^2 + \left(\frac{2}{3}\right)\dot{q}_2^2 + \frac{2}{6}\dot{q}_1\dot{q}_2\right] \tag{8.11}$$

The virtual work done by the aerodynamic pressure is given by

$$\delta W = \int (-p)\delta w\, dx \tag{8.12}$$

and using (8.9) in (8.12) we obtain

$$\delta W = Q_1\delta q_1 + Q_2\delta q_2 \tag{8.13}$$

where

$$Q_1 \equiv -\frac{\rho_\infty U_\infty^2}{M_\infty}q_2/2$$
$$Q_2 \equiv \frac{\rho_\infty U_\infty^2}{M_\infty}q_1/2$$

Using Lagrange's equations and (8.8), (8.11), (8.13) the equations of motion are

$$\begin{aligned}\frac{2}{3}ml\ddot{q}_1 + \frac{ml}{6}\ddot{q}_2 + kq_1 + \frac{\rho_\infty U_\infty^2}{2M_\infty}q_2 = 0\\ \frac{ml}{6}\ddot{q}_1 + \frac{2}{3}ml\ddot{q}_2 + kq_2 - \frac{\rho_\infty U_\infty^2}{2M_\infty}q_1 = 0\end{aligned} \tag{8.14}$$

In the usual way we seek an eigenvalue solution to assess the stability of the system, i.e., let

$$q_1 = \bar{q}_1 e^{i\omega t}$$
$$q_2 = \bar{q}_2 e^{i\omega t}$$

then (8.14) becomes (in matrix notation)

$$\left[-\omega^2 ml\begin{bmatrix}\frac{2}{3} & \frac{1}{6}\\ \frac{1}{6} & \frac{2}{3}\end{bmatrix} + \begin{bmatrix}k & 0\\ 0 & k\end{bmatrix} + \frac{\rho_\infty U_\infty^2}{2M_\infty}\begin{bmatrix}0 & 1\\ -1 & 0\end{bmatrix}\right]\begin{Bmatrix}\bar{q}_1 e^{i\omega t}\\ \bar{q}_2 e^{i\omega t}\end{Bmatrix} = \begin{Bmatrix}0\\ 0\end{Bmatrix} \tag{8.15}$$

We seek nontrivial solutions by requiring the determinant of coefficients to vanish which gives the following (nondimensional) equation after some algebraic manipulation

$$\frac{15}{36}\Omega^4 - \frac{4}{3}\Omega^2 + 1 + \lambda^2 = 0 \tag{8.16}$$

where

$$\Omega^2 \equiv \frac{\omega^2 ml}{k}, \quad \lambda \equiv \frac{\rho_\infty U_\infty^2}{2M_\infty k}$$

Solving (8.16) for Ω^2 we obtain

$$\Omega^2 = \frac{8}{5} \pm \frac{2}{5}[1 - 15\lambda^2]^{\frac{1}{2}} \tag{8.17}$$

When the argument of the square root becomes negative, the solutions for Ω^2 becomes a pair of complex conjugates and hence one solution for Ω will have a negative imaginary part corresponding to unstable motion. Hence, flutter will occur for

$$\lambda^2 > \lambda_F^2 \equiv \frac{1}{15} \tag{8.18}$$

The frequency at this λ_F is given by (8.17).

$$\Omega_F = \left[\frac{8}{5}\right]^{\frac{1}{2}}$$

For reference the natural frequencies($\lambda \equiv 0$) are from (8.17).

$$\Omega_1 = (\frac{6}{5})^{\frac{1}{2}} \quad \text{and} \quad \Omega_2 = (2)^{\frac{1}{2}}$$

From (8.15) (say the first of the equations) the eigenvector ratio may be determined

$$\text{1st Natural Mode: } \frac{\bar{q}_1}{\bar{q}_2} = +1 \quad \text{for} \quad \Omega = \Omega_1 \quad \text{at} \quad \lambda = 0$$

$$\text{2nd Natural Mode: } \frac{\bar{q}_1}{\bar{q}_2} = -1 \quad \text{for} \quad \Omega = \Omega_2 \quad \text{at} \quad \lambda = 0$$

and at flutter:

$$\text{Flutter Mode: } \frac{\bar{q}_1}{\bar{q}_2} = -4 + 15^{\frac{1}{2}} \quad \text{for} \quad \Omega = \Omega_F, \quad \lambda = \lambda_f$$

Sketches of the corresponding plate shapes are given below. The important features of this hinged rigid plate model which carry over to an elastic plate are:

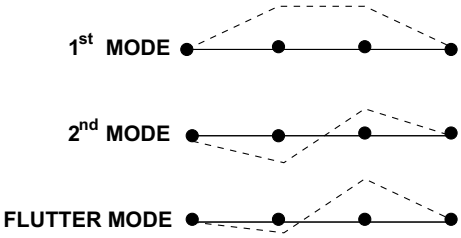

Fig. 44 Natural modes and flutter mode

(1) The flutter mechanism is a convergence of natural frequencies with increasing flow velocity. The flutter frequency is between the first and second natural frequencies. In this respect it is similar to classical bending-torsion flutter of an airfoil.

(2) The flutter mode shape shows a maximum nearer the rear edge of the plate (rather than the front edge) (Fig. 44).

There are, of course, some oversimplifications in the rigid plate model. For example, the plate length does not affect the flow velocity at which flutter occurs. For an elastic plate, it would. Also in subsonic flow the curvature of the plate has a strong influence on the aerodynamic pressure. In the rigid plate model, the curvature is identically zero, of course. Nevertheless the model serves a useful purpose in introducing this type of flutter problem. For a review of the recent literature on panel flutter, see Mei et al. [34].

References

1. Meirovitch L (1970) Methods of analytical dynamics. McGraw-Hill Book Co., New York
2. Bisplinghoff RL, Mar JW, Pian THH (1965) Statics of deformable solids. Addison-Wesley, Boston
3. Timoshenko SP, Goodier JN (1951) Theory of elasticity. McGraw-Hill, New York
4. Meirovitch L (1975) Elements of vibration analysis. McGraw-Hill, New York
5. Crandall S, Mark WD (1963) Random vibrations in mechanical systems. Academic, New York
6. Houbolt JC, Steiner R, Pratt KG (1964) Dynamic response of airplanes to atmospheric turbulence including flight data on input and response, NASA TR R-199
7. Acum WEA (1959) The comparison of theory and experiment of oscillating wings, vol. II, Chapter 10, AGARD manual on aeroelasticity
8. Pines S (1958) An elementary explanation of the flutter mechanism, In: Proceedings national specialists meeting on dynamics and aeroelasticit, Institute of the Aeronautical Sciences, Ft. Worth, Texas, pp 52–58
9. Ashley H, Zartarian G (1956) Piston theory-a new aerodynamic tool for the aeroelastician. J Aero Sci 23(12):1109–1118
10. Sears WR (1940) Operational methods in the theory of airfoils in non-uniform motion. J Franklin Inst 230:95–111
11. Jones RT (1946) Properties of low aspect-ratio pointed wing at speed below and above the speed of sound, NACA Report 835
12. Dowell EH, Widnall SE (1966) Generalized aerodynamic forces on an oscillating cylindrical shell: subsonic and supersonic flow. AIAA J 4(4):607–610

13. Widnall SE, Dowell EH (1967) Aerodynamic forces on an oscillating cylindrical duct with an internal flow. J Sound Vibr 1(6):113–127
14. Dowell EH (1968) Generalized aerodynamic forces on a flexible cylindrical shell undergoing transient motion. Q Appl Math 26(3):343–353
15. Hamming RW (1973) Numerical methods for scientists and engineers. McGraw-Hill, New York
16. Houbolt JC (1950) A recurrence matrix solution for the dynamic response of elastic aircraft. J Aero Sci 17(9):540–550
17. Hausner A (1971) Analog and analog/hybrid computer programming. Prentice-Hall, Inc, Hoboken
18. Savant CJ (1958) Basic feedback control system design. McGraw-Hill, New York
19. Garrick IE, Rubinow SL (1946) Flutter and oscillating air force calculations for an airfoil in a two-dimensional supersonic flow, NACA TR 846
20. Hassig HJ (1971) An approximate true damping solution of the flutter equation by iteration. J Aircraft 8(11):885–889
21. Eckhaus W (1971) Theory of transonic aileron buzz, neglecting viscous effects. J Aerospace Sci 29(11):712–718
22. Landahl M (1961) Unsteady transonic flow. Pergamon Press, London
23. Lambourne NC (1959) Flutter in one degree of freedom, vol. V, chap 5, AGARD Manual on Aeroelasticity
24. Abramson HN (1969) Hydroelasticity: a review of hydrofoil. Appl Mech Rev 22(2):115
25. Crisp JDC (1974) On the hydrodynamic flutter anomaly noise, shock and vibration conference. Monash University, Melbourne, Australia
26. Stenton TE (1968) Turbulence response calculations for the XB-70 airplane and preliminary comparison with flight data. Presented at the Meeting on aircraft response to turbulence. NASA Langley Research Center, pp 24–25
27. Weaver DS, Paidoussis MP (1977) On collapse and flutter phenomena in thin tubes conveying fluid. J Sound Vibr 50:117–132
28. Gregory RW, Paidoussis MP (1966) Unstable oscillation of tubular cantilevers conveying fluid. I. Theory. II. Experiments. Proceedings of the Royal Society A, vol. 293, pp. 512–527, 528–542
29. Paidoussis MP, Issid NT (1974) Dynamic instability of pipes conveying fluid. J. Sound Vibr 33(3):267–294
30. Chen SS (1975) Vibration of nuclear fuel bundles. Nuclear Eng Design 35:399–422
31. Paidoussis MP (1998) Fluid-structure interactions: slender structures and axial flow. Academic, New York
32. Dowell EH (1974) Aeroelasticity of plates and shells. Noordhoff International Publishing, Leydenm
33. Bolotin VV (1963) Non-conservative problems of the elastic theory of stability. Pergamon Press, Oxford
34. Mei C, Abdel-Motagaly K, Chen RR (1999) Review of nonlinear panel flutter at supersonic and hypersonic speeds. Appl Mech Rev 10:321–332

Nonsteady Aerodynamics of Lifting and Non-lifting Surfaces

Earl H. Dowell

Abstract The classical theory for unsteady potential flow models in the supersonic, Subsonic and transonic mach number ranges is presented including representative computational methods and results. The discussion with the simplest case of supersonic flow in two dimensions and then proceeds to consider the generalization to three dimensional flow, then subsonic flow and finally transonic flow. The discussion proceeds from the simplest to the most complex case and does not follow the historical order in which these subjects were treated. Also fourier and laplace transforms are used to obtain the key results even though other methods were used historically to first derive the governing integral equations.

Nomenculture

A	aerodynamic influence function; see Eq. (5.36)
a, b	see definitions following Eq. (5.1)
a_m, b_n	see equation preceding (5.10)
$\tilde{a}_0$	see equation following (5.26)
a_∞	free stream speed of sound
B	$\equiv -b_0$
C_p	$\equiv 2(p - p_\infty)/\rho_\infty U_\infty^2$; pressure coefficient due to airfoil motion
$C_{p_m s}$	mean steady pressure coefficient due to airfoil finite thickness at zero angle of attack
C_{L_α}	lift curve slope per degre
c	airfoil chord
d	see equation following (5.26)
$\tilde{d}$	see equation following (5.35)
e	see Eq. (5.30)
f	vertical airfoil displacement
h	rigid body translation of airfoil
Im	imaginary part

E. H. Dowell (✉)
Mechanical Engineering and Materials Science, Duke University, Durham, NC, USA
e-mail: earl.dowell@duke.edu

E. H. Dowell (ed.), *A Modern Course in Aeroelasticity*, Solid Mechanics and Its Applications 264, https://doi.org/10.1007/978-3-030-74236-2_4

i	$\equiv (-1)^{\frac{1}{2}}$
K	aerodynamic kernel function; see Eq. (5.55)
k	$\equiv \frac{\omega c}{U_\infty}$
$\tilde{k}$	see equation following (5.45)
L	lift
M	pitching moment about leading edge
M_∞	free stream Mach number
p	perturbation pressure; also Laplace Transform variable
Re	Real part
r	see Eqs. (5.37), (5.47) and (5.56)
t	time
U_∞	free stream velocity
w_a	downwash
x, y, z	spatial coordinated
x', y', z'	spatial coordinates
$\tilde{x}$	$\equiv \frac{a_0 x}{2b_0}$
$x_{c.p.}$	center of pressure; measured from leading edge
x_0	see equation preceding (5.10)
α	angle of attack
γ	ratio of specific heats; also Fourier transform variable
Φ	see Eq. (5.41)
ϕ	velocity potential
ψ	see Eq. (5.47)
ρ_∞	free stream density
Ω	see Eq. (5.42)
ω	frequency of airfoil oscillation
ξ, λ, η	dummy integration variables for x, y, z

Superscripts

0	basic solution
$\prime$	correction to basic solution
*	Laplace Transform
†	Fourier transform

Subscripts

U, L	upper, lower surfaces

1 Basic Fluid Dynamic Equations

Nonsteady aerodynamics is the study of *time dependent* fluid motion generated by (solid) bodies moving in a fluid. Normally (and as distinct from classical acuostics) the body motion is composed of a (large) steady motion, plus a (small) time dependent motion. In classical acoustics no (large) steady motions are examined. On the other hand, it should be said, in most of classical aerodynamic theory small time dependent motions are ignored, i.e. only small *steady* perturbations from the original steady motion are usually examined. However in a number of problems arising in aeroelasticity, such as a flutter and gust analysis, and also in fluid generated noise, such as turbulent boundary layers and jet wakes, the more general case must be attacked. It shall be our concern here.[1] The basic assumptions about the nature of the fluid are that it be inviscid and its thermodynamic processes be isentropic. We shall first direct our attention to a derivation of the Equations of motion, using the apparatus of vector calculus and, of course, allowing for a large mean flow velocity Let us recall some purely mathematical relationships developed in the vector calculus. These are all variations of what is usually termed Gauss' theorem.[2]

$$\text{I} \quad \iint c\vec{n}\, dA = \iiint \nabla c\, dV$$
$$\text{II} \quad \iint \vec{b}\cdot\vec{n}\, dA = \iiint \nabla\cdot\vec{b}\, dV$$
$$\text{III} \quad \iint \vec{a}(\vec{b}\cdot\vec{n})\, dA = \iiint [\vec{a}(\nabla\cdot\vec{b}) + (\vec{b}\cdot\nabla)\vec{a}]\, dV$$

Also

$$IV \quad \nabla(\vec{a}\cdot\vec{a}) = 2(\vec{a}\cdot\nabla)\vec{a} + 2\vec{a}\times(\nabla\times\vec{a}) \tag{IV}$$

In the above, V is an arbitrary closed volume, A its surface area and $\vec{a}$ and $\vec{b}$ are arbitrary vectors and c an arbitrary scalar.

1.1 Conservation of Mass

Consider an arbitrary but fixed volume of fluid, V, enclosed by a surface, A. $\vec{q}$ is the (vector) fluid velocity, dA is the surface elemental area, $\vec{n}$ is the surface normal, $\vec{q}\cdot\vec{n}$ is the (scalar) velocity component normal to surface, $\iint \rho\vec{q}\cdot\vec{n}\, dA$ is the rate of mass flow (mass flux) through surface, positive outward, $\partial/\partial t \iiint \rho\, dV$ is the rate of mass increase inside volume and $= \iiint(\partial\rho/\partial t)dV$ since V, through arbitrary, is fixed.

---

[1]References: Chap. 7, Liepmann [1]. Chapters 4, BA pp.70–81, Brief Review of Fundamentals; pp. 82–152, Catalog of available results with some historical perspective (1962). Chapters "Stall Flutter"–Aeroelastic Response of Rotorcraft, BAH, Detailed discussion of the then state-of-the art (1955) now largely of interest to aficionados. Read pp.188–200 and compare with Chap. 4, BA. AGARD, Vol., II.

[2]Hildebrand [2].

The physical principle of continuity of mass states that the fluid increase inside the volume = rate of mass flow *into* volume through the surface.

$$\int\int\int \frac{\partial \rho}{\partial t} dV = -\int\int \rho \vec{q} \cdot \vec{n} dA \tag{1.1}$$

Using II, the area integral may be transformed to a volume integral. Equation (1.1) then reads:

$$\iiint \frac{\partial \rho}{\partial t} dV = -\iiint \nabla \cdot (\rho \vec{q}) dV$$

or

$$\int\int\int [\frac{\partial \rho}{\partial t} + \nabla \cdot (\rho \vec{q})] dV = 0 \tag{1.2}$$

Since V is arbitrary, (1.2)

$$\frac{\partial \rho}{\partial t} + \nabla \cdot (\rho \vec{q}) = 0 \tag{1.3}$$

This is the conservation of mass, differential equation in three dimensions. Alternative forms are:

$$\frac{\partial \rho}{\partial t} + \rho \nabla \cdot \vec{q} + (\vec{q} \cdot \nabla)\rho = 0$$

$$\frac{D\rho}{Dt} + \rho(\nabla \cdot \vec{q}) = 0 \tag{1.4}$$

where

$$\frac{D}{Dt} \equiv \frac{\partial}{\partial t} + (\vec{q} \cdot \nabla)$$

1.2 Conservation of Momentum

The conservation or balance of momentum equation may be derived in a similar way.

$$\int\int\int \frac{\partial}{\partial t}(\rho \vec{q}) dV$$

is the rate of momentum increase inside the volume

$$\int\int \rho \vec{q} (\vec{q} \cdot \vec{n}) dA$$

is the rate of momentum flow (momentum flux) through surface, positive outward

$$\int\int -p\vec{n}\, dA$$

is the (pressure) force acting on the surface area enclosing the volume (recall $\vec{n}$ is positive outward)

The physical principal is that the total rate of change of momentum = force acting on V.

$$\int\int\int \frac{\partial(\rho\vec{q})}{\partial t} dV + \int\int \rho\vec{q}(\vec{q}\cdot\vec{n})dA = \int\int -p\vec{n}\, dA \tag{4.1}$$

Using I and III to transform the area integrals and rearranging terms,

$$\int\int\int \{\frac{\partial}{\partial t}(\rho\vec{q}) + \rho\vec{q}(\nabla\cdot\vec{q}) + (\vec{q}\cdot\nabla)\rho\vec{q} + \nabla p\} dV = 0 \tag{1.6}$$

Again because V is arbitrary,

$$\frac{\partial}{\partial t}(\rho\vec{q}) + \rho\vec{q}(\nabla\cdot\vec{q}) + (\vec{q}\cdot\nabla)\rho\vec{q} = -\nabla p \tag{1.7}$$

Alternative forms are

$$\frac{D}{Dt}(\rho\vec{q}) + \rho\vec{q}(\nabla\cdot\vec{q}) = -\nabla p$$

or

$$\rho\frac{D\vec{q}}{Dt} + \vec{q}[\rho\nabla\cdot\vec{q} + \frac{D\rho}{Dt}] = -\nabla\rho \tag{1.8}$$

where the bracketed term in (1.8) vanishes from (1.4).

Finally to complete our system of equations we have the isentropic relation,

$$p/\rho^{\gamma} = \text{constant} \tag{1.9}$$

Equations (1.3),(1.8) and (1.9) are five scalar equations (or two scalar plus one vector equations) in five scalar unknowns: p, ρ and three scalar components of the (vector) velocity, $\vec{q}$.

1.3 Irrotational Flow, Kelvin's Theorem and Bernoulli's Equation

To solve these nonlinear, partial differential equations we must integrate them. Generally, this is an impossible task except by numerical procedures. However, there is one integration that may be preformed which is both interesting theoretically and useful for application.

Consider the momentum equation which may be written

$$\frac{D\vec{q}}{Dt} = \frac{-\nabla p}{\rho} \tag{1.10}$$

On the right-hand side, using Leibnitz' Rule,[3] we may write

$$\frac{\nabla p}{\rho} = \nabla \int_{p_{ref}}^{p} \frac{dp_1}{\rho_1(p_1)} \tag{1.11}$$

where ρ_1, p_1 are dummy integration variables, and p_{ref} some constant reference pressure on the left-hand side

$$\frac{D\vec{q}}{Dt} \equiv \frac{\partial \vec{q}}{\partial t} + (\vec{q} \cdot \nabla)\vec{q}$$

In the above the second term may be written as

$$(\vec{q} \cdot \nabla)\vec{q} = \nabla \frac{(\vec{q} \cdot \vec{q})}{2} \quad \text{from IV}$$

and if we assume the flow is irrotational,

$$\vec{q} = \nabla \phi \tag{1.12}$$

where ϕ is the scalar velocity potential. Equation (1.12) implies and is implied by

$$\nabla \times \vec{q} = 0 \tag{1.13}$$

The vanishing of the curl of velocity is a consequence of Kelvin's Theorem which states that a flow which is initially irrotational, $\nabla \times \vec{q} = 0$, remains so at all subsequent time in the absent of dissipation, e.g., viscosity or shock waves. It can be proven using (1.3), (1.8) and (1.9). No additional assumptions are needed.

Let us pause to prove this result. We shall begin with the momentum equation.

$$\frac{D\vec{q}}{Dt} = -\frac{\nabla p}{\rho}$$

First form $\nabla\times$ and then dot the result into $\vec{n}_A\, dA$ and integrate over A. $\vec{n}_A$ is a unit normal to A and A itself is an arbitrary area of the fluid. The result is

$$\frac{D}{Dt} \int\int (\nabla \times \vec{q}) \cdot \vec{n}_A\, dA = -\int\int [\nabla \times (\frac{\nabla p}{\rho})] \cdot \vec{n}_A\, dA$$

[3]Hildebrand [2], pp. 348–353.

From Stokes Theorem,[4]

$$-\int\int[\nabla\times(\frac{\nabla p}{\rho})]\cdot\vec{n}_A\,dA=-\int\frac{\nabla p}{\rho}\cdot d\vec{r}$$
$$=-\oint\frac{dp}{\rho}$$

$d\vec{r}\equiv$ arc length along contour of the bounding arc of A. Since the bounding contour is closed, and ρ is solely a function of p,

$$\oint\frac{dp}{\rho}=0$$

Hence

$$\frac{D}{Dt}\int\int(\nabla\times\vec{q})\cdot\vec{n}_A\,dA=0$$

Since A is arbitrary

$$\nabla\times\vec{q}=\text{constant}$$

and if $\nabla\times\vec{q}=0$ initially, it remains so thereafter.

Now let us return to the integration of the momentum equation, (1.10). Collecting the several terms from (1.10)–(1.12), we have

$$\frac{\partial}{\partial t}(\nabla\phi)+\nabla\frac{(\nabla\phi\cdot\nabla\phi)}{2}+\nabla\int_{p_{ref}}^{p}\frac{dp_1}{\rho_1}=0 \tag{1.14}$$

or

$$\nabla[\frac{\partial\phi}{\partial t}+\frac{\nabla\phi\cdot\nabla\phi}{2}+\int_{p_{ref}}^{p}\frac{dp_1}{\rho_1}]=0$$

or

$$\frac{\partial\phi}{\partial t}+\frac{\nabla\phi\cdot\nabla\phi}{2}+\int_{p_{ref}}^{p}\frac{dp_1}{\rho_1}=F(t) \tag{1.15}$$

We may evaluate $F(t)$ by examining the fluid at some point where we know its state. For example, if we are considering an aircraft or missile flying at constant velocity through the atmosphere we know that far away from the body

$$\vec{q}=U_\infty\vec{i}$$

$$\phi=U_\infty x$$

$$p=p_\infty$$

[4]Hildebrand [2], p. 318.

If we choose as the lower limit, $p_{ref} = p_\infty$ then (1.15) becomes

$$0 + \frac{U_\infty^2}{2} + 0 = F(t)$$

and we find that F is a constant independent of space *and* time. Hence finally

$$\frac{\partial \phi}{\partial t} + \frac{\nabla \phi \cdot \nabla \phi}{2} + \int_{p_\infty}^{p} \frac{dp_1}{\rho_1} = \frac{U_\infty^2}{2} \tag{1.16}$$

(1.16) is usually referred to as Bernoulli's equation although the derivation for non-steady flow is due to Kelvin.

The practical value of Bernoulli's equation is that it allows one to relate p to ϕ. Using

$$\frac{p}{p_\infty} = (\frac{\rho}{\rho_\infty})^\gamma$$

one may compute from (1.16) (the reader may do the computation)

$$C_p = \frac{p - p_\infty}{\frac{\gamma}{2} p_\infty M^2} = \frac{2}{\gamma M^2}\{[1 + \frac{\gamma - 1}{2} M^2 (1 - \frac{(\vec{q} \cdot \vec{q} + 2\frac{\partial \phi}{\partial t})}{U_\infty^2})]^{\gamma/(\gamma-1)} - 1\} \tag{1.17}$$

where the Mach number is

$$M^2 \equiv \frac{U_\infty^2}{a_\infty^2}$$

and

$$a^2 \equiv \frac{dp}{d\rho} = \frac{\gamma p}{\rho}$$

a is the speed of sound.

1.4 Derivation of a Single Equation for Velocity Potential

Most solutions are obtained by solving this equation.

We shall begin with the conservation of mass equation (1.14)

$$\frac{1}{\rho}\frac{\partial \rho}{\partial t} + \frac{\vec{q} \cdot \nabla \rho}{\rho} + \nabla \cdot \vec{q} = 0 \tag{1.4}$$

Consider the first term. Using Leibnitz' rule we way write

$$\frac{\partial}{\partial t} \int_{p_\infty}^{p} \frac{dp_1}{\rho_1} = \frac{\partial \rho}{\partial t}\frac{dp}{d\rho}\frac{d}{dp}\int_{p_\infty}^{p} \frac{dp_1}{\rho_1} = \frac{\partial \rho}{\partial t} a^2 \frac{1}{\rho}$$

Thus

$$\frac{1}{\rho}\frac{\partial \rho}{\partial t} = \frac{1}{a^2}\frac{\partial}{\partial t}\int_{p_\infty}^{p}\frac{dp_1}{\rho_1} = \frac{1}{a^2}\frac{\partial}{\partial t}\left[\frac{\partial \phi}{\partial t} + \frac{\nabla\phi\cdot\nabla\phi}{2} + \frac{U_\infty^2}{2}\right] \tag{1.18}$$

from Bernouilli's equation (1.16).

In similar fashion, the second term may be written

$$\vec{q}\cdot\frac{\nabla\rho}{\rho} = \frac{-\vec{q}\cdot\nabla}{a^2}\left[\frac{\partial\phi}{\partial t} + \frac{\nabla\phi\cdot\nabla\phi}{2}\right] \tag{1.19}$$

Finally, the third term

$$\nabla\cdot\vec{q} = \nabla\cdot\nabla\phi = \nabla^2\phi \tag{1.20}$$

Collecting terms, and rearranging

$$\begin{aligned} &-\frac{1}{a^2}\left\{\frac{\partial^2\phi}{\partial t^2} + \frac{\partial}{\partial t}\left(\frac{\nabla\phi\cdot\nabla\phi}{2}\right) + \nabla\phi\cdot\frac{\partial}{\partial t}\nabla\phi + \nabla\phi\cdot\nabla\left(\frac{\nabla\phi\cdot\nabla\phi}{2}\right)\right\} \\ &\quad + \nabla^2\phi = 0 \\ &\nabla^2\phi - \frac{1}{a^2}\left[\frac{\partial}{\partial t}(\nabla\phi\cdot\nabla\phi) + \frac{\partial^2\phi}{\partial t^2} + \nabla\phi\cdot\nabla\left(\frac{\nabla\phi\cdot\nabla\phi}{2}\right)\right] = 0 \end{aligned} \tag{1.21}$$

Note we have not yet accomplished what we set out to do, since (1.21) is a single equation with *two* unknowns, ϕ and a. A second independent relation between ϕ and a is needed.

The simplest method of obtaining this is to use

$$a^2 \equiv \frac{dp}{d\rho}$$

and

$$\frac{p}{\rho^\gamma} = \text{constant}$$

in Bernoulli's equation. The reader may verify that

$$\frac{a^2 - a_\infty^2}{\gamma - 1} = \frac{U_\infty^2}{2} - \left(\frac{\partial\phi}{\partial t} + \frac{\nabla\phi\cdot\nabla\phi}{2}\right) \tag{1.22}$$

1.5 Small Perturbation Theory

Equations (1.21) and (1.22) are often too difficult to solve. Hence a simpler approximate theory is sought.

As in acoustics we shall linearize about a uniform equilibrium state. Assume

$$\begin{aligned} a &= a_\infty + \hat{a} \\ p &= p_\infty + \hat{p} \\ \rho &= \rho_\infty + \hat{\rho} \\ \vec{q} &= U_\infty \vec{i} + \hat{\vec{q}} \\ \phi &= U_\infty x + \hat{\phi} \\ \nabla\phi &= U_\infty \vec{i} + \nabla\hat{\phi} \end{aligned} \tag{1.23}$$

Note in the present case we linearize about a uniform flow with velocity, U_∞. Using (1.23) in (1.21) and retraining lowest order terms:

First term:

$$\nabla^2\phi \to \nabla^2\hat{\phi}$$

Second term:

$$\begin{aligned} &\frac{\partial}{\partial t}(\nabla\phi\cdot\nabla\phi) + \frac{\partial^2\phi}{\partial t^2} + \nabla\phi\cdot\nabla\left(\frac{\nabla\phi\cdot\nabla\phi}{2}\right) \\ &\quad = 2[U_\infty\vec{i} + \nabla\hat{\phi}]\cdot\frac{\partial}{\partial t}[U_\infty\vec{i} + \nabla\hat{\phi}] + \frac{\partial^2\hat{\phi}}{\partial t^2} \\ &\qquad + [U_\infty\vec{i} + \nabla\hat{\phi}]\cdot\nabla\left[\frac{U_\infty^2}{2} + U_\infty\vec{i}\cdot\nabla\hat{\phi} + \frac{1}{2}\nabla\hat{\phi}\cdot\nabla\hat{\phi}\right] \\ &\quad = 2U_\infty\frac{\partial^2\hat{\phi}}{\partial x\partial t} + \frac{\partial^2\hat{\phi}}{\partial t^2} + U_\infty^2\frac{\partial^2\hat{\phi}}{\partial x^2} + O(\hat{\phi}^2) \end{aligned}$$

Thus the linear or small perturbation equation becomes

$$\nabla^2\hat{\phi} - \frac{1}{a_\infty^2}\left[\frac{\partial^2\hat{\phi}}{\partial t^2} + 2U_\infty\frac{\partial^2\hat{\phi}}{\partial x\partial t} + U_\infty^2\frac{\partial^2\hat{\phi}}{\partial x^2}\right] = 0 \tag{1.24}$$

Note that we have replaced a by a_∞ which is correct to lowest order. By examining (1.22) one may show that

$$\hat{a} = -\frac{\gamma-1}{2}\frac{\left[\frac{\partial\hat{\phi}}{\partial t} + U_\infty\frac{\partial\hat{\phi}}{\partial x}\right]}{a_\infty} \tag{1.25}$$

Hence it is indeed consistent to replace a by a_∞as long as M is not too large where $M \equiv U_\infty/a_\infty$.

In a similar fashion the relationship between pressure and velocity potential, (1.17), may be linearized

$$C_p \simeq \frac{\hat{p}}{\frac{\gamma}{2} p_\infty M^2} = -\frac{2}{U_\infty}\frac{\partial \hat{\phi}}{\partial x} - \frac{2}{U_\infty^2}\frac{\partial \hat{\phi}}{\partial t}$$

or

$$\hat{p} = -\rho_\infty [\frac{\partial \hat{\phi}}{\partial t} + U_\infty \frac{\partial \hat{\phi}}{\partial x}] \tag{1.26}$$

1.5.1 Reduction to Classical Acoustics

By making a transformation of coordinates to a system at rest with respect to the fluid, we may formally reduce the problem to that of classical acoustics.

Define

$$x' \equiv x - U_\infty t$$

$$y' \equiv y$$

$$z' \equiv z$$

$$t' \equiv t$$

then

$$\frac{\partial}{\partial x} = \frac{\partial}{\partial x'}$$

$$\frac{\partial}{\partial t} = \frac{\partial x'}{\partial t}\frac{\partial}{\partial x'} + \frac{\partial t'}{\partial t}\frac{\partial}{\partial t'}$$

$$= -U_\infty \frac{\partial}{\partial x'} + \frac{\partial}{\partial t'}$$

and (1.24) becomes the classical wave equation

$$\nabla'^2 \hat{\phi} - \frac{1}{a_\infty^2}\frac{\partial^2 \hat{\phi}}{\partial t'^2} = 0 \tag{1.27}$$

and (1.26) becomes

$$\hat{p} = -\rho_\infty \frac{\partial \hat{\phi}}{\partial t'}$$

The general solution to (1.27) is

$$\hat{\phi} = f(\alpha x' + \beta y' + \epsilon z' + a_\infty t') + g(\alpha x' + \beta y' + \epsilon z' - a_\infty t')$$

where

$$\alpha^2 + \beta^2 + \epsilon^2 = 1$$

Unfortunately the above solution is not very useful, nor is the primed coordinate system, as it is difficult to satisfy the boundary conditions on the moving body in a coordinate system at rest with respect to the air (and hence moving with respect to the body). That is, obtaining solutions of (1.24) or (1.27) is not especially difficult per se. It is obtaining solutions subject to the boundary conditions of interest which is challenging.

1.5.2 Boundary Conditions

We shall need to consider boundary conditions of various types and also certain continuity conditions as well. In general we shall see that, at least in the small perturbation theory, it is the boundary conditions, rather than the equation of motions per se, which offer the principal difficulty.

The BODY BOUNDARY CONDITION states the normal velocity of the fluid at the body surface equals the normal velocity of the body.

Consider a body whose surface is described by $F(x, y, z, t) = 0$ at some time, t, and at some later time, $t + \Delta t$, by $F(x + \Delta x, y + \Delta y, z + \Delta z, t + \Delta t) = 0$. See Fig. 1

Now

$$\Delta F \equiv F(\vec{r} + \Delta\vec{r}, t + \Delta t) - F(\vec{r}, t) = 0$$

and also

$$\Delta F = \frac{\partial F}{\partial x}\Delta x + \frac{\partial F}{\partial y}\Delta y + \frac{\partial F}{\partial z}\Delta z + \frac{\partial F}{\partial t}\Delta t$$

$$= \nabla F \cdot \Delta\vec{r} + \frac{\partial F}{\partial t}\Delta t$$

Thus

$$\nabla F \cdot \Delta\vec{r} + \frac{\partial F}{\partial t}\Delta t = 0 \tag{1.28}$$

Now

Fig. 1 Body geometry

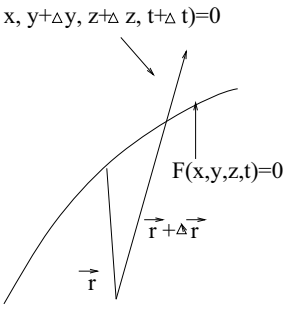

$$\vec{n} = \frac{\nabla F}{|\nabla F|} \quad \text{unit normal} \tag{1.29}$$

also

$$\vec{V} \equiv \lim_{\Delta t \to 0} \frac{\Delta \vec{r}}{\Delta t} \equiv \text{body velocity}$$

Thus the body *normal* velocity is

$$\begin{aligned} \vec{V} \cdot \vec{n} &= \frac{\Delta \vec{r}}{\Delta t} \cdot \frac{\nabla F}{|\nabla F|} \\ &= -\frac{\partial F}{\partial t} \frac{1}{|\nabla F|} \quad \text{from (4.1.28)} \end{aligned} \tag{1.30}$$

The boundary condition on the body is, as stated before, the normal fluid velocity equals the normal body velocity on the body. Thus, using (1.28) and (1.29) one has

$$\vec{q} \cdot \vec{n} = \vec{q} \cdot \frac{\nabla F}{|\nabla F|} = -\frac{\partial F}{\partial t} \frac{1}{|\nabla F|} \tag{1.31}$$

or

$$\frac{\partial F}{\partial t} + \vec{q} \cdot \nabla F = 0 \tag{1.32}$$

on the body surface

$$F = 0$$

Example. Planar (airfoil) surface

$$F(x, y, z, t) \equiv z - f(x, y, t)$$

where f is the height above the plane, $z = 0$, of the airfoil surface. See Fig. 2. Equation (1.32) may be written:

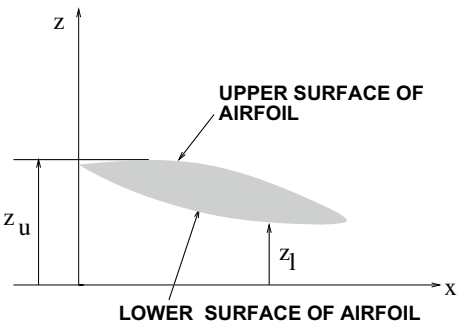

Fig. 2 Airfoil geometry

$$-\frac{\partial f}{\partial t}+[(U_\infty+u)\vec{\imath}+v\vec{\jmath}+w\vec{k}]\cdot\left[-\frac{\partial f}{\partial x}\vec{\imath}-\frac{\partial f}{\partial y}\vec{\jmath}+\vec{k}\right]=0$$

or

$$\frac{\partial f}{\partial t}+(U_\infty+u)\frac{\partial f}{\partial x}+v\frac{\partial f}{\partial y}=w \tag{1.33}$$

on

$$z=f(x,y,t) \tag{1.34}$$

One may approximate (1.33) and (1.34) using the concept of a Taylor series about $z=0$ and noting that $u \ll U_\infty$.

$$\frac{\partial f}{\partial t}+U_\infty\frac{\partial f}{\partial x}+v\frac{\partial f}{\partial y}=w \quad \text{on} \quad z=0 \tag{1.35}$$

Note

$$\begin{aligned} w_{z=f} &= w_{z=0}+\frac{\partial w}{\partial z}\Big|_{z=0} f+\text{H.O.T.} \\ &\simeq w_{z=0} \end{aligned}$$

to a consistent approximation within the context of small perturbation theory.

1.5.3 Symmetry and Anti-symmetry

One of the several advantages of linearization is the ability to divide the aerodynamic problem into two distinct cases, symmetrical (thickness) and anti-symmetrical (lifting) flow. If one denotes the upper surface by

$$f_{\text{upper}}=z_u(x,y,t)$$

and the lower surface by

$$f_{\text{lower}}=z_l(x,y,t)$$

then it is useful to write

$$\begin{aligned} z_u &\equiv z_t+z_L \\ z_l &\equiv -z_t+z_L \end{aligned} \tag{1.36}$$

where (1.36) defines z_t, thickness, and z_L, lifting contributions to z_u and z_l.

One may retreat the thickness and lifting cases separately (due to linearity) and superimpose their results for any z_u and z_l. The thickness case is much simpler than the lifting case as we shall see.

Recall (1.35), (we henceforward drop the $\hat{}$ on ϕ, p)

$$\frac{\partial f}{\partial t} + U_\infty \frac{\partial f}{\partial x} = \left.\frac{\partial \phi}{\partial z}\right|_{z=0^+ \text{ or } 0^-} \tag{1.35}$$

where + denotes the upper surface and—denotes the lower. From (1.35) and (1.36), one sees that

Thickness case

$$\frac{\partial \phi}{\partial z} \text{ is anti-symmetric with respect to } z \text{ (discontinuous across airfoil)}$$

hence ϕ is symmetric (and also p).

Lifting case

$$\frac{\partial \phi}{\partial z} \text{ is symmetric with respect to } z \text{ (continuous across airfoil)}$$

hence ϕ is anti-symmetric (and also p).

Consider now the pressure difference across the airfoil.

$$\Delta p \equiv p_l - p_u = -\rho \left[\frac{\partial \Delta \phi}{\partial t} + U_\infty \frac{\partial \Delta \phi}{\partial x} \right]$$

Thus $\Delta p = 0$ for the thickness case, i.e., there is no lift on the airfoil.

The OFF-BODY BOUNDARY CONDITIONS (these are really continuity conditions), state that p and $\vec{q} \cdot \vec{n}$ are continuous across any fluid surface. In particular, for $z = 0$,

$$p_u = p_l \quad \text{and} \quad \left.\frac{\partial \phi}{\partial z}\right|_u = \left.\frac{\partial \phi}{\partial z}\right|_l \tag{1.37}$$

(1.37) may be used to prove some interesting results.

Thickness case

$$\frac{\partial \phi}{\partial z} = 0 \quad \text{off wing}$$

This follows from the fact that since $\partial \phi / \partial z$ is anti-symmetric, one has

$$\left.\frac{\partial \phi}{\partial z}\right|_{0^+} = -\left.\frac{\partial \phi}{\partial z}\right|_{0^-}$$

But from the second of (1.37), this can only be true if

$$\left.\frac{\partial \phi}{\partial z}\right|_{0^+} = \left.\frac{\partial \phi}{\partial z}\right|_{0^-} = 0$$

Lifting case

$$p = 0 \quad \text{off wing}$$

This follows in a similar way using the anti-symmetry of p and the first of (1.37).

The BOUNDARY CONDITIONS AT INFINITY are conditions of finiteness or outwardly propagating waves (Sommerfeld radiation condition) which will be imposed at infinity, $z \to \pm\infty$.

2 Supersonic Flow

It is convenient to distinguish between various flow regimes on the basis of geometry (two or three dimensions) and Mach number (subsonic or supersonic). We shall not give a historical development, but shall instead begin with the simplest regime and proceed to the more difficult problems. Our main focus will be the determination of pressure distributions on airfoils and wings.

2.1 Two-Dimensional Flow

This flow regime[5] is the simplest as the fluid ahead of the body remains undisturbed and that behind the body does not influence the pressure distribution on the body. These results follow from the mathematics, but they also can be seen from reasonably simple physical considerations. Take a body moving with velocity, U_∞, through a fluid whose undisturbed speed of sound is a_∞, where $M \equiv U_\infty/a_\infty > 1$. At any point in the fluid disturbed by the passage of the body, disturbances will propagate to the right with velocity, $+a_\infty$, and to the left, $-a_\infty$ *with respect to the fluid*. That is, as viewed in the prime coordinate system. The corresponding propagation velocities as seen with respect to the body or airfoil will be:

$$U_\infty - a_\infty \quad \text{and} \quad U_\infty + a_\infty$$

Note these are both positive, hence the fluid ahead of the airfoil is never disturbed; also disturbance behind the airfoil never reach the body. For subsonic flow, $M < 1$, the situation is more complicated. Even for *three-dimensional, supersonic* flow one must consider possible effects of disturbances off the side edges in the third dimension. Hence the two-dimensional, supersonic problems offers considerable simplification.

One of the consequences of the simplicity, as we will see, is that no distinction between thickness and lifting cases need be made as far as the mathematics is concerned. Hence the body boundary conditions is (considering $z > 0$)

[5]See van der Vooren [3].

$$\left.\frac{\partial \phi}{\partial z}\right|_{z=0} = \frac{\partial z_a}{\partial t} + U_\infty \frac{\partial z_a}{\partial x} \equiv w_a \tag{2.1}$$

where one may use the notation $z_a \equiv f$ interchangeably and the equation of fluid motion is

$$\nabla^2_{x,z}\phi - \frac{1}{a^2_\infty}[\frac{\partial}{\partial t} + U_\infty \frac{\partial}{\partial x}]^2 \phi = 0 \tag{2.2}$$

2.2 *Simple Harmonic Motion of the Airfoil*

Most of the available literature is for simple harmonic motion, that is:

$$\begin{aligned} z_a &= \bar{z}_a(x)e^{i\omega t} \\ w_a &= \bar{w}_a(x)e^{i\omega t} \\ \phi &= \bar{\phi}(x,z)e^{i\omega t} \\ p &= \bar{p}(x,z)e^{iwt} \end{aligned} \tag{2.3}$$

Hence we shall consider this case first. Thus (2.1) becomes:

$$\frac{\partial \bar{\phi}}{\partial z}\cancel{e^{i\omega t}} = \bar{w}_a \cancel{e^{i\omega t}} \tag{2.4}$$

and (2.2)

$$\bar{\phi}_{xx} + \bar{\phi}_{zz} - \frac{1}{a^2_\infty}[-\omega^2\bar{\phi} + 2i\omega U_\infty \frac{\partial \bar{\phi}}{\partial x} + U^2_\infty \frac{\partial^2 \bar{\phi}}{\partial x^2}] = 0 \tag{2.5}$$

Since $\bar{\phi}$, $\partial\bar{\phi}/\partial x$, etc., are zero for $x < 0$, this suggests the possibility of using a Laplace Transform with respect to x, i.e.,

$$\Phi(p,z) \equiv \mathcal{L}\{\bar{\phi}\} = \int_0^\infty \bar{\phi} e^{-px} dx \tag{2.6}$$

$$W(p) \equiv \mathcal{L}\{\bar{w}_a\} = \int_0^\infty \bar{w}_a e^{-px} dx \tag{2.7}$$

Taking a transform of (2.4) and (2.5) gives:

$$\left.\frac{d\Phi}{dz}\right|_{z=0} = W \tag{2.8}$$

$$\frac{d^2\Phi}{dz^2} = \mu^2 \Phi \tag{2.9}$$

where

$$\mu^2 \equiv (M^2-1)p^2 + 2Mi\frac{\omega p}{a_\infty} - \frac{\omega^2}{a_\infty^2}$$
$$= (M^2-1)\{[p + \frac{iM\omega}{a_\infty(M^2-1)}]^2 + \frac{\omega^2}{a_\infty^2(M^2-1)^2}\}$$

Note $M \equiv U_\infty/a_\infty$. Equations (2.8) and (2.9) are now equations we can solve. The solution to (2.9) is

$$\Phi = Ae^{\mu z} + Be^{-\mu z} \tag{2.10}$$

Select $A \equiv 0$ to keep Φ finite as $z \to +\infty$. Hence

$$\Phi = Be^{-\mu z}$$

where B can be determined using (2.8). From the above,

$$\frac{d\Phi}{dz}|_{z=0} = -\mu B$$

Using this result and (2.8), one has

$$-\mu B = W$$

or

$$B = -W/\mu$$

and hence

$$\Phi = -(W/\mu)e^{-\mu z} \tag{2.11}$$

Inverting (2.11), using the convolution theorem,

$$\bar{\phi} = -\int_0^x \bar{w}_a(\xi)\mathcal{L}^{-1}\{\frac{e^{-\mu z}}{\mu}\}d\xi \tag{2.12}$$

and, in particular,

$$\bar{\phi}(x, z=0) = -\int_0^x \bar{w}_a(\xi)\mathcal{L}^{-1}\{\frac{1}{\mu}\}d\xi$$

From H. Bateman, 'Table of Integral Transforms', McGraw-Hill, 1954 [6].

$$\mathcal{L}^{-1}\{\frac{1}{\sqrt{p^2+\alpha^2}}\} = J_0(\alpha x)$$

$$\mathcal{L}^{-1}\{F(p+a)\} = e^{-ax}f(x)$$

where $\mathcal{L}^{-1}\{F(p)\} \equiv f(x)$. Thus

$$\mathcal{L}^{-1}\{\frac{1}{\mu}\} = \frac{\exp[-\frac{iM\omega}{a_\infty(M^2-1)}(x-\xi)]}{(M^2-1)^{\frac{1}{2}}} J_0[\frac{\omega}{a_\infty(M^2-1)}(x-\xi)] \tag{2.13}$$

$\mathcal{L}^{-1}\{e^{\mu z}/\mu\}$ may be computed by similar methods. In nondimensional terms,

$$\bar{\phi}(x^*,0) = -\frac{2b}{(M^2-1)^{\frac{1}{2}}} \int_0^{x^*} \bar{w}(\xi^*) \exp[-i\bar{\omega}(x^*-\xi^*)] J_0[\frac{\bar{\omega}}{M}(x^*-\xi^*)] d\xi^* \tag{2.14}$$

where

$$\bar{\omega} \equiv \frac{kM^2}{M^2-1}, \quad k \equiv \frac{2b\omega}{U_\infty} \text{is a reduced frequency and}$$

$$x^* \equiv x/2b, \quad \xi^* \equiv \xi/2b$$

One can now use Bernoulli's equation to compute p

$$p = -\rho_\infty[\frac{\partial\phi}{\partial t} + U_\infty \frac{\partial\phi}{\partial x}]$$

or

$$\bar{p} = -\rho_\infty[i\omega\bar{\phi} + U_\infty \frac{\partial\bar{\phi}}{\partial x}]$$

$$= \frac{\rho_\infty U_\infty}{2b}[\frac{\partial\bar{\phi}}{\partial x^*} + ik\bar{\phi}]$$

Using Leibnitz' rule,

$$\begin{aligned}\bar{p} = &-\frac{\rho_\infty U_\infty^2}{(M^2-1)^{\frac{1}{2}}}\{\int_0^{x^*}[ik\frac{\bar{w}_a}{U_\infty} + \frac{1}{U_\infty}\frac{d\bar{w}_a}{d\xi^*}]e^{-\cdots} J_0[\cdots]d\xi^* \\ &+ \frac{\bar{w}(0)}{U_\infty} e^{-i\omega x^*} J_0[\frac{\bar{\omega}}{M}x^*]\}\end{aligned} \tag{2.15}$$

2.3 *Discussion of Inversion*

Formally the inversion formula reads:

$$\bar{\phi}(x,z) = \frac{1}{2\pi i}\int_{-i\infty}^{i\infty} \Phi(p,z)e^{px}dp \tag{2.16}$$

Define $\alpha \equiv ip$, (α can be thought of as a Fourier transform variable), then

$$\bar{\phi}(x,z) = \frac{1}{2\pi}\int_{-\infty}^{\infty} \Phi(-i\alpha, z)e^{-i\alpha x}d\alpha \tag{2.17}$$

and

$$\mu = \sqrt{M^2-1}\sqrt{-[-\alpha + \frac{M\omega}{a_\infty(M^2-1)}]^2 + \frac{\omega^2}{a_\infty^2(M^2-1)^2}}$$

where

$$\Phi = \pm\frac{W}{\mu}e^{\pm\mu z} \tag{2.18}$$

Consider now μ as $\alpha = -\infty \to +\infty$. The quantity under the radical changes sign at

$$\alpha = \alpha_1,\ \alpha_2 = \frac{w}{a_\infty}\frac{1}{M\pm 1}$$

where $\mu = 0$. Thus

$$\mu = \pm i|\mu| \quad \text{for} \quad \alpha < \alpha_1 \quad \text{or} \quad \alpha > \alpha_2$$

$$= \pm|\mu| \quad \text{for} \quad \alpha_1 < \alpha < \alpha_2$$

where

$$|\mu| = \sqrt{(M^2-1)}\left| -[-\alpha + \frac{M\omega}{a_\infty(M^2-1)}]^2 + \frac{\omega^2}{a_\infty^2(M^2-1)^2}\right|^{\frac{1}{2}}$$

In the interval, $\alpha_1 < \alpha < \alpha_2$, we have seen we must select the minus sign so that Φ is finite at infinity. What about elsewhere? In particular, when $\alpha < \alpha_1$ and/or $\alpha > \alpha_2$?

The solution for $\phi = \bar{\phi}e^{i\omega t}$ has the form for $\alpha_1 < \alpha < \alpha_2$,

$$\phi = -\frac{1}{2\pi}\int_{-\infty}^{\infty} \pm\frac{W}{\mu}\exp(\pm\mu z\ -\ i\alpha x + i\omega t)d\alpha \tag{2.19}$$

In the intervals $\alpha < \alpha_1$ and/or $\alpha > \alpha_2$, (2.19) reads:

$$\phi = -\frac{1}{2\pi}\int_{-\infty}^{\infty} \pm i\frac{W}{|\mu|}\exp(\pm i|\mu|z\ -\ i\alpha x + i\omega t)d\alpha \tag{2.20}$$

To determine the proper sign, we require that solution represent an outgoing wave in the fluid fixed coordinate system, i.e., in the prime system. In the prime system $x' = x - U_\infty t,\ z' = z,\ t' = t$ and thus

$$\phi = -\frac{1}{2\pi}\int_{-\infty}^{\infty} \pm i\frac{W}{|\mu|}\exp[\pm i|\mu|z'\ - i\alpha x' + i(\omega - U_\infty\alpha)t']d\alpha \tag{2.21}$$

Consider a z', t' wave for fixed x'. For a wave to be outgoing, if $\omega - U_\infty \alpha > 0$ then one must choose—sign while if $\omega - U_\infty \alpha < 0$ then choose + sign. Note that

$$\omega - U_\infty \alpha = 0$$

when

$$\alpha = \alpha_3 \equiv \frac{\omega}{U_\infty} = \frac{\omega}{a_\infty M}$$

also note that

$$\frac{\omega}{a_\infty (M+1)} \equiv \alpha_1 < \alpha_3 < \alpha_2 \equiv \frac{\omega}{a_\infty (M-1)}$$

Thus the signs are chosen as sketched below.

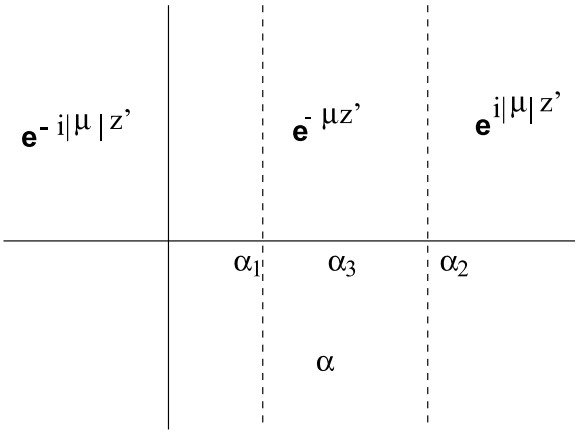

Here again

$$\alpha_1 \equiv \frac{\omega}{a_\infty} \frac{1}{M+1} \quad \alpha_2 \equiv \frac{\omega}{a_\infty} \frac{1}{M-1} \quad \alpha_3 \equiv \frac{\omega}{a_\infty} \frac{1}{M}$$

The reader may find it of interest to consider the subsonic case, $M < 1$, using similar reasoning.

Knowing the appropriate choice for μ in the several intervals, (2.19)–(2.21) may be integrated numerically, or by contour integration. The inversion formula used previously were obtained by contour integration.

2.4 *Discussion of Physical Significance of the Results*

Because of the complicated mathematical form of our solution, it is difficult to understand its physical significance. Perhaps it is most helpful for this purpose to consider the limits of low and high frequency.

One may show that (from (2.11) et. seq. or (2.15))[6]
$\omega \to 0$: *steady flow*

$$p(x) \to \frac{\rho_\infty U_\infty^2}{\sqrt{M^2-1}} \frac{w_a}{U}(x),\ p(x,z) = \frac{\rho_\infty U_\infty^2}{\beta} \frac{w_a(x-\beta z)}{U_\infty}$$

$$\frac{w_a}{U_\infty} \to \frac{\partial f}{\partial x} \quad \beta \equiv \sqrt{M^2-1}$$

$\omega \to \infty$: *highly unsteady flow*

$$p(x,t) \to \frac{\rho_\infty U_\infty^2}{M} \frac{w_a(x,t)}{U_\infty},\ p(x,z,t) = \frac{\rho_\infty U_\infty^2}{M} \frac{w_a}{U_\infty}(x - Mz,\ t)$$

$$\frac{w_a}{U_\infty} \to \frac{1}{U_\infty} \frac{\partial f}{\partial t} + \frac{\partial f}{\partial x}$$

The latter result may be written as

$$p = \rho_\infty a_\infty w_a$$

which is the pressure on a piston in a long, narrow (one-dimensional) tube with ω the velocity of the piston. It is, therefore, termed 'piston theory' for obvious reasons. Note that in the limits of low and high frequency the pressure at point x depends only upon the downwash at the same point. For arbitrary ω, the pressure a one point depends in general upon the downwash at all other points. See (2.15). Hence the flow has a simpler behavior in the limits of small and large ω than for intermediate ω. Also recall that low and high frequency may be interpreted in the time domain for transient motion as long and short time respectively. This follows from the initial and final value Laplace Transform theorems.[7] For example, if we consider a motion which corresponds to a step change in angle of attack, α, we have

$$f = -x\alpha \quad \text{for} \quad t > 0$$

$$= 0 \quad \text{for} \quad t < 0$$

$$w_a = -\alpha \quad \text{for} \quad t > 0$$

$$w_a / U_\infty = 0 \quad \text{for} \quad t < 0$$

[6] See the appropriate example problem in Appendix II for details.
[7] Hildebrand [2].

Hence for short time, (large w)

$$p = \frac{-\rho_\infty U_\infty^2}{M}\alpha$$

and long time, (small ω)

$$p = \frac{-\rho_\infty U_\infty^2 \alpha}{\sqrt{M^2 - 1}}$$

The result for short time may also be deduced by applying a Laplace Transform with respect to time and taking the limit $t \to 0$ of the formal inversion.

2.4.1 General Comments

A few general comments should be made about the solution. First of all, the solution has been obtained for simple harmonic motion. In principle, the solution for arbitrary time dependent motion may be obtained via Fourier superposition of the simple harmonic motion result. Actually it is more efficient to use a Laplace Transform with respect to time and invert the time variable prior to inverting the spatial variable, x. Secondly, with regard to the distinction between the lifting and thickness cases, one can easily show by direct calculation and using the method applied previously that

$$\begin{aligned} \textit{thickness}\quad & z = 0^+ \quad w = w_a \quad p = p^+ \\ & z = 0^- \quad w = -w_a \quad p = p^+ \end{aligned}$$

$$\begin{aligned} \textit{lifting}\quad & z = 0^+ \quad w = w_a \quad p = p^+ \\ & z = 0^- \quad w = w_a \quad p = -p^+ \end{aligned}$$

where p^+ is the solution previously obtained. Of course these results also follow from our earlier general discussion of boundary conditions.

2.5 Gusts

Finally it is of interest to consider how aerodynamic pressures develop on a body moving through a nonuniform flow, i.e., a 'gust'. If the body is motionless, the body boundary condition is that the total fluid velocity be zero on the body.

$$\left.\frac{\partial \phi}{\partial z}\right|_{z=0} + w_G = 0$$

where w_G is the specified vertical 'gust' velocity and $\partial\phi/\partial z$ is the perturbation fluid velocity resulting from the body passing through the gust field. Hence in our previous development we may replace w by—w_G and the same analysis then applies. Frequently one assumes that the gust field is 'frozen', i.e., fixed with respect to the fluid fixed coordinates, x', y', z', t'. Hence

$$w_G = w_G(x', y')$$

$$= w_G(x - U_\infty t, y)$$

Further a special case is a 'sharp edge' gust for which one simply has

$$w_G = w_0 \quad \text{for} \quad x' < 0$$

$$= 0 \quad \text{for} \quad x' > 0$$

or

$$w_G = w_0 \quad \text{for} \quad t > x/U_\infty$$

$$= 0 \quad \text{for} \quad t < x/U_\infty$$

These special assumptions are frequently used in applications.

Solutions for the sharp edge gust can be obtained through superposition of (simple harmonic motion) sinusoidal gusts. However, it is more efficient to use methods developed for transient motion. Hence before turning to three-dimensional supersonic flow, we consider transient motion. Transient solutions can be obtained directly (in contrast to Fourier superposition of simple harmonic motion results) for a two-dimensional, supersonic flow.

2.6 Transient Motion

Taking a Laplace transform with respect to *time* and a Fourier transform with respect to the *streamwise coordinate*, x, the analog of (2.11) is

$$\mathcal{L}F\{\phi\}_{\text{at } z=0} = -\frac{\mathcal{L}Fw_a}{\mu} \tag{2.22}$$

$i\omega \equiv s$ is the Laplace Transform variable (where ω was the frequency in the simple harmonic motion result), α is the Fourier transform variable (where $i\alpha \equiv p$ was the Laplace transform variable used in the previous simple harmonic motion result), $\mathcal{L} \equiv$ Laplace transform, $F \equiv$ Fourier transform, and

$$\mu^2 \equiv -(M^2-1)\alpha^2 + 2\frac{Msi}{a_\infty}\alpha + \frac{s^2}{a_\infty^2}$$

Inverting the Laplace Transform, and using $*$ to denote a Fourier transform

$$\begin{aligned}\phi^*|_{\text{at } z=0} &= -\int_0^t w^*(\tau)\mathcal{L}^{-1}\{\frac{1}{\mu}\}|_{t-\tau}d\tau \\ &= -a_\infty \int_\infty^t w^*(\tau)\exp[-i\alpha M a_\infty(t-\tau)]J_0[a_\infty\alpha(t-\tau)]d\tau\end{aligned} \tag{2.23}$$

Now from (1.26),

$$p^* = -\rho_\infty\left[\frac{\partial\phi^*}{\partial t} + U_\infty i\alpha\phi^*\right]$$

Thus using (2.23) and the above,

$$\begin{aligned}p^* &= \rho_\infty\left\{a_\infty w^*(t) - a_\infty^2\int_0^t w^*(\tau)\alpha\exp[-i\alpha M a_\infty(t-\tau)]J_1[\alpha a_\infty(t-\tau)]d\tau\right\} \\ &\equiv p_0^* + p_1^*\end{aligned} \tag{2.24}$$

Finally, a formal solution is obtained using

$$p = \frac{1}{2\pi}\int_{-\infty}^{\infty} p^* e^{i\alpha x}d\alpha \tag{2.25}$$

The lift is obtained by using (2.24) and (2.25) in its definition below.

$$L \equiv -2\int_0^{2b} p\,dx = -2\rho_\infty a_\infty\int_0^{2b} w\,dx - \frac{1}{\pi}\int_{-\infty}^{\infty} p_1^*\left[\frac{e^{i\alpha 2b}-1}{i\alpha}\right]d\alpha \tag{2.26}$$

In the second term the integration over x has been carried out explicitly.

2.7 *Lift, Due to Airfoil Motion*

Considering a translating airfoil, $w_a = -dh/dt$, for example, we have

$$w^* = -\frac{dh}{dt}\frac{[e^{-i\alpha 2b}-1]}{-i\alpha}$$

and

$$L = 2\rho_\infty a_\infty \frac{dh}{dt}(2b) + \rho_\infty a_\infty^2 \int_0^t \frac{dh}{dt}(\tau) K(t-\tau) d\tau \tag{2.27}$$

where

$$K(t-\tau) \equiv -\frac{1}{\pi} \int_{-\infty}^{\infty} \frac{\exp[-i\alpha M a_\infty (t-\tau)]}{\alpha} J_1[e^{i\alpha 2b} - 1][e^{-i\alpha 2b} - 1] d\alpha$$

K may be simplified to

$$K(t-\tau) = -\frac{4}{\pi} \int_0^{\infty} \frac{J_1[a_\infty \alpha (t-\tau)] \cos[\alpha M a_\infty (t-\tau)]}{\alpha} \cdot [1 - \cos \alpha 2b] d\alpha$$

One can similarly work out aerodynamic lift (and moment) for pitching and other motions.

2.8 *Lift, Due to Atmospheric Gust*

$$w_G(x - U_\infty t) = w_G(x')$$

x, t are coordinates fixed with respect to airfoil and x', t' are coordinates fixed with respect to atmosphere. At $t = t' = 0$ the airfoil enters the gust; the boundary condition is $w_a + w_G = 0$ or $w_a = -w_G$ on airfoil. See Fig. 3. Short and long time correspond to high and low frequency; hence it is of interest to use our previously developed approximate theories for these limits. Subsequently we treat the full transient case.

(i) Piston Theory (short t) on the upper and lower airfoil surfaces

$$p_u = -\rho_\infty a_\infty w_G$$

and

$$p_l = \rho_\infty a_\infty w_G$$

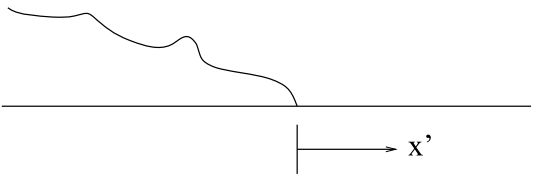

Fig. 3 Frozen gust geometry in fluid fixed coordinate system

Thus

$$L(t) = \int (p_l - p_u)dx$$
$$= 2\rho_\infty a_\infty \int_0^{2b} w_G(x - U_\infty t)dx$$

For simplicity, we first consider a sharp edge gust.

Let

$$w_G = w_0 \quad \text{for} \quad x' < 0 \quad \text{or} \quad x < U_\infty t,\ t > x/U_\infty$$
$$= 0 \quad \text{for} \quad x' > 0 \quad \text{or} \quad x > U_\infty t,\ t < x/U_\infty$$

Thus

$$L(t) = 2\rho_\infty a_\infty w_0 \int_0^{U_\infty t} dx$$
$$= 2\rho_\infty a_\infty w_0 U_\infty t \quad \text{for} \quad t < \frac{2b}{U_\infty} \tag{2.28}$$
$$= 2\rho_\infty a_\infty w_0 2b \quad \text{for} \quad t > \frac{2b}{U_\infty}$$

(ii) Static Theory (large t)

$$L(t) = \frac{2\rho_\infty U_\infty^2}{\sqrt{M^2-1}} \frac{w_0}{U_\infty} \int_0^{2b} dx = 4b \frac{\rho_\infty a_\infty w_0 M}{\sqrt{M^2-1}} \tag{2.29}$$

(iii) Full Transient Theory from (2.24),

$$p = \rho_\infty a_\infty [w_a(x,t) - a_\infty \int_0^t \alpha w_a^*(\alpha,\tau) e^{-(\cdots)} J_1(\cdots) d\tau] \tag{2.24}$$

Special case. Sharp Edge Gust

$$w_a = -w_G(x - U_\infty t) = -w_0 \quad \text{for} \quad x < U_\infty t$$
$$= 0 \quad \text{for} \quad x > U_\infty t$$

Thus

$$w_a^*(\alpha,\tau) = -\int_{-\infty}^{\infty} e^{-i\alpha x} w_G(x - U_\infty \tau)dx$$
$$= -w_0 \int_{-\infty}^{U_\infty \tau} e^{-i\alpha x} dx$$
$$= \frac{-w_0}{-i\alpha} e^{i\alpha x}\Big|_{-\infty}^{U_\infty \tau}$$
$$= \frac{w_0}{i\alpha} e^{i\alpha U_\infty \tau}$$

Using the above and (2.24),

$$p = \rho_\infty a_\infty [-w_G(x - U_\infty t) - \frac{a_\infty w_0}{2\pi} \times \int_{-\infty}^{\infty} \int_0^t \alpha \frac{e^{-i\alpha U_\infty t}}{i\alpha} e^{-(\cdot)} J_1(\,) d\tau e^{i\alpha x} d\alpha] \tag{2.30}$$

Again one may proceed further by computing the lift.

$$L = 2\rho_\infty a_\infty w_0 \begin{array}{ll} U_\infty t, & \text{for} \quad U_\infty t < 2b \\ 2b, & \text{for} \quad U_\infty t > 2b \end{array}$$
$$+2\rho_\infty \frac{a_\infty^2 w_0}{2\pi} \int_0^{2b} \int_{-\infty}^{\infty} \int_0^t \cdots d\tau d\alpha dx$$

Integrating over x first, and introducing non-dimensional notation

$$s \equiv \frac{tU_\infty}{2b} \qquad \alpha^* \equiv \alpha 2b$$

$$\sigma \equiv \frac{\tau U_\infty}{2b}$$

one obtains

$$\frac{L}{2\rho_\infty U_\infty^2 2b} = \frac{w_0}{U_\infty} \left[\frac{s}{M} - \frac{1}{M^2} \int_0^s F(s,\, \sigma) d\sigma \right] \tag{2.31}$$

where

$$F(s,\, \sigma) \equiv \frac{W_o}{U} \frac{1}{\pi} \int_0^\infty \frac{[-\cos \alpha^* s + \cos \alpha^* (1 - s)] J_1[\alpha^* \frac{(s-\sigma)}{M}]}{\alpha^*} d\alpha^*$$

General case. Arbitrary Frozen Gust

$$w_a^*(\alpha, \tau) = -\int_{-\infty}^{\infty} e^{-i\alpha x} w_G(x - U_\infty \tau) dx$$
$$= -\int_{-\infty}^{U\tau} e^{-i\alpha x} w_G(x - U_\infty \tau) dx$$

Let $x' = x - U_\infty t,\ dx' = dx$, then

$$w_a^* = -e^{-i\alpha U_\infty \tau} \int_{-\infty}^{0} e^{-i\alpha x'} w_G(x') dx'$$
$$= -e^{-i\alpha U_\infty \tau} w_G^*(\alpha)$$

Using above in (2.24), the pressure is

$$p = \rho_\infty a_\infty [-w_G(x - U_\infty t) + \frac{a_\infty}{2\pi} \int_{-\infty}^{\infty} \int_0^t w_G^* \alpha e^{-i\alpha U_\infty \tau} e^{-()} J_1() d\tau e^{i\alpha x} d\alpha]$$

and the lift,

$$L = 2\rho_\infty a_\infty \int_0^{2b} w_G(x - U_\infty t) dx - \frac{2\rho_\infty a_\infty^2}{2\pi} \int_0^{2b} \int_{-\infty}^{\infty} \int_0^t \cdots d\tau \, d\alpha \, dx$$

Integrating over x first,

$$\frac{L}{2\rho_\infty U_\infty^2 2b} = \int_0^{2b} \frac{w_G/U_\infty}{M} \frac{dx}{2b} - \frac{1}{M^2} \int_0^s F(s, \sigma) d\sigma \tag{2.32}$$

where now

$$F(s, \sigma) \equiv \frac{1}{\pi} \int_0^\infty \{W_I^* \{\cos[\alpha^*(1 - s)] - \cos \alpha^* s\} J_1[\frac{\alpha^*(s - \sigma)}{M}] + W_R^* \{\sin[\alpha^*(1 - s)] + \sin \alpha^* s\} J_1[\frac{\alpha^*(s - \sigma)}{M}]\} d\alpha^*$$

and

$$W^* \equiv \frac{w^*}{U_\infty 2b}$$

For an alternative approach to transient motion which makes use of an analogy between two-dimensional time dependent motion and three-dimensional steady motion, the reader may consult Lomax [4].

This completes our development for two-dimensional, supersonic flow. We now have the capability for determining the aerodynamic pressures necessary for flutter, gust and even, in principle, acoustic analyses for this type of flow. For the latter the pressure in the 'far field' (large z) is usually of interest. Now let us consider similar analyses for three-dimensional, supersonic flow.[8]

2.9 *Three Dimensional Flow*

We shall now add the third dimension to our analysis. As we shall see there is no essential complication with respect to solving the governing differential equation;

[8]References: BA, pp. 134–139; Landahl and Stark [5], Watkins [6].

the principal difficulty arises with respect to satisfying all of the relevant boundary conditions.

The convected wave equation reads in three spatial dimensions and time

$$\nabla^2\phi - \frac{1}{a_\infty^2}\left[\frac{\partial^2\phi}{\partial t^2} + 2U_\infty\frac{\partial^2\phi}{\partial x\partial t} + U_\infty^2\frac{\partial^2\phi}{\partial x^2}\right] = 0 \tag{2.33}$$

As before we assume simple harmonic time dependance.

$$\phi = \bar{\phi}(x, y, z)e^{i\omega t}$$

Further taking a Laplace transform with respect to x, gives

$$\frac{\partial^2\Phi}{\partial z^2} + \frac{\partial^2\Phi}{\partial y^2} = \mu^2\Phi \tag{2.34}$$

where

$$\Phi \equiv \mathcal{L}\bar{\phi} = \int_0^\infty \bar{\phi}e^{-px}dx$$

$$\mu = \sqrt{M^2-1}\left[\left(p + \frac{i\omega M}{a_\infty(M^2-1)}\right)^2 + \frac{\omega^2}{a_\infty^2(M^2-1)^2}\right]^{\frac{1}{2}}$$

To reduce (2.33) to an ordinary differential equation in z, we take a Fourier transform with respect to y. Why would a Laplace transform be inappropriate? The result is:

$$\frac{d^2\Phi^*}{dz^2} = (\mu^2 + \gamma^2)\Phi^* \tag{2.35}$$

where

$$\Phi^* \equiv F\Phi = \int_{-\infty}^\infty \Phi e^{-i\gamma y}dy$$

The solution to (2.34) is

$$\Phi^* = A\exp[+(\mu^2+\gamma^2)^{\frac{1}{2}}z] + B\exp[-(\mu^2+\gamma^2)^{\frac{1}{2}}z]$$

Selecting the appropriate solution for finiteness and/or radiation as $z \to +\infty$, we have

$$\Phi^* = B\exp[-(\mu^2+\gamma^2)^{\frac{1}{2}}z] \tag{2.36}$$

Applying the body boundary condition (as transformed)

$$\left.\frac{d\Phi^*}{dx}\right|_{z=0} = W^* \tag{2.37}$$

we have from (2.36) and (2.37)

$$B = -\frac{W^*}{(\mu^2+\gamma^2)^{\frac{1}{2}}}$$

and hence

$$\Phi^*_{z=0} = -\frac{W^*}{(\mu^2+\gamma^2)^{\frac{1}{2}}}$$

Using the convolution theorem

$$\bar{\phi}(x, y, z=0) = -\int_0^x \int_{-\infty}^{\infty} \bar{w}_a(\xi,\eta)\mathcal{L}^{-1}F^{-1}\frac{1}{(\mu^2+\gamma^2)^{\frac{1}{2}}}d\xi d\eta \tag{2.38}$$

Now let us consider the transform inversions, The Laplace inversion is essentially the same as for the two-dimensional case.

$$\mathcal{L}^{-1}\frac{1}{(\mu^2+\gamma^2)^{\frac{1}{2}}} = \frac{\exp[-\frac{iM\omega x}{\alpha_\infty(M^2-1)}]}{\sqrt{M^2-1}}J_0([\frac{\omega^2}{a_\infty^2(M^2-1)^2}+\frac{\gamma^2}{(M^2-1)}]^{\frac{1}{2}}x)$$

To perform the Fourier inversion, we write

$$\begin{aligned}
&F^{-1}\{\mathcal{L}^{-1}\{\frac{1}{(\mu^2+\gamma^2)^{\frac{1}{2}}}\}\}\\
&\quad= \frac{\exp[-\frac{iM\omega x}{\alpha_\infty(M^2-1)}]}{2\pi\sqrt{M^2-1}}\int_{-\infty}^{\infty} J_0\left(\left[\frac{\omega^2}{a_\infty^2(M^2-1)^2}+\frac{\gamma^2}{(M^2-1)}\right]^{\frac{1}{2}}x\right)e^{i\gamma y}d\gamma\\
&\quad= \frac{\exp[-\frac{iM\omega x}{\alpha_\infty(M^2-1)}]}{\pi\sqrt{M^2-1}}\int_0^{\infty} J_0(\cdots)\cos\gamma y\, d\gamma
\end{aligned}$$

where the last line follows from the evenness of the integrand with respect to γ. The integral has been evaluated in Bateman, [7], p. 55.

$$\begin{aligned}
\int_0^{\infty} J_0(\cdots)\cos\,\gamma y\, d\gamma &= [\frac{x^2}{M^2-1}-y^2]^{\frac{1}{2}}\cos[\frac{\omega}{a_\infty(M^2-1)^{\frac{1}{2}}}(\frac{x^2}{M^2-1}-y^2)^{\frac{1}{2}}]\\
&\qquad \text{for} \quad |y| < \frac{x}{\sqrt{M^2-1}}\\
&= 0 \quad \text{for} \quad |y| > \frac{x}{\sqrt{M^2-1}}
\end{aligned}$$

Thus finally

$$F^{-1}\mathcal{L}^{-1}\{\frac{1}{(\mu^2+\gamma^2)^{\frac{1}{2}}}\} = \frac{1}{\pi}\frac{\exp[-\frac{iM\omega}{a_\infty(M^2-1)}]x}{\sqrt{M^2-1}}$$
$$\cos\left[\frac{\omega}{a_\infty(M^2-1)^{\frac{1}{2}}}(\frac{x^2}{M^2-1}-y^2)^{\frac{1}{2}}\right]\left[\frac{x^2}{M^2-1}-y^2\right]^{\frac{1}{2}}$$
$$\text{for} \quad |y| < \frac{x}{\sqrt{M^2-1}}$$
$$= 0 \quad \text{for} \quad |y| > \frac{x}{\sqrt{M^2-1}}$$

Using the above in (2.37) and nondimensionalizing by $s \equiv$ wing semi-span and $b \equiv$ reference semi-chord,

$$\bar{\phi}(x^*,\ y^*,\ z=0)$$
$$= \frac{-s}{\pi}\int_0^{s^*}\int_{y^*-(2b/s)(x^*-\xi^*)/\beta}^{y^*+(2b/s)(x^*-\xi^*)/\beta} \bar{w}_a(\xi^*,\eta^*)\exp[-i\bar{\omega}(x^*-\xi^*)]\frac{\cos\frac{\bar{\omega}r^*}{M}}{r^*}d\xi^*\,d\eta^* \tag{2.39}$$

where

$$r^* \equiv [(x^*-\xi^*)^2 - \beta^2(\frac{s}{2b})^2(y^*-\eta^*)^2]^{\frac{1}{2}}$$
$$\beta \equiv \sqrt{M^2-1}$$
$$x^*, \xi^* \equiv x/2b, \xi/2b \qquad y^*, \eta^* \equiv y/s, \eta/s$$
$$k \equiv \frac{\omega 2b}{U_\infty}, \qquad \bar{\omega} \equiv \frac{kM^2}{(M^2-1)}$$

If $\bar{w}$ is known everywhere in the region of integration then (2.39) is a solution to our problem. Unfortunately, in many cases of interest, $\bar{w}_a$ is unknown over some portion of the region of interest. Recall that $\bar{w}_a$ is really $\frac{\partial\bar{\phi}}{\partial z}|_{z=0}$. In general this vertical fluid velocity is unknown off the wing. There are three principal exceptions to this:
(1) If we are dealing with a thickness problem then $\frac{\partial\phi}{\partial z}|_{z=0} = 0$ everywhere off the wing and no further analysis is required.
(2) Certain wing geometries above a certain Mach number will have undisturbed flow off the wing even in the lifting case. For these so-called 'supersonic planforms', $\frac{\partial\phi}{\partial z}|_{z=0} = 0$ off wing as well.
(3) Even in the most general case, there will be no disturbance to the flow ahead of the rearward facing Mach lines, $\eta = \pm\xi/\beta$, which originate at the leading most point of the lifting surface.

To make case (2) more explicit and in order to discuss what must be done for those cases where the flow off the wing is disturbed, let us consider the following figure; Fig. 4. Referring first to case (2), we see that if the slopes of the forward facing Mach lines (integration limits of (2.39)) and the rearward facing Mach lines

$$\eta = y \pm \frac{(x-\xi)}{\beta} \quad \text{and} \quad \eta = \pm\xi/\beta$$

are sufficiently small, i.e., $|\frac{1}{\beta}| \to 0$, then the regions where $\bar{w}_a$ is unknown, will vanish. This is what we mean by a 'supersonic planform'. The mathematical problem

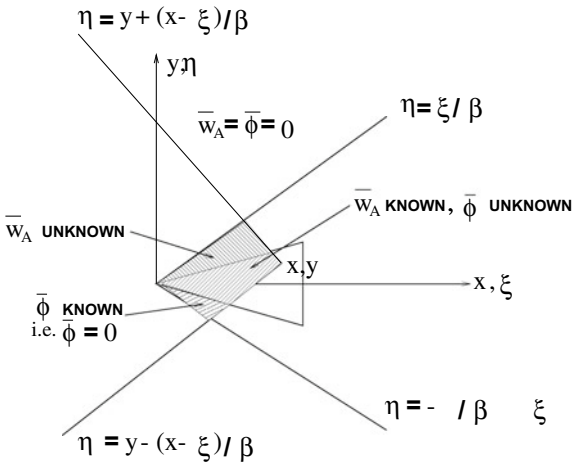

Fig. 4 Lifting surface geometry. A representative delta wing is shown

for these planforms is essentially the same as for a 'thickness problem' whether or not lift is being produced.

Finally let us consider the most difficult case where we have mixed boundary condition problems. In general analytical solutions are not possible and we resort to numerical methods. One such is the 'box' method. In this approach, the integral equation (2.39) is approximated by differences and sums, i.e.,

$$\frac{\bar{\phi}(x_i^*, y_j^*)}{U_\infty s} = \sum_{k=1}^{K} \sum_{l=1}^{L} A_{(ij)(kl)} \frac{\bar{w}_a(\xi_k^*, \eta_l^*)}{U_\infty} \tag{2.40}$$

where

$$A_{(ij)(kl)} \equiv -\frac{1}{\pi} \exp[-i\bar{\omega}(x_i^* - \xi_k^*)] \frac{\cos \frac{\bar{\omega}}{M} r^*_{(ij)(kl)}}{r^*_{(ij)(kl)}} \Delta\xi^* \Delta\eta^*$$

and

$$r^*_{(ij)(kl)} \equiv [(x_i^* - \xi_k^*)^2 - \beta^2 (\frac{s}{2b})^2 (y_j^* - \eta_l^*)^2]^{\frac{1}{2}}$$

$\Delta\xi^*, \Delta\eta^* \equiv$ dimensions of aerodynamic box

$A_{(ij)(kl)}$ aerodynamic influence coefficients; the velocity potential at point, ij, due to a unit 'downwash', $\bar{w}_a$, at point kl

Equation (2.40) can be written in matrix notation as:

$$\left\{ \bar{\phi} \right\} = \left[\; A \; \right] \left\{ \bar{w}_a \right\} \tag{2.41}$$

The system of linear equation may be separated as follows:

$$\left\{\begin{array}{c} \bar{\phi}(N1\times 1) \\ \text{unknown} \\ --- \\ \bar{\phi}(N2\times 1) \\ \text{known} \end{array}\right\} = \left[\begin{array}{c|c} A_1 & A_2 \\ (N1\times N1) & (N2\times N1) \\ \hline A_3 & A_4 \\ (N1\times N2) & (N2\times N2) \end{array}\right] \left\{\begin{array}{c} \bar{w}_a(N1\times 1) \\ \text{known} \\ --- \\ \bar{w}_a(N2\times 1) \\ \text{unknown} \end{array}\right\} \tag{2.42}$$

where

$N1$ number of boxes where $\bar{w}_a$ is known, and $\bar{\phi}$ is unknown (on wing)
$N2$ number of boxes where $\bar{w}_a$ is unknown, and $\bar{\phi}$ is known (on wing)

Using last $N2$ equations of (2.42)

$$\{\bar{\phi}_{\text{known}}\} = [A_3]\{\bar{w}_a\,\text{known}\} + [A_4]\{\bar{w}_a\,\text{unknown}\} \tag{2.43}$$

Solving for $\bar{w}_a\,\text{unknown}$

$$\begin{aligned} \{\bar{w}_a\,\text{unknown}\} &= [A_4]^{-1}\{\{\bar{\phi}_{\text{known}}\} - [A_3]\{\bar{w}_a\,\text{known}\}\} \\ &= -[A_4]^{-1}[A_3]\{\bar{w}_a\,\text{known}\} \end{aligned} \tag{2.44}$$

where we have noted that $\bar{\phi}_{\text{known}} = 0$. Using (2.44) in the first $N1$ equations of (2.42),

$$\begin{aligned} \{\bar{\phi}_{\text{unknown}}\} &= [A_1]\{\bar{w}_a\,\text{known}\} + [A_2]\{\bar{w}_a\,\text{unknown}\} \\ &= [[A_1] - [A_2][A_4]^{-1}[A_3]]\{\bar{w}_a\,\text{known}\} \end{aligned} \tag{2.45}$$

Computer programs have been written to preform the various computations.[9] Also it should be pointed out that in the evaluations of the 'aerodynamic' influence coefficients it is essential to account for the singular nature of the integrand along the Mach lines. This requires an analytical integration of (2.39) over each box with $\bar{w}$ assumed constant and taken outside the integral.

Extensions to this technique have been made to include more complicated geometries, e.g., nonplanar and multiple surfaces,[10] and also efforts have been made to include other physical effects.[11]

[9] Many Authors, Oslo AGARD Symposium [8].
[10] Many Authors, Oslo AGARD Symposium [8].
[11] Landahl and Ashley [9].

3 Subsonic Flow

Subsonic flow[12] is generally a more difficult problem area since all parts of the flow are disturbed due to the motion of the airfoil. To counter this difficulty an inverse method of solution has been evolved, the so-called 'Kernel Function' approach. To provide continuity with our previous development we shall formulate and solve the problem in a formal way through the use of Fourier Transforms. Historically, however, other methods were used. These will be discussed after we have obtained our formal solution. To avoid repetition, we shall treat the three-dimensional problem straight away.

Bernoulli's equation reads:

$$p = -\rho_\infty [\frac{\partial \phi}{\partial t} + U_\infty \frac{\partial \phi}{\partial x}] \tag{3.1}$$

It will prove convenient to use this relationship to formulate our solution in term of pressure directly rather than velocity potential.

3.1 Derivation of the Integral Equation by Transform Methods and Solution by Collocation

As before we will use the transform calculus. Since there is no limited range of influence in subsonic flow we employ Fourier transforms with respect to x *and* y. We shall also assume, as before, simple harmonic time dependent motion. Thus

$$\phi = \bar{\phi}(x, y, z)e^{i\omega t} \tag{3.2}$$

and transformed

$$\Phi^* = \int_{-\infty}^{\infty} \int \bar{\phi}(x, y, z) \exp(-i\alpha x - i\gamma y) dx\, dy \tag{3.3}$$

Hence (3.1) may be transformed

$$P^* = -\rho_\infty [i\omega + U_\infty i\alpha]\Phi^* \tag{3.4}$$

where

$$p = \bar{p}(x, y, z)e^{i\omega t}$$

$$P^* \equiv \int_{-\infty}^{\infty} \int \bar{p} \exp(-i\alpha x - i\gamma y) dx\, dy \tag{3.5}$$

[12]BA, pp. 125–133; Landahl and Stark, [5], Williams [10].

As in supersonic flow we may relate the (transformed) velocity potential to the (transformed) 'upwash' (see(2.26)et. seq.)

$$\Phi^*|_{z=0} = \frac{-W^*}{(\mu^2+\gamma^2)^{\frac{1}{2}}} \tag{3.6}$$

Substituting (3.6) into (3.4),

$$P^* = \rho_\infty \frac{[i\omega + U_\infty i\alpha]}{(\mu^2+\gamma^2)^{\frac{1}{2}}} W^*$$

or

$$\frac{\bar{W}^*}{U_\infty} = \frac{P^*}{\rho_\infty U_\infty^2} \frac{(\mu^2+\gamma^2)^{\frac{1}{2}}}{[\frac{i\omega}{U_\infty} + i\alpha]} \tag{3.7}$$

Inverting

$$\frac{\bar{w}}{U_\infty}(x,y) = \int_{-\infty}^{\infty}\int K(x-\xi, y-\eta)\frac{\bar{p}}{\rho_\infty U_\infty^2}(\xi,\eta)d\xi\, d\eta \tag{3.8}$$

where

$$K(x,y) \equiv \frac{1}{(2\pi)^2}\int_{-\infty}^{\infty}\int \frac{(\mu^2+\gamma^2)^{\frac{1}{2}}}{[\frac{i\omega}{U_\infty} + i\alpha]} \exp(i\alpha x + i\gamma y)d\alpha\, d\gamma$$

K is physically interpreted as the (non-dimensional) 'upwash', $\bar{w}/U_\infty$ at x, y due to a unit (delta-function) of pressure, $\bar{p}/\rho_\infty U_\infty^2$, at ξ, η. For lifting flow (subsonic or supersonic), $\bar{p} = 0$ off the wing; hence in (3.8) the (double) integral can be confined to the wing area. This is the advantage of the present formulation.

Now we are faced with the problem of extracting the pressure from beneath the integral in (3.9). By analogy to the supersonic 'box' approach we might consider approximating the integral equation by a double sum

$$\frac{\bar{w}_{ij}}{U_\infty} \simeq \Delta\xi\,\Delta\eta \sum_k \sum_l K_{(ij)(kl)} \frac{\bar{p}_{kl}}{\rho_\infty U_\infty^2} \tag{3.9}$$

In matrix notation

$$\left[\frac{\bar{w}}{U_\infty}\right] = [K\,\Delta\xi\,\Delta\eta]\left[\frac{\bar{p}}{\rho_\infty U_\infty^2}\right]$$

and formally inverting

$$\left[\frac{\bar{p}}{\rho_\infty U_\infty^2}\right] = (K\,\Delta\xi\Delta\eta)^{-1}\left[\frac{\bar{w}}{U_\infty}\right] \tag{3.10}$$

This solution is mathematically incorrect; worse, it is useless. The reason is that it is not unique unless an additional restriction is made, the so-called 'Kutta Condition'.[13] This restriction states that the pressure on the trailing edge of a thin airfoil must remain finite. For a lifting airfoil this is tantamount to saying it must be zero. This constraint is empirical in nature being suggested by experiment. Other constraints such as zero pressure at the leading edge would also make the mathematical solution unique; however, this would not agree with available experimental date. Indeed these data suggest a pressure maxima at the edge; the theory with trailing edge Kutta condition gives a square root singularity at the leading edge.

Although, in principle, one could ensure zero pressure at the trailing edge by using a constraint equation to supplement (3.9) and/or (3.10), another approach has gained favor in practice. In this approach the pressure is expanded in a series of (given) modes

$$\bar{p} = \sum_k \sum_l p_{kl} F_k(\xi) G_l(\eta) \tag{3.11}$$

where the functions $F_k(\xi)$ are chosen to satisfy the Kutta condition. (If the wing platform is other than rectangular, a coordinate transformation may need to be made in order to choose such functions readily.) The p_{kl} are, as yet, unknown.

Substituting (3.11) into (3.8) and integrating over the wing area

$$\frac{\bar{w}}{U_\infty}(x, y) = \sum_k \sum_l \frac{p_{kl}}{\rho_\infty U_\infty^2} \tilde{K}_{kl}(x, y) \tag{3.12}$$

where

$$\tilde{K}_{kl}(x, y) = \int\int K(x - \xi, y - \eta) F_k(\xi) G_l(\eta) d\xi \, d\eta$$

$\bar{K}$ is singular at $x = \xi,\ y = \eta$ (as we shall see later) and the above integral must be evaluated with some care.

The question remains how to evaluate the unknown coefficient, p_{kl} in terms of $\bar{w}/U_\infty(x, y)$? The most common procedure is collection. Equation (3.12) is evaluated at a number of points x_i, y_j, equal to the number of coefficients, p_{kl}. Thus (3.12) becomes

$$\frac{\bar{w}(x_i, y_j)}{U_\infty} = \sum_k \sum_l \frac{p_{kl}}{\rho_\infty U_\infty^2} \tilde{K}_{kl}(x_i,\ y_j) \tag{3.13}$$

Defining $\tilde{K}_{ijkl} \equiv \tilde{K}_{kl}(x_i,\ y_j)$, (3.13) becomes

$$\{\frac{\bar{w}_{ij}}{U_\infty}\} = [\tilde{K}_{(ij)(kl)}]\{\frac{p_{kl}}{\rho_\infty U_\infty^2}\}$$

[13] See Landahl and Stark or Williams, ibid.

Inverting

$$\{\frac{\bar{p}}{\rho_\infty U_\infty^2}\} = [\tilde{K}]^{-1}\{\frac{\bar{w}}{U_\infty}\} \tag{3.14}$$

This completes our formal solution. Relative to the supersonic 'box' method, the above procedure, the so-called 'Kernel Function' method, has proven to be somewhat delicate. In particular, questions have arisen as to:

1. the 'optimum' selection of pressure modes
2. the 'best' method for computing $\tilde{K}$
3. convergence of the method as the number of pressure modes becomes large

It appear, however, that as experience is acquired these questions are being satisfactorily answered at least on an 'ad hoc' basis.

In a later development an alternative approach for solving (3.8) has gained popularity which is known as the 'double lattice' method. In this method the lifting surface is divided into boxes and collocation is used for both the downwash and the pressure.[14]

3.2 An Alternative Determination of the Kernel Function Using Green's Theorem

The transform methods are most efficient at least for formal derivations, however historically other approaches were first used. Many of these are now only of interest to history, however we should mention one other approach which is a powerful tool for non-steady aerodynamic problems. This is the use of Green's Theorem.

First let us review the nature of Green's Theorem.[15] Our starting point is the Divergence Theorem or Gauss' Theorem.

$$\int\int\int \nabla \cdot \vec{b} dV = \int\int \vec{b} \cdot \vec{n} dS \tag{3.15}$$

S surface area enclosing volume V
$\vec{n}$ outward normal
$\vec{b}$ arbitrary vector

Let $\vec{b} = \phi_1 \nabla\phi_2$ where ϕ_1, ϕ_2 are arbitrary scalars. Then (3.15) may be written as:

$$\int\int\int \nabla \cdot \phi_1 \nabla\phi_2 dV = \int\int \vec{n} \cdot \phi_1 \nabla\phi_2 dS$$

[14]Albano and Rodden [11]. The downwash is placed at the box three-quarters chord and pressure concentrated at the one-quarter chord. For two-dimensional steady flow this provides an exact solution which satisfies the Kutta conditions. Lifanov, T.K. and Polanski, T.E., 'Proof of the Numerical Method of "Discrete Vortices" for Solving Singular Integral Equations', PMM (1975), pp. 742–746.

[15]References: Hildebrand [2] p. 312, Stratton [12], pp. 165–169.

Now use the vector calculation identity

$$\nabla \cdot c\vec{a} = c\nabla \cdot \vec{a} + \vec{a} \cdot \nabla c$$

c arbitrary scalar
$\vec{a}$ arbitrary vector

then $\nabla \cdot \phi_1 \nabla \phi_2 = \phi_1 \nabla^2 \phi_2 + \nabla \phi_2 \cdot \nabla \phi_1$ and (3.15) becomes

$$\int\int\int [\phi_1 \nabla^2 \phi_2 + \nabla \phi_2 \cdot \nabla \phi_1] dV = \int\int \vec{n} \cdot \phi_1 \nabla \phi_2 dS \tag{3.16}$$

This is the first form of Green's Theorem. Interchanging ϕ_1 and ϕ_2 in (3.16) and subtracting the result from (3.16) gives

$$\begin{aligned} \int\int\int [\phi_1 \nabla^2 \phi_2 + \phi_2 \nabla^2 \phi_1] dV &= \int\int \vec{n} \cdot (\phi_1 \nabla \phi_2 - \phi_2 \nabla \phi_1) dS \\ &= \int\int (\phi_1 \frac{\partial \phi_2}{\partial n} - \phi_2 \frac{\partial \phi_1}{\partial n}) dS \end{aligned} \tag{3.17}$$

This is the second (and generally more useful) form of Green's Theorem. $\partial/\partial n$ denotes a derivative in the direction of the normal. Let us consider several special but informative cases.

(a) $\phi_1 = \phi_2 = \phi$ in (4.3.16)

$$\int\int\int [\phi \nabla^2 \phi + \nabla \phi \cdot \nabla \phi] dV = \int\int \phi \frac{\partial \phi}{\partial n} dS \tag{3.18}$$

(b) $\phi_1 = \phi$, $\phi_2 = 1$ in (4.3.17)

$$\iiint \nabla^2 \phi \, dV = \iint \frac{\partial \phi}{\partial n} dS \tag{3.19}$$

(c) $\nabla^2 \phi_1 = 0$, $\phi_2 = 1/r$, $r \equiv \sqrt{(x - x_1)^2 + (y - y_1)^2 + (z - z_1)^2}$ in (4.3.17)

$$\iiint \phi_1 \nabla^2 (1/r) dV = \iint \left[\phi_1 \frac{\partial}{\partial n} - \frac{\partial \phi_1}{\partial n} \right] \frac{1}{r} dS \tag{3.20}$$

Now $\nabla^2 (1/r) = 0$ everywhere except at $r = 0$. Thus

$$\begin{aligned} \iiint \phi_1 \nabla^2 (1/r) dV &= \phi_1 (r = 0) \iiint \nabla^2 (1/r) dV \\ &= \phi_1 (r = 0) \iiint \nabla \cdot \nabla \frac{1}{r} dV \end{aligned}$$

and from the Divergence Theorem (3.15), this volume integral may be written as a surface integral, viz

$$\begin{aligned} &= \phi_1(r=0) \iint \nabla(1/r) \cdot \frac{\nabla r}{|\nabla r|} dS \\ &= \phi_1(r=0) \int_0^{2\pi} \int_0^{\pi} -\frac{1}{r^2} r^2 \sin\theta \, d\theta \, d\phi \\ &= -4\pi\phi_1(r=0) \end{aligned}$$

where we consider a small sphere of radius, ε, say, in evaluating the surface integral. Now

$$\phi_1(r=0) = \phi_1(x_1 = x,\ y_1 = y,\ z_1 = z) = \phi_1(x, y, z)$$

Thus (3.20) becomes

$$\phi_1(x, y, z) = -\frac{1}{4\pi} \iint \left[\phi_1 \frac{\partial}{\partial n} - \frac{\partial \phi_1}{\partial n} \right] \frac{1}{r} dS \tag{3.21}$$

The choice of $\phi_2 = 1/r$ may seem rather arbitrary. This can be motivated by noting that

$$\frac{\nabla^2 \phi_2}{4\pi} = -\delta(x - x_1)\delta(y - y_1)\delta(z - z_1)$$

Hence we seek a ϕ_2 which is the response to a delta function. This is what leads to the simplification of the volume integral.

3.3 Incompressible, Three-Dimensional Flow

To simplify matters we will first confine ourselves to $M = 0$. However, similar, but more complex calculations subsequently will be carried out for $M \neq 0$.[16] For incompressible flow, the equation of motion is

$$\nabla^2 \phi = 0$$

or

$$\nabla^2 p = 0$$

where ϕ and p are (perturbation) velocity potential and pressure respectively. Hence we may identify ϕ_1 in (3.21) with either variable as may be convenient. To confirm to convention in the aerodynamic theory literature, we will take the normal positive *into* the fluid and introduce a minus sign into (3.21) which now reads:

[16] Watkins, Woolston and Cunningham [13], Williams [14].

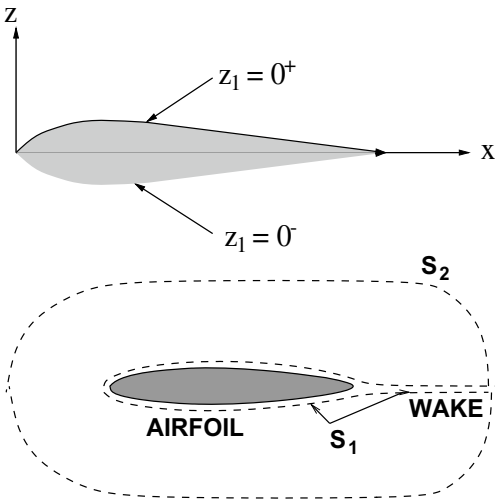

Fig. 5 Airfoil and flow field geometry

$$\phi_1(x, y, z) = \frac{1}{4\pi} \iint \left[\phi_1 \frac{\partial}{\partial n} - \frac{\partial \phi_1}{\partial n} \right] \frac{1}{r} dS \tag{3.22}$$

For example for a planar airfoil surface

$$\begin{array}{lllll} n & \text{on} & S & \text{at} & z_1 = 0^+ \quad \text{is} \quad +z_1 \\ n & \text{on} & S & \text{at} & z_1 = 0^- \quad \text{is} \quad -z_1 \end{array}$$

Note x, y, z is any given point, while x_1, y_1, z_1 are (dummy) integration variables. See Fig. 5 (top).

Let us identify the area S as composed of two parts, the area of the airfoil plus wake, call it S_1, and the area of a sphere at infinity, call it S_2. See Fig. 5 (bottom).
(i) *Thickness problem (nonlifting)*. Let $\phi_1 = \phi$, velocity potential. Because ϕ is bounded at $r \to \infty$, there is no contribution from S_2. Hence

$$\begin{aligned} \phi(x, y, z) = & \frac{1}{4\pi} \iint \left[\phi \frac{\partial}{\partial z_1} - \frac{\partial \phi}{\partial z_1} \right] \frac{1}{r} dS \\ & S_1 \text{ at } z_1 = 0^+ \\ & + \frac{1}{4\pi} \iint \left[\phi \left(-\frac{\partial}{\partial z_1} \right) - \left(-\frac{\partial \phi}{\partial z_1} \right) \right] \frac{dS}{r} \\ & S_1 \text{ at } z_1 = 0^- \end{aligned}$$

Now $\phi_{z_1=0^+} = \phi_{z_1=0^-}$ for thickness problem and

$$\left. \frac{\partial \phi}{\partial z_1} \right|_{z_1=0^+} = - \left. \frac{\partial \phi}{\partial z_1} \right|_{z_1=0^-}$$

Thus

$$\phi(x, y, z) = -\frac{1}{2\pi} \iint \frac{\partial \phi}{\partial z_1}|_{z_1=0^+} \frac{dS}{r}$$

and using the body boundary condition

$$= -\frac{1}{2\pi} \iint w_a \frac{dS}{r} \tag{3.23}$$

where

$$w_a = \frac{\partial z_a}{\partial t} + U_\infty \frac{\partial z_a}{\partial x}$$

Note this solution is valid for arbitrary time-dependent motion. Time only appears as a parameter in the solution $\phi(x, y, z) = \phi(x, y, z, t)$. This is a special consequence of $M \equiv 0$.

(ii) *Lifting problem*. For the lifting problem it again will prove convenient to use pressure rather than velocity potential. Equation (3.22) becomes

$$p(x, y, z) = \frac{1}{4\pi} \iint \left[(p_{z=0^+} - p_{z=0^-}) \frac{\partial}{\partial z_1} \left(\frac{1}{r} \right) - \left(\frac{\partial p}{\partial z_1}\Big|_{z_1=0^+} - \frac{\partial p}{\partial z_1}\Big|_{z_1=0^-} \right) \frac{1}{r} \right] dS$$

Now

$$p_{z_1=0^+} = p_{z_1=0^-}$$

for the lifting problem and

$$\frac{\partial p}{\partial z_1}\Big|_{z_1=0^+} - \frac{\partial p}{\partial z_1}\Big|_{z_1=0^-} = 0$$

Thus

$$p(x, y, z) = \frac{1}{4\pi} \iint \Delta p \frac{\partial}{\partial z_1} \left(\frac{1}{r} \right) dS \tag{3.24}$$

where

$$\Delta p = p_{z=0^+} - p_{z=0^-}$$

Equation (3.24) as it stands is not particularly helpful. We do not know either p or Δp. However we can relate p to something we do know, w. To simplify matters we shall specify harmonic motion,

$$p = \bar{p} e^{i\omega t}$$

$$\phi = \bar{\phi} e^{i\omega t}$$

hence from Bernoulli's equation

$$\bar{p} = -\rho_\infty \left[i\omega\bar{\phi} + U_\infty \frac{\partial \bar{\phi}}{\partial x} \right] \tag{3.25}$$

Solving (3.25), by variation of parameters,

$$\bar{\phi}(x, y, z) = -\int_{-\infty}^{x} \frac{\bar{p}}{\rho_\infty U_\infty}(\lambda, y, z) \exp\left[i \frac{\omega}{U_\infty}(\lambda - x) \right] d\lambda \tag{3.26}$$

and using (3.24), one has

$$\bar{\phi}(x, y, z) = -\int_{-\infty}^{x} \exp\left[i \frac{\omega}{U_\infty}(\lambda - x) \right] \cdot \left\{ \frac{1}{4\pi} \iint \frac{\Delta \bar{p}}{\rho_\infty U_\infty}(x_1, y_1, z_1 = 0) \frac{\partial}{\partial z_1} \left(\frac{1}{r(\lambda)} \right) dS \right\} d\lambda$$

where

$$r(\lambda) \equiv \sqrt{(\lambda - x_1)^2 + (y - y_1)^2 + (z - z_1)^2}$$
$$dS \equiv dz_1\, dy_1$$

Define

$$\xi = \lambda - x_1, d\lambda = d\xi, \lambda = \xi + x_1$$

and interchange order of integration with respect to ξ and S, then

$$\bar{\phi}(x, y, z) = -\frac{1}{4\pi} \iint \frac{\Delta \bar{p}}{\rho_\infty U_\infty}(x_1, y_1, z_1 = 0) \cdot \left\{ \int_{-\infty}^{x - x_1} \frac{\partial}{\partial z_1} \left(\frac{1}{r(\xi)} \right) \exp\left\{ i \frac{\omega}{U_\infty} [\xi - (x - x_1)] \right\} d\xi \right\} dS$$

Compute $\partial\bar{\phi}/\partial z$ and set it equal to $\bar{w}_a$ from body boundary condition, on $z = 0$.

$$\bar{w}_a = -\frac{1}{4\pi} \lim_{z \to 0} \iint \frac{\Delta \bar{p}}{\rho_\infty U_\infty} \times \left\{ \frac{\partial}{\partial z} \int_{-\infty}^{x - x_1} \frac{\partial}{\partial z_1} \left(\frac{1}{r} \right) \exp\left\{ i \frac{\omega}{U_\infty} [\xi - (x - x_1)] \right\} d\xi \right\} dS$$

Now

$$\frac{\partial}{\partial z} \left(\frac{1}{r} \right) = -\frac{\partial}{\partial z_1} \left(\frac{1}{r} \right)$$

therefore

$$\frac{\bar{w}_a}{U_\infty} = \iint \frac{\Delta \bar{p}}{\rho_\infty U_\infty^2}(x_1, y_1, z_1 = 0) K(x - x_1, y - y_1, 0) dx_1 dy_1 \tag{3.27}$$

where

$$K(x-x_1, y-y_1, 0) \equiv \frac{1}{4\pi} \lim_{z\to 0} \frac{\partial^2}{\partial z^2} \int_{-\infty}^{x-x_1} \frac{\exp\left\{\frac{i\omega}{U_\infty}[\xi-(x-x_1)]\right\} d\xi}{r}$$

and where

$$r \equiv \sqrt{\xi^2 + z^2 + (y-y_1)^2}$$

Equation (3.27), of course, has the same form as we had previously derived by transform methods.

The expression for the Kernel function may be simplified.

$$K(x-x_1, y-y_1, 0) = \frac{\exp\left[-\frac{i\omega}{U_\infty}(x-x_1)\right]}{4\pi} \int_{-\infty}^{x-x_1} \exp\left[\frac{i\omega\xi}{U_\infty}\right] \lim_{z\to 0} \frac{\partial^2}{\partial z^2}\frac{1}{r} d\xi$$

Now

$$\frac{\partial^2}{\partial z^2}\frac{1}{r} = -\frac{1}{2} r^{-3} 2 + (-1/2)(-3/2) r^{-5} (2z)^2$$

thus

$$\lim_{z\to 0} \frac{\partial^2}{\partial z^2}\frac{1}{r} = -[\xi^2 + (y-y_1)^2]^{-3/2}$$

and finally

$$K = -\frac{\exp\left[-\frac{i\omega}{U_\infty}(x-x_1)\right]}{4\pi} \int_{-\infty}^{x-x_1} \frac{\exp\left[+\frac{i\omega\xi}{U_\infty}\right]}{[\xi^2 + (y-y_1)^2]^{+3/2}} d\xi \tag{3.28}$$

The integral in (3.28) must be evaluated numerically.

3.4 Compressible, Three-Dimensional Flow

For the more general case of $M \neq 0$, we have an additional complication since

$$\nabla^2 \phi \neq 0$$

For simple harmonic motion, the equation of motion reads

$$\nabla^2 \bar{\phi} + \mathcal{L}\bar{\phi} = 0 \tag{3.29}$$

where

$$\mathcal{L} \equiv -\frac{1}{a^2}\left[(i\omega) + U\frac{\partial}{\partial x}\right]^2$$

By making a coordinate transformation we may reduce the compressible equation to a simpler form.[17] Defining

$$x^1 \equiv x,\ y^1 \equiv \beta y, \quad z^1 \equiv \beta z$$
$$\beta = \sqrt{1 - M^2}$$
$$\bar{\phi} \equiv \exp\left[i\frac{M^2}{(1 - M^2)}\frac{\omega}{U_\infty}x\right]\phi^*$$

The equation for ϕ^* is

$$\exp\left[i\frac{M^2}{(1 - M^2)}\frac{\omega}{U_\infty}x^1\right][\nabla^2\phi^* + k^2\phi^*] = 0 \tag{3.30}$$

where

$$k \equiv \left[\frac{M}{(1 - M^2)}\right]\frac{\omega}{U_\infty}$$

Note this equation is essentially the reduced wave equation. We shall use Green's Theorem on ϕ^* and then transform back to $\bar{\phi}$. Let

$$\nabla^2\phi_1^* + k^2\phi_1^* = 0 \tag{3.31}$$

$$\nabla^2\phi_2^* + k^2\phi_2^* = \delta(x^1 - x_1^1)\delta(y^1 - y_1^1)\delta(z^1 - z_1^1)$$

Solving for ϕ_2^*,

$$\phi_2^* = -\frac{e^{-ikr}}{4\pi r}$$

where

$$r = \sqrt{(x^1 - x_1^1)^2 + (y^1 - y_1^1)^2 + (z^1 - z_1^1)^2}$$

From (3.17),

$$\iiint [\phi_1^*(\delta - k^2\phi_2^*) - \phi_2^*(-k^2\phi_1^*)]dV = \iint \left[\phi_1^*\frac{\partial\phi_2^*}{\partial n} - \phi_2^*\frac{\partial\phi_1^*}{\partial n}\right]dS \quad (4.3.17a)$$

or

[17] By assuming a transformation of the form $e^{\Omega x}\phi^* = \bar{\phi}$, one can always determine Ω such that (3.29) reduces to (3.31).

$$\phi_1^*(x,y,z) = -\frac{1}{4\pi}\iint\left[\phi_1^*\frac{\partial}{\partial n} - \frac{\partial\phi_1^*}{\partial n}\right]\frac{e^{-ikr}}{r}dS \tag{4.3.21a}$$

or

$$\phi_1^*(x,y,z) = +\frac{1}{4\pi}\iint\left[\phi_1^*\frac{\partial}{\partial n} - \frac{\partial\phi_1^*}{\partial n}\right]\frac{e^{-ikr}}{r}dS \tag{4.3.22a}$$

(if we redefine the positive normal). Using symmetry and anti-symmetry properties of $\frac{\partial\phi_1^*}{\partial n}$ and ϕ_1^*

$$\phi_1^*(x,y,z) = \frac{1}{4\pi}\iint\Delta\phi_1^*\frac{\partial}{\partial z_1}\left\{\frac{e^{-ikr}}{r}\right\}dS \tag{4.3.24a}$$

where

$$\Delta\phi_1^* = \phi_{1_{z_1=0^+}}^* - \phi_{1_{z_1=0^-}}^*$$

and

$$-\frac{\partial\phi_1^*}{\partial z_1}\Big|_{z_1=0^+} + \frac{\partial\phi_1^*}{\partial z_1}\Big|_{z_1=0^-} = 0$$

Note $dS \equiv dx_1 dy_1$ and

$$(\frac{\partial}{\partial z_1})dx_1\,dy_1 = (\frac{\partial}{\partial z_1^1})dx_1^1 dy_1^1; \quad x_1 = x_1^1$$

From (4.3.24a) and the definition of ϕ^*

$$\begin{aligned}\bar{\phi}_1 &= \exp\left[i\frac{M^2}{(1-M^2)}\frac{\omega}{U_\infty}x\right]\phi_1^*(x,y,z)\\ &= \frac{\exp\left[i\frac{M^2}{(1-M^2)}\frac{\omega}{U_\infty}x\right]}{4\pi}\\ &\quad\times\iint\Delta\bar{\phi}_1\exp\left[-\frac{M^2}{(1-M^2)}\frac{\omega}{U_\infty}x_1\right]\frac{\partial}{\partial z_1}\left\{\frac{e^{-ikr}}{r}\right\}dS\end{aligned} \tag{3.32}$$

Identifying $\bar{\phi}_1$ with $\bar{p}$ and using (3.32) in (3.26),

$$\begin{aligned}\bar{\phi}(x,y,z,\omega) = &-\frac{1}{4\pi}\int_{-\infty}^{x}\exp\left[i\frac{M^2}{(1-M^2)}\frac{\omega}{U_\infty}\lambda\right]\exp\left[i\frac{\omega}{U_\infty}(\lambda-x)\right]\\ &\cdot\iint\frac{\Delta\bar{p}}{\rho_\infty U_\infty}\exp\left[-i\frac{M^2}{(1-M^2)}\frac{\omega}{U_\infty}x_1\right]\frac{\partial}{\partial z_1}\left\{\frac{e^{-ikr}}{r}\right\}dS\,d\lambda\end{aligned}$$

Define $\xi \equiv \lambda - x_1$, $d\lambda = d\xi$, $\lambda = \xi + x_1$ and interchange order of integration with respect to ξ and S,

$$\begin{aligned}\bar{\phi}(x, y, z, \omega) = &-\frac{1}{4\pi}\iint_{z_1=0}\frac{\Delta\bar{p}}{\rho_\infty U_\infty}(x_1, y_1, z_1)\\ &\cdot\left\{\int_{-\infty}^{x-x_1}\frac{\partial}{\partial z_1}\left\{\frac{e^{ikr}}{r}\right\}\exp\left[-i\frac{M^2}{(1-M^2)}\frac{\omega}{U_\infty}\xi\right]\right.\\ &\left.\cdot\exp\left(i\frac{\omega}{U_\infty}\xi\right)\exp\left[-i\frac{\omega}{U_\infty}(x-x_1)\right]d\xi\right\}dS\\ &= -\frac{1}{4\pi}\iint_{z_1=0}\frac{\Delta\bar{p}}{\rho_\infty U_\infty}(x_1, y_1, z_1)\exp\left[-\frac{i\omega}{U_\infty}(x-x_1)\right]\\ &\cdot\left\{\int_{-\infty}^{x-x_1}\exp\left[i\frac{1}{(1-M^2)}\frac{\omega}{U_\infty}\xi\right]\frac{\partial}{\partial z_1}\left\{\frac{e^{ikr}}{r}\right\}d\xi\right\}dS\end{aligned}$$

Compute $\partial\bar{\phi}/\partial z$ and set it equal to $\bar{w}_a$ from the body boundary condition on $z = 0$, noting that

$$\frac{\partial}{\partial z}\left\{\frac{e^{-ikr}}{r}\right\} = -\frac{\partial}{\partial z_1}\left\{\frac{e^{ikr}}{r}\right\}$$

The final result is

$$\frac{\bar{w}_a}{U_\infty} = \iint\frac{\Delta\bar{p}}{\rho_\infty U_\infty^2}(x_1, y_1, z_1 = 0)K(x - x_1, y - y_1, 0)dx_1dy_1 \tag{3.33}$$

where

$$K(x, y) = \lim_{z\to 0}\frac{\exp\left(-i\frac{\omega}{U_\infty}x\right)}{4\pi}\int_{-\infty}^{x}\exp\left[\frac{i}{(1-M^2)}\frac{\omega}{U_\infty}\xi\right]\frac{\partial^2}{\partial z^2}\left\{\frac{e^{ikr}}{r}\right\}d\xi$$

$$r \equiv [\xi^2 + (1-M^2)(y^2+z^2)]^{\frac{1}{2}}$$

That expression for K may be simplified as follows: Define a new variable, τ, to replace ξ by

$$(1-M^2)\tau \equiv \xi - Mr(\xi, y, z)$$

where one will recall

$$r(\xi, y, z) \equiv [\xi^2 + \beta^2(y^2+z^2)]^{\frac{1}{2}}$$

and

$$\beta^2 \equiv 1 - M^2$$

After some manipulation one may show that

$$\frac{d\tau}{[\tau^2 + y^2 + z^2]^{\frac{1}{2}}} = \frac{d\xi}{r}$$

and

$$\exp\left(+\frac{i\omega}{U_\infty}\frac{\xi}{(1-M^2)}\right)e^{-ikr}=\exp\left[i\frac{\omega}{U_\infty}\tau\right]$$

Thus

$$K=\lim_{z\to 0}\frac{\exp\left(-i\frac{\omega x}{U_\infty}\right)}{4\pi}\frac{\partial^2}{\partial z^2}\int_{-\infty}^{[x-Mr(x,y,x)]/(1-M^2)}\frac{\exp\left(\frac{i\omega\tau}{U_\infty}\right)}{[\tau^2+y^2+z^2]^{\frac{1}{2}}}d\tau \tag{3.34}$$

Taking the second derivative and limit as indicated in (3.34) and using the identity

$$\left[\frac{Mx+r}{(x^2+y^2)}\right]^2\equiv\frac{1}{\left[\frac{x-Mr}{(1-M^2)}\right]^2+y^2}$$

one finally obtains

$$\begin{aligned}K=&-\frac{1}{4\pi}\left\{\frac{M(Mx+r)}{r(x^2+y^2)}\exp\left[i\frac{\omega}{U_\infty}\frac{M}{(1-M^2)}(Mx-r)\right]\right.\\&\left.+\exp\left(-i\frac{\omega x}{U_\infty}\right)\int_{-\infty}^{(x-Mr)/(1-M^2)}\frac{\exp\left(i\frac{\omega\tau}{U_\infty}\right)}{[\tau^2+y^2]^{\frac{3}{2}}}d\tau\right\}\end{aligned} \tag{3.35}$$

This is one form often quoted in the literature. By expressing K in nondimensional form we see the strong singularity in K as $y\to 0$.

$$\begin{aligned}y^2K(x,y)=&-\frac{1}{4\pi}\left\{\frac{M(Mx/y+r/y)}{r/y[(x/y)^2+1]}\exp\left[i\frac{\omega y}{U_\infty}\frac{M}{(1-M^2)}\left(M\frac{x}{y}-\frac{r}{y}\right)\right]\right.\\&\left.+\exp\left(-i\frac{\omega x}{U_\infty}\right)\int_{-\infty}^{[x/y-M(r/y)]/(1-M^2)}\frac{\exp\left(\frac{i\omega y}{U_\infty}z\right)}{[z^2+1]^{\frac{3}{2}}}dz\right\}\end{aligned}$$

$$z\equiv\tau/y$$

Note that the compressible Kernel, K, has the same strength singularity as for incompressible flow and is of no more fundamental complexity.

There is a vast literature on unsteady aerodynamics within the framework of linearized, potential flow models. Among standard references one may mention the work of A. Cunningham[18] on combined subsonic-supersonic Kernel Function methods including an empirical correction for transonic effects and also the work of Morino[19] using Green's Theorem in a more general form for both subsonic and supersonic

[18]Cunningham [29].

[19]Morino, Chen and Suciu [15].

flow. For an authoritative overview, the papers by Rodden[20] and Ashley are recommended. The reader who has mastered the material presented so far should be able to pursue this literature with confidence. Before turning to representative numerical results the historically important theory of incompressible, two-dimensional flow will be presented.

3.5 *Incompressible, Two-Dimensional Flow*

A classical solution is due to Theodorsen[21] and others. Traditionally, the coordinate system origin is selected at mid-chord with $b \equiv$ half-chord. The governing differential equation for the velocity potential, ϕ, is

$$\nabla^2 \phi = 0 \tag{3.36}$$

with boundary conditions for a lifting, airfoil of

$$\frac{\partial \phi}{\partial z}\Big|_{z=0^+,0^-} = w_a \equiv \frac{\partial z_a}{\partial t} + U_\infty \frac{\partial z_a}{\partial x} \tag{3.37}$$

on airfoil, $-b < x < b$, on $z = 0$ and

$$p = -\rho_\infty \left[\frac{\partial \phi}{\partial t} + U_\infty \frac{\partial \phi}{\partial x} \right] = 0 \tag{3.38}$$

off airfoil, $x > b$ or $x < -b$, on $z = 0$ and

$$p, \phi \to 0 \quad \text{as} \quad z \to \infty \tag{3.39}$$

From (3.36), (3.37) and (3.39) one may construct an integral equation,

$$w_a = \frac{\partial \phi}{\partial z}|_{z=0} = -\frac{1}{2\pi} \int_{-b}^{\infty} \frac{\gamma(\xi, t)}{x - \xi} d\xi \tag{3.40}$$

where

$$\gamma(x, t) \equiv \frac{\partial \phi}{\partial x}\Big|_U - \frac{\partial \phi}{\partial x}\Big|_L \tag{3.41}$$

and

$$U \Rightarrow z = 0^+, \quad L \Rightarrow z = 0^-$$

[20]Rodden [16], Ashley and Rodden [17].

[21]Theodorsen [18]. Although this work is of great historical importance, the details are of less compelling interest today and some readers may wish to omit this section on a first reading. The particular approach followed here is a variation on Theodorsen's original theme by Marten Landahl.

Further definitions include

$$\text{'Circulation'} \equiv \Gamma(x) \equiv \int_{-b}^{x} \gamma(\xi) d\xi \Rightarrow \frac{\partial \Gamma}{\partial x} = \gamma(x)$$

$$\Delta\phi = \phi_L - \phi_U$$

$$C_p \equiv \frac{p}{\frac{1}{2}\rho_\infty U_\infty^2}$$

$$\Delta C_p \equiv C_{p_L} - C_{p_U}$$

From the above, and (3.41),

$$\Gamma(x,t) = \int_{-b}^{x} \gamma(\xi) d\xi = \int_{-b}^{x} \left[\frac{\partial \phi_U}{\partial \xi} - \frac{\partial \phi_L}{\partial \xi} \right] d\xi = -\Delta\phi(x), \tag{3.42}$$

Note: $\Delta\phi(x = -b) = 0$. Also from (3.38) and (3.41),

$$\Delta C_p = \frac{-2}{U_\infty^2} \left[\frac{\partial \Delta\phi}{\partial t} + U_\infty \frac{\partial \Delta\phi}{\partial x} \right]$$

and using (3.42)

$$\Delta C_p = \frac{2}{U_\infty^2} \left[\frac{\partial \Gamma}{\partial t} + U_\infty \frac{\partial \Gamma}{\partial x} \right] \tag{3.43}$$

Thus once γ (and hence Γ) is known, ΔC_p is readily computed. We therefore seek to solve (3.40) for γ. The advantage of (3.40) over (3.36)–(3.39) is that we have reduced the problem by one variable, having eliminated z. A brief derivation of (3.40) is given below.

Derivation of integral equation (3.40). A Fourier transform of (3.36) gives

$$\frac{d^2\phi^*}{dz^2} - \alpha^2 \phi^* = 0 \tag{4.3.36a}$$

where

$$\phi^*(\alpha, z, t) \equiv \int_{-\infty}^{\infty} \phi(x, z, t) e^{-i\alpha x} dx$$

Equation (3.37) becomes

$$\left. \frac{d\phi^*}{dz} \right|_{z=0} = w_a^* \tag{4.3.37a}$$

The general solution to (4.3.36a) is

$$\phi^* = Ae^{+|\alpha|z} + Be^{-|\alpha|z} \tag{4.3.38a}$$

From the finiteness condition, (3.39), we see that one must require that $A = 0$ for $z > 0$ (and $B = 0$ for $z < 0$). Considering $z > 0$ for definiteness, we compute from (4.3.38a)

$$\frac{d\phi^*}{dz}|_{z=0} = -|\alpha|B \tag{4.3.39a}$$

From (4.3.39a) and (4.3.37a),

$$B = -\frac{w_a^*}{|\alpha|} \tag{4.3.40a}$$

and from (4.3.38a) and (4.3.40a)

$$\phi^*|_{z=0^+} = \frac{-w_a^*}{|\alpha|} \tag{4.3.41a}$$

From (3.41)

$$\gamma^* = \left(\frac{\partial\phi}{\partial x}\right)^* \Big|_{z=0^+} - \left(\frac{\partial\phi}{\partial x}\right)^* \Big|_{z=0^-}$$

and using (4.3.41a)

$$\gamma^* = -2i\alpha\frac{w_a^*}{|\alpha|} \tag{4.3.42a}$$

Re-arranging (4.3.42a),

$$w_a^* = -\frac{|\alpha|}{2i\alpha}\gamma^*$$

and inverting back to physical domain (using the convolution theorem) we obtain the desired result.

$$w_a = -\frac{1}{2\pi}\int_{-b}^{\infty}\frac{\gamma(\xi, t)}{x - \xi}d\xi \tag{3.40}$$

where

$$\frac{1}{2\pi}\int_{-\infty}^{\infty} -\frac{|\alpha|}{2i\alpha}e^{+i\alpha x}d\alpha = -\frac{1}{2\pi x}$$

The lower limit $x = -b$ in (3.40) follows from the fact that $p = 0$ for $x < -b$ (on $z = 0$) implies that $\phi = \phi_x = 0$ for $x < -b$. This will be made more explicit when we consider $x > b$ where $p = 0$ does *not* imply $\phi = \phi_x = 0$! See discussion below.

Also one can calculate γ for $x > b$ in terms of γ for $b < x < b$ by using the condition that $\Delta C_p = 0$ (continuous pressure) for $x > b$. This is helpful in solving

(3.40) for γ in terms of w_a. From (3.43)

$$\Delta C_p = 0 \Rightarrow \frac{\partial \Gamma}{\partial t} + U_\infty \frac{\partial \Gamma}{\partial x} = 0$$

$$\Gamma = \Gamma(t - \frac{x}{U_\infty}) \tag{3.44}$$

3.5.1 Simple Harmonic Motion of an Airfoil

For the special case of simple harmonic motion, one has

$$\begin{aligned} w_a(x,t) &= \bar{w}_a(x) e^{i\omega t} \\ \gamma(x,t) &= \bar{\gamma}(x) e^{i\omega t} \\ \Gamma &= \bar{\Gamma} e^{i\omega t} \end{aligned} \tag{3.45}$$

(3.44) and (3.45) imply

$$\Gamma(x,t) = A \exp(i\omega[t - x/U_\infty])$$

The (integration) constant A may be evaluated by considering the solution at $x = b$.

$$\Gamma(x = b, t) = A \exp(i\omega[t - b/U_\infty])$$

$$\Gamma(x,t) = \bar{\Gamma}(b) \exp\{i\omega[t - (x-b)/U_\infty]\}$$

and

$$\bar{\gamma} = \frac{\partial \bar{\Gamma}}{\partial x} = \frac{-i\omega}{U_\infty} \bar{\Gamma}(b) \exp[-i\omega(x-b)/U_\infty] \tag{3.46}$$

Introducing traditional nondimensionalization

$$x^* \equiv \frac{x}{b}, \quad \xi^* \equiv \xi/b, \quad k \equiv \frac{\omega b}{U_\infty}$$

a summary of the key relations is given below

$$\bar{w}_a(x^*) = -\frac{1}{2\pi} \int_{-1}^{\infty} \frac{\bar{\gamma}(\xi^*)}{x^* - \xi^*} d\xi^* \quad \text{from (4.3.40)}$$

where

$$\frac{\bar{\gamma}(x^*)}{U_\infty} = -ik \frac{\bar{\Gamma}(b)}{U_\infty b} \exp[-ik(x^* - 1)]$$

for $x^* > 1$ from (3.46)

$$\frac{\bar{\gamma}(x^*)}{U_\infty b} = \int_{-1}^{x^*} \frac{\bar{\gamma}(\xi^*)}{U_\infty} d\xi^* \quad \text{definition}$$

$$\Delta \bar{C}_p = 2\left[\frac{\bar{\gamma}(x^*)}{U_\infty} + ik\frac{\bar{\gamma}(x^*)}{U_\infty b}\right] \quad \text{from (4.3.43)} \tag{3.47}$$

Special Case: Steady flow. For simplicity let us first consider steady flow, $\omega \equiv 0$. From (3.46) or (3.47)

$$\gamma = 0 \quad \text{for} \quad x^* > 1$$

and hence we have

$$w_a(x^*) = -\frac{1}{2\pi}\int_{-1}^{1} \frac{\gamma(\xi^*)}{x^* - \xi^*} d\xi^* \tag{3.48}$$

To solve (3.48) for γ, we replace x^* by u, multiply both sides of (3.48) by the 'the solving kernel'

$$\sqrt{\frac{1+u}{1-u}}\frac{1}{u - x^*}$$

and integrate $\int_{-1}^{1} \ldots du$. The result is

$$\int_{-1}^{1} \sqrt{\frac{1+u}{1-u}} \frac{w_a(u)}{u - x^*} du = -\frac{1}{2\pi}\int_{-1}^{1}\left[\sqrt{\frac{1+u}{1-u}}\frac{1}{u-x^*}\int_{-1}^{1}\frac{\gamma(\xi^*)}{u-\xi^*}d\xi^*\right]du$$

Now write $\gamma(\xi^*) = \gamma(x^*) + [\gamma(\xi^*) - \gamma(x^*)]$, then above may be written as

$$\begin{aligned}\int_{-1}^{1} \sqrt{\frac{1+u}{1-u}} \frac{w_a(u)}{u - x^*} du = &-\frac{1}{2\pi}\gamma(x^*)\int_{-1}^{1}\left\{\sqrt{\frac{1+u}{1-u}}\frac{1}{u-x^*}\int_{-1}^{1}\frac{d\xi^*}{u-\xi^*}\right\}du \\ &-\frac{1}{2\pi}\left\{\int_{-1}^{1}\sqrt{\frac{1+u}{1-u}}\frac{1}{u-x^*}\int_{-1}^{1}\frac{(\xi^*-x^*)}{u-\xi^*}F(\xi^*,x^*)d\xi^*du\right\}\end{aligned} \tag{3.49}$$

where

$$F(\xi^*, x^*) \equiv \frac{\gamma(\xi^*) - \gamma(x^*)}{\xi^* - x^*}$$

To simplify (3.49) we will need to know several integrals. To avoid a diversion, these are simply listed here and are evaluated in detail at the end of this discussion of incompressible, two-dimensional flow.

$$I_0 \equiv \int_{-1}^{1} \frac{d\xi^*}{x^* - \xi^*} = ln\left(\frac{1+x^*}{1-x^*}\right) \quad \text{for} \quad x^* < 1$$
$$= ln\left(\frac{x^*+1}{x^*-1}\right) \quad \text{for} \quad x^* > 1$$

$$I_1 \equiv \int_{-1}^{1} \sqrt{\frac{1+u}{1-u}} \frac{du}{u - x^*} = \pi \quad \text{for} \quad x^* < 1$$
$$= \pi \left[1 - \sqrt{\frac{x^*+1}{x^*-1}}\right] \quad \text{for} \quad x^* > 1$$

$$I_2 \equiv \int_{-1}^{1} \sqrt{\frac{1+u}{1-u}} ln\left|\frac{1-u}{1+u}\right| \frac{du}{u - x^*} = -\pi^2 \sqrt{\frac{1+x^*}{1-x^*}} \quad \text{for} \quad -1 < x^* < 1 \quad (3.50)$$

Now we can proceed to consider the several terms on the RHS of (3.49)

1st term. Now

$$\int_{-1}^{1} \frac{d\xi^*}{u - \xi^*} = ln\left|\frac{1+u}{1-u}\right| \quad \text{from} \quad I_0$$

$$I_3 \equiv \oint_{-1}^{1} \sqrt{\frac{1+u}{1-u}} \frac{1}{u - x^*} \int_{-1}^{1} \frac{d\xi^*}{u - \xi^*} du$$
$$= \int_{-1}^{1} \sqrt{\frac{1+u}{1-u}} \frac{1}{u - x^*} ln\left|\frac{1+u}{1-u}\right| du = +\pi^2 \sqrt{\frac{1+x^*}{1-x^*}} \quad \text{from} \quad I_2$$

$$\text{1st term} \quad = -\frac{\gamma I_3}{2\pi} = \frac{-\gamma(x^*)}{2} \pi \sqrt{\frac{1+x^*}{1-x^*}}$$

2nd term. Interchange order of integration;

$$I_4 \equiv \oint_{-1}^{1} [\xi^* - x^*] F(\xi^*, x^*) \int_{-1}^{1} \sqrt{\frac{1+u}{1-u}} \frac{du}{(u - x^*)(u - \xi^*)} d\xi^*$$

Now

$$\frac{1}{(u - x^*)(u - \xi^*)} = \frac{1}{x^* - \xi^*} \left[\frac{1}{u - x^*} - \frac{1}{u - \xi^*}\right]$$

from a partial fractions expansion.

$$I_4 = -\oint_{-1}^{1} F(\xi^*, x^*) \left\{ \int_{-1}^{1} \sqrt{\frac{1+u}{1-u}} \left[\frac{1}{u - x^*} - \frac{1}{u - \xi^*}\right] du \right\} d\xi^*$$
$$= -\oint_{-1}^{1} F(\xi^*, x^*) [\pi - \pi^0] d\xi^* \quad \text{from} \quad I_1$$

Finally then, from above and (3.49),

$$\int_{-1}^{1}\sqrt{\frac{1+u}{1-u}}\frac{w_a(u)}{u-x^*}du=-\frac{\pi}{2}\gamma(x^*)\sqrt{\frac{1+x^*}{1-x^*}}$$

or

$$\gamma(x^*)=-\frac{2}{\pi}\sqrt{\frac{1-x^*}{1+x^*}}\int_{-1}^{1}\sqrt{\frac{1+u}{1-u}}\frac{w_a(u)}{u-x^*}du \tag{3.51}$$

Note: Other 'solving kernels' exist, but they do not satisfy the Kutta condition, $\gamma(x^*)$ finite at $x^*=1$, i.e., finite pressure at the trailing edge.

One might reasonably inquire, how do we know what the solving kernel should be? Perhaps the most straightforward way to motivate the choice is to recognize that the solution for steady flow can be obtained by other methods. Probably the simplest of these alternative solution methods is to use the transformations $x^*\cos\theta$, $\xi^*=\cos\phi$ and expand γ and w_a in Fourier series in ϕ and θ. See BAH, p. 216. Once the answer is known, i.e., (3.51), the choice of the solving kernel is fairly obvious. The advantage of the solving kernel approach over the other methods is that it is capable of extension to unsteady airfoil motion where an analytical solution may be obtained as will be described below. On the other hand a method that is based essentially on the Fourier series approach is often employed to obtain numerical solutions for three-dimensional, compressible flow. This is the so-called Kernel Function approach discussed earlier.

In the above we have obtained the following integral relation: Given

$$f(x^*)=-\frac{1}{2\pi}\int_{-1}^{1}\frac{g(\xi^*)}{x^*-\xi^*}d\xi^*$$

with $g(1)$ finite or zero, then

$$g(x^*)=-\frac{2}{\pi}\sqrt{\frac{1-x^*}{1+x^*}}\int_{-1}^{1}\sqrt{\frac{1+\xi^*}{1-\xi^*}}\frac{f(\xi^*)}{\xi^*-x^*}d\xi^* \tag{3.52}$$

General case: Oscillating motion. We may employ the solving kernel approach to attack the unsteady problem also. Recall from (3.40), (3.43), (3.46) one has

$$\bar{w}_a(x^*)=-\frac{1}{2\pi}\int_{-1}^{1}\frac{\bar{\gamma}(\xi^*)}{x^*-\xi^*}d\xi^*-\frac{1}{2\pi}\int_{1}^{\infty}\frac{\bar{\gamma}(\xi^*)}{x^*-\xi^*}d\xi^* \tag{3.53}$$

$$\overline{\Delta C_p}=\frac{2\bar{\gamma}(x^*)}{U_\infty}+2ik\frac{\bar{\Gamma}(x^*)}{U_\infty b}=2\frac{\bar{\gamma}(x^*)}{U_\infty}+2ik\int_{-1}^{x^*}\frac{\bar{\gamma}(\xi^*)}{U_\infty}d\xi^* \tag{3.54}$$

$$\frac{\bar{\gamma}(x^*)}{U_\infty}=-ik\frac{\bar{\Gamma}(1)}{U_\infty b}\exp[-ik(x^*-1)]\quad\text{for}\quad x^*>1 \tag{3.55}$$

Substituting (3.55) into (3.53).

$$\bar{w}_a(x^*) = -\frac{1}{2\pi}\int_{-1}^{1}\frac{\bar{\gamma}(\xi^*)}{x^*-\xi^*}d\xi^* + \bar{G}(x^*) \tag{3.56}$$

where

$$\bar{G}(x^*) \equiv \frac{ik\bar{\Gamma}(1)}{2\pi b}\int_{+1}^{\infty}\frac{\exp[-ik(\xi^*-1)]}{x^*-\xi^*}d\xi^*$$

Invert (3.56) to determine $\gamma(x^*)$; recall the steady flow solution, (3.52).

$$\bar{\gamma}(x^*) = -\frac{2}{\pi}\sqrt{\frac{1-x^*}{1+x^*}}\int_{-1}^{1}\sqrt{\frac{1+\xi^*}{1-\xi^*}}\left\{\frac{\bar{w}_a(\xi^*)-\bar{G}(\xi^*)}{\xi^*-x^*}\right\}d\xi^* = -\frac{2}{\pi}\sqrt{\frac{1-x^*}{1+x^*}}$$

$$\times\int_{-1}^{1}\sqrt{\frac{1+\xi^*}{1-\xi^*}}\left\{\frac{\bar{w}_a(\xi^*)-\frac{ik\bar{\Gamma}(1)}{2\pi b}\int_1^\infty \exp[-ik(u-1)]/(\xi^*-u)du}{\xi^*-x^*}\right\}d\xi^* \tag{3.57}$$

Interchanging the order if integration of the term involving $\bar{\Gamma}(1)$ on the RHS side of (3.57) we may evaluate the integral over ξ^* and obtain

$$\bar{\gamma}(x^*) = +\frac{2}{\pi}\sqrt{\frac{1-x^*}{1+x^*}}$$
$$\left\{\int_{-1}^{1}\sqrt{\frac{1+\xi^*}{1-\xi^*}}\frac{\bar{w}_a(\xi^*)}{(x^*-\xi^*)}d\xi^* + ik\frac{\bar{\Gamma}(1)}{b}e^{ik}\int_1^\infty\frac{e^{-iku}}{x^*-u}du\right\} \tag{3.58}$$

(3.58) is not a complete solution until we determine $\bar{\Gamma}(1)$ which we do as follows. Integrating (3.58) with respect to x^* we obtain

$$\frac{\bar{\Gamma}(1)}{b} \equiv \int_{-1}^{1}\bar{\gamma}(x^*)dx^* = -2\int_{-1}^{1}\sqrt{\frac{1+\xi^*}{1-\xi^*}}\bar{w}_a(\xi^*)d\xi^*$$
$$-ik\frac{\bar{\Gamma}(1)}{b}e^{ik}\int_1^\infty\left[\sqrt{\frac{u+1}{u-1}}-1\right]e^{-iku}du \tag{3.59}$$

where the integrals in the right hand side with respect to x^* have been evaluated explicitly. We may now solve (3.59) for $\bar{\Gamma}(1)$. Recognizing that

$$\int_1^\infty\left[\sqrt{\frac{u+1}{u-1}}-1\right]e^{-iku}du = \frac{-\pi}{2}[H_1^{(2)}(k)+iH_0^{(2)}(k)] - \frac{e^{-ik}}{ik} \tag{3.60}$$

we determine from (3.59) and (3.60) that

$$\frac{\bar{\Gamma}(1)}{b} = 4\frac{e^{-ik}\int_{-1}^{1}\sqrt{\frac{1+\xi^*}{1-\xi^*}}\bar{w}_a(\xi^*)d\xi^*}{\pi ik[H_1^{(2)}(k) + iH_0^{(2)}(k)]} \tag{3.61}$$

$H_1^{(2)}$, $H_0^{(2)}$ are standard Hankel functions.[22] Equations (3.58) and (3.61) constitute the solution for $\bar{\gamma}$ in terms of $\bar{w}_a$. From $\bar{\gamma}$, we may determine $\overline{\Delta C_p}$ by using

$$\overline{\Delta C_p} = 2\frac{\bar{\gamma}(x^*)}{U_\infty} + 2ik\int_{-1}^{x^*}\frac{\bar{\gamma}(\xi^*)}{U_\infty}d\xi^*$$

After considerable, but elementary, algebra

$$\overline{\Delta C_p} = \frac{4}{\pi}\sqrt{\frac{1-x^*}{1+x^*}}\int_{-1}^{1}\sqrt{\frac{1+\xi^*}{1-\xi^*}}\left\{\frac{\bar{w}_a(\xi^*)/U_\infty}{x^*-\xi^*}\right\}d\xi^*$$

$$+\frac{4}{\pi}ik\sqrt{1-x^{*2}}\oint_{-1}^{1}\frac{W(\xi^*)d\xi^*}{U_\infty\sqrt{1-\xi^{*2}}(x^*-\xi^*)}$$

$$+\frac{4}{\pi}[1-C(k)]\sqrt{\frac{1-x^*}{1+x^*}}\int_{-1}^{1}\sqrt{\frac{1+\xi^*}{1-\xi^*}}\frac{\bar{w}_a(\xi^*)}{U_\infty}d\xi^* \tag{3.62}$$

where

$$W(\xi^*) \equiv \int_{-1}^{\xi^*}\bar{w}_a(u)du$$

and

$$C(k) \equiv \frac{H_1^{(2)}}{[H_1^{(2)} + iH_0^{(2)}]}$$

is Theodorsen's well known Function.

The lift may be computed as the integral of the pressure.

$$\bar{L} \equiv \frac{\rho U_\infty^2}{2}b\int_{-1}^{1}\overline{\Delta C_p}dx^* = \frac{\rho U_\infty^2}{2}b$$
$$\left\{-C(k)\int_{-1}^{1}\sqrt{\frac{1+\xi^*}{1-\xi^*}}\frac{\bar{w}_a(\xi)}{U_\infty}d\xi^* - ik\int_{-1}^{1}\sqrt{1-\xi^{*2}}\frac{\bar{w}_a(\xi^*)}{U_\infty}d\xi^*\right\} \tag{3.63}$$

[22] Abramowitz and Stegun [19].

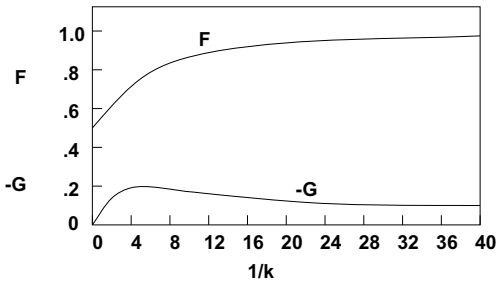

Fig. 6 The functions F and G against $\frac{1}{k}$. After Theodorsen [18]

Similarly for the moment about the point $x = ba$,

$$\bar{M}_y \equiv \frac{\rho U_\infty^2}{2} b^2 \int_{-1}^{1} \overline{\Delta C_p}[x^* - a]dx^* \tag{3.64}$$

In particular, for

$$z_a = -h - \alpha(x - ba)$$
$$\bar{z}_a = -\bar{h} - \bar{\alpha}(x - ba)$$

one has

$$\bar{w}_a = -i\omega\bar{h} - i\omega\bar{\alpha}(x - ba) - U_\infty\bar{\alpha} \tag{3.65}$$

Thus (3.65) in (3.63) and (3.64) give

$$\begin{aligned}
\bar{L} =& \pi\rho b^2[-\omega^2\bar{h} + i\omega U_\infty\bar{\alpha} + ba\omega^2\bar{\alpha}] \\
&+ 2\pi\rho U_\infty bC(k)[i\omega\bar{h} + U_\infty\bar{\alpha} + b(\frac{1}{2} - a)i\omega\bar{\alpha}] \\
\bar{M}_y =& \pi\rho b^2[-ba\omega^2\bar{h} - U_\infty b(\frac{1}{2} - a)i\omega\bar{\alpha} + b^2(\frac{1}{8} + a^2)\omega^2\bar{\alpha}] \\
&+ 2\pi\rho U_\infty b^2(\frac{1}{2} + a)C(k)[i\omega\bar{h} + U_\infty\bar{\alpha} + b(\frac{1}{2} - a)i\omega\bar{\alpha}]
\end{aligned} \tag{3.66}$$

Theodorsen's Function, $C(k) = F + iG$, is given below in Fig. 6.

3.5.2 Transient Motion

Using Fourier synthesis one may now obtain results for arbitrary time dependent motion from the simple harmonic motion results; using Fourier summation (integration) and (3.66),

$$
\begin{aligned}
L(t) =& \frac{1}{2\pi}\int_{-\infty}^{\infty} \bar{L}(\omega)_{\text{due to } h}\bar{h}(\omega)e^{i\omega t}d\omega \\
&+ \frac{1}{2\pi}\int_{-\infty}^{\infty} \bar{L}(\omega)_{\text{due to } \alpha}\bar{\alpha}(\omega)e^{i\omega t}d\omega \\
=& \frac{1}{2\pi}\int_{-\infty}^{\infty} \{\pi\rho b^2(-\omega^2) + 2\pi\rho U_\infty bC(k)(i\omega)\}\cdot \bar{h}(\omega)e^{i\omega t}d\omega \\
&+ \frac{1}{2\pi}\int_{-\infty}^{\infty} \{\pi\rho b^2(i\omega U_\infty + ba\omega^2) + 2\pi\rho U_\infty bC(k)(U_\infty + b(\frac{1}{2}-a)i\omega)\} \\
&\bar{\alpha}(\omega)e^{i\omega t}d\omega
\end{aligned}
\tag{3.67}
$$

where

$$
\bar{h}(\omega) = \int_{-\infty}^{\infty} h(t)e^{-i\omega t}d\omega
$$

and

$$
\bar{\alpha}(\omega) = \int_{-\infty}^{\infty} \alpha(t)e^{-i\omega t}d\omega \tag{3.68}
$$

Now

$$
\int_{-\infty}^{\infty} (i\omega)^n \bar{\alpha}e^{i\omega t}d\omega = \frac{d^n\alpha}{dt^n} \quad n = 1, 2\ldots \tag{3.69}
$$

Thus

$$
\begin{aligned}
L =& \pi\rho b^2\left[\frac{d^2h}{dt^2} + U_\infty\frac{d\alpha}{dt} - ba\frac{d^2\alpha}{dt^2}\right] \\
&+ \rho U_\infty b\int_{-\infty}^{\infty} C(k)f(\omega)e^{i\omega t}d\omega
\end{aligned}
$$

where

$$
\begin{aligned}
f(\omega) \equiv& i\omega\bar{h}(\omega) + U_\infty\bar{\alpha}(\omega) + b(\frac{1}{2}-a)i\omega\bar{\alpha}(\omega) \\
&\int_{-\infty}^{\infty}\left[\frac{dh}{dt} + U_\infty\alpha + b(\frac{1}{2}-a)\frac{d\alpha}{dt}\right]e^{-i\omega t}dt
\end{aligned}
\tag{3.70}
$$

Physically,

$$
\frac{dh}{dt} + U_\infty\alpha + b(\frac{1}{2}-a)\frac{d\alpha}{dt} = -w_a \quad \text{at} \quad x = b/2;
$$

$$
x = b/2 \text{ is } \frac{3}{4} \text{ chord of airfoil.}
$$

Similarly,

$$
\begin{aligned}
M_y =& \pi\rho b^2\left[ba\frac{d^2h}{dt^2} - U_\infty b(\frac{1}{2}-a)\frac{d\alpha}{dt} - b^2(\frac{1}{8}+a^2)\frac{d^2\alpha}{dt^2}\right] \\
&+ \rho U_\infty b^2(\frac{1}{2}+a)\int_{-\infty}^{\infty} C(k)f(\omega)e^{i\omega t}d\omega
\end{aligned}
\tag{3.71}
$$

Example I. Step change in angle of attack.

$$
\begin{aligned}
&h \equiv 0 \\
&\alpha = 0 \ \text{ for } \ t < 0 \\
&\quad = \alpha_0 \equiv \ \text{constant for} \quad t > 0 \\
&\qquad \frac{d\alpha}{dt} = \frac{d^2\alpha}{dt^2} = \frac{dh}{dt} = \frac{d^2h}{dt^2} = 0 \quad \text{for} \quad t > 0 \\
&\qquad f(\omega) = U_\infty \alpha_0 \int_0^\infty e^{-i\omega t} dt \\
&\qquad\quad = \frac{U_\infty \alpha_0}{-i\omega} e^{-i\omega t}|_0^\infty = \frac{U_\infty \alpha_0}{i\omega} \\
&\qquad\quad L = \rho U_\infty^2 b \alpha_0 \int_{-\infty}^\infty \frac{C(k)}{i\omega} e^{i\omega t} d\omega \\
&\qquad\quad\ = \rho U_\infty^2 b \alpha_0 \int_{-\infty}^\infty \frac{C(k)}{ik} e^{iks} dk
\end{aligned}
$$

where $s \equiv \frac{Ut}{b}$. Finally,

$$
L = 2\pi \rho U_\infty^2 b \alpha_0 \left\{ \frac{1}{2\pi i} \int_{-\infty}^\infty \frac{C(k)}{k} e^{iks} dk \right\} \tag{3.72}
$$

$\{\cdots\} \equiv \phi(s)$ is called the Wagner Function, see Fig. 7. Note that if α is precisely a step function, then L has a singularity a $t = 0$ from (3.70). Also shown is the K*ü*ssner function, $\psi(s)$, to be discussed subsequently. Note also that ϕ is the lift of the airfoil due to step change in angle of attack or more generally due to step change in $-w_a/U_\infty$ at $\frac{3}{4}$ chord.

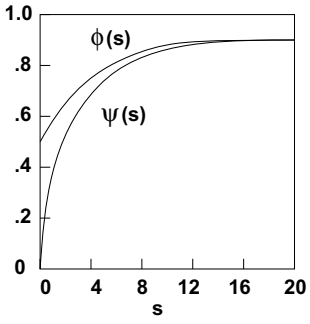

Fig. 7 Wagner's function $\phi(s)$ for indicial lift and K*ü*ssner's function $\psi(s)$ for lift due to a sharp-edged gust, plotted as functions of distance travelled in semichordlengths. After BAH, Fig. 5.21

Thus using the Duhamel superposition formula

$$\begin{aligned} L(t) =& \pi\rho b^2 \left[\frac{d^2h}{dt^2} + U_\infty \frac{d\alpha}{dt} - ba\frac{d^2\alpha}{dt^2}\right] \\ & - 2\pi\rho U_\infty b \left[w_{a_{\frac{3}{4}}}(0)\phi(s) + \int_0^s \frac{dw_{a_{\frac{3}{4}}}}{d\sigma}(\sigma)\phi(s-\sigma)d\sigma\right] \end{aligned} \tag{3.73}$$

Example II. Entrance into a sharp edged gust.

In the primed coordinate system, i.e., fixed with respect to the atmosphere, one has

$$\begin{aligned} w_G =& 0 \quad \text{for} \quad x' > 0 \\ =& w_0 \quad \text{for} \quad x' < 0 \end{aligned}$$

Note: The general transformation between fluid fixed and body fixed coordinate systems is

$$\begin{aligned} x' - x &= b - U_\infty t, \qquad x + b = x' + U_\infty t' \\ t' &= t \qquad\qquad\qquad t = t' \end{aligned}$$

The leading edge enters the gust at $t = t' = 0$ at

$$\begin{aligned} t &= 0, \qquad x' = x + b \\ t' &= 0. \end{aligned}$$

Thus in the coordinate system fixed with respect to the airfoil, one has

$$w_G = 0 \ \text{ for } \ x + b > U_\infty t \ \text{ or } \ \frac{x+b}{U_\infty} > t \tag{3.74}$$

$$= w_0 \ \text{ for } \ x + b < U_\infty t \ \text{ or } \ \frac{x+b}{U_\infty} < t$$

$$\begin{aligned} w_G(\omega) \equiv & \int_{-\infty}^{\infty} w_G e^{i\omega t} dt \\ =& w_0 \int_{(x+b)/U_\infty}^{\infty} e^{-i\omega t} dt \\ =& \frac{w_0}{i\omega} e^{-i\omega t}\Big|_{(x+b)/U_\infty}^{\infty} \\ =& \frac{w_0}{i\omega} \exp\left[-i\omega\frac{(x+b)}{U_\infty}\right] = \frac{w_0}{i\omega} e^{-ik} e^{ikx^*} \end{aligned}$$

where

$$x^* \equiv x/b \tag{3.75}$$

For

$$\bar{w}_a = -w_G \left(= -\frac{w_0}{i\omega} e^{-ik} e^{ikx^*} \right)$$

one finds from the oscillating airfoil motion theory that

$$\bar{L} = 2\pi\rho U_\infty b\{C(k)[J_0(k) - iJ_1(k)] + iJ_1(k)\}\frac{w_0}{i\omega}e^{-ik}$$

and

$$\bar{M}_y = b(\frac{1}{2} + a)\bar{L}$$

$$\begin{aligned} L(t) =& \frac{1}{2\pi}\int_{-\infty}^{\infty} \bar{L}(\omega) e^{i\omega t} d\omega \\ =& \rho U_\infty b w_0 \int_{-\infty}^{\infty} \frac{\{\cdots\}}{ik} e^{-ik} e^{iks} dk \\ =& 2\pi\rho U_\infty b w_0 \psi(s) \end{aligned} \tag{3.76}$$

where

$$\psi(s) \equiv \frac{1}{2\pi i}\int_{-\infty}^{\infty} \frac{\{\cdots\}}{k} \exp[ik(s-1)]dk \tag{3.77}$$

is called the K*ü*ssner function and was shown previously in Fig. 7. Finally then, using Duhamel's integral,

$$L = \pi\rho U b \left\{ w_G(0)\psi(s) + \int_0^s \frac{dw_G}{d\sigma}(\sigma)(s-\sigma)d\sigma \right\} \tag{3.78}$$

A famous controversy concerning the interpretation of Theodorsen's function for other than real frequencies (neutrally stable motion) took place in the 1950s. The issue has arisen again because of possible applications to feedback control of aeroelastic systems. For a modern view and discussion, the reader should consult Edwards, Ashley, and Breakwell [20]. Also see Sears, [10] in Chap. 3.

3.5.3 Evaluation of Integrals

For $x^* < 1$

$$\begin{aligned} I_0 \equiv \oint_{-1}^{1} \frac{d\xi^*}{x^* - \xi^*} &= \lim_{\epsilon\to 0}\left[\int_{-1}^{x^*-\epsilon} \frac{d\xi^*}{x^* - \xi^*} + \int_{x^*+\epsilon}^{1} \frac{d\xi^*}{x^* - \xi^*} \right] \\ &= \lim_{\epsilon\to 0}\left[-\int_{-1}^{x^*-\epsilon} \frac{d(x^* - \xi^*)}{(x^* - \xi^*)} - \int_{x^*+\epsilon}^{1} \frac{d(\xi^* - x^*)}{(\xi^* - x^*)} \right] \\ &= -ln(x^* - \xi^*)\Big|_{\xi^*-1}^{x^*-\epsilon} - ln(\xi^* - x^*)\Big|_{x^*+\epsilon}^{1} \\ &= -[ln\,\epsilon - ln(x^* + 1)] - [ln(1 - x^*) - ln\,\epsilon] = ln\left(\frac{1 + x^*}{1 - x^*}\right) \end{aligned}$$

Fig. 8 Integral contour

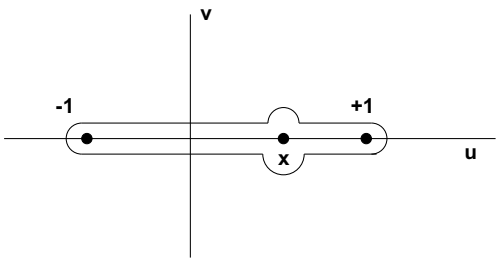

For $x^* > 1$, there is no need for a Cauchy Principal Value and

$$I_0 = ln\left(\frac{x^*+1}{x^*-1}\right)$$

$$I_1: \quad I_1 \equiv \oint_{-1}^{1} \sqrt{\frac{1+u}{1-u}} \frac{du}{u-x^*}$$

Use contour integration. Define $w \equiv u + iv$ (a complex variable whose real part is u) and

$$F(w) \equiv \left(\frac{w+1}{w-1}\right)^{\frac{1}{2}} \frac{1}{w-x^*}$$

Choose a contour as follows (Fig. 8).

Now

$$\frac{w+1}{w-1} = [R^2 + I^2]^{\frac{1}{2}} e^{-i\theta}$$

where

$$R \equiv \frac{(u+1)(u-1)+v^2}{(u-1)^2+v^2}, \qquad I \equiv \frac{-2v}{(u-1)^2+v^2}$$

$$\theta = \tan^{-1} I/R$$

(i) on top, $v = 0^+$, $\quad u - 1 < 0$

$$R < 0, \quad I = 0^- \Rightarrow \theta = -\pi$$

(ii) on bottom, $v = 0^-$, $u - 1 < 0$

$$R < 0, \quad I = 0^+ \Rightarrow \theta = +\pi$$

Thus

$$\left(\frac{w+1}{w-1}\right)^{\frac{1}{2}} = \sqrt{\frac{1+u}{1-u}}e^{-i\pi/2} \quad \text{on top}$$

$$= \sqrt{\frac{1+u}{1-u}}e^{+i\pi/2} \quad \text{on bottom}$$

Now $dw = du$ on top or bottom and $w - x^* = u - x^*$ except on arcs near $u = x^*$. On the arcs $w - x^* = \epsilon e^{i\theta},\ dw = \epsilon e^{i\theta} i d\theta$ where ϵ is radius of arc. Also

$$\left(\frac{w+1}{w-1}\right)^{\frac{1}{2}} = \sqrt{\frac{1+u}{1-u}}(-i) \quad \text{on top}$$

and $= \cdots (+i)$ on bottom. Thus

$$\zeta_1 \equiv \int_C F(w)dw = \overbrace{\int_{-1}^{x^*-\epsilon} + \int_{x^*+\epsilon}^{1} i\sqrt{\frac{1+u}{1-u}}\frac{du}{u-x^*}}^{\text{bottom}}$$

$$+ \overbrace{\int_{1}^{x^*+\epsilon} + \int_{x^*-\epsilon}^{-1} -i\sqrt{\frac{1+u}{1-u}}}^{\text{top}}\frac{du}{u-x^*} +$$

$$+ \quad \text{contributions from arcs which cancel each other}$$

$$\lim_{\epsilon\to 0}\zeta_1 = 2i\int_{-1}^{1}\sqrt{\frac{1+u}{1-u}}\frac{du}{u-x^*} = 2iI_1$$

ζ_1 can be simply evaluated by Cauchy's Theorem. As $w \to \infty,\ F(w) \to 1/w$.

$$\zeta_1 = \int_{\text{around arc at } \infty}\frac{dw}{w} = 2\pi i$$

$$I_1 = \frac{\zeta_1}{2i} = \frac{2\pi i}{2i} = \pi$$

For $x^* > 1$, I_1 is still equal to $\zeta_1/2\pi i$; however, now $\zeta_1 = \int_{\text{arc at infinity}} f(w)dw -$ Residue of F at x^*

$$= 2\pi i - 2\pi i\sqrt{\frac{x^*+1}{x^*-1}}$$

$$I_1 = \frac{\zeta_1}{2\pi i} = \pi\left[1 - \sqrt{\frac{x^*+1}{x^*-1}}\right]$$

A similar calculation gives I_2.

Evaluations of I_2

$$-I_2 \equiv \int_{-1}^{1} \sqrt{\frac{1+u}{1-u}} ln \left| \frac{1+u}{1-u} \right| \frac{du}{u-x^*}$$

Define

$$w \equiv u + iv$$

and

$$F(w) \equiv ln \left| \frac{w+1}{w-1} \right| \sqrt{\frac{w+1}{w-1}} \frac{1}{w-x^*}$$

The contour is the same as for I_1.

As before

$$\left(\frac{w+1}{w-1}\right)^{\frac{1}{2}} = \sqrt{\frac{1+u}{1-u}} e^{-i\pi/2} \quad \text{on top}$$

$$= \sqrt{\frac{1+u}{1-u}} e^{+i\pi/2} \quad \text{on bottom}$$

Also

$$ln\left(\frac{w+1}{w-1}\right) = ln\sqrt{R^2+I^2} + i\theta$$

$$= ln \left| \frac{u+1}{u-1} \right| - i\pi \quad \text{on top}$$

$$= ln \left| \frac{u+1}{u-1} \right| + i\pi \quad \text{on bottom}$$

Now $dw = du$ on top or bottom and $w - x^* = u - x^*$ *except* on arcs near $u = x^*$. On the arcs $w - x^* = \epsilon e^{i\theta}$, $dw = \epsilon e^{i\theta} i\, d\theta$ where ϵ is radius of arc. Thus

$$\zeta_2 \equiv \int_C F_2(w) dw = \int_{-1}^{x^*-\epsilon} + \int_{x^*+\epsilon}^{1} i \left\{ \sqrt{\frac{1+u}{1-u}} \left[ln \left| \frac{1+u}{1-u} \right| - i\pi \right] \right\} \times \frac{du}{u-x^*} \quad \text{bottom}$$

$$+ \int_{1}^{x^*+\epsilon} + \int_{x^*-\epsilon}^{-1} -i \left\{ \sqrt{\frac{1+u}{1-u}} \left[ln \left| \frac{1+u}{1-u} \right| - i\pi \right] \right\} \frac{du}{u-x^*} \quad \text{top}$$

$$- \int_{0}^{\pi} i\pi \sqrt{\frac{1+x^*}{1-x^*}} d\theta - \int_{-\pi}^{0} i\pi \sqrt{\frac{1+x^*}{1-x^*}} d\theta \quad \text{arcs}$$

Note: ln terms cancel and thus are omitted in the arc contributions. Cancelling π terms from bottom and top and adding arc terms, gives

$$\zeta_2 = \int_{-1}^{x^*-\epsilon} + \int_{x^*+\epsilon}^{1} i\sqrt{\frac{1+u}{1-u}} ln \left|\frac{1+u}{1-u}\right| \frac{du}{u-x^*}$$
$$+ \int_{1}^{x^*+\epsilon} + \int_{x^*-\epsilon}^{-1} -i\sqrt{\frac{1+u}{1-u}} ln \left|\frac{1+u}{1-u}\right| \frac{du}{u-x^*}$$
$$- 2i\pi^2\sqrt{\frac{1+x^*}{1-x^*}}$$

Adding bottom and top terms,

$$\lim_{\epsilon\to 0} \zeta_2 = 2i \int_{-1}^{1} \sqrt{\frac{1+u}{1-u}} ln \left|\frac{1+u}{1-u}\right| \frac{du}{u-x^*} - 2i\pi^2\sqrt{\frac{1+x^*}{1-x^*}}$$
$$= -2i I_2 - 2i\pi^2\sqrt{\frac{1+x^*}{1-x^*}}$$

ζ_2 can be simply evaluated by Cauchy's Theorem. As $w \to \infty,\ F_2(w) \to 0$.

$$\zeta_2 = 0 \Rightarrow I_2 = -\pi^2\sqrt{\frac{1+x^*}{1-x^*}}$$

4 Representative Numerical Results

Consider a flat plate airfoil, initially at zero angle of attack, which is given a step change in α, i.e.,

$$w = -U_\infty \alpha \quad \text{for} \quad t > 0$$
$$= 0 \qquad\quad \text{for} \quad t < 0$$

Although most calculations in practice are carried out for sinusoidal time dependent motion, for our purposes examining aerodynamic pressures due to this step change leads to more insight into the nature of the physical system. Of course, *in principle*, the results for sinusoidal motion (or a step change) may be superposed to obtain results for arbitrary time dependent motion.

It is traditional to express the pressure in nondimensional form

$$\frac{p}{\frac{\rho_\infty U_\infty^2 \alpha}{2}} \equiv \frac{p}{q\alpha}$$

as a function of nondimensional time,

$$s \equiv \frac{tU_\infty}{c/2}$$

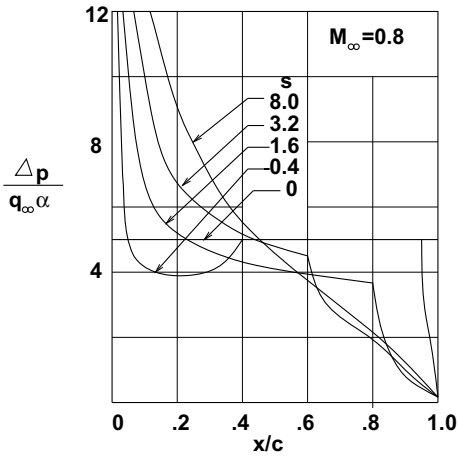

Fig. 9 Chordwise lifting pressure distributions

and M_∞. The results shown below are from an article by Lomax[23]; both subsonic and supersonic, two- and three dimensional results are displayed.

In Fig. 9 the chord-wise pressure distribution for two-dimensional flow is shown at several times, s, for a representative subsonic Mach number. For $s = 0$, the result is given by piston theory (as in supersonic flow)[24]

$$p = \rho_\infty a_\infty w$$

For a step change in α, piston theory gives

$$\frac{\Delta p}{\frac{\rho_\infty U_\infty^2 \alpha}{2}} = \frac{p_L - p_U}{\frac{\rho_\infty U_\infty^2 \alpha}{2}} = \frac{4}{M}$$

For $s \to \infty$, the result is also well known, with a square root singularity at the leading edge. Of course, the Kutta condition, $\Delta p = 0$, is enforced at the trailing edge for all s. As $s \to \infty$

$$\frac{\Delta p}{\frac{\rho_\infty U_\infty^2 \alpha}{2}} = \frac{4}{(1 - M^2)^{\frac{1}{2}}} \sqrt{\frac{c - x}{x}}$$

This result is implicit in the analysis of Sect. 3.

In Fig. 10 the chord-wise pressure distribution is shown at several times, s, for a representative supersonic Mach number. For $s = 0$ the result is again that given by piston theory

[23]Lomax [21].

[24]This can be shown by considering the transient analysis of Sect. 2 and noting it still applies for $t = 0^+$.

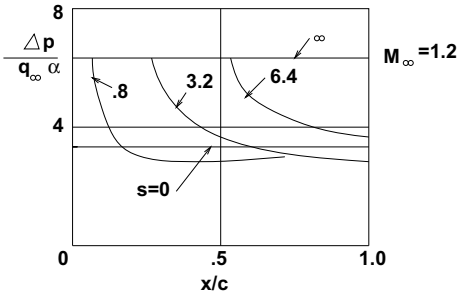

Fig. 10 Chordwise lifting pressure distribution

$$\frac{\Delta p}{\frac{\rho_\infty U_\infty^2 \alpha}{2}} = \frac{4}{M}$$

For $s \to \infty$, the result is (as previously cited in our earlier discussion, Sect. 2)

$$\frac{\Delta p}{\frac{\rho_\infty U_\infty^2 \alpha}{2}} = \frac{4}{(M^2-1)^{\frac{1}{2}}}$$

Indeed the pressure reaches this final steady state value at a finite s which can be determined as follows. All disturbances propagate *in the fluid* with the speed of sound, a_∞, but the airfoil moves faster with velocity $U_\infty > a_\infty$. Hence, the elapsed time for all disturbances (created by the step change of α for the airfoil) to move off the airfoil is the time required for a (forward propagating *in the fluid*) disturbance at the leading edge to move to the trailing edge, namely

$$t = c/(U_\infty - a_\infty)$$

or, in nondimensional form,

$$s \equiv \frac{tU_\infty}{c/2} = \frac{2M_\infty}{M_\infty - 1}$$

For

$$s > \frac{2M_\infty}{M_\infty - 1}$$

steady state conditions are obtained all along the airfoil. As can be seen from Fig. 10 for $s = 0^+$ the leading edge pressure instantly reaches its final steady state value. As s increases the steady state is reached by increasing portions of the airfoil along the chord. Note that the initial results, $s = 0$, and steady state results,

$$s \geq \frac{2M_\infty}{M_\infty - 1}$$

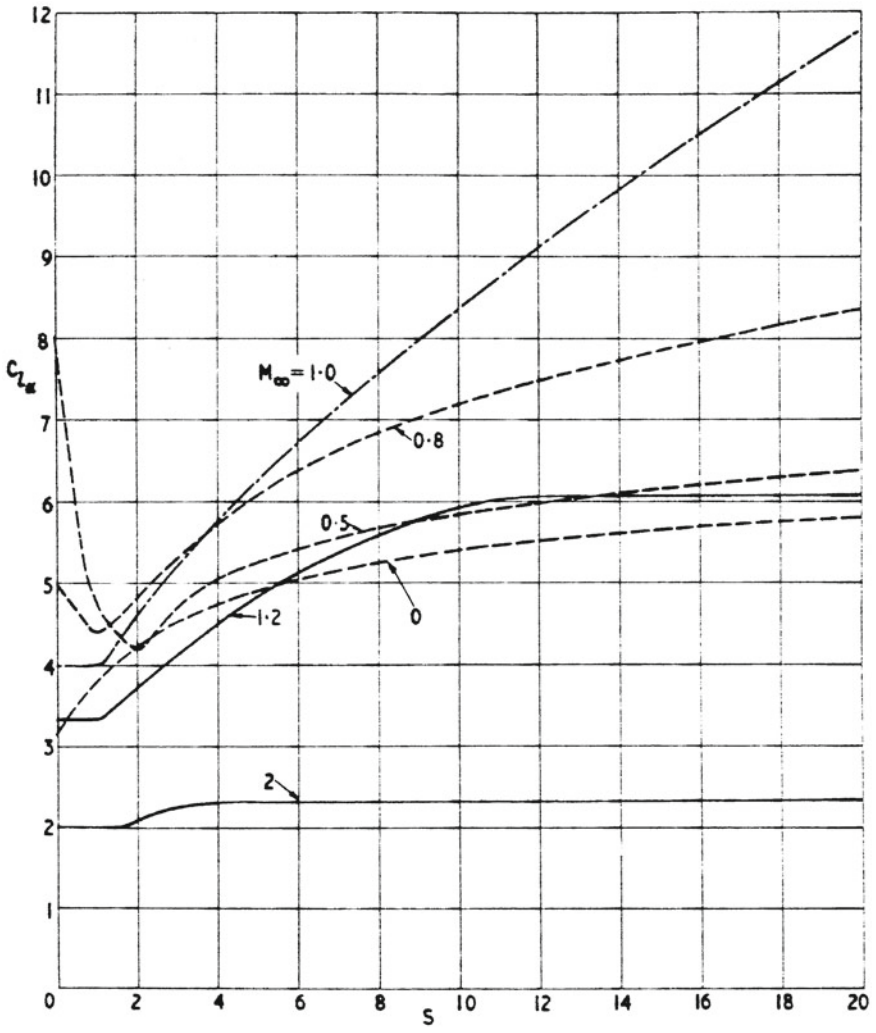

Fig. 11 Time history of lift curve slope

have a constant pressure distribution; however, for intermediate s, the pressure varies along the chord.

The pressure distributions may be integrated along the chord to obtain the total force (lift) on the airfoil.

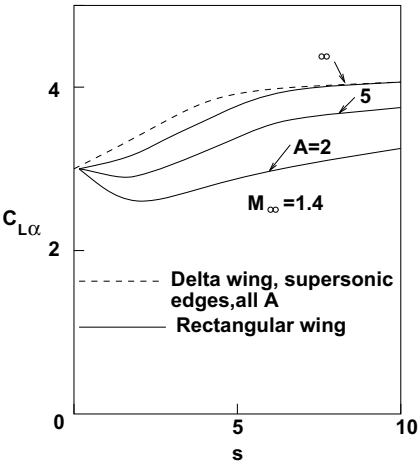

Fig. 12 Time history of lift curve slope

$$L \equiv \int_0^c \Delta p \, dx,$$

$$C_{L_\alpha} \equiv \frac{L}{\frac{\rho_\infty U_\infty^2 c\alpha}{2}}, \quad \text{lift curve slope}$$

Again the $s = 0$ result is that given by piston theory

$$C_{L_\alpha} = \frac{4}{M}$$

and the steady-state result is

$$C_{L_\alpha} = \frac{4}{(M^2 - 1)^{\frac{1}{2}}} \quad \text{for} \quad M_\infty > 1$$

and it is also known that

$$C_{L_\alpha} = \frac{2\pi}{(1 - M_\infty^2)^{\frac{1}{2}}} \quad \text{for} \quad M_\infty < 1$$

see Sect. 3. Results for C_{L_α} are shown in Fig. 11 for various Mach number.

Finally some representative results for *three-dimensional*, supersonic flow are shown in Fig. 12. The effect of three-dimensionality is to reduce the lift. For small aspect ratio, A, where

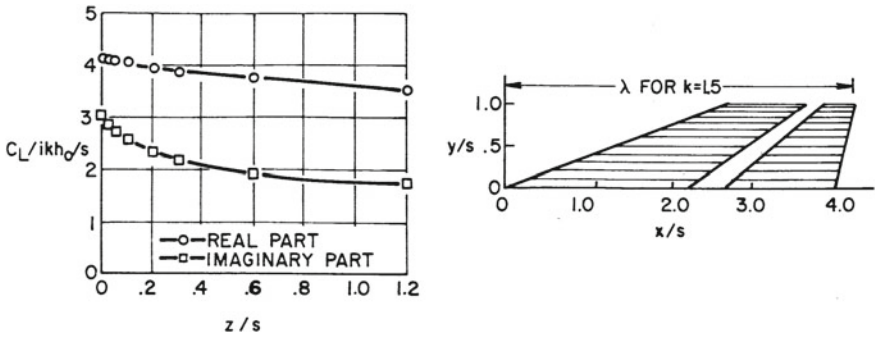

Fig. 13 Lift coefficient of plunging wing-tail combination for various vertical separation distances; simple harmonic motion

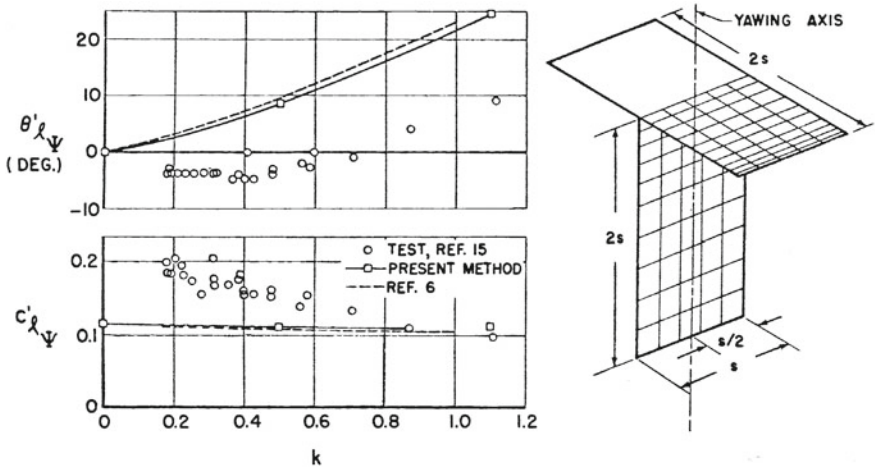

Fig. 14 Rolling moment coefficient of horizontal stabilizer for simplified T-tail oscillating in yaw about fin mid-chord; simple harmonic motion

$A \equiv$ maximum span squared/wing area it is known from slender body theory[25] (an asymptotic theory for $A \to 0$) that

$$C_{L_\alpha} = \frac{\pi}{2} A$$

for $s \to \infty$. Note however, that the $s = 0^+$ result is independent of A and is that given by piston theory.

Hence, piston theory gives the correct result for $s = 0^+$ for two- and three-dimensional flows, subsonic as well as supersonic. However, only for relatively high

[25]See Lomax, for example [21].

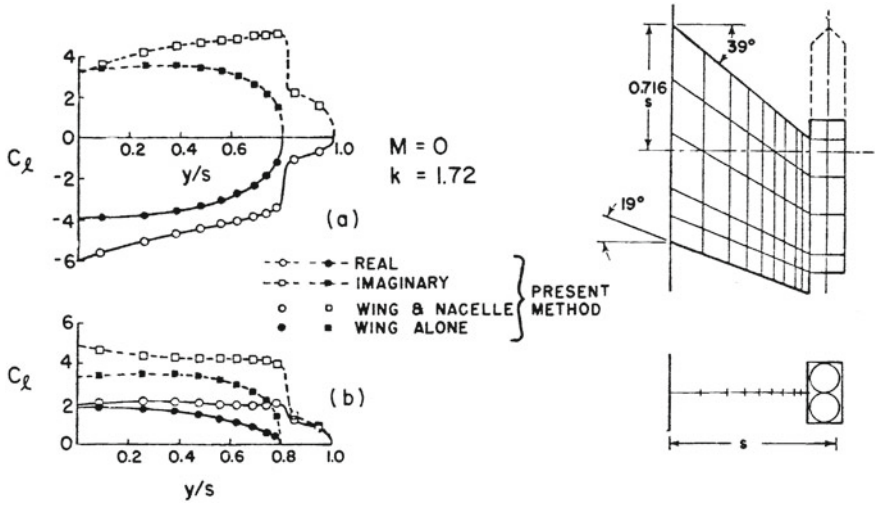

Fig. 15 Distribution of span load for wing with and without engine nacelle. **a** Plunging **b** pitching; simple harmonic motion

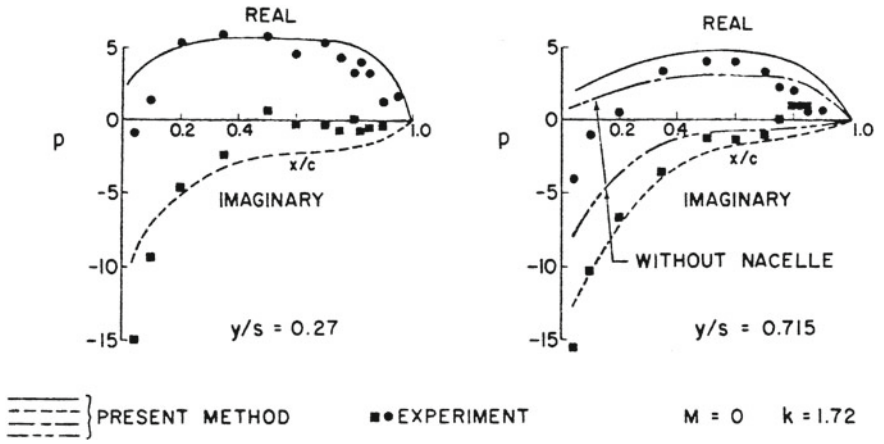

Fig. 16 Comparison of experimental and calculated lifting pressure coefficient on a wing-nacelle combination in plunge; simple harmonic motion

supersonic and nearly two-dimensional flow does it give a reasonable approximation for *all s*.

For subsonic flows, the numerical methods are in an advanced state of development and results have been obtained for rather complex geometries including multiple aerodynamic surfaces. In Figs. 13, 14, 15, 16 and 17representative data are shown. These are drawn from a paper by Rodden et al.,[26] Which contains an extensive

[26]Rodden, Giesing and K*álmán* [22].

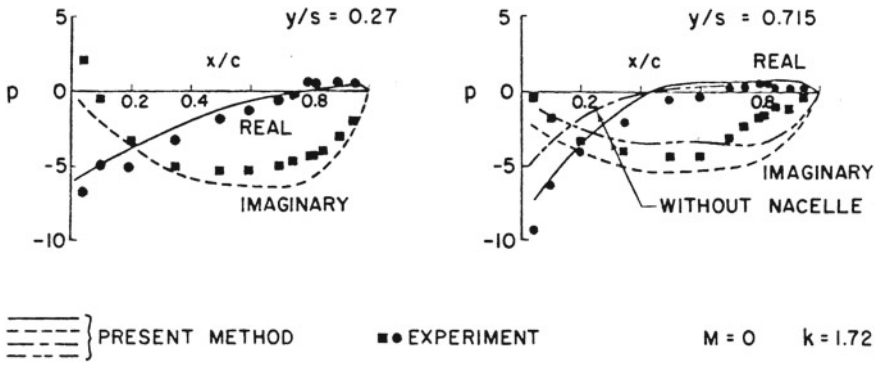

Fig. 17 Comparison of experimental and calculated lifting pressure coefficient on a wing-nacelle combination oscillating in pitch; simple harmonic motion

discussion of such data and the numerical techniques used to obtain them. Simple harmonic motion is considered where k is a non-dimensional frequency of oscillation. Comparison with experimental data are also shown.

5 Transonic Flow

Major progress has been made in recent years on this important topic. Here we concentrate on the fundamental ideas and explore one simple approach to obtaining solutions using the same mathematical methods previously employed for subsonic and supersonic flow.

The failure of the classical linear, perturbation theory in transonic flow is well known and several attempts have been made to develop a theoretical model which will give consistent, accurate results. Among the more successful approximate methods that builds upon the classical approaches for subsonic and supersonic flow is the 'local linearization' concept of Spreiter which has been generalized to treat oscillating airfoils in transonic flow [23]. Another valuable method is that of parametric differentiation as developed by Rubbert and Landahl [24]. 'Local linearization' is an ad hoc approximation while parametric differentiation is a perturbation procedure from which the result of local linearization may be derived by making further approximations. Several authors [25–28] have attacked the problem in a numerical fashion using finite differences and results have been obtained for two and three-dimensional, high subsonic flow. This continues to be an active subject of research and will be discussed further in chapter "Modeling of Fluid-Structure Interaction". Cunningham [29]. Has suggested a relatively simple, empirical modification of the classical theory.

In the present section a rational approximation method[27] is discussed which is broadly related to the local linearization concept. It has the advantages of (1) being simpler than the latter (2) capable of being systematically improved to obtain an essentially exact solution to the governing transonic equation. Although the method has been developed for treating infinitesimal dynamic motions of airfoils of finite thickness, it may also be employed (using the concept of parametric differentiation) to obtain solutions for nonlinear, steady nonlifting flows. This is a problem for which local linearization' was originally developed.

First, the basic idea will be explained for an infinitesimal steady motion of an airfoil of finite thickness in two-dimensional flow. Results will also be given for dynamic motion. The aerodynamic Green's functions for three-dimensional flow have also been derived. These are needed in the popular Mach Box and Kernel Function methods [31]. Using Green's functions derived by the present methods, three-dimensional calculations are effectively no more difficult than for the classical theory.

Analysis

From (1.21), Sect. 1, the full nonlinear equation for ϕ is

$$a^2\nabla^2\phi - \left[\frac{\partial}{\partial t}(\nabla\phi\cdot\nabla\phi) + \frac{\partial^2\phi}{\partial t^2} + \nabla\phi\cdot\nabla\left(\frac{\nabla\phi\cdot\nabla\phi}{2}\right)\right] = 0$$

In cartesian, scalar notation and re-arranging terms

$$\begin{aligned}&\phi_{xx}(a^2-\phi_x^2)+\phi_{yy}(a^2-\phi_y^2)+\phi_{zz}(a^2-\phi_z^2)\\&\quad-2\phi_{yz}\phi_y\phi_z-2\phi_{xz}\phi_x\phi_z-2\phi_{xy}\phi_x\phi_y\\&\quad-\frac{\partial}{\partial t}(\phi_x^2+\phi_y^2+\phi_z^2)-\frac{\partial^2\phi}{\partial t^2}=0\end{aligned} \tag{5.1}$$

Also we previously determined that ((1.22), Sect. 1)

$$\frac{a^2-a_\infty^2}{\gamma-1} = \frac{U_\infty^2}{2} - \left(\frac{\partial\phi}{\partial t} + \frac{\nabla\phi\cdot\nabla\phi}{2}\right) \tag{5.2}$$

Now let $\phi = U_\infty x + \hat{\phi}$, then (5.2) becomes

$$\frac{a^2-a_\infty^2}{\gamma-1} = -\left[\frac{\partial\hat{\phi}}{\partial t} + \frac{2U_\infty\frac{\partial\hat{\phi}}{\partial x} + \left(\frac{\partial\hat{\phi}}{\partial x}\right)^2 + \left(\frac{\partial\hat{\phi}}{\partial y}\right)^2 + \left(\frac{\partial\hat{\phi}}{\partial z}\right)^2}{2}\right]$$

[27]This section is a revised version of Dowell [30]. A list of nomenclature is given at the end of this section.

$$\cong -\left[\frac{\partial\hat{\phi}}{\partial t} + U_\infty \frac{\partial\hat{\phi}}{\partial x}\right]$$

or

$$a^2 \cong a_\infty^2 - (\gamma - 1)\left[\frac{\partial\hat{\phi}}{\partial t} + U_\infty \frac{\partial\hat{\phi}}{\partial x}\right] \tag{5.3}$$

(5.1) becomes

$$\begin{aligned}\hat{\phi}_{xx}\left(a_\infty^2 - (\gamma-1)\left[\frac{\partial\hat{\phi}}{\partial t} + U_\infty\frac{\partial\hat{\phi}}{\partial x}\right] - U_\infty^2 - 2U_\infty\frac{\partial\hat{\phi}}{\partial x}\right)\\ + \hat{\phi}_{yy}a_\infty^2 + \hat{\phi}_{zz}a_\infty^2 - \frac{\partial}{\partial t}\left(2U_\infty\frac{\partial\hat{\phi}}{\partial x}\right) - \frac{\partial^2\hat{\phi}}{\partial t^2} \cong 0\end{aligned} \tag{5.4}$$

where obvious higher order terms have been neglected on the basis of $\hat{\phi}_x, \hat{\phi}_y, \hat{\phi}_z \ll U_\infty$ and a_∞.

The crucial distinction in transonic perturbation theory is in the coefficient of $\hat{\phi}_{xx}$. In the usual subsonic or supersonic small perturbation theory one approximated it as simply

$$a_\infty^2 - U_\infty^2$$

However if $U_\infty = a_\infty$ or nearly so then the terms retained above become important. The time derivative term in the coefficient of $\hat{\phi}_{xx}$ may still be neglected compared to the next to last term in (5.4), but no further simplification is possible, in general. Hence, (5.4) becomes (dividing by a_∞^2)

$$\hat{\phi}_{xx}[1 - M_L^2] + \hat{\phi}_{yy} + \hat{\phi}_{zz} - \frac{1}{a_\infty^2}\left[2U_\infty\frac{\partial^2\hat{\phi}}{\partial x\partial t} + \frac{\partial^2\hat{\phi}}{\partial t^2}\right] = 0 \tag{5.5}$$

where

$$M_L^2 \equiv M_\infty^2\left[1 + \frac{(\gamma+1)\hat{\phi}_x}{U_\infty}\right], \quad M_\infty \equiv U_\infty/a_\infty$$

It may be shown that M_L is the consistent transonic, small perturbation approximation to the local (rather than free stream) Mach number. Hence, the essence of *transonic* small perturbation theory is the allowance for variable, local Mach number rather than simply approximating the local Mach number by M_∞ as in the usual subsonic and supersonic theories.

We digress briefly to show that in (5.4) the term

$$\hat{\phi}_{xx}\left[-(\gamma-1)\frac{\partial\hat{\phi}}{\partial t}\right] \tag{5.6}$$

may be neglected compared to

$$-2U_\infty \frac{\partial^2 \hat{\phi}}{\partial t \partial x} \tag{5.7}$$

This is done both for its interest in the present context as well as a prototype for estimation of terms in analyses of this general type.

We assume that a length scale, L, and a time scale, T, may be chosen so that

$$x^* \equiv x/L \quad \text{'is of order one'}$$
$$t^* \equiv t/T \quad \text{'is of order one'}$$

Hence, derivatives with respect to x^* or t^* do *not*, by assumption, change the order or size of a term. Thus (5.6) and (5.7) may be written (ignoring constants of order one like $\gamma - 1$ and 2) as

$$A \equiv \frac{\hat{\phi}_{x^*x^*}}{L^2} \frac{\hat{\phi}_{t^*}}{T} \tag{5.6}$$

and

$$B \equiv U_\infty \frac{\hat{\phi}_{t^*x^*}}{TL} \tag{5.7}$$

Hence

$$\frac{(A)}{(B)} \sim 0\left[\frac{\hat{\phi}}{U_\infty L}\right]$$

This ratio however, is much less than one by our original assumption of a small perturbation, viz.

$$\phi = U_\infty L x^* + \hat{\phi}$$

In the beginning we have assumed

$$\frac{\hat{\phi}}{U_\infty L x^*} \ll 1$$

Hence (5.6) may be neglected compared to (5.7).

Equation (5.5) is a nonlinear equation even though we have invoked small perturbation ideas. One may develop a linear theory by considering a steady flow due to airfoil shape, $\hat{\phi}_s$ and an infinitesimal time dependent motion of the airfoil superimposed, $\hat{\phi}_d$. For definiteness, one may consider ϕ_s as due to an airfoil of symmetric thickness at zero angle of attack. Thus let

$$\hat{\phi}(x, y, z, t) = \hat{\phi}_s(x, y, z) + \hat{\phi}_d(x, y, z, t) \tag{5.6}$$

and substitute into (5.5). The equations for ϕ_s is (by definition)

$$\hat{\phi}_{s_x x}[1 - M_{L_s}^2] + \hat{\phi}_{s_y y} + \hat{\phi}_{s_z z} = 0 \tag{5.7}$$

where

$$M_{L_s}^2 \equiv M_\infty^2 \left[1 + (\gamma + 1)\frac{\hat{\phi}_{s_x}}{U_\infty}\right]$$

The equation for $\hat{\phi}_d$ (neglecting products of $\hat{\phi}_d$ and its derivatives which is acceptable for sufficiently small time dependent motions) is

$$\hat{\phi}_{d_z z} + \hat{\phi}_{d_y y} - \frac{1}{a_\infty^2}\hat{\phi}_{d_t t} - 2\frac{U_\infty}{a_\infty^2}\hat{\phi}_{d_x t} - b\hat{\phi}_{d_x x} - a\hat{\phi}_{d_x} = 0 \tag{5.8}$$

where

$$b \equiv \left[M_\infty^2 - 1 + (\gamma + 1)\frac{\hat{\phi}_{s_x}}{U_\infty}M_\infty^2\right]$$

$$a \equiv (\gamma + 1)M_\infty^2\frac{\hat{\phi}_{s_x}}{U_\infty}$$

From Bernoulli's equation

$$C_{p_m s} \equiv \frac{\hat{P}_s}{\frac{\rho_\infty U_\infty^2}{2}} = -\frac{2\hat{\phi}_{s_x}}{U_\infty}$$

Hence, a and b may be written as

$$b \equiv \left[M_\infty^2 - 1 - \frac{(\gamma + 1)M_\infty^2 C_{p_m s}(x)}{2}\right]$$

$$a \equiv -(\gamma + 1)\frac{M_\infty^2}{2}\frac{dC_{p_m s}(x)}{dx}$$

$\hat{\phi}_d$ is velocity potential due to the infinitesimal motion (henceforth $\hat{}$ and d are dropped for simplicity). $C_{p_m s}$ is the mean steady pressure coefficient due to airfoil finite thickness and is taken as known. In general, it is a function of x, y, z and the method to be described will, in principle, allow for such dependence. However, all results have been obtained ignoring the dependence on y and z. See Refs. [23, 24, 32] for discussion of this point.

The (perturbation) pressure, p, is related to ϕ by the Bernoulli relations

$$p = -\rho_\infty\left[\frac{\partial\phi}{\partial t} + U_\infty\frac{\partial\phi}{\partial x}\right]$$

and the boundary conditions are

$$\frac{\partial \phi}{\partial z}|_{z=0} = w_a \equiv \frac{\partial f}{\partial t} + U_\infty \frac{\partial f}{\partial x}$$

on airfoil where

$$\begin{aligned} f(x, y, t) &\equiv \text{ vertical displacement of point } x, y \text{ on airfoil} \\ w_a &\equiv \text{ upwash velocity} \end{aligned}$$

and

$$p|_{z=0} = 0 \quad \text{off airfoil}$$

plus appropriate finiteness or radiation conditions as $z \to \infty$.

Note that Eq. (5.7) is nonlinear in $\hat{\phi}_s$. If one linearizes, as for example in the classical *supersonic* theory, one would set $M_L = M_\infty$ and obtain as a solution to (5.7)

$$\hat{p}_s = \frac{\rho_\infty U_\infty^2}{(M_\infty^2 - 1)^{\frac{1}{2}}} \frac{\partial f}{\partial x}$$

where $\partial f/\partial x$ is the slope of airfoil shape. As $M_\infty \to 1, \hat{p} \to \infty$ which is a unrealistic physical result of the linear theory. On the other hand if one uses

$$M_L = M_\infty \left[1 + (\gamma - 1) \frac{\hat{\phi}_{s_x}}{U_\infty} \right]^{\frac{1}{2}}$$

a finite result is obtained for $\hat{p}_s$ as $M_\infty \to 1$ which is in reasonable agreement with the experimental data.[28]

Equation (5.7) with the full expression for M_L is a nonlinear partial differential equation which is much more difficult to solve than its linear counterpart. However two types of methods have proven valuable, the numerical Finite difference methods [29] and various techniques associated with the name 'local linearization' as pioneered by Oswatitsch and Spreiter [33].

Once $\hat{\phi}_s$ is known (either from theory or experiment) (5.8) may be used to determine $\hat{\phi}_d$. Equation (5.8) is a linear differential equation with variable coefficients which depend upon $\hat{\phi}_s$. Hence, the solution for the lifting problem, $\hat{\phi}_d$, depends upon the thickness solution, $\hat{\phi}_s$, unlike the classical linear theory where the two may be calculated separately and the results superimposed. Again either finite difference methods or 'local linearization' may be employed to solve (5.8). Here we pursue an improved analytical technique to determine $\hat{\phi}_d$, which has been developed in the spirit of 'local linearization' ideas [30].

To explain the method most concisely, let $\phi_y = \phi_t = 0$ in Eq. (5.8), i.e., consider two-dimensional, steady flow.

---

[28] Spreiter [33].

[29] Ballhaus, Magnus and Yoshihara [34].

Assume[30]

$$a = \sum_{m=0}^{\infty} a_m (x - x_0)^m$$

$$b = \sum_{n=0}^{\infty} b_n (x - x_0)^n$$

and $\phi = \phi^0 + \phi'$ where, *by definition*,

$$\phi^0_{zz} - b_0 \phi^0_{xx} - a_0 \phi^0_x = 0 \tag{4.5.8a}$$

and ϕ^0 satisfies any nonhomogeneous boundary conditions on ϕ. The equation for ϕ' is thus from (5.8) and using the above

$$\phi'_{zz} - b_0 \phi'_{xx} - a_0 \phi'_x = \sum_{n=1}^{\infty} b_n (x - x_0)^n [\phi^0_{xx} + \phi'_{xx}] + \sum_{m=1}^{\infty} a_m (x - x_0)^m [\phi^0_{xx} + \phi'_{xx}] \tag{4.5.8b}$$

with homogeneous boundary conditions on ϕ'.

If $\phi' \ll \phi^0$, i.e., ϕ^0 is a good approximation to the solution, then ϕ' may be computed from (4.5.8b) by neglecting ϕ' in the right hand side. The retention of a_0 (but not b_1) in (4.5.8a) is the key to the method, even though this may seem inconsistent at first.

We begin our discussion with steady airfoil motion in a two-dimensional flow. This is the simplest case from the point of view of computation, of course; however, it is also the most critical in the sense that, as Landahl [32] and others have pointed out, unsteadiness and/or three-dimensionality alleviate the nonlinear transonic effects. Indeed, if the flow is sufficiently unsteady and/or three-dimensional, the classical linear theory gives accurate results transonically for thin wings.

Steady airfoil motion in two-dimensional, 'supersonic' ($b_0 > 0$) flow

Solution for ϕ^0. For $b_0 > 0$, x is a time-like variable and the flow is undisturbed ahead of the airfoil (as far as ϕ^0 is concerned). Hence, solutions may be obtained using a Laplace transform with respect to x. Defining

$$\phi^{0_*} \equiv \int_0^{\infty} \phi^0(x, z) e^{-px} dx$$

Equation (4.5.8a) becomes

[30]We expand in a *power* series about $x = x_0$; however, other series might be equally or more useful for some applications. Results suggest the details of a and b are unimportant.

$$\phi^{0_*}_{zz} - \mu^2 \phi^{0_*} = 0 \tag{5.9}$$

with

$$\mu^2 \equiv [b_0 p^2 + a_0 p]$$

Solving (5.9)

$$\phi^{0_*} = A_1^0 e^{-\mu z} + A_2^0 e^{+\mu z} \tag{5.10}$$

In order to satisfy finiteness/radiation condition at infinity, one selects $A_2^0 \equiv 0$. A_1^0 is determined from the (transformed) boundary condition,

$$\phi^{0_*}_z|_{z=0} = w^* \tag{5.11}$$

From (5.10) and (5.11),

$$\phi^{0_*}|_{z=0} = \frac{-w^*}{\mu} \tag{5.12}$$

Inverting (5.12)

$$\phi^0|_{z=0} = -\int_0^x b_0^{-\frac{1}{2}} \exp\left(\frac{-a_0\xi}{2b_0}\right) I_0\left[\frac{a_0\xi}{2b_0}\right] w(x-\xi)d\xi \tag{5.13}$$

It is of interest to note two limiting cases. As $a_0\xi/2b_0 \to 0$,

$$\phi^0|_{z=0} = -\int_0^x b_0^{-\frac{1}{2}} w(x-\xi)d\xi \tag{5.14}$$

the classical result. But, more importantly, as $a_0\xi/2b_0 \to \infty$,

$$\phi^0|_{z=0} = -\int_0^x (\pi a_0\xi)^{-\frac{1}{2}} w(x-\xi)d\xi \tag{5.15}$$

Hence, even when the effective Mach number at $x = x_0$ is transonic, i.e., $b_0 \equiv 0$, the present model gives a finite result. Before computing the correction, ϕ', to the velocity potential we shall exploit ϕ^0 to obtain several interesting result. For this purpose we further restrict ourselves to an airfoil at angle of attack, $w = -U_\infty \alpha$. From (5.15),

$$\frac{\phi^0_{z=0}}{U_\infty \alpha} = \frac{2b_0^{\frac{1}{2}}}{a_0} \tilde{x} e^{-x}[I_0(\tilde{x}) + I_1(\tilde{x})]; \qquad \tilde{x} \equiv \frac{a_0 x}{2b_0} \tag{5.16}$$

and the pressure on the *lower* aerodynamic surface is

$$\frac{C_p}{\alpha} \equiv \frac{p^0}{\frac{\rho_0 U_\infty^2 \alpha}{2}} = \frac{2\phi^0_x}{U_\infty \alpha}|_{z=0} = 2b_0^{-\frac{1}{2}} e^{-x} I_0(\tilde{x}) \tag{5.17}$$

The lift, moment and center of pressure may be computed.

$$
\begin{aligned}
L^0 &\equiv \int_0^C 2p^0 dx = \rho_\infty U_\infty^2 \alpha c 4(\pi a_0 c)^{-\frac{1}{2}} \tilde{L}^0 \\
\tilde{L}^0 &\equiv (\pi/2)^{\frac{1}{2}} \tilde{c}^{\frac{1}{2}} e^{-\tilde{c}} [I_0(\tilde{c}) + I_1(\tilde{c})]; \qquad \tilde{c} \equiv \frac{a_0 c}{2b_0}
\end{aligned}
\tag{5.18}
$$

$$
\begin{aligned}
M^0 &= \int_0^c 2p^0 x\, dx = L^0 c - \rho_\infty U_\infty^2 c^2 \frac{8}{3} (\pi a_0 c)^{-\frac{1}{2}} \tilde{M}^0 \\
\tilde{M}_0 &\equiv \frac{3}{4}(3\pi)^{\frac{1}{2}} \{e^{-\tilde{c}} I_1(\tilde{c}) [\tilde{c}^{-\frac{1}{2}} + \frac{2}{3}\tilde{c}^{\frac{1}{2}}] + \frac{2}{3} e^{-\tilde{c}} I_2(\tilde{c}) \tilde{c}^{\frac{1}{2}}\}
\end{aligned}
\tag{5.19}
$$

The center of pressure may be obtained from L^0 and M^0 in the usual way. We shall use and discuss these results for a particular airfoil later. But first let is consider the computations of ϕ'.

Solutions for ϕ'. For *simplicity*, we shall consider only a *linear* variation in mean pressure, $C_{p_m s}$, along the airfoil chord. hence, a_0, b_0 and b_1 are not zero and $b_1 = a_0$. All other a_m and b_n are zero. Assuming $\phi' \ll \phi^0$, the equation for ϕ' is

$$
\phi'_{zz} - a_0 \phi'_x - b_0 \phi'_{xx} = b_1 (x - x_0) \phi^0_{xx} \tag{5.20}
$$

Taking a Laplace transform of (5.20),

$$
\phi'^*_{zz} - \mu^2 \phi'^* = -b_1 \left[2p\phi^{0^*} + p^2 \frac{d\phi^{0^*}}{dp} + x_0 p^2 \phi^{0^*} \right] \tag{5.21}
$$

A particular solution of (5.21) is

$$
\phi'^*_p = (C_0 z + C_1 z^2) e^{-\mu z} \tag{5.22}
$$

where

$$
\begin{aligned}
C_0 &\equiv b_1 \left[\frac{A}{2\mu} + \frac{B}{4\mu^2} \right]; \qquad C_1 \equiv \frac{b_1}{4\mu} B \\
A &\equiv \frac{-2pw^*}{\mu} + \frac{p^2 w^*}{\mu^3} \frac{[2b_0 p + a_0]}{2} - x_0 \frac{p^2 w^*}{\mu} - \frac{p^2}{\mu} \frac{dw^*}{dp} \\
B &\equiv \frac{p^2 w^*}{\mu^2} \frac{[2b_0 p + a_0]}{2}
\end{aligned}
$$

The homogeneous solution for ϕ' is of the same form as for ϕ^0. After some calculation, applying homogeneous boundary condition to ϕ', we determine

$$
\phi'^*|_{z=0} = \frac{C_0}{\mu} \tag{5.23}
$$

Inverting (5.23) using the definitions of C_0, A, B above, and assuming $w = -U_\infty \alpha$ for simplicity, we have

$$\frac{\phi'}{U_\infty \alpha}|_{z=0} = \frac{b_0^{\frac{1}{2}}}{a_0}\{\, 2e^{-\tilde{x}}\tilde{x}I_1(\tilde{x}) - \left[\frac{d^2}{d\tilde{x}^2} + \frac{d}{d\tilde{x}}\right][e^{-\tilde{x}}\tilde{x}^2 I_2(\tilde{x})] + \frac{\tilde{c}2x_0}{c}e^{-\tilde{x}}\tilde{x}[I_0(\tilde{x}) + I_1(\tilde{x})]\,\}; \qquad \tilde{c} \equiv \frac{a_0 c}{2b_0} \tag{5.24}$$

The pressure coefficient corresponding to ϕ' is given by

$$C_p^0 = C'_{p1} + C'_{p2}$$

where

$$\begin{aligned} \frac{b_0^{\frac{1}{2}} C'_{p1}}{\alpha} &\equiv e^{-\tilde{x}}\{(2I_1 - I_0)(\tilde{x} - \tilde{x}^2) + I_2\tilde{x}^2\} \\ \frac{b_0^{\frac{1}{2}} C'_{p2}}{\alpha} &\equiv \tilde{c}\frac{2x_0}{c}e^{-\tilde{x}}\{2\tilde{x}(I_1 - I_0) + I_0\} \end{aligned} \tag{5.25}$$

As may be seen C'_{p1} is always a small correction to C_p^0; however, C'_{p2} may be large or small (particularly near the leading edge as $\tilde{x} \to 0$) depending on the size of

$$\frac{x_0}{c}\frac{a_0 c}{2b_0}$$

Since we are free to choose x_0 in any application, it is in our interest to choose it so that

$$C'_{p2} \ll C_p^0$$

More will be said of this in the following section.

We note that *higher* terms in the power series for a and b may be included and a solution for ϕ' obtained in a similar manner. The algebra becomes more tedious, of course.

Results and comparisons with other theoretical and experimental data

We have calculated two examples, a Guderley airfoil and a parabolic arc airfoil, both of 6% thickness ratio, τ, and for Mach numbers near one. These were chosen because they have smooth mean steady pressure distributions (at least for some Mach number range) and because other investigators have obtained results for these airfoils. These two airfoils and their mean, steady pressure distributions are shown in [23]. The Guderley airfoil had a linear mean pressure variation while the parabolic arc has a somewhat more complicated variation including a (theoretical) logarithmic singularity at the leading edge. For $M_\infty = 1$, when $C_{p_{ms}} = 0$ the local Mach number along the chord equals one and if one expanded about the point then $b_0 = 0$, and our procedure would fail in that $\phi' \gg \phi^0$. Hence, one is lead to believe that one should

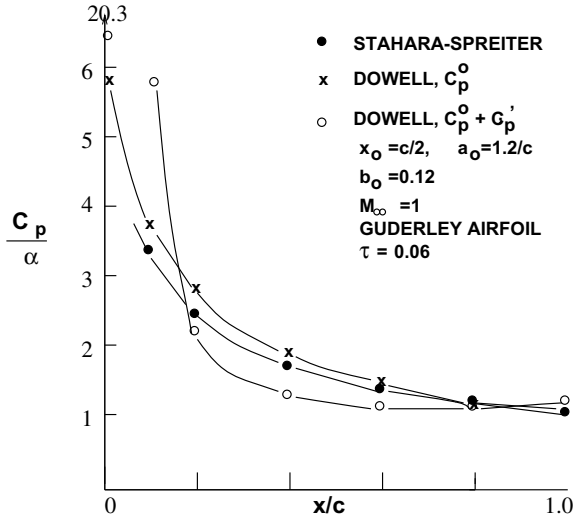

Fig. 18 Pressure distribution for Guderley airfoil at constant angle of attack

choose x_0 as far away from the sonic point, $C_{p_{ms}} \equiv 0$ at $M_\infty \equiv 1$, as possible. To fix this idea more concretely, we first considered the Guderley airfoil. *Guderley airfoil*. We have calculated C_p^0 and $C_p^0 + C_p'$ for $M_\infty = 1$. Two different choices of x_0 were used, $x_0 = c/2$ (Fig. 18) and c (Fig. 19). Results from Stahara and Spreiter [23] are also shown for reference. As can be seen for $x_0 = c/2$, the 'correction' term, C_{p2}', dominates the basic solution, C_p^0, as $x/c \to 0$. For $x_0 = c$, on the other hand, the correction term is much better behaved, in agreement with our earlier speculation about choosing x_0 as far as possible from the sonic point. Note that if, for example, we choose $x_0 = 0$ this would also work in principle, but now $b_0 < 0$, and a 'subsonic' solution would have to be obtained for ϕ^0.

Parabolic arc airfoil. Similar results have been obtained and are displayed in Fig. 20 ($x_0 = c/2$) and Fig. 21 ($x_0 = c_0$). Both of these solutions are well behaved in the sense that $C_p' < C_p^0$, though again the results for $x_0 = c$ appear to be better than those for $x_0 = c/2$. The relatively better behavior of the $x_0 = c/2$ results for the parabolic arc as compared with the Guderley airfoil is probably related to the sonic point being farther ahead of $x_0 = c/2$ for the former than the latter. See [23]. Also shown in Figs. 20 and 21 are the theoretical results of Stahara-Spreiter [23] and the experimental data of Knechtel [35]. Knechtel indicates the effective Mach number of his experiments should be reduced by approximately 0.03 due to wall interface effects. Also he shows that the measured mean steady pressure distributions at zero angle of attack, $C_{p_{ms}}$, agree well with the theoretical results of Spreiter [23, 36] for $M_\infty \geq 1$. However, for $M_\infty \leq 1$, $C_{p_{ms}}$ deviates from that theoretically predicted; see Fig. 22 taken from [35]. The change in slope for $C_{p_{ms}}$ near the trailing edge may be expected to be important for computing the lifting case. In Fig. 23 results are shown for $M_\infty = 0.9$ which dramatically make this point. Shock induced separation of the boundary layers is the probable cause of the difficulty.

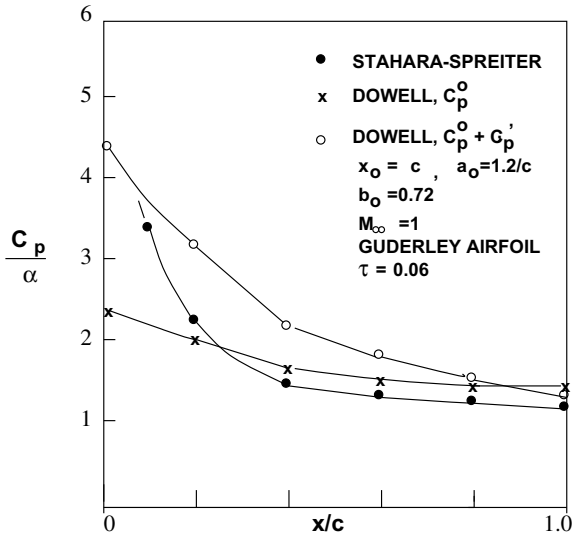

Fig. 19 Pressure distribution for Guderley airfoil at constant angle of attack

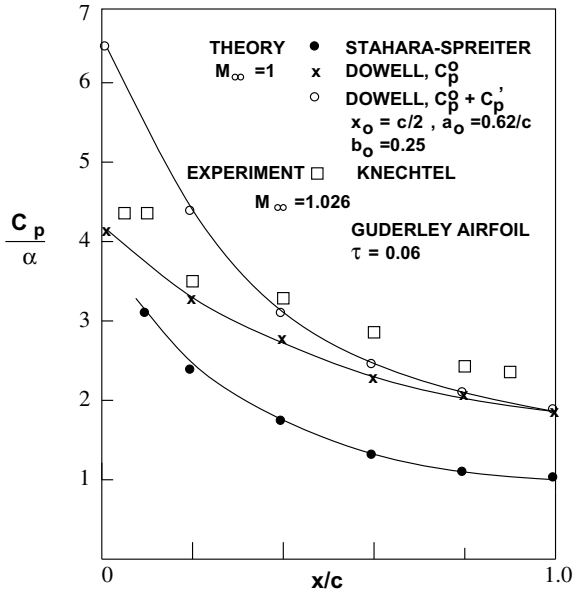

Fig. 20 Pressure distribution for parabolic arc airfoil at constant angle of attack

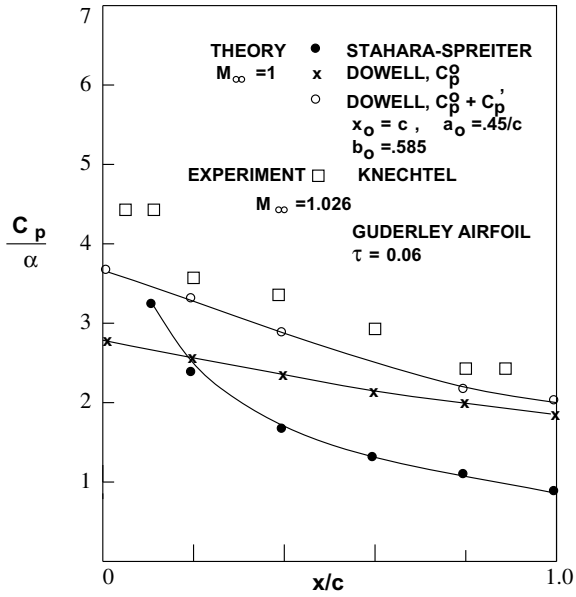

Fig. 21 Pressure distribution for parabolic arc airfoil at constant angle of attack

Finally, we present a graphical summary of lift curve slope and center of pressure for the parabolic arc airfoil comparing results of Knechtel's experimental data and the present analysis. See Fig. 24.

All things considered the agreement between theory and experiment is rather good; however, it is clear that is $C_{p_m s}$ varies in a complicated way one must go beyond the straight line approximation used in obtaining the present result. In principle this can be done; how much effort will be required remains to be determined.

Non-steady airfoil motion in two-dimensional, 'supersonic' $b_0 > 0$ flow

Solutions for ϕ^0. Again taking a Laplace transform with respect to x of (5.8) (for $\phi_{yy} \equiv 0$ and $a = a_0,\ b = b_0$) we obtain

$$\phi^{0^*}_{zz} - \mu^2 \phi^{0^*} = 0 \tag{5.26}$$

where $\mu \equiv [b_0 p^2 + \tilde{a}_0 p - d]^{\frac{1}{2}}$ and b_0 is as before

$$\tilde{a}_0 \equiv a_0 + \frac{2U_\infty}{a_\infty^2} i\omega; \qquad d \equiv \left(\frac{\omega}{a_\infty}\right)^2$$

and we have assumed simple harmonic motion in time. Solving (5.26) subject to the boundary condition, (5.11), and appropriate finiteness and/or radiation condition at infinity we have (after inversion).

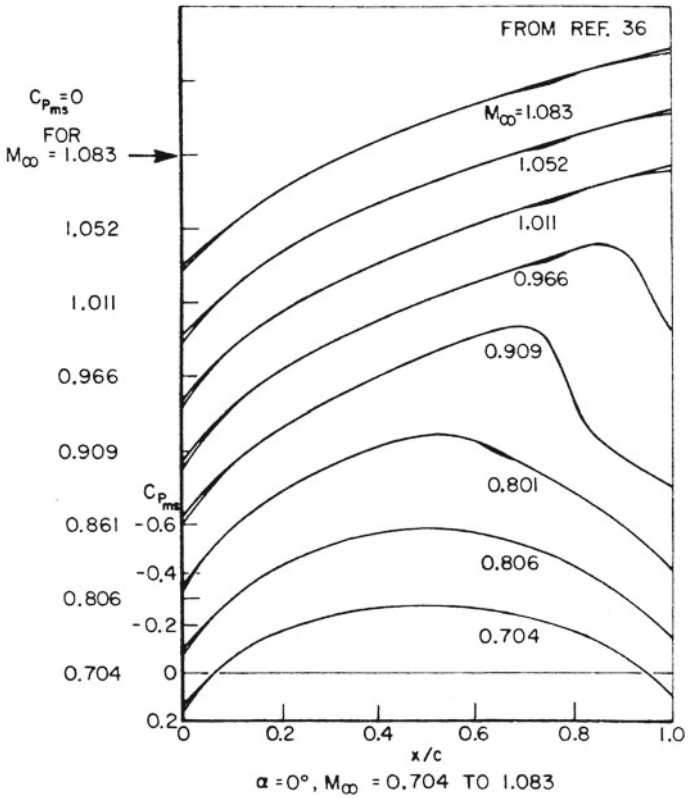

Fig. 22 Representative experimental pressure distribution for 6-percent-thick circular-arc airfoil with roughness elements near the leading edge

$$\phi^0|_{z=0} = -\int_0^x b_0^{-\frac{1}{2}} \exp\left(\frac{-\tilde{a}_0\xi}{2b_0}\right) I_0\left\{\left[\left(\frac{\tilde{a}_0}{2b_0}\right)^2 + \frac{d}{b_0}\right]^{\frac{1}{2}}\xi\right\} w_a(x-\xi)d\xi \tag{5.27}$$

The perturbation pressure on the lower surface is given by

$$p^0 = \rho_\infty[\phi_t^0 + U_\infty\phi_x^0] \tag{5.28}$$

which may be evaluated from (5.27) directly using Leibnitz' rule

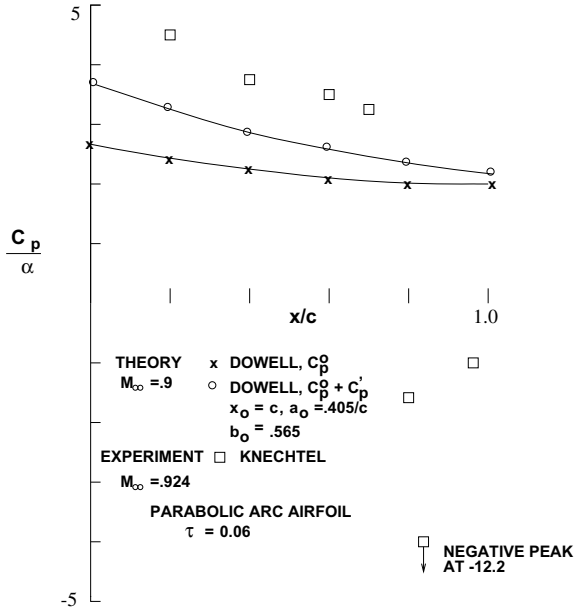

Fig. 23 Pressure distribution for parabolic arc airfoil at constant angle of attack

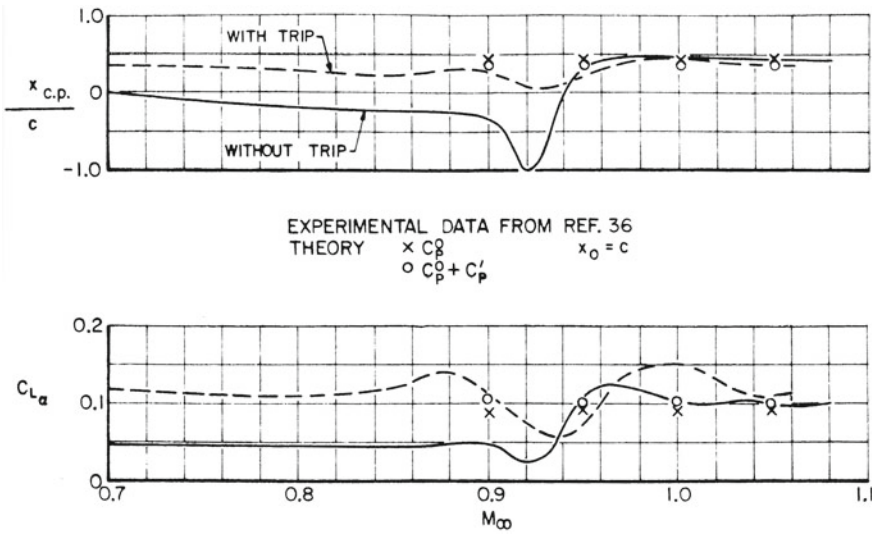

Fig. 24 Effects of boundary-layer trip in the variation with Mach number of lift-curve slope and center pressure of the circular-arc airfoil at $\alpha_o \simeq 0^o$

$$C_p^0 = \frac{p^0}{\frac{\rho_\infty U_\infty^2}{2}} = -2b_0^{-\frac{1}{2}} \left\{ \exp\left(\frac{-\tilde{a}_0 x}{2b_0}\right) I_0 \left[\left(\frac{\tilde{a}_0}{2b_0}\right)^2 + \frac{d}{b} \right]^{\frac{1}{2}} x \right\} \frac{w_a(0)}{U_\infty}$$
$$+ \int_0^x \exp\left(\frac{-\tilde{a}_0 \xi}{2b_0}\right) I_0 \left\{ \left[\left(\frac{\tilde{a}_0}{2b_0}\right)^2 + \frac{d}{b_0} \right]^{\frac{1}{2}} \xi \right\}$$
$$\cdot \left[i\omega \frac{w_a(x-\xi)}{U_\infty^2} + \frac{w_a'(x-\xi)}{U_\infty} \right] d\xi$$

where

$$w_a'(x) \equiv \frac{dw_a}{dx} \tag{5.29}$$

An alternative form for C_p^0 may be obtained by first interchanging the arguments x and $x - \xi$ in (5.27). For $a_0 = 0$, $b_0 \equiv M_\infty^2 - 1$ the above reduces to the classical result. For any a_0 and b_0 and $k \equiv \omega c / U_\infty$ large the results approach those of the classical theory and for $k \to \infty$ approach the 'piston' theory [31]. For the specific case of an airfoil undergoing vertical translation, $w = -h_t$, where h is vertical displacement and the h_t is the corresponding velocity, we have the following results,

$$\phi^0|_{z=0} = h_t b_0^{-\frac{1}{2}} \left[\left(\frac{\tilde{a}_0}{2b_0}\right)^2 + \frac{d}{b_0} \right]^{-\frac{1}{2}} e^{-e\tilde{x}} \tilde{x} \left\{ I_0(\tilde{x}) + \frac{I_1(\tilde{x})}{e} \right\}$$

where

$$\tilde{x} \equiv \left[\left(\frac{\tilde{a}_0}{2b_0}\right)^2 + \frac{d}{b_0} \right]^{\frac{1}{2}} x$$
$$e \equiv \frac{\tilde{a}_0}{2b_0} \left[\left(\frac{\tilde{a}_0}{2b_0}\right)^2 + \frac{d}{b_0} \right]^{-\frac{1}{2}} \tag{5.30}$$

In the limit as $b_0 \to 0$, (corresponding to $M_\infty \to 1$ in the classical theory)

$$\left[\left(\frac{\tilde{a}_0}{2b_0}\right)^2 + \frac{d}{b_0} \right]^{\frac{1}{2}} \to \frac{\tilde{a}_0}{2b_0}; \quad e \to 1$$

and

$$\phi^0|_{z=0} \to h_t 2 \left(\frac{x}{\tilde{a}_0 \pi}\right)^{\frac{1}{2}} \tag{5.31}$$

Using (5.30) or (5.31) in (5.28) gives the perturbation pressure. The latter form is particularly simple

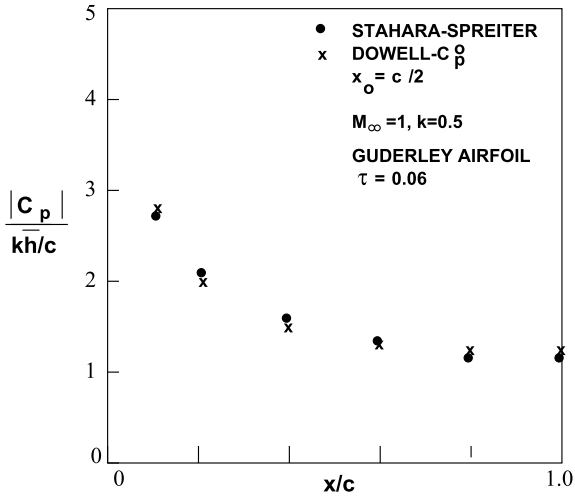

Fig. 25 Pressure distribution for Guderley airfoil oscillating in rigid body translation

$$\frac{C_p}{ik\frac{\bar{h}}{c}e^{i\omega t}} \equiv \frac{p}{\frac{\rho_\infty U_\infty^2}{ik\frac{\bar{h}}{c}e^{i\omega t}}} = (\pi\tilde{a}_0 c)^{-\frac{1}{2}}\left[2(x/c)^{-\frac{1}{2}} + i4k\left(\frac{x}{c}\right)^{\frac{1}{2}}\right] \tag{5.32}$$

where

$$h \equiv \bar{h}e^{i\omega t}; \qquad k \equiv \frac{\omega c}{U_\infty}$$

Solution for ϕ'. Park [37] has computed ϕ' and made comparisons with available experimental and theoretical data. It is well-known, of course, that for sufficiently large k the classical theory itself is accurate transonically [32]. Hence, we also expect the present theory to be more accurate for increasing k.

Results and comparison with other theoretical data

We have calculated a numerical example for the Guderley airfoil for $M = 1$ and $k = 0.5$ in order to compare with the results of Stahara-Spreiter [23]. We have chosen $x_0 = c/2$ for which

$$b_0 = 0.12; \qquad a_0 = 1.2/c$$

For such small b_0, we may use the asymptotic form for $b_0 \to 0$, (5.32), and the results are plotted in Figs. 25 and 26 along with the results of [23].

As $k \to 0$, the phase angle, Φ is a constant at 90° and the pressure coefficient amplitude is the same as that of Fig. 18. Presumably somewhat more accurate results could be obtained by choosing $x_0 = c$ and computing the correction, C_p'. However, the agreement is already good between the present results and those of [23].

As Stahara-Spreiter [23] point out even for k as large as unity there are still substantial quantitative differences between their results (and hence the present results)

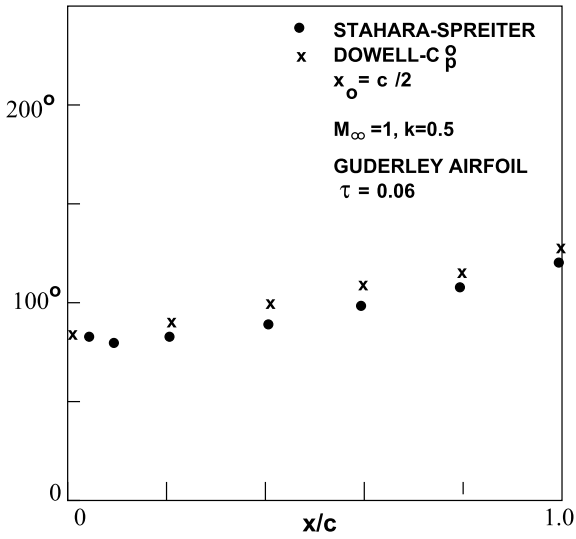

Fig. 26 Pressure-translation phase angle distribution

and those of the classical theory. However, for $k \gg 1$, one may expect the present theory and that of [23] to give results which approach those of the classical theory.

Non-steady airfoil motion in three-dimensional 'supersonic' $(b_0 > 0)$ *flow*

Solution for ϕ^0. We begin with (5.1) and take a Fourier transform with respect to y,

$$\phi^\dagger \equiv \int_{-\infty}^{\infty} \phi e^{-i\gamma y} dy \tag{5.33}$$

and a Laplace transform with respect to x,

$$(\phi^\dagger)^* \equiv \int_0^{\infty} (\phi^\dagger) e^{-px} dx \tag{5.34}$$

Equation (5.1) becomes

$$\phi_{zz}^{0*\dagger} - \mu^2 \phi^{0*\dagger} = 0 \tag{5.35}$$

where

$$\mu \equiv [b_0 p^2 + \tilde{a}_0 p - \tilde{d}]^{\frac{1}{2}}; \qquad b_0, \tilde{a}_0 \quad \text{as before}$$

and

$$\tilde{d} \equiv (\omega/a_\infty)^2 - \gamma^2$$

Solving (5.35) subject to the boundary condition, (5.11), and appropriate boundary finiteness/radiation conditions at infinity we have (after inversion)

$$\phi^0|_{z=0} = \int_0^x \int_{-\infty}^{\infty} A(x-\xi,\ y-\eta)w(\xi,\eta)d\xi\, d\eta \tag{5.36}$$

where

$$A(x,y) = \frac{-\exp\left(\frac{-\tilde{a}_0}{2b_0}x\right)}{\pi} r^{-1} \cosh\left\{\left[\left(\frac{\frac{\omega}{a_\infty}}{b_0}\right)^2 + \left(\frac{\tilde{a}_0}{2b_0}\right)^2\right]^{\frac{1}{2}} r\right\}$$

$$\text{for} \quad r^2 > 0, \quad \text{i.e.}$$

$$0 < |y| < x b_0^{-\frac{1}{2}}$$

$$= 0 \qquad \text{for} \quad r^2 < 0, \quad \text{i.e.}$$

$$x b_0^{-\frac{1}{2}} < |y|$$

and

$$r^2 \equiv x^2 - b_0^2 y^2 \tag{5.37}$$

A is the aerodynamic Green's function required in the Mach Box numerical lifting surface method [31].

For $b_0 \to M_\infty^2 - 1$; $a_0 \to 0$; $\tilde{a}_0 \to 2(i\omega U_\infty/a_\infty^2)$ and A reduces to the classical results. For $b_0 \to 0$, $R_e\tilde{a}_0 > 0$,

$$A \to -\frac{1}{2\pi x} e^{-\tilde{a}_0 y^2/4x} \quad \text{for} \quad x > 0; \quad |y| < \infty \tag{5.38}$$

For $b_0 \to 0$, $R_e\tilde{a}_0 < 0$,

$$A \to -\frac{1}{2\pi x} \exp\left(\frac{-\tilde{a}_0 x}{b_0}\right) \quad \text{for} \quad x > 0; \quad |y| < \infty \tag{5.39}$$

Non-steady airfoil motion in three-dimensional 'subsonic' ($b_0 < 0$) flow

Solution for ϕ^0. We begin with (5.1), assuming simple harmonic motion,

$$-b_0\phi^0_{xx} - \tilde{a}_0\phi^0_x + d\phi^0 + \phi^0_{yy} + \phi^0_{zz} = 0 \tag{5.40}$$

where $\tilde{a}_0$, b_0, d as before.

To put (5.40) in canonical form by eliminating the term ϕ_x, we introduce the new dependent variable, Φ

$$\phi^0 \equiv e^{\Omega x}\Phi \tag{5.41}$$

where Ω is determined to be

$$\Omega = -\tilde{a}_0/2b_0 \tag{5.42}$$

and the equation for Φ is

$$B\Phi_{xx} + \Phi\left[\frac{-\tilde{a}^2}{4B} + d\right] + \Phi_{yy} + \Phi_{zz} = 0 \tag{5.43}$$

and

$$B \equiv -b_0 > 0$$

We further define new independent variables,

$$x' \equiv x, \qquad y' \equiv B^{\frac{1}{2}} y, \qquad z' \equiv B^{\frac{1}{2}} z \tag{5.44}$$

then (5.43) becomes

$$\Phi_{x'x'} + \Phi_{y'y'} + \Phi_{z'z'} + \tilde{k}^2\Phi = 0 \tag{5.45}$$

where

$$\tilde{k}^2 \equiv \left(d - \frac{a^2}{4B}\right)/B$$

We are now in a position to use Green's theorem

$$\iiint [\Phi\nabla^2\psi - \psi\nabla^2\Phi]dV = \iint_s \left[\Phi\frac{\partial\psi}{\partial n} - \psi\frac{\partial\Phi}{\partial n}\right] dS \tag{5.46}$$

V volume enclosing fluid
S surface area of volume indented to pass over airfoil surface and wake
n outward normal.

We take Φ to be the solution we seek and choose ψ as

$$\psi \equiv \left(\frac{e^{-i\tilde{k}r}}{r}\right) \tag{5.47}$$

where

$$r \equiv [(x' - x_1')^2 + (y' - y_1')^2 + (z' - z_1')^2]$$

Note that

$$[\nabla^2 + \tilde{k}^2]\left(\frac{e^{-i\tilde{k}r}}{r}\right) = -4\pi\delta(x' - x_1')\delta(y' - y_1')\delta(z' - z_1') \tag{5.48}$$

Thus the LHS of (5.7) becomes $-4\pi\Phi(x', y', z')$. On the RHS, there is no contribution from the surface area of sphere at infinity. Thus (5.46) becomes

$$4\pi\Phi(x,y,z)=\iint_{S\ \text{airfoil plus wake}}\left[(\Phi_U-\Phi_L)\frac{\partial}{\partial z_1}\left(\frac{e^{-i\tilde{k}r}}{r}\right)-\left(\frac{e^{-i\tilde{k}r}}{r}\right)\frac{\partial}{\partial z_1}(\Phi_U-\Phi_L)\right]dx_1dy_1 \tag{5.49}$$

where

Φ_U, Φ_L upper, lower surface

$\frac{\partial}{\partial n}=\frac{-\partial}{\partial z_1}$ on upper/lower surface and we have returned to the original independent variables, x, y, z and x_1, y_1, z_1. Since Φ is an odd function of z_1, z_1,

$$\frac{\partial}{\partial z_1}(\Phi_U-\Phi_L)=0 \tag{5.50}$$

Also

$$\frac{\partial}{\partial z_1}\left(\frac{e^{-i\tilde{k}r}}{r}\right)=\frac{\partial}{\partial z}\frac{e^{-i\tilde{k}r}}{r}(-1) \tag{5.51}$$

Thus (5.49) becomes, re-introducing the original dependent variable, ϕ^0

$$\phi^0(x,y,z)=\frac{-e^{-\Omega x}}{4\pi}\iint\Delta\phi e^{-\Omega x_1}\frac{\partial}{\partial z}\left\{\frac{e^{-i\tilde{k}r}}{r}\right\}dx_1dy_1 \tag{5.52}$$

where

$$\Delta\phi\equiv\phi_U^0-\phi_L^0$$

Up to this point we have implicitly identified ϕ^0 with the velocity potential. However, *within the approximation*, $a=a_0,\ b=b_0,\ \phi=\phi^0,\ p=p^0, \phi$ and p satisfy the same equation, (5.40); hence, we may use (5.54) with ϕ^0 replaced by p^0. Further using Bernoulli's equation, (5.5), we may relate ϕ^0 to p^0

$$\phi^0(x,y,z)=-\int_{-\infty}^{x}\frac{p^0(\lambda,y,z)}{\rho_\infty U_\infty}\exp\left[\frac{i\omega(\lambda-x)}{U_\infty}\right]d\lambda \tag{5.53}$$

Substituting (5.52) into (5.53) (where (5.52) is now expressed in terms of p^0); introducing a new variable ξ and x_1, y_1; gives

$$\phi^0(x,y,z)=\frac{1}{4\pi}\iint\frac{\Delta p}{\rho_\infty U_\infty}(x_1,y_1)\exp\left[\frac{-i\omega(x-x_1)}{U_\infty}\right]\cdot\left\{\int_{-\infty}^{x-x_1}\exp\left(\frac{[\Omega+i\omega]\xi}{U_\infty}\right)\frac{\partial}{\partial z}\left\{\frac{e^{-i\tilde{k}r}}{r}\right\}d\xi\right\}dx_1\,dy_1 \tag{5.54}$$

Finally, computing from (5.56)

$$w = \frac{\partial \phi}{\partial z}\Big|_{z=0}$$

we obtain

$$\frac{w(x, y)}{U_\infty} = \iint \frac{\Delta p}{\rho_\infty U_\infty^2}(x_1, y_1) K(x - x_1, y - y_1) dx_1\, dy_1 \tag{5.55}$$

where

$$K \equiv \lim_{z \to 0} \frac{\exp\left[\frac{-i\omega(x-x_1)}{U_\infty}\right]}{4\pi} \int_{-\infty}^{x-x_1} \exp\left(\left[\Omega + \frac{i\omega}{U_\infty}\right]\xi\right) \frac{\partial^2}{\partial z^2}\left\{\frac{e^{-i\tilde{k}r}}{r}\right\} d\xi \tag{5.56}$$

and

$$r^2 \equiv [\xi^2 + B(y - y_1)^2]$$

The above derivation, though lengthy, is entirely analogous to the classical one. For $a_0 \to 0$, $B \to 1 - M_\infty^2$ we retrieve the known result [31].

It should be noted that in the above derivation we have assumed $\mathrm{Re}\,\tilde{a}_0 > 0$ and thus $\mathrm{Re}\,\Omega < 0$. This permits both the radiation and finiteness conditions to be satisfied as $z \to \pm\infty$. For $\mathrm{Re}\,\tilde{a}_0 < 0$ one may not satisfy both conditions and one must choose between them.

Asymmetric Mean Flow

In the above derivations we have assumed a mean flow about symmetrical airfoils at zero angle of attack and considered small motions of that configuration. It is of interest to generalize this to a mean flow about asymmetrical airfoils at nonzero angles of attack. First consider the Mach box form of the integral relation between velocity potential and downwash, cf. Eq. (5.36),

$$\phi_U = \iint A_U(x - \xi, y - \eta) w_U(\xi, \eta) d\xi\, d\eta \tag{5.57}$$

Here we have written the relation as though we knew w_U everywhere on $z = 0^+$. We do not, of course, and thus the need for the Mach box procedure [31]. Here A_U is that calculated using upper surface parameters, ignoring the lower surface. A similar relation applies for the lower surface with A_U replaced by $-A_L$. Hence, we may compute from (5.57) (for lifting motions where $w_U = w_L \equiv w$ on and off the airfoil)

$$\phi_U - \phi_L = \iint A(x - \xi, y - \eta) w(\xi, \eta) d\xi\, d\eta \tag{5.58}$$

where

$$A \equiv A_U + A_L$$

is the desired aerodynamic influence function. Note that A_U and A_L are the same basic function, but in one the upper surface parameters are used and in the other the lower surface parameters.

Using the Kernel Function approach the situation is somewhat more complicated. Here we have, cf. Eq. (5.55),

$$w_U = \iint K_U(x-\xi, y-\eta)\, p_U(\xi,\eta) d\xi\, d\eta \tag{5.59}$$

Note $K_U = 2K_{\Delta p}$ where $K_{\Delta p}$ is the Kernel Function for Δp when the lower surface mean flow parameters are the same as those of the upper surface.

A similar equation may be written for w_L and p_L with K_U replaces by $-K_L$. Again we note $w_L = w_U \equiv w$. These two integral equations must be solved simultaneously for p_U and p_L with given w. Hence, the number of unknowns one must deal with is doubled for different upper and lower surface parameters. This poses a substantial addition burden on the numerics. There is a possible simplification, however. Define

$$K \equiv \frac{K_U + K_L}{2}; \quad \Delta K \equiv \frac{K_U - K_L}{2} \tag{5.60}$$

If $(\Delta K/K)^2 \ll 1$, then on may simply use K, i.e., the average of the upper and lower surface kernel functions. Formally, one may demonstrate this using perturbation ideas as follows.

Using (5.59) (and its counterparts for the lower surface) and (5.60) one may compute

$$w_u + w_L \equiv 2w = \iint [K(p_U - p_L) + \Delta K(p_U + p_L)] d\xi\, d\eta$$

and

$$w_u - w_L \equiv 0 = \iint [K(p_U + p_L) + \Delta K(p_U - p_L)] d\xi\, d\eta \tag{5.61}$$

From the second of these equations, the size of the terms may be estimated.

$$\frac{p_U + p_L}{p_U - p_L} \sim 0\left(\frac{\Delta K}{K}\right)$$

Thus in the first of (5.61) the two terms on the right hand side are of order

$$K(p_U - p_L) \quad \text{and} \quad \frac{(\Delta K)^2}{K}(p_U - p_L)$$

The second terms may be neglected if

$$(\Delta K/K)^2 \ll 1 \tag{5.62}$$

and (5.61) may be approximated as

$$w(x, y) \approx \iint \frac{K}{2}(x - \xi, y - \eta)\Delta p(\xi, \eta) d\xi \, d\eta \tag{5.63}$$

where

$$\Delta p \equiv p_U - p_L$$

Equation (5.62) would not appear to be unduly restrictive condition for some applications.

The development in this section is *not* dependent upon the particular method used to compute K_U and/or K_L elsewhere in the text. The crucial assumptions are that (1) the oscillating motion is a small perturbation to the mean flow and (2) the difference between the upper and lower surface Kernel functions is small compared to either.

6 Concluding Remarks

A relatively simple, reasonably accurate and systematic procedure has been developed for transonic flow. A measure of the simplicity of the method is that all numerical results presented herein were computed by hand and analytical forms have been obtained for general 'supersonic' Mach number and airfoil motion for two-dimensional flow. For three-dimensional flow the relevant Green's functions have been determined which may be used in the Kernel Function and Mach Box numerical lifting surface methods.

This approach has been extended to include a more accurate form of Bernoulli's equation and airfoil boundary condition. Also numerical examples are now available for two dimensional airfoils in transient motion and three dimensional steady flow over a delta wing. Finally a simple correction for shock induced flow separationhas been suggested.[31]

For a highly readable survey of transonic flow, the reader should consult the paper by Spreiter and Stahara [39].

Also important advances in finite difference and finite element solutions are discussed in the following papers (all presented at the AIAA Dynamic Specialists Conference, San Diego, March 1977): Chan and Chen [40], Ballhaus and Goorjian [41] and Isogai [42].

In an important, but somewhat, neglected paper Eckhaus [43] gave a transonic flow model including shock waves which considered a constant supersonic Mach number ahead of the shock and a constant subsonic Mach number behind it. An obvious next step is to combine the Eckhaus and Dowell models. M.H. Williams [44] has extended Eckhaus' results by utilizing a somewhat broader theoretical formulation and obtaining more accurate and extensive solutions. He has compared his results

[31] Dowell [38].

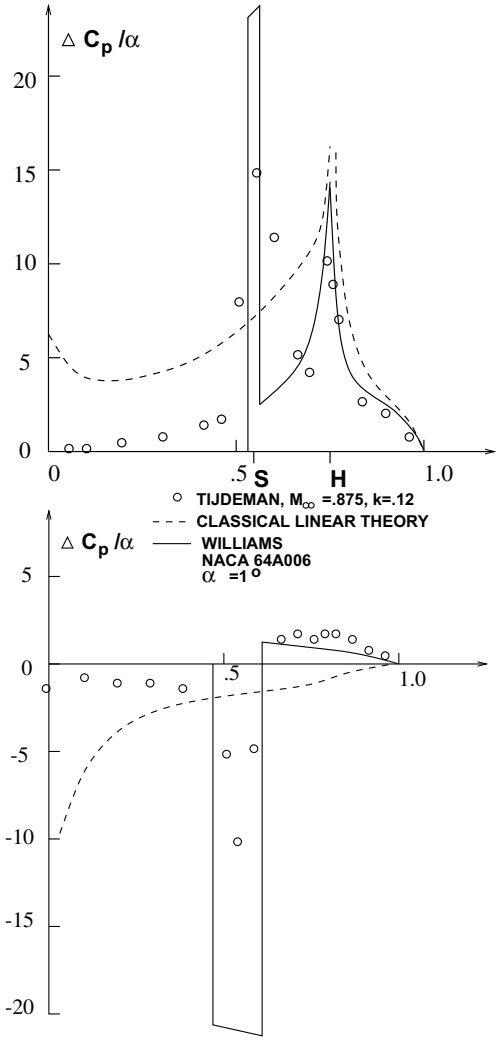

Fig. 27 **a** (top) In phase pressure, and **b** (bottom) out of phase pressure

to those of Tijdeman and Schippers [45] (experiment) and Ballhaus and Goorjian [41] (finite difference solutions) and obtain good agreement. The comparison with experiment is shown here in Fig. 27 for a NACA 64 A006 airfoil with a trailing edge quarter chord oscillating flap. The measured steady state shock strength and location for no flap. The measured steady state shock strength and location for no flap oscillation is used as an input to the theoretical model. Since the flap is downstream of the shock, the theory predicts no disturbance upstream of the shock. The experiment shows the upstream effect is indeed small. Moreover the agreement on the pressure peaks at the shock and at the slap hinge line is most encouraging. It would appear the transonic airfoil problem is finally yielded to a combination of analytical and

numerical methods. As Tijdeman and other have emphasized, however, the effects of the viscous boundary layer may prove significant for some applications. In particular the poorer agreement between theory and experiment for the imaginary pressure peak at the shock in Fig. 27 is probably due to the effects of viscosity. The same theoretical model has also been studied by Goldstein et al. for cascades with very interesting results [46]. Rowe, a major contributor to subsonic aerodynamic solution methods, has in the same spirit discussed how the classical boundary conditions and Bernoulli's equation can be modified to partially account for transonic effects as the airfoil critical mach number is approached [47].

For a broad-ranging survey of unsteady fluid dynamics including a discussion of linear potential theory, transonic flow, unsteady boundary layers, unsteady stall, vortex shedding and the Kutta-Joulowski trailing edge condition the paper by McCroskey [48] is recommended. For a discussion of the fundamentals of computational fluid dynamics of unsteady transonic flow, see chapter "Modeling of Fluid-Structure Interaction".

References

1. Liepmann HW, Roshko A (1957) Elements of gasdynamic. Wiley, New York
2. Hildebrand FB (1961) Advanced calculus for engineers. Prentice-Hall Inc, New York
3. van der Vooren AI (1959) Two-dimensional linearized theory, Vol. II, Chap. 2, AGARD manual on aeroelasticity
4. Lomax H, Heaslet MA, Fuller FB, Sluder L (1952) Two- and three-dimensional unsteady lift problems in high speed flight, NACA Report 1077
5. Landahl MT, Stark VJE (1968) Numerical lifting surface theory - problems and progress. AIAA J 6(11):2049–2060
6. Watkins CE, Runyan HL, Woolston DS (1955) On the kernel function of the integral equation relating the lift and downwash distribution of oscillating wings in subsonic flow, NACA TR-1234
7. Bateman H (1954) Table of integral transforms. McGraw-Hill, New York
8. Authors Many (1970) Oslo AGARD symposium unsteady aerodynamics for aeroelastic analyses of interfering surface, Tønsberg. Oslofjorden, Norway
9. Landahl MT, Ashley H (1959) Thickness and boundary layer effects, Vol. II, Chapter 9, AGARD manual on aeroelasticity
10. Williams DE (1959) Three-dimensional subsonic theor, Vol. II, Chapter 3, AGARD manual on aeroelasticity
11. Albano E, Rodden WP (1969) A doublet-lattice method for calculating life distributions on oscillating surfaces in subsonic flows. AIAA J. 279–285
12. Stratton JA (1941) Electromagnetic theory. McGraw-Hill, New York
13. Watkins CE, Woolston DS, Cunningham HJ (1959) A systematic kernel function procedure for determining aerodynamic forces on oscillating or steady finite wings at subsonic speeds, NASA Technical Report TR-48
14. Williams DE (1961) Some mathematical methods in three-dimensional subsonic flutter derivative theory, Great Britain Aeronautical Research Council, R&M 3302
15. Morino L, Chen LT, Suciu EO (1975) Steady and oscillatory subsonic and supersonic aerodynamics around complex configurations. AIAA J 368–374
16. Rodden WP (1976) State-of-the-Art in unsteady aerodynamics, AGARD Report No. 650

17. Ashley H, Rodden WP (1972) Wing-body aerodynamic interaction. Ann Rev Fluid Mech 4:431–472
18. Theodorsen T (1935) General theory of aerodynamic instability and the mechanism of flutter, NACA Report 496
19. Abramowitz M, Stegun IA (1965) Handbook of Mathematical functions, National Bureau of Standards, U.S. Printing Office
20. Edwards JV, Ashley H, Breakwell JB (1977) Unsteady aerodynamics modeling for arbitrary motions, AIAA Paper 77-451. In: AIAA dynamics specialist conference, San Diego
21. Lomax H (1960) Indicial aerodyamics, vol II, Chap 6, AGARD manual on aeroelasticity
22. Rodden WP, Giesing JP, Kalman TP (1970) New developments and applications of the subsonic doublet-lattice method for non-planar configurations. In: AGARD symposium on unsteady aerodynamics for aeroelastic analyses of interfering surfaces, Tonsberg, Oslofjorden, Norway
23. Stahara SS, Spreiter JR (1973) Development of a nonlinear unsteady transonic flow theory, NASA CR-2258
24. Rubbert P, Landahl M (1967) Solution of the transonic airfoil problem though parametric differentiation. AIAA J 470–479
25. Beam RM, Warming RF (1974) Numerical calculations of two-dimensional, unsteady transonic flows with circulation, NASA TN D-7605
26. Ehlers FE (1974) A finite difference method for the solution of the transonic flow around harmonically oscillating wings, NASA CR-2257
27. Traci RM, Albano ED, Farr JL Jr., Cheng HK (1974) Small disturbance transonic flow about oscillating airfoils, AFFDL-TR-74-37
28. Magnus RJ, Yoshihara H (1975) Calculations of transonic flow over an oscillating airfoil. AIAA Paper 75–98
29. Cunningham AM Jr (1975) Further Developments in the prediction of oscillatory aerodynamics in mixed transonic flow. AIAA Paper 75–99
30. Dowell EH (1975) A simplified theory of oscillating airfoils in transonic flow. In: Proceedings of symposium on unsteady aerodynamics. University of Arizona, pp 655–679
31. Bisplinghoff RL, Ashley H (1961) Principles of aeroelasticity. Wiley, New York
32. Landahl M (1961) Unsteady transonic flow. Pergamon Press, London
33. Spreiter JR (1975) Unsteady transonic aerodynamics-an aeronautics challenge. In: Proceedings of symposium on unsteady aerodynamics. University of Arizona, pp 583–608
34. Ballhaus WF, Magnus R, Yoshihara H (1975) Some examples of unsteady transonic flows over airfoils. In: Proceedings of a symposium on unsteady aerodynamics. University of Arizona, pp 769–792
35. Knechtel ED (1959) xperimental investigation at transonic speeds of pressure distributions over wedge and circular-arc airfoil sections and evaluation of perforated-wall interference, NASA TN D-15
36. Spreiter JR, Alksne AY (1957) thin airfoil theory based on approximate solution of the transonic flow equation, NACA TN 3970
37. Park PH (1976) Unsteady two-dimensional flow using dowell's method. AIAA J 1345–1346. Also see Isogai K (1974) A method for predicting unsteady aerodynamic forces on oscillating wings with thickness in transonic flow near mach number 1, National Aerospace Laboratory Technical Repoirt NAL-TR-368T, Tokyo, Japan, June 1974. Isogai, using a modified local linearization procedure, obtains aerodynamic forces comparable to Park's and these provide significantly better agreement with transonic flutter experiments on parabolic arc airfoils
38. Dowell EH (1977) a simplified theory of oscillating airfoils in transonic flow: review and extension, AIAA Paper 77-445. In: Presented at AIAA dynamic specialist conference, San Diego
39. Spreiter, J. R. and Stahara, S. S. (1976) Developments in Transonic Steady and Unsteady Flow Theory, Tenth Congress of the International Council of the Aeronautical Sciences, Paper No. 76–06
40. Chan STK, Chen HC, Finite element applications to unsteady transonic flow, AIAA Paper 77-446

41. Ballhaus WF, Goorjian PM Computation of unsteady transonic flows by the indicial method, AIAA Paper 77-447
42. Isogai K (1978) Oscillating arifoils using the full potential equation, AIAA Paper 77-448. Also see NASA TP1120
43. Eckhaus W (1962) A theory of transonic aileron buzz, neglecting viscous effects. J Aerosp Sci 712–718
44. Williams MH (1978) Unsteady thin airfoil theory for transonic flow with embedded shocks, Princeton University MAE Report No. 1376
45. Tijdeman H, Schippers P (1973) Results of pressure measurements on an airfoil with oscillating flap in two-dimensional high subsonic and transonic flow, National Aerospace Lab. Report TR 730780, The Netherlands
46. , , , W., and , J. J. () , , Vol. 83, 3 pp. 569-604
47. Rowe WS, Sebastian JD, Redman MC (1976) Recent developments in predicting unsteady airloads caused by control surfaces. J Aircraft 955–963
48. McCroskey WJ (1977) Some current research in unsteady fluid dynamics-the 1976 freeman scholar lecture. J Fluids Eng 8–39

Stall Flutter

Fernando Sisto

Abstract Stall flutter is an inherently nonlinear dynamic aeroelastic phenomena and this chapter presents phenomenological models that provide fundamental insights into this complex topic.

As the name implies, stall flutter is a phenomenon which occurs with partial or complete separation of the flow from the airfoil occurring periodically during the oscillation. In contrast to classical flutter (i.e., flow attached at all times) the mechanism for energy transfer from the airstream to the oscillating airfoil does not rely on elastic and/or aerodynamic coupling between two modes, nor upon a phase lag between a displacement and its aerodynamic reaction. These latter effects are necessary in a linear system to account for an airstream doing positive aerodynamic work on a vibrating wing. The essential feature of stall flutter is the *nonlinear* aerodynamic reaction to the motion of the airfoil/structure. Thus, although coupling and phase lag may alter the results somewhat, the basic instability and its principal features must be explained in terms of nonlinear normal force and moment characteristics.

1 Background

Stall flutter of aircraft wings and empennages is associated with very high angles of attack. Large incidence is necessary to induce separation of the flow from the suction surface. This type of operating condition and vibratory response was observed as long ago as World War I at which time stall flutter occurred during sharp pull-up maneuvers in combat. The surfaces were usually monoplane without a great deal of effective external bracing. The cure was to stiffen the structure and avoid the dangerous maneuvers whenever possible.

Electric power transmission cables of circular cross-section, or as modified by bundling or by ice accretion, etc., and structural shapes of various description are

F. Sisto (✉)
Mechanical Engineering Stevens Institute of Technology, Hoboken, NJ, USA
e-mail: fredsisto46@gmail.com

E. H. Dowell (ed.), *A Modern Course in Aeroelasticity*, Solid Mechanics and Its Applications 264, https://doi.org/10.1007/978-3-030-74236-2_5

classified as bluff bodies. As such they do not require large incidence for flow separation to occur. In fact incidence is chiefly an orientation parameter for these airfoils rather than an indication of the level of steady aerodynamic loading. Again, largely attributable to the nonlinearity in the force and moment as a function of incidence, such structures are prone to stall flutter. These vibrations are sometimes called 'galloping' as in the case of transmission lines. The number and classes of structures that potentially could experience stall flutter are very great, and include such diverse examples as suspension bridges, helicopter rotors and turbomachinery blades. More mundane examples are venetian blind slats and air deflectors or spoilers on automobiles.

The stall flutter of non-airfoil structures is described at greater length in chapter 'Aeroelasticity in Civil Engineering', along with galloping and buffeting. These are all closely related bluff body phenomena from the point of view of vortex method aerodynamics, a subject which is introduced later in the present chapter. The stall flutter of rotorcraft blades is described in greater detail in chapter 'Aeroelastic Response of Rotorcraft' where the special kinematic restraints of these rotating structures lead to a unique aeroelastic description. The stall flutter of turbomachinery blades is described more fully in chapter 'Aeroelasticity in Turbomachines', wherein it is observed that the aeroelastic behavior in stall flutter is distinct from both non-airfoil structures and rotorcraft blades.

When the flow field is measured or visualized during stall flutter oscillations it is observed that free vortices are generated in the vicinity of the separation points. These large vortical structures are shed periodically creating regions of reduced and even reversed velocity in the vicinity of the airfoil. For this reason the aforementioned technique known as the vortex method has been developed recently for the computational modelling of unsteady separation aerodynamics.

It may be shown that the mutual induction, or interaction, of as few as three vortices leads to chaotic behavior. Thus it is confirmed by computation that use of vortex method aerodynamics displays many of the nonlinear aeroelastic phenomena actually observed experimentally in conjunction with stall flutter.

2 Analytical Formulation

Although analysis of stall flutter based on computational unsteady aerodynamics is becoming feasible, it is nevertheless instructive to couch the problem in analytical terms so as to discriminate clearly the actual mechanism of instability [1]. We will consider two important cases: bending and twisting.

In the case of bending, or plunging displacement of a two-dimensional 'typical section' airfoil, let us assume that the force coefficient, including penetration well into the stall regime, is given by a polynomial approximation in α,

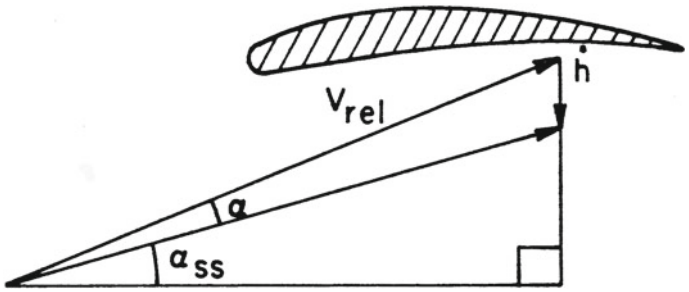

Fig. 1 Velocity triangle

$$-C_n = \sum_{n=0}^{v} a_n(\alpha_{ss})\alpha^n \qquad a_0 \cong -C_{nss}(\alpha_{ss}) \tag{2.1}$$

where α is the instantaneous departure from the steady state value of angle of attack, α_{ss}, attributable to vibration of the airfoil. This method of expressing the normal force characteristic gives a good local fit with a few terms. However, the coefficients, α_n, depend on the mean angle of attack,α_{ss}. Force has been taken to be positive in the same direction as positive displacement h. (In the usual (static) theory of thin unstalled and uncambered profiles $-C_n = \pi \sin 2\alpha_{ss}$. The α_n could then be obtained by deriving the Maclaurin series expansion of $\pi \sin 2(\alpha_{ss} + \alpha)$ considered as a function of α). In general the $-C_n$ function is an empirically determined function, or characteristic, when stall occurs on a cambered airfoil, but the procedure is still the same. The α_n are in fact given by the slope and higher order derivatives according to

$$a_n = -\frac{1}{n!}\frac{d^n C_n}{d\alpha^n}\bigg|_{\alpha=0} \tag{2.2}$$

We next consider a small harmonic bending oscillation

$$h = h_0 \cos \omega t$$

to exist and enquire as to the stability of that motion: Will it amplify or decay?

Under these circumstances, it is possible to interpret the instantaneous angle of attack perturbation to be given by (see Fig. 1)

$$\alpha = \arctan\left(\tan \alpha_{ss} + \frac{\dot{h}}{V \cos \alpha_{ss}}\right) - \alpha_{ss} \tag{2.3}$$

with Maclaurin series expansion in powers of $\dot{h}$ as follows

$$\alpha = \cos\alpha_{ss}\left(\frac{\dot{h}}{V}\right) - \frac{1}{2}\sin 2\alpha_{ss}\left(\frac{\dot{h}}{V}\right)^2 - \frac{1}{3}\cos 3\alpha_{ss}\left(\frac{\dot{h}}{V}\right)^3 + \frac{1}{4}\sin 4\alpha_{ss}\left(\frac{\dot{h}}{V}\right)^4 + \cdots \tag{2.4}$$

It should be noted that this incidence is relative to a coordinate system fixed to the airfoil. The dynamic pressure also changes periodically with time in this coordinate system according to

$$q_{\text{rel}} = \frac{1}{2}\rho V_{\text{rel}}^2 = \frac{1}{2}\rho V^2\left[1 + 2\sin\alpha_{ss}\left(\frac{\dot{h}}{V}\right) + \left(\frac{\dot{h}}{V}\right)^2\right] \tag{2.5}$$

It is assumed for simplicity that the single static characteristic of normal force coefficient versus angle of attack continues to be operative in the dynamic application described above. Thus, the expanded equation for the normal force $N = q(2b)C_n$ is given by

$$N = -\frac{1}{2}\rho V^2(2b)\left[1 + 2\sin\alpha_{ss}\left(\frac{\dot{h}}{V}\right) + \left(\frac{\dot{h}}{V}\right)^2\right]\sum_{n=0}^{v} a_n(\alpha_{ss})\left[\cos\alpha_{ss}\left(\frac{\dot{h}}{V}\right) - \frac{1}{2}\sin 2\alpha_{ss}\left(\frac{\dot{h}}{V}\right)^2 - \frac{1}{3}\cos 3\alpha_{ss}\left(\frac{\dot{h}}{V}\right)^3 + \frac{1}{4}\sin 4\alpha_{ss}\left(\frac{\dot{h}}{V}\right)^4 + \cdots\right]^n \tag{2.6}$$

with

$$\frac{\dot{h}}{V} = -\frac{\omega h_0}{V}\sin\omega t = -k\frac{h_0}{b}\sin\omega t \tag{2.7}$$

A slight concession to the dynamics of stalling may be introduced by the inclusion of a time delay, Ψ/ω, in the oscillatory velocity term appearing in the C_n expansion, i.e., within the summation of (2.6), but not in the development of q_{rel}. The latter is assumed to respond instantaneously to α or $\dot{h}$.

3 Stability and Aerodynamic Work

As is common with single degree of freedom systems such as that postulated above, the question of amplification or subsidence of the amplitude of the initial motion can easily be decided on the basis of the work done by this force acting on the displacement. Thus

$$\text{Work/Cycle} = \int_0^T N\dot{h}\,dt = \frac{1}{\omega}\int_0^{2\pi} N\dot{h}d(\omega t) \tag{3.1}$$

and since the frequency is effectively the number of cycles per unit time, the power may be expressed as

$$\mathbf{P} = \text{Power} = (\text{Work/Cycle})(\text{Cycles/Seconds}) = \frac{1}{2\pi}\int_0^{2\pi} N\dot{h}d(\omega t) \tag{3.2}$$

Using the previous expression for N and $\dot{h}$, it is clear that only even powers of $\sin\omega t$ in the integrand of the power integral will yield nonzero contributions. Also, terms of the form $\sin^n \omega t \cos\omega t$ will integrate to zero for any integer value of n including zero. Restricting the series expansions for $-C_n$ and α to their leading terms such that the power integral displays terms of vibratory amplitude up to the sixth power (i.e., up to h_0^6) results in

$$\mathbf{P} = \frac{1}{2}\rho V^3 b\left[A(\omega h_0/V)^2 + B(\omega h_0/V)^4 + C(\omega h_0\, V)^6 + \cdots\right] \tag{3.3a}$$

where

$$\begin{aligned}
A =& -2a_0 \sin\alpha_{ss} - a_1 \cos\alpha_{ss}\cos\psi \\
B =& -\frac{1}{4}a_1\left[-(\cos\,\alpha_{ss} - \cos 3\alpha_{ss})\left(1 + \frac{1}{2}\cos 2\psi\right)\right. \\
&\left. + (3\cos\alpha_{ss} - \cos 3\alpha_{ss})\cos\psi\right] \\
&-\frac{1}{4}a_2\left[(\sin\,\alpha_{ss} + \sin 3\alpha_{ss})\left(1 - \frac{3}{2}\cos\psi + \frac{1}{2}\cos 2\psi\right)\right] \\
&-\frac{3}{16}a_3\left[(3\cos\,\alpha_{ss} + \cos\,3\alpha_{ss})\cos\psi\right] \\
C =& -\frac{1}{16}a_1\left[(\cos\,3\alpha_{ss} - \cos\,5\alpha_{ss})\left(\frac{3}{2} + \cos 2\psi\right)\right. \\
&\left. -\frac{1}{16}(3\,\cos 3\alpha_{ss} - 2\cos\,5\alpha_{ss})\cos\psi - \frac{1}{3}\cos 3\alpha_{ss}\cos 3\psi\right] - \cdots
\end{aligned} \tag{3.3b}$$

The cubic dependence on V is a consequence of the dimensions of power, or work per unit time.

4 Bending Stall Flutter

The analytical expression for the aerodynamic power in a sinusoidal bending vibration is too cumbersome for easy physical interpretation. However, for very small amplitudes of motion, as might be triggered by turbulence in the fluid, or other 'noise' in the system, it is clear that the sign of the work flow will be governed by

the coefficient of $(\omega h_0/V)^2$. Assuming a small to moderate positive mean incidence, α_{ss}, the coefficient α_0 will be positive. With $\cos\Psi$ near unity, a positive power can only occur if α_1 is sufficiently negative, i.e., if the $-C_n$ versus α characteristic has a negative slope at the static operating incidence. More precisely, if $|\psi| < 90°$ and

$$a_1 < -2a_0 \tan \alpha_{ss} \sec \psi \tag{4.1}$$

the small amplitude vibration is unstable and the work flow will be such as to feed energy into the vibration and increase its amplitude.

In the previous expression for the power, (3.3a),

$$\mathbf{P}/\left(\frac{1}{2}\rho V^3 b\right) = A\,(\omega h_0/V)^2 + B\,(\omega h_0/V)^4 + C\,(\omega h_0/V)^6 \tag{4.2}$$

the coefficients A, B and C are complicated functions of ψ, α_{ss} and the α_n, the coefficients of the power series representation of the normal force characteristic. For example in the highly simplified case of $\alpha_{ss} = \psi = 0$, we obtain

$$A = a_1 = \frac{dC_n}{d\alpha}\bigg|_{\alpha=0}, \qquad B = \frac{1}{2}\frac{dC_n}{d\alpha}\bigg|_{\alpha=0} + \frac{1}{8}\frac{d^3C_n}{d\alpha^3}\bigg|_{\alpha=0}$$

and

$$C = \frac{1}{12}\frac{dC_n}{d\alpha}\bigg|_{\alpha=0} + \frac{1}{192}\frac{d^5C_n}{d\alpha^5}\bigg|_{\alpha=0} \tag{4.3}$$

In the general case A, B and C individually may be either positive, zero or negative. The several possible cases are of fundamental interest in describing possible bending stall flutter behavior. I. $A < 0,\ B < 0,\ C < 0$ No flutter is possible.

II. $A > 0,\ B > 0,\ C > 0$ Flutter amplitude grows from zero to very large values.

III. $A > 0,\ B < 0,\ C < 0$ Flutter amplitude grows smoothly from zero to a finite amplitude given by

$$(\omega h_0/V)^2_{\mathrm{III}} = \left(-|B| + \sqrt{B^2 + 4A|C|}\right)/2|C|$$

At this amplitude the power once again becomes zero.

IV. $A < 0,\ B > 0,\ C > 0$ No flutter at small amplitudes; if an external 'trigger' disturbance carries the system beyond a certain critical vibratory amplitude given by

$$(\omega h_0/V)^2_{\mathrm{IV}} = (-B + \sqrt{B^2 + 4|A|C})/2C$$

the flutter will continue to grow beyond that amplitude up to very large values. At the critical amplitude the power is zero.

V. $A > 0,\ B > 0,\ C < 0$ This is similar to case III except that the finite amplitude, or equilibrium, flutter amplitude

$$(\omega h_0/V)^2_{\mathrm{V}} = (B + \sqrt{B^2 + 4A|C|})/2|C|$$

might be expected to be somewhat larger.

VI. $A > 0,\ B < 0,\ C > 0$ This is similar to case IV except that the critical vibratory amplitude beyond which flutter may be expected to grow

$$(\omega h_0/V)^2_{\mathrm{VI}} = (|B| + \sqrt{B^2 + 4|A|C})/2C$$

is perhaps a larger value.

VII. $A > 0,\ B < 0,\ C > 0$ This case has behavior similar to case II if B is very small and similar to case III if C is very small and also very large amplitudes are excluded from consideration.

VIII. $A < 0.\ B > 0,\ C < 0$ This case behavior is similar to case I if B is very small and similar to case IV if C is very small and also very large amplitudes are excluded from consideration.

5 Nonlinear Mechanics Description

A number of these variations of power dependency on amplitude have been sketched in Fig. 2. Case II is an example of what may be termed 'soft flutter'; given an airstream velocity V, incidence α_{ss} and time delay ψ/ω such as produce values of A, B and C according to case II, the vibratory amplitude of flutter might be expected to grow smoothly from zero.

Cases III and V similarly are examples of soft flutter; in these cases however, the amplitude of vibration reaches a steady value and does not increase further. An equilibrium flutter amplitude is attained after a period of time and maintained thereafter. If, in either of these cases, one were to plot h versus $\dot{h}/\omega$ with time as a

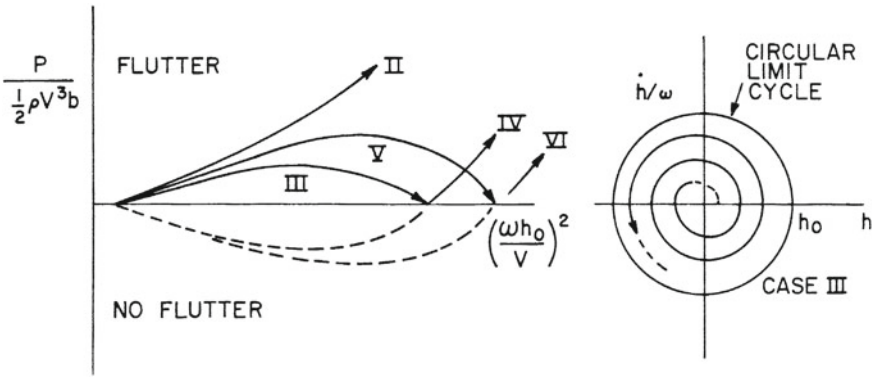

Fig. 2 Power versus amplitude

parameter, it would be found that the 'trajectory' of the 'characteristic point' would be a spiral around the origin, beginning at the origin at $t = 0$ and asymptotically approaching a circle of radius h_0 for very large time. In the parlance of nonlinear mechanics the circular path is a 'limit cycle' and hence most instances of stall flutter may be termed limit cycle vibrations.

Case IV, or alternatively case VI, describes a type of behavior which may be termed 'hard flutter'. In this situation when flutter appears as a self-sustaining oscillation, the amplitude is immediately a large finite value. Here the motion spirals away from the circular limit cycle to either large or smaller amplitudes in the phase plane (i.e., the $h, \dot{h}/\omega$ plane). This example is an instance in which the limit cycle is unstable. The slightest perturbation from an initially pure circular path, either to larger or smaller radii, will result in monotonic spiralling away from the limit cycle. The previous example of case III illustrated the case of a stable limit cycle.

The origin of the phase plane is also a degenerate limit cycle in the sense that the limit of a circle is a point in which case only path radii larger than zero have physical meaning. However, the origin may be an unstable limit cycle (soft flutter) or a stable limit cycle (hard flutter).

It is clear from a consideration of cases VII and VIII that more than two limit cycles may obtain; it is a theorem of mechanics that the concentric circles which are limit cycles of a given system are alternately stable and unstable.

6 Torsional Stall Flutter

With pure twisting motion of the profile, the analytical formulation is more complex stemming from the fact that the dynamic angle of incidence is compounded of two effects: the instantaneous angular displacement and the instantaneous linear velocity in a direction normal to the chord position; the second magnitude is linearly dependent upon the distance along the chord from the elastic axis and upon the frequency of vibration. Both components, of course, vary harmonically with the frequency ω. Thus, assuming a displacement $\theta_0 \cos \omega t$ the 'local' angle of attack becomes

$$\alpha = \theta_0 \cos \omega t + \arctan \left[\tan\, \alpha_{ss} - \frac{(x - x_0)\omega\theta_0}{V \cos\, \alpha_{ss}} \sin\, \omega t \right] - \alpha_{ss} \tag{6.1}$$

and the relative dynamic pressure becomes

$$q_{\text{rel}} = \frac{1}{2}\rho V_{\text{rel}}^2 = \frac{1}{2}\rho V^2 \left[1 + 2 \sin\, \alpha_{ss} \frac{\dot{\theta}(x - x_0)}{V} + \left(\frac{\dot{\theta}(x - x_0)}{V} \right)^2 \right] \tag{6.2}$$

Since the local incidence varies along the chord in the torsional case, it is not possible to formulate the twisting problem in a simple and analogous manner to the bending case unless a single 'typical' incidence is chosen. For incompressible potential flow,

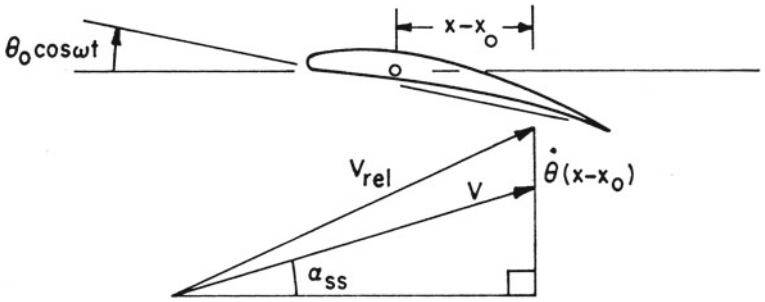

Fig. 3 Geometry

thin airfoil theory, it is known [2] that the three-quarter chord point is 'most representative' in relating changes in incidence to changes in aerodynamic reaction for an unstalled thin airfoil with parabolic camber. Replacing $x - x_0$ by a *constant*, say *eb*, for simplicity, one has by analogy with bending (Fig. 3)

$$\alpha = \theta_0 \cos \omega t + \cos\ \alpha_{ss}(-ek\theta_0) \sin \omega t - \frac{1}{2} \sin 2\alpha_{ss}(-ek\theta_0)^2 \cdot \sin^2 \omega t - \frac{1}{3} \cos 3\alpha_{ss}(-ek\theta_0)^3 \sin^3 \omega t + \frac{1}{4} \cdots \tag{6.3}$$

where α is, again, the departure in angle of attack from α_{ss}. The constant e will normally be of order unity for an elastic axis location forward of midchord.

From this point onward, the illustrative analysis involves the substitution of α into an analytical approximation for the aerodynamic moment coefficient

$$C_m = \sum_{n=0}^{v} b_n(\alpha_{ss})\alpha^n \tag{6.4}$$

In this equation, the b_n may be associated with the slope and higher order derivatives i.e.,

$$b_n = \frac{1}{n!} \frac{d^n C_m}{d\alpha^n} \Big|_{\alpha=0} \tag{6.5}$$

at the mean incidence point, in a manner analogous to the role of the a_n in the normal force coefficient.

The work done by the aerodynamic moment acting on the torsional displacement is given by

$$\text{Work/Cycle} = \int_0^T M\dot{\theta}\, dt = \frac{1}{\omega} \int_0^{2\pi} M\dot{\theta}\, d(\omega t) \tag{6.6}$$

and hence the work flow, or power, is

$$\mathbf{P} = \frac{1}{2\pi}\int_0^{2\pi} M\dot{\theta}d(\omega t) \tag{6.7}$$

Using the previously derived expressions contributing to the moment $M = q(2b)^2 C_m$ leads to

$$\begin{aligned} M =& \frac{1}{2}\rho V^2(2b)^2\left[1 + 2\sin\alpha_{ss}\left(\frac{\dot{\theta}eb}{V}\right) + \left(\frac{\dot{\theta}eb}{V}\right)^2\right] \\ &\cdot \sum_{m=0}^{v} b_n(\alpha_{ss})[\theta_0\cos\omega t - \cos\alpha_{ss}(ek\theta_0)\sin\omega t \\ &-\frac{1}{2}\sin 2\alpha_{ss}(ek\theta_0)^2\sin^2\omega t + \frac{1}{3}\cos 3\alpha_{ss}(ek\theta_0)^3\sin^3\omega t + \cdots\Bigg]^n \end{aligned} \tag{6.8}$$

and this expression, in turn inserted into the integrand of (6.7), will allow an analytical expression to be derived by quadrature.

At this stage in the development of torsional stall flutter, a key difference emerges more clearly when compared to bending stall flutter; a fundamental component of the moment coefficient appears ($b_1\theta_0\cos\omega t$) which is out of phase with the torsional velocity ($\dot{\theta} = -\omega\theta_0\sin\omega t$). Noting that $\dot{\theta}$ is the second factor in the integrand, it is seen that the final integrated expression for the power will have terms similar in nature to the expression derived for the bending case, and in addition may have terms proportional to

$$b_1\theta_0,\ b_2\theta_0^2,\ b_2\theta_0,\ b_3\theta_0^3,\ b_3\theta_0^2,\ \text{etc.},$$

It is not particularly instructive to set out this result in full detail.

However, let us consider briefly the case of very slow oscillations, so that terms proportional to higher powers of the frequency can be ignored. Then

$$\begin{aligned} \mathbf{P} &= -\frac{1}{2}\rho V^2(2b)^2\frac{\omega\theta_0}{2\pi}\sum_{n=0}^{v} b_n\theta_0^n\int_0^{2\pi}\cos^n(\omega t - \psi)\sin\ \omega t\, d(\omega t) \\ &= -\frac{1}{2}\rho V^3(4b)k\sin\psi\sum_{n=\text{odd}}^{v} b_n\theta_0^{n+1}\frac{1\cdot 3\cdot 5\cdots n}{2\cdot 4\cdot 6\cdots(n+1)} \end{aligned} \tag{6.9}$$

We conclude from this equation that the work flow again will be proportional to a sum of terms in even powers of the vibratory amplitude, but in this instance, the low frequency torsional stall flutter is critically dependent on the time lag ψ/ω between the oscillatory motion and the response of the periodic aerodynamic moment.

Torsional stall flutter is thus seen to be a much more complex phenomenon, with a greater dependence on time lag and exhibiting very strong dependence on the location of the elastic axis. For example, if the elastic axis were artificially moved rearward on an airfoil such as to reduce the effective value of the parameter e to zero, the airfoil

flutter behavior would be governed by exactly the same specialization of the analysis as was just termed 'low frequency'. Exactly the same terms would be eliminated from consideration. In qualitative terms one may also conclude that the actual behavior in torsional flutter in the general case (with $e \neq 0$) is some intermediate state between the low frequency behavior (critical dependence on sin ψ) and a type of behavior characteristic of bending stall flutter (critical dependence on the slope of a dynamic characteristic at the mean incidence).

7 General Comments

An interesting by-product of the nonlinear nature of stall flutter is the ability, in principle, to predict the final equilibrium amplitude of the vibration. This is in contradistinction to classical flutter in which only the stability boundary is usually determined. The condition for constant finite flutter amplitude is that the work, or power flow, again be zero. As we have seen this can be discerned when the power equation is set equal to zero; the resulting quadratic equation is solved for the squared flutter amplitude, either $(h_0/b)^2$ or θ_0^2 as the case may be. Since all the a_n or b_n coefficients are functions of α_{ss}, the two types of flutter are displayed in Fig. 4 as *presumed* functions of this parameter. Hard flutter displays a sudden jump to finite amplitude as a critical parameter is varied and a lower 'quench' value of that parameter where the vibration suddenly disappears. The two effects conspire to produce the characteristic hysteresis loop indicated by arrows in Fig. 4.

In summary then, stall flutter is associated with nonlinearity in the aerodynamic characteristic; the phenomenon may occur in a single degree of freedom and the amplitude of vibratory motion will often be limited by the aerodynamic nonlinearities. Although structural material damping has not been considered explicitly, it is clear that since damping is an absorber of energy its presence will serve to limit the flutter amplitudes to smaller values; damping limited amplitudes will obtain when

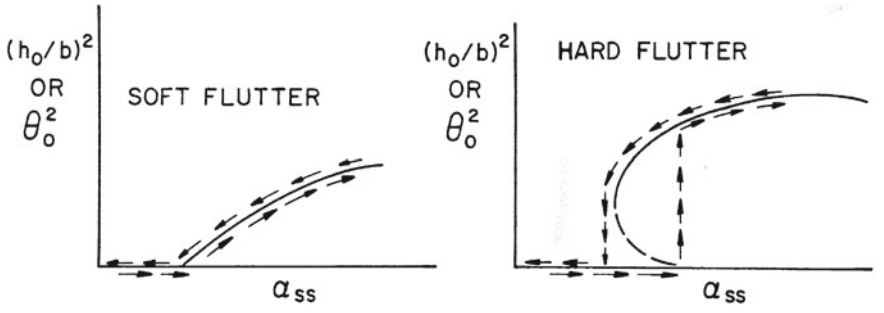

Fig. 4 Flutter amplitude versus steady state angle of attack

the positive power flow from airstream to airfoil equals the power conversion to heat in the mechanical forms of damping.

It is also clear that motion in a third degree of freedom is possible. Oscillatory surging of the airfoil in the chordwise direction can be related to a nonlinear behavior in the drag acting on the profile. However, airfoils are usually very stiff structurally in the chordwise direction and the drag/surging mechanism would normally be of importance only for bluff structural shapes such as bundles of electric power conductors suspended between towers, etc.

Under certain circumstances such as the example noted directly above, stall flutter in more than one degree of freedom may occur. In these cases, the dynamic characteristics of normal force, aerodynamic moment (and drag) become functions of an effective incidence compounded of many sources: plunging velocity, torsional displacement, torsional velocity and surging velocity. The resultant power equation will also contain cross-product terms in the various displacement amplitudes, and hence the equation cannot be used to predict stability or equilibrium flutter amplitudes without additional information concerning the vibration modes.

Perhaps the greatest deficiency in the theory, however, is the fact that even in pure bending motion or pure torsional motion, the dynamic force and moment are in fact frequency dependent: $a_n = a_n(\alpha_{ss}, k)$ and $b_n = b_n(\alpha_{ss}, k)$. And in general $a_0 \neq -C_{nss}$ and $b_0 \neq -C_{mss}$. In analogy with classical flutter it may be shown that even this dependence is deficient in that the characteristics in practice may be double valued. That is, for the same value of effective incidence α, the characteristic may have different values depending upon whether α is decreasing or increasing with time. Such a hysteretic characteristic is usually more pronounced at high frequencies of oscillation; an airfoil may have two lift or moment coefficients at a particular angle of attack even in the static case, depending upon how the operating point was approached.

It is for these reasons that practical stall flutter prediction has been at best a semi-empirical process, and often entirely empirical. A model is oscillated in torsion, or bending, in a wind tunnel under controlled conditions with parametric variation of reduced frequency, mean incidence and oscillatory amplitude. Various elastic axis locations also may be studied. Data which are taken may vary from instantaneous normal force and moment down to the actual time-dependent pressure distribution on the profile. Data reduction consists essentially of cross-plotting the various data so that flutter prediction for prototype application is largely a matter of interpolation in model data using dimensionless groups. Specific representative data will be taken up in subsequent chapters where stall flutter applications are studied.

An exception to the previous reliance on experimental data is a theory [3] which postulates that the departure of the normal force and/or aerodynamic moment from the classical (attached flow) values can be modelled by considering a flat plate with separated flow on the suction side. As the plate oscillates harmonically in time, the position of the separation point (from which emanates a free streamline) is also considered to move periodically with the same frequency as the oscillation. The movement of the separation point along the suction surface is between two arbitrarily

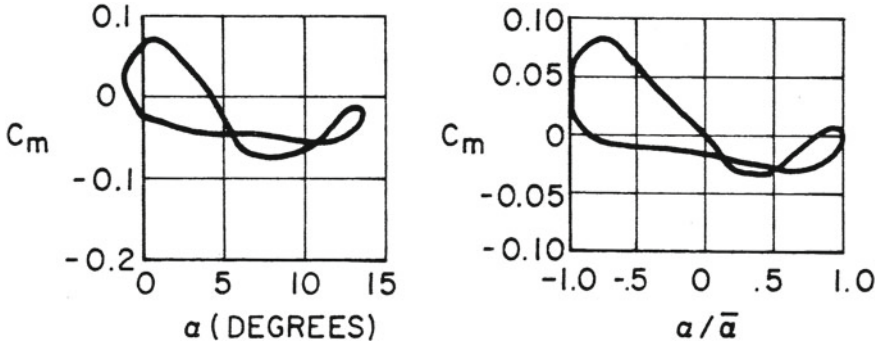

Fig. 5 Dynamic moment loops

specified upstream and downstream limits and with an arbitrarily specified phase angle with respect to the oscillatory motion.

Under these circumstances, it is possible to solve the unsteady flow problem (analogous to the classical Theodorsen solution for attached flow) with separation present. In effect the appropriate dynamic force and moment characteristics are generated for each function specifying the separation point movement and airfoil motion. The empirical part of the flutter prediction technique then resides in correlation of the separation point behavior as a function of the airfoil attitude and oscillatory motion. To illustrate the potential of the technique, two moment loops from the reference are shown in Fig. 5. The one on the left is from an experimental program [4], the one on the right is from [3]. Although the variation of moment with torsional displacement is remarkably similar, it must be emphasized that the particular choice of elastic axis location is different in experiment and theory, and the assumed separation point behavior in the theory was reasonable, but quite arbitrary and unrelated to the unknown separation point behavior in the experiment.

The method of modelling the separation region on the suction surface of the airfoil by a free streamline issuing from the 'separation' point has been generalized subsequently [5]. The method employs simultaneous integral equations and may be applied to subsonic, small perturbation flows of aeroelastic significance. In particular, for cascades of airfoils of interest in axial-flow compressors [6], the method has shown promise of improved stall flutter prediction. A type of stall resulting in a leading edge 'bubble' is also amenable to this type of small perturbation analysis [7] and is more appropriate for sharp leading edges with onset flows that result in reattachment of the separation streamline.

These free-streamline methods are useful when the reattachment point and/or separation point behavior can be predicted beforehand and the mean incidence is not excessive. An example is the thin airfoil with small leading edge radius at moderate incidence where the separation point is 'anchored' at the leading edge and reattachment does not occur.

8 Reduced Order Models

As noted in chapter 'Nonlinear Aeroelasticity', Nonlinear Aeroelasticity, reduced order models have been developed to help account for the effect of airfoil vibratory displacement, velocity and acceleration on the associated aerodynamic responses. Since the theoretical underpinning for these models is not firmly established for conditions of massive flow separation, the characteristics must be developed by model fitting from experimental data. For this reason these models have also been termed "semi-empirical".

In fact, a low order model is the quasisteady development presented in Sect. 2 for the nonlinear normal force and moment characteristics. The linear quasisteady development in chapter 'Dynamic Aeroelasticity' is another low order model. The steady flow aerodynamics example of that same chapter is of course the model of lowest possible order.

Reduced order modelling for stall flutter and bluff body aeroelasticity has been studied by a number of investigators. Some of these studies are described in chapter 'Nonlinear Aeroelasticity' and references to much of the recent literature may be found there. One important and representative study is that by Tang and Dowell [16] in which many of the characteristics attributable to aerodynamic nonlinearities appear. Example are the asymptotic approach to limit cycles and the development of chaotic pitch displacement and moment coefficient histories for particular values of the advance ratio.

9 Computational Stalled Flow

In recent years the so-called vortex method has begun to be used to model periodically separated flow from bluff bodies [8, 9] as well as streamlined shapes [10] such as airfoils. The vortex method is essentially a computational algorithm which tracks a large collection of discrete vortices in time. Since it is a time-marching procedure, the aerodynamic reactions are obtained with an evolving flow and the aeroelastic response of the structure must evolve in like manner. Hence stability of a specific structure oriented in a specific flow cannot be discriminated ab initio. The aeroelastic vibration develops in the course of time; hence the method might equally be termed computational fluid elasticity (CFE). The power of the method may be appreciated when it is realized that highly nonlinear aerodynamics (and structure as well) may be modelled and finite amplitudes of the flutter vibration may be predicted. The cost of computation is high since fairly long runs on supercomputers are required for acceptable accuracy.

The vortex method for modelling unsteady separated flow as initiated in [10] and modified in [11, 12] for oscillating airfoils, is based upon the following fluid dynamic system of equations.

For two-dimensional, viscous, incompressible flow past an infinite linear cascade of airfoils at high Reynolds number, the basic aerodynamic equations that govern the vorticity field derived in [8] are as follows. (For a single airfoil the formulation may be simplified from what is shown here).

Conservation of vorticity in the fluid requires

$$\frac{D\omega}{Dt} = v\nabla^2\omega \tag{9.1}$$

where the vorticity in the fluid field is

$$\omega = \frac{\partial v}{\partial x} - \frac{\partial u}{\partial y} \tag{9.2}$$

Vorticity within the solid is a continuation of the fluid field and represents the motion (vibration) of the solid

$$\omega = 2\Omega_m \tag{9.3}$$

The boundary conditions in terms of vorticity can be written as [8]

$$\oint \left(v\frac{\partial \omega}{\partial n} \right) ds = -2R_m \frac{d\Omega_m}{dt} \tag{9.4}$$

The system of equations governing the vorticity and the system governing the velocity and pressure are equivalent. A stream function ψ can be defined to satisfy the continuity equation

$$u = \frac{-\partial \psi}{\partial y} \quad \text{and} \quad v = \frac{\partial \psi}{\partial x} \tag{9.5}$$

Combining (9.2) and (9.5) results in the Poisson equation

$$\nabla^2\psi = \omega \tag{9.6}$$

The vortex method represents the vorticity field as the sum of a large number (N) of vortex blobs

$$\omega = \sum_{k-1}^{N} \omega_k \tag{9.7}$$

and the stream function induced by a collection of vortices is $\Sigma\psi_k$, where

$$\psi_k = (\Gamma_k/4\pi) ln|\sin[(2\pi/p)(z - z_k)]|^2 \tag{9.8}$$

Here $i = \sqrt{-1}$ and the complex variable notation $z = x + iy$ is used.

The instantaneous coordinates of the mth airfoil surface $[x(t), y(t)]$ under coupled bending-torsion with a frequency of f Hertz are given by

$$x(t) = x_0 - h\sin(2\pi\, ft + \mu + m\sigma)\sin\beta - y_0\,\theta\sin(2\pi\, ft + m\sigma) \tag{9.9a}$$

$$y(t) = y_0 + h\sin(2\pi\, ft + \mu + m\sigma)\cos\beta + x_0\,\theta\sin(2\pi\, ft + m\sigma) \tag{9.9b}$$

where (x_0, y_0) are coordinates for each airfoil without vibration and are measured from its centroid, assumed here for simplicity to coincide with the center of twist. The quantity μ refers to the intrablade phase angle which is the phase difference between the bending and torsional modes. On the other hand, the interblade phase angle, σ, represents the phase shift between neighboring blades. To obtain the corresponding boundary conditions, the nonpenetration condition is imposed as expressed by (1.32).

With the definition of the stream function $\partial\psi/\partial s = V_n$ where s and n are local coordinates parallel and normal to the wall, respectively, the incremental value of stream function along each airfoil surface can be determined by

$$d\psi|_s = \int_{s_0}^{s_0+\Delta s} V_n ds = \int_{s_0}^{s_0+\Delta s} (\dot{x}_b n_x + \dot{y}_b n_y) ds \tag{9.10}$$

This equation is used to determine the distribution of the values of the stream function along the boundary points of the airfoils, and then to solve the vorticity-stream function equations. As a consequence of the airfoil motion the values of the stream function are not constant along the boundary of the airfoil. It should also be mentioned that the no-slip condition reflecting the nonzero viscosity of the fluid is satisfied in a weak sense, as discussed in [8].

Computations based on this system of equations have shown [12] that the two-dimensional unsteady flow, as exemplified in a linear cascade of oscillating airfoils, is properly predicted for a range of reduced frequencies at low incidence. Results similar to those derivable analytically by the methods of Sect. 3 in chapter 'Nonsteady Aerodynamics of Lifting and Non-lifting Surfaces', and also in chapter 'Aeroelasticity in Turbomachines' for cascades, are confirmed by these computational procedures. With this validation in hand it is possible then to consider larger values of the mean incidence until stall is encountered, and compute the aerodynamic response under intermittent separation, and finally, under complete or 'deep' stall. The rapid change in amplitude and phase for lift due to plunging motion as the mean incidence is increased in steps is shown in the following table, along with streamline pattern at one instant for the highest incidence case, Fig. 6.

The presence of strong vortices in the flow illustrates an important stability modification mechanism present in stalled flow. These coherent structures are subject to a nonlinear eigenfunction/eigenfrequency interpretation associated entirely with the flow. A completely rigid airfoil (cascade of airfoils) is (are) subject to a flow instability identified as Karman vortex shedding [13] (propagating stall phenomenon). This unsteady periodic behavior has a characteristic frequency and the associated flow

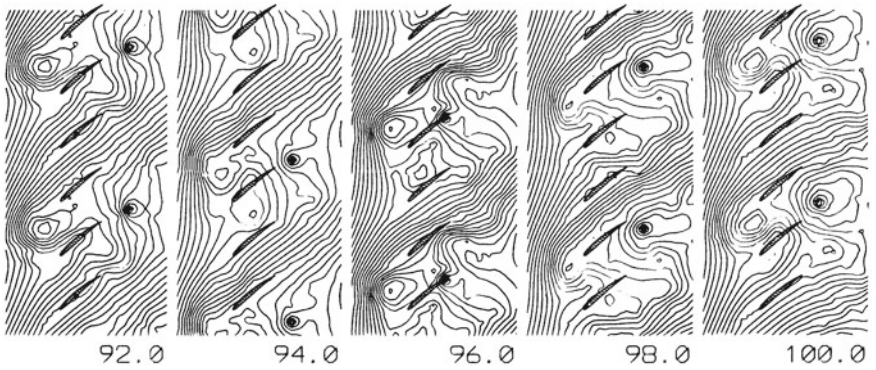

Fig. 6 Streamline pattern at several instants for bending vibrations in stall

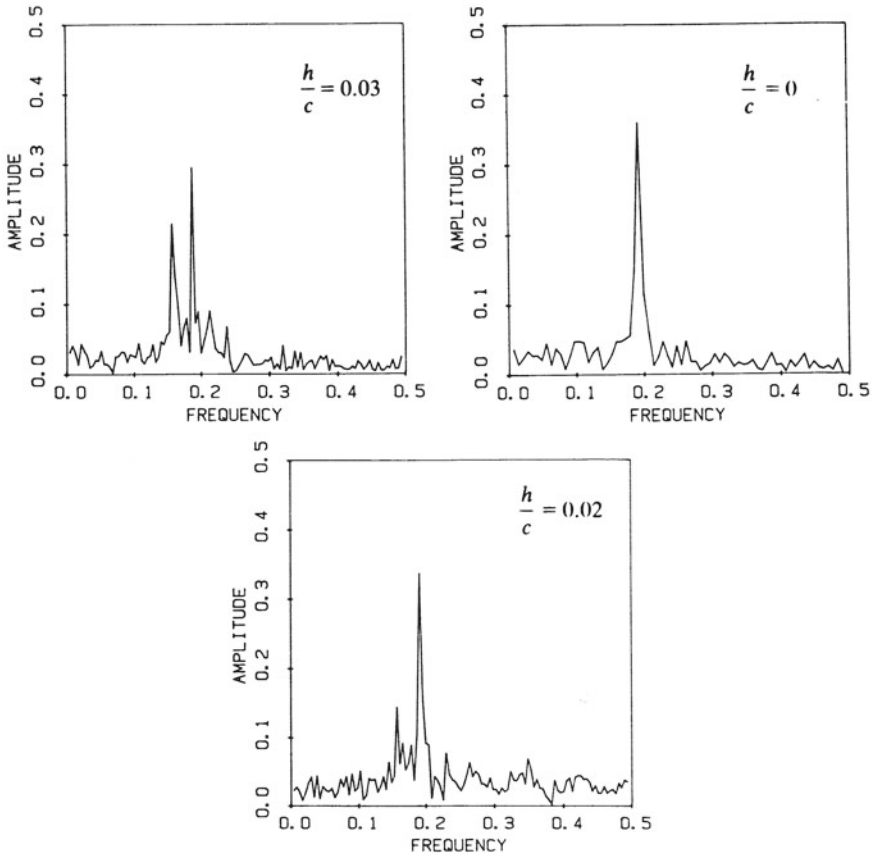

Fig. 7 Effect of vibration amplitude on lift amplitude and frequency

patten is in the guise of an eigenfunction. Thus stall flutter, in a modern interpretation, may be thought of as the aeroelastic coupling of fluid and structure through the vortex shedding and convection mechanism. If an airfoil natural frequency lies close to a natural frequency of the flow instability (either Karman vortex or propagating stall), the vibration of the blade can 'entrain' the stall frequency, resulting in the shift from a forced excitation at the 'stall natural frequency' to a self-excitation at the flutter frequency. This duality of frequencies may be observed in the lift response spectrum during the first few instants of the prescribed motion, Fig. 7, for several bending amplitudes.

In this figure two distinct frequencies are evident, one associated with the propagating stall that would be present in the absence of any vibration, and the other at the same frequency as the impressed vibration. At a later time the propagating frequency has shifted and is essentially equal to the vibration frequency (which is always taken to include the effect of apparent mass). Frequency synchronization has taken place.

Results of this nature have led to further modelling and computation with the conclusion that stall flutter can be predicted by a computational algorithm in which the airfoil motion is not prescribed beforehand. In [14, 15] the vortex method aerody-

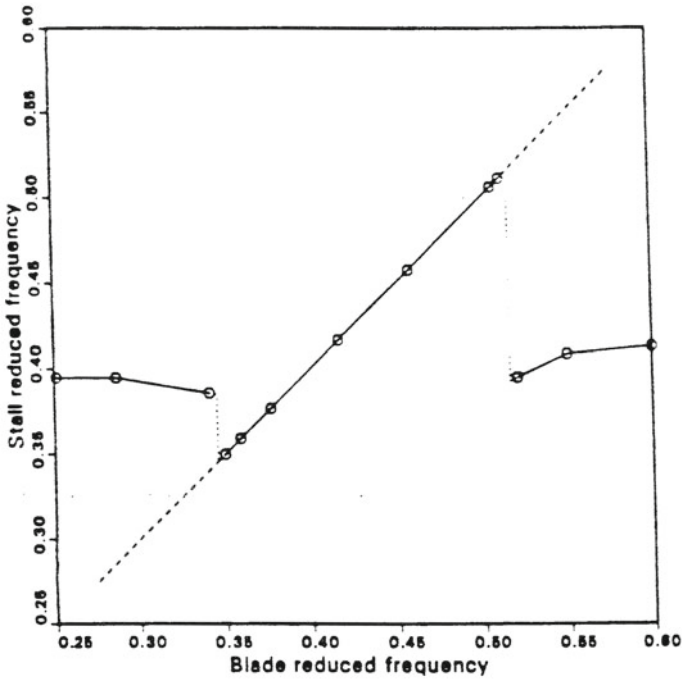

Fig. 8 Influence of blade-reduced frequency on the stall-reduced frequency for a cascade in torsional vibration. The plot shows the entrainment of stall frequency on a certain interval of blade frequency

namic subprogram is executed in parallel and interactively with a structural dynamics subprogram, the entire computation being carried forward in a time marching fashion.

Figure 8 from [14] is a computational confirmation of the frequency entrainment phenomenon previously hypothesized to occur for free vibrations. The temporal evolution of the streamline pattern and the accompanying blade vibratory motion for one datum point of Fig. 8 is shown in Fig. 9. The propagating stall frequency of a cascade of blade s with fixed geometry and onset flow is seen to be relatively unaffected by the presence of flexible blades except in the neighborhood of those blades having natural frequency near the intrinsic stall frequency. Within the interval of entrainment, however, the stall frequency is physically modified so as to synchronize with the blade

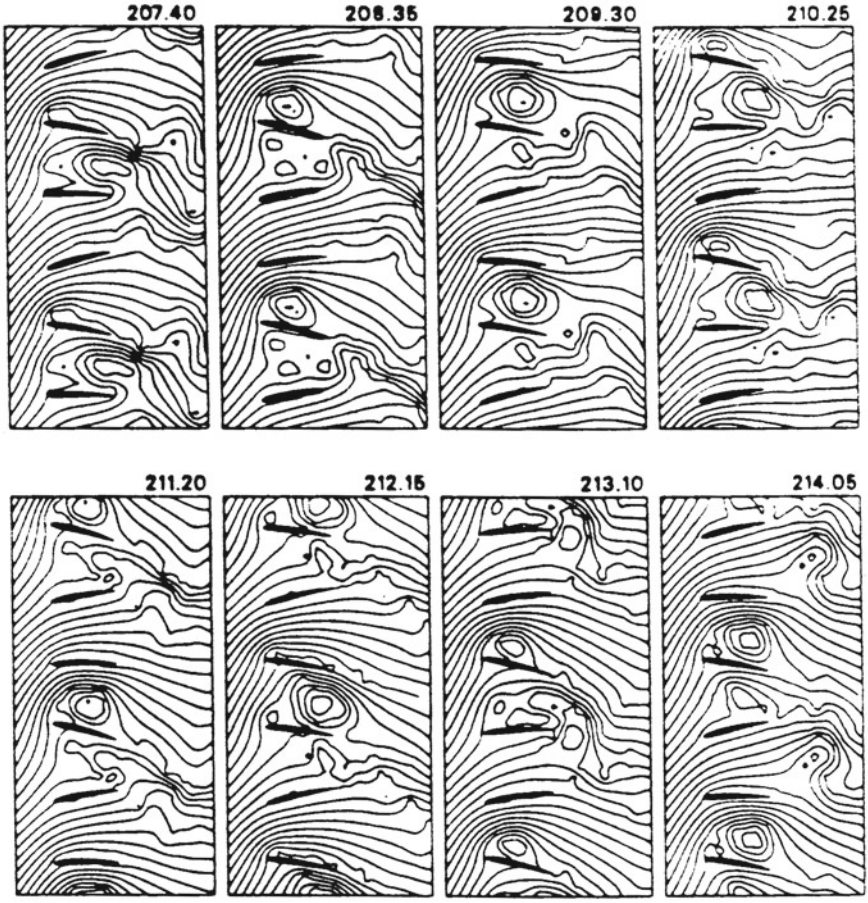

Fig. 9 Instantaneous streamline pattern for a cascade in torsional vibration at different time levels over a single period of oscillation (Cascade periodicity is three; stagger = 0 deg., inflow angle = 55 deg., blade natural frequency in vacuum = 0.13Hz, and the corresponding reduced frequency = 0.408.)

natural frequency. Within the entrainment interval stall flutter may be said to occur. In chapter 'Aeroelasticity in Civil Engineering' the synchronization phenomenon as applied to bluff bodies is discussed in greater detail. Further studies are underway to define the interval of synchronization as a function of the governing aeroelastic parameters and to further define the stall flutter behavior within this interval.

The vortex method possesses inherent limitations which are related to the two-dimensionality of the assumed flow and the necessity for a separation criterion embedded in a boundary layer subroutine. These limitations would be removed with the alternative development of Navier–Stokes solvers for full three-dimensional, unsteady, compressible flows. The principal difficulty to be overcome is the provision of an accurate turbulence model that will result in the necessary resolution of the scale of turbulence for typical cascade geometry. And the much greater number of computations required for this computational model, stemming from the multiplicity of blade passages, makes the forthcoming increase in computational speed a necessary adjunct. Supercomputers, probably involving parallel processing, are a necessity for reliable large scale Navier–Stokes solutions.

References

1. Sisto F (1953) Stall flutter in cascades. J Aeron Sci 20(9):598–604
2. Durand WF (Ed) (1963) Aerodynamic theory, Sec E, vol II. Dover Publications, New York
3. Sisto F, Perumal PVK (1974) Lift and moment prediction for an oscillating airfoil with a moving separation point. Trans ASME J Eng. Power Series A 96(4):372–378
4. Gray Lewis, Liiva J (1969) Wind tunnel tests of thin airfoils oscillating near stall, vol. USAAVLABS Technical Report II, 68-89B
5. Chi MR (1980) Unsteady aerodynamics in stalled cascade and stall flutter prediction. ASME Paper 80–C2/Aero-1
6. Chi RM, Srinavasan AV (1984) Some recent advances in the understanding and prediction of turbomachine subsonic stall flutter, ASME Paper 84-GT-151
7. Tokel H, Sisto F (1978) Dynamic stall of an airfoil with leading edge bubble separation involving time-dependent reattachment, ASME Paper 78-GT-94
8. Spalart PR (1983) Numerical simulation of separated flows, NASA-TM-84238
9. Lewis RI, Porterhouse DTC (1982) A generalized numerical method for bluff body stalling aerofoil flow, ASME Paper 82-GT-70
10. Spalart PR (1984) Two recent extensions of the vortex method, AIAA Paper No. 84-0343, Reno
11. Speziale CG, Sisto F, Jonnavithula S (1986) Vortex simulation of propagating stall in a linear cascade of airfoils. J Fluids Eng 108:304
12. Sisto F, Wu W, Thangam S, Jonnavithula S (1989) Computational aerodynamics of oscillating cascades with the evolution of stall. AIAA J 27(4):462–471
13. Fung YC (1955) Introduction to the theory of aeroelasticity. Wiley, New York
14. Sisto F, Thangam S, Abdelrahim A (1991) Computational prediction of stall flutter in cascaded airfoils. AIAA J 29(7):1161–1167
15. Sisto F, Thangam S, Abdelrahim A (1993) Computational study of stall flutter in linear cascades. ASME J Turbomach 115(1)
16. Tang DM, Dowell EH (1992) Chaotic stall response of helicopter rotor in forward flight. J Fluids Struct 6(6):311–335
17. Ekaterinaris JA, Platzer MF (1994) Numerical investigation of stall flutter, ASME Paper No. 94-GT-206

Aeroelasticity in Civil Engineering

Emil Simiu

Abstract Fluid-structure interaction occurs in civil engineering applications to flexible long span bridges and tall slender buildings. This chapter provides an authoritative account of current best practices and modeling methods.

Certain types of civil engineering structures can be subjected to aerodynamic forces generated by structural motions. These motions, called self-excited, are in turn affected by the aerodynamic forces they generate. Behavior associated with self-excited motions is called aeroelastic. The flutter of the Brighton Chain Pier Bridge (Fig. 1) and, more than one century later, the original Tacoma-Narrows Bridge (Fig. 2) are notorious examples of aeroelastic behavior. Tall chimneys and buildings may also respond aeroelastically and need to be designed accordingly. The John Hancock building in Boston, which has a relatively flat shape in plan (Fig. 3), has experienced across-wind and torsional motions of sufficient severity to warrant the installation of a large tuned-mass damper system at its top. These motions may have been due to aeroelastic effects.[1] Under certain conditions power lines experience aeroelastic behavior referred to as galloping.

Aeroelastic phenomena of interest in civil engineering differ from those studied in aeronautical engineering in two important ways. First, civil engineering structures are typically *bluff*, although in modern suspended-span[2] bridge design streamlined box-like deck shapes are increasingly being used. Second, unlike flows typically considered in aeronautical engineering, the flows in which civil engineering structures are immersed are in most cases *turbulent*. Atmospheric turbulence depends upon the thermal stratification of the flow. At very high wind speeds mechanical turbulence is dominant and the air flow may therefore be assumed to be neutrally stratified.

[1] Recent research on tall buildings with relatively large ratio between depth and width suggests that this was indeed the case—see Sect. 2.2.2. To the writers' knowledge, for legal or other reasons, detailed technical reports on the wind-induced behavior of the John Hancock building are not available in the public domain.

[2] The term "suspended-span bridge" covers both suspension bridges and cable-stayed bridges.

E. Simiu (✉)
National Institute for Standards and Technology, Gaithersburg, MD, USA
e-mail: emil.simiu@nist.gov; simiue@aol.com

E. H. Dowell (ed.), *A Modern Course in Aeroelasticity*, Solid Mechanics and Its Applications 264, https://doi.org/10.1007/978-3-030-74236-2_6

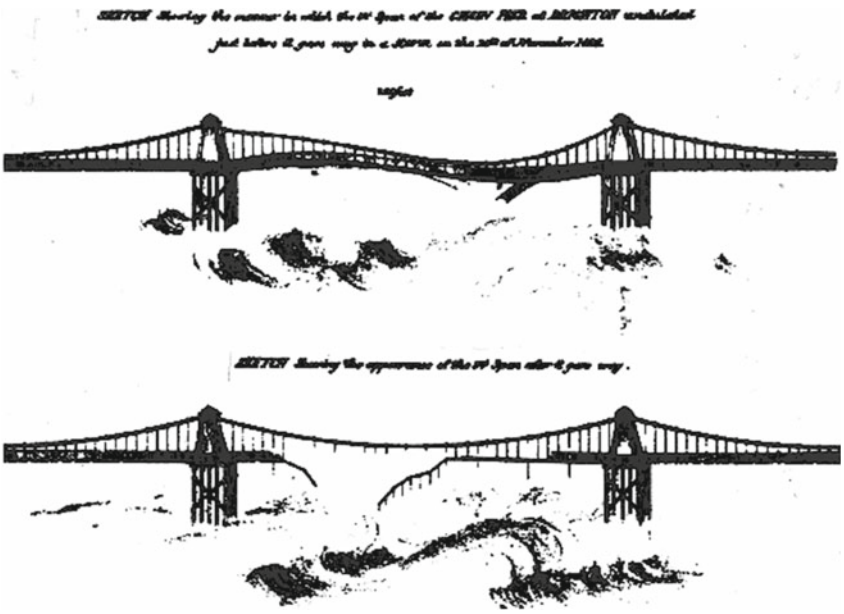

Fig. 1 Brighton Chain Pier Bridge failure, Nov. 29, 1836, as sketched by W. Reed. From J.S. Russell (1841) On the Vibration of Suspension Bridges and Other Structures, and the Means of Preventing Injury from this cause. Trans. Royal Scottish Soc. Arts, quoted in [113]

Standard atmospheric models commonly used in wind engineering are applicable in this case. However, atmospheric flows are not necessarily neutrally stratified—even at relatively high wind speeds. The actual flow turbulence may therefore differ substantially from, and in some cases be considerably weaker than, the turbulence inherent in standard models.

To estimate the effects of the interaction between aerodynamic forces and structural motions it is in principle necessary to solve the Navier–Stokes equations for turbulent flow with time-dependent boundary conditions dependent on the solutions themselves. This problem defies analytical capabilities. It is also difficult to solve dependably by computational fluid dynamic (CFD) methods, although continual progress is being made in this field, especially for non-turbulent flows.

Given the limitations of analytical and numerical procedures, the aeroelastic characterization of civil engineering structures relies largely on laboratory testing and empirical modeling. Such testing is not always without its problems, however, and for certain conditions it is necessary to assess carefully the applicability to the prototype of laboratory test results and the associated empirical models. There are two reasons for this. First, wind tunnels that achieve Reynolds numbers comparable to those typical of most types of civil engineering structures (e.g., high-pressure wind tunnels) are currently not capable of simulating atmospheric turbulence, which can significantly

Fig. 2 Flutter of the Tacoma Narrows Bridge, November 10, 1940. From F.B. Farquharson (ed.), *Aerodynamic Stability of Suspension Bridges*, 1949–1954

affect bluff body aerodynamic and aeroelastic behavior. Second, wind tunnels that simulate the features of atmospheric turbulence usually violate Reynolds number similarity requirements by factors of the order of 100–1,000. Nevertheless, for most structures with sharp edges at which flow separation must occur both in the prototype and the model, and for properly modeled structures with rounded shapes and rough or ribbed surfaces, it is assumed in most cases that the violation of Reynolds number similarity is relatively inconsequential, and that prudent use of laboratory test results is warranted.

This chapter is divided into two main parts. The first part is devoted to bluff body aeroelasticity fundamentals pertaining to vortex-shedding related phenomena (Sect. 1.1), galloping (Sect. 1.2), divergence (Sect. 1.3), flutter, and buffeting in the presence of aeroelastic effects (Sect. 1.4). The second part is concerned with applications to suspended-span bridges (Sect. 2.1), and tall chimneys and buildings (Sect. 2.2).

Fig. 3 John Hancock Building, Boston (by permission of Dr. DongHun Yeo)

1 Fundamentals

1.1 Vortex-Induced Oscillation

1.1.1 Vortex Shedding

The aeolian harp (named after Aeolus, the Greek god of winds) consists of a set of parallel strings which, when exposed to wind, experience vibrations that produce acoustical tones. The vibrations are caused by periodic lift forces associated with *vortex shedding*, and were studied by Strouhal in 1878 [1]. The shedding of vortices in the wake of circular cylinders was studied in 1908 by Bénard [2], after whom the vortices are named in France. A few years later it was also studied by von Kármán [3]. The orderly array of vortices that forms in the wake of a cylinder is known as a von Kármán street.[3] The character of the vortex shedding depends upon Reynolds number, the turbulence present in the oncoming flow, and the turbulence in the boundary layer that develops on the circular cylinder's surface. These factors control the interplay between viscous and inertial forces that determines the position of the boundary layer's separation point. Vortex shedding is not limited to circular cylinders; it also occurs in the wake of prismatic bodies (Fig. 4), and of non-cylindrical elongated bodies such as tapered chimneys.

For long rigid cylindrical bodies in flow with uniform mean speed, around which the flow may be assumed to be two-dimensional, the vortex shedding frequency f_s satisfies the relation

$$S = f_s D / U \tag{1.1}$$

where D is the across-flow dimension of the cylinder, U is the mean speed of the oncoming flow, and the Strouhal number S depends upon the cross-section of the cylinder. (The assumption that the flow is two-dimensional means that end effects are assumed to affect negligibly the overall model behavior.) For smooth circular cylinders S changes drastically at certain critical values of the Reynolds number (see, e.g., [4]). However, for circular cylinders with rough surfaces no such critical phenomena appear to have been observed [5, 6, p. 151]. The Strouhal number is listed in [6] for a variety of shapes of interest in structural engineering under uniform, smooth flow conditions.

The shedding of vortices in the wake of a body gives rise to an asymmetric flow (Fig. 4) and, therefore, to an asymmetric pressure field which induces on the body fluctuating *lift forces*, as well as relatively small drag force fluctuations. In air flow the latter may in most applications be assumed to be negligibly small. Various aspects of vortex shedding, including the dependence of the fluctuating lift force acting on a square cylinder upon the turbulence in the oncoming flow, are discussed, for example, in [6, 7].

[3] The late Professor Wallace Hayes of Princeton University sometimes called it "boulevard Bénard.".

Fig. 4 Flow around rectangular cylinder, Reynolds number Re=200. From Y. Nakamura, "Bluff Body Aerodynamics and Turbulence" *J. Wind Eng. Ind. Aerodyn.*, 49 (1993) 65–78

If the body is not perfectly rigid, or if it has elastic supports, it will experience motions due to the aerodynamic forces and, in particular, to the fluctuating lift force. As long as the motions are sufficiently small they do not affect the vortex shedding, and Eq. 1.1 remains valid. If the vortex-shedding frequency f_s, and therefore the frequency of the associated lift force, is equal to the natural frequency of vibration of the body f_n, then a relatively large motion amplification occurs. Experiments show that this is the case not only at the flow speed $f_n D/S$, but also at any flow speed U within an interval $f_n D/S - \Delta U < U < f_n D/S + \Delta U$, where $\Delta U/U$ depends upon cross-sectional shape and the mechanical damping, and is usually of the order of few percent. Within that interval the vortex shedding frequency no longer conforms to Eq. 1.1; rather, it aligns itself to the frequency of vibration of the body.

This is an aeroelastic effect: while the flow affects the body motion, the body motion in turn affects the flow insofar as it produces a synchronization of the vortex-shedding frequency with the frequency of vibration of the body. Synchronization occurs in a wide variety of physical, biological, and mathematical non-linear systems, including clocks attached to the same deformable wall, which tick in unison, women sleeping in the same room, who according to [8] tend to have their menses on the same day, and the famous van der Pol equation, among other nonlinear equations. In the vortex-shedding case the synchronization is referred to as *lock-in*.

Figure 5 shows measurements of the across-flow oscillations of an elastically supported circular cylinder in smooth flow and their spectral densities, and of flow velocity fluctuations and their spectral densities at 2.5 diameters downstream of and

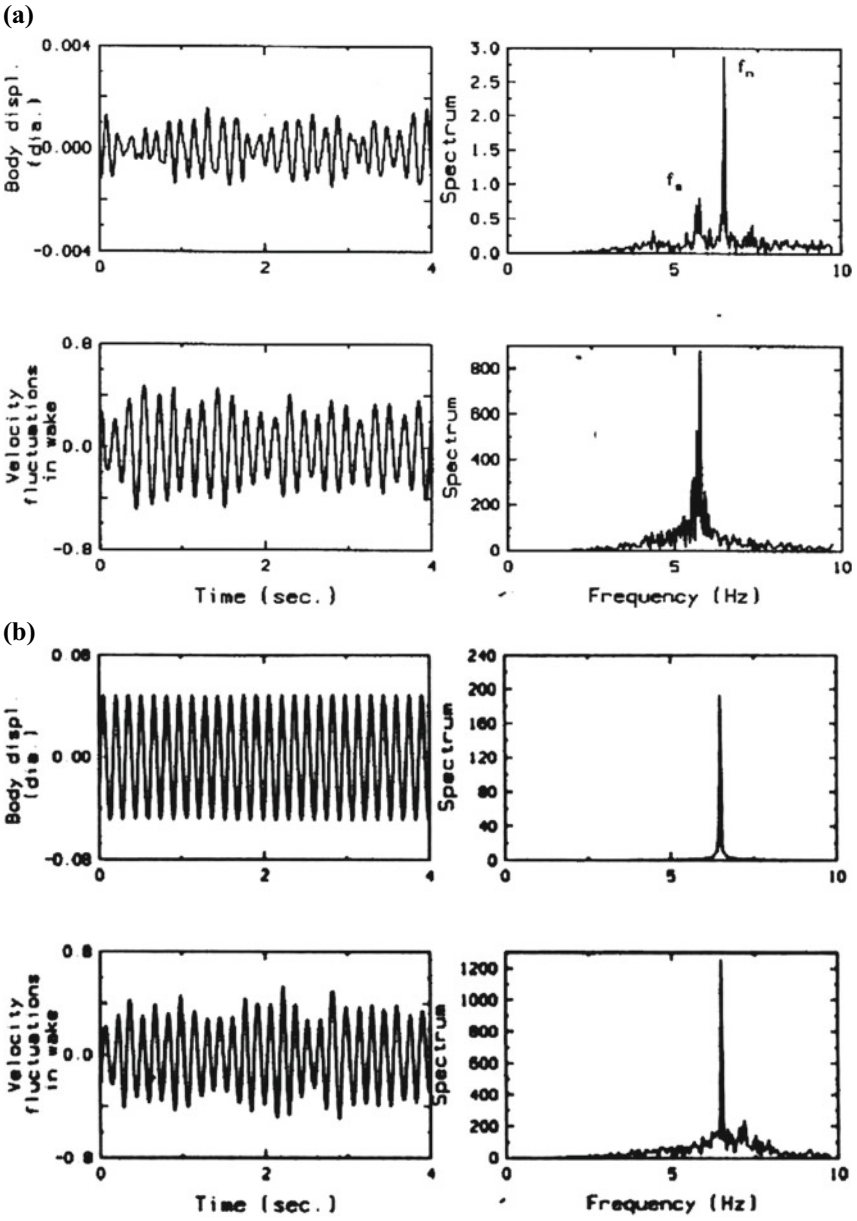

Fig. 5 **a** Response for $U/f_n D = 4.294$; $\zeta = 0.15\%$. **b** Response for $U/f_n D = 5.003$; $\zeta = 0.15\%$. **c** Response for $U/f_n D = 5.475$; $\zeta = 0.15\%$

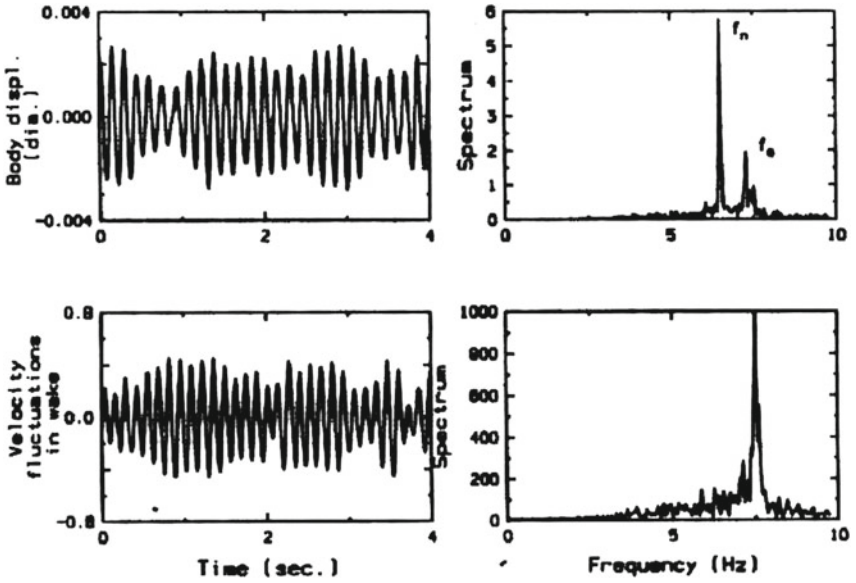

Fig. 5 (continued)

one diameter above the cylinder axis [9]. Note the significant increase in amplitude for $f_s = f_n$. However, even for $f_s = f_n$ the ratio of the amplitude to the diameter of the cylinder remains relatively small. This is typical of vortex-induced oscillations.

Up to a certain magnitude of the displacement the body motion results in a transfer of energy from the flow to the body. This transfer may be viewed as equivalent to a flow-induced negative aerodynamic damping. For larger displacements, however, there occurs a transfer of energy from the body to the flow. This helps to limit the amplitude of the motion and may be viewed as equivalent to a flow-induced positive damping.

Figure 6 reflects another aeroelastic phenomenon of interest in practice: the increased along-span correlation of the pressures acting on a circular cylinder as the oscillation amplitudes increase.

1.1.2 Modeling of Vortex-Induced Oscillations

The aeroelastic behavior of an oscillator is described by its equation of motion, in which the excitation term is the resultant of the flow-induced pressures. As was mentioned earlier, the latter can in principle be obtained from the solution of the Navier–Stokes equation with boundary conditions dependent upon the solution itself.

For many years mathematicians and engineers have tried to develop simplified empirical models. One justification for such models is that the collective behavior of a wide variety of systems with large numbers of degrees of freedom can be similar to

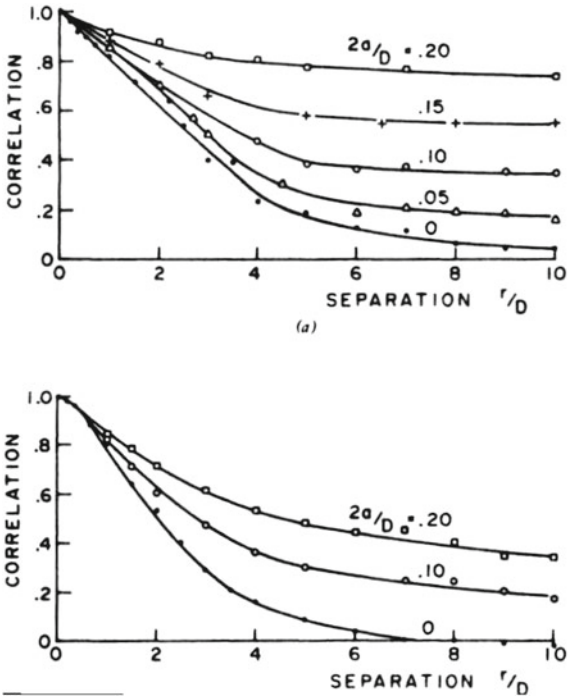

Fig. 6 Effect of increasing oscillation amplitude $a/2$ of a circular cylinder of diameter D on correlation between pressures at points separated by distance d along a cylinder generator: **a** smooth flow; **b** flow with turbulence intensity 11%. Reynolds number: $Re = 2 \times 10^4$

the behavior of simple low-degree-of-freedom systems representing them. (A flow interacting with a body is a system with an infinity of degrees of freedom.) The various empirical vortex-induced oscillation models contain adjustable parameters fitted to match experimental results. By construction, the solutions of the model equations with parameters fitted to those results provide a reasonable description of the observed aeroelastic motions. The user must be aware that the empirical model may not be valid as a motion predictor for conditions that differ significantly from the experimental conditions in which the fitted parameters were obtained. For long elastically-supported cylinders in uniform smooth flow we review a number of two-degree-of-freedom models, and a simpler but useful single-degree-of-freedom model.

1.1.3 Coupled Two-Degree-of-Freedom Equations: Wake Oscillator Models

Two-degree-of-freedom models entail two coupled equations, one describing the body motion, and one describing the wake motion. Various models, all derived from a generic model, were reviewed by Scanlan [10], whom we follow in the sequel. The generic model includes the equation of *body motion*

$$m[\ddot{y} + 2\zeta\omega_n\dot{y} + \omega_n^2 y] = F(\phi, \dot{\phi}, \ddot{\phi}), \tag{1.2}$$

where y is the across-flow body displacement, m is the body mass, ζ is the mechanical damping ratio, $\omega_n = 2\pi f_n$, ϕ is a representative wake variable, and

$$F(\phi, \dot{\phi}, \ddot{\phi}) = a_2\ddot{\phi} + \sum_{n=1}^{N} a_{2n-1}\dot{\phi}^{2n-1} + a_0\phi, \tag{1.3}$$

and the equation of *wake motion*

$$\ddot{\phi} + \sum_{m=1}^{M} b_{2m-1}\dot{\phi}^{2m-1} + b_0\phi = G(y, \dot{y}, \ddot{y}, \dddot{y}, \ddddot{y}), \tag{1.4}$$

where

$$G(y, \dot{y}, \ddot{y}, \dddot{y}, \ddddot{y}) = c_4\dddot{y} + c_3\ddot{y} + c_2\ddot{y} + \sum_{r}^{R} c_{2r-1}\dot{y}^{2r-1} + c_0 y. \tag{1.5}$$

The constants a^i, b^i, c^i must be identified by a combination of physical reasoning and experimental work. The system 1.2–1.5 is autonomous. Various models differ according to the meaning ascribed to the variable ϕ and the choice of non-zero constants a, b, and c.

The first wake oscillator model was proposed in 1955 by the great American mathematician Birkhoff[4] [11]. In the Birkhoff model the variable ϕ is the angle, denoted by α, between the axis of the vortex street and a fictitious lamellar mass, "something like the tail of a swimming fish," that extends a distance L aft of the cylinder, and oscillates at the Strouhal frequency from side to side across the wake.

Funakawa [12] pursued Birkhoff's basic idea by attributing to the wake oscillator a physical meaning associated with the mass of the "dead fluid" region in the near wake of the cylinder. He conducted experiments in uniform smooth flow in which a circular cylinder was subjected to harmonic oscillations at the Strouhal frequency. Details on the behavior of the "dead fluid" region were inferred from flow visualizations under lock-in conditions. The wake oscillator was assumed to act as a horizontal pendulum coupled to the cylinder motion and described by the equation

$$I\ddot{\alpha} + c\dot{\alpha} + k(\alpha + \frac{\dot{y}}{U}) = \omega_s^2 I\bar{\alpha}\sin\omega_s t \tag{1.6}$$

where $I = \frac{1}{4}\rho LH(D+L)^2$ is the moment of inertia of the wake oscillator, $H = 1.25D$, $L = 2.2D$, $k = \frac{1}{2}\rho U^2(2\pi)L(D+L)/2$ is the oscillator's moment stiffness, and $\bar{\alpha} = 2y_0/(D+L)$. Equation (1.6) was used by Funakawa to calculate drag and

[4] Birkhoff's contributions to the field of dynamical systems rank in importance with those of Poincaré, with whom he had close and fruitful scientific interactions.

lift forces induced by the wake oscillator on the cylinder through Magnus effects, and dependent on y, $\dot{y}$, and $\dot{y}^3$. There results from this model a van der Pol-type equation of motion of the body that contains two terms of aerodynamic origin. The first term is of the form $c_{1,aero}\dot{y}$ and reflects the transmission of energy from the flow into the body. Unlike a mechanical damping coefficient—which is associated with loss of energy by the system,—the aerodynamic damping coefficient $c_{1,aero} < 0$. The second term has the form $c_{2,aero}\dot{y}^3$, where the aerodynamic damping coefficient $c_{2,aero} > 0$. For small $\dot{y}$ the net aerodynamic damping due to the linear and nonlinear terms in $\dot{y}$ is negative, so that the displacement increases. For large $\dot{y}$ the net aerodynamic damping becomes positive, thereby limiting the amplitude of the body motion. A critique of Funakawa's model work led Nakamura [13] to propose a modified form of the Magnus lift force. A further modification was proposed by Tamura and Matsui [14].

In another family of circular cylinder vortex-induced oscillation models the parameter ϕ of Eq. (1.2) is taken to be the lift coefficient C_L. Hartlen and Currie [15] proposed the following model:

$$M\ddot{y} + C\dot{y} + Ky = \frac{1}{2}\rho U^2 D C_L(t) \tag{1.7}$$

$$\ddot{C}_L - a\omega_s \dot{C}_L + \frac{\gamma}{\omega_s}\dot{C}_L^3 + \omega_s C_L = b\dot{y} \tag{1.8}$$

where b is an adjustable parameter, $\alpha = \rho D^2/8\pi^2 S^2 M$, $y = 4\alpha/3C_{L_0}$, and C_{L_0} is the measured amplitude of the fluctuating lift coefficient on the stationary cylinder. Hartlen and Currie's model was subsequently modified by Skop [16] and Griffin [17], Landl [18], Wood [19], and Wood and Parkinson [20].

Dowell [21] developed a model in which C_L was also used as the wake oscillator variable. The model is based on four requirements:

1. At high frequencies a virtual mass relationship is preserved between lift and cylinder acceleration, that is,

$$8C_L = -B_1 \rho D^2 \frac{\ddot{y}^2}{2} (\omega \to \infty) \tag{1.9}$$

   where B_1 is a constant.
2. At low frequencies quasi-steady conditions hold between C_L and y, that is, for $\infty \to 0$

$$C_L = f(\frac{\dot{y}}{U}) = A_1(\frac{\dot{y}}{U}) - A_3(\frac{\dot{y}}{U})^3 + \cdots \tag{1.10}$$

   where $A_1, A_3 \ldots$ are constants.
3. For small C_L and $y \equiv 0$ the fluid oscillation has the Strouhal frequency, that is,

$$\ddot{C}_L + \omega_s^2 C_L = 0. \tag{1.11}$$

4. Characteristics of the van der Pol oscillator are included in the response of C_L. Conditions 1 to 4 lead to the equation

$$\ddot{C}_L - \epsilon\left[1 - 4\left(\frac{C_L}{C_{L_0}}\right)^2\right]\omega_s \dot{C}_L + \omega_s^2 C_L = -B_1\left(\frac{D}{U^2}\right)\dddot{y} + \omega_s^2\left[A_1\frac{\dot{y}}{U} - A_3\left(\frac{\dot{y}}{U}\right)^3 + A_5\left(\frac{\dot{y}}{U}\right)^5 - A_7\left(\frac{\dot{y}}{U}\right)^7\right] \tag{1.12}$$

in which the parameter ϵ must be determined experimentally. Two special features of Dowell's model are that it contains a fourth order coupling of y to C_L, and that the model can describe oscillations in a broader frequency range than is the case for other models. For details and comparisons with experiments see [21].

1.1.4 Single-Degree-of-Freedom Model of Vortex-Induced Response

The following simple single-degree-of-freedom model proposed by Scanlan [22] exhibits features of a van der Pol oscillator:

$$m(\ddot{y} + 2\zeta\omega_n\dot{y} + \omega_n^2 y) = \tfrac{1}{2}\rho U^2 D\left[Y_1(K)\left(1 - \epsilon\tfrac{y^2}{D^2}\right)\tfrac{\dot{y}}{U} + Y_2(K)\tfrac{y}{D} + C_L(K)\sin(\omega t + \phi)\right]. \tag{1.13}$$

In Eq. (1.13) $K = D\omega/U$, and the circular frequency ω satisfies the Strouhal relation $\omega = 2\pi SU/D$; $Y1$, $Y2$, ϵ, and C_L, a measure of the lift force that would occur in the absence of lock-in, must be fitted to experimental results. This model allows for negative and positive aerodynamic damping at low and high body displacements, respectively, that is, for the aeroelastic transfer of energy from the flow to the body or from the body to the flow according as the displacements are small or large. At lock-in $\omega \approx \omega_n$, and $Y_2(\omega_n) = 0$, $C_L(\omega_n) = 0$, since the last two terms within the square bracket of Eq. (1.13) are much smaller than the term—dominant by far—reflecting the aerodynamic damping effects. At steady amplitudes the average energy dissipation per cycle is zero, so that

$$\int_0^T \left|4m\zeta\omega - \rho U D Y_1(1 - \epsilon\frac{y^2}{D^2})\right| \dot{y}^2 dt = 0 \tag{1.14}$$

where $T = 2\pi/\omega$. The assumption that, for practical purposes, y is harmonic, that is, $y = y_0\cos\omega t$, implies

$$\int_0^T \dot{y}^2(t)dt = \omega y_0^2\pi. \tag{1.15}$$

$$\int_0^T y^2 \dot{y} dt = \omega y_0^2 \frac{\pi}{4}. \tag{1.16}$$

Equation (1.14) then yields

$$\frac{y_0}{D} = 2\left[\frac{Y_1 - 8\pi S_{scr} S}{\epsilon Y_1}\right]^{\frac{1}{2}} \tag{1.17}$$

where S_{scr} denotes the Scruton number, defined as

$$S_{scr} = \frac{\zeta m}{\rho D^2}. \tag{1.18}$$

The parameters Y_1 and ϵ may be evaluated from model tests. At the lock-in velocity the body is displaced to an initial amplitude $A_0 > y_0$ and then released. The body will then undergo a decaying oscillation until it levels out to the steady state motion with amplitude given by Eq. (1.17). It is shown in [23] that the amplitude of the decaying oscillation can be described by the expression

$$\frac{y(t)}{D} = \frac{y_0/D}{[1 - ((A_0^2 - y_0^2)/A_0^2)\exp(-\alpha y_0^2 U t/4D^3)]^{\frac{1}{2}}} \tag{1.19}$$

in which

$$\alpha = \frac{\rho D^2 Y_1}{2m}\epsilon. \tag{1.20}$$

The value of α is determined from the model tests as follows. Defining $R_n = A_0/A_n$, where A_n is the amplitude of the decaying oscillation at n cycles after the release,

$$\alpha = \frac{-4SD^2}{ny_0^2} ln\left[\frac{A_0^2 - R_n^2 y_0^2}{A_0^2 - y_0^2}\right]. \tag{1.21}$$

It follows that

$$Y_1 = \frac{m}{2\rho D^2}\left[\alpha \frac{y_0^2}{D^2} + 16\pi\zeta S\right], \tag{1.22}$$

$$\epsilon = \frac{2m\alpha}{\rho D^2 Y_1}. \tag{1.23}$$

Y_1 may be obtained by alternative identification techniques from section model tests of the type used to measure flutter coefficients (Sect. 2.1). Scanlan's model is the basis of procedures for the estimation of vortex-shedding effects on bridge decks (Sect. 2.1.3) and tall chimneys (Sect. 2.2).

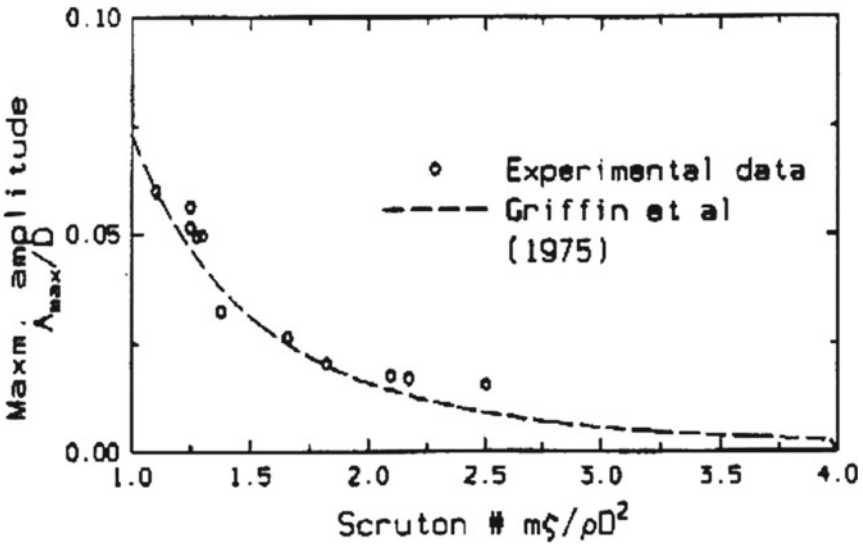

Fig. 7 Maximum amplitude as a function of Scruton number

Experimental data used in conjunction with a model similar to Eq. (1.17) yielded the values plotted in Fig. 7 [9]. Also plotted in Fig. 7 is the following empirical formula developed in [23]:

$$\frac{y_0}{D} = \frac{1.29}{[1 + 0.43(8\pi^2 S^2 S_{scr})]^{3.35}}. \tag{1.24}$$

For additional basic material on vortex-induced oscillation, see [24–28] and references listed in [10].

1.2 Galloping

In this section we study two types of galloping. *Across-wind galloping* is a large-amplitude oscillation (one to ten or more across-wind dimensions of the body) exhibited in a plane normal to the oncoming flow velocity by slender structures with certain types of cross-section. For example, ice-laden cables subjected to winds approximately normal to their span exhibit galloping oscillations in a vertical plane. For brevity we will refer to across-wind galloping simply as galloping. *Wake galloping* refers to oscillations of a downstream cylinder induced by the wake flow of an upstream cylinder, and has been observed in bundled power transmission-line cables.

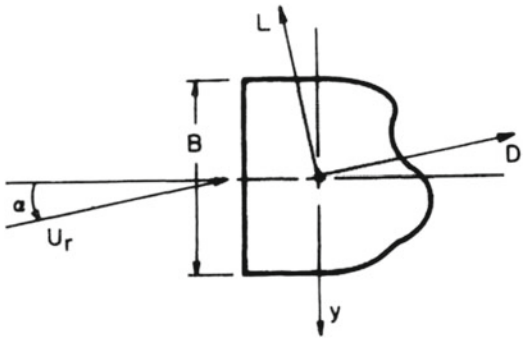

Fig. 8 Lift L and drag force D on a fixed bluff object

1.2.1 Equation of Motion of Galloping Bodies: The Glauert-Den Hartog Necessary Condition for Galloping instability

Pioneering contributions to the galloping problem are due to Glauert [29] and Den Hartog [30, 31]. Experience has shown that knowledge of the mean lift and drag coefficients obtained under static conditions as functions of angle of attack is sufficient for building a satisfactory analytical description of the galloping phenomenon; that is, galloping is governed primarily by quasi-steady forces. Deviations of the actual drag and lift forces from their mean static counterparts that occur during the galloping motion have a second-order effect, unless the oscillator can experience chaotic transitions, as suggested in Sect. 6.1.2.3.

We assume that the problem is two-dimensional, and consider the cross-section of a prismatic body in smooth flow (Fig. 8). Assume the body is *fixed* and that the angle of attack of the flow velocity U_r is α. The mean drag (mean force in the direction of U_r) and the mean lift (mean force in the direction normal to U_r) are, respectively,

$$D(\alpha) = \frac{1}{2} U_r^2 B C_D(\alpha) \tag{1.25}$$

$$L(\alpha) = \frac{1}{2} U_r^2 B C_L(\alpha) \tag{1.26}$$

Their projection on the direction y is

$$F_y(\alpha) = -D(\alpha) \sin\alpha - L(\alpha) \cos\alpha \tag{1.27}$$

We write $F_y(\alpha)$ in the alternative form

$$F_y(\alpha) = \frac{1}{2} U^2 B C_{Fy}(\alpha) \tag{1.28}$$

where

$$U = U_r \cos\alpha. \tag{1.29}$$

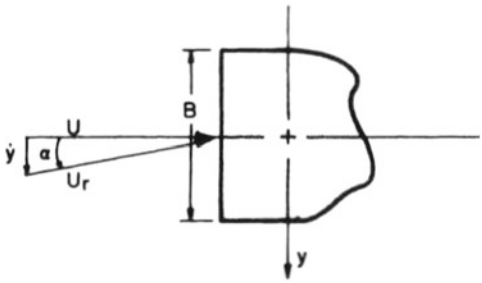

Fig. 9 Effective angle of attack on an oscillating bluff object

It follows from Eqs. (1.27) and (1.28) that

$$C_{Fy} = -[C_L(\alpha) + C_D(\alpha) \tan \alpha] \sec \alpha. \tag{1.30}$$

We now consider the case in which the same body *oscillates* in the across-wind direction y in flow with velocity U (Fig. 9).

The magnitude of the relative velocity of the flow with respect to the moving body is denoted by U_r and can be written as

$$U_r = (U^2 + \dot{y}^2)^{\frac{1}{2}}. \tag{1.31}$$

The angle of attack, denoted by α, is

$$\alpha = \arctan \frac{\dot{y}}{U}. \tag{1.32}$$

If the body has mass m per unit length, elastic supports, and linear viscous damping, its equation of motion is

$$m[\ddot{y} + 2\zeta \omega_n \dot{y} + \dot{\omega}_n^2 y] = F_y \tag{1.33}$$

where ζ is the damping ratio, ω_n is the circular natural frequency, and F_y is the aerodynamic force acting on the body. It is assumed that the mean aerodynamic drag and lift coefficients $C_D(\alpha)$ and $C_L(\alpha)$ for the oscillating body and for the fixed body are the same, so $F_y(\alpha)$ is given by Eqs. (1.28)–(1.32).

For incipient motion, where a may be assumed to be small,

$$\alpha \cong \frac{\dot{y}}{U} \cong 0,$$

$$F_y(\alpha)|_{\alpha=0} \cong \frac{\partial F_y}{\partial \alpha}|_{\alpha=0} \alpha. \tag{1.34}$$

For small α, Eqs. (1.28), (1.34) (in which it is recalled that U is constant), (1.30), and (1.32) yield

$$F_y(\alpha)|_{\alpha=0} \cong -\frac{1}{2}\rho U^2 B \left(\frac{dC_L}{d\alpha} + C_D\right)_0, \tag{1.35}$$

and the equation of motion of the body is

$$m[\ddot{y} + 2\zeta\omega_n\dot{y} + \omega_n^2 y] = -\frac{1}{2}\rho U^2 B \left(\frac{dC_L}{d\alpha} + C_D\right)_0 \frac{\dot{y}}{U} \tag{1.36}$$

In the right-hand side of Eq. (1.36) the coefficient of $\dot{y}$ may be viewed as an aerodynamic damping coefficient. The total aerodynamic damping coefficient—the factor d multiplying the derivative $\dot{y}$—is

$$2m\zeta\omega_n + \frac{1}{2}\rho U B \left(\frac{dC_L}{d\alpha} + C_D\right)_0 = d. \tag{1.37}$$

If $d > 0$ the fixed point $y = 0$, $\dot{y} = 0$ is stable, that is, small oscillations from the position of equilibrium $y = 0$ due to a small initial deviation from that position will decay in time, and the body will revert to its position of equilibrium. The body is then said to be aerodynamically stable. However, if $d < 0$, the fixed point $y = 0$, $\dot{y} = 0$ is unstable, and the body is said to be aerodynamically unstable.

A *necessary* condition for the occurrence of galloping motion is then

$$\left(\frac{dC_L}{d\alpha} + C_D\right)_0 < 0. \tag{1.38}$$

The inequality (1.38) is known as the Glauert-Den Hartog criterion. (A *sufficient* condition for the occurrence of galloping is $d < 0$.) Note, however, that Eq. (1.38) is applicable to galloping motion that starts from rest; a large triggering disturbance can in certain instances cause the occurrence of galloping even if Eq. (1.38) is not satisfied.

For reasons of symmetry circular cylinders cannot gallop: since the quasi-static mean lift force is identically zero for any angle of attack, $dC_L/d\alpha \equiv 0$. For an octagonal prism the lift and drag coefficients measured under static conditions are depicted in Fig. 10. It can be seen that for angles of attack $-5^\circ < \alpha < 5^\circ$, where α is defined in Fig. 10, the Glauert-Den Hartog criterion is satisfied.

1.2.2 Description of Galloping Motion

In Sect. 1.3 we were concerned with obtaining a necessary condition for the occurrence of galloping. In this section we consider bodies for which the total aerodynamic coefficient $d < 0$, and discuss the evolution in time of their galloping motion.

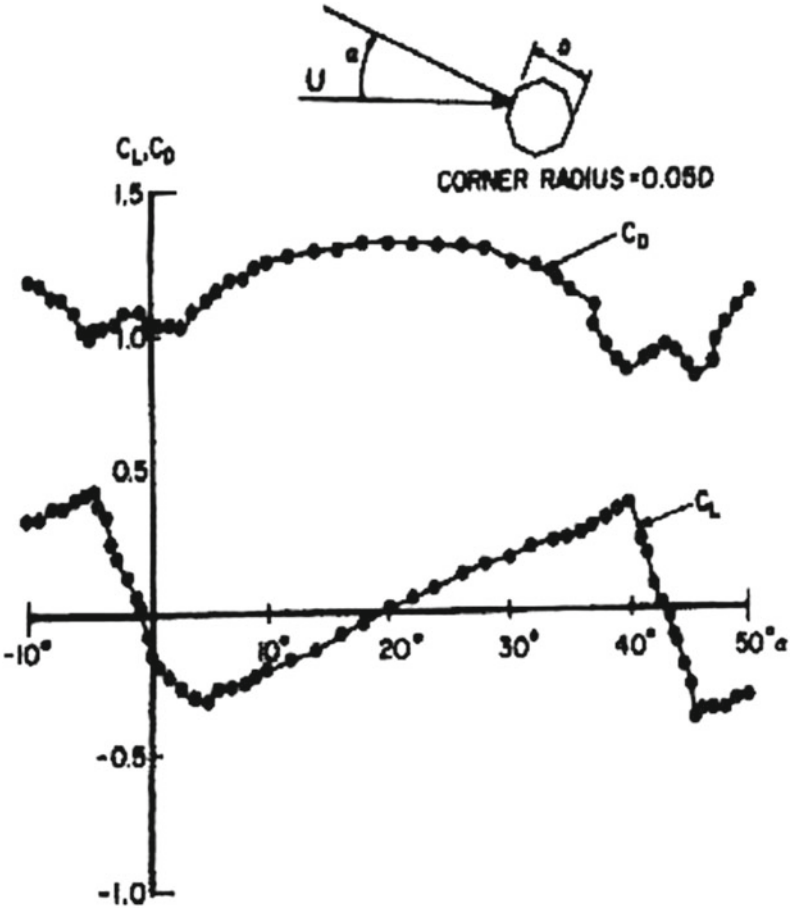

Fig. 10 Force coefficients on an octagonal cylinder

As shown by Eqs. (1.28), (1.30), and (1.32), the equation of motion of the galloping body (Eq. 1.33) is nonlinear. The description of the galloping motion is based on the development of the aerodynamic coefficient C_{F_y} in powers of $\dot{y}/U$ Since $\dot{y}/U = \tan\alpha$, [33] proposed the polynomial expression

$$C_{Fy} = A_1\frac{\dot{y}}{U} - A_2\left(\frac{\dot{y}}{U}\right)^2\frac{\dot{y}}{|\dot{y}|} - A_3\left(\frac{\dot{y}}{U}\right)^3 + A_5\left(\frac{\dot{y}}{U}\right)^5 - A_7\left(\frac{\dot{y}}{U}\right)^7, \quad (1.39)$$

where the constants A_i are determined by a least squares fit or another appropriate technique. The steady-state solution of the resulting equation of motion for a prismatic body with square cross-section is obtained by assuming

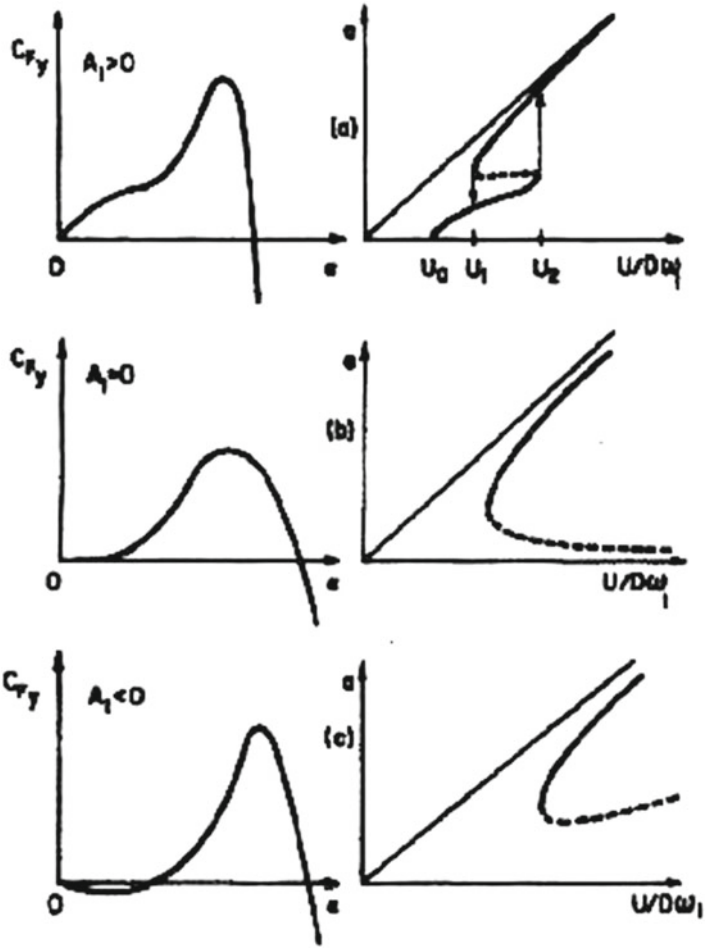

Fig. 11 Basic types of lateral force coefficients C_{f_y} and the corresponding galloping response amplitudes. From [32]

$$y = a\cos(\omega_n t + \phi) \tag{1.40a}$$

$$\dot{y} = -a\omega_n \sin(\omega_n t + \phi), \tag{1.40b}$$

in which α and ϕ are slowly varying functions of time, and by applying the Krylov and Bogoliuboff technique to the resulting equation of motion [34]. This leads to the identification of three basic types of curves C_{F_y} as functions of α, and of the corresponding curves α as functions of the reduced velocity $U/D\omega_n$. The observable amplitudes are those depicted in solid lines in Fig. 11. They correspond to stable limit cycles. Interrupted lines correspond to unstable limit cycles, which are not observable

in physical experiments. For $A_1 > 0$, if the speed increases from U_1 to U_2 a jump occurs from the lower to the upper curve; if the speed decreases from U_2 to U_0 the jump occurs from the upper to the lower curve.

The effect upon the galloping of non-uniform deflections along the span and of turbulence in the oncoming flow is discussed in [32]. Turbulence helps to render the oscillations unsteady and, depending upon its scale and intensity, it can reduce the magnitude of the aerodynamic damping to a degree that will prevent the occurrence of galloping. For additional studies of galloping see [35–37].

1.2.3 Chaotic Galloping of Two Elastically Coupled Square Bars

Experiments on a double galloping oscillator consisting of two elastically supported and coupled square prisms (Fig. 12) are described in [38]. The bars were observed to gallop in phase, but except for relatively low flow speeds U this oscillatory form alternated irregularly with a second oscillatory form wherein the two bars galloped with higher frequency in opposite phases (Fig. 13). The mean time between transitions from the first to the second oscillatory form decreased as the flow speed increased.

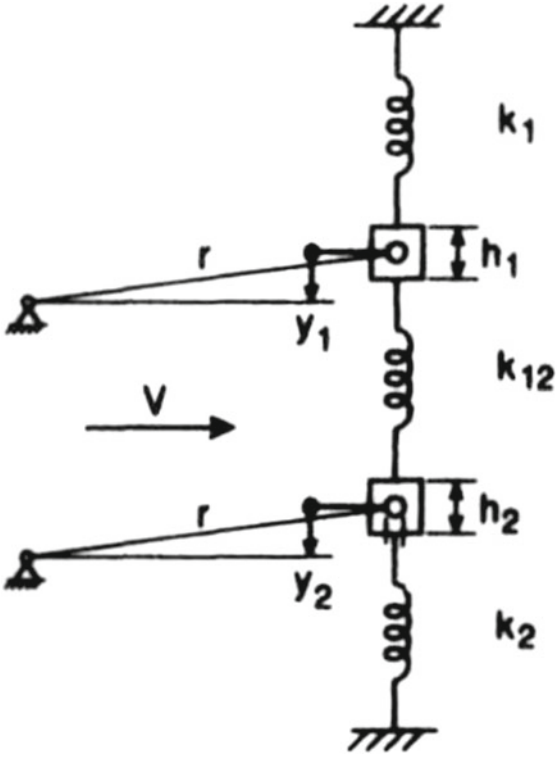

Fig. 12 Schematic of double galloping oscillator

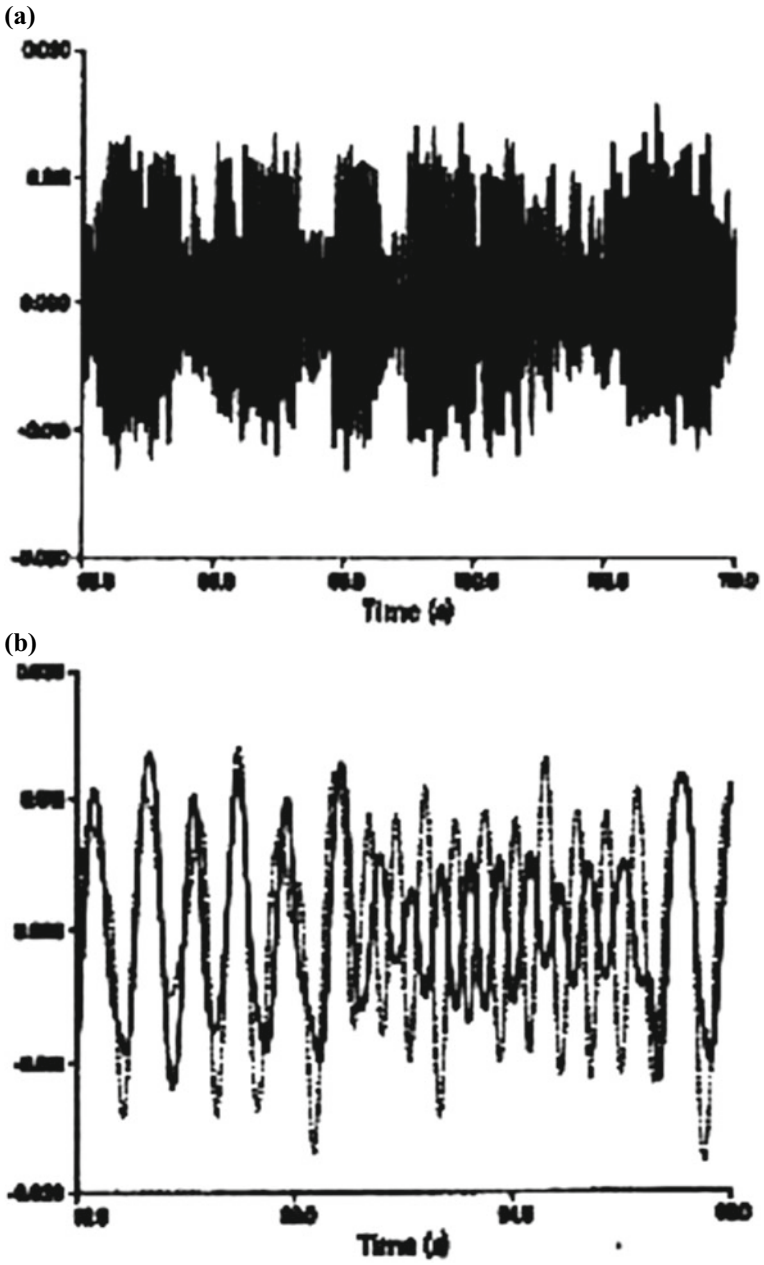

Fig. 13 **a** Observed time history of displacement y_1; **b** observed time history of displacement displacements y_1 (solid line) and y_2 (interrupted line). From [38]

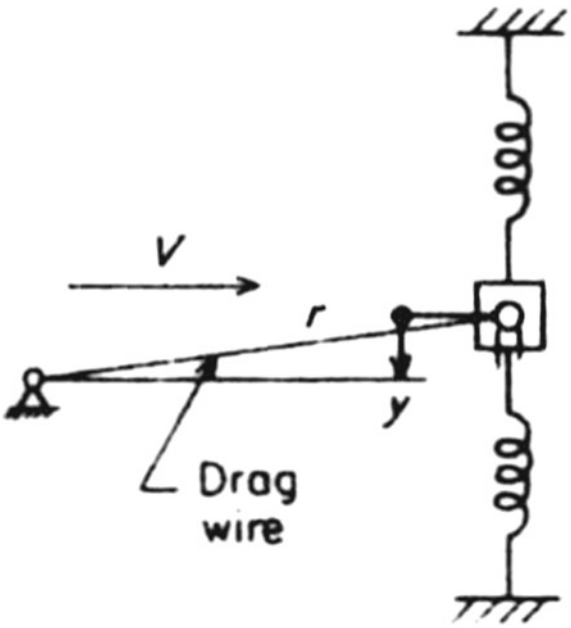

Fig. 14 Schematic of single galloping oscillator

A similar simple galloping oscillator is shown in Fig. 14. Observations show that its motion exhibits small deviations from periodicity (Fig. 15) that may be attributed to irregular flow fluctuations in the wake flow and to turbulence caused by experimental appurtenances. It follows that the actual aerodynamic forces acting on the oscillator deviate from the quasi-static model assumed in Sect. 6.1.2.1. Numerical simulations of the double galloping oscillator in which small random excitations were superimposed on the quasi-static aerodynamic forces yielded results similar to the experimental results of Fig. 13 [38].

It has been conjectured that galloping motions of the type shown in Fig. 13 are chaotic. The experimental results just reviewed have led to the development of a theory of chaotic dynamics occurring in a wide class of stochastic systems that can exhibit transitions between distinct oscillatory forms [39].

1.2.4 Wake Galloping: Physical Description and Analysis

We now consider the case of two circular cylinders of which one is located upstream of the other. Under certain conditions the downstream cylinder may experience wake galloping that is galloping induced by the wake of the upstream cylinder. Wake galloping arises in power transmission lines grouped in bundles as for example in Fig. 16. Since it occurs between spacers, it is referred to as subspan galloping.

We noted earlier that circular cylinders cannot experience across-wind galloping in uniform oncoming flow. However, the flow in the wake of an upstream cylinder is

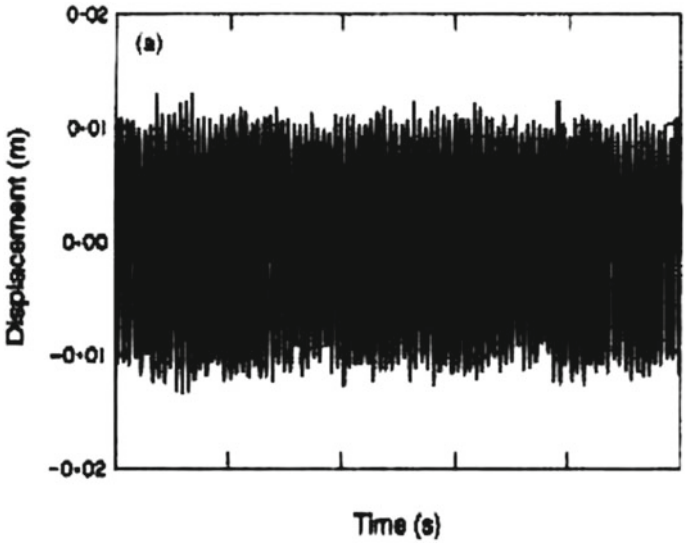

Fig. 15 Observed time history of displacement y

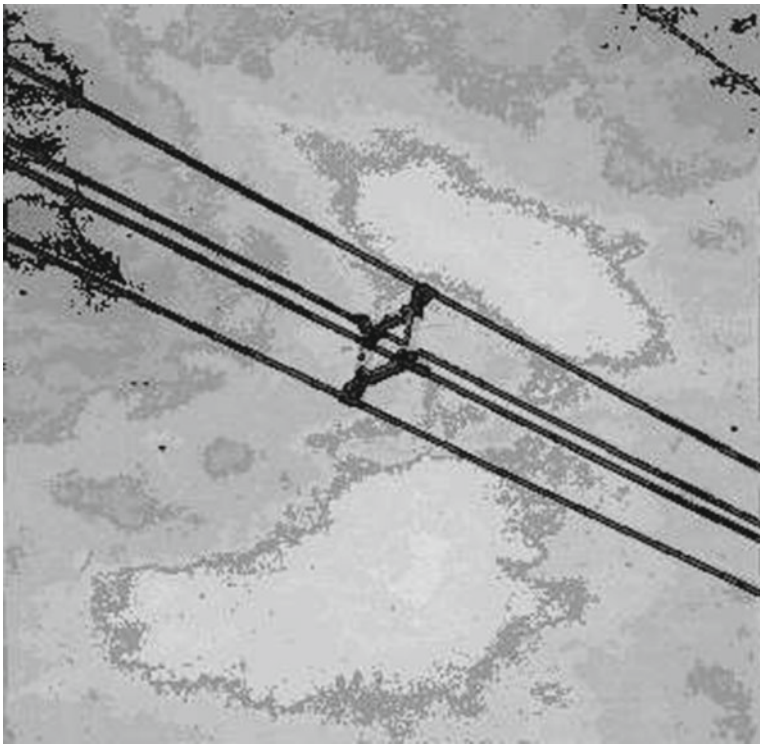

Fig. 16 Spacer in four-bundle power line

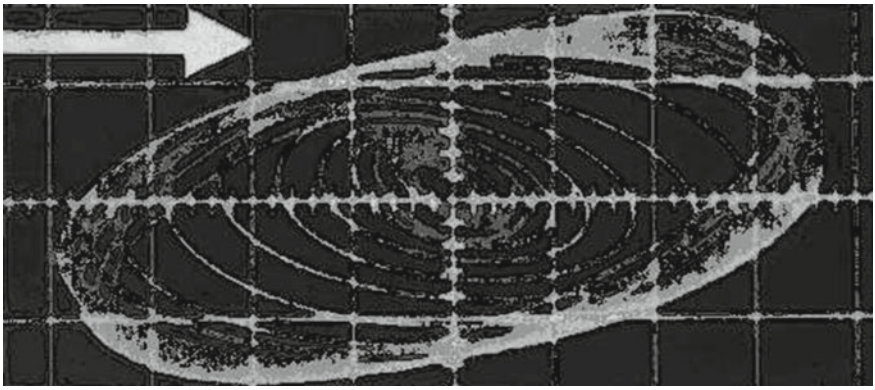

Fig. 17 Amplitude trace of a wake galloping orbit (courtesy of National Aeronautical Establishment, National Research Council of Canada)

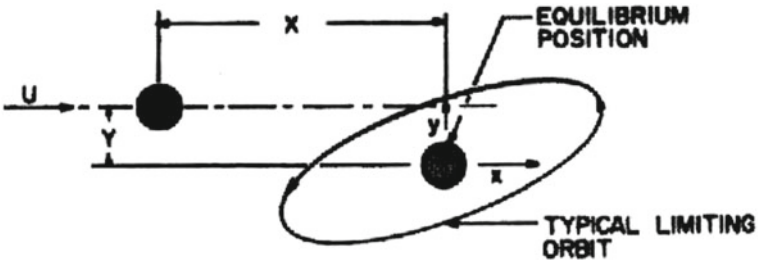

Fig. 18 Coordinates for wake galloping analysis [43]

sheared (i.e., non-uniform). If the distance between the upstream and the downstream cylinder is a few cylinder diameters, and the downstream cylinder is displaced into approximately the outer quarter of the wake, a galloping motion will begin from that displaced position, which grows in amplitude until it reaches a steady state elliptical orbit—a limit cycle—with the long axis oriented approximately along the flow velocity. An oscillograph trace of the galloping motion of a downstream cylinder supported elastically in both the flow direction and the direction normal to the flow is shown in Fig. 17. The direction of the motion on that orbit is downstream near the outer portion of the wake and upstream near the center of the wake, or clockwise in Fig. 17.

Wake galloping is analyzed by assuming two-dimensionality (i.e., uniform upstream flow and large ratio of subspan to cylinder diameter). The downstream cylinder is assumed to be elastically supported in both the horizontal and vertical direction about a position (X, Y), where X, Y are along-flow and across-flow coordinates centered on the upstream cylinder (Fig. 18). The equations of motion of the downward cylinder are written in terms of its excursions (x, y) away from the position (X, Y):

$$m\ddot{x} + d_x\dot{x} + K_{xx}x + K_{xy}y = F_x \tag{1.41a}$$

$$m\ddot{y} + d_y\dot{y} + K_{yx}x + K_{yy}y = F_y \tag{1.41b}$$

where m is the mass per unit length of the downstream cylinder, d_x, d_y are damping constants, K_{rs} $(r, s = x, y)$ are spring constants, and F_x, F_y are the flow-induced force components in the X and Y direction, written as

$$F_x = \frac{1}{2}\rho U^2 D\left\{\left(\frac{\partial C_x}{\partial x}x + \frac{\partial C_x}{\partial y}y\right) + C_y\frac{\dot{y}}{U_w} - 2C_x\frac{\dot{x}}{U_w}\right\} \tag{1.42a}$$

$$F_y = \frac{1}{2}\rho U^2 D\left\{\left(\frac{\partial C_y}{\partial x}x + \frac{\partial C_x}{\partial y}y\right) - C_x\frac{\dot{y}}{U_w} - 2C_y\frac{\dot{x}}{U_w}\right\} \tag{1.42b}$$

where U is the free upstream flow velocity, U_w is the average wake velocity in the U direction at (X, Y), and D is the cylinder diameter [40]. Expressions similar to Eq. 1.42a were first developed in [41, 42]. C_x, C_y are aerodynamic drag and lift coefficients. They, and their derivatives, are obtained by direct measurements of time-averaged values in the wind tunnel. The corresponding forces are self-excited: they vanish if the excursions x, y and their derivatives vanish. Cases of interest have included smooth circular cylinders and stranded wire cables.

An analytical solution of the problem can be obtained by assuming in Eqs. 1.41a and 1.42a

$$x = x_0 e^{\lambda t} \tag{1.43a}$$

$$y = y_0 e^{\lambda t} \tag{1.43b}$$

and using the condition that the determinant of the coefficients of Eq. 1.41a vanishes. The motions are unstable if the real part of the eigenvalue λ is smaller than zero. Stability boundaries can be obtained by seeking the vanishing real part of λ for a number of points X, Y. The agreement between theory and experiment was found to be reasonably good (Fig. 19) [43]. The corresponding orbits $[x(t), y(t)]$ may be calculated by using Eqs. 1.42a and 1.43a. For applications to cables see [40, 44, 45].

1.3 Torsional Divergence

Torsional divergence is an aeroelastic phenomenon that, like galloping, can be described by using aerodynamic properties measured on the body at rest. It can occur in bodies with relatively flat shapes, such as airfoils and lifting surfaces (see Sccts. 2.1–2.2) or bridge decks. It is also referred to as lateral buckling, and represents the condition wherein, given a slight deck twist, the drag load and the self-excited aerodynamic moment will precipitate a torsional instability.

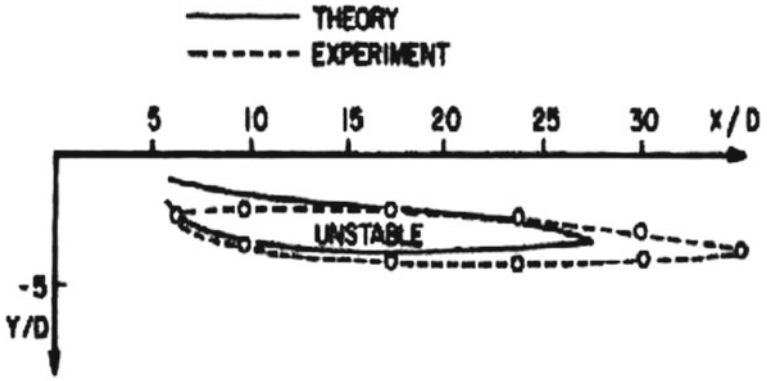

Fig. 19 Measured and predicted stabiloity boundaries for wake galloping [43]

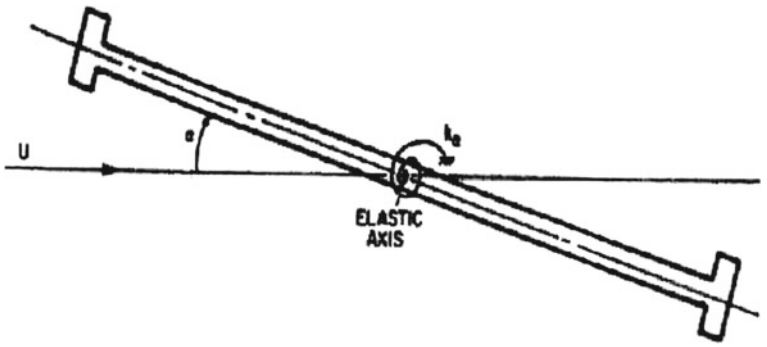

Fig. 20 Parameters for torsional divergence problem

We illustrate the divergence phenomenon by considering the bridge deck section of Fig. 20, in which U is the horizontal wind velocity, α is the angle of rotation about the bridge section's elastic center, and k_α is the torsional stiffness. The aerodynamic moment per unit span may be written as

$$M(\alpha) = \frac{1}{2}\rho U^2 B^2 C_M(\alpha) \tag{1.44}$$

where $C_M(\alpha)$ is the aerodynamic moment coefficient about the torsional axis and B is the bridge deck width. Typically $C_M(\alpha)$ is a monotonically increasing function of α. We denote $C_M(0)$ by C_{M0}. For small angles α, $M(\alpha)$ may be approximated to first order as

$$M(\alpha) = \frac{1}{2}\rho U^2 B^2 \left[C_{M0} + \frac{dC_M}{d\alpha}|_{\alpha=0}\alpha \right]. \tag{1.45}$$

By equating the aerodynamic torsional moment $M(\alpha)$ given by Eq. 1.45 to the internal torsional moment $k_\alpha \alpha$ we obtain

$$(k_\alpha - \lambda C'_{M0}) = \lambda C_{M0} \tag{1.46}$$

where $\lambda = \frac{1}{2}\rho U^2 B^2$ and $C'_{M0} = \frac{dC_M}{d\alpha}|_{\alpha=0}$, or

$$\alpha = \frac{\lambda C_{M0}}{k_\alpha - \lambda C'_{M0}}. \tag{1.47}$$

Since $\lambda > 0$, it follows from Eq. (1.47) that, provided $C'_{M0} > 0$, α approaches infinity (diverges) for $\lambda = \frac{k_\alpha}{C'_{M0}}$. (For $C'_{M0} < 0$, a case that occurs for some types of bridge decks, divergence does not occur.) The critical divergence velocity is therefore

$$U_{cr} = \sqrt{\frac{2k_\alpha}{\rho B^2 C'_{M0}}}. \tag{1.48}$$

The generalization of the problem to three dimensions and the role of the shape of the curve $C_M(\alpha)$ in the solution of the divergence problem are discussed in Sect. 6.2.1.2.

1.4 *Flutter and Buffeting in the Presence of Aeroelastic Effects*

Flutter is the term applied to aeroelastic phenomena occurring in flexible bodies with relatively flat shapes in plan (e.g., airfoils, rotor blades, turbomachinery blades, bridge decks) and involving oscillations with amplitudes that grow in time and can result in catastrophic structural failure. The term flutter is relatively recent and was first introduced in an aeronautical context; note that in Fig. 6.1 flutter is referred to as "undulation." As late as 1971 it has also been used to designate the wake galloping of conductor cables [42, 44], a usage that now appears to be obsolete. Like other aeroelastic phenomena, flutter entails the solution of equations of motion involving inertial, structural damping, restoring, and aerodynamic forces dependent upon the ambient flow and the shape and motion of the body.

For phenomena of interest in civil engineering the body motion is said to be *stable* from a flutter point of view if, assuming the absence of forcing terms, and given a sufficiently small disturbance from the body's position of equilibrium, the oscillations initiated by that disturbance will gradually die out, that is, the body will revert to its position of equilibrium. In dynamical systems theory that position is referred to as a *stable fixed point* (or a *sink*). In the presence of small forcing, solutions near the fixed point stay nearby, and the system is referred to as *linearly stable*. As the flow velocity increases, the aerodynamic forces acting on the body will also increase, and for a certain value of the flow velocity, called *critical flutter velocity*, or simply flutter

velocity, the stable fixed point in the dynamical system representing the body motion becomes neutrally stable—a *center*. At that velocity, in the absence of forcing, an initial small disturbance from equilibrium will result in steady harmonic, rather than decaying, oscillations. For velocities larger than the critical velocity the center turns into an *unstable fixed point*, also known as a *source*, and the oscillations initiated by a small disturbance will grow in time. The nonlinear dependence upon the motion of the aerodynamic forces and/or the body restoring force can result in a dynamical system in which the oscillations reach a periodic steady state by evolving on a *stable limit cycle*. In general, for flow velocities in excess of the critical velocity, the body will perform unacceptably from a service point of view, or can experience structural damage or collapse during the growing transient motion, that is, before its motion reaches a steady state.

The greatest difficulty in solving the flutter problem for bridges is the development of appropriate expressions for the aerodynamic forces due to the bridge deck motion. For thin airfoil flutter in incompressible flow it has been shown by Theodorsen [46] that the aerodynamic forces due to small oscillations can be derived from basic potential flow theory. To date perhaps the most influential contribution to solving the bridge flutter problem is a simple conceptual framework developed by Scanlan, who noted that the aerodynamic forces due to relatively small bridge deck oscillations can be characterized by fundamental quantities—aerodynamic derivatives or transforms thereof—obtained from measurements performed on the oscillating, rather than the fixed, body [47].

Computational fluid dynamics approaches currently being developed rest on the same basic idea. For some bridge decks it is possible to perform numerical computations of the motion-dependent aerodynamic forces, at least for smooth oncoming flow [48]. The latter restriction is not trivial, since turbulence, like the Reynolds number, can affect the aerodynamics and therefore aeroelastic behavior.

Although flutter is accompanied at all times by shedding of vortices with frequency equal to the flutter frequency, it is a phenomenon distinct from vortex-induced oscillation. The latter entails aeroelastic flow-structure interactions only for flow velocities at which the vortex-shedding frequency is close or equal to the structure's natural frequency. For velocities higher than those at which lock-in occurs the oscillations are significantly weaker than at lock-in (see Sect. 2.1). In contrast, for velocities higher than the critical flutter velocity the strength of flutter oscillations increases monotonically with flow velocity. As was pointed out by Scanlan and Billah [49], the statement made in some physics textbooks that the flutter of the original Tacoma Narrows bridge was a vortex-induced resonant oscillation conflates two distinct phenomena, and is therefore incorrect.

In Sect. 6.1.4.1 we consider the case of two-dimensional bridge deck behavior in smooth flow. Section 6.1.4.2 is concerned, in a two-dimensional context, with bridge deck flutter and buffeting in the presence of aeroelastic phenomena.

1.4.1 Formulation and Analytical Solution of the Two- Dimensional Bridge Flutter Problem in Smooth Flow

The equations of motion of a thin airfoil with linear restoring forces are written as

$$m\ddot{h} + S\ddot{\alpha} + c_h\dot{h} + C_h h = L_h \tag{1.49a}$$

$$S\dot{h} + I\ddot{\alpha} + c_\alpha\dot{\alpha} + C_\alpha\alpha = M_\alpha \tag{1.49b}$$

where h and α are the displacement due to vertical bending and the torsional angle, respectively. A unit span is acted upon by the aerodynamic lift L_h and moment M_α, and has mass m, mass moment of inertia I, static imbalance S (equal to m times the distance a between the center of mass and the elastic center), vertical and torsional restoring forces characterized by the stiffness C_h and C_α, respectively, and viscous damping coefficients c_h and c_α. Theodorsen showed that for small oscillations the expressions for L_h and M_α are linear in h and α and their first and second derivatives [46]. The coefficients in these expressions are referred to as *aerodynamic coefficients* or, more commonly, *flutter derivatives*, and are functions of the reduced frequency $b\omega/U$, where b is the half-chord of the airfoil, ω denotes circular frequency, and U is the smooth flow velocity.

Bridge decks are typically symmetrical, so the distance a and the imbalance S are zero. Scanlan and Tomko proposed expressions applicable to small oscillations that, like Theodorsen's expressions, are linear in h and α and their first and second derivatives [47]. However, as was noted earlier, the flutter derivatives must be obtained from laboratory measurements (or, if possible, by using computational fluid dynamics to solve the Navier–Stokes equation numerically). Tests showed that, just as for airfoils, the flutter derivatives are functions of the reduced frequency. In bridge engineering the reduced frequency is customarily defined as $B\omega/U$, where B is the whole width of the deck (unlike in aeronautical engineering, in which the half-chord is used), and U is the mean wind flow velocity; in addition, it is customary to write the expressions for the lift and moment in terms of real parameters and variables, rather than complex ones, as is common in aeronautical engineering. If the horizontal displacement p is also taken into account—which was not done in Scanlan's original formulation—the equations of motion of a two-dimensional section of a symmetrical bridge deck with linear viscous damping and restoring forces in smooth flow can be written as

$$\begin{aligned} m\ddot{h} + c_h\dot{h} + C_h h &= L_h \\ I\ddot{\alpha} + c_\alpha\dot{\alpha} + C_\alpha\alpha &= M_\alpha \\ m\ddot{p} + c_p\dot{p} + C_p p &= D_p \end{aligned} \tag{1.49c}$$

where h, α, and p are the displacement due to vertical bending, torsion, and horizontal bending, respectively. A unit span is acted upon by the aerodynamic lift L_h, moment M_α, and drag D_p, respectively, has mass m, mass moment of inertia I, vertical, torsional and horizontal restoring forces with stiffness C_h, C_α, and C_p, respectively, and viscous damping coefficients c_h, c_α, and c_p. The expressions for the aeroelastic

forces, including those induced by the horizontal bridge deck displacements p, are written in the form

$$L_h = \tfrac{1}{2}\rho U^2 B \left[K H_1^*(K)\tfrac{\dot{h}}{U} + K H_2^*(K)\tfrac{B\dot{\alpha}}{U} + K^2 H_3^*(K)\alpha + K^2 H_4^*(K)\tfrac{h}{B} + K H_5^*\tfrac{\dot{p}}{U} + K^2 H_6^*(K)\tfrac{p}{B} \right] \tag{1.50a}$$

$$M_\alpha = \tfrac{1}{2}\rho U^2 B \left[K A_1^*(K)\tfrac{\dot{h}}{U} + K A_2^*(K)\tfrac{B\dot{\alpha}}{U} + K^2 A_3^*(K)\alpha + K^2 A_4^*(K)\tfrac{h}{B} + K A_5^*\tfrac{\dot{p}}{U} + K^2 A_6^*(K)\tfrac{p}{B} \right] \tag{1.50b}$$

$$D_p = \tfrac{1}{2}\rho U^2 B \left[K P_1^*(K)\tfrac{\dot{h}}{U} + K P_2^*(K)\tfrac{B\dot{\alpha}}{U} + K^2 P_3^*(K)\alpha + K^2 P_4^*(K)\tfrac{h}{B} + K P_5^*\tfrac{\dot{p}}{U} + K^2 P_6^*(K)\tfrac{p}{B} \right] \tag{1.50c}$$

Equations (1.50a)–(1.50c) do not explicitly include terms in $\ddot{h}, \ddot{\alpha}$ and $\ddot{p}$ (i.e., added mass terms) which are negligible in wind engineering applications; however, they include terms in h and p whose function is to account for changes in the frequency of vibration of the body due to aeroelastic effects. Since these terms are out of phase with their first derivatives but in phase with added mass terms, the latter are in practice absorbed in the terms in h and p. The quantities $\alpha, \dot{h}/U$ and $B\dot{\alpha}/U$ are effective angles of attack and are therefore nondimensional, as are the coefficients H_i^*, A_i^* and P_i^*, to which the designation "flutter derivatives" or "Scanlan derivatives" is usually applied. Each term in Eqs. (1.50a)–(1.50c) can be viewed as similar in form to terms of the type

$$L = \frac{1}{2}\rho U^2 B C_L = \frac{1}{2}\rho U^2 B \frac{dC_L}{d\alpha}\alpha \tag{1.51}$$

for small angle of attack α. Terms such as $K H_i^*$ and $K^2 A_i^*$ are thus analogous to lift coefficient derivatives $dC_L/d\alpha$. These terms are *motional* aerodynamic derivatives, which go over into *steady-state* aerodynamic derivatives such as $dC_L/d\alpha$ for $K \to 0$ (zero frequency), meaning that they are obtained for the oscillating body, rather than under static conditions. The terms $K H_i^*$, $K^2 A_i^*$, and so forth, could be denoted by single symbols. Also, the asterisks could be omitted from the coefficients H_i^* and A_i^*. However, for historical reasons the notation that has gained currency is that of Eqs. (1.50a)–(1.50c). There is no fundamental reason why this could not change, as was suggested for example by Starossek, an advocate of complex, as opposed to real, notation [50]. The perception by some bridge engineers that real notation is more intuitive and transparent undoubtedly accounts for its current wider acceptance.

If plots of the flutter derivatives H_i^*, A_i^* and P_i^* are available from measurements as functions of reduced frequency K, the solution of the flutter equations can be obtained as follows. It is assumed that the expressions for h, α and p are proportional to $e^{i\omega t}$. These expressions are inserted in the equations of motion

$$m\ddot{h} + c_h\dot{h} + C_h h = L_h \tag{1.52a}$$

$$I\ddot{\alpha} + c_\alpha \dot{\alpha} + C_\alpha \alpha = M_\alpha \tag{1.52b}$$

$$m\ddot{p} + c_p \dot{p} + C_p p = D_p \tag{1.52c}$$

The determinant of the amplitudes of h, α, and p is then set to zero. For each value of K a complex equation in ω is obtained. For the lowest value of K denoted by K_c the corresponding equation yields a real (or nearly real) solution denoted by ω_c. The flutter velocity is

$$U_c = \frac{B\omega_c}{K_c}. \tag{1.53}$$

In Eqs. (1.50a)–(1.50c) the terms containing first derivatives of the displacements are measures of the aerodynamic damping. If, among these terms, only those associated with the coefficients H_1^*, A_2^*, and P_1^* are significant, the total (structural plus aerodynamic) damping can be written as

$$c_h - \frac{1}{2}\rho U^2 B K H_1^* \tag{1.54a}$$

$$c_\alpha - \frac{1}{2}\rho U^2 B K A_2^* \tag{1.54b}$$

$$c_p - \frac{1}{2}\rho U^2 B K P_1^* \tag{1.54c}$$

for the vertical, torsional, and horizontal degree of freedom, respectively. For the airfoil case horizontal displacements are negligible, and H_1^* and A_2^* are both negative for all K [6, 46]. The total damping is therefore positive for both h and α. It follows that, in incompressible flow, the airfoil is not capable of experiencing flutter in a single—vertical or torsional—mode. The mechanism for the occurrence of flutter in airfoils therefore always involves coupling between the vertical and torsional modes.

However, under the two-dimensionality assumption, and depending upon the coefficients H_1^* and A_2^*, such coupling is not always involved in the flutter of bridge decks. The original Tacoma Narrows bridge, which collapsed in November 1940, had negligible H_1^* values for all K, meaning that flutter in the vertical degree of freedom was not possible. However, A_2^* was positive for $K > 0.16$ or so. Assuming that the effect of horizontal deck motions was negligible, it is easy to see that, for sufficiently high flow velocity, the total damping given by Eq. (1.54b) is negative, and flutter involving only the torsional degree of freedom would occur. Torsional flutter has in fact occurred (Fig. 6.2) in wind with mean velocity of about 20 m/s. The bridge's susceptibility to flutter was due to the use of a section with an "H" shape (the horizontal line in the "H" representing the deck, and the vertical lines representing the girders supporting it). Owing to its inherent instability this type of bridge section should no longer be used.

An alternative approach to the assessment of a bridge's stability with respect to flutter involves *aerodynamic indicial functions* of a bridge deck section, representing the aerodynamic response of the section to a step change in angle of attack. These functions are derivable from the aerodynamic derivatives. Under the assumption that linear superposition is permissible they allow estimates of transient response. For basic material concerning aerodynamic indicial functions as applied to bridge decks see [51].

1.4.2 Bridge Section Response to Excitation by Turbulent Wind in the Presence of Aeroelastic Effects

The aerodynamic forces induced on a bridge by turbulent wind are due to

1. Aeroelastic forces associated with flutter derivatives
2. Vortex-induced forces
3. Randomly fluctuating forces induced by turbulent flow (buffeting forces).

The expressions for the aeroelastic forces have the same form as for the smooth flow case [Eqs. (1.50a)–(1.50c)]. However, the aerodynamic coefficients H_i^*, A_i^*, P_i^* should be obtained from measurements in turbulent flow, since turbulence may affect the aerodynamics of the bridge deck by changing the configuration of the separation layers and the position of reattachment points. As a simple example we show in Fig. 21 separation layers observed at the upwind corners of a rectangular shape in smooth and turbulent flow. Nearer the body the turbulence transports particles with higher

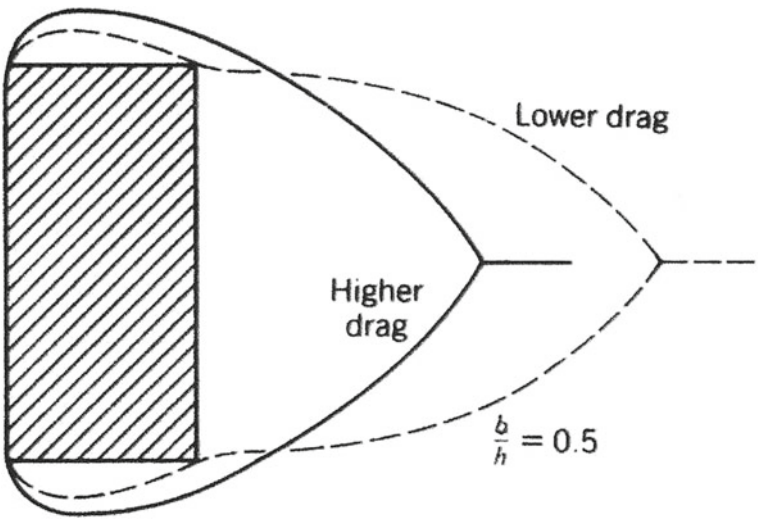

Fig. 21 Separation layers in smooth flow (solid line) and in turbulent flow (interrupted line). After [115]

momentum from the outer flow, thus bringing the separation layers closer to the body and causing reattachment of the flow. This change affects the aerodynamic response; in this particular example the turbulence results in a decreased drag force. Through more complex aerodynamic mechanisms, turbulence can affect the flutter derivatives and, therefore, the flutter velocity—in many instances favorably but possibly also unfavorably. Vortex-induced forces may be neglected unless lock-in occurs. The buffeting forces per unit span may be written as follows:

$$L_b = \frac{1}{2}\rho U^2 B\left[2C_L\frac{u(t)}{U} + \left(\frac{dC_L}{d\alpha} + C_D\right)\frac{w(t)}{U}\right] \tag{1.55a}$$

$$M_b = \frac{1}{2}\rho U^2 B\left[2C_M\frac{u(t)}{U} + \left(\frac{dC_M}{d\alpha}\right)\frac{w(t)}{U}\right] \tag{1.55b}$$

$$D_b = \frac{1}{2}\rho U^2 B\left[2C_D\frac{u(t)}{U}\right]. \tag{1.55c}$$

For example, Eq. (1.55c) is derived from the expression for the total (mean plus fluctuating) drag force D, where

$$D = \bar{D} + D_b = \frac{1}{2}\rho C_D B[U + u(t)]^2, \tag{1.56a}$$

U is the mean flow velocity, $u(t)$ is the horizontal component of the turbulent velocity fluctuation at time t, the mean drag force is defined as

$$\bar{D} = \frac{1}{2}\rho C_D B U^2, \tag{1.57a}$$

and the drag coefficient C_D is measured under turbulent flow conditions. For the two-dimensional case the solution of the buffeting problem in the presence of aeroelastic effects is obtained from Eqs. (1.52a)–(1.52c) in which the right-hand sides consist of the sums $L_h + L_b$, $M_\alpha + M_b$, $D_p + D_b$, respectively. However, even though the two-dimensional case can in some instances provide useful insights into the behavior of a bridge, to be useful in applications to actual bridges the solution must be obtained for the three-dimensional case where the bridge deformation and the aerodynamic forces are functions of position along the span. Such a solution is presented in Sect. 6.2.1.4.

2 Applications

2.1 Suspension-Span Bridges

This section is devoted to practical methods and results applicable to bridge design for wind. Section 6.2.1.1 is a brief overview of current wind tunnel testing methods. It includes examples of mean drag, lift, and moment coefficients measured on a fixed section model for various angles of inclination of the deck with respect to the horizontal, and examples of flutter derivatives obtained from an oscillating section model. Section 6.2.1.2 discusses the three-dimensional torsional divergence analysis of a full bridge. Section 6.2.1.3 is concerned with bridge response to vortex shedding. Section 6.2.1.4 is devoted to the flutter and buffeting analysis of a full-span bridge. Section 6.2.1.5 discusses factors that affect, and methods used to enhance, stability against flutter. Cables in cable-stayed bridges can exhibit severe vibrations due to the combined action of wind and rain. The excitation mechanism of the dynamic wind-water-cable interaction is discussed in [52]. The vibrations can be reduced by using various types of vibration mitigation devices, or by the mechanical processing of the cable surfaces (e.g., the creation on those surfaces of dimples or various protuberances) to prevent the formation of water rivulets on the cables [52–57].

2.1.1 Wind Tunnel Testing of Suspended-Span Bridges

Three types of wind tunnel tests are commonly used for suspended-span bridges:

1. *Tests on models of the full bridge*. Usual model scales are about 1:300–1:500. An example is shown in Fig. 22.
2. *Three-dimensional partial bridge models*. The supports for such partial models may consist of taut wires, and the tests are usually designed to mimic motion in the fundamental vibration mode of the bridge.
3. *Tests on section models*. Such tests are relatively inexpensive and yield basic information usable in parametric studies. They afford more flexibility than tests on models of the full bridge, which may be used to verify results of analyses based on section model tests. Also, they can be conducted in conventional wind tunnels at relatively large model scales (1:50 or even 1:25), thus allowing a better modeling of possibly important details and reducing possible distortions due to Reynolds number effects (Fig. 23).

Such distortions can be significant. Figure 24a, b show results of tests conducted in smooth flow in the high-pressure wind tunnel at Göttingen on a section model of the bridge over the Great Belt, Denmark [58]. It may be surmised that the presence of turbulence in the oncoming flow—which was not simulated in the high-pressure wind tunnel—would reduce those distortions by entraining fluid particles with higher momentum from the outer flow into the separation region, thus bringing the separation layers of Fig. 24a closer to those of Fig. 24b. It was concluded in [58] that the drag

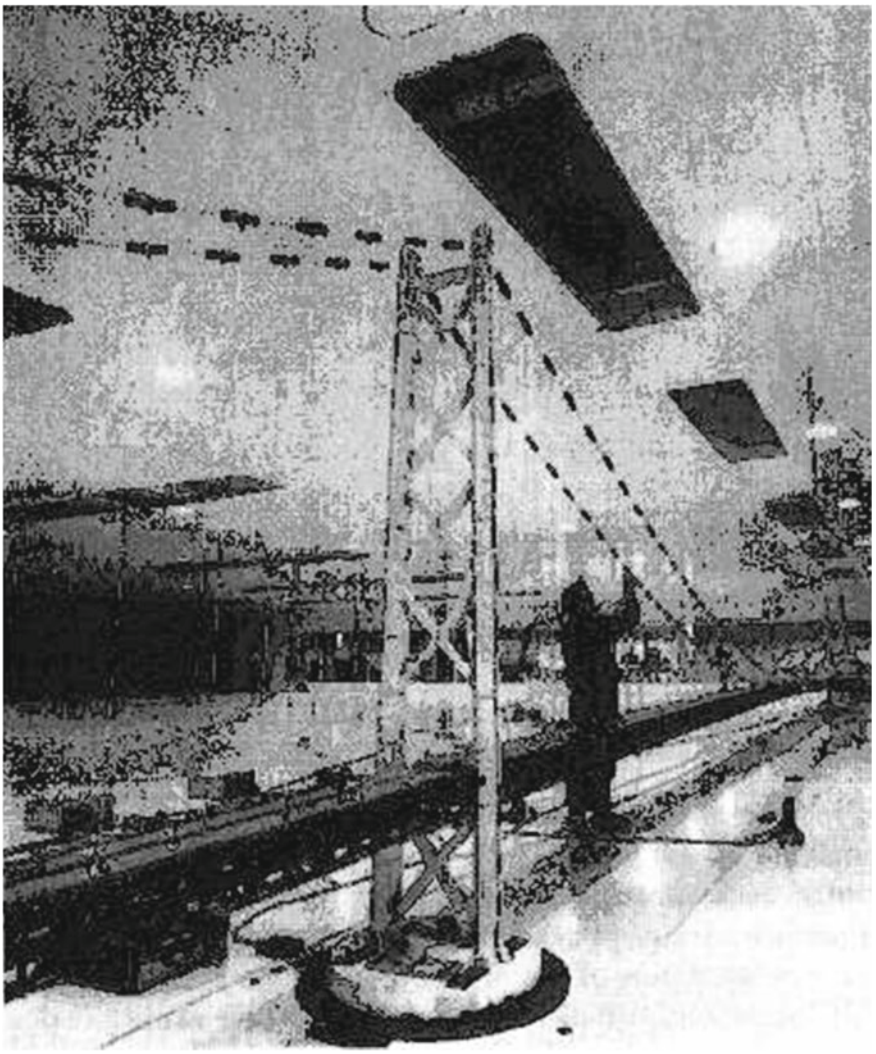

Fig. 22 Model of Akashi Strait suspension bridge (courtesy of T. Miyata, Yokohama National University, and M. Kitagawa, Honshu-Shikoku Bridge Authority, Tokyo)

coefficient obtained at the lower Reynolds numbers typical of conventional wind tunnels was in this case conservative for bridge design. From measurements reported for a series of deck shapes it was stated in [59] that, for those shapes, results obtained in conventional wind tunnel tests were conservative from the overall point of view of bridge design for wind. Whether or not such statements can be made in more general terms is not clear at this time.

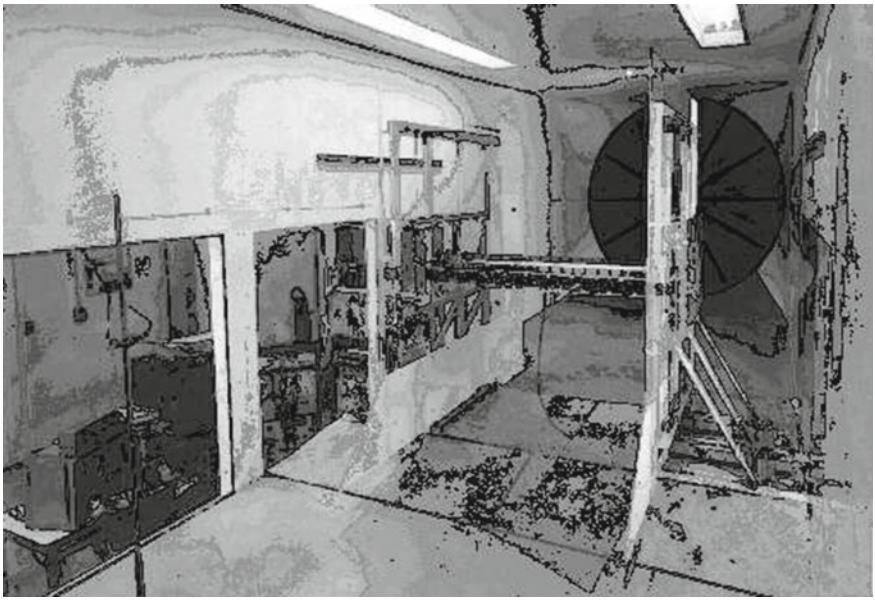

Fig. 23 Section model of the Halifax Narrows Bridge (courtesy of Boundary-Layer Wind Tunnel Laboratory, University of Western Ontario)

The information sought in section model tests consists of mean drag, lift, and moment coefficients measured under static conditions as functions of angle α, and of flutter derivatives. For some bridge decks flutter derivatives obtained under turbulent wind conditions yield higher critical flutter velocities than their smooth flow counterparts (e.g., [60]), but there are instances where this is not the case. For example, based on section model tests, the prototype flutter velocity for the renovated Lion's Gate Bridge was the same, to within about 2%, for both smooth and turbulent flow [61]. For important bridges it is prudent to perform tests under low or no turbulence conditions *and* under standard turbulence conditions.

For a section model of the New Burrard Inlet Crossing measured mean drag, lift, and moment coefficients plotted against the angle α are shown in Fig. 25 [62]. For a study of the Golden Gate Bridge measured flutter derivatives at a 0° mean angle of attack (angle of inclination between the mean position of the deck and the horizontal) are shown in Figs. 26 and 27 [6, 63]. Flutter derivatives measured at a 5° mean angle of attack are shown in Fig. 28 [63].

Measurements of flutter derivatives can be made with the section model being subjected to forced oscillations, or with the section model undergoing free oscillations [63]. Note that for an adequate modeling of the flutter of very long bridges (e.g., the Akashi-Kaikyo bridge, whose main span is 1,990 m long) all 18 flutter derivatives [see Eqs. (1.50a)–(1.50c)] are needed in the calculations [79].

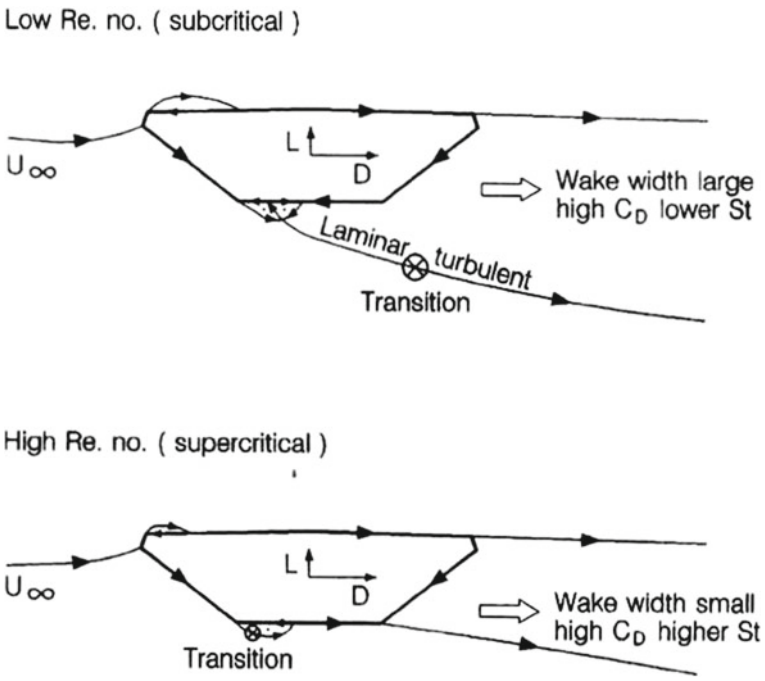

Fig. 24 Interpretation of oil flow pictures indicating flow fields at (a) low Reynolds numbers (sub-critical conditions) and (b) high Reynolds numbers (super-critical conditions)

Research on the identification of (i) coefficients for time domain flutter analysis and (ii) flutter derivatives, and on a suspension system for section model studies, is reported in [65–68].

2.1.2 Torsional Divergence Analysis for a Full Bridge

A linear torsional divergence analysis requires knowledge of the moment coefficient $C_M(\alpha)$ measured under static conditions and of the torsional flexibility matrix C_T, whose elements c_{ij} represent the torsional angles α_i at $x = x_i$ induced by a unit torsional moment acting at $x = x_j$. Let the torsional moments acting at $x = x_j$ be denoted by M_j. We de/note by $\{\alpha\}$ and $\{M\}$, respectively, the column vectors of the torsional angles α_i and of the moments

$$M_j = \frac{1}{2}\rho U^2 B^2 \Delta L_j C_M(\alpha_J) \tag{2.1}$$

where ΔL_j is the length of the span element associated with x_j, and $C_M(\alpha_j)$ is the moment coefficient corresponding to the angle α_j. The following matrix equation holds:

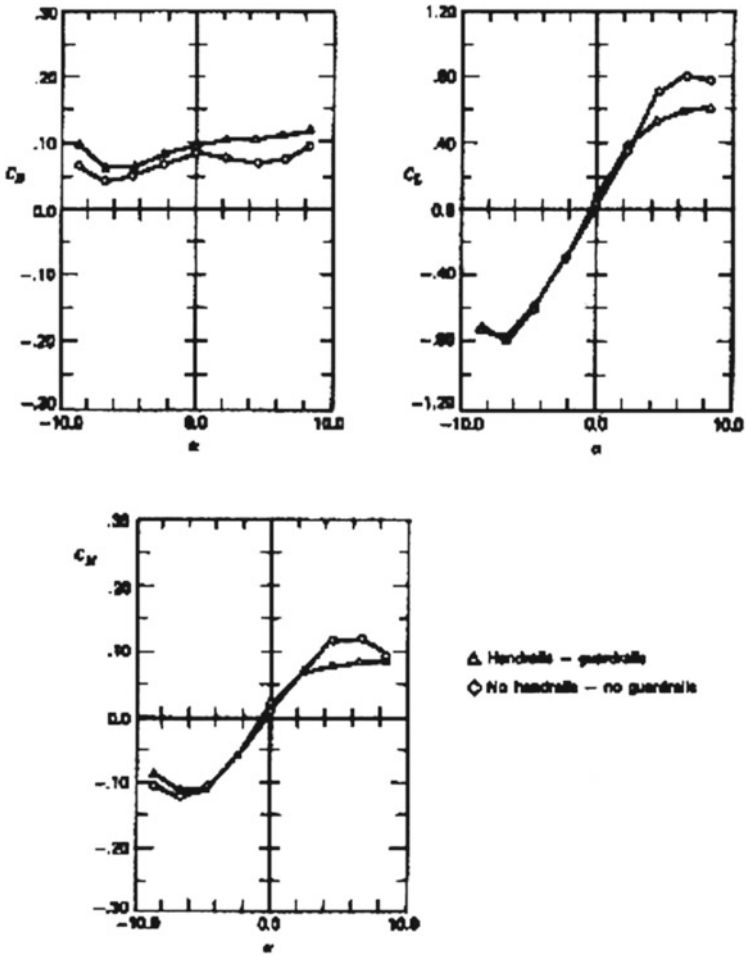

Fig. 25 Drag. lift, and aerodynamic coefficients for proposed deck of New Burrard Inlet Crossing [61] (courtesy of the National Aeronautical Establishment, National Research Council of Canada)

$$\{\alpha\} = C_T\{M\}. \tag{2.2}$$

In Eq. (2.2) the variables are torsional angles along the span. The velocity U_c for which the solution of Eq. (2.2) diverges is the *critical torsional divergence velocity*. If $C_M(\alpha)$ can be approximated by the linear function

$$C_M(\alpha) \approx \frac{dC_M}{d\alpha}\alpha + C_{M0} \tag{2.3}$$

where $C_{M0} = C_M^{(0)}$, then, using the notation

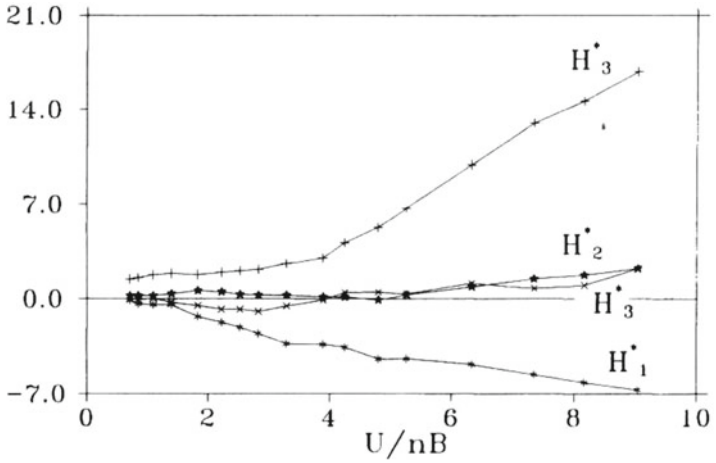

Fig. 26 Aerodynamic coefficients $H_i^*(i = 1, 2.3.4)$, Golden Gate Bridge (courtesy of Dr. J. D. Raggett, West Wind Laboratory, Carmel, CA)

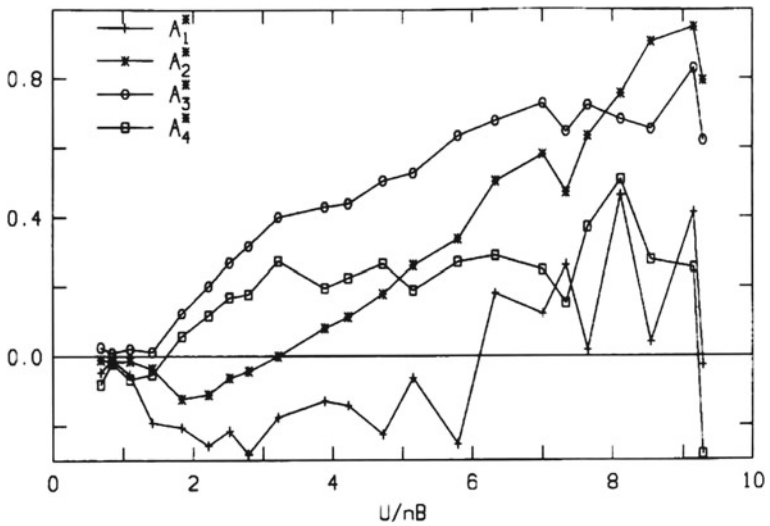

Fig. 27 A_i^* flutter derivatives of Golden Gate bridge at 0°$(i = 1, 2.3.4)$

$$\frac{1}{p} = \frac{1}{2}\rho U^2 B^2 \Delta L_i \tag{2.4}$$

where $\Delta L_i = \Delta L$ for all i, Eq. 2.2 can be written as

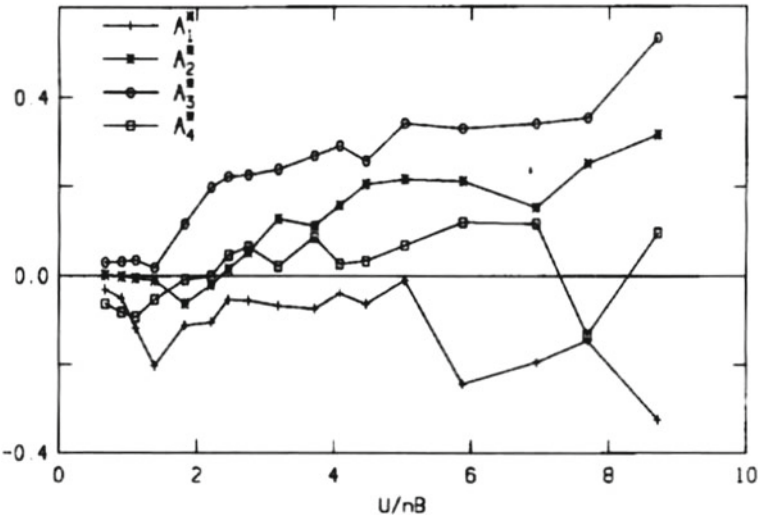

Fig. 28 A_i^* flutter derivatives of Golden Gate bridge at 5°($i = 1$, 2.3.4). From [63]

$$\{\alpha\} = C_T \frac{1}{p} \left\{ \frac{dC_M}{d\alpha} + C_{M0} \right\} \tag{2.5}$$

or

$$\left[pI - \frac{dC_M}{d\alpha} C_T \right] \{\alpha\} = C_T \{C_{M0}\}. \tag{2.6}$$

Equation (2.6) has divergent solutions if the determinant

$$\left| pI - \frac{dC_M}{d\alpha} C_T \right| = 0. \tag{2.7}$$

The largest eigenvalue of Eq. (2.7) yields the critical torsional divergence velocity through Eq. (2.4).

Note that if the moment induced by the mean wind speed is negative (i.e., if the bridge deck subjected to the action of the mean wind speed twists so that the wind approaches the upper side of the deck), according to the linear analysis torsional divergence will not occur. The case of the nonlinear dependence of C_M upon α can be dealt with by solving Eq. (2.2) in which C_M is expressed in terms of a power series in α.

2.1.3 Locked-In Vortex-Induced Response

Bridge decks supported by open trusses usually do not experience vortex-induced oscillations, owing to the shredding of the vorticity by the truss members. However,

vortex-induced response can be a problem for bluff bridge decks with a box or open-box shape. Aerodynamic design can help to reduce significantly or even eliminate this problem, as is seen in Fig. 29 [69], which shows the measured amplitudes of vortex-induced deflections for alternative shapes of the bridge section. The largest deflections occurred for the open-box section. A closed box fared better, possibly owing to its greater stiffness, rather than for aerodynamic reasons. However, the provision of fairings is advantageous from an aerodynamic viewpoint, as is, more generally, the extent to which the bridge section is streamlined. Flow visualizations showed that added fairings are effective in streamlining the flow when the deck is in a twisted position. This can be seen in Fig. 30b in which, owing in part to

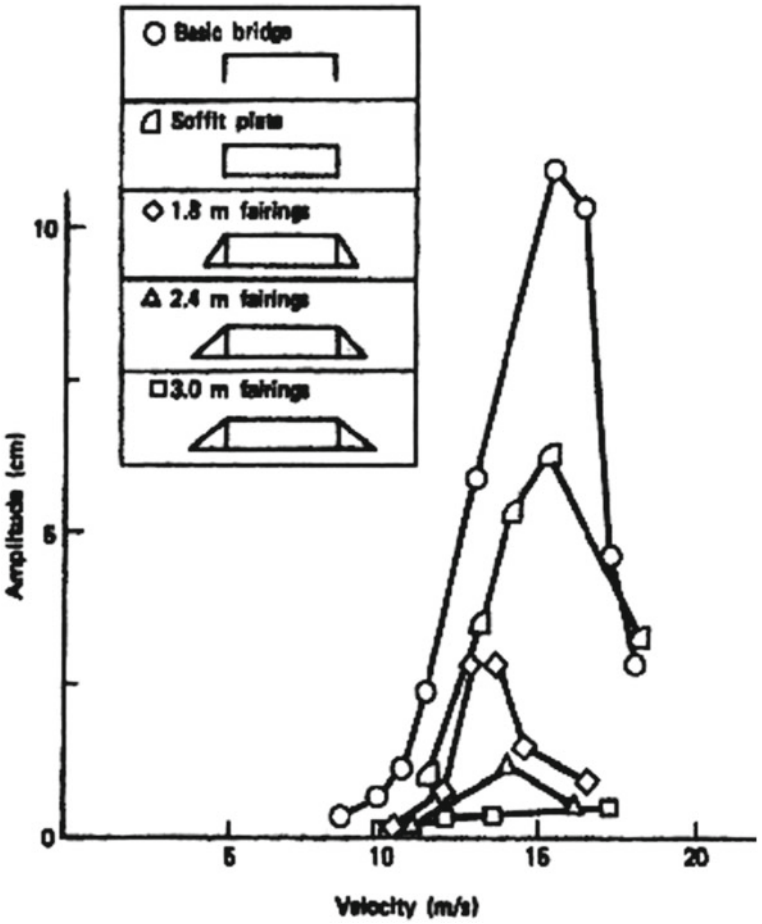

Fig. 29 Vertical amplitudes of vortex-induced deflections for various bridge deck sections of the proposed Long Creek's bridge [65] (courtesy of the National Aeronautical Establishment, National Research Council of Canada)

those fairings, the turbulence zone above the upper part of the deck is considerably smaller than for the section shown in Fig. 30a. For the Great Belt Bridge in Denmark vortex-induced response suppression was achieved with remarkable effectiveness by appending guide vanes to the bridge [70]. The steady-state amplitude h_0 of the vortex-induced response may be calculated by using Eq. (1.20), in which we substitute the notation $KH_1^*(K)$ for $Y_1(K)$. The result is

$$\frac{h_0}{B} = 2\left[\frac{H_1^* - 4\frac{\zeta m}{\rho B^2}}{\epsilon H_1^*}\right]^{\frac{1}{2}} \tag{2.8}$$

Equation (2.8) is applied to a full bridge as follows [6]. In the equation of motion of the bridge

$$m(\ddot{h} + 2\zeta\omega_h\dot{h} + \omega_h^2 h) = \frac{1}{2}\rho U^2 BKH_1^*(1 - \epsilon\frac{h^2(x,t)}{B^2})\frac{\dot{h}(x,t)}{U} \tag{2.9}$$

[see Eq. (1.20)], it is assumed

$$h(x,t) = \phi(x)B\xi(t), \tag{2.10}$$

where $\phi(x)$ is the dimensionless mode with frequency ω_n that responds to the locked-in vortex shedding, and the corresponding generalized coordinate is

$$\xi(t) = \xi_0 \cos\omega_h t. \tag{2.11}$$

Inserting h from Eq. (2.10) into (2.9) and multiplying the result by $B\phi(x)$, the motion of a segment of length dx associated with the spanwise coordinate x is described by the equation

$$\begin{aligned} m(x)B^2\ &\phi^2(x)[\ddot{\xi}(t) + 2\zeta\omega_h\dot{\xi}(t) + \omega_h^2\xi(t)]dx \\ &= \tfrac{1}{2}\rho U B^3 K H_1^*[1 - \epsilon\phi^2(x)\xi^2(t)]\dot{\xi}(t)\phi^2(x)f(x)dx \end{aligned} \tag{2.12}$$

in which we introduced a function $f(x)$ to account for the spanwise loss of coherence of the vortex-related forces. It is suggested in [6] that it may be appropriate to model the function $f(x)$ by the mode shape $\phi(x)$, normalized to unit value at its maximum ordinate. For example, if $\phi(x)$ is a half-sinusoid over a span l, it would be assumed

$$f(x) = \sin\pi x/l. \tag{2.13}$$

Integration of Eq. (2.12) over the full length of the bridge yields the equation

$$I\left[\ddot{\xi} + 2\zeta\omega_h\dot{\xi} + \omega_h^2\xi\right] = \frac{1}{2}\rho U B^2 LKH_1^*[C_2 - \epsilon C_4]\dot{\xi} \tag{2.14}$$

where I denotes the full-bridge generalized inertia of the mode $\phi(x)$, and

$$C_2 = \int_0^l \frac{\phi^2(x) f(x) dx}{l}, \quad C_4 = \int_0^l \frac{\phi^4(x) f(x) dx}{l}. \tag{2.15}$$

Under the assumption (2.13), $C_2 = 0.42$ and $C_4 = 0.34$. At steady-state amplitude, Eq. (2.14) and conditions similar to those that led to Eqs. (1.17) and (1.20) yield the amplitude

$$\xi_0 = 2\left[\frac{C_2 H_1^* - 4\zeta I/(\rho B^4 l)}{\epsilon C_4 H_1^*}\right]^{\frac{1}{2}}. \tag{2.16}$$

Numerical example: Response to vortex-shedding of the original Tacoma Narrows bridge [6]

The original Tacoma Narrows bridge experienced considerable vortex-induced oscillations before its collapse due to torsional flutter. Pertinent data are: $n_1 = 0.66\,\text{Hz}$ (natural frequency), $B = 11.9\,\text{m}$, $\rho = 1.23\,\text{kg/m}^3$, $m = 4250\,\text{kg/m}$, $I \cong \int_0^l mB^2\phi^2 dx$, $\phi = \sin \pi x/l$, so $I = mB^2 l/2\,\text{kg m}^2$. It is assumed $\zeta = 0.0025$, $\text{K} = B\omega/U = 3.13$, $U = 15.7$ m/s, $H_1^* = 1.19$, $\epsilon = 4170$ [6]. Inserting these values into Eq. (2.16), and remembering that $C_2 = 0.42$ and $C_4 = 0.34$, we obtain $\xi_0 = 0.03$. Equation (2.10) yields a peak-to-peak amplitude $2\xi_0 B = 0.71\,\text{m}$. This is reasonably consistent with observations at the site, according to which for the mode of the type considered in our calculations the double amplitude did not exceed 0.9 m.

According to [75], the vortex-induced response of a bridge in flow with low-frequency fluctuations is smaller than would be the case in smooth flow; this is attributed to the weakening effect on the vorticity shed in the bridge's wake of phase differences between the low-frequency flow fluctuations on the one hand and the bridge oscillations on the other. Wind tunnels tend to reproduce atmospheric turbulence scales inadequately. Therefore low-frequency flow fluctuations tend also to be reproduced inadequately, as are the inhibiting effects of those fluctuations on the vortex-induced oscillations. The latter may therefore be overestimated by laboratory test results.

2.1.4 Flutter and Buffeting of a Full-Span Bridge

In this section we extend to a full bridge the methods developed in Sect. 6.1.4.2 for the two-dimensional analysis of flutter and buffeting for bridge sections. We assume that the deformations are small so that the behavior of the bridge and of the aeroelastic and buffeting forces is linear.

Let $h(x,t)$, $p(x,t)$, and $\alpha(x,t)$ denote, respectively, the vertical, horizontal (sway), and torsional (twist) displacements of the spanwise station defined by the coordinate x; $h_i(x)$, $p_i(x)$, and $\alpha_i(x)$ the ith modal displacements at x; and $\xi_i(t)$,

I_i, ω_i and ζ_i the generalized coordinate, generalized inertia, natural frequency, and damping ratio in the ith mode. We have

$$h(x,t) = \sum_{i=1}^{N} h_i(x) B \xi_i(t) \tag{2.17a}$$

$$p(x,t) = \sum_{i=1}^{N} P_i(x) B \xi_i(t) \tag{2.17b}$$

$$\alpha(x,t) = \sum_{i=1}^{N} \alpha_i(x) \xi_i(t). \tag{2.17c}$$

The equation of motion in the ith mode is

$$I_i(\ddot{\xi}_i + 2\zeta_i \omega_i \dot{\xi}_i + \omega_i^2 \xi_i) = Q_i \tag{2.18}$$

where the Generalized force Q_i is defined by

$$Q_i = \int_0^l [(L_{ae} + L_b) h_i B + (D_{ae} + D_b) p_i B + (M_{ae} + M_b) \alpha_i] dx, \tag{2.19}$$

the aeroelastic lift, drag, and moment are

$$\begin{aligned} L_{ae} = \tfrac{1}{2}\rho U^2 B \Big[& K H_1^* \tfrac{\dot{h}}{U} + K H_2^* \tfrac{B\dot{\alpha}}{U} + K^2 H_3^* \alpha \\ & + K^2 H_4^* \tfrac{h}{B} + K H_5^* \tfrac{\dot{p}}{U} + K^2 H_6^*(K) \tfrac{p}{B} \Big] \end{aligned} \tag{2.20a}$$

$$\begin{aligned} D_{ae} = \tfrac{1}{2}\rho U^2 B \Big[& K P_1^* \tfrac{\dot{h}}{U} + K P_2^* \tfrac{B\dot{\alpha}}{U} + K^2 P_3^* \alpha \\ & + K^2 P_4^* \tfrac{p}{B} + K P_5^* \tfrac{\dot{p}}{U} + K^2 P_6^*(K) \tfrac{h}{B} \Big] \end{aligned} \tag{2.20b}$$

$$\begin{aligned} M_{ae} = \tfrac{1}{2}\rho U^2 B^2 \Big[& K A_1^* \tfrac{\dot{h}}{U} + K A_2^* \tfrac{B\dot{\alpha}}{U} + K^2 A_3^* \alpha \\ & + K^2 A_4^* \tfrac{h}{B} + K A_5^* \tfrac{\dot{p}}{U} + K^2 A_6^*(K) \tfrac{p}{B} \Big] \end{aligned} \tag{2.20c}$$

respectively, and the buffeting forces are

$$L_b = \frac{1}{2}\rho U^2 B \left[2C_L \frac{u(x,t)}{U} + \left(\frac{dC_L}{d\alpha} + C_D \right) \frac{w(x,t)}{U} \right] = \frac{1}{2}\rho U^2 B \breve{L}_b(x,t) \tag{2.21a}$$

$$D_b = \frac{1}{2}\rho U^2 B \left[2C_D \frac{u(x,t)}{U} \right] = \frac{1}{2}\rho U^2 B \breve{D}_b(x,t) \tag{2.21b}$$

$$M_b = \frac{1}{2}\rho U^2 B^2 \left[2C_M \frac{u(x,t)}{U} + \left(\frac{dC_M}{d\alpha} \right) \frac{w(x,t)}{U} \right] = \frac{1}{2}\rho U^2 B^2 \breve{M}_b(x,t). \tag{2.21c}$$

The aerodynamic coefficients and derivatives in Eqs. (2.21a)–(2.21c) should be based on measurements performed in turbulent flow, unless the flow is assumed to be smooth, in which case there is no buffeting by oncoming flow turbulence. Effects of turbulence created by the flow-structure interaction (signature turbulence) are assumed to be negligible. This assumption needs to be verified, and may not be acceptable (for example in the case of Fig. 30a). Effects of vortices shed in the wake of the deck may be assumed to be negligible unless the flow speed being considered is close to the speeds associated with lock-in.

The multimodal system of equations of motion of the bridge can be written in matrix notation:

$$\mathbf{I}\xi'' + \mathbf{A}\xi' + \mathbf{B}\xi = \mathbf{Q}_b(s) \tag{2.22}$$

where ξ is the generalized coordinate vector, $s = Ut/B$, and $\mathbf{I}$ is an identity matrix. $\mathbf{A}$ and $\mathbf{B}$ are the damping and stiffness matrices of the system, respectively, and include terms associated with both structural and aerodynamic damping and stiffness. $\mathbf{Q}_b$ is the generalized buffeting force vector. The terms of the matrices $\mathbf{A}$, $\mathbf{B}$, and $\mathbf{Q}_b$ are

$$A_{ij}(K) = 2\zeta_i K_i \delta_{ij} - \frac{\rho B^4 l K}{2I_i} \left[G^{H_1^*}_{h_i h_j} + G^{H_2^*}_{h_i a_j} + G^{H_5^*}_{h_i p_j} + G^{P_1^*}_{P_i P_j} + G^{P_2^*}_{p_i \alpha_j} + G^{P_5^*}_{p_i h_j} + G^{A_1^*}_{\alpha_i h_j} + G^{A_2^*}_{\alpha_i \alpha_j} + G^{A_5^*}_{\alpha_i p_j} \right] \tag{2.23a}$$

$$B_{ij}(K) = K_i^2 \delta_{ij} - \frac{\rho B^4 l K^2}{2I_i} \left[G^{H_3^*}_{h_i \alpha_j} + G^{H_4^*}_{h_i h_j} + G^{H_6^*}_{h_i p_j} + G^{P_3^*}_{P_i P_j} + G^{P_4^*}_{p_i p_j} + G^{P_6^*}_{p_i h_j} + G^{A_3^*}_{\alpha_i \alpha_j} + G^{A_4^*}_{\alpha_i h_j} + G^{A_6^*}_{\alpha_i p_j} \right] \tag{2.23b}$$

$$Q_{bi}(K) = \frac{\rho B^4 l}{2I_i} \int_0^l [\breve{L}_b(x,s) h_i + \breve{D}_b(x,s) p_i + \breve{M}_b(x,s) \alpha_i] \frac{dx}{l} \tag{2.23c}$$

where δ_{ij} is the Kronecker delta symbol, and the modal integrals are given by expressions of the type

$$G^{H_3^*}_{h_i \alpha_j} = \int_0^l H_3^*(K,x) h_i(x) \alpha_i(x) \frac{dx}{l}. \tag{2.24}$$

The coordinate x indexes information on the deck cross-section (which may vary along the span) and the mean angle of attack induced by the mean flow speed. For each vibration mode that angle of attack varies along the span. The flutter derivatives are therefore included under the integral sign [as in Eq. (2.24)] even if the cross-section of the deck is uniform along the span. Expressions of the type (2.24) imply that the aeroelastic forces are perfectly correlated along the span. This is not truly the case, but some measurements suggest that the error inherent in this assumption is small [76]. The equations of motion obtained by taking into account only diagonal terms ($i = j$) in the matrices $\mathbf{A}$ and $\mathbf{B}$ represent the single-degree-of-freedom, uncoupled

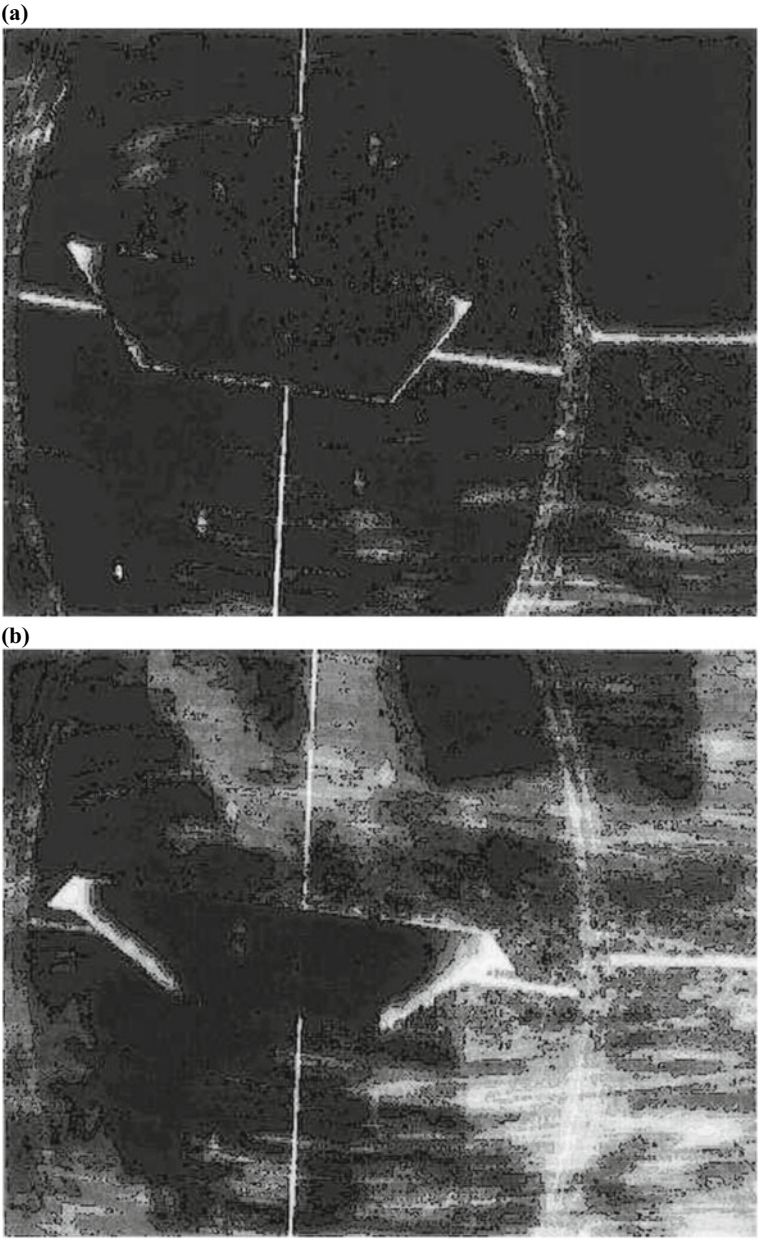

Fig. 30 **a** Visualization of water flow over a bridge model deck section (courtesy of the National Aeronautical Establishment, National Research Council of Canada). **b** Visualization of water flow over a partially streamlined bridge model deck section (courtesy of the National Aeronautical Establishment, National Research Council of Canada)

equations. The off-diagonal terms (corresponding to $i \neq j$) introduce the aeroelastic coupling.

Flutter analysis

Denote the Fourier transform of ξ_i by

$$\bar{\xi}_i(K) = \lim_{T\to\infty} \int_0^T \xi_i(s) e^{-jKs} ds \tag{2.25}$$

where $j = \sqrt{-1}$. The Fourier transform of Eq. (2.22) is

$$\mathbf{E}\bar{\xi} = \bar{\mathbf{Q}}_b \tag{2.26}$$

where the terms of the matrix $\mathbf{E}$ are

$$E_{ij} = -\omega^2 (B/U)^2 \delta_{ij} + j\omega (B/U) K A_{ij}(K) + B_{ij}(K). \tag{2.27}$$

The flutter condition is identified by solving the eigenvalue problem

$$E\bar{\xi} = 0. \tag{2.28}$$

Equation (2.28) has nontrivial solutions if the real and imaginary parts of the determinant of $\mathbf{E}$ vanish. The solutions of interest are sought as follows. For a fixed value of K seek the value of ω in the frequency range of interest until the real part of the determinant of $\mathbf{E}$ vanishes. Repeat the process for successive values of K until both the real part and the imaginary part of the determinant of $\mathbf{E}$ vanish for the same value of ω. That value of ω is the flutter frequency. The flutter speed is equal to $\omega B/K$, where K has the value that yielded the flutter frequency ω. For a multi-modal problem the same procedure must be carried out a number of times equal to the number of modes. The largest solution of K corresponds to the critical flutter condition. The mode corresponding to that solution is the dominant mode in the flutter condition. The eigenvector ξ yields the shape of the flutter oscillatory motion, that is, the relative participation in the flutter motion of each vibration mode [Eqs. (2.17a)–(2.17c)]. Note that in the linear formulation just described the flutter condition is independent of the buffeting excitation.

The flutter derivative P_1^* may be obtained by equating the following two expressions for the drag:

$$D = \frac{1}{2}\rho (U = \dot{p})^2 B C_D \tag{2.29a}$$

$$D = \frac{1}{2} \frac{\rho U^2 B K P_1^* \dot{p}}{U}. \tag{2.29b}$$

If the term in $\dot{p}^2$ is neglected from Eq. (2.29a),

$$P_1^* = -2C_D/K. \tag{2.30}$$

For a streamlined box and an H-shape section Eq. (2.30) was consistent with measurements up to reduced frequencies of $Un/B = 15$. However, for higher frequencies Eq. (2.30) was found to underestimate the measured values of P_1^*.

Buffeting analysis

We develop the buffeting analysis with a view to obtaining expressions for the spectral density of the bridge deck response. The Fourier transform of the generalized buffeting force may be written as

$$\bar{\mathbf{Q}}_b = \frac{1}{2}\rho B^4 l \begin{Bmatrix} \frac{1}{I_1}\int_0^l \bar{F}_{b_1}\frac{dx}{l} \\ \frac{1}{I_2}\int_0^l \bar{F}_{b_2}\frac{dx}{l} \\ \cdot \\ \cdot \\ \cdot \\ \frac{1}{I_n}\int_0^l \bar{F}_{b_n}\frac{dx}{l} \end{Bmatrix}, \tag{2.31}$$

$$\overline{F}_{bi}(x, K) = \overline{L}_b(x, K)h_i(x) + \overline{D}_b(x, K)p_i(x) + \overline{M}_b(x, K)\alpha_i(x, K) \tag{2.32}$$

or, in view of Eqs. (2.21a)–(2.21c) and (2.23c),

$$\begin{aligned} \overline{F}_{b_i}(x, K) = \tfrac{1}{U}\ \{&[2C_L h_i(x_A) + 2C_D p_i(x_A) + +2C_M\alpha_i(x_A)]\overline{u}(K) \\ &+[(C'_L + C_D)h_i(x_A) + C'_D p_i(x_A) + C'_M\alpha_i(x_A)]\overline{w}(K)\}. \end{aligned} \tag{2.33}$$

Denoting the transpose of the complex conjugate of the vector $\overline{\mathbf{Q}}_b$ by $\overline{\mathbf{Q}}_b^{*T}$, we have

$$\overline{\mathbf{Q}}_b\overline{\mathbf{Q}}_b^{*T} = \left(\frac{\rho B^4 l}{2}\right)^2$$

$$\begin{bmatrix} \frac{1}{I_1 I_1}\int_0^l\int_0^l \overline{F}_{b_1}\overline{F}^*_{b_1}\frac{dx_A}{l}\frac{dx_B}{l} & \cdots & \frac{1}{I_1 I_n}\int_0^l\int_0^l \overline{F}_{b_1}\overline{F}^*_{b_n}\frac{dx_A}{l}\frac{dx_B}{l} \\ & \cdot & \\ & \cdot & \\ \frac{1}{I_n I_1}\int_0^l\int_0^l \overline{F}_{b_n}\overline{F}^*_{b_1}\frac{dx_A}{l}\frac{dx_B}{l} & \cdots & \frac{1}{I_n I_n}\int_0^l\int_0^l \overline{F}_{b_n}\overline{F}^*_{b_n}\frac{dx_A}{l}\frac{dx_B}{l} \end{bmatrix} \tag{2.34}$$

By definition, the power spectral density of a function ϕ is

$$S_{\phi\phi}(\omega) = \lim_{T\to\infty} \frac{2}{T}\overline{\phi\phi} \tag{2.35}$$

where $\phi \equiv \phi(x_A)$ is a stationary stochastic process at a point with coordinate x_A. A similar expression holds for the cross-spectral density of $\phi(x_A)\phi(x_B)$. From Eqs. (2.34) and (2.35) a spectral density matrix with the following terms can be developed:

$$\begin{aligned} S_{Q_{b_i}} S_{Q_{b_j}}(K) = \left(\frac{\rho B^4 l}{2U}\right)^2 \frac{1}{I_i I_j} \int_0^l \int_0^l \{&\overline{q}_i(x_A)\overline{q}_j(x_B) S_{uu}(x_A, x_B, K) \\ &+ \bar{r}_i(x_A)\overline{r}_j(x_B) S_{ww}(x_A, x_B, K) \\ &+ [\overline{q}_i(x_A)\overline{r}_j(x_B) \\ &+ \overline{r}_i(x_A)\overline{q}_j(x_B)] C_{uw}(x_A, x_B, K)\} dx_A dx_B, \end{aligned} \tag{2.36}$$

$$\overline{q}_i(x) = 2[C_L h_i(x) + C_D p_i(x) + C_M \alpha_i(x)], \tag{2.37}$$

$$\overline{r}_j(x) = (C'_L + C_D) h_j(x) + C'_D p_j(x) + C'_M \alpha_j(x), \tag{2.38}$$

$S_{uu}(x_A,\ x_B,\ K)$ is the cross-spectral density of the horizontal wind speed fluctuations u at the spanwise coordinates x_A and x_B, $S_{ww}(x_A, x_B, K)$ is the cross-spectral density of the vertical wind speed fluctuations w at x_A and x_B, $C_{uw}(x_A, x_B, K)$ is the co-spectrum of u at x_A and w at x_B. It is assumed in Eq. (2.36) that the quadrature spectrum of u and w is negligible. Aerodynamic admittances are assumed to be equal to unity; in other words the dependence upon frequency of the relation between wind speed fluctuations and the fluctuating forces they induce is neglected. This may lead to a slight but likely negligible overestimation of the response. The power spectral density matrix $\mathbf{S}_{\xi\xi}$ of the generalized coordinate vector ξ is obtained from Eq. (2.39) in terms of the matrix $\mathbf{E}$ and the matrix $\mathbf{S}_{Q_b Q_b}$ of the spectral density of the generalized force vector $\mathbf{Q}_b$, that is,

$$\mathbf{S}_{\xi\xi}(K) = \mathbf{E}^{-1} S_{Q_b Q_b} \{[\mathbf{E}^*]^T\}^{-1} \tag{2.39}$$

The coupling between modes is due to the off-diagonal terms in the matrix $\mathbf{E}$. The power spectral density of the displacements, obtained from Eqs. (2.17a)–(2.17c), is

$$S_{hh}(x, K) = \sum_{i,j}\sum_{i,j} B^2 h_i(x) h_j(x) S_{\xi_i\xi_j}(K) \tag{2.40a}$$

$$S_{pp}(x, K) = \sum_{i,j}\sum_{i,j} B^2 p_i(x) p_j(x) S_{\xi_i\xi_j}(K) \tag{2.40b}$$

$$S_{\alpha\alpha}(x, K) = \sum_{i,j}\sum_{i,j} \alpha_i(x)\alpha_j(x) S_{\xi_i\xi_j}(K) \tag{2.40c}$$

where the summations are carried out over the number of modes being considered. The mean square values of the displacements are

$$\sigma_h^2(x) = \int_0^\infty S_{hh}(x, n)dn \tag{2.41a}$$

$$\sigma_p^2(x) = \int_0^\infty S_{pp}(x, n)dn \tag{2.41b}$$

$$\sigma_\alpha^2(x) = \int_0^\infty S_{\alpha\alpha}(x, n)dn \tag{2.41c}$$

where $n = \omega/2\pi$ is the frequency.

The cross-spectral density of the horizontal velocity fluctuations u, the cross-spectral density of the vertical fluctuations w, and the co-spectrum of u acting at x_1 and w acting at x_2 may be described empirically by the expressions

$$S_{uu}(x_1, x_2, n) \cong S_{uu}(\omega) \exp\left[\frac{c_u n|x_1 - x_2|}{U}\right] \tag{2.42a}$$

$$S_{ww}(x_1, x_2, n) \cong S_{ww}(\omega) \exp\left[\frac{c_w n|x_1 - x_2|}{U}\right] \tag{2.42b}$$

$$C_{uw}(x_1, x_2, n) \cong C_{uw}(\omega) \exp\left[\frac{c_{uw} n|x_1 - x_2|}{U}\right] \tag{2.42c}$$

respectively, where tentative values of the exponential decay coefficients in Eqs. (2.42a)–(2.42c) and (2.43a)–(2.43c) are $c_u \cong 15$, $c_w \cong 8$, $c_{uw} \cong 8$ [6]

$$S_{uu}(\omega) \equiv S_{uu}(x, x, \omega) = \frac{200 z u_*^2}{U(1 + 50nz/U)^{\frac{5}{3}}} \tag{2.43a}$$

$$S_{ww}(\omega) \equiv S_{ww}(x, x, \omega) = \frac{3.36 z u_*^2}{U(1 + 10nz/U)^{\frac{5}{3}}} \tag{2.43b}$$

$$C_{uw}(\omega) \equiv C_{uw}(x, x, \omega) = \frac{14 z u_*^2}{U(1 + 9.6nz/U)^{2.4}}, \tag{2.43c}$$

$$u_* = \frac{kU(z)}{ln(z/z_0)} \tag{2.44}$$

is the friction velocity, $k = 0.4$ is von Kármán's constant, z is the height of the bridge deck above water, and it may be assumed that for flow over water the roughness length is $z_0 = 0.003$–0.01 m, say. If the bridge span is over ground, rather than

over water, z_0 depends upon the terrain roughness, see, e.g., [6]. If topographic effects are significant, models such as Eqs. (2.43a)–(2.43c) and (2.44) may not be appropriate, and micrometeorological measurements should be performed (see, e.g., [78]). However it should be kept in mind that measurements conducted at low wind speeds, at which stable or unstable stratification effects could be significant, may not be representative of conditions occurring at the relatively high speeds for which aeroelastic and buffeting responses are significant.

To perform and validate calculations pertaining to a full bridge model tested in the wind tunnel it is necessary to use turbulence models consistent with the measured properties of the wind tunnel flow [78, 79]. It is noted in [76] that the large uncertainties associated with the spatial structure of low-frequency turbulence result in similarly large uncertainties in the estimation of buffeting response to which low-frequency vibration modes contribute significantly.

Details of the implementation of the flutter and buffeting analysis based on Eq. (2.26) are reported for the Akashi-Kaikyo Bridge (1,990 m main span) in [84]. One conclusion of the Akashi-Kaikyo flutter analyses was that disregarding cross-modal effects (off-diagonal terms in the matrix $\mathbf{E}$) yielded incorrect estimates of the flutter velocity. This conclusion was verified by observations on the full-scale model of the bridge. For a full model of the Straits of Messina Bridge calculations and wind tunnel measurements are reported in [80].

Analyses can be conducted by taking into account the buffeting response not only of the deck, but also that of a dynamic model of the entire bridge, including the cables and the bridge towers. Buffeting response calculations indicated that, for the Tsing Ma bridge in Hong Kong (1,377 m main span), the effect of including the cable and tower dynamics in the modeling was relatively small [109]. However, the longer the bridge, the more the effect of the tower dynamics becomes significant from an aeroelastic point of view. For example, according to calculations for a three-span bridge with a 3,000 m main span and 1,500 m side spans, replacing flexible steel pylons by stiffer, reinforced concrete pylons resulted in an increase of the critical flutter speed of about 25%, while for a bridge with a 2,000 m main span and 1,000 m side spans the increase was about 10% [81]. For the latter bridge replacing cables with allowable stress of about 1,000 MPa or less by cables with allowable stress of about 1,200 MPa or more (and a correspondingly lower moment of inertia) resulted in a decrease of the critical flutter speed of about 25%.

A case study: The Golden Gate Bridge

The Golden Gate bridge has a 1,280 m center span and two 343 m side spans. The elevation of the deck above water is 67 m. The calculated vibration modes, the modal frequencies, and the modal integrals (Eqs. 2.14) are given in Table 1 for the first eleven modes, ranked by order of increasing frequencies. Static force coefficients are listed in Table 2. A surface roughness length of 0.009 m was used in the calculations. The flutter derivatives were assumed to be independent of position along the span. However, the flutter velocities were calculated for five distinct sets of flutter derivatives, corresponding to $-5°$, $-2.5°$, $0°$, $2.5°$, and $5°$ mean angles of attack. Figures 26, 27

Table 1 Frequencies , Types of Modal Forms, and Modal Integrals for Golden Gate Bridge

Mode number	Freq. (Hz)	Type	$G_{h_i h_i}$	$G_{\alpha_i \alpha_i}$	$G_{p_i p_i}$
1	0.0490	LS	3×10^{-16}	8×10^{-5}	0.33
1	0.0490	LS	3×10^{-16}	8×10^{-5}	0.33
2	0.0870	VAS	0.3	1.9×10^{-15}	7.7×10^{-15}
3	0.1124	LAS	1.7×10^{-14}	1.24×10^{-2}	0.32
4	0.1285	VS	0.19	1.4×10^{-14}	8.3×10^{-14}
5	0.1340	VAS	0.34	2.7×10^{-14}	6.0×10^{-14}
6	0.1638	VS	0.34	1.8×10^{-14}	4.0×10^{-14}
7	0.1916	TAS	6.7×10^{-13}	0.32	0.033
8	0.1972	TS	2.5×10^{-12}	0.18	0.25
10	0.1988	VAS	0.18	9.6×10^{-12}	4.6×10^{-13}
11	0.2021	VS	0.26	8.0×10^{-15}	1.5×10^{-15}

Note Lateral; V: Vertical; T: Torsional; S; Symmetric; AS: Anti-symmetric

Table 2 Static Force Coefficients at 0° Angle of Attack for Golden Gate Bridge

C_D	C_L	C_M	C'_D	C'_L	C'_M
0.304	0.211	0.0044	0	3.25	−0.177

and 28 shows flutter derivatives H_i^* and A_i^* $(i = 1, 2, 3, 4)$ obtained in smooth flow from a 1:50 section model of the Golden Gate bridge for a zero-degree mean angle of attack [69]. For comparison flutter derivatives are shown in Fig. 28 for a 5° mean angle of attack [70]. Only the flutter derivatives H_i^*, A_i^* $(i = 1, 2, 3, 4)$, and P_1^* (given by Eq. 2.30) were accounted for in the calculations.

Buffeting calculations were carried out using flutter derivatives for the bridge at 0° mean angle of attack under a 22.2 m/s mean velocity. The largest values along the deck calculated for 2 % modal damping ratios and a mean wind speed of 34 m/s at the deck elevation were $\sigma_{hh} = 0.31$ m and $\sigma_{\alpha\alpha} = 0.77 \times 10^{-3}$ rad. Smaller assumed damping ratios would result in larger buffeting response (Tables 1 and 2).

For flutter calculations it was assumed that the damping ratios were 0.5 %. Calculations showed that, under the assumptions used, no flutter occurred for combinations including only the first six modes. Inclusion of the seventh mode, and of the seventh and eighth modes, yielded the reduced frequencies K, the circular frequencies ω, and the critical flutter velocities U_c listed in Table 3 for each of the five mean angles of attack. If a 1 % modal damping was assumed in the calculations, the multimodal flutter analysis yielded a flutter velocity of 44.6 m/s, rather than 22.0 m/s, as was the case for the assumption of a 0.5 % modal damping.

In addition to a multimodal analysis, a single-mode analysis was performed. Mode 7 yielded the lowest flutter velocity in all cases. The single-mode flutter velocities obtained were almost identical to those obtained by a multimodal analysis based on a combination of seven modes. This result, as well as the calculated shape of the

Table 3 Flutter Velocities for Golden Gate Bridge (0.5% Modal Damping Ratios)

Angle	−5°	−5°	−2.5°	−2.5°	0°	0°	2.5°	2.5°	5°	5°
Modes	7	8	7	8	7	8	7	8	7	8
K	1.27	1.27	1.28	1.28	1.34	1.34	1.43	1.43	1.49	1.49
$\omega(rad.)$	1.18	1.18	1.17	1.17	1.18	1.18	1.19	1.19	1.19	1.19
$U_c(m/s)$	25.5	25.5	25.2	25.2	24.1	24.1	22.7	22.7	22.0	22.0

oscillatory flutter motion, suggests that the flutter is dominated by mode 7, which is the first torsional asymmetric mode (i.e., the type of mode in which the flutter of the Tacoma Narrows bridge occurred—see Fig. 6.2).

In addition to section model tests in smooth flow, tests in flow with turbulence intensities 7.4 and 11 % were conducted for a 1:150 scale model of half the central span. Depending upon turbulence intensity, mean flutter velocities were about 10–20 % higher than the flutter velocity for smooth flow conditions [69, 83] (Table 3).

Before concluding this section we mention the development in [110] of a time domain approach for full bridges. The approach uses aerodynamic impulse response functions obtained from flutter derivatives by Fourier transformation. Unlike calculations in the frequency domain, which assume that the aeroelastic forces depend upon the mean deformation of the bridge, the time domain calculations use models of the aeroelastic forces that depend upon the instantaneous deformation induced by the buffeting. A numerical example included in [110] indicates that, for a 2,000 m span bridge with specified aeroelastic properties, the effect of this refinement on the flutter velocity and the buffeting response was relatively small.

We also refer the reader to research on the behavior of suspended-span bridges during construction [84–86], and on the effects of winds skewed with respect to the direction normal to the bridge span [69, 83].

2.1.5 Reduction of Bridge Susceptibility to Flutter

It has already been noted that "H-section" decks are prone to flutter. This is due both to their weak torsional stiffness and to their unfavorable aerodynamic properties. Roadways with slots, vents, or grills can significantly improve aeroelastic performance [91]. Even minor details such as deck railings can affect structural performance [92].

The design of long bridges to achieve satisfactory performance economically requires efficient aeroelastic design both through the selection of cross-sectional deck shapes with favorable flow patterns, *and* through aeroelastically effective structural design resulting in a reduction of modal and cross-modal integrals [see Eqs. (2.23a)–(2.23c) and (2.24)], particularly for torsional motions. Modal shapes consistent with such reduction can be achieved through the selection of a favorable ratio of side spans to main span, cross-sections stiffer near the supports and along the side spans than in the central part of the main span, stiff pylon towers, and stiff cables. For the

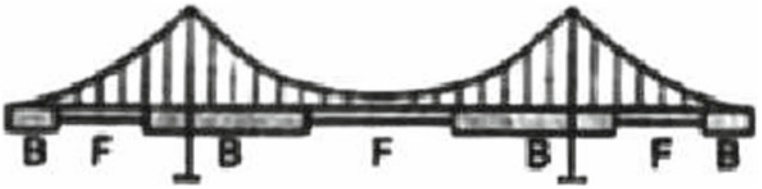

Fig. 31 Schematic of Akashi-Kiokyo suspension bridge . Note spanwise non-uniformity of the deck shape. From [71]

Akashi-Kiokyo Bridge the decks were of equal width throughout the bridge but had torsionally stronger and more bluff shapes near the supports and along the side spans (Fig. 31). The spindle-type suspension bridge concept depicted in Fig. 32 is aimed at achieving similar features more elegantly [92].

As an example of the role of aerodynamic refinements we briefly consider the "π-section" deck (Fig. 33). It was found that a ratio $C/D' = 2.0$ was optimal aerodynamically [73] ($C =$ deck floor overhang, $D' =$ girder depth). In addition the aeroelastic performance depends on the ratio r of solid traffic barrier height to outer

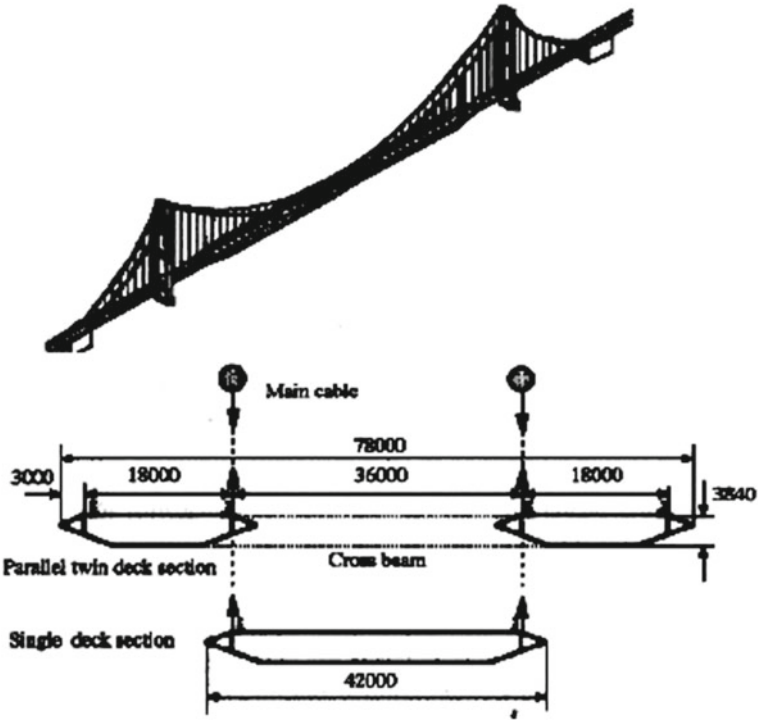

Fig. 32 Spindle-type suspension bridge concept. From [72]

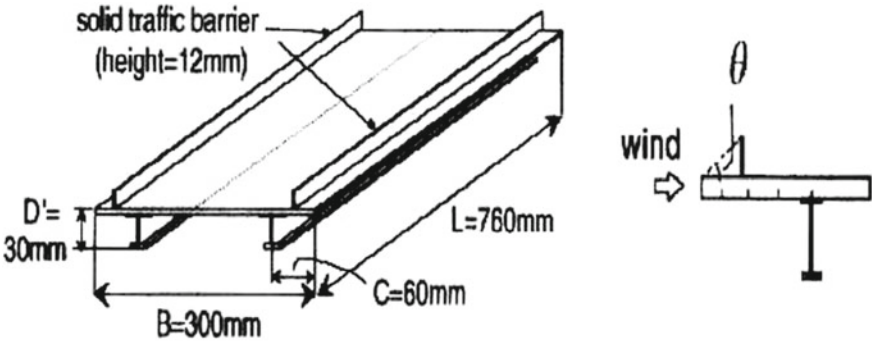

Fig. 33 A "π-section" deck. From [73]

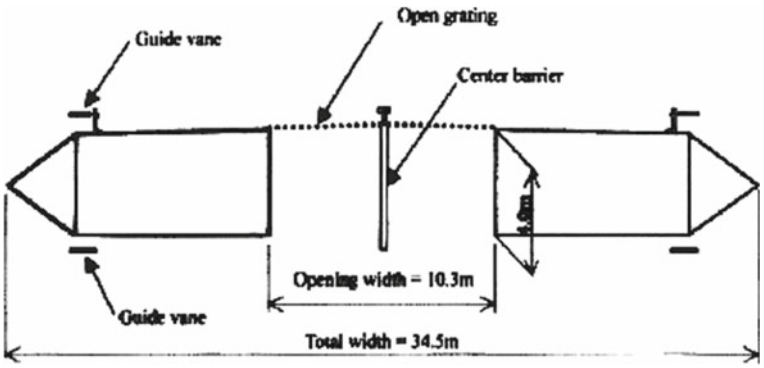

Fig. 34 Cross-section of slotted box girder. From [74]

pedestrian traffic strip width. For $\theta = \tan^{-1} r = 30°$ the torsional aerodynamic damping was found to be almost negligible in comparison with the case $\theta = 90°$ [93]. For this value of θ flow separation patterns result in aeroelastically beneficial reductions of unsteady pressures on the upper surface of the deck. It would be of interest to determine whether the reductions observed in the wind tunnel are Reynolds-number independent.

According to tests and calculations reported in [74], the slotted box girder shown in Fig. 34 is effective aerodynamically, as well as being efficient structurally, for a hypothetical suspension bridge with a 2,800 m main span and 1,100 m side spans. For a similar study of a suspension bridge with 2,500 m main span and 1,250 m side spans, with a deck consisting of a two-box girder over the mid-1,230 m of the central span and a box girder over the rest of the bridge, see [96].

2.2 Tall Chimneys and Stacks, and Tall Buildings

2.2.1 Tall Chimneys and Stacks

Tall chimneys and stacks can be affected by locked-in vortex-induced response. As was mentioned in Sect. 1.3, at lock-in Eq. (1.16) can be written approximately as

$$m(\ddot{y} + 2\zeta\omega_1\dot{y} + \omega_1^2 y) = \frac{1}{2}\rho U^2 D Y_1(K)(1 - \epsilon\frac{y^2}{D^2})\frac{\dot{y}}{U}. \tag{2.45}$$

In Eq. 2.45 $K = D\omega/U$, D is the diameter, U is the velocity, the circular frequency ω satisfies the Strouhal relation $\omega = 2\pi SU/D$, ω_1 is the fundamental natural frequency, and $Y_1(K)$ and ϵ must be fitted to experimental results. The right-hand side of Eq. 2.45 is approximated in [97] by the simplified expression

$$2\omega_1\rho D^2 K_{a0}(\frac{U}{U_{cr}})\left[1 - \frac{\eta_{rms}^2}{\lambda^2}\right]\dot{y} \tag{2.46}$$

where

$$\eta_{rms}^2 = \frac{\frac{1}{T}\int_0^T y^2 dt}{D^2}, \tag{2.47}$$

the numerator of Eq. 2.47 is an estimate of the variance of the fluctuating response, $K_{\alpha 0}(U/U_{cr}) > 0$ is an aerodynamic coefficient, $U_{cr} = \omega_1 D(2\pi S)$, S is the Strouhal number, and T is a sufficiently long time interval. If (2.45) is equated to the product $-2m\zeta_a\omega_n$, where ζ_α denotes the aerodynamic damping ratio, we may define a total damping ratio

$$\zeta_t = \zeta + \zeta_a, \tag{2.48}$$

where

$$\zeta_a = -2\frac{\rho D^2}{m}K_{a0}(\frac{U}{U_{cr}})\left[1 - \frac{\eta_{rms}^2}{\lambda^2}\right]\dot{y} \tag{2.49}$$

If $\eta_{rms} = \lambda$, then $\zeta_a = 0$. The response, including the effects of the aeroelastic forces, is obtained simply by substituting the total damping ratio ζ_t for the structural damping ratio ζ in the homogeneous equation of motion of the body. If $\eta_{rms} < \lambda$, then $\zeta_a < 0$, and the body extracts energy from the flow, that is, it can experience self-excited oscillations. If $\eta_{rms} > \lambda$, then $\zeta_a > 0$, and the body experiences no destabilizing aeroelastic effects. The approximate validity of the approach just described was verified against wind tunnel measurements of chimney response conducted at Reynolds numbers Re $\approx 600,000$ [97]. For reinforced concrete chimneys [98] suggests $\lambda \approx 0.4$.

It may be inferred from some measurements conducted in smooth flow that the largest value of the aerodynamic coefficient $K_{\alpha 0}$, denoted by $K_{\alpha 0\,\max}$, is of the order of unity (about 1.0 for Re $\leq 10^4$, about 1.4 for $10^4 <$ Re $< 10^5$, and about 0.8 for

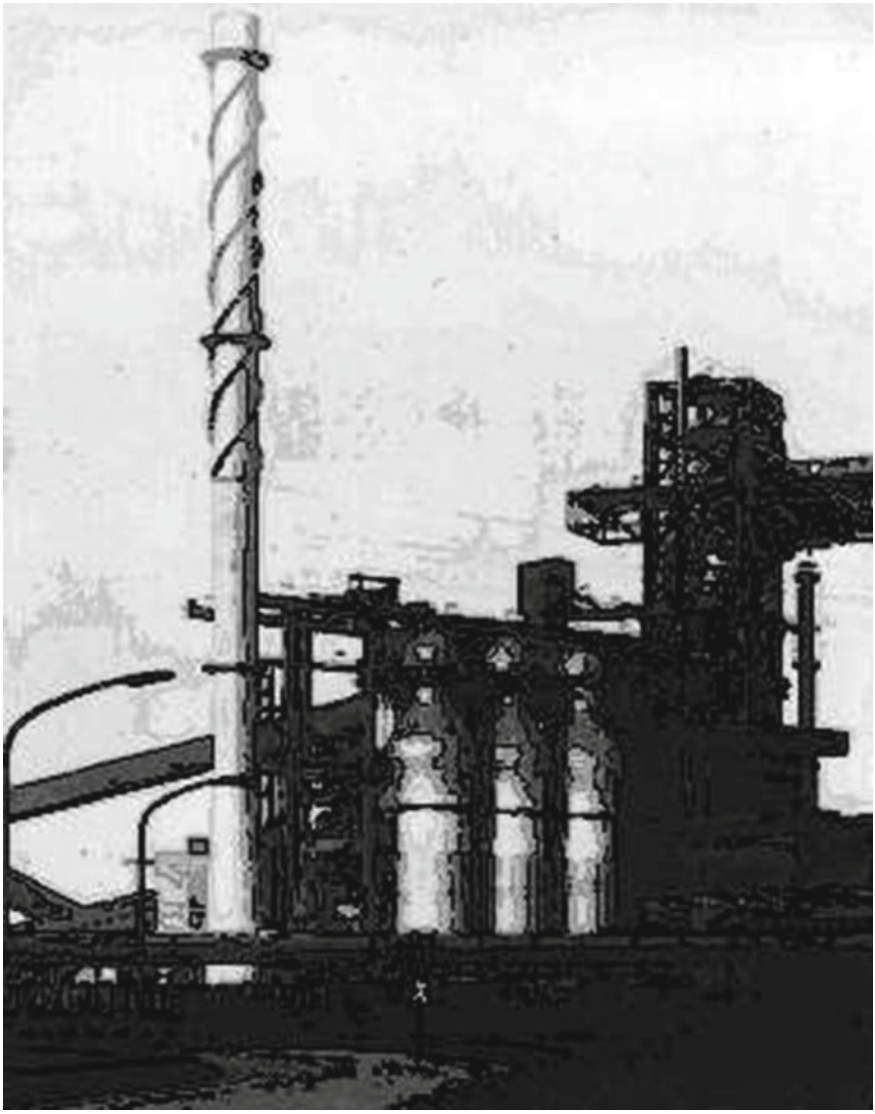

Fig. 35 Steel chimney with helical strakes. From *J. Wind Eng. Ind. Aerodyn.* 1 (1976) 341–347

Re $\geq 10^5$—see [98]). Ratios $K_{\alpha 0}/K_{\alpha 0\,\max}$ proposed in [98] as functions of the ratio U/U_{cr} and of turbulence intensity are shown in Fig. (35). More elaborate models of $K_{\alpha 0}$, applicable to chimneys with non-negligible end effects, are proposed in [98]; see also [6]. For response involving more than one mode of vibration [97] proposes, for each mode, expressions for the total damping similar to Eq. (2.48). In

these expressions modal aerodynamic damping ratios are derived by assuming that aeroelastic effects are linearly superposable.

The calculation of the total response of a chimney or stack to wind loading requires information or assumptions on the drag coefficient, Strouhal number, spectral density of the lift coefficient, spanwise wind loading correlation parameter, and aeroelastic parameter $K_{\alpha 0}$. The aerodynamic and aeroelastic information depends upon Reynolds number, chimney surface roughness, chimney aspect ratio and taper, and terrain roughness. For details see [6, 98, 99].

To reduce the vortex-induced response chimneys may be provided with hydraulic dampers or tuned mass dampers [100], or with aerodynamic devices referred to as spoilers. The latter are aimed at reducing or destroying the shed vortices' coherence along the height. A spoiler commonly used in the past for steel stacks with very light damping was developed on the basis of wind tunnel tests. It consists of three thin helical strakes applied over the top 33–40 % of the chimney (Fig. 35) [6, 101]. The strakes in use are rectangular in cross-section, with a height of 0.1–0.13 diameters, and a pitch of one revolution in 5 diameters. They increase significantly the drag force acting on the stacks. According to full-scale observations reported in [102], for large vibration amplitudes (e.g., 3–5 % of the diameter) the vortices re-establish themselves and the strakes become ineffective. An alternative type of spoiler device is a perforated shroud placed over the top 25 % of the stack [6, 103].

2.2.2 Tall Buildings

The response of tall (high-rise) buildings to wind loading may be divided into three categories:

- along-wind response, which consists of (a) the static response induced by the mean flow speed, and (b) the dynamic (buffeting) response induced mainly by longitudinal turbulent fluctuations in the oncoming flow (contributions by along-wind components of the signature turbulence, that is, of flow fluctuations due to the flow-structure interaction, are typically small)
- across-wind response due to signature turbulence, including vorticity shed in the building wake (contributions by lateral turbulent fluctuations in the oncoming flow are typically small)
- torsional response, due to the non-zero distance between the building's elastic center and the instantaneous point of application of the resultant wind loading.

This terminology pertains to the case where the mean wind speed is parallel to a principal axis of the building's horizontal cross section.

For isolated buildings in horizontal terrain with specified roughness simple procedures are available for relating the along-wind response to the oncoming turbulent flow (see, e.g., [6]). Expressions based on first principles are not available, however, for the estimation of the across-wind and torsional response. Nevertheless, some tentative empirical criteria have been developed from wind tunnel measurements. Let h_{rms} denote the rms value of the across-wind oscillations at the top of

the building. According to those criteria aeroelastic effects become significant if $h_{rms} > h_{rms\,cr}$, where $h_{rms\,cr}$ is a critical value. For buildings with a square shape in plan experiments reported in [104, 105] suggest that, if B denotes the side of the horizontal cross-section, it is conservative to assume $h_{rms\,cr}/B = 0.015$ for open terrain, $h_{rms\,cr}/B = 0.025$ for suburban terrain and, under the assumption that no neighboring building affects significantly the turbulent wind field, $h_{rms\,cr}/B = 0.045$ for centers of cities. For a variety of shapes tentative, crude empirical expressions and attendant data are available to describe the across-wind and torsional response for $h_{rms} < h_{rms\,cr}$ [6, 106]. According to [107], for some building shapes estimates based on those expressions appear to be significantly at variance with results based on [94].

Figure 36 [94] shows results of wind tunnel experiments obtained for four prismatic building shapes in smooth flow, flow over open terrain, and flow over urban terrain. Results for each case are given for three values of the structural damping ratio. The model scale was estimated to be about 1/600, and for all models the height H, the sectional area BD, and the specific mass were 0.5 m, 0.0025 m^2, and 120 kg/m^3, respectively. In Fig. 36, f_0, U, and h_{rms} denote, respectively, natural frequency of vibration in the fundamental mode, wind speed at building top, and rms of across-wind response at the building top. Additional results are reported in [108] for winds acting from various directions on the models described in [94] and on a model with a triangular shape in plan.

For tall buildings higher vibration modes typically do not make major contributions to the total response. In engineering practice information provided by sources such as [94, 104–108] is seldom if at all used for design purposes. Rather, each important tall structure is subjected to an ad-hoc aeroelastic wind tunnel test that reproduces the structure's main mechanical characteristics and built environment and allows testing for a sufficient number of wind speeds and directions. Recently, however, efforts have been made to develop for tall buildings an approach similar to the approach used for suspended-span bridges. Those efforts are still in the incipient stage. They entail primarily measurements used to estimate aerodynamic damping. For a tall building with a depth-to-width ratio of 2, $H/(BD)^{\frac{1}{2}} = 5$, and a linear fundamental modal shape, measurements of wind forces induced by across-wind harmonic forcing as well as by torsional harmonic forcing in smooth and turbulent flows were reported in [94], the wind direction being parallel to the long dimension of the rectangle. As is the case for chimneys (Eq. 2.47), the total damping ratio may be written as a sum of structural damping and aerodynamic damping. For flow over suburban terrain and for four values of the structural damping, Fig. 37 shows, for various structural across-wind and torsional damping ratios, denoted by h_{sx} and $h_{s\theta}$, nondimensional across-wind and torsional rms responses based on direct wind tunnel measurements and on analyses in which the measured aerodynamic damping ratios were used. In Fig. 37 U_H denotes the mean velocity at elevation H, B is the short dimension of the horizontal cross-section of the building, and n_x, n_θ denote the across-wind and torsional natural frequencies. Similar studies conducted on models with ratios $D/B = 1$ and $D/B = 3$ are reported in [111]. The framework developed in [95, 111] provides a useful basic understanding of aeroelastic effects on tall build-

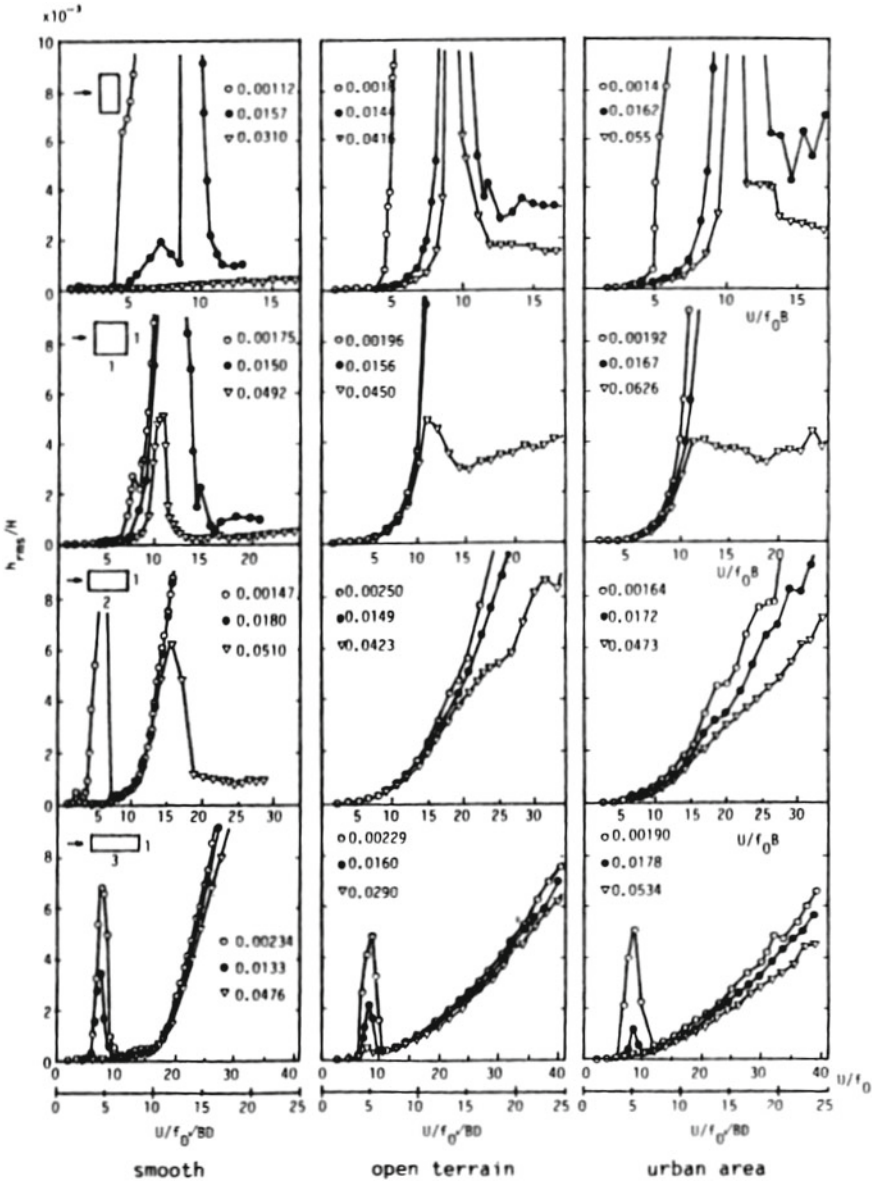

Fig. 36 Wind tunnel measurements of across-wind response of rectangular buildings (circles and triangles indicate damping ratios). From [94]

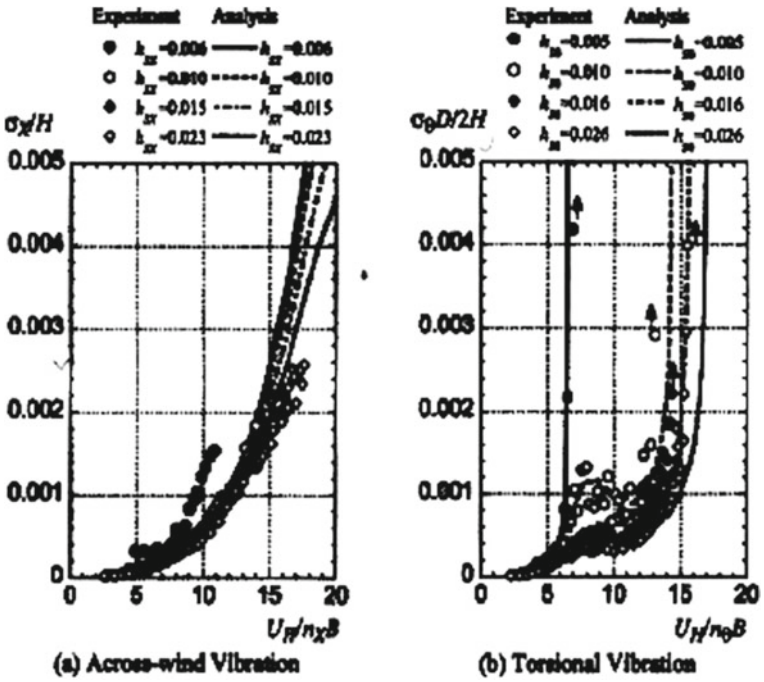

Fig. 37 Displacements of wind response obtained from response analysis accounting for measured aerodynamic damping and from wind tunnel tests on elastic model; shear flow corresponding to suburban terrain. From [95]

ings. However, until a sufficiently comprehensive database is developed, it cannot serve as a substitute for individual, ad-hoc wind tunnel tests, the more so as lock-in or galloping effects not accounted for in [95, 111] can play an important role in the response for reduced velocities larger than 5 or so [108].

Reference [112] discusses corrections to estimates of aeroelastic response obtained by current wind tunnel techniques.

References

1. Strouhal V (1870) Über eine besondere Art der Tonerregung. Annalen der Physik 5:216–250
2. Bénard H (1908) Formation de centres de gyration à l'arrière d'un obstacle en mouvement. Comptes rendus de l'Académie des sciences 147:839–842
3. von Kármán T (1911) Über den Mechanismus des Widerstandes den ein bewegter Körper in einer Flüssigkeit erfährt. Nachrichten der Königlichen Gesellschaft der Wissenschaften, Göttingen, pp 509–517
4. Roshko A (1961) Experiments on the flow past a circular cylinder at very high Reynolds number. J Fluid Mech 10:345–356

5. Shih WCI, Wang C, Coles D, Roshko A (1993) Experiments past rough circular cylinders at large Reynolds numbers. J Wind Eng Industr Aerodyn 49:351–358
6. Simiu E, Yeo D (2019) Wind Effects on Structures, Fourth ed. Wiley, Blackwell
7. Sarpkaya T (1978) Fluid forces on oscillating cylinders. J Waterw Ports Coast Ocean Eng Div ASCE 97:275–290
8. Bergé P, Pomeau Y, Vidal C (1984) Order within chaos. Wiley, New York
9. Goswami I, Scanlan RH, Jones NP (1993) Vortex-induced vibration of a circular cylinder in air: I new experimental data; II A new model. J Eng Mech 119:2270–2302
10. Scanlan RH (1995) Aeroelastic problems of civil engineering. In: Dowell EH (ed) A modern course in aeroelasticity. Kluwer Academic Publishers, Dordrecht
11. Birkhoff G (1953) Formation of vortex streets. J Appl Phys 24:98–103
12. Funakawa M (1969) The vibration of a circular cylinder caused by wake in a flow. Bulletin Jpn Soc Mech Eng 12:1003–1010
13. Nakamura Y (1969) Vortex excitation of a circular cylinder treated as a binary flutter. Rep Res Inst Appl Mech XVII:217–234 (Kyushu University)
14. Tamura Y, Matsui G (1979) Wake oscillator model of vortex-induced oscillation of a circular cylinder. In: Proceedings of the fifth conference on wind engineering, Ft. Collins, pp 1085–1094
15. Hartlen RT, Currie IG (1970) A Lift-oscillator model of vortex-induced vibration. J Eng Mech Div ASCE 96:577–591
16. Skop A, Griffin OM (1973) A model for the vortex-excited resonant response of bluff cylinders. J Sound Vib 27:225–233
17. Griffin OM, Skop A (1976) The vortex-excited oscillations of structures. J Sound Vib 44:303–305
18. Landl R (1975) A mathematical model for vortex-excited vibrations of bluff bodies. J Sound Vib 42:219–234
19. Wood KN (1976) Coupled oscillator models for vortex-induced oscillation of a circular cylinder. M.S. thesis, University of British Columbia
20. Wood KN, Parkinson GV (1977) A hysteresis problem in vortex-induced oscillations. In: Proceedings of the Canadian congress of applied mechanics, Vancouver, pp 697–698
21. Dowell EH (1981) Non-linear oscillator models in bluff body aeroelasticity. J Sound Vib 75:251–264
22. Simiu E, Scanlan RH (1978) Wind effects on structures. Wiley, New York
23. Griffin OM, Kop A, Ramberg SE (1975) The resonant vortex-excited vibration of structures and cable systems. Offshore technology conference paper OTC-2319, Houston, TX 1975
24. Blevins RD (1990) Flow-induced vibrations, 2nd edn. Van Nostrand Reinhold, New York
25. Iwan WD, Blevins RD (1974) A model for the vortex-induced oscillation of structures. J Appl Mech 41:581–585
26. Billah KYR (1989) A study of vortex-induced vibration. Doctoral Dissertation, Princeton University, Princeton
27. Berger H (1987) On a mechanism of vortex-induced oscillations of a cylinder. 7th international conference on wind engineering. Aachen, Germany, pp 169–177
28. Bearman P (1979) Pressure fluctuation measurements on an oscillating circular cylinder. J Fluid Mech 91:661–667
29. Glauert H (1919) Rotation of an airfoil about a fixed axis. Aeronautical Research Committee, R&M 595, Great Britain
30. Den Hartog JP (1932) Transmission line vibration due to sleet. Trans AIEE 51:1074–1076
31. Den Hartog JP (1956) Mechanical vibrations, 4th edn. McGraw-Hill, New York
32. Novak M (1972) Galloping oscillations of prismatic structures. J Eng Mech Div ASCE 98:27–46
33. Novak M (1969) Aeroelastic galloping of prismatic bodies. J Eng Mech Div ASCE 95:115–142
34. Kryloff N, Bogoliuboff N (1947) Introduction to nonlinear mechanics. Annals of mathematics studies, No. 11 (trans: Lefschetz S). Princeton University Press, Princeton

35. Mukhopadyay V, Dugundji J (1976) Wind excited vibration of a square section cantilever beam in smooth flow. J Sound Vib 45:329–339
36. Skarecky R (1975) Yaw effects on galloping instability. J Eng Mech Div ASCE 101:739–754
37. Richards DJB (1965) Aerodynamic properties of the severn crossing conductor. In: Proceedings of the symposium on wind effects on buildings and structures, vol II. National Physics Laboratory, H.M'.s Stationery Office, Teddington, UK, pp 688–765
38. Simiu E, Cook GR (1992) Empirical fluidelastic models and chaotic galloping?: a case study. J Sound Vib 154:45–66
39. Simiu E (2002) Chaotic transitions in deterministic and stochastic dynamical systems. Princeton University Press, Princeton
40. Scanlan RH (1972) A wind tunnel investigation of bundled power-line conductors, Part VI: Observations on the problem, Rep. LTR-LA-121, National Aeronautical Establishment, National Research Council, Ottawa, Canada
41. Simpson A (1970) Stability of subconductors of smooth cross-section. Proc Inst Electr Eng 117:741–750
42. Simpson A (1971) On the flutter of a smooth cylinder in a wake. Aeronaut Quart XXII:101–118
43. Wardlaw RL, Cooper KR, Scanlan RH (1973) Observations on the problem of subspan oscillation of bundled power conductors. DME/NAE Quarterly Bulletin, National Research Council, Ottawa, Canada, pp 1–20
44. Simpson A (1971) Wake-induced flutter of circular cylinders: mechanical aspects. Aeronaut Quart XXIII:101–118
45. Simpson A (1972) Determination of the natural frequencies of multi-conductor overhead transmission lines. J Sound Vibr 20:417–449
46. Theodorsen T (1935) General theory of aerodynamic instability and the mechanism of flutter, NACA Report 496
47. Scanlan RH, Tomko JJ (1971) Aircraft and bridge deck flutter derivatives. J Eng Mech Div ASCE 97:1717–1737
48. Thiesemann L, Starossek U (2002) Numerical evaluation of flutter derivatives. In: Grundmann H, Schuëller GI (eds) Structural dynamics. EURODYN2002, Bakkema, Lisse, vol 2, pp 1566–1581
49. Billah KY, Scanlan RH (1991) Resonance, Tacoma bridge failure, and undergraduate physics books. Am J Phys 59:118–124
50. Starossek U (1998) Complex notation in flutter analysis. J Struct Eng 124:975–977
51. Scanlan RH, Béliveau J-G, Budlong KS (1974) Indicial aerodynamic functions for bridge decks. J Eng Mech Div 100:657–672
52. Verwiebe C, Ruscheweyh H (1998) Recent research results concerning the exciting mechanism of rain-induced vibrations. J Wind Eng Ind Aerodyn 74–76:1005–1013
53. Flamand O (1994) Rain-wind induced vibrations of cables. In: Cable-stayed and suspended bridges, vol 2. Centre Scientifique et Technique du Bâtiment, Nantes, France
54. Kobayashi H, Minami Y, Miki M (1995) Prevention of rain-wind induced vibration of an inclined cable by surface processing. In: Wind engineering. Ninth international conference, vol 2. Wiley, New Delhi, pp 753–758
55. Matsumoto M, Yagi T, Goto M, Sakai S (1998) Rain-induced vibration of inclined cables at limited high reduced wind velocity region. J Wind Eng Ind Aerodyn 91:1–12
56. Matsumoto M, Shirato H, Yagi T, Goto M, Sakai S, Ohya J (1998) Field observation of the full-scale wind-induced cable vibration. J Wind Eng Ind Aerodyn 91:13–26
57. Persoon AJ, Noorlander K (1999) Full-scale measurements on the Erasmus bridge after wind/rain induced cable vibrations. In: Larsen A, Larsen GI, Livesey FM (eds) Wind engineering into the 21st century, vol 2. Bakkema, Rotterdam, pp 1019–1026
58. Schewe G, Larsen A (1998) Reynolds number effects in the flow around a bluff body bridge deck section. J Wind Eng Ind Aerodyn 74–76:829–838

59. Matsuda K, Tokushige M, Iwasaki T, Cooper KR, Tanaka H (1999) An investigation of Reynolds number effects on the steady and unsteady aerodynamics forces on a 1:10 scale bridge deck section model. In: Larsen A, Larsen GI, Livesey FM (eds) Wind engineering into the 21st century, vol 2. Bakkema, Rotterdam, pp 971–978
60. Simiu E (1971) Buffeting and aerodynamic stability of suspension bridges in turbulent wind. Doctoral Dissertation, Princeton University
61. Queen DJ, Vejrum T, Larose GL (1999) Aerodynamic studies of the Lions' Gate bridge–3 lane renovation. In: Larsen A, Larose GL, Livesey FM (eds) Wind engineering into the 21st century, vol 2. Bakkema, Rotterdam, pp 1027–1034
62. Wardlaw RL (1970) Static force measurements of six deck sections for the proposed new Burrard inlet crossing, Report RTR-LA-53. National Aeronautical Establishment, National Research Council, Ottawa
63. Raggett JD (1995) Section model wind tunnel studies, Report W920421. West Wind Laboratory, Calif, Carmel
64. Haan FL (2000) The effects of turbulence on the aerodynamics of long-span bridges. Doctoral Dissertation, Department of Civil Engineering, University of Notre Dame
65. Gan Chowdhury A, Sarkar PP (2005) Experimental identification of rational function coefficients for time-domain flutter analysis. Eng Struct 27(9):1349–1364
66. Sarkar PP, Gan Chowdhury A, Gadner TB (2004) A novel elastic suspension analysis for wind tunnel section model studies. J Wind Eng Ind Aerodyn 92(1):23–40
67. Gan Chowdhury A, Sarkar PP (2004) Identification of eighteen flutter derivatives of an airfoil and a bridge deck. Wind Struct 7(3):187–202
68. Gan Chowdhury A, Sarkar PP (2003) A new technique for identification of eighteen flutter derivatives using three-degree-of-freedom section model. Eng Struct 25(14):1763–1772
69. Jain A, Jones NP, Scanlan RH (1998) Effect of modal damping on bridge aeroelasticity. J Wind Eng Ind Aerodyn 77–78:421–430
70. Singh L, Jones NP, Scanlan RH, Lorendeaux O (1995) Simultaneous identification of 3-DOF aeroelastic parameters. In: Wind engineering. Ninth international conference, vol 2. Wiley, New Delhi, pp 972–977
71. Yamada M, Miyata T, Minh NN, Katsuchi H (1999) Complex flutter-mode analysis for coupled gust response of the Akashi-Kaikyo bridge model. In: Larsen A, Larose GL, Livesey FM (eds) Wind engineering into the 21st century. Tenth international conference on wind engineering, vol 2. Bakkema, Rotterdam, pp 1081–1088
72. Miyata T (1999) Comprehensive discussions on aeroelastic-coupled flutter control for very long suspension bridges. Long-span bridges and aerodynamics. Springer, Berlin, pp 181–200
73. Kubo Y, Sadashima K, Yamaguchi E, Kato K, Okamoto Y, Koga T (2002) Improvement of aeroelastic instability of shallow Π section. J Wind Eng Ind Aerodyn 89:1445–1457
74. Sato H, Hirahara N, Fumoto K, Hirano S, Kusuhara S (2002) Full aeroelastic model test of a super long-span bridge with slotted box girder. J Wind Eng Ind Aerodyn 90:2023–2032
75. Wardlaw RL, Goetler LL (1968) A wind tunnel study of modifications to improve the aerodynamic stability of the long Creek's bridge, Report LTR-LA-8. National Aeronautical Establishment, National Research Council, Ottawa
76. Larsen A, Esdahl S, Andersen JE, Vejrum T (2000) Storebælt suspension bridge–vortex shedding excitation and mitigation by guide vanes. J Wind Eng Ind Aerodyn 88:283–296
77. Utsunomy H, Nagao F, Noda M, Tanaka E (2001) Vortex-induced oscillation of a bridge in slowly fluctuating wind. J Wind Eng Ind Aerodyn 89:1689–1699
78. Barré C, Flamand O, Grillaud G (1999) The Millau viaduct—special wind studies for an exceptional structure. In: Larsen A, Larose GL, Livesey FM (eds) Wind engineering into the 21st century. Tenth international conference on wind engineering, vol 2. A.A. Bakkema, Rotterdam, pp 827–832
79. Katsuchi H, Jones NP, Scanlan RH (1999) Multimode coupled flutter and buffeting analysis of the Akashi-Kaikyo bridge. J Struct Eng 125:60–70
80. Diana G, Falco M, Bruni S, Cigada A, Larose GL, Damsgaard A, Collina A (1995) Comparisons between wind tunnel tests on a full aeroelastic model of the proposed bridge over Stretto di Messina and numerical results. J Wind Eng Ind Aerodyn 54(55):101–113

81. Miyata T (2002) Significance of aeroelastic relationship in wind-resistant design of long-span bridges. J Wind Eng Ind Aerodyn 77–78:1479–1492
82. Scanlan RH (1997) Amplitude and turbulence effects on bridge flutter derivatives. J Struct Eng 123:232–236
83. Irwin PA, Xie J, Dunn G (1995) Wind tunnel studies for the Golden Gate Bridge. Rowan, Williams, Davies, and Irwin, Guelph
84. Larsen A (1995) Prediction of aeroelastic stability of suspension bridges during erection. In: Wind engineering. Ninth international conference, vol 2. Wiley, New Delhi, pp 917–927
85. Brancaleoni F (1992) The construction phase and its aerodynamic issues. In: Larsen A (ed) Aerodynamics of large bridges. Bakkema, Rotterdam
86. Hansen SO, Thorbek LT, Krenk S, Clenance JC (1999) Dynamic response of suspension bridge decks during construction. In: Larsen A, Larose GL, Livesey FM (eds) Wind engineering into the 21st century. Tenth international conference on wind engineering, vol 2. Bakkema, Rotterdam, pp 899–906
87. Hosomi M, Koba K, Kobayashi H (1995) Effect of yawed wind on vortex excited response of bridge girder models. Ninth international conference on Wind engineering, vol 2. Wiley, New Delhi, pp 863–870
88. Tanaka H, Kimura K, Nakamura S, Larose GL (1995) Effects of wind yaw angles on bridge response. In: Wind engineering. Ninth international conference, vol 2. Wiley, New Delhi, pp 905–916
89. Zhu LD, Xu YL, Zhang F, Xiang HF (2002) Tsing Ma bridge deck under skew winds–Part I: aerodynamic coefficients. J Wind Eng Ind Aerodyn 90:781–805
90. Zhu LD, Xu YL, Xiang HF (2002) Tsing Ma bridge deck under skew winds–Part II: flutter derivatives. J Wind Eng Ind Aerodyn 90:807–837
91. Matsumoto M, Nakajima N, Taniwaki Y, Shijo R (2001) Grating effect on flutter instability. J Wind Eng Ind Aerodyn 89:1487–1498
92. Jones NP, Scanlan RH, Sarkar PP, Singh L (1995) The effect of section model details on aeroelastic parameters. J Wind Eng Ind Aerodyn 54–55:45–53
93. Kubo Y, Kimura K, Sadashima K, Okamoto Y, Yamaguchi E, Koga T, Kato K (2002) Aerodynamic performance of improved shallow Π shape bridge deck. J Wind Eng Ind Aerodyn 90:2113–2125
94. Kawai H (1992) Vortex-induced vibration of tall buildings. J Wind Eng Ind Aerodyn 41–44:117–128
95. Katagiri J, Okhuma T, Marukawa H (2001) Motion-induced wind forces acting on rectangular high-rise buildings with side ratio of 2. J Wind Eng Ind Aerodyn 89:1421–1432
96. Ogawa K, Shimodoi H, Oryu T (2002) Aerodynamic characteristics of a 2-box girder section adaptable for a super-long span suspension bridge. J Wind Eng Ind Aerodyn 90:2033–2043
97. Vickery BJ, Basu RI (1983) Across-wind vibrations of structures with circular cross-section, Part I: Development of a two-dimensional model for two-dimensional conditions'. J Wind Eng Ind Aerodyn 12:49–73
98. Basu RI, Vickery BJ (1983) Across-wind vibrations of structures with circular cross-section, Part II: Development of a mathematical model for full-scale application. J Wind Eng Ind Aerodyn 12:75–97
99. Uematsu Y, Yamada M (1995) Effects of aspect ratio and surface roughness on the time-averaged aerodynamic forces on cantilevered circular cylinders at high Reynolds numbers. J Wind Eng Ind Aerodyn 54–55:301–312
100. Ricciardelli F (2001) On the amount of tuned mass to be added for the reduction of the shedding-induced response of chimneys. J Wind Eng Ind Aerodyn 89:1539–1551
101. Scruton C (1963) Note on a device for the suppression of the vortex-excited oscillations of structures of circular or near-circular section, with special application to its application to tall stacks, NPL Aero Report No 1012. National Physical Laboratory, UK, Teddington
102. Ruscheweyh H (1994) Vortex-induced vibration. In: Sockel H (ed) Wind-excited vibrations. Springer, New York, pp 51–84

103. Walsh DE, Scruton RI (1970) Preventing wind-induced oscillations of structures of circular cross-section.In: Modern design of wind-sensitive structures. Construction Research and Information Association, London
104. Reinhold TA, Sparks PR (1980) The influence of wind direction on the response of a square-section tall building. In: Proceedings of the fifth international conference on wind engineering, Fort Collins, Colorado, 1979, Pergamon Press, Elmsford
105. Kwok CS, Melbourne WH (1981) Wind-induced lock-in excitation of tall structures. J Struct Div ASCE 107:52–72
106. Canadian structural design manual, Supplement No. 4 to the National Building Code of Canada. National Research Council of Canada, Ottawa, (1975)
107. Miyashita K et al (1993) Wind-induced response of high-rise buildings–effetcs of corner cuts or openings in square buildings. J Wind Eng Ind Aerodyn 50:319–328
108. Kawai H (1995) Effects of angle of attack on vortex induced vibration and galloping of tall buildings in smooth and turbulent boundary layer flows. J Wind Eng Ind Aerodyn 54:125–132
109. Xu YL (1999) Buffeting of the Tsing Ma Suspension bridge: analysis and comparison. In: Larsen A, Larose GL, Livesey FM (eds) Wind engineering into the 21st century. Tenth international conference on wind engineering, vol 2. pp 1075–1080
110. Chen X, Kareem A (2001) Nonlinear response analysis of long-span bridges under turbulent winds. J Wind Eng Ind Aerodyn 89:1335–1350
111. Katsumura A, Katagiri J, Marukawa H, Fujii K (2001) Effects of side ratio on characteristics of across-wind and torsional responses of high-rise buildings. J Wind Eng Ind Aerodyn 89:1433–1444
112. Zhou Y, Kareem A (2003) Aeroelastic balance. J Eng Mech 129:283–292
113. Farquharson F.B (ed) Aerodynamic stability of suspension bridges, Bulletin No. 116, University of Washington Engineering Experiment Station, Seattle, 1949-1954
114. Nakamura Y (1993) Bluff-body aerodynamics and turbulence. J Wind Eng Ind Aerodyn 49:65–78
115. Laneville A, Gartshore IS, Parkinson GV (1997) An explanation of some effects of turbulence on bluff bodies. In: Proceedings of the fourth international conference, Wind Effects on Buildings and Structures. Cambridge University Press, Cambridge

Aeroelastic Response of Rotorcraft

David A. Peters

Abstract Rotorcraft have particularly complex and often nonlinear aeroelastic phenomena. This chapter deals with those challenges including ground resonance, air resonance and various forms of aeromechanical instabilities.

In this chapter we will examine a number of aeroelastic phenomena associated with helicopters and other rotor or propeller driven aircraft. Certain areas have been selected for treatment to illustrate some significant stability problems which are associated with the design of helicopters. The approach to be followed employs simplified modelling of various problems such that physical insight into the nature of the phenomena can be obtained. In general, a complete and precise formulation of many of the problem areas discussed is highly complex and the reader is referred to the literature for these more detailed formulations.

A basic introduction to the mechanics and aerodynamics of helicopters may be found in [1, 2]. Extensive reviews of helicopter aeroelasticity may be found in [3, 4]. Reference [4] provides an excellent discussion of the considerations necessary in modelling helicopter aeroelasticity and illustrates the complexity of a general formulation as well as the care required to obtain a complete and precise analytical model.

Helicopter rotors in use may be broadly classified in four types, semi-articulated or teetering, fully-articulated, hingeless and bearingless. This classification is based on the manner in which the blades are mechanically connected to the rotor hub. The teetering rotor is typically a two-bladed rotor with the blades connected together and attached to the shaft by a pin which allows the two-blade assembly to rotate such that tips of the blades may freely move up and down with respect to the plane of rotation (flapping motion). In the fully-articulated rotor, each blade is individually attached to the hub through two perpendicular hinges allowing rigid motion of the blade in two directions, out of the plane of rotation (flapping motion) and in the plane of rotation (lag motion). The third type is the hingeless rotor in which the rotor blade

D. A. Peters (✉)
Mechanical Engineering, Washington University, St. Louis, MO, USA
e-mail: dap@wustl.edu

E. H. Dowell (ed.), *A Modern Course in Aeroelasticity*, Solid Mechanics and Its Applications 264, https://doi.org/10.1007/978-3-030-74236-2_7

is a cantilever beam, but with soft flexures near the root, simulating hinges. Fourth, bearingless rotors further replace the pitch bearing by the softness in torsion of the root of the blade. Thus, pitch changes are introduced through torsional deformations.

Because of their greater flexibility, elastic deformations of hingeless and bearingless rotors are significant in the analysis of the dynamics of the vehicle. Bending out of the plane of rotation is referred to as flap bending and in-plane as lag bending. These three rotor configurations are shown schematically in Fig. 1. Rotation of the blade about its long axis is controlled by a pitch change mechanism suitably connected to the pilot's stick. For further details see [1] for articulated rotors and [5] for hingeless rotors. Other variations in rotor hub geometry are found such as the gimballed rotor described in [6]. We will concentrate our discussion on the aeroelastic behavior of fully-articulated and hingeless rotors. However, it is important to realize that, for the aeroelastic analysis of rotors, the precise details of the hub and blade geometry must be carefully modelled.

Phenomena in helicopter aeroelasticity may be classified by the degrees-of-freedom which are significantly coupled. Typically, the dynamics of a single blade are of interest although coupling among blades can be present through the elasticity of the blade pitch control system or the aerodynamic wake [7]. The degrees-of-freedom of a single blade include rigid body motion in the case of the articulated system as well as elastic motion. Elastic motions of interest include bending in two directions and twisting or torsion. These elastic deformations are coupled in general. In addition to individual blade aeroelastic problems, the blade degrees-of-freedom can couple with the rigid body degrees-of-freedom of the fuselage in flight as well as the elastic deformations of the fuselage [8–10] or with the fuselage/landing gear system on the ground [10]. In fact, a complete aeroelastic model of the helicopter typically involves a dynamic model with a large number of degrees-of-freedom. We do not propose to examine these very complex models, but rather will consider simple formulations of certain significant stability problems which will give some insight into the importance of aeroelasticity in helicopter design. Avoiding resonances is also of considerable significance, but is not discussed here. First, aeroelastic phenomena associated with an individual blade are described and then those associated with blade/body coupling are examined. Finally, we will consider phenomena associated with the dynamics of the wake.

1 Blade Dynamics

Classical flutter and divergence of a rotor blade involving coupling of flap bending and torsion have not been particularly significant due to the fact that, in the past, rotor blades have been designed with their elastic axis, aerodynamic center, and center of mass coincident at the quarter chord.

In addition, blades are often torsionally stiff (a typical torsional frequency of a modern rotor blade is about 5–8 per revolution) which minimizes coupling between elastic flap bending and torsion. It is important to note that torsional stiffness con-

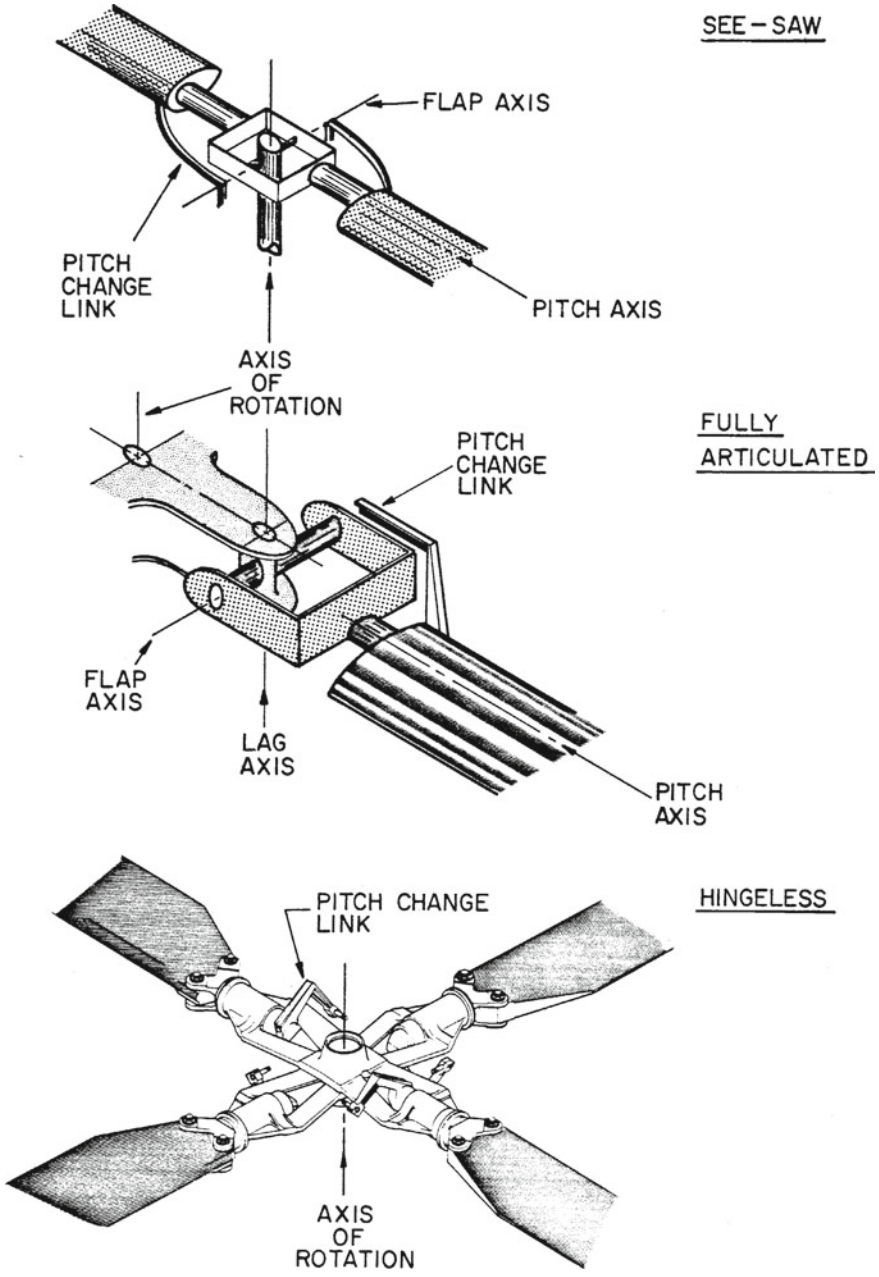

Fig. 1 Various rotor hub configurations

trol system flexibility is included as well as blade flexibility. Rotor systems with low torsional stiffness [11] have experienced flutter problems; and on hingeless and bearingless rotors, the blade section center of mass and elastic axis position can be moved from the quarter chord to provide a favorable effect on the overall flight stability [12] which may mean that these classical phenomena will have to be reviewed more carefully in the future. Sweep has also been employed on rotor blades [13] and this couples flap bending with torsion. However, we will not consider flutter and divergence here, but will instead concentrate on phenomena more frequently encountered in practice. Further discussion of classical bending-torsion flutter and divergence of rotor blade may be found in [3, 14].

1.1 Articulated, Rigid Blade Motion

In order to introduce the nature of rotor blade motion we first develop the equations of motion for the flapping and lagging of a fully articulated blade assuming that the blade is rigid. Consider a single blade which has only a flapping hinge located on the axis of rotation as shown in Fig. 2. The blade flapping angle is denoted by β_s and the blade rotational speed by Ω. We proceed to derive the equation of motion of the blade about the flapping axis. We assume that the rotor is in a hovering state with no translational velocity. It is most convenient to use a Newtonian approach to this problem. Since the flapping pin is at rest in space, we may write the equation of motion for the blade as follows [15]

$$\bar{\dot{H}}_P + \bar{\Omega}_B \times \bar{H}_P = \int_0^R \bar{\Upsilon} \times d\bar{F}_A \tag{1.1}$$

A blade-body axis system denoted by the subscript$_B$ is employed and $\bar{H}_P$ is the moment of momentum of the blade with respect to the flapping pin. $d\bar{F}_A$ is the aerodynamic force acting on the blade at the radial station $\bar{r}$. The gravity force on the blade is neglected owing to the comparatively high centripetal acceleration. Figure 2 also shows the coordinate system and variables involved. The blade is modelled as a very slender rod, and the body axes are principal axes such that the inertia characteristics of the blade are

$$I_B \cong I_y \cong I_z; \quad I_x \cong 0$$

Therefore

$$\bar{H} = (I_B q_B)\bar{j}_B + (I_B r_B)\bar{k}_B \tag{1.2}$$

where

$$\bar{\Omega} = p_B \bar{i}_B + q_B \bar{j}_B + r_B \bar{k}_B \tag{1.3}$$

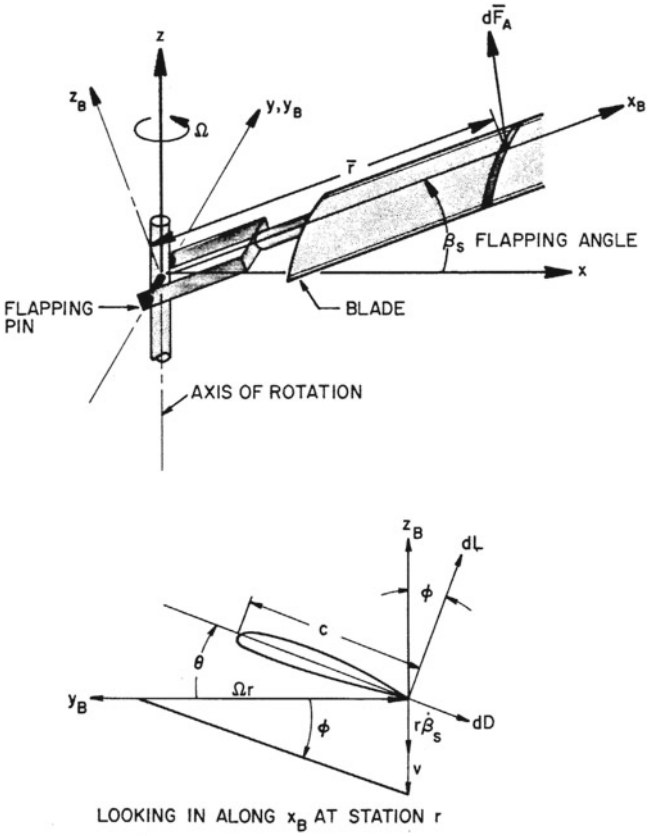

Fig. 2 Coordinate systems and aerodynamics for blade flapping analysis

The equation of motion, (1.1), becomes

$$I_B[\dot{q}_B - p_B r_B]\bar{j}_B + I_B[\dot{r}_B + p_B q_B]\bar{k}_B = \int_0^R \bar{r} \times d\bar{F}_A \tag{1.4}$$

Now we must express the angular body rates in terms of the variables of interest in the problem, Ω the angular velocity, and β_s the flap angle. The angular velocity must be resolved into the blade axis system by rotation through β_s, and then the flapping velocity $\dot{\beta}_s$ added.

$$\begin{Bmatrix} p_B \\ q_B \\ r_B \end{Bmatrix} = \begin{bmatrix} \cos\beta_s & 0 & \sin\beta_s \\ 0 & 1 & 0 \\ -\sin\beta_s & 0 & \cos\beta_s \end{bmatrix} \begin{Bmatrix} 0 \\ 0 \\ \Omega \end{Bmatrix} \begin{Bmatrix} 0 \\ -\dot{\beta}_s \\ 0 \end{Bmatrix}$$

That is

$$\begin{aligned} p_B &= \Omega \sin \beta_s \\ q_B &= -\dot{\beta}_s \\ r_B &= \Omega \cos \beta_s \end{aligned} \tag{1.5}$$

Substitution of (1.5) into (1.4) gives

$$I_B[-\ddot{\beta}_s - \Omega^2 \cos \beta_s \sin \beta_s]\bar{j}_B + [-2\Omega \sin \beta_s \dot{\beta}_s]\bar{k}_B = \int_0^R \bar{r} \times d\bar{F}_A \tag{1.6}$$

The first term on the left hand side is the angular acceleration of the blade about the y_B axis and the second term is the angular acceleration of the blade about the z_B axis (i.e., in the lag direction), which arises as a result of out-of-plane (flapping) motion of the blade. The aerodynamic force on the blade element is comprised of the lift and drag and is formulated from strip theory (usually called blade-element theory) [1, 2]. Also, see the discussion in Sect. 4 in Chap. 'Dynamic Aeroelasticity'. Three-dimensional effects are obtained by including the induced velocity which, for our purposes, may be calculated by momentum theory [1]. Thus from Fig. 2.

$$d\bar{F}_A = dL\bar{k}_B + (-dD - \phi dL)\bar{j}_B \tag{1.7}$$

where the inflow angle ϕ is assumed to be small and is made up of the effect of induced velocity (downwash) and the induced angle due to flapping velocity. Therefore

$$\begin{aligned} dL &= \frac{1}{2}\rho(\Omega r)^2 c\, dr a(\theta - \phi) \\ dD &= \frac{1}{2}\rho(\Omega r)^2 c\, dr \delta \\ \phi &= \frac{r\dot{\beta}_s + v}{\Omega r} \end{aligned}$$

Define

$$x \equiv \frac{r}{R}; \quad \lambda \equiv -\frac{v}{\Omega R}; \quad \gamma \equiv \frac{\rho a c R^4}{I_B} \quad \text{(the Lock number)} \tag{1.8}$$

Here the blade chord, c, and pitch angle, θ, are taken to be independent of x, for simplicity, although rotor blades are usually twisted. The blade section drag coefficient is denoted by δ and is also assumed to be independent of the radial station. Thus

$$dL = \frac{I_B \gamma \Omega^2}{R}\left[\theta - \frac{\dot{\beta}_s}{\Omega} + \frac{\lambda}{x}\right]x^2 dx$$

$$dD = \frac{I_B \gamma \Omega^2}{R}\left(\frac{\delta}{a}\right)x^2 dx \tag{1.9}$$

and

$$\bar{r} = xR\bar{i}_B$$

The total rotor thrust is found by integrating the lift along the radius, averaging over one revolution, and multiplying by the number of blades to give [1]

$$\frac{2C_T}{a\sigma} = \frac{\theta}{3} + \frac{\lambda}{2} \tag{1.10}$$

where

$$\sigma = \frac{bc}{\pi R}$$

and b is the number of blades. The thrust coefficient is

$$C_T = \frac{T}{\rho\pi R^2(\Omega/R)^2}$$

Momentum theory results in the following expression for the induced velocity

$$\lambda = -\sqrt{\frac{C_T}{2}}$$

so that the integral on the right-hand side of Eq. (1.6) becomes

$$\begin{aligned}\int_0^R \bar{r} \times d\bar{F}_A = &-\frac{I_B\gamma\Omega^2}{8}\left[\theta + \frac{4\lambda}{3} - \frac{\dot{\beta}_s}{\Omega}\right]\bar{j}_b \\ &+ \frac{I_B\gamma^2}{8}\left[-\frac{\delta}{a} + \frac{\dot{\beta}_s}{\Omega}\left(\frac{\dot{\beta}_s}{\Omega} - \theta\right) + \frac{4}{3}\left(\theta - 2\frac{\dot{\beta}_s}{\Omega}\right)\lambda + 2\lambda^2\right]\bar{k}_B\end{aligned} \tag{1.11}$$

The $\bar{j}_B$ components contribute to the flapping equation of motion which may be expressed from Eqs. (1.6) and (1.11) as

$$\ddot{\beta}_s + \frac{\gamma\Omega}{8}\dot{\beta}_s + \Omega^2 \cos\beta_s \sin\beta_s = \frac{\gamma\Omega^2}{8}\left[\theta + \frac{4\lambda}{3}\right] \tag{1.12}$$

The $\bar{k}_B$ component of Eq. (1.11) is the aerodynamic torque about the z_B axis or in the lag direction. There is a steady component and a component proportional to flapping velocity. Each of these components is important either for loads or for stability of the inplane motion.

If we assume that the flapping motion is small as is typical of rotor blade motion then the flapping equation becomes linear.

$$\ddot{\beta}_s + \frac{\gamma\Omega}{8}\dot{\beta}_s + \Omega^2\beta_s = \frac{\gamma\Omega^2}{8}\left[\theta + \frac{4\lambda}{3}\right] \tag{1.13}$$

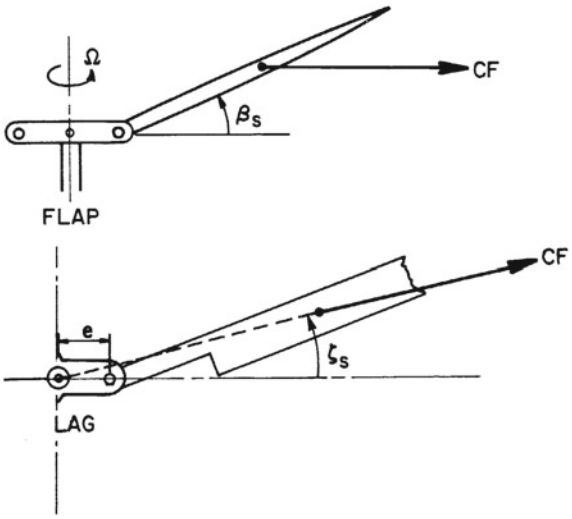

Fig. 3 Direction of centrifugal force for flap and lag motion

The linearized blade flapping equation may be recognized as a second order system with a natural frequency equal to the rotor angular velocity and a damping ratio equal to $\gamma/16$ which arises from the aerodynamic moment about the flapping pin. This motion is well damped as γ is between 5 and 15 for typical rotor blades. It is good that the system is well damped since the aerodynamic inputs characteristically occur in forward flight at Ω, and thus the blade flapping motion is forced at resonance.

The spring or displacement term can be interpreted as arising from the centrifugal force [1]. This same stiffening effect will appear in the flexible blade analysis and will increase the natural frequency as rotational speed is increased.

If the more general case of flapping in forward flight is considered, then the equation of motion for flapping (1.12) will contain periodic coefficients which can lead to instabilities [16]. However, the flight speed at which such instabilities occur is well beyond the performance range of conventional helicopters, unless they have positive pitch-flap coupling.

Now we include the lag degree-of-freedom to obtain a complete description of rigid motion of a fully-articulated rotor blade . The complete development of this two-degree-of-freedom problem is quite lengthy and will not be reproduced here [17].

Following the approach given above, assuming that the flap angle and lag angle are small and that the lag hinge and flap hinge are coincident and located a small distance e (hinge offset) from the axis of rotation as shown in Fig. 3, and further accounting for the effect of lag velocity on the aerodynamics forces acting on the blade, the lift is given by

$$dL = \frac{1}{2}\rho[\Omega + \dot{\zeta}_s r]^2 c\, dr a \left[\theta - \frac{(r\dot{\beta}_s + v)}{(\Omega + \dot{\zeta}_s)r}\right] \tag{1.14}$$

where the effect of the small distance e on the aerodynamics is neglected. The lag angle is defined as positive in the direction of rotor rotation. Care must be taken in formulating the inertial terms since we have noted above that a term like $\dot{\beta}_s \sin(\beta_s)$ is of significance in the equations of motion, and thus the small angle assumption must not be made until after the expressions for the acceleration have been obtained. Rotating by the flap angle first and then by the lag angle, the angular rates in the blade body axis system are given by

$$\begin{Bmatrix} p_B \\ q_B \\ r_B \end{Bmatrix} = \begin{bmatrix} \cos\zeta_s & \sin\zeta_s & 0 \\ -\sin\zeta_s & \cos\zeta_s & 0 \\ 0 & 0 & 1 \end{bmatrix} \begin{bmatrix} \cos\beta_s & 0 & \sin\beta_s \\ 0 & 1 & 0 \\ -\sin\beta_s & 0 & \cos\beta_s \end{bmatrix} \begin{Bmatrix} 0 \\ 0 \\ \Omega \end{Bmatrix} + \begin{bmatrix} \cos\zeta_s & \sin\zeta_s & 0 \\ -\sin\zeta_s & \cos\zeta_s & 0 \\ 0 & 0 & 1 \end{bmatrix} \begin{Bmatrix} 0 \\ -\dot{\beta}_s \\ 0 \end{Bmatrix} + \begin{Bmatrix} 0 \\ 0 \\ \dot{\zeta}_s \end{Bmatrix} \tag{1.15}$$

We must also account for the fact that the hinge point of the blade is no longer at rest but is accelerating [15]. Since the hinge point is located at a distance e from the axis of rotation, the equation of motion, (1.1), must be modified to read

$$\dot{\bar{H}}_P + \bar{\Omega}_B \times \bar{H}_P = \int_0^R \bar{r} \times d\bar{F}_A + \bar{E} \times M_B \bar{a}_P \tag{1.16}$$

where $\bar{a}_P$ is the acceleration of the hinge point

$$\bar{a}_P = \bar{\Omega} \times (\bar{\Omega} \times \bar{E}) + \dot{\bar{\Omega}} \times \bar{E} \tag{1.17}$$

$\bar{E}$ is the offset distance and M_B is the blade mass.

Accounting for all of these factors, and assuming that the flapping and lagging motion amplitudes are small, the equations of motion for this two-degree-of-freedom system may be expressed [17, 18] as

$$\begin{aligned} -\ddot{\beta}_s - \Omega^2\left(1 + \frac{3}{2}\bar{e}\right)\beta_s - 2\beta_s\dot{\zeta}_s\Omega &= -\frac{\gamma\Omega^2}{8}\left[\,\theta + \frac{4}{3}\lambda - \frac{\dot{\beta}_s}{\Omega} + \right. \\ \left.\left(2\theta + \frac{4}{3}\lambda\right)\frac{\dot{\zeta}_s}{\Omega}\,\right] - 2\beta_s\dot{\beta}_s\Omega + \ddot{\zeta}_s + \frac{3}{2}\bar{e}\Omega^2\zeta_s &= \frac{\gamma\Omega^2}{8}\left[\,-\left(\theta + \frac{8}{3}\lambda\right)\frac{\dot{\beta}_s}{\Omega} - \right. \\ \left.\left(2\frac{\delta}{a} - \frac{4}{3}\lambda\theta\right)\frac{\dot{\zeta}_s}{\Omega} - -\frac{\delta}{a} + \frac{4}{3}\lambda\theta + 2\lambda^2\,\right] \end{aligned} \tag{1.18}$$

where

$$\bar{e} = \frac{e}{R}$$

It has been assumed that the blade has a uniform mass distribution. These results can be displayed more conveniently by nondimensionalizing time by rotor angular velocity Ω and also expressing the variables as the sum of a constant equilibrium part and a perturbation

$$\begin{aligned} \beta_s &= \beta_0 + \beta \\ \zeta_s &= \zeta_0 + \zeta \end{aligned} \tag{1.19}$$

Retaining only linear terms, the equilibrium equations are

$$\begin{aligned} \beta_0 &= \frac{\gamma}{8(1+\frac{3}{2}\bar{e})}\left[\theta + \frac{4\lambda}{3}\right] \\ \zeta_0 &= \frac{\gamma}{12\bar{e}}\left[-\frac{\delta}{a} + \frac{4}{3}\lambda\theta + 2\lambda^2\right] = -\frac{1}{3}\frac{\gamma}{\bar{e}}\left(\frac{2C_q}{a\sigma}\right) \end{aligned} \tag{1.20}$$

The steady value of the flapping, β_0, is referred to as the coning angle. The steady value of the lag angle, ζ_0, is proportional to the rotor torque coefficient, c_q [1].

The perturbation equations are

$$\begin{aligned} &\ddot{\beta} + \frac{\gamma}{8} + \left(1 + \frac{3}{2}\bar{e}\right)\beta + \left[2\beta_0 - \frac{\gamma}{8}\left(2\theta + \frac{4}{3}\lambda\right)\right]\dot{\zeta} = 0 \\ &\left[-2\beta_0 + \frac{\gamma}{8}\left(\theta + \frac{8}{3}\lambda\right)\right]\dot{\beta} + \ddot{\zeta} + \frac{\gamma}{8}\left(2\frac{\delta}{a} - \frac{4}{3}\lambda\theta\right)\dot{\zeta} + \frac{3}{2}\bar{e}\zeta = 0 \end{aligned} \tag{1.21}$$

These equations describe the coupled flap-lag motion of a rotor blade. A number of features can be noted. The effect of the blade angular velocity on the lag frequency is much weaker than on flap frequency. The uncoupled natural frequency in flap expressed as a fraction of the blade angular velocity is

$$\frac{\omega_\beta}{\Omega} = \sqrt{1 + \frac{3}{2}\bar{e}} \tag{1.22}$$

and the coupled frequency in lag is

$$\frac{\omega_\zeta}{\Omega} = \sqrt{\frac{3}{2}\bar{e}} \tag{1.23}$$

For a typical hinge offset of $\bar{e} = 0.05$, the rigid flap frequency is

$$\frac{\omega_\beta}{\Omega} = 1.04$$

and the rigid lag frequency is

$$\frac{\omega_\zeta}{\Omega} = 0.27$$

The flap natural frequency is thus somewhat higher than the rotational speed, and the lag frequency is roughly one-quarter of the rotational speed. This difference is due to the weaker effect of the restoring moment due to centrifugal force in the lag direction as indicated in Fig. 3.

The uncoupled lag damping arises primarily from the blade drag and is equal to

$$D_L \equiv 2\frac{\delta}{a}\left(\frac{\gamma}{8}\right) \tag{1.24}$$

The lift curve slope of the blade, a, is the order of 6 per radian and the drag coefficient, δ, is the order of 0.015 giving a physical lag damping which is 0.005 times the flap damping or characteristically negligible. The damping ratio of the uncoupled lag motion for a Lock number of 8 is

$$\zeta_L = 0.009$$

This low value of aerodynamic damping indicates that structural damping will be of significance in estimating the lag damping. Any coupling between these equations which reduces the lag damping tends to result in an instability. Equation (1.21) can be rewritten

$$\begin{aligned} &\ddot{\beta} + \frac{\gamma}{8}\dot{\beta} + \left(1 + \frac{3}{2}\bar{e}\right)\beta + \left(\beta_0 - \frac{\gamma}{8}\theta\right)\dot{\zeta} = 0 \\ &-\frac{\gamma}{8}\theta\dot{\beta} + \ddot{\zeta} + \frac{\gamma}{8}\left[2\frac{\delta}{a}\right]\dot{\zeta}\frac{3}{2}\bar{e}\zeta = 0 \end{aligned} \tag{1.25}$$

where the equilibrium relationship for β_0 has been introduced (1.20) with the effect of hinge offset on coning neglected. It can be shown that the coupling present in this two-degree-of-freedom system arising from inertial and aerodynamic forces will not lead to an instability. However, the hinge offset or changes in minor features of the hub geometry can lead to instability. The equilibrium lag angle is proportional to rotor torque (Eq. (1.20)); and, consequently, it varies over a wide range from high power flight to autorotation as a result of the weak centrifugal stiffening. Thus, the simple pitch link geometry shown in Fig. 4 will produce a pitch change with lag depending upon the equilibrium lag angle. The blade pitch angle variation with lag angle can be expressed as

$$\Delta\theta = \theta_\zeta \zeta$$

This expression is inserted into Eq. (1.18). Retaining only the linear homogeneous terms, the perturbation equations are

$$\begin{aligned} &\ddot{\beta} + \frac{\gamma}{8}\dot{\beta} + \left(1 + \frac{3}{2}\bar{e}\right)\beta + \left(\beta_0 - \frac{\gamma}{8}\theta\right)\dot{\zeta} - \frac{\gamma}{8}\theta_\zeta\zeta = 0 \\ &\frac{-\gamma}{8}\theta\dot{\beta} + \ddot{\zeta} + \frac{\gamma}{8}\left[2\frac{\delta}{a}\right]\dot{\zeta}\frac{3}{2}\bar{e}\zeta - \frac{\gamma}{6}\lambda\theta_\zeta\zeta = 0 \end{aligned} \tag{1.26}$$

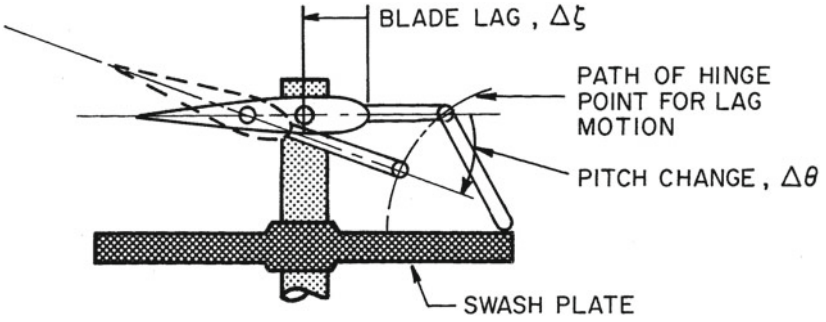

Fig. 4 Pitch-lag coupling due to pitch link geometry. Articulated rotor

We can now sketch a root locus for the effect of θ_ζ on the dynamics of this system. Expressing the equations of motion in operational notation, the root locus equation for variations in θ_ζ is

$$\frac{-\theta_\zeta \frac{\gamma\lambda}{6}\left[s^2 + \frac{3}{4}\frac{\beta_0}{\lambda}s + 1 + \frac{3}{2}\bar{e}\right]}{[s^2 + \frac{\gamma}{8}s + (1 + \frac{3}{2}\bar{e})][s^2 + \frac{\gamma}{8}[2\frac{\delta}{a}]s + \frac{3}{2}e] + \frac{\gamma}{8}\theta(\bar{\beta_0} - \frac{\gamma}{8}\theta)s^2} = -1 \qquad (1.27)$$

The root locus shown in Fig. 5 illustrates the effect of this geometric coupling, indicating that the critical case where instability occurs corresponds to the 180° locus (θ_ζ is positive). Recall that λ is negative. Thus, if forward lag produces an increase in pitch, an instability is likely to occur for a soft-inplane rotor. The effect is also proportional to thrust coefficient indicating that the instability is more likely to occur as the thrust is increased [18, 19]. Increasing thrust also increases the steady-state lag angle, hence increasing the geometric coupling for the geometry shown. In general, this instability tends to be of a rather mild nature, but it has destroyed tail rotors. Mechanical dampers are often installed about the lag axes for reasons to be discussed and these also provide additional lag damping and thus can alleviate the instability.

This example serves to illustrate that great care must be taken in the geometric design of the articulated rotor hub to avoid undesirable couplings and possible instabilities. We now turn to the elastic hingeless blade.

1.2 Elastic Motion of Hingeless Blades

The dynamics of a single hingeless blade will now be examined. Again we will use a simplified analysis which yields the essential features of the dynamic motion, and the reader is referred to the literature for a more detailed approach. In general, the flap and lag elastic deformations (as referred to a shaft axis system) are coupled as a result of the fact that the principal elastic axes of the blade will be inclined with

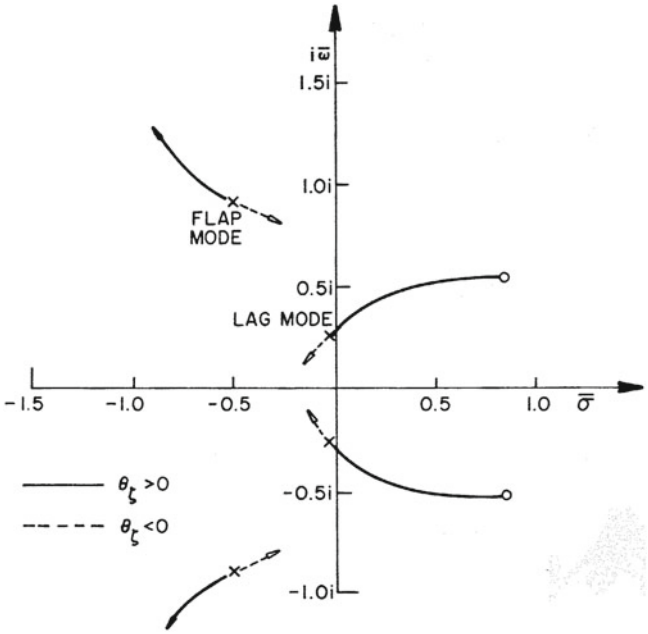

Fig. 5 Effect of pitch-lag coupling on flap-lag stability

respect to the shaft due to pitch angle. In fact, the term flexible "blade", as used here, includes the hub as well as the blade itself. "Hub" is used to refer to the portion of the blade structure inboard of the radial location where the pitch change takes place. The rotation of the blade principal elastic axes with blade pitch will depend upon the relative stiffness of the hub and the blade. It can be seen physically that, if the hub is soft in comparison to the blade, then the principal axes of this flexible system tend to remain fixed as the pitch of the blade is changed. However, if the hub is stiff and the blade is soft, the principal elastic axes rotate in a 1:1 relationship with blade pitch. An additional source of elastic coupling between flap and lag deflections arises from the built-in blade twist. A third source of elastic coupling between flap and lag arises from inclusion of torsion as a degree-of-freedom. For the typical rotor blade with a high torsional frequency, the effect of torsional flexibility on flap-lag coupling can be obtained through a quasistatic approximation to the torsional motion. That is, for a first-order estimate, the torsional inertia and damping can be neglected; and the coupling effects of torsional flexibility can be expressed in terms of geometric coupling similar in form to the hub geometry effects described in connection with the fully-articulated rotor. A detailed analysis of the flap-lag-torsion motion of a hingeless rotor blade may be found in [20, 21], and the complete equations of motion for elastic bending and torsion of rotor blades may be found in [22].

We now proceed to examine the flap-lag motion of a hingeless rotor blade from a simplified viewpoint.

If it is assumed that the rotor blade is untwisted, has zero pitch, and is torsionally rigid; the natural frequencies of the rotating blade can be expressed in terms of its mode shapes, ϕ, and derivatives with respect to radial distance ϕ' and ϕ'' as [23–25]

$$\omega_\beta^2 = \frac{\int_0^R EI_\beta(\phi_\beta'')^2 dr + \Omega^2 \int_0^R \left(\phi_\beta'\right)^2 (\int_r^R mn\, dn) dr}{\int_0^R m\phi_\beta^2 dr} \tag{1.28}$$

$$\omega_\zeta^2 = \frac{\int_0^R EI_\zeta(\phi_\zeta'')^2 dr + \Omega^2 \left\{\int_0^R \left(\phi_\zeta'\right)^2 (\int_r^R mn\, dn) dr - \int_0^R m\phi_\zeta^2 dr\right\}}{\int_0^R m\phi_\zeta^2\, dr}$$

m is the running mass of the blade and EI is the stiffness these expressions gives the nonrotating natural frequency and the second term gives the effect of centrifugal stiffening due to rotation. The coefficient of the square of the angular velocity Ω in the expression for flapping frequency is usually referred to as the Southwell coefficient. Note that the effect of the centrifugal stiffening is considerably weaker in the lag direction than in the flap direction as would be expected from the previous discussion of the articulated rotor.

The Southwell coefficient is denoted by K_s

$$K_s = \frac{\int_0^R (\phi_\beta')^2 \left(\int_r^R mn\, dn\right) dr}{\int_0^R m\phi_\beta^2 dr} \tag{1.29}$$

and the nonrotating frequencies are denoted by

$$\begin{aligned} \omega_{\beta_0}^2 &= \frac{\int_0^R EI_\beta(\phi_\beta'')^2 dr}{\int_0^R m\phi_\beta^2 dr} \\ \omega_{\zeta_0}^2 &= \frac{\int_0^R EI_\zeta(\phi_\zeta'')^2 dr}{\int_0^R m\phi_\zeta^2 dr} \end{aligned} \tag{1.30}$$

If the flap and lag mode shapes are assumed to be the same, the rotating frequencies can be written as

$$\begin{aligned} \omega_\beta^2 &= \omega_{\beta_0}^2 + K_s\Omega^2 \\ \omega_\zeta^2 &= \omega_{\zeta_0}^2 + (K_s - 1)\Omega^2 \end{aligned} \tag{1.31}$$

It is interesting to note that, if the mode shape is assumed to be that of a rigid articulated blade with hinge offset, $\bar{e}$, i.e.,

$$\begin{aligned} \phi &= 0 \quad 0 < x < \bar{e} \\ \phi &= (x - \bar{e}) \quad \bar{e} < x < 1 \end{aligned} \tag{1.32}$$

for a uniform mass distribution and small $\bar{e}$, then from (1.29)

$$K_s \equiv 1 + \frac{3}{2}\bar{e} \tag{1.33}$$

Thus the natural frequencies are from (1.30), (1.31) and (1.33)

$$\omega_\beta^2 = \Omega^2 \left(1 + \frac{3}{2}\bar{e}\right)$$

$$\omega_\zeta^2 = \Omega^2 \left(\frac{3}{2}\bar{e}\right) \tag{1.34}$$

reducing to the results for the rigid blade. For typical blade mass and stiffness distributions, the Southwell coefficient is of the order of 1.2 [24].

A simplified model for the elastic rotor blade follows. The elastic blade is modelled as a rigid blade with hinge offset $\bar{e}$ and two orthogonal springs (K_β and K_ζ) located at the hinge to represent the flap and lag stiffness characteristics. The natural frequencies for this model of the blade are

$$\begin{aligned} \omega_\beta^2 &= \frac{K_\beta}{I_B} + \left(1 + \frac{3}{2}\bar{e}\right)\Omega^2 \\ \omega_\zeta^2 &= \frac{K_\zeta}{I_B} + \left(\frac{3}{2}\bar{e}\right)\Omega^2 \end{aligned} \tag{1.35}$$

The spring constants K_β and K_ζ can be chosen to match the nonrotating frequencies of the actual elastic blade, and the offset is chosen to match the Southwell coefficient. In this way the dependence of frequency on rotor angular velocity is matched. Owing to the fact that the Southwell coefficient is close to unity (i.e., the equivalent offset, $\bar{e}$ is small), in many investigations the dependence of the Southwell coefficient on $\bar{e}$ is neglected [17] giving

$$\begin{aligned} \omega_\beta^2 &= \frac{K_\beta}{I_B} + \Omega^2 \\ \omega_\zeta^2 &= \frac{K_\zeta}{I_B} \end{aligned} \tag{1.36}$$

Thus, with this approximation there is no centrifugal stiffening in the lag direction. We will use this approximation in the analysis which follows. Recall that these frequencies are assumed to be uncoupled and therefore are defined with respect to the blade axes. Thus, they will appear coupled in a shaft oriented axis system. In order to include the effect of hub flexibility in the analysis, the hub (the portion of the blade system which does not rotate with pitch) is modelled by a second pair of orthogonal springs which are oriented parallel and perpendicular to the shaft and do not rotate when the blade pith is changed [17]. These spring constants are denoted K_{β_H} and K_{ζ_H}. The springs representing blade stiffness, ζ_B, are also located at the

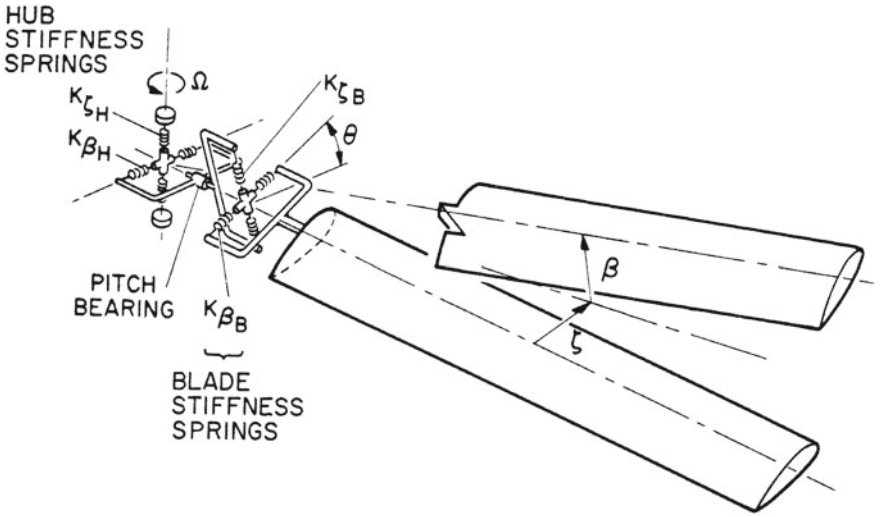

Fig. 6 Spring model for elastic blade and hub

root since offset has been neglected. However, this pair of springs rotate with the blade as pitch is changed. Figure 6 shows the geometry.

This model for the hub and blade gives rise to elastic coupling between flap and lag motion. Essentially, a mode shape $\phi = x$ is being employed to describe the elastic deflection of the blade in both directions such that the aerodynamic and inertial coupling terms developed for the articulated blade model (Eq. (1.21)) apply directly to this approximate model of the hingeless blade. The equations of motion for flap-lag dynamics are therefore

$$\begin{aligned} &\ddot{\beta} + \frac{\gamma}{8}\dot{\beta} + p^2\beta - \left\{\frac{\gamma}{8}\left(2\theta + \frac{4}{3}\lambda\right) - 2\beta_0\right\}\dot{\zeta} + z^2\zeta = 0 \\ &\left[-2\beta_0 + \frac{\gamma}{8}\left(\theta + \frac{8}{3}\lambda\right)\right]\dot{\beta} + z^2\beta + \ddot{\zeta} + \frac{\gamma}{8}\left(2\frac{\delta}{a} - \frac{4}{3}\lambda\theta\right)\dot{\zeta} + q^2\zeta = 0 \end{aligned} \tag{1.37}$$

where the difference between these equations of motion and those presented for the articulated blade (1.21) arise from the terms p, q, and z. p and q are the ratios of the noncoupled natural frequencies (i.e., those at zero pitch) to the rotor rpm, and z is the elastic coupling effect. For the spring model described above these terms can be expressed as [17]

$$p^2 = 1 + \frac{1}{\Delta}(\bar{\omega}_\beta^2 + R(\bar{\omega}_\beta^2)\sin^2\theta)$$

$$q^2 = \frac{1}{\Delta}(\bar{\omega}_\zeta^2 - R(\bar{\omega}_\zeta^2)\sin^2\theta)$$

$$z^2 = \frac{R}{2\Delta}(\bar{\omega}_\zeta^2 - \bar{\omega}_\beta^2)\sin 2\theta$$

$$\Delta = 1 + R(1-R)\frac{(\bar{\omega}_\zeta^2 - \bar{\omega}_\beta^2)^2}{\bar{\omega}_\zeta^2 \bar{\omega}_\beta^2}\sin^2\theta \tag{1.38}$$

$$\bar{\omega}_\beta^2 = \frac{K_\beta}{I_B\Omega^2}\bar{\omega}_\zeta^2 = \frac{K_\zeta}{I_B\Omega^2}$$

$$K_\beta = \frac{K_{\beta_B}K_{\beta_B}}{K_{\beta_B} + K_{\beta_B}} \quad K_\zeta = \frac{K_{\zeta_B}K_{\zeta_H}}{K_{\zeta_B} + K_{\zeta_H}} \quad R = \frac{\bar{\omega}_\zeta^2 \frac{K_\beta}{K_{\beta_B}} - \bar{\omega}_\beta^2 \frac{K_\zeta}{K_{\zeta_B}}}{\bar{\omega}_\zeta^2 - \bar{\omega}_\beta^2}$$

R is referred to as the elastic coupling parameter. The physical significance of this parameter can be understood by examining the relationship between the rotation of the principal axes of the blade-hub system, η, and the blade pitch angle, θ, [26]

$$\tan 2\eta = \frac{R\sin 2\theta}{R\cos 2\theta + (1-R)} \tag{1.39}$$

It can be seen from this expression that if $R = 0$ the principal axes remain fixed as blade pitch is changed and consequently there is no elastic coupling. The flap and lag natural frequencies are

$$p^2 = \bar{\omega}_\beta^2 + 1$$

$$q^2 = \bar{\omega}_\zeta^2$$

where $\bar{\omega}_\beta^2$ and $\bar{\omega}_\zeta^2$ are the dimensionless nonrotating frequencies. This is the case in which the hub is flexible and the blade is rigid. At the other limit $R = 1$, Eq. (1.39) indicates that the principal axes rotate in a 1:1 relationship with the blade pitch ($\eta = \theta$). In this case elastic coupling is present, and expressions for the natural frequencies (1.38) simply represent the fact that, as the blade is rotated through 90° pitch, the nonrotating frequencies must interchange. In addition to the case $R = 0$ where the elastic coupling between flap and lag vanishes, another interesting case exists in which no elastic coupling is present. This is the case referred to as matched stiffness, i.e., when the nonrotating frequencies of the blade are equal in both directions ($\bar{\omega}_\zeta = \bar{\omega}_\beta$). Various advantages accrue from this particular design choice as will be discussed below.

In principle, the designer has at his or her disposal the selection of the nonrotating frequencies of the blade. Consider some of the options in this regard. For simplicity, only the behavior of the rotor at zero pitch is examined. One choice is the matter of the hub stiffness relative to the blade stiffness which has an important impact on the flap-lag behavior of the rotor through the parameter R as will be discussed below. The flap frequency is largely chosen on the basis of the designed helicopter stability and control characteristics [5, 12]. Since the rotor blade is, in general, a long slender

member, the flap frequency will tend to be relatively near to the rotor rpm. Typical ratios of flap frequency to blade angular velocity for hingeless rotor helicopters are of the order of $p = 1.05 - 1.15$ [25] although at least one helicopter has flown with a flap frequency ratio of 1.4 [27]. The second major design decision is the choice of the lag frequency. Characteristically, the nonrotating lag frequency will tend to be considerably higher than the flap frequency owing to the larger dimensions of the blade and hub in the chordwise direction compared to the flapwise direction. As mentioned above, lag hinges are provided on articulated rotors to relieve lag stresses arising from flapping. Owing to the fact that the flap frequency is only slightly larger than once per revolution on a typical hingeless blade there will be considerable flap bending of the rotor blades. In fact, the amplitude of the vertical displacement of the blade tip on a hingeless blade will be quite similar to the flapping amplitude of the fully articulated rotor. The relationship between amplitude of tip motion of the hingeless blade and the flapping amplitude of the articulated blade is given by [28]

$$|\beta_H| = \frac{|\beta_A|}{\left\{1 + \left(\frac{8}{\gamma}(p^2 - 1)\right)^2\right\}^{\frac{1}{2}}}$$

Therefore, the inplane forces due to flap bending will cause the significant root stresses on a hingeless rotor. The dependence of these stresses on the selection of lag frequency can be seen by assuming that the flap and lag bending are loosely coupled ($z = 0$). The lag bending amplitude arising from sinusoidal flap bending at one per rev can be expressed from the Eq. (1.37), neglecting the lag damping, as

$$|\frac{\zeta}{\beta}| = \frac{\left[2\beta_0 - \frac{\gamma}{8}(\theta + \frac{8}{3}\lambda)\right]}{(q^2 - 1)} \tag{1.40}$$

The lag bending moment at the blade root, $K_\zeta \zeta$, thus varies as $q^2/(q^2 - 1)$ as shown in Fig. 7. It can be seen that if the lag frequency is selected above one per rev, large root bending stresses occur. The bending moment is reduced by choosing a lag frequency well below one per rev. A lag frequency below one per rev incidentally would be characteristic of a matched stiffness blade. For example, if

$$p^2 = 1.2 = \bar{\omega}_\beta^2 + 1$$

and

$$\bar{\omega}_\zeta^2 = \bar{\omega}_\beta^2$$

then

$$\bar{\omega}_\zeta = 0.45$$

Rotor blades are usually characterized by their lag frequency as soft inplane ($\bar{\omega}_\zeta < 1$) or stiff inplane ($\bar{\omega}_\zeta > 1$). Thus, rotor blade lag stresses an be reduced by choosing a

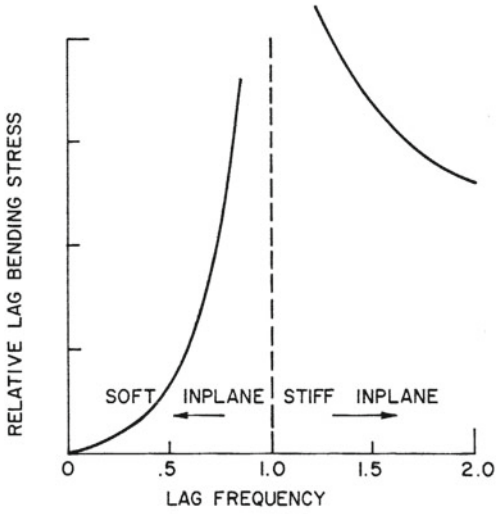

Fig. 7 Dependance of lag bending stress on lag frequency

soft inplane blade design and it should be kept in mind in the discussion that follows that there is a significant variation in the root bending stress with lag frequency. In the following, the influence of lag frequency on the dynamics of a hingeless blade is examined. Also it may be noted at this point that in contrast to the articulated rotor, in which large mechanical motion in lag allows mechanical lag dampers to be effective, this is usually more difficult with the hingeless rotor. Nevertheless, hingeless rotor helicopters have been equipped with lag dampers [10, 29].

Note also that if the lag frequency is selected such that the operating condition of the rotor is less than one per rev, then resonance in the lag mode will be encountered as the rotor is run up to operating speed.

Flap-lag stability characteristics as predicted by the equations of motion given by Eq. (1.37) are now examined. First consider the case in which the hub is considerably more flexible than the blade ($R = 0$). In Fig. 8 the stability boundaries given by Eq. (1.37) are shown as a function of flap and lag frequency and blade pitch angle for a typical rotor blade. This figure was obtained by determining the conditions under which Routh's discriminant equals zero. It can be seen that an approximately elliptical region of instability occurs which increases in extent as blade pitch is increased. It is centered around a lag bending frequency of 1.15 and flap frequency of 1.15 indicating that, in this particular case, flap-lag instability is more likely to be a problem for stiff inplane rotors. It can be seen that the stiff inplane blade ($1.1 < \bar{\omega}_\zeta < 1.2$) is destabilized with increasing pitch. Figure 9 shows root location of blade damping versus pitch angle (which relates to thrust coefficient). Clearly, the instabilities occur at high thrust. A family of plots can be seen for various values w_ζ. One can see that the stiff inplane rotors are more likely to be unstable. Figure 10 shows the effect of various ratios of hub stiffness to blade stiffness (different values of R) indicating the importance of careful modelling of the blade and hub in the

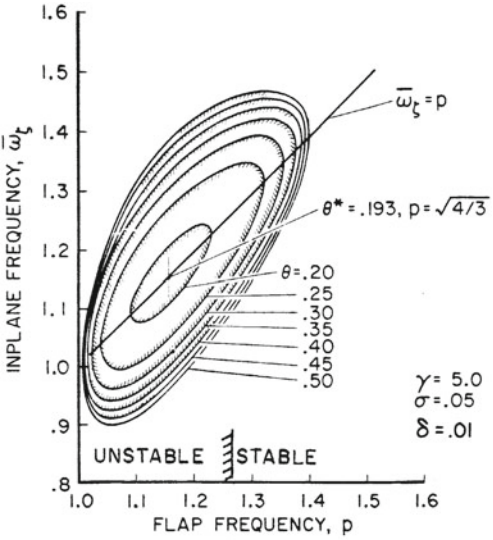

Fig. 8 Flap lag stability boundaries. $R = 0$, no elastic coupling [17]

study of flap-lag stability. This theory has been correlated with experiment in [30]. At large pitch angles where the blade encounters stall, wider ranges of instability occur as shown in [30]. This increase in the region of instability is primarily a result of the loss in flap damping owing to reduction in blade lift curve slope, a.

Various other configuration details have an impact on the flap-lag stability such as precone (the inclination of the blade feathering or pitch change axis with respect to a plane perpendicular to the hub). Precone is usually employed to relieve the root bending stresses that arise from the steady flap bending moment due to average blade lift. The blade may also have droop and sweep [21] (the inclinations of the blade axis with respect to the pitch change axis in the flap and lag directions respectively) which will also have an impact on the flap-lag stability. The presence of kinematic pitch-lag coupling will have important effects on hingeless blade stability which depend strongly on the lag stiffness and the elastic coupling parameter R [17]. Reference [31] provides a closed-form damping expression with a physical exploration of the effect of each parameter.

If torsional flexibility is included, elastic coupling between pitch, lag and flap will exist. This can be most readily understood by extending the simple spring model of blade flexibility to include a torsion spring. Consider a blade hub system as shown in Fig. 11 with a flap angle β and a lag angle ζ. Owing to the root spring orientation, there will be torques exerted about the torsion axis which depend on the respective stiffnesses in the two directions. Representing the torsional stiffness of the blade and control system by K_θ, the equation for torsional equilibrium is (neglecting torsional inertia and damping)

$$K_\theta \theta = (K_\beta - K_\zeta)\beta\zeta \tag{1.41}$$

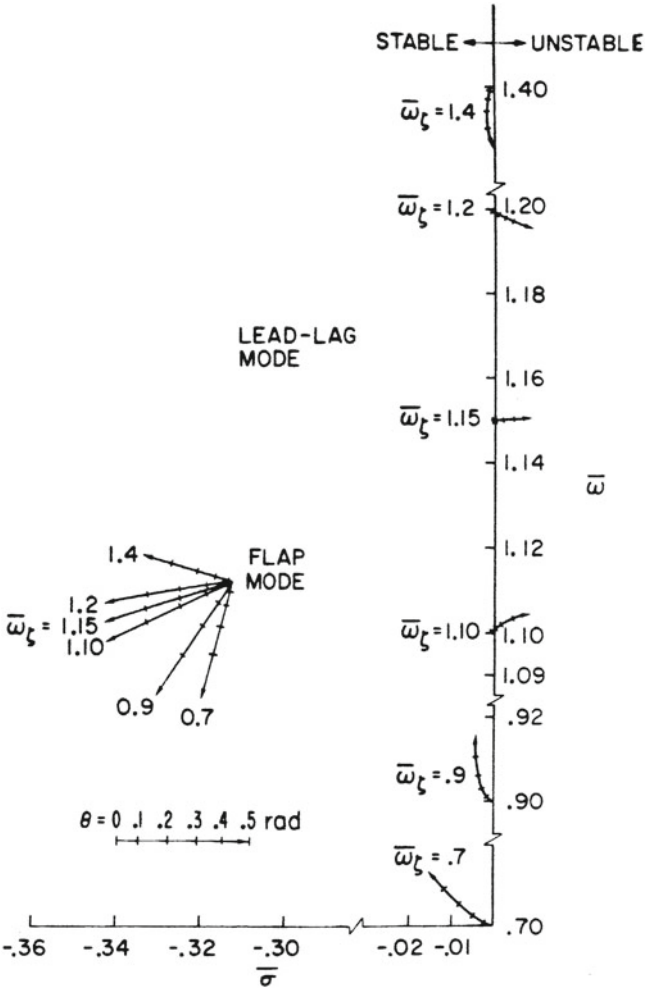

Fig. 9 Locus of roots for increasing blade pitch. $R = 0$, no elastic coupling

Linearizing about the blade equilibrium position, β_0, ζ_0,

$$\Delta\theta = \frac{1}{K_\theta}[(K_\beta - K_\zeta)\beta_0\Delta\zeta + (K_\beta - K_\zeta)\zeta_0\Delta\beta] \tag{1.42}$$

That is, torsional flexibility results in both pitch-lag coupling

$$\theta_\zeta = \left(\frac{K_\beta - K_\zeta}{K_\theta}\right)\beta_0 \tag{1.43}$$

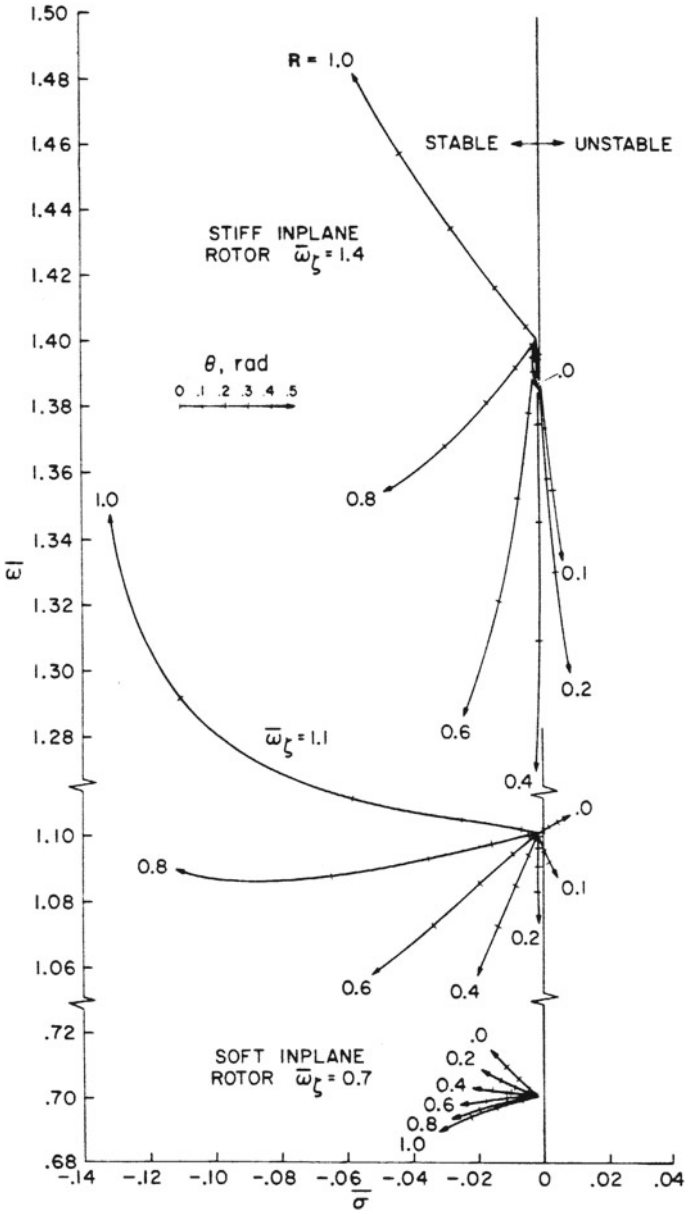

Fig. 10 Locus of roots for increasing blade pitch with various levels of elastic coupling [17]

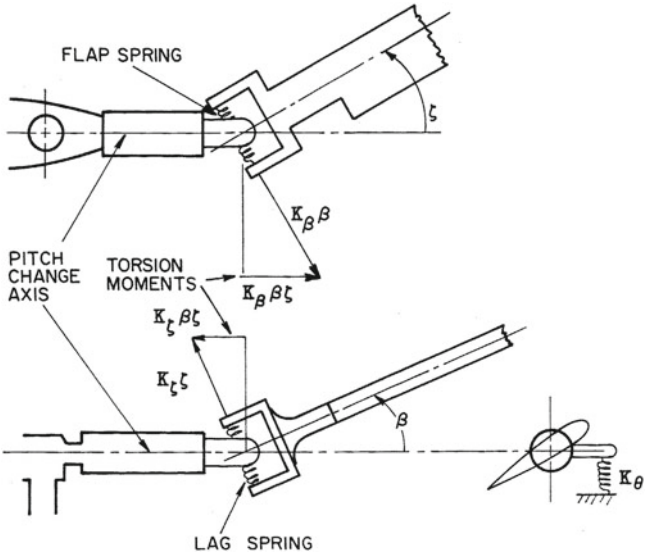

Fig. 11 Simplified blade model for flap-lag-torsion coupling

and pitch-flap coupling

$$\theta_\beta = \left(\frac{K_\beta - K_\zeta}{K_\theta}\right)\zeta_0 \tag{1.44}$$

These couplings depend both on the relative stiffness of the blade in the flap and lag directions and on the equilibrium values of the flap deflection and the lag deflection. A matched stiffness blade ($K_\beta = K_\zeta$) eliminates these couplings which is perhaps the primary reason for interest in a matched stiffness blade. For typical blade frequencies, K_ζ is larger than K_β and therefore θ_ζ tends to be negative and θ_β positive. θ_β is equivalent to what is usually referred to as a δ_3 hinge on an articulated blade. In powered flight ζ_0 is negative (1.20), and the sign of the effect is equivalent to negative ζ_3 [32]. This pitch change arising from flapping is statically destabilizing in the sense that an upward flapping produces an increase in pitch. If this term becomes sufficiently large, flapping divergence can occur. In autorotation, this coupling would change sign, as the equilibrium lag angle is positive. The characteristically negative value of pitch-lag coupling θ_ζ tends to produce a stabilizing effect in most cases as may be seen from the articulated rotor example. Negative values of θ_ζ can be destabilizing for a stiff inplane rotor with small values of R [17]. Precone, that is rotation of the pitch change axis in the flap direction, has a significant effect on the pitch-lag coupling. The coning angle β_0, in Eq. (1.43) refers only to the elastic deflection of the blade. Consequently, with perfect precone, that is, when the precone angle is equal to the equilibrium steady flap angle given by Eq. (1.20), the elastic deflection is zero and the pitch-lag coupling is zero. For excessive precone (i.e., if the rotor is operated well below its design thrust), β_0 is negative and a destabilizing

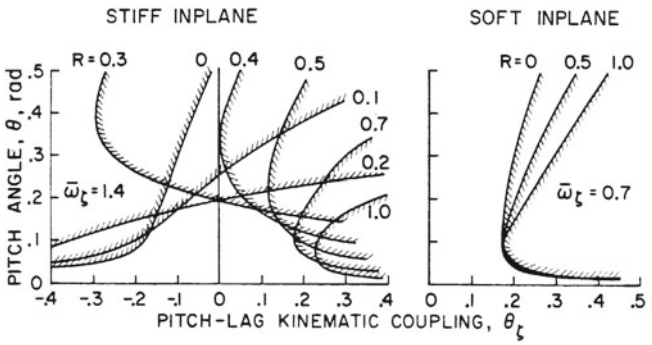

Fig. 12 Flap-lag stability boundaries as a function of pitch-lag coupling and elastic coupling [17]

pitch-lag coupling occurs. It should be noted that hub flexibility will also have an important impact on these kinematic couplings since it will determine the deflection of the pitch change axis. A precise formulation of flap-lag-torsion coupling as well as further discussion of its influence on blade stability can be found in [12]. Comparisons of theory and experiment can be found in [33].

In summary, a soft-inplane rotor blade tends to be less susceptible to isolated blade instabilities while the stiff-inplane blade tends to exhibit instabilities along with a considerably more complex behavior with changes in parameters. Figure 12 contrasts the effect of pitch-lag coupling on these two rotor blade types illustrating the complexity of the stability boundaries for the stiff inplane case in contrast to the soft inplane case which is quite similar to the articulated rotor.

2 Stall Flutter

A single degree-of-freedom instability encountered by helicopter blades which also occurs in gas turbines is referred to as stall flutter. The reader should consult Chap. 'Stall Flutter' for a discussion of stall flutter on a nonrotating airfoil. Stall flutter is primarily associated with high speed flight and maneuvering of a helicopter and arises from the fact that stalling of the rotor blade is encountered at various locations on the rotor disc. For a rotor blade, stall flutter does not constitute a destructive instability but rather produces a limit cycle behavior owing to the varying aerodynamic conditions encountered by the blade as it rotates in forward flight.

Consider the aerodynamic conditions existing on a rotor blade in high speed flight. On the advancing side of the rotor disc, the dynamic pressure depends on the sum of the translation velocity of the helicopter and the rotational velocity, while on the retreating side of the disc it depends on the difference between these two velocities. Consequently, if the rolling moment produced by the rotor is equal to zero, as required for equilibrium flight, the angle-of-attack of the blade is considerably smaller on the

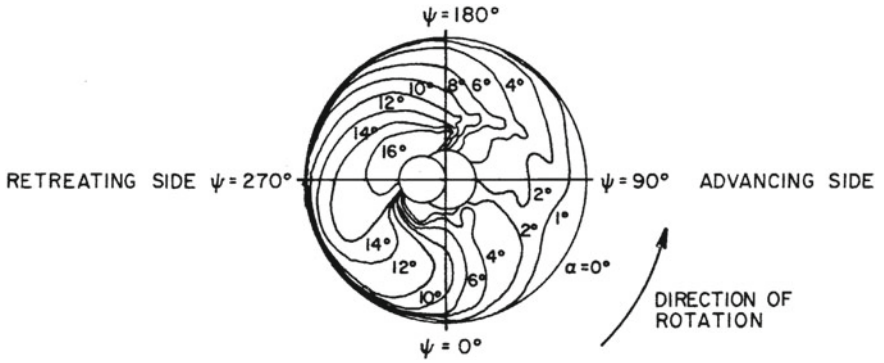

Fig. 13 Angle of attack distribution of helicopter rotor at 140 knots (advance ratio = 0.33) [34]

advancing side than on the retreating side. A typical angle-of-attack distribution at an advance ratio of 0.33 (140 kts) is shown in Fig. 13. This resulting distribution is produced by a combination of flapping or flap bending motion and the pilot's control input.

Note that on the advancing side the angle-of-attack is small and varies comparatively slowly with azimuth angle. On the retreating side the angle-of-attack is large and changes rapidly with azimuth angle. Consequently, prediction of the airload on the blade requires a model for the aerodynamics of the blade element which includes unsteady effects both in the potential flow region as well as in the stalled region. The source of the stall flutter instability is related to the unsteady aerodynamic characteristics of an airfoil under stalled conditions. Since the stalled region is only encountered by the blade over a portion of the rotor disc, however, if an instability of the aerodynamics at stall, it will not give rise to continuing unstable motion since a short time later the blade element will be at a low angle-of-attack, well below stall.

Owing to the complexity of the flow field around a stalled airfoil, we must have recourse to experimental data in order to determine the unsteady aerodynamic characteristics of an airfoil oscillating a high angle-of-attack. Experimental data are available in recent years on typical helicopter airfoil sections [34–36], which make it possible to characterize the aerodynamics of an airfoil oscillating about stall . In addition, a number of investigations have been conducted which give insight into the nature and complexity of the aerodynamic flow field under stalled conditions [37–39].

For a simplified treatment of stall flutter, it is assumed that the blade motion can be adequately described by a model involving only the blade torsional degree-of-freedom. The influence of flapping or heave motion of the section is neglected such that $\theta = \alpha$. The equation of motion for this single degree-of-freedom system is therefore

$$\ddot{\alpha} + \omega_\theta^2 \alpha = \left(\frac{\rho(\Omega R)^2 c^2}{2 I_\theta} \right) C_M(\dot{\alpha}) \tag{2.1}$$

where aerodynamic strip theory analysis is employed. Since the aerodynamic damping is a complex function of the angular velocity, it is convenient to express Eq. (2.1) as an energy equation by multiplying by $d\alpha$ and integrating over one cycle to obtain

$$\Delta\left\{\frac{\dot{\alpha}^2}{2}+\omega_\theta^2\frac{\alpha^2}{2}\right\}=\frac{\rho(\Omega R)^2c^2}{2I_\theta}\int C_M(\dot{\alpha})d\alpha \tag{2.2}$$

The left hand side of Eq. (2.2) expresses the change in energy over one cycle which is produced by the dependence of aerodynamic pitching moment on angle-of-attack rate as given by the right hand side. Figure 14 shows the time history of the pitching moment and normal force coefficients as a function of angle-of-attack for an airfoil oscillating at a reduced frequency typical of one per rev motion at three mean angles-of-attack. The arrows on the figure denote the direction of change of C_N and C_M. Note the large hysteresis loop which occurs in the normal force in the dynamic case when the mean angle-of-attack is near stall. In the potential flow region the effects are rather small and are predicted by Theodorsen's aerodynamic theory (see Chap. 'Nonsteady Aerodynamics of Lifting and Non-lifting Surfaces'). Proper representation of the unsteady lift behavior does have an important bearing on the prediction of rotor

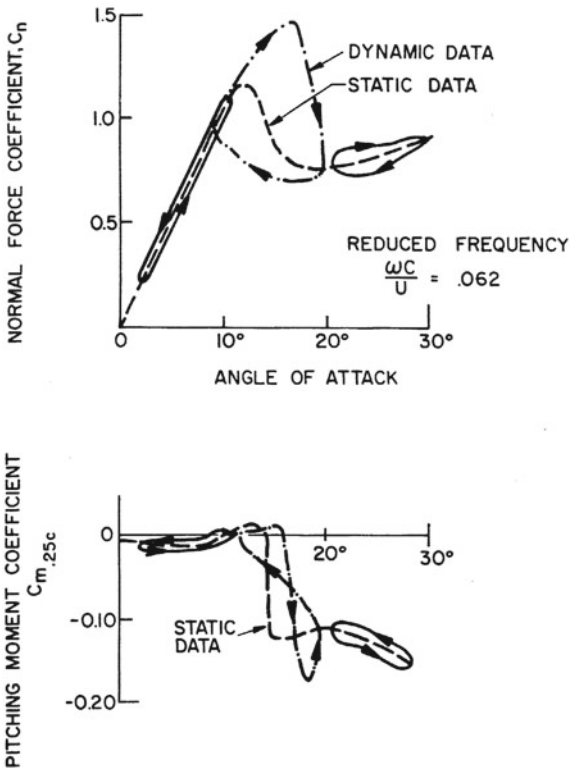

Fig. 14 Typical oscillating airfoil data [35]

performance, but will not be discussed further. The pitching moment characteristics are of primary interest here.

The pitching moment is well behaved in the potential flow region, and well above stall, resulting in small elliptically shaped loops over one cycle. In the vicinity of lift stall, two interesting effects occur; the average pitching moment increases markedly in a nose down sense, a phenomenon that is referred to as moment stall [35], and the moment time history looks like a figure eight. The change in energy over one cycle given by Eq. (2.2) is proportional to

$$\int C_M(\dot{\alpha}) d\alpha$$

The value of this integral is qual to the area enclosed by the loop, and its sign is given by the direction in which the loop is traversed. If the loop is traversed in a counter clockwise direction, then this integral will have a negative value indicating that energy is being removed from the structure or that there is positive damping. Thus the low and high angle-of-attack traces indicate positive damping. Near the angle-of-attack at which moment stall occurs statically, however, the figure-eight-like behavior indicates that there is essentially no net dissipation of energy over a cycle or possibly that energy is being fed into the structure (the integral on the right hand side of Eq. (2.2) is positive). This pitching moment characteristic gives rise to the phenomenon referred to as stall flutter. To actually encounter stall flutter, this behavior must occur over some appreciable span of the blade [40]. Reference [40] also discusses the importance of the rate of change of angle-of-attack with time on the dynamics of this process and concludes that delay in the development of dynamic stall depending upon $\dot{\alpha}$ is responsible for stall occurring over a significant radius of the blade with consequent effects on the rotor loads and vibrations. Of course, the rotor blade only encounters this instability over a small azimuth range and, consequently, the complete motion is essentially a limit cycle. The loss in damping at stall coupled with the marked change in the average pitching moment gives rise to large torsional motion with perhaps 2 or 3 cycles of the torsion excited before being damped by the low angle-of-attack aerodynamics. A typical time history of blade torsional motion and angle-of-attack when stall flutter is encountered is shown in Fig. 15. The dominant effect of the occurrence of stall flutter on a helicopter is to give rise to a marked increase in the vibratory loads in the blade pitch control system [40]. Reference [40] discusses approximate methods for incorporating unsteady stall aerodynamics into the rotor blade equations of motion. The most significant assumption in the analysis of rotor blade stall flutter relates to the applicability of two-dimensional data on airfoils oscillating sinusoidally to a highly three-dimensional flow field in which the motions are nonsinusoidal.

Further understanding of the aerodynamics of stall may make it possible to design airfoil sections that would minimize the occurrence of stall flutter and the associated control loads. Blade section design, however, has many constraints owing to the wide range in aerodynamic conditions encountered in one revolution; and the aerodynamic phenomena described appear to be characteristic of airfoils oscillating

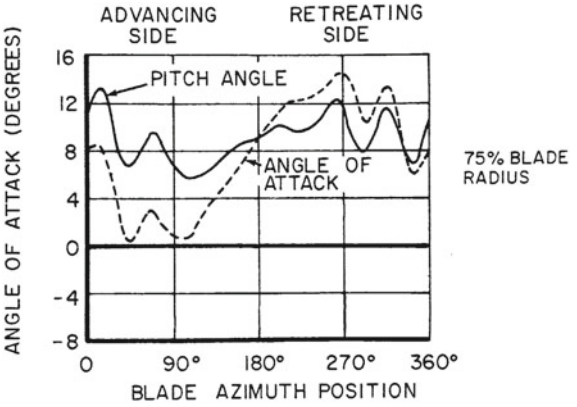

Fig. 15 Typical time history of blade motion for blade encountering stall flutter [42]

about an angle-of-attack beyond the onset of static stall. In more recent work, analytic methods have been developed to model dynamic stall [41, 42]; and CFD codes have been formulated to predict dynamic stall [43].

3 Rotor-Body Coupling

Another important topic is the aeroelastic instability of helicopters associated with coupling of blade motion and body motion. This problem is of considerable significance in articulated and hingeless rotor helicopter design, and was first encountered on autogiros. This violent instability was at first attributed to rotor blade flutter until a theory was developed during the period 1942–1947 showing it to be a new phenomenon. The instability is called *ground resonance*, and was first analyzed and explained by Coleman [44] who modelled the essential features of the instability for articulated rotor helicopters. The name ground "resonance" is somewhat confusing since, in fact, the dynamic system of the helicopter and blades is unstable. The instability occurs at a particular rotor angular velocity; and therefore it appears in some sense like a resonance, but it is not. Further, the ground enters the problem owing to the mechanical support provided the helicopter fuselage by the landing gear. The particularly interesting result obtained by Coleman is that the instability can be predicted neglecting the rotor aerodynamics; that is, ground resonance is purely a mechanical instability, the energy source being the rotor angular velocity. In the discussion below, Coleman's development is followed. Then there is qualitative discussion of the more complex formulation of this problem as applied to hingeless rotors. For an articulated rotor, the aerodynamics tend to be unimportant and only the lag degree-of-freedom needs to be included. For hingeless rotors, the flapping degree-of-freedom is important as well and aerodynamic forces play a significant role [10]. The addition of the flapping degrees-of-freedom leads to a similar instability in flight referred to as air resonance.

Following Coleman's analysis we consider a simplified model of a helicopter resting on the ground. The degrees-of-freedom assumed are: pitch and roll of the rotor shaft or pylon which arise from the landing gear oleo strut flexibility, and the lag degree-of-freedom of each rotor blade. Discussion is restricted to the case in which the rotor has three or more rotor blades and thus has polar symmetry. The two-bladed rotor is a somewhat more complex problem, and a few remarks on this special case are made at the end of this section. A four-bladed rotor system is used as the example since the approach is most easily visualized in this case. The generalization to three or more blades is described at the end of this section.

Consider the helicopter shown in Fig. 16. The system has six degrees-of-freedom: the lag motion of each of the four rotor blades and the two pylon deflections. Each rotor blade is modelled as an articulated blade with hinge offset $\bar{e}$. A spring is included at the root since a centering spring may be employed about the lag hinge.

A coordinate system is chosen that is fixed in space in order to allow the simplest mathematical treatment of the asymmetric stiffness and inertia characteristics associated with pitch and roll motion of the fuselage on the landing gear. If a rotating coordinate system is employed, then the differential equations describing the dynamics would involve periodic coefficients with attendant problems in unravelling the solution. In fact, it is this difference in the form of the equations of motion in fixed and rotating coordinate systems which gives rise to difficulties in analyzing the two-bladed rotor system with asymmetric pylon characteristics. The two-bladed rotor lacks polar symmetry; and, therefore, a fixed coordinate system approach will give rise to periodic coefficients from the rotor, while a rotating coordinate system analysis will give rise to periodic coefficients arising from the asymmetric pylon characteristics. Thus, periodic coefficients cannot be eliminated in the two-bladed case unless the pylon frequencies are equal. For a rotor with three or more blades, the use of a fixed coordinate system allows treatment of asymmetric pylon characteristics without encountering the problem of solving equations with periodic coefficients.

First we consider the equations of motion describing blade lag dynamics in a fixed coordinate system to illustrate the influence of coordinate system motion. All of our previous examples have used a coordinate system rotating with the blade. Simplification of this problem can be effected by defining new coordinates to describe the rotor lag motion. These new coordinates are linear combination of the lag motion of the individual blades. They usually are referred to as multi-blade coordinates [45] and are defined for a four-bladed rotor as

$$\begin{aligned}
\gamma_0 &= \frac{\zeta_1 + \zeta_2 + \zeta_3 + \zeta_4}{4} \\
\gamma_1 &= \frac{\zeta_1 - \zeta_3}{2} \\
\gamma_2 &= \frac{\zeta_2 - \zeta_4}{2} \\
\gamma_3 &= \frac{(\zeta_1 + \zeta_3) - (\zeta_2 + \zeta_4)}{4}
\end{aligned} \tag{3.1}$$

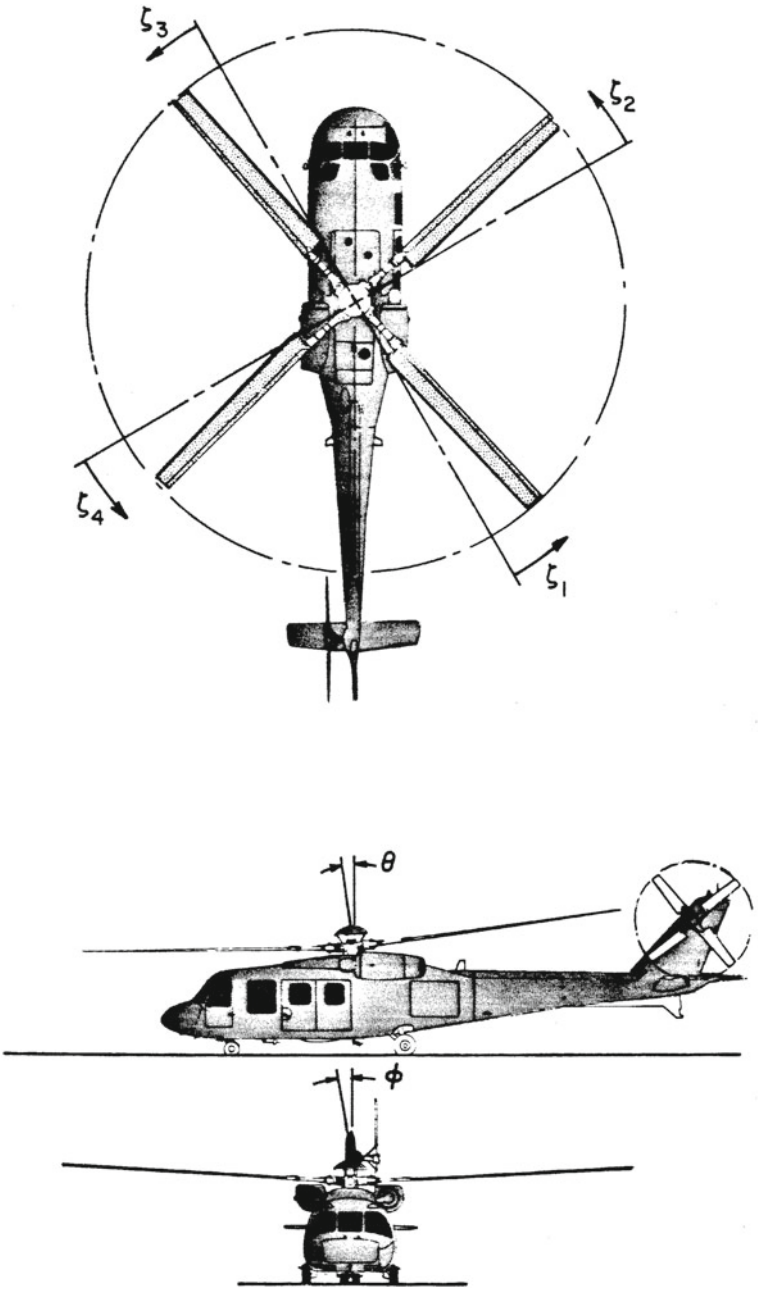

Fig. 16 Mechanical degrees of freedom for ground resonance analysis

The new coordinates, γ_1 and γ_2, describe the motion of the center of mass of the rotor system with respect to the axis of rotation and thus are responsible for coupling of rotor motion to pylon motion, while γ_0 and γ_3 describe motions of the rotor in which the center of mass of the rotor system remains on the axis of rotation. If $\gamma_1 = \gamma_2 = 0$, then motions corresponding to γ_0 and γ_3 are such that opposite blades move as though rigidly attached together with a vertical pin at the root. These motion variables, γ_0 and γ_3, are uncoupled for the dynamic problem of interest; and, consequently, the system is reduced to four degrees-of-freedom by introducing these coordinates as will be shown.

Now the equations of motion for γ_1 and γ_2 are developed in a moving coordinate system and then transformed to a stationary coordinate system. With the hub fixed, the lag motion of each blade without aerodynamics is, as shown earlier,

$$\ddot{\zeta}_i + \Omega^2(\bar{\omega}_\zeta^2)\zeta_i = 0 \quad i = (1, 2, 3, 4) \tag{3.2}$$

The natural frequency, $\bar{\omega}_\zeta^2$ arises from a mechanical spring on the hinge and the offset or centrifugal stiffening effect and is given by Eq. (1.35). The equations of motion for γ_1 and γ_2 are from (3.1) and (3.2)

$$\begin{aligned} \ddot{\gamma}_1 + \Omega^2(\bar{\omega}_\zeta^2)\gamma_1 &= 0 \\ \ddot{\gamma}_2 + \Omega^2(\bar{\omega}_\zeta^2)\gamma_2 &= 0 \end{aligned} \tag{3.3}$$

These equations may be thought of as describing the motion of the center of mass of the rotor system in two directions with respect to the coordinate system rotating at the rotor angular velocity Ω. Resolving to a fixed coordinate system as shown in Fig. 17,

$$\begin{aligned} \gamma_1 &= \Gamma_1 \cos \Omega t + \Gamma_2 \sin \Omega t \\ \gamma_2 &= -\Gamma_1 \sin \Omega t + \Gamma_2 \cos \Omega t \end{aligned} \tag{3.4}$$

Differentiating and substitution (3.4) into (3.3) we obtain the equations

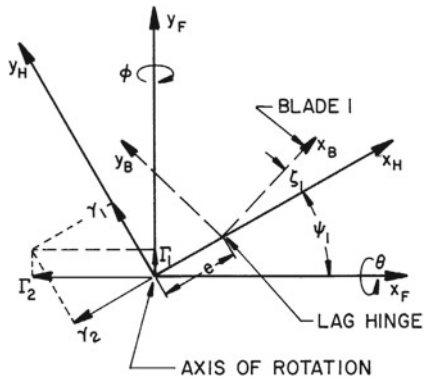

Fig. 17 Axis system and coordinates for ground resonance analysis

$$
\begin{aligned}
&[\ddot{\Gamma}_1 + 2\Omega\dot{\Gamma}_2 + \{\Omega^2(\bar{\omega}_\zeta^2 - 1)\}\Gamma_1]\cos\Omega t \\
&\quad + [\ddot{\Gamma}_2 - 2\Omega\dot{\Gamma}_1 + \{\Omega^2(\bar{\omega}_\zeta^2 - 1)\}\Gamma_2]\sin\Omega t = 0 \\
&[\ddot{\Gamma}_1 + 2\Omega\dot{\Gamma}_2 + \{\Omega^2(\bar{\omega}_\zeta^2 - 1)\}\Gamma_1]\sin\Omega t \\
&\quad - [\ddot{\Gamma}_2 - 2\Omega\dot{\Gamma}_1 + \{\Omega^2(\bar{\omega}_\zeta^2 - 1)\}\Gamma_2]\cos\Omega t = 0
\end{aligned} \tag{3.5}
$$

The second equation appears similar to the first with the coefficients of the sine and cosine terms reversed. Although the variables have been transformed to a fixed system, the equations of motion are still referred to a moving frame which accounts for the presence of the cosine and sine terms. To complete the transformation, multiply the first equation by $\cos(t)$ and add to the second equation multiplied by $\sin(t)$ to obtain one fixed-axis equation. Multiplying the first equation by $\sin(t)$ and subtracting from the second multiplied by $\cos(t)$ yields the second equation. The two equations of motion are

$$
\begin{aligned}
\ddot{\Gamma}_1 + 2\Omega\dot{\Gamma}_2 + \{\Omega^2(\bar{\omega}_\zeta^2 - 1)\}\Gamma_1 = 0 \\
\ddot{\Gamma}_2 - 2\Omega\dot{\Gamma}_1 + \{\Omega^2(\bar{\omega}_\zeta^2 - 1)\}\Gamma_2 = 0
\end{aligned} \tag{3.6}
$$

These are the equations of motion for the new lag coordinates (or CM motion) in the nonrotating coordinate system. Note that the variables are coupled due to the effects of rotation. The characteristic equation for the dynamics of the lag motion is now obtained from Eq. (3.6) as

$$
\{s^2 + \Omega^2(\bar{\omega}_\zeta^2 - 1)\}^2 + 4\Omega^2 s^2 = 0 \tag{3.7}
$$

The roots of this characteristic equation are

$$
\begin{aligned}
s_{1,2.} = \pm i\Omega(\bar{\omega}_\zeta + 1) \\
s_{3,4.} = \pm i\Omega(\bar{\omega}_\zeta - 1)
\end{aligned} \tag{3.8}
$$

Thus, the coordinate transformation has resulted in natural frequencies in the fixed coordinate system which are equal to the natural frequencies in the rotating system given by Eq. (3.3) ($\bar{\omega}_\zeta\Omega$) plus or minus the rotational speed (the angular velocity of the coordinate system). This is a basic characteristic of natural frequencies when calculated in rotating and fixed coordinate systems which must be kept in mind in analyzing rotating systems. At this point we consider one other aspect of the dynamics of this type of system which is helpful in visualizing the motion. Consider the eigenvectors describing the amplitude and phase of the two variables in transient motion. These ratios are obtained from the equations of motion and the characteristic roots.

$$
\left|\frac{\Gamma_1}{\Gamma_2}\right| = \frac{-2\Omega s}{s^2 + \Omega^2(\bar{\omega}_\zeta^2 - 1)}\Big|_{s_{1,2,3,4}}
$$

Therefore

$$\left|\frac{\Gamma_1}{\Gamma_2}\right| = \pm i|_{s_{1,2}}$$
$$\left|\frac{\Gamma_1}{\Gamma_2}\right| = \mp i|_{s_{3,4}} \tag{3.9}$$

The upper sign corresponds to the upper sign in the roots (3.8).

In either of these characteristic motions, Γ_1 and Γ_2 are of equal amplitude and Γ_1 either leads or lags Γ_2 by 90°. Thus the transient motion of the rotor system center of mass is a circular motion. This symmetry which occurs in many rotating systems permits an elegant formulation using complex coordinates [28, 44]. The two variables Γ_1 and Γ_2 can be combined into one single complex variable, as will be discussed below. Further, since the transient motion is circular, these modes are referred to as whirling modes; and the whirling may be described as either advancing or regressing depending upon whether the mode of motion corresponds to transient motion in the direction of rotor rotation or against the direction of rotation. Consider the root

$$s_1 = +i\Omega(\bar{\omega}_\zeta + 1)$$

corresponding to a counter clockwise rotation of the variables Γ_1 and Γ_2 in Fig. 17. From the eigenvectors (3.9), we see that Γ_1 leads Γ_2 by 90°. Thus Γ_1 reaches a maximum and then Γ_2 reaches a maximum and so the oscillation proceeds in the direction of rotation and is an advancing mode. Similarly, $s_2 = -\Omega(\bar{\omega}_\zeta + 1)$, corresponds to the two vectors rotating in a clockwise direction, but now Γ_1 lags Γ_2 and so this is also an advancing mode. Hence, the mode with frequency $(\bar{\omega}_\zeta)\Omega$ is an advancing mode. Following a similar argument for the mode $(\bar{\omega}_\zeta - 1)\Omega$ we find that it is a regressing mode, when $\bar{\omega}_\zeta$ is greater than 1. One must be careful of this terminology, since in a rotating coordinate system modes are also described as advancing and regressing modes, but because of the change in coordinate system angular velocity, modes may be regressing in the rotating system and advancing in the stationary system. From a geometric point of view, there are two whirling modes corresponding to the four characteristic roots. Use of complex coordinates helps to visualize the direction of rotation of the modes simply [28].

Thus, the transient motion of the center of mass of the rotor system may be described in terms of two circular or whirling modes. When viewed in the fixed frame of reference, one is an advancing whirl (in the same direction as the rotation of the rotor) and one is a regressing whirl at low rotor angular velocity ($\omega_\zeta > \Omega$) and a slow advancing whirl at larger angular velocities ($\omega_\zeta < \Omega$). Recall that the frequencies as seen in the rotating frame are simply equal to $\pm\omega_\zeta$ and one is an advancing mode while the other is always a regressing mode.

Now the effect of the pylon motion is added. It is assumed that the pylon is sufficiently long and the angular deflections are sufficiently small such that the hub motion lies in a horizontal plane. The equations of motion are developed using a Newtonian approach. First, a single blade is considered; and then the effects of the other blades are added. It is most convenient to derive the equations with the pylon

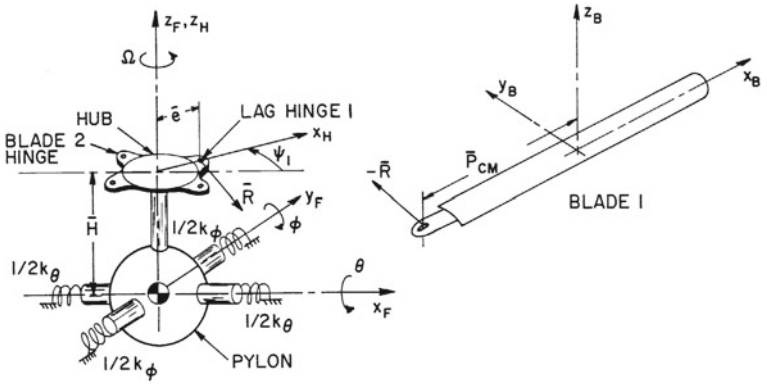

Fig. 18 Free body diagram for ground resonance analysis

or fuselage motion referred to a fixed axis system and the lag angle referred to a moving axis system and then to transform the lag angle to a fixed coordinate system. This will illustrate the manner in which periodic coefficients enter the equations. The equations of motion for the blade ad fuselage system may be written from the free body diagram shown in Fig. 18, as

$$\begin{aligned} \dot{\bar{H}}_B + \bar{\Omega}_B \times \bar{H}_B &= \bar{P}_{CM} \times \bar{R} \\ M_B \bar{a}_{CM} &= -\bar{R} \\ \dot{\bar{H}}_F &= \bar{H} \times \bar{R} \end{aligned} \tag{3.10}$$

where $\bar{R}$ is the reaction force at the hinge, $\bar{H}_B$ is the moment of momentum of the blade about its center of mass and $\bar{H}_F$ is the moment of momentum of the fuselage about its center of mass which is assumed fixed in space. $\bar{\Omega}_B$ is the angular velocity of the blade, $\bar{P}_{CM}$ is the distance from the hinge to the blade center of mass and $\bar{H}$ is the height of the rotor hub above the CM. The acceleration of the blade enter of mass in terms of the acceleration at the hinge point is

$$\bar{a}_{CM} = \bar{a}_E + \bar{\Omega}_B \times (\bar{\Omega}_B \times \bar{P}_{CM}) + \dot{\Omega}_B \times \bar{P}_{CM} \tag{3.11}$$

and the acceleration of the hinge in terms of the acceleration of the hub, $\bar{a}_0$, and the rotational velocity of the hub is

$$\bar{a}_E = \bar{a}_0 + \bar{\Omega} \times (\bar{\Omega} \times \bar{e}) + \dot{\bar{\Omega}} \times \bar{e} \tag{3.12}$$

The angular velocity of the hub is assumed constant. Three sets of unit vectors are defined. The subscript $_B$ refers to the set of unit vectors fixed to the blade, the subscript $_H$ to the set fixed in the hub and the subscript $_F$ refers to a set fixed in space. The lag

angle is assumed to be small, so that the relationships among these unit vectors for blade number 1 (Fig. 17) are

$$\begin{Bmatrix} \bar{i}_F \\ \bar{j}_F \\ \bar{k}_F \end{Bmatrix} = \begin{bmatrix} \cos\psi_1 & -\sin\psi_1 & 0 \\ \sin\psi_1 & \cos\psi_1 & 0 \\ 0 & 0 & 1 \end{bmatrix} \begin{Bmatrix} \bar{i}_H \\ \bar{j}_H \\ \bar{k}_H \end{Bmatrix} \tag{3.13}$$

$$\begin{Bmatrix} \bar{i}_H \\ \bar{j}_H \\ \bar{k}_H \end{Bmatrix} = \begin{bmatrix} 1 & -\zeta_1 & 0 \\ -\zeta_1 & 1 & 0 \\ 0 & 0 & 1 \end{bmatrix} \begin{Bmatrix} \bar{i}_B \\ \bar{j}_B \\ \bar{k}_B \end{Bmatrix} \tag{3.14}$$

The various quantities involved in the equations of motion are

$$\begin{aligned} \bar{H}_B &= I_{CM}(\Omega + \dot{\zeta}_1)\bar{k}_B + I_{CM}(\theta\cos\psi_1 + \dot{\theta}\sin\psi_1) \\ \bar{H}_F &= I_x\dot{\theta}\bar{i}_F + I_y\dot{\phi}\bar{j}_F \\ \bar{\Omega} &= \Omega\bar{k}_H + \dot{\theta}_{iF} + \dot{\phi}_{jF} \\ \bar{\Omega}_B &= (\Omega + \dot{\zeta}_1)\bar{k}_B + \dot{\theta}_{iF} + \dot{\phi}_{jF} \\ \bar{H} &= h\bar{k}_F \\ \bar{e} &= e\bar{i}_H \\ \bar{P}_{CM} &= r_{CM}\bar{i}_B \\ \bar{a}_0 &= \ddot{x}_H\bar{i}_F + \ddot{y}_H\bar{j}_F = h\ddot{\phi}\bar{i}_F - h\ddot{\theta}\bar{j}_F \end{aligned} \tag{3.15}$$

Substituting Eqs. (3.11)–(3.15) into the equations of motion (3.10) for the blade and body motion, noting that $\bar{R} = -M_B\bar{a}_{CM}$, we obtain one blade equation of motion and two body equations of motion

$$\begin{aligned} \ddot{\zeta}_1 + \frac{er_{CM}M_B}{I_B}\Omega^2\zeta_1 &= \frac{M_Br_{CM}h}{I_B}(\ddot{\theta}\cos\psi_1 + \ddot{\phi}\sin\psi_1) \\ (I_y + M_Bh^2)\ddot{\phi} &= M_Bh[e\Omega^2 + r_{CM}(\Omega + \dot{\zeta}_1)^2]\cos\psi \\ &\quad + M_Br_{CM}h(\ddot{\zeta}_1 - \Omega^2\zeta_1)\sin\psi_1 \\ (I_x + M_Bh^2)\ddot{\theta} &= -M_Bh[e\Omega^2 + rCM(\Omega + \dot{\zeta}_1)^2]\sin\psi_1 \\ &\quad + M_Br_{CM}h(\ddot{\zeta}_1 - \Omega^2\zeta_1)\cos\psi_1 \end{aligned} \tag{3.16}$$

The subscript 1 has been added to note that only one blade has been considered.

The equations of motion for the other three blades are identical to blade one with the azimuth angle suitably shifted, i.e., the equation of motion of blade 2 in terms of the azimuth angle of blade 1 is

$$\ddot{\zeta}_2 + \frac{er_{CM}M_B}{I_B}\Omega^2\zeta_2 = \frac{M_Br_{CM}h}{I_B}\left(\ddot{\theta}\cos\left(\psi_1 + \frac{\pi}{2}\right) + \ddot{\phi}\sin\left(\psi_1 + \frac{\pi}{2}\right)\right) \tag{3.17}$$

The equations of motion for the new coordinates, γ_0, γ_1, etc., are formulated by linear combinations of the blade equations and are

$$\begin{aligned}
\ddot{\gamma}_0 + \frac{er_{CM}M_B}{I_B}\Omega^2\gamma_0 &= 0 \\
\ddot{\gamma}_1 + \frac{er_{CM}M_B}{I_B}\Omega^2\gamma_1 &= \frac{M_B r_{CM} h}{I_B}(\ddot{\theta}\cos\psi_1 + \ddot{\phi}\sin\psi_1) \\
\ddot{\gamma}_2 + \frac{er_{CM}M_B}{I_B}\Omega^2\gamma_2 &= \frac{M_B r_{CM} h}{I_B}(-\ddot{\theta}\sin\psi_1 + \ddot{\phi}\cos\psi_1) \\
\ddot{\gamma}_3 + \frac{er_{CM}M_B}{I_B}\Omega^2\gamma_3 &= 0
\end{aligned} \tag{3.18}$$

We thus see as discussed earlier that γ_0 and γ_3 are not coupled to the hub motion and thus do not need to be considered further. Note that the equations of motion for γ_1 and γ_2 have periodic coefficients since $\psi_1 = \Omega t$. The influence of the other three blades must be added to the fuselage equations. The first equation becomes

$$\begin{aligned}
&(I_y + 4M_B h^2)\ddot{\phi} = \\
&\sum_{i=1}^{v} M_B h(e\Omega^2 + r_{CM}(\Omega + \dot{\zeta}_i)^2)\cos\left(\psi_1 + \frac{(i-1)\pi}{2}\right) \\
&+ M_b r_{CM} h(\ddot{\zeta}_i - \Omega^2\zeta_i)\sin\left(\psi_1 + \frac{(i-1)\pi}{2}\right)
\end{aligned} \tag{3.19}$$

and a similar form is obtained for the other fuselage equation. Using trigonometric identities and the definitions of the multi-blade coordinates (3.1) the two fuselage equations become, retaining only linear terms,

$$\begin{aligned}
(I_y + 4M_B h^2)\ddot{\phi} =& 2M_B r_{CM} h\{(\ddot{\gamma}_1 - 2\Omega\dot{\gamma}_2 - \Omega^2\gamma_1)\sin\psi_1 \\
&+ (\ddot{\gamma}_2 + 2\Omega\dot{\gamma}_1 - \Omega^2\gamma_2)\cos\psi_1\} \\
(I_y + 4M_B h^2)\ddot{\theta} =& 2M_B r_{CM} h\{(\ddot{\gamma}_1 - 2\Omega\dot{\gamma}_2 - \Omega^2\gamma_1)\cos\psi_1 \\
&- (\ddot{\gamma}_2 + 2\Omega\gamma_1 - \Omega^2\gamma_2)\sin\psi_1\}
\end{aligned} \tag{3.20}$$

Again we see that the coordinates γ_0 and γ_3 do not appear.

These equations involve periodic coefficients. The periodic coefficients are a consequence of defining the lag motion in a rotating system and the fuselage motion in a fixed system as noted earlier. The periodic coefficients can eliminated by transforming the lag motion to fixed coordinates as described above. This transformation involves the relationships given by Eq. (3.4). A centering spring about the lag hinge is incorporated in the lag equations such that the lag frequency is given by

$$\omega_\zeta^2 = \frac{K_\zeta}{I_B} + \frac{er_{CM}M_B}{I_B}\Omega^2$$

This is equivalent to Eq. (1.35) without the assumption of a uniform blade mass distribution. Employing Eq. (3.4) the blade Eq. (3.18) become

$$\begin{aligned} \ddot{\Gamma}_1 + (\omega_\zeta^2 - \Omega^2)\Gamma_1 + 2\Omega\dot{\Gamma}_2 &= \frac{M_B r_{CM} h}{I_B}\ddot{\theta} \\ -2\Omega\dot{\Gamma}_1 + \ddot{\Gamma}_2 + (\omega_\zeta^2 - \Omega^2)\Gamma_2 &= \frac{M_B r_{CM} h}{I_B}\ddot{\phi} \end{aligned} \tag{3.21}$$

The fuselage equations, including the effects of the supporting springs k_ϕ and k_θ are

$$\begin{aligned} (I_y + 4M_b h^2)\ddot{\phi} + k_\phi \phi &= 2M_B r_{CM} h\ddot{\Gamma}_2 \\ (I_x + 4M_b h^2)\ddot{\theta} + k_\theta \theta &= 2M_B r_{CM} h\ddot{\Gamma}_1 \end{aligned} \tag{3.22}$$

Equation (3.22) can be placed in the form given in [44] by converting the pylon rotations θ and ϕ to linear hub translations x and y. From Fig. 17, dropping the subscripts $_F$ on x and y,

$$x = h\phi, \bar{x} = \frac{x}{R}$$

$$y = -h\theta, \bar{y} = \frac{y}{R}$$

A uniform mass blade is assumed such that

$$I_B = M_B \frac{R^2}{3}$$

Define effective fuselage mass and spring constants by

$$M_{F_x} = \frac{I_y}{h^2} k_x = \frac{k_\phi}{h^2}$$

$$M_{F_y} = \frac{I_x}{h^2} k_y = \frac{k_\theta}{h^2}$$

These definitions eliminate the parameter h from Eqs. (3.21) and (3.22). Equations (3.21) and (3.22) become

$$\begin{aligned} \ddot{\Gamma}_1 + (\omega_\zeta^2 - \Omega^2)\Gamma_1 + 2\Omega\dot{\Gamma}_2 &= -\frac{3}{2}\ddot{y} \\ -2\Omega\dot{\Gamma}_1 + \ddot{\Gamma}_2 + (\omega_\zeta^2 - \Omega^2)\Gamma_2 &= \frac{3}{2}\ddot{x} \\ (M_{F_x} + 4M_B)\ddot{x} + k_x\bar{x} &= M_B\ddot{\Gamma}_2 \\ (M_{F_y} + 4M_B)\ddot{y} + k_y\bar{y} &= -M_B\ddot{\Gamma}_1 \end{aligned} \tag{3.23}$$

Note that the periodic coefficients will not be eliminated if we attempt to transform the body motion into rotating coordinates except in the special case where fuselage inertias and springs are identical about both axes. The procedure followed above for four blades will produce identical results for three or more blades. A generalized description of this procedure may be found in [6].

If the rotor has two blades, the only way to eliminate the periodic coefficients is to convert the pylon motion to rotating coordinates. Only in the special case of equal inertia and stiffness will the periodic coefficients be eliminated [44]. In general, if there is polar symmetry in one frame of reference and a lack of symmetry in the other frame, expressing the equation of motion in this latter frame will eliminate the necessity of dealing with periodic coefficients. With a two bladed rotor, the rotor lacks polar symmetry. If the support system also lacks polar symmetry, the periodic coefficients cannot be eliminated, and Floquet theory must be employed to analyze the stability of the system. The simplest case (equal support stiffness) of the two-bladed rotor is analyzed in the rotating system and the three or more bladed rotor in the fixed frame. Recall from the previous discussion that this will give quite a different picture of the variation of system natural frequencies with rpm. For simplicity, only the multibladed rotor with pylon symmetry is discussed which may be treated in either reference frame. The pylon characteristics are assumed to be

$$M_{F_x} = M_{F_y} = M_F$$

$$k_x = k_y = k_F$$

The important parameter governing the coupling between the blade motion and the fuselage motion is the ratio of the total blade mass to the total system mass defined by μ,

$$\mu = \frac{4M_B}{M_F + 4M_B}$$

It is convenient to nondimensionalize the time by the support frequency with the blade mass concentrated at the hub

$$\omega_F^2 = \frac{k_F}{M_F + 4M_B}$$

since rotor angular velocity is considered to be the variable parameter. The frequencies nondimensionalized in this fashion are denoted by $\hat{\omega}_\zeta$ and $\hat{\Omega}$. Introducing these definitions, Eq. (3.23) becomes,

$$
\begin{aligned}
&\ddot{\Gamma}_1 + (\hat{\omega}_F^2 - \hat{\Omega}^2)\Gamma_1 + 2\hat{\Omega}\dot{\Gamma}_2 + \frac{3}{2}\ddot{y} = 0 \\
&-2\hat{\Omega}\dot{\Gamma}_1 + \ddot{\Gamma}_2(\hat{\omega}_F^2 - \hat{\Omega}^2)\Gamma_{21} - \frac{3}{2}\ddot{x} = 0 \\
&\frac{\mu}{4}\ddot{\Gamma}_1 + \ddot{\bar{y}} + \bar{y} = 0 \\
&\frac{\mu}{4}\ddot{\Gamma}_2 + \ddot{\bar{x}} + \bar{x} = 0
\end{aligned}
\tag{3.24}
$$

The stability of the system defined by Eq. (3.24) is examined as a function of the various physical parameters of the problem. First, consider the limiting case in which the blade mass is zero ($\mu = 0$). This eliminates the coupling between the fuselage motion and the blade motion. The natural frequencies of the system are composed of the uncoupled blade dynamics and the fuselage dynamics. The roots of the characteristic equation are therefore

$$\pm i(\hat{\Omega} + \hat{\omega}_\zeta), \quad \pm i(\hat{\Omega} - \hat{\omega}_\zeta), \quad \pm i, \quad \pm i$$

The latter two pairs correspond to the fuselage motion and the former to the blade motion. The modes of motion are whirling or circular modes owing to polar symmetry. Figure 19 shows the whirling modes, i.e., only the four frequencies with signs that correspond to the direction of whirling, positive being an advancing mode. The frequencies are shown as a function of rotor angular velocity. In the numerical example shown, a centering spring (K_ζ) is included such that $\hat{\omega} = 0.3$ when the rotor is not rotating ($\hat{\Omega} = 0$) and the hinge offset $\bar{e} = 0.05$. ($\hat{\Omega} - \hat{\omega}_\zeta$) is a regressing mode when negative, ($\hat{\Omega} + \hat{\omega}_\zeta$) is an advancing mode. The fuselage modes ($\pm i$) are advancing and regressing modes respectively. These four whirling modes constitute the dynamics of the system in the limiting case of no hub mass. For comparison purposes, if the system is analyzed in the rotating frame, the result will be equivalent to subtracting the angular velocity $\hat{\Omega}$ from the frequencies shown in Fig. 19 resulting in the diagram shown in Fig. 20. Thus, the appearance of the figure depends upon the coordinate system. For two bladed rotors, one is likely to see a graph similar to Fig. 20; while, for multibladed rotor analysis, one usually sees the fixed coordinate plot shown in Fig. 19. It may be noted that at two rotor angular velocities ($\hat{\Omega} = 0.65$ and $\hat{\Omega} = 1.51$) the frequency of one of the blade modes is equal to a pylon mode. It would be expected that the coupling effects due to blade mass are most significant in these regions.

Next the influence of the mass ratio μ on the dynamics of the system is examined. It would be most convenient if root locus techniques could be used. This is not possible directly with Eq. (3.24) since μ does not appear linearly in the characteristic equation. Through introduction of complex coordinates, root locus techniques can be employed [28]. Define

$$\bar{z} = \bar{x} + i\,\bar{y}$$

$$\delta = \Gamma_2 - i\,\Gamma_1$$

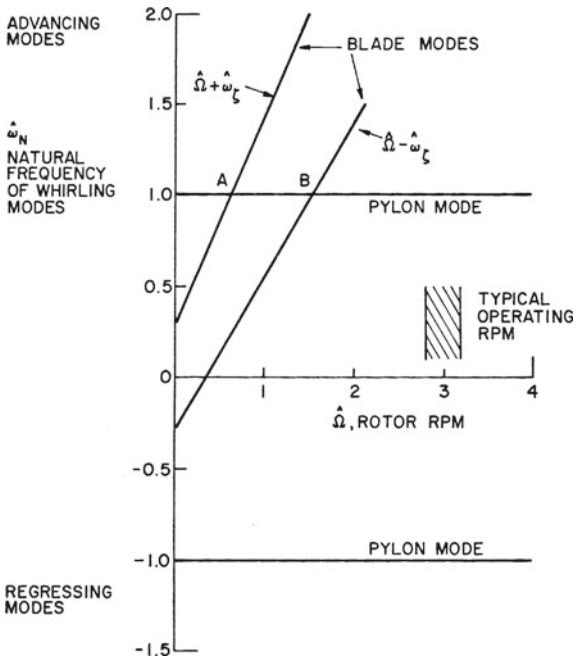

Fig. 19 Uncoupled whirling modes ($\mu = 0$). Fixed coordinate system

This coordinate change reduces the four Eq. (3.24) to two equations owing to the symmetry properties of these equations, i.e.,

$$\ddot{\delta} - 2i\hat{\Omega}\dot{\delta} + (\hat{\omega}_\zeta^2 - \hat{\Omega}^2)\delta - \frac{3}{2}\ddot{z} = 0 \tag{3.25}$$

$$-\frac{\mu}{4}\ddot{\delta} + \ddot{z} + \bar{z} = 0$$

We now have a fourth order system in place of an eighth order system (Eq. (3.24)), and the roots of this system are the whirling modes only, i.e.,

$$i(\hat{\Omega} + \hat{\omega}_\zeta)$$

$$i(\hat{\Omega} - \hat{\omega}_\zeta)$$

$$\pm i$$

The characteristic equation of this system can now be written as

$$(s^2 + 1)(s^2 - 2i\hat{\Omega}s + (\hat{\omega}_\zeta^2 - \hat{\Omega}^2)) - \frac{3}{8}\mu s^4 = 0$$

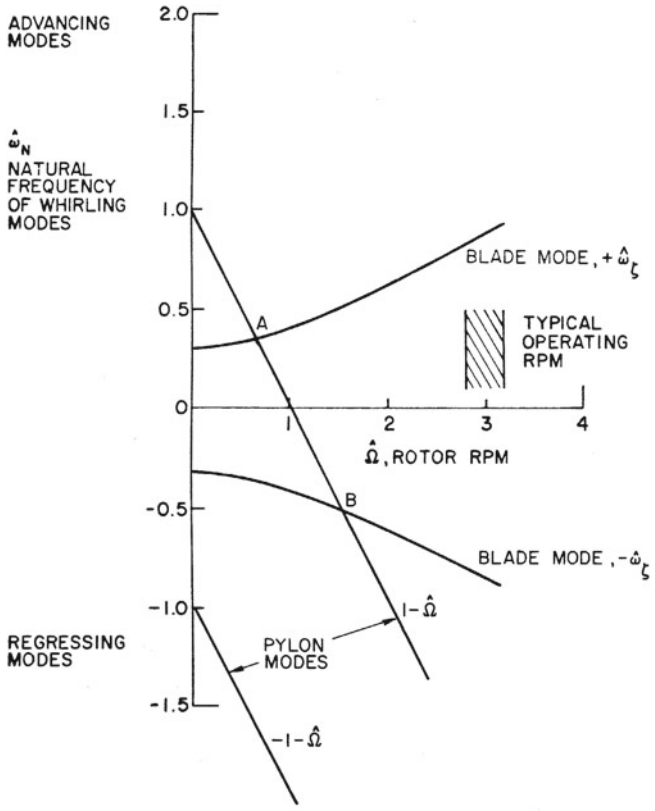

Fig. 20 Uncoupled whirling modes ($\mu = 0$). Rotating coordinate system

Now μ appears as a linear parameter and the characteristic equation can be written as

$$\frac{\frac{3}{8}\mu s^4}{(s^2+1)(s^2 - 2i\hat{\Omega}s + (\hat{\omega}_\zeta^2 - \hat{\Omega}^2))} = 1 \tag{3.26}$$

Equation (3.26) is in root locus form with μ as the variable parameter and a zero degree locus is indicated. The usual root locus rules apply to equations with complex coefficients as well as to those with real coefficients. Figure 21 shows root loci for increasing μ for two values of $\hat{\Omega}$ (0.2 and 1.3) and indicates that the influence of μ on the dynamics is quite different depending upon the sign of $(\hat{\Omega} - \hat{\omega}_\zeta)$[1]. When $(\hat{\Omega} - \hat{\omega})$ is negative, it can be seen from Fig. 21 that the coupling effect of increasing μ is to separate the system frequencies. However, when $(\hat{\Omega} - \hat{\omega}_\zeta)$ is positive, the two intermediate frequencies come together; and, if μ is sufficiently large, instability occurs. The most critical case occurs at intersection B of Fig. 19 (i.e., when the

[1] Recall $\hat{\omega}_\zeta = 0.3$

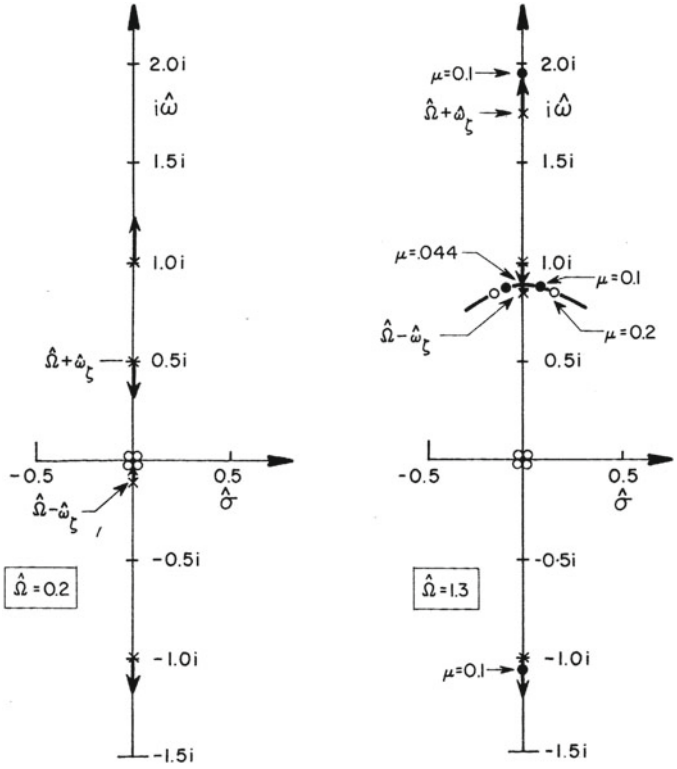

Fig. 21 Root locus for increasing blade mass ratio (μ) for two operating conditions

regressing mode frequency ($\hat{\Omega} - \hat{\omega}_\zeta$) = 1 such that the two intermediate frequencies are equal). At this operating condition, any value of μ causes instability. Intersection A is not critical because of the large separation of the two intermediate frequencies ($\hat{\Omega} + \hat{\omega}_\zeta$ and $\hat{\Omega} - \hat{\omega}_\zeta$). In the typical case, for an articulated rotor $\hat{\omega}_\zeta$ is the order 1.0 and $\hat{\Omega}$ at the operating condition ($\hat{\Omega}_{OP}$) is the order of 3.0, so that intersection B occurs below operating rpm. That is

$$\hat{\Omega}_{CR} = 1 + \hat{\omega}_\zeta \equiv 2$$

Thus, to completely eliminate the possibility of this instability which is called ground resonance, one must have $\hat{\Omega}_{CR} > \hat{\omega}_{OP} = 3$, and a very large offset is required since $\hat{\omega}_\zeta > 2$ and therefore, $\bar{\omega}_\zeta = 0.67$ which corresponds to a hinge offset of 0.3 (1.35) without a centering spring. Note that this ratio $\hat{\Omega}_{OP}$ is largely determined by considerations other than rotor stability, such as the rotor operating rpm and the shock absorbing character of the landing gear. Since this large hinge offset is not practical, a centering spring may be employed to increase $\bar{\omega}_\zeta$; however this will increase the root bending moment, the reason for which the lag hinge was installed.

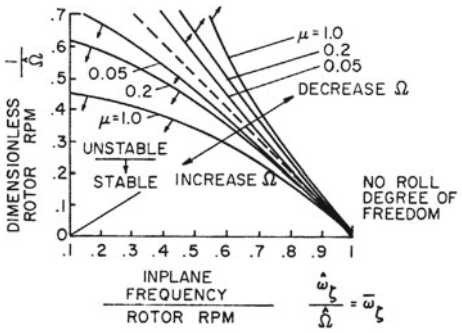

Fig. 22 Extent of unstable region for various mass ratios

The unstable region extends below and above this intersection to an extent depending upon the mass ratio as well as the other geometric parameters. Various criteria can be found in the literature as to the size of the unstable region as a function of mass ratio. A typical graph of the frequencies as well as the extent of the unstable region as a function of μ is shown in Fig. 22 taken from [10]. This result applies to the case where the pylon has only one degree-of-freedom in contrast to the example here where the pylon has two degrees-of-freedom.

Next we examine the influence of mechanical damping on the stability of the system. Damping in the rotating system (lag damping) and in the nonrotating system (pylon damping) are considered separately. Consider first the influence of damping on the pylon. This leads to terms $C_F\dot{\phi}$ and $C_F\dot{\theta}$ in Eq. (3.22). Adding this in complex form to the second of Eq. (3.25) and expressing the characteristic equation in root locus form yields

$$\frac{\hat{C}_F s[s^2 - 2i\hat{\Omega}s + (\hat{\omega}_\zeta^2 - \hat{\Omega}^2)]}{(s^2+1)(s^2 - 2i\hat{\Omega}s + (\hat{\omega}_\zeta^2 - \hat{\Omega}^2)) - \frac{3}{8}\mu s^4} = -1 \tag{3.27}$$

where

$$\hat{C}_F = \frac{C_F \omega_F}{k_f h^2}$$

This root locus has two zeros at the uncoupled lag-mode frequencies. Figure 23 shows the influence of increasing damping for two cases. In the first, μ is small so that the basic system is neutrally stable. Adding only fixed axis damping destabilizes the system. In the second case, where μ is large enough such that the basic system is unstable, no amount of damping will stabilize the system.

Now consider adding damping to the lag motion of the blades. It must be noted that this damping will be in the rotating coordinate system (about the blade hinge); and so, to directly add damping terms to the equations of motion, the rotating frame equations must be used. The damping then appears as $C_R\dot{\gamma}_1$ and $C_R\dot{\gamma}_2$. If the transformations are followed, this will ultimately result (in the rotating frame with complex notation) in the damping appearing in the first of Eq. (3.25) as

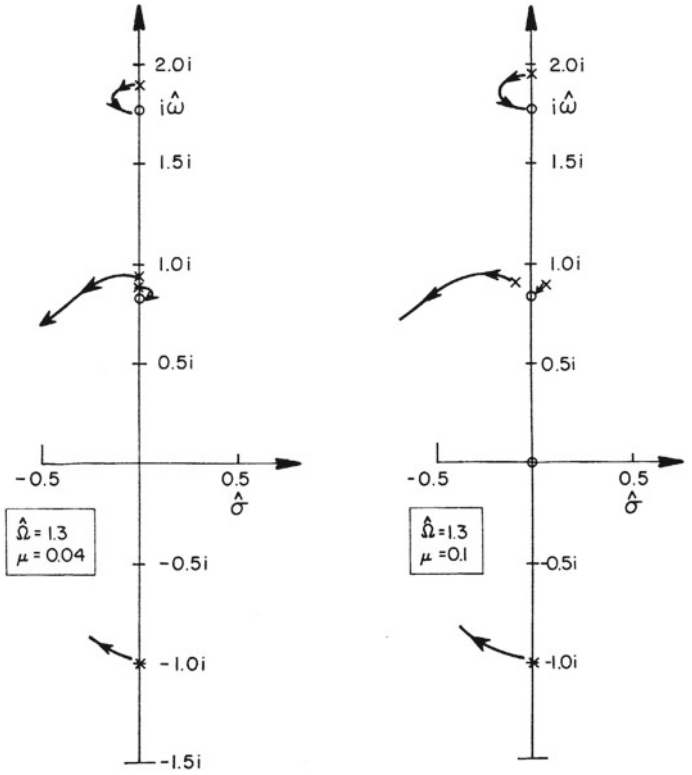

Fig. 23 Root locus for increasing pylon (fixed axis) damping on ground resonance stability

$$\hat{C}_R(\dot{\delta} - i\hat{\Omega}\delta)$$

The $i\hat{\Omega}$ term appears because rotating coordinate system damping is expressed with respect to a fixed frame. Adding this damping to the first of the two equations and expressing the characteristic equation in root locus form as

$$\frac{\hat{C}_R(s - i\hat{\Omega})(s^2 + 1)}{(s^2 + 1)(s^2 - 2i\hat{\Omega}s + (\hat{\omega}_\zeta^2 - \hat{\Omega}^2)) - \frac{3}{8}\mu s^4} = -1 \tag{3.28}$$

the root locus shown in Fig. 24 is obtained. Again it is interesting to note that adding damping only in the rotating frame results in destabilizing one of the fuselage modes when the system is initially neutrally stable (small μ). For large μ the situation is similar to the fixed axis damping case. These rather surprising effects of damping in a rotating system indicate that damping must be handled with considerable care. Owing to the order of the system, it is rather difficult to obtain physical insight into the source of these effects. A *combination* of damping in the rotating frame

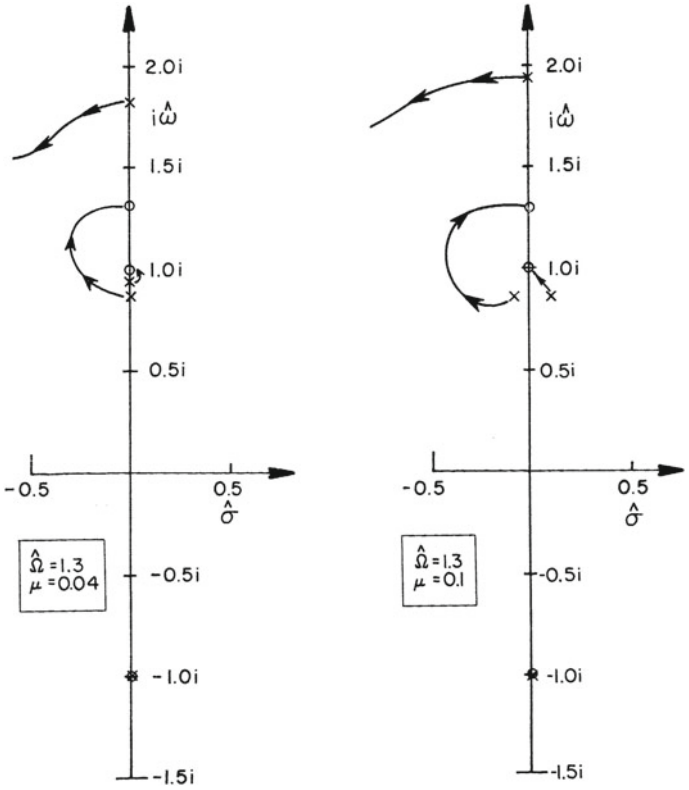

Fig. 24 Root locus for increasing lag (rotating axis) damping on ground resonance stability

(blades) and stationary frame (pylon) is required to stabilize the system; although, as can be seen from the root locus sketches, there will always be one zero near to the fuselage blade lag mode making it difficult to provide a large amount of damping in one of the modes. There would, of course, generally be damping in the pylons. Particularly on articulated rotors, blade lag dampers are added since, as noted, this region of instability must be traversed in bringing the rotor speed to operating rpm. Reference [44] presents boundaries showing the damping required to eliminate the instability region for articulated rotor helicopters.

The treatment of more general problems, including the blade flapping degrees of freedom and discussion of its importance in the hingeless rotor case, may be found in [8–10]. The two-bladed rotor is treated in [44].

Flapping motion of articulated rotors with small hinge offset does not produce appreciable hub moments; and, consequently, there is only weak coupling between the flapping motion and the pylon motion. The hingeless rotor, however, produces large hub moments; and, consequently, the flapping motion coupled into the pylon

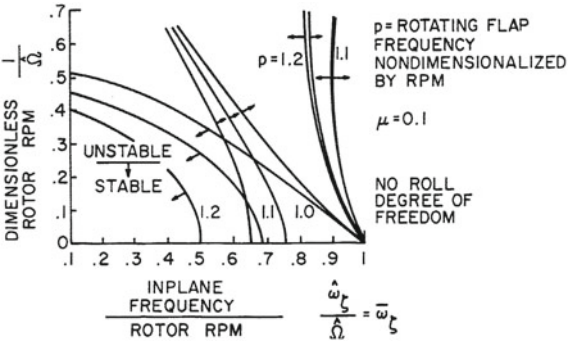

Fig. 25 Influence of flap frequency on ground resonance stability boundaries [10]

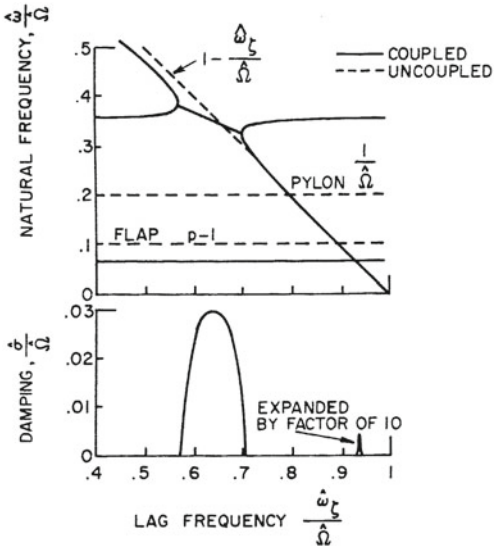

Fig. 26 Frequency and damping of rotor-body system. Flap, lag and pylon pitch degrees of freedom. No aerodynamics [10]

and lag dynamics [10]. Figure 25 shows the influence of the flapping frequency on the stability boundaries for $\mu = 0.1$.

There are now three frequencies involved in the problem: the pylon frequency, ω_F, the lag frequency, $\hat{\Omega} - \hat{\omega}_\zeta$ and the flap frequency p (p - 1 in the stationary frame). In addition to the destructive instability which occurs when the coupled pylon frequency is equal to the lag frequency ($\hat{\Omega} - \hat{\omega}_\zeta$), a mild instability occurs when the coupled flap frequency is equal to the lag frequency ($\hat{\Omega} - \hat{\omega}_\zeta$) as shown by Fig. 26. Note that pylon and flap frequencies are significantly changed by the coupling. The ground resonance problem for hingeless rotors thus becomes quite complex and difficult to generalize. The reader is referred to [10] for further details. It may be noted that a more detailed model of the rotor blades must be employed for hingeless rotors. Since both flap and lag degrees-of-freedom are involved, it is important to model the

coupling between these motions, which occurs as a result of hub and blade geometry. Aerodynamic forces and structural damping are also significant.

Air resonance refers to the form this dynamic problem takes with the landing gear restraint absent, that is, with the vehicle in the air. Coupling of flapping motion, body motion and lag motion is involved. Fuselage inertia and damping characteristics can have a significant impact on the stability. The air resonance problem is clearly asymmetrical; and, characteristically, the roll axis is more critical owing to its low inertia and small aerodynamic damping [8]. Furthermore, air resonance generally involves the unsteady flow field [46].

Since the primary source of damping in this physical system arises from flap bending, it is possible that the nature of the flight control system can have an impact on air resonance stability as shown in [47]. Essentially an attitude feedback from the body to cyclic pitch tends to maintain the rotor in a horizontal plane thus effectively removing the aerodynamic damping from the flapping/body dynamics. There are also other indications that the flight control system feedbacks have an impact on rotor system stability [48]; however, this problem does not appear to be well understood.

Another problem associated with propeller and prop/rotor driven aircraft which involves a blade motion-support coupling is whirl flutter which has been experienced on conventional aircraft [49] as well as on V/STOL aircraft [6]. This instability in the case of the conventional aircraft can be explained by considering only the wing as flexible (i.e., the propeller blades may be assumed to be rigid). For the tilt prop/rotor aircraft, where blade flexibility is important, the primary source of the instability is the same as in the rigid propeller case. It is a result of the aerodynamics characteristics of propellers and prop rotors at high inflows typical of cruising flight. It can be shown that the source of the whirl flutter instability is primarily associated with the fact that an angle-of-attack change on a propeller produces a yawing moment, and a sideslip angle produces a pitching moment. Further, the magnitude of this moment change grows with the square of the tangent of the inflow angle [6] and results in a rapid onset of the instability.

For the prop/rotor, a complex model with a large number of degrees-of-freedom is required to predict the dynamics of the system accurately [6]. The whirl flutter instability can occur on articulated rotors as well as hingeless rotors although for somewhat different physical reasons [50]. Here inplane force dependence on angular rate produces unstable damping moments acting on the support. The hingeless rotor which produces significant hub moments is similar to the rigid propeller. Young [51] has shown by a simplified analysis that, under certain circumstances, the occurrence of this instability can be minimized by a suitable selection of the flapping frequency. Reference [6] contains an excellent discussion of these various problem areas.

A typical predicted variation of damping with flight speed for a tilt-prop-rotor aircraft is shown in Fig. 27. As mentioned earlier, it is important in modelling this dynamic system to insure that the structural details of the hub, blade and pitch control system are precisely modelled. Reference [52] indicates the impact that relatively small modelling details can have on the flutter speed, as well as describing in detail the modelling requirements for prop-rotor whirl flutter.

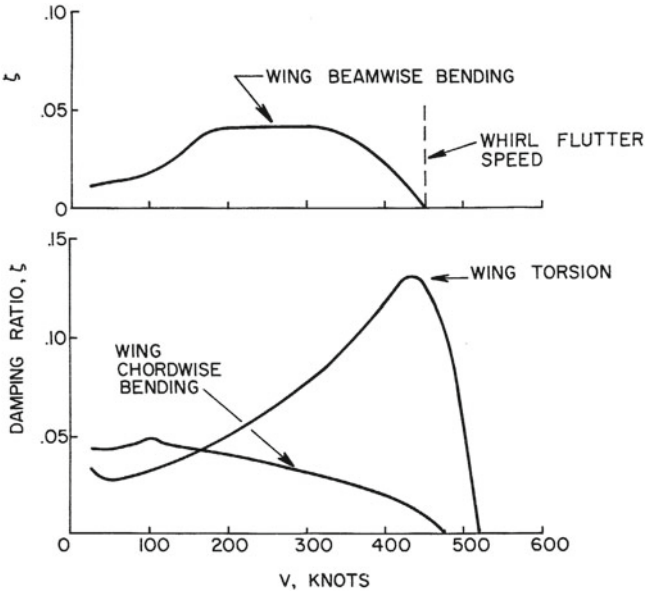

Fig. 27 Damping of wing bending modes as a function of airspeed. Tilt prop/rotor aircraft with gimballed rotor [6]

Aeroelastic analysis of two-bladed rotors requires special considerations since the two blades are connected together. The reader is referred to [53, 54] for the analysis of two-bladed rotors.

4 Unsteady Aerodynamics

Thus far in this chapter, we have utilized only the simplest quasi-steady,blade-element aerodynamics. However, it is well-known that the unsteady dynamics of the rotor flow field can have a profound effect on rotorcraft. This effect is routinely included in rotor vibration and performance codes through vortex-lattice waking modelling [55]. However, in rotor aeroelastic computations, which involve eigenvalue computations, the vortex wake is usually frozen in time. When not frozen in time, the eigenvalue computation can take hours of computing time [56]. Therefore, more approximate methods have been developed to include the important effects of wake dynamics in rotorcraft aeroelasticity. Some of the more useful ones are explained below.

4.1 Dynamic Inflow

Amer [57] analyzed the problem of rotor damping in roll and correlated the predicted data with flight test measurements in hover and forward flight. Amer observes that a discrepancy in damping is "due primarily to changes in induced velocity which occur during rolling (or pitching) because of changes in the distribution of thrust around the rotor disk". This observation more or less forms the stimulus for most of the subsequent dynamic inflow work. It fell to Sissingh [58], however, to explain this discrepancy by quantifying Amer's observation with the inclusion of variable inflow or, more precisely, of changes in induced velocities caused by transient changes in rotor disk loading. Starting from Glauert's classical momentum theory postulate, he gives the formula

$$k(\delta\lambda/\lambda) = \delta C_T/C_T \tag{4.1}$$

where $k = 2$ in hovering and $k = 1$ in forward flight with $V > 40$ mph ($\mu \ll \lambda$). For transitional flight conditions when induced flow λ cannot be neglected in comparison to μ, Sissingh suggests an "appropriate" value for $k(1 < k < 2)$ on an ad hoc basis.

It is easily seen that Eq. (4.1) follows from the classical results

$$\lambda = -\sqrt{C_T/2}, \quad \mu = 0 \tag{4.2}$$

$$\lambda = -C_T/2\mu, \quad \mu \gg \lambda \tag{4.3}$$

Sissingh was probably the first to initiate a systematic exposition that established a relation between instantaneous perturbations (or transients) in thrust δT, and perturbations in induced flow, $\delta\lambda$. The induced flow λ is an involved function of both radius, r, and spatial azimuth position, ψ. To arrive at a tractable model, he uses first harmonic inflow and lift distributions, without radial variation,

$$\lambda = \lambda_o + \lambda_s \sin\psi + \lambda_c \cos\psi \tag{4.4}$$

Here, λ_0 is the uniform inflow, while λ_s and λ_c are side-to-side and fore-to-aft inflow variations. His analysis convincingly shows that the inclusion of induced velocity perturbations, as typified in Eq. (4.4), improves correlation of predicted damping values with those of the flight test data of Amer. (Sissingh's distribution has been used by several other investigators [59–61].) As seen from this equation, the distribution has two disadvantages. first, it neglects the effects of radial variation completely. Second, it exhibits a discontinuity at $r = 0$. As a means of improving the inflow distribution to account for radial variation to some degree and to avoid discontinuity, Peters [62] approximates dynamic inflow perturbations in induced flow by a truncated fourier series with a prescribed radial distribution. The dynamic flow ν is perturbed with respect to the steady inflow λ such that the total inflow is

$$-\lambda = \bar{\lambda} + \nu \tag{4.5}$$

and dynamic inflow is

$$\nu = \nu_o + \nu_s \frac{r}{R} \sin\psi + \nu_c \frac{r}{R} \cos\psi \tag{4.6}$$

Similar to the development of [58], the inflow takes the form

$$\begin{Bmatrix} v_o \\ v_s \\ v_c \end{Bmatrix} = \frac{1}{V} \begin{bmatrix} 1/2 & 0 & 0 \\ 0 & 2 & 0 \\ 0 & 0 & 2 \end{bmatrix} \begin{Bmatrix} \delta C_T \\ -\delta C_L \\ -\delta C_M \end{Bmatrix} \tag{4.7}$$

where δC_T, δC_L, and δC_M are perturbations in thrust, roll-moment, and pitch-moment coefficients and where the mass-flow parameter, V, is obtained from momentum theory as

$$V = \frac{\mu^2 + \bar{\lambda}(\bar{\lambda} + \bar{\nu})}{\sqrt{\mu^2 + \bar{\lambda}^2}} \tag{4.8}$$

where $\bar{\nu}$ is the part of $\bar{\lambda}$ due to thrust (the remainder is due to climb) and 4μ is the ratio of forward speed to tip speed.

The preceding development from Eq. (4.7) implies that perturbations in disk loading (δC_T, δC_L, δC_M) create instantaneous perturbations in inflow (λ_0, λ_s, λ_c). In other words, the feedback between changes in disk loading and inflow takes place without time lag. However, in transient downwash dynamics, a large mass of air is involved; and it is natural to expect that mass effects will have an influence on the complete build up of inflow perturbations due to disk-loading perturbations and vice versa. That is, the feedback will have some form of time delay due to mass effects. This aspect of the problem was investigated by Carpenter and Fridovich [63] during the early 1950s. The inclusion of the mass effects forms an integral part of the development of unsteady inflow models as an extension of the quasi-steady inflow treated in the preceding paragraph. Substantial data-correlation experience with the quasi-steady momentum model clearly demonstrates that *unsteady* wake effects (not quasi-steady alone) play a dominant role in hover, in transitional flight, and at low collective pitch [61, 62]. We will bypass the mathematical details [64] and include the rate terms, $[M]$, in the quasi-steady equation:

$$\frac{1}{\Omega}[M] \begin{Bmatrix} \dot{v}_o \\ \dot{v}_s \\ \dot{v}_c \end{Bmatrix} + [L]^{-1} \begin{bmatrix} v_o \\ v_s \\ v_c \end{bmatrix} = \begin{Bmatrix} \delta C_T \\ -\delta C_L \\ -\delta C_M \end{Bmatrix} \tag{4.9}$$

where $[L]$ is the matrix of influence coefficients in Eq. (4.7); or, symbolically

$$\frac{1}{\Omega}[M]\{\dot{U}\} + [L]^{-1}\{U\} = \{\delta F\} \tag{4.10}$$

When premultiplied by $[L]$, Eq. (4.10) takes the form

$$[\tau]\{\dot{U}\} + \{U\} = [L]\{\delta F\} \tag{4.11}$$

where $[\tau] = [L][M]/\Omega$.

In Eq. (4.11), $[r]$ and $[L]$ have the physical significance of time constants and gains, respectively. The elements of $[\tau]$ can also be treated as filter constants. This means, unsteady inflow can be simulated by passing the quasi-steady inflow through a low-pass filter.

We now turn to the problem of evaluating these rate (or apparent mass) terms. This problem has been the subject matter of extensive studies. In [63], apparent mass terms are identified in terms of reaction forces (or moments) of an impermeable disk which undergoes instantaneously acceleration (or rotation) in still air. The problem of finding reactions on an impermeable disk basically leads to the solution of a potential flow problem in terms of elliptic integrals. The values for the apparent mass of air m_A and apparent inertia of air I_A are [64]:

$$m_A = \frac{8}{3}\rho R^3 \quad \text{and} \quad I_A = \frac{16}{45}\rho R^5 \tag{4.12}$$

In other words, these values represent 64 per cent of the mass and 57 percent of the rotary inertia of a sphere of air or radius R; and we have a diagonal $[M]$ matrix with

$$m_{11} = m_A \rho \pi R^3 = 8/(3\pi) \tag{4.13}$$

$$m_{22} = m_{33} = I_A \rho \pi R^5 = 16/(45\pi) \tag{4.14}$$

which give time constants of 0.4244/V for δC_T and 0.2264/V for δC_L or δC_M. Given the complexity of the actual apparent mass terms of a lifting rotor, it would seem that the methodology adopted to arrive at the time constants is at best a crude approximation. Surprisingly, tests of Hohenemser et al. [59], and more recent analytical studies of Pitt and Peters [64] arrive at time constants or mass terms which are within a few percent of those given by Eq. (4.12). From the symmetry of the flow problem in hover, it is clearly seen that M is a diagonal matrix with $m_{22} = m_{33}$. Therefore, we have

$$[M] = \begin{bmatrix} \frac{8}{3\pi} & 0 & 0 \\ 0 & \frac{16}{45\pi} & 0 \\ 0 & 0 & \frac{16}{45\pi} \end{bmatrix} \tag{4.15}$$

Equation (4.9) with $[M]$ and $[L]^-1$ from Eqs. (4.15) and (4.7) forms the theory of dynamic inflow in hover. Numerous correlations with experimental data have shown the model accurate and crucial in rotor aeroelastic modelling. This includes frequency response [59, 62], control derivatives [62], and air and ground resonance [65]. Figures 28 and 29, taken from [65], show measured and computed frequencies of a ground-resonance model versus rotor speed. Figure 28 has no dynamic inflow modelling, and Fig. 29 includes modelling of the type of Eq. (4.9). We are particularly interested in the range $300 < \Omega < 1000$ in which ground resonance can occur. The

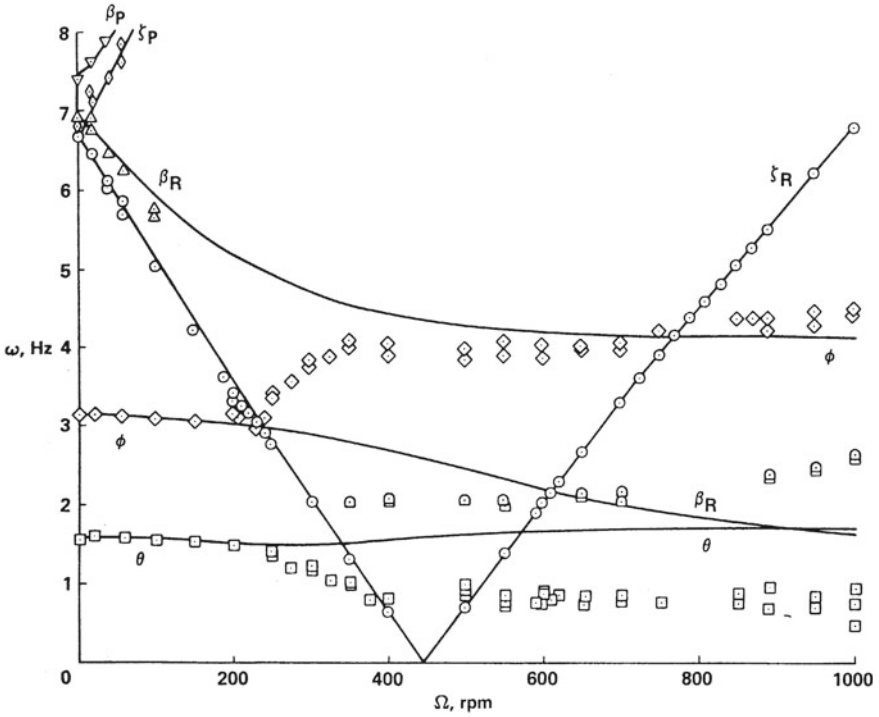

Fig. 28 Influence of unsteady aerodynamics on hingeless rotor ground resonance. Comparison of measured modal frequencies, and calculations without dynamic inflow

modes, labelled on the basis of theoretical eigenvectors are: regressing inplane (ζ_R), regressing flapping (β_R), roll (ϕ), pitch (θ). Note that in Fig. 28, the regressing inplane mode shows good frequency correlation; but all other modes are significantly off of the correct frequency. In Fig. 29, a new mode appears (due to the added inflow degrees of freedom). It is labelled λ and is a mode dominated by inflow motions. The new results show excellent correlation of all frequencies with the exception of a roll-pitch coupling for $200 < \Omega < 400$. The results show that the regressing flap mode becomes critically damped at $\Omega = 750$, and that the measured modes are crucially impacted by the dynamic inflow.

One of the interesting aspects of the dynamic inflow theory refers to the formulation of equivalent Lock number and drag coefficient (γ^* and C_d^*) [66]. This formulation reveals that there is an intrinsic correlation between downwash dynamics and unsteady airfoil aerodynamics. After all, any three-dimensional automatically includes induced flow theory as a local approximation to transient downwash dynamics. Further,dynamic inflow decreases lift and increases profile drag. Therefore, we should expect an equivalent γ (or γ^*) that is lower than γ, and an equivalent C_d (or C_d^*) that is higher than C_d. Thus, the $\gamma^* - C_d^*$ concept leads to one of the simplest methods of crudely accounting for dynamic inflow in conventional "no-inflow"-

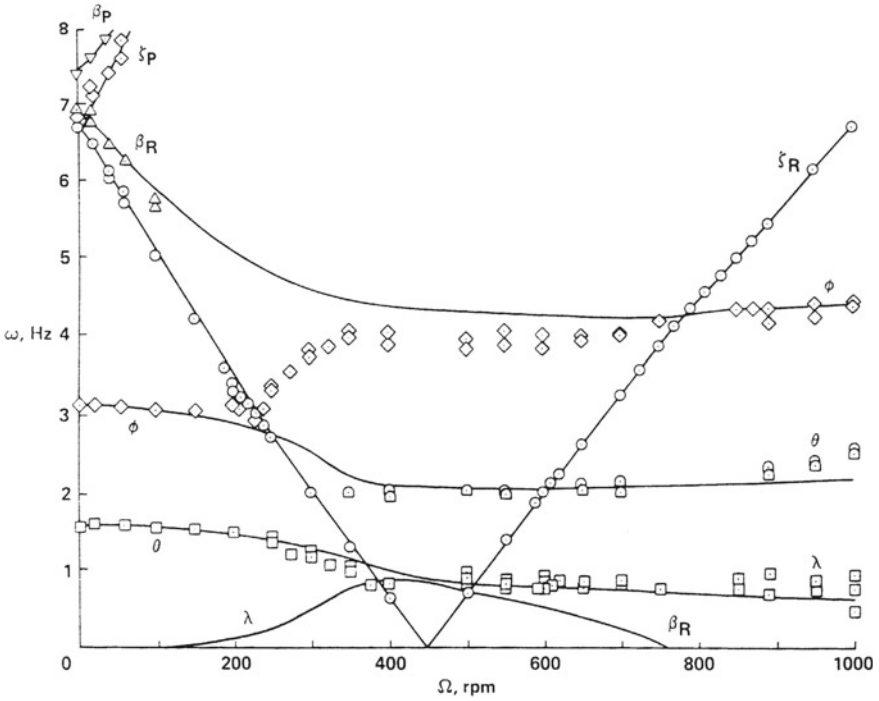

Fig. 29 Influence of unsteady aerodynamics on hingeless rotor ground resonance. Comparison of measured modal frequencies, and calculations including dynamic inflow

programs. One simply must change γ to γ^* and C_d to C_d^*. Furthermore, the concept brings out the physics of dynamic inflow in a simple and visible manner.

In quasi-steady inflow theory, apparent mass effects are neglected. Therefore, the inflow differential equations reduce to algebraic equations without increasing the system dimension. If we stipulate the condition of axial flow (e.g., $\mu = 0$) in the quasi-steady formulation, we may obtain γ_* and C_d^*, directly as detailed in [66].

$$\gamma^* = \gamma/(1 + \frac{a\sigma}{8V}) \tag{4.16}$$

and

$$(C_d/a)^* = \frac{C_d}{a}\left(1 + \frac{a\sigma}{8V}\right) + \frac{a\sigma}{8V}(\bar{\theta} - \phi)^2 \tag{4.17}$$

where $(\bar{\theta} - \phi)$ can be approximated by $6C_T/a\sigma$.

In forward flight, the model of Eq. (4.9) can be used but with alterations to the $[L]$ matrix. In [64], a general $[L]$ matrix is defined based on potential flow theory. A new parameter, X, is introduced which is defined as the tangent of one-half of the wake skew angle. In hover or axial flight, $X = \tan(0) = 0$ and, in edgewise flight, X

$= \tan(\pi/4) = 1$. Thus, S varies from zero to one as we transition from axial flight to edgewise flight. The corresponding $[L]$ matrix is

$$[L] = \frac{1}{V}\begin{bmatrix} \frac{1}{2} & 0 & -\frac{15\pi}{64}X \\ 0 & 2(1+X^2) & 0 \\ \frac{15\pi}{64}X & 0 & 2(1-X^2) \end{bmatrix} \tag{4.18}$$

In axial flow, $X = 0$; and this matrix reduces to the momentum-theory values in Eq. (4.7). In edgewise flow, significant couplings develop between thrust and the fore-to-aft gradient in flow (and between pitch moment and uniform flow). Equation (4.18) has been proven accurate by exhaustive correlations with forward-flight data [67].

4.2 Frequency Domain

The theory of dynamic inflow treats low-frequency inflow effects in the range of 0/rev to 2/rev. For high-frequency effects, investigators traditionally have relied upon frequency-domain aerodynamics such as the Theodorsen function [68]. However, the wake model for Theodorsen theory is flat two-dimensional for rotor work. A very useful alternative is Loewy theory [69]. The model for the Loewy theory is similar to that for the Theodorsen theory except that the wake is assumed to return in an infinite number of layers spaced apart by a fixed distance, h semi-chords. The resultant lift-deficiency function (the Loewy function) takes the following form

$$C'(k) = \frac{1}{1 + A(k)} \tag{4.19}$$

$$A(k) = \frac{Y_0(k) + iJ_0(k)(1+2W)}{J_1(k)(1+2W) - iY_1(k)} \tag{4.20}$$

$$W = [\exp(kh + 2\pi i\omega/Q) - 1]^{-1} \tag{4.21}$$

where k is the rotating-system reduced frequency, Y_n and J_n are Bessel Functions, ω is the frequency per revolution as seen in the non-rotating system, and Q is the number of blades.

W is called the wake-spacing function. For infinite wake spacing ($h \to \infty$), $W \to 0$; and consequently, Eq. (4.19) reduces to Theodorsen theory. For finite wake spacing, W becomes largest when ω is an integer multiple of Q, and the resulting $C'(k)$ is low. Thus, lift is lost when the shed vorticity of successive layers is aligned. For small k, the near-wake approximation for $A(k)$ is [71]

$$A(k) \approx \pi k\left(\frac{1}{2} + W\right) \tag{4.22}$$

The above theory has a connection to dynamic inflow theory (although the latter is in the time-domain). In particular, when ω is an integer multiple of Q and k is small, we can write

$$A(k) \approx \pi k \left(\frac{1}{kh}\right) = \frac{\pi}{h} \tag{4.23}$$

Now, if we note that $a = 2\pi$ for Loewy theory and that $h = 4v/\sigma$, where $\sigma = 2bQ/\pi R$ (where $b =$ semi-chord). Then

$$A = \frac{\sigma a}{8V}, \quad C'(k) = \frac{1}{1 + \frac{\sigma a}{8V}} \tag{4.24}$$

which is the quasi-steady approximation for dynamic inflow, γ^*/γ.

Thus, $C'(k)$ tends to oscillate between $\frac{1}{1+\sigma a/8V}$ and 1 (as ω is varied). The lowest points are at integer multiple of Q, and the highest points are at odd multiples of $Q/2$.

An alternative theory for $C'(k)$ is given by Miller [70], which neglects the W in the denominator of $A/(k)$. Both theories have the same near-wake approximation. In order to apply a lift deficiency function to rotor problems, one must also account for the effect of $C'(k)$ on lift and drag. This can be accomplished through the C_D^* approach.

$$a^* = aC'(k) = \frac{a}{1 + A(k)} \tag{4.25}$$

$$C_D^* = C_D + \frac{A(k)}{1 + A(k)}(\bar{\theta} - \phi)^2 \tag{4.26}$$

Despite the elegance and power of lift-deficiency functions, their use in rotor problems has been limited by several shortcomings. First, the theories are limited to a two-dimensional approximation in axial flow. Second, they are in the frequency domain, which is inconvenient for periodic-coefficient eigen-analysis (although finite-state approximations can be obtained) [72]. Third, Loewy theory exhibits a singularity as ω and k approach zero simultaneously. Due to these drawbacks, investigators often use dynamic inflow for the low-frequency effects (since it is a three-dimensional neglect wake effects in other frequency ranges.

4.3 Finite-State Wake Modelling

More recently, a complete three-dimensional wake model has been developed that includes dynamic inflow and the Loewy function implicitly [73]. In this theory, the induced flow on the rotor disk is expressed as an expansion in a Fourier series (azimuthally) and in special polynomials (radially) in powers of $\bar{r} = r/R$.

$$\nu(\bar{r},\ \psi,\ t) = \sum_{m=0}^{\infty} \sum_{n=m+1}^{\infty} \sum_{m+3}^{\infty} \hat{\phi}_n(\bar{r})[\alpha_n^m \cos m\psi + \beta_n^m \sin m\psi] \tag{4.27}$$

where

$$\hat{\phi}_n^m(\bar{r}) = \frac{1}{2}\sqrt{\pi(2n+1)} \sum_{q=m,m+2,\ldots}^{n-1} \bar{r}^q \frac{(-1)^{(q-m)/2}(n+q)!}{(q-m)!(q+m)!(n-q-1)!} \tag{4.28}$$

and α_n^m and β_n^m are the expansion coefficients. Thus, α_1^0, α_2^1, and β_2^1 take on the role of ν_o, ν_c and ν_s in dynamic inflow; and the higher-order terms allow a more detailed inflow model to any order desired. When the above expansion is combined with an acceleration-potential for the three-dimensional flow field, differential equations are formed that are similar in character to dynamic inflow.

$$\frac{1}{\Omega}\{\dot{\alpha}_n^m\} + [L^c]^{-1}\{\alpha_n^m\} = \{\tau_n^{mc}\} \tag{4.29}$$

$$\frac{1}{\Omega}\{\dot{\beta}_n^m\} + [L^s]^{-1}\{\beta_m^n\} = \{\tau_n^{ms}\} \tag{4.30}$$

The $[L]$ matrices are influence coefficients that depend on X (tangent of one-half of the wake skew angle). They are partitioned by the harmonic numbers m, r (m = inflow harmonic, r = pressurewithin each mr partition) there is a row-column pair (j, n) for the inflow and pressure shape function, respectively.

$$\begin{aligned}
[L_{jn}^{om}]^c &= \frac{1}{V} X^m \Gamma_{jn}^{0m} \\
[L_{jm}^{rm}]^c &= \frac{1}{V}[X^{|m-r|} + (-1)^\ell X^{|m+1|}]\Gamma_{jn}^{rm} \\
[L_{jn}^{rm}]^c &= \frac{1}{V}[X^{|m-r|} - (-1)^\ell X^{|m+r|}]\Gamma_{jn}^{rm}
\end{aligned} \tag{4.31}$$

where ℓ = min(r,m) and

$$\begin{aligned}
\Gamma_{jn}^{rm} &= \frac{(-1)^{\frac{n+j-2r}{2}} 4\sqrt{(2n+1)(2j+1)}}{\pi(j+n)(j+n+2)[(j-n)^2-1]} \quad \text{for} \quad r+m \text{ even} \\
\Gamma_{jn}^{rm} &= \frac{sgn(r-m)}{\sqrt{(2n+1)(2j+1)}} \quad \text{for} \quad r+m \text{ odd},\ j = n \pm 1 \\
\Gamma_{jn}^{rm} &= 0 \ \text{ for } \ r+m \text{ odd},\ j \neq n \pm 1
\end{aligned} \tag{4.32}$$

The right hand sides of Eqs. (4.29)–(4.30) are generalized forces obtained from the integral over each blade of the circulatory lift per unit length (and then summed over all the blades, the q-th blade being at ψ_q).

$$\tau_n^{oc} = \frac{1}{2\pi}\sum_{q=1}^{Q}\left[\int_0^1 \frac{L_q}{\rho\Omega^2 R^3}\hat{\phi}_n^0(\bar{r})d\bar{r}\right]$$

$$\tau_n^{mc} = \frac{1}{\pi}\sum_{q=1}^{Q}\left[\int_0^1 \frac{L_q}{\rho\Omega^2 R^3}\hat{\phi}_n^m(\bar{r})d\bar{r}\right]\cos(m\psi_q) \tag{4.33}$$

$$\tau_n^{ms} = \frac{1}{\pi}\sum_{q=1}^{Q}\left[\int_0^1 \frac{L_q}{\rho\Omega^2 R^3}\hat{\phi}_n^m(\bar{r})d\bar{r}\right]\sin(m\psi_q)$$

It is interesting to note that τ_1^{0c}, τ_2^{1c}, and τ_2^{1s} are proportional to C_T, C_M, and C_L (respectively). Thus, when only these three are present, we recover dynamic inflow. The higher expansion terms are taken to the same order as we take velocity expansions.

The L_q terms (lift per unit length of q-th blade) can be inserted in Eq. (4.33) from any lifting theory. When they are taken from blade element theory (and when the radial direction is neglected), one can prove that the system of Eqs. (4.29)–(4.30)

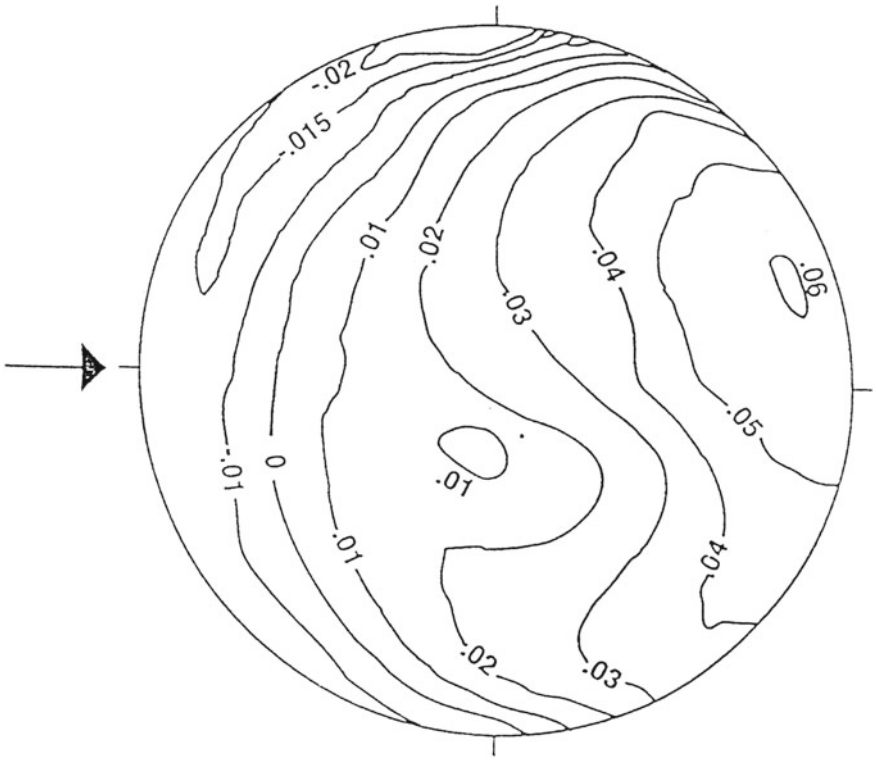

Fig. 30 Experimental induced inflow distribution. Tapered blade, $\mu = 0.15$

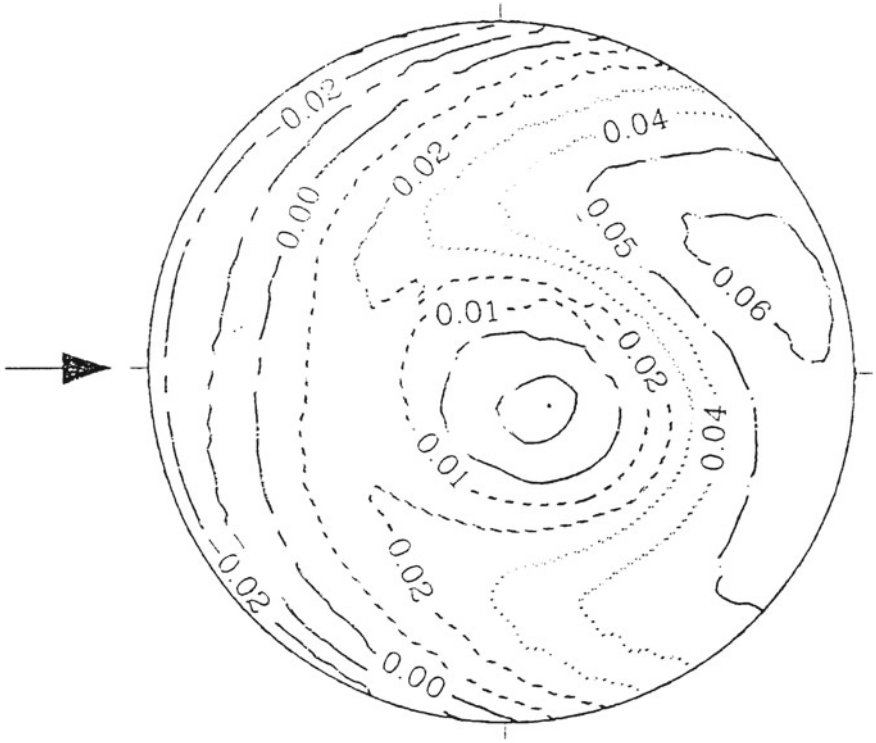

Fig. 31 Theoretical induced inflow distribution, tapered, blades with fuselage, $\mu = 0.15$, $C_r = 0.0064$, $\alpha = 3°$, $M = 4$, $S = 33$

reduces to the Loewy theory for $X = 0$ (axial flow) [73]. It should be pointed out that these equations are perturbation equations with ν and L_q taken as perturbations with respect to a steady state. A complete, nonlinear theory is available [74] but is not presented here.

Figures 30 and 31 show measured and calculated induced flows on a rotor at $\mu = 0.15$, from [74]. The calculations are based on the finite-state model. The major features of the flow-field are captured by the model. In [33], the new wake model is used to greatly improve correlation of stability computations with experimental data.

5 Summary

In recent years, rotor aeroelasticity has relied more heavily on unsteady aerodynamic modelling to improve predictive capabilities. The major modelling tools are dynamic inflow, lift-deficiency functions, and finite-state modelling. The last of these includes the other two as special cases.

References

1. Gessow A, Myers GC Jr (1952) Aerodynamics of the helicopter. The Macmillan Company, New York
2. Bramwell ARS (1976) Helicopter dynamics. Wiley, New York
3. Loewy RG (1969) Review of rotary wing V/STOL dynamics and aeroelastic problems. J Am Helicopter Soc 14(3):323
4. Friedmann P (1977) Recent developments in rotary wing aeroelasticity, Paper no. 11, Second European rotorcraft and powered lift aircraft forum
5. Hohenemser KH (1974) Hingeless rotorcraft flight dynamics. Agardograph 197
6. Johnson W (1974) Dynamics of tilting proprotor aircraft in cruise flight, NASA TN D-7677
7. Manjunath A, Nagabhushanam J, Gaonkar G, Peters D, Su A (1992) Flap-lag damping in hover and forward flight with a three-dimensional wake. In: Proceedings of the 48th annual forum of the American Helicopter Society, Washington
8. Burkham JE, Miao WL (1972) Exploration of aeroelastic stability boundaries with a soft-inplane hingeless-rotor model. J Am Helicopter Soc 17(4):2735
9. Donham RE et al (1969) Ground and air resonance characteristics of a soft in-plane rigid-rotor system. J Am Helicopter Soc 14(4):3341
10. Ormiston RA (1977) Aeromechanical stability of soft inplane hingeless rotor helicopters, Paper no. 25, Third European rotorcraft and powered lift aircraft forum, Aix-en-Provence, France
11. Goland L, Perlmutter AA (1957) A comparison of the calculated and observed flutter characteristics of a helicopter rotor blade. J Aeronaut Sci 24(4):281290
12. Reichert G, Huber H (1973) Influence of elastic coupling effects on the handling qualities of a hingeless rotor helicopter. In: Agard conference proceedings no. 121 advanced rotorcraft
13. Lentine FP et al (1968) Research in manuverability of the XH-51A compound helicopter, USA AVLABS TR 6823
14. Ham ND (1973) Helicopter blade flutter, AGARD report 607
15. Shames IH (1958) Engineering mechanics. Prentice-Hall Inc, Englewood Cliffs
16. Peters DA, Hohenemser KH (1971) Application of the floquet transition matrix to problems of lifting rotor stability. J Am Helicopter Soc 16(2):25–33
17. Ormiston RA, Hodges DH (1972) Linear flap-lag dynamics of hingeless helicopter rotor blades in hover. J Am Helicopter Soc 17(2):214
18. Chou PC (1958) Pitch lag instability of helicopter rotors. Institute of Aeronautical Sciences Preprint 805
19. Bennett RM, Curtiss HC Jr (1960) An experimental investigation of helicopter stability characteristics near hovering flight using a dynamically similar model. Princeton University Department of Aeronautical Engineering Report 517
20. Hansford RE, Simons IA (1973) Torsion-flap-lag coupling on helicopter rotor blades. J Am Helicopter Soc 18(4):212
21. Hodges DH, Ormiston RA (1976) Stability of elastic bending and torsion of uniform cantilever rotor blades in hover with variable structural coupling, NASA TN D-8192
22. Hodges DH, Dowell EH (1974) Non-linear equations of motion for the elastic bending and torsion of twisted nonuniform rotor blades, NASA TN D-7818
23. Flax AH, Goland L (1951) Dynamic effects in rotor blade bending. J Aeronaut Sci 18(12):813829
24. Yntema RT (1955) Simplified procedures and charts for rapid estimation of bending frequencies of rotating beams, NACA TN 3459
25. Young MI (1962) A simplified theory of hingeless rotors with application to tandem helicopters. In: Proceedings of the 18th annual national forum. American Helicopter Society, pp 3845
26. Curtiss HC Jr (1975) Sensitivity of hingeless rotor blade flap-lag stability in hover to analytical modelling assumptions, Princeton University Department of Aerospace and Mechanical Sciences Report 1236
27. Halley DH (1973) ABC helicopter stability, control and vibration evaluation on the Princeton dynamic model track, American Helicopter Society Preprint 744

28. Curtiss HC Jr (1973) Complex coordinates in near hovering rotor dynamics. J Aircr 10(5):289296
29. Berrington DK (1974) Design and development of the Westland Sea Lynx. J Am Helicopter Soc 19(1):1625
30. Ormiston RA, Bousman WG (1975) A study of stall-induced flap-lag instability of hingeless rotors. J Am Helicopter Soc 20(1):2030
31. Peters DA (1975) An approximate closed-form solution for lead-lag damping of rotor blades in hover. NASA TM X- 62:425
32. Gaffey TM (1969) The effect of positive pitch-flap coupling (negative δ_3) on rotor blade motion stability and flapping. J Am Helicopter Soc 14(2):4967
33. de Andrade D, Peters D (1992) On a finite-state inflow application to flap-lag-torsion damping in hover. In: Proceedings of the eighteenth European rotorcraft forum, Avinon, France, Paper no. 2
34. Ham ND, Garelick MS (1968) Dynamic stall considerations in helicopter rotors. J Am Helicopter Soc 13(2):4955
35. Liiva J, Davenport FJ (1969) Dynamic stall of airfoil sections for high-speed rotors. J Am Helicopter Soc 14(2):2633
36. Martin JM et al (1974) An experimental analysis of dynamic stall on an oscillating airfoil. J Am Helicopter Soc 19(1):2632
37. McCroskey WJ, Fisher RK Jr (1972) Detailed aerodynamic measurements on a model rotor in the blade stall regime. J Am Helicopter Soc 17(1):2030
38. Johnson W, Ham ND (1972) On the mechanism of dynamic stall. J Am Helicopter Soc 17(4):3645
39. Ericsson LE, Reding JP (1972) Dynamic stall of helicopter blades. J Am Helicopter Soc 17(4):3645
40. Tarzanin FJ Jr (1975) Prediction of control loads due to blade stall. J Am Helicopter Soc 17(2):3346
41. Leishman JG, Beddoes TS (1989) A semi-empirical model for dynamic stall. J Am Helicopter Soc 34(3):317
42. Peleau B, Petot D (1989) Aeroelastic prediction of rotor loads in forward flight. Vertica 13(2):107118
43. Narramore JC, Sankar LN, Vermeland R (1988) An evaluation of a navier-stokes code or calculation of rereating blade stall on helicopter rotor. In: Proceedings of the 44th annual forum of the American Helicopter Society, Washington, pp 797808
44. Coleman RP, Feingold AM (1957) Theory of self-excited mechanical oscillations of helicopter rotors with hinged blades, NACA TN 3844
45. Hohenemser KH, Yin SK (1972) Some applications of the method of multi-blade coordinates. J Am Helicopter Soc 17(3):312
46. Gaonkar GH, Mitra AK, Reddy TSR, Peters DA (1982) Sensitivity of helicopter aeromechanical stability to dynamic inflow. Vertica 6:5975
47. Lytwyn RT et al (1971) Airborne and ground resonance of hingeless rotors. J Am Helicopter Soc 16(2):29
48. Briczinski S, Cooper DE (1974) Flight investigation of rotor/vehicle state feedback, NASA CR-132546
49. Reed WH III (1967) Review of propeller-rotor whirl flutter, NASA TR R-264
50. Hall EW Jr (1966) Prop-rotor stability at high advance ratios. J Am Helicopter Soc 11(2):1126
51. Young MI, Lytwyn RT (1967) The influence of blade flapping restraint on the dynamic stability of low disc loading propeller-rotors. J Am Helicopter Soc 12(4):3854
52. Johnson W (1975) Analytical modelling requirements for tilting prop rotor aircraft dynamics, NASA TN D-8013
53. Shamie J, Friedmann P (1976) Aeroelastic stability of complete rotors with application to a teetering rotor in forward flight. American Helicopter Society Preprint No. 1031
54. Kawakami N (1977) Dynamics of an elastic seesaw rotor. J Aircr 14(3):225330

55. Landgrebe AJ (1969) An analytical method for predicting rotor wake geometry. J Am Helicopter Soc 14(4):2032
56. Kwon OJ, Hodges DH, Sankar LN (1991) Stability of hingeless rotors in hover using threed-imensional unsteady aerodynamics. In: Proceedings of the 45th annual national forum of the American Helicopter Society, Boston, 1989, and Journal of the American Helicopter Society, vol 36, No. 2 pp 2131
57. Amer KB (1950) Theory of helicopter damping in pitch or roll and comparison with flight measurements. NACA, TN, p 2136
58. Sissingh GJ (1952) The effect of induced velocity variation on helicopter rotor damping pitch or roll, Aeronautical Research Council (Great Britain), A.R.C. Technical Report G.P. No. 101 (14,757)
59. Hohenemser KH (1974) Hingeless rotorcraft flight dynamics, AGARD-AG-197
60. Curtiss HC Jr, Shupe NK (1971) A stability and control theory for hingeless rotors. Annual national forum of the American Helicopter Society, Washington, D. C
61. Ormiston RA, Peters DA (1972) Hingeless helicopter rotor response with non-uniform inflow and elastic blade banding. J Aircr 9(10):730736
62. Peters DA (1974) Hingeless rotor frequency response with unsteady inflow. In: Presented at the AHS/NASA Ames specialists meeting on rotorcraft dynamics, NASA SP-362
63. Carpenter PJ, Fridovich B (1953) Effect of a rapid blade pitch increase on the thrust and induced velocity response of a full scale helicopter rotor, NASA TN 3044
64. Pitt DM, Peters DA (1981) Theoretical prediction of dynamic inflow derivatives. Vertica 5(1):2134
65. Johnson W (1982) Influence of unsteady aerodynamics on hingeless rotor ground resonance. J Aircr 29(9):668673
66. Gaonkar GH, Mitra AK, Reddy TSR, Peters DA (1982) Sensitivity of helicopter aeromechanical stability to dynamic inflow. Vertica 6(1):5975
67. Gaonkar GH, Peters DA (1986) Effectiveness of current dynamic-inflow models in hover and forward flight. J Am Helicopter Soc 31(2):4757
68. Theodorsen T (1949) General theory of aerodynamic instabilities and the mechanism of flutter, NACA TR 496
69. Loewy RG (1957) A two-dimensional approach to the unsteady aerodynamics of rotary wings. J Aerosp Sci 24(2):8298
70. Wayne Johnson (1980) Helicopter theory. Princeton University Press, Princeton
71. Miller RH (1964) Rotor blade harmonic air loading. AIAA J 2(7):12541269
72. Friedman PP, Venkatesan C (1985) Finite state modeling of unsteady aerodynamics and its application to a rotor dynamics problem. Eleventh European rotorcraft forum, London, Paper no, p 77
73. Peters DA, Boyd DD, He CJ (1989) Finite-state induced-flow model for rotors in hover and forward flight. J Am Helicopter Soc 34(4):517
74. Peters DA, He CJ (1991) Correlation of measured induced velocities with a finite-state wake model. J Am Helicopter Soc 36(3):5970

Aeroelasticity in Turbomachines

Fernando Sisto

Abstract Turbomachines also prone to various types of dynamic instabilities and responses that in some respects are similar to those of classical aeroelasticity as described in earlier chapters. However the complications of rotating flows and structures provide new challenges as described in this chapter, also see the related discussion in chapters "Modeling of Fluid-Structure Interaction and Modern Analysis for Complex" and "Nonlinear Unsteady Flows in Turbomachinery".

The advent of the jet engine and the high performance axial-flow compressor toward the end of World War II focussed attention on certain aeroelastic problems in turbomachines.

The concern for very light weight in the aircraft propulsion application, and the desire to achieve the highest possible isentropic efficiency by minimizing parasitic losses led inevitably to axial-flow compressors with cantilever airfoils of high respect ratio. Very early in their development history these machines were found to experience severe vibration of the rotor blades at part speed operation; diagnosis revealed that these were in fact stall flutter (see chapter "Stall Flutter") oscillations. The seriousness of the problem was underlined by the fact that the engine operating regime was more precisely termed the 'part corrected speed' condition, and that in addition to passing through this regime at ground start up, the regime could be reentered during high flight speed conditions at low altitude. In either flight condition destructive behavior of the turbojet engine could not be tolerated.

In retrospect it is probable that flutter had occurred previously in some axial flow compressors of more robust construction and in the later stages of low pressure axial-flow stream turbines as well. Subsequently a variety of significant forced and self-excited vibration phenomena have been detected and studied in axial-flow turbomachinery blades.

In 1987 and 1988 two volumes of the AGARD *Manual on Aeroelasticity in Turbomachines* [1, 2] were published with 22 chapters in all. The sometimes disparate topics contributed by nineteen different authors and/or co-authors form a detailed and extensive reference base related to the subject material of the present chapter.

F. Sisto (✉)
Mechanical Engineering, Stevens Institute of Technology, Hoboken, NJ, USA

E. H. Dowell (ed.), *A Modern Course in Aeroelasticity*, Solid Mechanics and Its Applications 264, https://doi.org/10.1007/978-3-030-74236-2_8

The reader is urged to refer to the AGARD compendium for in-depth development and discussion of many of the topics to be introduced here, and for related topics (such as the role of experimentation) not included here.

1 Aeroelastic Environment in Turbomachines

Consider an airfoil or blade in an axial flow turbine or compressor which is running at some constant rotational speed. For reasons of steady aerodynamic and structural performance the blade has certain geometric properties defined by its length, root and tip fixation, possible mechanical attachment to other blades and by the chord, camber, thickness, stagger and profile shape which are functions of the radial coordinate. Furthermore, the blade may be constructed in such a manner that the line of centroids and the line of shear centers are neither radial nor straight, but are defined by schedules of axial and tangential coordinates as functions of radius. In fact, in certain cases, it may not be possible to define the elastic axis (i.e., the line of shear centers). The possibility of a built-up sheet metal and spar construction, a laid-up plastic laminate construction, movable or articulated fixations and/or supplemental damping devices attached to the blade would complicate the picture even further.

The blade under consideration, which may now be assumed to be completely defined from a geometrical and kinematical point of view, is capable of deforming[1] in an infinite variety of ways depending upon the loading to which it is subjected. In general, the elastic axis (if such can be defined) will assume some position given by axial and tangential coordinates which will be continuous functions of the radius (flapwise and chordwise bending). About this axis a certain schedule of twisting deformations may occur (defined, say by the angular displacement of a straight line between leading and trailing edges). Finally, a schedule of plate type bending deformations may occur as functions of radius and the chordwise coordinate. (Radial extensions summoned by centrifugal forces may further complicate the situation).

Although divergence is not a significant problem in turbomachines, an alternative static aeroelastic problem, possibly resulting in the measurable untwist and uncamber of the blades, can have important consequences with respect to the steady performance and with respect to the occurrence of blade stall and surge.

One has now to distinguish between steady and oscillatory phenomena. If the flow through the machine is completely steady in time and there are no mechanical disturbances affecting the blade through its connections to other parts of the machine, the blade will assume some deformed position as described above (and as compared to its manufactured shape) which is also steady in time. This shape or position will depend on the elastic and structural properties of the blade and upon the steady aerodynamic and centrifugal loading. (The centrifugal contribution naturally does not apply to a stator vane.)

[1] Deformations are reckoned relative to a steadily rotating coordinate system in the case of a rotor blade.

Consider the situation, however, where dynamic disturbances may exist in the airstream, or may be transmitted through mechanical attachments from other parts o the structure. Due to the unsteadiness of the aerodynamic and/or the external forces the blade will assume a series of time-dependent positions. If there is a certain repetitive nature with time of the displacements relative to the equilibrium position, the blade is said to be executing vibrations, the term being taken to include those cases where the amplitude of the time-dependent displacements is either increasing, decreasing or remaining constant as time progresses.

It is the prediction and control of these vibrations with which the turbomachine aeroelastician is concerned. Once the blade is vibrating the aerodynamic forces are no longer a function only of the airstream characteristics and the blade's angular position and velocity in the disturbance field, but depend in general upon the blade's vibratory position, velocity and acceleration as well. There is a strong interaction between the blade's time-dependent motion and the time-dependent aerodynamic forces which it experiences. It is appropriate at this point to note that in certain cases the disturbances may be exceedingly small, serving only to 'trigger' the unsteady motion, and that the vibration may be sustained or amplified purely by the interdependence or feedback between the harmonic variation with time of the blade's position and the harmonic variation with time of the aerodynamic forces (the flutter condition).

A further complication is that a blade cannot be considered as an isolated structure. There exist aerodynamic and possibly structural coupling between neighboring blades which dictate a modal description of the entire vibrating bladed-disk assembly. Thus an interblade phase angle, σ, is defined and found to play a crucial role in turbomachine aeroelasticity . Nonuniformities among nominally 'identical' blades in a row, or stage, are found to be extremely important in turbomachine aeroelasticity; stemming from manufacturing and assembly tolerances every blade row is 'mistuned' to a certain extent, i.e., the nominally identical blades in fact are not identical.

2 The Compressor Performance Map

The axial flow compressor, and its aeroelastic problems, are typical; the other major important turbomachine variant being the axial flow turbine (gas or steam). In the compressor the angle of attack of each rotor airfoil at each radius r is compounded of the tangential velocity of the airfoil section due to rotor rotation and the through flow velocity as modified in direction by the upstream stator row. Denoting the axial component by V_x and the angular velocity by Ω as in Fig. 1, it is clear that the angle of attack will increase inversely with the ratio $\phi = V_x/(r\Omega)$. In the compressor, an increase in angle of attack (or an increase in 'loading') results in more work being done on the fluid and a greater stagnation pressure increment Δp_0 being imparted to it. Hence the general aspects of the single 'stage' (i.e., pair of fixed and moving blade rows) characteristics in Fig. 2 are not without rational explanation. Note that

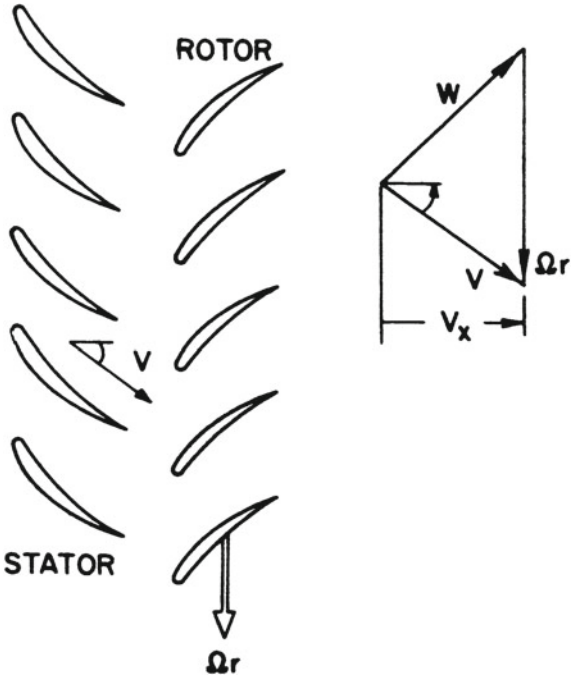

Fig. 1 Velocity triangle in an axial compressor

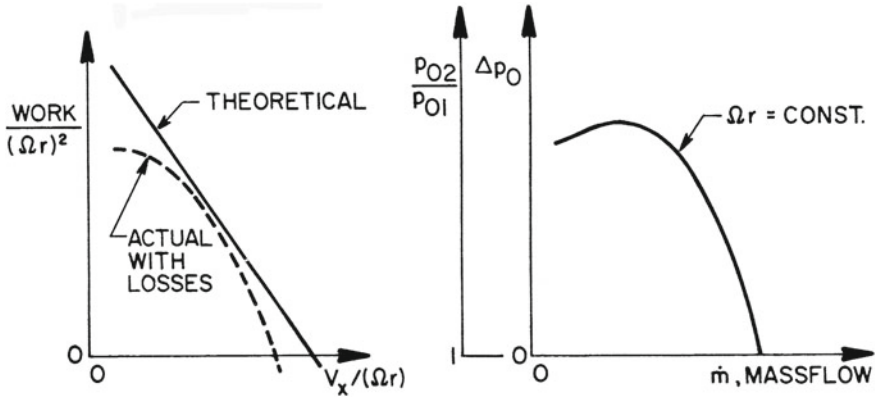

Fig. 2 Work and pressure ratio relationships

the massflow through the stage equals the integral over the flow annulus of the product of V_x and fluid density.

When the various parameters are expressed in dimensionless terms, and the complete multistage compressor is compounded of a number of states, the overall compressor 'map', or graphical representation of multistage characteristics, appears as in

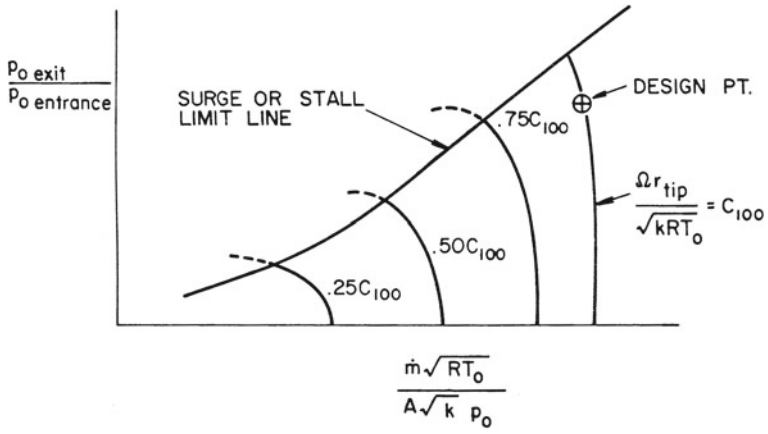

Fig. 3 Compressor map

Fig. 3, where $\dot{m}$ is massflow, γ and R are the ratio of specified heats and gas constant, respectively; T_0 is stagnation temperature and A is a reference flow area in the compressor. Conventionally the constants γ and R are omitted where the identity of the working fluid is understood (e.g., air). The quantity A is a scaling parameter relating the absolute massflow of geometrically similar machines and is also conventionally omitted. The tangential velocity of the rotor blade tip, Ωr_{tip}, is conventionally replaced by the rotational speed in rpm. The latter omission and replacement are justified when discussing a particular compressor.

An important property of the compressor map is the fact that to each point there corresponds theoretically a unique value for angle of attack (or incidence) at any reference airfoil section in the compressor. For example, taking a station near the tip of the first rotor blade as a reference, contours of incidence may be superposed on the map coordinates. In Fig. 4 such angle contours have been shown for a specific machine. As defined here, a_i is the angle between the relative approach velocity W and the chord of the airfoil. Here again axial velocity V_x (or massflow) is seen to display an inverse variation with respect to angle of attack as a line of constant rotational speed is traversed. The basic reason such incidence contours can be established is that the two parameters which locate a point on the map, $\dot{m}\sqrt{T_0/p_0}$ and $\Omega r/\sqrt{T_0}$, are effectively a Mach number in the latter case and a unique function of Mach number in the former case. Thus the 'Mach number triangles' are established which yield the same 'angle of attack' as the velocity triangles to which they are similar, Fig. 5.

As a matter for later reference, contours of $V/(v\omega)$ for a particular stator airfoil, or else $W/(b\omega)$ for a particular rotor airfoil, can be superimposed on the same map, provided the environmental stagnation temperature, T_0, is specified. These contours are roughly parallel, though not exactly, to the constant rotational speed lines. The natural frequency of vibration, ω, tends to be constant for a rotor blade at a given rotational speed; and of course a stator blade's frequency does not depend directly on rotation. However, upon viewing the velocity triangles in Fig. 5, it is clear that if Ωr

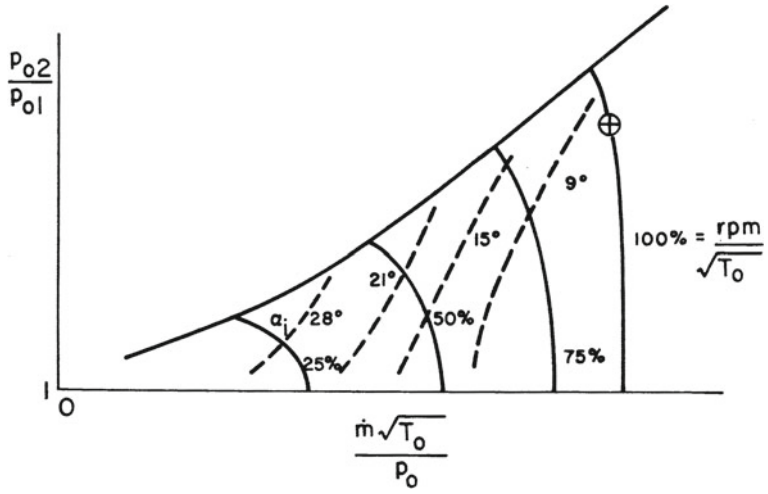

Fig. 4 Map showing incidence as a parameter

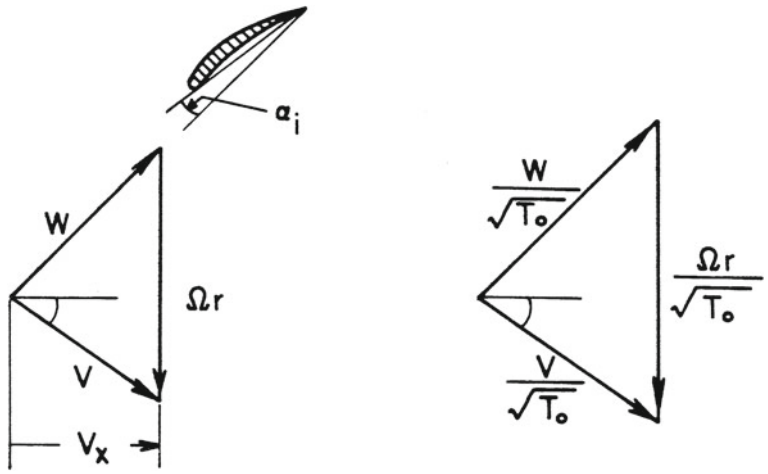

Fig. 5 Velocity and Mach number correspondence

is kept constant and the *direction* of V is kept constant, the size of W may increase or decrease as V_x (or massflow) is changed. In fact, if the angle between V and W is initially close to 90 degrees, a not uncommon situation, the change in the magnitude of W will be minimal. For computing the stator parameter, $V/(b\omega)$, the direction of W *leaving* a rotor is considered to be virtually constant, and the corresponding changes in V (length and direction) as V_x is varied lead to similar conclusions with regard to angle of attack and magnitude of V experienced y the following stator. The values of $W/(b\omega)$ increase with increasing value of Ωr_{tip}, since the changes in W

(or V) will dominate the somewhat smaller changes in the appropriate frequency ω, at least in the first few stages of the compressor. Compressibility phenomena, when they become significant will sometimes alter these general conclusions.

3 Blade Mode Shapes and Materials of Construction

Flutter and vibration of turbomachinery blades can and do occur with a wide variety of these beam -like structures and their degrees of end restraint. Rotor blades in use vary from cantilever with perfect root fixity all the way to a single pinned attachment such that the blade behaves in bending like a pendulum 'flying out' and being maintained in a more or less radial orientation by the centrifugal (rather than a gravity) field. Stator vanes may be cantilevered from the outer housing or may be attached at both ends, with degrees of fixity ranging from 'encastred' to 'pinned'.

The natural modes and frequencies of these blades, or blade -disc systems when the blades are attached to their neighbors in the same row or the discs are not effectively rigid, are obtainable by standard methods of structural dynamics. Usually twisting and two directions of bending are incorporated in a beam -type finite element analysis. If plate-type deformations are significant, the beam representation must be replaced by more sophisticated plate or shell elements which recognize static twist and variable thickness.

In predicting the first several natural modes and frequencies of rotor blades it is essential to take into account the effect of rotor rotational speed. Although the description is not analytically precise in all respects, the effect of rotational speed can be approximately described by stating $\omega_n^2 = \omega_{0n}^2 + K_n\Omega^2$ where ω_{0n} is the static (nonrotating) frequency of the rotor blade and the Southwell coefficient K_n is a proportionality constant for any particular blade in the nth mode. The effect is most pronounced in the natural modes which exhibit predominantly bending displacements; the modes associated with the two gravest frequencies are usually of this type, and it is here that the effect is most important. A positive Southwell coefficient represents a centrifugal stiffening of the blade, increasing the natural frequency. Disk rotation rate also produces a softening effect that can reduce the Southwell coefficient. This softening effect is typically significant for only the first mode. High temperatures in high pressure turbines operating at high power levels can reduce the modulus of elasticity of the blades, reducing the static natural frequency ω_{0n}. As high engine power tends to occur at high rotor speeds, thermal effects can cause the frequency of some blade modes to decrease with increasing speed. Other factors also need to be considered, such as blade fixity boundary condition (fixed-fixed in stators versus fixed-free in rotors), and disk flexibility.

Materials of construction are conventionally aluminum alloys, steel or stainless steel (high nickel and/or chromium content). However, in recent applications titanium and later beryllium have become significant. In all these examples, considering flutter or forced vibration in air as the surrounding fluid, the fluid/structural mass ratios are such that the critical mode and frequency may be taken to be one or a combination of the modes calculated, or measured, in a vacuum.

More recently there has been a reconsideration of using blades and vanes made of laminated materials such as glass cloth, graphite or metal oxide fibers laid up in polymeric or metal matrix materials and molded under pressure to final airfoil contours. Determining the modes and frequencies of these composite beams is more exacting. However, once determined, these data may be used in the same manner as with conventional metal blades. It should also be noted that aeroelastic programs related to turbomachinery often make a great deal of practical use out of mode and frequency data determined experimentally from prototype and development hardware.

A major consideration in all material and mode of construction studies is the determination of mechanical damping characteristics. Briefly stated the damping may be categorized as material or structural. The former is taken to describe a volume-distributed property in which the rate of energy dissipation into heat (and thus removed from the mechanical system) is locally proportional to a small power of the amplitude of the local cyclical strain. The proportionality constant is determined by many factors, including the type of material, state of mean or steady strain, temperature and other minor determinants.

The structural damping will usually be related to interfacial effects, for example in the blade attachment to the disk or drum, and will depend on normal pressure across the interface, coefficient of friction between the surfaces, mode shape of vibration, and modification of these determinants by previous fretting or wear. Detailed knowledge about damping is usually not known with precision, and damping information is usually determined and used in 'lumped' or averaged fashion. Comparative calculations may be use to predict such gross damping parameters for a new configuration, basing the prediction on the known information for an existing and somewhat similar configuration. By this statement it is not meant to imply that this is a satisfactory state of affairs. More precise damping prediction capabilities would be very welcome in modern aeroelastic studies of turbomachines, and some studies of this nature are reported in Refs. [1, 2].

The aeroelastic response is central to the analysis of fatigue and fracture of turbomachinery blades. The question of crack initiation, crack propagation and destructive failure cannot be addressed without due attention being given to the type of excitation (forced or self-excited) and the parametric dependencies on the nonsteady aerodynamic forces. This may be appreciated when it is noted that the modal shape functions, frequencies and structural damping of a blade change with the crack growth of the specimen. This concatenation of aeroelasticity and blade failure prediction is presently an active area of research and development.

4 Nonsteady Potential Flow in Cascades

Unwrapping an annulus of differential height dr from the blade row flow passage of an axial turbomachine results in a two-dimensional representation of a cascade of airfoils and the flow about them. The airfoils are identical in shape, equally spaced, mutually congruent and infinite in number.

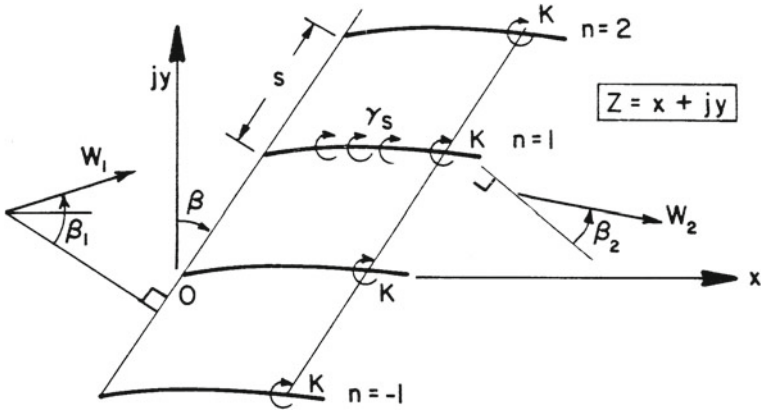

Fig. 6 Cascade camberlines modelled by vortex sheets

When a cascade is considered, as opposed to a single airfoil, the fact that the flexible blades may be vibrating means that the relative pitch and stagger may be functions of time and also position in the cascade. The steady flow, instead of being a uniform stream, will now undergo turning; large velocity gradients may occur in the vicinity of the blades and in the passages between them. These complications imply that the blade thickness and steady lift distribution must be taken into account for more complete fidelity in formulating the nonsteady aerodynamic reactions. See chapters by Whitehead and Verdon in Ref. [1].

A fundamental complication which occurs is the necessity for treating the wakes of shed vorticity from *all* the blades in the cascade.

Assume the flow is incompressible. Standard methods of analyzing steady cascade performance provide the steady vorticity distribution common to all the blades, $\gamma_s(x)$, and its dependence on W_1 and β_1. As a simple example of cascading effects consider only this steady lift distribution on each blade in the cascade and compute the disturbance velocity produced at the reference blade by a vibration of al the blades in the cascade.

In what follows the imaginary index j for geometry and the imaginary index i for time variation (i.e., complex exponential) cannot be 'mixed'. That is $ij \neq -1$. Furthermore, it is convenient to replace the coordinate normal to the chord, z, by y and the upwash on the reference airfoil w_a by v. The velocities induced by an infinite column of vortices of equal strength, τ, are given by (Fig. 6)

$$\delta[u(z) - jv(z)] = \frac{j\Gamma}{2\pi} \sum_{n=-\infty}^{\infty} \frac{1}{Z - \zeta_n} \tag{4.1}$$

where the location ζ_n of the nth vortex

$$\zeta_n = \xi + jnse^{-j\beta} + jY_n(\xi_n, t) + X_n(t) \tag{4.2}$$

indicates small deviations from uniform spacing s, ($Y_n \ll s$, $X_n \ll c$). The point Z is on the zeroth or reference blade

$$Z = x + jY(x, t) + X(t) \tag{4.3}$$

and the location of the vortices will ultimately be congruent points on different blades so that

$$\xi_n = \xi + ns \sin \beta \tag{4.4}$$

(The subscript naught, indicating the zeroth blade, is conventionally omitted.) Finally, harmonic time dependence with time lag $-r$ between the motions of adjacent blades[2] is indicated by

$$Y_n(\xi_n, t) = e^{in\omega r}\, Y(\xi, t) \tag{4.5}$$

With these provisions the Cauchy kernel in (4.1) may be written

$$\frac{1}{Z - \zeta_n} = \frac{1}{x - \xi - jnse^{-j\beta} + j[Y(x, t) - Y_n(\xi_n, t)] + X(t) - X_n(t)} \tag{4.6}$$

and summing (4.5) over all blades

$$\sum_{n=-\infty}^{n=\infty} \frac{1}{Z - \zeta_n} = \frac{1}{x - \xi + j[Y(x, t) - Y(\xi, t)]} + \sum_{n=-\infty}^{\infty'} \frac{1}{Z - \zeta_n} \tag{4.7}$$

where the primed summation indicates $n = 0$ is excluded. The first term on the RHS of (4.7) is a self-induced effect of the zeroth foil. The part $Y(x, t) - Y(\xi, t)$ is conventionally ignored in the thin-airfoil theory; it is small compared to $x - \xi$ and vanishes with $x - \xi$. Hence the first term supplies the single airfoil or self-induced part of the steady state solution. Expanding the remaining term yields

$$\begin{aligned} \sum{}' \frac{1}{Z - \zeta_n} \cong \sum{}' \frac{1}{x - \xi - jns\, e^{-j\beta}} + j \sum{}' \frac{Y_n(\xi_n,\, t) - Y(x,\, t)}{(x - \xi - jns\, e^{-j\beta})^2} \\ + \sum{}' \frac{X_n(t) - X(t)}{(x - \xi - jns\, e^{-j\beta})^2} + \cdots \end{aligned} \tag{4.8}$$

[2] This so-called 'periodicity assumption' of unsteady cascade aerodynamics lends order, in principle and often in practice, to the processes of cascade aeroelasticity. The mode of every blade is assumed to be identical, with the same amplitude and frequency but with the indicated blade-to-blade phase shift. Such a blade row, would be termed 'perfectly tuned'. Absent this assumption, the cascade representing a rotor of n blades could have n distinct components (type of mode, modal amplitude, frequency).

where the last two summations on the RHS of (4.8) are the *time-dependent portions*. The corresponding unsteady induced velocities from (4.1) may be expressed as follows using the preceding results

$$\delta[\tilde{u}(x')-j\tilde{v}(x')] \simeq -\frac{\gamma_s(\xi')\delta\xi'}{2\pi c}\mathbf{P}^2\Big\{\sum{}' \frac{e^{in\omega\tau}Y(\xi',\,t)-Y(x',\,t)}{(\chi-jn\pi)^2} + \frac{1}{j}\sum{}' \frac{e^{in\omega\tau}X(t)-X(t)}{(\chi-jn\pi)^2}\Big\} \tag{4.9}$$

where the primed variables are dimensionless w.r.t. the chord,

$$P = \pi e^{j\beta}c/s \tag{4.10}$$

$$\chi = P(x'-\xi') \tag{4.11}$$

and $\tilde{u}$, $\tilde{v}$ are the time dependent parts of u, v. The local chordwise distribute vortex strength $\gamma_s(\xi)d\xi$ has replaced τ the discrete vortex strength in the last step, (4.9). With the notation

$$q = 1-\omega\tau/\pi \tag{4.12}$$

the summations may be established in closed form. For example, when the blades move perpendicular to their chordlines with the same amplitude all along the chord (pure bending) the displacement function is a constant

$$Y = -\bar{h}e^{i\omega t} = -h \tag{4.13}$$

and, upon integrating over the chord in (4.9), one obtains

$$\tilde{u}(x') - j\tilde{v}(x') = \frac{\mathbf{P}^2}{2\pi c}\int^{1_0\gamma_s}(\xi')\sum{}' \frac{e^{in\omega\tau}h(t)-h(t)}{(\chi-jn\pi)^2}d\xi' \tag{4.14}$$

or

$$\tilde{u} = -\frac{h}{2\pi c}\int_0^1 \gamma_s(\xi')[F-iI]d\xi' \tag{4.15a}$$

$$\tilde{v} = -\frac{h}{2\pi c}\int_0^1 \gamma_s(\xi')[G+iH]d\xi' \tag{4.15b}$$

where

$$F+iG = \mathbf{P}^2\frac{q\sinh\chi\,\sinh q\chi-\cosh\chi\,\cosh q\chi+1}{\sin h^2\chi} \tag{4.15c}$$

$$H+iI = \mathbf{P}^2\frac{q\sinh\chi\,\cosh q\chi-\cosh\chi\,\sinh q\chi}{\sin \mathrm{h}^2\chi} \tag{4.15d}$$

Similar disturbance velocity fields can be derived for torsional motion, pure chordwise motion, etc. Another separate set of disturbance fields may be generated to take account of the blade thickness effects by augmenting the steady vorticity distribution $\gamma(x)$ by, say $-j\epsilon(x)$, the steady source distribution, in the above development.

The net input to the computation of oscillatory aerodynamic coefficients is then obtained by adding the $\tilde{v}$ of all the effects so described to the LHS of the integral equation which follows

$$\overbrace{v_1(x) + v_2(x) + v_3(x)}^{\text{on } y=0,\ 0<x<c} = \frac{1}{2\pi}\int_0^c [\gamma_1(\xi) + \gamma_2(\xi) + \gamma_3(\xi)]K(\xi - x)d\xi + \frac{1}{2\pi}\int_c^\infty [\gamma_1(\xi) + \gamma_2(\xi) + \gamma_3(\xi)]K(\xi - x)d\xi \tag{4.16}$$

In this formulation v_1 may be identified with the unsteady upwash, if any, convected as a gust with the mean flow and v_2 is the unsteady upwash attributable to vibratory displacement of all the blades in the cascade, where each blade is represented by steady vortex and source/sink distribution. It is v_2 that was described for one special component (pure bending) in the derivation of $\tilde{v}$ leading to (4.15b).

The component v_3 may be identified with the unsteady upwash elative to the zeroth airfoil occasioned by its harmonic vibration.

Since we are dealing here with a linear problem each of the subscripted subproblems may be solved separately and independently of the others. It is also important to note that since the vortex distributions γ_1, γ_2 and γ_3 representing the lift distributions on the cascade chordlines are unsteady they must give rise to distributions of free vortices in the wake of each airfoil of the cascade. In other words vortex wakes emanate from the trailing edge of each airfoil and are convected downstream: at a point with fixed coordinates in the wake, the strength of the vortex element instantaneously occupying that point will vary with time. Hence, the integral equation will in general contain a term that is an integral over the wake ($c < \xi < \infty$) to account for the additional induced velocities from the infinite number of semi-infinite vortex wakes. The kernel $\frac{1}{2}\pi K(\xi - x)$ accounts in every case for the velocity induced at $(x, 0)$ by a vortex element at the point $(\pi, 0)$ on the chord or wake of the reference, or zeroth, airfoil plus an element of equal strength located at the congruent point $(\pi + ns\sin\beta, ns\cos\beta)$ of every other profile of the cascade or its wake. The form of K may in fact be derived by returning to the previous derivation for $\tilde{v}$ in (4.9) and (4.15b) and extracting the terms

$$\overbrace{\frac{1}{\xi - x}}^{\text{isolated airfoil}} + \overbrace{\sum_{n=-\infty}^{\infty} \frac{1}{\xi - x + jns\,e^{-j\beta}}}^{\text{cascade effect}} \tag{4.17}$$

In this expression the signs have been changed to imply calculations of positive v (rather than $-jv$) and with each term it is now necessary to associate a strength

$\gamma_r(\xi)\exp(in\omega r)$ ($r = 1, 2$ or 3) since the inducing vortexes now pulsate rather than being steady in time. The kernel now appears as

$$\frac{1}{2\pi}K(\xi - x) = \frac{1}{2\pi}\sum_{n=-\infty}^{\infty}\frac{e^{in\omega\tau}}{\xi - x + jns\exp(-j\beta)} \tag{4.18}$$

which may be summed in closed form to yield

$$\frac{1}{2\pi}K(\xi - x) = \frac{e^{j\beta}}{2s} \cdot \frac{\cosh[(1-\sigma/\pi)\pi\exp(j\beta)(\xi - x)/s] + ij\ \sinh[(1-\sigma/\pi)\pi\ \exp(j\beta)(\xi - x)/s]}{\sinh[\pi\exp(j\beta)(\xi - x)/s]} \tag{4.19}$$

where $\sigma = \omega\tau$ is known as the interblade phase angle, an assumed constant.

The term for $n = 0$ in the summation (4.18) is

$$\frac{1}{2\pi}K_0(\xi - x) = \frac{1}{2\pi}\frac{1}{\xi - x} \tag{4.20}$$

which is the kernel for the isolated airfoil. Hence, the added complexity of solving the cascaded airfoil problem is attributed to the additional terms giving the more complicated kernel displayed in (4.19).

In contradistinction to the isolated airfoil case, solutions of the unsteady aerodynamics integral equation cannot be solved in closed form, or in terms of tabulated functions, for arbitrary geometry (β and s/c) and arbitrary interblade phase angle, σ. In fact, as noted previously, the thickness distribution of the profiles and the steady lift distribution become important when cascades of small space/chord ratio are considered to vibrate with nonzero interblade phasing. Consequently, solutions to the equation are always obtained numerically. It is found that the new parameters β, s/c and σ are strong determinants of the unsteady aerodynamic reactions. A tabular comparison of the effect of these variables on the lift due to bending taken from the data in [3] appears below. In this chart, the central stencil gives the *lift coefficient* for the reference values of $s/c = 1.0$, $\beta = 45°$, $\sigma = 0.4pi$. Other values in the matrix give the coefficient resulting from changing one and only one of the governing parameters.

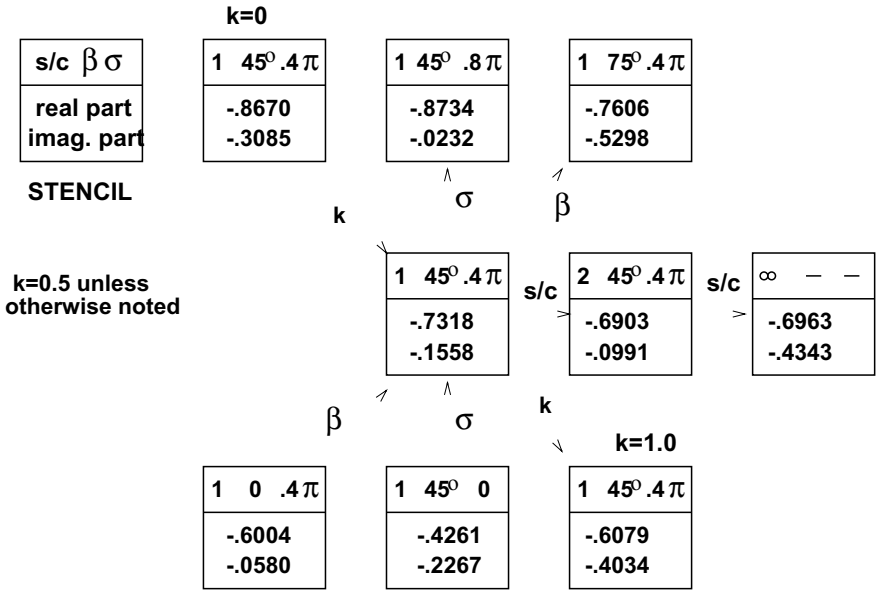

The effects of thickness and steady lift cannot be easily displayed, and are conventionally determined numerically for each application. See Chap. III in [1].

5 Compressible Flow

The linearized problem of unsteady cascade flow in a compressible fluid may be conveniently formulated in terms of the acceleration potential, $-p/\rho$, where p is the perturbation pressure, i.e., the small unsteady component of fluid pressure. Using the acceleration potential as the primary dependent variable, a number of compact solutions have been obtained for the flat plate cascade at zero incidence. The most reliable in subsonic flow is that due to Smith [4], and in supersonic flow the solutions of Verdon [5] and Adamczyk [6] are representative.

Supersonic flow relative to the blades of a turbomachine is of practical importance in steam turbines and near the tips of transonic compressor blades. In these cases the axial component of the velocity remains subsonic; hence analytic solutions in this flow regime (the so-called subsonic leading edge locus) are of the most interest. It may be that in future applications the axial component will be supersonic. In this event the theory actually becomes simper so that the present concentration on subsonic values of M_{axial} represents the most difficult problem. Currently efforts are underway to account for such complicating effects as changing back-pressure on the stage, flow turning, shock waves, etc.

To illustrate the effect of varying the Mach number from incompressible on up to supersonic, a particular unsteady aerodynamic coefficient has been graphed in Fig. 7 as a function of the relative Mach number. It is seen that the variation of the coefficient

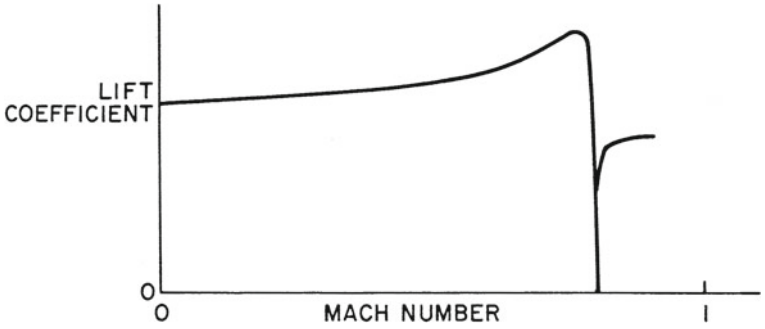

Fig. 7 The aerodynamic resonance phenomenon

in the subsonic regime is not great except in the immediate neighborhood of the so-called 'resonant' Mach number, or the Mach number at which 'aerodynamic resonance' occurs.

It is possible to generalize the situation with respect to compressibility by indicating that the small disturbance approximations are retained, but the velocities, velocity potential, acceleration potential, or pressure (in every case the disturbance component of these quantities) no longer satisfy the Laplace equation, but rather an equation of the following type.

$$(1 - M^2)\phi_{xx} + \phi_{yy} = \frac{1}{a^2}\phi_{tt} - 2\frac{M}{a}\phi_{xt} = 0 \tag{5.1}$$

Here M is the relative Mach number and a is the sound speed. Note that the presence of time derivatives make this partial differential equation hyperbolic whatever the magnitude of M, a situation quite different from the steady flow equation.

Although the above equation is appropriate to either subsonic or supersonic flow, the resonance phenomenon occurs in the regime of subsonic axial component of the relative velocity when geometric and flow conditions satisfy a certain relationship.

Equating the time of propagation of a disturbance along the cascade to the time for an integral number of oscillations to take place plus the time lag associated with the interblade phase angle, σ, yields

$$\frac{s}{V_p^+} = \frac{2\pi v}{\omega} - \frac{\sigma}{\omega} \tag{5.2a}$$

$$\frac{s}{V_p^-} = \frac{2\pi v}{\omega} + \frac{\sigma}{\omega} \tag{5.2b}$$

where $V_p^{\pm}$, the velocity of propagation, has two distinct values associated with the two directions along the cascade, see Fig. 8.

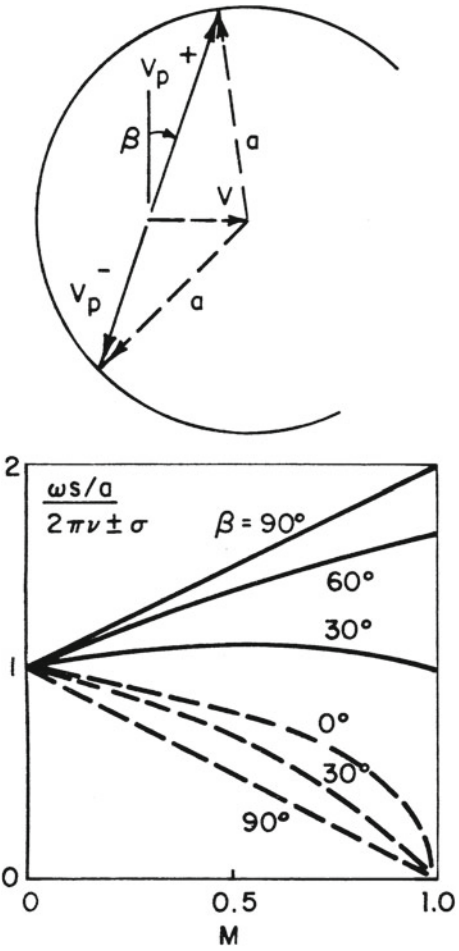

Fig. 8 Resonant values of governing parameters

$$V_p^{\pm} = a[\sqrt{1 - M^2 \cos^2 \beta} \pm M \sin \beta] \tag{5.3}$$

These expressions can be reduced to the equation

$$\frac{\omega s}{a} = (2\upsilon\pi \pm \sigma)(\sqrt{1 - M^2 \cos^2 \beta} \mp M \sin \beta) \tag{5.4}$$

where υ may be any positive integer, and with the upper set of signs may also be zero.

Equation (5.4) may be graphed and potential acoustic resonances discerned by plotting the characteristics of a given stage on the same sheet for possible coincidence. (It is convenient to take β as the parameter with axes $\omega s/a$ and M.) Acoustic resonances of the variety described above may be dangerous because they account for

the vanishing, or near vanishing, of all nonsteady aerodynamic reactions including therefore the important aerodynamic damping. Although it is difficult to establish with certainty, several cases of large vibratory stresses have been correlated with the onset of acoustic resonance. It should be recognized that the effects of blade thickness and nonconstant Mach number throughout the field are such as to render the foregoing formulation somewhat approximate.

The foregoing development may also be based more rigorously on the theoretically derived integral equation relating the harmonically varying downwash on the blade to the resulting harmonically varying pressure difference across the blade's thickness. Symbolically

$$\bar{v}_a(x) = \int_0^c K(\xi - x)\Delta\bar{p}_a(\xi)d\xi \tag{5.5}$$

and the acoustic resonance manifests itself by a singularity appearing in the kernel K for special values of k, s, c, τ and β of which K is a function. Under this circumstance the downwash υ_a can only remain finite, as it must physically, by a vanishing of Δp_a as noted above. The previous development shows why the compressible flow solutions have received such an impetus from, and are so closely related to, the acoustic properties of compressor and fan cascades.

Thus the field of aeroacoustics, as exemplified in the text of Goldstein [7], and the field of turbomachine aeroelasticity are in a synergistic relationship. This is discussed more fully in [1].

The acoustic resonance phenomenon, as just described results from standing waves in blade-fixed coordinates, albeit with impressed throughflow velocity, of the fluid occupying the interblade passages.

6 Periodically Stalled Flow in Turbomachines

Rotating, or propagating, stall are terms which describe a phenomenon of circumferentially asymmetric flow in axial compressors. Such a flow usually appears at rotationally part-speed conditions and manifests itself as one or more regions of reduced (or even reversed) throughflow which rotate about the compressor axis at a speed somewhat less than rotor speed, albeit in the same direction.

A major distinction between propagating stall and surge is that in the former case the integrated massflow over the entire annulus remains steady with time whereas in the latter case this is not true. The absolute propagation rate can be brought to zero or even made slightly negative by choosing pathological compressor design parameters.

If the instigation of this phenomenon can be attributed to a single blade row (as it obviously must in a single-stage compressor) then insofar as this blade row is concerned, it represents a periodic stall ing and unstall ing of each blade in the row. Later or preceding blade rows (i.e., half-stage) may or may not experience individual

blade stall periodically, depending on the magnitude of the flow fluctuation at that stage, as well as the cascade stall limits in that stage.

The regions of stall ed flow may extend across the flow annulus (full span) or may be confined either to the root or tip regions of the blades (partial-span stall) The number of such regions which may exist in the annulus at any one time varies from perhaps 1 to 10 with greater numbers possible in special types of apparatus.

The periodic loading and unloading of the blades may prove to be extremely harmful if a resonant condition of vibration obtains. Unfortunately the frequency of excitation cannot be accurately predicted at the present time so that avoidance of resonance is extremely difficult.

The results of various theories concerning propagating stall are all moderately successful in predicting the propagational speed. However the number of stall patches which occur (i.e., the circumferential wavelength of the disturbance) seems to be analytically unpredictable so that the frequency of excitation remains uncertain. Furthermore, the identification of the particular stage which is controlling the propagating stall , in the sense noted above, is often uncertain or impossible.

This situation with regard to propagating stall has recently been impacted by a CFD approach using the vortex method of description. In chapter "Stall Flutter" the vortex method was applied to the analysis of stall flutter. The earlier application, however, was to propagating (or rotating) stall, i.e. for the flow instability which can occur with completely rigid blades. The vortex method has been intensively developed for propagating stall prediction and results [9] indicate that success in the long sought objective of wavelength prediction is at hand. Improvements that are required for more useful results are in the boundary layer subroutine executed at each time step for each blade) and in the enlargement of computing capacity to handle the number of blades in realistic annular cascades. A further improvement that is desirable is in the vortex merging algorithm. The vortex method is a time-marching CFD routine in which the location of a large number of individual vortices are tracked on the computational domain. New vortices are created at each time step to satisfy the boundary conditions and separation criteria. Hence, to limit the total number of vortices in the field after many time steps, it is necessary to merge individual vortices, preferably downstream of the cascade. Many merging criteria may be considered, related to the strength and position of the candidate vortices.

Although the precise classification of vibratory phenomena of an aeromechanical nature is often somewhat difficult in turbomachines because of the complication due to cascading and multistaging, it is nevertheless necessary to make such distinctions as are implied by an attempt at classification. The manifestation of stall flutter in turbomachines is a good example of what is meant. When a given blade row, or cascade, approaches the install ing incidence in some sense (i.e., stall ing defined by rapid increase of relative total pressure loss, or defined by rapid increase in deviation angle, or defined by the appearance of flow separation from the suction surface of the blades, etc.) it is found experimentally that a variety of phenomena may exist. Thus the region of reduced throughflow may partially coalesce into discrete patches which propagate relative to the cascade giving rise to the type of flow instability previously discussed under rotating stall. There is no dependence on blade flexibility.

Under certain other overall operating conditions it is found that in the absence of, or even coexistent with, the previous manifestation, the blades vibrate somewhat sporadically at or near their individual natural frequencies. There is no immediately obvious correlation between the motions of adjacent blades, and the amplitudes of vibrations change with time in an apparently random manner. (We exclude here all vibration attributable to resonance with the propagating stall frequency, should the propagation phenomenon also be present.) This behavior is termed stall flutter or stall ing flutter and the motion is often in the fundamental bending mode. Another term is random vibration. Since the phenomenon may be explained on the basis of nonlinear mechanics, (see the chapter on Stall Flutter) the sporadicity of the vibration can be attributed provisionally to the fact that the excitation has not been strong enough to cause 'entrainment of frequency', a characteristic of many nonlinear systems. Hence, each blade vibrates, *on the average*, as if the adjacent blades were not also vibrating. However, a careful analysis demonstrates that the instantaneous amplitude of a particular blade is effected somewhat by the 'instantaneous phase difference' between its motion and the motion of the adjacent blade(s). One must also speak of 'instantaneous' frequency since a frequency modulation is also apparent. As a general statement it must be said that the frequency, amplitude and phase of adjacent blades are functionally linked in some complicated aeromechanical manner which results in modulations of all three qualities as functions of time. While the frequency modulation will normally be small (perhaps less than 1 or 2%) the amplitude and the phase modulations can be quite large. Here the term phase difference has been used rather loosely to describe the relationship between two motions of slightly different frequency. Since this aerodynamic coupling would also depend on the instantaneous amplitude of the adjacent blade(s), it is not surprising that the vibration gives a certain appearance of randomness. On the linear theory for identically tuned blades one would not expect to find sporadic behavior as described above. However, it is just precisely the failure to satisfy these two conditions that accounts for the observed motion; the average blade system consists of an assembly of slightly detuned blades (nonidentical frequencies) and furthermore the oscillation mechanism is nonlinear.

Application of vortex method aerodynamics to a cascade of elastically supported blades recently has demonstrated [12], in a computational sense, the features of randomness and sporadicity as described above.

When the relative magnitudes of the nonsteady aerodynamic forces increase it may be expected that entrainment of frequency will occur. In certain nonlinear systems it can be shown that the 'normalized' frequency interval $(\omega - \omega_0)/\omega$ (where ω is the impressed frequency and ω_0 is the frequency of self-excitation) within which one observes entrainment, is proportional to h/h_0, where h is the amplitude of the impressed motion and h_0 is the amplitude of the self-excited oscillation. In case of entrainment one would expect to find a common phase difference between the motion of adjacent blades which implies also motion with a common flutter frequency. This latter phenomenon is also termed stalling flutter, although the term limit-cycle vibration is sometimes used to emphasize the constant-amplitude nature of the motion, which is often in the fundamental torsional mode.

Finally it should be noted that the distinction between blade instability (flutter) and flow instability (rotating stall) is not always perfectly distinct. When the sporadic stall flutter occurs it is clear that there is no steady tangentially propagating feature of the instability. Similarly, when propagating stall occurs with little or no vibration (stiff blades away from resonance) it is apparent that the instability is not associated with vibratory motion of the blade. However, the limit cycle type of behavior can be looked upon (due to the simultaneously observed constant interblade phase relationship) as the propagation of a disturbance along the cascade. Furthermore, the vorticity shed downstream of the blade row would have every aspect of a propagation stall region. For instance if the interblade phasing was 180 degrees the apparent stall region would be on one blade pitch in tangential extent and each would be separated by one blade pitch of unstall ed throughflow. The tangential wavelength is two blade pitches. Because of the large number of such regions, and the small tangential extent of each, this situation is still properly termed stall flutter since the blades are controlling and the blade amplitudes are constant. At the other extreme when one or two stall patches appear in the annulus it is obvious that the flow instability is controlling and then the phase relationships between adjacent blade's motions may appear to be rather sporadic. At any rate, in the middle ground between these extremes it is probable that a strong interaction between flow stability and blade stability exists and the two phenomena cannot be easily separated.

Another distinction may be attempted to assist in understanding the operative phenomena. When a *single airfoil* is subjected to an increasing angle of attack an instability of the fluid may arise, related to the Karman vortex frequency or the extension of this concept to a distributed frequency spectrum. If the frequency of this fluid instability coincides with the natural frequency of the blade in any mode the phenomenon is termed buffeting. If the dynamic moment coefficient (or force coefficient) attains a negative slope a self-excited vibration known as stall flutter occurs. The two phenomena may merge when airfoil vibration exerts some influence on the vortex shedding frequency. Stall -flutter is usually observed in the torsional mode and buffeting in the bending mode, but this distinction is not always possible. These concepts cannot be carried over directly to the cascade where steady bending amplitudes of the limit cycle variety have been observed. The explanation rests on the additional degrees of freedom present in the cascaded configuration.

7 Stall Flutter in Turbomachines

On account of the foregoing complications and the very recent emergence of quantitative CFD-based theories noted in chapter "Stall Flutter" it is not surprising that past prediction for turbomachines has rested almost entirely on correlation of experimental data. The single most important parameter governing stall ing is the incidence, and the reduced frequency has been seen in all aeroelastic formulations to exert a profound influence. Hence it is not surprising that these variables have been used to correlate the data.

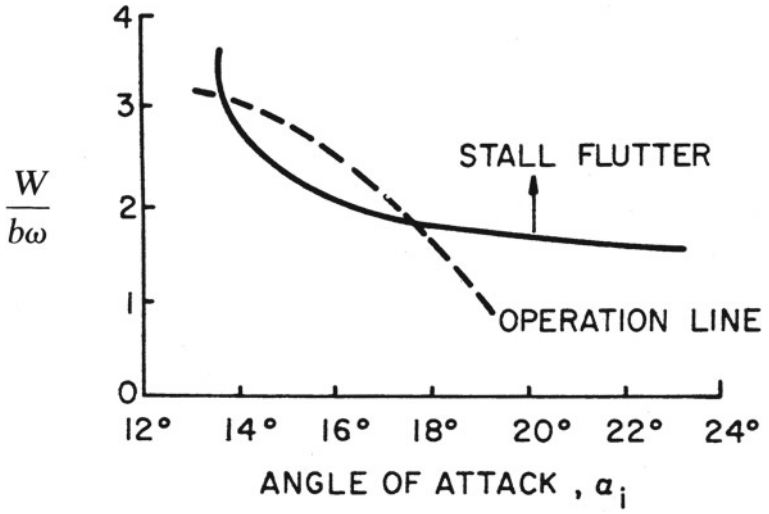

Fig. 9 Experimental stall flutter correlation

Typically stall flutter will occur at part-speed operation and will be confined to those rotor stages operating at higher than average incidence. With luck the region of flutter will be above the operating line on a compressor map and extend up to the surge line. Under less fortunate circumstances the operating line will penetrate the flutter region. The flutter boundary will have the appearance shown on Fig. 9. Contours of constant flutter (or limit cycle oscillation) stress (or tip amplitude) will run more or less parallel to, and within, the boundary. Traditional parameters for this typical experimental correlation are reduced velocity, $W/b\omega$, (the inverse of reduced frequency) and incidence, at some characteristic radius such as 75% or 80% of the blade span for a cantilever blade. The curve is typical of data obtained in turbomachines or cascades; essentially a new correlation is required for each major change of any aerodynamic variable (Mach number, stagger, blade contour, etc.). The structural mode shape will usually be first torsion. The single contour shown in the previous figure is for that level of cyclic stress (or strain) in the blade material that is arbitrarily taken to represent some distinct and repeatable measurement attributable to the flutter vibration and discernible above the 'noise' in the strain measuring system. A typical number might be a stress of 10,000 kPa used to define the flutter boundary. However, small changes in relative airspeed, W, may increase the flutter stress substantially, or, in the case of 'hard' flutter, a small increase in incidence might have a similar effect. Hence, in keeping with the nonlinear behavior described in chapter "Stall Flutter", the contours of constant flutter stress may be quite closely spaced in some regions of the correlation diagram.

Naturally, when considering three-dimensional effects it is the net energy passing from airstream to airfoil that determines whether flutter will occur, or not. The stall ed tip of a rotor blade, for example, must extract more energy from the airstream than

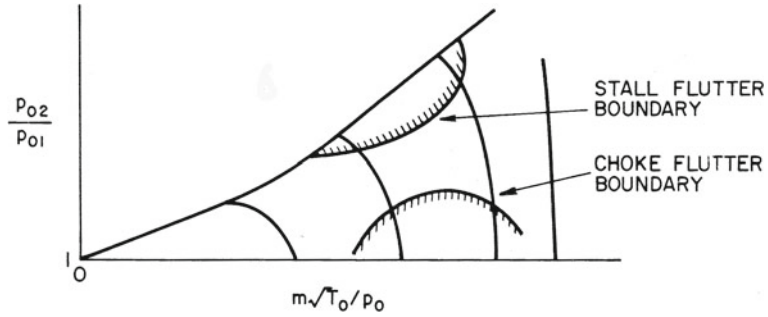

Fig. 10 Stall flutter boundary

is put back into the airstream by airfoil sections at smaller radii and that is dissipated from the system by damping.

This total description of stall flutter in turbomachine rotor blades is consistent with the appearance of the stall flutter boundary as it appears on the following typical compressor performance map (Fig. 10), the vibrations are usually confined to the first two or three stages. This figure may be viewed in conjunction with the performance map on Fig. 4 which shows typical angles of attack for a rotor blade tip in the first stage of a compressor. Keeping in mind that the mass flow parameter $\dot{m}\sqrt{T_0/p_0}$ is virtually proportional to the throughflow velocity in the first few stages of a compressor, it is clear that any typical operating line as shown on the compressor map will traverse the flutter boundary somewhat as the dotted line on Fig. 9.

This explains the general shape and location of the region of occurrence of stall flutter. Experimental determinations confirm increasing stresses as the region is penetrated from below and the specific behavior is a function of the aeroelastic properties of the individual machine, consistent with the broad principles enunciated here.

8 Choking Flutter

In the middle stages of a multistage compressor it may be possible to discern another region on the compressor map wherein so-called choking flutter will appear. This will normally occur at part-speed operation and will be confined to those rotor stages operating at lower than average incidence (probably negative values are encountered). The region of flutter will normally lie below the usual operating line on a compressor map, but individual stages may encounter this type of instability without greatly affecting operating line; this is particularly true when the design setting angle of a particular row of rotor blades has been arbitrarily changed from the average of adjacent stages through inadvertence or by a sequence of aerodynamic redesigns.

The physical manifestation of choking flutter is usually discriminated by a plot of a stage's operating line on coordinates of relative Mach number vs. incidence, as

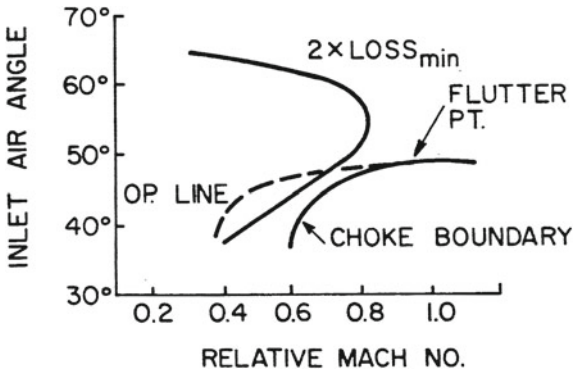

Fig. 11 Choking flutter correlation

in Fig. 11. On these same coordinates the choke boundaries are shown; a coincidence or intersection of these graphs indicate the possible presence of choking flutter and is usually confined to a very small range of incidence values. The mechanism of choking flutter is not fully understood. It is related to compressibility phenomena in the fluid and separation of the flow is probably also involved. The graph labelled '$2 \times Loss'_{min}$ is a locus of constant aerothermodynamic loss coefficient (closely related to the drag coefficient of an airfoil); the interior of the nose-shaped region representing low values of loss, or efficient operation of the compressor stage. The curve labelled 'choke boundary' represents the combination of relative Mach number and flow angle at which the minimum flow area between adjacent blades (the throat) is passing the flow with the local sonic velocity. Presumably separation of the flow at the nose of each airfoil on the pressure surface, and the *relative* motion between adjacent blades as they vibrate, conspire to change the effective throat location in a time dependent manner. These oscillatory changes effect the pressure distribution on each blade in such a fashion (including a phase angle) as to pump energy from the airstream into the vibration and thus sustain the presumed motion.

Experimental results [13, 14] bear out the general description of choking flutter described above. The analytically-based predictions [15, 16] lend further credence to the mechanism, although the aerodynamic formulation is confined to quasisteady time dependence. Ultimately a satisfactory explanation and prediction technique will be likely attained with a time marching computational capability using the compressible Navier-Stokes equations.

Choking flutter occurs in practice with sufficient frequency and destructive potential as to be an important area for current research efforts as noted above.

9 Aeroelastic Eigenvalues

Traditionally the analytical prediction of flutter has been conducted by computation of the aeroelastic eigenvalues for the particular system under investigation. In turbomachines the eigenvalue determinations have been conducted in the frequency

domain, and the unsteady aerodynamics, excluding separated or choked flow, have been based on the solutions of the small disturbance equations as described in [3–6] and elsewhere, and as reviewed effectively in the AGARD Manual [1]. A representative sample analysis for the steady loading effect in an infinite cascade was introduced in Sect. 4. In the literature a large number of additional effects are treated, including compressibility, finite flow deflection, three-dimensionality, finite shock strength and shock movement, section thickness and turbine-type geometry.

In every case, however, the initial formulation of the eigenvalue problem for an N-bladed annular cascade results in a system of mN equations, where m is the number of degrees of freedom (or else structural modes) assigned to each blade. Since the disc on which the turbomachine blades are attached will not be completely rigid, these modeshapes will be 'system' modes in which nodal circles and diameters may be discerned on the disc proper (and its extension into the flow annulus).

$$-\omega^2[M_n]\{q_n\} + [M_n\omega_n^2(1 + ig_n)]\{q_n\} = \pi b^3\omega^2[F]\{q_n\} \tag{9.1}$$

In (9.1) the aeroelastic equation has been specialized for one degree of freedom per blade ($m = 1$); hence n ranges from 0 to N-1. This equation, adapted from Crawley's Chap. 19 in [2], assumes harmonic time dependence at frequency ω and the nth blade has its individual mass, M_n, natural frequency, ω_n, and the structural damping coefficient, g_n. The development leading to (9.1) parallels that for (3.7.32) for a single foil. (The principal result of considering $m > 1$ is to replace each matrix element by a submatrix and enlarge the displacement vector, $\{q_n\}$).

When the blades on the disc are structurally uncoupled (rigid disc and no interconnecting shrouds or lacing wires) the square matrices on the LHS are diagonal and the equations are coupled only through the aerodynamic force matrix

$$[F] = \begin{bmatrix} F_0 & F_{N-1} & F_{N-2} & \dots & F_1 \\ F_1 & F_0 & F_{N-1} & \dots & F_2 \\ \cdot & \cdot & \cdot & & \cdot \\ \cdot & \cdot & \cdot & & \cdot \\ F_{N-1} & F_{N-2} & F_{N-3} & \dots & F_0 \end{bmatrix} \tag{9.2}$$

The matrix is completely populated and each element is an aerodynamic influencecoefficient: the force effect on the row-identified blade due to the motion of the column-identified blade. These are the terms derivable from the previously described analytical theories under the assumption of constant interblade phase angle, σ, and harmonic displacement given by

$$q_n = Re[\bar{q}_n \exp(i\omega t)] \tag{9.3}$$

although Fourier decomposition of the aerodynamic force is necessary to obtain the form implied by (9.1) and (9.2).

For a 'tuned' stage the mass, natural frequency and damping coefficient for every blade are the same so that the N equations are identical ($[F]$ is circulant) and the

complex eigenvalues

$$\omega = \omega_R + i\omega_I \tag{9.4}$$

may be obtained from any one of the individual blade equations. Since there are N possible tuned values of σ, there are N possible $[F]$ matrices and N corresponding eigenvalues. The particular eigenvalue that obtains in practice will be for those values of airspeed W (embedded in F) and g_n that just produce $\omega_I = 0$. That is, the typical V, g plot is replaced by a family of contours with σ as the parameter. The critical flutter speed is then obtained by minimizing W with respect to σ, see [10]. In this sense the aeroelastic behavior of tuned cascades is a straightforward extension of the single airfoil procedure, to include an additional parameter, the interblade phase angle.

One of the most intensive recent efforts in turbomachine aeroelastic studies has been in the area of 'mistuned' blade rows. When the mass and/or stiffness of all airfoils are not identical, or the coupling through the discs or shrouds is not uniform, then structural mistuning is present. Analogous aerodynamic mistuning results from nonuniform blade spacing, setting angle of section profile. Such mistuned stages are inevitably manufactured, subject in degree to inspection and tolerance acceptance procedures at assembly. The general effect of mistuning is to reduce the symmetry and cyclical nature of the matrices in the flutter equation, (8.9.1). The character of the eigenvalue plots and the eigenfunctions become more varied. Thus, at flutter, all blades are found to vibrate with the same frequency; the relative blade amplitudes and phase angles are constant with respect to time, but not with respect to location in the blade row. For each of the eigensolutions, however, there may be associated a 'tuned' interblade phase angle [2]. The most significant effect of mistuning is to change the value of ω_I. If the shift of the least stable eigenvalue is in the direction of increased stability, the proclivity to flutter is reduced and it is for this reason that mistuning is considered to be a powerful design tool for improving aeroelastic stability in cascaded airfoils. Figures 12a and 12b adapted from [11] show the effect of mistuning on the position of the eigenvalues (actually $i\omega$ rather than ω) for a 14-blade cascade.

It is demonstrated that a necessary but not sufficient condition for aeroelastic stability is that the blades be self-damped; the effect of a blade's motion upon itself must be to contribute positive aerodynamic damping. The unsteady interactions amongst or between blades in the cascade are destabilizing for at least one possible σ. This blade-to-blade destabilizing interference is reduced by mistuning and is hence desirable. Mistuning, however, can never produce stability when self-damping is negative. With nonzero structural damping, blades of larger (blade to air) mass ratio are relatively more stable.

The effect of kinematic coupling (e.g. the presence of some bending displacements in a predominantly torsional mode) may be quite important in determining stability whereas dynamic coupling (e.g. through the aerodynamic reactions) is usually not strong enough to be of significance. The effect of mean loading is speculated as being a possible source of flutter near stall, and stability trends with reduced velocity are

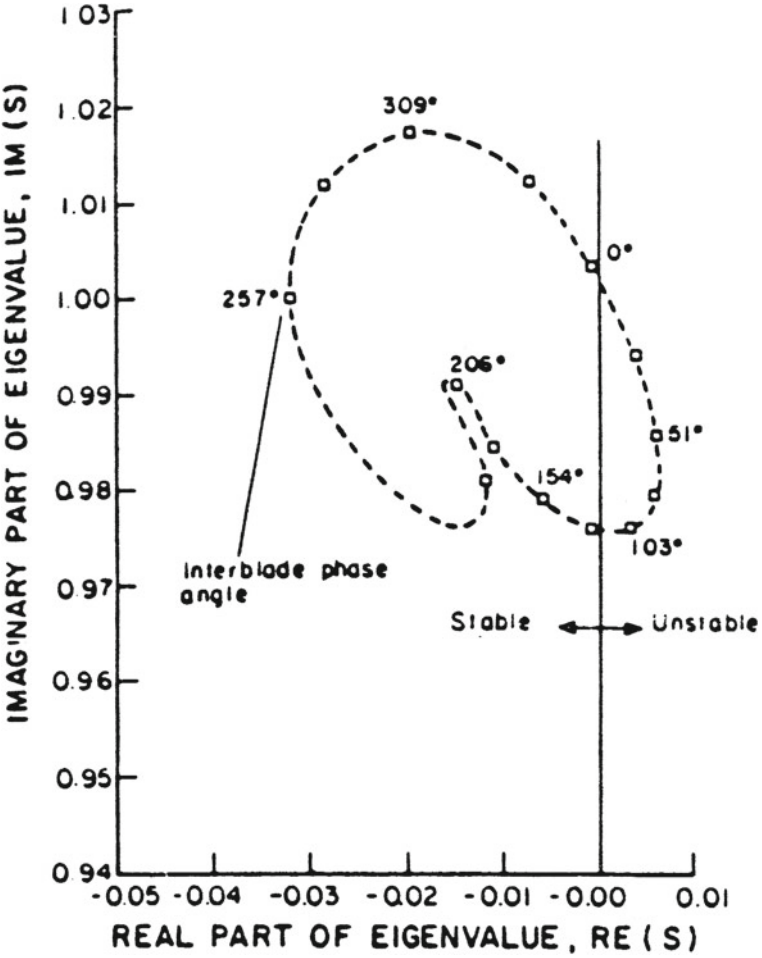

Fig. 12 **a** Aeroelastic eigenvalues of a 14-bladed tuned rotor. **b** Eigenvalues of the same rotor with 'optimal' mistuning

discussed qualitatively in [2], noting both structural and aerodynamic implications of the reduced frequency parameter.

Optimal mistuning as an intentional manufacturing procedure at assembly is an important concept, although it must be tempered with the knowledge that, under forced aerodynamic resonance, so-called 'rogue' blades may be identified which will vibrate at dangerously high amplitude. More research on mistuning may be expected to yield increasingly practical results for the turbomachine aeroelastician to apply beneficially, see [17–19].

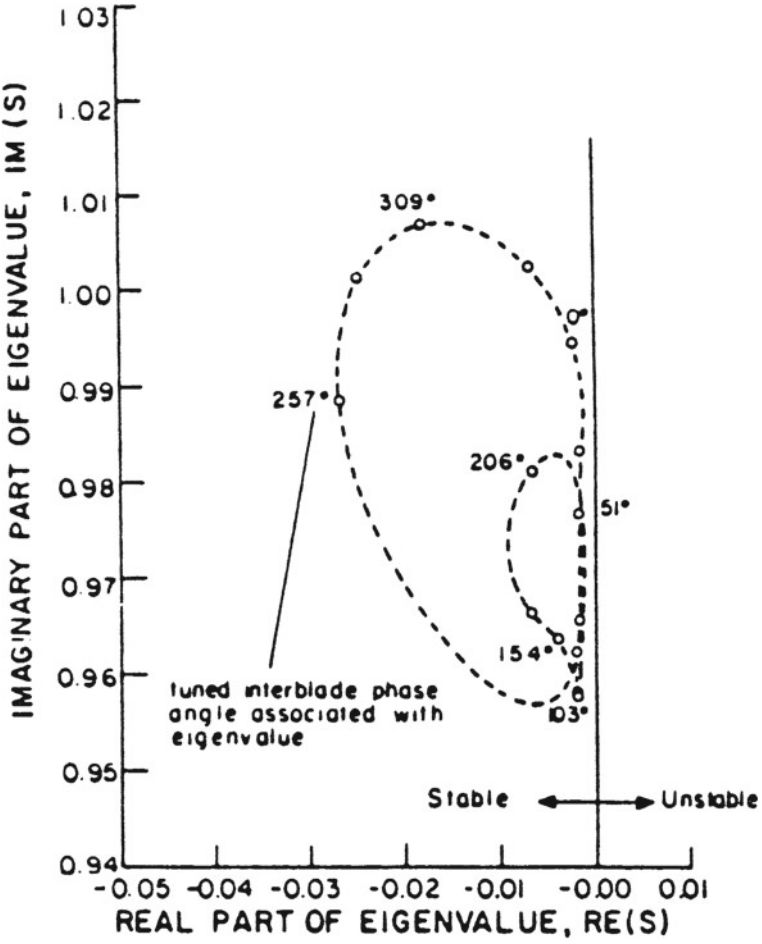

Fig. 12 (continued)

10 Recent Trends

A number of supersonic flutter regimes have been encountered in practice, see Regions III, IV and V in Fig. 13. Only Region III flutter, in either pitching or plunging, will usually be encountered along a normal operating line, and then only at corrected overspeed conditions. Supersonic aerodynamic theories have been developed to explain and confirm Region III flutter. Low incidence formulations were reported by a number of investigators, with greatest interest being attached to the onset flows having a subsonic axial component. The survey papers by Platzer [21–24] give an excellent summary of the early aerodynamics literature and experience

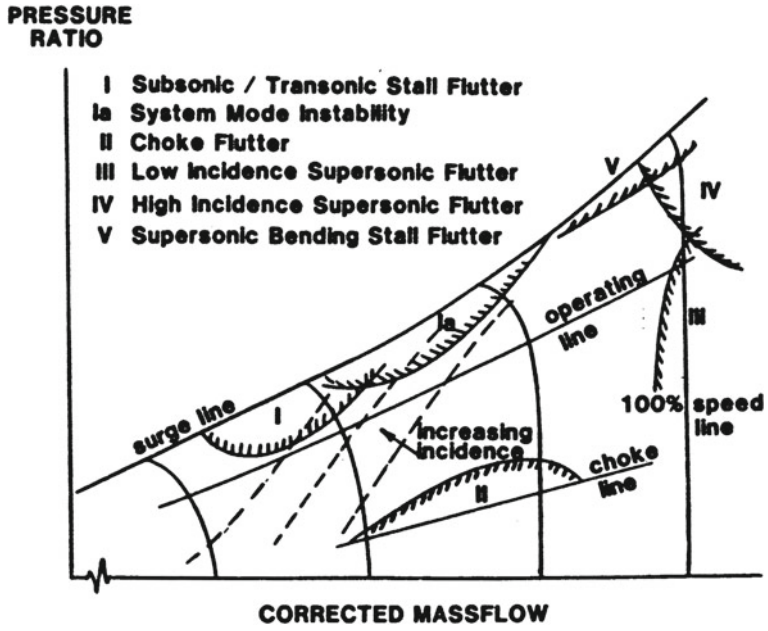

Fig. 13 Axil compressor or fan characteristic map showing principle types of flutter and region of occurrence

up to 1982 including summaries of relevant papers by authors in the former Soviet Union.

Regions IV and V in Fig. 13 are at higher compressor pressure ratio, above the normal equilibrium operating line, and, in Region V, may involve stall ing at supersonic blade relative Mach number. Unsteady aerodynamic analyses appropriate to this regime have been presented [25, 26]. For the first time account was taken of the effect of shock waves which may appear when the surface Mach number exceeds unity. Flutter observed in these regions have been mostly flexural, although not exclusively. In Region V stall ing of the flow has been implicated since the region is in the neighborhood of the surge or stall limit line. Hence Region V is provisionally termed 'supersonic bending stall flutter' and it is assumed that there is a detached bow shock at each blade passage entrance; i.e., the passage is unstarted. By contrast, the flutter mechanism in Region IV is thought to involve an in-passage shock wave whose oscillatory movement is essential for the instability mechanism.

A counterclockwise continuation around Fig. 13 returns one to Region I, divided earlier in Fig. 10 and which, it now appears, should be divided into more than one subregion. The so-called system mode instability seems to be associated with the upper end of this region, and although the blade loading is high, flutter may not involve flow separation as an essential part of the mechanism. Instead it has been hypothesized [27] that even with a subsonic onset flow the surface Mach number can exceed unity locally and oscillating shocks may help explain the appearance

of negative aerodynamic damping. It seems that these instability mechanisms (separation, oscillating shocks) may both appear in this general region of the fan or compressor map, although not both at the same time in a particular machine. Thus the non-aerodynamic factors, which are not revealed by the map parameters and are discussed in Sect. 1, may determine which, if any, of these flutter types will manifest itself in any particular instance. The clarification of this matter is still required so that Region I is now provisionally labelled Subsonic/Transonic Stall Flutter and System Mode Instability. Region II, discussed in Sect. 8 and of relatively lesser importance, is associated with choking of the passage and is labelled Choke Flutter. As such the role of oscillatory shock waves is again indicated to be important. Hence for relatively low negative incidence and high enough subsonic relative Mach numbers, appropriate to a middle stage of a multistage compressor, the mechanism of choke flutter has many similarities to the transonic stall flutter of Region I. In addition, some authors [28] add a second sub-region at a larger negative incidence and lower relative Mach number, and term it negative incidence stall flutter. The choke flutter mechanism is still controversial; it may involve the type of machine (fan, compressor or turbine), type of stage (front, middle, or rear) and structural details (shrouded vs unshrouded, disc vs drum, etc.).

Three-dimensional unsteady cascade flow was first formulated in the 1970s [29, 30]. In order to apply two-dimensional theory to the aeroelastic problems of real blade systems one must either use a representative section analysis or else apply the strip hypothesis; i.e., the aerodynamics at one radius is uncoupled from the aerodynamics at any other radius. In particular, it is known that at 'aerodynamic resonance' the strip theory breaks down and the acoustic modes are strongly coupled radially.

Along with aerodynamic advances the structural description of the blade d-disc assembly [31, 32], has received a great impetus, and the importance of forward and backward travelling waves has been firmly established. Within a particular number of nodal diameters, coupling between modes has been shown to be significant [33] and the role of the 'twin modes' (i.e. $\sin n\phi$ and $\cos n\phi$) in determining propagation has been clarified. Ford and Foord [34] have used the twin mode concept in both analysis and flutter measurement. Furthermore, the number of nodal diameters affects the fundamental natural frequencies slightly so that they cluster together. Coupling of modes with closely spaced frequencies by aerodynamic means therefore becomes appreciable and the resulting flutter mode may contain significant content from two or three modes with consecutive numbers of diametral nodes.

A great concentration of studies recently has been in the area of Computational Fluid Dynamics (CFD) coupled with a Finite Element Method (FEM) description of the blade and disk structure. Typically these sets of governing equations are solved interactively in a time marching fashion to yield the developing flutter amplitudes. Stability limits are not determined directly per se. For nonlinear systems the limit cycle amplitudes are predicted while for linear systems the temporal growth of amplitude identifies those values of the operating variables that lie within the instability boundary.

Usually in these models only spanwise displacements in plunging, pitching and surging are allowed, leading to beam -type finite elements for representing a tapered,

twisted blade of variable cross-section [35, 36]. Consequently, when plate- or shell-type elements are necessitated by airfoil thicknesses on the order of 4 or 5%, the chordwise deformations cannot be neglected and full three-dimensional FEM packages must be utilized. Essentially the camber schedule of the blade profiles change with time in these cases.

The FEM-based structural analysis is also essential for static aeroelastic studies in the nascent field of compliant blade performance modification. The compliance of the blade in an annular cascade represents a *passive* means of controlling the aerothermodynamic performance of the turbomachine by aeroelastic tailoring. This topic comes under the overarching subject of aeroservoelasticity, the application of automatic control theory to fundamental aeroelastic problems. In the blading of turbomachinery the enhanced compliance, and its chordwise distribution, are introduced intentionally by design. The resulting configuration must be checked for freedom from dynamic aeroelastic instability, or flutter, over the entire operating range of the compressor map such as that appearing in Fig. 4. It may be remarked that the concept of performance "map" will have to be extended to include the parametric ependence of performance on a representative value of a new dimensionless quantity: the ratio of the dynamic pressure of the fluid to the Young's modulus of the structure. In effect the augmentation of compliance introduces variable geometry into the turbomachine blading.

The small compliance, or conversely great rigidity, of conventional blades is responsible for only slight amounts of untwist and uncambering. In the design and development of traditional turbomachines these effects, in turn, have been reflected in very slight corrections to the aerothermodynamic performance as compared to assuming complete rigidity of the airfoils. This situation will be changed with the application of static aeroservoelasticity to the design of turbomachines with compliant blades.

Applications of unsteady Navier-Stokes codes to cascaded airfoils appear in references [37][38] and [39]. These early studies using Navier-Stokes solvers for unsteady flows with moving boundaries are chiefly of interest for computational prediction. At present the needed confidence and accuracy are not being obtained because of the inadequacy of the turbulence model in the CFD code and the extreme requirements on computer capacity alluded to above.

Subjects receiving attention recently that have not been treated fully include such topics as finite shock motion, variable shock strength, thick and highly cambered blades in a compressible flow, and the effects of curvilinear wakes and vorticity transport. These and other large amplitude and therefore nonlinear perturbations, which prevent the linear super-position implicit in classical modal analysis, have certain implications relative to the traditional solutions of the aeroelastic eigenvalue problem. The field of aeroelasticity in turbomachines continues to be under active investigation, driven by the needs of aircraft powerplant, gas turbine and steam turbine designers.

References

1. Platzer MF, Carta FO (eds) (1987) AGARD manual on aeroelasticity in axial-flow turbomachines, unsteady aerodynamics vol 1, AGARDograph No.298
2. Platzer MF, Carta FO (eds) (1988) Ibid vol 2, structural dynamics and aeroelasticity, AGARDograph No. 298
3. Whitehead DS (1960) Force and moment coefficients for vibrating aerofoils in cascade, ARC R & M 3254. London
4. Smith SM (1972) Discrete frequency sound generation in axial flow turbomachines, ARC Ri & M 3709. London
5. Verdon JM, Caspar JR (1984) A linearized unsteady aerodynamic analysis for transonic cascades. J Fluid Mech 149:403–429
6. Adamczyk JJ, Goldstein ME (1978) Unsteady flow in a supersonic cascade with subsonic leading edge locus. AIAA J 16(12):1248–1254
7. Goldstein ME (1976) Aeroacoustics. McGraw-Hill Publishing Company, New York
8. Speziale CG, Sisto F, Jonnavithula S (1986) Vortex simulation of propagating stall in a linear cascade of airfoils. ASME J Fluids Eng 108(3):304–312
9. Sisto F, Wu W, Thangam S, Jonnavithula S (1989) Computational aerodynamics of oscillating cascades with the evolution of stall. AIAA J 27(4):462–471
10. Tanida Y, Saito Y (1977) On choking flutter. J Fluid Mech 82:179–191
11. Jutras RR, Stall one MJ, Bankhead HR, (1980) Experimental investigation of flutter in midstage compressor designs. AIAA Paper 80–0786:729–740
12. Micklow J, Jeffers J (1981) Semi-Actuator disc theory for compressor choke flutter, NASA Contractor Report 3426
13. Tang ZM, Zhou S (1983) Numerical prediction of choking flutter of axial compressor blades. AIAA Paper 83–0006, Reno
14. Lane F (1956) System mode shapes in the flutter of compressor blade rows. J Aeronaut Sci 23(1):54–66
15. Crawley EF, Hall KC (1985) Optimization and mechanism of mistuning in cascades. J Eng Gas Turbines Power 107(2):418–426
16. Bendiksen OO, Valero NA (1987) Localization of natural modes of vibration in bladed disks. ASME Paper 87-GT-47, Anaheim, California
17. Kaza KR, Kielb RE (1982) Flutter and response of a mistuned cascade in incompressible flow. AIAA J 20(8):1120–1127
18. Srinavasan AV (1980) Influence of mistuning on blade torsional flutter, NASA CR-165137
19. Platzer MF (1975) Transonic blade flutter: a survey. Shock Vib Dig 7(7):97–106
20. Platzer MF (1977) Unsteady flows in turbomachines-a review of current developments. In: AGARD-CP-227 unsteady aerodynamics, Ottawa
21. Platzer MF (1978) Transonic blade flutter: a survey of new developments. Shock Vib Dig 10(9):11–20
22. Platzer MF (1982) Transonic blade flutter: a survey of new developments. Shock Vib Dig 14(7):3–8
23. Adamczyk JJ (1978) Analysis of supersonic stall bending flutter in axial-flow compressor by actuator disc theory. NASA, Technical Paper, p 1345
24. Adamczyk JJ, Stevens W, Jutras R (1982) Supersonic stall flutter of high-speed fans. Trans ASME J Eng Power 104(3):675–682
25. Stargardter H (1979) Subsonic/Transonic stall flutter study, Final Report, NASA CR-165256, PWA 5517–31
26. Fleeter S (1979) Aeroelasticity research for turbomachine applications. J Aircr 16(5):320–326
27. Namba M (1972) Lifting surface theory for a rotating subsonic or transonic blade row, Aeronautical Research Council, R & M 3740. London
28. Salaun P (1974) Pressions aerodynamiques instationnaires sur une grille annulaire en eccoulement subsonique, Publication ONERA No. 158

29. Ewins DJ (1973) Vibration characteristics of bladed disc assemblies. J Mech Eng Sci 15(3):165–186
30. Srinivasan AV (ed) (1976) Structural Dynamic Aspects of Bladed Disk Assemblies. In: Proceedings ASME Winter Annual Meeting, New York
31. Chi RM, Srinicasan AV (1984) Some recent advances in the understanding and prediction of turbomachine subsonic stall flutter, ASME Paper 84-GT-151
32. Ford RAJ, Foord CA (1979) An analysis of aeroengine an flutter using twin orthogonal vibration modes, ASME Paper 79-GT-126
33. Sisto F, Chang AT (1984) A finite element for vibration analysis of twisted blades based on beam theory. AIAA J 22(11):1646–1651
34. Sisto F, Chang AT (1985) Influence of rotation and pretwist on cantilever fan blade flutter, In: Proceedings of 7th international symposium on airbreathing engines, Beijing
35. Rai MM (1987) Navier-Stokes simulations of rotor-stator interaction using patched and overlaid grids. AIAA J Propul Power 3(9):387–396
36. Schroeder LM, Fleeter S (1988) Viscous aerodynamic analysis of an oscillating flat plate airfoil with locally analytic solution. AIAA Paper 88–0130, Jan 1988
37. Clarkson JD, Ekaterinaris JA, Platzer MF (1991) Computational investigation of airfoil stall flutter. In: Sixth international symposium on unsteady aerodynamics and aeroacoustics and aeroelasticity of turbomachines and propeller, Notre Dame, Sept 1991

Modeling of Fluid-Structure Interaction

Earl H. Dowell and Kenneth Hall

Abstract Modeling of aerodynamic forces has now moved beyond the classical potential flow theory at least in the research community and to some degree in engineering practice. These more sophisticated fluid models are based upon the Euler or Navier- Stokes equations and require substantial computer resources. This has led to the search for reduced order models that retain the higher physical fidelity of such flow models while still permitting computationally feasible solutions as described in this chapter.

In the course of preparing this chapter, a bibliography of over 500 references was prepared and is available from the authors in electronic form upon request.

1 The Range of Physical Models

1.1 The Classical Models

The physical models used in treating fluid-structure interaction phenomena vary enormously in their complexity and range of applicability. The simplest model is the very popular "piston theory," which may be thought of as the limit of potential-flow models as the frequency of an oscillating body in a fluid becomes large. It also may be thought of as the double limit as the Mach number becomes large, but the product of the Mach number and amplitude of oscillation normalized by body chord remains small compared with unity. This simplest theory expresses the fluid pressure p on the oscillating body at some point x,y and some time t as a simple linear function of the motion at that same point and instant in time. That is,

$$p = (\rho U/M)\left[\frac{\partial w}{\partial t} + U\frac{\partial w}{\partial x}\right], \tag{1}$$

E. H. Dowell (✉) · K. Hall
Mechanical Engineering and Materials Science Duke University, Durham, NC, USA
e-mail: earl.dowell@duke.edu

E. H. Dowell (ed.), *A Modern Course in Aeroelasticity*, Solid Mechanics and Its Applications 264, https://doi.org/10.1007/978-3-030-74236-2_9

where w is a function of x, y and t and is the instantaneous deflection of the body in the fluid stream, p, U, and M are the free-stream density, velocity, and Mach number, respectively. This simple fluid mechanics model has been very popular with structural engineers because it allows the fluid pressure to be incorporated into a standard structural dynamic with a minimum of additional complexity. But this fluid model is physically useful over only a limited range of flow conditions, and its primary value is in checking the results from more complex fluid models in the appropriate limit. There is a nonlinear version of the piston theory, but it still is limited in the frequency or Mach number range where it is useful. Lighthill [29], in a classic paper on the subject, notes the analogy with the pressure on a piston face with a certain oscillating velocity.

The full-potential theory is a much more formidable model to consider, however. Even if one assumes the flow is inviscid and irrotational, the full potential-flow theory requires the solution of a nonlinear wave equation for the velocity potential whose gradient gives the local fluid velocity components and from which the fluid pressure may be determined via Bernoulli's equation. See, for example, Dowell et al. [8]. A well-known simplification is to assume that the motion of the body is small and the body profile is thin and thus derive a small-perturbation form of the potential-flow theory that leads to the celebrated linear convected-wave equation for the velocity potential Φ; that is,

$$\nabla^2 \Phi - \frac{D^2 \Phi}{Dt^2} = 0. \tag{2}$$

where ∇^2 is the Laplacian operation and D/Dt is the substantial derivative, which is, in turn,

$$\frac{D}{Dt} \equiv \frac{\partial}{\partial t} + U \frac{\partial}{\partial x}, \tag{3}$$

The solution of the linear convected-wave equation forms the basis for many of the fluid-structure interaction models that have been used for fluid-structure interaction stability and response analyses of aircraft. These are termed "flutter" or "gust response" analyses. See for example the texts by Bisplinghoff et al. (1955) and Fung [16]. Note that, in deriving Eq. 2, the steady flow about which dynamic perturbations are taken is a simple, uniform-constant-velocity flow. While a great deal of understand of unsteady flows has been gained from the study of Eq. 2, for some flows of interest, a more complex steady flow must be considered, as is discussed below.

Solving the convected-wave equation per se is not the primary difficulty in determining the pressure on a wing; rather it is the satisfaction of appropriate boundary conditions. For example, for a thin wing undergoing bending structural oscillations, it is required that the (small-perturbation) pressure be zero in the plane of the wing off the wing surface, but that the fluid velocity normal to the wing surface be equal to the body or structural velocity on the body surface. Note that, from symmetry and antisymmetry considerations, one need only consider the fluid in the region above (or below) the plane defined by the wing (which is treated as a planar body undergoing

oscillations normal to its surface within the small-perturbation approximation). This gives rise to a mixed-boundary value problem since the boundary conditions involve both the unknown velocity potential and its gradient over different portions of the fluid boundary or solution domain.

The solution to this mixed-boundary problem can be obtained by invoking Green's theorem or Fourier transforms methods to reduce the convected-wave equation, a partial differential equation in three spatial dimensions with suitable boundary conditions, to an integral equation that relates the downwash created by the body oscillations (the bracketed term in Eq. 1) to the pressure on the wing. In some contexts this would be called a boundary element approach. Formally,

$$\left[\frac{\partial w}{\partial t} + U\frac{\partial w}{\partial x}\right] = \int_0^t \left[\iint_{wing} K(x - x^*, y - y^*, t - t^*) \times p(x^*, y^*, t^*)\mathrm{d}x^*\mathrm{d}y^*\right]\mathrm{d}t^* \tag{4}$$

Here K is a Green's function, also sometimes called a kernel function, which can be expressed in terms of elementary functions although in a rather elaborate form. Form the standpoint of the fluid mechanician, to determine a solution to Eq. 4 is to find the unknown pressure p for a prescribed downwash. Of course the structural analyst thinks of solving a companion structural model to determine the body motion and hence the downwash for a prescribed pressure. The fluid-structure interaction solution requires that we solve the fluid and structural models simultaneously for the unknown pressure and body motion. Normally the solution of Eq. 4 is the more difficult part of the fluid-structure interaction analysis, not least because the Green's function K is a highly singular function that varies as $(y - y^*)^{-2}$ as y approaches y^*. Nevertheless, successful numerical techniques have been devised to effect solutions to Eq. 13.4. Most such solutions are for the special but important case of simple harmonic motion in time. Of course, from Fourier theory one can in principle determine solutions for arbitrary time-dependent motion by superposition of the solutions for harmonic motion. For a thorough elaboration of solution techniques for Eq. 4 for both subsonic and supersonic flow, see the well-known text by Fung [16], Bisplinghoff et al. (1955), and Dowell et al. [8]. These solutions today remain the most commonly used in the design aircraft and are still important for turbomachinery applications as well. Even so, it has been known for many years that the classical small-perturbation theory has some substantial limitations. For example, when the flow is transonic with the Mach number near unity, then shock waves may form, and these must be taken into account for a physically faithful analysis. Also, in turbomachinery flows, the turning angles are often so large as to require a nonlinear modeling of the steady flow at the very least.

1.2 The Distinction Between Linear and Nonlinear Models

There are two distinct approaches here. The simplest, although still more complex than the classical theory of the linear convected-wave equation, is to first determine a fully nonlinear solution for the steady (time-independent) flow about the body when the body is not in motion. Thus, the steady-flow solution varies with spatial position unlike the assumed uniform steady flow of the classical theory. For a transonic flow, the nonlinear static solution may include a shock wave. Then one considers a small dynamic perturbation about this steady flow or static solution and assumes that the subsequent shock motion and all other flow variable vary in a linear fashion with the body motion. This is usually called a time-linearized or dynamically linear (but statically linear) model. Such models are discussed in more depth later, in the section entitled Time-Linearized Models. The governing equation for the dynamically perturbed flow is still a linear convected-wave equation, but now the coefficients in the partial differential equation depend on the steady flow and hence vary with the spatial coordinates throughout the flow field. For subsonic flow or supersonic flow or supersonic flow with a Mach Number well removed from unity, this steady flow may be approximated by a uniform steady flow with a constant flow velocity U everywhere in the flow field as in the classical theory for airfoils and wings. Again, for flows in turbomachinery, one may find the classical approximation less useful.

The solution of the time-linearized equations rather than the full nonlinear equations usually leads to at least an order of magnitude reduction in computer costs and is often sufficient for describing accurately many interesting physical phenomena, for example, the onset of instabilities of the fluid-structure system or even of the fluid alone. The concept of time linearization may be used not only for potential-flow models, but also in the context of the more elaborate and general Euler equations for an inviscid rotational flow or even the Navier-Stokes equations for a viscous flow. As an example of a time-linearized analysis for the Navier-Stokes equations, one may recall the much studied hydrodynamic stability theory; for example, see the well-known text by Lin [30].

The other approach is of course to attempt to determine a fully dynamically nonlinear solution. This approach is discussed in more depth in the section entitled Nonlinear Dynamical Models and involves the numerical solution of a nonlinear convected-wave equation for potential flow and more elaborate equations for the Euler or Navier-Stokes models. Once one is committed to determining nonlinear solutions, be they steady (static) or unsteady, then normally a finite-difference scheme in the spatial variable will be required that converts the nonlinear partial differential equation model in space and time to a very large system of ordinary differential equations (ODEs) in time only. The size of the system is often very large indeed, involving 10^4 to $\geq 10^6$ ODEs. This is the field of computational fluid dynamics (CFD). See, for example, various review articles on the CFD approach to unsteady aerodynamics by Tijdeman and Seebass [45], McCroskey [32], Seebass et al. (1986) and Nixon [34] and Edwards et al. [10].

1.3 Computational Fluid Dynamics Models

With a CFD approach, one can in principle consider not only the potential-flow models of irrotational flow, but also the inviscid rotational models of the Euler equations and indeed the viscous models of the Navier-Stokes equations. As is well known, however, the computational resources required to treat the Navier-Stokes equations de novo even today are beyond our capabilities, and therefore various empirical models of turbulence have been developed so that solutions to the Navier-Stokes equations can be made computationally tractable. Such empirical models of turbulence effectively allow one to construct a mathematical model that avoids the nonlinear dynamics of the transition from laminar to turbulent flow. In this review, we discuss only briefly the basic elements of the CFD approach. However, as will be emphasized, the important work that has been done over many years by the CFD community is now beginning to bear fruit for fluid-structure interaction analysis with the advent of what is usually called reduced-order modeling.

1.4 The Computational Challenge of Fluid Structure Interaction Modeling

The fluid-structure interaction analyst has a special challenge. If one wished to obtain solutions for many difference combinations of structural and fluid parameters, then the solutions to the CFD and other fluid models must be made as computationally efficient as possible. Typically a design team may wish to evaluate thousands of parameter variations as various structural elements are changed in the design process. For many years, in the analysis of complex structures, the finite-element model for a structural body undergoing oscillations has been "reduced" in size by first finding the natural or eigenmodes of the structure and then recasting the finite-element structural model in terms of these modes, using, for example, Lagrange's equations from classical dynamics. Typically a finite-element structural model of a few thousand degrees of freedom has been reduced to a modal model with a few tens of degrees of freedom. See, for example, Dowell et al. [8]. This reduces not only the size of the model but also the computational cost by orders of magnitude, while providing new insights into the physical phenomena through a consideration of the structural modal behavior. Such an approach has only recently been proposed and successfully pursued for fluid models. However in the last few years it has been shown that such an approach gives remarkable benefits in terms of computational cost savings and also in terms of increasing our insight into the dynamics of fluid models by considering their modal structure. Hence, in this review considerable attention is given to these new developments. See the section entitled Reduced-Order Models below. Now, we turn to a more thorough exposition of some of the issues we have touched upon so far.

2 Time-Linearized Models

Time-linearized models are a broad and very interesting class of fluid models that are extremely powerful and useful in dealing with fluid-structure interaction phenomena. First, a few special cases that are well known in the literature are considered, and then the general case is treated. For the reader who prefers deductive to inductive reasoning, the general case is treated at the end of this section and may be consulted first. The basic notion is that a steady-flow field is first determined that is the base flow about which a dynamic, small perturbation is considered. Only linear terms in the dynamic perturbation are retained, and thus the governing equations for the dynamic perturbation are linear in the dynamic or time-dependent unknowns with coefficients that depend on the (nonlinear) base steady-flow or static-equilibrium solution.

2.1 Classical Aerodynamic Theory

In classical aerodynamics, the base flow is taken to be the simplest imaginable, that is, a uniform steady flow. Physically this may be thought of as the flow around an infinitesimally thin, flat plate aligned with a uniform oncoming flow velocity. Or to say it another way, any thickness or profile deviation from a thin flat plate gives rise to a small perturbation to the uniform flow itself so that the effects of finite thickness, airfoil or wing profile (camber or curvature), and airfoil or wing motion can be treated separately as linear perturbations to the uniform steady flow, and therefore their effects may simply be added together or superimposed. Hence, the governing equation for a potential flow is Eq. 13.2, as previously discussed. Much of the literature on fluid-structure interaction uses this model. And it is perhaps the simplest model that is based on time linearization. However there are others.

2.2 Classical Hydrodynamic Stability Theory

One of the most fascinating issues in unsteady fluid mechanics is the transition from laminar to turbulent flow. Some of the most famous investigators in the field of fluid mechanics have addressed this issue, for example, Werner Heisenberg, G.I. Taylor, and Theodore Von Karman (see Lin [30]). A central question is under what circumstances a laminar flow loses its stability and begins the process of transition to turbulence. Hydrodynamic-stability theory examines the small dynamic perturbation of a laminar flow field and determines the condition for the loss of stability. The theory is a subtle one, and a connected and authoritative account is provided by Lin [30] in his celebrated book. The best known aspect of this theory is that which considers the stability of a parallel shear flow. In this model the underlying steady flow is a nonlinear viscous solution to Navier-Stokes equations, but to simplify the model and

subsequent calculations, the steady flow is often assumed to vary only normal to a flat plate of infinite extent, but not to vary in the flow direction or in the spanwise direction. Hence, the steady flow is a function of only one spatial variable in the direction transverse to the plate and the flow. Therefore, in the dynamic perturbation analysis, the governing equation is a linear one show coefficients depend only on the transverse spatial variable. This allows a Fourier decomposition in both time and the spatial direction aligned with the flow (and in the spanwise direction as well). This leads then to the famous Orr-Sommerfeld equation which has challenged fluid mechanicians for many years. The assumption of a parallel shear flow over an infinite plate may or may not model all the interesting physics of a spatially evolving viscous steady flow on an airfoil, of course. The invocation of this severe assumption is a measure of the complexity of considering the spatially developing, steady-boundary layer and its dynamic perturbation when the hydrodynamic-stability theory was first being developed more than 50 years ago. This restrictive assumption has been attacked by subsequent investigators, but the range of geometries considered to date has still been somewhat limited.

2.3 Parallel Shear Flow with An Inviscid Dynamic Perturbation

A further simplification to hydrodynamic-stability theory that is sometimes useful is to neglect the viscous terms in the dynamic perturbation per se, but still include their effect in determining the steady flow. This may be thought of as an inviscid perturbation about the viscous steady flow. While such a model clearly cannot treat the stability of the viscous steady-flow field per se, it may be useful in computing the pressure on a wall over which the boundary layer thickness does not vary greatly. By scaling arguments, one may deduce when the neglect of the viscous terms in the dynamic perturbations may be justified. Such a model has been proposed by Miles [33] and Anderson and Fung [1] in the context of fluid-structure interaction and has been applied successfully by Dowell [6] to the determination of the stability of an elastic plate interacting with a flow stream, the so-called panel flutter problem. Dowell has shown that the boundary layer effect on the unsteady aerodynamic pressure is most pronounced for transonic flows and is relatively less important for subsonic and supersonic flows, in agreement with the experimental evidence.

Formally, for a slowly varying boundary layer thickness, one may also determine the solution for the pressure on an airfoil or wing, using the shear flow model. Specifically, one may derive a new Kernel or Green's function so that the solution techniques of classical aerodynamics may be applied. But this model has not been widely used, although it may have some utility for treating the effect of a boundary layer on a wing control surface, for example (see Chi and Dowell [4]).

2.4 General Time-Linearized Analysis

To consider the most general case, we consider a generic form of a CFD model in which, for example, a finite-difference technique is used to convert the partial differential equations of a nonlinear flow model, whether potential, Euler, or Navier-Stokes, to a large system of ODEs in time. Thus, formally, one has

$$\frac{\partial}{\partial t}\{\mathbf{q}\} = \{\mathbf{Q}(\mathbf{q})\} + \{\mathbf{B}(x, y, z, t)\}. \tag{5}$$

Here $\mathbf{q}$ is a vector of unknown variable to be determined throughout the flow field, $\mathbf{Q}$ is a known function of the $\mathbf{q}$ (i.e. for a given $\mathbf{q}$, one knows $\mathbf{Q}$), and $\mathbf{B}$ is some known function that expresses the motion of a structure or body in the fluid. Of course there are additional parameters determined by the far upstream conditions and the properties of the fluid, for example, the upstream Mach number. Formally, a dynamic-perturbation analysis may proceed as follows: one sets

$$\mathbf{B} = \mathbf{B_0} + \hat{\mathbf{B}}(t),$$

$$\mathbf{q} = \mathbf{q_0} + \hat{\mathbf{q}}(t). \tag{6}$$

Where $\mathbf{B_0}$ and $\mathbf{q_0}$ depend only on x, y, z, but not on t, that is, they form a steady-flow solution to Eq. 13.5. Substituting Eq. 13.6 into Eq. 13.5 and retaining only linear terms in $\hat{\mathbf{q}}$, one has the governing linear small-perturbation equations for $\hat{\mathbf{q}}$ which have coefficients that depend on the steady-flow solution, $\mathbf{q_0}$, as follows:

$$\frac{\partial}{\partial t}\{\mathbf{q}\} = \left[\frac{\partial \mathbf{Q}}{\partial \mathbf{q}}\bigg|_{q=q_0}\right]\{\hat{\mathbf{q}}\} + \{\hat{\mathbf{q}}\}. \tag{7}$$

Standard and novel means for solving large systems of such equations have been developed.

Note that if $\hat{\mathbf{B}} = 0$ in Eq. 7, then one has a eigenvalue problem. This can be exploited effectively by first solving the eigenvalue/eigenvector problem and reconstituting Eq. 7 in terms of a small number of eigenvectors or eigenmodes. This leads to one class of so-called reduced-order models (ROMs). All such ROMs, which are discussed in more detail below, are based on this notion of a few dominant modes that may be represented by some relatively small linear combination of eigenmodes. However, even without appealing to eigenmodes per se, the solution of Eq. 7 offers an attractive and powerful way of describing unsteady flows. This is especially the case if we consider simple harmonic motion and use a Fourier series (for periodic motion) or Fourier integral (for arbitrary time-dependent motion) to construct the solution for any time dependence from the basic solution of harmonic motion.

Here we emphasize the physical effects that such time-linearized models may include. For example, the steady flow may include shock waves and also separated flows. The dynamic perturbation ansatz does require that the oscillations of shocks

or separated flow regions be sufficiently small, but there are many flow conditions in which that is true. For example, if a small dynamic perturbation is assumed, it is required that shock wave motions be small compared with the airfoil or wing chord and that the dynamic variation in shock strength, for example, the jump in pressure through the shock, be small compared with that of the steady shock. Similar restrictions apply to separated flow regions. Also, of course, limit cycle oscillations due to fluid nonlinearities are not modeled when time linearization is assumed. Note, however, that the effects of turbulence can be included formally within the framework of the empirical turbulence models frequently used in CFD application, e.g. Baldwin-Lomax models, $k - \epsilon$ models, etc. In this regard it is worth noting that to construct a dynamical perturbation model one needs to be able to differentiate $\mathbf{Q}$ with respect to $\mathbf{q}$. Doing this for the original fluid equations, e.g. Euler or Navier-Stokes, is not a problem, at least formally. However some empirical turbulence models introduce nondifferentiable functions that can pose practical computational difficulties in constructing dynamic-perturbation models. Of course, if one has an exact steady-flow solution of the steady Navier-Stokes equations, then a dynamic-perturbation analysis follows without any especial difficulty. In particular it may be noted that such models allow, in principle, a hydrodynamic-stability analysis that fully accounts for the spatial distribution of a laminar steady flow prior to its becoming unstable.

2.5 Some Numerical Examples

As a typical example, we show results from a computation by Florea et al. [14] for a separated flow over a cascade of airfoils. One purpose of this example is to show that one can calculate quantities such as the time variation of boundary layer thickness and skin friction as well as pressure or pitching moment on an airfoil with such models. Here an empirical turbulence model has been used in the CFD code, and a time-linearized solution has been developed. See Figs. 1 and 2.

3 Nonlinear Dynamical Models

A nonlinear dynamical model is almost invariably cast in the form of a CFD model with spatial discretization by finite-difference techniques or other methods. Thus one starts with a system of ODEs such as those of Eq. 13.5. The most popular form of solution for such equations has been a time-marching technique. However, there are severe practical computational difficulties associated with the size of such system of equations, which may be on the order of 10^6, and equally important, with the small step in time that one must take with such equations because of numerical stability considerations. In the language of numerical analysis, these equations are "stiff." The end result has been that such models have been infrequently used beyond the research community. Even for research purposes, when such CFD models are used

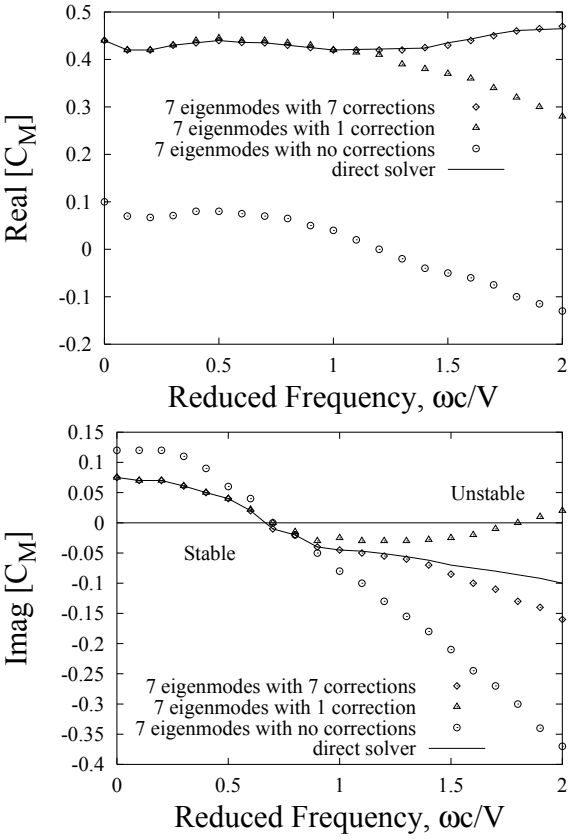

Fig. 1 Real and imaginary (Imag) pitching moment for airfoils pitching about a point near midchord for a range of reduced frequencies. $\Omega = 62^0; \sigma = 90^0$. (Republished from Florea et al. [14] with permission)

in combination with structural models, the range of the parameter space that can be explored has been relatively modest. Nevertheless, substantial progress has been made and some techniques have been developed to make such models more attractive computationally. Three are discussed here. First to be discussed are harmonic-balance techniques, which effect a solution in the frequency domain. Second are system identification techniques that allow the nonlinear (and linear) models to be expressed more compactly. The latter, used in combination with the third approach, i.e. reduced-order-modeling techniques, offers considerable promise for future development, as does the harmonic-balance methodology.

3.1 Harmonic Balance Method

In the harmonic-balance method, one takes the time dependence of the solution to be a Fourier series in time, for example,

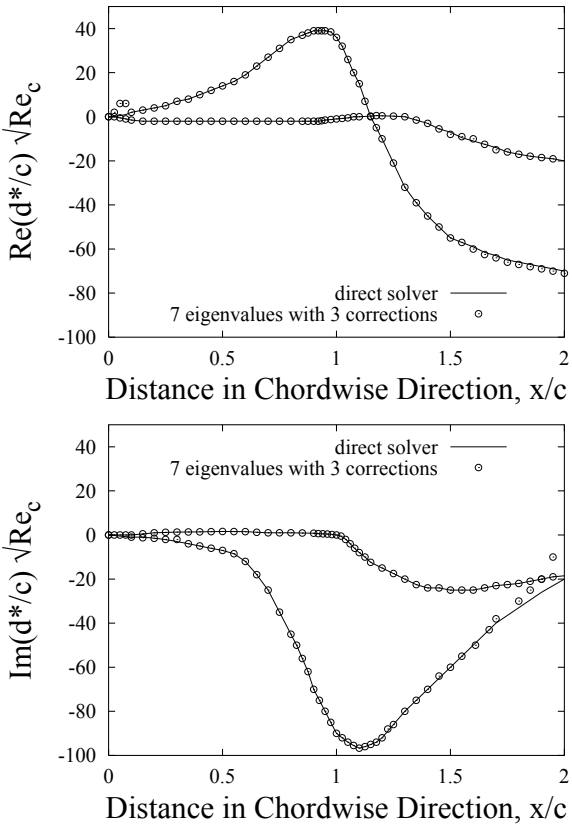

Fig. 2 Real and imaginary (Im) parts of unsteady displacement thickness for airfoils pitching about a point near midchord. $\Omega = 62^0$; $\sigma = 90^0$; $\bar{\omega}$=0.5. (Republished from Florea et al. [14] with permission)

$$\mathbf{q} = \sum_m \mathbf{q_m} e^{i\omega_0 mt}. \tag{8}$$

Lan and his coworkers (Greco et al. [17, 18] and Hwang and Lan [26]) have used a single term in such a Fourier expansion and investigated the nonlinear potential-flow model in a series of interesting papers. Of course for sufficiently small amplitudes of airfoil or wing motion (and therefore fluid motion), a single-term approximation may suffice. In the limit of infinitesimal motion, such an analysis becomes a time-linearized model. More recently, Hall and his coworkers (2000) have considered multiple harmonic terms in the Fourier series and developed computationally efficient methods for extracting the nonlinear solution to the Euler equations. Lan and his coworkers (Greco et al. [17, 18] and Hwang and Lan [26]) have applied his method to airfoils and wings, while Hall developed his methodology for turbomachinery applications to cascades of airfoils. Hall et al. [19] have shown that a few harmonics are normally sufficient to describe the flow field accurately, even for rather large

airfoil and fluid motions. Both Lan and Hall note that a harmonic balance approach allows the analyst to take advantage of the many computational-solution techniques that have been developed for steady-flow solvers over the years.

3.2 System Identification Methods

Several authors have considered system identification methods. Among these, Silva [40, 41] has suggested the adaptation of the Volterra/Wiener approach that has been developed in the field of signal processing. Formally, by considering a small number of inputs (structural motions) and outputs (e.g. lift and moment on an airfoil), the nonlinear input/output relationships can be modeled with a relatively small number of equations. This approach has considerable promise; however, if the inputs or outputs of interest change, then the model must be reconstructed. Also the dynamics of the system are essentially treated as a "black box", and the internal dynamics of the total governing equations and hence the fluid are to some degree masked by this approach.

Silva chooses the integral formulation for the input/output model and defines a hierarchy of impulse or temporal Green's functions. For example, if $y(t)$ is a typical output and u an input, then following Volterra and Wiener, one may postulate a form of input/output relationship as follows:

$$y(t) = \sum_n \int_{-\infty}^{\infty} h_n(\sigma_1^*, \sigma_2^*, ...) u(t - \sigma_1^*) u(t - \sigma_2^*) ....\mathrm{d}\sigma_1^* \mathrm{d}\sigma_2^* ... \tag{9}$$

The corresponding differential equation form is

$$\frac{\partial y}{\partial t} = A_0 + A_1 y + A_2 y^2 + ... + A_n y^n + Bu \tag{10}$$

Silva suggests techniques for deducing h_n in Eq. 9, and there are also methods in the literature for deducing the coefficients, A_0, A_1, $.....A_n$, etc, in Eq. 10, given u and with y determined by a numerical simulation. Please note that, formally, Eq. 10 may be obtained from Eq. 5 by expanding $\mathbf{Q}(\mathbf{q})$ in a Taylor series and noting that there exists a linear transformation between y and $\mathbf{q}$. Note that, while Eqs. 9 and 10 are written here as scalar equations for simplicity, there are generalizations to a vector form available.

3.3 Nonlinear Reduced-Order Models

Of course formally one may determine a modal representation for q from a time-linearized analysis and use these modes to reduce the full nonlinear dynamical model

(see Eq. 5). Such a technique has been used for structural models of relatively high dimension for some years, (e.g. see Dowell [7]), but it is only now being explored for CFD models. The nonlinear dynamic models are a subject of current research, but it does appear that there are several promising alternatives that may lead to advances in our ability to deduce more compact models, which will lead to a greater understanding of such models and improve their computational efficiency.

3.4 Reduced-Order Models

The use of CFD models for systematically investigating unsteady aerodynamic flows has been a goal since the advent of the computer age. Many investigators have demonstrated the potential utility of CFD for improving the physical modeling of complex unsteady flows. However, until recently the computational cost associated with the high dimensionality of these models has precluded their use in routine applications for studying aeroelastic phenomena. Thus the research literature has been voluminous, but the applications in industry have been relatively few in number.

Recent work on a conceptually novel and computationally efficient technique for computing unsteady flows based on the modal character of such flows is described below. Eigenmode-based, reduced-order models (ROMs) are given prominence although other related modal descriptions also prove useful and are discussed as well.

Why study the eigenmodes of unsteady aerodynamic flows? This is perhaps the fundamental question most often asked, although occasionally someone will express surprise that eigenmodes even exist for these flows. The reason are several:

1. Eigenvalues and eigenmodes for these flows do exist! So perhaps they can tell us something about the basic physical behavior of the flow field.
2. Indeed, if a relatively small number of eigenmodes are dominant, this immediately suggests a way to construct an efficient computational aerodynamic model using these dominant modes.
3. Constructing the aerodynamic model in eigenmodal form is a particularly attractive way to combine the eigenmode aerodynamic model with a number of degrees of freedom for a given desired level of accuracy. These aeroelastic models will be especially useful for design studies, including the active control of such systems.
4. Finally, as will be seen, alternative modal descriptions are available. While their usefulness is predicated on the existence of eigenmodes, these other modal descriptions seek to induce more information on the flow response to enhance the accuracy of a reduced model of a given dimension or reduce the dimension for a required accuracy compared with a standard eigenmode representation. Moreover, for one descriptor, the so-called proper orthogonal decomposition (POD) modes, one may avoid the necessity of a tedious direct eigenvalue evaluation of the CFD equations, a major advantage of using these modes.

For a more in depth discussion of this work, see, for example, Hall [21], Dowell et al. [5, 9]; earlier work is noted in those references.

3.5 Constructing Reduced Order Models

There are two distinct ways of going about constructing ROMs, although there are many variations on the basic themes. One approach is to characterize the aerodynamic flow field in terms of a relatively small number of global modes. By a mode we mean a distribution of flow field variables that characterizes a gross motion of the flow. The conceptually simplest way of choosing such a set of modes is to consider the eigenmodes of the flow field. Of course, such modes form a complete set, and any flow field distribution can be expressed in terms of such eigenmodes. Formally, the eigenvectors are used to effect a linear transformation from the original set of (local) flow variables used in the CFD model, such as pressure, density, and velocity components at a spatial grid point, to a new modal set of global coordinates. The new modal equations are uncoupled due to the orthogonality of the eigenvectors. In particular any alternative modal selection, and we consider several, can always be expressed in terms of such eigenmodes.

Indeed, it is the existence of eigenmodes that underpins any modal description of the flow. As with other simpler mechanical systems, it is the hope and expectation, borne out in the results to be shown later, that a relatively small number of modes will prove adequate to describe the flow. Thus, a typical CFD model, which may have 10^4 to 10^6 or more degrees of freedom, may be reduced to a model containing only 10^1 to 10^2 modes, which is capable of accurately describing the pressure on an oscillating aerodynamic surface.

The second category of ROMs does not explicitly rely on a modal description per se, but rather appeals to the idea that only a small number of inputs, that is, structural motions or modes, and a correspondingly small number of outputs, that is, generalized forces or specific integrals of the aerodynamic pressure distribution weighted by the structural mode shapes, are of interest. Hence one may construct, for example, a transfer function matrix whose size is determined by the number of inputs and outputs. Typically the size of this matrix will be on the order of the number of structural modes. The transfer functions are determined numerically using a systems identification technique from time simulations calculated by using the CFD code. If the number or type of inputs, that is, the structural modes, changes during an aeroelastic simulation, then the aerodynamic-transfer functions may need to be recalculated. On the other hand, the CFD code does not require deconstruction to determine aerodynamic modal information, thereby saving this additional effort but also foregoing the additional insight and flexibility gained by knowing the aerodynamic modes. Changes in the structural modes do not change the aerodynamic eigenmodes, of course, but changes in the structural modes may require recalculation of the transfer functions of aerodynamic input/output models.

3.6 Linear and Nonlinear Fluid Models

Two points that arise in the use of a model representation are worthy of mention. For nonlinear dynamical systems, it is possible to extend the idea of a linear eigenmode itself to nonlinear eigenmodes. See, for example, the book by Troger and Steindl [46] and Chap. 7 of the present book for a readable account of these ideas. This point has some theoretical interest. However, these nonlinear eigenmodes still lead to coupled modal equations, so their value in practice is often not substantially greater than that of linear eigenmodes for ROM systems of several (say 10 or more) degrees of freedom.

The second noteworthy point is that, if one determines the linear eigenmodes for say one airfoil-Mach number combination and then uses an eigenvector transformation for another airfoil-Mach number combination, then the corresponding modal equations will also be coupled even in the linear terms. This, of course, is because we have used the eigenmodes of one fluid system to represent the dynamics of a different fluid system. That is, orthogonality of the modes only holds for eigenmodes used for the same dynamical system from which they are derived. Nevertheless, if the eigenvectors do not change appreciably with, for instance, Mach number, these coupled modal equations may still be adequate, and thus one may avoid recomputing the eigenvector for each change in Mach number.

3.7 Eigenmode Computational Methodology

For the simpler (lower dimensional) fluid models, for example, a two-dimensional vortex lattice model of unsteady flow about an airfoil, the size of the eigenvalue matrix is on the order of 100×100. For such matrices, standard eigenvalue extraction numerical procedures may be used. We have used EISPACK, a standard algorithm and computer code available in most computational centers in the United States.

For more complicated fluid models (e.g. the full potential models or Euler models), the order of the eigenvalue matrix may be in the range of 1000–10,000 squared or greater. For matrices of this size, new developments in eigenvalue extraction have been required. We have used methods based on the Lanczos algorithm. For the full-potential equation (1000×1000), an efficient and effective algorithm is described by Hall et al. [22]. For the Euler equations ($10^4 \times 10^4$), the paper by Romanowski and Dowell [37] will be of interest. The discussion by Mahajan et al. [31] is also recommended to the reader. As the extensions to three-dimensional and viscous flows are made, further developments in eigenvalue and eigenmode determination will likely be required or desired.

To improve the convergence of the eigenmode ROM representation, that is, to reduce the number of eigenvectors retained, a so-called static-correction method is useful, as was first noted by Hall. In this approach, Eq. 7 is first solved by setting the

left-hand side to zero, and then a correction is determined by expanding the difference between this solution and the full solution of Eq. 7 in terms of eigenmodes.

However an alternative method may be preferable, as described below.

3.8 *Proper Orthogonal Decomposition Modes*

Given the difficulty of extracting eigenmodes for very high-dimensional systems (e.g. $> 10^4$), it is of great interest to note that a simpler modal approach is available, as recently developed by Romanowski [36]. This approach adapts a methodology from the fields of nonlinear dynamics and signal processing, that is, the POD or Karhunen-Loeve (KL) modal representation. See Romanowski [36] for an introduction to the relevant literature in this field.

Here we quote Romanowski's account of the essence of the method.

> Karhunen-Loeve Decomposition (KL Decomposition) [also called proper orthogonal decomposition (POD)] has been used for a broad range of dynamic system characterization and data compression applications. The procedure, which is briefly summarized below, results in an optimal basis for representing the given data ensemble.
>
> The instantaneous flow field vector, $\mathbf{q}_j$, is retained at J discrete times, such that $j = 1, 2, 3, ...J$. A caricature flow field, $\tilde{\mathbf{q}}_j$, is defined as the deviation of each instantaneous flow field from the mean flow field, $\bar{\mathbf{q}}_j$, of the ensemble:
>
> $$\tilde{\mathbf{q}}_j = \mathbf{q}_j - \bar{\mathbf{q}}_j. \qquad (9)^* \qquad (11)$$
>
> A[1] matrix Φ is formed as the ensemble of the two-point correlation of the caricature flow fields, such that
>
> $$\Phi_{jk} = \tilde{\mathbf{q}}_j^T \tilde{\mathbf{q}}_k^T. \qquad (10) \qquad (12)$$
>
> References (10) and (12) [of Romanowski 1996] show that solving the eigenvalue problem
>
> $$[\Phi]\{\mathbf{v}\} = \lambda\{\mathbf{v}\} \qquad (11) \qquad (13)$$
>
> produces an optimal set of basis vectors, $[\mathbf{V}] = [\{\mathbf{v}_1\}, \{\mathbf{v}_2\}, ...\{\mathbf{v}_j\}]$ for representing the flow field ensemble. Additionally, the magnitude of the eigenvalue, λ_j gives a measure of the participation of the jth KL [or POD] eigenvector in the ensemble. Therefore, a reduced set of basis vectors can easily be found by limiting the set to only those KL eigenvectors corresponding to sufficiently large eigenvalue.

Since the number of time steps and thus the order of matrix needed to compute a reasonable and useful set of KL or POD modes is typically on the order of 1000, the determination of POD modes is computationally very inexpensive, especially as compared to determining the eigenmodes of the original fluid dynamics model. In the subsequent section, results using POD modes are shown to be in excellent agreement with those obtained from the full-order model and also the ROM based on eigenmodes. It also might be noted that one can first use the POD decomposition to reduce the order of the original model and then do a further eigenmode analysis of the ROM, a technique that may be useful for some applications.

[1] The first equation number is from the original reference Romanowski [36].

As a final comment on the POD or KL methodology, it is important to note that a similar calculation may be done in the frequency domain by assuming simple harmonic solutions and replacing the data at discrete time steps with data at discrete frequencies over a frequency internal of interest. Kim [28] has used the POD frequency domain method for a vortex lattice fluid model and Hall et al. [20] and Thomas et al. [44] have done so for an Euler fluid model, including shock waves at transonic conditions.

3.9 Balanced Modes

Baker et al. [2] have used this methodology originally developed in the controls community to develop reduced-order aerodynamic models. Rule et al. [38] have explored this method as well. This basic notion is that balanced modes are in some sense an optimal descriptor within the framework of POD modes for a given family of inputs or structural motions and the aerodynamic outputs of interest. See also the discussion of balanced modes in the Appendix.

3.10 Synergy Among the Modal Methods

In light of the above discussion, the following methodology appears to be a practical and perhaps even an optimum approach. With a given CFD model, a set of POD modes can be constructed with on the order of $10^2 - 10^3$ degrees of freedom. Then, using the POD modes and the corresponding ROM (POD/ROM), a further reduction may be obtained by extracting eigenmodes or balanced modes from the POD/ROM. For some applications in which the smallest possible model is desired, for example, design for active control of an aeroelastic system, this further reduction will be desirable and perhaps essential. However, for validation studies where the identification and understanding of the most critical modes for stability are the primary issue, one may prefer to retain a POD/ROM or an eigenmode ROM.

3.11 Input/Output Models

There is a long tradition of developing aerodynamic transfer function representations from numerical data for simple harmonic motion dating from the time of Jones's approximation to the Theordorsen function. Much of the relevant literature is summarized by Karpel [27], whose own contribution was to develop a state-space or transfer function representation of minimum order for a given level of accuracy by using transfer function ideas based on data for simple harmonic motion. Hall et al. [20] have recently discussed such models in light of the more recent developments

in aerodynamic modal representations. Their discussion follows. See Bisplinghoff et al. (1955) and Karpel [27] for references to the original literature.

> Investigators have developed a number of techniques to reduce the complexity of unsteady aerodynamic models. R.T. Jones approximated indicial lift functions with series of exponentials in time. Such series have particularly simple Laplace transforms, i.e., rational polynomials in the Laplace variables, making them especially useful for aeroelastic computations. Pade approximants are rational polynomials whose coefficients are found by least-squares curve fitting the aerodynamic loads computed over a range of frequencies. Vepa [48], Edwards [11], and Karpel [27] developed various forms of the matrix Pade approximant technique. Their approach reduces the number of so-called augmented states needed to model the various unsteady aerodynamic transfer functions (lift due to pitching, pitching moment due to pitching, etc.) by requiring that all the transfer functions share common poles.
>
> . . . [A POD or eigenmode model] is similar in form to that obtained using a matrix Pade approximate for the unsteady aerodynamics...and has some of the same advantages of the Pade approach. Both methods produce low degree-of-freedom models. Furthermore, both require the aerodynamic lift and moment transfer functions to share common eigenvalues (although the zeros are obviously different). This is appealing because physically the poles should be independent of the type of transfer function. However, the present (modal) approach has several advantages over the matrix Pade approximate method. The present method attempts to compute the actual aerodynamic poles, or at least the poles of a rational CFD model. The Pade approach, on the other hand, selects pole locations by some form of curve fitting (of aerodynamic data for simple harmonic motion). In fact, some Pade techniques can produce unstable aerodynamic poles, even for stable aerodynamic systems.

It is interesting that the notion of a transfer function can be extended to nonlinear dynamical systems where the counterpart is usually called a describing function. Ueda and Dowell [47] pioneered and discussed this approach. The describing function may be considered a single harmonic-balance method.

In the time domain transfer functions can be inverted to form convolution integrals. Silva [40, 41] has recently pioneered the extension of these ideas to nonlinear aerodynamic models, using the concept of a Volterra integral.

3.12 Structural, Aerodynamic, and Aeroelastic Modes

Structural modes have a long and rich tradition. The novelty of much that is being discussed here is to extend such ideas to aerodynamic flows that also possess a modal character, albeit a more complex one. And finally there are aeroelastic modes one may consider.

For the determination of structural modes, one normally neglects dissipation or damping and thus only models kinetic energy (or inertia) and potential strain energy (or stiffness) of the structure. The eigenvalues are real (the natural frequencies squared) as are the corresponding eigenmodes. Physically, if one excites the structure with a simple harmonic oscillation at a frequency near that of an eigenvalue, the structure will perform a simple harmonic oscillation at that same frequency, whose spatial distribution is given by the corresponding eigenvector.

For aerodynamic modes (and also for aeroelastic modes), the physical interpretation as well as the mathematical determination of the eigenvalues and eigenvectors or eigenmodes is more subtle and difficult, but still rewarding. First of all, the eigenvalues are complex, with the real and imaginary parts of the eigenvalue giving the oscillation frequency and rate of growth or decay (damping) of the eigenmode. As for a structural modes, if one is clever enough to excite only a single aerodynamic eigenmode, then an oscillation will occur whose spatial distribution is given by the corresponding eigenvector. However, the eigenvalues of an aerodynamic flow are closely spaced together, typically much more closely than the eigenvalues for structural modes. Indeed, if the aerodynamic computational domain were extended to infinity, then the eigenvalues would no longer be discrete but rather would form a continuous distribution for most aerodynamic flows. Thus, exciting only a single aerodynamic mode experimentally is a difficult feat. For some turbomachinery flows with bounded flows between blades in a cascade, discrete well-spaced eigenvalues are possible that have a resonant character (see Hall et al. [22]). This is also true for some aerodynamic eigenmodes in a wind tunnel, of course. And these have been observed experimentally (see Parker [35]).

Aeroelastic modes are those that exist when the structural and aerodynamic modes are fully coupled; that is, oscillations of a fluid mode excite all structural modes and vice verse. In general, these aeroelastic modes also have complex eigenvalues and eigenvectors. At low speeds (well below the flutter speed, for example) one may usually identify the structural and aerodynamic eigenvalues separately, because structural/aerodynamic coupling is weak. However, as the flutter speed if approached, the eigenvalues and eigenvectors may change substantially, and the fluid and structural modes become more strongly coupled. It is even possible for a mode that is aerodynamic in origin at low speeds to become the critical flutter mode at higher speeds, although normally it is one or more of the structural modes that become unstable as the flow velocity approaches the flutter speed.

Winther et al. [49] have suggested using aeroelastic modes to reduce the total number of modes to be used in a simulation of overall aircraft motion. This seems like an idea worth exploring, although aeroelastic modes by definition vary with flow condition, that is, dynamic pressure and Mach number, and thus the aeroelastic modes at one flight condition will not be the aeroelastic modes at another. Of course, if one uses a sufficient number of aeroelastic modes, they will be able to describe accurately the system dynamics at any flight condition, but that tends to defeat the purpose of minimizing the number of modes in the representation.

Also it should be noted that the particular implementation of aeroelastic modes in Winther et al. [49] does not include aerodynamic states or modes per se, which limits that particular approach when the aerodynamic modes themselves are active and couple strongly with the structural modes. This is probably the exceptional case, but one which can occur.

3.13 Representative Results

Dowell et al. [9] have discussed (a) comparisons of the ROM to classical unsteady, incompressible aerodynamic theory, (b) reduced-order calculations of compressible unsteady aerodynamics based on the full-potential equation, (c) reduced-order calculations of unsteady flow about an isolated airfoil based on the Euler equations, (d) reduced-order calculations of unsteady viscous flows associated with cascade stall flutter, and (e) linear flutter analyses using ROMs.

In the present discussion, recent results for transonic flows with shock waves, including viscous and nonlinear effects, are emphasized. Before turning to these, however, we consider some fundamental results concerning the effects of spatial discretization and a finite computational domain.

3.13.1 The Effects of Spatial Discretization and A Finite Computational Domain

For simplicity, we use a classical numerical model, the vortex lattice method, for an incompressible potential fluid, to illustrate the points we wish to make. Compressible potential-flow models and Euler flow CFD models have provided numerical results consistent with those obtained from the vortex lattice models in this regard. The results discussed here are from Heeg and Dowell [24].

In CFD there are two approximations that are nearly universal to all such models. One is the construction of a computational grid that determines the limits of spatial resolution of the computational model. The second is the approximation of an infinite fluid domain by a finite spatial domain. It is a principal purpose of the present discussion to note that the computational grid determines not only the spatial resolution obtainable by the CFD model, but also the frequency or temporal resolution that can be obtained. Further, as is shown, the finiteness of computational domain determines the resolution of the eigenvalue distribution for a CFD model. Both of these observations have important ramifications for assessing the CFD model and its ability to provide an adequate approximation to the original fluid model on which it is founded, as well as being helpful in constructing and understanding ROMs.

In the following discussion, we consider both discrete-time and continuous-time eigenvalues. Even in a high dimensional system such as usually encountered with CFD, the relationship between any dynamical variable, such as vortex strength, velocity potential, flow velocity, density, pressure, etc, and its time evolution as expressed for the determination of eigenvalues and eigenvectors is a simple one. For a given dynamic variable $\hat{\mathbf{q}}$, which changes with time t, the eigenvalue relationship from a time-linearized model is

$$\hat{\mathbf{q}} = \mathbf{A}e^{\lambda t}, \tag{14}$$

where λ is the continuous-time eigenvalue. For a discrete time representation in which the time step is Δt, we define the discrete-time eigenvalue z as the ratio of $\hat{\mathbf{q}}$ to its value one time step earlier. It is easily seen then that

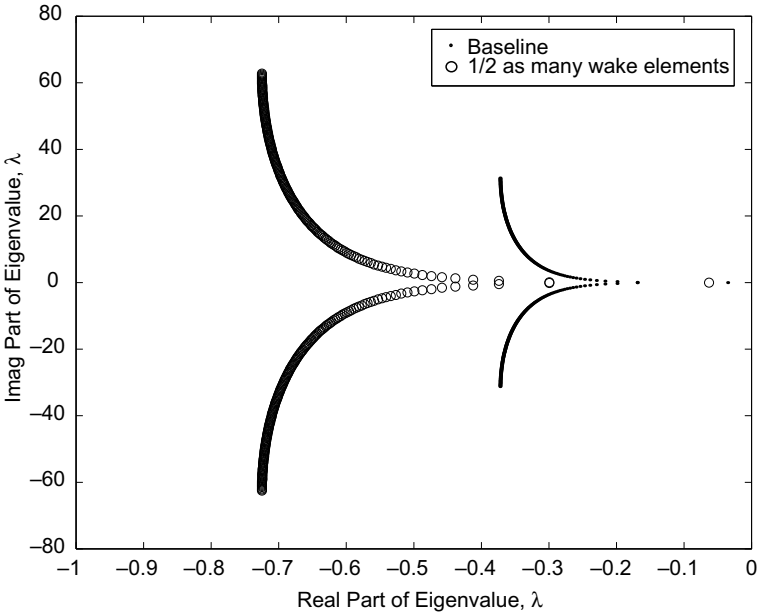

Fig. 3 Influence of varying the number of aerodynamic elements of the vortex-lattice model, while maintaining the number of elements. Shown are continuous-time real and imaginary (Imag) eigenvalues, λ. (Republished from Heeg and Dowell [24] with permission)

$$z = e^{\lambda \Delta t}$$

or

$$\lambda = \log(z/\Delta t). \tag{15}$$

It will be useful in our discussion to consider both λ and z.

Here we use the vortex lattice model, because (a) it is one of the simplest CFD models, (b) it has been widely used, and (c) among practitioners, it is thought to be well understood in terms of its capability and limitations. As noted earlier, similar results are obtained from more elaborate CFD models, which include the effects of flow compressibility, rotationality, and/or viscosity.

As an example, we consider the flow over an airfoil with a certain number of vortex elements on the airfoil and in the wake. Initially, we select 20 elements on the airfoil and 360 elements in the wake. The length of the finite wake extends 18 chord lengths. The eigenvalues and eigenmodes of the flow can be computed by now well-established methods for a relatively small eigenvalue system, for example, < 1000.

The eigenvalue distribution for λ is shown in Fig. 3. Note that the real part of the eigenvalue is the damping and the imaginary part is the frequency of the eigenvalue. We now study the effects of (a) refining the vortex lattice grid and (b) changing the

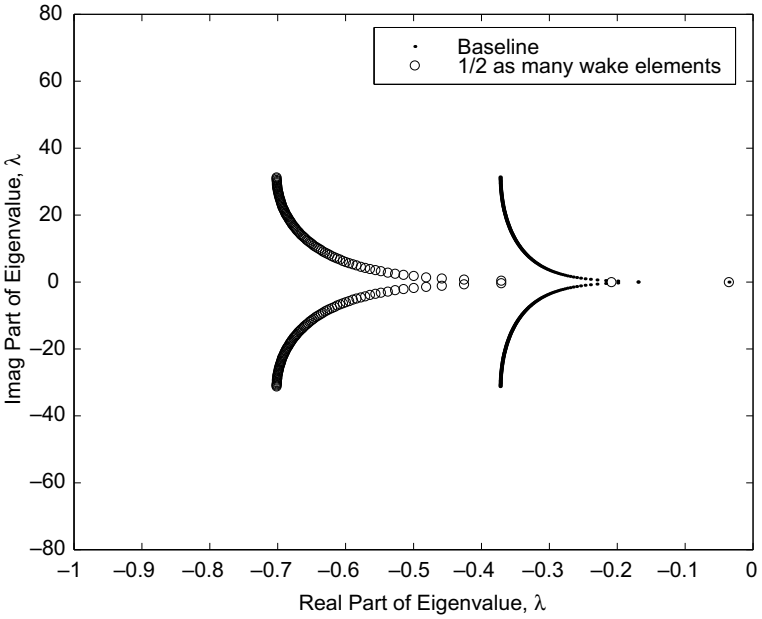

Fig. 4 Influence of varying the number of aerodynamic elements in the wake of the vortex-lattice model, while maintaining the element size. Shown are continuous-time real and imaginary (Imag) eigenvalues, λ. (Republished from Heeg and Dowell [24] with permission)

extent of the wake length. Note that, In Fig. 3, the baseline configuration's eigenvalue with the largest imaginary part has the value of 10π. When we next halve the element size while maintaining the same number of wake elements, thus shortening the wake, the total number of eigenvalues remains constant. However, the frequency range of the original eigenvalues has doubled. Thus we see that refining the grid has led to increasing the frequency range of the eigenvalue distribution. The spacing of the eigenvalues has also increased by about a factor of two. As is seen in the next paragraph, the latter result is because the computational domain has been reduced by nearly half, that is, the wake length is shorter.

Now consider what happens as the extent of the wake length is decreased while the grid spacing is held constant. In Fig. 4, the baseline configuration is compared to an aerodynamic model that has half as many aerodynamic elements in the wake. Now we see that the spacing between eigenvalues has increased by about a factor of two, but the largest imaginary part of the eigenvalue distribution (frequency) is unchanged. Hence, the effect of extending the wake length (for a fixed-grid resolution) is to refine the resolution of the eigenvalue distribution, but not to change the maximum frequency of the eigenvalue distribution. A more in-depth interpretation of this behavior is given by Heeg and Dowell [24] along with further details and numerical examples.

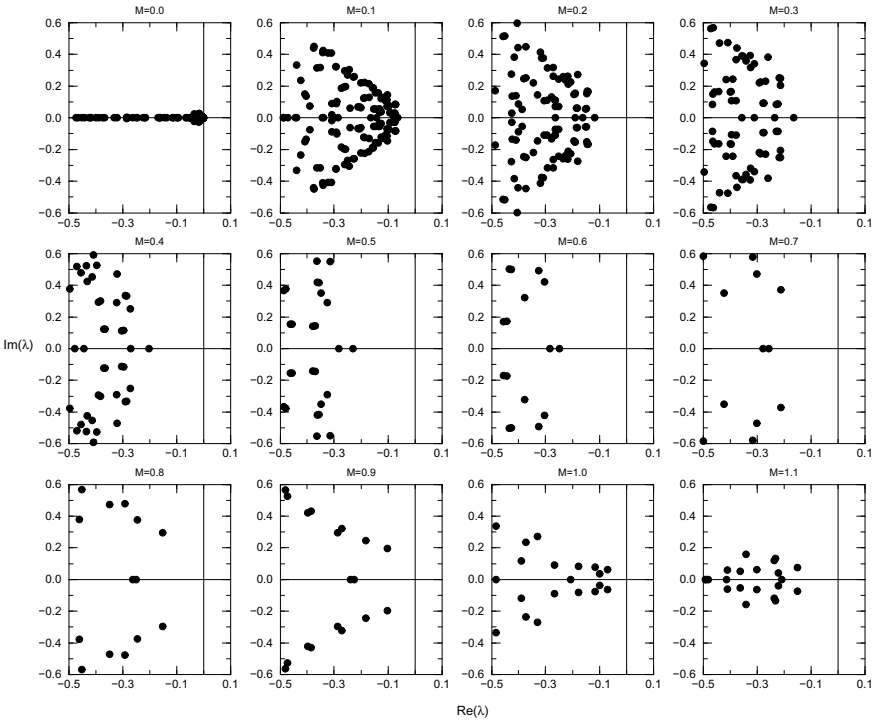

Fig. 5 Full aerodynamic eigenspectrums. Re, real; Im, imaginary, M, Mach number. Flat-plate airfoil (16 × 8 mesh). (Republished from Thomas et al. [44] with permission)

3.13.2 The Effects of Mach Number and Steady Angle of Attack: Subsonic and Transonic Flows

Here we examine some recent results from Hall et al. [20] and Thomas et al. [44] and also Florea et al. [15]. Hall et al. used an Euler equation flow model with a frequency domain POD method, and Thomas et al. used a transonic potential-flow model with a now standard eigenvalue, eigenmode formulation. Although different flow models and modal representations were used, the results of these two studies lead to similar conclusions regarding the nature of the flow and the efficacy of a modal representation of the aerodynamic flow.

In Fig. 5, the full eigenvalue spectrum for a flat plate airfoil using a coarse computational grid is shown to elucidate the effects of Mach number from $M = 0$ to $M = 1.1$. These results are from Thomas et al. [44]. Interestingly, the eigenvalue spectrum changes notably over this range. For $M = 0$, all of the eigenvalues are real and negative. Hence none of the eigenmodes have an oscillatory character. For any $M > 0$, however, eigenvalues that are complex conjugates appear along with real eigenvalues. The eigenvalue pattern continues to evolve as the Mach number increases, with another significant change in character occurring in the transonic

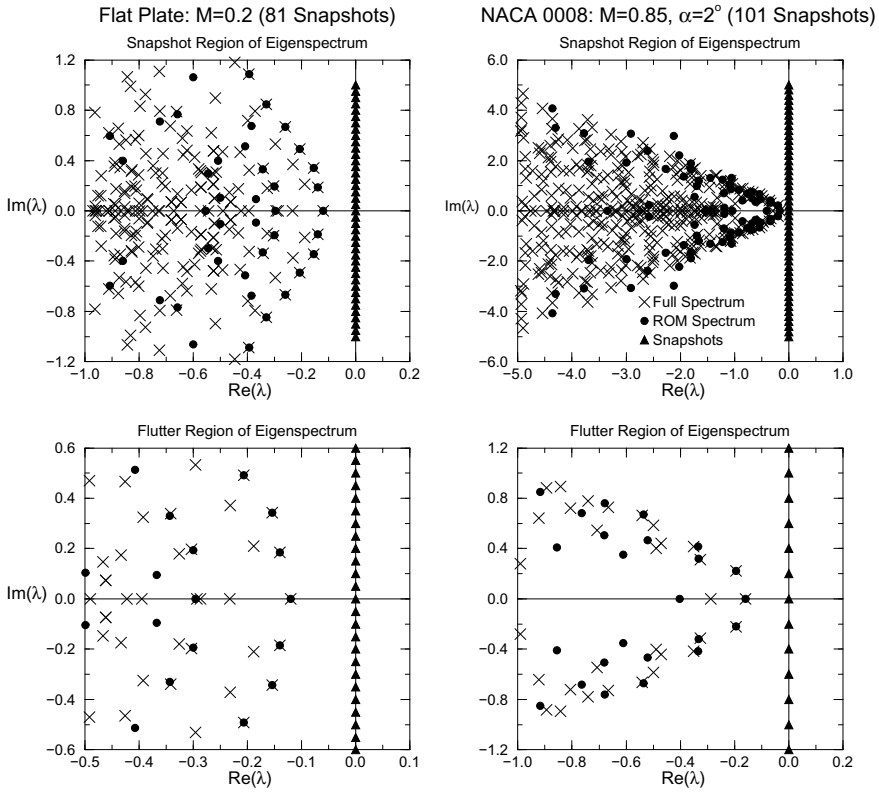

Fig. 6 A comparison of the full and ROM aerodynamic eigenspectrums. Re (λ), real eigenvalues; Im(λ), imaginary eigenvalues; M, Mach number; α, angle of attack. (Republished from Thomas et al. [44] with permission)

range from $M = 0.9$ to $M = 1.1$. The corresponding eigenmodes have also been determined, including the characteristic pressure distributions on the airfoil. Typically, the eigenmode that corresponds to the smallest negative real eigenvalue has a pressure distribution similar to that for steady flow at a constant angle of attack.

As an aside, it is very interesting that the eigenvalues for $M = 0$ are distributed along the real axis in Fig. 5, whereas in Fig. 3 they are distributed along the imaginary axis. In both cases these represent discrete approximation to a branch cut. It is well known from Theordorsen's theory for that the branch cut can be placed along a line emanating from near the origin of the complex plane (see Dowell et al. [8]). The results of Figs. 3 and 5 indicate that different CFD models for the same physical flow may place this branch cut along distinctly different rays from the origin. In Fig. 6, results are shown for a flat plate $M = 0.2$ and 0.9 and an NACA 0008 airfoil at $M = 0.85$. For the latter, a shock is present. Results are shown for a finer mesh that is typical of CFD calculations, and results are shown from the full eigenspectrum and those eigenvalues of the flow obtained by using 100 POD modes to construct a ROM.

The POD modes were determined using solutions at discrete values, often called snapshots in the POD literature, computed at uniformly distributed frequencies in the range $-1.0 < Im[\lambda] < 1.0$. The dominant eigenmodes are well approximated by the POD/ROM model. Note the characteristic distribution pattern of the eigenvalues as a function of Mach number, including with and without shock. Further results have been obtained for an NACA 64A006 airfoil (see Florea et al. [15]). The CFD grid is shown in Fig. 7, and the steady-flow pressure distribution is shown in Fig. 8.

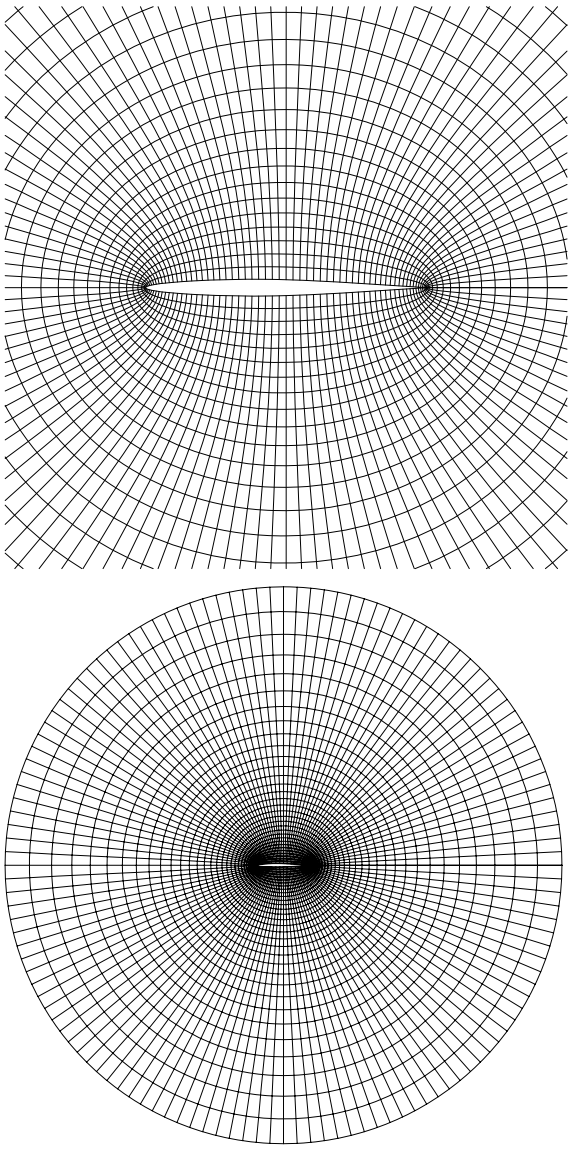

Fig. 7 Computational grid used for an NACA 64A006 airfoil. (Republished from Hall et al. [20] with permission)

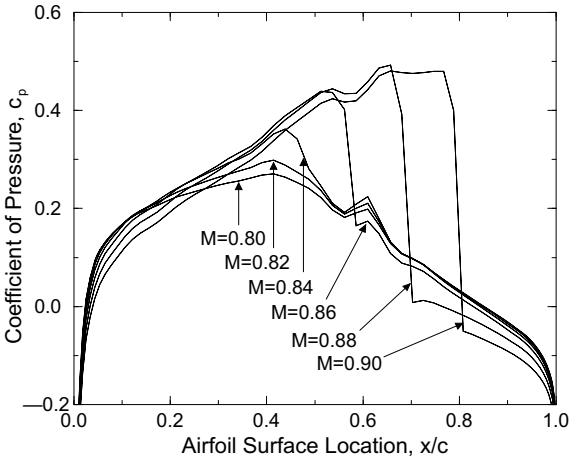

Fig. 8 Steady-background-flow surface pressure coefficient. M, Mach number. (Republished from Hall et al. [20] with permission)

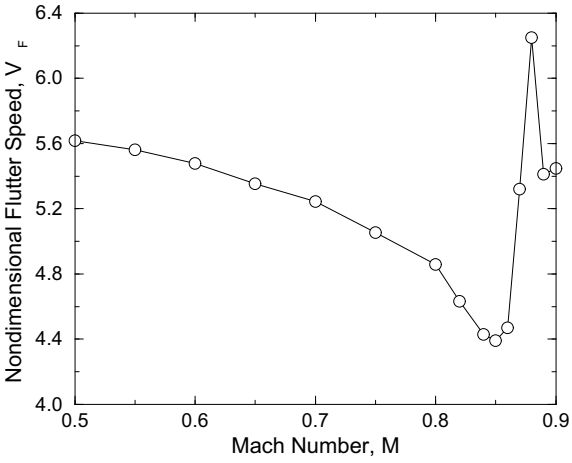

Fig. 9 Flutter speed variation (V_F) with Mach number (M). (Republished from Hall et al. [20] with permission)

Note that a shock is distinctly present for $M > 0.86$. For this airfoil, a bending/torsion flutter analysis is conducted over the Mach number range $M = 0.5 - 0.9$. The flutter boundary is shown in Fig. 9. Root loci for the two dominant aeroelastic modes (which originate in the plunging and pitching structural modes at low Mach number) are shown in Fig. 10 for Mach numbers in the range $M = 0.8 - 0.9$. These root loci show that in the Mach number range where the position of the shock on the airfoil moves appreciably, the critical eigenmode for flutter changes from the plunging mode to the pitching mode. There is a corresponding and sharp change in the flutter boundary (cf Fig. 9). One of the benefits of a reduced-order-modal representation of the aerodynamic flow is the capability and ease of constructing such root loci, which provide a significantly improved understanding of transonic flutter over other methods of stability analysis, for example, time-marching solutions.

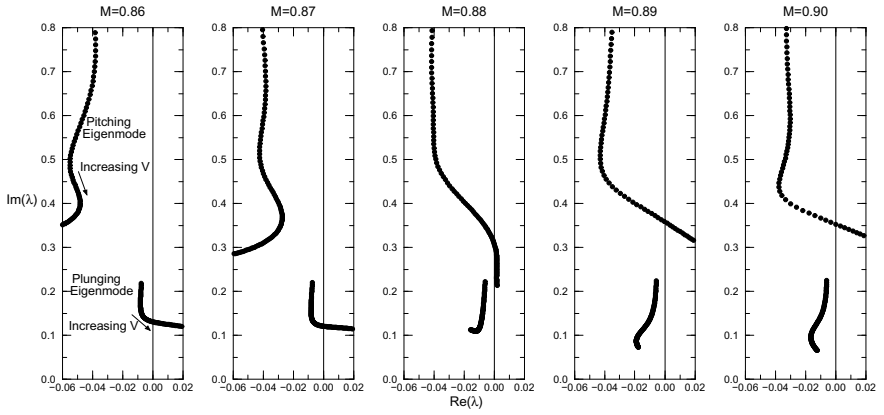

Fig. 10 Loci of pitching and plunging roots of aeroelastic system. Re(λ), real eigenvalues; Im(λ), imaginary eigenvalues; M, Mach number; V, variation. (Republished from Hall et al. [20] with permission)

We now turn to some complementary results from Florea et al. [15], who have studied an NACA 0012 airfoil and an MBB A3 airfoil. We present results only for the former airfoil here. The grids used for the CFD models are shown in Fig. 11. In addition to the basic grid, a refined grid in the vicinity of the shock wave was also considered. In Fig. 12, the steady flow pressure distribution is shown form $M = 0.75$ and several steady angles of attack. The corresponding eigenvalue distributions are shown in Fig. 13. Somewhat surprisingly perhaps, the eigenvalue distribution does not change radically with angle of attack changes, even though the flow at zero angle of attack is shockless, while that at a 2^0 angle of attack has a strong shock.

Another comparison of eigenvalue distributions is shown in Fig. 14 where the angle of attack is held at 0, but a range of Mach numbers is considered. Although over the full range of Mach numbers the eigenvalue distribution does change, there is not radical change in the high subsonic, transonic range per se.

Finally, in Fig. 15, a comparison is shown between the results of the full CFD model ($>$ 5000 degrees of freedom) and those from a ROM. Two different versions of the ROM are used with 67 and 160 degrees of freedom, respectively. Good correlation is obtained between the full CFD model and the ROM for lift and moment on an oscillating airfoil over a wide range of reduced frequencies.

The Effects of Viscosity

Epureanu et al. (2000) have considered the effects of viscosity by using the POD methodology in the frequency domain. Also see the earlier results by Florea et al. [13] using the direct eigenvalue approach. The results of Epureanu et al. (2000) are for a cascade of airfoils. The basic flow model uses a potential description in the outer

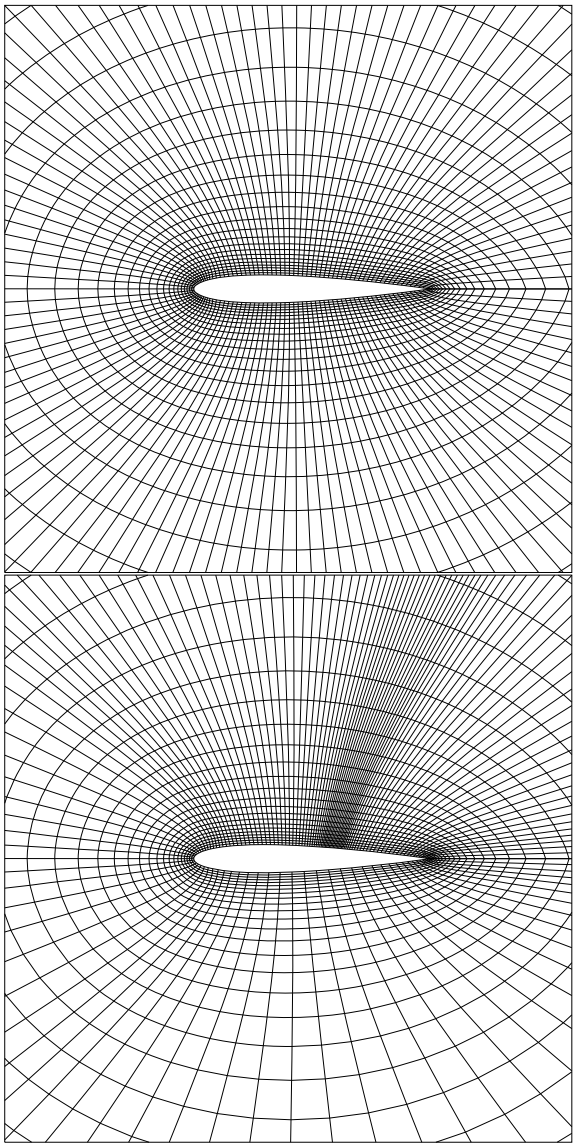

Fig. 11 Typical 129 × 43-node grid about an NACA 0012 isolated airfoil. (Top) initial grid; ($bottom$) locally refined grid. (Republished from Florea et al. [15] with permission)

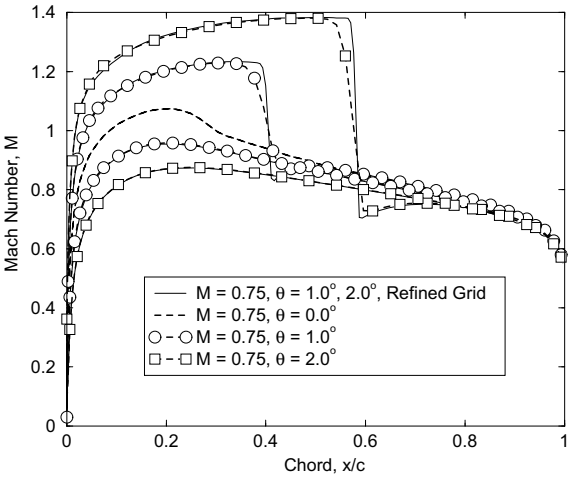

Fig. 12 Steady Mach number (M) and pressure distribution on surface of NACA 0012 airfoil at different angles of attack. Freestream Mach number $M_\infty = 0.75$. (Republished from Florea et al. [15] with permission)

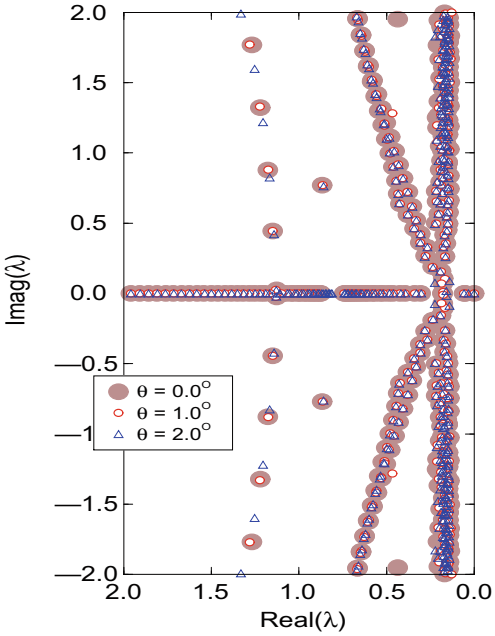

Fig. 13 Real [Real(λ)] and imaginary [Imag(λ)] eigenvalues of unsteady flow about NACA 0012 airfoil at different angles of attack, M_∞=0.75. (Republished from Florea et al. [15] with permission)

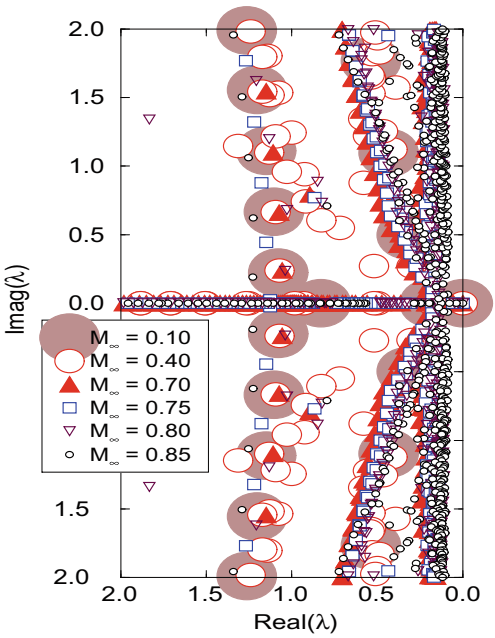

Fig. 14 Real [Real(λ)] and imaginary [Imag(λ)] eigenvalues of unsteady flow about NACA 0012 airfoil for different Mach number (M) at zero angles of attack. (Republished from Florea et al. [15] with permission)

inviscid region and a simplified integral boundary layer model in the inner region. The solution domain is shown in Figs. 16 and 17. A comparison of results from this model wit a Navier-Stokes solver has shown reasonable agreement. Comparisons have also been made with experimental data showing reasonable correlation.

Representative comparisons are shown between the full CFD model and a POD/ROM in Fig. 18 for a pressure distribution at fixed interblade phase angle and frequency, in Fig. 19 for lift versus interblade phase angle for a fixed frequency, and in Fig. 20 for lift versus reduced frequency for a fixed interblade phase angle. The results are in generally good agreement given the complexity of the flow. A reduction in degrees of freedom by two orders of magnitude or more is realized for this example. Note that no more degrees of freedom are required to model viscous flows than those required for inviscid flows, when considering aerodynamic pressures on a airfoil.

3.13.3 Nonlinear Aeroelastic Reduced-Order Models

One of the remaining challenges is to construct nonlinear aerodynamic ROMs. An example of a shock wave undergoing large oscillations in a one-dimensional channel has been treated by Hall in an as yet unpublished work (KC Hall, unpublished observations). However, no results from ROMs for flows about an airfoil undergoing large motions have yet been reported in the literature.

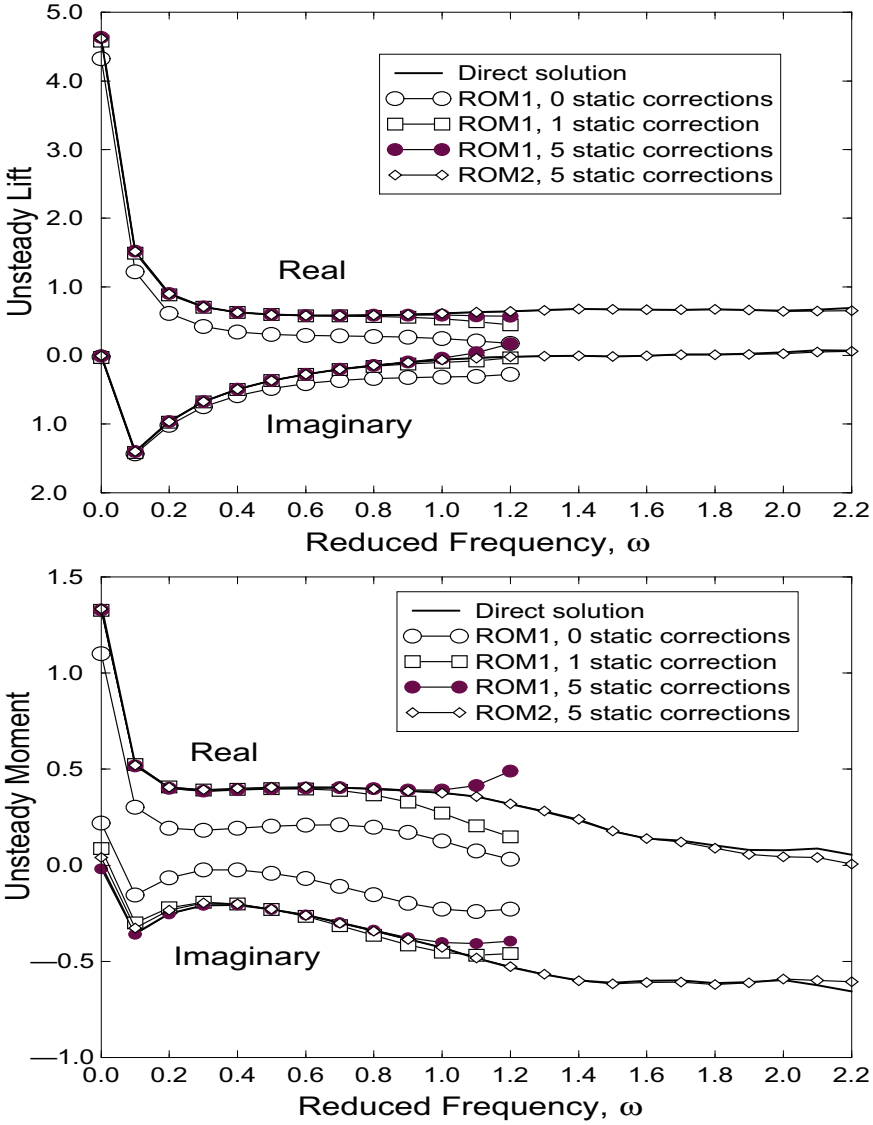

Fig. 15 Unsteady lift (*top*) and moment (*bottom*) on NACA 0012 airfoil pitching about its mid-chord ROM, reduced-order model. Mean flow conditions: $\theta = 2^0$, M_∞=0.75. Locally refined grid. (Republished from Florea et al. [15] with permission)

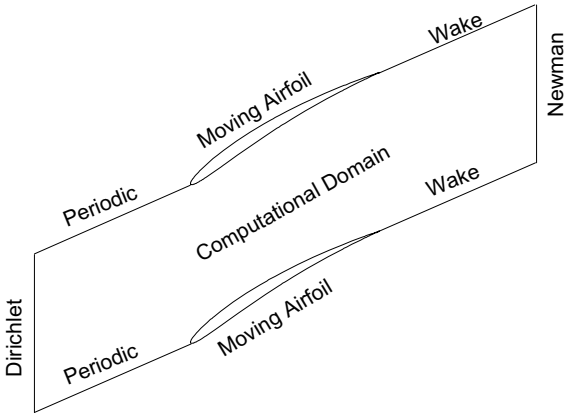

Fig. 16 Solution domain and boundary conditions used to calculate the inviscid flow. (Republished with permission from Epureanu et al. [12])

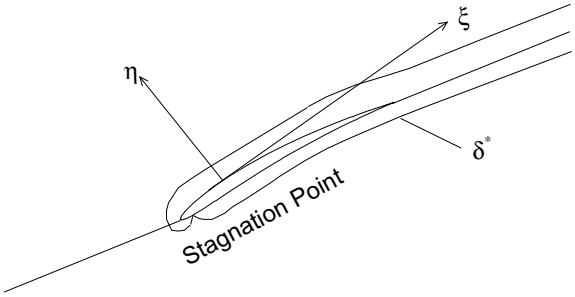

Fig. 17 Solution domain used to calculate the inviscid flow. Special local analytic solution is used at the stagnation point. The system of coordinates along the airfoil surface is indicated by ξ and η. A typical displacement thickness is sketched along the airfoil and wake. (Republished with permission from Epureanu et al. [12])

On the other hand, an example wing problem has been examined with a linear ROM vortex lattice aerodynamic model and a nonlinear structural model for a delta wing. The details are presented by Tang et al. [43]. Physically, a low Mach number and small angle of attack flow about a platelike structure undergoing oscillations on the order of the plate thickness are considered. For a plate, oscillations of this magnitude give rise to strong geometric structural nonlinearity. The consequence of this structural nonlinearity is that, once the flutter speed is exceeded, the wing goes into a limit cycle oscillation (LCO) of bounded amplitude. Of course, a purely linear aeroelastic model would predict exponentially growing oscillations for flow conditions beyond the flutter boundary. The use of ROMs for the fluid and structure makes calculations of this type of LCO practical.

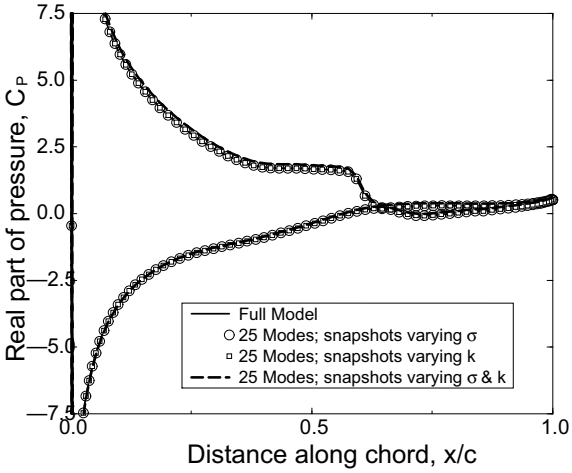

Fig. 18 Real part of the coefficient of pressure C_p obtained by using 25 POD modes when the interblade phase angle σ is 90^0, the reduced frequency k is 0.85, and the upwind far-field Mach number M is 0.5. (Republished with permission from Epureanu et al. [12])

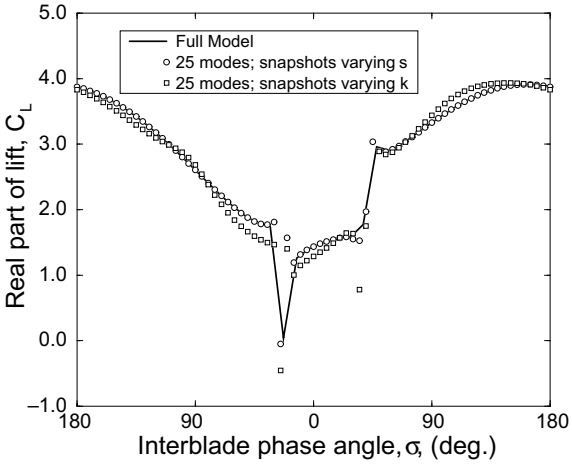

Fig. 19 Real part of the coefficient of lift C_L obtained by using 25 POD modes when the reduced frequency k is 0.85, and the upwind far-field Mach number M is 0.5. (Republished with permission from Epureanu et al. [12])

The geometry of the delta wing and its wake is shown if Fig. 21. A comparison between theory and experiment is shown in Fig. 22 for the flutter boundary and in Fig. 9.23 for the limit cycle oscillation.

4 Concluding Remarks and Directions for Future Research

With the construction of ROMs based on rigorous fluid dynamical theory, it is now possible to (a) provide a practical approach for constructing highly efficient, accurate, unsteady aerodynamic models suitable for fluid/structure modeling, (b) calculate true damping and frequency for all coupled fluid/structural (aeroelastic) modes at

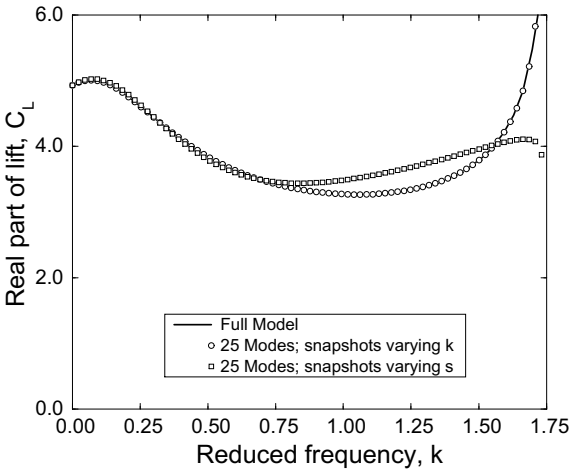

Fig. 20 Real part of the coefficient of lift C_L obtained by using 25 POD modes when the interblade phase angle σ is 90^0 and the upwind far-field Mach number M is 0.5. (Republished with permission from Epureanu et al. [12])

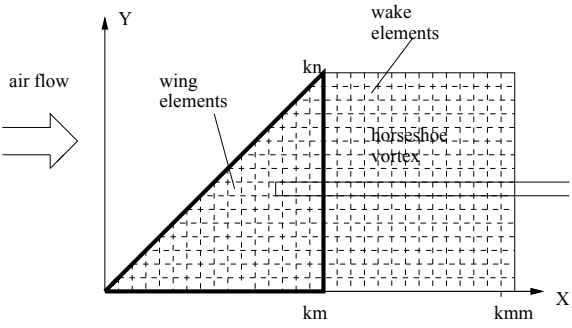

Fig. 21 Aeroelastic model of delta wing using vortex-lattice aerodynamic model. (Republished with permission from Tang et al. [43])

all parameter conditions, and (c) provide greater physical insight from aeroelastic analysis.

What more might the future bring?

Using fully (dynamically) nonlinear models, one should be able to develop rigorous ROMs that will accurately model large and violent aircraft motions, for example. For aeroacoustics phenomena in which the far-field radiation pattern is of prime interest, the eigenmode-ROM concept should work well also, but far-field boundary conditions will need special attention for this (or any other) approach. See Hardin and Hussaini [23] for a discussion of the present state-of-the-art in computational aeroacoustics. Finally, regarding turbulence and turbulence models, if we use a standard turbulence model, for example, κ-ϵ, etc, then the present method formally goes through. However, it is possible that the real value of the eigenmodal ROM approach will be to encourage the development of better turbulence models.

Is it possible that one could attack the full Navier-Stokes equations using the eigenmode-ROM methodology? The answer is that in some sense such work has already begun. The classical hydrodynamic-stability theory is an eigenmode

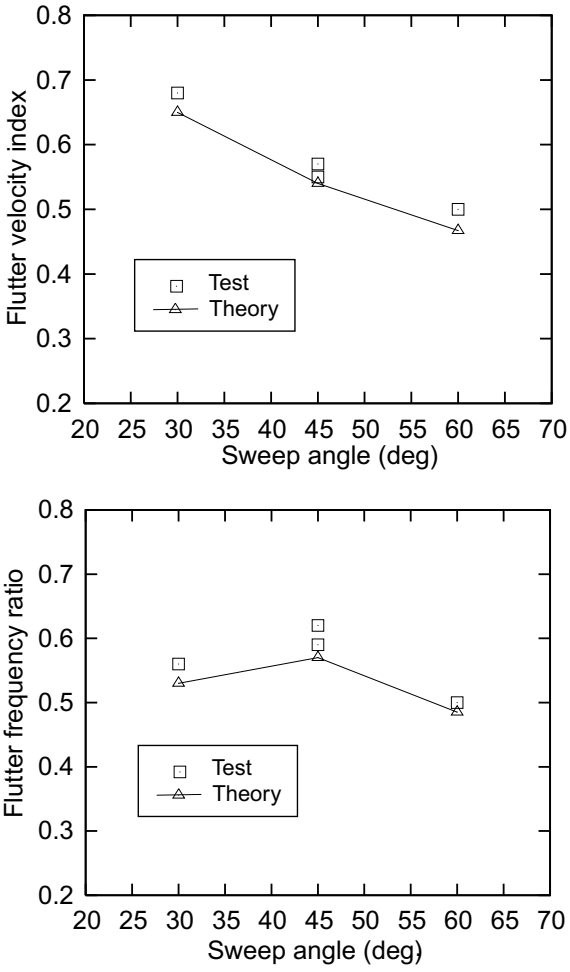

Fig. 22 Variation of flutter velocity index (*top*) and flutter frequency ratio (*bottom*) with sweep angle. (Republished with permission from Tang et al. [43])

approach based on the boundary layer approximation combined with a highly simplified geometry, a flat plate of infinite extent. However, the work per se, now some 50–70 years ago in its origins, did not lead to advances much beyond the limitations of the classical infinite geometry. Already, models with an outer inviscid model combined with viscous boundary layer theory have been developed, and some encouraging preliminary results are emerging. See Florea et al. [13] and Epureanu et al. 2000. Thus, one might hope to overcome that classical geometrical limitation and treat the larger-scale viscous motions about an airfoil or wing with a modern ROM. With these large-scale motions determined, it might even be possible to refine the eigenmode representation to determine local flow behavior. Clearly this is only a hypothesis, but a very intriguing one. It is certainly an open question as to the resolutions of turbulence length scales one may achieve with a given eigenmode or POD expansion.

The recent work of K.Y. Tang et al. [42] on ROMs in low-Reynolds-number flows using KL or POD modes is interesting in this regard. Also, see the pioneering work of Holmes et al. [25] discussed in their stimulating book.

Appendix: Singular-Value Decomposition, Proper Orthogonal Decomposition, and Balanced Modes

Let q_j^n be the nth flow variable at some spatial point at some time j where $n = 1, 2, ...N$ and $j = 1, 2, ...J$. Now from the matrix, $\tilde{\mathbf{Q}}$, as

$$[\tilde{\mathbf{Q}}] = \begin{bmatrix} q_1^1 & \cdots & q_J^1 \\ . & & . \\ . & & . \\ . & & . \\ q_1^N & \cdots & q_J^N \end{bmatrix}. \tag{16}$$

Again note that total number of time step is J, and the total number of flow variables is N. For a typical CFD calculation, J might be 1000, and N might be 10000 or more. Hence N is much greater than J.

Now assume a singular value decomposition of $\tilde{\mathbf{Q}}$; that is

$$\tilde{\mathbf{Q}} = \mathbf{U}\Sigma\mathbf{V}^T, \tag{17}$$

where $\mathbf{U}$ is a unitary matrix of dimension $N \times n$ and $\mathbf{V}$ is also a unitary matrix of dimension $J \times n$. We may select n and typically n will be less than J. Note that

$$[\mathbf{U}^T\mathbf{U}] = [\mathbf{I}]_{n\times n} \quad , \quad [\mathbf{V}^T\mathbf{V}] = [\mathbf{I}]_{n\times n}, \tag{18}$$

and Σ is a diagonal matrix of singular values; that is,

$$[\Sigma] = \begin{bmatrix} \sigma_1 & & & \\ & \sigma_2 & & \\ & & . & \\ & & & \sigma_n \end{bmatrix}. \tag{19}$$

We order these singular values such that

$$\sigma_1 \geq \sigma_2 \geq ..... \geq \sigma_n. \tag{20}$$

Now form Φ, the correlation matrix for the POD method:

$$\Phi = \tilde{\mathbf{Q}}^T\tilde{\mathbf{Q}} = \mathbf{V}\Sigma^T\mathbf{U}^T\mathbf{U}\Sigma\mathbf{V}^T = \mathbf{V}\Sigma^T\Sigma\mathbf{V}^T. \tag{21}$$

Equation 21 implies that $\mathbf{V}$ is the eigenvector of the correlation matrix and the corresponding eigenvalues are the squares of the singular values.

From Eq. 17, one may computer (assuming that $\mathbf{V}$ is normalized so that the magnitude of each eigenvector is unity),

$$\tilde{\mathbf{Q}}\mathbf{V} = \mathbf{U}\Sigma\mathbf{V}^T\mathbf{V} = \mathbf{U}\Sigma. \tag{22}$$

One may also compute $\mathbf{U}$ from Eq. 22, and further one may compute $\tilde{\mathbf{Q}}$ from a knowledge of $\mathbf{U}$, $\mathbf{V}$, and the singular values using Eq. 17. Usually it is easier to compute $\tilde{\mathbf{Q}}$ directly from Eq. 16, however. The representation of Eq. 17 may be useful if we choose to decompose $\tilde{\mathbf{Q}}$ such that

$$\tilde{\mathbf{Q}}(\mathbf{U}\Sigma^{\frac{1}{2}})(\Sigma^{\frac{1}{2}}\mathbf{V}^T). \tag{23}$$

With this decomposition the POD modes are said to be "balanced," and these are often put forth as an optimum choice for mode selection.

If there is a truncation in the singular values, that is, if we choose n to be less than J which is much less than N, then Eq. 17 may be written in a reduced form. The corresponding reduced form for $\tilde{\mathbf{Q}}$ approaches the original $\tilde{\mathbf{Q}}$ if the neglected singular values or POD eigenvalues are sufficiently small compared with those retained.

Denoting $\mathbf{V}$ as the eigenvector matrix for the correlation matrix of dimension $J \times n$, noting that $\tilde{\mathbf{Q}}$ is a matrix $N \times J$, and defining $\mathbf{a}$ as the new unknowns to be determined, which are the n modal amplitudes of the POD modes, then one may write the original flow variables, $\mathbf{q}$, as

$$\{\mathbf{q}(t)\}_{N\times 1} = [\tilde{\mathbf{Q}}]_{N\times J}[\mathbf{V}]_{J\times n}\{\mathbf{a}\}_{n\times 1}. \tag{24}$$

Substituting this expression into Eq. 5 of the main text, that is,

$$\frac{\partial}{\partial t}\{\mathbf{q}\} = \{\mathbf{Q}(\mathbf{q})\} + \{\mathbf{B}\}u, \tag{25}$$

and premultiplying by the transpose of $\tilde{\mathbf{Q}}$ [$\mathbf{V}$] gives a ROM in terms of the new unknowns $\mathbf{a}$, where the dimension of the vector $\mathbf{a}$ is $n \times 1$ with n chosen to be less than J. For simplicity, in Eq. 25, only a single scalar input, u, is shown. The generalization to multiple inputs is clear. If $\mathbf{Q}(\mathbf{q})$ in Eq. 25 is expanded in a Taylor series about a steady-flow solution (the time-linearized model corresponds to retaining only linear terms in $\mathbf{q}$ in the Taylor series), then a particularly simple and attractive form of the ROM is obtained.

There is another interesting case to consider which may arise when experimental data rather than numerical data from a CFD code are used to construct a ROM. In this case the number of low variables that are observed or measured, N, will be relatively small and typically N will be less than J, the total number of time steps for which

data are obtained. Formally the calculation still goes through, but now the number of flow variables modeled is much smaller than for a CFD code. Ideally these flow variables would be related to the amplitudes of the dominant modes of the flow.

References

1. Anderson WJ, Fung YC (1962) The effect of an idealized boundary layer on the flutter of cylindrical shells in supersonic flow, Rep. SM 62–49, California Institute of Technology. Pasadena, California
2. Baker ML, Mingori DL, Goggin PJ (1996) Approximate subspace iteration for constructing internally balanced reduced order models of unsteady aerodynamic systems. AIAA Paper 96–1441, presented at AIAA/ASME/ASCE/AHS/ASC Struct., Structures, Structural Dynanamics and Materials. Conference 37th, Salt Lake City, Utah
3. Bisplinghoff RL, Ashley H, Halfman RL (1995) Aeroelasticity. Addison-Wesley, Cambridge
4. Chi MR, Dowell EH (1977) Variable thickness shear layer aerodynamics revisited. AIAA J 15(5):745–747
5. Dowell EH, Hall KC, Thomas JP, Florea R, Epureanu BI, Heeg J (1999) Reduced order models in unsteady aerodynamics. AIAA paper 99–1261, presented at AIAA/ASME/ASCE/AHS/ASC Structures, Structural Dynanamics, and Materials. Conference 40th, St. Louis, Missouri
6. Dowell EH (1971) Generalized aerodynamic forces on a flexible plate undergoing transient motion in a shear flow with an application to panel flutter. AIAA J 9(5):834–841
7. Dowell EH (1975) Aeroelasticity of plates and shells. Noordhoff International Pub, Leiden
8. Dowell EH, Crawley EF, Curtiss HC Jr, Peters DA, Scanlan RH, Sisto F (1995) A modern course in aeroelasticity, 3rd edn. Kluwer Academic Publishers, Dordrecht
9. Dowell EH, Hall KC, Romanowski MC (1997) Eigenmode analysis in unsteady aerodynamics: reduced order models. Appl Mech Rev 50(6):371–386
10. Edwards JW, Malone JB, Batina JT, Lee EM, Kleb WL et al (1991) Transonic unsteady aerodynamics and aeroelasticity, AGARD-CP-507. Presented at AGARD Structure and Materials Panel, San Diego
11. Edwards JW (1979) Applications of Laplace transform methods to airfoil motion and stability calculations. AIAA Paper 79–0772, presented at AIAA Structures, Structures, Structural Dynanamics and Materials. Conference 20th, St. Louis, Missouri
12. Epureanu BI, Hall KC, Dowell EH (2001) Reduced order model of unsteady viscous flows in turbomachinery using viscous-inviscid coupling. J Fluids Struct 15(2):255–273
13. Florea R, Hall KC, Cizmas PGA (1998) Reduced-order modeling of unsteady viscous flows in a compressor cascade. AIAA J 36(6):1039–1048
14. Florea R, Hall KC, Cizmas PGA (1996) Reduced order modeling of unsteady viscous flow in a compressor cascade. AIAA paper 96–2572, presented at AIAA/ASME/SAE/ASEE, Joint Propulsion Conference, 32nd, Lake Buena Vista, Florida
15. Florea R, Hall KC, Dowell EH (1999) Eigenmode analysis and reduced order modeling of unsteady transonic full potential flow around isolated airfoils. Presented at CEAS/AIAA/ICASE/NASA Langley International Forum on Aeroelasticity and Structural Dynamics, Williamsburg, Virginia
16. Fung YC (1955) An introduction to the theory of aeroelasticity. Wiley, New York
17. Greco PC Jr, Lan CE, Lim TW (1995) Unsteady transonic aerodynamics in frequency domain and calculation of flutter characteristics of aircraft. SAE Technical paper, Ser. 951182, presented at SAE International Aviation Meeting and Exposition, Wichite, Kansas,
18. Greco PC Jr, Lan CE, Lim TW (1997) Frequency domain unsteady transonic aerodynamics for flutter and limit cycle oscillation prediction. AIAA paper 97–0835, presented at AIAA Aerospace Sciences Meeting, 35th, Reno, Nevada

19. Hall KC, Thomas JP, Clark WS (2000) Computation of unsteady nonlinear flows in cascades using a harmonic balance technique. In: 9th international symposium on unsteady aerodynamics aeroacoustics and aeroelasticity of turbomachines (ISUAAAT), Lyon, France, Sept 2000
20. Hall KC, Thomas JP, Dowell EH (1999) Reduced-order modeling of unsteady small-disturbance flows using a frequency-domain proper orthogonal decomposition technique. AIAA Paper 99–0655, presented at AIAA Aerospace Sciences Meeting and Exhibit, 37th, Reno, Nevada
21. Hall KC (1994) Eigenanalysis of unsteady flows about airfoils, cascades, and wings. AIAA J 32(12):2426–2432
22. Hall KC, Florea R, Lanzkron PJ (1995) A reduced order models of unsteady flows in turbomachinery. J Turbomach 117(3):375–383
23. Hardin JC, Hussani MY (eds) (1993) Computational aeroacoustics. ICASE/NASA LaRC Ser. New York, Springer, p 513
24. Heeg J, Dowell EH (1999) The discrete and finite domain approximations in CFD models: insights from eigenanalysis. Presented at CEAS/AIAA/ICASE/NASA Langley International Forum on Aeroelasticity and Structural Dynamics, Williamsburg, Virginia
25. Holmes P, Lumley JL, Berkooz G (1996) Turbulence, coherent structures, dynamical systems and symmetry. Cambridge University Press, Cambridge, p 420
26. Hwang H, Lan CE (1989) Direct solution of unsteady transonic flow equations in frequency domain. AIAA Paper 89–0641, presented at AIAA Aerospace Science Meeting, 27th, Reno, Nevada
27. Karpel M (1982) Design for active flutter suppression and gust alleviation using statespace aeroelastic modeling. J Aircr 19(3):221–227
28. Kim T (1998) Frequency-domain Karhunen-Loeve method and its application to linear dynamic system. AIAA J 36(11):2117–2123
29. Lighthill MJ (1953) Oscillating airfoils at high mach number. J Aeronaut Sci 20(6):402–406
30. Lin CC (1955) The theory of hydrodynamic stability. Cambridge University Press, Cambridge, p 155
31. Mahajan AJ, Bakhle MA, Dowell EH (1994) A new method for aeroelastic stability analysis of cascades using nonlinear, time-marching cfd solvers. AIAA Paper 94–4396, presented at AIAA/USAF/NASA/ISSMO Symposium on Multidisciplinary Analysis and Optimization, 5th, Panama City, Beach, Florida, Structures, Structural Dynanamics and Materials, Conference 40th, St. Louis, Missouri
32. McCroskey WJ (1982) Unsteady airfoils. Annu Rev Fluid Mech 14:285–311
33. Miles JW (1967) On the generation of surface waves by shear flows, part5. J Fluid Mech 30(1):163–175
34. Nixon D (ed) (1989) Unsteady transonic aerodynamics. In: Progress in Astronautics and Aeronautics, vol 120. AIAA, Washington, p 385
35. Parker R (1967) Resonance effects in wake shedding from parallel plates: calculation of resonant frequencies. J Sound Vib 5(2):330–334
36. Romanowski MC (1996) Reduced order unsteady aerodynamic and aeroelastic models using Karhunen-Loeve eigenmodes. AIAA Paper 96–3981, presented at AIAA/NASA/ISSMO Symposium on Multidisciplinary Analysis and Optimization, 6th, Bellevue, Washington
37. Romanowski MC, Dowell EH (1996) Reduced order euler equations for unsteady aerodynamic flows: numerical techniques. AIAA Paper 96–0528, presented at AIAA Aerospace Sciences Meeting, 34th, Reno, Nevada
38. Rule JA, Cox DE, Clark RL (2000) Aerodynamic model reduction through balanced realization. AIAA J (in press)
39. Seebass AR, Fung KY, Przybytkowski SM (1983) Advances in the understanding and computation of unsteady transonic flows. In: Krothapalli A, Smith CA (eds) Proceedings of the internatinal symposium recent advances in aerodynamics, Stanford University, August 22–26, 1983, Springer, New York, pp 3–77
40. Silva WA (1997) Discrete-time linear and of nonlinear aerodynamic impulse responses for efficient (CFD) analyses. PhD thesis, College of William and Mary, p 159

41. Silva WA (1993) Application of nonlinear systems theory to transonic unsteady aerodynamic responses. J Aircr 30(5):660–668
42. Tang KY, Graham WR, Peraire J (1996) Active flow control using a reduced order model and optimum control. AIAA paper 96–1946, presented at AIAA Fluid Dynamics Conference, 27th, New Orleans, Los Angels
43. Tang DM, Herry JK, Dowell EH (1999) Limit cycle oscillations of delta wing models in low subsonic flow. AIAA J 37(11):1355–1362
44. Thomas JP, Hall KC, Dowell EH (1999) Reduced order aeroelastic modeling using proper orthogonal decompositions. Presented at CEAS/AIAA/ICASE/NASA Langley International Forum on Aeroelasticity and Structural Dynamics, Williamsburg, Virginia
45. Tijdeman H, Seebass R (1980) Transonic flow past oscillating airfoils. Annu Rev Fluid Mech 12:181–222
46. Troger H, Steindl A (1991) Nonlinear stability and bifurcation theory: an introduction for engineers and applied scientists. Springer, New York
47. Ueda T, Dowell EH (1984) Flutter analysis using nonlinear aerodynamic forces. J Aircr 21(2):101–109
48. Vepa R (1976) On the use of pade approximates to represent aerodynamic loads for arbitrary small motions of wings. Presented at AIAA Aerospace Sciences Meetings, 14th, Washington DC
49. Winther BA, Goggin PJ, Dykman JR (1998) Reduced order dynamic aeroelastic model of development and integration with nonlinear simulation. AIAA Paper 98–1897, presented at AIAA/ASME/ASCE/AHS/ASC Structures, Structures, Structural Dynanamics and Materials. 39th, Long Beach, California

Experimental Aeroelasticity

Earl H. Dowell

Abstract This is a brief account of the basic elements underlying experiments in Aeroelasticity.

Much of this text has been devoted to mathematical modeling of physical phenomena in the field of aeroelasticity. Yet one of the most challenging and important aspects of the subject is the conduct of physical experiments. Experiments are useful for many purposes, e.g. to assess the accuracy and validity of theoretical models, to study phenomena beyond the current reach of theory, and/or to verify the safety and integrity of aeroelastic systems through wind tunnel tests or flight tests. A thorough exposition of this topic would require a volume in itself. Here a few of the fundamental aspects of experimental aeroelasticity are discussed. The focus is on aeroelastic tests per se rather than structural dynamic tests or unsteady aerodynamic measurements. However the latter will be touched on as well insofar as they are relevant to our principal topic.

For authoritative treatment of this subject the discussion by Ricketts [1] is highly recommended.

Before an aeroelastic experiment is conducted, it is usual to make measurements of the natural modes and frequencies of the structural model. Hence our discussion begins there.

1 Review of Structural Dynamics Experiments

In the jargon of the practitioners, these are referred to as ground vibration tests or GVT. The basic requirements are a means for exciting (forcing) the structure into its resonant, natural modes and also a means for measuring the response of the structure. For excitation systems a variety of devices have been used including those that provide mechanical forces, electromagnetic forces and acoustical excitation.

E. H. Dowell (✉)
Mechanical Engineering and Materials Science Duke University, Durham, NC, USA
e-mail: earl.dowell@duke.edu

E. H. Dowell (ed.), *A Modern Course in Aeroelasticity*, Solid Mechanics and Its Applications 264, https://doi.org/10.1007/978-3-030-74236-2_10

The choice of excitation depends primarily upon the level of force required and the range of frequency to be covered. For lightly damped systems excited in a resonant mode, the force level needed can be estimated as the mass of the structure times the frequency squared times (twice) the critical damping ratio times the amplitude of response required, i.e. the inertial and stiffness terms nearly cancel and the exciting force is balanced by structural dissipation or damping. The response amplitude required is typically determined by the sensitivity of available response measurement instrumentation or perhaps the need for the response to be in a certain linear (or less usually, nonlinear) range of response.

In practical terms mechanical excitation systems are used for low frequencies (say 1–100 Hz), electromagnetic exciters (shakers) are used for moderate frequencies (say 10–1000 Hz) and acoustic excitation at high frequencies (say 100–10000 Hz).

The response measurement systems may be either mechanical (strain gauges or accelerometers), electromagnetic (some electromagnetic devices may be used as either exciters or response measurement devices) or, more recently piezoelectric devices[1] that may be used to either serve as exciter or responder.

The basic measurement technique is to excite the system at its resonant frequencies (usually having theoretical calculations as a guide) with the excitation and response devices placed at locations on the structure expected to have large response. Multiple exciters are used to distinguish between symmetric and anti-symmetric natural modes or to excite modes with complex shapes. In principle, a continuous distribution of excitation with a distribution of force amplitude proportional to the expected (mass weighted) natural mode (and therefore orthogonal to all other natural modes) is optimum. Rarely can so many exciters be used in practice to approach this ideal.

If a pure frequency excitation is used, then a transient decay time history or a half-power frequency response plot may be used to estimate modal natural frequency and damping (e.g. see Thomson[2] or any standard text on vibration theory).

Also a random excitation over the range of relevant frequencies may be used to identify multiple modes with one excitation. This is used only when test time is limited. Another possibility is pulse excitation in the time domain and the use of Fast Fourier transform theory to extract information on multiple natural modes. Commercial hardware and software is now widely available to perform the latter measurement.[3] However for precise work the old fashioned methods may still be preferred.

Of course, if any significant nonlinearities are present, nonlinear theory must be used to guide the form of excitation, measurement and data interpretation. The range of possibilities is too extensive to be easily summarized. But the presence of higher harmonics in the response measurement is often a key observation that suggests nonlinearities are present and important.

---

[1] See Crawley [2].

[2] See Thomson [3].

[3] See, e.g., ZONIX, HEWLETT PACKARD and other manufacturers' catalogs and equipment manuals.

2 Wind Tunnel Experiments

With the presence of flow the environment for excitation and measurement of response is more complex, but the basic devices for creating, measuring and interpreting the responses remain the same as for the simpler structural dynamics experiments. Sometimes the aerodynamic turbulence in the tunnel is used to provide a random excitation and, of course, for self-excited instabilities (e.g. flutter) no special requirements are (in principle) necessary to excite the aeroelastic system. Nevertheless, where practicable, it is desirable to have an excitation system available of the conventional sort, e.g. mechanical, electromagnetic, acoustic, or perhaps, piezoelectric. Such excitations allow one to conduct sub-critical response experiments(i.e. experiments conducted below the flutter boundary). One of the principal challenges in flutter testing is to be able to extrapolate to flutter (critical) conditions from sub-critical measurements.

2.1 Sub-critical Flutter Testing

By monitoring the change of modal damping with change in flow dynamic pressure, for example, one may try to anticipate the value of dynamic pressure for which the modal damping will become zero and then negative. However, because of the sometimes complicated and rapid variation of damping with dynamic pressure and the necessity to monitor several potentially critical modes, it is often difficult to extrapolate to this flutter condition. Indeed extrapolation techniques for this purpose remain an active area of research.[4]

For certain types of flutter, monitoring the changes in modal frequencies may also be a useful guide to help predict the onset of flutter.

2.2 Approaching the Flutter Boundary

For low speed (incompressible flow) flutter tests, the flutter boundary is normally approached by increasing the flow velocity in suitable increments. For high speed (compressible flow) flutter tests, the Mach number is normally fixed, and the flutter boundary is approached by increasing the wind tunnel stagnation pressure, and hence dynamic pressure, in suitable increments. Then the Mach number is changed and the process repeated. At very high Mach numbers, a blow-down (transient flow) wind tunnel may be the only flow facility available. However, a continuous flow, closed return tunnel is to be preferred when available in order to assure well defined flow conditions and give adequate time for accurate response measurements.

[4] See Matsuzaki [4].

2.3 Safety Devices

Normally some provision will be made for suppression of the flutter response by a rapidly applied restraint to the flutter model, in order to protect the model from damage due to flutter.

2.4 Research Tests Versus Clearance Tests

Research tests are normally conducted to provide experimental data for comparison with theory and hence usually rather detailed data sets are obtained over a wide range of flow and/or structural parameters. Clearance tests are designed simply to show a particular flutter model is unlikely to encounter an instability over a range of anticipated operational conditions.

2.5 Scaling Laws

By expressing the aeroelastic equations of motion in non-dimensional form or by simply using dimensional analyses, it is possible to relate the behavior of the small scale models typically tested in wind tunnels so that of full-scale aircraft in flight.[5] Often not all relevant non-dimensional parameters can be matched between tunnel scale and flight scale due to the imitations of modal fabrication and wind tunnel flow conditions. Selecting an appropriate set of scaling parameters is a matter of intelligent application of theory (i.e. matching those non-dimensional parameters that are most important and sensitive as predicted by analysis) and judgement based upon experience. Normally modal frequency ratios, reduced frequency, Mach number and a non-dimensional ratio of dynamic pressure to model stiffness are matched. Frequently fluid/structural mass ratio is not.

Wind tunnel tests are extraordinarily valuable and often fill in gaps in our knowledge where theory is unavailable or unreliable.

3 Flight Experiments

Virtually all the previous comments for wind tunnel tests apply to flight tests as well. However the need for safety is now paramount and the challenges of providing a well defined excitation force are considerably higher. Also the test procedure is necessarily different.

[5] See Dugundji and Calligeros for a particularly valuable discussion [5].

3.1 Approaching the Flutter Boundary

Normally the flutter boundary has been estimated from a suitable combination of analysis and wind tunnel experiment prior to the flight test and presented in terms of altitude (corresponding to a certain static or dynamic pressure) vs Mach number. Usually the Mach number at which flutter will occur increases with increasing altitude. Hence flutter testing normally begins at high altitude (this also provides more margin for emergency procedures including the pilot leaving the aircraft). At fixed altitude the Mach number is increased in small increments until flutter occurs or the maximum Mach number capability of the aircraft is reached.

When is flight flutter testing required?

For new aircraft, for substantial modifications of existing aircraft and for new uses of an existing aircraft, flutter testing is usually required.

3.2 Excitation

Several excitation methods have been proposed and used. None are clearly superior. Use of existing hardware, e.g. control stick raps, electronic inputs to the control system, or atmospheric turbulence, obviously minimize cost. On the other hand, add-on devices, such as oscillating vanes, inertial mass oscillations, or pyrotechnic devices presumably give greater control and range to the excitation. The rotating slotted cylinder device proposed by Reed[6] shows promise of being a good compromise between cost and performance. Examples of excitation systems that have been used in practice are shown in Fig. 1.[7]

3.3 Examples of Recent Flight Flutter Test Programs

To remind the reader of the danger inherent in such tests, Fig. 2 shows the loss of a substantial portion of the tail surface from the recent flutter testing of the F-117A Stealth fighter. Other examples of recent programs are described in Table I (Fig. 3).

[6] See Reed [6].

[7] After Reed [6]. All Figures and Tables in this chapter are drawn from [6].

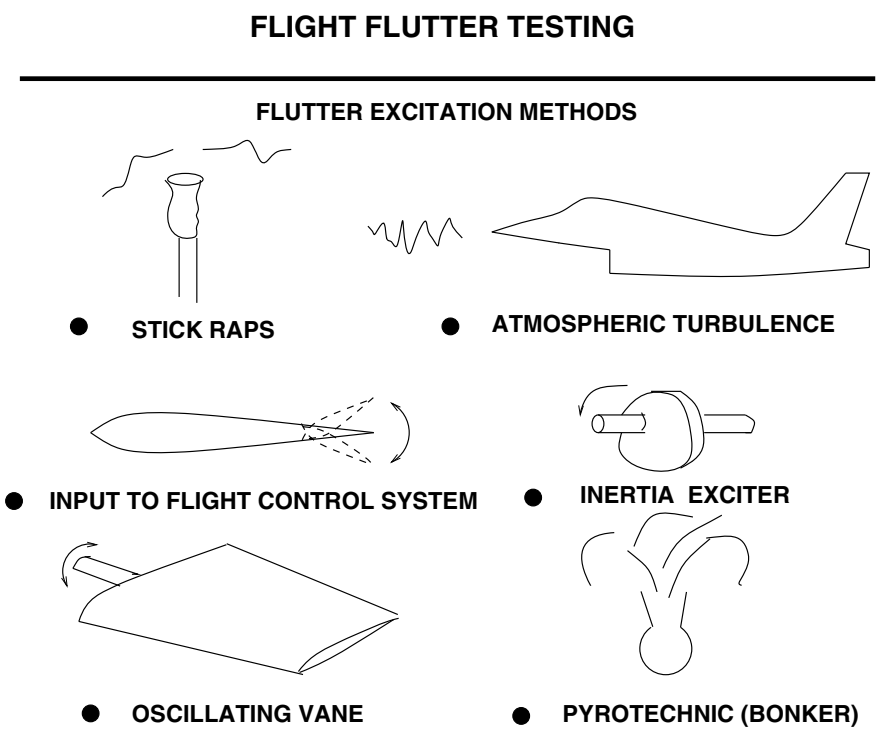

Fig. 1 Various devices for exciting an aircraft structure

4 The Role of Experimentation and Theory in Design

In designing a new aircraft with acceptable aeroelastic behavior, a synergistic combination of theory, wind tunnel tests and flight tests is normally employed. Here a brief overview is presented of how this is usually done.

One measure of the relative importance of each of these synergistic elements is their cost. Baird[8] has estimated these for the F-14 aircraft. See Table II (Fig. 4).

In Table III (Fig. 5) a flow chart is shown that indicates the interaction among these elements. Note that each element normally influences another. For example, analysis and wind tunnel tests help define the flight flutter test program. Conversely any anomalies determined during flight test will almost assuredly lead to additional analysis and wind tunnel tests.

[8] Baird [7].

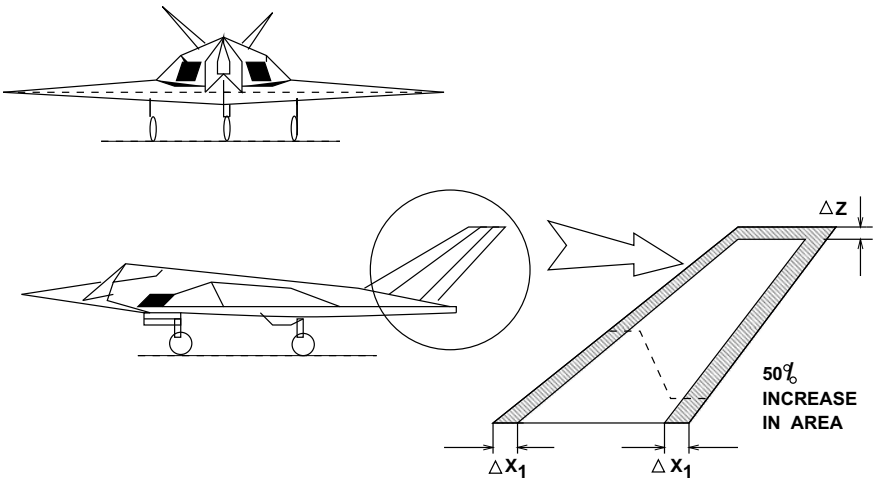

Fig. 2 Loss of aircraft tail structure due to flutter

Finally, although the emphasis here has been on flutter experiments, gust response experiments or static aeroelastic behavior may be the subject of tests as well. The techniques employed are similar to those for flutter, with pilot and aircraft safety usually not as much a critical concern as with flutter tests.

FLIGHT FLUTTER TESTING

EXAMPLES OF RECENT FLIGHT FLUTTER TEST PROGRAMS

- **X-29 FORWARD SWEPT WING DEMONSTRATOR**
  - THREE DIFFERENT FLIGHT CONTROL SYSTEMS TO TEST
  - NEW STRUCTURE
  - 218+ TEST POINTS TO CLEAR THE FLIGHT ENVELOPE
  - EXCITATION: TURBULENCE AND ROTATY INERTIA SHAKERS FOR THE FLAPERONS
- **F-18 HARV AIRPLANE (TO BE TESTED SUMMER 1991)**
  - MODIFICATION: TURNING VANES-STRUCTURE AND FLIGHT CONTROL LAWS
  - EXCITATION: COMMANDS TO THE FLIGHT CONTROL SURFACES
  - TWO DIFFERENT FLIGHT CONTROL SYSTEMS TO TEST
  - ESTIMATE OVER 80 TEST POINTS TO CLEAR FLIGHT ENVELOPE
    - ANGLE OF ATTACK RANGE: 0° TO 70°
    - MACH NUMBER:MULTIPLE POINTS UP TO 0.7 MACH
- **SCHWEIZER 1-36 DEEP-STALL SAILPLANE**
  - MODIFICATION:HORIZONTAL STABILIZER MODIFIED TO PIVOT TO 70° FOR CONTROLLABITY RESEARCH WITH COMPLETELY STALLED
  - GROUND TEST PERFORMED PRIOR TO FLIGHT TEST DUE TO NONLINEAR STRUCTURAL DYNAMICS BEHAVIOR OF TAIL
  - EXCITATION: TURBULENCE- DATA ACQUIRED AT CONSTANT SPEED DURING CONTINUOUS DESCENT IN ALTITUDE BANDS OF $\pm$1000 FEET ABOUT TEST ALTITUDE
  - STABILITY ANALYSIS: CLEARED IN REAL TIME BY MONITORING STRIP CHARTS
- **AFTI/F-16 AEROSERVOELASTIC AND FLUTTER TEST**
  - MODIFICATION: DIGITAL FLIGHT CONTROL SYSTEM AND CANARDS
  - EXCITATION: TURBULENCE AND STICK RAPS
  - STABILITY ANALYSIS: RECURSIVE IDENTIFICATION ALGORITHM USED TO SEPARATE CLOSELY SPACED MODES

Fig. 3 Table I for flight flutter testing

Fig. 4 Table II for F-14 flutter prevent program relative costs

F-14 FLUTTER PREVENT PROGRAM RELATIVE COSTS

• ANALYSIS	29 %	
• WIND TUNNEL	27 %	71 %
• GVT	19 %	
• FLIGHT FLUTTER TEST	25 %	

R and D COST 0.5 %

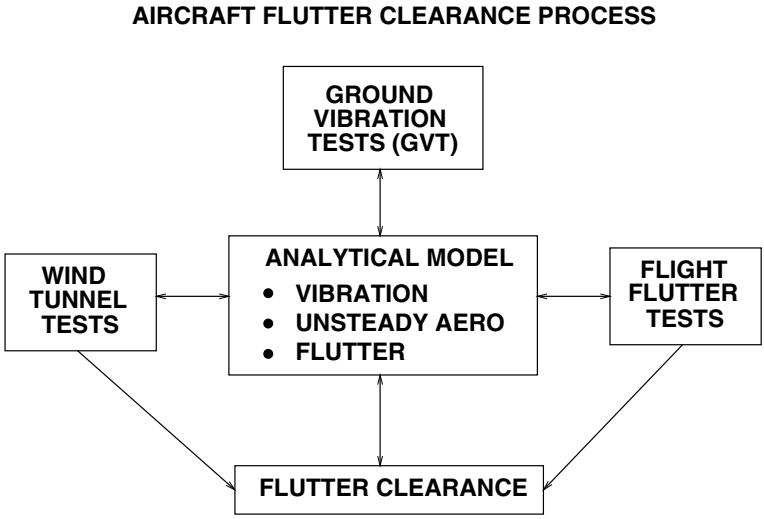

Fig. 5 Table III for aircraft flutter clearance process

References

1. Ricketts R (1990) Experimental aeroelasticity. AIAA Paper 90–0978
2. Crawley EF, Lazarus KB (1991) Induced strain actuation of isotropic and anisotropic plates. AIAA J 29(6):944–951
3. Thomson WT (1993) Theory of vibration with applications. Springer, Boston. https://doi.org/10.1007/978-1-4899-6872-2_9
4. Matsusaki Y, Ando Y (1981) Estimation of flutter boundary from random responses due to turbulence of subcritical speeds. J Aircract 18(10):862–868
5. Dugundji J, Calligeros JM (1962) Similarity laws for aerothermoelastic testing. J Aerospace Sci 29(8):935–950
6. Reed WH III (1991) Flight flutter testing: equipment and techniques, Presented at the FAS Southwest Region Annual Designer Conference. Ft, Worth, Texas
7. Baird EFJ, Personal communication with W. H. Reed III

Nonlinear Aeroelasticity

Earl H. Dowell

Abstract This is an introduction and overview of the work that has been done in nonlinear aeroelasticity prior to the last decade. Many of the issues discussed here are still under active investigation. Of particular interest are the limit cycle oscillations that may occur once the dynamic stability (flutter) boundary has been exceeded.

1 Introduction

Nonlinear aeroelasticity has been a subject of high interest for the last decade and the literature is now extensive.[1] An account of the state of the art is provided as of this writing with an emphasis on key ideas and results. These demonstrate our current theoretical, computational and experimental capabilities and the degree to which correlation among results from these several approaches agree or disagree. An exhaustive literature survey is not attempted here; however a bibliography of over eight hundred citations is available in electronic form from the first author upon request. The particular results and methods described must inevitably reflect the authors' knowledge and experience, but we have made an effort to be comprehensive in terms of ideas and representative with respect to results.

The chapter begins with a discussion of generic nonlinear aeroelastic behavior especially as it relates to Limit Cycle Oscillations (LCO); then the important studies that come from flight experience with LCO are noted which have stimulated much of the other research on the subject. Next a summary is provided of the primary physical sources of fluid and structural nonlinearities that can lead to nonlinear aeroelastic response in general and LCO more particularly.

A broad overview of unsteady aerodynamic models, both linear and nonlinear, is then given before turning to the heart of the chapter that provides a critique of

[1] This chapter is based upon an invited paper prepared by E.H. Dowell, J.W. Edwards and T. Strganac, "Nonlinear Aeroelasticity," *Journal of Aircraft*, Vol. 40, No .5, 2003, pp.857–874.

E. H. Dowell (✉)
Mechanical Engineering and Materials Science, Duke University, Durham, NC, USA
e-mail: earl.dowell@duke.edu

E. H. Dowell (ed.), *A Modern Course in Aeroelasticity*, Solid Mechanics and Its Applications 264, https://doi.org/10.1007/978-3-030-74236-2_11

the results obtained to date via various methods, using as a framework correlations between theory and experiment or alternative theoretical models. For these correlations unsteady aerodynamic forces per se, flutter boundaries and limit cycle oscillations are each considered in turn. For limit cycle oscillations (1) airfoils with stiffness nonlinearities, (2) delta wings with geometrical plate nonlinearities, (3) very high aspect ratio wings with both structural and aerodynamic nonlinearities, (4) nonlinear structural damping and (5) aerodynamic flows with large shock motions and flow separation are each discussed. A brief mention is also made of recent studies of active control of nonlinear aeroelastic systems.

The chapter concludes with a summary of major lessons learned by the research and development community to date and offers suggestions for future work that appear particularly attractive at this time.

2 Generic Nonlinear Aeroelastic Behavior

There are several basic concepts that will be helpful for the reader to keep in mind throughout the discussion to follow. The first is the distinction between a static nonlinearity and a dynamic one. In the aeroelasticity literature the term "linear system" may either mean a (mathematical or wind tunnel) model or flight vehicle that is both statically and dynamically linear in its response or one that is nonlinear in its static response, but linear in its dynamic response. So we will usually qualify the term "linear model" further by noting whether the system is dynamically linear or both statically and dynamically, i.e. wholly, linear.

An example of a system which is wholly linear is a structure whose deformation to either static or dynamic forces is (linearly) proportional to those forces. An aerodynamic flow is wholly linear when the response (say change in pressure) is (linearly) proportional to changes in downwash or fluid velocities induced by shape or motion of a solid body in the flow. This is the domain of classical small perturbation aerodynamic theory and leads to a linear mathematical model (convected wave equation) for the fluid pressure perturbation or velocity potential. Shock waves and separated flow are excluded from such flow models that are both statically and dynamically linear. A wholly linear aeroelastic model is of course one composed of wholly linear structural and aerodynamic models.

A statically nonlinear, but dynamically linear structure is one where the static deformations are sufficiently large that the static response is no longer proportional to the static forces and the responses to the static and dynamic forces cannot be simply be added to give meaningful results. Buckled skin panels (buckling is a nonlinear static equilibrium that arises from a static instability) that dynamically respond to (not too large) acoustic loads or the prediction of the onset of their dynamic aeroelastic instability (flutter) are examples where a statically nonlinear, but dynamically linear model may be useful.

In aerodynamic flows, shock waves and separated flows are themselves the result of a dynamically nonlinear process. But once formed they may often be treated in

the aeroelastic context as part of a nonlinear static equilibrium state (steady flow). Then the question of the dynamic stability of the statically nonlinear fluid-structural (aeroelastic) system may be addressed by a linear dynamic perturbation analysis about this nonlinear static equilibrium. Sometime such aerodynamic flow models are call time linearized.

Of course if one wishes to model nonlinear limit cycle oscillations and the growth of their amplitude as flow parameters are changed, then either or both the structural and the aerodynamic model must be treated as dynamically nonlinear. Often a single nonlinear mechanism is primarily responsible for the limit cycle oscillation. However, one may not know a priori which nonlinearity is dominant unless one has designed a mathematical model, wind tunnel model or flight vehicle with the chosen nonlinearity. Not the least reason why limit cycle oscillations are more difficult to understand in flight vehicles (compared to say mathematical models) is that rarely has a nonlinearity been chosen and designed into the vehicle. More often one is dealing with an unanticipated and possibly unwanted nonlinearity. Yet sometimes that nonlinearity is welcome because without it the limit cycle oscillation would instead be replaced by catastrophic flutter leading to loss of the flight vehicle.

It must be emphasized that the variety of possible nonlinear aeroelastic response behaviors is not limited to 'Limit Cycle Oscillations (LCO)' per se. In the context of nonlinear system theory [1], an LCO is one of the simplest dynamic bifurcations, a 'first stop on the road to chaos,' so to speak. Other common possible behaviors include higher harmonic and subharmonic resonances, jump-resonances, entrainment, beating (which can be due to either linear or nonlinear coupling), and period doubling to name only a few. These behaviors have been delineated and studied using low order model problems in the nonlinear dynamics literature; however in aeroelastic wind tunnel and flight testing, the detailed knowledge required to identify these nonlinear behaviors has rarely been available. Also, experience indicates that the concept of LCO is a good general description for many nonlinear aeroelastic behaviors. Thus, we will limit ourselves herein to the use of the generic term, LCO, acknowledging that this is an oversimplification.

Now let us turn to the generic types of nonlinear dynamic response that may occur, i.e. limit cycle oscillations and the variation of their amplitude with flight speed (or wind tunnel velocity). Of course the frequency of the LCO may vary with flight parameters as well, but usually the frequency is near that predicted by a classical linear dynamic stability (flutter) analysis.

The generic possibilities are indicated in Fig. 1 where the limit cycle amplitude is plotted verses some system parameter, e.g. flight speed. In Fig. 1a, an aeroelastic system is depicted that is stable to small or large disturbances (perturbations) below the flutter (instability) boundary predicted by a linear dynamical model. Beyond the flutter boundary, LCO arise due to some nonlinear effect and typically the amplitude of the LCO increases as the flight speed increases beyond the flutter speed. In Fig. 1b, the other generic possibility is shown. While again LCO exist beyond the flutter boundary, now LCO may also exist below the flutter boundary, if the disturbances to the system are sufficiently large. Moreover both stable (solid line) and unstable (dotted line) LCO now are present. Stable LCO exist when for any sufficiently small

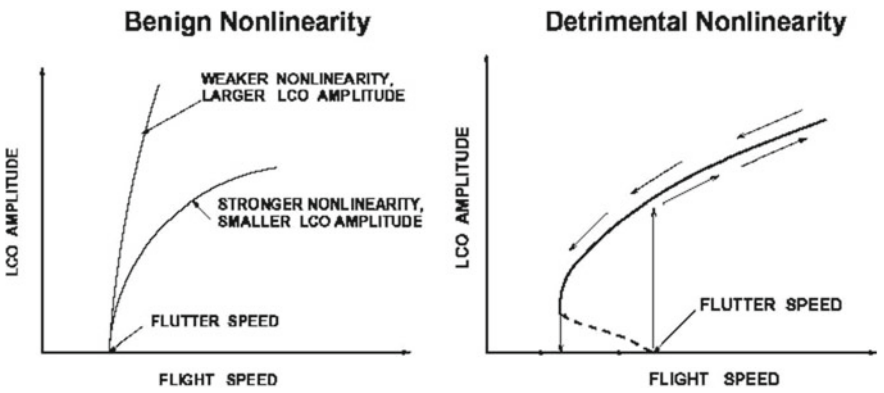

Fig. 1 Schematic of Limit Cycle Oscillation response

disturbance, the motion returns to the same LCO at large time. Unstable LCO are those for which any small perturbation will cause the motion to move away from the unstable LCO and move toward a stable LCO. Theoretically, in the absence of any disturbance both stable and unstable LCO are possible dynamic, steady state motions of the system. Information about the size of the disturbance required to move from one stable LCO to another can also be obtained from data such as shown in Fig. 1b. Note also the hysteretic response as flight speed increases and then decreases.

3 Flight Experience with Nonlinear Aeroelastic Effects

Much of the flight experience with aircraft has been documented by the Air Force Flight Test Center at Eglin AFB and is described in several publications by Denegri and his colleagues, [3–6]. Most of this work has been in the context of the F-16 aircraft. Denegri distinguishes among three types of LCO based upon the phenomenological observations in flight and as informed by classical linear flutter analysis. "Typical LCO" is when the LCO begins at a certain flight condition and then with say an increase in Mach number at constant altitude the LCO response smoothly increases. "Flutter", as distinct from LCO, is said to occur when the increase in LCO amplitude with change in Mach number is so rapid that the safety of the vehicle is in question. And finally "atypical LCO" is said to occur when the LCO amplitude first increases and then decreases and perhaps disappears with changes in Mach number. Often changes in flight vehicle angle of attack lead to similar generic LCO responses to those observed with changes in Mach number.

It has long been recognized [7] that the addition of external stores to aircraft changes the dynamic characteristics and may adversely affect flutter boundaries. Limit cycle oscillations (LCO) remain a persistent problem on high performance fighter aircraft with multiple store configurations. Using measurements obtained

from flight tests, Bunton and Denegri [8] describe LCO characteristics of the F-16 and F/A-18 aircraft. While LCO can be present in any sort of nonlinear system, in the context of aeroelasticity, LCO typically is exhibited as an oscillatory torsional response of the wing, the amplitude of which is limited, but dependent on the nature of the nonlinearity as well as flight conditions, such as speed, altitude, and Mach number. The LCO motion is often dominated by antisymmetric modes. LCO are not described by standard linear aeroelastic analysis, and they may occur at flight conditions below those at which linear instabilities such as flutter are predicted. Although the amplitude of the LCO may be above structural failure limits, more typically the presence of LCOs results in a reduction in vehicle performance, leads to airframe-limiting structural fatigue, and compromises the ability of pilots to perform critical mission-related tasks. When LCO are unacceptable for flight performance, extensive and costly flight tests for aircraft/store certification are required.

Denegri [3, 4] suggests that for the F-16, the frequencies of LCO might be identified by linear flutter analysis; however, linear analysis fails to predict the oscillation amplitude or the onset velocity for LCO. No definitive theory has been forwarded to explain completely the mechanisms responsible for F-16 LCO. Denegri notes that while linear techniques have been used to predict the frequency of LCOs, linear analysis cannot consistently predict where within the flight envelope the onset of the oscillations will occur. Thus, nonlinear analysis will be necessary to predict the onset of the LCO and their amplitudes with changing flight conditions. Such nonlinear analysis would be a useful and valuable tool for reducing the amount of flight testing necessary for aircraft/store certification.

3.1 Nonlinear Aerodynamic Effects

There are several other flight experiences with limit cycle oscillations in addition to the F-16 including those for example with the F-18, the B-1 and B-2. Most of these LCO have been attributed by a majority of investigators to nonlinear aerodynamic effects due to shock wave motion and/or separated flow. However, there is the possibility that nonlinear structural effects involving stiffness, damping or freeplay may play a role as well. Indeed, much of the present day research and development effort is devoted to clarifying the basic mechanisms responsible for nonlinear flutter and LCO. For an authoritative discussion of these issues see Cunningham et al., [9–11]; Denegri et al. [3–6] on the F-16 and F-18, Dobbs et al. [12]; Hartwich et al. [13] on the B-1 and Dreim et al., [14] on the B-2. Recent experimental evidence from wind tunnel tests is beginning to shed further light on these matters as are advances in mathematical and computational modeling.

In addition to the above studies, many aircraft with freeplay in their control surfaces have experienced LCO as well.

3.2 Freeplay

There have been any number of aircraft that have experienced flutter induced limit cycle oscillations as a result of control surface freeplay. Not surprisingly perhaps these are not well documented in the public literature, but are more known by word of mouth among practitioners and perhaps documented in internal company reports and/or restricted government files.

A recent and notable exception is the account in Aviation Week and Space Technology [15] of a flutter/limit cycle oscillation as a result of freeplay. In many ways this account is typical. The oscillation is of limited amplitude and there was a reported disagreement between the manufacturer and the regulating governmental agency as to whether this oscillation was or was not sufficiently large as to be a threat to the structural integrity of the aircraft structure.

3.3 Geometric Structural Nonlinearities

Another not infrequently encountered and documented case is the limit cycle oscillation that follows the onset of flutter in plate-like structures. The structure has a nonlinear stiffening as a result of the tension induced by mid-plane stretching of the plate that arises from its lateral bending. This is most commonly encountered in what is often called panel flutter where a local element of a wing or fuselage skin encounters flutter and then a limit cycle oscillation. There have been many incidents reported in the literature dating back to the V-2 rocket of World War II, the X-15, the Saturn Launch Vehicle of the Apollo program and continuing on to the present day. Some of these are discussed in a monograph by Dowell [16] and also a NASA Special Publication Dowell [17].

It has been recently recognized that low aspect ratio wings may behave as structural plates and the entire wing may undergo a form of plate-like flutter and limit cycle oscillations. This has been seen in both wind tunnel models and computations. However there is not yet a clearly documented case of such behavior in flight.

4 Physical Sources of Nonlinearities

These have been identified through mathematical models (in almost all cases), wind tunnel tests (in several cases) and flight tests (less often). Among those most commonly studied and thought to be among the more important are the following. Large shock motions may lead to a nonlinear relationship between the motion of the structure and the resulting aerodynamic pressures and forces that act on the structure. If the flow is separated (perhaps in part induced by the shock motion) this may also create

a nonlinear relationship between structural motion and the consequent aerodynamic flow field.

Structural nonlinearities can also be important and are the result of a given (aerodynamic) force on the structure creating a response that is no longer (linearly) proportional to the applied force. Freeplay and geometric nonlinearities are prime examples (already mentioned). But the internal damping forces in a structure may also have a nonlinear relationship to structural motion, with dry friction being an example that has received some attention. Because the structural damping is usually represented empirically even within the framework of linear aeroelastic mathematical models, not much is known about the fundamental mechanisms of damping and their impact on flutter and LCO.

All of these nonlinear mechanisms have nevertheless received attention by the mathematical modeling community and several have been the subject of wind tunnel tests as well. In some cases good correlation between theory and experiment has been obtained for limit cycle oscillation response.

5 Efficient Computation of Unsteady Aerodynamic Forces: Linear and Nonlinear

The literature on unsteady aerodynamic forces alone is quite extensive. A comprehensive assessment of current practice in industry is given by Yurkovich, Liu and Chen [18]. An article that focuses on recent developments is that of Dowell and Hall [19]. They also developed a bibliography of some five hundred items available in electronic form from the authors. Other recent and notable discussions include those of Bennett and Edwards [20] and Beran and Silva [21]. Much of the present focus of work on unsteady aerodynamics is on developing accurate and efficient computational models. Standard computational fluid dynamic [CFD] models that include the relevant fluid nonlinearities are simply too expensive now and for some time to come for most aeroelastic analyses. Thus there has been much interest in reducing computational costs while retaining the essence of the nonlinear flow phenomena.

There are three basic ideas that are currently being pursued with some success in retaining the accuracy associated with state-of-the-art CFD models while reducing aerodynamic model size and computational cost, [19, 21]. One is to consider a small (linear) dynamic perturbation about a (nonlinear) mean steady flow. The steady flow may include both the effects of a shock wave and flow separation, but any shock or flow separation region motion is considered in the dynamically linear approximation. That is, it is assumed that the shock motion or the separation point motion, for example, is linearly proportional to the motion of the structure. This is sufficient to assess the linear stability of the aeroelastic system, but not to determine LCO amplitudes due to nonlinear aerodynamic effects. Of course in those cases where the structural nonlinearities are dominant, this simpler aerodynamic model is all one needs to determine LCO. This approach has enormous computational advantages as

the computational cost is comparable to that of a steady flow CFD model since the unsteady calculation per se uses a linear model. And if a structural parameter study is conducted to determine the flutter boundary, the computational cost is no more than for classical aerodynamic methods.

Moreover this approach can be extended to NONLINEAR unsteady flows by expanding the flow solution in terms of a Fourier series in time. This assumes the flow motion is periodic in time of course and is most effective if the number of important harmonics needed in the Fourier Series is small. However this is true of many (but not all) flows of interest. Here the computational cost is a small multiple (say a factor of three) of the cost of a steady flow solution. This is the second major idea, and the harmonic balance method is much faster for determining the LCO than a time marching methods typically by one to two orders of magnitude.

The third major idea is to determine the dominant spatial modes of the flow field and use these, rather than many local grid points, to represent the flow. This is a class of so called Reduced Order Models. The reduction is from the very large number of local grid points (on the order of a million or more) to a small number of spatial modes (typically less than one hundred). The reduction in computational cost for aeroelastic analysis is several orders of magnitude, i.e., a factor of one thousand or more. This approach has been used for potential flow, Euler flow and Navier-Stokes flows (with a turbulence model) for small dynamic perturbations about a nonlinear mean steady flow (recall the first major idea discussed above). Current research is underway to consider nonlinear unsteady flows. Kim and Bussoletti [22] have discussed how one can construct an optimal reduced-order aeroelastic model within the framework of time linearized CFD models. While in principle fluid eigenmodes can be used, and indeed they provide the underlying framework for reduced order modeling, the technique known as proper orthogonal decomposition has proven to be the most computationally attractive method for constructing a set of global modes for the reduced order model. With a reduced order model, the aeroelastic computations are no more expensive than using classical aerodynamics. Moreover one can compute the true aeroelastic damping and frequency of each system mode.

A parallel approach to the last idea is to use the ideas of transfer functions (sometimes called describing function s in the nonlinear case) in the frequency domain or Volterra series in the time domain to create small computational models from large CFD codes [19, 21]. In this approach the form of the transfer function or describing function (or its time series equivalent) is assumed and the coefficients of the reduced order model are determined from data generated by the CFD code in a time simulation. A good discussion of this approach is contained in Beran and Silva [21] and in a series of papers by Silva [23–28]. Again this approach is most fully developed for the dynamically linear case and the dynamically nonlinear case is currently a subject of active research. Raveh, Levy and Karpel [29] have offered a recent and useful discussion of how these ideas can be implemented within the framework of an Euler based, CFD model and provided an example of the well studied AGARD 445.6 wing. Also see Raveh [30].

All of these ideas, individually or in combination, provide the promise of dramatic reductions in computational costs for unsteady transonic flows including the effects

of shock motion and flow separation. In addition progress continues to be made in improving the computational efficiency of time marching simulations Farhat et al. [31, 32]. And the ideas of dynamic (time) linearization and reduced order modeling can be used in either the time or frequency domains. For a more thorough discussion of these ideas, see chapter "Modeling of Fluid-Structure Interaction".

6 Correlations of Experiment/Theory and Theory/Theory

Much of what we know about the state of the art with respect to nonlinear aeroelasticity comes from the study of correlations between experiment and theory and between various levels of theoretical models. Hence the remainder of this chapter is largely devoted to such correlations and the lessons learned from them. The correlations selected are to the best of our knowledge representative of the state of the art. We shall consider correlations for aerodynamic forces per se, transonic flutter boundaries, and limit cycle oscillations.

6.1 Aerodynamic Forces

Roughen, Baker and Fogarty [33] have compared the results of several theoretical models with the experimental data from the Benchmark Active Controls Technology (BACT) wing. The BACT wing is a rectangular planform with a NACA 0012 airfoil profile. The model has a trailing edge control surface extending from 45–75% span. Previously Schuster et al. [34] had compared results from a Navier-Stokes CFD model (ENS3DAE) to these experimental data. Roughen et al. used an alternative Navier-Stokes CFD model (CFL3D) and also a classical potential flow model (Doublet Lattice). Correlations were made at several subsonic to transonic Mach numbers. As they note.

"For the purely subsonic condition ($M = 0.65$)....there is relatively good agreement between the doublet-lattice results, the Navier-Stokes results and the test data. This is not surprising because the flow is entirely subsonic and well behaved (there is no shock wave and no flow separation)." However at $M = 0.77$ "transonic effects begin to become apparent in these results. For the most part, the observations about the results and the qualitative correlation between doublet lattice, Navier-Stokes, and experimental results are similar to the subsonic results. However, there are some important differences that appear in the neighborhood of the supersonic pocket (near the mild and relatively weak shock wave).....There is clearly a bump in the unsteady pressure magnitude (near the shock wave position).....Little nonlinear amplitude dependence is seen (however) except near the trailing edge."

For $M = 0.82$ there is a strong shock near 40% chord. "The presence of the shock is also clearly evident in the steady-state pressure distribution shown in Fig. 2. The effects of the shock are also quite obvious in the unsteady pressure results. See Fig. 3.

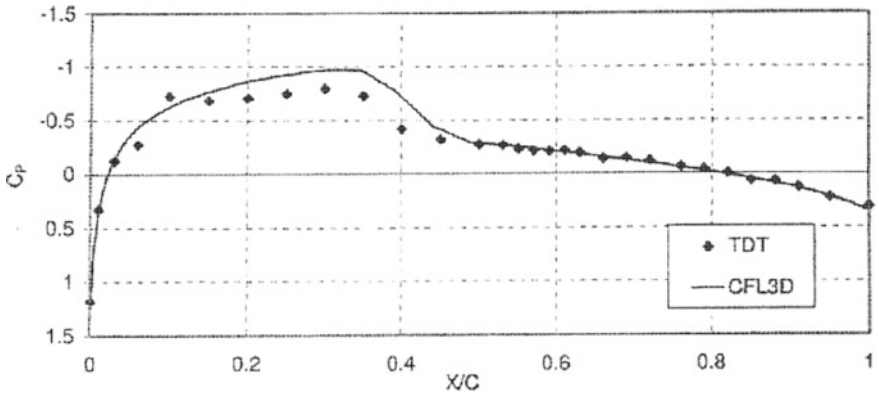

Fig. 2 Steady state pressure distribution for BACT odel

In the unsteady pressure magnitudes, there is a clear peak in the unsteady pressure at approximately 35% local chord in the experimental results and at 40% local chord in the Navier-Stokes results. The peak, which represents the shock doublet Ashley [35] caused by the unsteady motion of the shock, is absent in the linear doublet lattice results [N5K code]. Quantitatively, the correlation of the shock doublet peak between experimental and Navier-Stokes results is disappointing. The CFD results predict a shock doublet of approximately double the amplitude of that seen in the experimental results.... possible contributors to this inaccuracy (in the theory) are the chordwise grid resolution and the Baldwin-Lomax turbulence model. Correlation between CFD solutions and the experiment is excellent away from ...the shock."

More recent calculations for this configuration have improved the quantitative results from the CFD mathematical models, but not wholly resolved the differences between theory and experiment at the highest Mach number, $M = 0.82$. See the valuable and insightful discussion of results using the CFL3D and ENS3DAE computer models by Bartels and Schuster [36].

Another valuable correlation among several theoretical results and that of experiment is based upon the experimental work of Davis and Malcolm [37]. Several investigators have compared the results of transonic potential flow and Euler flow models with these experimental data. A NACA 64A010A airfoil was studied, again in the high subsonic/transonic Mach number range. See Fig. 4 for a comparison of lift and moment magnitude and phase for a pitching airfoil. As can be seen the general trends are well predicted by all theories with the Euler model being in somewhat better agreement with the experimental data overall. The most recent Euler results were obtained using the Harmonic Balance method and the number of data points calculated were correspondingly more numerous. For this comparison the mean angle of attack of the airfoil was a 0 degrees. However Davis and Malcolm also considered a mean angle of attack of 4 degrees for which the flow is separated and results for the magnitude of the unsteady lift are shown in Fig. 5 for both mean angles of attack as a function of the amplitude of the oscillating or unsteady angle of

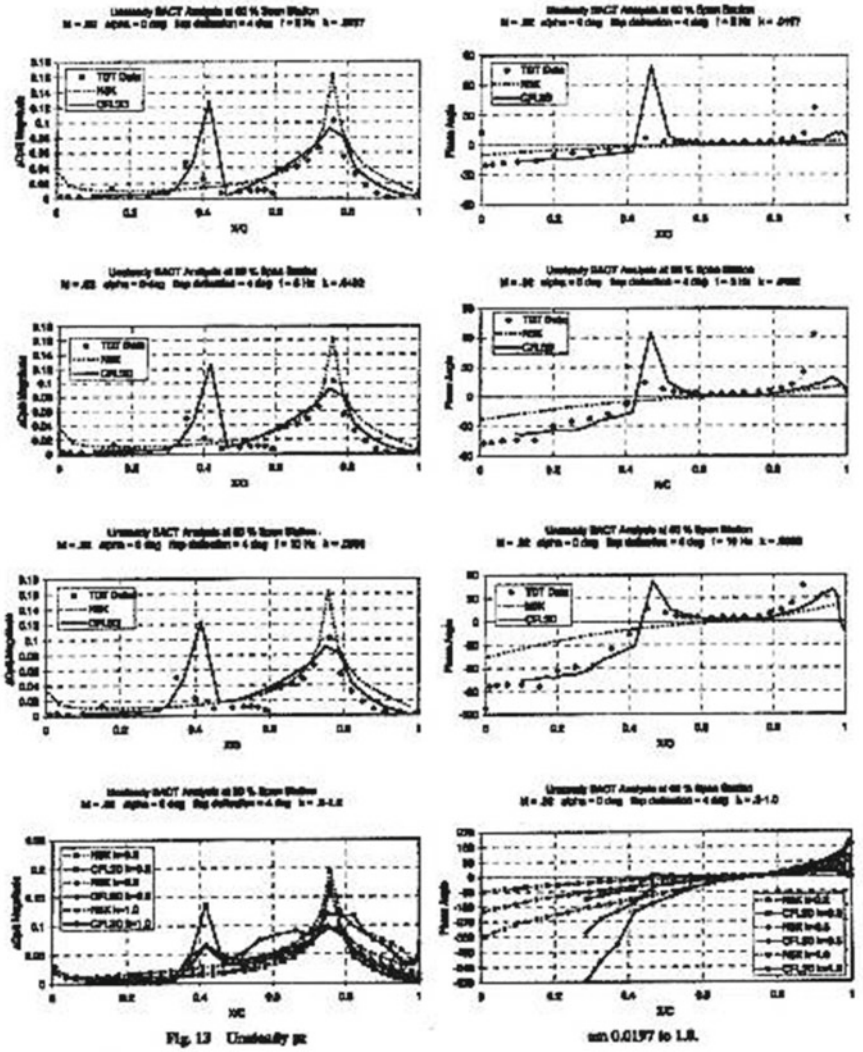

Fig. 3 Unsteady pressure distribution of BACT model

attack. What is immediately clear is that for the mean angle of attack of zero there is a significant range of unsteady angle of attack for which the aerodynamic flow is dynamically linear. However that range is much smaller when the mean angle of attack is increased to 4 degrees and the flow is separated. Results from both potential flow and Euler flow models correlate well with the experiment for a mean angle of attack of 0 degrees when the flow is attached, but not for the case of a mean angle of attack of 4 degrees when the flow is separated. It would be very valuable

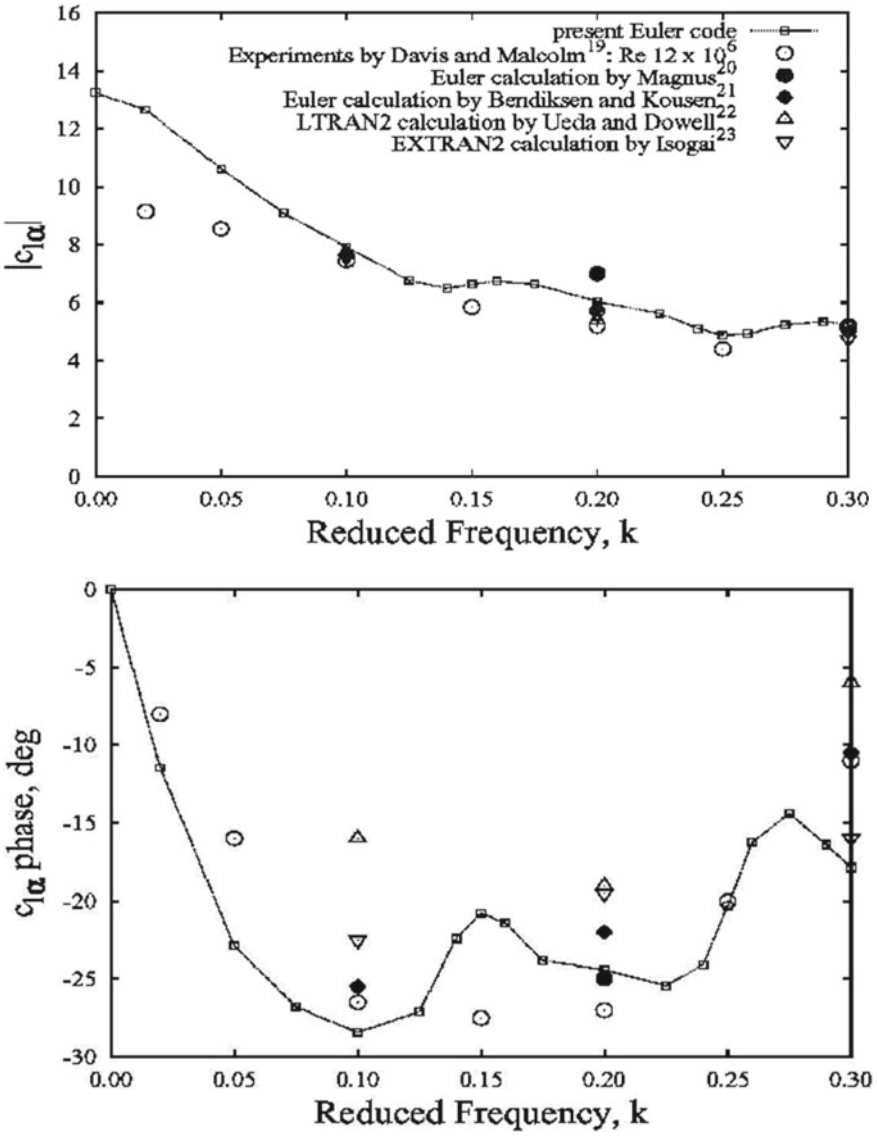

Fig. 4 **a** Lift Magnitude due to pitching $+/-\ 1^\circ$ at the quarter-chord for $M = 0.8$ verses reduced frequency $k \equiv \frac{\omega b}{U_\infty}$ for NACA64A010 airfoil. **b** Lift phase. **c** Moment magnitude. **d** Moment phase

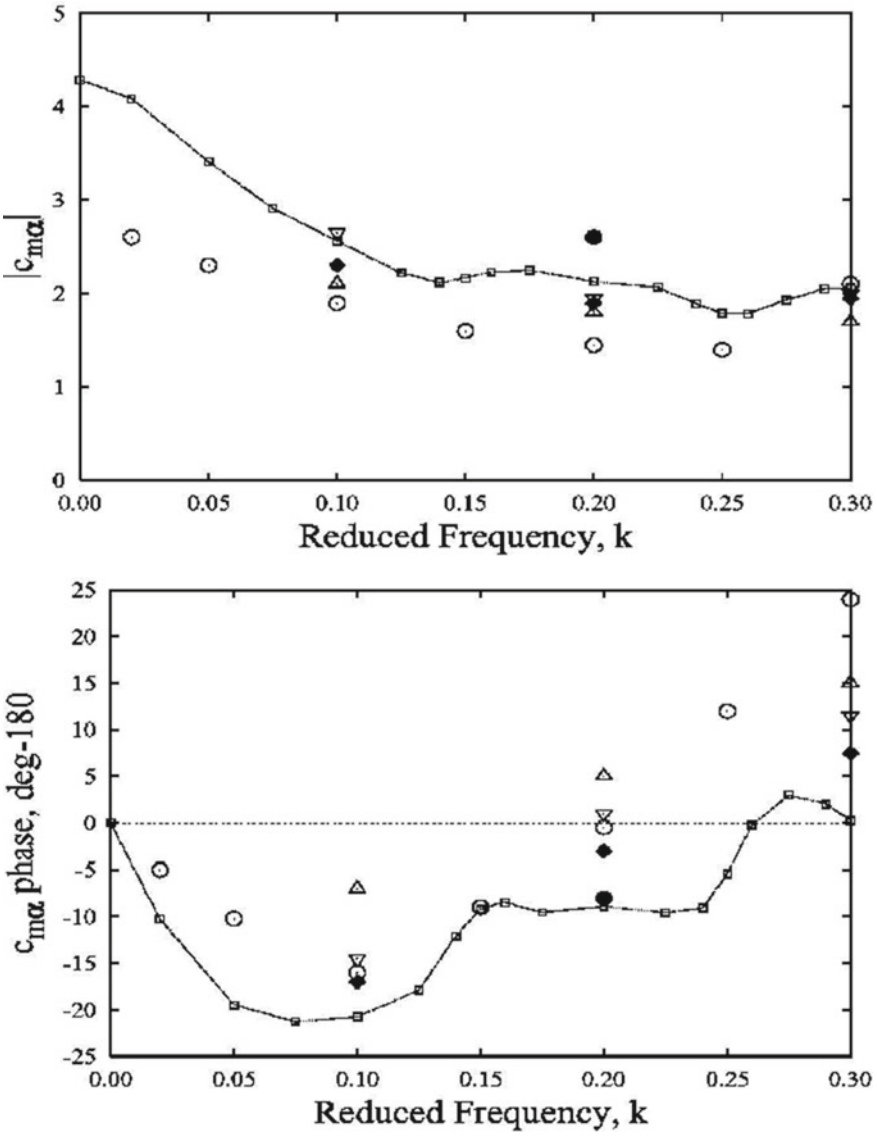

Fig. 4 (continued)

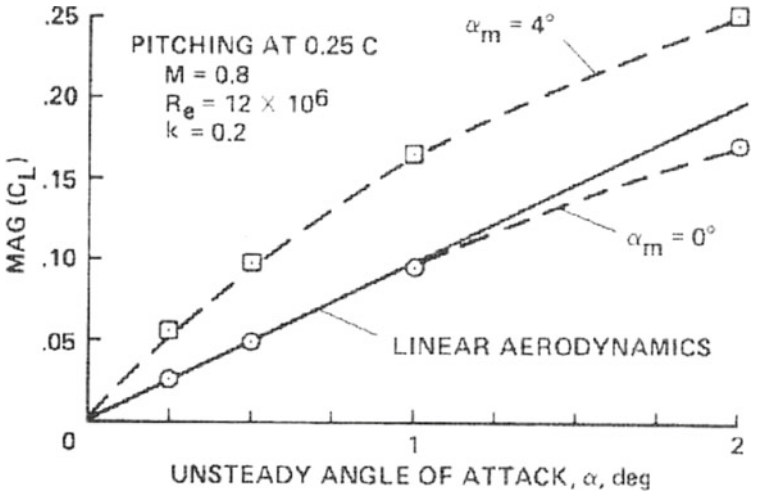

Fig. 5 Unsteady lift magnitude verses unsteady angle of attack magnitude

to have results from a Navier-Stokes model for the latter case. McMullen, Jameson and Alonso [38] have also done calculations for this set of experimental data using the harmonic balance method and obtained similar results. They have done a careful grid convergence study as well.

Finally the valuable study of Krieiselmaieer and Laschka [39] is noted. In this work they develop a time linearized Euler model and compare the results obtained to those from a fully dynamically nonlinear Euler model. The cases considered are a NACA 0012 airfoil in subsonic flow, the NACA 64A010 in transonic flow and a 3% parabolic arc airfoil in supersonic flow, as well as the three-dimensional flow about the LANN wing. Their principal conclusions are that the computational cost of the time linearized code is about an order of magnitude less than that of the fully nonlinear code (consistent with the findings of other investigators) and that the results from the two theoretical models are in good agreement for the cases and parameter ranges investigated. As already noted previously, a time linearized flow model is sufficient to predict the flutter boundary per se, but of course cannot predict LCO amplitudes.

A recent NATO report by a Research and Technology Organization Working Group Ruiz-Calavera [40] provides a comprehensive experimental data base drawn from many sources in the literature for the verification and validation of computational unsteady aerodynamic computational codes. Comparisons of the experimental data with selected aerodynamic computer models and codes are also provided. Additional such theoretical/experimental correlations may be expected using this unique collection of data. See especially the paper 8C by Schuster and Bartels in [40].

7 Flutter Boundaries in Transonic Flow

7.1 AGARD 445.6 Wing

Bennett and Edwards [20] have discussed the state of the art of Computational Aeroelasticity (CAE) in a relatively recent paper and made several insightful comments about various correlation studies. The NASA Langley team pioneered in providing correlations for the AGARD 445.6 wing in the transonic flow region. In Fig. 6 a comparison of flutter speed index (FSI) and flutter frequency is shown as a function of Mach number between the results from experiment and theory. The theoretical results are for transonic nonlinear potential flow theory without (CAP-TSD) and with (CAP-TSDV) a boundary layer model to account for viscous flow effects; and also for an Euler (CFL3D-Euler) and Navier-Stokes (CFL3D-NS) flow model. For this thin wing, there are no significant transonic effects in the steady flow over the wing surface at the Mach numbers with experimental results except for M = 0.96 where there is a very weak shock on the surface. For the subsonic conditions, all computational results are in very good agreement with experiment. The two low supersonic test conditions have been problematic for CAE. Inviscid computations have produced high flutter speed index values relative to the experimental FSI and viscous computations have accounted for about one half the difference between theory and experiment. Several investigators have now done similar Euler calculations and obtained similar results Farhat and Lesoinne [41–43]; Ravfeh, Levy and Karpel [44]; Thomas, Dowell and Hall [45, 46]. The excellent agreement of the wholly linear theory results with experiment should probably be regarded as fortuitous. Also

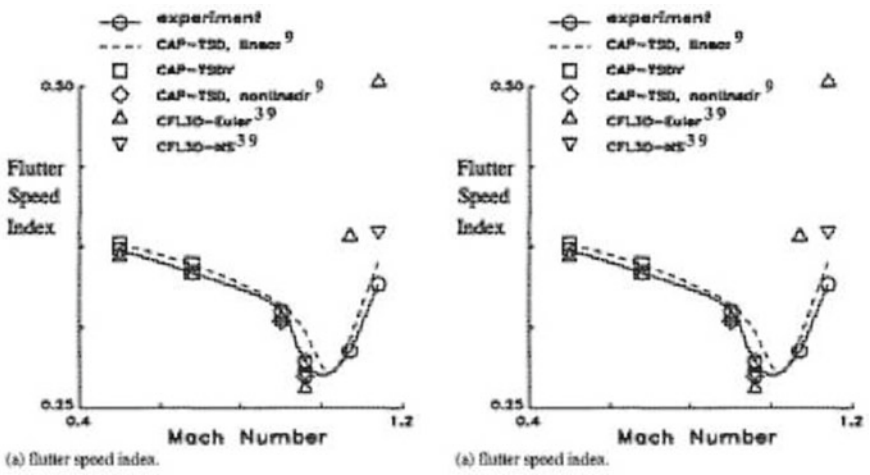

Fig. 6 **a** Flutter speed index and flutter frequency verses mach number for AGARD 445.6 wing. **b** Flutter frequency verses mach number

and interestingly, Gupta [47], who also used an Euler based CFD model, obtains results in better agreement with experiment at the low supersonic conditions, though in less good agreement with experiment than the other Euler based results at subsonic conditions. Thus, CAE computations for this low supersonic region have unresolved issues which probably involve details such as wind tunnel wall interference effects and flutter test procedures, as well as CAE modeling issues.

7.2 HSCT Rigid and Flexible Semispan Models

Two semispan models representative of High Speed Civil Transport (HSCT) configurations were tested in the NASA Langley Research Center Transonic Dynamics Tunnel (TDT) in heavy gas. A Rigid Semispan Model (RSM) was tested mounted on an Oscillating Turn Table (OTT) and on a Pitch And Plunge Apparatus (PAPA). The RSM/OTT test Scott et al. [48] acquired unsteady pressure data due to pitching oscillations and the RSM/PAPA test acquired flutter boundary data for simple pitching and plunging motions. The FSM test Silva et al. [49] involved an aeroelastically-scaled model and was mounted to the TDT sidewall. The test acquired unsteady pressure data and flutter boundary data. Figure 7 Scott et al. [48] shows the unexpectedly large effect of mean angle of attack upon the flutter boundaries for the RSM/PAPA model. Flutter of thin wings at subsonic conditions is typically independent of angle-of-attack within the linear flow region. Figure 8 Silva et al. [49] shows a summary of the flutter and high dynamic response regions for the RSM. Squares indicate conditions where forced response measurements due to trailing edge control surface oscillations were made. The 'analysis' flutter boundary is from an early finite element model.

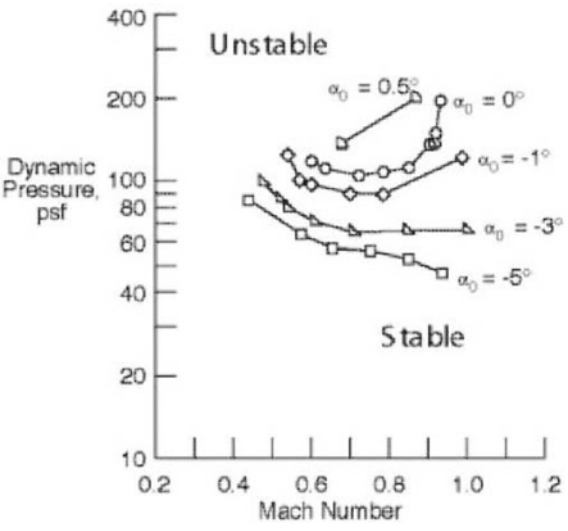

Fig. 7 Flutter dynamic pressure verses mach number for various mean angles of attack

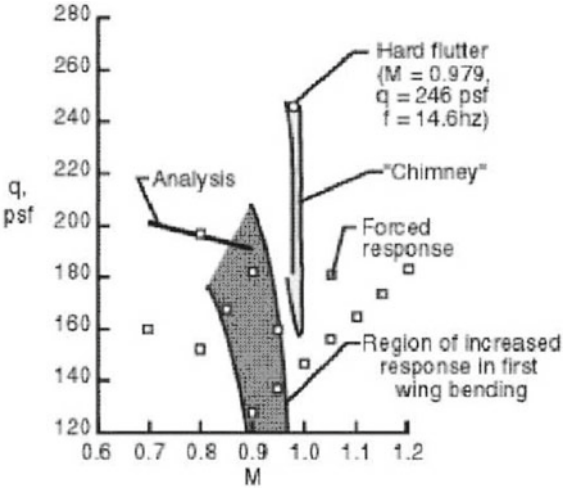

Fig. 8 Dynamic pressure verses mach number: depicting regions of distinct response for HSCT model

Updated modeling places the (linear) flutter boundary slightly above the indicated 'hard flutter' point. A region of increased response in first wing bending (8.5 Hz.) was encountered in the Mach number range of 0.90–0.98. Finally, an narrow region of LCO behavior, labelled 'chimney', was encountered for M = 0.98–1.00 and over a wide range of dynamic pressures. Response frequency ranged from 11.9 to 14.0 Hz. And the region was traversed a number of times prior to encountering the hard flutter point at M = 0.979 and q = 246 pounds per square foot where the model was lost.

7.3 Benchmark Active Control Technology (BACT) Model

This rectangular wing model had a panel aspect ratio of two and a NACA 0012 airfoil section. See Bennett et al. [50, 51] and Ruiz-Calavera [40, 52]. It was mounted on a pitching and plunging apparatus which allowed flutter testing with two simple degrees of freedom. It was extensively instrumented with unsteady pressure sensors and accelerometers and it could be held fixed (static) for forced oscillation testing or free for dynamic response measurements. Data sets for trailing-edge control surface oscillations and upper-surface spoiler oscillations for a range of Mach numbers, angle of attack, and static control deflections are available. The model exhibited three types of flutter instability illustrated in Fig. 9.

A classical flutter boundary is shown, for $\alpha = 2$ deg as a conventional boundary versus Mach number with a minimum, the transonic 'dip', near M = 0.77 and a subsequent rise. Stall flutter was found, for $\alpha > 4$ deg near the minimum of the flutter boundary (and at most tunnel conditions where high angles of attack could be attained). Finally, a narrow region of instability occurs near M = 0.92 consisting of plunging motion at the plunge mode wind-off frequency. This type of transonic

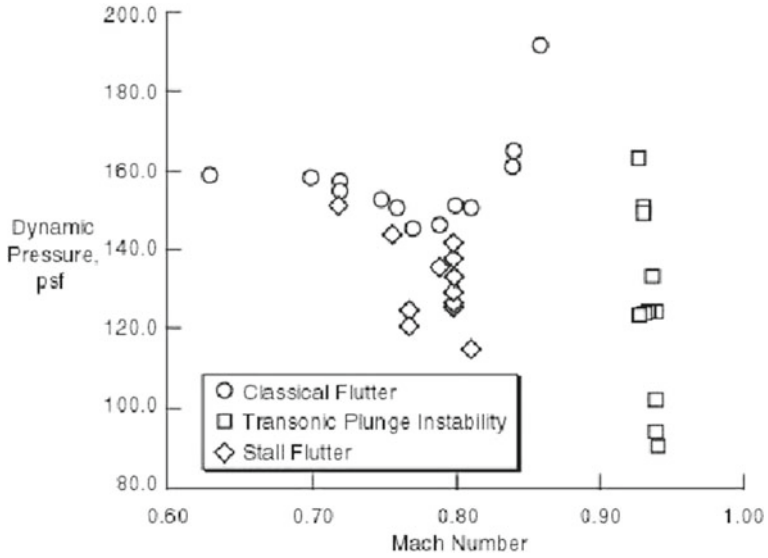

Fig. 9 Dynamic pressure verses mach number: depicting regions of distinct response for BACT model

instability has sometimes been termed single-degree-of-freedom flutter. It is caused by the fore and aft motion of symmetric shocks on the upper and lower surfaces for this wing. It was very sensitive to any biases and does not occur with nonzero control surface bias or nonzero alpha. Such a stability boundary feature is often termed a 'chimney' since the oscillations are typically slowly diverging or constant amplitude (LCO) and it is found, sometimes, that safe conditions can be attained with small further increases in Mach number. Note that the Mach number for the plunge instability decreases slightly with increasing pressure.

7.4 Isogai Case a Model

Another benchmark case often used for theoretical/theoretical comparisons is the famous Isogai Case A, again for a NACA 64A010 airfoil with certain structural parameters that lead to a complex transonic flutter boundary for a plunging and pitching airfoil. A recent study is that by Hall, Thomas and Dowell [53, 54] that includes comparisons with the earlier results of Isogai [55], Ehlers and Weatherill [56] and Edwards et al. [57]. The latter results were all obtained using nonlinear potential flow models (in some cases they were time linearized, which should make no difference for determining the flutter boundary per se), while the results of Hall et al. were obtained using a time linearized Euler model. There is encouraging agreement among all models for this complex transonic flutter boundary as seen in Fig. 10. Note

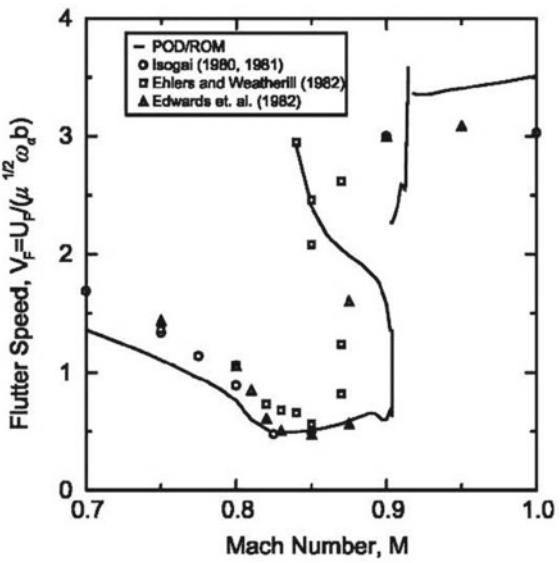

Fig. 10 Flutter speed index verses mach number for Isogai case A

the rapid change in flutter speed index as the Mach number is varied. This is associated with a change in the critical flutter mode (eigenvector). Two additional studies by Prananta et al. [58] and Bohbot and Darracq [59] have included turbulence modeling for this case. Their results show that viscosity reduces the extent of the transonic dip in the flutter boundary significantly and eliminates the double valued FSI that are seen over a portion of the Mach number range in the inviscid calculations. Bohbot and Darracq also show a significant decrease in LCO amplitude due to viscosity at $M = 0.9025$.

Bendiksen[60–62] has made two important observations about transonic flutter boundaries. One is with respect to an experimental study done some years ago at NASA Langley to consider the effects of airfoil thickness ratio Dogget, Rainey and Morgan [63] for the same airfoil profile. Bendiksen notes that the family of results for the variation of flutter speed index with Mach number for the several thickness ratios can be reduced to a single curve when the data are replotted using (nonlinear potential flow) transonic steady flow similarity variables. These similarity parameters rescale the aerodynamic pressure using non-dimensional parameters that combine the Mach number and thickness ratio. Essentially this rescaling shows an equivalence between changes in Mach number and thickness ratio in the transonic range. As the rescaling is based upon steady flow similarity variables, it presumably works best when the reduced frequency is small as might be the case for bending/torsion flutter, but perhaps not for single degree of freedom flutter due to negative damping. See, for example, Dowell et al. [64] for a discussion of various types of flutter that may occur. Implicitly the success of this rescaling also supports the more general observation that for transonic flow it is important to model accurately the position and strength of

the shock wave for steady flow conditions before attempting unsteady aerodynamic or aeroelastic calculations.

The other important point made by Bendiksen is that in the transonic range the flutter speed index may vary rapidly, not only because of a change in flutter type or mode (as has been noted by several investigators), but also because of the substantial changes in mass ratio that may occur in wind tunnel test trajectories. This may explain in part the so called "chimneys" in flutter boundaries that have been observed in transonic flutter wind tunnel test data.

In this regard it is interesting to note that Denegri [3] presents flight test data showing LCO at nearly constant Mach number over large variations of altitude. Many "typical LCO" encounters result in termination of testing due to increasing response levels with each increase in Mach number because of concern for aircraft safety. Some "non-typical LCO" encounters are reminiscent of the "chimney" feature in that response levels increased to a maximum and then decreased with increasing Mach number.

8 Limit Cycle Oscillations

8.1 Airfoils with Stiffness Nonlinearities

Many investigators have considered such a configuration with a variety of nonlinear stiffness modes. For a description of the work on freeplay nonlinearities including a discussion of the literature, see the article by Dowell and Tang [65] which focuses on correlations between theory and experiment. In general good quantitative correlation is found for simple wind tunnel models and the basic physical mechanism that leads to LCO appears well understood. Among the important insights developed include the demonstration that the LCO amplitude and the effect of mean angle of attack on LCO amplitude both simply scale in proportion to the range of freeplay present in the aeroelastic system.

Here we consider in more depth the valuable and recent work of the Texas A&M team [66–71]. They have conducted experiments with their Nonlinear Aeroelastic Test Apparatus (NATA) in a low speed wind tunnel, and these investigations of typical section models provided validation of their theoretical models. See Fig. 11. The NATA testbed has been used to investigate both linear and nonlinear responses of wing sections as well as the development of active control methods. Three wing sections have been used in their research: a NACA 0015 wing section without a control surface; a NACA 0015 wing section with a 20% chord full span trailing edge control surface; and, a NACA 0012 wing section with a 15% chord, full span leading edge and a 20% chord, full span trailing edge control surfaces. The pitch and plunge stiffness of the NATA is provided by springs attached to cams with shapes prescribed to impart specific response. For example, a parabolic pitch cam yields a spring hardening response tailored to mimic the response of interest. With

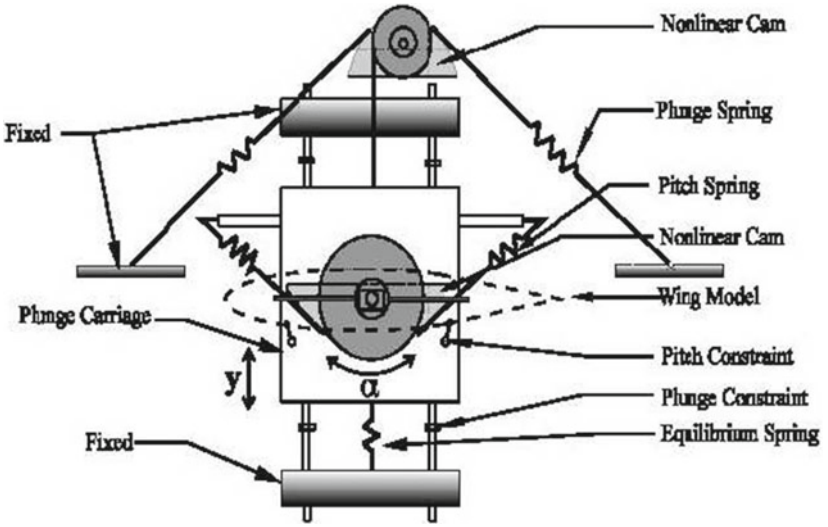

Fig. 11 The nonlinear aeroelastic test apparatus (NATA) in Texas A&M's 2'x3' wind tunnel

such a nonlinear pitch cam in place, the system will experience LCO response. It is noteworthy that similar nonlinear spring hardening behavior has been observed in static measurements of the F/A-18 wing Thompson and Strganac [71]. A polynomial representation of the spring hardening behavior provides a quite effective model of the response. Encoders are use to measure all motions.

The experimental and analytical efforts of O'Neil, et al. used a model with a nonlinear structural stiffness. In these studies, the stiffness grew (i.e., spring-hardened) in a smooth, continuous manner with amplitude of motion. The effect on flutter of a structure with stiffness that grew in a cubic manner was investigated, and the results showed that LCOs occurred and the stability boundary was insensitive to initial conditions. As the freestream velocity was increased, the amplitude of the LCO increased and less time was required to reach the LCO. A representative result for LCO shown as phase plane diagrams is presented in Fig. 12.

8.2 Nonlinear Internal Resonance Behavior

Unusual findings from a wind tunnel experiment have been a motivation for studies of the possible presence of internal resonance's in aeroelastic systems. Internal resonance (IR) occurs as a result of nonlinearities present in the system, and leads to an exchange of energy between the system modes. The amount of energy that is exchanged depends on the type of nonlinearity and the relationship of the linear natural frequencies. IR exists when the linear natural frequencies of a system are commensurable, or nearly so, and the nonlinearities of the system provide a source

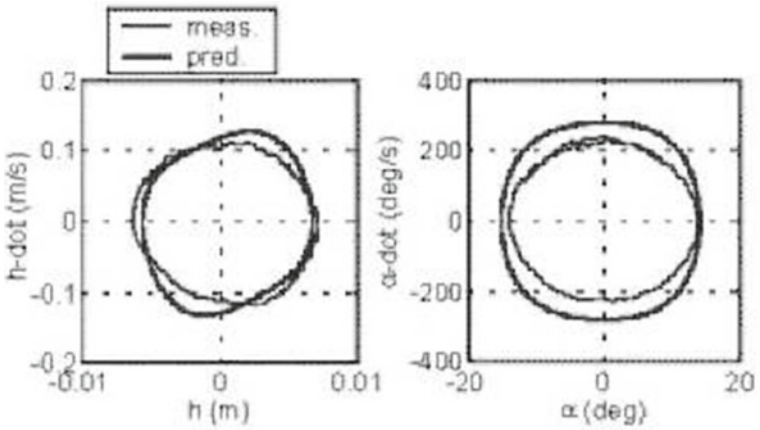

Fig. 12 Large amplitude LCO's, induced by a hardening in structural stiffness, as measured with the NATA

of coupling. Commensurability is defined as

$$m_1\omega_1 + m_2\omega_2 + \ldots + m_n\omega_n \approx 0$$

where m_n are positive or negative integers, and ω_n are the natural frequencies of the system. Although an integer natural frequency ratio does not guarantee IR, it does form a necessary condition for IR. IR has been shown to exist in many systems, and its presence depends on the geometry, composition of nonlinearities and boundary conditions.

During wind tunnel tests by Cole [72] intended to verify the aeroelastic stability of a new wing design, an unexpected flutter-type response occurred at dynamic pressures much lower than analysis had predicted. It is important to note that predictive tools based upon linear theory were used. For the physical structure, the natural frequency of the second bending mode of the wind tunnel model was slightly more than twice the natural frequency of the first torsional mode. However, since frequencies in an aeroelastic system depend on the aerodynamic loads, a system's frequencies may be tuned as the velocity changes. In Cole's experiments, a resonance-type condition may have been reached before linear flutter conditions. Consequently, it was considered that the inaccurate predictions were due to the limitations presented by the use of linear theory.

In an attempt to explain the unexpected experimental results, Oh, Nayfeh and Mook [73] developed an experiment to examine the structural dynamic behavior of Cole's experiments. These experiments were conducted in the absence of any aerodynamic loads. They determined, theoretically and experimentally, the linear natural frequencies and the mode shapes, and also experimentally showed that an antisymmetric vibration mode of a cantilever metallic plate was indirectly excited by a 2:1 internal resonance mechanism. To explain the experimental results, they referred

to the study of Pai and Nayfeh [74] in which they considered nonlinear beam theory. The two-to-one IR was present since the natural frequency of the second bending mode being nearly twice the natural frequency of the first torsional mode. Their experiment consisted of a base excitation being applied to a cantilevered plate with the same aspect ratio as Cole's wing. However, in this study the second bending mode was excited by a shaker rather than by aerodynamic forces.

Internal resonance has been used to suppress the vibrations of flexible structures. Studies show that during the resonance, the nonlinear modal amplitudes exchanged energy back and forth over time, even in the presence of damping. It was also shown that in the presence of an external excitation, the internal resonances give rise to coupling between the modes, leading to several motions including nonlinear periodic, almost periodic, and chaos.

Although many researchers have investigated IR in various types of mechanical systems, relatively little attention has been given to the study of IR in aeroelastic systems. Stearman, et al. [75] studied resonances in aeroelastic systems, and showed that both combination-type and parametric resonances can occur. These resonances occurred if

$$\Omega_f \approx 2\omega_n/k \quad \text{and} \quad \Omega_f \approx |\omega i \pm \omega_j|/k$$

where k is an integer, Ω_f is the frequency of the external forcing function, ω_i, ω_j and ω_n are normal mode frequencies. Their study explored the use of statistical techniques to analyze flight test data.

Gilliatt et al. [76] and Chang et al. [77] both studied the possible presence and effects of internal resonances in aeroelastic systems. Gilliatt, in particular, was motivated by the experimental findings of Cole. The two degree-of-freedom model of O'Neil's research was a basis for the study, and a quasi-steady aerodynamic model was extended to include stall effects which introduced strong cubic nonlinearities into the equations of motion. The system parameters were selected to permit the aeroelastic frequencies to pass through a 3:1, 2:1, and 1:1 ratio as the flowfield velocity was increased. Gilliatt found that the presence of cubic nonlinearities in the aeroelastic system led to a 3:1 internal resonance.

8.3 Delta Wings with Geometrical Plate Nonlinearities

At low Mach numbers, see for example Tang and Dowell [78], good correlation has been demonstrated between theory and experiment for LCO amplitudes and frequencies. Since these results are well documented elsewhere, see also Dowell and Tang [65], here the recent work of Gordnier et al. [79, 80] that has extended these correlations into the transonic range is emphasized. In Fig. 13 a cropped delta wing planform is shown. This configuration had been investigated experimentally by Schairer and Hand [81] and the theoretical calculations were done by Gordnier et al. using both Euler and Navier-Stokes flow models. Initially the theoretical calculations were done using a linear structural model, which gave predicted LCO amplitudes much greater

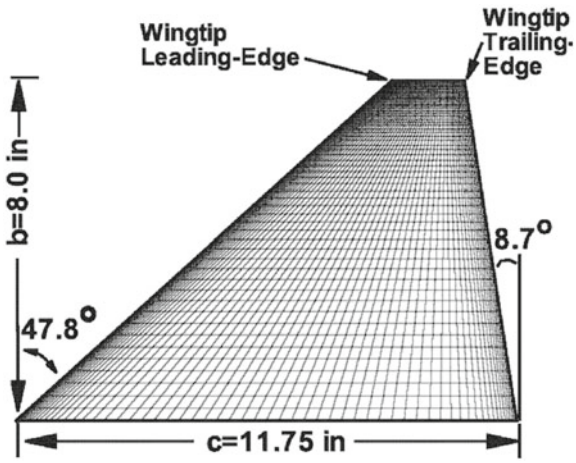

Fig. 13 Planform of a cropped delta wing

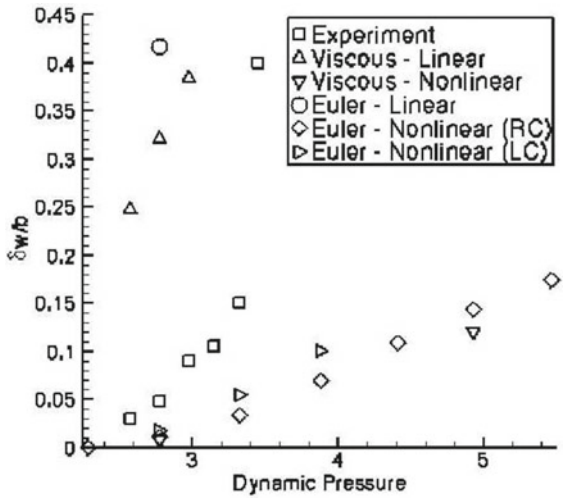

Fig. 14 LCO response verses dynamic pressure: correlation of experiment with various theoretical models for cropped delta wing

than those observed experimentally. This led Gordnier to include nonlinearities in the structural model (tension induced by bending) via Von Karman's nonlinear plate theory that provided much improved correlation between theory and experiment. See Fig. 14 which shows a plot of LCO amplitude versus flow dynamic pressure at a fixed transonic Mach number. Note that the effects of viscosity are modest based upon the comparisons of results using the Euler verses Navier-Stokes models. Also the much improved agreement obtained with the nonlinear structural model suggests that aerodynamic nonlinearities per se are not as significant for this configuration as are the structural nonlinearities as Gordnier notes in his conclusions. Perhaps the most significant impact of this example is to illustrate that even for a transonic flow, there are cases where structural nonlinearities may be dominant.

It is also interesting to note that for this example that the most significant aerodynamic nonlinearity was associated with leading edge vortices rather than shock motion. This nonlinear aerodynamic flow mechanism has also been studied by Mook and colleagues, e.g. Preidikman et al. [82] at low Mach numbers in a series of papers. As Gordnier and Mook note nonlinear vortex flow phenomena may be important when structural nonlinearities are weaker and the corresponding structural motions greater. Of course if the mean angle of attack is sufficiently large (say 10 degrees or more) then vortex formation may be important for even smaller wing oscillations.

8.4 Very High Aspect Ratio Wings with Both Structural and Aerodynamic Nonlinearities

Notable contributions have been made by Patil, Hodges and Cesnik [83, 84] and Tang and Dowell [85]. This case has been discussed in some depth by Dowell and Tang [65] and that discussion will not be repeated here. In summary, however, both structural geometrical nonlinearities (associated with torsional motion and bending both transverse and parallel to the beam /rod chord) and aerodynamic nonlinearities (associated with flow separation and wing stall) have been shown to be important. Also wing stall has been shown to lead to hysteretic LCO response with increases and decreases in flow velocity. The correlation of theory and experiment is good, albeit the extant theory uses a semi-empirical model to account for wing stall. Again it would be highly desirable to use a Navier-Stokes flow model for correlation with this experiment and indeed this case is a good benchmark for such flow models.

Further recent work has been done by Kim and Strganac [86] who used the equations of Crespo da Silva [87] to examine store-induced LCOs for the cantilevered wing-with-store configuration. These equations contain structural coupling terms and quadratic and cubic nonlinearities due to curvature and inertia. Several possible nonlinearities, including aerodynamic, structural, and store-induced sources, were considered. Structural nonlinearities were derived from large deformations. Aerodynamic nonlinearities were introduced through a stall model. Store-induced nonlinearities were introduced by kinematics of a suspended store. All of these nonlinearities retained cubic nonlinear terms. To examine systematically the response characteristics, phase plane analysis was performed and the effect of each nonlinearity, as well as combinations of the nonlinearities were studied. Although various forms of nonlinear responses were found, of interest was the finding of LCO response at speeds below the flutter velocity. Furthermore, an unstable boundary was found, above which responses were attracted to the LCO and below which the responses were attracted to the nominal static equilibria. Of special importance, such subcritical response was found for only the case in which complete consideration of structural, aerodynamic, and store-induced nonlinearities was given. This suggested that studies of nonlinear aeroelasticity must sometimes consider a full aircraft configuration. A representative result is shown in Fig. 15.

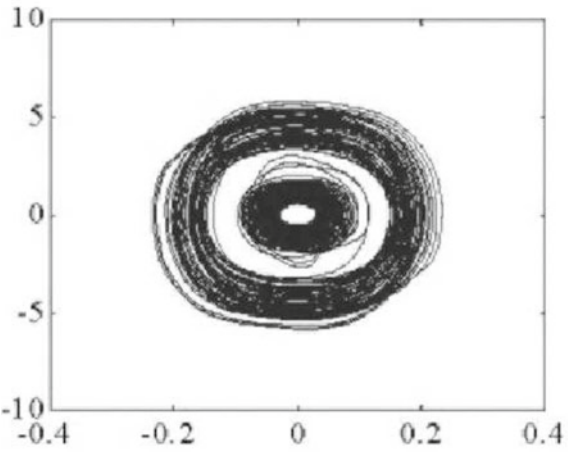

Fig. 15 LCO response of the cantilevered wing-with-store configuration

Thompson and Stragnac [71] studied the effects of structural nonlinearities and store configuration nonlinearity. Thompson showed that although store-induced kinematic nonlinearities might be considered negligible in practice, they may introduce atypical behavior that would not be predicted by linear system analysis.

8.5 Nonlinear Structural Damping

Even linear aeroelastic models often use empirical models of structural damping; thus little is known fundamentally about how to model structural damping for LCO. However an interesting and insightful hypothesis has been offered by Chen, Saarhaddi and Liu [88]. If one assumes that the structural damping increases with amplitude of structural motion (there is some experimental evidence to suggest this may be the case), and if the negative aerodynamic damping associated with flutter remains sufficiently small beyond the flutter boundary, then the nonlinear increase in structural damping may offset the negative aerodynamic damping and this will lead to a nonlinear, neutrally stable motion, i.e., LCO. Liu et al. have performed calculations based upon this hypothesis that appear consistent with some of the LCO observed in the F-16 aircraft.

8.6 Large Shock Motions and Flow Separation

These aerodynamic nonlinearities are both the most difficult to model theoretically and also to investigate experimentally. Hence it is perhaps not surprising that our correlations between theory and experiment are not yet what we might like them to

be. As a corollary one might observe that it will in all likelihood be easier to design a favorable nonlinear structural element to produce a benign LCO, than to assure that flow nonlinearities will always be beneficial with respect to LCO.

8.6.1 NACA 64A010A Conventional Airfoil Models

In Fig. 16 recent results are shown for the LCO of a NACA 64A010 airfoil in plunge and pitch as predicted by an Euler flow model Kholodar, Thomas, Dowell and Hall [89]. Here the LCO amplitude is plotted versus the flutter speed index (FSI) for a range of Mach number. As can be seen the LCO is relatively weak (the curves of the figure are nearly vertical) for most Mach numbers. And for those Mach numbers where the LCO is relatively strong, it can be either benign (the curves bend to the right) or detrimental (the curves bend to the left) leading to LCO below the flutter boundary. This example also points out the substantial amount of data needed to assess LCO under these circumstances. A Navier-Stokes model has also been used to assess LCO of this configuration for a more limited range of parameters. The results (not shown) indicate a modest effect of viscosity provided the mean angle of attack is sufficiently small and no flow separation occurs.

8.6.2 NLR 7301 Supercritical Airfoil Models

Another configuration of interest is the supercritical airfoil, NLR 7301, which has been studied experimentally by Schewe and his colleagues [90–93]. This has in turn

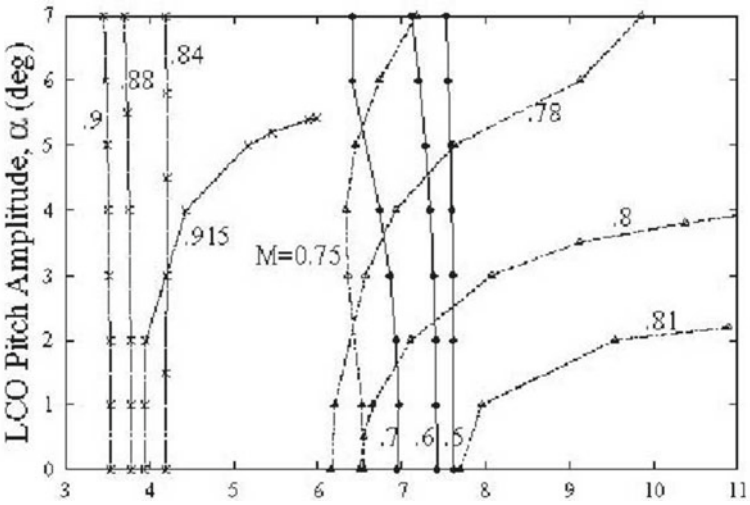

Fig. 16 LCO amplitude verses reduced velocity for NACA 64A010 airfoil

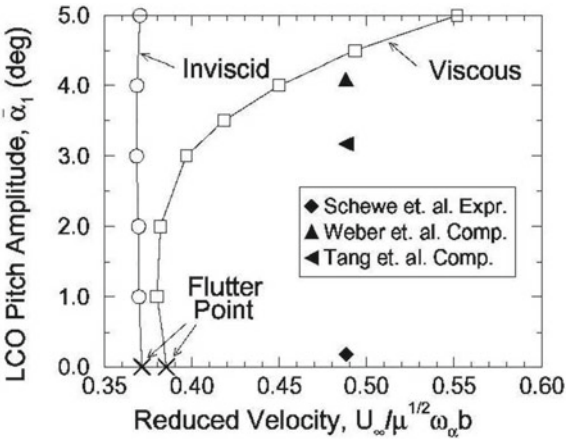

Fig. 17 LCO amplitude verses reduced velocity for NCR 7301 supercritical airfoil

inspired several theoretical studies using either an Euler or Navier-Stokes flow model. A correlation among several theoretical models and the result of experiment is shown in Fig. 17. This figure is drawn from the paper by Thomas, Dowell and Hall [94] who used a harmonic balance LCO solution method. Results are also shown from Weber et al. [95] and Tang et al. [96] both of whom used the more computationally demanding time marching technique. Note that there is only a single data point from the latter as is the case from the experiment. However it is clear that to have a more meaningful correlation it is highly desirable to provide results for LCO amplitude over a range of FSI and Mach number. Hence it is not yet clear what the conclusion should be with respect to correlation between theory and experiment. It does appear that the several theoretical results are in reasonable agreement. More correlations with the experimental data are needed.

Computational conditions are sensitive and care must be taken to achieve reasonable steady initial pressure distributions for this configuration. Also, the LCO conditions appear to be very sensitive to details of the computations. Tang et al. give results from the CFL3D-NS code illustrating effects of turbulence models, single-block and multi-block (parallel), multigrid subiterations, and time step. Agreement for the LCO motion amplitudes has been difficult to achieve for this case even including the effects of wind tunnel wall interference. Castro et al. [97].

8.6.3 AGARD 445.6 Wing Models

The AGARD 445.6 wing has been discussed earlier in terms of its flutter boundary; now we turn to very recent results from Thomas, Dowell and Hall [9i8] for LCO. The correlation between theory and experiment for the flutter boundary is again shown in Fig. 18 where the Euler flow model is that of Thomas et al. The flutter boundary correlation is consistent with that discussed earlier relative to Fig. 6. But now we have in additional results for LCO amplitude versus FSI for various Mach number.

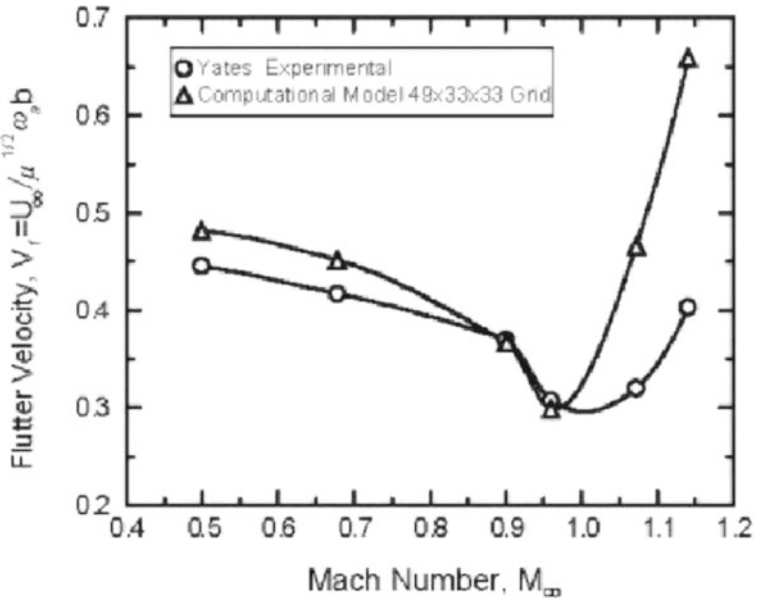

Fig. 18 Flutter speed index verses mach number for AGARD wing 445.6: comparison of theory and experiment

See Fig. 19. Note that a value of first mode non-dimensional modal amplitude of $\xi = .012$ as shown in this figure corresponds to a wing tip deflection equal to one fourth of the wing half-span. Note also that in general the LCO is predicted to be weak and there is no Mach number for which a benign LCO is predicted. Indeed the strongest LCO is detrimental and occurs at the low supersonic Mach numbers, i.e. $M = 1.141$ and 1.072. This means that LCO may occur below the flutter boundary at these two Mach numbers and perhaps this explains at least in part why flutter (or LCO) in the experiment occurs below the predicted flutter boundary.

Small amplitude LCO behavior for the AGARD 445.6 wing has also been calculated by Edwards [99]. The majority of published calculations for this wing model (actually a series of models with similar planforms) are for the "weakened model ♯3" tested in air, since this test covered the largest transonic Mach number range and showed a significant transonic dip in the flutter boundary. The focus on this particular configuration may be in some ways unfortunate, in that the model tested in air resulted in unrealistically large mass ratios and small reduced frequencies. Weakened models ♯5 and ♯6 were tested in heavy gas and had smaller mass ratios and higher reduced frequencies. Very good agreement was obtained with experiment for flutter speed index using the CAP-TSDV code over the Mach number range tested. For the highest Mach number tested, $M = 0.96$, it was noted that damping levels extracted from the computed transients were amplitude dependent, an indicator of nonlinear behavior. It was also found that small amplitude divergent (in time) responses used

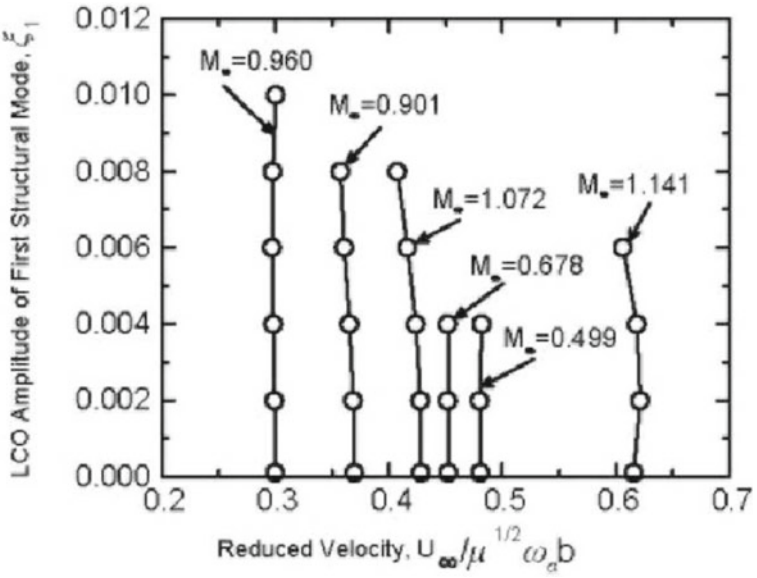

Fig. 19 LCO amplitude verses reduced velocity for various mach numbers: AGARD 445.6 wing

to infer the flutter boundary would transition to LCO when the calculation was continued further in time. The wing tip amplitude of the LCO was approximately 0.12 inches peak-to-peak, a level that is unlikely to be detected in wind tunnel tests given the levels of model response to normal wind tunnel turbulence.

8.6.4 MAVRIC Wing Flutter Model

This business jet wing-fuselage model Edwards [99, 100] was chosen by NASA Langley Research Center's Models For Aeroelastic Validation Involving Computation (MAVRIC) project with the goal of obtaining experimental wind-tunnel data suitable for Computational Aeroelasticity (CAE) code validation at transonic separationonset conditions. LCO behavior was a primary target. An inexpensive construction method of stepped-thickness aluminum plate covered with end-grain balsa wood and contoured to the desired wing profile was used. A significant benefit of this method was the additional strength of the plate that enabled the model to withstand large amplitude LCO motions without damage.

The model was instrumented with three chords of unsteady pressure transducers and eight accelerometers. It was tested in air and in heavy gas and with three wingtip configurations: clean, winglet, and pencil tipstore. Figure 20 shows the Flutter Speed Index (FSI) boundary versus Mach number from an earlier test of this model Edwards [101], including computed CAE code comparisons. The experimental flutter boundary shows a gradual decrease in dynamic pressure, reaching a minimum

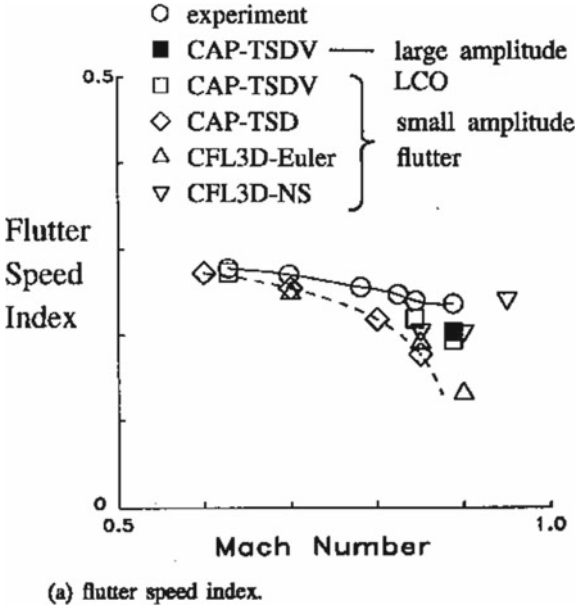

(a) flutter speed index.

Fig. 20 Flutter speed index verses mach number for MAVRIC model

at M = 0.89. The structural modifications and added instrumentation resulting in the MAVRIC model had very little effect upon the flutter boundary. Both the Transonic Small Disturbance CAP-TSDV and the higher level CFL3D codes are in good agreement with experiment at the lower Mach numbers. Both inviscid codes, CAP-TSD and CFL3D-Euler, increasingly depart from experimental values approaching the minimum FSI value. This emphasizes the necessity of the inclusion of viscous shock-boundary layer interaction effects for LCO-like motions. Both viscous codes, CAP-TSDV and CFL3D-NS, are in good agreement with experiment at M = 0.89 where small amplitude, time-marching responses were used to identify the flutter boundary.

The behavior of the MAVRIC model as flutter was approached during the wind tunnel test indicated that wing motions tended to settle to a large amplitude LCO condition, especially in the Mach number range near the minimum FSI conditions. Figure 21 [Edwards [102]] indicates the ability of the CAP-TSDV code to simulate these large amplitude LCO motions. Large and small initial condition disturbance transient responses clearly show the six inch peak-to-peak wingtip motions observed in the tests. Such large amplitude aeroelastic motions have not been demonstrated by RANS codes which have difficulty maintaining grid cell structure for significant grid deformations. Figure 22 Edwards et al. [100] shows the map of the regions of LCO found in the MAVRIC test in the vicinity of the minimum FSI (clean wingtip, deg.). Numbers for the several contours in the figure give the half-amplitude of wingtip LCO motions, in g's, in the indicated regions. Two regions, signified by 'B', are regions where 'beating' vibrations were observed. For this test condition, wing

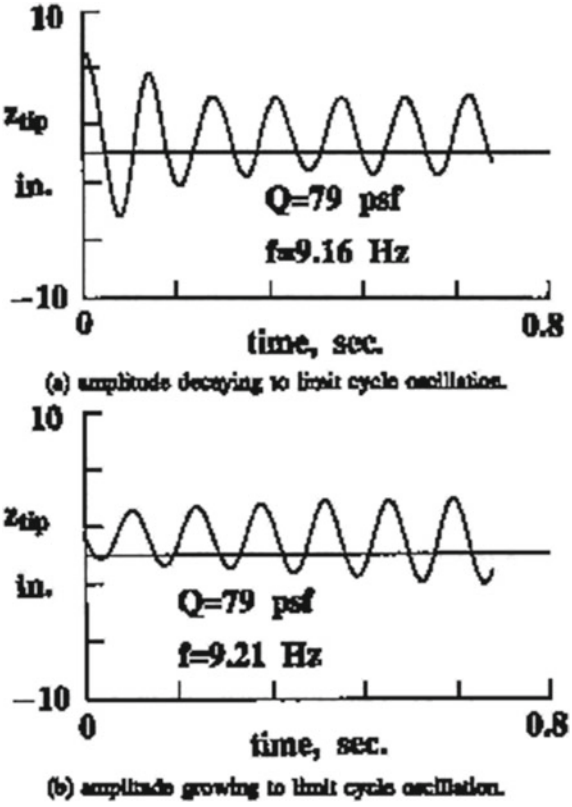

Fig. 21 Transient response leading to a LCO: simulation for MAVRIC wing

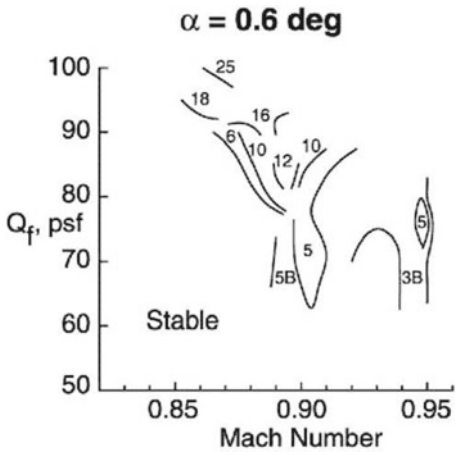

Fig. 22 Dynamic pressure verses mach number contours of constant LCO amplitude for MAVRIC wing

motions are predominantly of the wing first bending mode at a frequency of 7–8 Hz. (wind-off modal frequency is 4.07 Hz.). Two chimney features are seen, at M = 0.91 and at M = 0.94. Edwards discusses flutter model responses which are indicative of more complex nonlinear behaviors than are commonly attributed to LCO. Thus, flutter test engineers are familiar with responses such as 'bursting' and 'beating,' commonly used as indicators of the approach to flutter (and LCO).

8.6.5 Clipped-Tip Delta Wing Control Surface Buzz Model

Parker et al. [103] describe a test of a clipped-tip delta wing model with a full span control surface. The leading-edge sweep was 60°, the biconvex wing profile had thickness of 3% of local chord, and the constant chord control surface length was approximately 13% of the root chord. The control surface was mounted on two flexure springs. The tests were conducted in air which is of concern since there are known to be severe Reynolds number and/or transition effects for this tunnel at dynamic pressures below 50–75 pounds per square foot Edwards et al. [100]. Pak and Baker [104] have performed computational studies of this case. They compare the experimental buzz boundary with time-marching transient responses calculated with the CFL3D-NS code and the CAP-TSDV code, respectively. Both codes capture LCO behavior near the experimental buzz conditions with the higher level code appearing to have better agreement for the experimental trend versus Mach number. The responses offer excellent insight into issues and problems of the use of CAE time-marching codes for LCO-like studies. The record lengths of a number of the responses, which are extremely expensive to compute, are not sufficient for clear determination of the response final status. Also, LCO behaviors can result from very delicate force balances and settling times to final LCO states can require many cycles of oscillation.

8.6.6 Residual Pitch Oscillations on the B-2

The B-2 bomber encountered a nonlinear aeroelastic Residual Pitch Oscillation (RPO) during low altitude high speed flight. See Dreim et al. [14]. Neither the RPO or any tendency of lightly damped response had been predicted by wholly linear aeroelastic design methods. The RPO involved symmetric wing bending modes and rigid body degrees of freedom. It was possible to augment the CAP-TSDV aeroelastic analysis code with capability for the longitudinal short-period rigid body motions, vehicle trim, and the full-time active flight control system including actuator dynamics. This computational capability enabled the analysis of the heavyweight, forward center of gravity flight condition. The simulation predicts open loop instability at M = 0.775 and closed loop instability at M = 0.81 in agreement with flight test. In order to capture the limit cycle behavior of the RPO it was necessary to include modeling of the nonlinear hysteretic response characteristic of the B-2 control surfaces for small amplitude motions. This is caused by the small overlap of the servohydraulic

control valve spool flanges with their mating hydraulic fluid orifices. With this realistic actuator modeling also included, limited amplitude RPO motions similar to those measured in flight were simulated as shown. A lighter weight flight test configuration exhibited very light damping near M = 0.82 but did not exhibit fully developed RPO. Instead damping increased with slight further increase in speed, typical of hump mode behavior. The CAP-TSDV simulations did not capture this hump mode behavior.

8.6.7 Rectangular Goland Wing Model with Tip Store

We conclude this section with a discussion of the recent and valuable papers by Beran et al. [105] and Huttsell et al. [106]. In the paper by Beran et al. comparisons were made between the predictions of a fully nonlinear potential flow plus boundary layer model (CAP-TSDV) and the results from classical fully linear theory (doublet lattice). The Goland wing was used for this study which is a rectangular planform with a 4% parabolic arc airfoil. In Fig. 23 flutter boundaries and what is termed a LCO boundary are shown for the two theoretical methods. Results for the wing alone and for a wing with a tip store are given. Beran et al. note that for this configuration the aerodynamic effect of the tip store is small, but the effect of tip store dynamics (inertia)

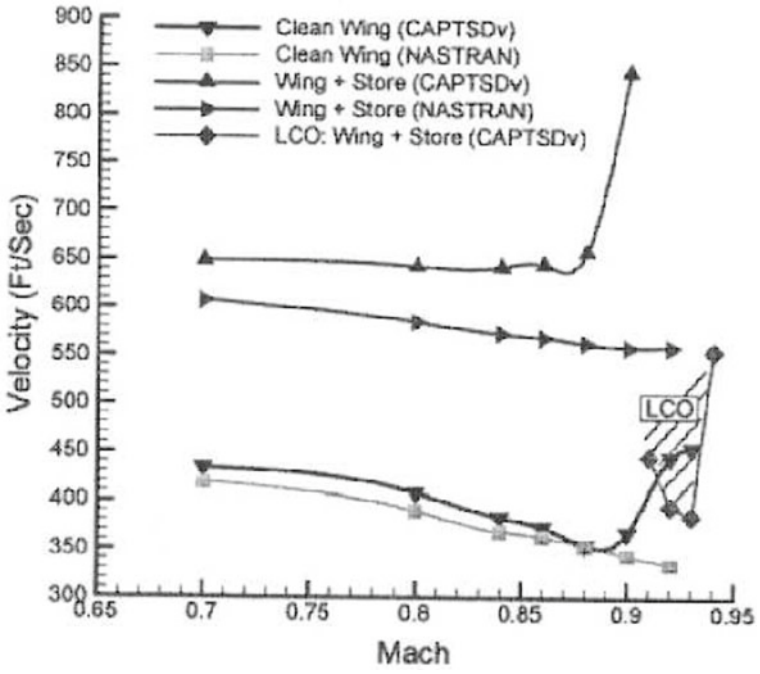

Fig. 23 Flutter and LCO boundaries: velocity verses mach number for goland wing

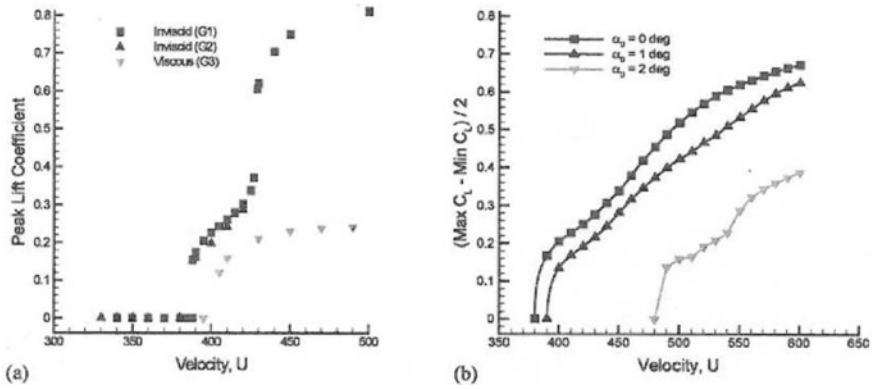

Fig. 24 LCO response verses flow velocity. An example of hysteresis for goland wing

is important as seen in the figure. Note also that the two flow models give results in good agreement for the subsonic Mach number range, but differ substantially in the transonic range. Beran et al. distinguish between the flutter boundary (for the wing plus tip store) and the LCO boundary. However based upon the work of others that show that rapid changes in flutter (and LCO) modes may occur, it seems likely that these are both flutter boundaries per se. At the subsonic Mach number it is likely that no LCO was observed in these time simulations because the LCO is very weak. That is at subsonic Mach numbers the time simulation shows a rapidly exponentially diverging oscillation typical of a linear dynamical system. LCO was observed over a narrow range of transonic Mach number (again consistent with the findings of other investigators for other configurations) where the aerodynamic nonlinearity is strong enough that a time simulation will reach a finite steady state LCO amplitude in a reasonable amount of computational time. However if the initial disturbance to the system is small enough or there is little hysteresis in the dependence of LCO steady state amplitude on speed index, then the boundary for the onset of LCO should be essentially the same as the flutter boundary. There is some mild hysteretic LCO behavior for this configuration as is discussed further in the paragraph after next.

In Fig. 24a the LCO amplitude is shown as a function of flow velocity for various theoretical models. Results are shown with and without store aerodynamics (again the differences are small) and with and without the effects of viscosity. As can be seen there is little effect of viscosity on the flow velocity at the onset of flutter and LCO, but the effect on LCO amplitude per se is substantial. (The abrupt increase in LCO response for the inviscid model may be indicative of unrealistic shock motions.) Recall the results of Thomas, Dowell and Hall [94] for the NLR 7301 airfoil which showed similar behavior when comparing LCO response from inviscid and viscous flow models. And also recall the results of Bohbot and Darracq [59] for the Isogai Case A.

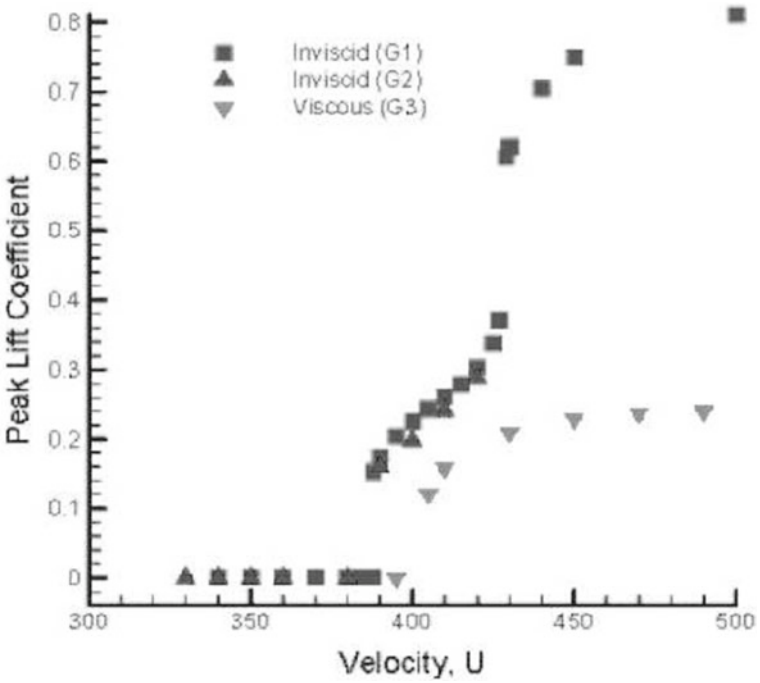

Fig. 25 LCO response verses flow velocity for goland wing

In Fig. 24b inviscid flow results are shown for various mean angles of attack. The results are qualitatively similar, but the effect of increased angle of attack is to increase the flow velocity at which flutter and LCO occur.

In Fig. 25, the results of Fig. 24 are shown again for increasing flow velocity (Perturbed Rigid IC) and decreasing flow velocity (Path Following IC). The results display hysteresis with the LCO amplitude observed being path dependent. As the flow velocity is increased and given a sufficiently small initial condition (IC) disturbance, no flutter or LCO is seen until a velocity of about 390 ft/s; but when the airfoil is then allowed to oscillate in the LCO and the flow velocity is now decreased, LCO continues until a lower velocity is reached of about 385 ft/s. Although the range of flow velocity over which hysteresis is observed is relatively small in this example, there is every reason to expect that for other parameter choices the range of hysteresis can be greater.

8.6.8 Time Marching Codes Compared to Various Experimental Results

In the paper by Huttsell et al. [106] several state of the art time marching CFD codes are used to investigate flutter and LCO for challenging cases drawn from flight

or wind tunnel tests. The CAP-TSD, CAP-TSDV, CFL3D and ENS3DAE codes are all used. The results are extremely helpful in providing a realistic assessment of the state of the art of these codes and they are also indicative of future needs for improvements. For the F-15 example, difficulty was encountered in producing a computational grid with negative fluid volumes being encountered. For the AV8-B a steady state flow field could not be found due to oscillations in the numerical solver from one iteration to the next. These difficulties are not unusual for CFD codes in the present authors' experience. Sometimes the difficulty in achieving a steady flow solution is attributed to shedding in the flow field, but in the absence of a full nonlinear dynamic CFD calculation, that must remain a speculation. For the B-2 example encouraging agreement was obtained for the frequency and damping variation of the critical flutter (and LCO) mode as a function of flight speed using the CAP-TSDV code. For the B-1 estimates of the damping associated with LCO were favorably compared to those found in wing tunnel tests using the CFL3DAE code. It is not entirely clear what the "damping" of an LCO means, however, since by definition LCO is a neutrally stable motion. Two control surface "buzz" cases were considered and CFL3DAE had some success in predicting the behavior observed in the wind tunnel for a NASP like configuration.

As Huttsell et al. note, additional work is needed to improve CFD model robustness, computational efficiency and grid generation deformation strategies.

8.7 Abrupt Wing Stall

Although not usually classified as a nonlinear aeroelastic response or LCO, abrupt wing stall (AWS) appears to share some of the same basic characteristics. A joint Navy/NASA/ Air Force program over the last several years has addressed this class of phenomena Woodson [107]. Chambers [108] has presented a valuable historical account of AWS and drawn lessons learned from a number of aircraft programs. Much of the recent work on AWS has been motivated by experiences with the F-18.

Briefly AWS is encountered when the aircraft is at a sufficiently high angle of attack for flow separation to occur and the flow then begins to oscillate including shock oscillations if the local Mach number is large enough. For large angles of attack sonic conditions may be reached locally even for relatively low free stream Mach numbers. This oscillating flow may be asymmetric from one wing to the other and therefore the aircraft will roll. If this rolling motion is a transient the motion is usually called "wing drop" while if it is periodic in the roll angle it is called "wing rock". Wing rock has been modeled Nayfeh, Elzebda, Mook [109], Ericcson [110] as a limit cycle oscillation due to nonlinear self-excited coupling between the aerodynamic flow and the rolling motion of the aircraft. Wing drop has been modeled by including this effect Kokolios and Cook [111] and also the oscillating aerodynamic rolling moment that may occur even in the absence of aircraft motion. This oscillating aerodynamic moment is due to a nonlinear self-excitation of the flow

in the absence of aircraft motion and thus this moment is an "external" excitation as far as the vehicle motion is concerned.

Since the dominant aircraft motion is rigid body roll rather than the an elastic structural mode of the wing, for example, abrupt wing stall is not usually thought of as being an aeroelastic issue per se. Yet from a dynamics perspective many of the issues with respect to aerodynamic modeling and aircraft motion are similar to those nonlinear phenomena discussed previously in this paper. Valuable free-to-roll wind tunnel model studies have been performed at NASA Langley Research Center by Lamar et al. [112] as have some CFD simulations of AWS. Several sessions and papers devoted to this topic have been presented at the recent 2003 AIAA Aerospace Sciences Meeting.

8.8 Uncertainty Due to Nonlinearity

There has been recent and renewed interest in the impact of uncertainties on aerospace system response. Here two scenarios that have been reported by operators of current aerospace systems are discussed and the relationship of uncertainty to nonlinearity is noted.

8.8.1 Scenario I

One scenario that has been reported is the following. An aircraft in straight and level flight does not experience flutter or LCO; however when the aircraft is maneuvered LCO does occur and then when the aircraft is returned to straight and level flight the LCO persists. The question is, how has the maneuver generated LCO that persists in straight and level flight when LCO did not occur before the maneuver?

With the framework of a linear aeroelastic model, such behavior is not possible, but an explanation is possible for a nonlinear aeroelastic system as a result of hysteresis. That is, if the disturbance to a nonlinear system is sufficiently small, LCO will not occur, but if a sufficiently large disturbance is applied to the system, e.g., a maneuver, then LCO may be induced. And once LCO exists, it may persist even if one returns to the nominal original flight condition. Such behavior has been observed in both mathematical and experimental wind tunnel models where the nonlinear effect producing the LCO and hysteretic response is due to either structural freeplay or flow separation.

In this scenario the uncertainty is because two different nonlinear response states are possible at the same parameter condition (flight speed and altitude) and the prior history of the system is critical in determining its response.

8.8.2 Scenario II

In another scenario that has been observed, two distinct, but nominally identical systems (aircraft) are flown through the same trajectory and one encounters LCO but the other does not. The question is, how is this possible? Again insights obtained from nonlinear aeroelastic models may offer an explanation.

Consider an aircraft with freeplay as an example. Now it is very difficult to maintain the same amount of freeplay in each and every aircraft. So what might happen if two otherwise identical aircraft have different amounts of freeplay? For the aircraft with the smaller freeplay, the LCO amplitude (which scales in proportion to the magnitude of freeplay) might not be noticeable because it is too small. However for the aircraft with the larger freeplay the LCO may be detectable. From recent theoretical and experimental studies of freeplay as discussed by Dowell and Tang [65], not only is it known that LCO amplitudes increase in proportion to the magnitude of the freeplay, but also that the magnitude of the angle of attack required to suppress LCO due to freeplay scales in proportion to the magnitude of the freeplay. Thus the aircraft with the larger freeplay will not only have a LCO of larger amplitude, but it will also experience freeplay over a larger range of angle of attack, again making it more likely that LCO will be observed.

These two scenarios and their possible explanation point up the importance of developing a fundamental understanding of the underlying structural and fluid nonlinearities that may occur in aeroelastic systems in dealing with the uncertainties and apparent paradoxes that have been observed in practice.

9 Concluding Remarks

Substantial progress has been made in modeling and understanding nonlinear aeroelastic phenomena. Experimental and theoretical investigations have shown good correlation for a number of nonlinear physical mechanisms. As a broad generalization, one may say that our understanding of and correlation among alternative theoretical models and experiment is further advanced for nonlinear structural mechanisms such as freeplay and large deflection geometric nonlinearities of beam s and plates, than it is for nonlinear fluid mechanisms such as large shock motions and separated flows. Nevertheless accurate and much more computationally efficient theoretical models are now becoming available for nonlinear aerodynamic flows and there is cause for optimism in addressing these issues going forward.

As has been emphasized throughout this chapter, a number of physical mechanisms can lead to nonlinear aeroelastic response including the impact of steady flow fluid or static structural nonlinearities in changing the flutter boundary of an aeroelastic system. Of course dynamic nonlinearities play a critical role in the development of limit cycle oscillations, hysteresis in flutter and LCO response, and the sensitivity of both to initial and external disturbances.

The good news for the flight vehicle designer is that because of nonlinear aeroelastic effects, finite amplitude oscillations can in some cases replace what would otherwise be the rapidly growing and destructive oscillations of classical flutter behavior. A careful consideration and design of favorable nonlinearities offers a new opportunity for improved performance and safety of valuable wind tunnel models, flight vehicles, their operators and passengers. And once nonlinear aeroelastic models have reached a state of maturity sufficient for their consideration in the design process, then active and adaptive control can potentially provide for even greater flight vehicle performance. The discussion of active and adaptive control is beyond the scope of this paper, but the reader may wish to consult the work of Heeg [113], Lazarus, et al. [114, 115], Ko, et al. [68–70], Block and Strganac [67], Vipperman, et al. [116], Bunton and Denegri [8], Clark et al. [117], Frampton et al. [118], Rule et al. [119], Richards et al. [120] and Platanitis and Strganac [121].

References

1. Dowell EH, Edwards JW, Strganac T (2003) Nonlineaeroelasticity. J Aircr 40(5):857–874
2. Thompson JMT, Stewart H (1988) Nonlinear dynamics and chaos. Wiley, New York
3. Denegri CM Jr (1997) Correlation of classical flutter analyses and nonlinear flutter responses characteristics. International forum on aeroelasticity and structural dynamics, Rome, Italy, June, pp 141–148
4. Denegri CM Jr, Cutchins MA (1997) Evaluation of classical flutter analysis for the prediction of limit cycle oscillations. AIAA Paper 97–1021
5. Denegri CM Jr (2000) Limit cycle oscillation flight test results of a fighter with external stores. J Aircr 37(5):761–769
6. Denegri CM Jr, Johnson MR (2001) Limit cycle oscillation prediction using artificial neural networks. J Guid Control Dyn 24(5):887–895
7. AGARD Specialists meeting on wings-with-stores flutter. In: 39th meeting of the structures and materials panel, AGARD Conference proceedings No. 162, Munich, Germany, Oct 1974
8. Bunton RW, Denegri CM Jr (2000) Limit cycle oscillation characteristics of fighter aircraft. J Aircr 37(5):910–918
9. Cunningham AM Jr (1999) A generic nonlinear aeroelastic method with semi-empirical nonlinear unsteady aerodynamics. Vol 1 and 2, AFRL-VA-WP-R-1999-3014
10. Cunningham AM Jr (1998) The role of nonlinear aerodynamics in fluid-structure interactions, AIAA Paper 98–2423
11. Cunningham AM Jr, Geurts EGM (1998) Analysis of limit cycle oscillation/transonic high alpha flow visualization, AFRL-VA-WP-TR-1998-3003, Part I, Jan
12. Dobbs SK, Miller GD, Stevenson JR (1985) Self induced oscillation wind tunnel test of a variable sweep wing. In: 26th AIAA/ASME/ASCE/AHS structures, Structural dynamics and materials conference. AIAA Paper 85–0739-CP. Orlando, FL, April, pp 15–17
13. Hartwich PM, Dobbs SK, Arslan AE, Kim SC (2000) Navier-Stokes computations of limit cycle oscillations for a B-1-Like configuration. AIAA Paper 2000–2338, AIAA Fluids 2000. Denver
14. Dreim DR, Jacobson SB, Britt RT (1999) Simulation of non-linear transonic aeroelastic behavior on the B-2, NASA CP-1999-209136. CEAS/AIAA/ICASE/NASA Langley international forum on aeroelasticity and structural dynamics, pp 511–521
15. Croft J (2001) Airbus elevator flutter: annoying or dangerous, Aviation week and space technology

16. Dowell EH (1972) Panel flutter, NASA special publication, SP-8004
17. Dowell EH (1975) Aeroelasticity of plates and shell. Kluwer academic publishers, New York
18. Yurkovich RN, Liu DD, Chen PC (2001) The state-of-the-art of unsteady aerodynamics for high performance aircraft. AIAA Paper 2001–0428
19. Dowell EH, Hall KC (2001) Modeling of fluid-structure interaction. Annu Rev Fluid Mech 33:445–490
20. Bennett RM, Edwards JW (1998) An overview of recent developments in computational aeroelasticity. AIAA Paper No. 98–2421, presented at the AIAA fluid dynamics conference, Albuquerque, NM
21. Beran P, Silva W (2001) Reduced-order modeling: new approaches for computational physics. AIAA Paper 2001–0853, 39th Aerospace sciences meeting and exhibit. Reno
22. Kim T, Bussoletti JE (2001) An optimal reduced order aeroelastic modeling based on a response - based modal analysis of unsteady CFD models. AIAA Paper 2001–1525
23. Silva WA (1993) Application of nonlinear systems theory to transonic unsteady aerodynamic responses. J Aircr 30(5):660–668
24. Silva WA (1993) Extension of a nonlinear system theory to general-frequency unsteady transonic aerodynamic responses. In: 34th AIAA structures, structural dynamics, and materials conference. Reston
25. Silva WA (1993) Extension of a nonlinear systems theory to transonic unsteady aerodynamic responses. AIAA Paper 93–1590
26. Silva WA (1997) Discrete-time linear and nonlinear aerodynamic impulse responses for efficient (CFD) analyses. Ph.D Thesis, college of William Mary, Williamsburg, Oct
27. Silva WA (1997) Identification of linear and nonlinear aerodynamic impulse response using digital filter techniques. AIAA atmospheric flight mechanics conference, Reston, VA, pp 584–597
28. Silva WA (1999) Reduced-order models based on linear and nonlinear aerodynamic impulse response. International forum on aeroelasticity and structural dynamics, NASA Langley research center, Hampton, pp 369–379
29. Raveh D, Levy Y, Karpel M (2000) Aircraft aeroelastic analysis and design using CFD-based unsteady loads. AIAA Paper 2000–1325, 41st AIAA/ASME/ASCE/AHS/ASC structures, Structural dynamics, and materials conference and exhibit. Atlanta, GA, April
30. Raveh DE (2001) Reduced-order models for nonlinear unsteady aerodynamics. AIAA J 39(8):1417–1429
31. Farhat C, Geuzaine P, Brown G, Harris C (2002) Nonlinear flutter analysis of an F-16 in stabilized, accelerated, and increased angle of attack flight conditions. AIAA Paper 2002–1490
32. Farhat C, Harris C, Rixen D (2000) Expanding a flutter envelope using accelerated flight data: application to An F-16 fighter configuration. AIAA Paper 2000–1702
33. Roughen KM, Baker ML, Fogarty T (2001) Computational fluid dynamics and doublet-lattice calculation of unsteady control surface aerodynamics. J Aircr 24(1):160–166
34. Schuster DM, Edwards JW, Bennett RM (2000) An overview of unsteady pressure measurements in the transonic dynamics tunnel. AIAA Paper No. 2000–1770, presented at the AIAA dynamics specialists conference, Atlanta
35. Ashley H (1980) Role of shocks in the 'Sub-Transonic' flutter phenomenon. J Aircr 17:187–197
36. Bartels RE, Schuster DM (2000) A comparison of two navier-stokes aeroelastic methods using BACT Benchmark experimental data. J Guid Control Dyn 23(5):1094–1099
37. Davis SS, Malcolm GN (1980) Transonic shock-wave/boundary layer interactions on an oscillating airfoil. AIAA J 18(11):1306–1312
38. McMullen M, Jameson A, Alonso JJ (2002) Application of a nonlinear frequency domain solver to Euler and Navier-Stokes equations. AIAA Paper 2002–0120. In: 40th AIAA Aerospace sciences meeting and exhibit. Reno
39. Kreiselmaier E, Laschka B (2000) Small disturbance Euler equations: efficient and accurate tool for unsteady load prediction. J Aircr 37(5):770–778

40. Ruiz-Calavera LP (ed) (2000) Verification and validation data for computational unsteady aerodynamics codes, Research and technology organization TW-26
41. Farhat C, Lesoinne M (1998) A conservative algorithm for exchanging aerodynamic and elastodynamic data in aeroelastic systems. AIAA Paper 98–0515
42. Farhat C, Lesoinne M (1998) A higher-order subiteration free staggered algorithm for nonlinear transient aeroelastic problems. AIAA J 36(9):1754–1756
43. Farhat C, Lesoinne M (1998) Enhanced partitioned procedures for solving nonlinear transient aeroelastic problems. AIAA Paper 98–1806
44. Raveh DE, Levy Y, Karpel M (2001) Efficient aeroelastic analysis using computational unsteady aerodynamics. J Aircr 38(3):547–556
45. Thomas JP, Dowell EH, Hall KC (2001) Nonlinear inviscid aerodynamic effects of transonic divergence, flutter and limit cycle oscillations. In: AIAA Paper 2001–1209, presented at 42nd AIAA/ASME /ASCE /AHS /ASC structures, Structural dynamics and materials conference, Seattle
46. Thomas JP, Dowell EH, Hall KC (2001) Three-dimensional transonic aeroelasticity using proper orthogonal decomposition based reduced order models. AIAA Paper 2001–1526, presented at 42nd AIAA/ASME /ASCE/AHS /ASC structures, Structural dynamics, and materials conference and exhibit. Seattle, WA, April, pp 16–19
47. Gupta KK (1996) Development of a finite element aeroelastic analysis capability. J Aircr 33(5):995–1002
48. Scott RC, Silva WA, Florance JR, Keller DF Measurement of unsteady pressure data on a large HSCT semi-span wing and comparison with analysis. AIAA Paper 2002–1648
49. Silva WA, Keller DF, Florance JR, Cole SR, Scott RC (2000) Experimental steady and unsteady aerodynamic and flutter results for HSCT semi-span models, 41st structures, Structural dynamics and materials conference. AIAA No. 2000–1697, April
50. Bennett RM, Eckstrom CV, Rivera JA Jr, Danberry BE, Farmer MG, Durham MH (1991) The Benchmark aeroelastic models program: description and highlights of initial results, NASA TM 104180
51. Bennett RM, Scott RC, Wieseman CD (2000) Computational test cases for the Benchmark active controls model. J Guid Control Dyn 23(5):922–929
52. Ruiz-Calavera LP et al. (1999) A new compendium of unsteady aerodynamic test cases for CFD: summary of AVTWG-003 activities, International forum on aeroelasticity and structural dynamics
53. Hall KC, Thomas JP, Dowell EH (2000) Proper orthogonal decomposition technique for transonic unsteady aerodynamic flows, AIAA Paper 99–0655. AIAA J 38(10):1853–1862
54. Hall KC, Thomas JP, Dowell EH (1999) Reduced-order modeling of unsteady small disturbance flows using a frequency-domain proper orthogonal decomposition technique. AIAA Paper 99–0655, presented at 37th AIAA Aerospace sciences meeting and exhibition. Reno
55. Isogai K (1979) On the transonic-dip mechanism of flutter of sweptback wing. AIAA J 17(7):793–795
56. Ehlers FE, Weatherhill WH (1982) A harmonic analysis method for unsteady transonic flow and its application to the flutter of airfoils, NASA CR-3537
57. Edwards JW, Bennett RM, Whitlow W Jr, Seidel DA (1983) Time-marching transonic flutter solutions including angle-of-attack effects. J Aircr 20(11):899–906
58. Prananta BB, Hounjet JHL, Zwaan RJ (1998) Two-dimensional transonic aeroelastic analysis using thin-layer Navier-Stokes methods. J Fluids Struct 12:655–676
59. Bohbot J, Darracq D (2001) Time domain analysis of two D.O.F. airfoil flutter using an Euler/turbulent Navier-Stokes implicit solver, International forum on structural dynamics, Vol II, Madrid, Spain, June, pp 75–86
60. Bendiksen OO (2001) Energy approach to flutter suppression and aeroelastic control. J Guid Control Dyn 24(1):176–184
61. Bendiksen OO (2002) Transonic flutter. In: AIAA Paper 2002–1488, 43rd AIAA/ASME /ASCE/AHS /ASC structures, Structural dynamics and materials conference, Denver, CO, April

62. Bendiksen OO (2001) Transonic flutter and the nature of the transonic dip, IFASD 2001, Vol 11, Madrid, Spain
63. Dogget RV Jr, Rainey AG, Morgan HG (1959) An experimental investigation of aerodynamic effects of airfoil thickness on transonic flutter characteristics, NASA TM X-79
64. Dowell EH, Crawley EF, Curtiss HC Jr, Peters DA, Scanlan RH, Sisto F (1995) A modern course in aeroelasticity, 3rd edn. Kluwer Academic Publishers, Dordrecht/Boston, p 699
65. Dowell EH, Tang DM (2002) Nonlinear aeroelasticity and unsteady aerodynamics, AIAA paper 2002–0003. The Theodore von Karman lecture. AIAA J 40(9), 1697–1707
66. O' Neil T, Gilliat H, Strganac T (1996) Investigation of aeroelastic response for a system with continuous structural nonlinearities. AIAA Paper 96–1390
67. Block JJ, Strganac TW (1998) Applied active control for a nonlinear aeroelastic structure. J Guid Control Dyn 21(6):838–845
68. Ko J, Kurdila AJ, Strganac TW (1997) Nonlinear control of a prototypical wing section with torsional nonlinearity. J Guid Control Dyn 20(6):1181–1189
69. Ko J, Strganac TW, Kurdila AJ (1999) Adaptive feedback linearization for the control of a typical wing section with structural nonlinearity. Nonlinear Dyn 18(3):289–301
70. Ko J, Strganac TW, Kurdila AJ (1998) Stability and control of a structurally nonlinear aeroelastic system. J Guid Control Dyn 21(5):718–725
71. Thompson DE, Strganac TW (2000) Store-induced limit cycle oscillations and internal resonance in aeroelastic systems. In: 41st AIAA structures, Structural dynamics and materials conference. AIAA Paper 2000–1413
72. Cole SR (1990) Effects of spoiler surfaces on the aeroelastic behavior of a low-aspect ratio wing. In: 31st AIAA structures. Structural dynamics and materials conference. AIAA Paper 90–0981:1455–1463
73. Oh K, Nayfeh AH, Mook DT (1994) Modal interactions in the forced vibration of a cantilever metallic plate. Nonlinear Stoch Dyn 192:237–247
74. Pai PF, Nayfeh AH (1990) Three-dimensional nonlinear vibrations of composite beams-I: equations of motion. Nonlinear Dyn 1:477–502
75. Stearman RO, Powers EJ, Schwarts J, Yurkorvich R (1991) Aeroelastic system identification of advanced technology aircraft through higher order signal processing. 9th International modal analysis conference. Florence, Italy, April, pp 1607–1616
76. Gilliatt HC, Strganac TW, Kurdila AJ (1997) Nonlinear aeroelastic response of an airfoil, 35th Aerospace sciences meeting and exhibit. AIAA Paper 97–0459. Reno, pp 258–266
77. Chang JH, Stearman RO, Choi D, Powers EJ (1985) Identification of aeroelastic phenomenon employing bispectral analysis techniques. Int Modal Anal Conf Exhibit 2:956–964
78. Tang DM, Dowell EH (2001) Effects of angle of attack on nonlinear flutter of a delta wing. AIAA J 39(1):15–21
79. Gordnier RE, Melville RB (1999) Physical mechanisms for limit-cycle oscillations of a cropped delta wing. AIAA Paper 99–3796, Norfolk
80. Gordnier RE, Melville RB (2001) Numerical simulation of limit-cycle oscillations of a cropped delta wing using the full Navier-Stokes equations. Int J Comput Fluid Dyn 14(3):211–224
81. Schairer ET, Hand LA (1997) Measurement of unsteady aeroelastic model deformation by stereo photogrammetry. AIAA Paper 97–2217
82. Preidikman S, Mook DT (2000) Time domain simulations of linear and nonlinear aeroelastic behavior. J Vib Control 6(8):1135–1175
83. Patil MJ, Hodges DH, Cesnik C (1999) Nonlinear aeroelasticity and flight dynamics of high-altitude long-endurance aircraft. AIAA Paper 99–1470
84. Patil MJ, Hodges DH, Cesnik CE (2000) Nonlinear aeroelastic analysis of complete aircraft in subsonic flow. J Aircr 37(5):753–760
85. Tang DM, Dowell EH (2001) Experimental and theoretical study on aeroelastic response of high-aspect-ratio wings. AIAA J 39(8):1430–1441
86. Kim K, Strganac T (2002) Aeroelastic studies of a cantilever wing with structural and aerodynamic nonlinearities. In: AIAA Paper 2002–1412, 43rd AIAA/ASME/ASCE/AHS/ACS structures, Structural dynamics and materials conference, Denver, CO, April

87. Crespo da Silva MRM, Glynn CC (1978) Nonlinear flexural-torsional dynamics of inextensional beams-I: equations of motions. J Struct Mech 6(4):437–448
88. Chen PC, Sarhaddi D, Liu DD (1998) Limit cycle oscillation studies of a fighter with external stores. AIAA Paper 98–1727
89. Kholodar DB, Thomas JP, Dowell EH, Hall KC (2002) A parametric study of transonic airfoil flutter and limit cycle oscillation behavior. In: AIAA Paper 2002–1211, presented at the AIAA/ASME/ASCE/AHS SDM Conference. Denver, CO, April
90. Knipfer A, Schewe G (1999) Investigations of and oscillation supercritical 2-D wing section in a transonic flow, 36th Aerospace sciences meeting and exhibit. AIAA Paper No. 99–0653
91. Schewe G, Deyhle H (1996) Experiments on transonic flutter of a two-dimensional supercritical wing with emphasis on the nonlinear effects, proceeding of the royal aeronautical society conference on unsteady aerodynamics, London, UK, July 17–18
92. Schewe G, Knipfer A, Henke H (1999) Experimentelle und numerisch Untersuchung zum transonischen Flgelflattern im Hinblick auf nichtlineare Effecte, unpublished manuscript
93. Schewe G, Knipfer A, Mai H, Dietz G (2002) Experimental and numerical investigation of nonlinear effects in transonic flutter, English version (Translated by Dr. W.F. King III), German aerospace center DLR final report number DLR IB 232–2002 J 01, corresponds to final report for BMBF: Nichtlineare Effekte beim transsonischen Flattern (FKZ 13 N 7172), and internal report DLR IB 2001 J03, Accessed 25 Jan 2002
94. Thomas JP, Dowell EH, Hall KC (2002) Modeling viscous transonic limit cycle oscillation behavior using a harmonic balance approach. AIAA Paper 2002–1414, presented at 43rd AIAA/ASME/ASCE/AHS/ASC structures, Structural dynamics, and materials conference and exhibit. Denver, CO, April, pp 22–25
95. Weber S, Jones KD, Ekaterinaris JA, Platzer MF (1999) Transonic flutter computations for a 2-D supercritical wing. AIAA Paper 99–0798, 36th Aerospace sciences meeting and exhibit. Reno
96. Tang L, Bartels RE, Chen PC, Liu DD (2001) Simulation of transonic limit cycle oscillations using a CFD time-marching method. In: AIAA Paper 2001–1290, 42nd AIAA/ASME/ASCE/AHS/ASC structures, Structural dynamics and materials conference, Seattle. WA, April
97. Castro BM, Ekaterinaris JA, Platzer MF (2002) Navier-Stokes analysis of wind-tunnel interference on transonic airfoil flutter. AIAA J 40(7):1269–1276
98. Thomas JP, Dowell EH, Hall KC (2001) A harmonic balance approach for modeling threedimensional nonlinear unsteady aerodynamics and aeroelasticity, IMECE paper 2003–32532
99. Edwards JW (1998) Calculated viscous and scale effects on transonic aeroelasticity, AGARDR-822, Numerical unsteady aerodynamic and aeroelastic simulation, Mar, pp. 1-1-1-1
100. Edwards JW, Schuster DM, Spain CV, Keller DF, Moses RW (2001) MAVRIC Flutter model transonic limit cycle oscillation test. AIAA Paper No. 2001–1291
101. Edwards JW (1996) Transonic shock oscillations and wing flutter calculated with an interactive boundary layer coupling method, NASA TM-110284
102. Edwards, J.W., Private communication
103. Parker EC, Spain CV, Soistmann DL (1991) Aileron Buzz investigated on several generic NASP wing configurations. AIAA Paper 91–0936
104. Pak C, Baker ML (2001) Control surface buzz analysis of a generic nasp wing. AIAA Paper 2001–1581
105. Beran PS, Khot NS, Eastep FE, Snyder RD, Zweber JV, Huttsell LJ, Scott JN (2002) The dependence of store-induced limit-cycle oscillation predictions on modeling fidelity, RTO applied vehicle technology panel symposium on reduction of military vehicle acquisition time and cost through advanced modeling and virtual product simulation, Paper # 44. France, Paris
106. Hutsell L, Schuster D, Volk J, Giesing J, Love M (2001) Evaluation of computational aeroelasticity codes for loads and flutter. AIAA Paper 2001–569

107. Woodson SH (2001) Wing drop, article in the McGraw-Hill 2002 yearbook of science and technology. McGraw-Hill, New York
108. Chambers JR (1999) Historical review: perspective on experiences with uncommanded lateral motions at high-subsonic and transonic speeds. Ball aerospace & technologies report, Aerospace systems division
109. Nayfeh AH, Elzebda JM, Mook DT (1989) Analytical study of the subsonic wing-rock phenomenon for slender delta wings. J Aircr 26(9):805–809
110. Ericsson LE (2001) Flow physics generating highly nonlinear lateral stability characteristics of 65-degree delta-wing-body. J Aircr 38(5):932–934
111. Kokolios A, Cook SP (2001) Modeling abrupt wing stall from flight test data, 32nd Annual symposium of the society of flight test engineers. Seattle
112. Lamar JE, Hall RM, Sanders EN, Cook SP, Grove DV (2003) Status and plans of abrupt wing stall figures-of-merit (FOM) studies from experimental and computational fluid dynamics, NASA technical report in preparation
113. Heeg J (1993) Analytical and experimental investigation of flutter suppression by piezoelectric actuation, NASA Technical paper 3241
114. Lazarus KB, Crawley EF, Lin CY (1991) Fundamental mechanism of aeroelastic control with control surface and strain actuation. 32nd AIAA/ASME/ASCE/AHS SDM Conference. Baltimore, MD, April, pp 1817–1831
115. Lazarus KB, Crawley EF, Lin CY (1997) Multi-variable active lifting surface control using strain actuation: analytical and experimental results. J Aircr 34(3):313–321
116. Vipperman JS, Barker JM, Clark RL, Balas GS (1999) Comparison of μ- and H2-synthesis controllers on an experimental typical section. J Guid Control Dyn 22(2):278–285
117. Clark RL, Frampton KD, Dowell EH (2000) Control of a three degree of freedom airfoil with limit cycle behavior. AIAA J Aircr 37(3):533–536
118. Frampton KD, Clark RL (2000) Experiments on control of limit cycle oscillations in a typical section. AIAA J Guid Control Dyn 23(5):956–960
119. Rule JA, Richard RE, Clark RL (2001) Design of an aeroelastic delta wing model for active flutter control. AIAA J Guid Control Dyn 24(5):918–924
120. Richard RW, Rule JA, Clark RL (2001) Genetic spatial optimization of active elements on an aeroelastic delta wing. ASME J Vib Acoust 123:466–471
121. Platanitis G, Strganac T (2002) Control of a wing section with nonlinearities using leading and trailing edge control surfaces. In: AIAA Paper No. 2002–1718, 43rd AIAA/ASME/ASCE/AHS/ACS structures, Structural dynamics and materials conference, Denver, CO, April

Aeroelastic Control

Robert Clark

Abstract Active control of aeroelastic systems is a subject of continuing interest and this chapter provides an introduction to this fascinating topic.

1 Introduction

Aeroelastic phenomena, as described throughout this text, occur due to a feedback effect between the unsteady aerodynamics and the structural dynamics of an airfoil or vehicle. This two-way exchange of energy is what distinguishes aeroelastic phenomena from driven vibration problems in structural dynamics. The presence of feedback also provides much common ground between the disciplines of control theory and aeroelasticity. In particular, the concept of stability is central to both fields, and the accuracy of models are judged largely on the ability to predict the conditions under which an instability will occur.

In control theory, linear time invariant (LTI) models form the basis for most types of analysis and design. Models of this form, and extensions to linear parameter varying systems, will be assumed for the methods discussed in this chapter. The dynamics of lightly damped structures are well described by this type of model. Using spatial expansions based on orthogonal functions [1], low order models can be constructed that predict vibration accurately, particularly for small displacements. Fluid dynamics, however, exhibit behavior on a wide range of scales and often are sensitive to nonlinearities present in the physics. Nevertheless, as was discussed in Chap. 9, many important cases of aeroelastic phenomena can be predicted with time-linearized aerodynamic models. These models can account for effects such as shock, separation and even turbulence in the steady solution, and the dynamic behavior is treated as a linear perturbation about this solution. With this linear dynamic simplifi-

R. Clark (✉)
Mechanical Engineering and Materials Science Duke University, Durham, NC, USA
e-mail: rclark@rochester.edu

E. H. Dowell (ed.), *A Modern Course in Aeroelasticity*, Solid Mechanics and Its Applications 264, https://doi.org/10.1007/978-3-030-74236-2_12

cation, tools such as eigenvector analysis or singular value analysis become possible, and aerodynamic models may be reduced in order similar to what is commonly done with finite element structural models.

In this chapter some basic concepts from control theory will be reviewed, including state-space modeling, balanced realization theory, and extensions to linear parameter varying models. This is a relatively narrow presentation of control theory, and the content is in no way meant to be comprehensive. Rather the intent is to introduce the reader to possibilities with simple examples serving as vehicles for the concepts presented. The broader area of controlling aeroelastic vehicles is described in the work on aeroservoelasticity from Noll [2], the literature survey of Livne [3], and a series of results from NASA sponsored research programs [4, 5].

Specifically, active flutter suppression is developed for two example systems, a typical section model and a flexible delta wing. Experimental results are presented for both with feedback control based upon fixed as well as gain-scheduled compensators. A unifying theme to the presentation is the applicability of Hankel singular values from the initial model reduction stage, aerodynamic, structural, or aeroelastic, to the design of actuator and sensor systems for selectively targeting modes of the system. Thus, we have chosen to provide an integrated design perspective for the presentation of aeroelastic control.

2 Linear System Theory

The design of feedback control systems is dominated by the use of linear time invariant (LTI) input/output models. The concepts described below are detailed in standard linear systems texts including [6–9], and are provided here largely to introduce the notation and terminology, which are also standard but may vary somewhat from previous notation in this book.

2.1 System Interconnections

The state-space model of an LTI system that is driven by inputs $u \in \mathbf{R}^p$ and observed by outputs $y \in \mathbf{R}^q$ is,

$$\begin{bmatrix} \dot{x} \\ y \end{bmatrix} = \left[\begin{array}{c|c} A & B \\ \hline C & D \end{array}\right] \begin{bmatrix} x \\ u \end{bmatrix} \tag{1}$$

where $A \in \mathbf{R}^{n\times n}$, $B \in \mathbf{R}^{n\times p}$, $C \in \mathbf{R}^{q\times n}$, and $D \in \mathbf{R}^{q\times p}$. This complete model is often denoted by a single symbol, G, that can be either the transfer function matrix

$$G(s) = C(sI - A)^{-1}B + D, \tag{2}$$

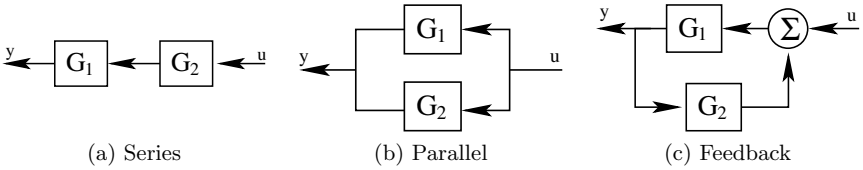

Fig. 1 Interconnection of systems G_1 and G_2

where s is a Laplace transform variable [8], or equivalently a state space realization

$$G(s) := \left[\begin{array}{c|c} A & B \\ \hline C & D \end{array}\right]. \tag{3}$$

State-space models can be developed at a subsystem level and combined by various interconnections into full system models. Several important interconnections are shown in the block diagrams of Fig. 1. Note that outputs appear on the left in these block diagrams, consistent with the equations they represent. The series connection of two systems G_1 and G_2, as shown in Fig. 1a, is

$$G_1(s)G_2(s) := \left[\begin{array}{cc|c} A_1 & B_1C_2 & B_1D_2 \\ 0 & A_2 & B_2 \\ \hline C_1 & D_1C_2 & D_1D_2 \end{array}\right] \tag{4}$$

and the parallel connection, as shown in Fig. 1b, is

$$G_1(s) + G_2(s) := \left[\begin{array}{cc|c} A_1 & 0 & B_1 \\ 0 & A_2 & B_2 \\ \hline C_1 & C_2 & D_1 + D_2 \end{array}\right] \tag{5}$$

Finally the feedback connection of systems G_1 and G_2 as shown in Fig. 1c is,

$$\left[\begin{array}{cc|c} A_1 + B_1R_u^{-1}D_2C_1 & B_1R_u^{-1}C_2 & B_1(I + R_u^{-1}D_2D_1) \\ B_2R_y^{-1}C_1 & A_2 + B_2R_y^{-1}D_1C_2 & B_2R_y^{-1}D_1 \\ \hline (I + D_1D_2R_y^{-1})C_1 & D_1R_u^{-1}C_2 & D_1(I + D_2R_y^{-1}D_1) \end{array}\right] \tag{6}$$

where

$$R_u = (I - D_2D_1)^{-1}, \qquad R_y = (I - D_1D_2)^{-1} \tag{7}$$

and simplifies considerably if either system is strictly proper (i.e., D_1 or D_2 is zero).

The feedback connection is often defined in terms of a linear fractional transformation (LFT) on the systems involved. The LFT is a convenient formalism for feedback effects and is commonly used in robust control design. It provides the ability to view uncertainty in a model as an unknown feedback effect and in so doing

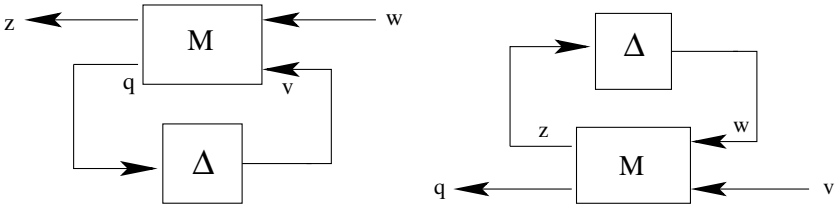

(a) Lower LFT, $\mathcal{F}_l(M, \Delta)$ (b) Upper LFT, $\mathcal{F}_u(M, \Delta)$

Fig. 2 Linear fractional transformation of Δ on M

unifies many methods of analysis and design [9, 10]. To understand the mechanics of an LFT explicitly, consider the mapping

$$\begin{bmatrix} z \\ q \end{bmatrix} = \begin{bmatrix} M_{11} & M_{12} \\ M_{21} & M_{22} \end{bmatrix} \begin{bmatrix} w \\ v \end{bmatrix} \tag{8}$$

and the feedback relationship $v = \Delta q$, as shown in Fig. 2a. The relationship between z and w is given by the lower LFT,

$$\begin{aligned} z &= \left(M_{11} + M_{12}\Delta(I - M_{22}\Delta)^{-1}M_{21}\right) w \\ &= \mathcal{F}_l(M, \Delta)w \end{aligned} \tag{9}$$

Similarly, the upper LFT results if Δ relates w and z as shown in Fig. 2b, and this is given by,

$$\begin{aligned} q &= \left(M_{22} + M_{21}\Delta(I - M_{11}\Delta)^{-1}M_{12}\right) v \\ &= \mathcal{F}_u(M, \Delta)v \end{aligned} \tag{10}$$

A useful property of the LFT is that algebraic combinations of LFTs which occur due to parallel, series, or feedback connections preserve the LFT structure. Therefore, systems with multiple LFTs can be represented by a single LFT of augmented dimensions. The general linear robust control problem is represented by the block diagram of Fig. 3, where Δ represents the effect of uncertainty on the system model, and K represents a feedback control law. The closed-loop transfer function of interest is

$$T_{zw} = \mathcal{F}_l(\mathcal{F}_u(T, \Delta), K). \tag{11}$$

The linear optimal control problem involves finding K to minimize T_{zw} with $\Delta = 0$, while robust control seeks the same objective with only limited knowledge of the uncertainty model Δ.

In principle the uncertainty Δ can be made large enough to contain all the feedback effects of aerodynamics on a system. Then the aeroelastic control problem is just regulation of the structural model while retaining stability in the presence of the uncertainty. Such a design is a first pass at including aerodynamics in a structural

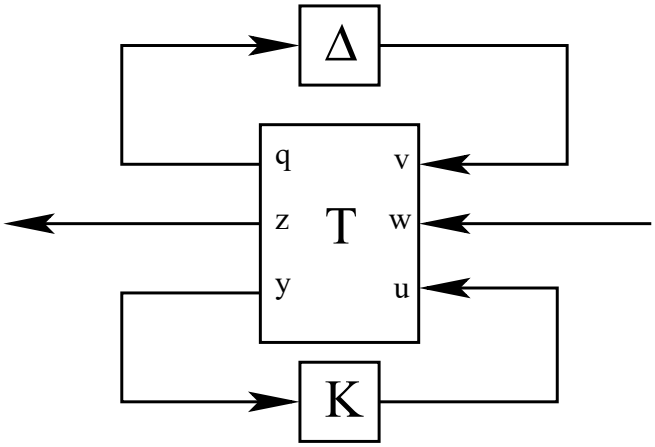

Fig. 3 General LFT framework for linear robust control problems

vibration problem, however, the performance would be limited by the large uncertainty. To obtain acceptable performance an explicit model for the aerodynamics is needed. A method for obtaining suitable reduced order models will be outlined in Sect. 3.

2.2 Controllability and Observability

The LTI system of (1) is said to be controllable if for any initial condition, $x(0)$, any target state, x_1, and any final time, t_f, there exists an input signal, $u(t)$, defined in the interval $t \in [0, t_f]$ that will cause the system to satisfy $x(t_f) = x_1$. In fact this control signal can be explicitly calculated as,

$$u(\tau) = -B^T e^{A^T(t_f-\tau)} W_c(t_f)^{-1}(e^{At_f}x(0) - x_1); \tag{12}$$

where W_c, the controllability Gramian, is

$$W_c(t_f) = \int_o^{t_f} e^{A\tau} B B^T e^{A^T\tau} d\tau. \tag{13}$$

The condition for existence of this signal is the invertibility of the matrix $W_c(t_f)$ for any final time t_f. For stable systems, only the infinite time Gramian, $W_c(\infty)$ need be calculated. The solution to (13) with infinite final time can be found from the positive definite solution to the Lyapunov equation,

$$AW_c + W_c A^T + BB^T = 0 \tag{14}$$

If the matrix W_c is full rank, and therefore invertible, the system is said to be controllable. Otherwise the system has at least some states which are not controllable from the input.

A dual problem to that of system controllability is observability. A system is said to be observable if for any time $t_f > 0$, the initial state $x(0)$ can be determined from the output history $y(t)$ over the interval $t \in [0, t_f]$. The infinite time observability Gramian can be found as the solution to,

$$A^T W_o + W_o A + C^T C = 0. \tag{15}$$

and the system is observable if W_o is full rank.

Controllability and observability of a system is a standard assumption for many problems involving the design of optimal control laws. In practice it is rare to find models built from physical principles that contain non-obvious unobservable or uncontrollable subspaces. However these Gramians can provide more information about a system than just a discrete test of controllability or observability. The numerical conditioning of W_c (W_o) provides measure of the relative degree of controllability (observability). For example if the singular values of W_c are spread over a wide range, then the inverse will be ill-conditioned and from (12) one would expect large control forces to reach a nominal x_1, say on the unit ball, $\|x_1\| = 1$.

Clearly the conditioning of this matrix depends upon the units, and more generally on the coordinates, of the internal state vector x. These coordinates are not unique and an LTI system will have a family of equivalent models related by similarity transformations. Transforming the state vector by any nonsingular matrix T as $\hat{x} = Tx$, yields equivalent realizations with the same input/output properties.

$$G(s) = C(sI - A)^{-1}B + D := \left[\begin{array}{c|c} T^{-1}AT & T^{-1}B \\ \hline CT & D \end{array}\right]. \tag{16}$$

A particularly useful coordinate system is called balanced coordinates, and is defined as the coordinate system in which the observability and controllability Gramians are diagonal and equal, $W_c = W_o$. For a stable, observable and controllable system such a realization always exists and is, by convention, ordered in such a way as to relate the first state of the model to the largest singular value of W_c, the second state to the second largest singular value of W_c, and so forth. These singular values are called the Hankel singular values (HSV) and they play an important role in model reduction as well as system realization theory [11, 12]. The technique for calculating transformations to balanced coordinates was first introduced in [13] and is described in detail in several textbooks, including [7, 9, 10].

It should also be noted that the absence of controllability and/or observability isn't always a negative thing. Control system design can be accomplished as long as one can control or observe the modes of the system that are important for the desired performance. As will be discussed later in Sect. 4, we can use the concept of Hankel singular values in the context of controllability and observability to selectively

couple to some modes and intentionally minimize coupling to others. This leads to the incorporation of control concepts in the physical *design* of a system.

3 Aeroelasticity: Aerodynamic Feedback

From spacecraft pointing to automotive ride quality many problems in structural dynamics involve the response of a system to external disturbances. Aeroelastic responses differ from these in that the source of the disturbance is strongly influenced by the structural response. This coupling is itself a feedback effect with the aerodynamics providing a flow-dependent feedback that can destabilize the system either through divergence or flutter. To study the aeroelastic problem as a feedback interconnection it is convenient to develop approximate LTI models in state-space form.

In this section state-space LTI models are constructed for two simple aeroelastic systems. The first is a typical section airfoil coupled with reduced order 2D potential flow. The combined system is shown to match standard results in the prediction of flutter, and also to match published results in the prediction of limit cycle oscillations. The second system is a uniform delta wing coupled to a reduced-order 3D potential flow model. Both these models are sized with consideration to available experimental hardware.

3.1 Development of a Typical Section Model

The typical section airfoil shown in Fig. 4 is standard in the analysis of rigid-body aeroelastic flutter [14, 15] and was covered in some detail in Chap. 3 of this book. The structural model for the system can be obtained by expressing the kinetic and potential energies in a set of generalized coordinates and applying Lagrange's equation [1]. The potential energy is stored exclusively in the systems springs and can be written as

$$U = \frac{1}{2}\left(K_h h^2 + K_\alpha \alpha^2 + K_\beta \beta^2\right). \tag{17}$$

where the coordinates and spring constants are as shown in Fig. 4. The kinetic energy is given by

$$T = \frac{1}{2}\int_{-b}^{b} \rho(x)\dot{r}(x)^2 dx. \tag{18}$$

where $\rho(x)$ is the linear density, $r(x)$ gives the position of the airfoil in an inertial frame and b is the semi-chord. For small angles, motion in the horizontal direction is negligible and the motion in the vertical direction can be written

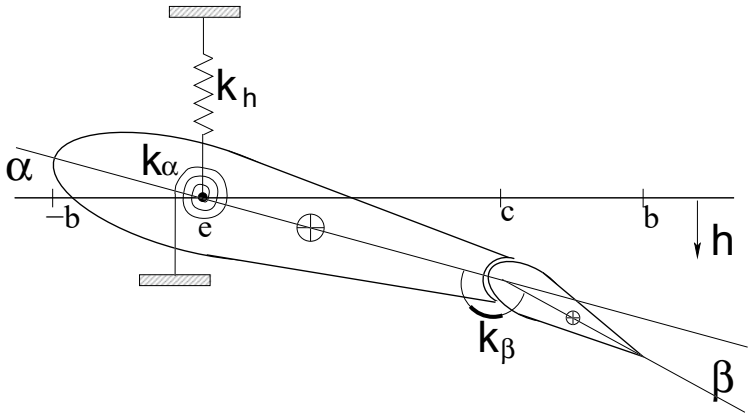

Fig. 4 Typical section airfoil model

$$r(x) \approx \begin{cases} -h - (x-e)\alpha & -b < x < c \\ -h - (x-e)\alpha - (x-c)\beta & c < x < b \end{cases} \tag{19}$$

where e is the elastic axis, c is the flap hinge-line, and by convention h, the vertical displacement of the elastic axis, is positive downward. Substituting this approximation into (18) yields,

$$T = \frac{1}{2}(M\dot{h}^2 + I_\alpha\dot{\alpha}^2 + I_\beta\dot{\beta}^2) + \dot{\alpha}\dot{h}S_\alpha + \dot{\beta}\dot{h}S_\beta + \dot{\alpha}\dot{\beta}(I_\beta + (c-e)S_\beta). \tag{20}$$

where the mass is

$$M = \int_{-b}^{b} \rho(x)dx, \tag{21}$$

and the inertias and mass imbalance terms are defined as,

$$I_\alpha = \int_{-b}^{b} \rho(x)(x-e)^2dx \qquad S_\alpha = \int_{-b}^{b} \rho(x)(x-e)dx \tag{22}$$

$$I_\beta = \int_{c}^{b} \rho(x)(x-c)^2dx \qquad S_\beta = \int_{c}^{b} \rho(x)(x-c)dx. \tag{23}$$

Lagrange's equation,

$$\frac{\partial}{\partial t}\left(\frac{\partial(T-U)}{\partial\dot{q}_i}\right) - \frac{\partial(T-U)}{\partial q_i} = Q_i, \tag{24}$$

relates the motion in coordinates q_i to forces Q_i in those coordinates. Choosing generalized coordinates as pitch(α), flap(β), and plunge(h) and substituting (20) and (17) into (24) yields the following equations of motion,

$$\begin{pmatrix} I_\alpha & I_\beta + (c-e)S_\beta & S_\alpha \\ I_\beta + (c-e)S_\beta & I_\beta & S_\beta \\ S_\alpha & S_\beta & M \end{pmatrix} \begin{pmatrix} \ddot{\alpha} \\ \ddot{\beta} \\ \ddot{h} \end{pmatrix} + \begin{pmatrix} K_\alpha & 0 & 0 \\ 0 & K_\beta & 0 \\ 0 & 0 & K_h \end{pmatrix} \begin{pmatrix} \alpha \\ \beta \\ h \end{pmatrix} = \begin{pmatrix} M_\alpha \\ M_\beta \\ -L \end{pmatrix} \tag{25}$$

where M_α, M_β, L are torque about the elastic axis, torque about the flap hinge, and lift force, respectively. With the choice of state vector,

$$x_s = \begin{bmatrix} \alpha & \beta & h & \dot{\alpha} & \dot{\beta} & \dot{h} \end{bmatrix}^T \tag{26}$$

and position measurements, y, this can be written in state-space form as,

$$\begin{bmatrix} \dot{x_s} \\ y \end{bmatrix} = \left[\begin{array}{cc|c} 0 & I & 0 \\ \mathbf{M}^{-1}\mathbf{K} & 0 & \mathbf{M}^{-1} \\ \hline I & 0 & 0 \end{array}\right] \begin{bmatrix} x_s \\ u \end{bmatrix} \tag{27}$$

where the mass matrix $\mathbf{M}$ is first term in (25) and $\mathbf{K}$ is the diagonal stiffness matrix from (25).

3.2 Aerodynamic Model, 2D

The structural model above must be coupled to an aerodynamic model to form the complete system. Analytic aerodynamic models, such as those of Theodorsen [14], have been used to study harmonic oscillations of the aeroelastic structure and used to predict important features, such as the flutter boundary. Approximations to these solutions are possible, both in the frequency and time domain [16–18], and have been used to study a variety of aeroelastic problems, including the typical section model [19–21].

In this work a vortex lattice formulation is used to represent the aerodynamics, and balanced model reduction is applied to generate a reduced-order model. The vortex-lattice approach admits general non-harmonic motions, as well as harmonic oscillations and can be extended to airfoils with more complex geometries. Balanced model reduction retains fidelity in the aerodynamic model with respect to external effects on the structure. Extensions of this type of model reduction to larger and more complex fluid dynamic models is an active area of research [22–24].

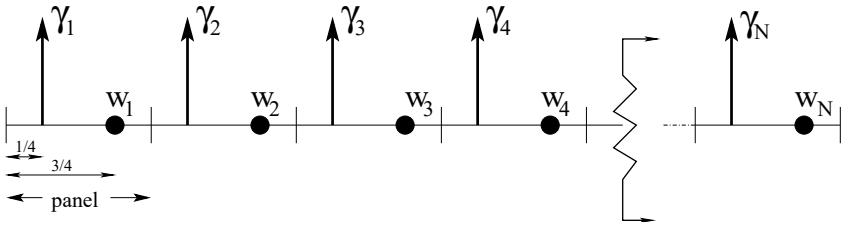

Fig. 5 Arrangement of point vortices and control points for two dimensional vortex lattice aerodynamic model

The fluid is assumed to be incompressible, irrotational, and inviscid. Following the development in [25] the 2D airfoil and a finite portion of the wake behind the airfoil is divided into N equal length elements, as shown in Fig. 5. Each panel element has a point vortex of strength γ at the quarter chord and a collocation point at the three-quarter-chord. The 2D wash at the collocation points on the airfoil can be described by the potential equation,

$$w_i^n = \sum_{j=1}^{N} K_{ij}\gamma_j^n, \qquad i = \{1, 2, \ldots, M\} \tag{28}$$

where the wash, w_i is described at M points on the airfoil, and influenced by vortex strength γ_j both on the airfoil ($1 \leq j \leq M$) and in the wake ($M + 1 \leq j \leq N$). For a 2D system the kernel function K_{ij} is given by,

$$K_{ij} = \frac{1}{2\pi(x_i - \zeta_j)} \tag{29}$$

where x_i and ζ_j are the ith wash collocation and jth point vortex locations, respectively.

The first wake term, γ_{M+1}^n, is given by the time rate of change of the circulation about the airfoil, as shown in (30). The vorticity simply convects along the wake with the freestream, as in (31). Since the wake is finite, vorticity on the final wake element is allowed to accumulate with a relaxation factor $\hat{\alpha} < 1$, as given in (32). Together these conditions,

$$\gamma_{M+1}^{n+1} = -\sum_{j=1}^{M}(\gamma_j^{n+1} - \gamma_j^n) \tag{30}$$

$$\gamma_i^{n+1} = \gamma_{i-1}^n, \quad \text{for } i = \{M + 2, M + 3, \ldots N - 1\} \tag{31}$$

$$\gamma_N^{n+1} = \gamma_{N-1}^n, +\hat{\alpha}\gamma_N^n \tag{32}$$

along with (28) constitute N linear equations in the N unknowns γ_i. The set of N equations can be written in matrix form,

$$\Gamma^{n+1} = \mathcal{A}\Gamma^n + \mathcal{B}w^n \tag{33}$$

where $\mathcal{A} \in \mathbf{R}^{N\times N}$, $\mathcal{B} \in \mathbf{R}^{N\times M}$ are constants, $\Gamma = [\gamma_1,\ \gamma_2,\ \ldots\ \gamma_n]^T$ is a state vector. The input to this system is the normal wash and is fully defined by the airfoil motion. Enforcing a non-penetration condition on the airfoil, for the geometry of Fig. 4 and small angle conditions, the wash is given by,

$$w_j = \begin{cases} \alpha U + \dot{\alpha}(x_j - e) + \dot{h} & \text{for } x_j < c \\ (\alpha+\beta)U + (\dot{\alpha}+\dot{\beta})(x_j - e) + \dot{h} & \text{for } x_j > c \end{cases} \tag{34}$$

Finally, outputs from the aerodynamic model relevant to the coupled system are the moment about the elastic axis, moment about the flap hinge, and the lift. These can be calculated as,

$$\begin{aligned} M_\alpha &= \int_{-b}^{b} \rho(e-x)\Delta p \\ M_\beta &= \int_{-b}^{b} \rho(c-x)\Delta p \\ L &= \int_{-b}^{b} \rho\Delta p \end{aligned} \tag{35}$$

where the pressure difference across the airfoil is given by Bernoulli's equation,

$$\Delta p = U\gamma(x) + \frac{d}{dt}\int_{-b}^{x} \gamma(\hat{x})d\hat{x} \tag{36}$$

The discretization of these integrals yields the expression of lift and moments as linear sums of γ_i and so forms an output equation for the state model,

$$y = \mathcal{C}\Gamma^n + \mathcal{D}w^n \tag{37}$$

where the outputs are lift and moments, $y = \left[M_\alpha,\ M_\beta,\ L\right]^T$.

3.3 Balanced Model Reduction

The model described by (33) and (37) is conveniently in the form of a discrete-time state-space system. This model can be converted to continuous-time, and coupled directly with (25) for aeroelastic analysis. However the vortex lattice model can be quite large, with a state for each discrete vortex. For efficient control design this model needs to be reduced to one of lower order.

One method of model reduction is to transform the aerodynamic model into a new coordinate system where the new states are orthogonal distributions of vorticity, ordered by their coupling to the input/output mapping. Such an ordering is achieved by transformation of the model into balanced coordinates. Model reduction then involves simply truncating the less important states.

For the reduced model to be applicable to the widest range of conditions it is useful to non-dimensionalize the inputs and outputs before balancing. Here we take non-dimensional time to be $s = tU/b$ and the non-dimensional input from the airfoil to be,

$$\hat{u} = \left[\alpha,\ \beta,\ \frac{h}{b},\ \frac{d\alpha}{ds},\ \frac{d\beta}{ds},\ \frac{dh/b}{ds}\right]^T \tag{38}$$

and the outputs to be lift and moment coefficients,

$$\begin{aligned}\hat{y} &= \left[C_\alpha, C_\beta,\ C_L\right]^T \\ &= \left[\frac{M_\alpha}{2\pi\rho U^2 b^2},\ \frac{M_\beta}{2\pi\rho U^2 b^2},\ \frac{L}{2\pi\rho U^2 b}\right]^T\end{aligned} \tag{39}$$

To illustrate the level of model reduction possible, a vortex lattice model was constructed for a simple flat plate airfoil with 20 vortices along the plate, and an additional 160 vortices in the wake. Figure 6 shows the Hankel singular values for each state in the balanced system. Since the states are ordered, simply truncating the model will yield a reduced order model whose magnitude error is, at worst, twice

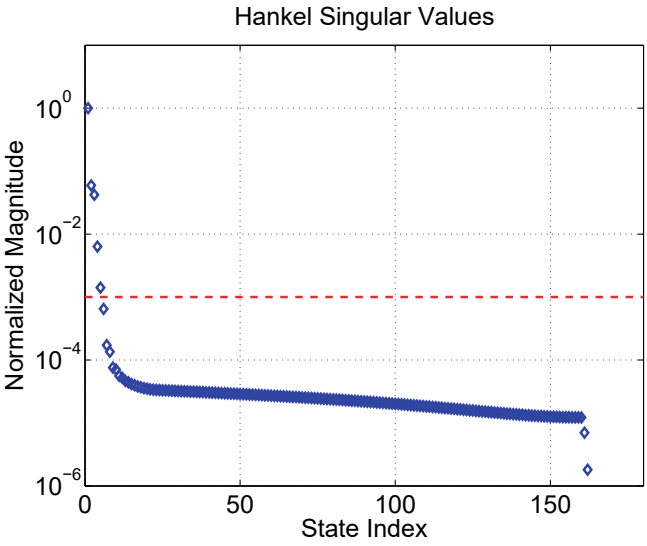

Fig. 6 Hankel singular values for balanced realization of flat-plate aerodynamic model

the sum of the truncated Hankel singular values [9]. Therefore, if a system G_a is a state-space model corresponding to the N vortex lattice equations and $\hat{G}_a$ is a nth order model found through balancing, the following holds

$$\|\hat{G}_a - G_a\|_\infty < 2\sum_{i=n}^{N} \sigma_i \tag{40}$$

where σ_i is the ith Hankel singular value. For practical purposes states whose contribution to the input/output map is three or four orders of magnitude below the dominant state may be truncated without significant errors. For the simple flat-plate airfoil a 5th order model was realized, corresponding to truncating all states whose contribution was three orders of magnitude down from the dominant state. The error bound for this case, calculated as twice the sum of the truncated singular values, is 1.6%. This is an upper bound on magnitude error (over all frequencies) in the prediction of lift and moment outputs, from harmonic plunge and pitch inputs.

Figure 7 shows the transient response of this system to a step input in angle of attack. The response matches well with the Wagner function, an analytic solution to this problem [15] given as

$$\phi(s) = \frac{2}{\pi}\int_0^\infty \left(\frac{J_1(J_1+Y_0)+Y_1(Y_1-J_0)}{(J_1+Y_0)^2+(Y_1-J_0)^2}\right)\frac{\sin(ks)}{k}dk \tag{41}$$

where J_i and Y_i are Bessel functions of the first and second kind, respectively, and are functions of the reduced frequency, k.

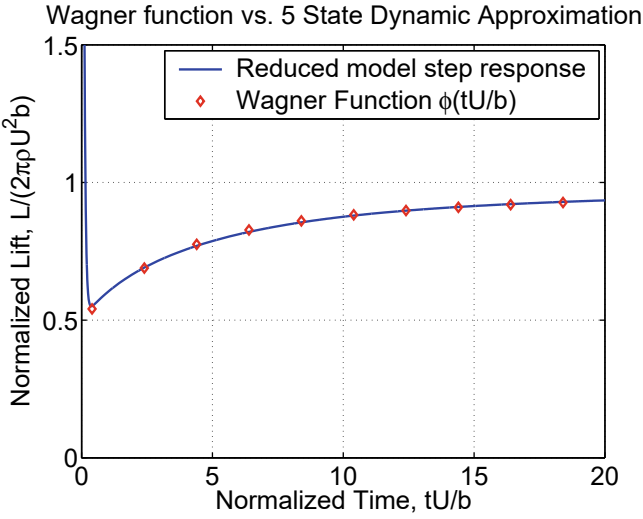

Fig. 7 Comparison of the Wagner function and step response of reduced order aerodynamics model

3.4 Combined Aeroelastic Model

The structural and aerodynamic models developed above can be coupled to form a model for the aeroelastic system. At a given flowspeed the dynamics are linear, and we can use eigenvalues of the system to assess stability properties. Figure 8 shows a root locus type plot of the system's eigenvalues as flowspeed is varied. The two oscillatory poles are related to the pitch and plunge dynamics of the typical section model. The real poles, and others outside the range of the plot, are related to flap dynamics and to the 5th order reduced-order aerodynamic model. For this example, the typical section has an elastic axis at 0.4 semichords forward of the center, and flap hinge 0.6 semichords aft of the center. Mass and inertial properties are also chosen as in reference [19], where a similar analysis is done using both an analytic solution to the aerodynamics and an approximation using rational functions. The results here, which are based on the reduced order vortex lattice code, compare well with these previous results. This root locus plot shows a behavior typical of bending-torsion flutter. From an undamped structural model, the initial effect of flow is to add damping to the all the modes. As the frequencies of pitch and plunge dominated motions coalesce the lower frequency becomes undamped, eventually destabilizing at the flutter boundary.

Finally, although the dynamics predicted by this model are linear it is possible to incorporate structural non-linearities into the model without dramatically changing the formulation. Previous studies on a typical section model [20, 21, 26] have shown a nonlinear spring response in the flap will produce limit-cycle behavior at flowspeeds well below the linear flutter boundary. To incorporate such an effect into the model it

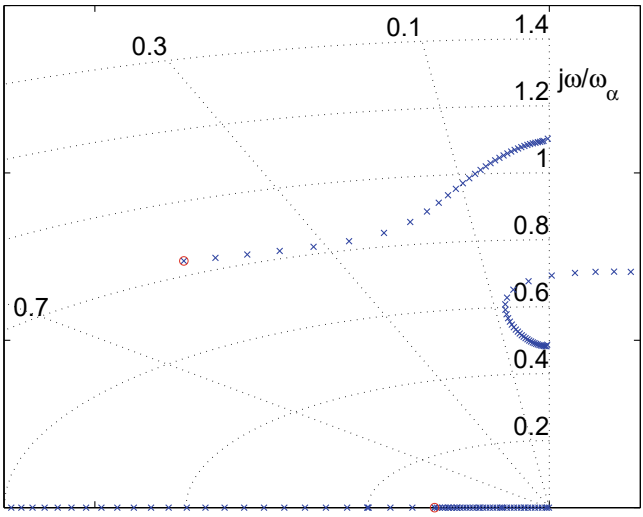

Fig. 8 Root locus showing variation of system eigenvalues with reduced order aerodynamic model, parameters chosen as in [19]

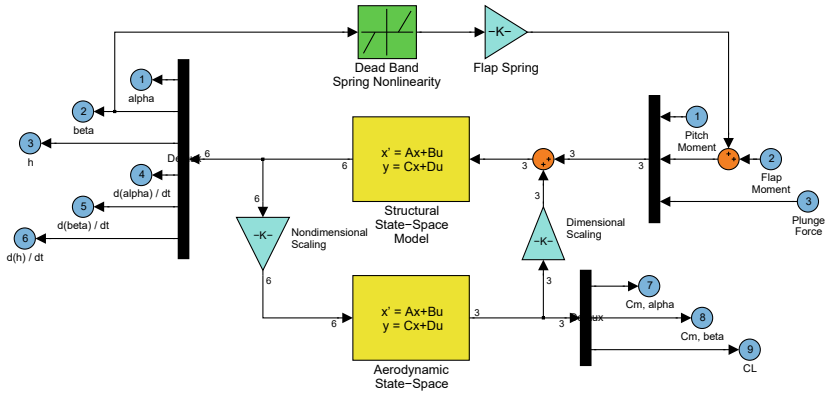

Fig. 9 Coupled aeroelastic system with deadband nonlinearity

Table 1 Physical parameters for typical section model

Elastic axis 1/4 chord	e	−0.063 m
Hingeline 3/4 chord	c	0.063 m
Mass	M	1.72 Kg
Pitch inertia	I_α	7.07e-3 Kg m^2
Flap inertia	I_β	1.68e-4 Kg m^2
Wing mass imbalance	S_α	4.49e-2 Kg m
Flap mass imbalance	S_β	2.03e-3 Kg m
Pitch stiffness	K_α	19.6 Nm/rad
Flap stiffness	K_β	2.0 Nm/rad
Plunge stiffness	K_h	1480 N/m

is useful to isolate the nonlinearity as a feedback effect. This corresponds to having a nominal linear model in an LFT configuration with the nonlinearity. In the structural model of (25) the flap spring stiffness, K_β, can be set to zero, and its effect replaced with an outer feedback loop between flap position and the moment applied to the flap. Such an arrangement is shown in Fig. 9, where the nonlinearity is deadband in the response of the flap spring.

This system has two distinct linear regions. Within the deadband region it appears that there is no physical restoring spring in the flap position, and outside the region it has the a nominal stiffness K_β. The switching between these systems, however, is discontinuous and occurs twice per flap oscillation. The dynamics, therefore, exhibit a variety of nonlinear behavior. The work here uses physical parameters as in Table 1, consistent with those used in [20] and a 5th order aerodynamic model as described above. The simulations were executed directly from the diagram of Fig. 9 using integration routines within the commercially available (Mathworks, Inc.) `Simulink` software. With the deadband set to zero, the system was linear and had a predicted

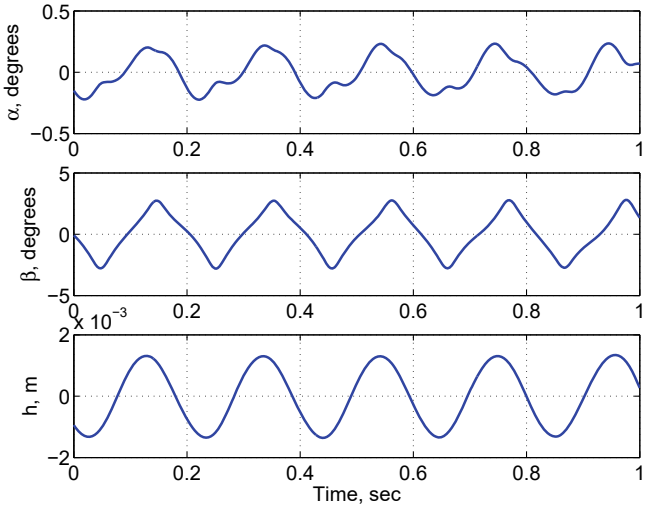

Fig. 10 Limit cycle behavior of nonlinear system at 30% of linear flutter speed

flutter boundary of 23.4 m/s, with an unstable oscillation at 6.1 Hz. With a deadband of 2.12 degrees, however, the system exhibited limit cycles starting at about 28% of the linear flutter speed. These limit cycles, shown in Fig. 10 at 30% of the flutter speed, compare well with earlier results [20].

3.5 Development of a Delta Wing Model

True flutter phenomena occur due to distributed flexibility in an aircraft wing, conditions which are only coarsely approximated by the rigid body dynamics of the typical section model. A more realistic system, that still lends itself to analytic study, is a uniform and flexible delta wing [27, 28]. Here a delta wing model is developed which incorporates piezoelectric sensors and actuators to allow for aeroelastic control. The model also serves as a basic design platform for shaping the open-loop dynamics of the structure through optimal actuator and sensor placement, as detailed in the next section.

Basic physics of the delta wing model include the structural and transduction device dynamics, and their interaction with the unsteady aerodynamic loads. The structural model is readily developed through finite element analysis or an assumed modes approach as outlined by Richard et al. [29]. For the purpose of this example, the structural model is formed using the assumed modes method outlined in [30]. This general approach follows the work of Anderson et al. [31] by finding the assumed mode shapes applicable to a clamped-free-free-free ($CFFF$) rectangular plate and transforming these functions into a trapezoidal domain. A one-hundred mode (two-

hundred state) model is generated with Lagrange's equations (the products of ten assumed chordwise and ten assumed spanwise beam modes), and the model is later reduced to include fifty states.

Initially, the out-of-plane assumed modal displacements of a rectangular $CFFF$ plate are represented as the product of clamped-free (η) and free-free (μ) beam modes for a given assumed plate mode (i) as in Eq. 42, where the i indice extends over all combinations of j and k. These beam mode products are used for simplicity since they satisfy the geometric (and natural) boundary conditions for the $CFFF$ plate.

$$\Phi_i(x, y) = \eta_j(x)\mu_k(y) \tag{42}$$

The beam modes are defined based upon the general beam solution Eq. (43) with boundary conditions specific to the problem.

$$W(x) = A_1\sin(\gamma_i x) + A_2\cos(\gamma_i x) + A_3\sinh(\gamma_i x) + A_4\cosh(\gamma_i x) \tag{43}$$

The free-free case requires: $W''(0) = 0$, $W'''(0) = 0$, $W''(L) = 0$, and $W'''(L) = 0$, giving the mode shapes described in Eq. (44). The clamped-free case requires the conditions: $W(0) = 0$, $W'(0) = 0$, $W''(L) = 0$, and $W'''(L) = 0$, which yields the mode shapes described by Eq. (45). The eigenvalues are represented by parameters α_j and β_k, and L_x and L_y are the x and y dimensions of the plate.

$$\begin{aligned} \eta_j(x) &= \cos(\alpha_j x) + \cosh(\alpha_j x) + A[\sin(\alpha_j x) + \sinh(\alpha_j y)] \\ A &= \left[\frac{\cos(\alpha_j L_x) - \cosh(\alpha_j L_x)}{\sin(\alpha_j L_x) - \sinh(\alpha_j L_x)}\right] \end{aligned} \tag{44}$$

$$\begin{aligned} \mu_k(y) &= \cos(\beta_k y) + \cosh(\beta_k y) + B\,[-\sin(\beta_k y) + \sinh(\beta_k y)] \\ B &= \left[\frac{\sin(\beta_k L_y) - \sinh(\beta_k L_y)}{\cos(\beta_k L_y) + \cosh(\beta_k L_y)}\right] \end{aligned} \tag{45}$$

Using the assumed mode shapes developed for the rectangular plate, a coordinate transformation is performed to map them into non-dimensional trapezoidal coordinates. The transformation is shown in Fig. 11. The transformation is normalized by span (Sp) and root chord (C) dimensions to yield a unit square, and the taper ratio (TR) is defined as the tip chord dimension divided by the root chord. By this definition, the delta wing would have a taper ratio of zero but numerical considerations limit this value to a finite taper ratio: $TR = \epsilon > 0$. In addition to this transformation, the Jacobian is required due to integration of the shape functions necessary in the model development. Allowing for the intermediate step of non-dimensionalizing x and y by C and S_p respectively (yielding $\hat{x}$ and $\hat{y}$), the Jacobian is defined as follows:

$$\mathbf{J}\left(\frac{\hat{x}, \hat{y}}{u, v}\right) \equiv \begin{vmatrix} \frac{\partial \hat{x}}{\partial u} & \frac{\partial \hat{x}}{\partial v} \\ \frac{\partial \hat{y}}{\partial u} & \frac{\partial \hat{y}}{\partial v} \end{vmatrix} = \frac{Sp}{2C}\left[1 - v\,(1 - TR)\right] \tag{46}$$

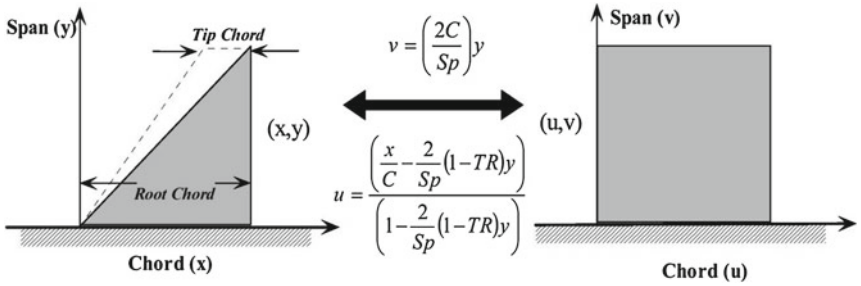

Fig. 11 Coordinate transformation from dimensionalized rectangular to non-dimensional trapezoidal domain

Table 2 Delta wing model parameters

Geometry	45° LE × 90° TE delta, clamped at root
Proportions	0.381 m (15 × 15 in.)
Material	Acrylic
Thickness (h_s)	1.58×10^{-3} m (0.062")
Elastic modulus (E_s)	4.2×10^9 N/m
Poisson ratio (υ_s)	0.45
Density (ρ_s)	1.009×10^3 kg/m^3

These transformations along with the Jacobian allow for the integration of assumed rectangular plate mode shape functions necessary for the calculation of energy functions used to develop the equations of motion.

Upon developing expressions for the kinetic and potential energy, Lagrange's equations Eq. (24) can be applied to obtain the structural equations of motion, which upon solving the discrete eigenvalue problem resulting from the assumed-modes approach, can be expressed in the following well recognized form:

$$\begin{bmatrix} \dot{r} \\ \ddot{r} \end{bmatrix} = \begin{bmatrix} 0 & I \\ -\omega^2 & -2\zeta\omega \end{bmatrix} \begin{bmatrix} r \\ \dot{r} \end{bmatrix} + \begin{bmatrix} 0 \\ I \end{bmatrix} [R] \tag{47}$$

with r and R representing modal states and forces. The ζ matrix is a diagonal representation of approximate proportional modal damping coefficients, introduced to bound the response at resonance, and ω is the matrix of system natural frequencies.

For the example presented, the geometric and material parameters were selected to model a wing of appropriate mass and stiffness to facilitate experimental implementation in the low-speed wind tunnel located at Duke University (Table 2). These parameters correspond to a model of appropriate dimensions and sufficient flexibility to produce flutter within the operating range of the wind tunnel. The material properties were obtained from [32] as average properties for acrylic.

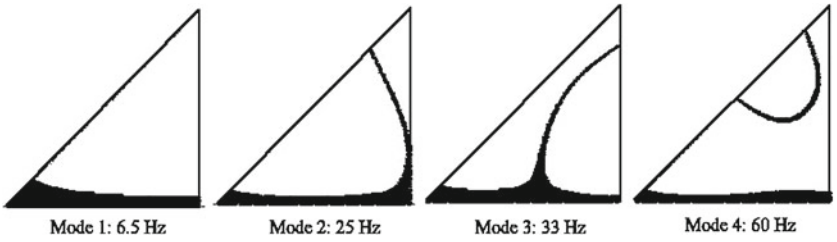

Fig. 12 Invaccuo mode shape node-line predictions for first four structural modes

At this point in the development, the model can be used to predict the no-flow mode shapes of the wing and associated natural frequencies for a given set of parameters. Plots of these predicted mode shapes with nodal lines can be seen in Fig. 12.

3.6 Transducer Effects

To complete the design model, one must incorporate the dynamics of the transduction devices. Here, induced-strain, surface-mounted, piezoelectric transducers were selected for actuators and sensors.

A technique for incorporating the electro-mechanical coupling effects of surface mounted piezostructures was developed in [33]. A brief presentation of the model is discussed herein; however greater details of the modeling specific to the example here can be found in [34]. The piezoelectric patches relate to the structure through the Θ and C_p matrices shown in Eqs. (48) and (49).

$$\left[M_s + M_p\right]\ddot{q} + \left[K_s + K_p\right]q = B_f F + \Theta V \tag{48}$$

$$Y = \Theta^T q + C_p V \tag{49}$$

The general definitions of the Θ and C_p matrices are shown in Eqs. (50) and (51), with the first part of the integrand in Eq. (50) representing the mechanical portion and the later electrical part being coupled to it through the piezoelectric material constant matrix, e^T. The M_p and K_p terms in Eqs. (48) and (49) represent the mass and stiffness characteristics of the patches and are generally small compared to the corresponding terms for the wing structure. The details of Eqs. (50) and (51) can be found in [33] or [30].

$$\Theta = \int_{V_p} [L_w \Phi_r R_s]^T e^T [R_E L_\varphi \Phi_v] dV_p \tag{50}$$

$$C_p = \int_{V_p} [\Phi_v L_\varphi R_E]^T \varepsilon^S [R_E L_\varphi \Phi_v]\, dV_p \tag{51}$$

These equations can be substantially simplified for cases involving thin patches with symmetric strain constants ($d_{31} = d_{32}$), which are part of the e^T and ε^S terms. The simplified equations are taken from [30] and are shown in Eqs. (52) and (53) for mode j. In the simplified Θ equation, the electro-mechanical coupling constant is composed of the piezoelectric strain constant for the x and y directions, the piezoelectric modulus of elasticity and the Poisson's ratio ($d_{31},\ E_p,\ \nu_p$). The integrated potential distribution term consists of the plate and patch thicknesses, ($h_s,\ h_p$), and the chord length, (C). The integrand involves only the jth mode shape function for the plate with the limits of integration corresponding to the x and y domains of the patch. The full matrix has rows corresponding to particular modes (j) and columns corresponding to patches (m). For this simplified case, the capacitance function (C_p) forms a diagonal matrix whose entries consist of the piezoelectric-dielectric constants, area, and thicknesses ($\varepsilon_m^S,\ A_{pm}, h_{pm}$). The diagonal nature of Eq. (53) reflects the fact that capacitance is only relevant for the collocated sensoriactuator case (i.e., when the transducer is used for both sensing and actuation [35].)

$$\Theta_j = \left(\frac{d_{31}E_p}{1-\nu_p}\right)\left(\frac{h_s + h_p}{2C^2}\right) \int_{y_1}^{y_2}\int_{x_1}^{x_2}\left[\frac{\partial^2 \Phi_{jm}(x,y)}{\partial x^2} + \frac{\partial^2 \Phi_{jm}(x,y)}{\partial y^2}\right] dxdy \tag{52}$$

$$C_p = \begin{bmatrix} \frac{\varepsilon_1^S A_{p1}}{h_{p1}} & & \mathbf{0} \\ & \searrow & \\ \mathbf{0} & & \frac{\varepsilon_m^S A_{pm}}{h_{pm}} \end{bmatrix} \tag{53}$$

These equations are used to model the effect of piezoelectric patches (sensors or actuators) mounted on the delta wing structure. The computational difficulties in this approach result from the integral in Eq. (52). As long as the patches are rectangular and orthogonal to the base, simple numerical integration schemes can be used. However, for calculating odd-shaped, rotated, or numerous patches, straightforward use of this method is too computationally intensive.

To address this issue, a contiguous grid was developed over the entire surface of the wing [36]. A compromise between computational efficiency and accuracy determines the resolution of the grid. The general idea is to save, in advance, the calculated electromechanical coupling characteristics of very small piezoelectric elements, which can be used later, through numerical integration, to compute the electromechanical coupling coefficient for individual actuator or sensor patches. The size of these elements allow for further simplification of Eq. (52) as shown in Eq. (54). The justification for this is quite straightforward. If the individual elements used to represent a distributed sensor or actuator are sufficiently small compared to the wavelengths of the modes of interest, a zero-order approximation to the integral can be used. Therefore, by taking the value of the shape function at the center of an

element (x_c, y_c) and multiplying by the area (A_E), the integral can be approximated as follows:

$$\int_{y_1}^{y_2}\int_{x_1}^{x_2}\left[\frac{\partial^2\Phi_{jm}(x,y)}{\partial x^2}+\frac{\partial^2\Phi_{jm}(x,y)}{\partial y^2}\right]dxdy \approx \left[\frac{\partial^2\Phi_{jm}(x_c,y_c)}{\partial x^2}+\frac{\partial^2\Phi_{jm}(x_c,y_c)}{\partial y^2}\right]\mathbf{A}_E \tag{54}$$

Due to the linear nature of the electro-mechanical coupling effects of the patches, large patches can be constructed by summing the effects of elements within the large patch boundaries as illustrated in Eq. (55) with the variables Θ_m and Θ_E corresponding to an overall patch and its component elements respectively, and **N** being the number of constituent elements. Similarly, the capacitance effects can be determined by summing the component element capacitance effects. Since all of the elements are of constant dimensions, the capacitance is the same for all elements and the summation reduces to the simple expression of Eq. (56).

$$\Theta_m = \sum_{\mathbf{E=1}}^{\mathbf{N}}\Theta_E \tag{55}$$

$$\mathbf{C}_{p_m} = \mathbf{N}\mathbf{C}_{p_E} \tag{56}$$

Using this approach allows for the necessary element characteristics to be calculated once for a given wing geometry. The process requires that the Θ_E and C_{p_E} vectors be calculated for all of the elements and saved for later patch construction. The computational advantages gained from this approach result from the fact that much of the required computations are performed outside of the optimization routine - apriori. Thus, the cost of calculating the elements' coupling does not factor into the efficiency needs of the algorithm. Computational gains and modeling errors that result from this approach can be found in the work of Richard [34] (Fig. 13).

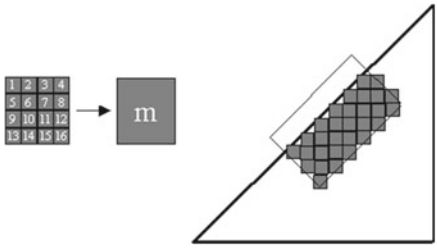

Fig. 13 Patch building through summation of piezoelectric elements

3.7 Aerodynamic Model, 3D

A reduced order aerodynamic model was developed based upon the vortex lattice approach. Thus, assumptions include subsonic, inviscid, incompressible, and irrotational flow as has been previously discussed in this chapter and book. The first step in the process is to develop a grid for the wing and wake as illustrated in Fig. 14 with vorticity points at the quarter chord, and downwash observation points at the three-quarter chord of each grid block. The grid is structured such that the grid blocks are of like size and shape in the unit square computational domain consistent with the structural model. The grid used in this example has 8 chordwise blocks, 15 spanwise blocks, and 4 chords of wake leading to a model with 600 vorticity states.

As detailed in the previous section, the order of this model can be readily reduced using balanced realization theory. Applying this model reduction technique, it was possible to reduce the number of states included in the aerodynamic model from 600 to 50. The relative magnitudes of the balanced system Gramians (i.e., the HSVs) are illustrated in Fig. 15. The sum of all of the truncated Gramians totals less than 5% of the non-truncated Gramian sum.

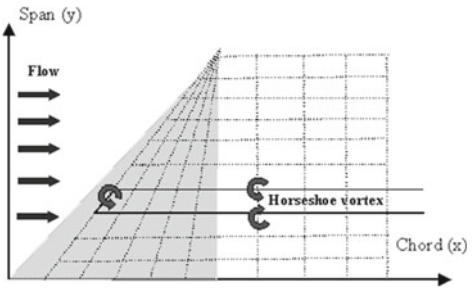

Fig. 14 Vortex lattice construction grid for wing and wake

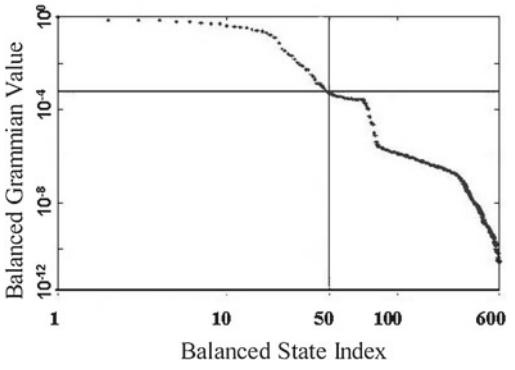

Fig. 15 Relative magnitude of Gramians in balanced system

3.8 *Coupled System*

The aeroelastic system is developed by coupling the structural and aerodynamic models through feedback. The two systems were constructed with this goal in mind and their input/output requirements were modeled so as to facilitate this step. Once coupled, the model can be used to predict characteristics such as flutter speed, flutter frequency, mode shape progression with flow, and general system response traits for any flow speed below the linear instability boundary. It is now possible to use this model to predict the onset of flutter (based on the assumption of linear instability being the driving mechanism). By plotting the aeroelastic system roots at progressively increasing flow speeds, trends of root migration can be followed that clearly show the roots of the second mode moving into the right half plane (Fig. 16). In contrast, each of the other modes show substantially increased damping, and thus, reduced response. The instability takes place at a flow speed of 31.5 m/s for the system parameters outlined in Table 2. Although the non-linear effects involved with flutter can be expected to somewhat alter the frequency of oscillation, it can be expected to be in the vicinity of the 18 Hz prediction of the linear model.

The aeroelastic model can also be used to predict the progression of mode shapes with increasing flow speed. Since the root migration identifies the second mode as the mode of interest, the emphasis here is placed on how that mode shape changes as the system approaches flutter. The areas of lowest average maximum displacements are shown in Fig. 17 with respect to increasing flow speed. This figure clearly shows the nodal centers moving toward the interior of the wing as the flow speed is increased.

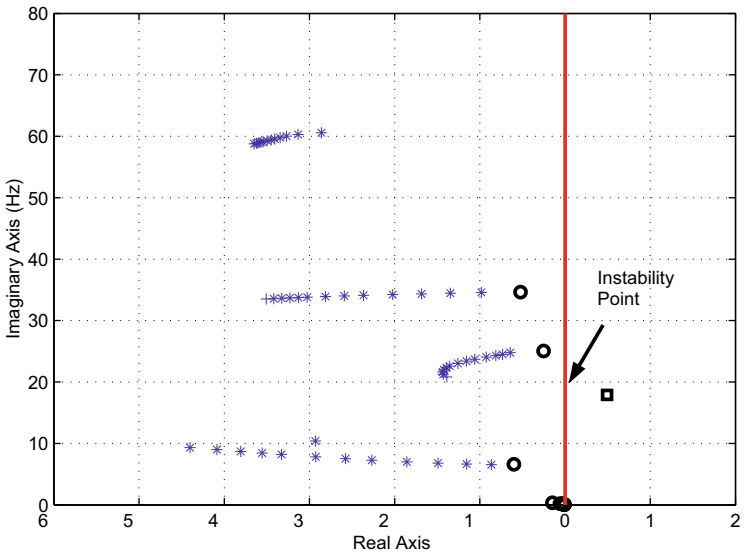

Fig. 16 Aeroelastic root migrations with flow

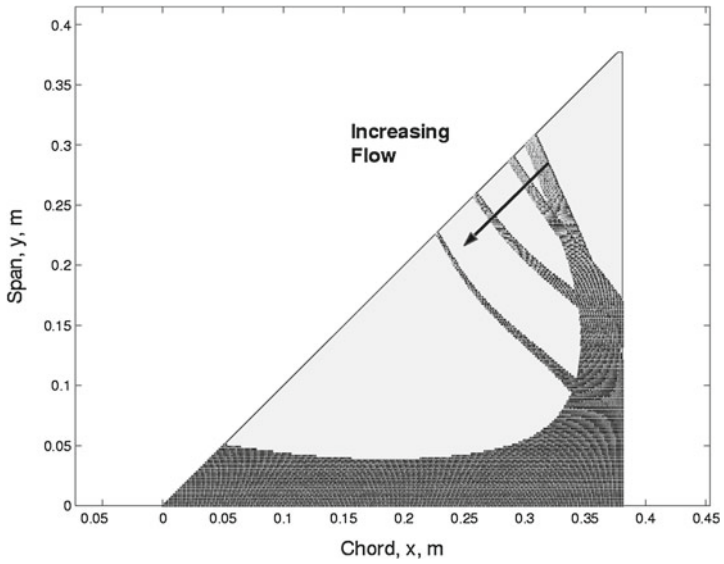

Fig. 17 Mode shape progression of second aeroelastic mode with flow speed

This pre-flutter, combined torsional/bending mode, in addition to the clear trend shown in Fig. 16, points to the fact that flutter results from a coalescence of the first structural mode (primarily bending) and the second structural mode (primarily torsional). This is consistent with the concept of modal coalescence described in this text. There is also the implication that the ideal placement of sensors and actuators for control of this mode should change between the no-flow case and the pre-flutter case.

4 Open-Loop Design Considerations

In a feedback control system, the actuator input signals are created by modifying the temporal response of the sensor signals with a compensator. The optimum controller - temporal compensator, is usually realized by frequency-shaping the system open- and closed-loop transfer functions [30]. Although much can be accomplished with the optimization (and in practice the iterative tuning) of a control law, the final performance of a system depends very much on how difficult the problem is to begin with. Previous work in adaptive structures has also shown that optimum compensator design may be augmented by considering the design of the *spatial compensator* of the control system [30]. Spatial compensation is defined as the influence of the type, placement, size, and shape of the transducers on the open-loop response and, as a result, the closed-loop temporal compensator design. When combined, the temporal and spatial compensator's form the complete control system for any structure.

While much of an airframe design may be fixed by other criteria, the choice of actuator and sensor locations is often determined by a combination of physical restraints and requirements of the control system. These choices frame the dynamics, and if possible, it is best to make those decisions an integral part of the design, with an eye toward the final control objectives. The Hankel Singular Values (HSVs) that play a key role in model reduction can also be utilized early in the design to facilitate the choice of actuator and sensor locations.

HSVs and the Modal Model

In models with lightly damped dynamics the HSVs can be related directly to modal parameters through a very simple expression. For the purpose of development, cast the structural model from the actuator input, $u(t)$, to the measured output of the sensor, $y(t)$, in modal form such that

$$\begin{aligned} \ddot{\mathbf{q}} + \text{diag}(2\zeta_i\omega_i)\dot{\mathbf{q}} + \text{diag}(\omega_i^2)\mathbf{q} &= \hat{\mathbf{B}}\text{u} \\ y &= \hat{\mathbf{C}}\mathbf{q} \end{aligned} \tag{57}$$

where ω_i and ζ_i are the natural frequency and damping ratio of the ith mode, respectively. Defining the state vector as

$$\mathbf{x} = [\dot{q}_1, \omega_1 q_1, \ldots, \dot{q}_{N_m}, \omega_{N_m} q_{N_m}]^T \tag{58}$$

produces a state space representation such that

$$\begin{aligned} \dot{\mathbf{x}} &= \mathbf{A}\mathbf{x} + \mathbf{B}u \\ y &= \mathbf{C}\mathbf{x} \end{aligned} \tag{59}$$

where $\mathbf{A} = \text{diag}(\mathbf{A}_\text{i})$, $\mathbf{B} = [\mathbf{B}_1^T, \ldots, \mathbf{B}_{N_m}^T]^T$, $\mathbf{C} = [\mathbf{C}_1, \ldots, \mathbf{C}_{N_m}]$. The submatrices are defined as

$$\mathbf{A}_i = \begin{bmatrix} -2\zeta_i\omega_i & -\omega_i \\ \omega_i & 0 \end{bmatrix} \tag{60}$$

$$\mathbf{B}_i = \begin{bmatrix} \mathbf{b}_i^T \\ \mathbf{0} \end{bmatrix} \tag{61}$$

and

$$\mathbf{C}_j = \begin{bmatrix} \mathbf{c}_j, \mathbf{0} \end{bmatrix} \tag{62}$$

where $\mathbf{b}_i^T$ is the ith row of $\hat{\mathbf{B}}$ and $\mathbf{c}_j$ is the jth column of $\hat{\mathbf{C}}$ [37].

Williams [37] demonstrated that the square of the ith HSV of a lightly damped structure can be approximated by the following expression:

$$\sigma_i^2 \approx \frac{\left[\mathbf{b}_i^T \mathbf{b}_i\right]\left[\mathbf{c}_i^T \mathbf{c}_i\right]}{\left(4\zeta_i \omega_i\right)^2}, \tag{63}$$

where σ_i is the approximation of the ith HSV. As indicated in Eq. (63), the ith HSV is proportional to the time constant ($\tau_i = 1/(\zeta_i \omega_i)$) of the ith structural mode and the modal participation coefficients for each actuator and sensor. The numerator of Eq. (63) thus provides a measure of the degree of coupling between the actuator inputs and measured outputs relative to the structural modes. Physically, the HSV is a measure of the amount of energy that can be stored in the system from the inputs and the amount of energy that can be retrieved by the outputs [38]. Thus, the HSV can be used to measure the effectiveness of a particular actuator/sensor pair for coupling, or not coupling, to structural modes.

From a practical perspective, it should be noted that not all models can be described purely in modal form, and in fact, most experimental models, obtained from system identification, will often incorporate first-order dynamics as well with real poles. However, when optimizing actuator/sensor designs, one usually targets the lightly damped modes of the system since the actuator/sensor design is an integral part of the structural dynamics. Thus, one can effectively ignore the first order dynamics in this portion of the design, but certainly not in the design of the temporal compensator.

4.1 Optimization Strategy

There are numerous means for optimization; however, the one thing common to all schemes is the choice of the cost function, which effectively defines the problem. Since the Hankel singular values provide a measure of the degree of coupling for a chosen path, one must decide how to use this information in design.

The design metric for frequency-shaping with spatial compensators is developed from the work presented by Smith and Clark [39], Clark and Cox [40], Lim [41], and Lim and Gawronski [42]. As detailed in these references, methods for optimizing or selecting the appropriate spatial aperture (i.e, size and location) of actuators and sensors using Hankel singular values of the open-loop controllability and observability Gramians are developed.

The first step in developing any compensator design metric is to cast the control problem into proper form. Figure 18 shows a block diagram of the two-port or two-input, two-output (TITO) closed-loop system. The system $T(s)$ is composed of the generalized plant, $P(s)$, with controller, $K(s)$. The transfer matrix $P(s)$ in Fig. 18 represents the dynamics of the adaptive structure and transducer coupling, and is written in equation form as:

$$\begin{bmatrix} z(s) \\ y(s) \end{bmatrix} = \begin{bmatrix} P_{zw}(s) & P_{zu}(s) \\ P_{yw}(s) & P_{yu}(s) \end{bmatrix} \begin{bmatrix} w(s) \\ u(s) \end{bmatrix}. \tag{64}$$

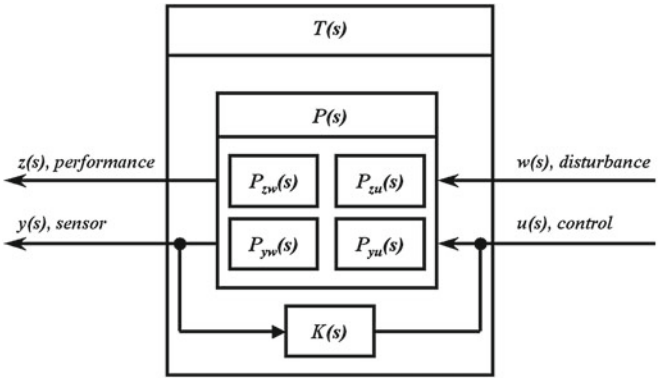

Fig. 18 Block diagram of generalized plant with feedback controller

As shown by Fig. 18 and Eq. (64), $P(s)$ is partitioned according to the input-output variables, and four sub-matrices are identified. The upper-left transfer matrix, P_{zw}, represents the path from the input disturbance signals to the measured performance. The lower-right transfer matrix, P_{yu}, is the path from the input actuator signal to the response of the sensor, and is determined by the selection of transducer type, placement, size, and/or shape. The cross transfer matrices P_{zu} and P_{yw} show that the design of the control transducers also affects system performance and that the disturbance signals affect the measured outputs, respectively.

Each transfer matrix is formed from the states of the system and the respective input-output characteristics. When optimized, the design of the spatial compensators ideally alters the coupling characteristics of the system for increased performance and robustness.

The Hankel singular values (HSVs) from the input actuator signal to the sensor output are written as

$$\sigma_{yu} = \text{diag}(\sigma_{yu1}, \ldots, \sigma_{yun}, \ldots, \sigma_{yuN_m}). \tag{65}$$

The HSVs defined by Eq. (65) provide a measure of the degree of coupling between each of the N_m modes associated with the transducer path of the control problem.

A spatial compensator design metric based entirely upon evaluating Eq. (65) was presented by Lim and Gawronski [42]. In this case, the HSVs defined by Eq. (65) were computed from a predetermined set of candidate transducer locations and the optimum location is defined by the path which provided the greatest HSV measurement. The conclusion being that selecting transducer locations with the largest degree of coupling increases control system efficiency and, thus, performance.

Lim [41] recognized that the purpose of the control problem defined in Fig. 18 is to reduce/control the measure of performance, $z(s)$, and that Eq. (65) could be weighted by a measure of the system performance to provide for spatial compensator designs that are efficient at coupling the modes with the greatest effect on the measured performance.

Again using HSVs, a measure of the degree of coupling of each mode associated with the performance-disturbance path, P_{zw}, is

$$\Sigma_{zw} = \text{diag}(\sigma_{zw1}, \ldots, \sigma_{zwn}, \ldots, \sigma_{zwN_m}) \tag{66}$$

and the design metric defined by Lim [41] is written as

$$J_{qp} \equiv \sum_{i=1}^{N_m} \frac{\sigma^2_{y_p u_q i}}{\bar{\sigma}^2_{yui}} \sigma^2_{zwi}, \tag{67}$$

where J_{qp} is the metric for the q-th candidate sensor and p-th candidate actuator. The value $\bar{\sigma}^2_{yui}$ is the squared HSVs of the system where all possible actuators and sensors are considered; it is used to normalize the HSV calculations. As shown in [41], Eq. (67) is a computationally efficient means of determining transducer designs that increase system performance.

Based upon Eq. (67), Clark and Cox [40] developed a design metric which also provided for system robustness. This metric emphasizes coupling to modes within the bandwidth of control, but de-emphasizes coupling to modes outside the performance bandwidth. This metric was later refined by Smith and Clark [39] as well as Richard and Clark [34]. Defining a binary selection vector with 1's corresponding to the targeted modes of the system and 0's elsewhere, a metric can be developed to emphasize actuator/sensor selection that provides desired coupling to select modes and effectively penalizes coupling to modes unimportant in the control system design. Thus, one can effectively impose a level of roll-off in the frequency response by penalizing coupling to higher-order modes. This can be readily implemented by constructing binary selection vectors related to modes desired for performance, Λ_{perf} (with unity on-switches and zeros as off-switches), and a binary selection vector to identify modes unimportant for performance, identified as Λ_{robust} here. It should be noted that an ideal actuator/sensor choice would be one that coupled only to the modes desired for enhanced control system performance. This would lead to an identified system model with very few modes in the identified path and thus a low-order compensator – an inherently simpler design problem. The two metrics (desirable and undesirable) can be expressed in terms of the HSVs as follows:

$$J_{perf} = \sum_{i=1}^{N} \Lambda_{perf} \frac{\sigma_{yu_i}}{\bar{\sigma}_{yu_i}} \sigma_{zw_i} \tag{68}$$

$$J_{robust} = \sum_{i=1}^{N} \Lambda_{robust} \frac{\sigma_{yu_i}}{\bar{\sigma}_{yu_i}} \sigma_{yu_i} \tag{69}$$

These two metrics yield scores for a given actuator/sensor pair that correspond to their beneficial and detrimental modal coupling. Note that each metric is normalized by $\bar{\sigma}_{yu_i}$, which as detailed by Lim, represents the root-mean-square of the sum of

the HSVs over all possible actuator-sensor paths for a given mode. This approach works well when one is trying to select an actuator and sensor from a fixed array of candidate sensors and actuators (i.e., when all possible actuator-sensor paths are known in advance). However, when designing without such constraints, one must provide a normalizing estimate, and the simplest estimate is to use the maximum for each mode over a given set of actuator-sensor candidates. This does not guarantee that the normalized metric will be less than unity, but it will be of order unity for scaling purposes. The performance metric used in the delta wing model presented can be expressed as follows:

$$J = \frac{J_{perf}}{J_{robust}} \tag{70}$$

Thus, J is maximized when J_{perf} is large and J_{robust} is small, indicating that the actuator-sensor path maximizes coupling to the desired modes and minimizes coupling to modes that are not important for controlling the desired dynamic response of the structure.

4.2 Optimization Results

A genetic algorithm was used to optimize the design of the actuator and sensor concurrently so as to achieve the desired coupling and decoupling to modes within the bandwidth of interest. Details of the optimization can be found in the work of Richard [34]. However, the primary mode targeted for coupling is the second mode since this mode is observed to destabilize as the flutter boundary is approached. Coupling to higher order modes (greater than the sixth mode) is penalized to impose a level of roll-off in the frequency response from input to output and reduce coupling to modes unimportant for control. Coupling to other structural modes (below mode seven) is neither emphasized or penalized so as not to overly constrain the design. Thus $\Lambda_{perf} = [0\ 1\ 0\ 0\ \ldots]$ and $\Lambda_{robust} = [0\ 0\ 0\ 0\ 0\ 0\ 1\ 1\ 1\ \ldots]$. A genetic algorithm was structured so as to allow for optimization of the angle of orientation and dimensions of the actuator and sensor. For the case presented, the dimensions of the actuator were constrained to a maximum of 2 inches in both x and y.

The initial conditions for actuator and sensor dimensions and orientation were selected arbitrarily, and hundreds of cases were executed to determine if the optimization would lead to similar results. The design results are presented in Fig. 19. Several design results are depicted in this figure, and it should be noted that the results emphasized in bold are representative of the design used for the experimental test system. The optimal actuators are located closest to the leading edge of the delta wing and the sensors are depicted near the trailing edge. The dominant peak in the frequency response corresponds to the second structural mode, and the diminished coupling at higher frequency is readily noted, which is a form of "loop-shaping" by design. A plot of the performance metric as a function of the number of itera-

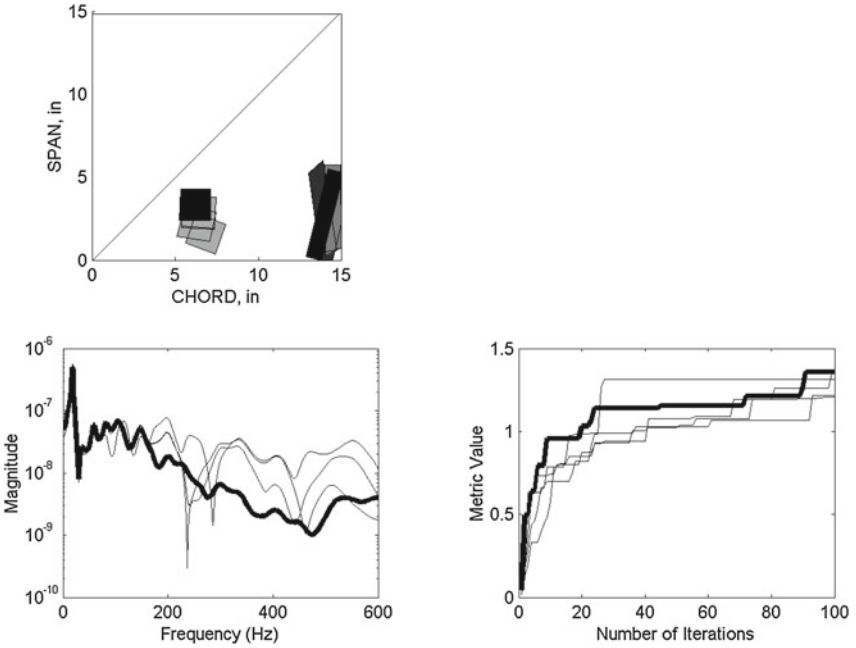

Fig. 19 Optimization results for patches with maximum 2 × 2 inch actuators

tions within the optimization routine is also displayed. As indicated by the results, despite the fact that the initial conditions for the actuator and sensor dimensions and orientation were selected arbitrarily, the optimal results are very similar.

5 Control Law Design

The general diagram of Fig. 3 provides a basis for understanding much of modern and robust control design. The control objectives are best viewed in terms of the transfer function path through the system T_{zw}. This path is defined by the control designer and not limited by physical inputs or outputs of the system. Through the application of static, or possibly dynamic, weighting functions on this path a wide variety of possible performance objectives may be defined.

With $\Delta = 0$ the problem of finding a K that minimizes the performance path $\|T_{zw}\|$ is a linear optimal control problem. With appropriately chosen inputs, w, and outputs, z, minimizing the H_2 norm is equivalent to the linear quadratic regulator problem with optimal estimation (LQR/LQG) [43]. In addition to minimizing $\|T_{zw}\|$ when $\Delta = 0$, requiring stability for the interconnection $\mathcal{F}_l(\mathcal{F}_u(T, \Delta), K)$ for non-zero Δ is the robust control problem. Typically, Δ is an unknown but norm bounded and the problem is scaled such that $\|\Delta\|_\infty < 1$. Then the stability requirement can be

enforced (with some conservatism) by the small-gain condition $\|T_{qv}\|_\infty < 1$. This forms the basis of robust control design via H_∞ methods [9].

In both the case of quadratic regulation and robust control the optimization problem is to find a state-space system K that will minimize $\|T_{zw}\|$. With the controller K an LTI model of the same order as the augmented plant matrix T, this optimization problem reduces to the solution of two coupled second order algebraic equations, called Riccati equations. Although the algebraic Riccati equations must be evaluated numerically, efficient procedures exist to do this and the time required to solve the problem depends on the order of the system, and not the problem data. This avoids some of the pitfalls of nonlinear optimization, and helps account for the wide generality of modern control theory.

In this section quadratic optimal control laws (the H_2 problem) are posed for both the typical section and delta wing models. Rationale for the system augmentation and control weightings are detailed and predicted extension of the flutter boundary under active control is shown for both models.

5.1 Control of the Typical Section Model

Consider the typical section model defined above with the trailing edge flap as the control surface and position measurements available from each axis.

The control design includes weights typical of Linear Quadratic Gaussian (LQG) control laws, including a trade-off between performance and control effort and between sensor noise and process noise. This basic design technique has been successfully applied to a typical section airfoil under a variety of experimental conditions [44–46].

Pitch-plunge coupling is known to be the flutter mechanism in this system, with the system destabilizing quickly (with respect to variations in flow speed) after the frequencies of these motions coalesce. With the goal of extending the flutter boundary a reasonable control objective would be to reduce coupling in the system for the model just below the flutter boundary. To achieve this an objective function, T_{zw}, is defined as the transfer function from a disturbance in plunge to the response in pitch. This will cause the control action to try and alter dynamics of the closed-loop system such that the coupling between these motions is reduced. Without further augmentation, however, the optimization problem is not well posed. The coupling can be made very small, but this will require control authority exceeding that available from the flap. To limit control effort, outputs of the the objective path, T_{zw}, are augmented with the control signal. In a similar fashion the plunge disturbance input is augmented with additive inputs at the sensors, and this is used to reduce the sensitivity of the control action to sensor noise.

Figure 20 shows the problem in block diagram form, with the design weights shown as triangular signal gain blocks. Without loss of generality the performance weight, Q, and the level of disturbance input Q_w can be set to unity, as these weights are trade-offs in the optimization problem with the control effort R and sensor noise

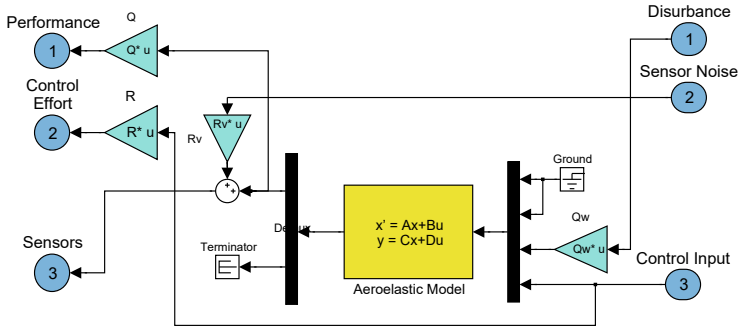

Fig. 20 Block diagram showing system augmentation for H_2 control design problem

Q_v, respectively. The sensor noise level Q_v was set independently for each channel, and at a level which gives a physically appropriate sensor/noise ratio. Here, given the resonate response near the flutter boundary, the sensor noise is scaled to be two orders of magnitude below the peak harmonic response at the sensors from a unit disturbance input. The only remaining design freedom is the level of the control effort penalty. This was determined through iterative design, checking closed-loop response to ensure the system does not saturate the control surface, in either harmonic or transient response.

In Fig. 21 the open and closed loop transfer functions are shown from the disturbance (a force in plunge) to the change in angle of attack. Although the closed loop response is still lightly damped, it is significantly attenuated due to the action of control. Therefore, although this model may not have significantly more damping than the open-loop model, the attenuated coupling should allow for an increased flutter boundary. The root loci of Fig. 22 confirms that this is the case. Under closed loop control the flutter boundary is extended by 19% to 27.8 m/s, and the locus is altered such that flowspeed variations cause a change in frequency, rather than damping, in the region near the design condition.

There are, however, some obvious limitations to this approach. In the design only the performance of the control law at a single flowspeed is considered. By choosing an open-loop model near the flutter boundary we have operated on a critical region, however, at points off of this flow condition the performance is not optimized. From the loci in Fig. 22 it can be seen that the closed loop system is actually unstable for all flowspeeds up to 11.2 m/s. Also, although the flutter boundary is extended damping is actually decreased at most flowspeeds in the closed-loop response. In practice this may lead to unacceptably large vibrations, or show a sensitivity to model errors. Some of this could be addressed by tuning the control weights and by including additional transfer functions in the performance path. However, as will be seen in a later section, by using linear parameter varying models and convex optimization for the control design it is possible to incorporate eigenvalue constraints directly and to optimize performance over a range of flow conditions.

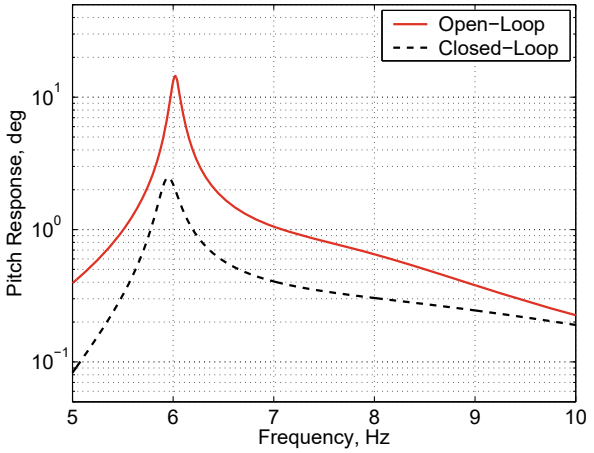

Fig. 21 Open and Closed loop gain from a force disturbance in plunge to motion in the pitch axes for the typical section model at $U = 23$ m/s near the open-loop flutter boundary of $U_f = 23.4$ m/s

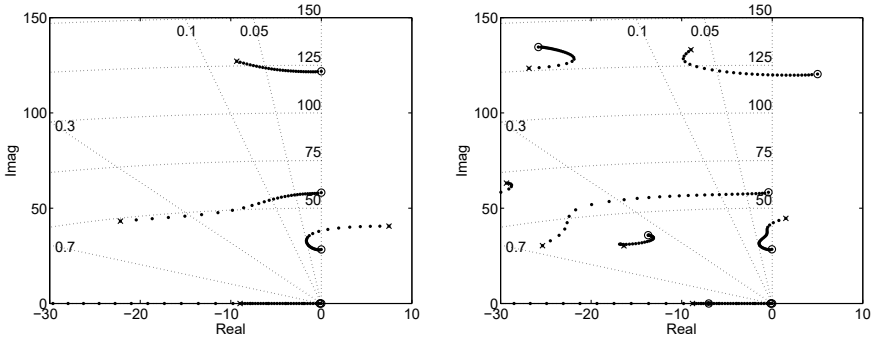

(a) Open-loop root locus, $U_f = 23.4$ m/s

(b) Closed-loop root locus, $U_f = 27.8$ m/s

Fig. 22 Root Loci as flowspeed is varied from 0 m/s (Circle) to 30 m/s (X). The closed-loop system is unstable below 11.2 m/s and above 27.8 m/s

5.2 Control of the Delta Wing Model

Through H_2-synthesis, a temporal compensator can be designed so as to minimize the response of the second mode in order to extend the flutter boundary. Since the dynamics of the system vary as a function of flow-speed, one must select a flow speed for design unless gain scheduling is incorporated. For the example presented, the pre-flutter condition of 30 m/s was selected for design.

Figure 20 shows the H_2 design problem in block diagram form as detailed in the previous section. Control design for the delta wing is consistent with the approach outlined for the typical section model, and uses the same system augmentation in

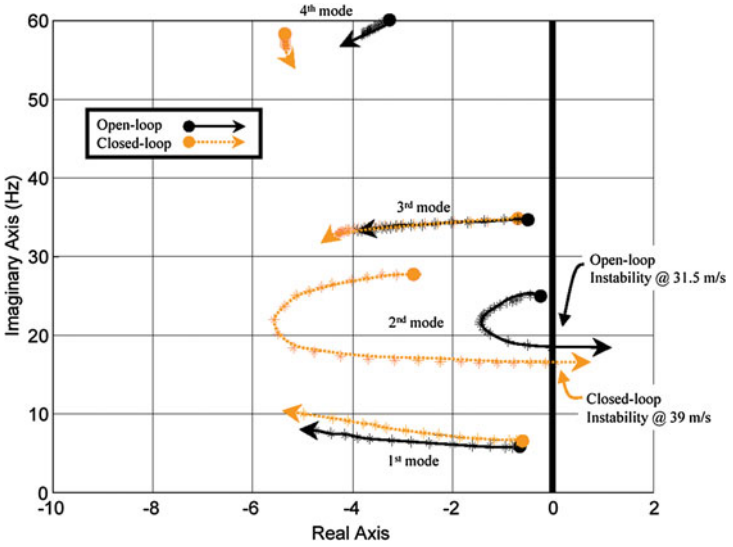

Fig. 23 Closed-loop aeroelastic root migrations

defining the optimization path T_{zw}. The performance weight, Q, and the level of disturbance input Q_w are again set to unity. The sensor noise level Q_v was set at a level which gives a physically appropriate sensor/noise ratio, approximately two orders of magnitude below the peak response.

Given that the actuator-sensor path was designed so as to provide roll-off at higher frequencies, this results in a control design that effectively precludes any significant emphasis on high-frequency dynamics since the signal to noise ratio is poor by design at higher frequencies . The remaining degree of freedom in design is the level of the control effort penalty. An iterative design process was conducted, checking closed-loop response to ensure the system does not saturate the piezoelectric transducer.

Results illustrating the migration of the closed-loop poles as a function of flow-speed are depicted in Fig. 23 along with the migration of the open-loop poles. As indicated, the predicted instability of the closed-loop system occurs at a flow-speed of 39 m/s, yielding a 20% extension of the flutter boundary.

6 Parameter Varying Models

Gain scheduling of control laws is a technique for overcoming some of the limitations of single-point designs, and has been successfully applied in a variety of aerospace and industrial systems [47]. Of relatively recent interest in control theory is the use of Linear Matrix Inequalities to design gain-scheduled controllers [48, 49] using an

extension of linear models to systems with linear or affine parametric dependence. Such models are called Linear Parameter Varying (LPV) and take the form,

$$S(\theta) = \left[\begin{array}{c|c} A(\theta) & B(\theta) \\ \hline C(\theta) & D(\theta) \end{array}\right] \tag{71}$$

for a parameter vector $\theta \in \mathrm{R}^N$. Since the dependence of the state matrices on θ is affine we can write,

$$S(\theta) = S_0 + \sum_{i=1}^{N} \theta_i S_i \tag{72}$$

This structure includes a much wider range of dynamic models than LTI systems, and provides acceptable approximations to many nonlinear problems of engineering significance. Stability, system norms, and other properties can be established for models where the variations are slow, remain within constant bounds, or are arbitrarily fast. By allowing this same form for the control law, controllers can be designed which are implicitly gain-scheduled and vary with parameters of the plant.

6.1 Linear Matrix Inequalities

The design of LPV gain-scheduled control laws follows a similar development as linear optimal control, but the optimization problem results in a series of linear matrix inequalities (LMIs) as constraints, with an objective function that is linear or affine in the problem's unknowns. With constraints posed as an LMI, or combinations of LMIs, the resulting optimization problems are convex, and very efficient numerical techniques exist for their solution [50, 51]. The development of control synthesis methods using LMIs is an active area of research and will be summarized only briefly here. The interested reader is referred to the references for background on the use of LMIs in system theory [52–54], the formulation of LMI control objectives [55–58], and the design of gain-scheduled controllers for LPV systems [48, 49, 59, 60].

A Linear Matrix Inequality (LMI) is a system of equations in which some unknown or decision variable is written as an affine function of symmetric matrix quantities. The equation is satisfied if the matrix function is either strictly positive (or negative) definite. The canonical form for such an equation is,

$$F(x) = F_0 + \sum_{i=0}^{m} x_i F_i > 0 \tag{73}$$

where $x \in \mathbf{R}^m$, and $F_i = F_i^T \in \mathbf{R}^{n\times n}$. The greater-than symbol implies that $F(x)$ is positive definite, that is,

$$q^T F(x) q > 0, \quad \forall q \in \mathrm{R}^n \tag{74}$$

Individual LMIs can be combined in a straightforward manner by diagonally augmenting the equations into a larger LMI. For example, the pair of conditions that $F(x) > 0$ and $G(x) < 0$ can be written as the single LMI,

$$\begin{bmatrix} F(x) & 0 \\ 0 & -G(x) \end{bmatrix} > 0 \tag{75}$$

All LMIs can be written in the canonical form of (73), however, sometimes these equations arise more naturally in matrix form with the unknowns appearing as elements of a symmetric matrix. So long as products of unknowns do not appear in these equations, the LMIs still have a convex solution and can be transformed into the form of (73) by finding the terms F_i as a basis for $F(x)$ corresponding to the i_{th} variable [52].

6.2 LMI Controller Specifications

In this section two useful controller specifications, the H_2 norm of a transfer function and a regional pole placement condition, are developed in terms of linear matrix inequalities involving the state-space models. With these criteria defined in terms of LMIs, it will be possible to pose convex optimization problems for control laws which address the issues of control design for various flow conditions and allow direct control over system eigenvalues.

The H_2 norm of a system is the sum of the root-mean-square (RMS) responses to unit impulses and can be written,

$$\|G\|_2 = \sqrt{\sum_{i=1}^{m} \int_0^\infty \hat{y}_i^2(t)dt}. \tag{76}$$

where $\hat{y}_i$ is the response to a unit impulse $\delta(t)$ on the ith input. For a finite H_2 norm the system's feed through matrix D must be zero, and the output is given by,

$$\hat{y}_i(t) = Ce^{At}B_i\delta(t). \tag{77}$$

Substituting $\hat{y}$ into (76) yields,

$$\begin{aligned} \|G\|_2^2 &= \text{trace} \int_0^\infty \hat{y}^T \hat{y}\, dt \\ &= \text{trace}\, B^T \left(\int_0^\infty e^{A^T t} C^T C e^{At} dt \right) B \\ &= \text{trace}\, B^T W_o B \end{aligned} \tag{78}$$

where W_o, the observability Gramian, is calculated as the solution to the following Lyapunov equation,

$$A^T W_o + W_o A + C^T C = 0. \tag{79}$$

Therefore, a system's H_2 norm will be below a level, γ, if a solution $P > 0$ exists such that,

$$A^T P + P A + C^T C < 0 \tag{80}$$

$$\text{trace}\, B^T P B < \gamma^2 \tag{81}$$

Making the variable substitution $Q = P^{-1}$ and introducing a free variable $Z > 0$ this condition can be written,

$$\begin{aligned} Q A^T + A Q + Q C^T C Q &< 0 \\ B^T Q^{-1} B - Z &< 0 \\ \text{trace}\, Z &< \gamma^2 \end{aligned} \tag{82}$$

Finally, the Schur complement (see e.g. [52]) of (82) yields the following LMIs,

$$\begin{bmatrix} AQ + QA^T & QC^T \\ CQ & -I \end{bmatrix} < 0, \quad \begin{bmatrix} Z & B^T \\ B & Q \end{bmatrix} > 0, \quad \text{trace}\, Z < \gamma^2 \tag{83}$$

which are jointly convex in the unknowns Q, Z, and γ^2.

Existence of $Q > 0$ and $Z > 0$ that satisfy the inequalities in (83) establish that the system's H_2 norm is below γ. Determination of such solutions can be found numerically as a convex feasibility problem. Furthermore, a convex optimization problem may be posed that exploits the freedom in Q and Z to find a minimal value γ^2. This value of γ is the system H_2 norm.

In order to address system damping directly it is desirable to specify in the controller design that closed loop poles are contained in regions of the left-half plane. Pole-placement is a traditional technique in control design, but it is seldom used in high order systems because uniquely specifying all the eigenvalue locations produces a highly constrained problem, and can require large amounts of control effort. Regional pole placement defines regions of the left half plane where closed loop poles may reside, and unlike exact pole-placement allows additional design freedom for minimizing the control effort required.

Following the development in [57, 61], let a region of the complex plane, $\mathcal{D}$ be defined by the symmetric matrix L, square matrix M, and the condition,

$$\mathcal{D} = \{z \in \mathbf{C} \mid L + Mz + M^T \bar{z} < 0\}, \tag{84}$$

where $\bar{z}$ is the complex conjugate of z. The matrix A will have its eigenvalues in the region $\mathcal{D}$ if there exists a matrix $X > 0$ such that,

$$L \otimes X + M \otimes (AX) + M^T \otimes (XA^T) < 0 \tag{85}$$

where $\otimes$ is the Kronecker product. The Kronecker product of two matrices creates a block matrix, whose $(i_{\text{th}}, j_{\text{th}})$ block is the second operand scaled by an element of the first. Specifically for $C = A \otimes B$ we have,

$$C = \begin{bmatrix} A_{11}B & \cdots & A_{1m}B \\ \vdots & \ddots & \vdots \\ A_{n1}B & \cdots & A_{nm}B \end{bmatrix} \tag{86}$$

Several important regions can be described by (84), for example with

$$L = \alpha, \;\; M = 0 \tag{87}$$

the region is defined by $z + \bar{z} < -\alpha$ which requires eigenvalues to have a real component more negative then $-\alpha/2$. In this case of $L = 0$ the region is just the left-half plane and the LMI condition of (85) reduces to the familiar Lyapunov equation for stability of state-space systems,

$$AX + XA^T < 0, \quad X > 0 \tag{88}$$

A condition of minimum damping, $\zeta = \cos(\theta)$, is a region of the left half plane bounded by cones of angle θ off the real axis. This region is described by (84) with $L = 0$ and

$$M = \begin{bmatrix} \cos(\theta) & -\sin(\theta) \\ -\sin(\theta) & \cos(\theta) \end{bmatrix}, \tag{89}$$

and the LMI constraint is the existence of a matrix $X > 0$ that solves,

$$\begin{bmatrix} \sin(\theta)(AX + XA^T) & \cos(\theta)(AX - XA^T) \\ \cos(\theta)(XA^T - AX) & \sin(\theta)(AX + XA^T) \end{bmatrix} < 0 \tag{90}$$

More complex geometries are possible with other choices for L and M, and arbitrary convex regions can be defined by looking at the intersection of the regions outlined above. Since in all cases the constraint equation is an LMI, the solutions to multiple constraints remains convex and numerically tractable.

6.3 An LMI Design for the Typical Section

It is possible to use these LMI equations to pose convex optimization problems and solve for Lyapunov matrices that verify if a system's H_2 norm is below a certain bound or its eigenvalues exist within a specified region. However, the power in this method is not in the analysis of systems, but it is in the ability to work directly from a set of analysis equations to pose a control synthesis problem, and to extend this to the synthesis of controllers for parameter varying plants. There are several additional steps which must be taken to achieve this end. Specifically these steps are: the assumption of a common Lyapunov function for all constraints, a nonlinear substitution of variables to restore convexity to the synthesis problem, and a finite parameter expansion on which to gain schedule the resulting controller. We treat these conditions only briefly here, and refer the reader to the references for a more complete development.

The synthesis of a controller requires that a single common Lyapunov function be used to enforce the design constraints. This means that the term Q in the H_2 norm bound of (83) and the term X in the pole placement criteria of (90) must be equal. This is the primary source of conservatism in the control law synthesis. It is possible for a system to meet both criteria, but this may not be provable with a single Lyapunov function. Although it is difficult to quantify the conservatism in general, in practice many problems allow sufficient freedom that this process, sometimes called Lyapunov shaping, yields suitable results.

In the control synthesis problem, the system of interest for the LMI conditions is the closed-loop model after feedback has been applied. With the controller model unknown, this introduces additional unknowns into the LMI conditions as can be seen from substituting (6) for the system in (83) and (90). These unknowns appear in the equations in products with one another, and therefore the resulting matrix inequality is not linear in the unknowns and cannot be solved by convex optimization. However, as was developed in [58], a combination of congruence transformation and substitution of variables exists which converts this problem into one which has a linear dependence on a new set of unknowns. Once solved this variable substitution can be inverted to yield a state-space model for the controller.

The extension of the control synthesis problem to LPV models is straightforward. Since changes in flowspeed will be slow compared to the dynamics of the system the dynamic effects due to the rate of change in flowspeed can be safely ignored. The aerodynamic model depends on flowspeed and dynamic pressure, and it can be written in state-space form in terms of an expansion with U and U^2,

$$\begin{aligned} S_a(\theta) &= \left[\begin{array}{c|c} A(\theta) & B(\theta) \\ \hline C(\theta) & D(\theta) \end{array}\right] \\ &= \begin{bmatrix} A_0 & B_0 \\ C_0 & D_0 \end{bmatrix} + \begin{bmatrix} A_1 & B_1 \\ C_1 & D_1 \end{bmatrix} U + \begin{bmatrix} A_2 & B_2 \\ C_2 & D_2 \end{bmatrix} U^2 \end{aligned} \tag{91}$$

The design constraints are then written for systems over a grid of speeds throughout the range of interest. Solving the optimization problem over the grid of constraints will yield a fixed control law that can operate over this range. However, the proposed control structure may be given the same functional dependence as the plant model, and performance greatly improved through gain scheduling. That is, each unknown of the optimization problem is written as a quadratic function of flowspeed. This triples the number of unknowns, but gives rise to a resulting control law that is gain-scheduled as a function of the aerodynamics.

The procedure outlined above was followed for the typical section model, producing a gain-scheduled controller for flutter suppression, see Cox [70]. For the H_2 norm condition the system was given the same performance weights as the previous example, except now the H_2 norm optimization is carried out over grid of flowspeeds extending to 30 m/s, approximately 27% past the open loop flutter boundary. Furthermore, the pole placement condition was also part of the constraint set and this required that all the system's eigenvalues have at least 5% damping throughout the flow range.

Performance of the resulting gain-scheduled controller is shown in the root locus plot of Fig. 24 for a flowspeed range of 5 m/s to 30 m/s. The flowspeed range here does not extend to zero speed, as it was too difficult for the system to achieve the damping specification at these low flowspeeds with only an inertial response from the flap actuator. The transfer function of the path from a disturbance force in plunge to the response in pitch at a flowspeed of 23 m/s is shown in Fig. 25. The peak attenuation of this path is less than for the single objective, single-point design shown in Fig. 21. The response, however, is much more damped due to the inclusion of the pole placement constraint and, unlike the single-point design, well damped responses occur over the entire range of flow conditions.

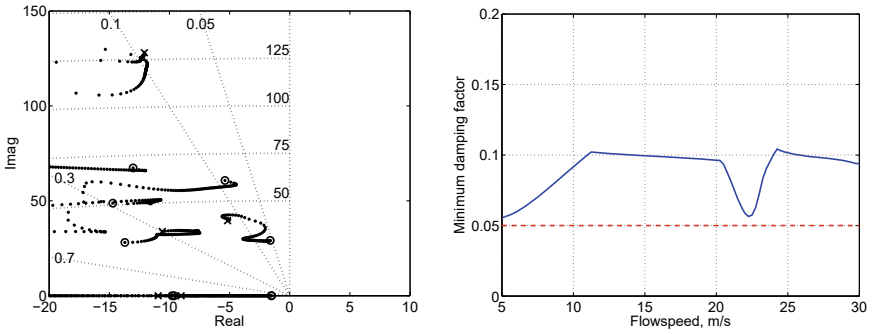

(a) Closed-loop root locus, $5 < U < 30$ m/s

(b) Minimum damping factor

Fig. 24 Root Loci as flowspeed is varied from 5 m/s (Circle) to 30 m/s (X) with gain-scheduled LPV control law. Closed-loop system retains minimum of 5% damping through the design range

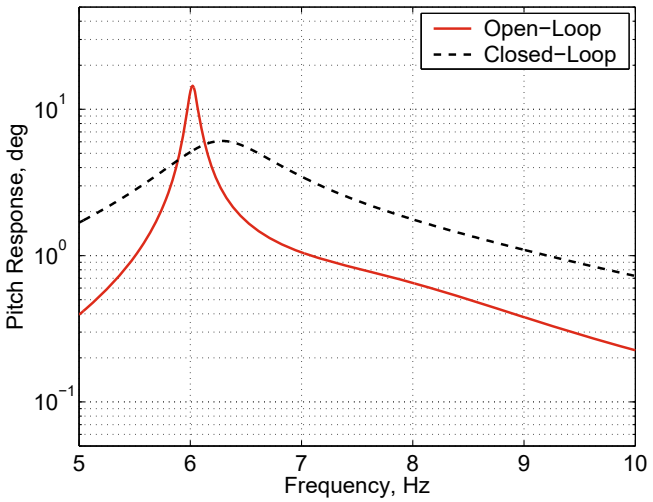

Fig. 25 Open and Closed loop (LPV controller) gain from a force disturbance in plunge to motion in the pitch axes for the typical section model at $U = 23$ m/s near the open-loop flutter boundary of $U_f = 23.4$ m/s

7 Experimental Results

In this section experimental results are presented for aeroelastic control of both the typical section and delta wing models. Physical parameters for these models correspond to those detailed in Tables 1 and 2. The delta wing results are based on a system with sensor and actuator placement designed for optimal coupling to the destabilizing flutter mode. The control law design is based on an identified LTI model for a flow condition just below the flutter speed. The typical section design is also based upon identified models, however, these models have an LPV form and the design criteria includes performance specifications over a range of flow conditions. The resulting typical section control law is also in LPV form, and therefore operates as a gain scheduled controller.

7.1 Typical Section Experiment

The typical section model provides a convenient analytic tool due to its relatively tractable modeling, yet it exhibits may of the dynamic features of more complex systems. Experimental investigations based on a typical section rig can also be informative, if for nothing else, in order to verify the practicality of control designs and to expose any sensitivity in the methods to more realistic conditions. The model shown in the photographs of Fig. 26 is a rigid airfoil with a NACA-0012 profile with an

(a) Full span typical section model

(b) Actuator and flexible support rig

Fig. 26 Photos of typical section model mounted in flexible support wind tunnel mount

actuated full length trailing edge flap. Similar hardware has been the focus of previous studies in both active control of flutter [44] and in experimental investigations of limit cycle oscillations [20, 21, 26, 62–64]. The model was mounted in the Duke University wind tunnel in a support system that provides flexible and lightly damped response to motions in both pitch and plunge. The flap was also held with a restoring spring and connected to a linear induction motor for control. The model was instrumented with variable differential transformers (RVDTs) that provide position measurements in each axis. Physical properties for the model are similar to those provided in Table 1, with the addition of a 0.32 Kg motor mounted near the elastic axis.

7.2 LPV System Identification

Under different flow conditions the typical section model varies dramatically. In order to apply system identification, data was taken at a number of flowspeeds below the flutter boundary. The system's flap actuator was driven by white noise and outputs from the three position sensors were recorded. Independently each of these data sets could be fit quite accurately with a low order model using subspace identification algorithms [11, 12, 65]. However, the coordinate system used for these realizations

is not consistent and it cannot be made consistent without full measurement of the state. Here full measurement is clearly not possible since the state includes dynamics associated with modes of the unsteady flow.

The ambiguity of coordinates makes this collection of identified models unsuitable for LPV control. Solving for a parameter dependent Lyapunov function over a grid of models is not meaningful if the internal state vector is not consistent among these different grid points. One method to determine an LPV model that reflects the experimental data is to use the identified model of the system at zero flowspeed and couple this to an analytic model for the aerodynamics. In order to couple this model to the aerodynamic model, however, inputs are required for forces in the pitch and plunge directions. To obtain these experimentally would require calibrated force transducers in these directions that did not impart mass or stiffness loading to the structure.

Here an alternative approach was taken using optimization codes designed for tuning of specific parameters in a model [70]. The model at zero flowspeed was identified using a subspace identification algorithm. This was reduced to 8 states with little loss of fidelity. The missing information in coupling the identified structural model and the analytic aerodynamic model is the influence matrix, B, that defines the effect of moment and force inputs on the identified state. Moments in the flap should closely follow inputs to the flap actuator, however there is no guidance in choosing influence coefficients for forces in pitch and plunge. With the pitch and plunge influence coefficients free and the flap constrained to be a scaled version of the actuator input, the problem has 17 unknown parameters. A key to improving the solvability of this problem was to choose a decoupled coordinate system for the structural model. In modal coordinates the A matrix is block diagonal and the effect of perturbations in elements of the B matrix is more clearly delineated, improving convergence of the nonlinear optimization.

With the structural model in modal canonical form a set of parameters was found that allowed the model to fit well at a flowspeed of 21 m/s. This is a condition where the influence of aerodynamics is significant but far enough below the flutter point where the response is not dominated by a single resonance. The model was most accurate at this condition, however, it was still fairly accurate at other flow conditions indicating that the optimization problem was not over-parameterized. A comparison of the experimentally determined spectra and the frequency responses of the LPV identified model is shown in Fig. 29, at the end of this section.

Another measure of the models accuracy is is ability to predict the transition to flutter. The LPV model can be evaluated at any flowspeed, and used to determine the systems eigenvalues. Figure 27a shows a root locus for the identified model as a function of increasing flowspeed. The locus starts with lightly damped motion in pitch, plunge and flap. As flow increases both initially gain damping, then the plunge mode starts to lose damping, and eventually becomes unstable. This is similar to the behavior of the analytic typical section model shown in Fig. 22a. The most notable difference being the lower flap frequency (due to loading from the control actuator),

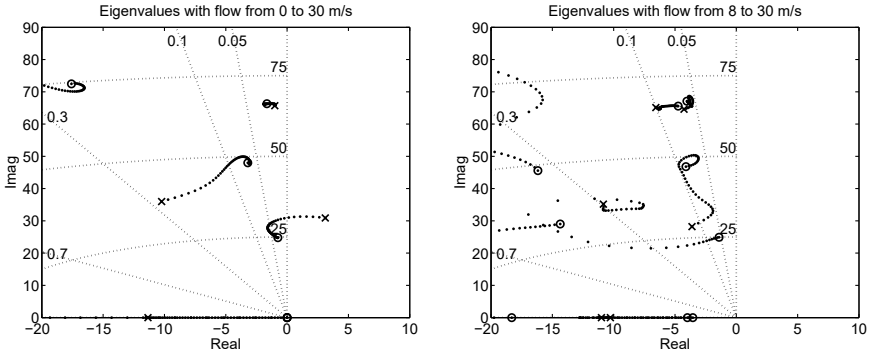

(a) Open-Loop Locus, 0 m/s to 30 m/s

(b) Closed-Loop Locus, 8 m/s to 30m/s

Fig. 27 Root Locus of **a** open-loop identified LPV model, with a flutter prediction at 26.8 m/s. In **b**, predicted closed-loop locus with LPV design and constraint of 5% damping

and the presence of damping in the identified model. An experimental test of the model revealed that flutter occurred at 25.1 m/s, slightly below the predicted flutter speed of 26.8 m/s from the identified LPV model.

7.3 Closed-Loop Results

A controller was designed using the identified LPV model and following the same multiobjective procedure described in Sect. 5. The goal was a reduced H_2 transfer function from a plunge disturbance to an output that included both pitch and plunge. The regional pole-placement conditions were set to 5% damping in all the modes, over a flow range that extended from 8 m/s to 30 m/s. The solution to this problem was found through convex optimization of the resulting LMIs, using semidefinite programming software described in [66]. The resulting continuous controller was discretized through a Tustin transformation, and implemented digitally at a sample rate of 250 Hz.

A series of manual disturbance tests were performed for the open and closed loop system at several flowspeeds below the flutter boundary. These results, presented in Fig. 30, show the increase in damping of plunge motion in the closed loop system. The damping increase is greatest at the intermediate flowspeed of 16 m/s, and decreases again at higher flowspeeds. There is also an increase in the frequency of the response with flowspeed. This is consistent with the location of the dominant poles in the predicted closed-loop root locus of Fig. 27b. The system remains stable and relatively well damped past the open-loop flutter boundary as shown in the response plots of Fig. 28.

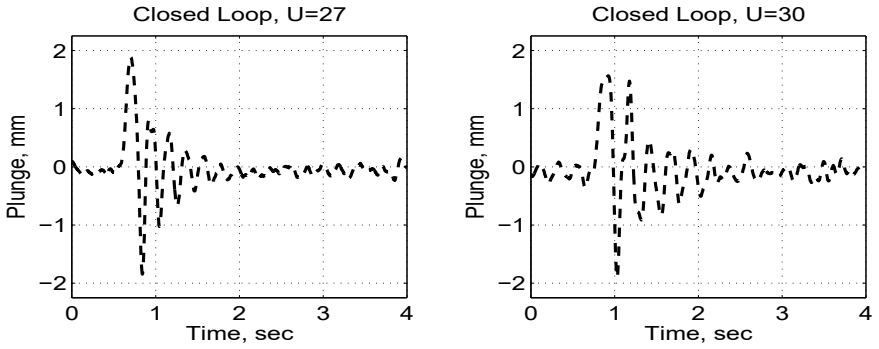

Fig. 28 Closed loop disturbance response in plunge for flow conditions above the open-loop flutter boundary

Finally, a white noise dither signal was added at the flap for both open and closed loop operation. This provided a calibrated input from which full bandwidth responses could be computed from the signals auto and cross spectra. The open and closed-loop frequency responses below the flutter boundary are shown in Fig. 31. Above the flutter boundary only closed loop response is available, and this is shown in Fig. 32 (Fig. 29).

7.4 Delta Wing Experiment

Material properties for the experimental test-rig were provided in Table 2. In order to test the no-flow simulation results against experimental measurements, the test rig is driven by an acoustic disturbance, and point velocities are measured with a laser vibrometer (VPI 4000 scanning laser). The first step in the process is to measure the frequency response between the band-limited random acoustic disturbance and point velocity measurements. From these measurements, the resonant frequencies of the structure are easily identified. The structure is then driven with a harmonic input corresponding to each of the measured resonant frequencies, with velocity measurements being obtained over a grid covering the entire wing. These grid measurements yield an RMS velocity magnitude map over the entire surface for a given frequency, providing a graphical image of the mode shape. A comparison of these simulated and measured structural mode shapes for the wing without transducers can be seen in Fig. 33.

The frequencies of these modes, and the analytic predictions, are listed in Table 3. These frequencies prove to be somewhat sensitive to certain parameter modifications, most notably thickness. Tests showed a variation of nearly $\pm 3\%$ over the entire wing structure which may contribute to the observed errors.

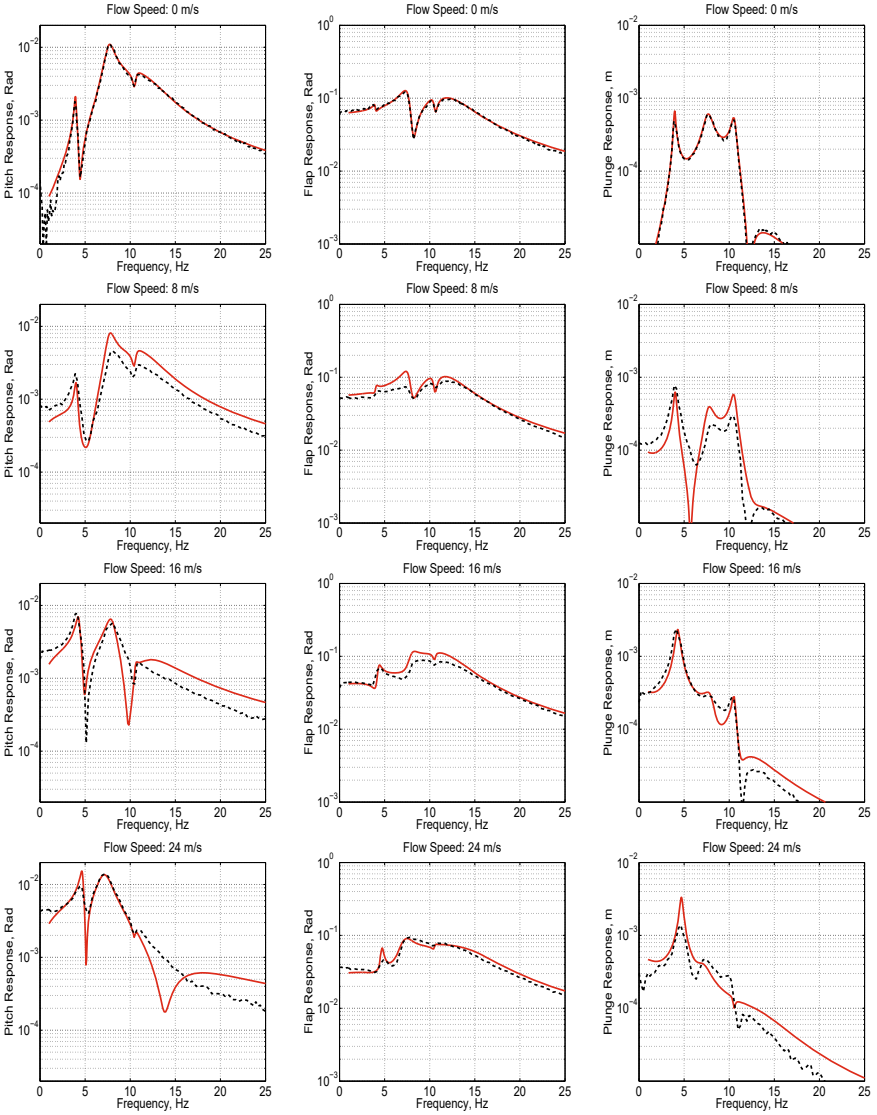

Fig. 29 Comparison of LPV model obtained through tuned aeroelastic coupling (solid) and transfer functions based on spectra from experimental data (dashed)

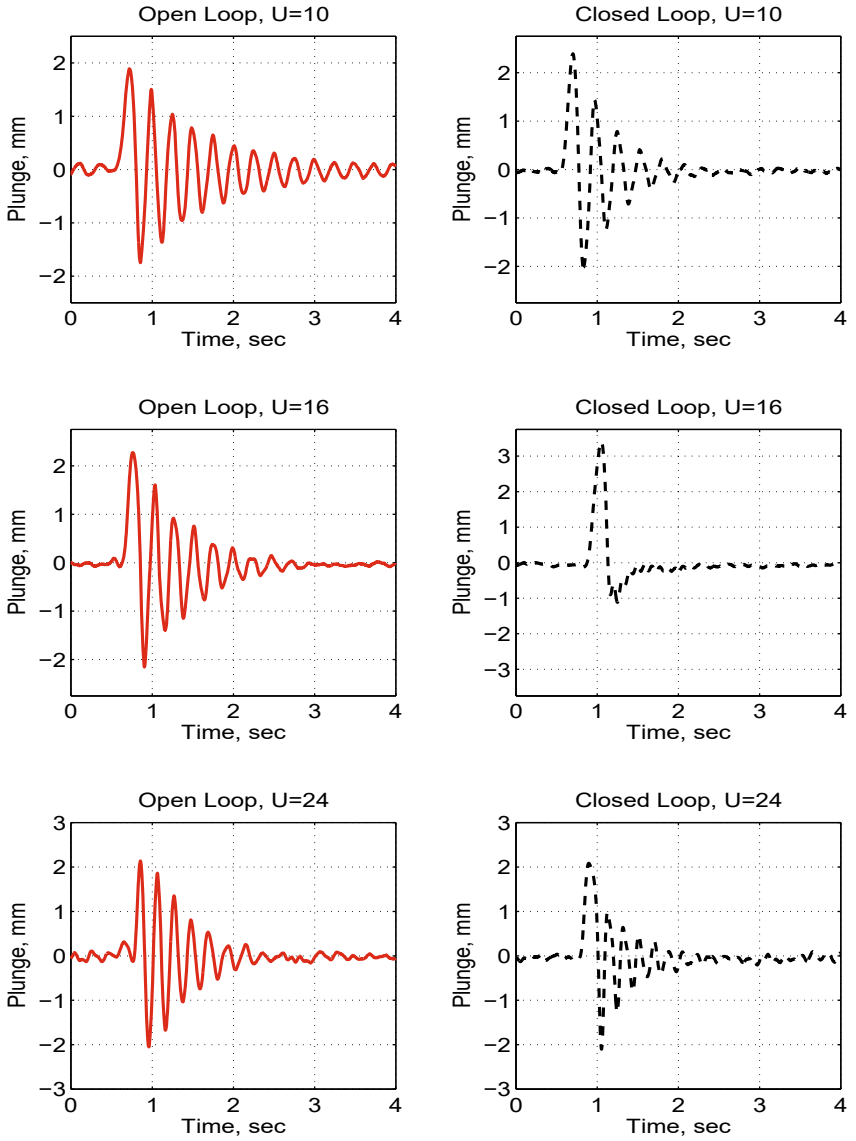

Fig. 30 Open and Closed loop disturbance response in plunge

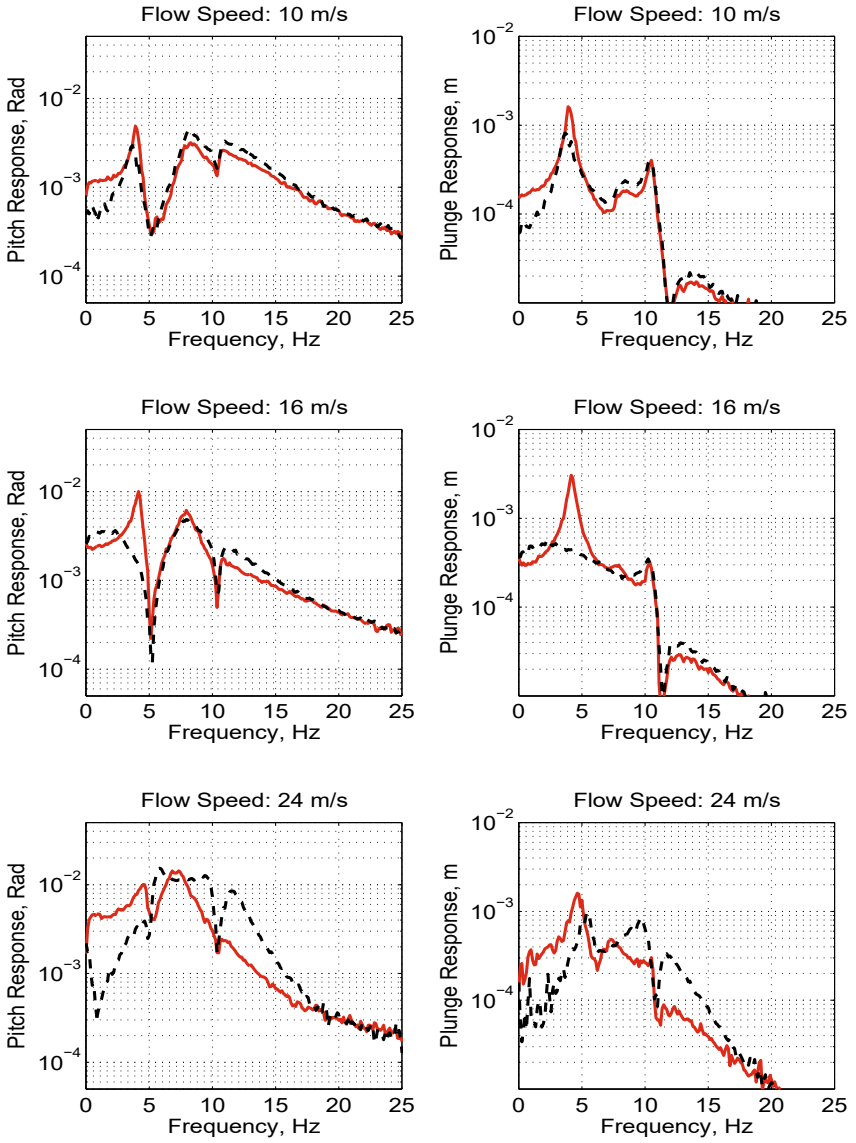

Fig. 31 Comparison of open (solid) and closed (dashed) loop transfer functions from spectral data with flap excitation

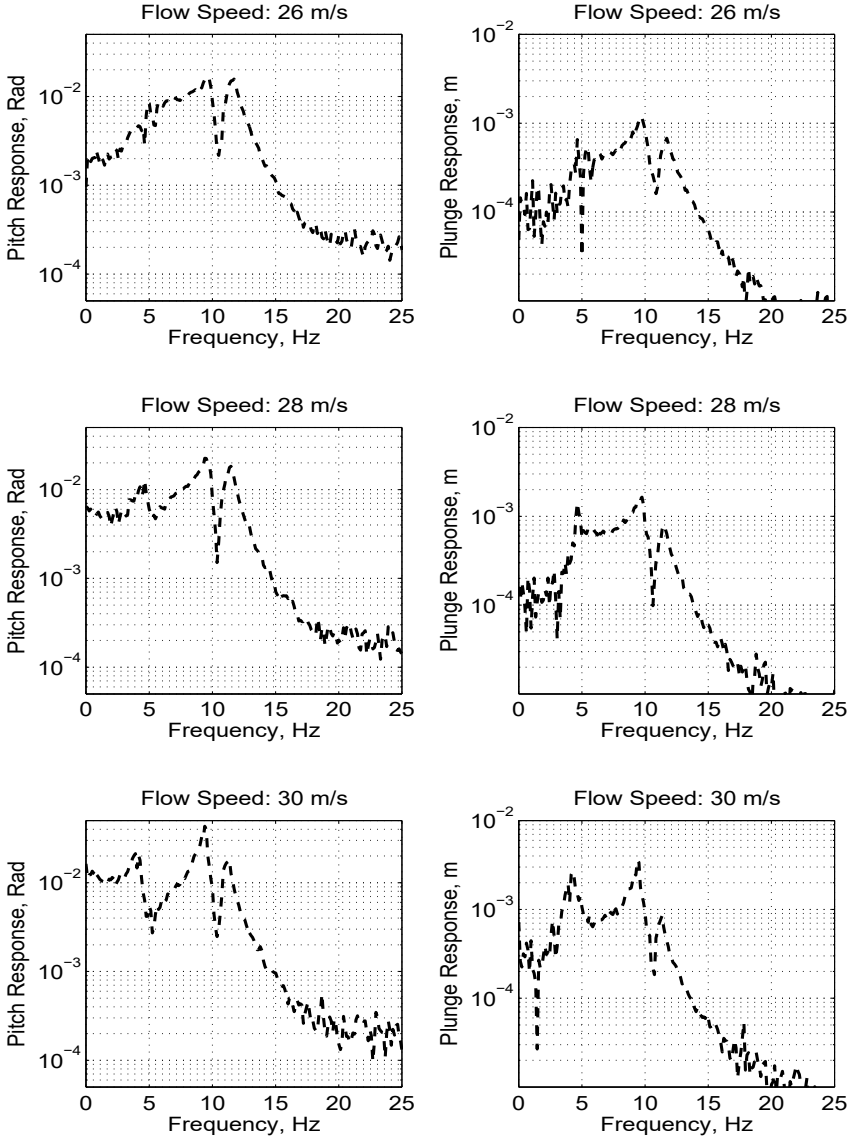

Fig. 32 Closed loop transfer functions from spectral data with flap excitation

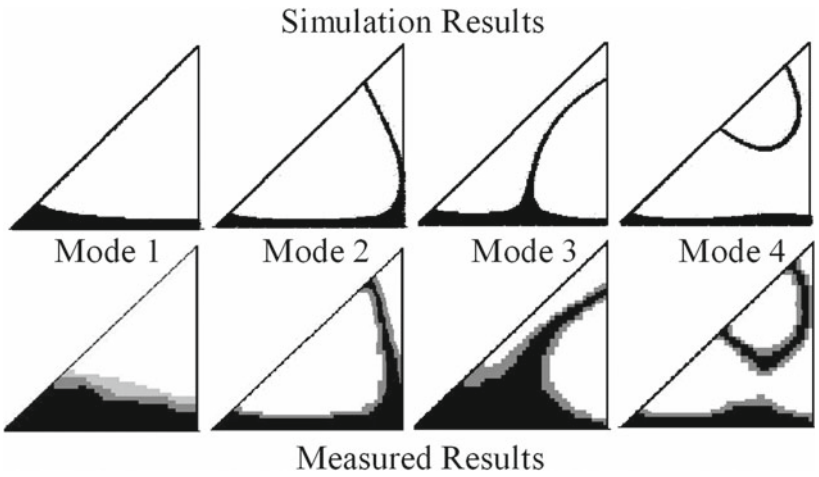

Fig. 33 Comparison of predicted and measured delta wing mode shapes

Table 3 Comparison of predicted and measured delta wing frequencies

	Predicted (Hz)	Measured (Hz)	% Error
Mode 1	6.5	5.75	3.8%
Mode 2	25	24.75	1%
Mode 3	33	32.5	1.5%
Mode 4	60	59.75	0.5%

The actuator for the active wing is constructed from 0.015 inch nominally thick PZT material with silver electrode layers. The sensor is made from two layers of 0.003 inch polyvinylidene fluoride (PVDF) material. These dual sensor layers are wired in parallel and oriented orthogonal to each other in order to eliminate the directional bias typically associated with this material.

For control system design, system identification was employed to obtain an estimate of the transfer function from actuator to sensor. Since the structural response of the wing is modified upon attaching the actuator and sensor, system identification is important to the successful implementation of a compensator. Although analytic models are critical to understating a physical system and its dynamic behavior, there is no substitute for an experimentally identified model of the system when designing a controller. Factors such as damping, actuator dynamics, and phase effects from signal conditioning circuitry are often omitted or ignored in analytical models, but are critical to the accurate prediction of the system response.

Subspace system identification techniques, such as the Eigensystem Realization Algorithm (ERA) [67], and the N4SID algorithm [68], allow for the generation of state-space models from multivariable input/output data sets generated with a frequency rich input signal. Order for the identified model can be prescribed, or

determined by over-fitting the data and choosing a reasonable truncation point by looked at the Hankel singular values. The later approach was taken for this work.

Wind tunnel testing of the non-active wing demonstrates a flutter boundary of 35 m/s at 19 Hz showing a 10% variation in the observed flutter boundary from the predicted response of 31.5 m/s at 18.5 Hz. Here, the flutter boundary is considered to be the point at which clear harmonics appear in the measured frequency response. The analysis and design presented is restricted to linear modeling techniques. As was shown in [69], structural non-linearities can lead to limit cycle oscillations (LCOs) consistent with those observed in this experiment. However, as will be shown, the LCO can be eliminated and the onset of flutter delayed by designing a compensator based on a pre-flutter, linear model of the system.

As predicted by the analytical model, the wing response is dominated by the second mode as the flow speed progresses toward the flutter boundary. Additionally, a gradual reduction in the frequency of the second mode from a no-flow frequency of 25 Hz toward a flutter frequency in the vicinity of 18 Hz is also observed and consistent with the predicted response.

To demonstrate the progression of the mode shape as a function of flow speed, the second mode was driven harmonically, and the laser vibrometer was used to measure point-velocities over a grid sufficient for generating a contour plot of the mode shape. These plots are generated for flow speeds varying from 0 m/s to the pre-flutter condition of 31 m/s. A comparison of the experimentally determined mode shape progression with the predicted progression can be seen in Fig. 34. The inferred nodal regions in the experimental plots demonstrate a tendency in low velocity areas similar to that found in the analytical model. The experimental results are limited by noise due to turbulence as well as nonlinearities in the response associated with LCO that dominates at the onset of flutter.

Given the observed correlation between the experimental and analytical model, the final test involves the design and implementation of a dynamic compensator using the optimally designed actuator and sensor. The compensator is designed from an identified model of the experimental test structure. However, the chosen inputs and outputs for the design are consistent with that of the analytical model, and the compensator is designed through H_2 synthesis. The controller is implemented on a digital signal processor and interfaced through analog to digital and digital to analog converters with the hardware.

Experimental results from the closed-loop response are presented in Fig. 35. The flutter boundary is increased from 33.5 m/s to 37.8 m/s – a 13% increase. The magnitude of both the open-loop frequency response (measured at 33.5 m/s) and the closed-loop frequency response (measured at 37.5 m/s) from the actuator to the measured velocity at the tip of the wing is illustrated in Fig. 35. The harmonics used to define the onset of flutter are clearly observed as evidenced by the dramatic spikes in frequency intervals of approximately 18 Hz in the open-loop response. The lack of harmonics in the closed-loop response, in addition to the substantial reduction in magnitude of the second mode, shows significant control effect.

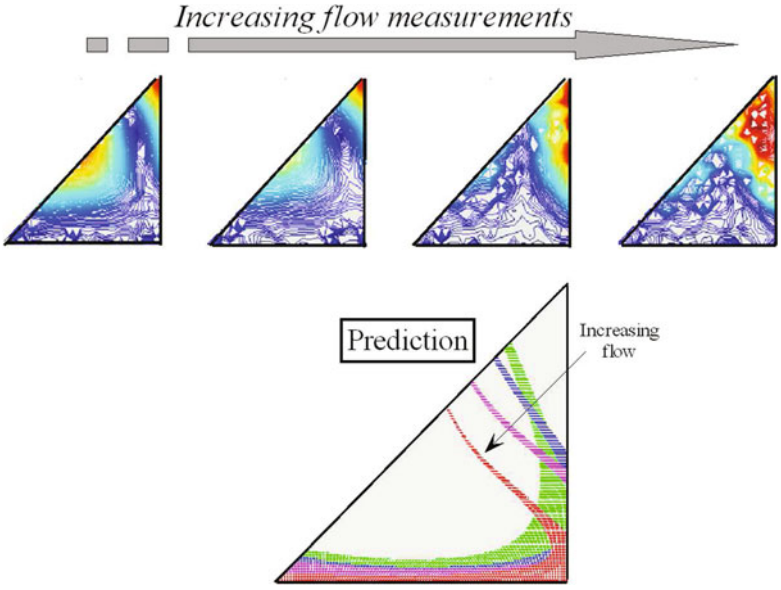

Fig. 34 Progression of second mode shape with flow speed

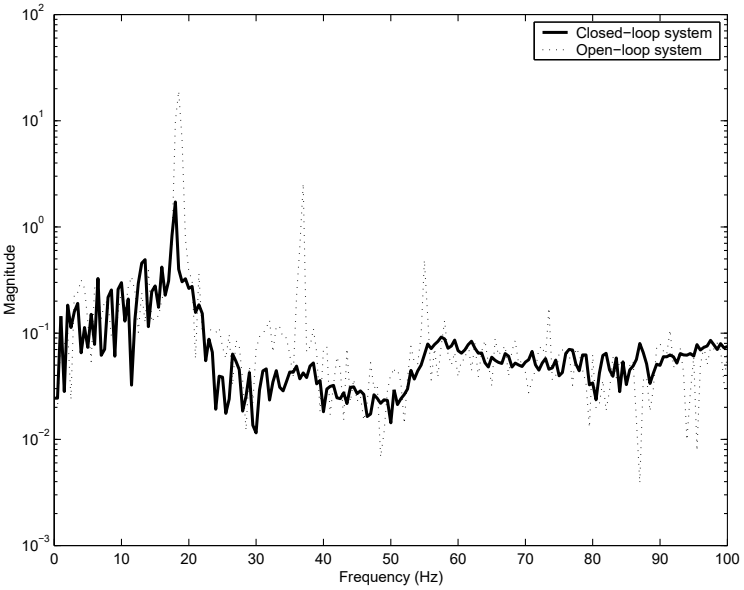

Fig. 35 Comparison of open-loop and closed-loop system, configuration Case 1 at 37.5 m/s

8 Closing Comments on Aeroelastic Control

Within this chapter, we have presented a unified approach to aeroelastic system modeling and control based upon linear analysis tools. These models capture the basic physics (structural, aerodynamic, or aeroelastic) and are often suitable for design purposes, even in systems where nonlinear considerations are required for final verification analysis. Model reduction was shown to enable significant simplification, without a critical loss of accuracy, by focusing on physically relevant input/output paths and a bandwidth of interest. Such model reduction was shown to be not only useful in the design of compensators, but also in the physical design of systems to determine optimal actuator and sensor placement. These models were also extended to encompass parameter varying systems, and shown to permit explicit design of gain scheduled control laws.

Although the models presented within this chapter are relatively simple, the basic tools used are applicable to more complex aeroelastic systems and afford the same advantages to designers. The "great divide" in design frequently occurs when the design of the structure and that of the control system are separated. When properly integrated, one can effectively *design the structure to be controlled*, which can greatly reduce the order of the compensator required to achieve the desired objective and further improve robustness with respect to performance and stability.

There are a number of frontiers yet to be addressed if we are to transition these tools to modern day design practice. Reduced-order aerodynamic models which incorporate the effects of compressibility, viscosity, and/or nonlinearity are critical to extending the applicability of the approach presented to a wider range of missions and models. Furthermore, one must also address the impact of model uncertainty in such systems and develop design philosophies which minimize the effect of uncertainties on closed-loop performance. Finally, although gain scheduling overcomes some of the pitfalls of single-point control designs, the final answer may be in adaptive control systems that combine both the identification of parameter dependent models and the design of control laws. Each of these are topics of active research interest, and exploiting the progress in these areas in the multidisciplinary field of aeroservoelasticity will provide opportunities to improve radically the design and performance of future aircraft.

References

1. Meirovitch L (1980) Computational methods in structural dynamics. Sijhoff and Noordhoff, Rockville, Maryland
2. Noll TE (1993) Structural dynamics and aeroelasticity, vol 5 of flight-vehicle materials, structures, and dynamicsassessment and future directions, chapter Aeroservoelasticity, ASME, pp 179212
3. Livne E (2018) Aircraft active flutter suppression: state of the art and technology maturation needs. J Aircr 55(1):410–450

4. Perry BI, Cole SR, Miller GD (1995) Summary of the active flexible wing program. AIAA J Aircr 32(1):1015
5. Mukhopadhyay V (2000) Benchmark active control technology: part I. J Guid Control Dyn 23(5):913
6. Kailath T (1980) Linear systems. Prentice-Hall, Englewood Cliffs
7. Maciejowski JM (1989) Multivariable feedback design. Addison- Wesley, New York
8. Ogata K (1997) Modern control engineering, 3rd edn. Prentice-Hall, Upper Saddle River
9. Zhou K, Doyle JC (1998) Essentials of robust control. Prentice-Hall, Upper Saddle River
10. Skogestad S, Postlethwaite I (1996) Multivariable feedback control: analysis and design. Wiley, Chichester
11. Ljung L (1987) System identification: theory for the user. Prentice Hall, Englewood Cliffs
12. Juang J-N (1994) Applied system identification. Prentice Hall, Englewood Cliffs
13. Moore BC (1981) Principal component analysis in linear systems: controllability, observability and model reduction. IEEE Trans Autom Control 26(1):1732
14. Theodorsen T (1935) General theory of aerodynamic instability and the mechanism of flutter. Technical report, NACA
15. Bisplinghoff RL, Ashley H, Halfman RL (1955) Aeroelasticity. Addison-Wesley, Cambridge
16. Sears WR (1940) Operational methods in the theory of airfoils in non-uniform motion. J Frankl Inst 230:95111
17. Jones RT (1940) The unsteady lift of a wing of finite aspect ratio. Technical report, NACA
18. Peters DA, Karunamoorthy S, Cao WM (1995) Finite state induced flow models; part I twodimensional thin airfoil. J Aircr 32:313322
19. Edwards JW, Ashley H, Breakwell JV (1979) Unsteady aerodynamic modeling for arbitrary motions. AIAA J 17:365374
20. Conner MD, Tang DM, Dowell EH, Virgin LN (1997) Nonlinear behavior of a typical airfoil section with control surface freeplay: a numerical and experimental study. J Fluids Struct 11:89109
21. Tang DM, Dowell EH, Virgin JN (1998) Limit cycle behavior of an airfoil with a control surface. J Fluids Struct 12:839858
22. Baker ML, Mingori DL, Goggin PJ (1996) Approximate subspace iteration for constructing internally balanced reduced order models of unsteady aerodynamic systems. AIAA structures structural dynamics and materials conference. Salt Lake City, Utah
23. Holmes P, Lumley JL, Berkooz G (1996) Turbulence, coherent structures, dynamical systems and symmetry. Monographs on mechanics. Cambridge University Press, Cambridge
24. Tang DM, Kholodar D, Juang JN, Dowell EH (2001) System identification and proper orthogonal decomposition method applied to unsteady aerodynamics. AIAA J 39(8):15691576
25. Hall KC (1994) Eigenanalysis of unsteady flows about airfoils, cascades, and wings. AIAA J 32(12):24262432
26. Tang DM, Klolodar D, Dowell EH (2000) Nonlinear response of airfoil section with control surface freeplay to gust loads. AIAA J 38(9):15431557
27. Tang DM, Henry JK, Dowell EH (1999) Limit cycle oscillations of delta wing models in low subsonic flow. AIAA J 37(11):13551362
28. Tang DM, Dowell EH (2001) Effects of angle of attack on nonlinear flutter of a delta wing. AIAA J 39(1):1521
29. Richard RE, Rule JA, Clark RL (2001) Genetic spatial optimization of active elements on an aeroelastic delta wing. ASME J Vib Acoust 123(4):466471
30. Clark RL, Gibbs GP, Saunders WR (1998) Adaptive structures, dynamics and control. Wiley, New York
31. Andersen BW (1954) Vibration of triangular cantilever plates by the ritz method. J Appl Mech 21:365370
32. Gere JM, Timoshenko SP (1990) Mechanics of materials, 3rd edn. PWS publishing, Boston
33. Hagood NW, ChungWH, Von Flotow A (1990) Modeling of piezoelectric actuator dynamics for active structural control, In: Proceedings of the 31st AIAA/ASME/ASCE/AHS structures, structural dynamics and materials conference, 24 April , pp 22422256 or AIAA-90-1087-CP

34. Richard R (2002) Optimized flutter control for an aeroelastic delta wing. PhD thesis, Duke University
35. Cole DG, Clark RL (1994) Adaptive compensation of piezoelectric sensoriactuators. J Intell Mater Syst Struct 5:665672
36. Richard RE, Clark RL (2003) Delta wing flutter control using spatially optimized transducers. J Intell Mater Syst Struct 14:677691
37. Williams T (1990) Closed-form grammians and model reduction for flexible space structures. IEEE Trans Autom Control 35(3):379382
38. Boyd S, Baratt C (1991) Linear controller design: limits of performance. Prentice-Hall, Englewood Cliffs
39. Smith CC, Clark RL (1999) Tradeoffs in design complexitytemporal versus spatial compensation. J Sound Vib 228(5):11821194
40. Clark RL, Cox DE (1999) Band-limited actuator and sensor selection for disturbance rejection. AIAA J Guid Control Dyn 22(5):740743
41. Lim KB (1997) Disturbance rejection approach to actuator and sensor placement. J Guid Control Dyn 20(1):202204
42. Lim KB, Gawronski W (1996) Hankel singular values of flexible structures in discrete time. J Guid Control Dyn 19(6):13701377
43. Anderson B, Moore J (1990) Optimal control: linear quadratic methods. Information and system sciences series. Prentice-Hall, Englewood Cliffs
44. Vipperman JS, Clark RL, Conner M, Dowell EH (1998) Experimental active control of a typical section using a trailing-edge flap. J Aircr 35(2):224229
45. Vipperman JS, Clark RL, Conner M, Dowell EH (1999) Comparison of μ and H_2 synthesized controllers on an experimental typical section. AIAA J Guid Control Dyn 22(2):278285
46. Frampton KD, Clark RL (2000) Experiments on control of limit cycle oscillations in a typical section. AIAA J Guid Control Dyn 23(5):956960
47. Leith DJ, Leithhead WE (2000) Survey of gain-scheudling analysis and design. Int J Control 73(11):10011025
48. Packard A (1994) Gain scheduling via linear fractional transformations. Syst Control Lett 22:7992
49. Apkarian P, Gahient P (1995) A convex characterization of gain-scheduled H_∞ controllers. IEEE Trans Autom Control 40(5):853864
50. Nesterov Y, Nemirovsky A (1994) Interior-point polynomial methods in convex programming. Studies in applied mathematics. SIAM, Philadelphia
51. Renegar J (2001) A mathematica view of interior-point methods in convex optimization. MPSSIAM series on optimization. SIAM, Philadelphia
52. Boyd S, ElGhaoui L, Feron E, Balakrishnan V (1994) Linear matrix inequalities in system and control theory. Studies in applied sciences. SIAM, Philadelphia
53. ElGhaoui L, Niculescu SI (eds) (2000) Advances in linear matrix inequality methods in control. Advances in design and control. SIAM, Philadelphia
54. Dullerud GE, Paganini F (1999) A course in robust control theory: a convex approach vol.36 of texts in applied mathematics. Springer, New York
55. Packard A, Zhou K, Pandey P, Becker G (1991) A collection of robust control problems leading to lmis, In: Proceedings of the 30th conference on decision and control, Brighton, England, December 1991, pp 12451250
56. Gahinet P (1994) Explict controller formulas for lmi-based H_{infty} synthesis, In: Proceedings of the IEEE American Control conference, pp 23962400
57. Chiali M, Gahinet P (1996) H_{infty} design with pole placement constraints: an lmi approach. IEEE Trans Autom Control 41(3):358367
58. Scherer C, Gahinet P, Chilali M (1997) Multiobjective output-feedback control via lmi optimization. IEEE Trans Autom Control 42(7):896911
59. Apkarian P, Adams RJ (1998) Advanced gain-scheduling techniques for uncertain systems. IEEE Trans Control Syst Technol 6(1):2132

60. Barker JM, Balas GJ (2000) Comparing linear parameter-varying gain-scheduled control techniques for active flutter suppression. J Guid Control Dyn 23(5):948955
61. Chiali M, Gahinet P (1999) Robust pole placement in lmi regions. IEEE Trans Auto Control 44(12):22572270
62. Cox DE (2003) Control design for parameter dependent aeroelastic systems. PhD. thesis, Duke University
63. Conner M (1996) Nonlinear aeroelasticity of an airfoil section with control surface freeplay. PhD thesis, Duke University
64. Trickey ST (2000) Global and local dynamics of an aeroelastic system with a control surface freeplay nonlinearity. PhD thesis, Duke University
65. Trickey ST, Virgin LN, Dowell EH (2002) The stability of limit-cycle oscillations in a nonlinear aeroelastic system. Proc Math Phy Eng Sci 458(2025):22032226
66. Overschee PV, Moor BD (1996) Subspace identification of linear systems: theory, implementation, applications. Kluwer Academic Publishers, Dordrecht
67. Sturm JF (1999) Using (SeDuMi 1.02), A (MATLAB) toolbox for optimization over symmetric cones. Optimization methods and software, pp 625653
68. Juang JN, Pappa RS (1985) An eigensystem realization algorithm for modal parameter identification and model reduction. J Guid Control Dyn 8(5):620627
69. Overschee PV, Moor BD (1994) N4sid: subspace algorithms for the identification of combined deterministic-stochastic systems. Automatica 30:7593
70. Tang DM, Dowell EH, Hall KC (1999) Limit cycle oscillations of a cantilevered wing in low subsonic flow. AIAA J 37(3):364371

Modern Analysis for Complex and Nonlinear Unsteady Flows in Turbomachinery

Kenneth Hall

Abstract The field of turbomachinery is undergoing major advances in aeroelasticity and this chapter provides an overview of these new developments in the key enabling methodology of unsteady aerodynamic modeling. Also see the earlier discussions in chapters "Aeroelasticity in Turbomachines" and "Modeling of Fluid-Structure Interaction."

In this chapter, we review the state of the field of computational unsteady aerodynamics, particularly frequency domain methods used for the calculation of the unsteady aerodynamic forces arising in turbomachinery aeroelasticity problems [1]. While the emphasis here is on turbomachinery aerodynamics, the methods described in this chapter have analogues for the analysis of isolated airfoils, wings, and even whole aircraft, as well as rotorcraft.

The two main aeromechanics problems in turbomachinery are flutter and gust response. In the flutter problem, the unsteady aerodynamic loads acting on a cascade of turbomachinery airfoils arise from the motion of the airfoils themselves. In the gust response problem, the original excitation arises away from the blade row in question. Typical sources of excitation are wakes or potential fields from neighboring blade rows or support structures (struts), inlet distortions, and hot streaks from the combustor.

More recently, a third class of aeromechanical problems has been identified [1]. This class of problems is akin to galloping of power lines or buffeting of aircraft wings. Examples include so-called separated flow vibrations and non-synchronous vibrations. In separated flow vibrations, the flow over a row of airfoils is separated, or nearly so. The flow itself is unstable, producing unsteady air loads with broadband frequency distributions that excite the airfoil at all frequencies producing a large response at the natural structural frequencies of the airfoil. Non-synchronous flow

K. Hall (✉)
Mechanical Engineering and Materials Science Duke University, Durham, NC, USA
e-mail: kenneth.c.hall@duke.edu

[1] Portions of this chapter were excepted from prior papers written by the author and his students, including W. S. Clark, C.B. Lorence, P. D. Silkowski, and D. M. Voytovich. Their contributors are gratefully acknowledged.

E. H. Dowell (ed.), *A Modern Course in Aeroelasticity*, Solid Mechanics and Its Applications 264, https://doi.org/10.1007/978-3-030-74236-2_13

vibrations, on the other hand, are similar to separated flow vibrations in that the source of the excitation is thought to be a fluid dynamics instability (rather than an aeroelastic instability), except that non-synchronous vibrations can also occur well away from a stalled condition and the response tends to be at a single frequency. If this fluid dynamic natural frequency happens to be close to a structural natural frequency, then the fluid dynamic instability frequency can "lock on" to the structural frequency of the airfoils resulting in a large-amplitude vibration.

Most unsteady flows of interest in turbomachinery aeromechanics are periodic in time, and for many of these flows, the unsteadiness in the flow is also relatively small compared to the mean steady flow. Thus, the flow may be decomposed into two parts: a nonlinear steady or mean flow, plus a dynamically linear small perturbation unsteady flow. In general, the steady flow is described by a set of nonlinear partial differential equation, whereas the unsteady small-perturbation flow is described by a set of linear variable coefficient partial differential equations that are hyperbolic in time. Because the unsteady perturbation flow is periodic in time, we may, without loss of generality, represent the unsteady flow as a Fourier series in time with coefficients that vary spatially. Each Fourier coefficient is described by a set of partial differential equations in which time does not appear explicitly. Such equations are called "time-linearized" equations, and their solution is one of the main topics of this chapter.

Working in the frequency domain rather than the time domain has a number of distinct advantages. The available frequency solution techniques tend to be much more computationally efficient than the equivalent time domain techniques. Additionally, certain parts of the unsteady flow problem—for instance, the description of the behavior of acoustic, vortical, and entropic waves—are simplified in the frequency domain.

In the case where the unsteadiness in the flow is large, the time-linearized equations are not valid. Fortunately, however, the unsteady flow may still be calculated in the frequency domain using a recently developed harmonic balance technique.

Finally, although the emphasis in this chapter is on unsteady aerodynamics associated with aeromechanical problems, frequency domain techniques can be used to solve of wide variety of problems, including performance, unsteady heat transfer, aeroacoustic, and flow stability problems.

1 Linearized Analysis of Unsteady Flows

Recently, a number of investigators have developed linearized Euler and Navier–Stokes solvers to predict unsteady flows in turbomachinery. To motivate these methods, consider the two-dimensional Euler equations, given by

$$\frac{\partial \hat{\mathbf{U}}}{\partial t} + \frac{\partial \hat{\mathbf{F}}}{\partial x} + \frac{\partial \hat{\mathbf{G}}}{\partial y} = 0 \tag{1.1}$$

where $\hat{\mathbf{U}}$ is the vector of conservation variables, and $\hat{\mathbf{F}}$ and $\hat{\mathbf{G}}$ are so-called flux vectors. These are given by

$$\hat{\mathbf{U}} = \begin{bmatrix} \hat{\rho} \\ \hat{\rho}\hat{u} \\ \hat{\rho}\hat{v} \\ \hat{e} \end{bmatrix}, \quad \hat{\mathbf{F}} = \begin{bmatrix} \hat{\rho}\hat{u} \\ \hat{\rho}\hat{u}^2 + \hat{p} \\ \hat{\rho}\hat{u}\hat{v} \\ \hat{\rho}\hat{u}\hat{h}_0 \end{bmatrix}, \quad \hat{\mathbf{G}} = \begin{bmatrix} \hat{\rho}\hat{v} \\ \hat{\rho}\hat{u}\hat{v} \\ \hat{\rho}\hat{v}^2 + \hat{p} \\ \hat{\rho}\hat{v}\hat{h}_0 \end{bmatrix} \tag{1.2}$$

where $\hat{\rho}$ is the density, $\hat{u}$ and $\hat{v}$ are the x and y components of velocity, $\hat{p}$ is the static pressure, $\hat{e}$ is the total internal energy, and $\hat{h}_0$ is the total enthalpy. The pressure, energy, and total enthalpy can in turn be expressed in terms of the conservation variables.

The flow is assumed to be composed of a mean flow plus an unsteady perturbation flow that is harmonic in time, so that

$$\hat{\mathbf{U}}(x, y, t) = \mathbf{U}(x, y) + \mathbf{u}(x, y)e^{j\omega t} \tag{1.3}$$

where the perturbation amplitude $\mathbf{u}(x, y)$ is small compared to the mean flow $\mathbf{U}(x, y)$, and ω is the frequency of the unsteadiness. This assumption is substituted into the Euler equations, Eq. (1.1), and the result is expressed as a perturbation series in the small parameter. The collected zeroth-order terms result in the steady Euler equations, which are solved using now conventional computational fluid dynamic techniques. The collected first-order terms give the linearized Euler equations, i.e.,

$$j\omega\mathbf{u} + \frac{\partial}{\partial x}\left(\frac{\partial \mathbf{F}}{\partial \mathbf{U}}\mathbf{u}\right) + \frac{\partial}{\partial y}\left(\frac{\partial \mathbf{G}}{\partial \mathbf{U}}\mathbf{u}\right) = 0 \tag{1.4}$$

where $\partial\mathbf{F}/\partial\mathbf{U}$ and $\partial\mathbf{G}/\partial\mathbf{U}$ are steady flow Jacobians. These equations are solved subject to appropriate "upwash" boundary conditions at the airfoil surface, far-field boundary conditions, and periodicity conditions that allow the computational domain to be reduced to a single blade passage.

One of the earliest linearized Euler solvers was developed by Ni and Sisto [2]. So that they could make use of more traditional time marching CFD algorithms, Ni and Sisto introduced a pseudo-time term τ into the linearized Euler equations, i.e.,

$$\frac{\partial \mathbf{u}}{\partial \tau} + j\omega\mathbf{u} + \frac{\partial}{\partial x}\left(\frac{\partial \mathbf{F}}{\partial \mathbf{U}}\mathbf{u}\right) + \frac{\partial}{\partial y}\left(\frac{\partial \mathbf{G}}{\partial \mathbf{U}}\mathbf{u}\right) = 0 \tag{1.5}$$

where now $\mathbf{u} = \mathbf{u}(x, y, \tau)$. This additional term makes the equations hyperbolic in pseudo time, and hence they may be marched in pseudo time using traditional CFD techniques. As time advances, the solution reaches a steady state and the additional term goes to zero. Thus the solution to the original linearized Euler equations [Eq. (1.4)] is obtained. The results of this early analysis, however, were limited to flat plate cascades with homentropic flows.

Hall and Crawley [3] discretized the linearized Euler equations using a finite volume scheme, and assembled the resulting equations into a large sparse set of matrix equations which were then solved using LU decomposition. Shock fitting and shock capturing were used to explicitly model the motion of wakes and shocks. However, due to the complexity of the shock fitting algorithm, only a few model transonic flows problems were computed. Nevertheless, this work demonstrated the feasibility of using the linearized Euler equations to model transonic flows, at least for cases where the motion of the shock is not too large.

In recent years, a number of investigators [4–8] have continued to develop the linearized Euler technique using pseudo time marching.

The time-linearized technique has been extended to three-dimensional inviscid (Euler) flows [9, 10] and to two and three-dimensional viscous (Navier–Stokes) flows [11–13] in turbomachinery.

The time-linearized frequency-domain approach has a number of distinct advantages over a conventional time-domain approach. By using pseudo time marching, conventional steady CFD techniques may be used to solve the time-linearized equations. Thus, acceleration techniques such as local time stepping and multiple grid acceleration techniques may be used to accelerate convergence. Furthermore, by using complex periodicity conditions, the computational domain can be reduced to a single blade passage. The result is that time-linearized solutions can be obtained in computational times comparable to the time required to obtain a *steady* flow solution.

One feature of most linearized Euler and Navier–Stokes solvers is the use of harmonically deforming computational meshes [7]. The use of the deforming grid eliminates the need for a troublesome extrapolation term appearing in the upwash boundary condition applied at the airfoil surface, but also produces an inhomogeneous term in the linearized Euler equation, Eq. (1.4), that depends on the mean flow and the prescribed grid motion.

One important aspect of a linearized Euler analysis is how shocks are treated. Two approaches have been used. Hall and Crawley [3] used shock fitting to model shocks within a linearized framework. Shock fitting, while providing explicit descriptions of the shock motion, is somewhat difficult to implement for general cascade flows which may have rather complicated shock features. For this reason, shock capturing is favored. However, until recently it was not known whether shock capturing correctly predicts the unsteady aerodynamic loads induced by the unsteady shock motion.

The situation is shown graphically in Fig. 1. Shown are the mean and unsteady shock trajectories on the surface of an airfoil or channel. Also shown are typical unsteady flow quantities, e.g., pressure. In a linearized analysis, the motion of the shock appears as an impulse in pressure. At this impulse, the pressure is not small (in fact it is of the same order as the mean flow pressure), and therefore, one might conclude that the linearization would break down at this point. Lindquist and Giles [14] argued that to obtain the proper shock impulse, one must faithfully linearize a conservative discretization of the Euler equations. Hall et al. [8] demonstrated that the correct shock impulse is produced if a conservative discretization of the Euler equations is used, and further, that the shock is smoothed so that it is smeared over several grid points.

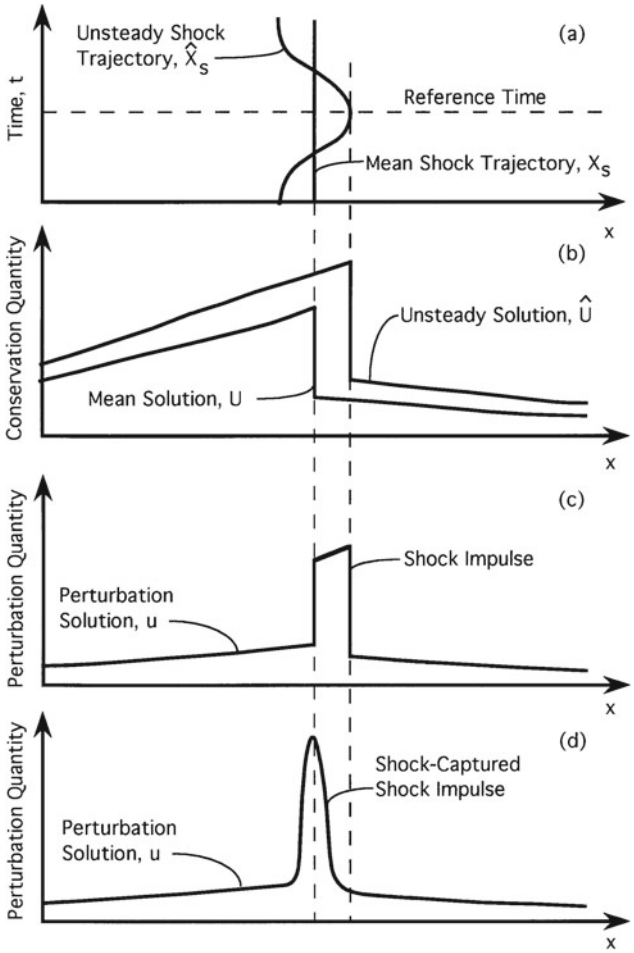

Fig. 1 Trajectory of shock in a channel or on airfoil surface and corresponding effect on unsteady flow quantities. After Hall, Clark, and Lorence [8]. Published with permission from ASME

A typical transonic analysis is shown in Figs. 2 and 3. Shown in Fig. 2 is the computed steady distribution for the Tenth Standard Configuration [15, 16], one of a series of Standard Configurations used to validate unsteady aerodynamic models. Shown in Fig. 3 is the computed unsteady pressure distribution on the airfoils of this cascade for the case where the airfoils vibrate in plunge with a reduced frequency $\overline{\omega}$ of 1.287 with an interblade phase angle σ of -90 deg. Shown are two solutions, one computed with a time-linearized flow solver, and one computed using a conventional time-domain flow solver [17]. Note the very good agreement between the two solutions everywhere except at the shock impulse. However, even though the details

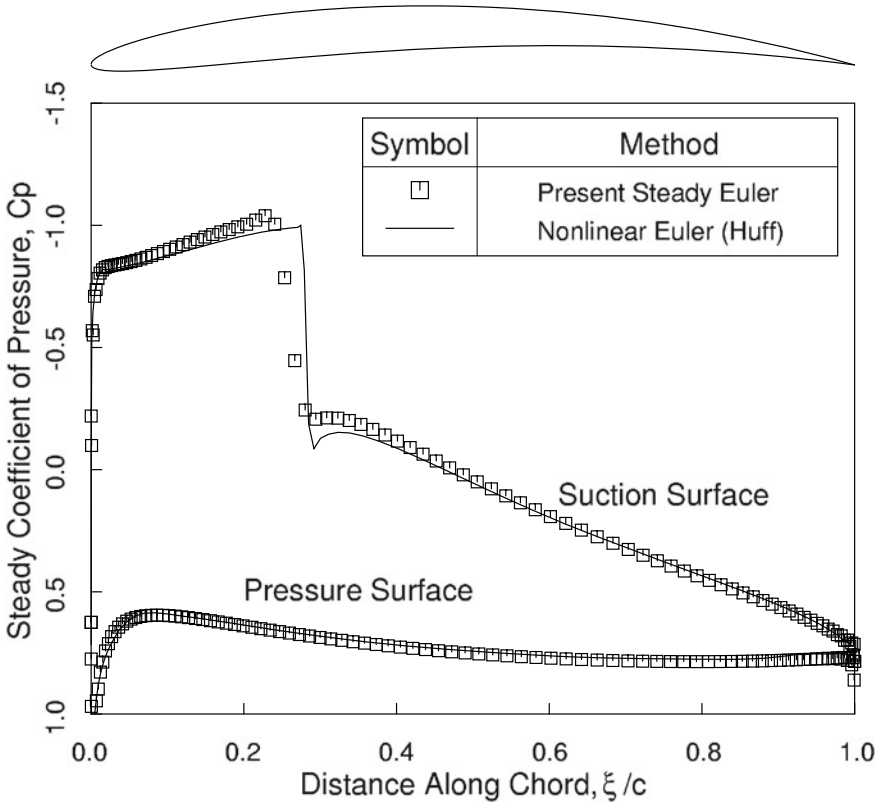

Fig. 2 Steady surface pressure for the Tenth Standard Configuration transonic compressor cascade. After Hall, Clark, and Lorence [8]. Published with permission from ASME

of the shock impulse differ between the two solutions, the integrated force is very nearly equal. The integrated unsteady lift differs by just 2%.

The time-linearized approach can also be applied equally well viscous flows using the Reynolds averaged Navier–Stokes equations and/or three-dimensional flows. As an example, consider the case of the front stage of a modern front stage transonic compressor rotor shown in Fig. 4. Shown are the blades of the rotor together with the computed streamlines associated with the steady flow at a particular operating condition. These results were computed using a steady Navier–Stokes flow solver that uses the Spalart–Allmaras [18] turbulence model to predict turbulent viscosity. Note the clearly visible tip vortex due to leakage flow through the tip clearance.

Next, the rotor blades are assumed to vibrate in their first bending mode (and at the natural frequency of that mode) with zero interblade phase angle. Figure 5 shows the computed steady and unsteady pressure distributions for this compressor rotor near the midspan of the blade computed using the time-linearized technique.

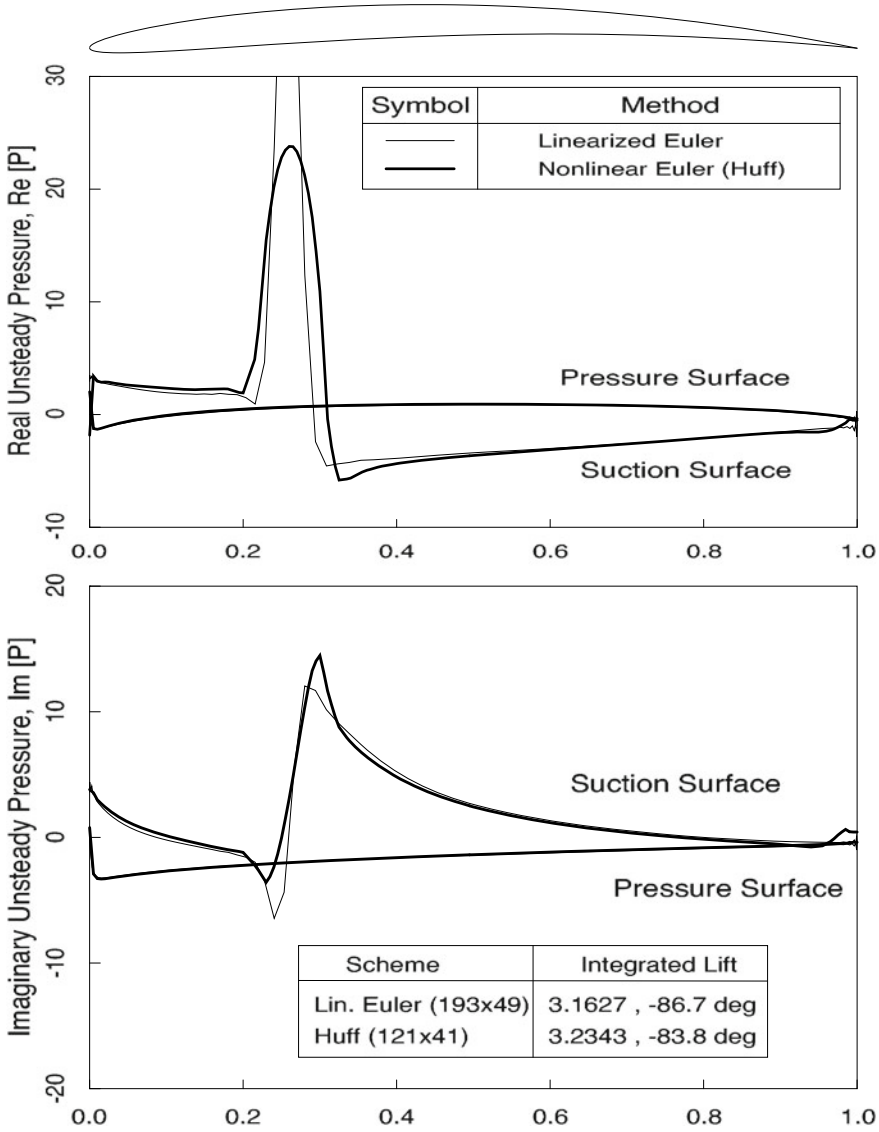

Fig. 3 Real and imaginary unsteady surface pressure for the Tenth Standard Configuration cascade vibrating in plunge with a reduced frequency $\overline{\omega}$ of 1.287 with an interblade phase angle σ of -90 deg. After Hall, Clark, and Lorence [8]. Published with permission from ASME

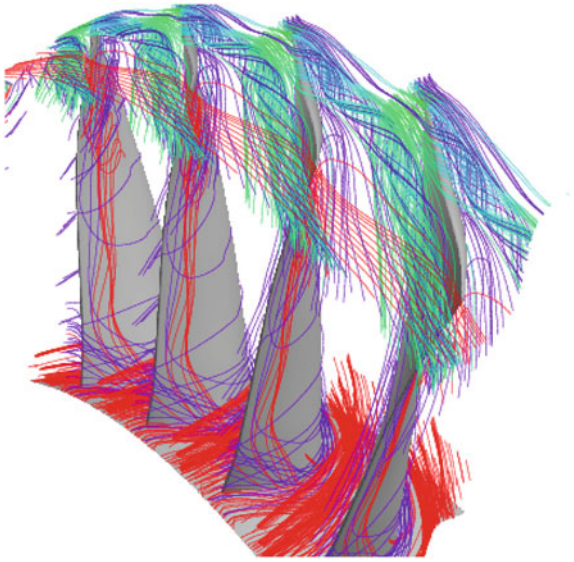

Fig. 4 Computed steady streamline patterns for a modern front stage compressor rotor

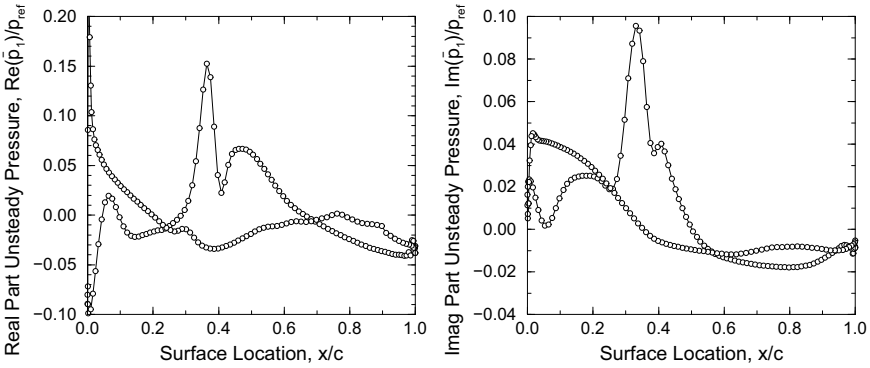

Fig. 5 Unsteady pressure distribution near the midspan station of a front stage compressor rotor. The airfoil vibrates in its first bending mode with an interblade phase angle of zero. After Hall et al. [34]

A shock impulse is seen in the unsteady pressure distribution on the surface of the airfoil at about 35% of the chord.

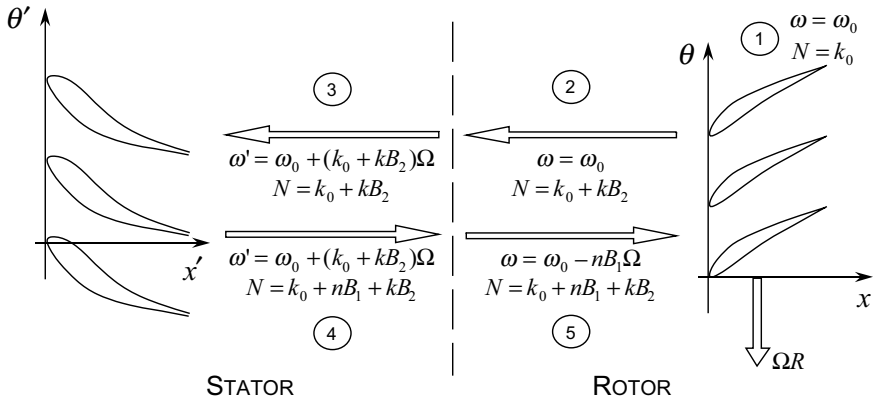

Fig. 6 Kinematics of mode scattering and frequency shifting in a multistage machine. After Silkowski and Hall [20]. Published with permission from ASME

2 Analysis of Unsteady Flows in Multistage Machines

[2]Unsteady fluid motion is essential to gas turbine engine operation. Only through unsteady flow processes can a machine do work on a fluid to increase its total enthalpy. This unsteadiness is provided in compressors and turbines by relative motion of adjacent stators and rotors. Unfortunately, this motion also produces undesirable aeroacoustic and aeroelastic phenomena, i.e., tonal noise and forced blade vibrations induced by rotor/stator interactions. Furthermore, the aeroelastic (flutter) stability of a rotor can be profoundly influenced by the presence of nearby stators and rotors.

Most current unsteady aerodynamic theories model a single blade row in an infinitely long duct, ignoring potentially important multistage effects. However, unsteady flows are made up of acoustic, vortical, and entropic waves. These waves provide a mechanism for the rotors and stators of multistage machines to communicate with one another. For example, consider the case of a row of vibrating rotor blades (see Fig. 6).

The blades will respond aerodynamically, producing acoustic, vortical, and entropic waves which propagate away from the rotor. Some of these waves will then impinge on the neighboring stators. The stators will in turn respond aerodynamically, again producing waves, some of which will impinge upon the original rotor, and so on. In other words, wave behavior makes unsteady flow in turbomachinery fundamentally a multistage phenomenon.

The basic time-linearized Euler and Navier–Stokes approach can be extended to the case of multistage flows [19]. For a given multistage fan or compressor, one first generates a computational mesh for each blade row. Unlike time-domain multistage

[2] Portions of this section originally appeared in [20] and are reprinted here with permission from ASME.

analyses, the computational mesh for each blade row need only include a single passage.

Having generated a computational mesh, the steady flow is computed using the steady Euler or Navier–Stokes equations and conventional computational fluid dynamic (CFD) techniques, with so-called "mixing planes" (the inter-row computational boundaries of the computational grid) used to couple together the solutions computed in the individual blade rows. The solution in each blade row is computed independently, except that at each time step in the pseudo time marching, the flow at the inter-row computational boundaries between two blades rows is updated so that the circumferentially averaged flow at the inlet (or exit) of one blade row is matched the circumferentially averaged flow at the exit (or inlet) of the neighboring blade row.

For the unsteady flow solution, the process is similar. However, instead of a single solution in each passage, several linearized unsteady flow calculations are performed simultaneously in each blade row, one corresponding to each spinning mode retained in the model. Each spinning mode is identified by a set of integers that describe the scattering process that creates the mode (n and k in Fig. 6). These integers, along with the frequency and interblade phase angle of the initial disturbance and the blade counts in each blade row, determine the interblade phase angle and frequency of the mode. The only coupling among the various spinning modes is at the inter-row boundaries.

The advantages of this approach are several. First, unlike time-domain techniques where many blade passages are required to model each blade row, only a single passage is required for each row. Second, as in the single blade row computations, a pseudo time marching technique is used to march the solution to steady state, and acceleration techniques such as multigrid may be used. Finally, as a practical matter, only a handful of spinning modes are usually needed to obtain accurate solutions. These three factors mean that memory requirements and computational time required to compute the unsteady multistage solution are greatly reduced compared to time domain solvers. A typical unsteady multistage flow calculation might take on the order of just ten times the computational time required for a single steady blade row flow computation.

As an example, consider the case of the front stage of a modern compressor. This three-dimensional configuration consists of three blade rows (IGV/rotor/stator). Figure 7 shows the static pressure distribution near the midspan location computed using a steady Euler multistage flow solver. Note, that the contours at the inter-row boundaries are not continuous since only the circumferential averages of the flows in each blade row match at the boundaries.

Next, the middle blade row (rotor) is assumed to vibrate in its first bending mode and frequency. Figure 8 shows the real and the imaginary parts of the unsteady pressure on the rotor row for an interblade phase angle of -30. deg. The multistage solution was computed using one and eight spinning modes in the coupling procedure. One can see that there is significant difference between the isolated and coupled (multistage) computations.

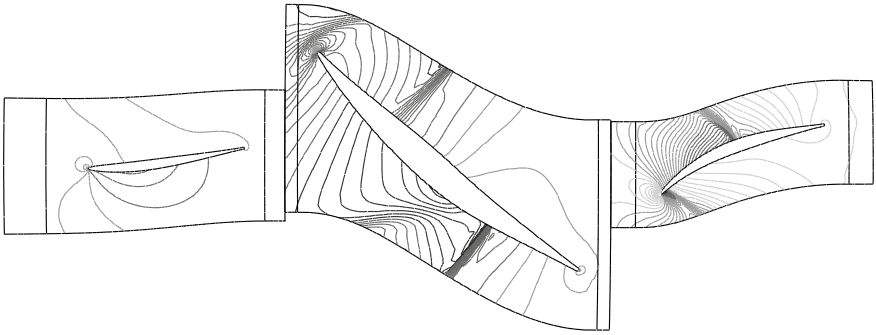

Fig. 7 Pressure contours at the midspan of a front stage compressor. After Hall et al. [34]

The unsteady pressure distribution can be integrated to obtain the unsteady modal force acting on the rotor blades due to their vibration. Figure 9 shows the real and imaginary parts of the computed generalized forces on the rotor blades as a function of interblade phase angle. Note the significant difference between the forces computed using a single blade row (the rotor) and three blade rows (the rotor and the upstream IGV and downstream stator). Clearly, multistage effects are important. However, the generalized force computed using just one spinning mode is in very good agreement with the force computed using eight spinning modes, indicating the dominant coupling is in the fundamental mode.

These results, and earlier two-dimensional results produced by Hall and Silkowski [20–22], confirm that the aerodynamic damping of a blade row that is part of a multistage machine can be significantly different than that predicted using an isolated blade row model. This is an important result since most unsteady aerodynamic theories currently used in industry assume that the blade row can be modeled as isolated in an infinitely long duct. However, a good estimate of the aerodynamic damping can be obtained using just a few spinning modes in the model. In fact, most of the unsteady aerodynamic coupling between blade rows occurs in the fundamental spinning mode, that is, the spinning mode associated with the original disturbance. Scattered modes are relatively less important.

Although not shown here, Hall and Silkowski [20–22] have shown that the two neighboring stator blade rows adjacent to a rotor have the strongest influence on the unsteady aerodynamic response of the rotor. The next nearest blade rows are less important, but can have a modest influence. As a practical matter, this means that only three blade rows need to be included in most unsteady flow computations.

Finally, we note that while the frequency domain multistage analysis presented here is for small disturbance (linearized) flows, the method has been extended to model nonlinear unsteady multistage flows using the harmonic balance technique [23, 24].

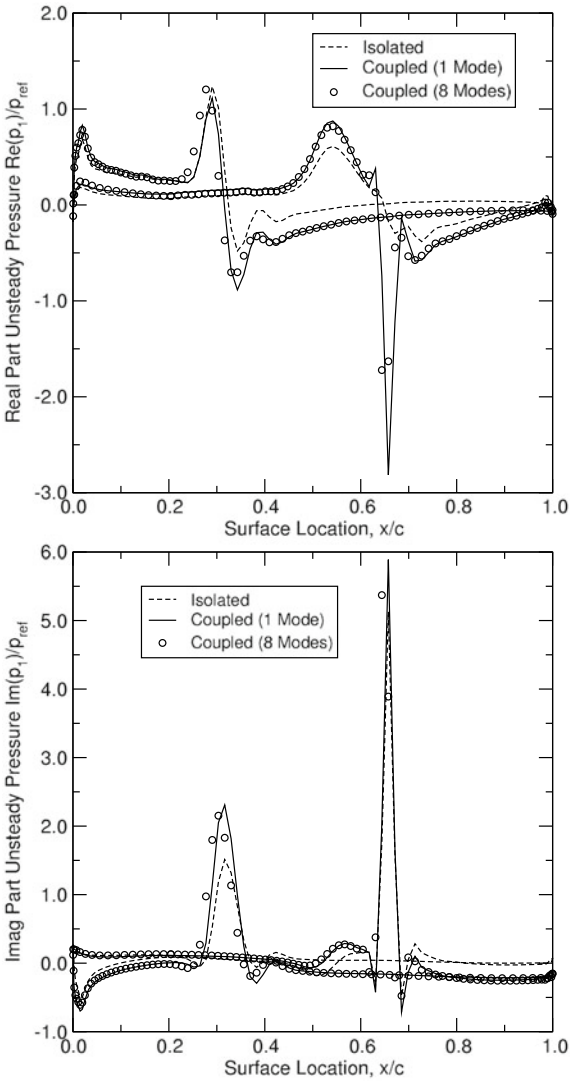

Fig. 8 Unsteady pressure distribution on the surface of rotor blades vibrating in first bending with σ =-30°. After Hall et al. [34]

3 The Harmonic Balance Method for Nonlinear Unsteady Aerodynamics

A number of investigators have developed frequency domain analyses of nonlinear unsteady flows [25–33]. While the methods differ somewhat in detail, most can be viewed as a form of harmonic balance. To motivate the development of the harmonic balance analysis, and for simplicity, we assume for the moment that the flow in a blade row is two-dimensional, inviscid, and non-heat-conducting, with constant specific

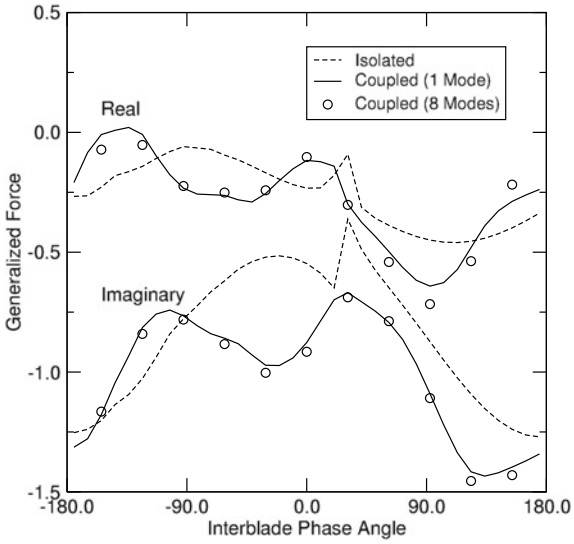

Fig. 9 Generalized force acting on rotor blades vibrating in first bending. After Hall et al. [34]

heats. Thus, the flow may be modeled by the two-dimensional Euler equations, Eq. (1.1).

In this section, we consider unsteady flows that are temporally and spatially periodic. In particular, temporal periodicity requires that

$$\mathbf{U}(x, y, t) = \mathbf{U}(x, y, t + T) \tag{3.1}$$

where T is the temporal period of the unsteadiness. Similarly, for cascade flow problems arising from vibration of the airfoils with fixed interblade phase angles σ, or incident gusts that are spatially periodic, spatial periodicity requires that

$$\mathbf{U}(x, y + G, t) = \mathbf{U}(x, y, t + \Delta T) \tag{3.2}$$

where G is the blade-to-blade gap, and ΔT is the time lag associated with the interblade phase lag. As an example, consider a cascade of airfoils where the source of aerodynamic excitation is blade vibration with a prescribed interblade phase angle σ and frequency ω. Then $T = 2\pi/\omega$ and $\Delta T = \sigma/\omega$.

Because the flow is temporally periodic, the flow variables may be represented as a Fourier series in time with spatially varying coefficients. For example, the conservation variables may be expressed as

$$\rho(x, y, t) = \sum_n R_n(x, y) e^{j\omega nt}$$

$$\rho u(x, y, t) = \sum_n U_n(x, y) e^{j\omega nt}$$

$$\rho v(x, y, t) = \sum_n V_n(x, y) e^{j\omega n t}$$

$$\rho e(x, y, t) = \sum_n E_n(x, y) e^{j\omega n t} \tag{3.3}$$

where in principle the summations are taken over all integer values of n. In practice, these series are truncated to a finite number of terms, $-N \leq n \leq +N$.

Next, at least conceptually, we substitute the series expansions for ρ, ρu, ρv, and ρe into the Euler equations, Eq. (1.1). The result is expanded in a Fourier series, with terms grouped by frequency. Using a traditional harmonic balance approach, each frequency component must vanish. Collecting the resulting harmonic balance equations together into one vector equation gives

$$\frac{\partial \tilde{\mathbf{F}}(\tilde{\mathbf{U}})}{\partial x} + \frac{\partial \tilde{\mathbf{G}}(\tilde{\mathbf{U}})}{\partial y} + \tilde{\mathbf{S}}(\tilde{\mathbf{U}}) = 0 \tag{3.4}$$

where

$$\tilde{\mathbf{U}} = \begin{Bmatrix} R_0 \\ U_0 \\ V_0 \\ E_0 \\ R_{+1} \\ U_{+1} \\ V_{+1} \\ E_{+1} \\ \vdots \end{Bmatrix}, \qquad \tilde{\mathbf{S}} = j\omega \begin{Bmatrix} 0 \cdot R_0 \\ 0 \cdot U_0 \\ 0 \cdot V_0 \\ 0 \cdot E_0 \\ +1 \cdot R_{+1} \\ +1 \cdot U_{+1} \\ +1 \cdot V_{+1} \\ +1 \cdot E_{+1} \\ \vdots \end{Bmatrix} \tag{3.5}$$

The vectors $\tilde{\mathbf{F}}$ and $\tilde{\mathbf{G}}$ are much more complicated, but can be written as a nonlinear functions of the vector of Fourier coefficients of the conservation variables $\tilde{\mathbf{U}}$.

Finally, we note the conservation variables are real quantities, so that

$$U_{-n} = \overline{U}_n \tag{3.6}$$

where $\overline{U}_n$ is the complex conjugate of U_n. Thus, we only need to store Fourier coefficients for non-negative n. If N harmonics are retained in the Fourier series representation of the flow, then $2N + 1$ coefficients are stored for each flow variable (one for the zeroth harmonic or mean flow, and $2N$ for the real and imaginary parts of the remaining harmonics).

Computation of the harmonic fluxes is difficult and computationally expensive; on the order of N^3 operations are required, so that the cost of the harmonic balance analysis grows rapidly with the number of harmonics. Also, this approach is not readily applicable to viscous flows, because turbulence models tend to be quite complex, and not readily expressed in simple algebraic forms.

To alleviate these problems, we note that alternatively, one can reconstruct the Fourier coefficients of the conservation variables $\tilde{\mathbf{U}}$ and the flux vectors $\tilde{\mathbf{F}}$ and $\tilde{\mathbf{G}}$ from a knowledge of the temporal behavior of $\mathbf{U}$, $\mathbf{F}$, and $\mathbf{G}$ at $2N + 1$ equally spaced points over one temporal period. In other words,

$$\tilde{\mathbf{U}} = \mathbf{E}\mathbf{U}^* \tag{3.7}$$

where $\mathbf{U}^*$ is the vector of conservation variables at $2N + 1$ equally spaced points in time over one temporal period, and $\mathbf{E}$ is matrix that is the discrete Fourier transform operator. Conversely,

$$\mathbf{U}^* = \mathbf{E}^{-1}\tilde{\mathbf{U}} \tag{3.8}$$

where $\mathbf{E}^{-1}$ is the corresponding inverse Fourier transform operator. Similar expressions hold for the flux vectors.

Substitution of Eq. (3.7) into Eq. (3.3) gives

$$\frac{\partial \mathbf{E}\mathbf{F}^*}{\partial x} + \frac{\partial \mathbf{E}\mathbf{G}^*}{\partial y} + j\omega \mathbf{N}\mathbf{E}\mathbf{U}^* = 0 \tag{3.9}$$

where $\mathbf{N}$ is a diagonal matrix with n in the entries corresponding to the nth harmonic. Pre-multiplying Eq. (3.9) by $\mathbf{E}^{-1}$ gives

$$\frac{\partial \mathbf{F}^*}{\partial x} + \frac{\partial \mathbf{G}^*}{\partial y} + \mathbf{S}^* = 0 \tag{3.10}$$

where

$$\mathbf{S}^* = j\omega \mathbf{E}^{-1}\mathbf{N}\mathbf{E}\mathbf{U}^* \approx \frac{\partial \mathbf{U}^*}{\partial t} \tag{3.11}$$

The product $j\omega \mathbf{E}^{-1}\mathbf{N}\mathbf{E}$ is just the spectral operator that approximates $\partial/\partial t$. The advantage of Eq. (3.10) over the original form of the harmonic balance equations, Eq. (3.4), is that the fluxes in Eq. (3.10) are much easier to compute. The fluxes are simply computed at each of the $2N + 1$ time levels in the usual way, using Eq. (1.2). Also, the alternate form of the harmonic balance equations can easily be applied to more complex flow equations, such as the Navier–Stokes equations, whereas the original form, Eq. (3.4), cannot.

To solve the harmonic balance equations, we introduce a "pseudo-time" term so that the equations may be marched to a steady state condition using a conventional computational fluid dynamic scheme. Using the harmonic balance form of the Euler equations as an example, we let

$$\frac{\partial \mathbf{U}^*}{\partial \tau} + \frac{\partial \mathbf{F}^*}{\partial x} + \frac{\partial \mathbf{G}^*}{\partial y} + \mathbf{S}^* = 0 \tag{3.12}$$

where τ is a fictitious time, used only to march Eq. (3.12) to steady state, driving the pseudo time term to zero. Note that pseudo-time harmonic balance equations, Eq. (3.12), are similar in form to the original time-domain form of the Euler equations, Eq. (3.7). However, the conservation variable vector, $\mathbf{U}^*$ and flux vectors $\mathbf{F}^*$ and $\mathbf{G}^*$ are now $2N+1$ larger than the original vectors $\mathbf{U}$, $\mathbf{F}$, and $\mathbf{G}$. Furthermore, the physical time derivative term is replaced by the time spectral term $\mathbf{S}^*$, and the pseudo time term is added.

The time spectral term $\mathbf{S}^*$ requires $\mathcal{O}(N^2)$ operations to compute (or $\mathcal{O}(N\log(N))$ if an FFT is used). However, the calculation of the flux vector terms is greatly simplified, requiring only $\mathcal{O}(N)$ computations. As a practical matter, the flux calculations, and other calculations requiring $\mathcal{O}(N)$ computations, require much more computational time than the relatively simple time derivative term. Thus, the computational time scales like the number of Fourier terms retained in the solution, at least for modest sized N.

Although the harmonic balance technique has been described using the Euler equations, the method can be readily applied to the Reynolds averaged Navier–Stokes equations. As an example, we apply the harmonic balance technique to a representative flutter problem. We consider a two-dimensional section near the tip of the front stage transonic rotor of a modern high pressure compressor.

At this spanwise station, the inflow Mach number M is 1.27, the inflow angle Θ, measured from the axial direction, is 59.3°, and the Reynolds number Re is about 1.35×10^6. The computational grid used is an H-O-H grid, which has good resolution near the airfoil surface for resolving viscous boundary layers, as well as good resolution in the far field for modeling outgoing waves.

Shown in Fig. 10 is the steady flow (i.e., no unsteady disturbances) in the blade row computed using a grid with 193×33 nodes in the O-grid section. Note the fairly complex shock structure, with a shock extending from the leading edge both above and below the airfoil. This shock impinges on the suction surface of the airfoil, causing a local strong adverse pressure gradient, which causes the boundary layer to separate. The rapid growth of the boundary layer results in an oblique shock forming just upstream of the separation point. Also, the flow accelerates over the front portion of the pressure surface resulting in a weak normal shock at about 40% of the chord on the pressure surface.

Next, we consider the unsteady aerodynamic response of the rotor for the case where the airfoils vibrate harmonically in pitch about their midchords with a reduced frequency $\overline{\omega}$ equal to 1.0 (based on chord and upstream velocity), an interblade phase angle σ equal to 30°, and amplitude $\overline{\alpha}$. Shown in Fig. 11 is the mean pressure distribution (the zeroth Fourier component) computed for a pitching amplitude $\overline{\alpha} = 1.0°$. The harmonic balance solution was computed using one, three, five, and seven harmonics ($N = 1, 3, 5,$ and 7). Note that the mean pressure distributions computed with various numbers of harmonics are different. However, the solutions converge rapidly as the number of harmonics is increased.

Next, we consider the first harmonic of the unsteady pressure distribution on the airfoil surface. This component is important, because it is the only component that contributes to aerodynamic damping for harmonic pitching motion of the airfoil.

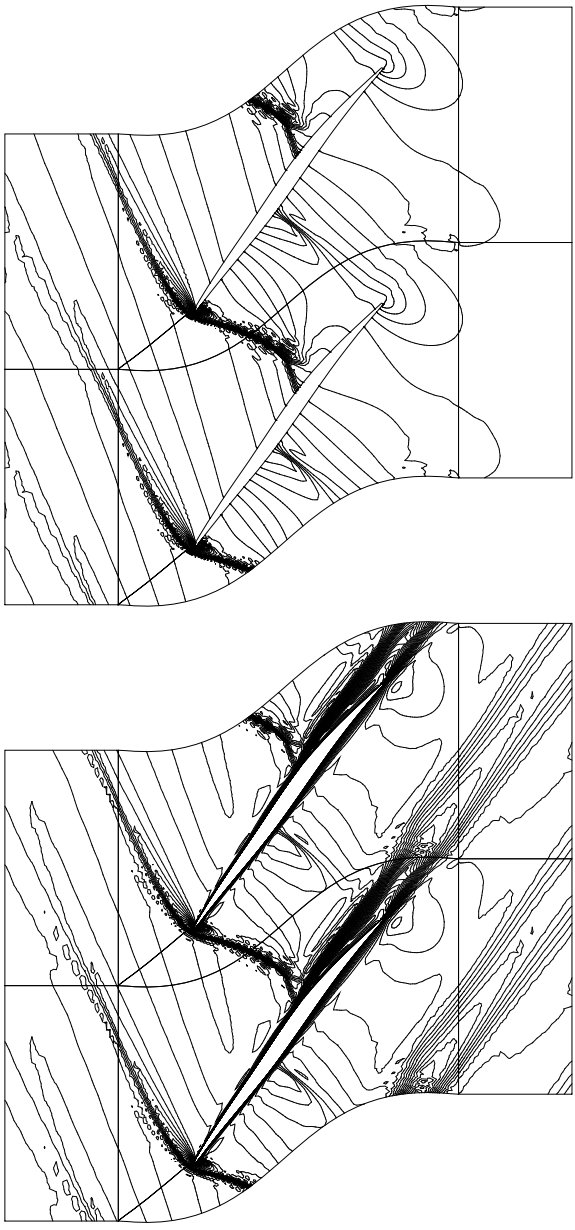

Fig. 10 Computed steady pressure (top) and Mach number (bottom) contours for transonic viscous flow through front stage compressor rotor. After Hall, Thomas, and Clark [32]

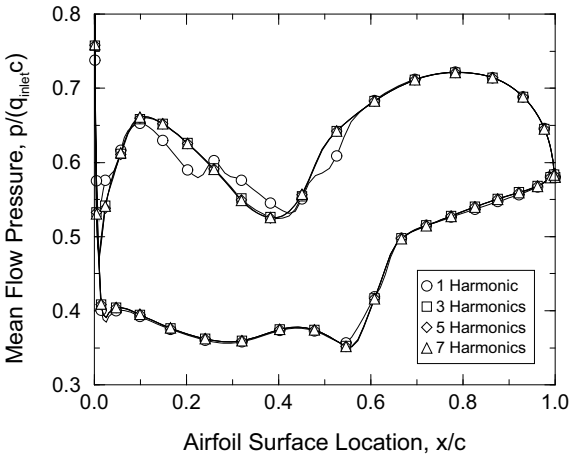

Fig. 11 Zeroth harmonic (mean flow) of unsteady pressure distribution for front stage compressor rotor airfoils vibrating in pitch with $\overline{\omega} = 1.0$ and $\sigma = 30°$, and $\overline{\alpha} = 1.0°$. After Hall, Thomas, and Clark [32]

Shown in Fig. 12 is the first harmonic of the unsteady pressure on the airfoil surface, scaled by the amplitude of the pitching amplitude. As in the case of the mean flow, the unsteady pressure distributions computed with various numbers of harmonics are different, but again the solutions converge rapidly as the number of harmonics is increased.

To demonstrate the influence of nonlinearities on the unsteady flow, we again plot the zeroth and first harmonics of the unsteady flow in Fig. 13. In these results, the larger amplitude motion solutions are computed using five harmonics so that the results are converged in the harmonic balance sense. The pressure distributions are plotted for several pitching amplitudes. The pressure distributions associated with the larger amplitude pitching motion is seen to be substantially different from the small amplitude case. In the small-amplitude case, the mean pressure distribution shows signs of very sharp shocks. For the larger amplitude motion, the shocks get "smeared" out. Physically, this is because the shocks oscillate, and when temporally averaged, the shocks appear smeared. Of course, when viewed at any instant in time, the shocks are sharp. Also shown are the real and imaginary parts of the first harmonic of the unsteady pressure. In the small-amplitude case, very large and narrow peaks of pressure are seen. These are the so-called "shock impulses" associated with the unsteady motion of the shock. As the amplitude of the pitching vibration is increased, these peaks are reduced and spread out, because the shock motion is larger and the resulting shock impulse is spread over a larger chordwise extent.

By appropriate integration of the first harmonic of the unsteady pressure distribution, one can obtain the first harmonic of the pitching moment. The imaginary part determines the aeroelastic stability of the rotor. In the absence of mechanical damping, the rotor is stable only if the imaginary moment is less than zero for all interblade phase angles. Shown in Fig. 14 is the pitching moment as a function of interblade phase angle for several pitching amplitudes. For small amplitude motions, the rotor is unstable for interblade phase angles σ between $-10°$ and $+60°$. Thus, the

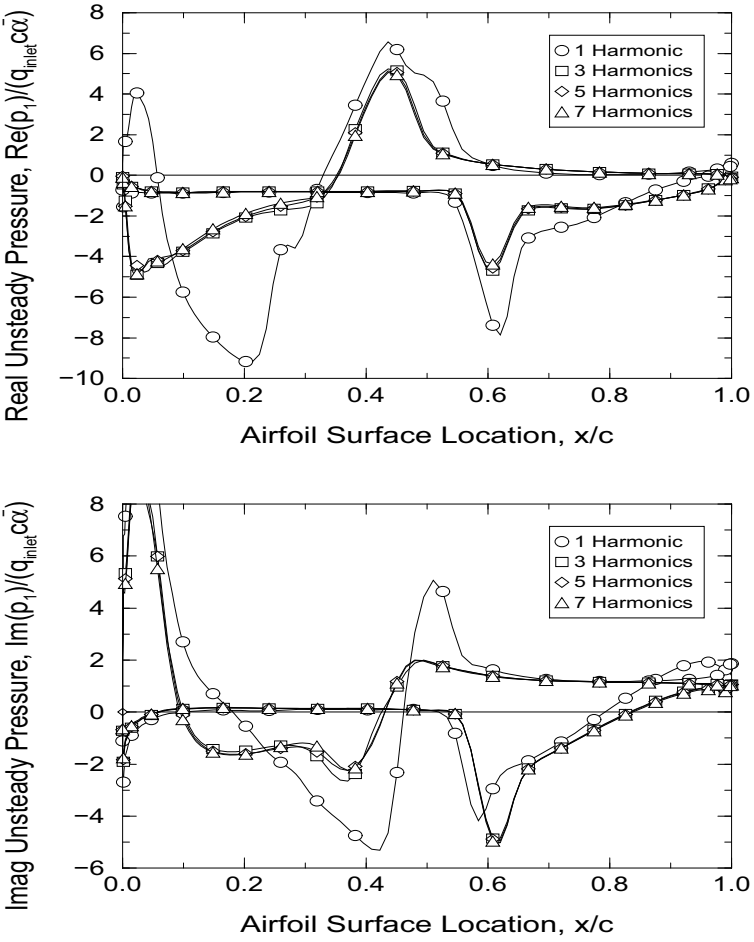

Fig. 12 First harmonic of unsteady pressure distribution for front stage compressor rotor airfoils vibrating in pitch with $\overline{\omega} = 1.0$, $\sigma = 30°$, and $\overline{\alpha} = 1.0°$. After Hall, Thomas, and Clark [32]

amplitude of an initially infinitesimal motion will grow. As the motion grows, however, the aerodynamic damping of the least stable interblade phase angle goes to zero. This is seen more clearly in Fig. 15. Shown is the pitching moment for $\sigma = +30°$ as a function of pitch amplitude computed using one, three, five and seven harmonics. Clearly, the solution computed with just one harmonic is not converged (except at very small amplitudes), and gives erroneous results. However, with three or five harmonics, the solution is converged to engineering accuracy. Note that the imaginary moment is positive (unstable) for small amplitude motions, but goes to zero at a pitching amplitude of about 0.7°. Thus, the blade will vibrate in a stable limit cycle with with this pitch amplitude. It is also remarkable that the nonlinear fluid dynamics effects are important at such a small geometric displacement.

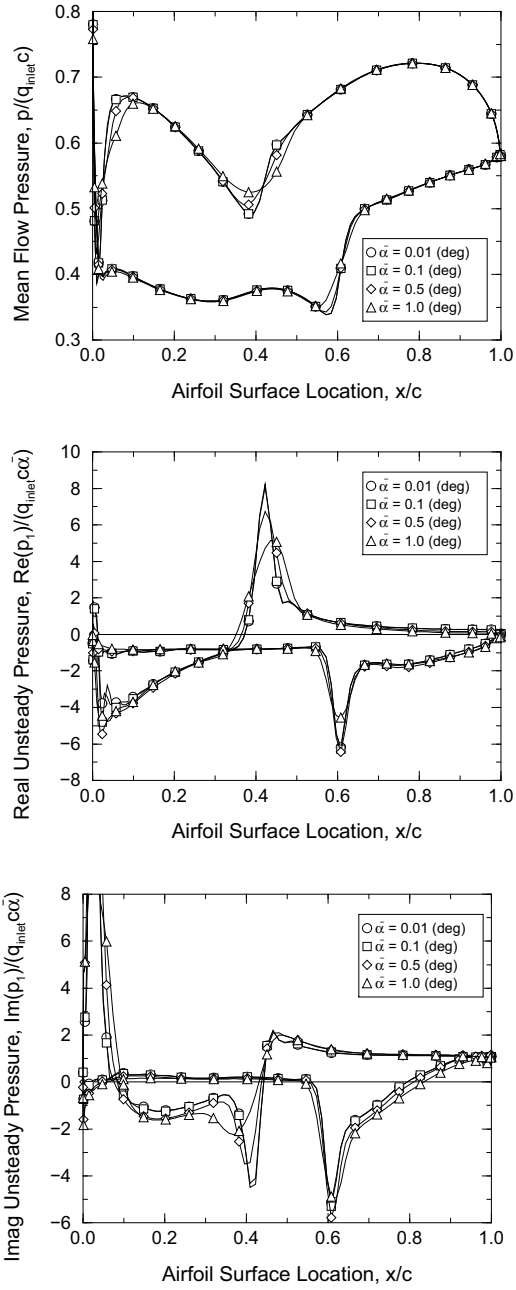

Fig. 13 Unsteady pressure distribution for front stage compressor rotor airfoils vibrating in pitch with $\overline{\omega} = 1.0$ and $\sigma = 30°$. Top: zeroth harmonic. Middle and bottom: first harmonic. After Hall, Thomas, and Clark [32]

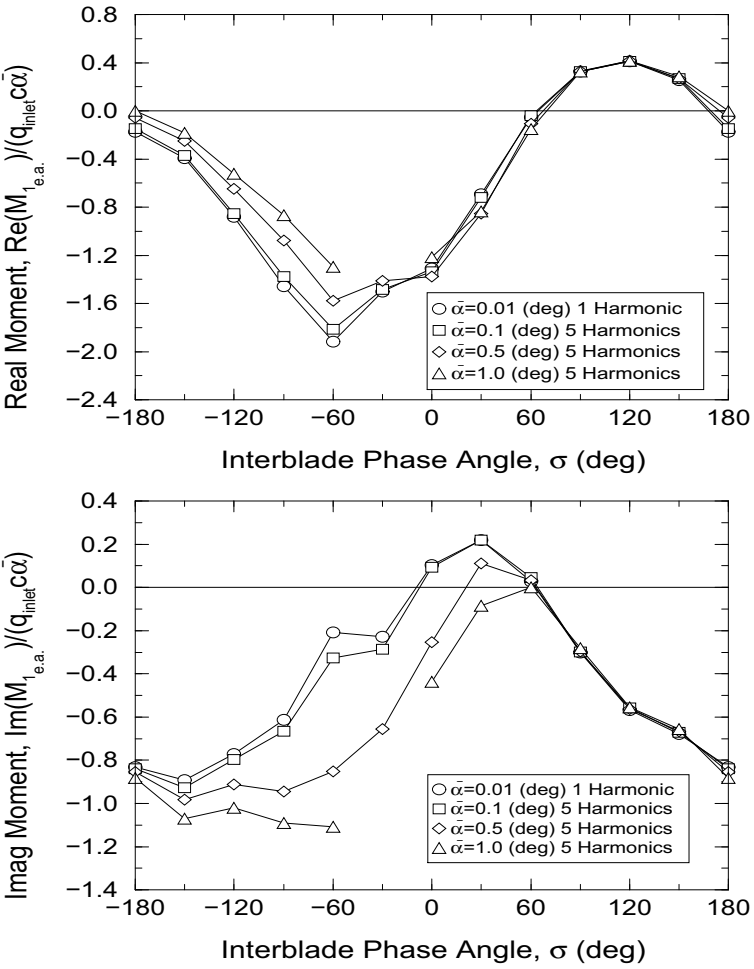

Fig. 14 First harmonic of unsteady pitching moment for front stage compressor rotor airfoils vibrating in pitch with $\bar{\omega} = 1.0$. After Hall, Thomas, and Clark [32]

We next consider the computational efficiency of the present method. Shown in Fig. 16 are the convergence histories for the steady flow and harmonic balance calculations. Note that except for $N = 7$, the steady flow solver and harmonic balance flow solver converge in about the same number of iterations. For the $N = 7$ case, the harmonic balance solution does not converge. Fortunately, we have found that three to five harmonics are more than adequate to obtain mode converged solutions of the zeroth and first harmonic components of the unsteady flow, and the harmonic balance solver usually converges for this number of harmonics.

Finally, the CPU time per iteration of the harmonic balance flow solver for one, three, five, and seven harmonics was found to be 2.15, 4.62, 7.45, and 10.29 times

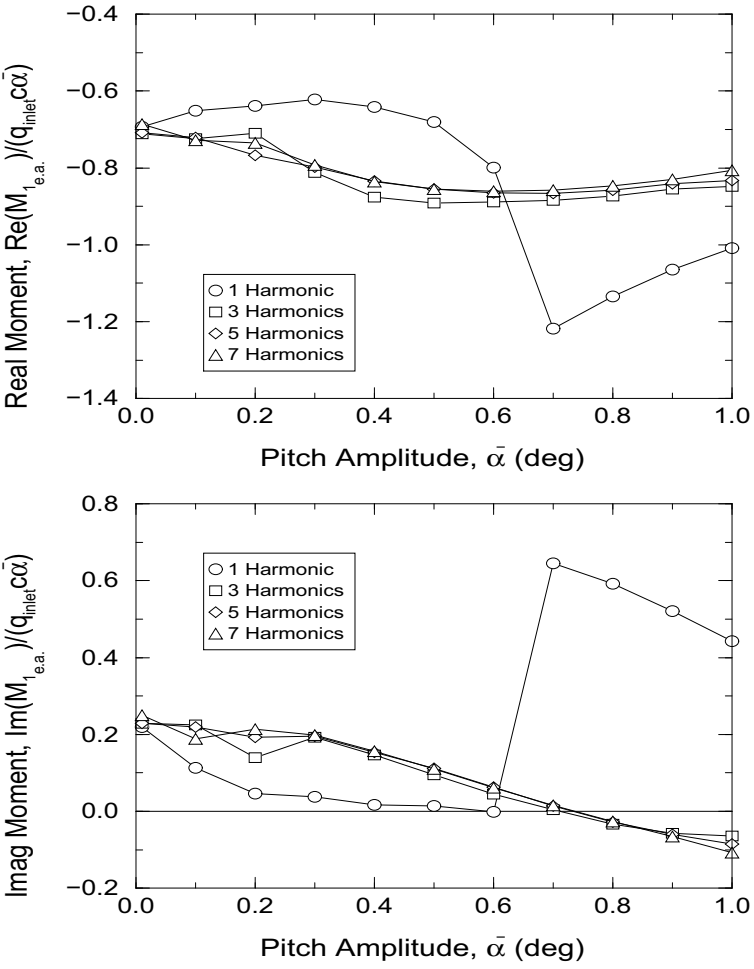

Fig. 15 First harmonic of unsteady pitching moment for front stage compressor rotor airfoils vibrating in pitch with $\sigma = 30°$. After Hall, Thomas, and Clark [32]

the cost per iteration of the steady flow solver. Even using seven harmonics, the cost to compute the fully nonlinear, viscous, transonic flow about a vibrating blade row is only about ten times the cost of a comparable steady flow calculation.

The instability found in the example shown in Fig. 16 merits further discussion. The computational scheme used to compute the solution in this case used an explicit Lax–Wendroff scheme. For a conventional time-marching analysis, the Lax–Wendroff scheme is stable for CFL numbers less than some finite number. In one-dimensional inviscid problems, for example, the CFL number on a cartesian grid is defines as

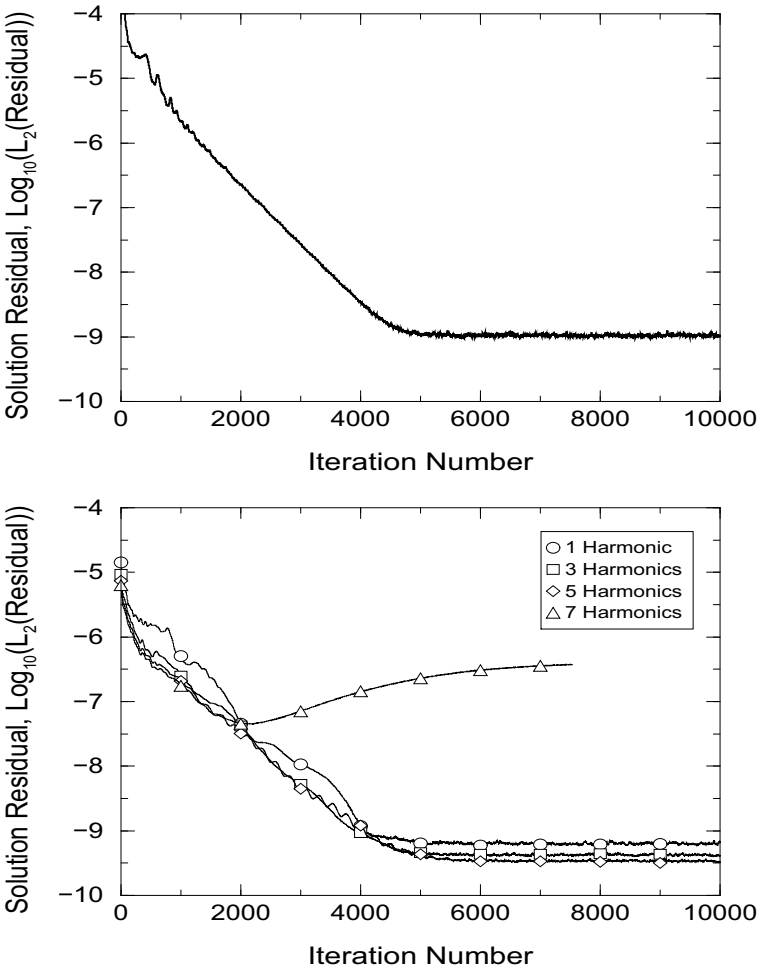

Fig. 16 Convergence history for steady flow solver (top) and harmonic balance flow solver (bottom) with $\sigma = 30°$, $\overline{\omega} = 1.0$, and $\overline{\alpha} = 1.0°$. After Hall, Thomas, and Clark [32]

$$C = \left(\frac{|u_{\max}|}{\Delta x} \right) \Delta t \tag{3.13}$$

where $|u_{\max}|$ is the largest characteristic speed of the flow. For a conventional time-domain analysis, one finds that the Lax–Wendroff scheme is stable so long as $C \leq 1$. For CFL numbers greater than unity, the unstable modes are short wavelength "sawtooth" modes.

For the harmonic balance analysis, however, the source term $\mathbf{S}^*$ in Eq. (3.12) renders the Lax–Wendroff scheme *unconditionally unstable* on very large grids, and conditionally stable on grids of finite extent. A Fourier stability analysis (which is

valid on large grids) shows that the unstable modes for the harmonic balance method are *long* wavelength modes, and the boundary conditions help stabilize the scheme.

In general, the stability computational schemes applied to the harmonic balance equations depends on *two* non-dimensional numbers, the CFL number and the grid reduced frequency, defined by

$$\overline{\omega} = \frac{N\omega\Delta x}{|u_{\min}|} \tag{3.14}$$

where $|u_{\min}|$ is the smallest characteristic speed. Large values of $\overline{\omega}$ tend to make explicit schemes unstable, even with the stabilizing influence of boundary conditions, which explains the non-convergence seen in Fig. 16 for the $N = 7$ case. More recently, a number of researchers have developed implicit schemes to improve the stability of the method [35–38].

4 Conclusions

Frequency domain techniques for computing unsteady flows in turbomachinery have evolved considerably over the past several decades. These techniques are capable of computing both small-disturbance unsteady flows (using the time-linearized approach) and large amplitude flows (using the harmonic balance approach). In addition, the frequency domain approaches have been applied to the difficult but important problem of computing unsteady flows in multistage machines. In all cases, the frequency domain solvers have a number of distinct advantages over their time-domain equivalents. Using complex periodicity conditions, the computational domain can be reduced to a single blade passage (in each row). Furthermore, using the pseudo time marching technique, the governing Euler and Navier–Stokes equations can be solved using steady-state acceleration techniques such as local time stepping and multigrid acceleration. The result is that computing these very complex unsteady flows in turbomachinery—and other problems involving temporally and spatially periodic flows—is only modestly more expensive than solving a steady flow problem.

References

1. Kielb RE, Barter JW, Thomas JP, Hall KC (2003) Blade excitation by aerodynamic instabilities a compressor blade study. ASME Paper GT-2003-38634
2. Ni R, Sisto F (1976) Numerical computation of nonstationary aerodynamics of flat plate cascades in compressible flow. Trans ASME J Eng Power 98:165–170
3. Hall KC, Crawley EF (1989) Calculation of unsteady flows in turbomachinery using the linearized Euler equations. AIAA J 27(6):777–787
4. Clark W (1992) Prediction of unsteady flows in turbomachinery using the linearized Euler equations on deforming grids. Masters thesis, Duke University

5. Holmes DG, Chuang HA (1993) 2D linearized harmonic Euler flow analysis for flutter and forced response. In: Atassi HM (ed) Unsteady aerodynamics, aeroacoustics, and aeroelasticity of turbomachines and propellers. Springer, New York
6. Kahl G, Klose A (1993) Time linearized euler calculations for unsteady quasi-3D cascade flows. In: Atassi HM (ed) Unsteady aerodynamics, aeroacoustics, and aeroelasticity of turbomachines and propellers. Springer, New York
7. Hall KC, Clark WS (1993) Linearized Euler prediction of unsteady aerodynamic loads in cascades. AIAA J 31(3):540–550
8. Hall KC, Clark WS, Lorence CB (1994) A linearized Euler analysis of unsteady transonic flows in turbomachinery. J Turbomach 116:477–488
9. Lorence CB (1991) An investigation of three-dimensional unsteady flows in turbomachinery using the linearized Euler equations. Masters thesis, Duke University
10. Hall KC, Lorence CB (1993) Calculation of three-dimensional unsteady flows in turbomachinery using the linearized harmonic Euler equations. J Turbomach 115(4):800–809
11. Holmes D, Mitchell B, Lorence CB (1997) Three-dimensional linearized Navier-Stokes calculations for flutter and forced response. Presented at the 8th international symposium on unsteady aerodynamics, aeroacoustics, and aeroelasticity of turbomachines and propellers, Stockholm, Sweden
12. Clark W (1998) Investigation of unsteady viscous flows in turbomachinery using a linearized Navier-Stokes analysis. Ph.D. thesis, Duke University
13. ClarkWS Hall KC (2000) A time-linearized Navier-Stokes analysis of stall flutter. J Turbomach 122:467–476
14. Lindquist DR, Giles MB (1994) On the validity of linearized Euler equations with shock capturing. AIAA J 32:46–53
15. Bolcs A, Fransson TH (1986) Aeroelasticity in turbomachines. Comparison of theoretical and experimental results. Technical Report AFOSR-TR-87-0605, Air Force Office of Scientific Research, Washington
16. Fransson TH, Verdon JM (1993) Panel discussion on standard configurations for unsteady flow through vibrating axial-flow turbomachine cascades. In: Atassi HM (ed) Unsteady aerodynamics, aeroacoustics, and aeroelasticity of turbomachines and propellers. Springer, New York
17. Huff DL, Swafford TW, Reddy TSR (1991) Euler flow predictions for an oscillating cascade using a high resolution wave-split scheme. ASME Paper 91-GT-198
18. Spalart P, Allmaras S (1994) A one-equation turbulence model for aerodynamics flows. La Recherche Aerospatiale 1:5–21
19. Smelova NV (2000) Calculation of three-dimensional unsteady multistage flows in turbomachinery. Ph.D. thesis, Duke University, Durham, NC 27708
20. Silkowski PD, Hall KC (1998) A coupled mode analysis of unsteady multistage flows in turbomachinery. J Turbomach 120(3):410–421
21. Hall KC, Silkowski PD (1997) The influence of neighboring blade rows on the unsteady aerodynamic response of cascades. J Turbomach 119(1):83–95
22. Silkowski PD (1996) A coupled mode method for multistage aeroelastic and aeroacoustic analysis of turbomachinery. Ph.D. thesis, Duke University, Durham
23. Ekici K, Hall KC (2007) Nonlinear analysis of unsteady flows in multistage turbomachines using harmonic balance. AIAA J 45(5):1047–1057
24. Gopinath A, Van Der Weide E, Alonso J, Jameson A, Ekici K, Hall KC (2007) Three-dimensional unsteady multi-stage turbomachinery simulations using the harmonic balance technique, In 45th AIAA aerospace sciences meeting and exhibit, January, p 892
25. Giles MB (1992) An approach for multi-stage calculations incorporating unsteadiness. ASME Paper 92-GT-282
26. Ning W, He L (1998) Computation of unsteady flows around oscillating blades using linear and non-linear harmonic Euler methods. J Turbomach 120(3):508–514
27. He L, Ning W (1998) Efficient approach for analysis of unsteady viscous flows in turbomachines. AIAA J 36(11):2005–2012

28. Vasanthakumar P, Chen T, He L (2000) Three-dimensional viscous computation of blade flutter and forced response using nonlinear harmonic approach
29. Chen T, Vasanthakumar P, He L (2001) Analysis of unsteady bladerow interaction using nonlinear harmonic approach. AIAA J Power Propul 17(3):651–658
30. McMullen M, Jameson A, Alonso JJ (2001) Acceleration of convergence to period steady state in turbomachinery flows. AIAA Paper 2001–0152
31. McMullen M, Jameson A, Alonso JJ (2002) Application of a non-linear frequency domain solver to the Euler and Navier-Stokes equations. AIAA Paper 2001–0120
32. Hall KC, Thomas JP, Clark WS (2002) Computation of unsteady nonlinear flows in cascades using a harmonic balance technique. AIAA J 40(5):879–886
33. Thomas JP, Dowell EH, Hall KC (2002) Nonlinear inviscid aerodynamic effects on transonic divergence, flutter and limit cycle oscillations. AIAA J 40(4):638–646
34. Hall KC, Thomas JP, Ekici K, Voytovich DM (2003) Frequency domain techniques for complex and nonlinear flows in turbomachinery. AIAA paper 2003–3998
35. Sicot F, Puigt G, Montagnac M (2008) Block-Jacobi implicit algorithms for the time Spectral method. AIAA J 46(12):3080–3089
36. Woodgate MA, Badcock KJ (2009) Implicit harmonic balance solver for transonic flow with forced motions. AIAA J 47(4):893–901
37. Su X, Yuan X (2009) Implicit solution of time spectral method for periodic unsteady flows. Int J Numer Methods Fluids 63:860–870
38. Thomas JP, Custer CH, Dowell EH, Hall KC, Corre C (2013) Compact implementation strategy for a harmonic balance method within implicit flow solvers. AIAA J 51(6):1374–1381

Some Recent Advances in Nonlinear Aeroelasticity

Earl H. Dowell

Abstract This brings the discussion of nonlinear aeroelasticity up to date. See the earlier discussion in Chap. 11. Much of the recent advances are based on new understanding of such subjects as limit cycle oscillations due to structural non-linearities, including freeplay, and fluid nonlinearities associated with unsteady separated flow including self excited flow oscillations variously called buffet or non-synchronous vibration.

As the reader now knows, aeroelasticity is the field that examines, models and seeks to understand the interaction of the forces from an aerodynamic flow and the deformation of an elastic structure. The forces produce deformation, but the structural deformation in turn changes the aerodynamic forces. This feedback between force and deformation leads to a variety of dynamic responses of the fluid and the structure including flutter (a Hopf bifurcation), limit cycle oscillations and sometimes chaos. Selected recent advances in nonlinear aeroelasticity and fluid-structure interaction are reviewed to identify and model the fundamental elements that they share. Topics discussed include the following. following.[1]

- Transonic and Subsonic Panel Flutter
- Freeplay Induced Flutter and Limit Cycle Oscillations (LCO)
- Reduced Order Modeling (ROM) of Unsteady Aerodynamics
- Eigenmodes and POD Modes
- High Dimensional Harmonic Balance (HDHB)
- Nonlinear ROM based upon POD and HDHB
- Transonic Flutter and LCO of Lifting Surfaces
- Flight Experience
- Efficient and Accurate Computation of Aerodynamic Forces
- Experimental/Theoretical Correlations
- Aerodynamic LCO: Buffet, Abrupt Wing Stall and Non-Synchronous Vibration

[1] This chapter is based upo a AIAA SDM lecture given in 2010.

E. H. Dowell (✉)
Mechanical Engineering and Materials Science Duke University, Durham, NC, USA
e-mail: earl.dowell@duke.edu

E. H. Dowell (ed.), *A Modern Course in Aeroelasticity*, Solid Mechanics and Its Applications 264, https://doi.org/10.1007/978-3-030-74236-2_14

1 Introduction

Some twenty plus years ago I had the pleasure of giving the SDM lecture in Mobile, Alabama and am happy to have the opportunity to do so again here in Orlando. When asked to give this SDM lecture, I mentioned my previous experience and suggested that being asked to do so again might be considered double jeopardy. But I was assured that no one would remember my earlier talk! However, I do recall that twenty years ago a then radical idea was discussed in the lecture, i.e. that one could use the eigenmodes of an aerodynamic flow to construct a modal model of the flow much as has been done for many years for structures. Whether that suggestion inspired anyone other than our group at Duke, I cannot be sure. But in any event, reduced order modeling of flow fields and their interaction with structural response is today a flourishing topic. Indeed reduced order modeling is now pervasive in many fields of engineering and science, no doubt having been discovered and rediscovered many times by many investigators. And the topic has been generalized in at least three significant ways that I will discuss in this lecture. Given the title of this lecture you will not be surprised that one of the generalizations is to treat the *nonlinear as well as linear dynamics of aeroelastic or fluid-structural systems*. Thus the major theme of this talk is the modeling of nonlinear aeroelastic systems both mathematically and computationally as well as experimentally.

2 Motivation and Goals

The motives for pursuing research and developing methods that are useful in practice are many. But to provide a context and rationale for much of the work to be described in this lecture, perhaps a few words about goals will be helpful.

When my contemporaries and I first began the study and practice of aeroelasticity, and for a number of years thereafter, any difference between theory and experiment of design and reality was often attributed to nonlinear effects. However, it was generally understood that trying to model such *nonlinear effects* was not to be expected or attempted. Since then many studies of nonlinear effects have been undertaken and today the subject is treated in review articles [1–4] and indeed in textbooks [5, 6]. An engineer today no longer has the luxury of simply ignoring such effects and one of my predictions is that some years from now an SDM Lecturer will be discussing the favorable effects that can be created by a judicious analysis and design of nonlinearities in aeroelastic systems. Of course there are unfavorable and indeed potentially catastrophic consequences of nonlinearities in aeroelastic systems as well, as is also the case when an aeroelastic system is analyzed and designed with linear models.

The motivation for *reduced order modeling* is much the same for fluid systems as for structural systems. In either case, a relative small number of modes is often (but not always!) sufficient to describe the dynamics of a structural or fluid system. In

the case of a structure an initial mathematical/computational model may consist of a finite element representation with several thousand degrees of freedom while for a computational fluid dynamics (CFD) model there may be millions of degrees of freedom. If one can use say one hundred modes or less to describe the structure or the fluid, then clearly there is a great potential for savings in the cost of the computation. Indeed at any given point in time of the state of the art in computer hardware and software, there will be computations that are only feasible if one uses a reduced order model.

But here it is worth noting that another very important advantage of reduced order models is the greater physical insight they may give to the investigator. While a dynamical system with one hundred degrees of freedom or less may be still one of considerable complexity, it pales in complexity compared to a system with thousands not to mention millions of degrees of freedom. Moreover it is often the case that the response of the aeroelastic system is governed by an even smaller number of modes than the structural or fluid system individually. This is because the fluid and structural modes of greatest interest will be those that match most closely in both the spatial (wavelength) and temporal (frequency) domains. In the field of acoustics this matching of frequency and wavelength is called "coincidence". Lest one think this means that reduced order models may be smaller than in fact they reasonably can be, it is well to point out two important facts. First, it cannot always be anticipated which fluid and structural modes will be most important for an aeroelastic system and thus more modes must be retained than would otherwise be the case (once the most dominant aeroelastic modes are determined!). Secondly, if one wishes to control or modify the aeroelastic system, some of the fluid, structural, and/or aeroelastic or coupled fluid-structural modes that may not have been important before can now become important. Therefore and again, more modes must be retained as control of the system is considered.

It is sometimes said that the use of modes is only possible for a linear system. It is now widely, though not universally, appreciated that modes can be used for nonlinear systems as well. Having said that, for linear systems the use of eigenmodes is almost always the preferred choice for constructing a reduced order model. But for nonlinear systems other choices of modes may be preferred, e.g. the modes that can be constructed from Proper Orthogonal Decomposition, so called POD modes. These modes have been used very successfully by Dowell and colleagues at Duke, Beran and colleagues at the Air Force Research Laboratory (AFRL) and by Farhat and colleagues at Stanford.

Finally, one can think of modes as a form of generalized Fourier series in the spatial domain. Therefore it is perhaps not surprising that a Fourier Series in time can also be very useful if the temporal response is periodic. As was the case for eigenmodes versus POD modes for the representation of the spatial domain of nonlinear systems, for nonlinear systems a standard Fourier Series or classical Harmonic Balance method may not be the best choice for describing the temporal response. The Higher Order Harmonic Balance method developed by Hall and his colleagues at Duke has proven to be a very effective method and it has now also been adopted and exploited by Jameson and colleagues at Stanford and Badcock and colleagues

at Liverpool. A related method has also been developed by Beran and colleagues at AFRL.

The remainder of the chapter is organized as follows. In Sect. 3. A transonic panel flutter and the effect of a viscous boundary layer is treated, in Sect. 3. B the structural nonlinearity of freeplay and its effect on flutter and limit cycle oscillations (LCO) is discussed, in Sect. 3. C reduced order modeling is summarized, in Sect. 4 transonic flutter and LCO of lifting surfaces is reviewed and, finally, in Sect. 5 aerodynamic limit cycle oscillations are discussed, e.g. buffet, abrupt wing stall and non-synchronous vibration. The present discussion is not meant to be exhaustive of the study of either nonlinear aeroelasticity or the reduced order modeling. For example, the nonlinear aeroelasticity of very high aspect ratio, flexible wings is not treated here (for an introduction to that topic, see [2]) or the use of Volterra series for reduced order modeling (for an introduction to that topic see [4]). Also rotorcraft and turbomachinery aeroelasticity, morphing aircraft and other important topics are not treated here, but are nonetheless active areas of research as seen in papers in the literature. The topics that have been chosen for this chapter are representative of the active and productive work underway and are those for which the present authors can claim some personal experience.

3 Current Examples of Recent Advances

3.1 Transonic and Subsonic Panel Flutter

Although the vast majority of the literature on panel flutter analysis is devoted to high supersonic/hypersonic flow, many of the flutter incidents in practice have occurred in the low supersonic/transonic Mach number regime. A recent paper by Hashimoto, Aoyama and Nakamura [7] provides new insight into the importance of a viscous fluid boundary layer on the transonic flutter boundary. Previous work by Dowell [8] had shown this effect as well. But whereas Dowell used what is sometimes called a shear flow model that dates back to work of Lighthill and others, the more recent work of Hashimoto et al. uses a modern CFD code that solves the Navier-Stokes equations within the framework of a Reynolds Averaged Navier-Stokes model. The shear flow model by contrast uses a mean flow that represents the boundary layer, but neglects the viscosity in the small perturbation equations of the fluid that arise from the panel oscillation. The more rigorous fluid model shows improved agreement with the excellent experiments of Muhlstein, Gaspers and Riddle [9].

Figure 1 is a schematic of the panel and flow geometry. Figure 2 shows the comparison between theory and experiment where the experimental data have been extrapolated to zero boundary layer thickness, $\delta/a = 0$, where δ is the boundary layer thickness and a is the panel length. The theoretical results from Dowell are for transonic potential flow and those from Hashimoto et al. are for inviscid Euler flow. The plot is of a non-dimensional dynamic pressure versus Mach number. The good

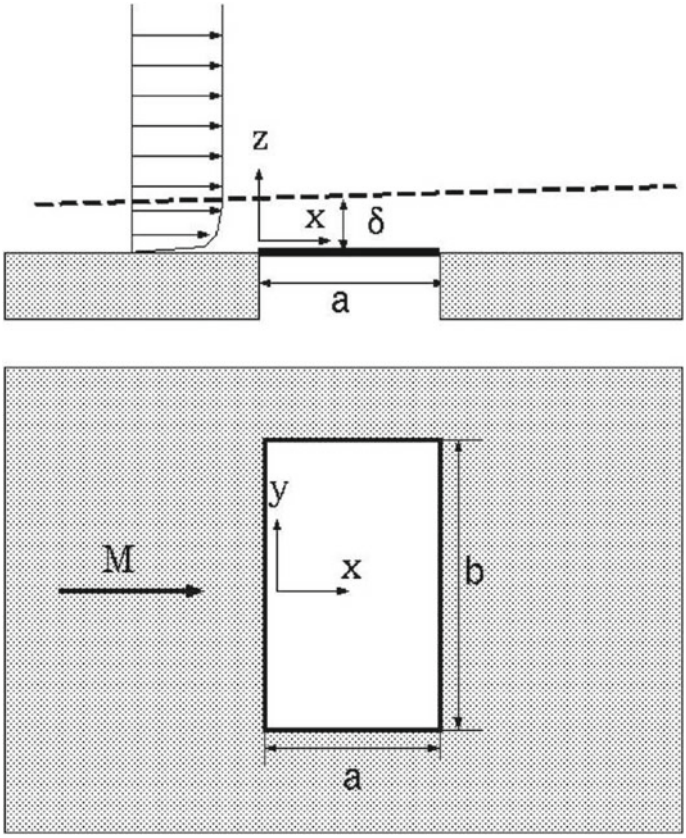

Fig. 1 Schematics of panel flutter problem

agreement among all results is encouraging. Turning now to the case for a boundary layer thickness of $\delta/a = 0.1$, a similar comparison is shown in Fig. 3. Note that the flutter boundary predicted by theory and that determined experimentally has been very substantially changed from that for $\delta/a = 0$, especially in the lower Mach number range. The dynamic pressure for flutter at $M = 1.1$ has been increased by a factor of 2–3 due to the viscous boundary layer. While the shear flow model used by Dowell is a substantial improvement over an inviscid analysis that neglects the boundary layer effect, the RANS flow model of Hashimoto et al. is a notable further improvement and agrees better with experiment.

Moreover, as Hashimoto et al. note this is an excellent test case for new developments in CFD methodology for aeroelastic analysis in general and gives considerable confidence in the basic theory. They have also shown that in this particular case the results are not sensitive to the empirical turbulence model used in the RANS flow model.

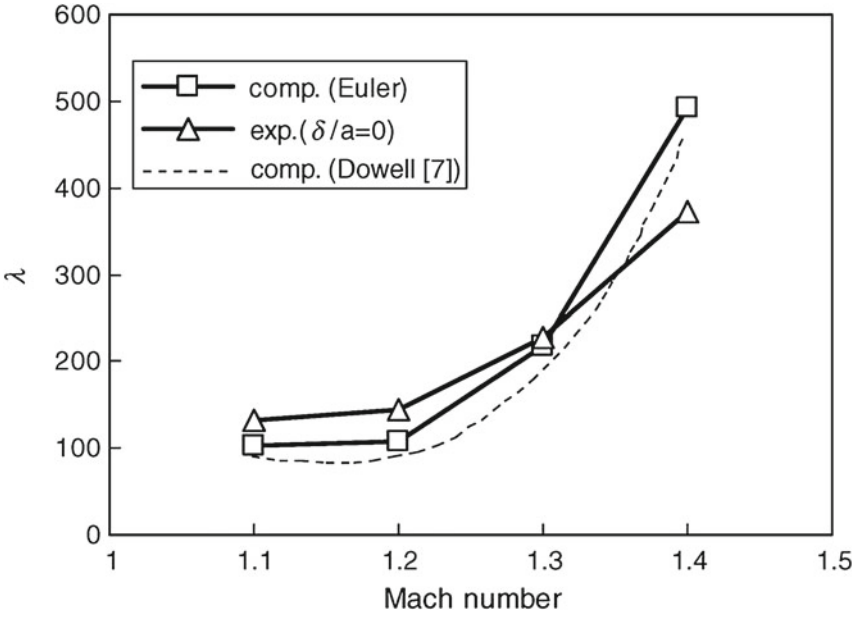

Fig. 2 Flutter boundary (Inviscid Case)

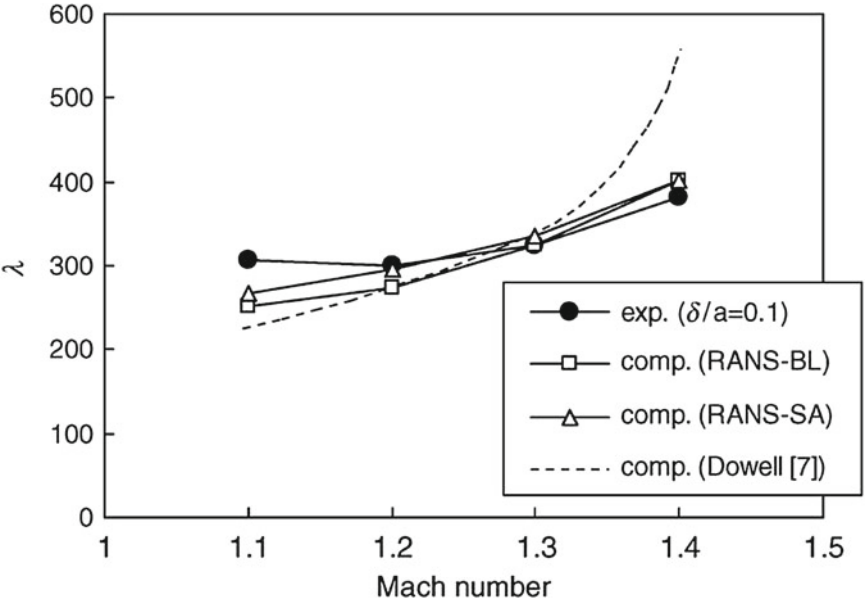

Fig. 3 Flutter boundary (Viscous Case)

While subsonic panel flutter is unusual in aerospace applications it has been known for many years that panel flutter may occur at subsonic conditions under some circumstances [10]. Most notably if the trailing edge of the panel is free, then flutter will occur in subsonic flow. But, if the trailing edge, as well as the leading edge, of the panel is fixed then divergence (a static aeroelastic instability) will occur rather than flutter. Panel divergence is a form of aeroelastic buckling and, when the panel is in a buckled state, then oscillations in the flow due for example to engine or boundary layer noise may cause a buckled panel to "oil can" from one buckled state to another. This is sometimes referred to as "dynamic buckling" [10]. In experiments as well as in nonlinear numerical simulations it may be difficult to distinguish between limit cycle oscillations due to flutter and oil canning due to dynamic buckling.

The classical example of subsonic panel flutter was described in the paper by Dugundji and colleagues [11] who considered a panel on an elastic foundation that can lead to a form of traveling wave flutter. Here recent work on subsonic flutter is emphasized. See [12, 13]. The work of Tang, Yamamoto and Dowell [12] is for a panel clamped at its leading edge, but free on both side edges and, most importantly, free on its trailing edge. Both theoretical and experimental work has been done and the agreement between theory and experiment is very good for the prediction of flutter flow velocity and frequency. However, in the experiments, hysteresis is observed that this is not predicted by the theory which includes a nonlinear structural model and a nonlinear vortex lattice aerodynamic model [12, 13]. Moreover the amplitude of the limit cycle oscillation (LCO) that is observed in the experiment after the onset of flutter and indeed at lower flow velocities due to hysteresis is some two to three times greater than that predicted by the theoretical model. Currently the most plausible hypothesis for the differences between theory and experiment is that vortex shedding and flow separation may occur at the large amplitudes of the LCO. These effects are not included in the vortex lattice aerodynamic model, but would be included in a viscous flow model based upon the Navier-Stokes equations.

Because the LCO amplitudes are on the order of the panel chord (LCO amplitudes of panels which are fixed on two opposing edges are typically much smaller and on the order of the panel thickness [11]), Tang, Paidoussis and Jiang [13] have suggested such a LCO is a prime candidate for energy harvesting. And they have analyzed this configuration inter alia using a similar theoretical model and obtained similar results.

Figure 4 shows a stroboscopic picture of the panel in LCO during a wind tunnel test [12]. Note the amplitude of the LCO relative to the panel chord.

This configuration is also an example of what is sometimes referred to as "flag flutter", but here the bending stiffness of the panel is dominant over the tension/membrane stiffness of the panel where the latter might be induced by gravity or shear stresses produced by a viscous flow. So this is a rather stiff "flag". Current applications to micro airvehicles and coverings for gaps in conventional wing/control surfaces during landing may give rise to renewed interest in subsonic panel flutter for panels and/or thin membranes where both the bending stiffness and membrane stiffness may be important.

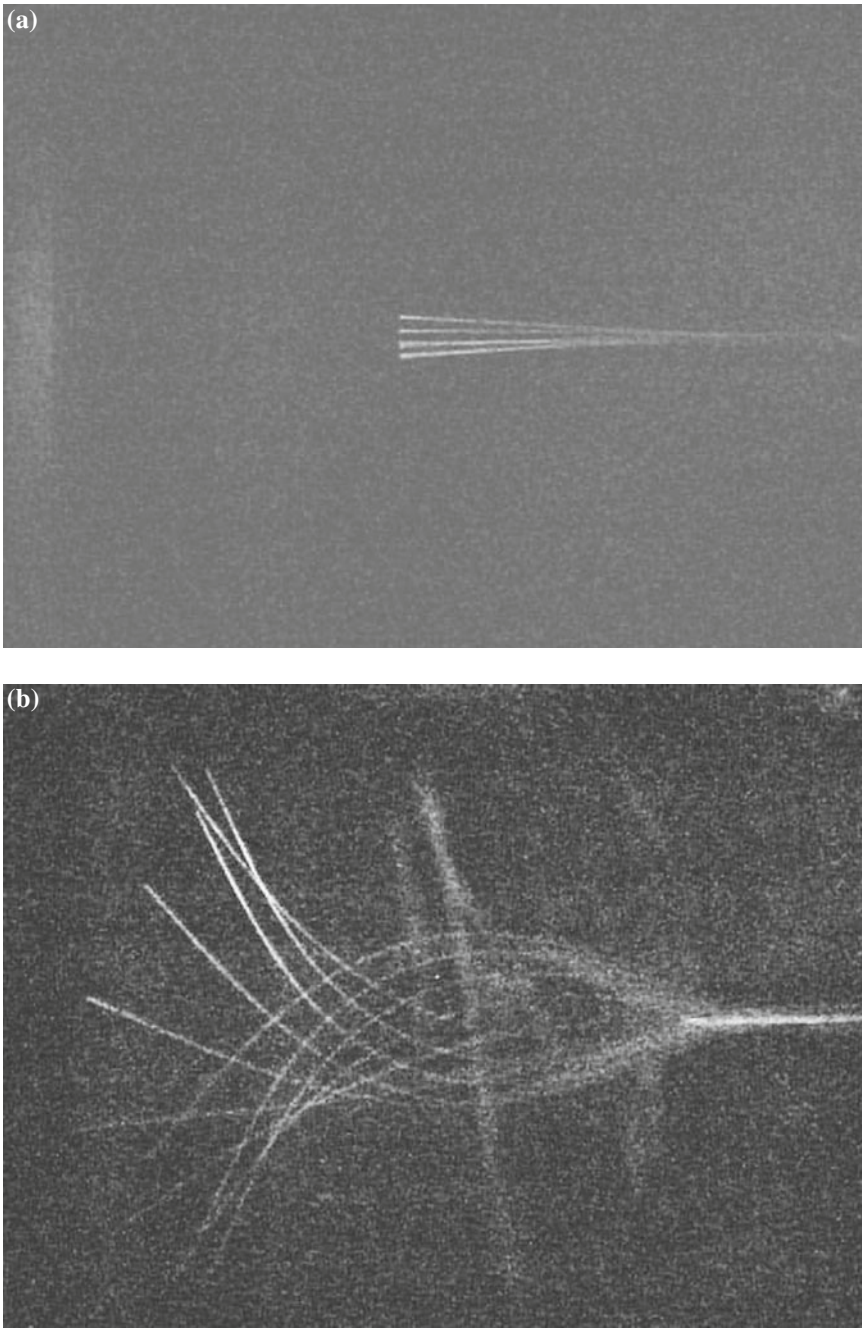

Fig. 4 **a** Flutter oscillations of an elastic panel with a clamped leading edge and all other edges free. Subsonic flow is from right to left for a small amplitude. **b** For a large amplitude

3.2 *Freeplay Induced Flutter and Limit Cycle Oscillations*

Freeplay is a concern with respect to control surface attachments, but it has also been suggested as a possible source of flutter and limit cycle oscillations in wing/store attachments. The latter is still an open area of investigation, but recent progress for freeplay in control surfaces offers an opportunity to enhance both analysis and design methods and may lead to a paradigm shift in design criteria.

Here a brief review of history is provided, the results of recent advances in understanding based upon computations and wind tunnel testing are summarized and the current design criteria and the data on which they are based are reinterpreted in light of recent advances.

Figure 5 is taken from one of a series of early reports [14] on the effect of freeplay on control surface flutter and limit cycle oscillations (LCO) conducted at the Wright Air Development Center, the predecessor to the Air Force Research Laboratory. It is plot of the putative flutter velocity versus the total angular freeplay in an all movable control surface. The relevant conclusions drawn at that time from these data were the following.

> The test data also show the variation in flutter speed as a function of free-play....

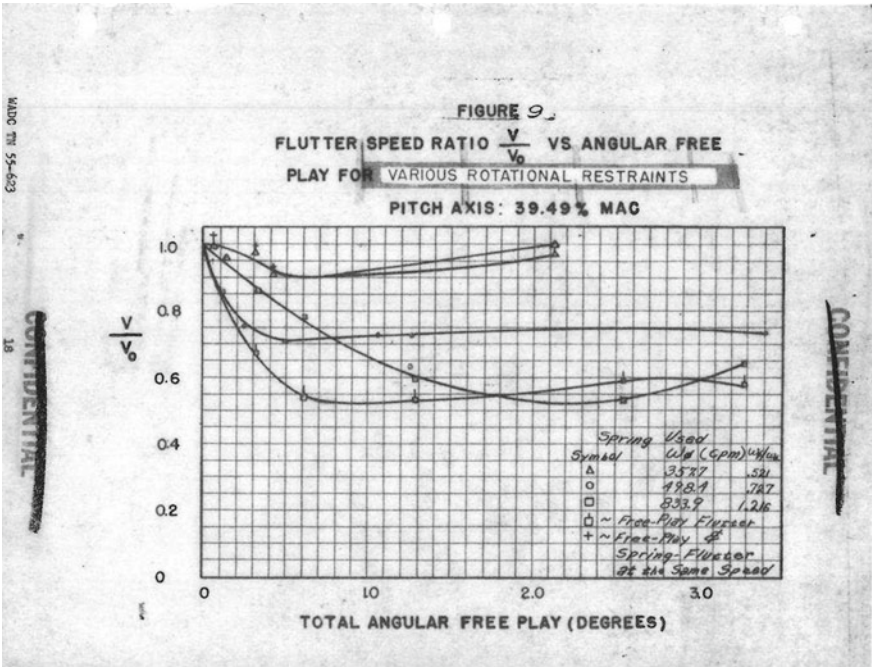

Fig. 5 Flutter velocity versus freeplay

Fig. 6 Photograph of the experimental model with gust generator in the wind tunnel test

> Free-play in all movable controls should be limited to + or −1/64° unless it can be shown by means of experimental flutter model data that reasonable deviations from this free-play limit can be tolerated for the particular all-movable control design being considered.

This limit of + or −1/64° remains today more than fifty years later as the basic design criterion to preclude freeplay induced flutter (and limit cycle oscillations).

Recent computational and experimental work [15–18] has shed new light on these earlier results. It is now understood that in fact, for an unloaded control surface, the flow velocity at which limit cycle oscillations (LCO) begins is independent of the degree of freeplay. Note that even in Fig. 5 the early tests concluded that the flutter velocity was independent of the freeplay angle as this angle became large.

However, it is now known that the amplitude of the LCO and the amount of loading required to preclude LCO is strongly dependent on the degree of freeplay. In fact the LCO amplitude scales in proportion to the degree of freeplay and the amount of loading required to suppress flutter/LCO does as well. For example, the LCO amplitude will be of the order of the degree of freeplay and if the loading is due to placing the airfoil at an angle of attack, the angle of attack required to totally eliminate freeplay is about five times the degree of freeplay. Thus for a freeplay of 1/64° the LCO amplitude will be about 1/64° and an angle of attack of 5/64° is sufficient to suppress the LCO altogether. This then likely explains the apparent variation of the flutter speed with freeplay angle shown in Fig. 5 from the earlier tests. For small freeplay angles, it is likely the LCO amplitude was undetectable and/or unavoidable small amounts of angle of attack were sufficient to load the wing so that LCO was suppressed.

More recent investigations by Tang and Dowell [15, 16], Lee et al. [17] and Schlomach [18] have confirmed the effect of freeplay and loading on LCO. Figures

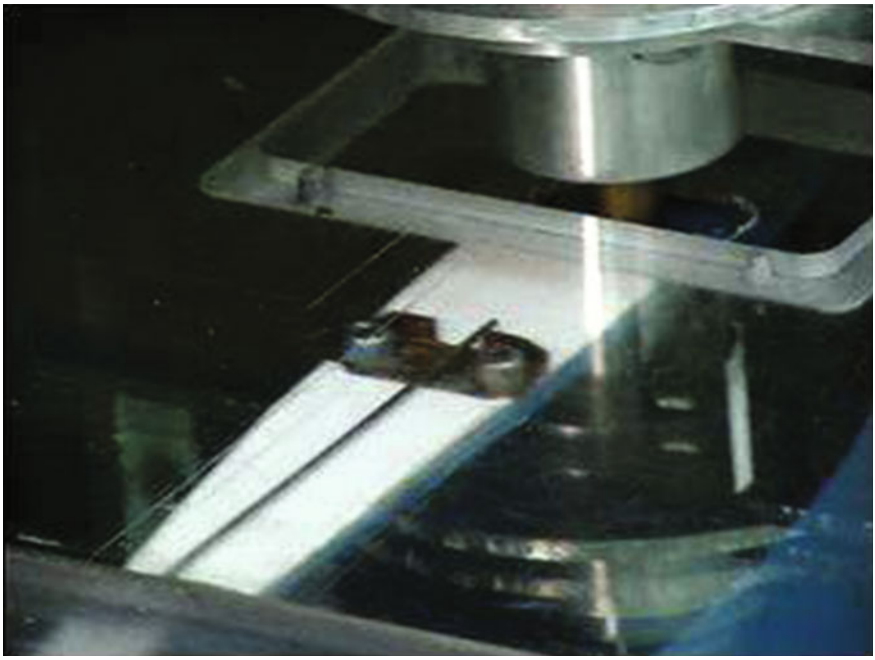

Fig. 7 Close-Up of freeplay mechanism

6 (full model view) and 7 (close up of the wire beam that moves between two rigid stops to produce freeplay) show the wind tunnel model from [11–13]. Figure 8 shows the LCO amplitude of the model versus flow velocity for plunge, pitch and flap (control surface) degrees of freedom of this model as well as the LCO frequency. Note the computational results are in very good agreement with the wind tunnel test data. These results are for zero angle of attack and a freeplay angle of 2.12°. If the angle of attack is increased to 8°, as shown in Fig. 9 the range of flow velocity for which LCO exists is much decreased and a further increase in angle of attack to 10° suppresses the LCO altogether. Note however that the flow velocity at which the LCO begins is not much changed by the angle of attack change. Results (not shown) also show that varying the degree of freeplay simply changes the LCO amplitude in proportion while the LCO frequency is unchanged [15–17].

Current work is underway to include the effect of a feedback control system in this model.

The excellent work of Schlomach [18] for the F-35 program has provided independent verification of the above results and extended them into the high subsonic/transonic flow regime. As expected the quantitative agreement between theory and experiment is less satisfactory in the transonic regime because of the challenging environment for modeling the aerodynamic forces. However, even so, the same scaling laws for the effect of freeplay and loading were also found in this study.

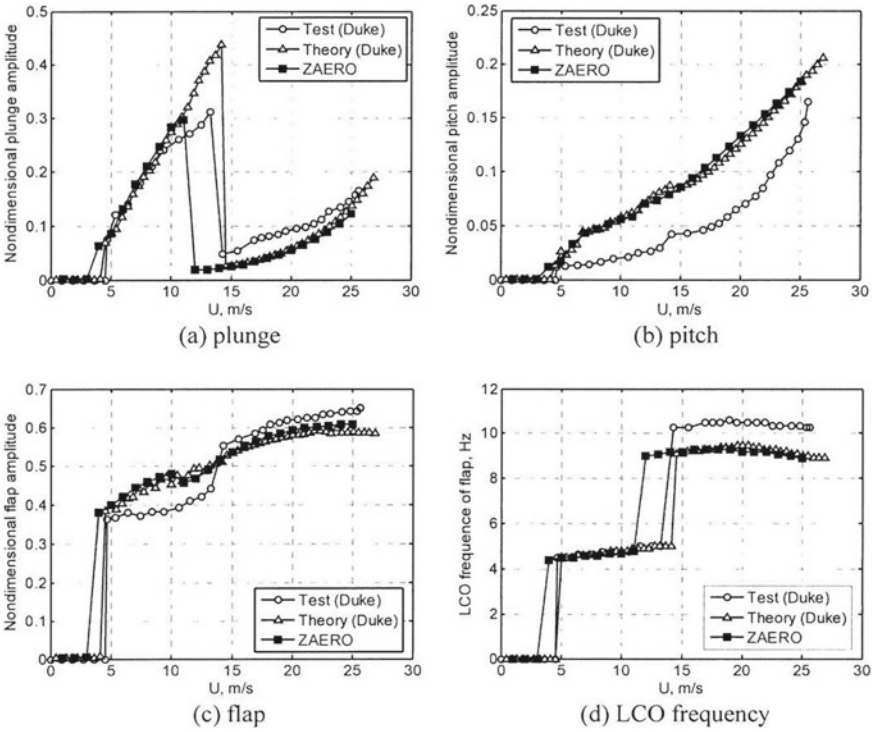

Fig. 8 Theoretical and experimental LCO R.M.S. Response amplitudes and frequency for the initial pitch angles of $\alpha = 0$ and $\delta = 2.12°$

3.3 Reduced Order Modeling of Unsteady Aerodynamics

For an expanded discussion and reviews of this topic, see [1–6].

3.3.1 Eigenmodes and POD Modes

The original impetus for such models was the thought that by using the eigenmodes of a computational fluid dynamics (CFD) model, one might construct a modal model of the fluid that is the counterpart for the modal model of a structure obtained from a finite element model (FEM). [1–6] And this turns out to be possible with some notable caveats. First of all, finding the eigenmodes of a CFD model is itself a formidable task because of the very large number of degrees of freedom in a typical CFD model. And indeed the use of Proper Orthogonal Decomposition (POD) to find a suitable set of fluid modes proves to be far more practical. However it is worth noting in passing that using POD modes one may find a good approximation to the

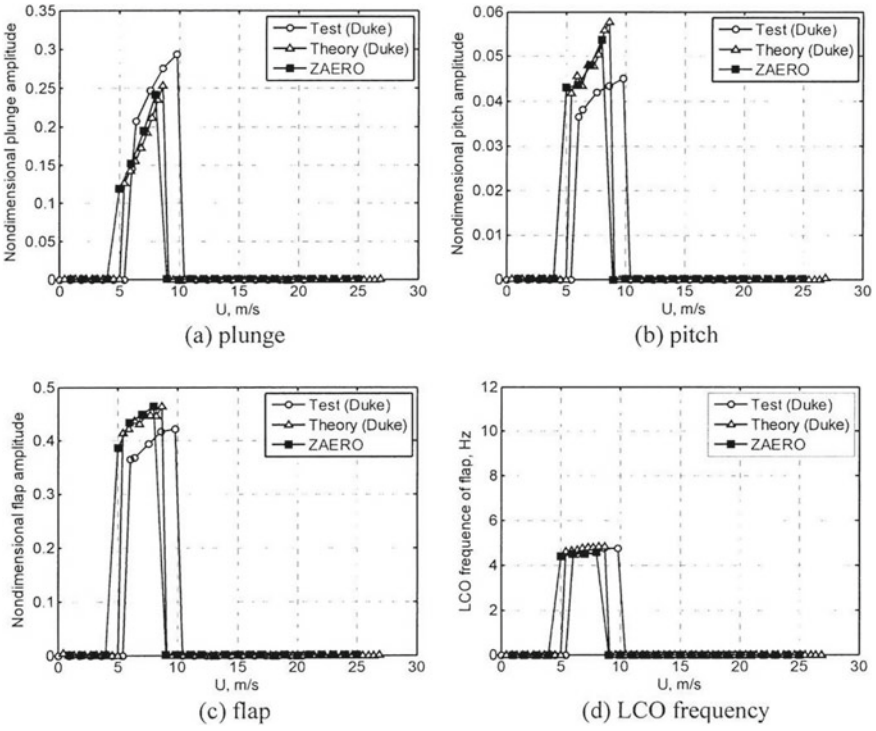

Fig. 9 Theoretical and experimental LCO R.M.S. Response amplitudes and frequency for the initial pitch angles of $\alpha = 8°$ and $\delta = 2.12°$

dominant eigenmodes of a CFD model. Normally however one uses the POD modes themselves in an aeroelastic analysis. [3]

Also it is worth noting that the fluid modal model is non-self adjoint and thus the fluid eigenvalues are complex with each fluid mode eigenvalue having both a frequency and a damping. Thus both the system and its adjoint must be considered when constructing the orthogonality relations for the complex eigenmodes. And perhaps most importantly, the eigenmodes and the POD modes can be very sensitive to small changes in system parameters, most notably there is a sensitivity to Mach number. Thus when using POD modes it is most convenient to fix the Mach number and vary the altitude or flow density for example. However Farhat [19–21] and his colleagues have made very good progress in showing how one may interpolate POD modes obtained at two different Mach numbers to obtain a good ROM model at intermediate Mach numbers thereby expanding the range of application of such ROMs. This interpolation proves to be surprisingly subtle.

For a chronological development of this approach including the seminal paper by Romanowski [22], the reader may consult [22–29]. There is a discussion of the eigenmode and/or POD mathematical technique in most of these papers and readily accessible accounts are available in [3–6].

3.3.2 High Dimensional Harmonic Balance

Here the essential idea is that most aeroelastic responses of interest are periodic in time. As those who have tried to compute the periodic in time limit cycle oscillation (LCO) using a time marching CFD code have observed, it takes a very long time to do so while waiting for the transient oscillation to decay in order to reach the steady state LCO. Indeed at the flutter point in parameter space which is usually the point at which LCO also begins, the damping in the critical aeroelastic mode is strictly speaking zero and the transient never decays. But even near the flutter point, the transients are usually very long.

Thus it is natural to ask can one avoid computing the transient solution and computei the LCO directly. Classical Harmonic Balance has been used successfully in pursuit of this goal for low dimensional systems, e.g. the Duffing and Van der Pol oscillators. However for the high dimensional systems of interest using a nonlinear CFD model, the classical method becomes practically impossible. Thus Hall and colleagues [3] developed a significant extension to the classical Harmonic Balance method that is particularly useful for high dimensional dynamical systems such as those arising from CFD models. Other investigators have found this approach useful as well. See the work of Jameson et al. [30, 31] and Badcock [32].

For a chronological development of this approach including the seminal paper by Hall, Thomas and Clark [33], see [33–39]. For an accessible account of the mathematical formulation of the High Dimensional Harmonic Balance method, see [34, 40]. Beran and Lucia [35] have developed a related approach that has some interesting alternative ideas.

For systems that are not strictly periodic in time, but have two fundamental periods or frequencies, the classical and Higher Order Harmonic Balance Methods can also be useful if a Fourier Series for each period is constructed. If the system is nonlinear then the coupling between the (as well as within each of the) components of the two Fourier Series must be taken into account. While a system with only two fundamental periods may be thought to be rather limited from a mathematical point of view, in point of fact it includes systems of interest to aeroelasticians, e.g. an aeroelastic system undergoing a limit cycle oscillation of a certain period or frequency which is then excited by an external dynamic force such as a gust with its own characteristic frequency.

3.3.3 Nonlinear Reduced Order Models Based Upon POD Modes and High Dimensional Harmonic Balance

Thomas, Dowell and Hall [40] have recently combined the advantages of POD modes and High Dimensional Harmonic Balance to construct nonlinear reduced order models. In this approach, the solution is expanded in a Taylor Series with respect to CFD code parameters including variables such as Mach and the amplitude of the structural motion. If this expansion were done for each of the many fluid variable degrees of freedom that may number in the millions or more, the computation would quickly get out of hand. However if one relates the many flow variables through a coordinate transformation to the modal amplitudes of a relatively small number of POD modes, then the computational model can be made very efficient. The key then is to be able to differentiate the CFD code and its flow variables with respect to the POD modal amplitudes and this can be accomplished using adjoint automatic differentiation software that is now widely available [40]. In [40] this reduced order model is constructed in combination with a High Dimensional Harmonic Balance (HDHB) solver. In principle this POD approach could also be combined with a time marching solution algorithm, but that would not exploit the considerable advantages of the HDHB method.

A representative result [40] is shown in Fig. 10 where the results of the full CFD model and the reduced order model (ROM) are compared in a plot of LCO amplitude versus a reduced (non-dimensional) velocity. Results are shown for both a first and second order ROM. As can be seen the second order ROM is a distinct improvement

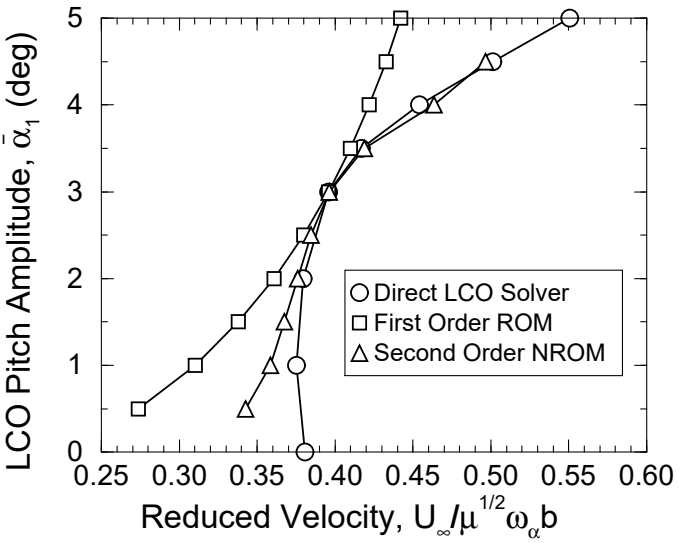

Fig. 10 LCO response trends for the nlr 7301 aeroelastic configuration including reduced-order-model results

over the first order ROM. Of course in principal one can go to a third order ROM etc. However in practice a better strategy is to choose a small number of full order solutions and expand in a Taylor Series up to say second order about each of them. Referring to Fig. 10, it is seen that the common point on the three curves is the point about which the Taylor Series has been expanded. By choosing a few more such points, the several Taylor Series can be blended to produce the entire LCO response with sufficient accuracy.

4 Transonic Flutter and LCO of Lifting Surfaces

This section[2] begins with a discussion of generic nonlinear aeroelastic behavior of wings especially as it relates to Limit Cycle Oscillations (LCO); then the important studies that come from flight experience with LCO are noted which have stimulated much of the other research on the subject. Next a summary is provided of the primary physical sources of fluid and structural nonlinearities that can lead to nonlinear aeroelastic response in general and LCO more particularly.

A brief summary of unsteady aerodynamic models, both linear and nonlinear, is then given before turning to the heart of the section that provides a critique of the results obtained to date via various methods using as a framework correlations between theory and experiment.

4.1 Generic Nonlinear Aeroelastic Behavior

There are several basic concepts that will be helpful for the reader to keep in mind throughout the discussion to follow. The first is the distinction between a static nonlinearity and a dynamic one. In the aeroelasticity literature the term "linear system" may either mean a (mathematical or wind tunnel) model or flight vehicle that is both statically and dynamically linear in its response or one that is nonlinear in its static response, but linear in its dynamic response. So we will usually qualify the term "linear model" further by noting whether the system is dynamically linear or both statically and dynamically, i.e. wholly linear.

An example of a system which is wholly linear is a structure whose deformation in response to either static or dynamic forces is (linearly) proportional to those forces. An aerodynamic flow is wholly linear when the response (say change in pressure) is (linearly) proportional to changes in downwash or fluid velocities induced by the shape or motion of a solid body in the flow. This is the domain of classical small perturbation aerodynamic theory and leads to a linear mathematical model (convected wave equation) for the fluid pressure perturbation or velocity potential. Shock waves and separated flow are excluded from such flow models that are both statically and

[2] This section is an abbreviated and revised version of [1]

dynamically linear. A wholly linear aeroelastic model is of course one composed of wholly linear structural and aerodynamic models.

A statically nonlinear, but dynamically linear structure is one where the static deformations are sufficiently large that the static response is no longer proportional to the static forces and the responses to the static and dynamic forces cannot simply be added to give meaningful results. Buckled skin panels (buckling is a nonlinear static equilibrium that arises from a static instability) that dynamically respond to (not too large) acoustic loads or the prediction of the onset of their dynamic aeroelastic instability (flutter) are examples where a statically nonlinear, but dynamically linear model may be useful.

In aerodynamic flows, shock waves and separated flows are themselves the result of a dynamically nonlinear process. But once formed they may often be treated in the aeroelastic context as part of a nonlinear static equilibrium state (steady flow). Then the question of the dynamic stability of the statically nonlinear fluid-structural (aeroelastic) system may be addressed by a linear dynamic perturbation analysis about this nonlinear static equilibrium. Sometime such aerodynamic flow models are call time linearized.

Of course if one wishes to model limit cycle oscillations and the growth of their amplitude as flow parameters are changed, then either or both the structural and the aerodynamic model must be treated as dynamically nonlinear. Often a single nonlinear mechanism is primarily responsible for the limit cycle oscillation. However, one may not know apriori which nonlinearity is dominant unless one has designed a mathematical model, wind tunnel model or flight vehicle with the chosen nonlinearity. Not the least reason why limit cycle oscillations are more difficult to understand in flight vehicles (compared to say mathematical models) is that rarely has a nonlinearity been chosen and designed into the vehicle. More often one is dealing with an unanticipated and possibly unwanted nonlinearity. Yet sometimes that nonlinearity is welcome because without it the limit cycle oscillation would instead be replaced by catastrophic flutter leading to loss of the flight vehicle.

It must be emphasized that the variety of possible nonlinear aeroelastic responses is not limited to 'Limit Cycle Oscillations (LCO)' per se. In the context of nonlinear system theory [41], an LCO is one of the simplest dynamic bifurcations. Other common possible nonlinear responses includei higher harmonic and subharmonic resonances, jump-resonances, entrainment, beating and period doubling to name only a few. These responses have been studied using low order model problems in the nonlinear dynamics literature; however in aeroelastic wind tunnel and flight testing the detailed knowledge required to identify these nonlinear responses has rarely been available.

Now consider the generic types of nonlinear dynamic response that may occur, i.e. limit cycle oscillations and the variation of their amplitude with flight speed (or wind tunnel velocity). Of course the frequency of the LCO may vary with flight parameters as well, but usually the frequency is near that predicted by a classical linear dynamic stability (flutter) analysis.

The generic possibilities are indicated in Fig. 11a and b where the limit cycle amplitude is plotted versus some system parameter, e.g. flight speed. In Fig. 11a, an

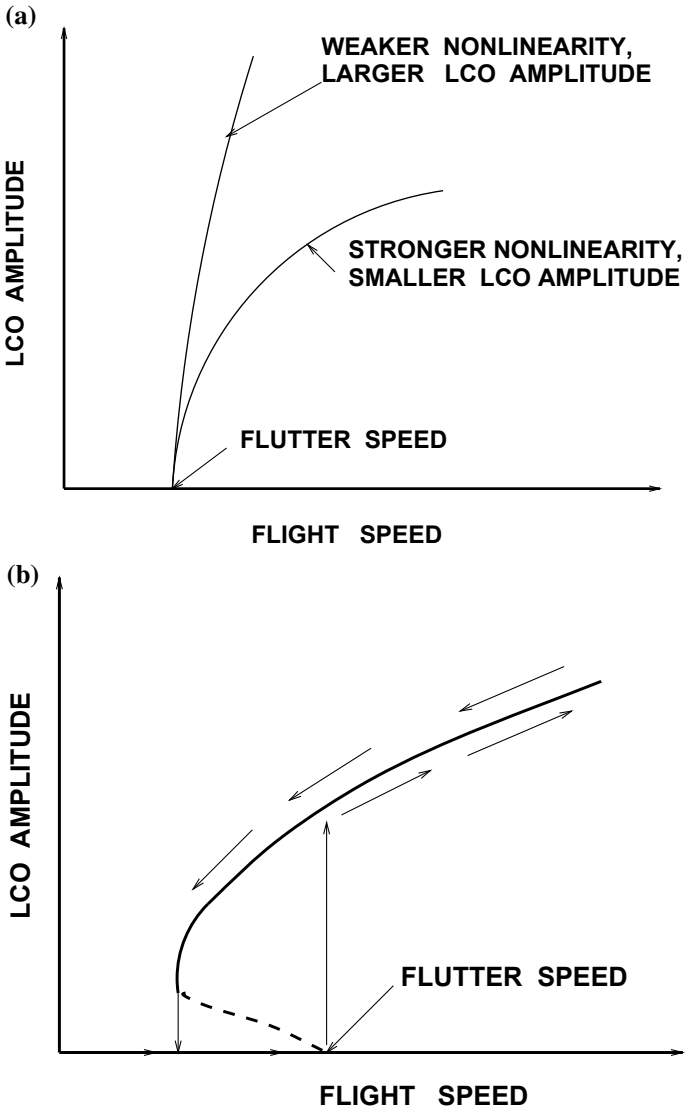

Fig. 11 **a** Schematic of limit cycle oscillation response for benign nonlinearity. **b** Schematic of limit cycle oscillation response for detrimental nonlinearity

aeroelastic system is depicted that is stable to small or large disturbances (perturbations) below the flutter (instability) boundary predicted by a linear dynamical model. Beyond the flutter boundary, LCO arise due to some nonlinear effect and typically the amplitude of the LCO increases as the flight speed increases beyond the flutter speed. In Fig. 11b, the other generic possibility is shown. While again LCO exist

beyond the flutter boundary, now LCO may also exist below the flutter boundary, if the disturbances to the system are sufficiently large. Moreover both stable (solid line) and unstable (dotted line) LCO now are present. Stable LCO exist when for any sufficiently small disturbance, the motion returns to the same LCO at large time. Unstable LCO are those for which any small perturbation will cause the motion to move away from the unstable LCO and move toward a stable LCO. Theoretically, in the absence of any disturbance both stable and unstable LCO are possible dynamic, steady state motions of the system. Information about the size of the disturbance required to move from one stable LCO to another can also be obtained from data such as shown in Fig. 11b. Note also the hysteretic response as flight speed increases and then decreases.

4.2 Flight Experience with Nonlinear Aeroelastic Effects

Much of the flight experience with aircraft LCO has been documented by the Air Force SEEK EAGLE Office at Eglin AFB and is described in several publications by Denegri and his colleagues [42–45]. Most of this work has been in the context of the F-16 aircraft. Denegri distinguishes among three types of LCO based upon the phenomenological observations in flight and as informed by classical linear flutter analysis. "Typical LCO" is when the LCO begins at a certain flight condition and then with say an increase in Mach number at constant altitude the LCO response smoothly increases. "Flutter", as distinct from LCO, is said to occur when the increase in LCO amplitude with change in Mach number is so rapid that the safety of the vehicle is in question.i And finally "atypical LCO" is said to occur when the LCO amplitude first increases and then decreases and perhaps disappears with changes in Mach number. This is also sometimes called a "hump" mode. Often changes in flight vehicle angle of attack lead to similar generic LCO responses to those observed with changes in Mach number.

It has long been recognized [46] that the addition of external stores to aircraft changes the dynamic characteristics and may adversely affect flutter boundaries. Limit cycle oscillations (LCO) remain a persistent problem on high performance fighter aircraft with multiple store configurations. Using measurements obtained from flight tests, Bunton and Denegri [47] describe LCO characteristics of the F-16 and F/A-18 aircraft. While LCO can be present in any sort of nonlinear system, in the context of aeroelasticity, LCO typically is exhibited as an oscillatory response of the wing, the amplitude of which is limited, but dependent on the nature of the nonlinearity as well as flight conditions, such as speed, altitude, and Mach number. The LCO motion is often dominated by antisymmetric modes. LCO are not described by standard linear aeroelastic analysis, and they may occur at flight conditions below those at which linear instabilities such as flutter are predicted. Although the amplitude of the LCO may rise above structural failure limits, more typically the presence of LCOs results in a reduction in vehicle performance, leads to airframe-limiting structural fatigue, and compromises the ability of pilots to perform critical

mission-related tasks. When LCO are unacceptable, extensive and costly flight tests for aircraft/store certification are required.

Denegri [42, 43] suggests that for the F-16, the frequencies of LCO might be identified by linear flutter analysis; however, linear analysis fails to predict the oscillation amplitude or the onset velocity for LCO. Thus, nonlinear analysis will be necessary to predict the onset of the LCO and their amplitudes with changing flight conditions.

4.2.1 Nonlinear Aerodynamic Effects

There are several other flight experiences with limit cycle oscillations in addition to the F-16 including those for example with the F-18, the B-1 and B-2. Most of these LCO have been attributed by investigators to nonlinear aerodynamic effects due to shock wave motion and/or separated flow. However, there is the possibility that nonlinear structural effects involving stiffness, damping or freeplay may play a role as well. Indeed, much of the present day research and development effort is devoted to clarifying the basic mechanisms responsible for nonlinear flutter and LCO. For an authoritative discussion of these issues see Cunningham et al. [48–50], Denegri [41–45] on the F-16 and F-18, Dobbs [51], Hartwich [52] on the B-1 and Britt, Jacobsen and Dreim [53] on the B-2. Recent experimental evidence from wind tunnel tests is beginning to shed further light on these matters as are advances in mathematical and computational modeling.

4.2.2 Freeplay

There have been any number of aircraft that have experienced flutter induced limit cycle oscillationsi as a result of control surface freeplay. These are not well documented in the public literature, but are more known by word of mouth among practitioners and perhaps documented in internal company reports and/or restricted government files.

A recent and notable exception is the account in Aviation Week and Space Technology by Croft [54] of a flutter/limit cycle oscillation as a result of freeplay. In many ways this account is typical. The oscillation is of limited amplitude and there was a reported disagreement between the manufacturer and the regulating governmental agency as to whether this oscillation was or was not sufficiently large as to be a threat to the structural integrity of the aircraft structure. See also Sect. 3 of this paper.

4.2.3 Geometric Structural Nonlinearities

Another not infrequently encountered and documented case is the limit cycle oscillation that follows the onset of flutter in plate-like structures. The structure has a nonlinear stiffening as a result of the tension induced by mid-plane stretching of the plate that arises from its lateral bending. This is most commonly encountered in

what is often called panel flutter where a local element of a wing or fuselage skin encounters flutter and then a limit cycle oscillation.i There have been many incidents reported in the literature dating back to the V-2 rocket of World War II, the X-15, the Saturn Launch Vehicle of the Apollo program and continuing on to the present day. Some of these are discussed in a monograph by Dowell [55] and also a NASA Special Publication by Dowell [56]. See also Sect. 3 of this paper.

It has been recently recognized that low aspect ratio wings may behave as structural plates and thus the entire wing may undergo a form of plate-like flutter and limit cycle oscillations. This has been seen in both wind tunnel models and computations to be discussed later. However there is not yet a clearly documented case of such behavior in flight.

4.3 Physical Sources of Nonlinearities

Several physical sources of nonlinearities have been identified through mathematical models (in almost all cases), wind tunnel tests (in several cases) and flight tests (less often). Among those most commonly studied and thought to be important are the following. Large shock motions may lead to a nonlinear relationship between the motion of the structure and the resulting aerodynamic pressures and forces that act on the structure. If the flow is separated (perhaps in part induced by the shock motion) this may also create a nonlinear relationship between structural motion and the consequent aerodynamic flow field.

Structural nonlinearities can also be important and are the result of a given (aerodynamic) force on the structure creating a response that is no longer (linearly) proportional to the applied force. Freeplay and geometric nonlinearities are prime examples (already mentioned). But the internal damping forces in a structure may also have a nonlinear relationship to structural motion, with dry friction being an example that has received limited attention to date. Because the structural damping is usually represented empirically even within the framework of linear aeroelastic mathematical models, not much is known about the fundamental mechanisms of damping and their impact on flutter and LCO.

All of these nonlinear mechanisms have nevertheless been considered by the mathematical modeling community and several have been the subject of wind tunnel tests as well. In some cases good correlation between theory and experiment has been obtained for limit cycle oscillation response.

4.4 *Efficient and Accurate Computation of Unsteady Aerodynamic Forces: Linear and Nonlinear*

The literature on unsteady aerodynamic forces alone is quite extensive. A comprehensive assessment of current practice in industry is given by Yurkovich, Liu and Chen [57]. An article that focuses on recent developments is that of Dowell and Hall [3]. Other recent and notable discussions include those of Bennett and Edwards [58] and Lucia, Beran and Silva [4]. Much of the present focus of work on unsteady aerodynamics is on developing accurate and efficient computational models. Standard computational fluid dynamic [CFD] models and solution methods that include the relevant fluid nonlinearities are simply too expensive now and for some time to come for most aeroelastic analyses. Thus there has been much interest in reducing computational costs while retaining the essence of the nonlinear flow phenomena. See Sect. 3 of this paper.

4.5 *Experimental/Theoretical Correlations*

Much of what we know about the state of the art with respect to nonlinear aeroelasticity comes from the study of correlations between experiment and theory and between various levels of theoretical models. Hence the remainder of this discussion is largely devoted to such correlations and the lessons learned from them. The correlations selected are representative of the state of the art for transonic flutter boundaries and limit cycle oscillations.

4.5.1 Flutter Boundaries in Transonic Flow

AGARD 445.6 WING MODELS

Bennett and Edwards [58] have discussed the state of the art of Computational Aeroelasticity (CAE) in a relatively recent paper and made several insightful comments about various correlation studies. The NASA Langley team pioneered in providing correlations for the AGARD 445.6 wing in the transonic flow region. For this thin wing, there are no significant transonic effects in the steady flow over the wing surface at the Mach numbers with experimental results except for $M = 0.96$ where there is a very weak shock on the surface. For the subsonic conditions, all computational results are in very good agreement with experiment. However, the two low supersonic test conditions have been problematic for CAE. Inviscid flow (Euler) computations have produced high flutter speed index (FSI) values relative to the experimental FSI and viscous flow (Navier-Stokes) computations have accounted for about one half the difference between theory and experiment. Several investigators have now done similar Euler calculations and obtained similar results [59–61]. The excellent agreement of the wholly linear theory results with experiment should probably be regarded

as fortuitous. Interestingly, Gupta [62], who also used an Euler based CFD model, obtains results in better agreement with experiment at the low supersonic conditions, though in less good agreement with experiment than the other Euler based results at subsonic conditions. Thus, CAE computations for this low supersonic region have unresolved issues which probably involve details such as wind tunnel wall interference effects and flutter test procedures, as well as CAE modeling issues.

HSCT Rigid and Flexible Semispan Models

Two semispan models representative of High Speed Civil Transport (HSCT) configurations were tested in the NASA Langley Research Center Transonic Dynamics Tunnel (TDT) in heavy gas. A Rigid Semispan Model (RSM) was tested mounted on an Oscillating Turn Table (OTT) and on a Pitch And Plunge Apparatus (PAPA). The RSM/OTT test [63] acquired unsteady pressure data due to pitching oscillations and the RSM/PAPA test acquired flutter boundary data for simple pitching and plunging motions. The RSM test [64] involved an aeroelastically-scaled model and was mounted to the TDT sidewall. The test acquired unsteady pressure data and flutter boundary data. The results show the unexpectedly large effect of mean angle of attack upon the flutter boundaries for the RSM/PAPA model. Flutter of thin wings at subsonic conditions is typically independent of angle-of-attack within the linear flow region. A region of increased response in first wing bending (8.5 Hz.) was encountered in the Mach number range of 0.90–0.98. Finally, a narrow region of LCO behavior, labeled 'chimney', was encountered for $M = 0.98 - 1.00$ and over a wide range of dynamic pressures.

Benchmark Active Control Technology (BACT)

This rectangular wing model had an aspect ratio of two and a NACA 0012 airfoil section [65, 66]. It was mounted on a pitching and plunging apparatus which allowed flutter testing with two structural degrees of freedom. It was extensively instrumented with unsteady pressure sensors and accelerometers and it could be held fixed (static) for forced oscillation testing or free for dynamic response measurements. Data sets for trailing-edge control surface oscillations and upper-surface spoiler oscillations for a range of Mach numbers, angle of attack, α, and static control deflections are available. The model exhibited three types of flutter instability.

A classical flutter boundary was found for $\alpha = 2°$, as a conventional boundary of flow density versus Mach number with a minimum, the transonic 'dip', near $M = 0.77$ and a subsequent rise. Stall flutter was found, for near the minimum of the flutter boundary (and at most tunnel conditions where high angles of attack could be attained). Finally, a narrow region of instability occurred near $M = 0.92$ consisting of plunging motion at the plunge mode wind-off frequency. This type of transonic instability has sometimes been termed single-degree-of-freedom flutter. It is caused by the fore and aft motion of symmetric shocks on the upper and lower surfaces for this wing. It was very sensitive to any biases and did not occur with nonzero control surface bias or nonzero alpha. Such a stability boundary feature is sometimes termed a 'chimney' since the oscillations are typically slowly diverging or constant amplitude (LCO) and it is found, sometimes, that safe conditions can be attained with small further increases in Mach number.

Computational studies by Kholodar et al. [67] were conducted to correlate with the flutter boundary obtained experimentally by Rivera et al. [67]. Kholodar's inviscid calculation agreed very well with the experimental findings except for M ≈ 0.88 to M ≈ 0.95 where a "plunge instability region" occurred.

Experimental data for the flutter boundary were not obtained at Mach numbers just below the plunge instability region. Using an inviscid aerodynamic model in the flutter calculations, no flutter solutions could be obtained for $0.82 < M < 0.92$ except at very low flow densities (inverse mass ratios). This is approximately the same region for which experimental results were unavailable. Kholodar conjectured this indicated that in this region, the flutter mass ratio (inversely proportional to flow density or dynamic pressure) rose precipitously as the airfoil entered a single degree-of-freedom flutter mode. Conversely, flow density (or inverse mass ratio) dropped precipitously.

Viscous CFD results obtained by Schwarz et al. [68] revealed a number of surprising characteristics. First, whereas inviscid aerodynamics made flutter solutions difficult to find in the region $0.82 \leq M \leq 0.91$ due to the sharp increase in flutter mass ratio, μ; by contrast, viscous results on a 193 x 49 CFD grid yielded readily detectable solutions. However, these viscous solutions showed some sensitivity to Mach number.

A grid refinement study was performed by Schwarz et al. [68] to verify the results obtained on the nominal 193 x 49 grid. The flutter condition was recomputed on a coarser 97 x 25 grid and also a fine 385 x 97 grid at select Mach numbers, chosen to be representative of the range of Mach numbers examined. This study showed that the coarse 97 x 25 grid had insufficient resolution and produced results in poor agreement with experiment at low subsonic as well as transonic Mach numbers.

Results on the 385 x 97 computational mesh agreed with those on the nominal 193 x 49 mesh except for a narrow range of transonic Mach numbers. For M ≈ 0.84–0.86, computations on this mesh showed flow shedding to be occurring, a phenomenon not seen on the coarser meshes (shedding or buffeting is an LCO of the flow alone, even in the absence of structural motion). The range in which this shedding occurred agrees very closely with the Mach number range for which experimental results were not obtained, approximately $0.82 < M < 0.88$. As seen in Fig. 12, predictions on the 193 x 49 and 385 x 97 viscous grids largely agreed outside of this shedding region.

Shedding or buffeting prohibits a linear flutter analysis at the Mach numbers for which it occurs, because it violates the assumption that the flow behaves in a dynamically linear way for small motions of the airfoil. Still, the present calculation provides an insight into the flutter experiment. The occurrence of shedding correlates with the range of Mach numbers for which airfoil motions became erratic in the experiments, indicating that shedding may have led to this unusual behavior.

F-16

The computed flutter boundaries for eight F-16 wing/store configurations are shown in Fig. 13 in terms of altitude versus Mach number based upon standard atmospheric conditions. Note the Mach number range over which flutter may occur varies substantially from one configuration to the next. In these calculations, the viscous Reynolds

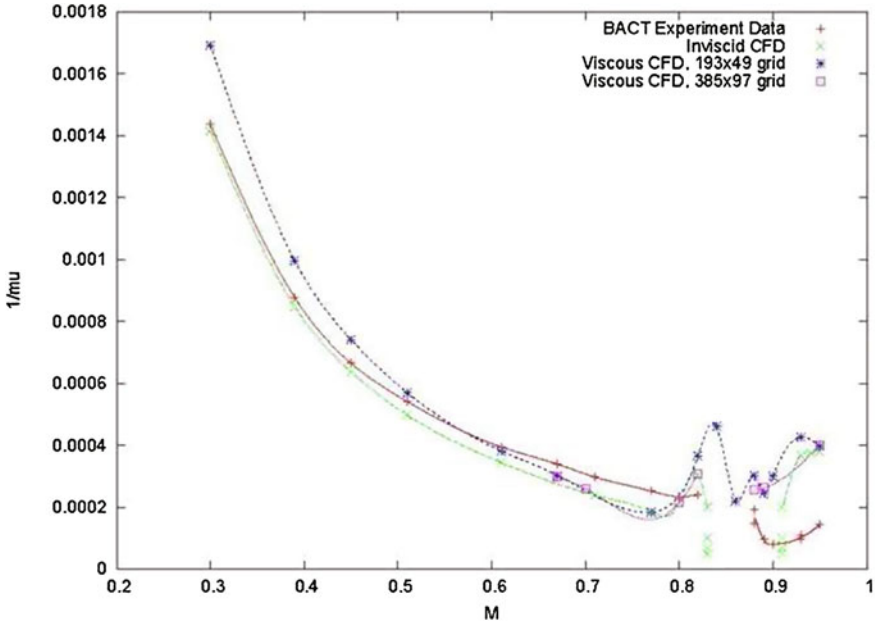

Fig. 12 Flutter inverse mass ratio versus Mach number from viscous and inviscid CFD results and experimental data from Rivera [67]

Averaged Navier Stokes (RANS) version of the Duke University harmonic balance solver was used [69]. Calculations for some of these configurations were also done using an Euler version of the CFD code. In general, the Euler code provides similar trends for the flutter onset boundary, but there are some quantitative differences, i.e. as much as 25

Note that in Fig. 13 there are no results for Configuration #7. This is because no flutter or LCO was found in the Mach number range shown which is in agreement with the flight test results. Also for configuration #6, flight tests were stopped at Mach numbers less than the highest shown in Fig. 13. Again no flutter or LCO was found in the flight test in agreement with the computations. Moreover the computed flutter boundaries shown in Fig. 13 generally agree reasonably well with the flight test results as seen in Fig. 14. Note that a range of Mach number is shown for configuration #5 for both computed and flight test results in Fig. 14. This is because flutter and LCO occur over a range of Mach number for configuration #5 with flutter/LCO starting at the lowest Mach number shown and ending at the highest Mach number shown. Recall Fig. 13. This is sometimes called a "hump" flutter/LCO mode.

A comparison between measured and computed frequencies at Mach numbers just beyond the onset of LCO for the several configurations where LCO was observed shows the agreement is generally quite good and it is noted that the LCO frequency does not vary rapidly with Mach number [69].

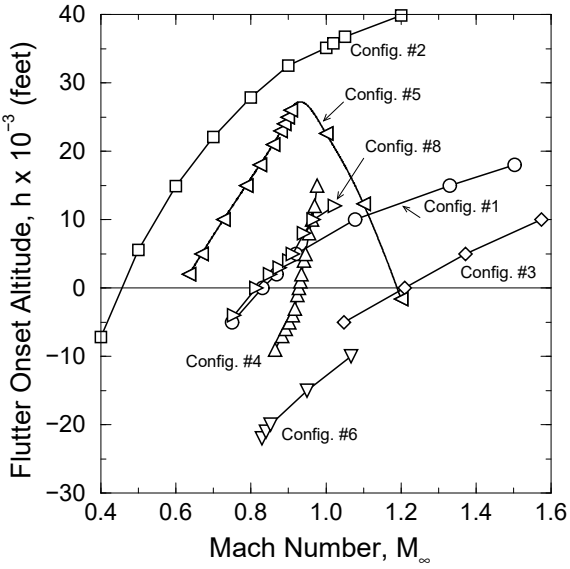

Fig. 13 Computed F-16 fighter flutter onset altitude versus mach number

4.5.2 Limit Cycle Oscillations

Airfoils with structural stiffness and freeplay nonlinearities

Some investigators have considered configurations with a variety of nonlinear stiffness and freeplay structural nonlinearities. For a description of the work on freeplay nonlinearities, see the article by Dowell and Tang [70] which focuses on correlations between theory and experiment as well as Sect. 3.2 of the present paper. In general good quantitative correlation is found for simple wind tunnel models and the basic physical mechanism that leads to LCO appears well understood. Among the important insights developed include the demonstration that the LCO amplitude and the effect of mean angle of attack on LCO amplitude both simply scale in proportion to the range of freeplay present in the aeroelastic system. This result has received further confirmation from the excellent study of Schlomach for the F-35 aircraft program [18]. An example of another stiffness nonlinearity is described next.

Delta wings with geometrical plate nonlinearities

At low Mach numbers good correlation has been demonstrated between theory and experiment for LCO amplitudes and frequencies. Since these results are well documented elsewhere, see Dowell and Tang [70], here the recent work of Gordnier et al. [71, 72] that has extended these correlations into the transonic range for a cropped delta wing planform is emphasized. This configuration had been investigated experimentally by Schairer and Hand [73] and the theoretical calculations were done by Gordnier et al. using both Euler and Navier-Stokes flow models. Initially the theoretical calculations were done using a linear structural model, which gave predicted LCO amplitudes much greater than those observed experimentally. This led Gordnier to

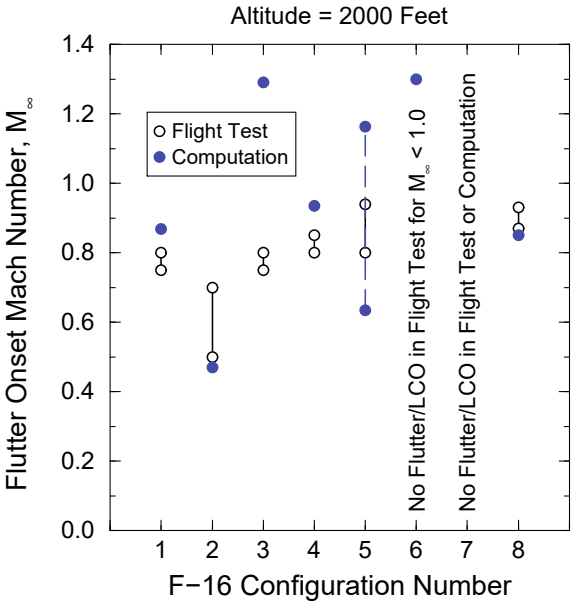

Fig. 14 Flutter mach number characteristics for each F-16 fighter configuration

include nonlinearities in the structural model via Von Karman's nonlinear plate theory that provided much improved correlation between theory and experiment. Note that the effects of viscosity are modest based upon the good agreement of results using the Euler vs Navier-Stokes models. Also the much improved agreement obtained with the nonlinear structural model suggests that aerodynamic nonlinearities per se are not as significant for this configuration as are the structural nonlinearities.

Large shock motions and flow separation
These aerodynamic nonlinearities are both the most difficult to model theoretically and also to investigate experimentally. Hence it is not surprising that our correlations between theory and experiment are not yet what we might like them to be. As a corollary one might observe that it will in all likelihood be easier to design a favorable nonlinear structural element to produce a benign LCO, than to assure that flow nonlinearities will always be beneficial with respect to LCO.

4.5.3 AGARD 445.6 Wing Models

The AGARD 445.6 wing has been discussed earlier in terms of its flutter boundary; now we turn to results from Thomas, Dowell and Hall [74] for LCO. The correlation between theory and experiment for the flutter boundary is shown in Fig. 15 where the Euler flow model is that of Thomas et al. But now we have in addition results for LCO amplitude versus FSI for various Mach number. See Fig. 16. Note that a value of first mode non-dimensional modal amplitude of $\xi = 0.012$ as shown in this

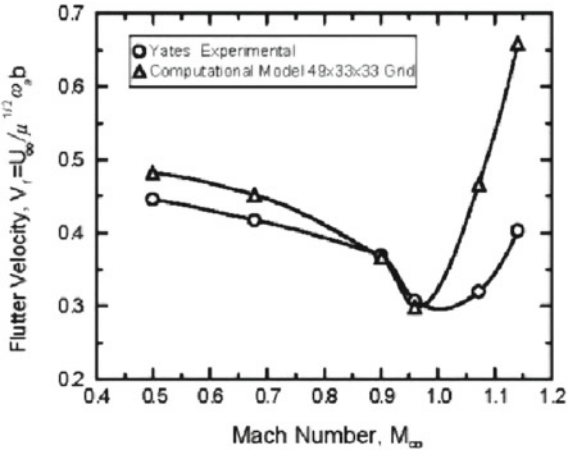

Fig. 15 Flutter speed index versus mach number for AGARD wing 445.6: comparison of theory and experiment

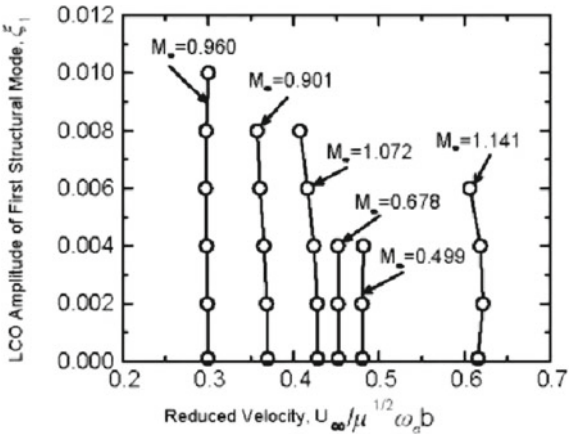

Fig. 16 LCO amplitude versus flutter speed index (Reduced Velocity) for various mach number for AGARD 445.6 Wing

figure corresponds to a wing tip deflection equal to one fourth of the wing half-span. Note there is no Mach number for which a benign LCO is predicted and subcritical LCO is predicted at M = 1.141 and 1.072. This means that LCO may occur below the flutter boundary at these two Mach numbers and perhaps this explains at least in part why flutter (or really an unstable LCO) occurred in the experiment below the predicted flutter boundary.

Small amplitude LCO behavior for the AGARD 445.6 wing has also been calculated by Edwards [75]. The majority of published calculations for this wing model (actually a series of models with similar planforms) are for the "weakened model #3" tested in air, since this test covered the largest transonic Mach number range and showed a significant transonic dip in the flutter boundary. The focus on this particular configuration may be in some ways unfortunate, in that the model tested in air resulted in unrealistically large mass ratios and small reduced frequencies. Weakened

models #5 and #6 were tested in heavy gas and had smaller mass ratios and higher reduced frequencies. Very good agreement was obtained with experiment for flutter speed index using the CAP-TSDV code over the Mach number range tested. For the highest Mach number tested, M = 0.96, it was noted that damping levels extracted from the computed transients were amplitude dependent, an indicator of nonlinear behavior. It was also found that small amplitude divergent (in time) responses used to infer the flutter boundary would transition to LCO when the calculation was continued further in time. The wing tip amplitude of the LCO was approximately 0.12 inches peak-to-peak, a level that is unlikely to be detected in wind tunnel tests given the levels of model response to normal wind tunnel turbulence.

4.5.4 MAVRIC Wing Flutter Model

This business jet wing-fuselage model (see Edwards [76, 77]) was chosen by NASA Langley Research Center's Models For Aeroelastic Validation Involving Computation (MAVRIC) project with the goal of obtaining experimental wind-tunnel data suitable for Computational Aeroelasticity (CAE) code validation at transonic separation onset conditions. LCO behavior was a primary target. An inexpensive construction method of stepped-thickness aluminum plate covered with end-grain balsa wood and contoured to the desired wing profile was used. A significant benefit of this method was the additional strength of the plate that enabled the model to withstand large amplitude LCO motions without damage.

The behavior of the MAVRIC model as flutter was approached during the wind tunnel test indicated that wing motions tended to settle to a large amplitude LCO condition, especially in the Mach number range near the minimum FSI conditions. Figure 17 demonstrates [77] the ability of the CAP-TSDV code to simulate these large amplitude LCO motions. Large and small initial condition disturbance transient responses clearly show the six inch peak-to-peak wingtip motions observed in the tests. Such large amplitude aeroelastic motions have not been demonstrated by RANS CFD codes which have difficulty maintaining grid cell structure for significant grid deformations. Figure 18 shows the map of the regions of LCO found in the MAVRIC test in the vicinity of the minimum FSI (clean wingtip, $\alpha = 6°$) [77]. Numbers for the several contours in the figure give the half-amplitude of wingtip LCO motions, in g's, in the indicated regions. Two regions, signified by 'B', are regions where 'beating' vibrations were observed. For this test condition, wing motions are predominantly of the wing first bending mode at a frequency of 7–8 Hz. (wind-off modal frequency is 4.07 Hz.). Two chimney features are seen, at M $\sim$ 0.91 and at M $\sim$ 0.94. Edwards discusses flutter model responses which are indicative of more complex nonlinear behaviors than are commonly attributed to LCO. Thus, flutter test engineers are familiar with responses such as 'bursting' and 'beating', commonly used as indicators of the approach to flutter (and LCO).

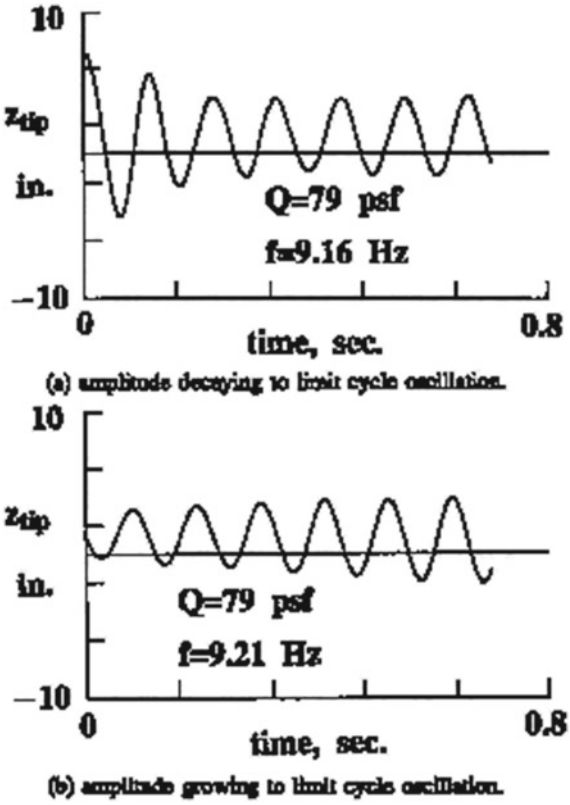

Fig. 17 Transient response leading to a LCO: simulation for mavric wing

4.5.5 Clipped-Tip Delta Wing Control Surface Buzz Model

Parker et al. [78] describe a test of a clipped-tip delta wing model with a full span control surface. The tests were conducted in air which is of concern since there are known to be severe Reynolds number and/or transition effects for this tunnel at dynamic pressures below 50–75 pounds per square foot. Pak and Baker [79] have performed computational studies of this case. They compare the experimental buzz boundary with time-marching transient responses calculated with the CFL3D-NS code and the CAP-TSDV code, respectively. Both codes capture LCO behavior near the experimental buzz conditions with the higher level code appearing to have better agreement for the experimental trend versus Mach number. The record lengths of a number of the responses, which are extremely expensive to compute, are not sufficient for clear determination of the response final status. Also, LCO behaviors can result from very delicate force balances and settling times to final LCO states can require many cycles of oscillation.

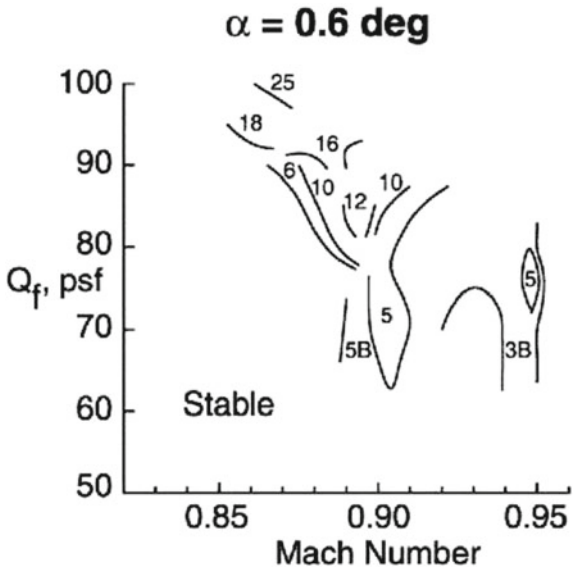

Fig. 18 Dynamic pressure versus mach number contours of constant LCO amplitude for mavric wing

4.5.6 Residual Pitch Oscillations on the B-2

The B-2 bomber encountered a nonlinear aeroelastic Residual Pitch Oscillation (RPO) during low altitude high speed flight [53]. Neither the RPO nor any tendency of lightly damped response had been predicted by wholly linear aeroelastic design methods. The RPO involved symmetric wing bending modes and rigid body degrees of freedom. It was possible to augment the CAP-TSDV aeroelastic analysis code with capability for the longitudinal short-period rigid body motions, vehicle trim, and the full-time active flight control system including actuator dynamics. This computational capability enabled the analysis of the heavyweight, forward center of gravity flight condition [53]. The simulation predicts open loop instability at $M = 0.775$ and closed loop instability at $M = 0.81$ in agreement with flight test. In order to capture the limit cycle behavior of the RPO it was necessary to include modeling of the nonlinear hysteretic response characteristic of the B-2 control surfaces for small amplitude motions. This is caused by the small overlap of the servohydraulic control valve spool flanges with their mating hydraulic fluid orifices. With this realistic actuator modeling also included, limited amplitude RPO motions similar to those measured in flight were simulated. A lighter weight flight test configuration exhibited very light damping near $M = 0.82$ but did not exhibit fully developed RPO. Instead damping increased with slight further increase in speed, typical of hump mode behavior. The CAP-TSDV simulations did not capture this hump mode behavior.

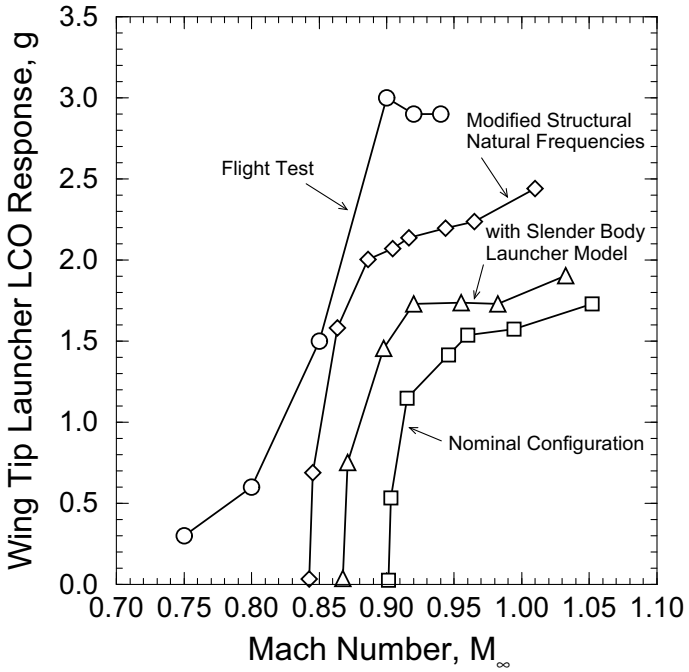

Fig. 19 F-16 configuration #1 computed and flight test forward wingtip launcher accelerometer LCO response level versus mach number for an altitude of 2000 feet and a mean angle-of-attack of $\alpha = 1.5^{\circ}$

4.5.7 F-16

In Fig. 19, a comparison of computational and flight test results is shown for Configuration #1 for both the flutter boundary and also for LCO response [69]. This is a plot of wing tip acceleration response versus Mach number at a fixed altitude of 2000 feet. The flight test results are shown by the curve with open circles. Three different computational results are shown. The curve with open squares shows the results for the nominal configuration with the aerodynamics of the stores neglected. The curve with open triangles includes the effects of the aerodynamics of the wing tip launcher using slender body aerodynamic theory. Note this curve is in better agreement with the flight test data. Finally the curve with open diamonds is for a one percent change in one of the structural frequencies. Here the computational model has been "tuned" to the experiment to give better agreement with the measured LCO frequency. That in turn has led to better agreement between computation and measurement for the LCO amplitude. Of course if a change in structural frequency in the opposite direction is made, this leads to poorer agreement between computations and flight test with the LCO response curve moving a similar amount from the nominal response but in the opposite direction. So what has been shown by the "tuning" is that the results for this configuration are sensitive to small plausible changes in the structural frequencies.

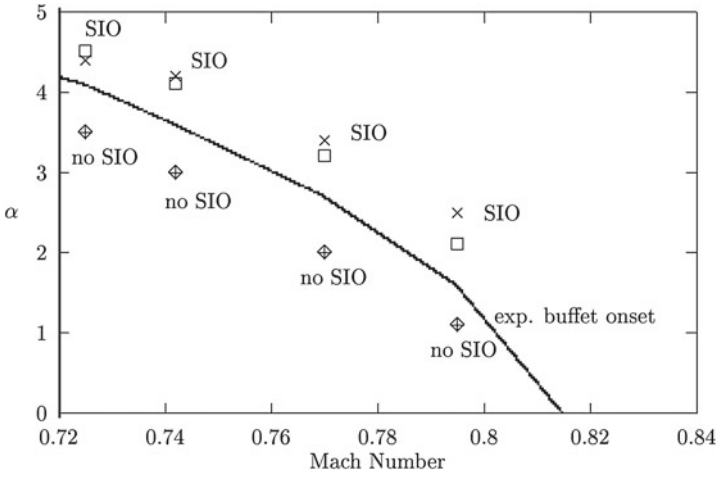

Fig. 20 Buffet boundary: angle of attack versus mach number

A final word about the correlation between computations and flight test is warranted. Note that the computations show a precise Mach number at which flutter and the onset of LCO occurs, i.e. when the wing tip acceleration is zero. This is because we have neglected the gust response of the aircraft to atmospheric turbulence as is traditional in flutter and LCO calculations. Of course in the flight test there is always some (small) response even when there is no flutter or LCO due to atmospheric turbulence. Thus it is impossible to define a precise Mach number at which flutter begins from the flight test data shown in Fig. 20. Indeed inferring a flutter Mach number from flight test data is a difficult art and requires a deeper study of the test data than simply a plot such as shown in Fig. 19. On the other hand, for the present purpose, this is not crucial. From Fig. 19, it is clear that neither flutter nor LCO is occurring for Mach numbers less than $M_\infty = 0.8$, but flutter onset and LCO do occur for Mach numbers greats than $M_\infty = 0.85$. And thus one can compare the computed flutter Mach number to this range from the test data. For LCO per se, the major goals are predicting the maximum LCO response level and the frequency and structural modal content of the LCO. The frequency and modal content are well predicted by the computational model [69], and the maximum response is reasonably well predicted as well for this configuration. See Fig. 19. Note in particular that both flight test and computations show the flutter and LCO motion is anti-symmetric.

4.5.8 Time Marching Codes Compared to Various Experimental Results

In the paper by Huttsell et al. [80] several state of the art time marching CFD codes are used to investigate flutter and LCO for challenging cases drawn from flight or wind tunnel tests. The CAP-TSD, CAP-TSDV, CFL3D and ENS3DAE codes are all used.

The results are extremely helpful in providing a realistic assessment of the state of the art of these codes and they are also indicative future needs and improvements. For the F-15 aircraft example, difficulty was encountered in producing a computational grid with negative volumes being encountered. For the AV8-B aircraft a steady state flow field could not be found due to oscillations in the numerical solver from one iteration to the next. These difficulties are not unusual for CFD codes in the present authors' experience. Sometimes the difficulty in achieving a steady flow solution is attributed to shedding in the flow field, but in the absence of a full nonlinear dynamic CFD calculation, that must remain a speculation. For the B-2 aircraft example encouraging agreement was obtained for the frequency and damping variation of the critical flutter (and LCO) mode as a function of flight speed using the CAP-TSDV code. For the B-1 estimates of the damping associated with LCO were computed using the CFL3DAE code and favorably compared to those found in wind tunnel tests. It is not entirely clear what the "damping" of an LCO means, however, since by definition LCO is a neutrally stable motion. Two control surface "buzz" cases were considered and CFL3DAE had some success in predicting the behavior observed in the wind tunnel for a NASP like configuration.

As Huttsell et al. [80] note, additional work is needed to improve CFD model robustness, computational efficiency and grid deformation strategies.

5 Aerodynamic LCO: Buffet, AWS and NSV

The aerodynamic flow field itself can become unstable even in the absence of any structural motion. Of course, once the flow field becomes unstable, then oscillations in the flow will begin and due to aerodynamic nonlinearities such as shock motion and/flow separation a limit cycle oscillation may (and usually will) occur. This purely aerodynamically generated LCO may then drive the structure into motion and the structural motion may in turn modify the LCO. Often in practice it is difficult to distinguish this type of LCO from one that occurs because of an inherent aeroelastically generated LCO in which the aerodynamic flow per se is stable. Of course in mathematical models this distinction can be (but is not always) made clear. But in a wind tunnel or flight test it is more difficult to distinguish between these two different LCO scenarios.

Even so, in recent years considerable progress has been made in understanding aerodynamically generated LCO and subsequent aeroelastic effects. This progress is briefly summarized here and the promise of greater progress in the future is substantial.

In classical aerodynamics the transition from laminar to turbulent flow is one of the most important examples of a steady (laminar) fluid flow becoming unstable and thus leading to a (turbulent) fluid flow LCO. Determining the properties of this LCO of turbulence remains one of the great unresolved issues of all of science and engineering. However there are also other examples of flow instabilities which go by such names as buffet, abrupt wing stall (AWS) and non synchronous vibration (NSV),

that have received much attention in aerospace (and other) research and engineering applications. Typically, in these examples the flow is already turbulent, but a further dynamic instability occurs whose intensity is far greater than typical turbulence (e.g. the oscillating lift coefficient is of order unity) and whose length scale is of the order of the airfoil or wing dimensions. By contrast, turbulence per se occurs over a great range of length scales including length scales much smaller than a wing chord or span and the intensity is a small fraction of the mean flow values.

Here we discuss the work of Edwards [81], Barakos [82] and Raveh [83–85] on buffet and are content to cite some of the key literature on AWS and NSV.

There is a well known experiment by McDevitt and Okuno [86] that considers the dynamic instability of the flow about a NACA 0012 airfoil in transonic flow conditions at certain prescribed angles of attack. The airfoil itself does not move, but the flow oscillates in what today might be called a limit cycle oscillation (LCO), but is more commonly referred to as a buffeting flow. Several investigators have undertaken computations to compare with these experiments. Edwards [77] has considered a potential flow model for the outer flow coupled to an integral boundary layer model and shown excellent agreement with the measured data for the buffet (LCO) boundary. This boundary is expressed in terms of angle of attack versus Mach number and separates the no buffet (no LCO) region from the buffet (LCO) region. Barakos [78] has also done an interesting study where various turbulence models are used in a Reynolds Averaged Navier-Stokes (RANS) computation and shown that the k-omega and Spalart-Allmaras turbulence models also give good correlation for the buffet (LCO) boundary and the buffet (LCO) frequency. Figure 20 is a comparison of the computed and measured buffet boundary from Barakos [78], who also shows that other commonly used turbulence models such as k-epsilon fail altogether to predict the buffet boundary. Hence buffet experiments [82] and correlations with computational models may give essential and fundamental insights into the required computational fluid dynamics (CFD) models for unsteady aerodynamic flows.

Very recently Raveh et al. [83–85] have studied the effect of a prescribed airfoil motion on a buffeting flow. Many interesting findings have been uncovered including the possibility of "lock-in". Lock-in occurs when response at the inherent flow buffet frequency is suppressed and the flow as well as the airfoil oscillates at the frequency of the prescribed airfoil motion. This occurs for certain combinations of the airfoil motion amplitude and frequency. The larger the airfoil motion, the wider the range of structural frequency (near the buffet flow frequency) for which lock-in will occur. Recently Raveh et al. [84] have considered the case of an elastically mounted airfoil which is free to move, but for which there is no prescribed motion. Again lock in is found under certain conditions. It is an open question of how often this may occur in wind tunnel tests or flight tests of aeroelastic systems. However the BACT wind tunnel model discussed earlier [65–68], an elastically mounted rigid wing with a NACA 0012 airfoil profile, is an intriguing example of where such oscillations may have occurred.

Figure 21 is from [85] and shows the time histories of lift on the NACA 0012 airfoil as the angle of attack is increased in prescribed steps of 0.5° from 4.5° and then decreased in steps starting from 8.5°. Outside the range of angle of attack for

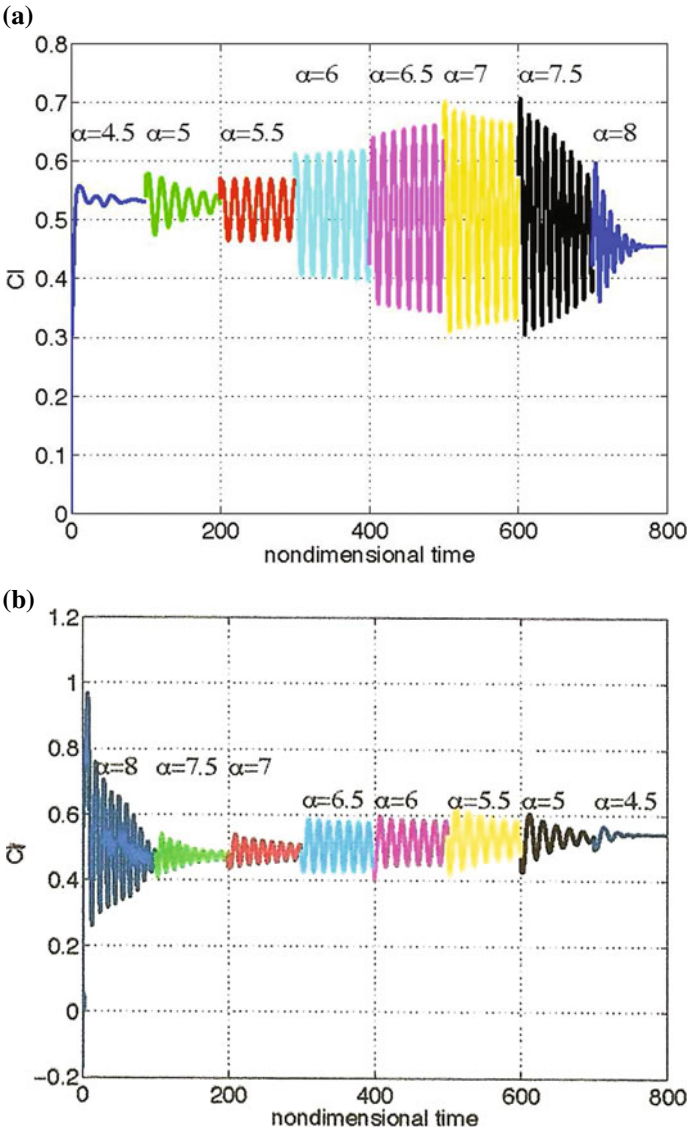

Fig. 21 **a** Lift coefficient versus time in response to the step-up increments to the mean flow angle of attack; Mach 0.72, Re 1E7. **b** Lift coefficient versus time in response to the step-down increments to the mean flow angle of attack; Mach 0.72, Re 1E7

which buffet occurs, a transient decay of the lift illustrates the approach to a time independent steady flow. By contrast, inside the range of angle of attack for which buffet occurs, the long time response is a periodic oscillation of the lift (and other flow variables).

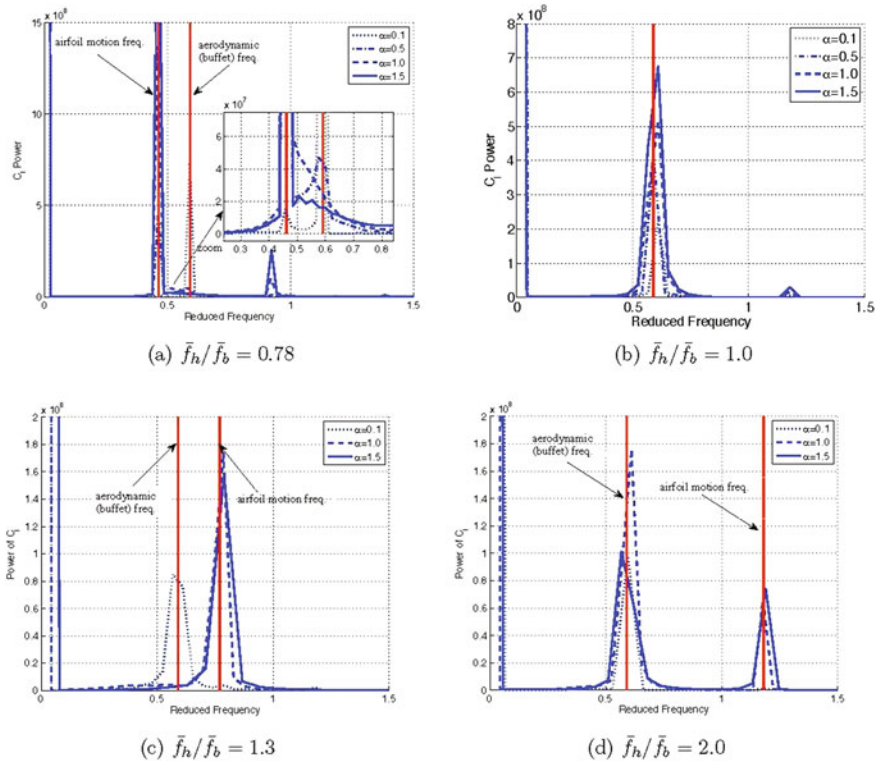

Fig. 22 Frequency content of lift coefficient response to prescribed airfoil motion of various amplitudes and frequencies: $\alpha_m = 6°$, Mach 0.72, Re 1E7

Then a prescribed airfoil motion is added and the effect of this motion on the buffet limit cycle oscillation is found. Figure 22 is also from [85] and shows the lift response on the airfoil for various cases of prescribed airfoil motion amplitudes and frequencies. This illustrates the approach to lock in when the frequency and amplitude of the prescribed motion are in the appropriate ranges. Figure 23 shows the range for which lock-in occurs in a plot of motion amplitude versus frequency.

The study of buffeting (and its counterparts of abrupt wing stall and non-synchronous vibration) appears ripe for even more significant advances and also suggests the need for further experiments building on the earlier wind tunnel tests of McDevitt and Okuno and the NASA Langley team with the BACT wind tunnel model. In particular the computational results suggest that one can exit the buffet region by continuing to increase the angle of attack at a given Mach number. Also the computational models are now capable of predicting the buffeting (LCO) amplitudes. Neither of these predictions have yet been validated by experiments, but these important issues could be addressed in new experiments that extend the earlier test results.

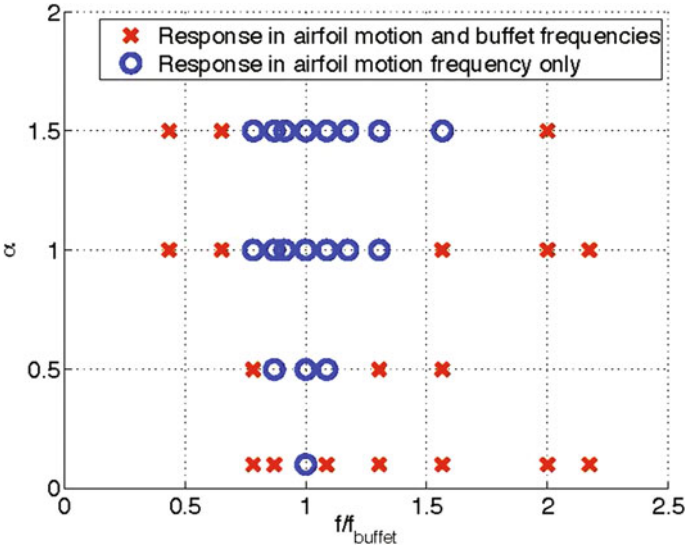

Fig. 23 Lock-in map of shock buffet; $\alpha_m = 6°$, Mach 0.72, Re 1E7

Abrupt Wing Stall (AWS) appears to be a particular form of buffet, but with two possible caveats. First of all, the instability of the aircraft flow field appears to be asymmetric and/or anti-symmetric with respect to the fuselage and thus gives rise to an oscillating rolling moment that leads to what is sometimes called "wing drop". At least a dozen distinct aircraft have encountered this phenomenon over several decades, but the ability to predict when it will occur is still beyond current computational modeling methods. Nevertheless there is real hope that this will become possible with a suitable CFD model in the near to mid-term future. Also it is still uncertain to what degree aeroelastic feedback is an issue including the rigid body motions in roll. Much of the recent work on AWS has been done in the context of the F-18 program which devoted very substantial effort to resolving this issue for that aircraft. For a summary and citation to recent literature, see for example [1].

Non-Synchronous Vibration (NSV) appears to be in substantial part a form of buffet encountered in turbomachinery. For an introduction to the literature on NSV, see [87]. It has also been called "Vortex Induced Vibration (VIV)". This first attempt by Duke University to investigate NSV was in 2003 by Kielb, Hall, Barter and Thomas. This study presented experimental evidence of NSV in the form of strain gauge data on a compressor test rig as well as unsteady casing pressure measurements. Using computational fluid dynamics, the NSV frequency was determined, and was within 9 percent of the experimental frequency. Other results from this study include identifying NSV as arising from an unsteady suction side vortex and a tip flow instability.

While a large-scale computational fluid dynamic simulation was a good way to search for NSV, Sanders points out in 2005 that the underlying flow physics must

first be understood, then increasingly complex configurations can be studied [88]. As a result, several works focused on cylinders, symmetric airfoils, and cascades, rather than full annulus compressors and turbines. In addition, advanced computational methods such as the Harmonic Balance method and Reduced Order Modeling (see chaps. 13 and 9 respectively) replace traditional time-marching simulations when applicable.

Spiker analyzed a cylinder under enforced motion near the lock-in region [89]. Lock-in occurs when the shedding frequency jumps onto the enforced frequency. This behavior was validated experimentally as well. Results agreed very well for a two-dimensional cylinder, moderately well for a two-dimensional airfoil, yet not so well for the three-dimensional case. In addition, the harmonic balance method was used to analyze the behavior of flow through cascades. The design methods resembled those of linear flutter analyses, but for the nonlinear behavior of LCO associated with NSV.

Clark's work primarily focused on coupled mode flutter; however, work was also completed on NSV [90]. He proposed a Reduced Order Model to study NSV around a cylinder. It was a coupled model, one degree of freedom captured the motion of a cylinder with mass, stiffness, and damping while the other captured the oscillatory motion of the wake. The latter utilized a Van der Pol Oscillator to capture the lock-in behavior of a cylinder experiencing NSV as well as a stable limit cycle oscillation (LCO). Clark later expanded on the model, incorporating Proper Orthogonal Decomposition (POD).

To further explore cylinders, Besem expanded on the work using POD to study cylinders vibrating transversely and in line with the flow [91]. It was concluded that transverse oscillations lead to alternating shedding while inline oscillations lead to symmetric shedding. These conclusions came from utilizing POD methods to create a ROM, which can predict results faster and as accurate as full computational models, requiring at least two degrees of freedom and two harmonics. In addition, Besem and Tang performed experimental studies on the lock-in region for a NACA 0012 airfoil [92]. They found that the lock-in region to experiments is wider, capturing the chaotic edge region between locked and unlocked. In addition, the locked-in region can be split into two groups: positive and negative equivalent aerodynamic damping.

Current work includes extending the van der Pol based ROM, further experimental studies, and more complex CFD simulations. Results by Hollenbach [93] show greater agreement to experimental LCO lock-in data using a 2 DOF ROM for a cylinder in transverse flow, utilizing system identification methods to tune the coefficients and including nonlinear stiffness terms. Figure 24 shows the improved results, which can be compared to those found in [94]. In addition, further studies on lock-in for the flow around a NACA 0012 airfoil are being conducted to develop an understanding of the behavior of the unsteady pressures for increasing oscillation amplitude.

One of the most interesting aspects of buffet is the relatively benign time signatures of the lift (and moment) oscillations on an airfoil or wing. See Fig. 21. The lift oscillation is not only periodic, but nearly simple harmonic. Yet this is a result of a nonlinear limit cycle oscillation of the fluid and involves substantial shock oscillations and in at least some cases separated flow. How can this be?

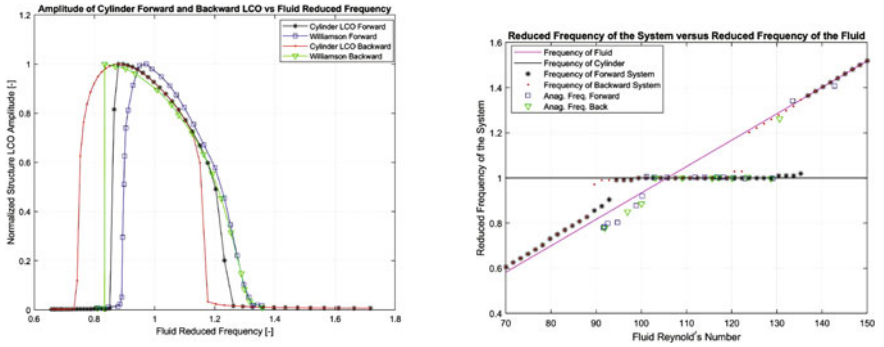

Fig. 24 Normalized LCO amplitude of ROM compared data. **a** Amplitude of cylinder forward and backward LCO versus fluid reduced frequency and **b** reduced frequency of the system versus fluid Reynold's number

Some years ago, Williams [95] showed using transonic potential flow theory that as the motion of an airfoil or wing becomes small, the shock displacement is linearly proportional to the airfoil or wing motion and the lift and moment (and indeed all generalized forces) are linearly proportional to the airfoil or wing motion. This is a remarkable result because the pressure distribution along the airfoil is highly nonlinear even for small motions if one examines a position on the airfoil over which the shock moves. Williams was able to show these results analytically for the potential flow model and subsequent numerical computations using Euler and Navier-Stokes fluid models have confirmed a similar result.

A recent paper by Woodgate and Badcock [96] has a nice result that graphically illustrates this point for an Euler flow model. At the many points along the airfoil that are not traversed by the shock motion, the pressure is nearly harmonic in time as illustrated by the nearly elliptical phase plane plot of pressure versus angle of oscillating motion of the airfoil (not shown here). On the other hand at the points along the airfoil that are traversed by the shock motion, the pressure time history although periodic has many higher harmonics as well. These computations were done using a harmonic balance method [3, 4] and Woodgate and Badcock show that many higher harmonics are indeed needed to resolve the local pressure time history when the point on the airfoil is traversed by the shock. In Fig. 25 results are shown for one, two, four, eight and sixteen harmonics. The good news for the modeling of aeroelastic systems is that the generalized forces including lift and moment do not usually have this higher harmonic content unless the airfoil or wing motions are very large (an effective angle of attack near the stall angle) because of the spatial filtering that occurs due to integration over the airfoil chord or wing area when computing lift, moment and other generalized forces.

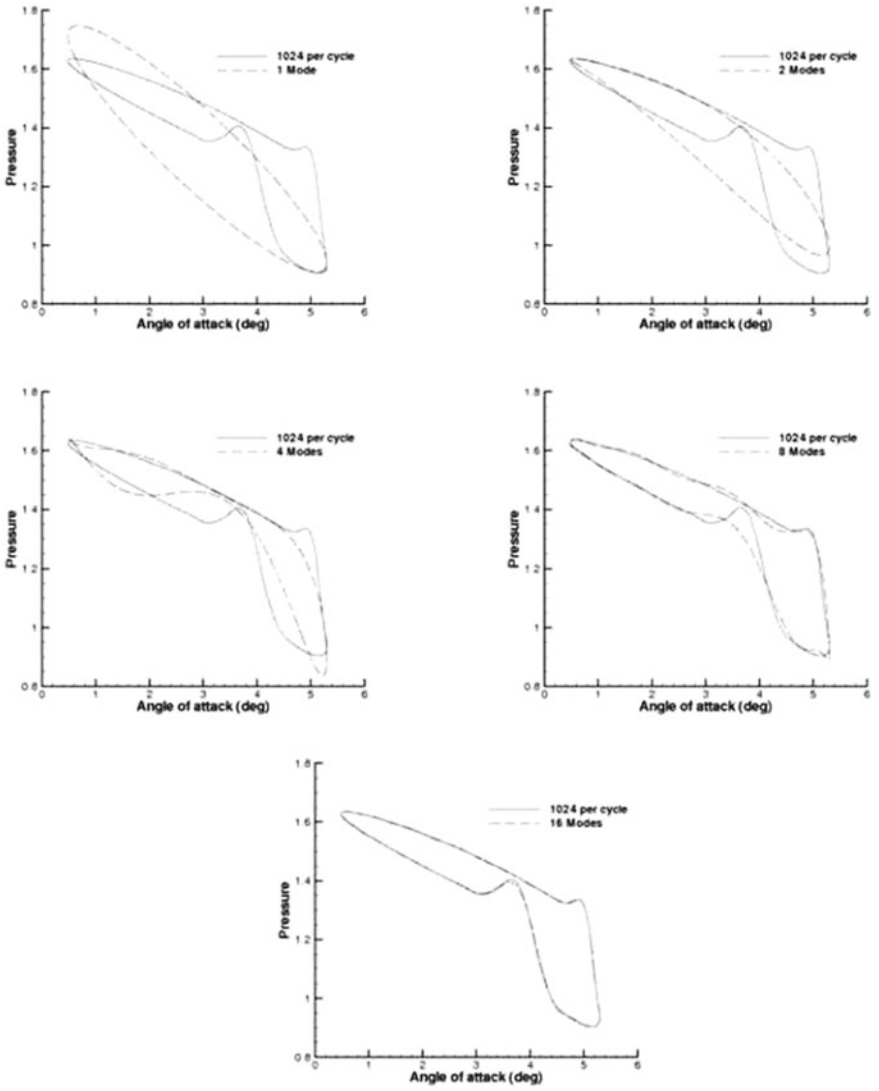

Fig. 25 Pressure versus angle of attack

6 Concluding Remarks

Substantial progress has been made in modeling and understanding nonlinear aeroelastic phenomena. Experimental and theoretical investigations have shown good correlation for a number of nonlinear physical mechanisms. As a broad generalization, one may say that our understanding of and correlation among alternative theoreti-

cal models and experiment is further advanced for nonlinear structural mechanisms such as freeplay and large deflection geometric nonlinearities of beams and plates, than it is for nonlinear fluid mechanisms such as large shock motions and separated flows. Nevertheless more accurate and much more computationally efficient theoretical models are now becoming available for nonlinear aerodynamic flows and there is cause for optimism in addressing these issues going forward.

As has been emphasized throughout this paper, a number of physical mechanisms can lead to nonlinear aeroelastic response including the impact of static (steady flow) fluid or static structural nonlinearities in changing the flutter boundary of an aeroelastic system. Of course dynamic nonlinearities play a critical role in the development of limit cycle oscillations, hysteresis in flutter and LCO response, and the sensitivity of both to initial and external disturbances.

The good news for the flight vehicle designer is that because of nonlinear aeroelastic effects, finite amplitude oscillations can in some cases replace what would otherwise be the rapidly growing and destructive oscillations of classical flutter behavior. A careful consideration and design of favorable nonlinearities offers a new opportunity for improved performance and safety of valuable wind tunnel models, flight vehicles, their operators and passengers.

Finally and inevitably some important topics have been omitted due to space and time limitations. The insightful article on rotorcraft aeroelasticity by Friedmann [97] is highly recommended; for turbomachinery aeroelasticity, see the authoritative volume edited by Hall, Kielb and Thomas [98] and for an entrée to the literature on morphing aircraft such as the folding wing concept see the paper by Attar et al. [99]. The work of Batina [100] on advanced concepts in transonic small disturbance potential flow theory and computation also reminds us that there are still valuable opportunities for significant advances in that field as well.

References

1. Dowell EH, Edwards JW, Strganac TW (2003) Nonlinear aeroelasticity. J Aircr 40(5):857–874
2. Dowell EH, Tang DM (2002) Nonlinear aeroelasticity and unsteady aerodynamics. AIAA J 40(9):1697–1707
3. Dowell EH, Hall KC (2001) Modeling of fluid-structure interaction. Annu Rev Fluid Mech 33:445–490
4. Lucia DJ, Beran PS, Silva WA (2004) Reduced-order modeling: new approaches for computational physics. Prog Aerosp Sci 40(1–2):51–117
5. Dowell EH, Clark R, Cox D, Curtiss HC Jr, Edwards JW, Hall KC, Peters DA, Scanlan R, Simiu E, Sisto F, Strganac TW (2004) A modern course in aeroelasticity, 4th edn. Kluwer Academic, Boston
6. Dowell EH, Tang DM (2003) Dynamics of very high dimensional systems. World Scientific, Singapore (See especially Chaps. 4, 13 and 14)
7. Hashimoto A, Aoyama T, Nakamura Y (2009) Effects of turbulent boundary layer on panel flutter. AIAA J 47(12):2785–2791
8. Dowell EH (1973) Aerodynamic boundary layer effects on flutter and damping of plates. J Aircr 10(12):734–738

9. Muhlstein L, Gaspers P, Riddle D (1968) An experimental study of the influence of the turbulent boundary layer on panel flutter. NASA TN D4486
10. Dugundji J, Dowell E, Perkin B (1963) Subsonic flutter of panels on a continuous elastic foundation. AIAA J 1(5):1146–1154
11. Dowell EH (1975) Aeroelasticity of plates and shells. Kluwer Academic Publishers, Dordrecht (See Appendix II)
12. Tang DM, Yamamoto H, Dowell EH (2003) Flutter and limit cycle oscillations of twodimensional panels in a three- dimensional axial flow. J Fluids Struct 17:225–242
13. Tang L, Paidoussis M, Jiang J (2009) Cantilevered flexible plates in axial flow: energy transfer and the concept of a Flutter-Mill. J Sound Vib 326:263–276
14. Hoffman NR (1955) Subsonic flutter model tests of an all-movable stabilizer with 35 degree sweepback. WADC Tech Note 55-623
15. Tang D, Dowell EH, Virgin LN (1998) Limit cycle behavior of an airfoil with a control surface. J Fluids Struct 12(7):839–858
16. Tang D, Dowell EH (2010) Aeroelastic airfoil with freeplay at angle of attack with gust excitation. AIAA J 48(2):427–442
17. Lee D, Chen P, Tang D, Dowell E (2010) Nonlinear gust response of a control surface with freeplay. AIAA 2010-3116, presented at the 51st AIAA SDM conference, Orlando
18. Schlomach C (2009) All-moveable control surface freeplay. NASA Langley Research Center, Hampton (Presentation to the Aerospace Flutter and Dynamics Council)
19. Lieu T, Farhat C, Lesoinne A (2006) Reduced-order fluid/structure modeling of a complete aircraft configuration. Comput Methods Appl Mech Eng 195(41–43):5730–5742
20. Lieu T, Farhat C (2007) Adaptation of aeroelastic reduced-order models and application to an F-16 configuration. AIAA J 45(6):1244–1257
21. Amsallem D, Farhat C (2008) Interpolation method for adapting reduced-order models and application to aeroelasticity. AIAA J 46(7):1803–1813
22. Romanowski MC (1996) Reduced order unsteady aerodynamic and aeroelastic models using kahunen-loeve eigenmodes [pod modes], AIAA paper 96-3981, presented at the AIAA/NASA/ISSMO symposium on multidisciplinary analysis and optimization. Bellevue, Washington
23. Hall KC, Thomas JP, Dowell EH (2000) Proper orthogonal decomposition technique for transonic unsteady aerodynamic flows. AIAA J 38(10):1853–1862
24. Thomas JP, Dowell EH, Hall KC (2003) Three-dimensional aeroelasticity using proper orthogonal decomposition based reduced order models. J Aircr 40(3):544–551
25. Dowell EH, Thomas JP, Hall KC (2004) Transonic limit cycle oscillation analysis using reduced order models. J Fluids Struct 19(1):17–27
26. Beran PS, Lucia DJ (2004) Reduced-order modeling of limit-cycle oscillation for aeroelastic systems. J Fluids Struct 19(5):575–590
27. Lucia DJ, Beran PS (2004) Reduced-order model development using proper orthogonal decomposition and Volterra theory. AIAA J 42(6):1181–1190
28. Mortara SA, Slater J, Beran P (2004) Analysis of nonlinear aeroelastic panel response using proper orthogonal decomposition. J Vib Acoust 126(3):416–421
29. Anttonen JSR, King PI, Beran PS (2005) Applications of multi-POD to a pitching and plunging airfoil. Math Comput Model 42(3–4):245–259
30. McMullen M, Jameson A (2006) The computational efficiency of non-linear frequency domain methods. J Comput Phys 212(2):637–661
31. McMullen M, Jameson A, Alonzo J (2006) Demonstration of nonlinear frequency domain methods. AIAA J 44(7):1428–1435
32. Timme S, Badcock K (2009) Implicit harmonic balance solver for transonic flow with forced motions. AIAA J 47(4):893–901
33. Hall KC, Thomas JP, Clark WS (2002) Computation of unsteady nonlinear flows in cascades using a harmonic balance technique. AIAA J 40(5):879–886
34. Thomas JP, Dowell EH, Hall KC (2004) Modeling viscous transonic limit cycle oscillations behavior using a harmonic balance approach. J Aircr 41(6):1266–1274

35. Beran PS, Lucia DJ (2005) A reduced order cyclic method for computation of limit cycles. Nonlinear Dyn 39(1–2):143–158
36. Liu L, Thomas JP, Dowell EH, Attar PJ, Hall KC (2006) A comparison of classical and high dimensional harmonic balance approaches for a duffing oscillator. J Comput Phys 215(1):298–320
37. Dowell EH, Hall KC, Thomas JP, Kielb RE, Spiker MA, Denegri Jr CM (2007) A new solution method for unsteady flows around oscillating bluff bodies. In: Proceedings of the IUTAM symposium on fluid-structure interaction in ocean engineering, Springer
38. Custer CH, Thomas JP, Dowell EH, Hall KC (2009) A nonlinear harmonic balance method for the CFD code OVERFLOW 2. In: International forum on aeroelasticity and structural dynamics, Seattle, paper 2009-050
39. Thomas JP, Custer CH, Dowell EH, Hall KC (2009) Unsteady flow computations using a harmonic balance approach implemented about the OVERFLOW 2 flow solver. In: 19th AIAA computational fluid dynamics conference, San Antonio, paper 2009-4270
40. Thomas JP, Dowell EH, Hall KC (2010) Using automatic differentiation to create nonlinear reduced order model aerodynamic solver. AIAA J 48(1):19–24
41. Thompson JMT, Stewart HB (1988) Nonlinear dynamics and chaos. Wiley, New York
42. Denegri CM Jr (1997) Correlation of classical flutter analyses and nonlinear flutter responses characteristics. In: International forum on aeroelasticity and structural dynamics, Rome, pp 141-148
43. Denegri CM Jr, Cutchins MA (1997) Evaluation of classical flutter analysis for the prediction of limit cycle oscillations. AIAA paper 97-1021
44. Denegri CM Jr (2000) Limit cycle oscillation flight test results of a fighter with external stores. J Aircr 37(5):761–769
45. Denegri CM Jr, Johnson MR (2001) Limit cycle oscillation prediction using artificial neural networks. J Guidance Control Dyn 24(5):887–895
46. (1974) AGARD Specialists meeting on wings-with-stores flutter, 39th meeting of the structures and materials panel, AGARD conference proceedings no 162, Munich
47. Bunton RW, Denegri CM Jr (2000) Limit cycle oscillation characteristics of fighter aircraft. J Aircr 37(5):916–918
48. Cunningham AM Jr (1999) A generic nonlinear aeroelastic method with semi-empirical nonlinear unsteady aerodynamics, vol 1 and 2, AFRL-VA-WP-R-1999-3014
49. Cunningham AM Jr (1998) The role of nonlinear aerodynamics in fluid-structure interactions, AIAA paper 98-2423
50. Cunningham AM Jr, Geurts EGM (1998) Analysis of limit cycle oscillation/transonic high alpha flow visualization, AFRL-vA-WP-TR-1998-3003, Part I
51. Dobbs SK, Miller GD, Stevenson JR (1985) Self induced oscillation wind tunnel test of a variable sweep wing, AIAA paper 85-0739-CP presented at 26th AIAA/ASME/ASCE/AHS structures, structural dynamics and materials conference, Orlando, pp 15–17
52. Hartwich pM, Dobbs SK, Arslan AE, Kim SC (2000) Navier-stokes computations of limit cycle oscillations for a B-1-like configuration, AIAA paper 2000-2338, AIAA Fluids 2000, Denver
53. Dreim DR, Jacobson SB, Britt RT (1999) Simulation of non-linear transonic aeroelastic behavior on the B-2, NASA CP-1999-209136. CEAS/AIAA/ICASE/NASA Langley international forum on aeroelasticity and structural, Dynamics, pp 511–521
54. Croft J (2001) Airbus elevator flutter: annoying or dangerous? Aviation week and space technology
55. Dowell EH (1975) Aeroelasticity of plates and shell. Kluwer Academic, Dordrecht
56. Dowell EH (1972) Panel flutter. NASA Special Publication, Washington (SP-8004)
57. Yurkovich RN, Liu DD, Chen PC (2001) The state-of-the-art of unsteady aerodynamics for high performance aircraft, AIAA paper 2001-0428, aerospace sciences conference
58. Bennett RM, Edwards JW (1998) An overview of recent developments in computational aeroelasticity, AIAA paper no. 98-2421, presented at the AIAA fluid dynamics conference, Albuquerque

59. Farhat C, Lesoinne M (1998) Enhanced partitioned procedures for solving nonlinear transient aeroelastic problems. AIAA Paper 98-1806
60. Raveh DE, Levy Y, KarpelM, (2001) Efficient aeroelastic analysis using computational unsteady aerodynamics. J Aircr 38(3):547–556
61. Thomas JP, Dowell EH, Hall KC (2001) Three-dimensional transonic aeroelasticity using proper orthogonal decomposition based reduced order models, AIAA Paper 2001-1526, presented at 42nd AIAA/ASME/ASCE/AHS/ASC structures, structural dynamics, and materials conference and exhibit, Seattle, pp 16-19
62. Gupta KK (1996) Development of a finite element aeroelastic analysis capability. J Aircr 33(5):995–1002
63. Scott RC, Silva WA, Florance JR, Keller DF (2010) Measurement of unsteady pressure data on a large HSCT semi-span wing and comparison with analysis, AIAA, pp 2002–1648
64. Silva WA, Keller DF, Florance JR, Cole SR, Scott RC (2000) Experimental steady and unsteady aerodynamic and flutter results for HSCT semi-span models. In: 41st structures, structural dynamics and materials conference, AIAA, no 2000–1697
65. Bennett RM, Eckstrom CV, Rivera JA Jr, Danberry BE, Farmer MG, Durham MH (1991) The benchmark aeroelastic models program: description and highlights of initial results, NASA TM 104180
66. Bennett RM, Scott RC, Wieseman CD (2000) Computational test cases for the benchmark active controls model. J Guidance Control Dyn 23(5):922–929
67. Kholodar DE, Dowell EH, Thomas JP, Hall KC (2004) Limit-Cycle oscillations of a typical airfoil in transonic flow. J Aircr 41(5):911-917 (AIAA)
68. Schwarz JB, Dowell EH, Thomas JP, Hall KC, Rausch RD, Bartels RE (2009) Improved flutter boundary prediction for an isolated two degree of freedom airfoil. J Aircr 46(6):2069–2076
69. Thomas JP, Dowell EH, Hall KC (2009) Theoretical predictions of limit cycle oscillations for flight flutter testing of the f-16 fighter. J Aircr 46(5):1667–1672
70. Dowell EH, Tang D (2002) Nonlinear aeroelasticity and unsteady aerodynamics. AIAA J 40(9):1697–1707
71. Gordnier RE, Melville RB (1999) Physical mechanisms for limit-cycle oscillations of a cropped delta wing. AIAA Paper, Norfolk
72. Gordnier RE, Melville RB (2001) Numerical simulation of limit-cycle oscillations of a cropped delta wing using the full Navier-stokes equations. Int J Comput Fluid Dyn 14(3):211–224
73. Schairer ET, Hand LA (1997) Measurement of unsteady aeroelastic model deformation by stereo photogrammetry, AIAA Paper 97-2217
74. Thomas JP, Dowell EH, Hall KC (2002) A harmonic balance approach for modeling three-dimensional nonlinear unsteady aerodynamics and aeroelasticity, IMECE-2002-32532. Presented at the ASME international mechanical engineering conference and exposition, New Orleans, Louisiana
75. Edwards JW (1998) Calculated viscous and scale effects on transonic aeroelasticity, paper no.1 in Numerical unsteady aerodynamic and aeroelastic simulation. AGARD Report 822
76. Edwards JW, Schuster DM, Spain CV, Keller DF, Moses RW (2001) MAVRIC flutter model transonic limit cycle oscillation test, AIAA p 2001-1291
77. Edwards JW (1996) Transonic shock oscillations and wing flutter calculated with an interactive boundary layer coupling method, NASA TM-110284
78. Parker EC, Spain CV, Soistmann DL (1991) Aileron buzz investigated on several generic NASP wing configurations, AIAA Paper 91-0936
79. Pak C, Baker ML (2001) Control surface buzz analysis of a generic NASP wing, AIAA Paper 2001-1581
80. Huttsell L, Schuster D, Volk J, Giesing J, Love M (2001) Evaluation of computational aeroelasticity codes for loads and flutter, AIAA Paper 2001-569
81. Edwards JW (2008) Calculated viscous and scale effects on transonic aeroelasticity. J Aircr 45(6):1863–1871

82. Barakos G, Drikakis D (2000) Numerical simulation of transonic buffet flows using various turbulence closures. Int J Heat Fluid Flow 21:620–626
83. Raveh D (2009) A numerical study of an oscillating airfoil in transonic buffeting flows. AIAA J 47(3):505–515
84. Raveh D, Dowell EH (2009) Aeroelastic response of airfoil in buffeting transonic flows. In: International forum on aeroelasticity and structural dynamics, Seattle, IFASD-2009-161
85. Raveh D, Dowell EH (2012) Frequency lock-in phenomenon for oscillating airfoils in buffeting flows. Accept Publ J Fluids Struct
86. McDevitt JB, Okuno AF (1985) Static and dynamic pressure measurements on a NACA 0012 airfoil in the AMES high Reynolds number facility, NASA TP 2485
87. Kielb R, Barter JT, Hall KC (2003) Blade excitation by aerodynamic instabilities-a compressor blade study, ASME GT-2003-38634, ASME Turbo Expo Conference
88. Sanders AJ (2005) Nonsynchronous vibration (NSV) due to a flow-induced aerodynamics instability in a composite fan stator. ASME
89. Spiker M (2008) Development of an efficient design methods for non-synchronous vibrations. Doctoral dissertation. Duke University
90. Clark S (2013) Design for coupled-mode flutter and non-synchronous vibration in turbomachinery. Doctoral dissertation. Duke University
91. Besem F (2015) Aeroelastic instabilities due to unsteady aerodynamics. Doctoral dissertation. Duke University
92. Besem F, Kamrass J, Thomas J, Tang D, Kielb R (2016) Vortex-induced vibration and frequency lock-in of an airfoil at high angles of attack. J Fluids Eng. ASME
93. Hollenbach, R, Kielb, R, Hall, K (2022) Extending a van der pol based reduced-order model for fluid-structure applied to non-synchronous vibrations in turbomachinery. J Turbomach. pp 1–14
94. Clark S, Kielb R, Hall K (2013) A Van Der Pol based reduced-order model for nonsynchronous vibration (NSV) in turbomachinery. ASME, Turbo Expo
95. Williams MH (1979) Linearization of unsteady transonic flows containing shocks. AIAA J 17(4):394–397
96. Woodgate MA, Badcock KJ (2009) Implicit harmonic balance solver for transonic flow with forced motions. AIAA J 47(4):893–901
97. Friedmann PO (2004) Rotary-wing aeroelasticity: current status and future trends. AIAA J 42(10):1953–1972
98. Hall KC, Kielb RE, Thomas JP (eds) (2003) Unsteady aerodynamic, aeroacoustics and aeroelasticity of turbomachines. In: Proceedings of the 10th international symposium held at Duke University. Springer
99. Attar P, Tang D, Dowell EH (2009) Nonlinear aeroelastic study for folding wing structures, presented at the NATO AVT-168 symposium on morphing structures
100. Batina J (2005) Introduction of the asp3d computer program for unsteady aerodynamics and aeroelastic analyses, NASA TM-2005-213909

Aeroelastic Models Design/Experiment and Correlation with New Theory

Deman Tang and Earl H. Dowell

Abstract Several examples of experimental model designs, wind tunnel tests and correlation with new theory are presented in this chapter. The goal is not only to evaluate a new theory, new computational method or new aeroelastic phonomenon, but also to provide new insights into nonlinear aeroelastic phenomena, flutter, limit cycle oscillation (LCO), gust response and energy harvesting from a large flapping flag response. The experiments are conducted in a standard low speed wind tunnel. Similar experiments in a high speed wind tunnel would be very valuable.

1 Introduction

A very important function of wind tunnel models and testing is to verify a new aeroelastic theory or a new computational method. For this purpose, experimental aeroelastic model design and manufacturing of scaled models, model ground vibration test and wind tunnel testing are essential to success. In the past 20 years, the Duke aeroelastic group has designed many aeroelastic models and conducted wind tunnel tests to evaluate new theoretical aeroelastic theories and new computations methods. They include:

1. A high aspect ratio wing model. Several correlation studies for flutter and limit cycle oscillation [1], limit cycle hysteresis response [2], gust response for clamped and flexibly suspended models [3, 4] and Flutter/LCO suppression [5] were performed.
2. Wing like plate models, delta wing-store, flapping flag, yawed plate and folding wing. The wind tunnel tests were used to evaluate the von Karman nonlinear plate theory and a new nonlinear inextensible beam and plate theory and also some high

D. Tang · E. H. Dowell (✉)
Mechanical Engineering and Materials Science Duke University, Durham, NC, USA
e-mail: earl.dowell@duke.edu

D. Tang
e-mail: demantang148@gmail.com

E. H. Dowell (ed.), *A Modern Course in Aeroelasticity*, Solid Mechanics and Its Applications 264, https://doi.org/10.1007/978-3-030-74236-2_15

fidelity computational methods. Based on these models several correlation studies for flutter/LCO [6–16] and gust response studies [17–19] were performed.

3. Airfoil section with control surface freeplay. The wing tunnel tests were used to evaluate new approachs for the freeplay nonlinear and gust responses including Duke computational codes using the Peter's finite state airload aerodynamic theory, harmonic balance method and the time marching integration based on state space equations [20–24] and the ZAERO code [25] based on the computational fluid dynamic (CFD) theory conducted by ZONA Technology, Inc.
4. All-movable tail with freeplay model at the root [26, 27] to similar horizontal tail in the actuating mechanism freeplay nonlinearity of aircraft. Based on this model a computational code has been developed and evaluated.
5. A free-to-roll fuselage flutter model [28]. From measured wind tunnel data, one evaluates the predicted symmetric and anti-symmetric flutter/LCO theory.
6. A experimental oscillating airfoil model at high angles of attack for measuring aerodynamic response. A frequency "Lock-in" phenomenon is found in buffeting flow and compared to the theoretical results [29]. Also a experimental airfoil model with a partial-span control surface is conducted to measure the flap response of the partial-span induced by the buffeting flow [30].
7. The structural design of RSC/airfoil gust generator that is used to create a lateral gust in the Duke University low speed wind tunnel has been developed. The design principle of this generator has been verified by the coorelation between the experimental and numerical simulation when the RSC rotating angle is statically rotated from 0° to 180°, see [59, 60]. Using this gust generator, the theoretical and experimental correlation study of gust response for a high-aspect-ratio wing model was used to evaluate the gust flowfield and nonlinear beam structural theory.
8. Two experimental models are constructed, i.e. partially covered and fully covered, cantilevered plates with piezoelectric patch and film sensor that are used to study energy harvesting from a large flapping flag response, see [63–65]. Two different experimental methods are used to obtain large flapping vibrations, a mechanically forced vibration and a limit cycle oscillation from an aeroelastic responses. AC voltage outputs from the piezo patch or film sensors and a DC power extraction through a AC/DC convert circuit are obtained. These experiments are used to evaluate a new computational model and code for an aero-electromechanical interaction system.

Several examples of model designs, wind tunnel tests and experimental/theoretical correlation studies with the theory are presented in this chapter. The goal is not only to evaluate a new theory, new computational method or new aeroelactic phonomenon, but also to provide new insights into nonlinear aeroelastic phenomena, flutter/LCO and gust response and energy harvesting.

2 Experimental Models for Measuring Flutter/Limit Cycle Oscillation (LCO) Response to Evaluate A Nonlinear Structural Theory

Theoretical and experimental correlation study for the aeroelastic stability and response of an aircraft with a high-aspect-ratio wing and low-aspect-ratio wing have been studied for many years from subsonic to supersonic flow. Most investigators have used linear beam and plate theories to simplify the wing structural model. However, a geometric structural nonlinearity may arise from the coupling between elastic flap or vertical bending, chordwise or edgewise bending and torsion for very high aspect ratio wings typical of Uninhabited Air Vehicles (UAV) and also for the low aspect ratio wings. Here, two kinds of experimental wing models, a high altitude long endurance (HALE) model and a wing-like (plate) model are considered to evaluate the new nonlinear structural theories.

2.1 High Altitude Long Endurance Models (Nonlinear Beam Structural Theory and ONERA Aerodynamic Model)

An experimental high-aspect ratio wing aeroelastic model with a tip mass has been constructed and a wind tunnel test conducted to measure the static aeroelastic response, flutter and limit cycle oscillations. The goal is to assess experimentally the theoretical results using nonlinear structural and aerodynamic theories. The theoretical structural equations of motion are based on nonlinear beam theory by Hodges and Dowell [31] and the ONERA aerodynamic stall model [32].

The experimental model includes two parts: a high-aspect ratio wing with a slender body at the tip and a root support mechanism. The wing is rectangular, untwisted and flexible in the flap, lag and torsional directions. The wing is constructed from a precision ground flat steel spar with mass uniformly distributed along the wing span. The spar is 45.72 cm in length, 1.27 cm in width and 0.127 cm in thickness. It is inserted tightly into the wing root mechanism. In order to reduce torsional stiffness, the spar has multiple thin flanges along the span. The flange width is 0.127 cm and it is 0.318 cm in deep. There are 2×33 flanges uniformly and symmetrically distributed along the wing span and center line of the spar. There are 18 pieces of NACA 0012 airfoil plate uniformly distributed along the span. The pieces of the airfoil plate are made of aluminum alloy with 0.254 cm thickness. A precision aerodynamic contour of the wing model is obtained. Each airfoil plate has a slot 1.27 cm in width and 0.127 cm in thickness at the symmetry line. The spar is inserted through these airfoil plate slots and they are permanently bonded together. Each space between two airfoil plates is filled with a light wood (bass) covering the entire chord and span which provides the aerodynamic contour of the wing. This wood provides a slight additional mass and a small addition to the bending and torsion stiffness.

A slender body is attached to the elastic axis of the wing tip. The slender body is an aluminum bar, 0.95 cm in diameter and 10.16 cm in length. A paraboloidal forebody and an aftbody with 1.14 cm length are fixed to two ends of the bar. The forebody and aftbody are made of brass.

The slender body is symmetrical and is designed to provide enough torsional inertia to reduce the natural torsional frequency sufficiently to induce flutter in the velocity range of the wind tunnel.

The root support mechanism is a socket that allows a change of the steady angle of attack at the root. The root socket is mounted to the mid point of side-wall of the wind tunnel

Figure 1a shows a photograph of the aeroelastic wing model in the wind tunnel.

Axial strain gages for bending modes and a 45° oriented strain gage for torsional modes were glued to the root spar to measure the bending-torsional deflections of the wing. Signals from the strain gages were conditioned and amplified before their

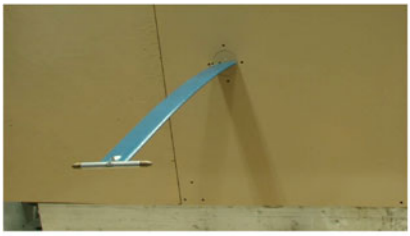

(a) Photograph

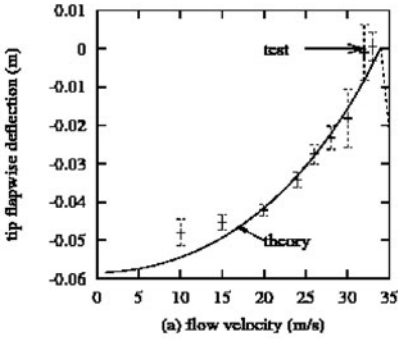

(b) Static deflection

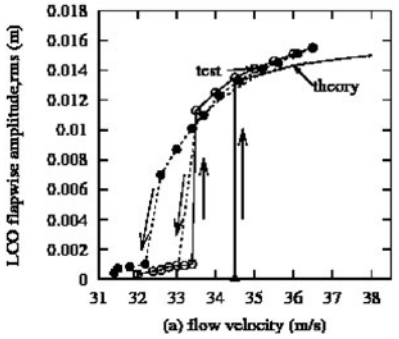

(c) LCO amplitude

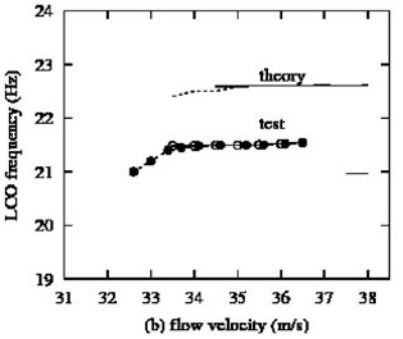

(d) LCO frequency

Fig. 1 HALE experimental model and correlation analyses; **a** photograph of model, **b** static aeroelastic deflections at the wing tip **c** LCO amplitude, **d** LCO frequency versus flow velocity for pitch angle of attack $\theta_0 = 1.0°$

Table 1 Experimental wing model data

Wing properties	
Span (L)	0.4508 m
Chord (c)	0.0508 m
Mass per unit length	0.2351 kg/m
Mom. Inertia (50% chord)	0.2056×10^{-4} kgm
Spanwise elastic axis	50% chord
Center of gravity	49% chord
Flap bending rigidity (EI_1)	0.4186 Nm^2
Chordwise bending rigidity (EI_2)	0.1844×10^2 Nm^2
Torsional rigidity (GJ)	0.9539 Nm^2
Flap structural modal damping (ξ_W)	0.02
Chordwise structural modal damping (ξ_v)	0.025
Torsional structural modal damping (ξ_ϕ)	0.031
Slender body properties	
Radius (R)	0.4762×10^{-2} m
Chord length (c_{SB})	0.1406 m
Mass (M)	0.0417 kg
Mom. Inertia (I_x)	0.9753×10^{-4} kgm^2
Mom. Inertia (I_y)	0.3783×10^{-5} kgm^2
Mom. Inertia (I_z)	0.9753×10^{-4} kgm^2

measurement through a gage conditioner and a low-pass filter. A micro-accelerometer is mounted at the mid-span of the wing. The output signals from these transducers are directly recorded on a computer with data-acquisition and analysis software, Lab-VIEW 5.1.

A Helium-Neon Laser with 0.8mw randomly polarized and wavelength 633 (nm) is mounted on the top of the tunnel. The top of the tunnel is made of a glass plate with a thickness of 1.27 cm. A mirror, 1.27 cm in diameter, is fixed on the tip of the wing. A "mirror" deflection technique is used to determine the geometric twist angle and the vertical or flapwise bending slope at the wing tip.

All static, flutter and LCO response tests were performed in the Duke University low speed wind tunnel. The wind tunnel is a closed circuit tunnel with a test section of $0.7 \times 0.53\,\mathrm{m}^2$ and a length of 1.52 m. The maximum air speed attainable is 89.3 m/s.

The basic parameters of the experimental wing model were obtained from standard static and vibration tests and are listed in the Table 1.

We use a "mirror" deflection technique to measure the tip static aeroelastic deflections of the wing. A point determined by a reflected light source is marked on a readout grid paper placed on the top of the wind tunnel when the wing is undeflected. The readout grid paper is calibrated in the tip flap and twist deflections before the test.

The reflected light source point with wing deflection as marked on the readout paper is then determined as the flow velocity is varied.

Figure 1b shows the the theoretical and experimental results of the tip flapwise deflection for a steady angle of attack, $\theta_0 = 1°$. The solid line indicates the theoretical results and the bar indicates the measured data. The experimental data appear have some scatter due to the turbulent aerodynamic noise, although the noise is small. A very high measurement sensitivity is obtained from the mirror technique. We use a bar in the figure to indicate the magnitude of the response uncertainty. As shown Fig. 1b, the tip deflection increase with increasing flow velocity, but the tip deflection is always negative until the flow velocity reaches 34.5 m/s. At that velocity the aerodynamic forces provide sufficient lift to overcome the effect of gravity. At $U = 34.5$ m/s, the system enters into the flutter instability range. The consequent LCO has a certain non-zero mean or temporal average and this is shown by a dashed line in Fig. 1b. Also with LCO, aerodynamic stall occurs and the lift coefficient C_l suddenly decreases. The measured data in Fig. 1b are acquired before the onset of flutter and LCO. The experimental data fall near the theoretical curves in Fig. 1b. In general, the agreement is good except for some points at $U = 10$ and 15 m/s. In the higher flow velocity range, the data fluctuation increases due to greater aerodynamic turbulence.

A typical LCO amplitude and LCO frequency versus flow velocity for $\theta_0 = 1°$ and at the mid span position are shown in Fig. 1c and d, respectively. The theoretical and experimental amplitudes are taken as rms average values from a 50 s sampling interval. The symbols, $\circ$ and $\bullet$, indicate the experimental results for increasing and decreasing flow velocity, respectively. The solid and broken lines (without symbols) indicate the theoretical results for increasing and decreasing flow velocity, respectively. The symbol, $\triangle$, indicates the linear flutter velocity which is calculated from the perturbation eigenvalue solution. For the increasing flow velocity case, the theoretical limit cycle oscillation occurs when the flow velocity is larger than the perturbation flutter velocity and the amplitude has a jump from almost rest to a larger value. Once the onset of LCO occurs, the amplitude increases smoothly with increasing the flow velocity. When $U > 38.6$ m/s, a numerical or possibly a physical divergence is found in the theoretical model. For the case of decreasing flow velocity, as shown by the broken line, the LCO amplitude decreases, but does not exactly coincide with those for the increasing velocity case. Also there is a jump in the LCO response at $U = 33.5$ m/s which is a distinctly lower velocity than that found for the increasing velocity case (i.e. $U = 34.5$ m/s).

The present experimental and theoretical results provide new insights into nonlinear aeroelastic phenomena of LCO beyond the linear flutter speed for high aspect ratio wings. Also these results show the nonlinear equations and stall aerodynamic equations provided by Hodges and Dowell and ONERA, respectively, provide useful and accurate results for HALE vehicles.

2.2 *Flapping Flag and Yawed Plate Models (Nonlinear Inextensible Beam and Plate Theory)*

There is a substantial literature on inextensible beam theory, but relatively little on inextensible plate theory. A notable exception is the work of J. G. Simmonds and colleagues [33–36] on inextensible plate theory. His approach is quite different from the present one and ultimately leads to a system of ordinary differential equations for the plate deformation for a one dimensional generator curve from which the entire plate deformation may then be deduced. In the present new inextensible theory of beam and plate deformation as described in [37], the formulation is based upon Hamilton's Principle in terms of a single unknown, i.e. the beam or plate deformation normal to its surface. The present approach has some substantial computational advantages, but certainly the work of Simmonds is elegant and pioneering.

The interaction between a cantilevered elastic plate and a uniform axial flow is a canonical fluid-structure interaction problem. If the flow is oriented *parallel* to the clamped leading edge the system is described as a wing-like configuration. If the flow is oriented *normal* to the clamped edge then the system is referred to as flag-like. There is extensive research on the aeroelastic response of the wing-like configuration due to the similarities between the simple cantilevered beam and aircraft wings. The present study differs from the classic explorations of the swept wing due to the application of the clamped boundary condition. For a traditional swept wing configuration the clamp is applied parallel to the flow, changing the shape of the structure for every angle (it is called the yaw angle, β, in the present paper). For the current study the clamped edge is rotated with the structure. In this case the second classic fluid structure interaction problem for a clamped-free elastic plate will be considered, i.e. the flag-like configuration.

References [12, 13] focus on exploring the transition of the limit cycle oscillation (LCO) response from a small yaw angle (flapping flag response for $\beta = 0$) to a large yaw angle (wing-like response, $\beta = 90°$) of a cantilever plate as the angle between the clamped edge and free stream velocity changes. In particular, [37] presents a nonlinear structural model for the rotated aeroelastic system. One creates the aeroelastic model by coupling this newly developed inextensible nonlinear plate structural model with a rotated vortex lattice aerodynamic model. The theoretical predictions were validated with aeroelastic experiments. Three distinct configurations, $\beta = 0°, 45°$ and $90°$ were explored that show markedly different LCO transition behaviors.

Table 2 contains the material properties and geometry of the configuration. Table 3 shows the results of the ground vibration experiments in bending and torsion. The first column has the theoretical predictions using a ANSYS structural model with the parameters listed in Table 2. There is very good agreement between the theory (ANSYS code) and the experiment for all of the bending and torsion modes.

The goal of the aeroelastic experiments was to quantify the LCO amplitude of the flapping flag ($\beta = 0°$) as shown in Fig. 2a. To capture the LCO amplitude, a Light Emitting Diode, LED, was placed at the tip and mid-span of the structure. Using 3D

Table 2 Experimental plate properties

ρ_s	E	h	L	C
2840 kg/m^3	70.6E9 N/m^2	0.381 mm	275 mm	151 mm

Table 3 Vibration test results

Mode	ANSYS code Freq (Hz)	Experiment Freq (Hz)	Error (%)
1st Bending	4.16	3.95	5.06
2nd Bending	25.84	24.98	3.3
3rd Bending	72.12	69.91	3.06
4th Bending	144.06	142.37	1.1
1st Twist	15.91	15.13	3.45
2nd Twist	45.73	49.05	7.16

RPS video the path of the LED can be traced. Additionally the color coherence of the LED light, made it easier to use automated filtering in Matlab to track the path. To determine the amplitude of the oscillation, the code averages the snapshots from a full second of the video (30 frames) to get the average path. The script then automatically identifies the pixel of the far left and far right portion of the path and calls this the LCO amplitude. This amplitude is then synchronized with the wind tunnel velocity data to get the amplitude as a function of the velocity. The amplitude is converted to a real length using the camera calibration conducted before the experiment that calculates the pixels per centimeter in the plane of the LED. This method is able to provide the LCO amplitude to +/− 1 cm. This could be improved by using a camera with a higher resolution. For the detail experimental measurement, see Ref. [12].

The experimental data are presented as the measured nondimensional peak displacement from the panel tip. Figure 2b shows the nondimensional rms flap amplitude versus the flow velocity. The theoretical results include two nonlinear cases: a full stiffness nonlinearity only and a full stiffness nonlinearity plus an inertia nonlinearity. The experimental results contain the LCO amplitude data for all of three different runs. The theoretical LCO responses are bursts or intermittent motion while the experimental results are primarily a single harmonic oscillation.

The experimental linear flutter speed can be estimated using an extrapolation method (this method is also used for other yaw angles), i.e. an extrapolation of LCO response to zero amplitude. The experimental flutter speed is $U_f = 21.35$ m/s and the theoretical flutter speed is $U_f = 20.45$ m/s for $\beta = 0°$.

It is interesting that the theoretical results for the full nonlinearities (inertia plus stiffness) agree best with experiment for the LCO amplitude. However when only

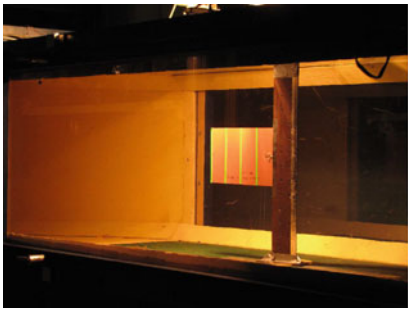

(a) $\beta = 0^0$

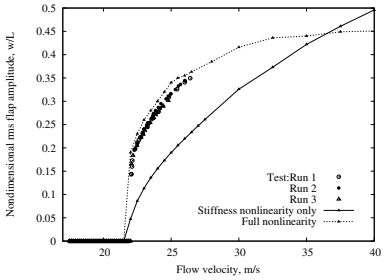

(b) RMS amplitude

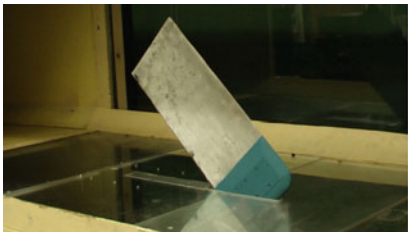

(c) $\beta = 45^0$

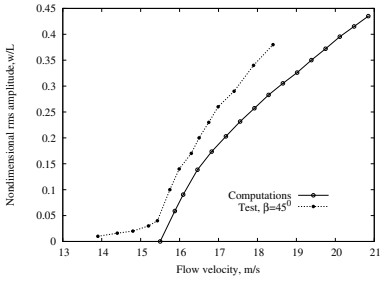

(d) RMS amplitude

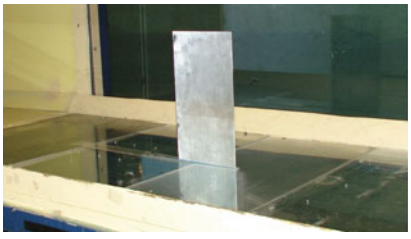

(e) $\beta = 90^0$

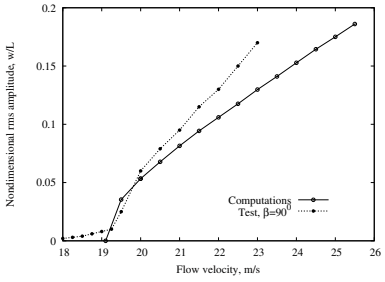

(f) RMS amplitude

Fig. 2 Yawed plate models and correlation analyses; **a**, **c** and **e** for photographs and **b**, **d** and **e** for LCO rms amplitude versus the flow velocity for the yaw angle of $\beta = 0°$, $45°$ and $\beta = 90°$, respectively

the stiffness nonlinearity is included the response is a single dominant frequency as found in the experiment.

For $\beta = 45°$ and $\beta = 90°$ yawed plates, to capture the LCO amplitude, a micro-accelerometer was placed at the trailing edge of these plate structuries. Even though the micro-accelerometer is only 2.6 g, we include this weight in the computational model.

Figure 2c, d show the computational and experimental correlations of the LCO displacement response rms amplitude versus the flow velocity for the yaw angle of $\beta = 45°$. The correlation between the computations and experiments is reasonably good beyond the flutter speed. There are some smaller response amplitudes at lower flow velocities ($U < 15.75$ m/s) in the experiment. From the experimental curve of the LCO amplitude versus the flow velocity, the experimental flutter speed is $U_f = 15.6$ m/s and the theoretical flutter speed is $U_f = 16.2$ m/s for $\beta = 45°$.

For $\beta = 90°$, the plate is a wing-like. Figure 2e, f show the computational and experimental correlations of the LCO displacement response rms amplitude and corresponding LCO frequency versus the flow velocity for the yawed angle of $\beta = 90°$. The correlation between the computations and experiments is fair beyond the flutter speed. There are some smaller response amplitudes at lower flow velocities ($U < 19$ m/s) in the experiment due to flow turbulence. The experimental flutter speed is $U_f = 19.3$ m/s and theoretical flutter speed is $U_f = 18.7$ m/s for $\beta = 90°$.

By comparing computations and experiments for the LCO response of the several yawed plate configurations, it is shown that the present inextensible beam or plate theory as provided by Dowell and Tang [37] produces results in good agreement with the measured rms LCO amplitude. These theories have only a single unknown variable, i.e. the transverse deflection of the beam or plate structure. This is very attractive for computations.

2.3 Free-to Roll Fuselage Flutter Model (Symmetric and Anti-symmetric Flutter/LCO Theory)

A flutter model is often made using a semi-span wind-tunnel model with the root of the semi-span wing model clamped on the tunnel side wall. The experimental data obtained from such a model is suitable for computational aeroelasticity code validation. References [38–41] are studies with typical subsonic and transonic flutter semi-span models. The boundary conditions of these experimental flutter modes are different from those of an actual aircraft, but the experimental data from the wind tunnel test may still be useful for evaluating the theory.

A fuselage which is free to roll is designed, but the vertical rigid body translation (plunge) and rotation (pitch) of the fuselage are constrained.The full span wing is a cropped delta wing plate for simplicity. The right and left wings are structurally symmetric. The full span wing dynamics are modeled using a linear plate wing structure theory. A three-dimensional time domain vortex lattice aerodynamic model is also used to investigate flutter of the linear aeroelastic system and results are correlated with experiment. See Ref. [28] for more detail.

The experimental model consists of a right and left wing and a fuselage (slender body). For simplicity, the wing model is a cropped delta wing configuration which is constructed from a aluminum plate of thickness 0.0127 cm and has 40° leading edge sweep and 0° trailing edge sweep. The root chord is 12.7 cm and the halfspan length

is 11.68 cm. The material properties of the wing are: mass density of 0.00284 kg/cm^2, Young's modulus of 720000 kg/cm^2 and a Poisson's ratio of 0.3.The right and left wing model is assumed to be rigidly clamped along the full root chord of the wing. The total rolling inertia about the fuselage center axis for the right and left wings is $J_w = 3.859e^{-5}$ kgm^2. A photograph of the aeroelastic model in the wind tunnel is shown in Fig. 3a.

The fuselage has a circular cross-section with a diameter of 2.54 cm. It includes two parts. The front part is a slender body with a parabolic forebody which can rotate about the fuselage center axis and supports the wings. The rear part is a non-rotating slender body with a parabolic aftbody which is used to support the front portion of the slender body and is connected to the wind tunnel floor by a support or sting rod. The rolling inertia about the fuselage center axis for the rotating slender body is $J_f = 11.19e^{-5}$ kgm^2.

The wings are allowed to rotate (roll) about the center axis of the fuselage. The free or clamped mechanism for the rotation is provided by an electrical magnet brake that is used to provide rolling free or rolling clamped boundary conditions. Two strain gauges attached near the root of the two wings are used to measure the wing elastic deflections.

Because the experimental structural model has nonlinear behavior, the self-excited aeroelastic response represents a limit cycle oscillation(LCO) when the flow velocity is higher than the linear flutter speed. The linear critical flutter boundary is estimated from the LCO responses. The structural nonlinearity arises from a nonlinear strain-displacement relationship due to large structural deformations of the plate-like wings.

Figure 3b shows the measured rms LCO amplitude (microstrain) from the strain guage at the wing root versus the flow velocity from U = 14 m/s to 18 m/s for three cases. One is for the symmetric mode, i.e. in the rolling fixed case. The other two cases are for the anti-symmetric mode with $J_f/J_w = 2.9$ and 13.5. The data are acquired when the response achieves a steady state limit cycle oscillation. The response is given by a rms value over the total sampling length. For the rolling fixed case, there are very small rms amplitudes from U = 14 to 17 m/s. It is believed that these responses are induced by the randomly fluctuating flow of the wind tunnel. At U = 17.1 m/s, the LCO rms amplitude jumps to a high amplitude response with a certain oscillating frequency. As the flow velocity continues to increase from U = 17.1 m/s, the LCO rms amplitude increases. An intersection between the extrapolated LCO amplitude curve and the flow velocity axis is defined as the linear critical flutter speed. This estimated value is about $U_f = 17.05$ m/s. Similar to the symmetric mode case, for the anti-symmetric mode flutter at $J_f/J_w = 2.9$ and 13.5, the experimentally estimated linear critical flutter speeds are $U_f = 16.6$ m/s and 16.7 m/s, respectively.

Figure 3c shows the theoretical and experimental (estimated) critical flutter boundary versus J_f/J_w from $J_f/J_w = 0$ to 50. For the theoretical anti-symmetric mode flutter, the flutter speed increases as J_f/J_w increases but the increase is small. For the theoretical symmetric mode flutter, the flutter boundary does not change with J_f/J_w as expected. When J_f/J_w becomes large, the linear flutter speed for the anti-symmetric mode approaches that for the symmetric mode. The experimental results for the anti-symmetric mode at $J_f/J_w = 2.9$, 13.5 and 38 are plotted in this figure as

(a) Measurement model

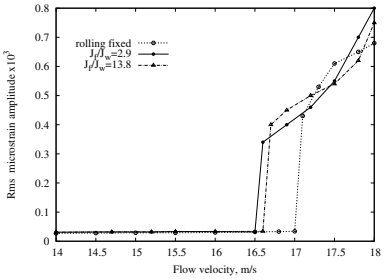

(b) Measured LCO

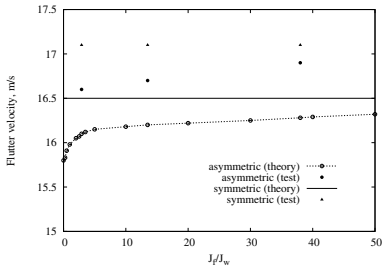

(c) Flutter velocity

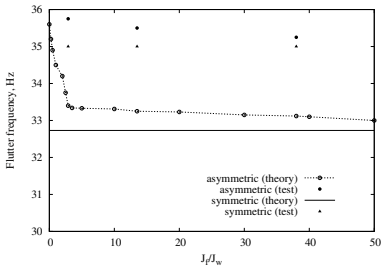

(d) Flutter frequency

Fig. 3 Free-to-roll experimental model and correlation analyses; **a** photograph of the model, **b** measured LCO rms amplitude versus flow velocity for symmetric mode (rolling fixed) and anti-symmetric mode at $J_f/J_w = 2.9$ and 13.5, **c** and **d** flutter speed and frequency versus J_f/J_w

indicated by symbol of • and for the symmetric mode (rolling fixed case) is indicated by symbol of a black triangle. The maximum difference is 3.5% for the flutter speed. Figure 3d shows the corresponding flutter frequency. The maximum difference is 3.5% for the flutter speed and 7.5% for the flutter frequency.

The experimentally observed flutter mode is anti-symmetric, although theory suggests the symmetric mode flutter speed is only modestly higher than that for the anti-symmetric modes. Correlation between theory and experiment for flutter speed and frequency is good including the trends obtained when varying the ratio of fuselage to wing inertia.

3 Experimental Models for Measuring Flutter/LCO Response to Evaluate Nonlinear Freeplay Theory

The freeplay nonlinearity usually occurs in the following components of an aircraft: (a) between the main wing and the control surface actuating mechanism; (b) between the all-movable horizontal or vertical tail and the stabilizer or control actuat-

ing mechanism. In this section, two typical experimental models have been designed and constructed to simulate these freeplay nonlinearities. 1. an airfoil section with control surface freeplay and 2. all-movable tail with stabilizer freeplay.

3.1 Airfoil Section with Control Surface Freeplay

Early theoretical studies of aeroelastic systems with structural freeplay were carried out on analog computers by linearizing the system about the nonlinearity via describing functions or harmonic balance or by time marching integration based on the state-space model. One of the compelling advantages of using harmonic balance or describing functions for aeroelastic systems is that traditional linear analytical tools, such as eigenanalysis, can be used for the determination of system stability while still allowing for the prediction of some nonlinear behavior. However, the response of a true nonlinear system may be dependent on the initial conditions, and the describing function approach does not permit a full exploration of this effect. The dependence on initial conditions and the wide variety of nonlinear behavior exhibited by systems with freeplay show the importance of incorporating this common physical nonlinearity into the theoretical model. In addition, the freeplay nonlinearity will likely have a significant effect on the response of the system to a control law designed for the nominal linear system.

In the present correlation study, a new nonlinear aerodynamic model, a finite state incompressible airloads model, developed by Peters [42] called "Duke code" and a ZAERO code based on CFD technology and nonlinear structural dynamics developed by ZONAT Technology, Inc [25] have been used.

3.1.1 Experimental Model and Measurement System

The two-dimensional NACA 0012 rectangular wing model includes two parts: a main wing with a 19 cm chord and 52 cm span; and a flap with a 6.35 cm chord and 52 cm span, which is mounted at the trailing edge of the main wing using two pairs of micro-bearing with a pin. The main wing is constructed from an aluminum alloy circular spar beam with a diameter of 2.54 cm and a wall thickness of 0.32 cm. The beam runs through 14 pieces of NACA 0012 aluminum airfoil plate and serves as the pitch axis, located at the quarter-chord location from the leading edge. A 0.254 mm thick aluminum sheet covers the entire chord and span, providing the aerodynamic contour of the wing. In addition, an aluminum tube with 1.27 cm diameter is mounted from wing tip to wing tip at a location of 3.175 cm from the leading edge. The chordwise center of gravity can be adjusted by adding or subtracting a balance weight from this tube.

The flap is constructed in a similar manner with an aluminum alloy tube spar beam (1.27 cm diameter and 0.158 cm wall-thickness) passed through the leading edge of 14 pieces of NACA 0012 wood airfoil plate. The flap is also covered with the same

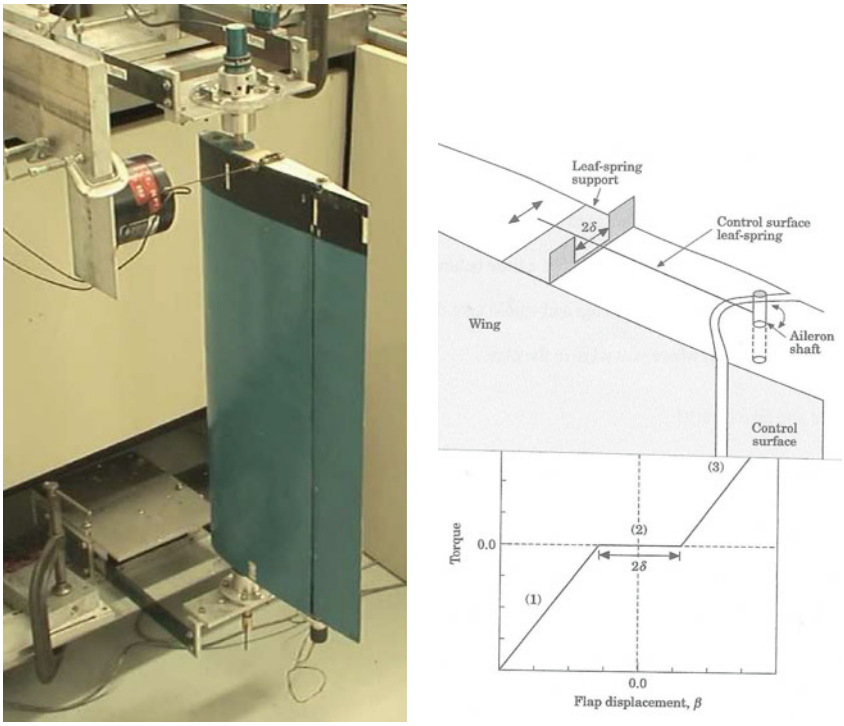

(a) Experimental model (b) Schematic

Fig. 4 Photograph of the experimental model **a** and schematic of freeplay mechanism and restoring moment with a symmetric freeplay region **b**

type of aluminum sheet. Figure 4a shows the photograph of the experimental model including the ground vibration test.

A rotational axis comprised of the micro-bearings and pin allows the flap to have a rotational degree of freedom relative to the main wing. A steel leaf-spring is inserted tightly into a slot of the tube spar beam at one end of the flap. The free end of the leaf spring is inserted into a support block mounted on the main wing. The schematic of freeplay mechanism and restoring moment with a symmetric freeplay region, see Fig. 4b. The amount of structural stiffness that the leaf-spring provides can be adjusted by moving the support block toward or away from the rotational axis of the flap or by changing the diameter of the leaf-spring. Freeplay is incorporated by using a support block that allows the free end of the leaf-spring to move through a given range of motion before encountering resistance.

The support mechanisms for the entire model are mounted outside of the wind tunnel, at the top and bottom. The support mechanism at each end is a bi-cantilever beam made of two steel leaf-spring which are 20.32 cm long, 2.86 cm wide, and

0.102 cm thick. The distance between the two cantilever beams is 15.24 cm. A support block joins the free ends of the bi-cantilevered beams on both the top and the bottom and is free to move in the plunge direction. Figure 4a shows the plunging motion of the support structure. An identical structure is located on the bottom side of the wind tunnel. The two support blocks are the only parts of the support mechanism that move with the model, and this motion is restricted to the plunge degree of freedom. The pitch axis of the main wing is mounted to the upper and lower support blocks through a pair of precision bearings which have small amount of dry friction in the ball. This design allows the model to have a plunge motion that is independent of the pitch degree of freedom. At the upper bracket, there is a spring wire inserted tightly into the pitch axis of the wing. The ends of the spring wire are simply supported on the bracket, which provides an adjustable pitch stiffness. The bracket is mounted on the upper support mechanism by three screws. The bracket allows rotation around the pitch axis when the screws are used to adjust the initial pitch angle.

The pitch angle of the main wing is measured by a rotational velocity displacement transducer, R30, which is fixed at the upper end of the pitch axis. The angular displacement transducer was calibrated and showed excellent linear response characteristic and high sensitivity. The plunge displacement is measured using another R30 which determines the motion of the upper support block. The flap rotational motion relative to the main wing is measured by a micro-RVDT which is mounted on the flap axis outside of the main wing. These three measurement signals are independent of one another.

The output from these transducers is amplified and directly recorded by data acquisition system, LabView 8.0 version in the computer. The digitized response data can be graphically displayed either on-line or off-line as a time history, phase plane plot, FFT, PSD, or Poincare map. In order to make a comparison of the theoretical and experimental data, a measurement system calibration was completed before the wing tunnel test. The dynamic calibration coefficients were determined by a ground vibration test. The system parameters for the experimental model are shown in Table 4.

From the experimental ground vibration results, a comparison of the structural natural frequencies for the numerical and experimental systems is given in Table 5.

3.1.2 Correlation Study $\alpha_0 = 0°$

For the flutter/LCO test, a freeplay gap, $2 \times \delta = 2 \times 2.12°$, is used. A nondimensional r.m.s amplitude normalized by the freeplay gap is introduced here for LCO amplitude. The pitch and flap motions are nondimensionalized by the freeplay gap, i.e. by $2 \times \delta$. For the plunge motion, it is nondimensionalized by $2 \times \pi\delta b/180°$.

When the freeplay gap is set zero, the measured flutter flow velocity is 26.5 m/s for zero initial angle of attack. Because in this flow velocity range the model motion is very large we use an external device to limit the plunge motion amplitude. The measured flutter frequency is about 6.25 Hz.

Table 4 Experimental plate properties

Model parameters:	
Chord	0.254 m
Span	0.52 m
Semi-chord (b)	0.127
Elastic axis (a) w/r/t (b)	−0.5
Hinge line (c) w/r/t (b)	0.5
Mass parameters:	
Mass of wing	0.713 kg
Mass of aileron	0.18597 kg
Mass/length of wing-aileron	1.73 kg/m
Mass of support blocks	0.467 × 2 kg
Total mass per span, M_h	3.625 kg/m
Inertial parameters:	
S_α (per apn)	0.0726 kg
S_β (per span)	0.00393 kg
I_α (per span)	0.0185 kgm
I_β (per span)	0.00025 kgm
Stiffness parameters:	
K_α (per span)	46.88 kgm/s^2
K_β (per span)	2.586 kgm/s^2
K_h (per span)	2755.4 kg/ms^2
Damping parameters:	
ζ_α (half-power)	0.0175
ζ_β (half-power)	0.032
ζ_h (half-power)	0.0033

Table 5 Model natural frequencies

	Computational	Experimental	% Difference
ω_α (coupled)	8.32 Hz	8.45 Hz	1.6
ω_β (coupled)	17.64 Hz	17.37 Hz	1.5
ω_h (coupled)	4.37 Hz	4.45 Hz	1.83
U_F (m/s)	27.3	26.5	2.9
ω_F (Hz)	6.05	6.25	3.3

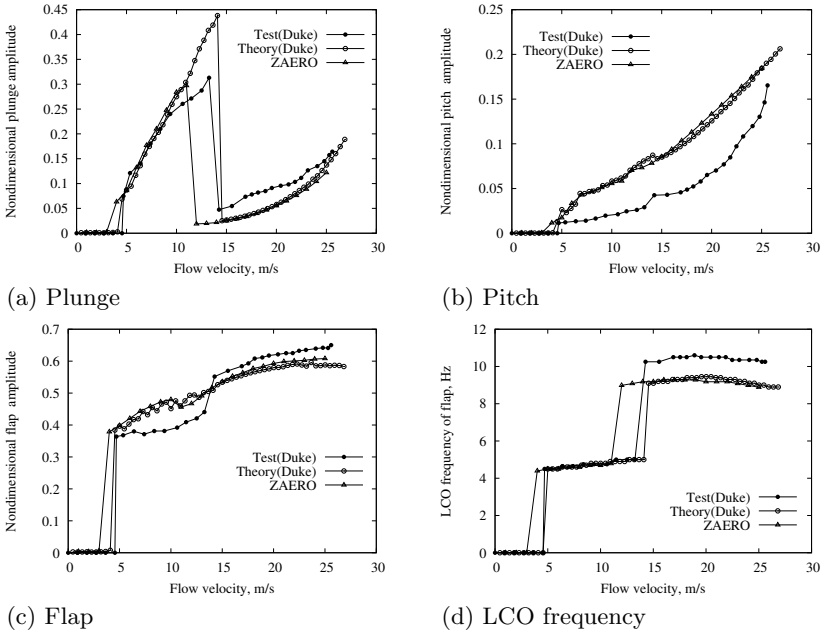

Fig. 5 Theoretical and experimental LCO rms response amplitudes and frequency for the initial pitch angle of $\alpha_0 = 0$ and $\delta = 2.12°$

Figure 5 shows the nondimensional plunge, pitch, flap LCO amplitudes and LCO frequency versus the flow velocity for the initial pitch angle, $\alpha_0 = 0$. The motion may be periodic or non-periodic or chaotic. Here we use r.m.s amplitude to present the LCO motion versus the flow velocity.

As shown Fig. 5, when the flow velocity, U, is less than 4.67 m/s no LCO occurs both for the theory and experiment. When U is between 4.67 and 13.26 m/s for the experiment and 4.55 and 14.1 m/s for the theory, the motion is dominated by the plunge degree of freedom and has an oscillation frequency of about 4.5–5 Hz for both the theory and experiment. When U is between 13.26 and 25.6 m/s for the experiment and 14.1 and 27.4 m/s for the theory, the motion is dominated by the flap degree of freedom and has an oscillation frequency of about 10–10.5 Hz for the experiment and 9–9.5 Hz for the theory. When U is greater than 25.6 m/s, the experimental LCO amplitude abruptly increases and the test is stopped to protect the model (this is called the catastrophic flutter speed). This flow velocity is close to the experimental flutter speed (26.5 m/s) of the linear structure without freeplay. However the theoretical catastrophic flutter speed is 27.4 m/s and is slightly higher than the theoretical linear flutter speed (27.3 m/s). For comparison, the computational results using CFD code, ZAERO, provided by ZONA Technology, Inc, are also presented in this figure.

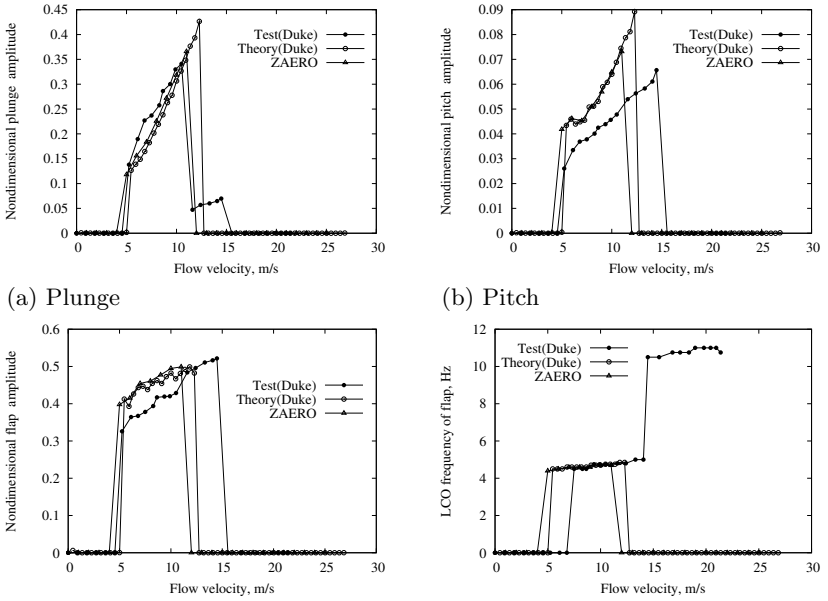

Fig. 6 Theoretical and experimental LCO rms response amplitudes and frequency for the initial pitch angle of $\alpha_0 = 6^\circ$ and $\delta = 2.12^\circ$

3.1.3 Correlation Study for $\alpha_0 \neq 0$

Experimental measurement for the several initial pitch angles of attack from $\alpha_0 = 2^\circ$ to 8° are made to study the correlation. Here only one case ($\alpha_0 = 6^\circ$) is shown Fig. 6. Summarizing the correlation results from $\alpha_0 = 2^\circ$, to $\alpha_0 = 8^\circ$, the following observations may be made.

1. The flow velocity corresponding to a change in the LCO behavior from a lower frequency oscillation to a higher frequency oscillation changes modestly in the experiments as α_0 increases.
2. The flow velocity corresponding to catastrophic flutter (very large LCO amplitude) also decreases as the initial pitch angle increases. The experimental results are 25.6 m/s for $\alpha_0 = 0^\circ$; 25.05 m/s for $\alpha_0 = 2^\circ$; 23.96 m/s for $\alpha_0 = 4^\circ$; 21.48 m/s for $\alpha_0 = 6^\circ$ and 20.43 m/s for $\alpha_0 = 8^\circ$.
3. When α_0 equals 8°, the flow velocity range for the LCO becomes quite small and when α_0 is larger than 8° the LCO disappears both for the theory and test.

3.2 All-Movable Tail Model with Freeplay

Experimental models have been constructed by previous investigators that had freeplay nonlinearity in an all-movable tail in the actuating mechanism at the root, see Ref. [43–45]. These early experiments were interpreted in terms of a reduction in flutter speed due to freeplay. However, the early works did not provide a LCO correlation analysis induced by the freeplay nonlinearity. Inspired by the early WADC (Wright Air Development Center) all-movable tail model, a similar experimental model was designed and tested. A computational code based on the linear three-dimensional time domain vortex lattice aerodynamic model and freeplay structural nonlinearity has been developed to study the flutter and also nonlinear limit cycle oscillations induced by a freeplay gap in the actuating mechanism at the root of the tail as well as the effects of the root rotation angle (nominal angle of attack) on LCO response. The tail model is mounted vertically in the wind tunnel. The effect of the gravity load is not considered in the computations and experiment discussed here although a later study included the effects of gravity by testing the model in a horizontal mount.

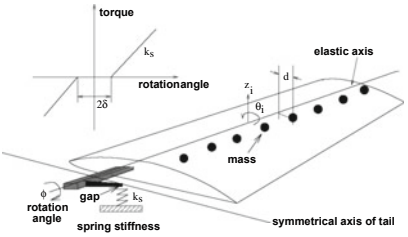

(a) Schematic of model

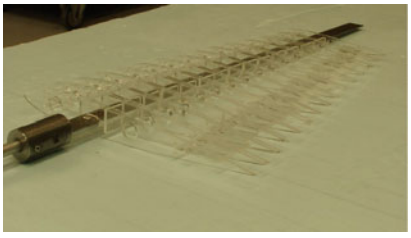

(b) Spar and airfoil ribs

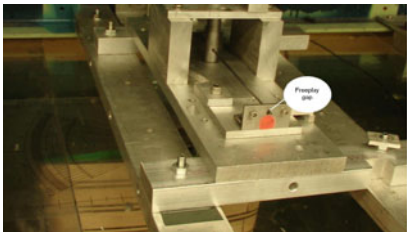

(c) Freeplay mechanism

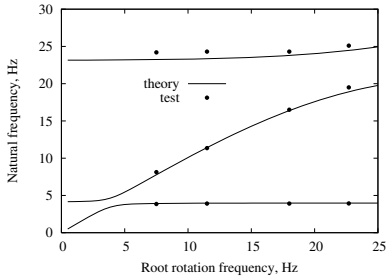

(d) Natural frequency

Fig. 7 **a** Schematic of the all-movable tail model with free play in the root rotation mechanism, **b** and **c** photographs of the model configuration and freeplay at root support mechanisms, **d** natural frequency versus uncoupled rotation frequency, ω_ϕ at the root

3.2.1 Experimental Model and Measurement System

A uniformly tapered wing from root to tip was designed to simulate a conventional unswept horizontal stabilizer. The schematic of the all-movable horizontal tail model with free play gap in the root rotation mechanism is shown in Fig. 7a. The experimental model includes two parts: a tapered wing and an actuating mechanism with torsional free play gap at the root. The tail wing is untwisted and flexible in the flap, lag and torsional directions. The root chord is 24.7 cm and tip chord is 13.2 cm and the span is 39.7 cm. The sweep angle of the lead edge is 5.7°.

The wing is constructed from a precision ground flat steel spar with mass uniformly distributed along the wing span. The spar is 39.7 cm in length, 1.905 cm in width and 0.127 cm in thickness. It is inserted tightly into the wing root mechanism. The spar elastic axis is located at 33% of the local chord aft of the leading edge which is consistent with the location for the axis of rotation of the tail, see Fig. 7b

There are 14 pieces of 2.6 cm wide sections uniformly attached to the spar along the span. Each section consists of a pair of ribs with NACA 0012 airfoil plate made of plastic material with 0.15 cm thickness. Each airfoil plate is fabricated using a Laser Printer and CAD software. Each airfoil section is constructed from two plastic airfoil plates and balsa wood. The wing is assembled by inserting the steel spar through a small slot cut through each of the sections. An additional 0.2 cm thick sheet of balsa wood is placed between each section and the wing is permanently bonded. The balsa wood placed between the airfoil sections provides some additional mass and stiffness in the bending and in torsion.

The support mechanism for the entire tail model is mounted outside of the wind tunnel at the top. The wing spar axis is mounted to support blocks through a pair of precision bearings which have a small amount of dry friction in the ball, but this dry friction is not accounted for in the computational code. There is a spring wire inserted tightly into a rotational axis between two bearings. The free end of the spring wire is simply supported on a bracket of the support block. The amount of rotational stiffness that the spring wire provides can be adjusted by moving the support block toward or away from the rotational axis of the wing. Each freeplay gap is incorporated by using a support block with a different size hole that allows the free end of the spring wire to move through a given range of motion before encountering resistance. A photograph of the spring wire assembly for the rotation stiffness (with freeplay) is shown in Fig. 7c. The bracket is mounted on the support mechanism by screws. The bracket allows rotation around the pitch axis when the screws are used to adjust the nominal pitch angle.

The root pitch angle of the wing is measured by a rotational velocity displacement transducer, R30, which is fixed at free end of the support block. The angular displacement transducer was calibrated and showed excellent linear response characteristic and high sensitivity. A 45° oriented strain gage for torsional modes were glued to the root spar to measure the torsional elastic deflections of the tail. Signals from the strain gages were conditioned and amplified before their measurement through a gage conditioner and a low-pass filter. A micro-accelerometer is mounted at the

tip-span of the tail. The output signals from these transducers are directly recorded on a computer with data-acquisition and analysis software, Lab-VIEW 7.1.

A ground vibration test of the model was used to determine the natural frequencies and the modal damping. Figure 7d shows the theoretical and experimental natural frequencies at zero airspeed versus the uncoupled rotation frequency, ω_ϕ. The first mode is dominated by the first bending and the second is dominated by the first torsion. The third mode is dominated by the second bending. When the tail wing is cantilevered, $\omega_\phi = \infty$, the first two theoretical bending frequencies 3.99, 23.1 Hz and the first torsion frequency is 30.2 Hz. The experimental results are 4.0, 25.1 for bending and 27.75 Hz for torsion. In this case the agreement between the theory and experiment is good. Also it is found that the frequencies are close to the corresponding $\omega_\phi = \infty$ values (as shown in Fig. 7d) over the higher ω_ϕ range. This means the coupling between the bending and torsion modes is weak.

3.2.2 LCO Correlation Study for $\alpha_0 = 0°$

Four typical freeplay gaps are selected. These are $\delta = 0.1°, 0.25°, 0.5°$ and $1°$. The military specification (MIL-SPEC) confines the freeplay limit of all-moveable control surfaces to be less than $0.034°$ (peak-to peak value) to achieve the goal of no freeplay induced LCO during normal operation of aircraft. In the present study, the maximum freeplay gap is limited to $\pm 1°$. The uncoupled rotation frequency, ω_ϕ, is chosen to be 7.5 Hz, corresponding to root rotation stiffness, $k_s = 2.895$ N-m. Considering the effects of flight loads on tail freeplay induced LCO, the initial angles of attack vary from $\alpha_0 = 0°$ to $6°$. The purpose of these computations is to determine the nominal angles of attack for which when the freeplay induced LCO disappears.

Depending on the initial conditions and physical parameters, the response may be either LCOs or chaotic oscillations, i.e. the oscillation is generally around one of two equilibrium positions ($\pm\delta$), and the particular equilibrium position depends upon the initial conditions. Thus the oscillating displacement is essentially random with respect to time. In this study, we used a velocity response for the bending motion and a torsional rate for the torsional motion to present the LCO response behavior. A rms amplitude for the bending displacement velocity at the tail tip and a rms amplitude for the rotation angle at the root are calculated.

Figure 8a and b show the rms LCO amplitude of the bending velocity and at the tail tip (a) and the rms LCO amplitude of the root rotational angle motion (b) versus the flow velocity for the initial disturbance angle, $+\delta$ at the root. The flow velocity range is from 0 to 22 m/s. Note that the linear flutter speed without freeplay is 23 m/s. In these figures results are included for four freeplay gaps, $\delta = 0.1°, 0.25°, 0.5°$ and $1°$. From Fig. 8, the following observations may be made.

(1). The theoretical LCO occurs over essentially the whole flow velocity range for which when $U > 0$. There is an oscillating divergence from the LCO motion when the flow velocity is greater than the linear flutter speed, i.e. $U \geq U_f$. The experimental LCO occurs when flow velocity is larger than about 5 m/s. Below 5 m/s there is no

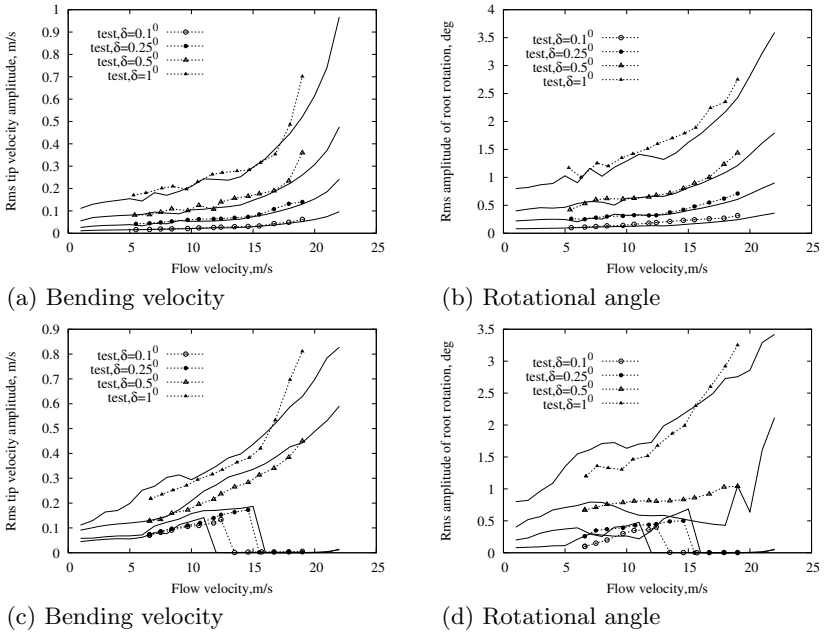

(a) Bending velocity (b) Rotational angle

(c) Bending velocity (d) Rotational angle

Fig. 8 Correlation analyses for the all-movable model; **a** tip bending velocity at tip and **b** root rotational angle at root versus the flow velocity for $\alpha_0 = 0°$ and **c**, **d** for $\alpha_0 = 2°$

measured LCO due to a dry friction torque in the root rotation mechanism. Without this dry friction torque, LCO is predicted to occur at even lower flow velocities.

(2). The rms amplitude for both the bending and torsional response increases as the flow velocity increases.

(3). The rms amplitude for the root rotational angle response oscillates around the gap region. The amplitude varies with the flow velocity which depends upon the initial conditions.

(4). As expected the rms amplitude for both the bending and torsional response increases as the freeplay gap increases.

3.2.3 LCO Correlation Study for $\alpha_0 \neq 0°$

Five typical nominal angles of attack, $\alpha_0 = 1°, 2°, 4°, 6°$ and $8°$ and four freeplay gap values as described before. Only one case is presented here. Figure 8c, d show the rms LCO amplitude for a nominal angle of attack, $\alpha_0 = 2°$. For two free play gaps, $\delta = 0.1°$ and $\delta = 0.25°$, LCO disappears above a certain flow velocity. The corresponding flow velocities for which LCO disappears, U_{no-LCO}, are 12 m/s for the theory and 13.5 for the test in the case of $\delta = 0.1°$ and 16 m/s for the theory and

Table 6 Flow velocity at which LCO disappeared, U_{no-LCO} m/s

α_0 / δ	0.1°	0.25°	0.5°	1.0°
1°	17/(15.7) m/s	None	None	None
2°	12/(13.5) m/s	16/(14.6) m/s	None	None
4°	8/(0) m/s	13/(11) m/s	16/(14.1)	None
6°	0/(0) m/s	10/(0) m/s	15/(13)	17/(14.7)
8°	0/(0) m/s	0/(0) m/s	13.5/(0)	15.5/(12)

14.6 m/s for the test in the case of $\delta = 0.25°$ respectively. When $\delta > 0.25°$, LCO response occurs over the whole flow velocity range $U_f > U > 0$.

Summarizing the theoretical and experimental results for $\alpha_0 = 1°$ to 8°, a disappearance of the LCO boundary is listed in Table 6. Note that the values in the parenthesis show the results from the tests. Also as the nominal angles of attack increases from 1° to 8°, the following observations may be made.

(1). The flow velocity for LCO disappearing increases when the angle of attack decreases for a given freeplay gap.

(2). The freeplay boundary for LCO disappearing increases when the angle of attack increases for a given flow velocity.

(3). As expected the LCO rms amplitude for both the bending and torsional responses increases with increased freeplay gaps. These results are similar to those for $\alpha_0 = 0°$.

(4). Note that LCO also disappears for flow velocities less than about 6.5 m/s which is attributed again to the presence of friction in the root support mechanism.

The quantitative agreement between the theory and experiment is reasonably good for zero and non-zero angles of attack. The fair to good quantitative agreement between theory and experiment verifies that the present method has reasonable accuracy and good computational efficiency for the flutter/LCO analysis.

4 Experimental Models for Measuring Aerodynamic Response Phenomenon in Buffeting Flow

In earlier computational work by Raveh and Dowell, Ref. [46, 47], large shock oscillations (buffet oscillations) are observed for a certain combination of Mach number and steady mean angle of attack even in the absence of structural motion. Also in lower Reynolds number flow, bluff bodies in cross flow [48], and a flat plate at high angles of attack [49] are observed to have the nonlinear oscillations induced by the buffeting flow. In the buffeting flow there is a very interesting phenomenon called "frequency Lock-in". Under certain flow conditions, the shedding frequency can lock into the natural frequency of the structure. In this Lock-in region, the structural

response amplitude can reach a limit cycle oscillation that may cause high cycle fatigue and eventually failure.

Two experimental models were constructed to observe the buffeting flow oscillation. One is to find lock-in region by measuring the pressure variation on the oscillating airfoil surface at high angles of attack. Another is to construct a partial-span control surface (flap) attached to near the mid-span of a NACA0012 airfoil model with and without freeplay gaps at high angle of attack and to measure the flap response induced by the buffeting flow.

4.1 An Oscillating Airfoil Section Model in Buffeting Flow

4.1.1 Experimental Model and Measurement System

In order to observe the dynamic and static pressure distribution and measure the aerodynamic loading due to a high nominal angle of attack and a small pitching oscillation through wind tunnel tests, a typical section wing model was constructed. Design of the typical section took into account the fact that it must accommodate a root pitching oscillation, mount 20 micro-pressure sensors, PCB model 103B01, for dynamic pressure measurement and 20 orifices for the static pressure taps at the mid-span and also be mounted in the Duke University wind tunnel using an existing pitch oscillating testing rig.

The profile of the typical section is a NACA 0012 symmetrical airfoil, having a chord length of 0.2554 m, which nicely accommodates 20 dynamic pressure sensors and 20 static pressure taps. The span, $l = 0.52$ m of the typical section was dictated by the height of the wind tunnel, as the typical section is to be mounted vertically. Eight pieces of NACA0012 airfoil ribs made of aluminum material with 0.64 cm thickness are used for high chordwise stiffness and for adequate housing for bearings supporting the small strip hinge. In addition,a mid-span aluminum rib with 1.27 cm thickness provides support for 20 pressure sensors, see Fig. 9a. The airfoil ribs are placed on three spars that, in addition to being structural elements, have specific functional roles.The spar placed at the quarter chord is an aluminum tube and serves to mount the model on the testing rig that is connected to a pitch oscillating testing rig to create an airfoil pitch oscillation.

The mid-span airfoil rib is specially made to measure the dynamic pressure distribution at mid-span and provide support for the 20 micro-pressure sensors. There are 20 orifices of 1.16 mm diameter for the pressure taps which are symmetrically distributedover the upper and lower surfaces, respectively. The orifice positions in terms of percentage chord from the leading edge are 0.06, 0.12, 0.18, 0.3, 0.42, 0.49, 0.54, 0.61,0.74 and 0.92. The pressure sensor is bolted on the mid-span airfoil rib and installed with an adhesive mounting ring to prevent a pressure leak between the pressure surface of the sensor and the airfoil orifice.The dimensions of the pressure sensor are 9.5 mm diameter, 7 mm height. The weight is 3.26 g. The signal/noise is 60 db, i.e. the uncertainty is 0.1%. The dynamic range is 77 db and the frequency range

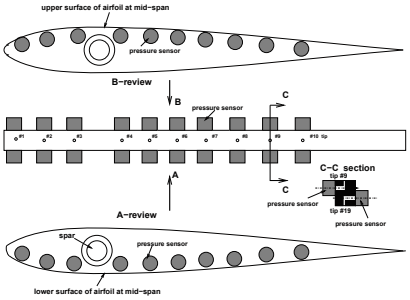

(a) Schematic of pressure measurement

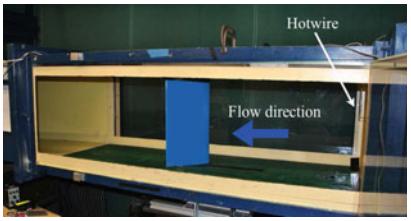

(b) Photograph of model

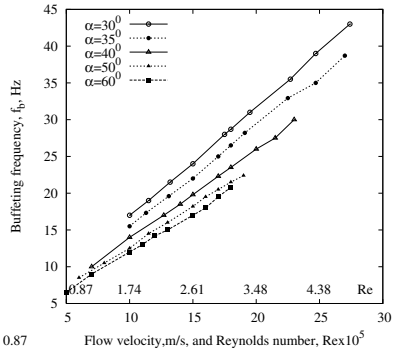

(c) Buffeting frequency

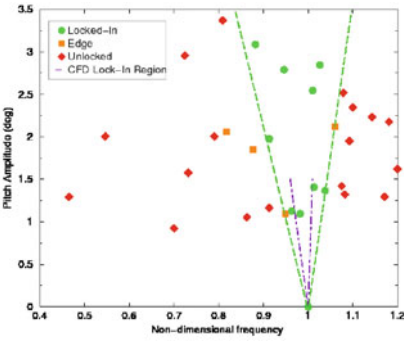

(d) Lock-in region

Fig. 9 Oscillating airfoil model in the buffeting flow and correlation analyses; **a** schematic of pressure measurement, **b** experimental model in wind tunnel at high angles of attack, **c** buffet frequency varies flow velocity and Reynolds number, Re, for "onset" boundary of the buffet flow for nominal angles of attack, $\alpha = 30°$ to 60°, **d** experimental and theoretical lock-in region for $\alpha = 40°$ and the Reynolds number, $R_e = 100000$ (U = 5.8 m/s)

is 5 Hz–13 kHz. Details of the dynamic pressure measurement device are shown in Fig. 9a. All the structural elements are held together by epoxy resin and mechanical elements (bolts, pins etc). They are covered with 0.25 mm in thick aluminum foil (called skin).

The root airfoil pitch excitation was performed by a pitch oscillatory shake table which is mounted to a very heavy support frame that is attached to the ground. The shake table is driven using a DC servo motor through a cam.The driving frequency is controlled by a D/A NB-MIO-16 system. A nearly pure single harmonic excitation is provided. A photograph of the wind tunnel model and the pressure measurement system in the model is shown in Fig. 9b.

For the dynamic pressure measurement, the output of each pressure sensor and pitch oscillating displacement was directly recorded on a PC computer through signal conditioners, PCB models481A02, 442C04 and a data acquisition package which

consisted of a 20-channel analog to digital (A/D) plug-in interface board, a BNC termination box,and data acquisition and analysis software, LabVIEW version 9.0.

4.1.2 Correlation Analyses for Frequency Lock-in Region

In this section, for comparison with the experimental results, the computational fluid dynamic analyses of NACA0012 are conducted using a nonlinear, frequency domain, harmonic balance (HB) code [50]. The viscous, Reynolds-averaged Navier–Stokes equations are solved for a 2D slice using a Spalart–Allmaras turbulence model. The O-grid contains 385 points in the circumferential direction, 97 points in the radial direction and extent approximatery 20 diameters from the airfoil.

Aerodynamic response at buffet flow conditions with no pitch excitation were measured for different flow velocities from U = 5 m/s to 27.5 m/s and several nominal angles of attack, $\alpha = 30°$ to 60°. The results are shown in Fig. 9c in a plot of buffeting frequency versus flow velocity and corresponding Reynolds number for the "onset" boundary of the buffet flow.

For aerodynamic response to pitch exciton in the buffeting flow, a pitch sinusoidal excitation at the airfoil root is added. The pitch excitation amplitudes, θ_0, are considered in the present experiment from $\theta_0 = 0.8°$ to 3.4°. The excitation frequency, f_e ($\omega_e = 2\pi f_e$) varies from 5 to 12.5 Hz for the nominal angle of attack, $\alpha = 40°$ and the flow velocity, U = 5.8 m/s and Reynolds number $R_e = 100{,}000$.

Figure 9d shows the experimental lock-in region found by enforcing the airfoil oscillations at a fixed amplitude and frequency. The non-dimensionalized frequency is defined as f_e/f_b. The angle of attack is 40° and the Reynolds number is 100000 (U = 5.8 m/s). Figure 9d and other comparable data may be found in Besem et al. [51]. The diamond symbols represent conditions where the shedding and enforced frequencies are unlocked, the circle symbols show lockin conditions, and the square symbols have a chaotic behavior that can be attributed to the edge of the lock-in region. The "V" shape is similar to the numerical results conducted by HB code [50], though the lock-in region is narrower numerically, which can be attributed to the chaotic behavior on the edges of the lock-in region. In the experiments, it is difficult to separate the frequencies due to the motion and due to the shedding because of the noise in the measurements. However, the computational code solution will only converge if the two frequencies are perfectly Locked-in. This explains why the edges of the Lock-in region are difficult to compare with the experiments.

From Fig. 9c and 9d the following observations may be made.

(1). The buffeting frequency is almost directly proportional to the flow velocity or Reynolds number for any nominal angle of attack.

(2). The buffeting frequency (the starting points of the curves) depends on a combination of nominal angle of attack and flow velocity or Reynolds number.

(3). As the nominal angle of attack increases the buffeting frequency decreases for a certain flow velocity or Reynolds number.

4.2 An Airfoil with and without Freeplay Control Surface in Buffeting Flow

4.2.1 Experimental Model and Measurement System

The airfoil experimental model and the pressure measurement system are the same as described above. This model is mounted vertically to a very heavy support frame that allows one to adjust the nominal angle of attack of this model. The rotation center is at the one quarter chord of the airfoil. A photograph of the experimental model is shown in Fig. 10a.

Based on the above model, a partial span control surface (flap) with 5.08 cm chord and 5.08 cm span is mounted on the wing model at span location, y = 28 cm and chord location of x = 20 cm. The flap pitch rotation axis is placed at x = 20 cm. The rotation axis is comprised of two micro-bearings and allows the flap to have a rotational degree of freedom relative to the main wing. A steel leaf-spring is inserted tightly into a slot of the rotation axis of the flap.The free end of the leaf-spring is inserted into a support block mounted on the main wing. The amount of structural stiffness that the leaf-spring provides can be adjusted by moving the support block toward or away from the rotational axis. Freeplay is incorporated by using a support block that allows the free end of the leaf-spring to move through a given range of motion before encountering resistance. A schematic of the leaf spring assembly for the partial control surface (with freeplay) is shown in Fig. 10b.

Two strain gauges are glued to both sides near the fixed end of the leaf-spring and are used to measure the flap pitch angle. The pitch angle calibration has been made from the strain gages. There is almost a linear relationship between the output voltage and the input pitch angle within 15°. The average sensitive coefficient is 1.115 degree/voltage. For the dynamic pressure and flap pitch angle measurements, the output of each pressure sensor and pitch angle were directly recorded on a PC computer through signal conditioners and a data acquisition package which consisted of a 20-channel analog to digital (A/D) plug-in interface board, a BNC termination box, and data acquisition and analysis software, LabVIEW version 9.0.

Because of unavoidable freestream and boundary layer turbulence irregularities, the free stream turbulence levels are about 1% of the nominal velocity. In order to remove this randomness from the pressure data, an ensemble averaging procedure over a total of 20 records was carried out. The response is given by a rms value over the total sampling length for the experimental data. For the FFT analysis of these experimental data, an ensemble averaged FFT analysis has been used. Twenty (20) test time samples are taken to do the FFT analysis and an averaged FFT amplitude and frequency are determined.

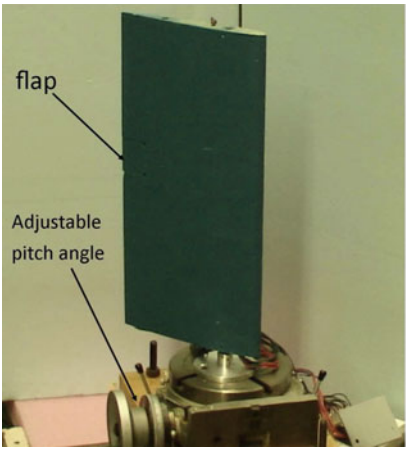

(a) Photograph

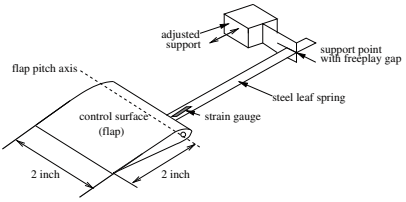

(b) Schematic of flap

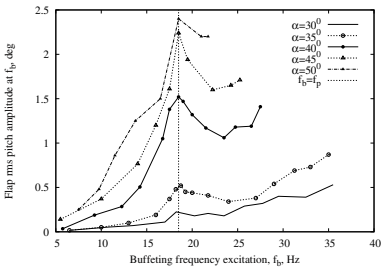

(c) RMS amplitude

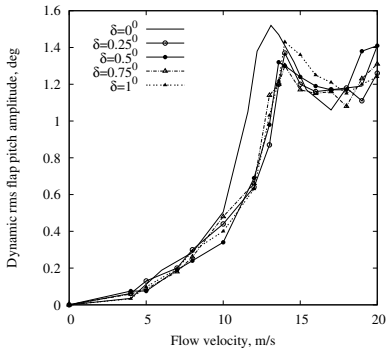

(d) RSM amplitude

Fig. 10 Experimental Freeplay model and correlation analyses in buffet flow; **a** photograph of model, **b** schematic of a portion of main wing-partial span surface assembly, **c** dynamic rms flap pitch amplitude versus buffet frequency for $\alpha = 30°$ to $50°$ without freeplay, **d** dynamic rms flap pitch amplitude versus flow velocity for $\alpha = 40°$ and freeplay gap, $\delta = 0.25°$ to $1.0°$

4.2.2 Measured Aeroelastic Response of the Flap Induced by Buffeting Flow

The experimental flap pitch stiffness is $k_p = 0.0569\,\text{Nm/rad}$ and the flap pitch moment of inertia is $J_p = 0.42155E^{-5}\,\text{kgm}^2$ and the corresponding flap pitch natural frequency is $f_p = 18.25\,\text{Hz}$. All aeroelastic flap response tests were performed for nominal angles of attack from $\alpha_0 = 30°$ to $50°$ and the flow velocity varies from 5 m/s to 26 m/s. Four freeplay gap ranges are considered in the wind tunnel tests, $\delta = \pm 0.25°$, $\pm 0.5°$, $\pm 0.75°$ and $\pm 1.0°$.

Figure 10c shows flap rms pitch amplitude versus the buffeting frequency, for the nominal angles of attack $\alpha_0 = 30°$ to 50° without freeplay gap. There is a local peak amplitude for each nominal angle of attack. Corresponding to these peak amplitudes, the flap is excited by a larger aerodynamic load with a certain excitation frequency, i.e the buffet frequency, f_b.[1] At the peak response values, the buffeting frequencies are close to the flap natural frequency, f_p. We use a dotted line to connect these peak points in this figure. The rms dynamic flap responses are created by two different types of flow separation: one is due to a randomly fluctuating flow as shown for $\alpha_0 < 28°$ and the other is due to a von Karman street vortex flow that has a dominant frequency when $\alpha_0 > 30°$. The fluctuating flow has a white noise characteristic and the noise strength increases as the flow velocity increases. This noise excitation always leads to an increase in rms flap amplitude with increased flow velocity, but the von Karman street vortex flow or buffeting flow significantly increases the rms flap amplitude when the buffeting frequency is close to the flap natural frequency.

Generally, the rms flap response amplitude increases as the nominal angle of attack increases. For example, when $\alpha_0 = 30°$, the buffet flow strength, i.e the peak value at the buffeting frequency, is relatively weak. Indeed, for the range of $28° < \alpha_0 < 30°$ it is difficult to identify the dominant buffeting frequency from the measured flap response due to the weak buffeting flow. When $\alpha_0 > 40°$ the buffet flow strength is stronger and the effect on the flap response is significant.

The dynamic rms amplitude of the flap pitch angle versus the flow velocity for four freeplay gaps at nominal angle of attack, $\alpha_0 = 40°$ is shown in Fig. 10d. The dynamic rms amplitude does not increase monotonically with an increased flow velocity. There is a local peak amplitude for each freeplay gap. Corresponding to these peak amplitudes, the flap is excited by a larger aerodynamic load with a buffeting flow frequency, f_b and these buffeting frequencies are close to the flap natural frequency, f_p. Corresponding to the peak amplitude, the flow velocity, $U_{p-p} = 13.1$ m/s and frequency $f_b = 18.5$ Hz for no freeplay gap. The U_{p-p} values for different freeplay gaps are also very close to U = 13.1 m/s. The corresponding f_{p-p} values for different freeplay gaps are very close to the buffeting frequency, f_b. It is interesting to note that the peak rms amplitude for different freeplay gaps are also close to the value for no freeplay case. This means the effect of the freeplay gap on the dynamic response of the flap motion is small.

Due to the larger static preload of the aerodynamic forces, the flap pitch motion is always near to one side of the freeplay boundary. The flow buffeting frequency versus the flow velocity can be determined from measured flap motion. The results show that the flow buffeting frequency is almost independent of the freeplay gaps, as expected.

The buffet flow occurs at large angles of attack and leads to a larger preload due to the aerodynamic forces and thus a larger static pitch equilibrium position. In this case no limit cycle oscillations (LCO) of the flap pitch motion induced by the freeplay gap were found. The flap pitch motions are around the upper boundary of

[1] Recall that the buffet frequency is given in Fig. 9c as a function of flow velocity for the various angles of attack.

the freeplay gap only. Buffeting flow excitation leads to a large dynamic response when the buffeting frequency is close to the flap natural frequency.

5 Design of A Gust Generator and Gust Responses to Linear and Nonlinear Structural Models

In recent years, various mechanisms for creating an oscillating flow in a wind tunnel have been developed for the purpose of studying the response of linear and nonlinear structural modes to gust excitation. These methods include oscillating biplane vanes mounted on the side walls of the test section entrance [52], a cascade of oscillating airfoils [53], fixed airfoils with oscillating flaps [54], fixed airfoils with oscillating jet flaps [55] and airfoils with circulation control [56]. These conventional gust generators require mechanical complexity to achieve the required sinusoidal lateral and longitudinal gust amplitude over a useful frequency range. Thus, there is a need for a new concept for a gust generator with a high degree of mechanical simplicity, controllability and reliability. A flight flutter excitation system invented by Reed [57] has been employed successfully in aircraft aeroelastic response investigations. This excitation system has a very simple configuration and can produce high-force aerodynamic excitation with minimal power and torque input.

5.1 Structural Design of RSC Gust Generator and Measurement of Gust Angles

5.1.1 Structural Design of RSC Gust Generator

The design of the new gust generator is similar to that of two parallel airfoils with circulation control or oscillating jet flaps. The latter needs an air supply source and a more complex airfoil configuration to control the circutation or jet, and thus, the gust magnitude. The former uses the local inflow airstream as an energy source. The gust generator can induce a controlled gust field in the test section by means of a fixed airfoil with a rotating slotted cylinder (RSC) at its trailing edge. Here the lateral and longitudinal gust intensities are controlled by the RSC. The extremely simple RSC/airfoil system combined with low cost is a major advantage of this gust system. A gust generator based on the previous flight flutter excitation system was designed by Dynamic Engineering Incorporated and made and installed by the Duke aeroelastic group in the Duke University low speed wind tunnel.

The structural design of gust generator can be used to create a lateral gust or a longitudinal gust that depends on RSC rotation direction. If two parallel RSC/airfoils have the same rotating direction, it creates lateral gust else is longitudinal gust. Here the structural design for lateral gust generator is described below.

The basic design of the gust generator consists of an aluminum frame as a drive support system that is inserted at the bottom near the test section entrance of the wind tunnel. The frame holds two SRC/airfoils and also a motor drive system. The photograph of the gust generator is shown in Fig. 11a. Each RSC/airfoil is a symmetrical airfoil with a 2.54 cm diam. RSC located at the trailing edge. The RSC/airfil is simply constructed using a fine-grain wood over an aluminum spar, with a chord length of 10.16 cm, spar length of 52.6 cm and a NACA 0015 airfoil profile. The distance between adjacent RSC/airfoil is 30.5 cm. The cylinder is made from an aluminum tube with an o.d. of 2.54 cm and thickness of 0.32 cm. The slot is symmetrical with a 45° center angle. The slot is divided into two spanwise segments, supported by an intermediate ring with a diameter of 2.54 cm and a width of 0.25 cm. The gap between the o.d. of RSC and the trailing edge of the airfoil is 0.32 cm. A photograph of the RSC/airfoil is shown in Fig. 11c.

The RSC has two tip bearings that are centrally mounted on the ceiling plate of the wind tunnel and the bottom plate of the frame. The frame is mounted to a very heavy support table that is attached to the ground. A photograph of the frame is shown in Fig. 11d. The frame is 15.24 cm in width and 10.16 cm tall.

Rotation of the RSC is provided by a DC servomotor DM-326. The interface between the motor and cylinder is located on the lower part of the frame through a motor drive system of timing belts and lightweight pulleys.

There are two modes of gust excitation considered in this generator: sine dwell with a single frequency and linear frequency sweep. These are controlled by a Macintosh II-Ci personal computer. The control program is included so that the experimentalist can stop the frequency sweep and dwell at any frequency during the test run.

5.1.2 Gust Flowfield Measurement

The lateral velocity Δw (or hence, α_g, which is equal to Δw/U), was measured with a differential pressure probe mounted on a bar that is located a certain position in the gust flowfield. The bar was attached to a stand fixed on a support table that can be adjusted to any position.

The pressure probe consisted of two tubes or claws, oriented at 90° to one another in the horizontal plane for measuring the lateral gust and a pitot tube at the center of the probe for measuring the longitudinal gust. The photograph of probe is shown in Fig. 11b. The ends of the tubes protrude from a slender aerodynamic housing, which is oriented in the wind tunnel such that the angle between the tubes is bisected by the freesteam. The tubes are connected to two ± 0.1804-psi differential pressure transducers with a high level voltage output, which is located ourside of the wind tunnel and measures the pressure difference in the lateral direction. The configuration of this probe is similar to a yaw meter of the five-hole probe. For the principle of the gust flowfield measurement, see Ref. [58]. The relationship between the output voltage from the differential pressure transducers and lateral gust angle was obtained by using a statical or a dynamical calibration.

(a) Photograph of gust generator

(b) Photograph of probe

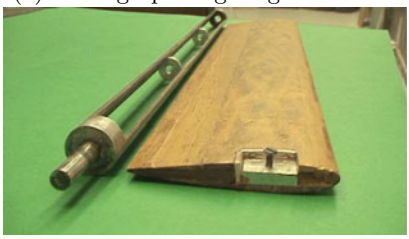

(c) Photograph of RSC/airfoil

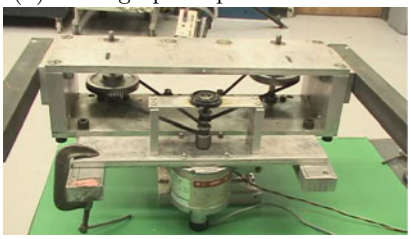

(d) Photograph of side frame

Fig. 11 Structural design of RSC/airfoil gust generator and gust angle measurement in Duke University low speed wind tunnel; **a** photograph of the RSC/airfoil gust generator, **b** photograph of the probe, **c** photograph of the RSC/airfoil, **d** photograph of the frame

5.2 Verification of Design Principle of RSC Gust Generator

The design principle is based on Biot–Savart law of the aerodynamic theory. The lift generated by each RSC/airfoil can be considered as a linear segment vortex of a circulation located at the quarter chord of the combinated RSC/airfoil. A static equivalent lift coefficient from both a numerical computation and an experiment study can be used to verify the design principle of gust generator and obtain an optimal design of this gust generator. The equivalent lift coefficient is defined as

$$C_{Leq} = 2(L_{airfoil} + L_{rsc})/[\rho U^2(c + d)]$$

where $L_{airfoil}$ is airfoil lift force per span length and L_{rsc} is RSC lift force per span length, c and d is airfoil chord length and cylinder diameter.

5.2.1 Experimentally Measured Lift Forces of Arfoil and RSC

The experimental model and measurement technique are described below.

A two-dimensional NACA 0012 airfoil model measuring 30.48 cm in chord and 53.3 cm in span was mounted vertically across the test section from the tunnel floor. The airfoil is set at zero angle of attack. A gap of approximately 0.16 cm existed between the ends of the model and the wind tunnel walls. There are 35 orifices 0.12 cm in diameter used for pressure taps that are symmetrically distributed over the upper and lower surfaces of the midspan, respectively. These orifices are connected to a scanivalve system, a standard static pressure measurement system in the wind tunnel.

The RSC is made by using a special manufacturing technique. The cylinder itself is made from a special tube with an o.d. of 7.62 cm and thickness of 0.95 cm. The slot is symmetrical with a 45° center angle. A top plate with a thickness of 0.635 cm is mounted on the top end of the RSC and a root bracket fixed on the bottom end of RSC that is connected to a rotating support of a wind tunnel balance. The RSC is mounted vertically and cantilevered from the rotating support behind the airfoil. The gap between the top of RSC and the ceiling of tunnel is 0.16 cm. The gap between the o.d. of the RSC and the trailing edge of airfoil can be adjusted by moving the airfoil root support.

The RSC is statically rotated from 0° to 180° and then the pressure distribution on the airfoil surface and the lift force, $L_{airfoil}$, of the RSC are measured. The output of the measured static pressure through the scanivalve system was directly recorded on a Macintosh IIci computer through a data acquisition package. NB-MIO-16 board and an analysis software, LabVIEW 2. The wind tunnel balance with a readout instrument was used to measure directly the lift force, L_{rsc}, of the RSC system. A rotating controller was used to control the rotational angle of the RSC from 0° to 180°.

5.2.2 Correlation Between Experiment and Numerical Simulation

Based on the experimental model, the flowfield around a combinated RSC/airfoil is numerically simulated using the general purpose finite element program FIDAP. The flow is assumed to be quasisteady, turbulent, incompressible and two dimensional. The turbulence is modeled far from the walls by a high Reynolds number $\kappa - \epsilon$ model. In the near wall region, which includes the viscous sublayer, the mixing length concept is used to model turbulence. The variation of lift as a function of the rotation angle and as a function of the gap between the airfoil and RSC is calculated.

Three typical RSC/airfoil gaps are selected in the experiment and computation. A nondimensional gap, $\bar{e}$ is normalized by the airfoil chord length. There are $\bar{e} = 0.03$, 0.08 and 0.3. The flow velocity is U = 20 m/s. A typical theoretical and experimental equivalent lift coefficients C_{Leq} versus statically rotational angle of RSC is shown in Fig. 12a for nondimensional gap $\bar{e} = 0.08$ and U = 20 m/s. From the FFT analysis of these data, the theoretical and experimental equivalent lift coefficient are 0.31 and

0.39, respectively, for the dominant periodic component. The maximum lift response is located at a rotational angle, $\phi_s = 20°$ and the minimum lift response is located at $\phi_s = 70°$. At $\phi_s = 45°$ and $\phi_s = 135°$ the lift response are zero. These results are physically plausible due to the RSC symmetry at a zero lift position. The agreement between theory and experiment is good.

The purpose of these test and computation is not only to do verification of design principle of RSC gust generator, but also to observe the variation of the lift coefficient induced by rotating the RSC and the effects of the RSC position. As shown in Fig. 12b and c, it is found that the lift coefficient decreases as the gap value increases. It is believed that the lift coefficient should be zero when the gap value is large enough. Also note that the differences between the experimental and the numerically simulated lift coefficients increases as the gap decreases.

For more details of the experimental measurements and numerical simulation method see Refs. [59, 60].

5.3 Gust Responses for High-Aspect-Ratio Wing

Theoretical and experimental correlation analyses of the static aeroelastic response, flutter and limit cycle oscillations have been discussed in the Sect. 2.1. The experimental wing model and experimental measured system are also described in this Sect. 2.1 and also used in this gust response correlation analysis. The goal of this section is to assess experimentally the theoretical correlation of gust responses to a single harmonic and sweep frequency gust excitations using nonlinear structural beam theory and linear gust aerodynamic theories. The experimental model is vertically mounted on the ceiling of the wind tunnel and behind the RSC gust generator that is described above. A photograph of the experimental model and gust generator in the wind tunnel is shown Fig. 13. Dur to the wing is in the vertical status, the effects of wing gravity is neglected in the correlation study.

5.3.1 Responses to A Single Harmonic Gust Excitation

In order to obtain a more meaningful correlation between theory and experiment, the gust angles of attack for a single harmonic are measured and quantitatively calibrated. A typical time history and corresponding FFT analysis of the gust angle of attack are shown in Fig. 14a and b for $U = 25\,\text{m/s}$ and gust frequency $\omega = 18.5\,\text{Hz}$. As shown in the FFT analysis of Fig. 14b, the gust load is not a pure sinusoid. The second harmonic component is small however. Similar results are found for other gust frequencies. Figure 14c shows the measured gust angle of attack (α_G) versus gust excitation frequency (Hz) for a flow velocity of $U = 25\,\text{m/s}$. In this figure, a symbol, $\circ$, indicates the measured first harmonic component and the symbol, $\bullet$, indicates the second harmonic component. The solid line is a least-square curve fitting of the experimental data. A formula based upon the measured experimental gust angle of attack is constructed as

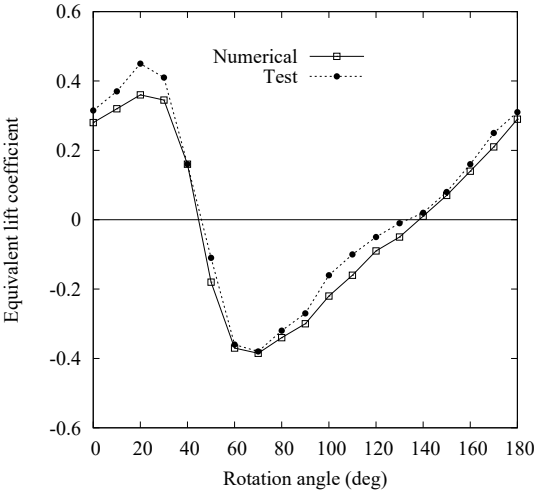

(a) Gap, $\bar{e}$=0.08

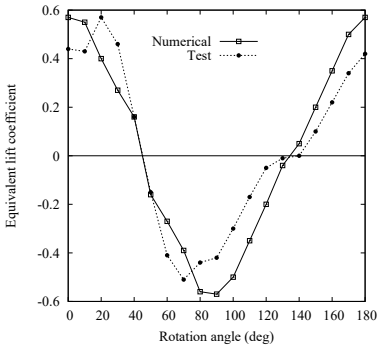

(b) Gap, $\bar{e}$=0.03

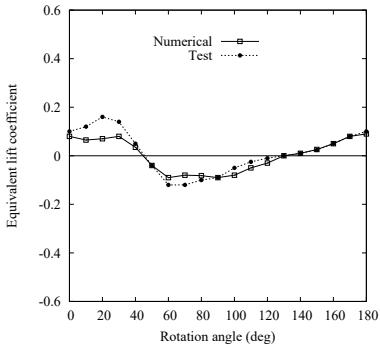

(c) Gap, $\bar{e}$=0.3

Fig. 12 Theoretical and experimental static equivalent left coefficients of RSC/airfoil versus statically rotational angle of RSC for nondimensional gap between the RSC and the airfoil trailing edge and flow velocity U = 20 m/s; **a** for $\bar{e} = 0.08$, **b** for $\bar{e} = 0.03$ and **c** $\bar{e} = 0.3$

$$\alpha_G(t) = \overline{\alpha}_{G1} \sin \omega t + \overline{\alpha}_{G2} \sin(2\omega t + \Delta\phi)$$

where $\Delta\phi$ is a possible phase difference between first and second gust frequencies. However, it is difficult to determine $\Delta\phi$ due to the flow field created by the present RSC gust generator. Thus we assume $\Delta\phi = 0$ as an approximation in the theoretical computations.

Using experimental gust angle versus gust frequency (Fig. 14c), the correlation analyses between the theoretical and experimental results for the mid-span velocity response (rms) versus gust excitation frequency at the flow velocity $U = 25$ m/s is

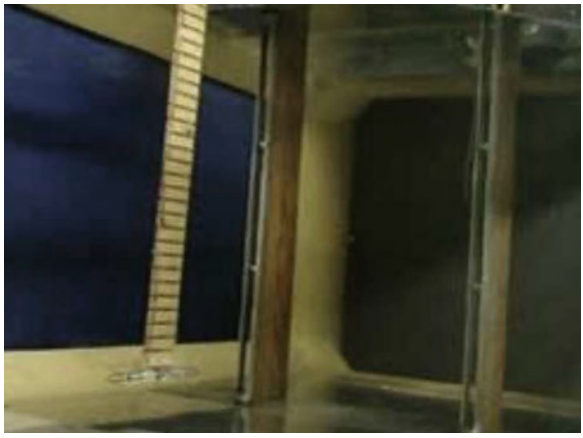

Fig. 13 Photograph of the experimental model and gust generator in the wing tunnel

shown in Fig. 14d ($\theta_0 = 2°$). Two dominant peaks are found. One is at a frequency, 19 Hz, which corresponds to the second flapwise bending mode and the other is near 22–23 Hz, which corresponds to the first torsional mode. The theoretical and experimental results verify that the correlation is good.

5.3.2 Responses to A Frequency Sweep Gust Excitation

Before the test, the frequency sweep gust excitation values are measured and quantitatively calibrated. The measured point of the probe is located at the position of the wing model. Figure 15a shows a measured time of continuous linear frequency sweep gust angle of attack for $U = 25$ m/s. The gust strength (angle of attack) is not constant with time as expected from theory. For the measured lateral gust, the minimum and maximum frequencies are 0 and 40 Hz, and the sweep duration T is 4 s. For convenient application in the gust response analysis, a formula based upon experimental gust angle of attack data is constructed,

$$\alpha_G(t) = \overline{\alpha}_G(t) \sin\left(\omega_1 + \frac{\omega_2 - \omega_1}{2T} t\right) t$$

and where $\alpha_G(t)$ is given by

$$\overline{\alpha}_G(t) = \sum_{i=0}^{4} c_i t^i$$

and $c_0, \ldots c_4$ are determined by the least-square curve fitting method of the experimental data.

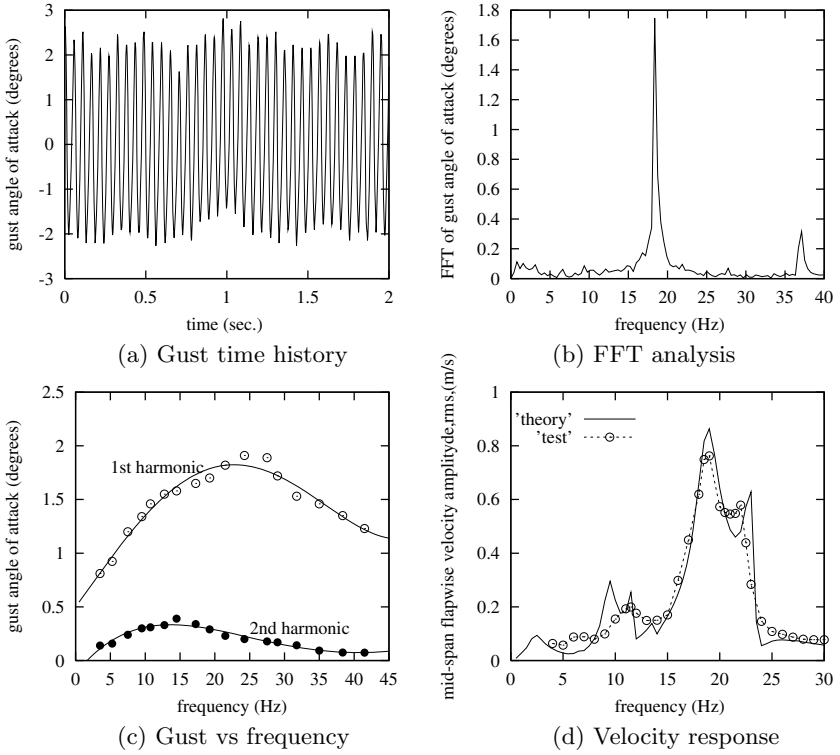

Fig. 14 Gust response to a harmonic excitation for the flow velocity U = 25 m/s; **a** time history of single harmonic gust excitation for gust frequency, $\omega = 18.5$ Hz, **b** FFT analysis of the time history, **c** gust angle of attack versus gust frequency, experimental data points are indicated by the circles. Solid lines are curve fits, **d** theoretical and experimental velocity response (rms) to gust excitation frequency at mid-span for $\theta_0 = 2°$

An envelope of the numerical gust simulation is plotted in Fig. 15a as indicated by the broken line that is applied to the theoretical computations.

Figure 15b shows a corresponding power spectra density (PSD) plot and comparison between the measured continuous linear frequency sweep gust (solid line) and the numerical gust simulation (broken line) for $U = 25$ m/s. The experimental PSD is based on an average over 20 sweep periods.

Using the above formula of the experimental frequency sweep gust envelope, (Fig. 15a), the correlation analyses between the theoretical and experimental results for the mid-span flapwise velocity at flow velocity of $U = 25$ m/s and a steady angle of attack, $\theta_0 = 2°$ are shown in Fig. 16a–c. There are ten sweep periods in 40 s and the total sampling length is 51,200 points for the measured data. Figure 16a and b is one sweep period of the total sampling length for the theoretical and experimental

time histories of the mid-span flapwise velocity response. Corresponding to Fig. 16a and b, theoretical (solid line) and experimental (dashed line) PSD results are shown in Fig. 16c for an average over 10 sweep periods. The agreement between theory and experiment is reasonably good. The peak frequencies of the PSD analysis are very similar to Fig. 14d. It further confirms our previous conclusions for the single harmonic excitation.

In addition to the high-aspect-ratio wing model [3], studies of gust response for other linear and nonlinear structural models have been made. These are:

1. A flexibly suspended high-aspect-ratio wing model [4];
2. A delta wing model [17, 18];
3. A wing-store model including a freeplay in the store support [19];
4. An airfoil section wing control surface freeplay [22, 23];
5. An airfoil with electro-magnetic dry friction damper [24];
6. An All-movable tail model including a freeplay in the control system [26].

6 Aero-Electromechanical Interaction: Theoretical and Experimental Correlation of Energy Harvesting

Recently energy harvesting from fluid-structural interaction has been studied theoretically and experimentally. Many papers on nonlinear beams and plates in axial flow from Paidoussis' group [61] (Cantilevered flexible plates in axial flow: Energy transfer and the concept of flutter-mill; The dynamics of variants of two-dimensional cantilevered flexible plates in axial flow) and also from Michelin's group [62] (Energy harvesting efficiency of piezoelectric flags in axial flows; Influence and optimization

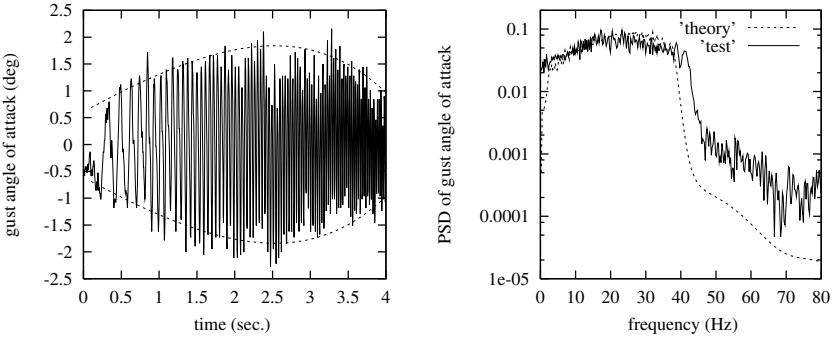

(a) Time history (b) PSD analysis

Fig. 15 Gust response to a linear frequency sweep excitation for the flow velocity U = 25 m/s; **a** time history of frequency sweep gust excitation, **b** for PSD analysis of the gust excitation.

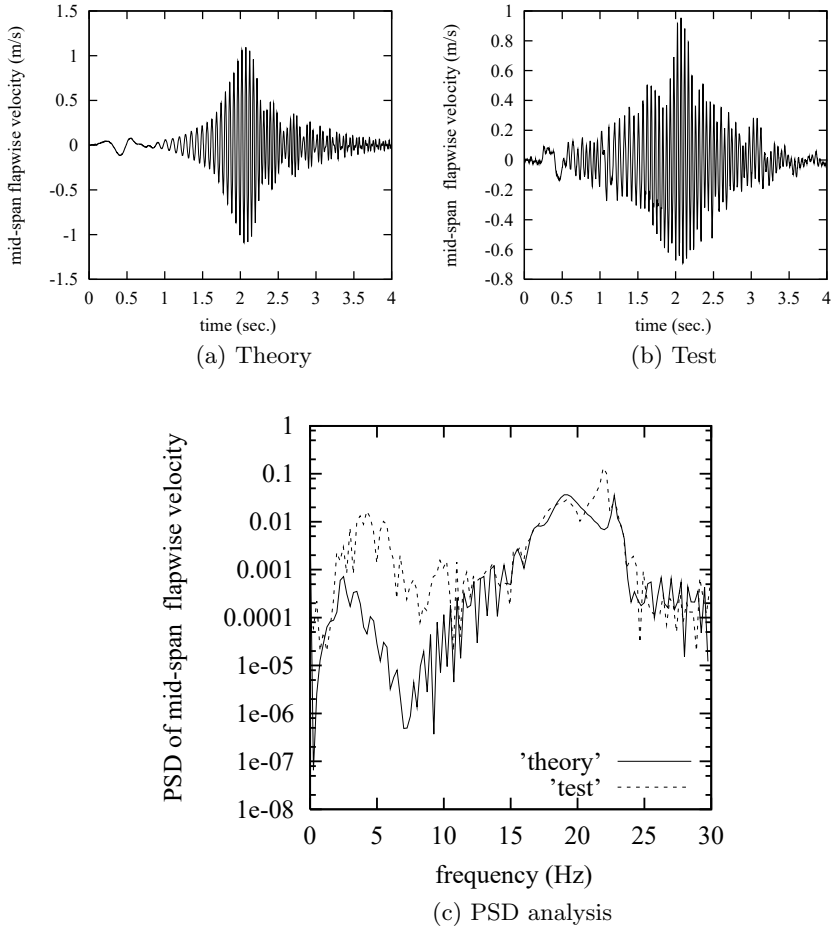

Fig. 16 Gust response to a linear frequency sweep excitation for the flow velocity U = 25 m/s; **a** theoretical velocity time history of mid-span flapwise for $\theta_0 = 2°$, **b** for measured time history at mid-span flapwise, **c** PSD analyses for both the theoretical and experimental times for $\theta_0 = 2°$

of the electrodes position in a piezoelectric energy harvesting flag) have developed new computational methods about fluid-electric-mechanical coupling system and provided very useful information.

Modeling of aero-electromechanical interaction in active flutter suppression and in energy harvesting extraction from a large nonlinear aeroelastic response has been studied and developed theoretically and experimentally in the Duke Aeroelastic group [63–65]. For the former, two typical example systems, a typical section model and a flexible delta wing have been described by David Cox in chapter "Aeroelastic Control". For the energy harvesting project, the inextensible beam and plate theory

developed by this group has provided a strong theoretical foundation. This theoretical approach has been applied to nonlinear aeroelastic response analysis and aero-electromechanical coupling model analysis and also correlated with results from wind tunnel experiments.

The studies of energy harvesting include experimentally aeroelastic model design with partly and fully covered piezoelectric and piezo film sensor attached to a beam or plate, experimentally electromechanical model design and power energy measurement from large structural response and also the theoretical and experimental correlation both for the flapping response from wind tunnel testing and energy harvesting. Theoretically, the structural dynamic equation includes the effects of the mass and stiffness of piezoelectric sheets and the stiffness nonlinearity form inextensible beam and plate theory. Also the linear electric equation includes these nonlinear terms from the above effects. To find a optimal energy extraction, the fully covered piezoelectric plate is rotated from a position with the clamped edge normal to the flow (0°) to where the clamped edge is aligned with the flow (90°), i,e the yaw angle, β varies from 0° to 180°. Thus, this numerical simulation provides a better option of the yawed plate. Two cases of the theoretical and experimental correlation are considered. One is an experiment for a large flapping response created by an external force vibration excitation near the second bending natural frequency. This experiment not only evaluates the theoretical aero-electromechanical coupling model, but also the nonlinear inextensible beam theory when the electric circuit is closed. Another experiment is for a large flapping response created by a limit cycle oscillation of a fluttering flag providing an aeroelastic energy harvester created for piezoelectric power generation in an aerodynamic flow field. AC voltage outputs from the piezo patch or film sensors and a DC power extraction through a AC/DC convert circuit are obtained. These experiments are used to evaluate a new computational model and code for an aero-electromechanical system. These provide a good physical understanding of the flutter/LCO and the energy harvester characteristics of this aero-electromechanical system.

There are several alternative strategies for energy harvesting including energy harvesting from fluid-structural interaction. Based upon the present and prior work the following may stated with some confidence. Self excited nonlinear oscillations arising from the dynamic instability of the corresponding linear fluid-structural system will provide larger energy/power levels than alternative concepts based upon stable dynamical systems excited into resonance. Most of the concepts previously studied in the literature lead to milliwatts of power typically, with a few that might reach a watt. As shown in Ref. [64] by the numerical simulation for a comparable sized system, the tens of watts can be theoretically achieved and scaling laws have been developed that allow one to to increase power levels to even greater levels with systems of greater size and improved piezoelectric patches with larger coupling coefficient.

Table 7 Geometric and material properties

Parameter	P-876A12	DT2-028K/L	DT4-028K/L
Piezo-Sheet numbers, m	#1, 2, 3	#6, 7, 9	#4, 5, 8
Length (l_p, l_{t1}, l_{t2}, L) (mm)	61	73	171
Width (b_p, b_t, b) (mm)	35	16	16
Thickness (t_p, t_t, t_s) (mm)	0.5	0.04	0.04
Mass density (ρ_p, ρ_t, ρ_s) (kg/m^3)	4666	1789	1789
Elastic modulus (E_p, E_t, E_s) (GPa)	23.3	3.0	3.0
Coupling coefficient (e_{31}^p, e_{31}^t) (C/m^2)	−0.6	−0.01	−0.01
Permitivity constant ($\epsilon_{33}^p, \epsilon_{33}^t$) (F/m)	$33.63e^{-9}$	$107e^{-12}$	$107e^{-12}$

6.1 Experimental Model and Measurement System

6.1.1 Experimental Model for Partly Covered Piezoelectric Patch and Piezo Film Sensors

A 6061-T6 aluminum elastic plate was used as a substrate lamination. One end was clamped to a heavy support that was fixed on the ground and the other end is free. The length, width and thickness are 513, 101.6 and 0.375 (mm) of the substrate plate and the mass density and elastic modulus are 2840 kg/m^3 and 68.9 GPa. Two kinds of piezoelectric patches, P-876A12 and piezo film sensors, DT2-028K/L, DT4-028K/L were bonded to the substrate on both surfaces or only on one surface. A schematic of the distribution of the piezoelectric patches and piezo film sensors is shown in Fig. 17a. The material properties and geometry of the substrate laminate and the piezoelectric patches and piezo film sensors are shown in Table 7.

6.1.2 Experimental Model for Full Covered Piezo Film Sensors

The same cantilever elastic plate was used as a substrate, but twelve (12) piezo film sensors, DT4-028K/L were bonded to the substrate on both sides. A photograph of the distribution of the piezo film sensors is shown in Fig. 17b.

The flexible plate has several piezoelectric patches and piezo film sensors attached and is placed in a uniform axial flow. This flexible system can be considered as a flap-

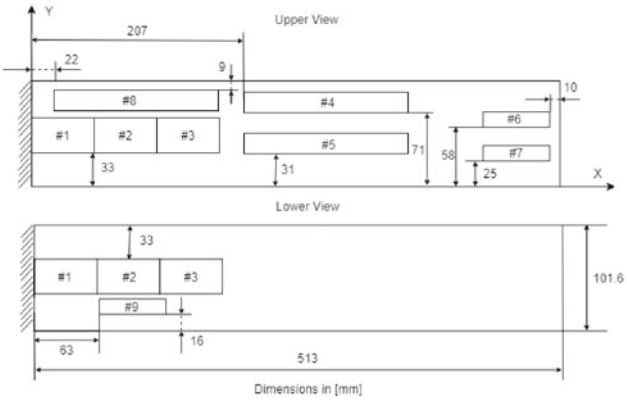

(a) Schematic

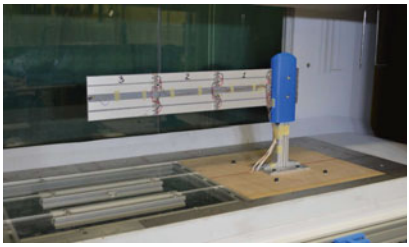

(b) Photograph

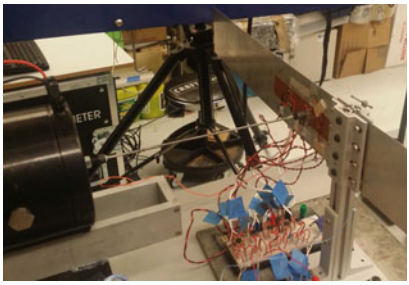

(c) Photograph

Fig. 17 Schematic of the distribution of the partly corvered piezoelectric patches and piezo film sensors (**a**), photograph of the aeroelastic model (fully covered model) in the wind tunnel (**b**), and photograph of the forced vibration test setup (**c**)

ping flag model, i.e a non-uniform beam model. The stiffness and mass distributions are variable along the elastic axis.

6.1.3 Experimental Setup and Measurement Data Acquisition

In both cases the aluminum plate is cantilevered horizontally, flag configuration, from a stiff vertical aluminum profile. The data is acquired with m+p VibPilot 24bit 8ch DAQ. The AC voltages from piezo elements are rectified through full-wave DF04S rectifier. Tip acceleration is measured with PCB 352C22 accelerometer.

Dynamic responses and energy harvesting from a forced vibration test.

The plate is excited through *B&K* 4809 shaker, positioned horizontally and attached to the plate through Dytran 1022V force sensor. The shaker is controlled through the DAQ unit with compatible amplifier. The applied force and tip accel-

eration are acquired directly. The excitation is pure sine with pre-set frequency. A photograph of the forced vibration test setup is shown in Fig. 17c.

LCO aeroelastic response and energy harvesting from the wind tunnel test.

The cantilevered plate is placed inside the wind tunnel, with aluminum profile covered with 3d printed plastic shroud to reduce vortex shedding. Air speed is measured with a pitot tube sensor and acquired directly together with tip acceleration and voltage outputs in the DAQ unit. The air speed is increased manually with data recorded constantly during the tests. The tip deflection was measured with an accelerometer and the defection inferred from that. Given a dominant single frequency in the response, this is straightforward. A photograph of the aeroelastic model (fully covered model) in the wind tunnel is shown in Fig. 17b.

6.2 Theoretical/Experimental Correlations

6.2.1 Dynamic Response and Power Extraction from Force Vibration for Partly Covered Beam Model

Figure 18a shows the stiffness and mass per length distribution for the partly covered piezoelectric patch and piezo film sensors. The piezoelectric patch of P-876A12 provides a large additional stiffness and mass near the root of the cantilever beam. However the piezo film sensors of DT2-028 K/L and DT4-028K/L provide very small additional stiffness and mass. The weight of the accelerometers is accounted for in the computational model. The weight of the wires was added as distributed mass in the model. A finite element method (FEM) is used to calculate the eigenvalues and eigenvectors. The first five (5) natural frequencies of the beam are 1.74, 8.67, 22.85, 45.53 and 73.73 Hz.

A standard hammer test was performed in order to identify the dynamic properties of the experimental model. The first two natural frequencies are 1.23 and 8.6 Hz. An experimental model to be subjected to a dynamic loading was constructed. A periodic dynamic point force, $f_0 \sin(\omega t)\delta(x_f - L)$ is applied near the root of the cantilever beam, where ω is the external frequency and is set close to the experimental second natural frequency, 8.6 Hz. Note that the theoretical second natural frequency is 8.67 Hz. The force driving point is at x = 60 mm. First five bending modes are considered in the calculations and the modal damping is $\xi = 0.015$ for all modes. The external force f_0 varies from 0.4 N to 14.4 N.

Figure 18b shows the nondimensional response amplitude, wtip/L at the tip for the external force amplitude from 0.4 N to 14.4 N for the theoretical computations and 1.42 N to 13.2 N for the experiment. For comparison the results without the electric coupled equations are also plotted in this figure. It is found that the nonlinear forces are dominated by those of the structure. The linear and nonlinear electric forces induced by the piezoelectric patch and piezo film sensor are smaller. The correlation is reasonably good, but there are some differences between the computations and experiment. The source of the difference may come from both the computa-

tional model and the experimental measurement. The theoretical modal damping does not exactly match the experimental model, because it varies when the excitation frequency is equal to the second natural frequency. Also for the experimental measurement it is difficult to control the excitation frequency to be at exactly the second natural frequency. Although there are some differences, these results still provide a good experimental verification of the inextensible beam theory.

The theoretical output sinusoidal voltage signal generated from the piezoelectric patch converts to a DC voltage through an AC/DC convert circuit and is directly connected with the capacitor. The algorithm of the conversion is based on the assumption that the external electric circuit has a small effect on the voltage output of the piezoelectric patch, and hence the amplitude of the voltage output on the patch remains unchanged during the charging process. The DC amplitude remains the AC amplitude. The experimental output voltage signal generated from the piezoelectric patch converts to a DC voltage through an AC/DC convert circuit. The electric circuit is shown in Fig. 18c.

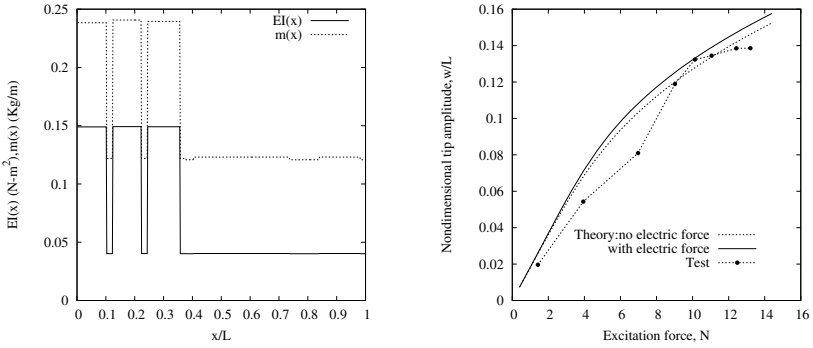

(a) EI-m vs x (b) Tip Disp.

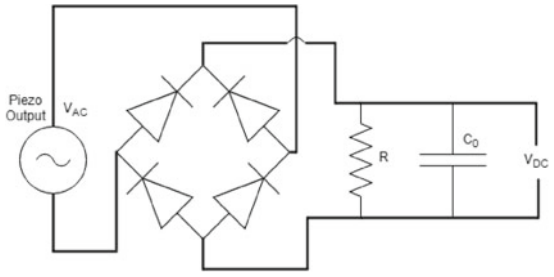

(c) AC/DC circuit

Fig. 18 Large response from a force vibration: stiffness and mass per length distribution for the partly covered piezoelectric patch and piezo film sensors (**a**), nondimensional peak tip amplitude, w_{tip}/L (**b**), and schematic of AC/DC convert circuit of the experiment. R is an effective resistance and C_0 is a capacitance, $C_0 = 22\mu F$ (**c**)

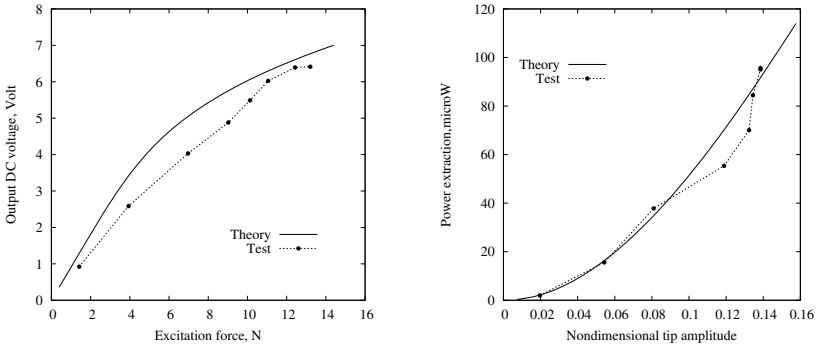

(a) DC output (b) Power extraction

Fig. 19 Power extraction from a force vibration: output DC voltage (**a**) and power extraction (**b**) from #4 piezo film sensor

Figure 19a shows the DC output voltage at #4 piezo film sensor and the external force amplitude from 0.4 N to 14.4 N. As expected the DC output voltage increases as the external force increases. The correlation is reasonably good, but there are some differences between the computations and experiments. The source of the error may come from the determination of the piezoelectric properties such as the coupling constants, e_{31}^p, e_{31}^t and permittivity constants, ϵ_{33}^p, ϵ_{33}^t. Here the piezo film coupling constant is obtained from the experimental tip response and the corresponding AC output voltage using the linear electric equation. Also the differences may come from the AC/DC conversion. The theoretical AC/DC conversion assumes that the peak value of the generated AC voltage from the piezo film sensor is close to the converted DC voltage. The experimental AC/DC convert has difference in these voltages of about 8–10

Corresponding to this output voltage of the #4 film sensor, the power extraction can be calculated as

$$P_{DC} = V_{DC}^2 / R$$

where R is an effective resistance, $R = 430\,\text{k}$ Ohm.

The theoretical and experimental correlation of a typical element is shown in Fig. 19b for the power output for piezoelectric patch, P-876A12 at #4. The correlation is good.

6.2.2 Aeroelastic Response and Power Extraction from Flag Flutter for Partly Covered Model

A linear vortex lattice aerodynamic model was used. For the structural modal equation, the Runge–Kutta Fourth order algorithm is used and for the aerodynamic and

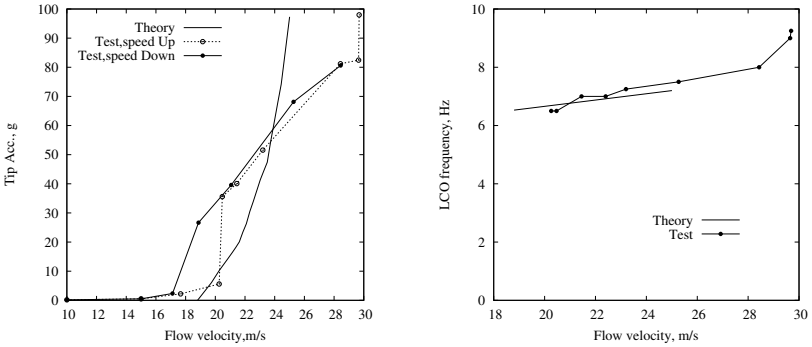

(a) Tip Acc. (b) LCO frequency

Fig. 20 Tip response from a large aeroelastic response of partially covered model: tip acceleration responses versus flow velocity, U (**a**), LCO frequency (**b**)

electric network equations the finite-difference method is used to calculate the nonlinear responses, peak output voltage and power extraction of this piezoelectric-aeroelastic system.

Figure 20a shows the acceleration peak amplitude in g at the tip for flow speeds from 18.8 m/s to 25 m/s for the theory and 10 to 29.7 m/s for the experiment. The theoretical tip acceleration as indicated by solid line rapidly increases as flow speed increases. For the experimental measurement, two different LCO responses for increasing and decreasing flow velocity were observed. The symbols, ∘ plus broken line and • plus solid line, indicate the experimental results for increasing and decreasing flow velocity, respectively. With increasing flow velocity, we find a jump at $U = 20.6$ m/s which is similar to the theoretical results at $U = 18.8$ m/s as shown by the solid line. As the flow velocity increases further, the LCO amplitude that is measured has a larger increase than that found from theory. When the flow velocity is decreased, we find another jump at $U = 18.87$ m/s as shown in Fig. 21a and as indicated by the symbol, • with a solid line. The experimental linear critical flutter boundary is estimated from this figure. An intersection between the extrapolated LCO amplitude curve and the flow velocity axis is defined as the linear critical flutter boundary. The estimated experimental flutter velocity is 20.36 m/s and frequency is 6.4 Hz. Corresponding to the experimental acceleration peak response, the measured dominant LCO frequency are obtained. The theoretical and experimental LCO frequencies are shown in Fig. 20b. The experimental LCO frequency is similar to the theoretical frequency. As shown in Fig. 20a a hysteresis response was observed in the experimental measurement but not in the theoretical response.

Corresponding to the DC voltage outputs of #3, P-876-A12 patch and the film sensors of #4 and 6, the DC power extraction can be calculated with the effective resistance, $R = 750$ k Ohm. Figure 21a–c show the theoretical and experimental correlation of power extraction versus increasing flow velocity for patches #3, 4 and 6.

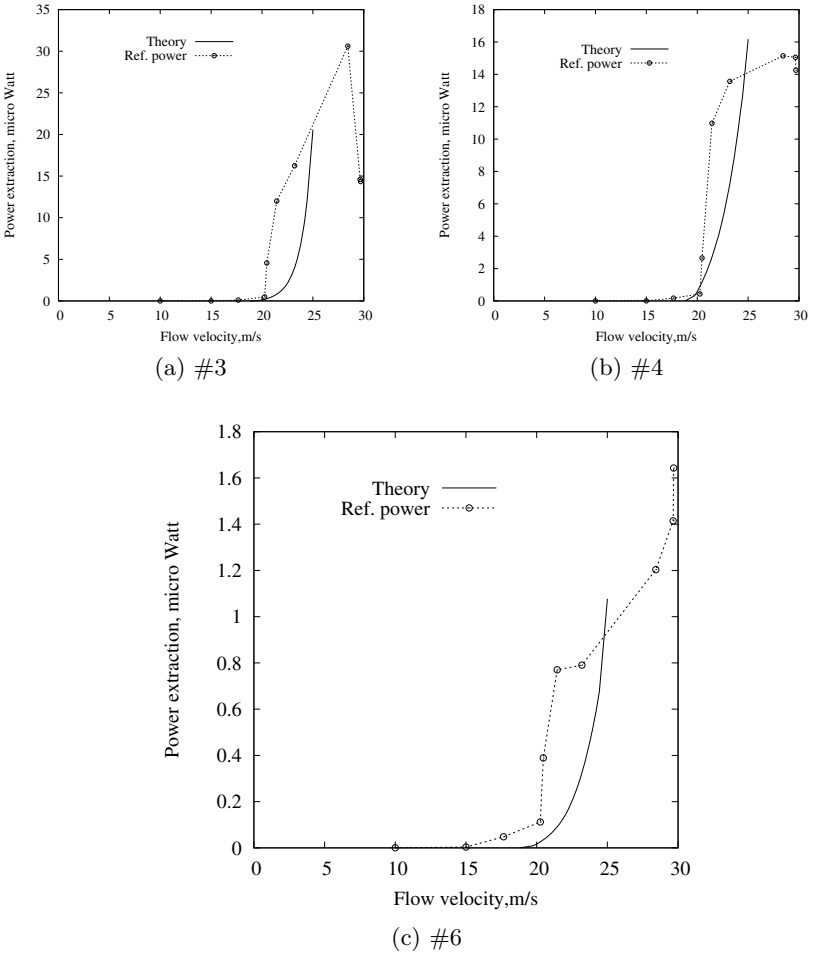

Fig. 21 Power extraction from a large aeroelastic response of partially covered model: power extraction from piezoelectric patch at #3 (**a**) and piezo film sensors at #4 (**b**) and #6 (**c**)

Considering the effect of experimental AC/DC converter on the power extraction, a reference power, ($P_{Ref.}$) concept is introduced. This is defined as

$$P_{Ref.} = V_{AC,test}^2 / R$$

This means the AC/DC converter has zero voltage drop, i.e no energy loss in the convert process. Thus, $P_{DC} = P_{Ref.}$. Here $V_{AC,test}$ is the measured AC voltage output. This reference power, "Ref. power", is indicated in the figure. The electric power extraction increases as the flow velocity increases as expected. Film sensor #6 provides much lower power extraction than patch #4 although they are both film sensors.

This is because #6 patch is near the beam tip and the bending curvature velocity at #6 is smaller than those at #4 and also #3. Piezo patch #3 provides much larger power extraction than patch #4. This is because #3 patch has a larger electric-mechanical coupling coefficient, e_{31}, than those of film sensor although the bending curvature velocity at #3 is smaller than those at #4. It is also found that the theoretical results are closer to the "Ref. power" results, i.e. the experimental results when the non-ideal experimental AC/DC converter is neglected.

6.2.3 Aeroelastic Response and Power Extraction from Flag Flutter for Fully Covered Model

As shown in Fig. 17b of the fully covered model by the film sensors, DT4-028 K/L, the aeroelastic model is considered as a uniform flag plate. The structural natural frequencies and mode shapes can be calculated for a uniform cantilevered beam. The experimental first natural bending frequency is $f_1 = 1.44$ Hz. The theoretical first five (5) bending natural frequencies are 1.44, 9.02, 25.27, 49.5 and 81.86 Hz. The theoretical linear flutter speed and frequency are $U_f = 21.25$ m/s and $\omega_f = 6.24$ Hz. The theoretical computations for the fully covered plate are similar to those for the partly covered plate for the nonlinear structural modal and linear electric and aerodynamic equations. The same algorithm and aerodynamic parameters are used.

Figure 22a shows the acceleration peak amplitude in g at the beam tip for flow speeds from 19.27 m/s to 28.15 m/s. The theoretical tip acceleration as indicated by solid line rapidly increases as the flow speed increases. For the experimental measurement, two different LCO responses for increasing and decreasing flow velocity were observed. The symbols, ∘ plus broken line and • plus solid line, indicate the experimental results for increasing and decreasing flow velocity, respectively. With increasing flow velocity, we find a jump at $U = 23.03$ m/s which is similar to the theoretical results at $U = 23.03$ m/s as shown by the solid line. As the flow velocity increases further, the LCO amplitude measured has dropped down, but the theoretical LCO amplitude continues to increase. This drop down phenomenon in the experiment may be created by a effect similar to that of a nonlinear stalled airfoil because of the large flag motions. When the flow velocity is decreased, another jump range from $U = 21.7$ m/s to 19.1 m/s was found as shown in Fig. 22a and as indicated by the symbol, • with a solid line. The experimental linear critical flutter boundary is estimated from this figure. The experimental flutter speed and frequency are 20.36 m/s and 7.25 Hz. The correlation is reasonably good.

Figure 22b show the theoretical and experimental AC output voltage from the film sensors, DT4-028K/L at #2. Due to different positions in the x axis, the output voltages for #1 and #3 are different with #2. Near the root of the plate, #1 film provides a lower AC voltage output and #2 patch provides a higher AC voltage output. This is because the bending curvature velocity at #2 is larger than those at #1 and also at #3. Due to hysteresis, the measured AC output voltage has two different results for increasing and decreasing flow velocity. The theoretical results are closer

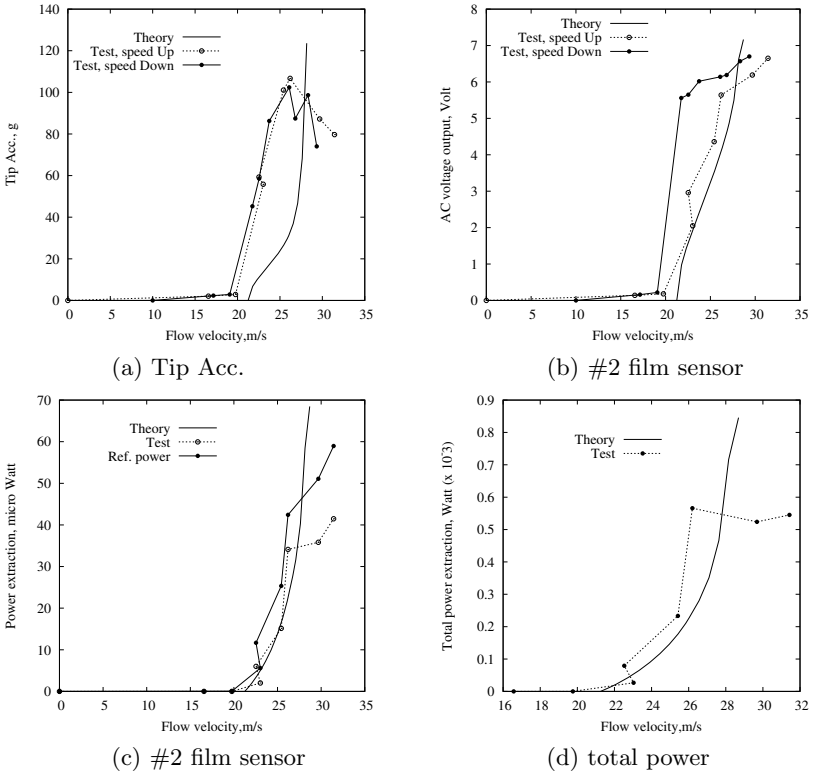

Fig. 22 Power extraction from a large aeroelastic response of fully covered model: peak amplitudes versus flow velocity for the tip acceleration (**a**), the theoretical and experimental AC output voltage from #2 (**b**), DC power extraction from film sensors at #2 (**c**), total DC power extraction (**d**) versus increasing flow velocity

to those from the experiment for increasing flow velocity than from the experiment for decreasing flow velocity.

Figure 22c shows the theoretical and experimental correlation of power extraction versus the increasing flow velocity for the film sensor of #2. Considering the effect of experimental AC/DC converter on the power extraction, "Ref. power" is also plotted in this figure. The electric power extraction increases as the flow velocity increase as expected. The film sensor of #2 provides much higher power extraction than the patches of #1 and 3. This is because #2 has the larger bending curvature velocity. The theoretical results are reasonably close to both the "Ref. power" and the real "Test" results.

Figure 22d shows the total theoretical and experimental power extraction versus the increasing flow velocity for the fully covered plate. The fully covered plate has total 24 film sensors bonded to the substrate for both surfaces and each power

extraction is based on a single film sensor. The total power extraction should be and is assumed to be the sum of each single film sensor. The theoretical and experimental correlation is reasonably good. In the total power extraction analysis, it found that #2 film sensor provides maximum contribution over the total power for both the theoretical and experimental results. More than half of the total power extraction comes from the film sensors at #2 position. This means that it is very important to consider the optimal position of the piezo patch or film sensor.

Summarizing the correlation results, the following conclusion may be made.

1. The inextensible beam theory has been verified by the dynamic force vibration test with larger flapping response. A good correlation between the theory and experiment was obtained for the structural motion.

2. A large LCO response beyond the linear flutter speed was observed from the wind tunnel experiment and correlated with results from the computational model for both experimental models. A good correlation for the linear flutter speed verifies that the theoretical linear piezoelectric-aeroelastic model is accurate. A reasonably good correlation for the LCO response shows the new computational code and the nonlinear inextensible beam theory is useful. A hysteresis response of LCO in the experimental measurement and amplitude drop down in the higher flow velocity were observed in the experiment, but not found in the computations.

3. The DC power extraction from the piezoelectric network equation depends on the dynamic vibration amplitude or the LCO amplitude as well as the LCO mode and the position of piezo patch or film sensor along the flow direction. This is because the best position with a larger bending curvature velocity provides a larger power extraction. Also the DC power extraction depends on AC/DC convert circuit and there is an opportunity for improvement in the experimental model in this respect.

4. Given the complexity of the interaction among the structural deformation, the aerodynamic flow field and the electrical field, the agreement between experiment and the computational model is in fact encouraging. The basic structural plus aerodynamic model has been studied by the authors and others and reported separately. Not surprisingly, the added complexity of the electrical field leads to larger differences in the results between the experiment and the computational model compared to that of the aerodynamic plus structural model alone. However, it is clear that the basic physics of the experiment is being captured by the theoretical/computational model. But there is always room for improvement of course.

7 Conclusions

This overview of wind tunnel model design and testing conducted at Duke University over the last twenty years has demonstrated that a standard low speed wind tunnel may be used as a test bed for a wide range of models to investigate linear and nonlinear phenomena in aeroelasticity. The data acquired have been used to validate and improve theoretical/computational models that in turn have provided a basis for high speed flow prediction of comparable phenomena. Flutter, gust response, limit

cycle oscillations and energy harvesting have been among the fundamental physical phenomena that have been studied for models with a range of nonlinear elements in the structures (including freeplay and nonlinear geometric, i.e. strain-displacement relations) or aerodynamic flows (including flow separation over bluff bodies and airfoils at high angles of attack). Correlation between theory and experiment has been encouraging and ever better as the state of the art has progressed.

Acknowledgements The authors would like to thank all those colleagues who have contributed to these studies over the years including the following: Peter Attar, Fanny Besem, PC Chen, Paul G. A., Cixmas, Mark Connor, Levin, Dani, Chuck Denegri, Henri Gavin, Chad Gibbs, Adam Grasch, James Henry, Denis Kholodar, Bob Kielb, D-H Lee, Daniella Raveh, Anosh Sethna, Meredith Spiker, Jeff Thomas, Steve Trickey, Lawrie Virgin, Ivan Wang, Hiroshi Yamamoto, Minghui Zhao

References

1. Tang DM, Dowell EH (2001) Experimental and theoretical study on aeroelastic response of high-aspect ratio wings. AIAA J 39(8):1430–1441
2. Tang DM, Dowell EH (2002) Limit cycle hysteresis response for a high-aspect ratio wing model. J Aircr 39(5):885–888
3. Tang DM, Dowell EH (2002) Experimental and theoretical study of gust response for a high-aspect ratio wing. **40**(3):419–429
4. Tang DM, Grasch A, Dowell EH (2010) Gust response for flexibly suspended high-aspect ratio wing. AIAA J 48(10):2430–2444
5. Tang DM, Dowell EH (2009) Flutter/LCO suppression of high aspect ratio wings. J R Aeron Soc 113(1144):409–416
6. Tang DM, Henry JK, Dowell EH (1999) Limit cycle oscillations of delta wing models in low subsonic flow. AIAA J 37(11):1355–1362
7. Tang DM, Dowell EH (2001) Effects of angle of attack on nonlinear flutter of a delta wing. AIAA J 39(1):15–21
8. Tang DM, Attar PJ, Dowell EH (2006) Flutter/LCO analysis and experiment for a wing-store model. AIAA J 44(7):1662–1675
9. Tang DM, Dowell EH (2006) Flutter and limit cycle oscillations for a wing-store model with freeplay. J Aircr 43(2):487–503
10. Attar PJ, Dowell EH, Tang DMI (2005) Modeling the LCO of a delta wing model with an external store using a high fidelity structural model. In: AIAA SDM conference, April, AIAA paper 2005-1913
11. Tang DM, Yamamoto H, Dowell EH (2003) Experimental and theoretical study on limit cycle oscillations of two-dimensional panels in axial flow. J Fluids Struct 17(2):225–242
12. Gibbs C, Sethna A, Wang I, Tang DM, Dowell EH (2014) Aeroelastic stability of a cantilevered plate in yawed subsonic flow. J Fluids Struct 49:450–462
13. Tang DM, Gibbs C, Dowell EH (2015) Nonlinear aeroelastic analysis with inextensible plate theory including correlation with experiment. AIAA J 53(5):1299–1308
14. Attar PJ, Dowell EH, Tang DM (2003) A theoretical and experimental investigation of the effects of a steady angle of attack on the nonlinear flutter of a delta wing plate model. J Fluids Struct 17(2):243–259
15. Tang DM, Dowell EH (2008) Theoretical and experimental aeroelastic study for folding wing structures. J Aircr 45(4):1136–1147
16. Peter JA, Tang DM, Dowell EH (2010) Nonlinear aeroelastic study for folding wing structures. AIAA J 48(10):2187–2195

17. Tang DM, Henry JK, Dowell EH (2000) Nonlinear aeroelastic response of a delta wing to periodic gust. J Aircreft 37(1):155–164
18. Tang DM, Henry JK, Dowell EH (2002) Effects of steady angle of attack on nonlinear gust response of a delta wing model. J Fluids Struct 16(8):1093–1110
19. Tang DM, Dowell EH (2006) Experimental and theoretical study of gust response for a wing-store model with freeplay. J Sound Vib 295:659–684
20. Conner MC, Tang DM, Dowell EH, Virgin LN (1997) Nonlinear behavior of a typical airfoil section with control surface freeplay: a numerical and experimental study. J Fluids Struct 11:89–112
21. Tang DM, Dowell EH, Virgin LN (1998) Limit cycle behavior of an airfoil with a control surface. J Fluids Struct 12(7):839–858
22. Tang DM, Kholodar D, Dowell EH (2000) Nonlinear aeroelastic response of a airfoil section with control surface freeplay to gust loads. AIAA J 38(9):1543–1557
23. Tang DM, Dowell EH (2010) Aeroelastic airfoil with free play at angle of attack with gust excition. AIAA J 48(2)(Feb.):427–442
24. Tang DM, Gavin HP, Dowell EH (2004) Study of airfoil gust response alleviation using an electro-magnetic dry friction damper - Part 2: experiment. J Sound Vib 267:875–897
25. Dong-Hwan L, Chen PC, Tang DM, Dowell EH (2010) Nonlinear gust response of a control surface with freeplay AIAA 2010–3116. In: 51st AIAA/ASME/AHS/ASC structures, structural dynamics and materials conference, 12–15 April. Oriando, Floriad
26. Tang DM, Dowell EH (2011) Aeroelastic response induced by freeplay: Part II, theoretical/experimental correlation analysis. AIAA J 49(11):2543–2554
27. Tang DM, Dowell EH (2013) Computational/experimental aeroelastic study for a horizontal tail model with freeplay. AIAA J 51(2):341–352
28. Tang DM, Dowell EH (2014) Effects of a free-to-roll fuselage on wing flutter: theory and experiment. AIAA J 52(12):2625–2632
29. Tang DM, Dowell EH (2014) Experimental aerodynamic response for an oscillating airfoil in buffeting flow. AIAA J 52(6):1170
30. Tang DM, Dowell EH (2013) Experimental aeroelastic response for a freeplay control surface in buffeting flow. AIAA J 51(12):2852–2861
31. Hodges DH, Dowell EH (1974) Nonlinear equations of motion for the elastic bending and torsion of twisted nonuniform rotor blades, NASA TN D-7818
32. Tran CT, Petot D (1981) Semi-empirical model for the dynamic stall of airfoils in view to the application to the calculation of responses of a helicopter blade in forward flight. Vertica 5(1):35–53
33. Simmonds JG, Libal A (1979) Exact equations for the inextensional deformation of cantilevered plates. J Appl Mech 46:631–636
34. Simmonds JG, Libal A (1979) Alternate exact equations for the inextensional deformation of arbitrary. Quadrilateral, and triangular plates. J Appl Mech 46:895–900
35. Simmonds JG (1981) Exact equations for the large inextensional motion of plates. J Appl Mech 48:109–112
36. Darmon P, Benson RG (1986) Numerical solution to an inextensible plate theory with experimental results. J Appl Mech 53:886–890
37. Tang DM, Zhao M, Dowell EH (2014) Inextensible beam and plate theory: computational analysis and comparison with experiment. J Appl Mech 81(6)
38. Molyneux WG (1950) The flutter of swept and unswept wing with fixed-root conditions. Aeronautical Research Council Reports and Memoranda No. 2796
39. Yates EC (1985) AGARD standard aeroelastic configurations for dynamic response I-Wing 445.6, AGARD Report, No. 765
40. Weatin MF, Goes LC, Ramos RL, Silva RG (2009) Aeroservoelastic modeling of a flexible wing for wind tunnel flutter test. In: Proceedings of 20th international congress of mechanical engineering (p. 9), Gramado, RS
41. Edwards JW, Schuster DM, Spain CV, Keller DF, Moses RM (2014) MAVRIC Flutter Model Transonic Limit Cycle Oscillation Test, NASA/TM-2001-210877. Langley Reseach Center, Hampton, Virginia. AIAA J 52(12):2625–2632

42. Peters DA, Cao WM (1995) Finite state induced flow models, part i: two-dimensional thin airfoil. J Aircr 32(2):313–322
43. Niles RH, Spielberg IN (1954) Subsonic flutter tests of an unswept all-movable horizontal tail, WADC TR-54-53, AD 39949
44. Niles RH (1955) Subsonic flutter model tests of an all-movable stabilizer with 35^0 Sweepback. WADC technical Note 55-623, AD 91593
45. Cooley DE, Murphy JA (1958) Subsonic flutter model tests of a low aspect ratio unswept all-movable tail, WADC-TR-58-31, AD 142337
46. Raveh Daniella E (2009) Numerical study of an oscillating airfoil in transonic buffeting flows. AIAA J 47(3):505–515
47. Raveh DE, Dowell EH (2011) Frequency lock-in phenomenon for oscillating airfoils in buffeting flows. J Fluids Struct 27(1):89–104
48. Dowell EH, Hall KC, Thomas JP, Kielb RE, Spiker MA, Denegri Jr CM (2007) A new solution method for unsteady flows around oscillating bluff bodies. In: IUTAM symposium on fluid-structure interaction in ocean engineering: Proceeding of the IUTAM symposium held in Hamburg, Germany, Springer, p. 37
49. Chen J, Fang YC (1998) Lock-on of vortex shedding due to rotational oscillations of a flat plane in a uniform stream. J Fluid Struct 12(6):779–798
50. Hall KC, Thomas JP, Clark WS (2002) Computation of unsteady nonlinear flows in cascades using a harmonic balance technique. AIAA J 40(5):879–886
51. Besem F, Kamrass JD, Thomas JP, Tang DM, Kielb RE (2016) Vortex-induced vibration and frequency lock-in of an airfoil at high angles of attack. J Fluids Eng Trans ASME 138(1)
52. Gilman J Jr, Bennett RM (1966) A wind tunnel technique for measuring frequency response functions for gust load analyses. J Aircr 3(6):535–540
53. Buell DA (1969) An experimental investigation of the velocity fluctuations behind oscillating vanes, NASA TN D-5542
54. Bicknell J, Parker AG (1972) A wind-tunnel stream oscillating apparatus. J Aircr 9(6):446–447
55. Poisson-Quinton P (1972) Note on a new V/STOL rig in the SI modane sonic tunnel. Third AGARD Meeting on V/STOL Tunnels, INERA, Amsterdam
56. Ham ND, Bauer PH, Lawrence TL (1974) Wind tunnel generation of sinusoidal lateral and longitudinal gust by circulation control of twin parallel airfoils, NASA CR 137547. Aeroelastic and Structures Research Lab, TR 174–3
57. Reed WH, III (1991) Conceptual design of a wind tunnel gust generator and rotor blade with feedback control. Dynamic Engineering Inc, Document D-409. Newport News, VA
58. Yates ECJr, Fox AG (1963) Steady-state characteristics of a differential-pressure system for evaluating angle of attack and sideslip of ranger IV vehicle, NASA TN D-1966
59. Tang DM, Cizmas Paul GA, Dowell EH (1996) Experiments and analysis for a gust generator in a wind tunnel. J Aircraft 33(1):139–148
60. Cizmas PGA, Tang DM, Dowell EH (1996) Flow about a slotted cylinder-airfoil combination in a wind tunnel. J Aircraft 33(4):716–721
61. Tang L, Paidoussis MP, Jiang J (2009) Cantilevered flexible plates in axial flow: energy transfer and the concept of flutter-mill. J Sound Vib 326:263–276
62. Michelin S, Doare O (2013) Energy harvesting efficiency of piezoelectric flaps. J Fluid Mech 714:489–504
63. Dunnmon JA, Stanton SC, Mann BP, Dowell EH (2011) Power extraction from aeroelastic limit cycle oscillations. J Fluids Struct 27(8):1182–1198
64. Tang Deman, Dowell EH (2018) Aeroelastic response and energy harvesting from a cantilevered piezoelectric laminated plate. J Fluids Struct 76:14–36
65. Tang Deman, Levin Dani, Dowell EH (2019) Experimental and theoretical correlations for energy harvesting from a large flapping flag response. J Fluids Struct 86:290–315

Fluid/Structural/Thermal/Dynamics Interaction (FSTDI) in Hypersonic Flow

Earl H. Dowell

Abstract Hypersonic flight is a major technical challenge and substantial efforts are currently underway to provide the understanding and technology required to design and operate effectively and safely a hypersonic aircraft for commercial or military purposes. Leyva [1] has recently described the essence of this challenge. The present chapter provides a summary of the past, present and proposed work for fluid/structural/thermal dynamics interaction.

1 An Introduction and Overview

There are several key physical phenomena that can occur in hypersonic flight that involve fluid/structural/thermal/dynamics interaction (FSTDI). *This chapter is not a review of the all the many papers that have been published that one might cite; there are literally thousands. It is an effort to bring some order to this complex multidisciplinary topic for the benefit of current and future research teams.* In the beginning of the discussion, issues involving only two disciplines are identified that need further work as well as issues that are relatively well understood. Then the discussion moves to issues involving three disciplines (FSI) and finally to FSTDI in its full four discipline form.

To bring some order to the complexity, the focus will be on (1) response of structures to known turbulent flows, (2) global dynamic instability of the flow field due to shock wave/boundary layer interaction, (3) dynamic instability of the combined fluid structural system (flutter and limit cycle oscillations), and (4) effects of the thermal fields on the foregoing as well as vice versa.

The discussion is inspired by the notion of simpler "unit projects" that are important components of the full FSTDI challenge. In any of these projects a close interaction of theory/computations and experiments is needed. Theory/computation can be a great help in designing and interpreting the results of experiments and of course experiments can help assess the validity of the theoretical/computational model as

E. H. Dowell (✉)
Mechanical Engineering and Materials Science Duke University, Durham, NC, USA
e-mail: earl.dowell@duke.edu

E. H. Dowell (ed.), *A Modern Course in Aeroelasticity*, Solid Mechanics and Its Applications 264, https://doi.org/10.1007/978-3-030-74236-2_16

well as uncover previously unknown physical phenomena. In thinking about the role of theory/computation in designing and interpreting experiments, it is useful to consider theory/computation as being a map to our ultimate destination. Even if the map is imperfect (as it always is), we are more likely to have a more productive and less costly journey when using a map to design and interpret the results of experiments.

As Peretz Friedmann [2] has pointed out, building on the seminal work of John Dugundji and John Calligeros [3] on aerothermoelastic scaling, the total number of significant non-dimensional parameters relevant to FSTDI and which must be accounted for in both theory and experiment is very large. Indeed it is not possible to design a model scale experiment that has all of the same (and potentially important) non-dimensional parameters as a full scale vehicle. Hence any experiment can at most represent an idealization of what the full scale vehicle will experience; but model scale experiments can be very valuable if all the relevant non-dimensional parameters are taken into account in the design of the experiment and the results correlated with current and future theoretical/computational models.

These non-dimensional parameters include the following: Mach number, Reynolds Number, the ratio of flow dynamic pressure to structural stiffness, the ratio of fluid mass to structural mass, the ratio of static pressure loading to structural stiffness, and the ratio of thermal stress induced by a temperature difference between the flexible structure and its surrounding structure to flexible structure stiffness as well as the geometry (e.g. length to width ratio) and boundary conditions of the structure. When multiple disciplines are involved the number of relevant non-dimensional parameters is indeed daunting.

Even for classical wing flutter, in experimental models, usually only the Mach number and flow dynamic pressure to structural stiffness are the same at model scale and full scale while the Reynolds number and the ratio of fluid mass to structural mass are not. This choice is dictated in part by necessity and in part by theory which suggests that the results are usually less sensitive to these latter two parameters. For the greater number of relevant parameters for FSTDI in hypersonic flow, theory and computations are even more valuable as a guide to the design and interpretation of experiments.

1.1 Two Disciplines Interaction

These multidisciplinary interactions can be usefully depicted in the form of a matrix as shown in Fig. 1 where both the horizontal and vertical components are four dimensional, i.e. representing the (F) fluid, (S) structural, (T) thermal and (D) dynamics disciplines.

The elements of this matrix have either XXX suggesting this two discipline interaction is very challenging and important to FSTDI; XX suggesting it is challenging and may be important or X suggesting the interaction is not as challenging to model and may usually be considered separately from FTSDI per se. Of course different observers may have different views on this categorization of the several elements

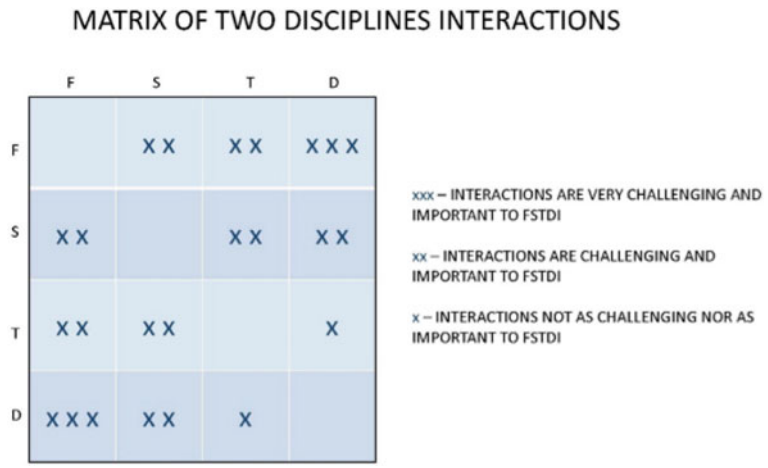

Fig. 1 Two disciplines interaction

and indeed as advances or new discoveries are made, the assessment of the elements of this matrix may change. Note that the matrix is symmetric.

Also note that there are only six unique elements in the matrix. The evaluation of the six X, XX, or XXX elements (at least in the authors' minds) are justified as follows.

Fluid/Structural (FS) Interaction: This describes the static deflection of the structure under fluid loading and also a possible change in the steady flow over the structure due to the static structural deformation. This is a well-studied issue and the interaction is usually modest and well understood.

Fluid/Thermal (FT) Interaction: This is the heating due to fluid flow and is well studied even without reference to FSTDI per se.

Fluid/Dynamics (FD): This name can be confusing because the study of fluids in general is often called fluid dynamics. But here we are concerned with time dependent phenomena and, in particular, the dynamics of turbulence due to the transition from laminar to turbulent flow as a consequences of the laminar flow becoming dynamically unstable. Note however that even when the flow has become turbulent a further dynamic instability may occur due to separated flow arising from shock wave-boundary layer interaction. Some would say that this interaction is the most demanding to model in all of FSTDI both theoretically/computationally and experimentally. The dynamics of turbulence and shock-wave boundary layer interaction represent two of the great unsolved problems in engineering and science and both provide an important source of excitation that may lead to significant structural response. Given that both phenomena represent the nonlinear dynamics of a fluid arising from dynamic instabilities they may prove to share certain fundamental characteristics.

Thermal/Structural (TS): Buckling of the structure due to thermal stress is perhaps the most important issue here and again this issue is well studied even without

considerations of FSTDI. However there is a concern that a buckled structural may increase the heat transfer to the structure from the fluid and this is the theme of a wind tunnel investigation by Michael Spottswood and his team at AFRL [4] that was conducted in 2019.

Structural/Dynamics (SD): Determining the natural modes and frequencies of a structure is an essential part of any FSDI or FSTDI investigation. However when flexible plates are clamped (or pinned or otherwise fixed) on all edges or two opposite edges, they will often have natural modes and frequencies that are sensitive to static pressure and thermal loadings. Thus the SD investigation needs to be more extensive when these two types of loadings are important, as they often are in high speed flows.

Thermal/Dynamics (TD): Usually the dynamics of the thermal field is not a major concern on the time scale of interest for FSDI and FSTD, though one should always check make sure that neglecting this effect is well founded in a given experiment or flight vehicle design.

1.2 Three Disciplines (FSD) Interaction

Next, interactions among three disciplines are considered. There are several distinct physical phenomena that may be of interest and a brief summary of the state of the art and the need for further investigation is provided. Later in the chapter a more extended discussion of available theoretical/computational results and experimental results and their correlation will be provided. This is the basis for the brief assessments of the state of the art provided below.

Flutter And Limit Cycle Oscillations

There is a well characterized set of experimental data [5, 6] for flutter in the Mach number range of $M = 1.1$–5 for plates clamped on all edges that has been well correlated with theoretical/computational models. Qualitative experimental data are also available for limit cycle oscillations that are consistent with theory and computations. However quantitative experimental data for limit cycle oscillations are lacking. For cantilevered plates, flutter and limit cycle oscillation data are available for low subsonic flow that agree well with theory/computation [7]. However experimental flutter data are lacking for all $M > 1$ for a cantilevered plate.

Plate Response To Turbulent Boundary Layer Pressure Oscillations And/Or Engine Exhaust Flow Oscillations

A well-established theoretical/computational approach is available for determining such responses given the oscillating pressures from measurements over rigid surfaces. It is thought that the aerodynamic damping due to structural motion can be determined from a range of theoretical fluid models, but experimental confirmation is lacking [6].

Buffet Or Flow Oscillations Due To Shock-Boundary Layer Interaction Leading To Separated Flow

It is now well established that such flow oscillations are often due to a global dynamic instability of the flow (which may already be turbulent) and some success has been obtained in correlating experiments and theoretical/computational model for airfoils and wings. Most of the work has been in the transonic range where such phenomena have been observed on high performance aircraft and in wind tunnel models. See Gianellis et al. [8] for a recent review of the literature. The shock oscillations observed in hypersonic flow over ramps may have a similar character, but the theory is less well developed and no successful correlation between theory and experiment has yet been achieved [9–11].

Once the flow oscillations are established then the structure may respond and changes in the flow pressure oscillations due to structural motion are thought to be important. The flow over a blunt cylinder that induces a Von Karman vortex street is broadly analogous and successful correlations between theory and experiment have been achieved for a cylinder supported on springs as an example of a flexible body. In this case, fully coupled fluid structure dynamic interaction occurs. However experiments are lacking for $M > 1$ for any structure including airfoils and wings [6].

Changes In The Flow Dynamics Due To Structural Motion

These changes are usually modeled theoretically by potential flow theory or RANS models for structural response investigations including flutter. However a long sought goal is to modify the dynamics of the flow so that (1) the transition from laminar to turbulent flow is delayed or (2) the intensity level of turbulence is reduced. Despite great efforts over many years at low speeds as well as higher speeds, this goal has remained elusive. In a recent supersonic experiment over a ramp with a compliant material (rubber) ahead of the ramp, Narayanaswamy [12] found that the pressure oscillation on the flexible wall near the shock location could be reduced. This is an interesting result and provides a challenge to theoretical/computational models to correlate with this experimental result.

1.3 Four Disciplines (FSTD) Interaction

The role of the thermal field may be several fold. First of all the structure may buckle. A buckled structure is more likely to flutter if near the onset of the buckled condition and the limit cycle oscillations may be larger than for an unbuckled plate. Indeed this is true for any form of fluid excitation of the structure, e.g. due to turbulent boundary layer pressure oscillations or those due to an engine exhaust. For flutter and limit cycle oscillations there is a key experiment for a single elastic plate at $M = 3$ [5] that has been well correlated with a theoretical/computational model. But additional experimental data for a wider range of parameters is highly desirable.

Some investigators are also concerned about material degradation due to high temperatures, but this is a concern quite aside from FSTD interactions. As noted previously there is concern that structural response may in turn increase the heat flux to the structure. Also, for some reentry vehicles, striations have been observed on the nose cone that it is suggested are due to the interaction of the fluid forces and viscoelastic nature of the structure induced by high heating rates. However the data in the open literature are not yet conclusive.

1.4 Distinction Between a Plate with All Fixed (Clamped) Edges and a Cantilevered Plate (Clamped on One Edge Only)

Much of the recent interest in FSTDI has been for plates that are clamped on all edges or a cantilevered plate that is clamped only at its leading edge [13–23]. Within the framework of linear structural theory, there is no fundamental distinction between the two configurations with respect to the natural modes, the onset of flutter or the response to fluid fluctuations in the boundary layer (with or without shock waves and flow separation). However in experiments and within the framework of nonlinear theory for plate response to boundary layer pressure oscillations or the onset of flutter and the nature of the limit cycle oscillations, there are important fundamental differences between the two plate configurations as follows [5–7].

In a well-designed experiment for plates clamped on all edges, the static pressure differential across the plate and the thermal stresses must be controlled as they can substantially change the plate natural frequencies, the plate dynamic response to turbulent pressure oscillations, the onset of flutter and the amplitude of the limit cycle oscillations. Also it is desirable to measure the natural modes and frequencies for the anticipated range of static pressure differentials and thermal stresses.

By contrast for a cantilevered plate, with flow on both sides of the plate the static pressure differential need not be controlled to the same degree, provided the flow is unobstructed and flows smoothly on both sides of the plate. However the flows on both sides of the panel may interact through the motion of the plate and this must be taken into account in the theoretical/computational models. Also the thermal stresses will be relieved because of the free edges of the cantilevered plate; thus the control of thermal stresses is less of an issue for a cantilevered plate than a plate with more restrained boundary conditions.

In the post flutter/limit cycle regime the response of plates clamped on all sides is also quite different from the response of a cantilevered plate. For an all clamped panel the amplitude of the limit cycle oscillations (LCO) will be on the order of the thickness of the plate if the plate is initially flat. If the plate has curvature (either due to its manufactured shape or due to plate buckling), then the amplitude of the LCO will be on the order of the height of the plate above the plane formed by the plate edges (rise height). By contrast, for a cantilevered plate, the amplitude of LCO

will be on the order of a significant fraction of the plate chord. For subsonic flows, both theory and experiment show that the flow over a cantilevered plate remains attached and nonlinear fluid effects are modest. The dominant nonlinearities are in the plate. However if the flow has shocks and/or the flow is separated then nonlinear aerodynamic effects may be expected as well. The cantilevered plate is relatively unexplored both theoretically/computationally and experimentally for $M > 1$ [7].

Also it might be noted that in subsonic flow, plates with various other edge support conditions have been studied including plates with only side edges clamped and also all edges clamped except for the trailing edge which is free. Also studied in subsonic flow is the case of a cantilevered plate at various yaw angles to the oncoming fluid flow. It would be very valuable to extend these studies to $M > 1$.

2 Correlations of Theory and Experiment

2.1 Introduction

There are several physical phenomena of interest as described below. Usually in a given experiment or computational model, only one of these is the principal focus. However it has happened that more than one of these have occurred in a single experiment, though not always planned.

2.2 Physical Phenomena of Interest

The principal physical phenomena of interest are the following:

1. ***A turbulent boundary layer or jet excites a flexible structure*** (panel or control surface) with random-like pressure fluctuations possibly leading to short-time or long-time (fatigue) failure. An open question is to what degree the structural motion might in turn change the fluid flow.
2. ***A shock wave oscillates ahead of or on the flexible structure.*** The basic physical mechanism that causes the shock oscillations (even in the absence of structural motion) is still unresolved. The two prime candidates are (1) the shock and flow field are excited into a resonance due to the turbulent boundary layer pressure fluctuations as considered by Touber and Sandham [24] and/or (2) the flow field becomes dynamically unstable and creates a limit cycle oscillation that is most visible in the shock motion, e.g. see Crouch [25]. Both physical mechanisms involve shock wave boundary layer interaction. There is a substantial literature on the second physical mechanism at lower Mach numbers especially in the transonic range, e.g. see the recent review paper by Giannellis [8].
3. ***A fully coupled fluid structure interaction (FSI) may lead to a dynamic instability (flutter) and subsequent limit cycle oscillation*** of the structure and flow.

This may include shock wave boundary layer interaction (SWBLI) as well, but can occur even when SWBLI is not a major contributor. Structural failure is the primary concern when flutter and/or limit cycle oscillations occur.

4. *Fluid flow-structural-thermal coupling may lead to (1) buckled structures and (2) possibly substantial increases in heat fluxes.* Often this issue can be treated as a static (rather than a dynamic) phenomenon. However if oscillating fluid forces act on a buckled structure, the structural response may be substantially greater than for an unbuckled structure, if near the onset of buckling. Conversely, if the structure is well into the buckled regime, it may be stiffer than the unbuckled structure.

2.3 Key Parameters for Experiments and Theory

One of the major challenges of fluid structure interaction at any Mach number is the large number of physical parameters that must be taken into account in designing an experiment and must be included in a mathematical model that hopes to correlate with experimental results. On the fluid side there is the Mach number and Reynolds Number, while on the structural side there are of course the geometrical and materials constants. But when fluid structure interaction is important there are several additional non-dimensional parameters that are of interest including the ratio of fluid to structural mass, the ratio of fluid pressure to structural stiffness forces and also the ratio of static pressure differential across the structure to stiffness forces and the ratio of thermal stress forces to structural stiffness forces. Formally other non-dimensional parameters appear as discussed in some depth by Dugungji and Calligeros [3] and more recently by Friedmann [2]. But even the parameters mentioned above lead to the following formidable list.

M: Mach number (almost always matched in a wind tunnel experiment or flight test program)

Re: Reynolds number (almost never matched in a wind tunnel experimental program, unless there is substantial evidence that viscous effects are important)

μ: Ratio of fluid to structural mass; typically this fluid density multiplied by a characteristic length (e.g. wing chord) divided by structural mass per unit area or fluid density multiplied by a characteristic length cubed divided by the total mass of the structure (often not matched in wind tunnel experiments and usually less important than the next parameter)

Λ: Ratio of fluid pressure forces (e.g. fluid dynamic pressure) to structural stiffness forces (e.g. mass per unit area multiplied by a natural frequency squared multiplied by a characteristic length) (almost always matched in wind tunnel experiments and flight tests)

ΔP: As above with dynamic pressure replaced by the static pressure differential acting across the structure. (For thin panels this parameter is critical and in

early wind tunnel experiments this parameter was uncontrolled and unmeasured which often led to great scatter in the measured data.)

ΔT: As above with pressure replaced by the temperature differential between the flexible structure and a connected fixed structure multiplied by the thermal expansion coefficient and the modulus of elasticity. (Thin panels are easily buckled due to thermal stresses in a high speed fluid flow and this parameter is critical to modeling this effect.)

2.4 Representative Correlations of Theory and Experiment

Here several representative results are discussed for the various physical phenomena of interest which will give insights into the state of the art for both computational models and experiments.

Structural Response to Pressure Oscillations from a Turbulent Boundary Layer or Jet Noise

The standard theoretical/computational model on this topic dates to early work of Coe and colleagues at NASA Ames Research Center and Maestrello and colleagues at NASA Langley Research Center. Readily accessible treatments of the standard model are available in the books by Lin [26], Dowell [27] and Dowell and Tang [28]. In the standard theoretical and computational models the pressure oscillations are taken from measured data and simple scaling laws are used to make a universal model for the pressure acting on the structure. The key parameters for expressing the pressures, p, are the flow dynamic pressure, q; Mach number; and reduced frequency, $k = \omega c/U$ where c is a characteristic length which might be the boundary layer thickness or the jet engine nozzle diameter.

This the following non-dimensional relationship is often assumed with a possible (usually weaker) dependence on Reynolds number,

$$p/q = F(M, k)$$

Note the pressure is usually expressed in the frequency domain in terms of its power spectra. With the pressure modeled, standard methods random vibration analysis are then used to compute the structural response. A compact discussion of this approach appears in Crandall and Mark [29] and Dowell [27].

A key uncertainty in such an analysis is the representation of the damping. Although it is common to include a structural damping term in the model, usually the dominant physical source of the damping is the change in fluid pressure due to structural motion. This aerodynamic damping can be modeled and indeed often requires the same model as that needed for dynamic stability (flutter) analysis.

There are various comparisons between theory and experiment in literature, but the uncertainties in the representation of the pressure loading and damping have often led to at best only qualitative agreement between theory and experiment for structural

response levels. On the other hand, there is usually good agreement on the resonant response frequencies and the theoretical models are often useful in comparing the relative response of one structural configuration to another. Also for intense noise levels from a jet for example, the structure may respond well into the nonlinear range. See the review of the literature by Clarkson [30].

Shock Wave Oscillations Arising from Interaction with a Boundary Layer

There are three relative recent overviews of this topic that are highly recommended due to Dolling [9], Clement and Narayanaswamy [10] and Gaitonde [31]. The title of the 2001 article by David Dolling, "Fifty Years of Shock Wave/Boundary Layer Interaction Research: What Next?", is a reminder that this is a long standing and challenging issue. Determining the cause of shock oscillation is important for applications and still an open question. It is often perceived to be a low frequency phenomenon since a reduced frequency based upon boundary layer thickness is much less than 1. Or to say it another way, if we assume the proper scaling for frequency is in terms of reduced frequency, then the characteristic length scale is much larger than a boundary layer thickness. This is perhaps initially surprising, but recent work at transonic Mach numbers has shown that in fact shock oscillations may occur due to interaction of the shock with a separated flow and the characteristic length scale is the airfoil or wing chord. Thus the reduced frequency with this characteristic length is of order 1.

Note that it is now accepted that shock oscillations in flow over ramps in hypersonic flow do involve interaction of the shock with flow separation. See Clemens and Narayanaswamy [10]. They present a reduced frequency based upon the amplitude of the shock oscillation and it is also much less than 1; but is essentially and remarkably constant for a wide range of flow geometries. They also note the shock oscillation when it occurs has an amplitude proportional to the separation length. Since the separation length is much larger than the shock oscillation amplitude, it may be that the characteristic length scale might better be based upon the former rather than the latter. However both shock oscillation amplitude and separation length are outputs (results) rather than inputs (causes), so that still leaves open the question of what length scale is best used to predict the onset of shock oscillations. Recent work suggests it may be the distance from the leading edge to the shock location.

Dynamic Instability (Flutter) and Limit Cycle Oscillations

When flutter and limit cycle oscillations occur, the integrity and possible failure of the structure is of great concern. A fuller discussion of some of these results is available in Dowell [5] including citations to the original research articles.

As seen in Fig. 2, there is good correlation between theory and experiment for the Mach number range from 2 to 5. For the lower Mach number range the measured dynamic pressure for flutter was above that computed by an inviscid aerodynamic model. Later it was discovered that the viscous boundary layer accounted for this difference was associated with a change in the flutter mechanism from coalescing frequency flutter for the higher the Mach numbers to single degree of freedom flutter in the first panel mode at the lower (but still supersonic) Mach numbers.

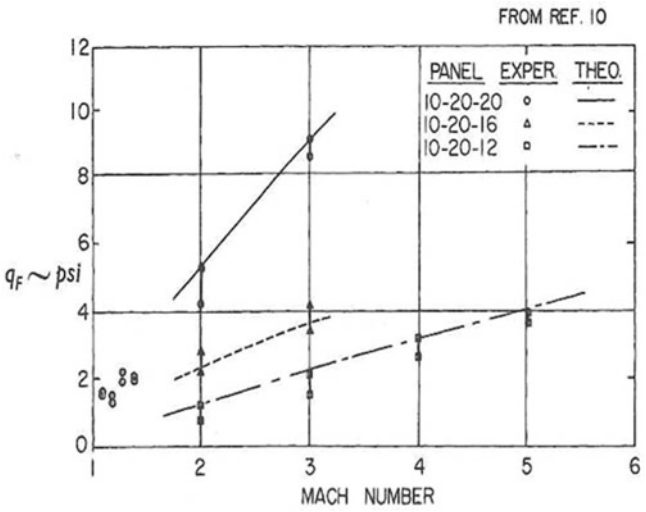

Fig. 2 Flutter boundary for a rectangular plate; flow dynamic pressure versus M from $M = 1.2$–5

The now classic experiment of Muhlstein and Gaspers [5] for the lower supersonic Mach number range controlled the thickness of the boundary layer. Results are shown in Fig. 3a for zero boundary layer thickness (as extrapolated) and a boundary layer thickness to panel length ratio of 0.1. Also shown in Fig. 3b are theoretical results from a shear layer model (where viscosity is included in the mean steady flow, but not in the dynamic perturbation due to panel motion) and also from a full RANS computation by Hashimoto et al. [32]. The agreement between experiment and the two theoretical models is very satisfying and suggests a good fundamental understanding of the flutter phenomenon for $M < 5$. Later experiments and computations by Vedeneev [33] suggested that single degree of freedom flutter in higher panel modes may also occur when great efforts are made to minimize the boundary layer thickness and the structural damping as well.

It is now well established that a static pressure differential across the panel can stiffen the panel. This nonlinear effect raises the natural frequencies of the panel and also increases the dynamic pressure required for flutter. Figure 4 shows theoretical results for completely clamped edges and for edges which are clamped with respect to motion normal to the panel but free to move in the plane of the panel. Also shown are experimental results which agree more closely with the free in plane motion model. This was also found to be true when comparing theoretical and experimental results for the panel natural frequencies [not shown]. Citations on Figs. 3, 4 and 5 are to the original references as discussed in [5].

A key experiment was performed at NASA Langley Research Center [5] and the results are shown in Fig. 5 in a plot of [non-dimensional] dynamic pressure at which flutter (and thus limit cycle oscillations) were observed versus a [non-dimensional] temperature difference between the panel and its support structure. Typically the

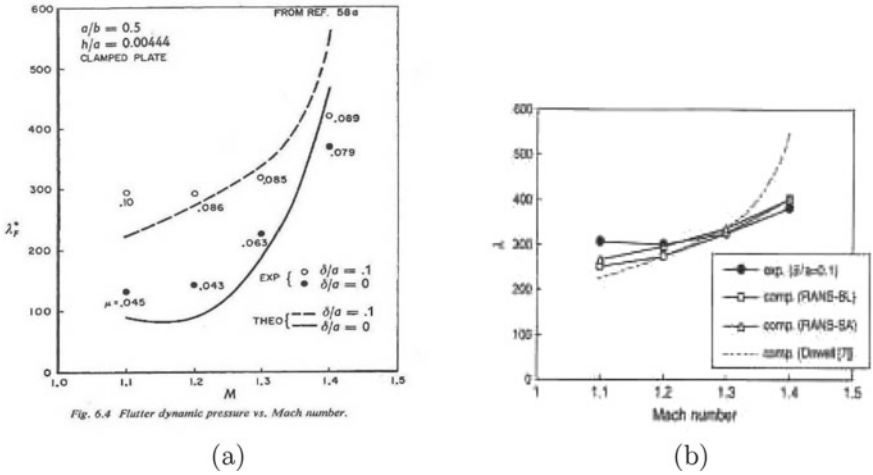

Fig. 3 **a** Flutter boundary for a rectangular plate including the effects of a viscous boundary layer; **b** flow dynamic pressure versus Mach number with different ratios of boundary layer thickness to panel length

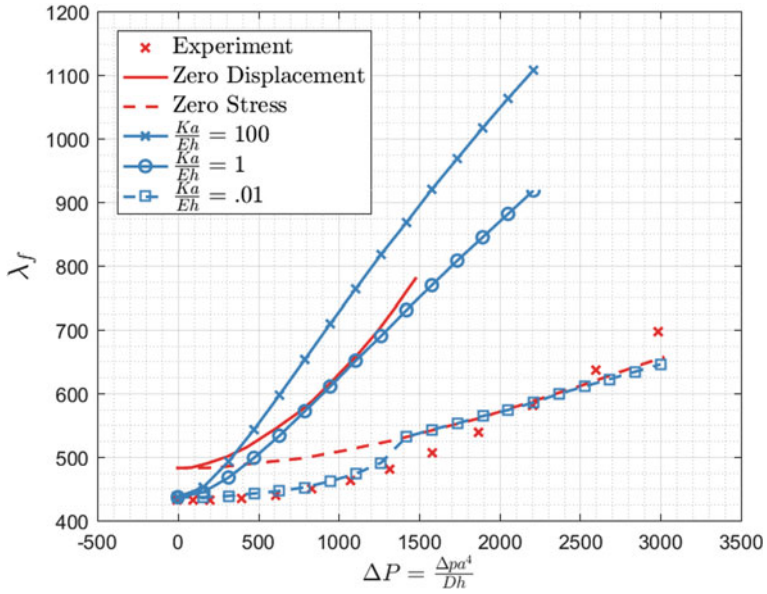

Fig. 4 Flutter boundary for a rectangular plate including the effects of static pressure differential: flow dynamic pressure versus static pressure differential for fixed Mach number

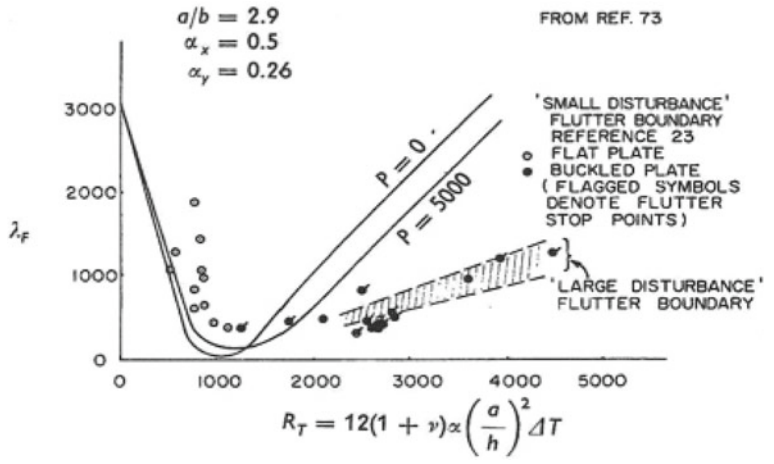

Fig. 5 Flutter boundary for a rectangular plate including the effects of thermal stress; flow dynamic pressure versus non-dimensional temperature differential for fixed $M = 3$ and fixed static pressure differential

panel temperature is higher and thus a compressive thermal stress is induced into the panel that may lead to buckling. For the range of temperatures shown buckling did indeed occur and thus there is hysteresis in the flutter boundary. For a given level of flow dynamic pressure flutter occurs at a certain temperature differential and then flutter stops at a yet higher temperature. This is because a buckled panel stiffens at sufficiently high temperatures and thus stops the flutter. This was the experimental protocol followed and produces the "large disturbance" flutter boundary shown in the figure for both theory and experiment. However the theory also predicts a small disturbance flutter boundary that might be seen if the panel was initially buckled at some temperature and then the flow dynamic pressure was increased to reach this flutter boundary.

Another example of the subtlety of the flutter phenomenon is that a curved plate which is stiffer than a flat plate may in fact have a lower dynamic pressure for flutter if the curvature is in the direction of the flow. This is because the effect of the curvature on panel stiffness is selective in that it raises the first mode frequency, but does not change the second mode frequency. Thus the two modal frequencies are closer together due to curvature and flutter is more likely. The experimental results are due to Anderson [5] and the theoretical results are due to Dowell [5] and Amirzadegan and Dowell [34]. In Fig. 6 the flutter dynamic pressure is plotted versus H/h where H is the maximum rise height of the curved plate and h is the plate thickness. Note that there is a theoretically predicted change in flutter mode for H/h near 8 and a near jump in the dynamic pressure. However the flutter frequency does not change radically (not shown).

There is also an early literature on flutter of cylindrical shells and it would now seem timely to revisit that configuration. A recent paper by Cesnik [35] et al. on this topic suggests renewed interest in this configuration. Also Goldman et al. have studied

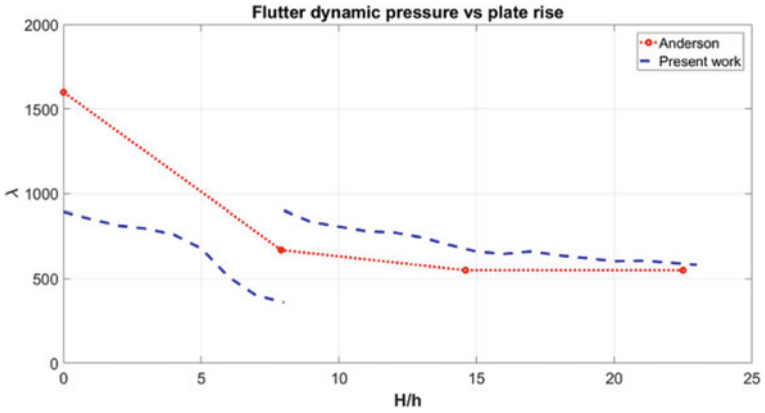

Fig. 6 Flutter boundary for a square plate with streamwise curvature

conical shells in the context of the Hypersonic Inflatable Aerodynamic Decelerator that was motivated by a wind tunnel experiment at NASA Langley which showed flutter oscillations [36].

Limit Cycle Oscillations

There are few measurements of limit cycle oscillation (LCO) amplitude for $M > 1$. However it is generally found that for flat plates the LCO amplitude is of the order of the panel thickness, h, while for a streamwise curved plate the LCO amplitude is of the order of the rise height, H, as predicted by theory. There are more detailed and quantitative measurements for $M < 1$ for a cantilevered plate, as well as other boundary conditions, and these agree well with the appropriate structural theory, [7].

Fluid Flow-Structural-Thermal Interaction

Thermal stresses can substantially decrease the stiffness of the structure and this in turn reduces the natural frequencies and make the structure more prone to experience flutter and limit cycle oscillations. If one of the resonant frequencies goes to zero as the thermal stress reaches a critical level, then buckling may occur. Buckling is a static instability, as distinct from a dynamic instability, and in some cases may be tolerated. Moreover a buckled structure may recover its stiffness in the post-buckled region. However the large static deformations associated with buckling may lead to an increase in the heat flux due the "aerodynamic roughness" of the deformed structure. This is an important issue that is not well explored in the open literature. However there is experimental and theoretical/computational work underway to address this concern [4]. This is discussed elsewhere in this chapter and it is to be expected that correlations between measurements and computations will be available in the near future. Also one may buckle a relatively stiff structure with mechanical forces (rather than thermal stresses) and measure the increase in heat flux. The current experiment by Spottswood and colleagues at AFRL is a notable effort in this regard [4].

2.5 Summary of the State of the Art Based upon Correlations of Theory and Experiment and Opportunities to Advance the State of the Art

Structural Response to Pressure Oscillations from a Turbulent Boundary Layer or Jet Noise

A standard computational approach is available that relies on measurement of random pressures due to a turbulent boundary layer or jet noise and an empirical model of damping. Opportunities exist to improve this approach by using computational fluid dynamics (CFD) simulations to compute these random pressure fields and various levels of aerodynamic modeling (from potential flow theory to a Navier-Stokes model) to represent the fluid damping due to structural motion.

Shock Wave Oscillations Arising from Interaction with a Boundary Layer

The basic physical mechanism that leads to shock oscillations is still uncertain. There is an opportunity for both Navier-Stokes based computational models and for experiments to determine whether the basic mechanism is a result of a global dynamic instability of the flow field (bifurcation) or the resonant response of the global flow to pressure fluctuations in the boundary layer or possibly some combination of the two mechanisms.

For recent developments in the transonic flow range, see [37–39].

Dynamic Instability (Flutter) and Limit Cycle Oscillations (LCO)

There is a now a substantial body of theoretical-experimental correlation evidence for $M < 5$ that gives a basis for future progress in investigating the hypersonic Mach number range, $M > 5$. Experiments for $M > 5$ are needed and these will be challenging. However using the best available theoretical/computational models should provide a firm basis for design of these experiments and correlation with measurements. Thermal stresses may and likely will be important.

For recent work on the effect of a shock standing on the panel for flutter and LCO, see [40–43]. For a computational design study in support of a proposed hypersonic plate flutter experiment, see [44].

Fluid Flow-Structural-Thermal Interaction

It is well established that buckling of flexible structures may occur in high speed flows and considerable effort in structural design is devoted to avoiding buckling or making sure that a buckled panel does not lead to plastic deformation of the material. However even elastic buckling (buckling deformation that occurs below the yield stress of the material) may be a concern if it leads to higher heat fluxes. Current experiments are exploring this important issue [4].

3 Current Experimental Programs and Complementary Computational Results

There are several experiments underway in hypersonic FSTDI. A brief description of each is provided including preliminary comparisons between theory/computations and experiment.

3.1 Air Force Research Laboratory (SM Spottswood, R Perez, T Berberniss) with Computational Support from Duke University (M Freydin, EH Dowell)

Several experiments were conducted at the AFRL Research Cell 19 (RC-19) facility between the years 2011 and 2017 and they are continuing. The RC-19 is a continuous Mach 1.5–3 supersonic wind tunnel modified to test elastic plates with an optional impinging shock. The most recent set of experiments is described in detail in [45] including an overview of previous related work. The experimental campaign was aimed at testing new measurement techniques and produce data for validation of computational methods and theoretical models. Full-field measurement techniques (3D DIC, PSP, TSP) allowed measuring the deformation, static pressure, and temperature across the plate at sufficiently high sampling rates to allow dynamic analysis of the fluid-structure system.

Notable experiments include a transient wind tunnel start-up where a 30 s measurement of the plate deformation showed the onset of flutter, a sporadic limit cycle oscillation, and the final stabilization of the plate which is attributed to buckling due to aerodynamic heating. In a recent theoretical computation by Freydin et al. [46] a qualitative correlation with experiment was demonstrated and the stability transitions were analyzed using stability maps in the freestream static pressure versus temperature differential plane. Figure 7 shows the measured and computed displacement at 25% chord versus time during the transient, supersonic wind tunnel start where flutter starts around 5s and stops near 25s. Temperature differential was measured during the experiment near the edge of the plate and used in the theoretical computations. However because the thermocouple was installed near one of the edges of the plate, the measurement is not likely representative of the mean (or maximum) temperature on the plate. To address this issue, several temperature differential scaling values were considered. Figure 8 shows a stability map for static pressure differential of 3kPa, which remained approximately constant during the experiment. Three temperature differential scaling values are considered and their respective trajectory in the stability plane is plotted with ‘x’ marking 5s intervals. Note that for scaling of one the trajectory ends inside the flutter region and the plate does not stabilize during the 30s transient. Also note that the stability map includes instability regions attributed to two coupled mode instability labelled ‘Flutter’ as well as a cavity-plate coupling instability labelled ‘A’ and ‘B’. For more details on Figs. 7 and 8 see [46].

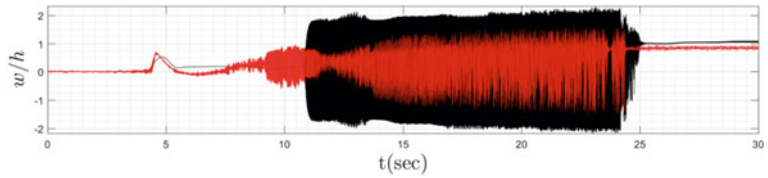

Fig. 7 Experiment (red) and theory (black)—displacement versus time, computed with cavity dynamics and a scaled, uniform temperature differential $1.25 \times \Delta T(t)$ [46]

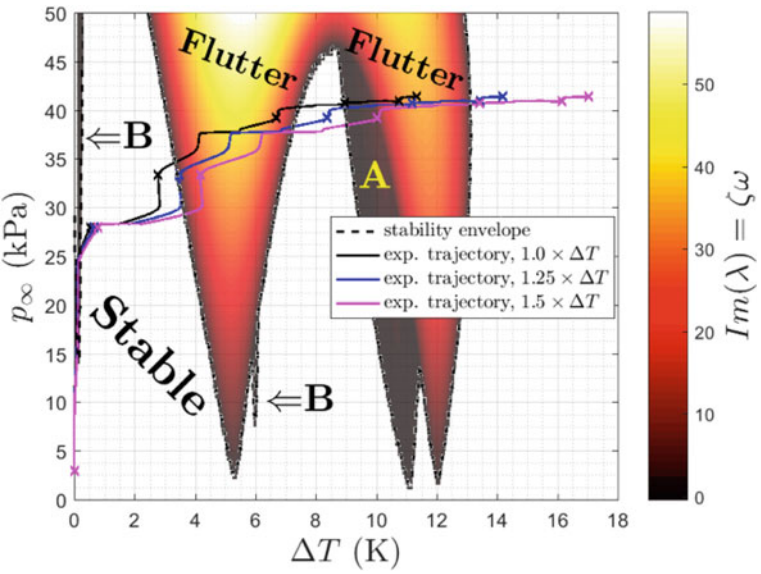

Fig. 8 Stability map for a static pressure differential of 3kPa and with cavity dynamic coupling [46]

In another experiment, the static pressure differential was decreased by modulating the pressure inside a cavity and the freestream conditions were held constant. An increase in LCO amplitude was measured at first, while subsequent decrease in static pressure differential caused the plate to intermittently transition between large and small amplitude response. A similar behavior was observed in the theoretical computations [46]. At the end of the set of experiments a high-cycle fatigue crack was identified near the trailing edge of the plate.

3.2 *University of New South Wales (A Neely and G Currao) with Computational Support from Duke University (M Freydin, K McHugh and EH Dowell)*

Several experiments [47] have been conducted in a heated Ludwieg (hypersonic expansion) tube, a facility in which compressed gas in a tube is suddenly released and forms a pressure wave as it travels the length of a tube to the test section apparatus. In this system, test times are on the order of less than one second. In the experiments of interest, plates have been studied with varying boundary conditions to represent several structural components of aircraft.

One experiment tested a cantilevered plate clamped at its leading edge to represent a flexible control surface. The plate was positioned with an initial angle of attack of 20° to the freestream flow, and the flow conditions were well below the predicted flutter boundary. A schematic is shown in Fig. 9. As expected, the plate statically deflected due to the pressure differential across the plate, and measured motion was a damped oscillation with a frequency near the fundamental resonant frequency of the plate. Shown in Fig. 10 are Schlieren images of the deflected plate at select times, which show several characteristics of the system. Firstly, the leading edge shock can be clearly seen, and the static as well as dynamic deflection of the plate can be discerned by comparing time points. For this case, the damping was well predicted by aerodynamic theory. It is interesting to note that the aerodynamic theory used to correlate with experiment was piston theory which is the correct limit of potential flow theory at high Mach number. The free stream condition was that behind the shock of course. The Euler equations would also be expected to provide good correlation

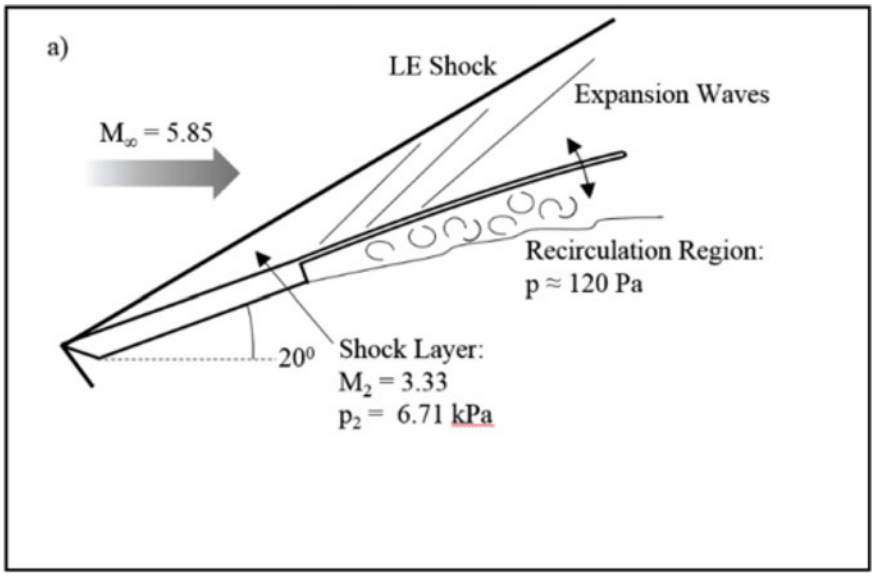

Fig. 9 Schematic of cantilevered trailing edge with initial angle of attack

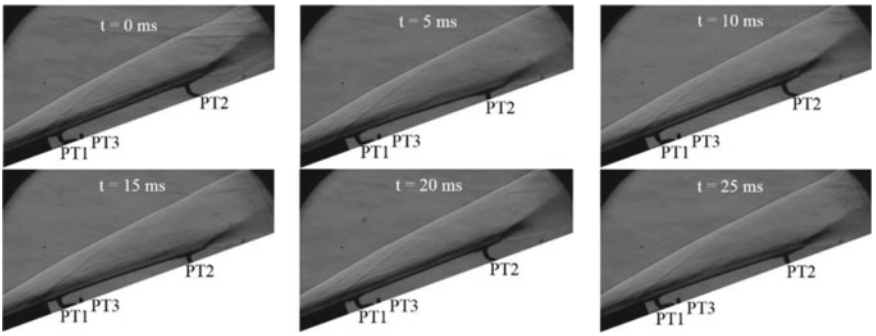

Fig. 10 Schlieren imagery of the cantilevered plate subject to Mach 5.85 flow. The leading edge shock is clearly seen. Several time points illustrate oscillatory behavior of the system. PT1-3 are Pressure Transducers

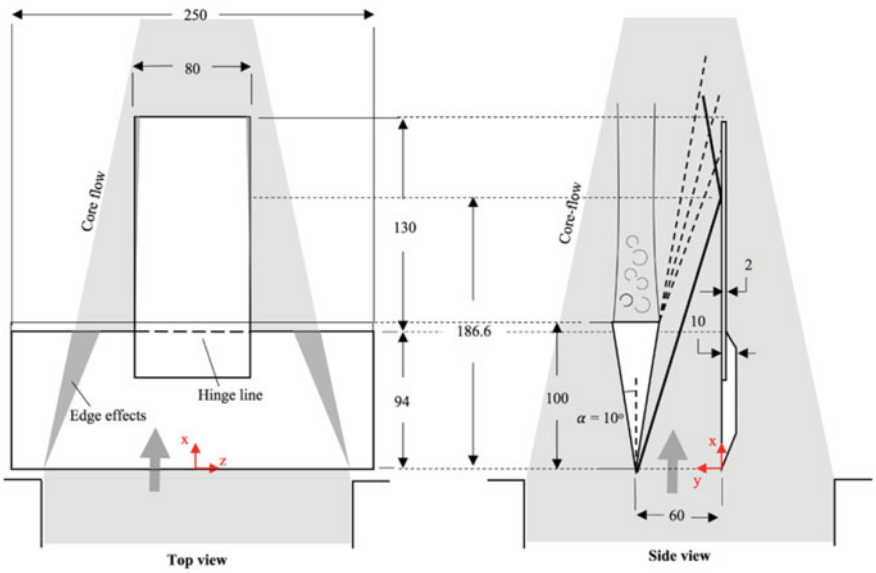

Fig. 11 Schematic of system with rigid wedge to generate a steady oblique shock impinging on a compliant cantilevered flat plate. Note that the wedge shock generator is wide enough such that the entire test plate is within the core flow. The thick solid line on the Side View represents the compression shock and the dotted lines are the expansion fan

with experiment and agree with potential flow theory for the relatively small motions measured. The good correlation between theory and experiment also suggests that viscous flow effects were not significant for predicting the damping of the model.

Another experiment tested a flat plate clamped at its leading edge with zero angle of attack, but with an oblique shock impinging upon it to create a pressure differential. A schematic of this system is shown in Fig. 11. Again, the freestream flow was below the flutter boundary, the plate experienced a static deflection with dynamic oscillations around this deflection, and piston theory predicted nicely the pressure

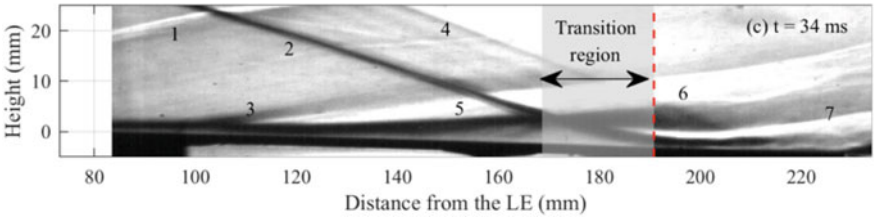

Fig. 12 Schlieren imagery of the deflected cantilevered plate fixed at its leading edge with an impinging shock. Note the labeled characteristics. The dark line (2) is the impinging shock, which causes the recirculation zone marked by the dark region under the dividing shear layer (5). Shocks (3) and (7) stem from the separation and reattachment points, respectively

on the plate due to the flow field. However, there was more of an offset in pressure—i.e. the system was not quasi-steady—because the deflection of the plate altered the effects of the impinging shock. In other words, the deflected plate resulted in a weaker shock because it introduces expansion waves. Figure 12 shows the Schlieren imagery from this case. In this experiment, it was shown that the boundary layer transitions from laminar to turbulent in the area of separation over the plate, and that RANS calculations under-predicted the heat transfer to the plate.

Plans are currently underway for a flat plate clamped on its leading and trailing edges to be tested with a nominal freestream Mach number of $M = 5.8$ and a local Mach number behind the shock of $M = 4.27$. The plate is mounted on a wedge and the angle of inclination of the wedge can be varied to change the local flow including the Mach number. The plate is designed to encounter flutter for the flow conditions expected, which include a static pressure differential across the panel and thermal stress within the panel, which raises and lowers the flutter boundary, respectively. Experimental challenges include the relative short test time—less than 1 s—due to the nature of the hypersonic expansion tube constraints. Flutter frequencies of several hundred Hz are predicted and flutter and subsequent limit cycle oscillations will occur if, as designed, the effects of static pressure differential and thermal stresses are offsetting. Figure 13 shows a schematic of the model and Fig. 14 shows a predicted time history of the plate in a flutter/limit cycle oscillation [44].

3.3 Sandia (K Caspers) with Supporting Computations from the Duke Team

A flexible plate with spanwise curvature is fixed at its edges and embedded in an otherwise rigid cone structure. It was tested in a hypersonic flow at $M = 6$ and 8 and was well below the flutter boundary as computed by the Duke University team. Limited correlations between measured and computed natural frequencies showed good agreement. The panel was responding to the random pressure fluctuations in the turbulent boundary layer augmented by spark excitation. Figure 15a, b shows a picture of the experimental model.

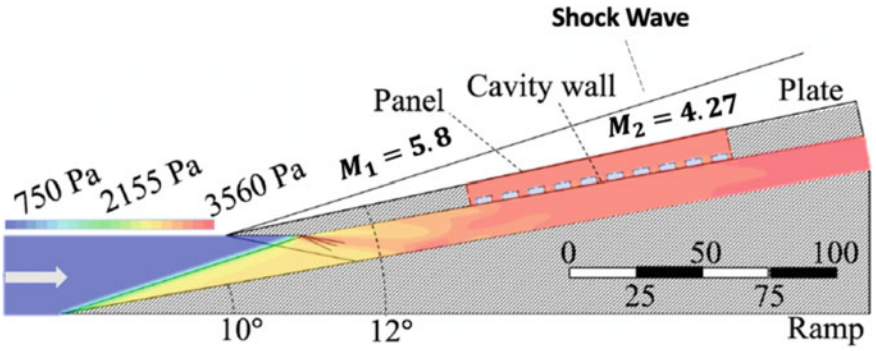

Fig. 13 Schematic of proposed experiment in which a flat plate clamped at its leading and trailing edges and free on sides parallel to the flow is acted upon by heated flow such that the panel flutters

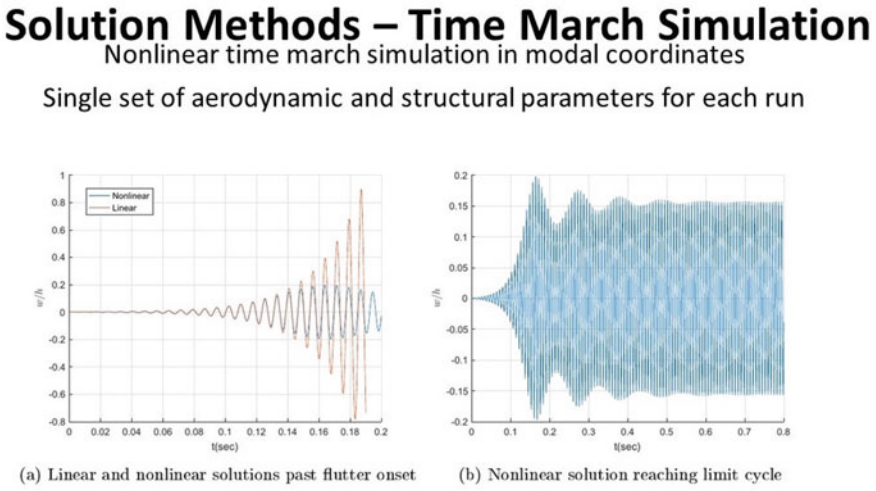

Fig. 14 Displacement at $x/a = 0.8$, linear and nonlinear solutions past flutter onset condition (left), and nonlinear solution reaching limit cycle oscillation (right)

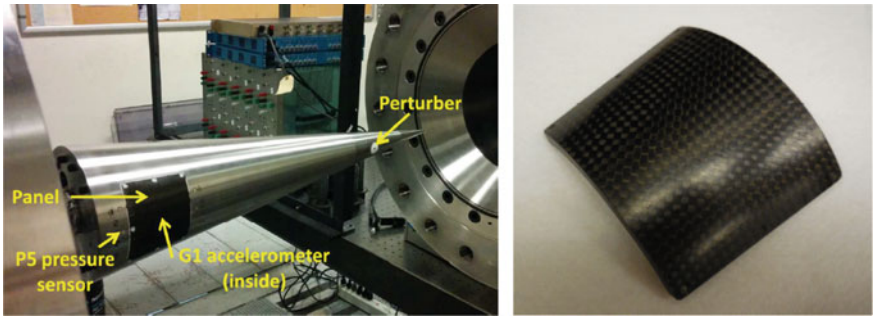

Fig. 15 **a** Flexible panel mounted flush in a rigid cone. **b** Close up view of flexible panel

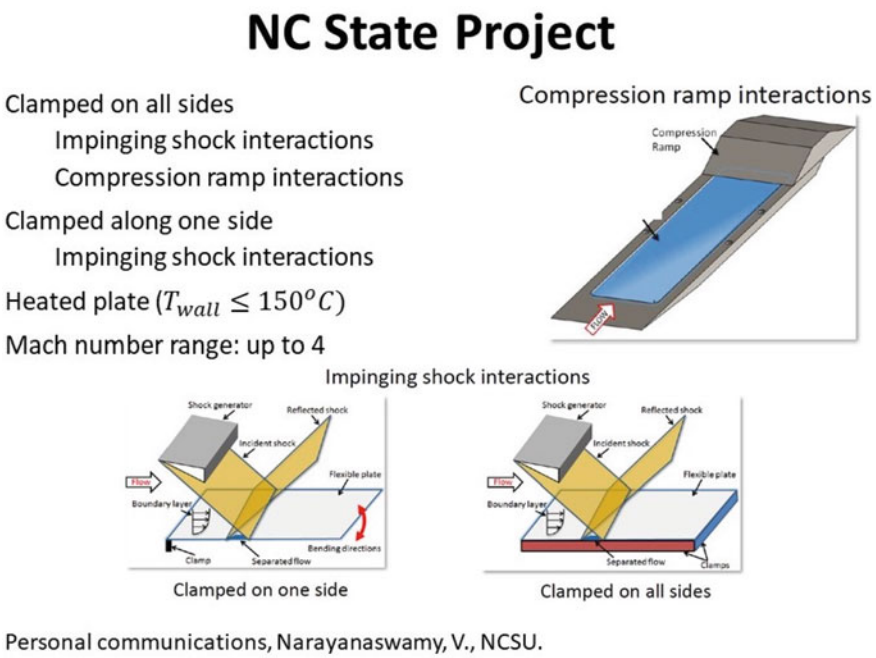

Fig. 16 Schematic of wind tunnel experimental model

3.4 North Carolina State University (V Narayanaswamy) with Computational and Experimental Support from Duke University (M Freydin, D Levin, EH Dowell)

A flat flexible plate clamped on all edges has been tested at $M = 4$ with a shock impinging on the plate. The plate has been constructed and correlations between theory and experiment have made for the plate natural frequencies and modes. A shallow cavity beneath the panel allows the static pressure across the panel to be controlled. The acoustic dynamics of this cavity can change the lowest natural frequency of the plate. This change can be accounted for by a well established theoretical model. A schematic of the experimental model is shown in Fig. 16.

In recent experiments [48], natural frequencies of the plate were measured in several configurations: mounted with/without cavity, with static pressure differential, and with a uniform temperature differential. The cavity was found to have a small stiffening effect on the first natural frequency and a negligible effect on higher modes. Static pressure differentials of up to 10psi was also shown to have negligible effect on the natural frequencies. The relative insensitivity of the plate to these effects allows the isolation of other effects planned for the wind tunnel experiment (shock-wave boundary-layer interaction, aerodynamic heating). Lastly, the plate was heated uniformly and the variation of natural frequencies versus temperature was measured

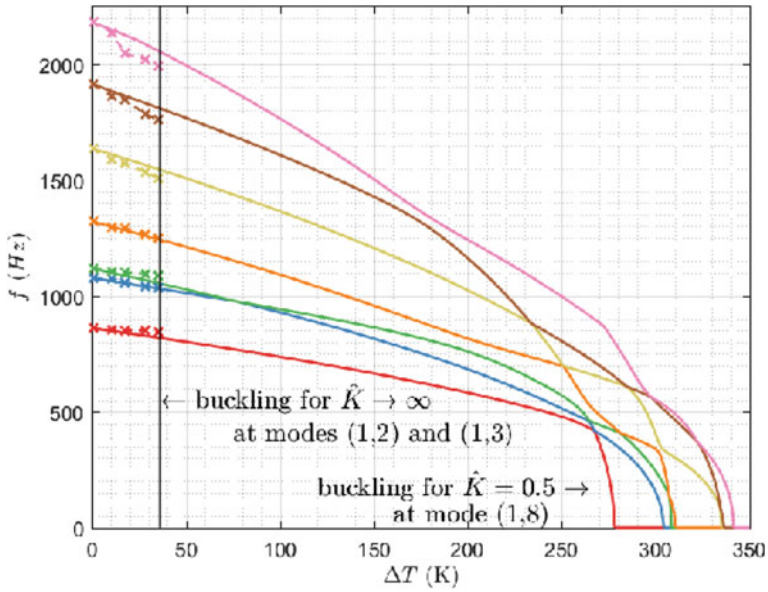

Fig. 17 Frequencies vs ΔT from experiment (dashed with crosses) and calibrated theory with in-plane stiffness $\hat{K} = 0.5$ (lines) shown for 7 leading natural modes [48]

and plotted in Fig. 17. The experimental results were correlated with a recently theoretical model that allows setting the stiffness of the in-plane boundary support [54]. It was shown that the tested plate has relatively soft in plane edge supports and that a uniform temperature difference of up to 35K is expected to reduce the leading natural frequencies of the plate by less than 10%. Note that for the limiting case of rigidly fixed in-plane edges, the plate is expected to buckle at 35K.

3.5 University of Maryland (S Laurence, T Whalen) and NASA Langley Research Center (G Buck) with Computational Support from Duke University (M Freydin, EH Dowell)

A flexible square plate clamped on all edges has been tested at $M = 6$ in a NASA Langley Research Center wind tunnel with flow conditions well below the computed flutter boundary. The plate was mounted on a compression corner (with its leading edge at the corner) and deformation was measured using photogrammetry in response to the ramp-induced shock-wave boundary layer interaction. A picture of the experimental model is shown in Fig. 18. Static deformation on the order of the plate thickness was measured and correlated with theory. Good agreement was obtained when the combined effects of static pressure and temperature differentials were considered with the nonlinear plate model.

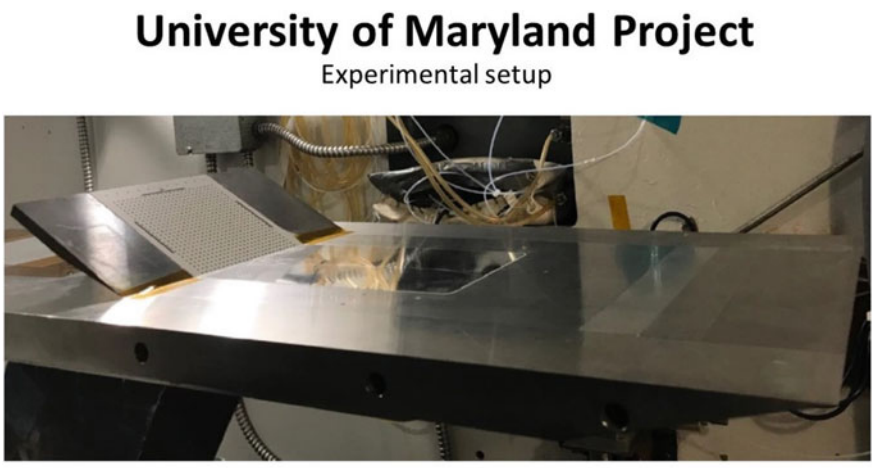

Fig. 18 Flexible panel mounted on a ramp in the wind tunnel

Preliminary correlations between computations and experiment show that the natural frequencies of the fluid-structure system are changed due to the flow with the static pressure differential and thermal stresses being the major contributors to these frequency changes. Figure 19 shows frequency (normalized by value measured outside of the wind tunnel $f_{\text{Exp}}^{(2,2)} = 3\,\text{kHz}$) versus ramp angle measured in the experiment and obtained using theory with and without the effects of static pressure and temperature differentials. Two papers have been published [49, 50] describing this work. Initial correlations between theory and experiment are encouraging and further wind tunnel experiments are planned in which the temperature distribution across the plate as well as flow properties behind the corner will be measured. Also the cavity beneath the panel will be sealed and the pressure measured there. These additional measurements will allow for a more complete and accurate correlation between theory and experiment.

4 Computational Models and Methods

4.1 Computational Models (Fluids)

Fluid models may be at one of several levels including:

Model 1: Potential flow model (with piston theory as the limiting case when $M \gg 1$)
Model 2: Euler flow model (includes the effects of shocks but ignores viscosity)
Model 3. Navier-Stokes model (includes shocks and viscosity)

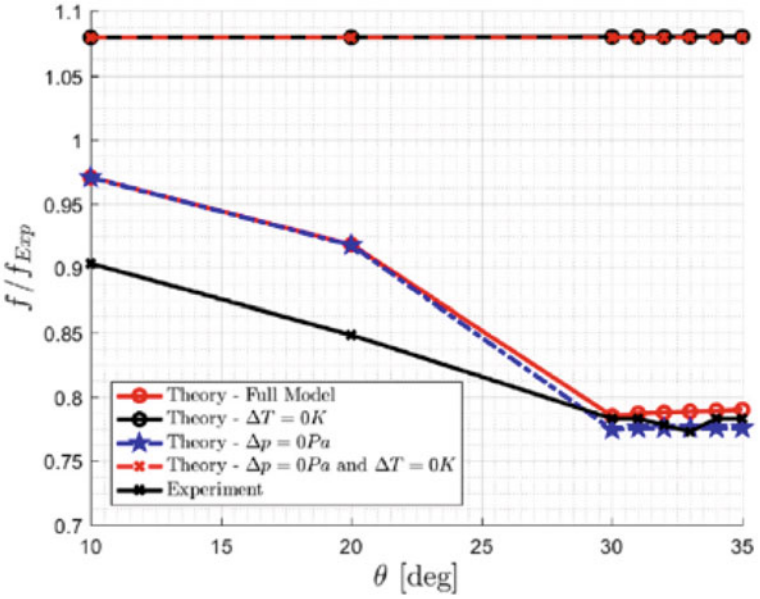

Fig. 19 Normalized frequency vs. θ for mode (2, 2) [45]

In principle the models are more physically accurate as one moves from Model 1 to Model 2 to Model 3. However because the computational challenges also increase, it is not always the case that a more accurate answer is obtained because of theoretical and computational limitations. In particular the use of empirical turbulence models remains a source of fundamental concern with respect to Reynolds Average Navier-Stokes (RANS) models. While Large Eddy Simulation (LES) models (still empirical but said to be an improvement on RANS models) and even Direct Navier-Stokes (DNS) models are in principle feasible, only now are such computations underway which show promise. But these are not currently and routinely used for FSTDI work.

4.2 Computational Models (Structures)

Model 1: Plates with all edges fixed

Here the primary nonlinear physical effect is nonlinear stiffness which is well described by the Von Karman plate theory for flat and curved plates for which the deflections are small (enough) compared to the plate length and width. Typically the deflections are on the order of the thickness for a flat plate and on the order of the rise height for a curved plate. Efficient and accurate computational methods are available using a modal expansion. For simple geometries these modes are known and can

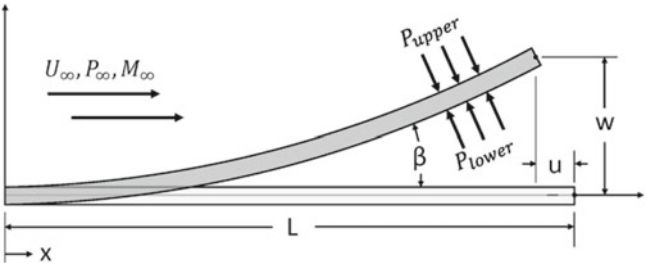

Fig. 20 Schematic of cantilevered plate fixed at its leading edge with supersonic flow moving over both sides

be prescribed analytically. For more complex geometries these modes need to be determined by finite element computations or by using a component mode model.

Model 2: Plates with only one edge fixed

Here the nonlinear deflections are much larger than those on the fully clamped plate, i.e. on the order of the plate length. See Fig. 20 for a schematic of a plate fixed at its leading edge with the trialing edge free. Flow moves over both sides of the plate from left to right at high Mach number. For the cases examined to date, an inextensible beam or plate model has proven accurate and again a modal based computational method is efficient. The inextensibility condition states that the arclength of the beam (or the arclength of the fibers in the two planar dimensions of the plate) is constant. This allows for a simplification of the potential energy expression of the beam or plate, which is advantageous for FSTDI computations.

Recent work at Duke University [51] has explored the post-critical behavior of a cantilevered plate in supersonic and hypersonic flow. Researchers used the inextensible beam model as the structural model (because spanwise bending is small) coupled with Piston Theory as the aerodynamic theory of choice for flows between $2 < M < 6$. It was found that the model was very sensitive to the inclusion of several nonlinearities in the mathematical model. For deflections on the order of the beam length, the geometric nonlinearities include third order nonlinear stiffness and nonlinear inertia. For these large deflections, third order Piston Theory was shown to be more accurate than first order Piston Theory. In addition, because of the large slope of the beam, a geometric modification to Piston Theory was added to ensure that the pressure always acted normal to the instantaneous slope of the plate. This modification is normally negligible for cases of fully clamped or fully pinned beams and plates, but for these large deflections it was shown that its inclusion is necessary to develop bounded limit cycle oscillation (LCO) solutions. In fact, the nonlinearity introduced by this modification is strong enough to produce bounded LCO behavior even for modeling cases with linear fluid and structural models.

Figure 21 compares the plate's LCO behavior at Mach 4 for various modeling conditions, and illustrates the sensitivity of the models to various nonlinear terms. It shows the root mean square (RMS) of the beam tip during LCO versus the nondi-

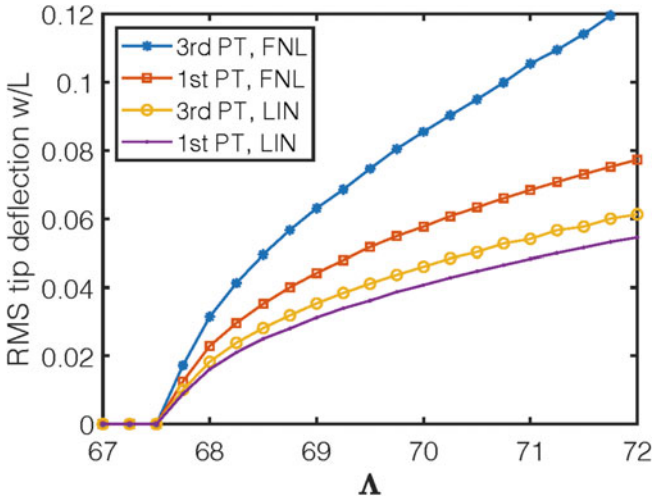

Fig. 21 Limit Cycle Oscillation behavior from various models including first order Piston Theory (1st PT), third order Piston Theory (3rd PT), linear structure (LIN) and a fully nonlinear structure (FNL). Note the system's high sensitivity to included nonlinearities which drive the response magnitude upwards

mensional fluid dynamic pressure parameter lambda. For each case the nonlinear modification to Piston Theory is included to ensure that pressure always acts normal to the plate surfaces. For the case of linear first order Piston Theory (1st PT) and linear structural theory (LIN) in purple, the structural response is the smallest of the group. Including third order Piston Theory (3rd PT) but keeping linear structural theory, the result is slightly larger. This is due to the higher order Piston Theory terms adding more dynamic pressure to the structure. However even larger is the case with first order Piston Theory but a fully nonlinear structure (FNL), offering insight into the considerable effect of the nonlinear structural inertia which increases deflection levels. Finally, the case with the largest deflection is that which employs third order Piston Theory and fully nonlinear structural modeling. This case includes the most physical nonlinearities in the model and therefore is thought to be the most accurate to model a potential experiment. Note that the RMS response of this case is more than double that of the linear fluid and structural model, and this result should be considered when planning an experimental effort.

To assess the accuracy of Piston Theory for this configuration, an Euler CFD simulation was performed at Mach 4 using the structural motion computed from the modal solution to calculate pressures on the plate. See Fig. 22 for a pressure contour plot from the Euler CFD solution and Fig. 23 for the comparison between aerodynamic theories at the plate's largest deflection. It can be seen that third order Piston Theory is very accurate compared to the Euler solution for the range of lambda values considered, whereas first order Piston Theory is only accurate at lower lambda levels.

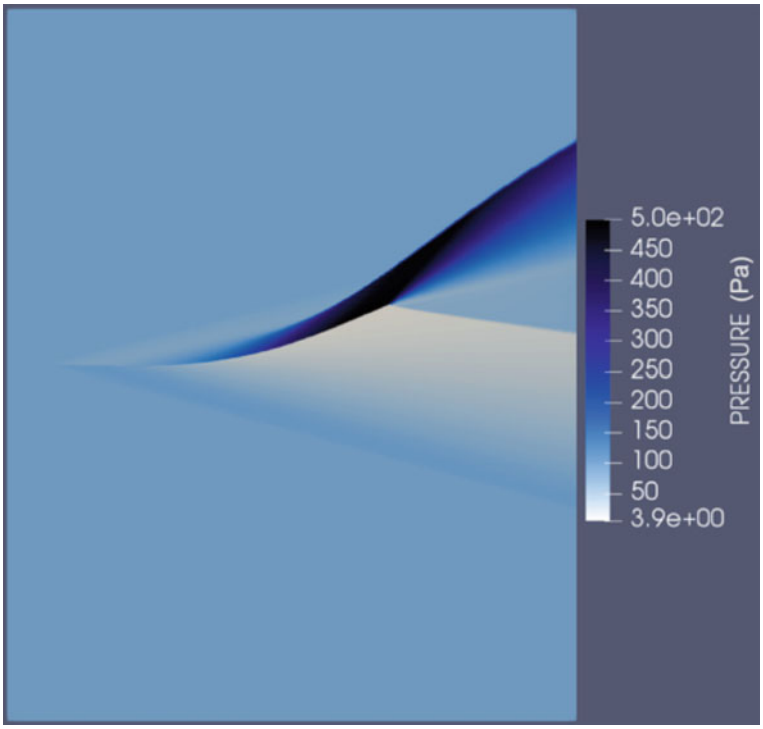

Fig. 22 Pressure contour plots from Euler CFD solution of beam in Mach 4 flow at beam's largest deflection

Because in this configuration the plate is free on three sides, thermal expansion is not a cause of instability. Therefore, for this computational study thermal effects were not included.

4.3 Computational Models (Thermal)

If the computation of the thermal field can be done prior to the modeling of the fluid and structure and if the structural motion does not significantly change the thermal field, then the thermal field can be taken as an input to the fluid-structure-dynamic interaction computation. This approach has often proved sufficiently accurate and is computationally efficient. Thus the thermal field is said to be "uncoupled" from the rest of the computational model.

However, in those cases where the thermal field is changed by the FSTDI, then a more complex approach must be pursued including the coupled interaction of the thermal field model with the fluid and structural models. When coupling the heat equation with the structure and fluid dynamics there are two main questions. First,

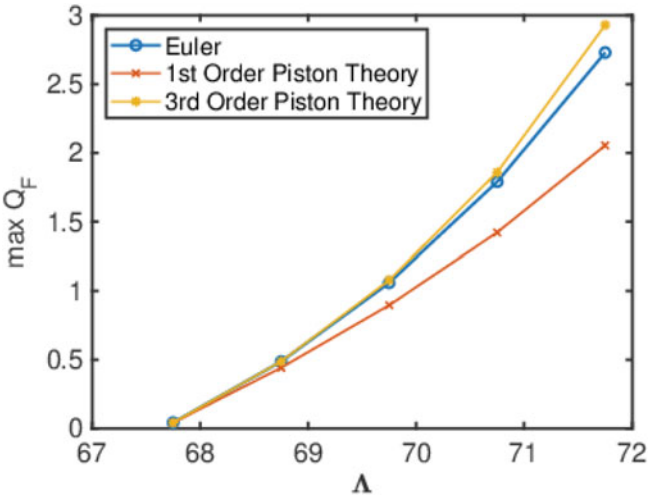

Fig. 23 Maximum aerodynamic pressure versus Lambda ratio of fluid dynamic pressure to structural stiffness for Euler CFD, 1st order Piston Theory, and 3rd order Piston Theory

there is the question of time scale differences between the thermal and fluid-structure dynamics which may affect how the dynamic coupling is implemented. Thermal time scales are typically orders of magnitude larger than that of the fluid-structure and thus the possible thermal model change is usually held constant for several fluid-structure time steps. The sensitivity of the solution to this assumption should be investigated for each problem separately. It is expected that problems with complicated geometries and impinging shocks should be more sensitive to the coupling time step than simpler geometries with uniform flow and without shocks.

The second question is how one models the heat flux from the boundary layer to the structure in super/hypersonic flow. A widely used semi-empirical model is the Eckert's reference enthalpy method [52]. See Anderson [53] for an insightful discussion of this model. In a temperature range where the heat capacity can be assumed constant, the method is simplified to the reference temperature method. This approach provides a simple relation between the flow conditions at the edge of the boundary layer above a point on the elastic structure, the local temperature of the structure, and the local heat flux. The accuracy of this model is well established for rigid structures, but for the coupled FSTI experimental data is lacking.

The enthalpy reference method can be thought of as the rough equivalent of Piston Theory for the aerodynamic heat flux. However, in contrast to Piston Theory, it is not easily incorporated in a modal fluid-structure solver due to complicated dependency of the heat flux on the motion of the structure. Two main approaches were considered to address this problem. One is solving the heat equation in physical coordinates. This increases computational complexity because it adds an additional step of transforming the thermal field to modal coordinates and the displacement field to physical coordinates to implement the coupling. However because the time

scale of the thermal field is substantially longer than that of the fluid-structure, the heat equation terms may be evaluated less often. A second approach that is currently under investigation is to linearize the temperature reference method in terms of the local transverse downwash and the structure temperature. In physical coordinates, this will result in the following heat flux term,

$$Q^{\text{aero}} \approx Aw_a + BT^w + C, \qquad w_a = \frac{\partial w}{\partial t} + U_1 \frac{\partial w}{\partial x}$$

And in modal coordinates

$$Q^{\text{aero}} = A_{nk}\dot{w}_k + U_1 A_{nk} w_k + B_{nk} T_j^w + C_n$$

The coefficients A, B, and C depend only on the chordwise coordinates x (due to variation of the local Reynolds number) and can easily be incorporated in a modal structural solver. The local downwash term can be used with (1st or higher order) Piston Theory to evaluate the local pressure change at the edge of the boundary layer (and compute all other parameters) to include the effect of structure motion on the thermal field.

More accurate models for aerodynamic heating include the boundary layer theory, on which the semi-empirical method of reference enthalpy is based. And of course the above discussed Navier-Stokes model can be used. When strong gradients in the temperature field of the fluid are expected, for example due to shock-wave boundary-layer interaction, only the latter flow model is expected to provide accurate results for the local heat flux near the surface of the structure.

5 Concluding Remarks on the State of the Art and Prospects for Future Work

A turbulent boundary layer or jet excites a flexible structure

To predict the response of a flexible structure one needs to know (1) the oscillating pressures from the flow field even in the absence of structural motion and (2) then also the fluid pressures due to the structural motion. Computations and experiments are underway to determine (1) and, if good correlations are obtained, this will give important confidence in the use of CFD models. Such models may be at the RANS, LES or DNS level. For (2) the flow model need not be the same as for (1). Indeed what is sometimes called Enhanced Piston Theory (i.e. piston theory with the local spatial flow parameters such as Mach number and static pressure determined from steady flow CFD computations or experiment) may often be sufficient.

Once the panel motion is determined, a CFD simulation with now known panel motion may be used to assess the change in the flow field due to panel motion.

Studies to determine the elements of all of the above are underway by various investigators.

A shock wave oscillates ahead of or on the flexible structure

Determination of the physical source of the shock oscillations due to shock wave boundary layer interaction is a challenge of long standing and still an active area of research. As mentioned earlier there is still some uncertainty about the fundamental physical mechanism. However recent work suggests that a global dynamic instability of the flow field may occur under certain conditions, e.g. when a ramp angle reaches a certain critical value. This fascinating subject is discussed in detail from a FSTDI perspective in an Appendix C with citations to the relevant literature. An assessment of the current state of the art and the identification of tasks to advance the state of the art are also provided in the appendix.

A fully coupled fluid structure interaction leading to flutter and limit cycle oscillations (LCO)

The state of the art is generally satisfactory when the flow is attached and Enhanced Piston Theory may be used to describe the oscillating fluid pressures due to structural motion. But for separated flows this is a topic of active research. Often the challenge is to characterize fully all the many flow and structural parameters that may influence the onset of flutter and LCO. Recent studies have emphasized the importance of in plane as well as out of plane boundary conditions, curvature, and mechanical and thermal loadings for the structure.

Fluid flow-structural-thermal coupling may lead to (1) buckled structures and (2) possible substantial increases in heat fluxes

Experiments are underway and new computational models have been developed and correlations of experimental and theoretical data are now possible. There is reason for cautious optimism.

References

1. Leyva A (2017) The relentless pursuit of hypersonic flight. Phys Today 70(11):30–36
2. Huang D, Friedmann P, Rokita T (2019) Aerothermoelastic scaling laws for configurations with hypersonic skin panels with arbitrary flow orientation. AIAA J 57(10):4377–4392
3. Dugundji J, Calligeros J (1962) Similarity laws for aerothermoelastic testing. J Aerosp Sci 26(2):935–950
4. Spottswood SM, Personal communication
5. Dowell EH (1975) Aeroelasticity of plates and shells. Springer, Berlin
6. Dowell EH (ed) Sisto F, Scanlan R, Simiu E, Curtiss HC, Jr., Peters D, Hall K, Edwards J, Strganac T, Clark R, Cox D, Tang D (2015) A modern course in aeroelasticity, 5th edn, Springer, See especially Chaps. 9, 11 and 14
7. Tang D, Dowell EH (2016) Experimental aeroelastic models design and wind tunnel testing for correlation with new theory. Aerospace 3(12). https://doi.org/10.3390
8. Giannelis NF, Vio GA, Levinski O (2017) A review of recent developments in the understanding of transonic shock buffet. Prog Aerosp Sci 92:39–84

9. Dolling DS (2001) Fifty years of shock-wave boundary layer interaction research: what next? AIAA J 39(8):1517–1531
10. Clemens NT, Narayanaswamy V (2014) Low-frequency unsteadiness of shock wave/turbulent boundary layer interactions. Annu Rev Fluid Mech 46:469–492
11. Funderburk ML, Narayanaswamy V (2017) Experimental investigation of shock boundary layer interactions in axisymmetric isolator geometries. In: AIAA propulsion and energy forum, joint propulsion conference (July 10–12)
12. Narayanaswamy V, Currao GMD, Neely AJ, Buttsworth DR, Gai Sl (2017) Hypersonic fluid-structure interaction on a cantilevered plate. In: 7th European conference for aeronautics and space sciences, p 13
13. Currao GMD, Neely AJ, Buttsworth DR, Gai Sl (2017) Hypersonic fluid-structure interaction on a cantilevered plate. In: 7th European conference for aeronautics and space sciences
14. Currao GMD, Neely AJ, Buttsworth DR, Choudhury R (2016) Measurement and simulation of hypersonic fluid-structural interaction on a cantilevered plate in a Mach 6 flow. In: AIAA Sci Tech, 15th dynamics specialists conference (January 4–8)
15. Wang L, Currao GMD, Han F, Neely AJ, Young J, Tian F-B (2017) An immersed boundary method for fluid-structure interaction with compressible multi-phase flows. J Comput Phys 346:131–151
16. Casper KM, Beresh SJ, Henfling JF, Spillers RW, Hunter P (2016) Fluid-structure interactions using controlled disturbances on a slender cone at Mach 8. In: AIAA SciTech, 54th aerospace sciences meeting (January 4–6)
17. Casper KM (2017) Fluid-structure interactions on a slender cone under quiet flow conditions at Mach 6. In: AIAA SciTech, 58th structures, structural dynamics and materials conference (January 9–13)
18. Laurence S, Personal communication
19. Spottswood SM, Eason TG, Beberniss T (2012) Influence on shock-boundary layer interactions on the dynamic response of a flexible panel. In: Proceedings of the ISMA-21-2, Sept 17–19. Belgium, Leuven, pp 603–616
20. Spottswood SM, Eason TG, Beberniss T (2013) Full-field dynamic response and displacement measurements of a panel excited by shock boundary layer interaction. AIAA Paper 2013–2016
21. Willems S, Gulhan A, Esser B (2013) Shock induced fluid-structure interaction on a flexible wall in supersonic turbulent flow. Prog Flight Phys 5:285–308
22. Gogulapati A, Deshmukh R, Crowell A, McNamara J, Vyas V, Wang X, Mignolet M, Beberniss T, Spottswood S, Eason T (2014) Response of a panel to shock impingement: modeling and comparison with experiments. AIAA 2014–0148
23. Gogulapati A, Deshmukh R, Crowell A, McNamara J, Vyas V, Wang X, Mignolet M, Beberniss T, Spottswood S, Eason T (2015) Response of a panel to shock impingement: modeling and comparison with experiments-part 2. AIAA 2015–0685
24. Touber E, Sandham ND (2011) Low-order stochastic modelling of low-frequency motions in reflected shock-wave/boundary-layer interactions. J Fluid Mech 671:417–465
25. Crouch JD, Barbarak A, Magidor D, Travin A (2009) Origin of transonic buffet on airfoils. J Fluid Mech 628:357–369
26. Lin YK (1967) Probabilistic theory of structural dynamics. McGraw-Hill
27. Dowell EH et al (2015) A modern course in aeroelasticity, 5th edn. Springer, Appendix A
28. Dowell EH, Tang D (2003) Dynamics of very high dimensional systems. World Scientific
29. Crandall SH, Mark WD (1963) Random vibrations. Academic Press
30. Clarkson BH (1994) Review of sonic fatigue technology, NASA CR 4587
31. Gaitone DV (2015) Progress in shock wave/boundary layer interactions. Prog Aerosp Sci 71:80–99
32. Hashimoto A, Aoyama T, Nakamura Y (2009) Effects of turbulent boundary layer on panel flutter. AIAA J 47:2785–2791
33. Vedeneev V (2010) Experimental observations of single mode panel flutter in supersonic gas flow. J Fluids Struct 26(5):2785–2791

34. Amirzadegan S, Dowell EH (2019) Correlation of experimental and computational results for flutter of a streamwise curved plate. AIAA J 57(8):3556–3561
35. Klock R, Cesnik C (2019) Local aeroelastic instability of high speed cylindrical vehicles. AIAA J 57(6):2553–2561
36. Goldman B, Dowell EH, Scott RC (2015) Aeroelastic stability of a thermal protection system for an inflatable aerodynamic decelerator. J Spacecr Rocket 52(1):144–156
37. Raveh D, Dowell EH (2011) Frequency lock-in phenomenon for oscillating airfoils in buffeting flows. J Fluids Struct 27:89–104
38. Raveh D, Dowell EH (2014) Aeroelastic responses of elastically suspended airfoil systems in transonic buffeting flows. AIAA J 52:926–934
39. Bastos K, Dowell EH (2019) Computation of buffet oscillations at high Reynolds number over an airfoil at high angle of attack, accepted for presentation at the international forum on aeroelasticity and structural dynamics. June Savannah, GA
40. Visbal MR (2012) On the interaction of an oblique shock with a flexible panel. J Fluids Struct 30:219–225
41. Visbal MR (2014) Viscous and inviscid interactions of an oblique shock with a flexible panel. J Fluids Struct 48:27–45
42. Boyer N, McNamara J, Visbal M (2016) Study on shock-induced panel flutter in 2-D laminar flow. AIAA Paper 2016–1091
43. Boyer NR, McNamara JJ, Gaitinonde DV, Barnes CJ, Visbal MV (2017) Study on shock induced panel flutter in 3-D inviscid flow. In: AIAA SciTec, 58th structures, structural dynamics and materials conference (January 9–13)
44. Freydin M, Dowell EH, Currao GMD, Neely AJ (2019) Computational study for the design of a hypersonic panel flutter experiment, accepted for presentation at the international forum on aeroelasticity and structural dynamics, June, Savannah, GA
45. Spottswood SM, Beberniss TJ, Eason TG, Perez RA, Donbar JM, Ehrhardt DA, Riley ZB (2019) Exploring the response of a thin, flexible panel to shock-turbulent boundary-layer interactions. J Sound Vib 443, 74–89. ISSN 0022-460X
46. Freydin M, Dowell EH, Spottswood SM, Perez RA (2020) Nonlinear dynamics and flutter of plate and cavity in response to supersonic wind tunnel start. Nonlinear Dyn (July)
47. Currao GMD, Neely AJ, Kennell CM, Gai SL, Buttsworth DR (2019) Hypersonic fluid structure interaction on a cantilevered plate with shock impingement. AIAA J 57, 4819–4834
48. Freydin M, Levin D, Dowell EH, Varigonda SV, Narayanaswamy V (2020) Natural frequencies of a heated plate: theory and experiment. AIAA J 58(11):4969–4973
49. Freydin M, Dowell EH, Whalen T, Laurence S (2020) A theoretical computational model of a plate in hypersonic flow. J Fluids Struct 93, UNSP 102858 (February)
50. Whalen T, Laurence S, Schoneich A, Sullivan B, Bodony D, Freydin M, Dowell EH, Buck G (2020) Hypersonic fluid-structure interactions in compression corner shock-wave boundary-layer interaction. AIAA J 58(9):4090–4105
51. McHugh KA, Freydin M, Bastos KK, Beran PS, Dowell EH (2021) Flutter and limit cycle oscillations of a cantilevered plate in supersonic flow. J Aircr 58(2):266–278
52. Eckert ERG (1956) Engineering relations for heat transfer and friction in high-velocity laminar and turbulent boundary-layer flow over surfaces with constant pressure and temperature. Trans ASME 78(6):1273–1283
53. Anderson JD (2019) Hypersonic and high temperature gas dynamics, 3rd edn, an AIAA Book
54. Freydin M, Dowell EH (2021) Nonlinear theoretical aeroelastic model of a plate: free to fixed in-plane boundaries. AIAA J 59(2):653–672

Appendix A
A Primer for Structural Response to Random Pressure Fluctuations

A.1 Introduction

In this appendix[1] we shall treat the response of a structure to a convecting - decaying random pressure field. The treatment follows along conventional lines after Powell [1] and others. That is, the pressure field is modelled as a random, stationary process whose correlation function (and/or power spectra) is determined from experimental measurements. Using this empirical description of the random pressure, the response of the structure is determined using standard methods from the theory of linear random processes [2,3]. The major purpose of the appendix is to provide a complete and detailed account of this theory which is widely used in practice (in one or another of its many variants). A second purpose is to consider systematic simplifications to the complete theory. The theory presented here is most useful for obtaining analytical results such as scaling laws or even, with enough simplifying assumptions, explicit analytical formulae for structural response.

It should be emphasized that, if for a particular application the simplifying assumptions which lead to analytical results must be abandoned, numerical simulation of structural response time histories may be the method of choice [4,5]. Once one is committed to any substantial amount of numerical work (e.g., computer work) then the standard power spectral approach loses much of its attraction.

A.2 Excitation-Response Relation For The Structure

In the present section we derive the excitation-response relations for a flat plate. It will be clear, however, that such relations may be derived in a similar manner for any linear system.

[1] This Appendix is based upon a report by E.H. Dowell and R. Vaicaitis of the same title Princeton University AMS Report No. 1220, April 1975.

E. H. Dowell (ed.), *A Modern Course in Aeroelasticity*, Solid Mechanics and Its Applications 264, https://doi.org/10.1007/978-3-030-74236-2

The equation of motion of the small (linear) deformation of a uniform isotropic flat plate is

$$D\nabla^4 w + m\frac{\partial^2 w}{\partial t^2} = p \tag{A.1}$$

where w is the plate deflection, p the pressure loading and the other terms are defined in the Nomenclature. Associated with (I.1) are the natural modes and frequencies of the plate which satisfy

$$D\nabla^4 \psi_n - \omega_n^2 m\psi_n = 0 \tag{A.2}$$

where ω_n is the frequency and $\psi_n(x, y)$ the shape of the nth natural mode. In standard texts it is shown that the ψ_n satisfy an orthogonality condition

$$\iint \psi_n \psi_m dxdy = 0 \quad \text{for} \quad m \neq n \tag{A.3}$$

If we expand the plate deflection in terms of the natural modes

$$w = \sum_n q_n(t)\psi_n(x, y) \tag{A.4}$$

then substituting (A.4) into (A.1), multiplying by ψ_m and integrating over the plate area we obtain

$$M_m[\ddot{q}_m + \omega_m^2 q_m] = Q_m \qquad m = 1, 2, \ldots \tag{A.5}$$

where we have used (A.2) and (A.3) to simplify the result. M_m and Q_m are defined as

$$\begin{aligned} M_m &\equiv \iint m\psi_m^2 dxdy \\ Q_m &\equiv \iint p\psi_m dxdy \\ \cdot &\equiv d/dt \end{aligned} \tag{A.6}$$

For structures other than a plate the final result would be unchanged, (A.5) and (A.6); however, the natural modes and frequencies would be obtained by the appropriate equation for the particular structure rather than (A.1) or (A.2). Hence, the subsequent development, which depends upon (A.5) only, is quite general.

Before proceeding further we must consider the question of (structural) damping. Restricting ourselves to structural damping only we shall include its effects in a gross way by modifying (A.5) to read

$$M_m[\ddot{q}_m + 2\zeta_m\omega_m\dot{q}_m + \omega_m^2 q_m] \equiv Q_m \tag{A.7}$$

where ζ_m is a (nondimensional) damping coefficient usually determined experimentally. This is by no means the most general form of damping possible. However,

given the uncertainly in our knowledge of damping from a fundamental theoretical viewpoint (see [6]) it is generally sufficient to express our meager knowledge. If damping is inherent in the material properties (stress-strain law) of the structure, the theory of viscoelasticity may be useful for estimating the amount and nature of the damping. However, often the damping is dominated by friction at joints, etc., which is virtually impossible to estimate in any rational way.

Now let us turn to the principal aim of this section, the stochastic relations between excitation (pressure loading), and response (plate deflection or stress). We shall obtain such results in terms of correlation functions and power spectra.

The correlation function of the plate deflection w is defined as

$$R_w(\tau; x, y) \equiv \lim_{T\to\infty} \frac{1}{2T} \int_{-T}^{T} w(x, y, t) w(x, y, t+\tau) dt \tag{A.8}$$

Using (A.4) we obtain

$$R_w(\tau; x, y) = \sum_m \sum_n \psi_m(x, y) \psi_n(x, y) R_{q_m q_n}(\tau) \tag{A.9}$$

where

$$R_{q_m q_n}(\tau) \equiv \lim_{T\to\infty} \frac{1}{2T} \int_{-T}^{T} q_m(t) q_n(t+\tau) dt \tag{A.10}$$

is defined to be the cross-correlation of the generalized coordinates , q_m. Defining power spectra

$$\Phi_w(\omega; x, y) = \frac{1}{\pi} \int_{-\infty}^{\infty} R_w(\tau; x, y) e^{-i\omega\tau} d\tau \tag{A.11}$$

$$\Phi_{q_m q_n}(\omega) \equiv \frac{1}{\pi} \int_{-\infty}^{\infty} R_{q_m q_n}(\tau) e^{-i\omega\tau} d\tau \tag{A.12}$$

we may obtain from (A.9) via a Fourier transform

$$\Phi_w(\omega; x, y) = \sum_m \sum_n \psi_m(x, y) \psi_n(x, y) \Phi_{q_m q_n}(\omega) \tag{A.13}$$

(A.9) and (A.13) relate the physical deflection, w, to the generalized coordinates , q_m.

Consider next similar relations between physical load p and Generalized force Q_m. Define the cross-correlation.

$$R_{Q_m Q_n}(\tau) \equiv \lim_{T\to\infty} \frac{1}{2T} \int_{-T}^{T} Q_m(t) Q_n(t+\tau) dt \tag{A.14}$$

Using the definition of Generalized force (A.6)

$$Q_m(t) \equiv \iint p(x, y, t)\psi_m(x, y)dxdy$$

$$Q_n(t+\tau) \equiv \iint p(x^*, y^*, t+\tau)\psi_n(x^*, y^*)dx^*dy^*$$

and substituting into (A.14) we obtain

$$R_{Q_m Q_n}(\tau) = \iiiint \psi_m(x, y)\psi_n(x^*, y^*) \cdot R_p(\tau; x, y, x^*, y^*)dxdy\ dx^*dy^* \tag{A.15}$$

where we define the pressure correlation

$$R_p(\tau; x, y, x^*, y^*) \equiv \lim_{T\to\infty} \frac{1}{2T}\int_{-T}^{T} p(x, y, t)p(x, y, t)p(x^*, y^*, t+\tau)dt \tag{A.16}$$

Note that a rather extensive knowledge of the spatial distribution of the pressure is required by (A.16).

Again defining power spectra

$$\Phi_{Q_m Q_n}(\omega) \equiv \frac{1}{\pi}\int_{-\infty}^{\infty} R_{Q_m Q_n}(\tau)e^{i\omega\tau}d\tau \tag{A.17}$$

$$\Phi_p(\omega; x, y, x^*, y^*) \equiv \frac{1}{\pi}\int_{-\infty}^{\infty} R_p(\tau; x, y, x^*, y^*)e^{-i\omega\tau}dt \tag{A.18}$$

we may obtain from (A.15)

$$\Phi_{Q_m Q_n}(\omega) = \iiiint \psi_m(x, y)\psi_n(x^*, y^*) \cdot \Phi_p(\tau; x, y, x^*, y^*)dxdy\ dx^*dy^* \tag{A.19}$$

Finally, we must relate the generalized coordinates to the generalized forces . From (A.7) we may formally solve (see [2], for example or recall Sect. 3.3)

$$q_n(t) = \int_{-\infty}^{\infty} I_n(t-t_1)Q_n(t_1)dt_1 \tag{A.20}$$

where the 'impulse function' is defined as

$$I_n(t) \equiv \frac{1}{2\pi}\int_{-\infty}^{\infty} H_n(\omega)e^{i\omega\tau}d\omega \tag{A.21}$$

and the 'transfer function' is defined as

$$H_n(\omega) \equiv \frac{1}{M_n[\omega_n^2 + 2\zeta_n i\omega_n\omega - \omega^2]}$$

Also

$$H_n(\omega) = \int_{-\infty}^{\infty} I_n(t)e^{-i\omega\tau}dt$$

which is the other half of the transform pair, cf (A.21).

From (A.20) and (A.10)

$$R_{q_m q_n}(\tau) = \lim_{T\to\infty} \frac{1}{2T} \iiint_{-T}^{T} I_m(t-t_1)I_n(t+\tau-t_2)Q_m(t_2)dt_1dt_2dt$$

Performing a change of integration variables and noting (A.14),

$$R_{q_m q_n}(\tau) = \iint_{-\infty}^{\infty} I_m(\xi)I_n(\eta)R_{Q_m Q_n}(\tau-\eta+\xi)d\xi d\eta \tag{A.22}$$

Taking a Fourier transform of (A.22) and using the definitions of power spectra (A.12) and (A.17), we have

$$\Phi_{q_m q_n}(\omega) = H_m(\omega)H_n(-\omega)\Phi_{Q_m Q_n}(\omega) \tag{A.23}$$

Summarizing, the relations for correlation functions are (A.9), (A.15) and (A.22) and for power spectra (A.13), (A.19) and (A.23). For example, substituting (A.19) into (A.23) and the result into (A.13) we have

$$\Phi_w(\omega; x, y) \sum_m \sum_n \psi_m(x, y)\psi_n(x, y)H_m(\omega)H_n(-\omega)$$

$$\cdot \iiint \psi_m(x, y)\psi_n(x^*, y^*)$$

$$\cdot \Phi_p(\omega; x, y, x^*, y^*)dxdy\,dx^*dy^* \tag{A.24}$$

This is the *desired final result* relating the physical excitation to the physical response in stochastic terms.

A.3 Sharp Resonance or Low Damping Approximation

Often (I.24) is approximated further. Two approximations are particularly popular and useful. The first is the 'neglect of off-diagonal coupling'. This means omitting all terms in the double sum except those for which $m = n$. The second is the 'white

noise' approximation which assumes that Φ_p is essentially constant relative to the rapidly varying transfer functions $H_m(\omega)$. Making both of these approximations in (A.24) we may obtain the mean square response

$$\bar{w}^2(x, y) \equiv R_w(\tau = 0; x, y) = \int_0^\infty \Phi_w(\omega; x, y) d\omega$$

$$\approx \frac{\pi}{4} \sum_m \frac{\psi_m^2(x, y)}{M_m^2 \omega_m^3 \zeta_m} \iiint \psi_m(x, y) \psi_m(x^*, y^*)$$

$$\cdot \Phi_p(\omega_m; x, y, x^*, y^*) dx dy\, dx^* dy^* \tag{A.25}$$

Of course, only one or the other of these approximations may be made, rather than both. However, both stem from the same basic physical idea: The damping is small and hence, H_m has a sharp maximum near $\omega = \omega_m$. That is

$$H_m(\omega_m) H_n(-\omega_m) \ll |H_m(\omega_m)|^2$$

$$H_m(\omega_n) H_n(-\omega_n) \ll |H_n(\omega_n)|^2$$

and the 'neglect of off-diagonal coupling' follows. Also

$$\int \Phi_p |H_m(\omega)|^2 d\omega \approx \Phi_p(\omega_m) \int |H_m(\omega)|^2 d\omega$$

and (A.25) follows by simple integration.

Not that if we take the spatial mean square of (A.24) then using orthogonality (for a uniform mass distribution)one may show that the off-diagonal terms do not contribute (see Powell [1]).

Finally note that if we desire stress rather than deflection, then it may be shown that analogous to (A.25)one obtains

$$\bar{\sigma}^2 = \frac{\pi}{4} \sum_m \frac{\sigma_m^2(x, y)}{M_m^2 \omega_m^3 \zeta_m} \iiint \psi_m(x, y) \psi_m(x^*, y^*)$$

$$\cdot \Phi_p(\omega_m; x, y, x^*, y^*) dx dy\, dx^* dy^* \tag{A.26}$$

where σ_m is stress due to $w = \psi_m$.

Nomenclature

a	Plate length
b	Plate width
D	$Eh^3/12(1 - \upsilon^2)$, Plate bending stiffness
E	Modulus of elasticity

H_n	Plate transfer function
h	Plate thickness
I_n; I	Plate impulse function; see equation (A.21)
K_n^2	$= \frac{m\omega_n^2 a^4}{D}$
M_m	Plate generalized mass
m	Plate mass/area
n	normal
p	Pressure on plate
Q_m	Generalized force on plate
q_n	Generalized plate coordinate
R	Correlation function
t	Time
w	Plate deflection
x, y, z	Cartesian Coordinates
∇^2	Laplacian
Φ	Power spectral density
ρ_m	Plate density
σ	stress
τ	Dummy time
ζ_m	Modal damping
ω_m	Modal frequency

References

1 Powell A (1958) Chapter 8 in book In: Random vibration Crandall SH (ed). Technology Press, Cambridge, Mass
2 Laning JH, Battin RH (1956) Random processes in automatic control. McGraw-Hill, New York, N.Y.
3 Lin YK (1967) *Probabilistic Theory of Structural Dynamics*, McGraw-Hill, New York, N.Y.
4 Dowell EH (1974) Aeroelasticity of plates and shells. Noordhoff International Publishing, Leyden, The Netherlands.(Now published by Springer)
5 Vaivaitis R, Dowell EH, Ventres CS (1974) Nonlinear panel response by a Monte Carlo approach. AIAA J 12(5):685–691
6 Lazan BJ (1968) Damping of materials and members in structural mechanics. Pergamon Press, New York, N.Y.

Appendix B
Some Example Problems

Problems such as these have been used successfully as homework assignments. When used as a text, the instructor may wish to construct variations on these problems.

B.1 For Chapter "Static Aeroelasticity"

Questions

Typical section with control surface, see Fig. B.1.

1. Compute $q_{REVERSAL}$ for finite K_δ and show it is the same as computed in the text for $K_\delta \to \infty$.
2. Compute $q_{DIVERGENCE}$ explicitly in terms of K_α, K_δ, etc.

Beam-rod model

3. Compute $q_{DIVERGENCE}$ using one and two models with uniform beam-rod eigenfunctions.

Assume

$$GJ = GJ_0[1 - y/l]$$

How do these results compare to those for

$$GJ = GJ_0 \sim \text{ constant?}$$

E. H. Dowell (ed.), *A Modern Course in Aeroelasticity*, Solid Mechanics and Its Applications 264, https://doi.org/10.1007/978-3-030-74236-2

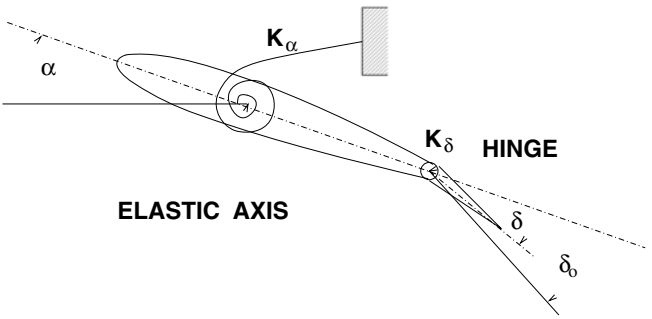

Fig. B.1

Answers

1. The two equations of static moment equilibrium are as follows:

$$eqS\left(\frac{\partial C_L}{\partial \alpha}\alpha + \frac{\partial C_L}{\partial \delta}\delta\right) + qSc\frac{\partial C_{MAC}}{\partial \delta}\delta - K_\alpha \alpha = 0 \quad \text{(about elastic axis)}$$

$$qSc\left(\frac{\partial C_H}{\partial \alpha}\alpha + \frac{\partial C_H}{\partial \delta}\delta\right) - K_\delta(\delta - \delta_0) = 0 \quad \text{(about high axis)}$$

These equations are given in matrix form as follows:

$$\begin{bmatrix} eqS\frac{\partial C_L}{\partial \alpha} - K_\alpha & eqS\frac{\partial C_L}{\partial \delta} + qSc\frac{\partial C_{MAC}}{\partial \delta} \\ qSc\frac{\partial C_H}{\partial \alpha} & qSc\frac{\partial C_H}{\partial \delta} - K_\delta \end{bmatrix}\begin{bmatrix} \alpha \\ \delta \end{bmatrix} = \begin{bmatrix} 0 \\ -K_\delta \cdot \delta_0 \end{bmatrix}$$

Solving for α and δ, one obtains

$$\alpha = \frac{\begin{vmatrix} 0 & eqS\frac{\partial C_L}{\partial \delta} + qSc\frac{\partial C_{MAC}}{\partial \delta} \\ -K_\delta \cdot \delta_0 & qSc\frac{\partial C_H}{\partial \delta} - K_\delta \end{vmatrix}}{\Delta} = \frac{K_\delta \cdot \delta_0 qS\left(e\frac{\partial C_L}{\partial \delta} + c\frac{\partial C_{MAC}}{\partial \delta}\right)}{\Delta} \quad \text{(B.1)}$$

$$\delta = \frac{\begin{vmatrix} eqS\cdot\frac{\partial C_L}{\partial \alpha} - K_\alpha & \dot{0} \\ qSc\frac{\partial C_H}{\partial \alpha} & -K_\delta \cdot \delta_0 \end{vmatrix}}{\Delta} = \frac{-K_\delta \cdot \delta_0\left(eqS\frac{\partial C_L}{\partial \alpha} - K_\alpha\right)}{\Delta} \quad \text{(B.2)}$$

where

$$\Delta \equiv \begin{vmatrix} eqS\frac{\partial C_L}{\partial \alpha} - K_\alpha & eqS\frac{\partial C_L}{\partial \delta} + qSc\frac{\partial C_{MAC}}{\partial \delta} \\ qSc\frac{\partial C_H}{\partial \alpha} & qSc\frac{\partial C_H}{\partial \delta} - K_\delta \end{vmatrix} \quad \text{(B.3)}$$

If control surface reversal occurs when $q = q_R$, then

$$L = qS\left[\frac{\partial C_L}{\partial \alpha}\alpha + \frac{\partial C_L}{\partial \delta}\delta\right] = 0$$

for $q = q_R$, i.e.,

$$\left[\frac{\partial C_L}{\partial \alpha}\alpha + \frac{\partial C_L}{\partial \delta}\delta\right] = 0 \qquad \text{(B.4)}$$

$$\text{at } \; q = q_R$$

Substitution of (B.1) and (B.2) into (B.4) gives

$$0 = \frac{\partial C_L}{\partial \alpha} \cdot \frac{K_\delta \cdot \delta_0}{\Delta} q_R S\left(e\frac{\partial C_L}{\partial \delta} + c\frac{\partial C_{MAC}}{\partial \delta}\right) - \frac{\partial C_L}{\partial \delta} \cdot \frac{K_\delta \cdot \delta_0}{\Delta}\left(eq_R S\frac{\partial C_L}{\partial \delta} - K_\alpha\right)$$

$$= \frac{K_\delta \cdot \delta_0}{\Delta}\left(\cancel{eq_R S\frac{\partial C_L}{\partial \alpha}\frac{\partial C_L}{\partial \delta}} + q_R S\frac{\partial C_L}{\partial \alpha}\frac{\partial C_{MAC}}{\partial \delta} - \cancel{eq_R S\frac{\partial C_L}{\partial \alpha}\frac{\partial C_L}{\partial \delta}} + K_\alpha\frac{\partial C_L}{\partial \delta}\right)$$

$$= \frac{K_\sigma \cdot \delta_0}{\Delta}\left(q_R Sc\frac{\partial C_L}{\partial \alpha}\frac{\partial C_{MAC}}{\partial \delta} + K_\alpha\frac{\partial C_L}{\partial \alpha}\right)$$

Thus the reversal dynamic pressure q_R for finite K_δ is

$$q_R = \frac{\frac{K_\alpha}{Sc}\left(\frac{\partial C_L}{\partial \delta} \Big/ \frac{\partial C_L}{\partial \alpha}\right)}{\frac{-\partial C_{MAC}}{\partial \delta}}$$

which is identical with q_R when $K_{\delta \to \infty}$!

2. The divergence dynamic pressure is determined by $\Delta = 0$. That is,

$$\left(eqS\frac{\partial C_L}{\partial \alpha} - K_\alpha\right)\left(qSc\frac{\partial C_H}{\partial \delta} - K_\delta\right) - qSc\frac{\partial C_H}{\partial \alpha}\left(eqS\frac{\partial C_L}{\partial \delta} + qSc\frac{\partial C_{MAC}}{\partial \delta}\right) = 0$$

$$q^2S^2c^2\left(\bar{e} \cdot \frac{\partial C_L}{\partial \alpha}\frac{\partial C_H}{\partial \delta} - \bar{e}\frac{\partial C_H}{\partial \alpha}\frac{\partial C_L}{\partial \delta} - \frac{\partial C_{MAC}}{\partial \delta}\right)$$

$$-qSc\left(K_\alpha \cdot \frac{\partial C_H}{\partial \delta} + K_\delta \cdot \bar{e}\frac{\partial C_L}{\partial \alpha}\right) + K_\alpha K_\delta = 0$$

$$(\bar{e} \equiv e/c) \qquad \text{(B.5)}$$

If $A \neq 0$ (A is defined below),

$$q = \frac{1}{Sc} \cdot \frac{B \pm \sqrt{B^2 - 4AC}}{2A}$$

where

$$A \equiv \bar{e}\left(\frac{\partial C_L}{\partial \alpha}\frac{\partial C_H}{\partial \delta} - \frac{\partial C_H}{\partial \alpha}\frac{\partial C_L}{\partial \delta}\right) - \frac{\partial C_{MAC}}{\partial \delta}$$

$$B \equiv K_\alpha \frac{\partial C_H}{\partial \delta} + K_\delta \bar{e}\frac{\partial C_L}{\partial \alpha}$$

$$C \equiv K_\alpha K_\delta$$

Then divergence occurs when $AB > 0$ and $B^2 - 4AC \geq 0$ (for which e.g., (B.5) has two positive roots), and the divergence dynamic pressure q is

$$q_D = \min\left[\frac{1}{Sc}\cdot\frac{B+\sqrt{B^2-4AC}}{2A}, \frac{1}{Sc}\frac{B-\sqrt{B^2-4AC}}{2A}\right]$$

If $A = 0$, then divergence occurs when $B > 0$, and the divergence dynamic pressure q_D is

$$q_D = \frac{1}{Sc}\cdot\frac{C}{B}$$

To sum up, divergence occurs when
(a)

$$\left\{\bar{e}\left(\frac{\partial C_L}{\partial \alpha}\frac{\partial C_H}{\alpha\delta} - \frac{\partial C_H}{\partial \alpha}\frac{\partial C_L}{\partial \delta}\right) - \frac{\partial C_{MAC}}{\partial \delta}\right\}\left(K_\alpha\frac{\partial C_H}{\partial \delta} + K_\delta\bar{e}\frac{\partial C_L}{\partial \alpha}\right) > 0$$

and

$$\left(K_\alpha\frac{\partial C_H}{\partial \delta} - K_\delta\bar{e}\frac{\partial C_L}{\partial \alpha}\right)^2 + 4K_\alpha K_\delta\left(\bar{e}\frac{\partial C_H}{\partial \alpha}\frac{\partial C_L}{\partial \delta} + \frac{\partial C_{MAC}}{\partial \delta}\right) \geq 0$$

and the divergence dynamic pressure q_D is

$$K_\alpha\frac{\partial C_H}{\partial \delta} + K_\delta\bar{e}\frac{\partial C_L}{\partial \alpha} - \sqrt{\left(K_\alpha\frac{\partial C_H}{\partial \delta} - K_\delta\bar{e}\frac{\partial C_L}{\partial d}\right)^2}$$

$$q_D = \frac{+4K_\alpha K_d\left(\bar{e}\frac{\partial C_H}{\partial \alpha}\frac{\partial C_L}{\partial \delta} + \frac{\partial C_{MAC}}{\partial \delta}\right)}{2Sc\left\{\bar{e}\left(\frac{\partial C_L}{\partial \alpha}\frac{\partial C_H}{\partial \delta} - \frac{\partial C_{HL}}{\partial \alpha}\frac{\partial C_L}{\partial \delta}\right) - \frac{\partial C_{MAC}}{\partial \delta}\right\}}$$

when

$$\bar{e}\left(\frac{\partial C_L}{\partial \alpha}\frac{\partial C_H}{\partial \delta} - \frac{\partial C_H}{\partial \alpha}\frac{\partial C_L}{\partial \sigma}\right) - \frac{\partial C_{MAC}}{\partial \delta} > 0$$

and

$$K_\alpha\frac{\partial C_H}{\partial \delta} + K_\delta\bar{e}\frac{\partial C_L}{\partial \alpha} + \sqrt{\left(K_\alpha\frac{\partial C_H}{\partial \delta} - K_\delta\bar{e}\frac{\partial C_L}{\partial \alpha}\right)^2}$$

Fig. B.2

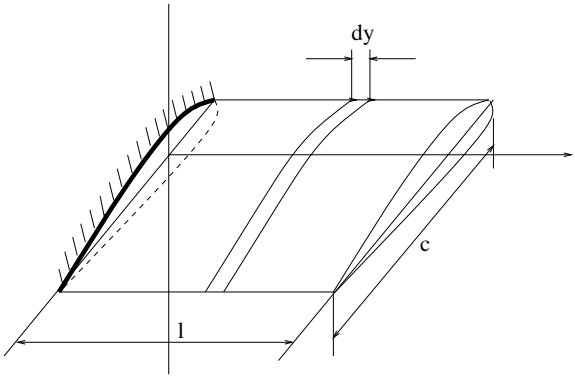

$$q_D = \frac{+4K_\alpha K_\delta \left(\bar{e}\frac{\partial C_H}{\partial \alpha}\frac{\partial C_L}{\partial \delta} + \frac{\partial C_{MAC}}{\partial \delta}\right)}{2Sc\left\{\bar{e}\left(\frac{\partial C_L}{\partial \alpha}\frac{\partial C_H}{\partial \delta}\right) - \frac{\partial C_H}{\partial \alpha}\frac{\partial C_L}{\partial \delta}\right\}}$$

when

$$\bar{e}\frac{\partial C_L}{\partial \alpha}\frac{\partial C_H}{\partial \delta} - \frac{\partial C_H}{\partial \alpha}\frac{\partial C_L}{\partial \delta} - \frac{\partial C_{MAC}}{\partial \delta} < 0$$

or,

(b)

$$\bar{e}\left(\frac{\partial C_L}{\partial \alpha}\frac{\partial C_H}{\partial \delta} - \frac{\partial C_H}{\partial \alpha}\frac{\partial C_L}{\partial \delta}\right) - \frac{\partial C_{MAC}}{\partial \delta} = 0$$

and

$$K_\alpha \frac{\partial C_H}{\partial \delta} + K_\delta \bar{e}\frac{\partial C_L}{\partial \alpha} > 0$$

and the divergence dynamic pressure q_D is

$$q_D = \frac{K_\alpha K_\delta}{Sc\left(K_\alpha \frac{\partial C_H}{\partial \delta} + K_\delta \bar{e}\frac{\partial C_L}{\partial \alpha}\right)}$$

3. The equation of static torque equilibrium for a beam rod, see Fig. B.2, is

$$\frac{d}{dy}\left(GJ\frac{d\alpha_e}{dy}\right) + M_y = 0 \tag{B.6}$$

where

$$\begin{aligned} M_y &= M_{AC} + L_e \\ &= qc^2 C_{MAC_0} + eqc\frac{\partial C_L}{\partial \alpha}(\alpha_0 + \alpha_e) \end{aligned} \tag{B.7}$$

If we put $\gamma = [1 - y/l]$ and $y = l\bar{y}$, then, from (B.6) and (B.7), we have

$$\frac{d}{d\bar{y}}\left(\gamma\frac{d\alpha_e}{d\bar{y}}\right)+\frac{qcel^2\frac{\partial C_L}{\partial\alpha}}{GJ_0}\alpha_e=-\frac{qcl^2}{GJ_0}\left(c\cdot C_{MAC_0}+e\frac{\partial C_L}{\partial\alpha}\alpha_0\right) \tag{B.8}$$

(1) Eigenvalues and functions for constant wing properties. Putting

$$\lambda^2\equiv\frac{qcel^2\frac{\partial C_L}{\partial\alpha}}{GJ_0}$$

we have the characteristic equation as follows

$$(B.7)\rightarrow\frac{d^2\alpha_e}{d\bar{y}^2}+\lambda^2\alpha_e=0\qquad(\gamma=1\ \text{ for constant wing properties})$$

Hence, $\alpha_e=A\sin\lambda\bar{y}+B\cos\lambda\bar{y}$.
As boundary conditions are

$$\begin{aligned}\alpha_e&=0\ \text{ at }\ \bar{y}=0\rightarrow B=0\\ \frac{d\alpha_e}{d\bar{y}}&=0\ \text{ at }\ \bar{y}=1\rightarrow A\lambda\cos\lambda-B\lambda\sin\lambda\rightarrow\cos\lambda=0\end{aligned}$$

(If $\lambda=0$ then $\alpha_e\equiv 0$, which is of no physical interest.)
So

$$\text{Eigenvalues: }\ \lambda_m=(2m-1)\frac{\pi}{2},\ m=1,2\ldots$$
$$\text{Eigenfunctions: }\ \alpha_m=\sin\lambda_m\bar{y}$$

We first find the divergence dynamic pressure for the wing with constant properties. Let

$$\alpha_e=\sum_m a_n\alpha_n,\qquad K\equiv-\frac{qcl^2}{(GJ)_0}\left(cC_{MAC_0}+e\frac{\partial C_L}{\partial\alpha}\alpha_0\right)=\sum_n A_n\alpha_n$$

Then

$$\sum_n a_n\left(\frac{d^2\alpha_n}{d\bar{y}^2}+\lambda^2\alpha_n\right)=K$$

As

$$\frac{d^2\alpha_n}{d\bar{y}^2}=-\lambda_n^2\alpha_n$$

so

$$\sum_n a_n(\lambda^2-\lambda_n^2)\alpha_n=K$$

$$\sum_n a_n \int_0^1 (\lambda^2 - \lambda_n^2)\alpha_n \alpha_m d\bar{y} = \int_0^1 K\alpha_m d\bar{y} = \frac{1}{2}A_m$$

since

$$\begin{aligned}\int_0^1 \alpha_n \alpha_m d\bar{y} &= \frac{1}{2}\delta_{mn} \\ &= \frac{1}{2} m = n \\ &= 0 m \neq n\end{aligned}$$

Hence

$$\begin{aligned}\frac{a_m}{2}(\lambda^2 - \lambda_m^2) &= \frac{1}{2}A_m \\ a_m &= \frac{A_m}{\lambda^2 - \lambda_m^2}\end{aligned}$$

Thus

$$\alpha_e = \sum_n \frac{A_n}{\lambda^2 - \lambda_n^2} \cdot \alpha_n$$

$\alpha_e \to \infty$ when

$$\lambda = \lambda_m = (2m-1)\frac{\pi}{2}$$

hence, the divergence dynamic pressure q_D, corresponds to the minimum value of λ_m, i.e., $\pi/2$. Thus

$$q_D = \frac{GJ_0}{cel^2 \frac{\partial C_L}{\partial \alpha}} \frac{\pi^2}{4}$$

for constant wing properties.

(2) $GJ = GJ_0(1 - y/l) = GJ_0(1 - \bar{y})$, variable wing properties. We assume for simplicity that only the torsional stiffness varies along span and that other characteristics remain the same.

Putting

$$\alpha_e = \sum_n b_n \cdot \alpha_n, \qquad K \equiv -\frac{qcl^2}{GJ_0}\left(cC_{MAC_0} + e\frac{\partial C_L}{\partial \alpha}\alpha_0\right) = \sum_n A_n \alpha_n$$

and

$$\lambda^2 \equiv \frac{qcel^2}{GJ_0}\frac{\partial C_L}{\partial \alpha}$$

we get from (B.8)

$$\sum_n b_n \left\{\frac{d}{d\bar{y}}\left(\gamma \frac{d\alpha_n}{d\bar{y}}\right) + \lambda^2 \alpha_n\right\} = K$$

$$\text{therefore} \quad \sum_n b_n \int_0^1 \left\{ \frac{d}{d\bar{y}} \left(\gamma \frac{d\alpha_n}{d\bar{y}} \right) + \lambda^2 \alpha_n \right\} \alpha_m d\bar{y} = \int_0^1 K \alpha_m dy = \frac{1}{2} A_m$$

$$\text{therefore} \quad [C_{mn}]\{b_n\} = \frac{1}{2} A_m (\text{for finite } n) \tag{B.9}$$

where

$$\begin{aligned} C_{mn} &= \int_0^1 \left\{ \frac{d}{d\bar{y}} \left(\gamma \frac{d\alpha_n}{d\bar{y}} \right) + \lambda^2 \alpha_n \right\} \alpha_m d\bar{y} \\ &= -\int_0^1 \gamma \frac{d\alpha_n}{d\bar{y}} \frac{d\alpha_m}{d\bar{y}} d\bar{y} + \frac{\lambda^2}{2} \delta_{mn} \end{aligned}$$

($\gamma \frac{d\alpha_n}{d\bar{y}} \alpha_m = 0$ at $\bar{y} = 0$ and 1 because of the boundary conditions for eigenfunctions.)
(1) One mode model. The assumed mode is as follows:

$$\alpha_1 = \sin \lambda_1 \bar{y} = \sin \frac{\pi}{2} \bar{y} \rightarrow \frac{d\alpha_1}{d\bar{y}} = \frac{\pi}{2} \cos \frac{\pi}{2} \bar{y}$$

Equation (B.9) is

$$C_{11} b_1 = \frac{A1}{2} \tag{B.10}$$

where

$$C_{11} = -\int_0^1 (1 - \bar{y}) \left(\frac{d\alpha_1}{d\bar{y}} \right)^2 d\bar{y} + \frac{\lambda^2}{2}$$

$$\text{therefore} \quad C_{11} = \frac{\lambda^2}{2} - \frac{\pi^2 + 4}{16}$$

From (B.10),

$$b_1 = \frac{A_1}{\lambda^2 - \frac{\pi^2 + 4}{8}}$$

Then divergence occurs when

$$\lambda^2 = \frac{\pi^2 + 4}{8}$$

and

$$q_D = \frac{GJ_0}{cel^2 \frac{\partial C_L}{\partial \alpha}} \frac{\pi^2 + 4}{8} = (q_D)_{\text{const. wing prop.}} \times 0.703$$

(2) Two mode model. Assumed modes are

$$\alpha_1 = \sin\lambda_1\bar{y} = \sin\frac{\pi}{2}\bar{y} \Rightarrow \frac{d\alpha_1}{d\bar{y}} = \frac{\pi}{2}\cos\frac{\pi}{2}\bar{y}$$
$$\alpha_2 = \sin\lambda_2\bar{y} = \sin\frac{3}{2}\pi\bar{y} \Rightarrow \frac{d\alpha_2}{d\bar{y}} = \frac{3}{2}\pi\cos\frac{3}{2}\pi\bar{y}$$

Equation (B.9) is as follows:

$$\begin{bmatrix} C_{11} & C_{12} \\ C_{21} & C_{22} \end{bmatrix}\begin{bmatrix} b_1 \\ b_2 \end{bmatrix} = \frac{1}{2}\begin{bmatrix} A_1 \\ A_2 \end{bmatrix} \tag{B.11}$$

where

$$C_{11} = -\int_0^1 (1-\bar{y})\left(\frac{d\alpha_1}{d\bar{y}}\right)^2 d\bar{y} + \frac{\lambda^2}{2} = \frac{\lambda^2}{2} - \frac{\pi^2+4}{16}$$
$$C_{12} = -\int_0^1 (1-\bar{y})\frac{d\alpha_2}{d\bar{y}}\frac{d\alpha_1}{d\bar{y}}d\bar{y} = -\frac{3}{4}$$
$$C_{21} = -\int_0^1 (1-\bar{y})\frac{d\alpha_1}{d\bar{y}}\frac{d\alpha_2}{d\bar{y}}d\bar{y} = C_{12} = -\frac{3}{4}$$
$$C_{22} = -\int_0^1 (1-\bar{y})\left(\frac{d\alpha_2}{d\bar{y}}\right)^2 d\bar{y} + \frac{\lambda^2}{2} = \frac{\lambda^2}{2} - \frac{9\pi^2+4}{16}$$

Then equation (B.11) is as follows:

$$\begin{bmatrix} \lambda^2 - \frac{\pi^2+4}{8} & -\frac{3}{2} \\ -\frac{3}{2} & \lambda^2 - \frac{9\pi^2+4}{8} \end{bmatrix}\begin{bmatrix} b_1 \\ b_2 \end{bmatrix} = \begin{bmatrix} A_1 \\ A_2 \end{bmatrix}$$

Thus divergence occurs when

$$\begin{vmatrix} \lambda^2 - \frac{\pi^2+4}{8} & -\frac{3}{2} \\ -\frac{3}{2} & \lambda^2 - \frac{9\pi^2+4}{8} \end{vmatrix} = 0$$

$$\text{therefore} \quad \lambda^2 = \frac{5\pi^2+4}{8} \pm \frac{1}{2}\sqrt{\pi^4+9}$$

q_D is given by the smaller value of λ^2, i.e.,

$$q_D = \frac{GJ_0}{cel^2\frac{\partial C_L}{\partial\alpha}} \times \left(\frac{5\pi^2+4}{8} - \frac{1}{2}\sqrt{\pi^4+9}\right)$$
$$= (q_D)_{const.wingprop.} \times 0.612$$

Fig. B.3

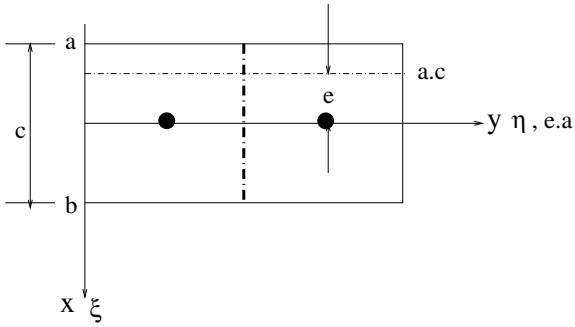

Question

Beam-rod model, see Fig. B.3

4. For a constant GJ, etc. wing, use a two 'lumped element' model and compute the divergence dynamic pressure. Neglect rolling. Compare your result with the known analytical solution. How good is a one 'lumped element' solution?

Answer
4.
(a) Two lumped element model

$$\alpha(y) = \int_0^1 C^{\alpha M}(y, \eta) M(\eta) d\eta \tag{B.12}$$

where
$C^{\alpha M}(y, \eta)$: twist about y axis at y due to unit moment at η

$$M(\eta) = \int_a^b p(\xi, \eta) \xi d\xi$$

Equation (B.12) in matrix form is

$$\{\alpha\} = [C^{\alpha M}]\{M\}\Delta\eta \tag{B.12}$$

where from structural analysis,

$$[C^{\alpha M}] = \begin{bmatrix} \frac{l/4}{GJ} & \frac{l/4}{GJ} \\ \frac{l/4}{GJ} & \frac{3l/4}{GJ} \end{bmatrix} \tag{B.13}$$

and $C^{\alpha M}(i, j)$ is the twist at i due to unit moment at j. Using an aerodynamic 'strip theory' approximation, the aerodynamic moment may be related to the twist,

$$\{M\} = qce\frac{\partial C_L}{\partial \alpha}\begin{bmatrix}1 & 0\\ 0 & 1\end{bmatrix}\{\alpha\} = qce\frac{\partial C_L}{\partial \alpha}\{\alpha\} \tag{B.14}$$

From (B.12) and (B.14), one has

$$\{\alpha\} = [C^{\alpha M}]\{M\}\Delta\eta = qCe\frac{\partial C_L}{\partial \alpha}[C^{\alpha M}]\Delta\eta\{\alpha\}$$

or rewritten, using $\Delta\eta = l/2$,

$$\left[\begin{bmatrix}1 & 0\\ 0 & 1\end{bmatrix} - \frac{1}{2}qce\frac{\partial C_L}{\partial \alpha}\frac{l^2}{4GJ}\begin{bmatrix}1 & 1\\ 1 & 3\end{bmatrix}\right]\{\alpha\} = \begin{Bmatrix}0\\ 0\end{Bmatrix} \tag{B.15}$$

Setting the determinant of coefficients to zero, gives

$$|\ \ | = 0 \rightarrow 2Q^2 - 4Q + 1 = 0 \tag{B.16}$$

where

$$Q = \frac{l^2}{8GJ}qce\frac{\partial C_L}{\partial \alpha}$$

Solving (B.16), on obtains

$$Q = \frac{2 \pm \sqrt{2}}{2}$$

The smaller Q gives the divergence q_D

$$\begin{aligned} q_D =& 4(2 - \sqrt{2})\frac{GJ/l}{(lc)e\frac{\partial C_L}{\partial \alpha}} \\ \doteq& 2.34\frac{GJ/l}{(lc)e\frac{\partial C_L}{\partial \alpha}} \end{aligned}$$

(b) One lumped element model

$$\alpha = qce\frac{\partial C_L}{\partial \alpha}C^{\alpha M}\Delta\eta\alpha$$

where

$$\Delta\eta = l, \qquad C^{\alpha M} = \frac{l/2}{GJ}$$

$$\left(1 - qCe\frac{\partial C_L}{\partial \alpha}\frac{l/2}{GJ}\right)\alpha = 0$$

$$\text{therefore} \quad q_D = 2\frac{GJ/l}{(lc)e\frac{\partial C_L}{\partial \alpha}}$$

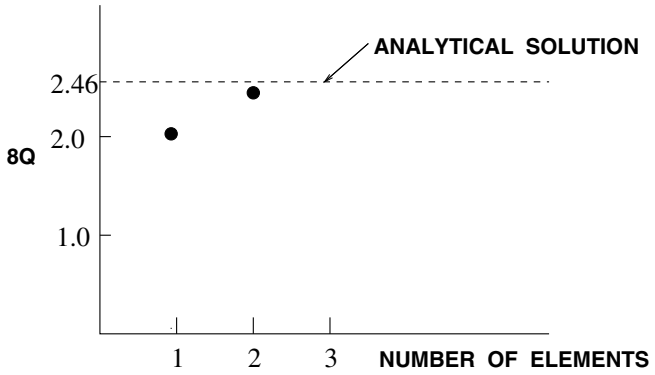

Fig. B.4

Fig. B.5

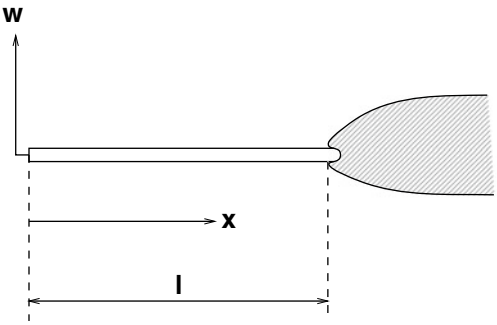

Recall that the analytical solution is (cf. Section 2.2)

$$q_D = \left(\frac{\pi}{2}\right)^2 \frac{GJ}{l}/(lc)e\frac{\partial C_L}{\partial \alpha}$$
$$= 2.46\cdots$$

A comparison of the several approximations is given below. In the two element model the error is about 5%, see Fig. B.4.

Question

5. Consider a thin cantilevered plate of length l and width b which represents the leading edge of a wing at supersonic speeds. See Fig. B.5.

The aerodynamic pressure loading (per unit chord and per unit span) at high speeds is given by (Sect. 3.4 and 4.2)

$$p = \frac{2\rho U^2}{(M^2-1)^{\frac{1}{2}}}\frac{\partial w}{\partial x} \quad \text{Sign convention:} \quad p \text{ down}, \quad w \text{ up}$$

where M is the mach number and w is the transverse deflection (not the downwash!). Compute the divergence speed.
(1) Work out a formal mathematical solution, without numerical evaluation, using classical differential equation methods.
(2) How would you use Galerkin's method with an assumed mode of the form

$$w = a\{2(1 - x/l)^2 - \frac{4}{3}(1 - x/l)^3 + \frac{1}{3}(1 - x/l)^4\}$$

to obtain a numerical answer? What boundary conditions on w does the assumed mode satisfy?

Answer

(1) The governing equilibrium equation is

$$EI\frac{\partial^4 w}{\partial x^4} = -p = -\frac{2\rho U^2}{(M^2 - 1)^{\frac{1}{2}}}\frac{\partial w}{\partial x}$$

Define

$$K \equiv \left[\frac{2\rho U^2}{(M^2 - 1)^{\frac{1}{2}}}\right]\left[\frac{1}{EI}\right]$$

then the equation above becomes

$$\frac{\partial^4 w}{\partial x^4} + K\frac{\partial w}{\partial x} = 0 \tag{B.17}$$

The boundary conditions are:

$$w(l) = \frac{\partial w}{\partial x}(l) = \frac{\partial^2 w}{\partial x^2}(0) = \frac{\partial^3 w}{\partial x^3}(0) = 0 \tag{B.18}$$

The characteristic equation of differential equation (B.17) is

$$\gamma^4 + K\gamma = 0 \tag{B.19}$$

The roots are $\gamma_1 = 0$ and $\gamma_2,\ \gamma_3,\ \gamma_4$ such that $\gamma^3 = -K$. Now

$$(-K)^{\frac{1}{3}} = K^{\frac{1}{3}} e^{i\frac{1}{3}(\pi + 2n\pi)}, \qquad n = 0, 1, 2$$

and defining $K^1 = K^{\frac{1}{3}}$ the roots $\gamma_2,\ \gamma_3,\ \gamma_4$ become

$$\gamma_2 = K^1 e^{i\pi/3} = K^1[\cos\pi/3 + i\sin\pi/3] = K^1\left[\frac{1}{2} + i\frac{\sqrt{3}}{2}\right]$$
$$\gamma_3 = K^1 e^{i\pi} = K^1[\cos\pi + i\sin\pi] = K^1[-1]$$
$$\gamma_4 = K^1 e^{i5\pi/3} = K^1\left[\cos\frac{5\pi}{3} + i\sin\frac{5\pi}{3}\right] = K^1\left[\frac{1}{2} - i\frac{\sqrt{3}}{2}\right]$$

Therefore $w(x)$ has the form:

$$w(x) = b_1 + b_2 e^{-K^1 x} + e^{K^1(x/2)}\left[b_3\cos\left(K^1\frac{\sqrt{3}}{2}x\right) + b_4\sin\left(K^1\frac{\sqrt{3}}{2}x\right)\right]$$

$$w'(x) = -b_2 K^1 e^{-K^1 x} + \frac{K^1}{2}e^{K^1(x/2)}\Big[(b_3+b_4\sqrt{3})\cos\left(K^1\frac{\sqrt{3}}{2}x\right) + (b_4 - b_3\sqrt{3})\sin\left(K^1\frac{\sqrt{3}}{2}x\right)\Big]$$

$$w''(x) = b_2 K^{1^2} e^{-K^1 x} + \left(\frac{K^1}{2}\right)e^{K^1(x/2)}\Big[(2\sqrt{3}b_4 - 2b_3)\cos\left(K^1\frac{\sqrt{3}}{2}x\right) + (2\sqrt{3}b_3 + 2b_4)\sin\left(K^1\frac{\sqrt{3}}{2}x\right)\Big]$$

$$w'''(x) = -b_2 K^{1^3} e^{-K^1 x} - K^{1^3} e^{K^1(x/2)}\left[b_3\cos\left(K^1\frac{\sqrt{3}}{2}x\right) + b_4\sin\left(K^1\frac{\sqrt{3}}{2}x\right)\right] \tag{B.20}$$

Using boundary conditions (B.18), we obtain from (B.20),

$$w(l) = 0 = b_1 + b_2 e^{-K^1 l} + e^{K^1}\frac{1}{2}\left[b_3\cos\left(K^1\frac{\sqrt{3}}{2}l\right) + b_4\sin\left(K^1\frac{\sqrt{3}}{2}l\right)\right]$$

$$\frac{\partial w}{\partial x}(l) = 0 = --b_2 K^1 e^{-K^1 l} + \frac{K^1}{2}e^{K^1}\frac{l}{2}\Big[(b_3 + b_4\sqrt{3})\cos\left(K^1\frac{\sqrt{3}}{2}l\right) + (b_4 - b_3\sqrt{3})\sin\left(K^1\frac{\sqrt{3}}{2}l\right)\Big]$$

$$\frac{\partial^2 w}{\partial x^2}(0) = 0 = b_2 K^{1^2} + \left(\frac{K^1}{2}\right)^2(2\sqrt{3}b_4 - 2b_3)$$

Fig. B.6

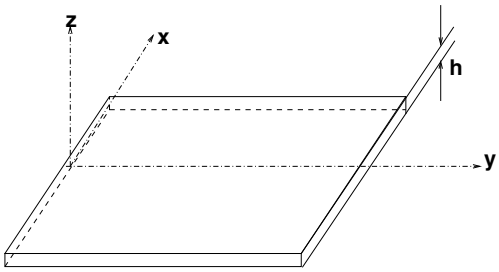

$$\frac{\partial^3 w}{\partial x^3}(0) = 0 = -b_2 K^{1^3} - b_3 K^{1^3} \tag{B.21}$$

The condition for nontrivial solutions is that the determinant of coefficients of the system of linear, algebraic equations given by (B.21) be zero. This leads to

$$e^{-\frac{3}{2}K''} = -2\cos\left(\frac{\sqrt{3}}{2}K''\right) \tag{B.22}$$

where

$$K'' \equiv K^1 l$$

In order to find the solution to equation (B.22), one would plot on the same graph as a function of K'' the right and left sides of this equation and note the points (if any) of intersection. The first intersection for $K'' > 0$ is the one of physical interest. Knowing this particular K'', call it K''_D, one may compute

$$U_D^2 = \frac{K_D''^3 (M^2 - 1)^{\frac{1}{2}} EI}{2\rho l^3}$$

to find the speed U at which divergence occurs (Fig. B.6).
(2) This is left as an exercise for the reader.

Questions

Sweptwing divergence

6. Derive the equations of equilibrium and associated boundary conditions, (2.6.1, 2.6.2, 2.6.11 and 2.6.12) from Hamilton's Principle. Note that Hamilton's Principle is the same as the Principle of Virtual Work for the present static case.

For a constant property sweptwing undergoing bending only, use classical solution techniques to compute the lowest eigenvalue corresponding to divergence. That is from (2.6.10)–(2.6.12), show that $\lambda_d = -6.33$.

- Now use Galerkins method to compute an approximate λ_D. For h, assume that

$$h = a_0 + a_1\tilde{y} + a_2\tilde{y}^2 + a_3\tilde{y}^3 + a_4\tilde{4}$$

From the boundary conditions (2.6.11), (2.6.12) show that

$$\begin{aligned} a_0 &= b_0 = 0 \\ a_3 &= -4a_4 \\ a_2 &= 6a_4 \end{aligned}$$

and thus $h = a_4(\tilde{y}^3 - 4\tilde{y}^3 + 6\tilde{y}^2)$. Using this representation for h, compute λ_D. How does this compare to the exact solution?

- Now consider both bending and torsion for a constant property wing. Assume

$$\alpha = b_0 + b_1\tilde{y}^2 + b_2\tilde{y}^3$$

Determine the possible form of α from the boundary conditions.

Determine λ_D for $GJ/EI = 1$, $\bar{e}/\bar{c} = 0.5$, $l/\bar{c} = 10$. Compare to the earlier result for bending only. Plot your result in terms of $\tilde{\lambda}_D$ vs Λ where $\tilde{\lambda}_D \equiv q(\partial \bar{C}_L/\partial\alpha)(\bar{c}l^3/EI)$.

B.2 For Sect. 3.1

Question

Starting from

$$U = \frac{1}{2}\iiint [\sigma_{xx}\epsilon_{xx} + \sigma_{xy}\epsilon_{xy} + \sigma_{yx}\epsilon_{yx} + \sigma_{yy}\epsilon_{yy}]\, dx\, dy\, dz$$

and

$$\begin{aligned} \epsilon_{xx} &= -z\frac{\partial^2 w}{\partial x^2} \\ \epsilon_{yy} &= -z\frac{\partial^2 w}{\partial y^2} \\ \epsilon_{xy} &= -z\frac{\partial^2 w}{\partial x \partial y} \\ \sigma_{xx} &= \frac{E}{(1-\nu^2)}[\epsilon_{xx} \nu \epsilon_{xy}] \\ \sigma_{yy} &= \frac{E}{(1-\nu^2)}[\epsilon_{yy} \nu \epsilon_{xx}] \\ \sigma_{xy} &= \epsilon_{xy} = \sigma_{yx} \\ w &= w(x, y) \text{ only} \end{aligned}$$

1. Compute $U = U(w)$
2. For $w = -h(y) - a\alpha(y)$, compute $U = U(h, \alpha)$
3. Using a kinetic energy expression

$$T = \frac{1}{2} \iiint \rho \left(\frac{\partial w}{\partial t} \right)^2 dx\, dy\, dz$$

compute $T = T(h, \alpha)$
4. Assume $h(y) = q_h f(y)$

$$\alpha(y) = q_\alpha g(y)$$

where $f,\ g$ are specified.

Determine equations of motion for q_h, q_α using Lagrange's Equations, where the virtual work done by aerodynamic pressure, p, is given by

$$\delta w = \iint p \delta w\, dx\, dy$$

5. Return to 1; now assume

$$w = \sum_m q_m \psi_m(x, y)$$

where ψ_m is specified. Determine equations of motion for q_m.

Answer

1. Potential energy U:

$$U = \frac{1}{2} \iiint (\sigma_{xx}\epsilon_{xx} + \sigma_{xy}\epsilon_{xy} + \sigma_{yx}\epsilon_{yx} + \sigma_{yy}\epsilon_{yy})\, dx\, dy\, dz$$

where

$$\begin{aligned}
\epsilon_{xx} &= -z \frac{\partial^2 w}{\partial x^2} \\
\epsilon_{xy} &= -z \frac{\partial^2 w}{\partial x \partial y} = \epsilon_{yx} \\
\epsilon_{yy} &= -z \frac{\partial^2 w}{\partial y^2} \\
\sigma_{xx} &= \frac{E}{1 - \nu^2} (\epsilon_{xx} \nu \epsilon_{yy}) \\
\sigma_{xy} &= \frac{E}{1 + \nu} \epsilon_{xy} \\
\sigma_{yy} &= \frac{E}{1 - \nu^2} (\epsilon_{yy} \nu \epsilon_{xx})
\end{aligned}$$

Thus

$$\sigma_{xx}\epsilon_{xx} + \sigma_{xy}\epsilon_{xy} + \sigma_{yx}\epsilon_{yx} + \sigma_{yy}\epsilon_{yy}$$

$$= \frac{E}{1-\nu^2}(\epsilon_{xx} + \nu\epsilon_{yy}) \cdot \epsilon_{xx} + 2\frac{E}{1+\nu}\epsilon_{xy}^2 + \frac{E}{1-\nu^2}(\epsilon_{yy} + \nu\epsilon_{xx})\epsilon_{yy}$$

$$= \frac{E}{1-\nu^2}(\epsilon_{xx}^2 + 2\nu\epsilon_{xx} + \epsilon_{yy}^2) + \frac{2E(1-\nu)}{1-\nu^2}\epsilon_{xy}^2$$

$$= \frac{E}{1-\nu^2}\left\{z^2\left(\frac{\partial^2 w}{\partial z^2}\right)^2 + 2\nu \cdot z^2\left(\frac{\partial^2 w}{\partial x^2}\right)\left(\frac{\partial^2 w}{\partial y^2}\right) + z^2\left(\frac{\partial^2 w}{\partial y^2}\right)^2 \right.$$

$$\left. +2(1-\nu)z^2\left(\frac{\partial^2 w}{\partial x \partial y}\right)\right\}$$

$$= \frac{Ez^2}{1-\nu^2}\left\{\left(\frac{\partial^2 w}{\partial x^2}\right) + \left(\frac{\partial^2 w}{\partial y^2}\right)^2 + 2\nu\left(\frac{\partial^2 w}{\partial x^2}\right)\left(\frac{\partial^2 w}{\partial y^2}\right) + 2(1-\nu)\left(\frac{\partial^2 w}{\partial x \partial y}\right)^2\right\}$$

$$U = \frac{1}{2}\iiint \frac{Ez^2}{1-\nu^2}\Big[\left(\frac{\partial^2 w}{\partial x^2}\right)^2 + \left(\frac{\partial^2 w}{\partial y^2}\right)^2 + 2\nu\left(\frac{\partial^2 w}{\partial x^2}\right)\left(\frac{\partial^2 w}{\partial y^2}\right) + 2(1-\nu) \times \left(\frac{\partial^2 w}{\partial x \partial y}\right)^2\Big] dx\, dy\, dz$$

$$= \frac{1}{2}\iint D\left[\left(\frac{\partial^2 w}{\partial x^2}\right)^2 + \left(\frac{\partial^2 w}{\partial y^2}\right)^2 + 2\nu\left(\frac{\partial^2 w}{\partial x^2}\right)\left(\frac{\partial^2 w}{\partial y^2}\right) + 2(1-\nu)\left(\frac{\partial^2 w}{\partial x \partial y}\right)^2\right] dx\, dy \tag{B.23}$$

where

$$D \equiv \frac{E}{1-\nu^2}\int z^2 dz$$

2. For $w = -h(y) - x\alpha(y)$

$$\frac{\partial^2 w}{\partial y^2} = -\frac{\partial^2 h}{\partial y^2} - x\frac{\partial^2 \alpha}{\partial y^2}$$

$$\frac{\partial^2 w}{\partial x \partial y} = -\frac{\partial \alpha}{\partial y}$$

$$\frac{\partial^2 w}{\partial x^2} = 0$$

Hence, from (B.23), we have

$$U = \frac{1}{2}\iint D\Big[\left(\frac{\partial^2 h}{\partial y^2}\right)^2 + 2\left(\frac{\partial^2 h}{\partial y^2}\right)\left(\frac{\partial^2 \alpha}{\partial y^2}\right) \cdot x + \left(\frac{\partial^2 \alpha}{\partial y^2}\right)^2 \cdot x^2 + 2(1-\nu)\left(\frac{\partial \alpha}{\partial y}\right)^2\Big] dx\, dy \tag{B.24}$$

Using the estimates,

$$\frac{\partial \alpha}{\partial y} \sim \frac{\alpha}{l}, \quad x \sim c, \quad \frac{h}{l} \sim \alpha$$

we see the second and third terms can be neglected compared to the first and fourth for $c/l \ll 1$. Thus U becomes

$$U = \frac{1}{2} \int EI \left(\frac{\partial^2 h}{\partial y^2} \right)^2 dy + \frac{1}{2} \int GJ \left(\frac{\partial \alpha}{\partial y} \right)^2 dy$$

where

$$EI = \int D dx, \qquad GJ = \int 2D(1-\nu) dx$$

Note that if $\frac{h}{c} \sim \alpha$ is used as an estimate, then to deduce the final expression for U from (B.24), it is required that $\int Dx dx = 0$ which defines the position of the "elastic axis".

3. For $w = -h(y,t) - \alpha(y,t)x$,

$$T = \frac{1}{2} \iiint \rho \left(\frac{\partial w}{\partial t} \right)^2 dx dy dz$$

$$= \frac{1}{2} \int [m\dot{h}^2 + 2S_\alpha \dot{h}\dot{\alpha} + I_\alpha \dot{\alpha}^2] dy$$

where: $m \equiv \int \rho \, dx dz$; $S_\alpha \equiv \int \rho x \, dx \, dz$; and $I_\alpha \equiv \int \rho x^2 dx dz$.

Recall

$$\delta W = \int -L\delta h dy + \int My\delta\alpha dy$$

Using the above expression for U, T and δW, one can derive the governing partial differential equations for h and α and the associated boundary conditions from Hamilton's principle.

4. Now $w(z, y, t) = q_h(t) \cdot f(y) + q_\alpha(t) g(y) x$ and therefore

$$\frac{\partial w}{\partial t} = \dot{q}_h f(y) + \dot{q}_\alpha g(y) x \qquad \cdot \equiv \frac{d}{dt}$$

$$
\begin{aligned}
T =& \frac{1}{2}\iiint \rho\left(\frac{\partial w}{\partial t}\right)^2 dxdydz \\
=& \frac{1}{2}\iiint \rho(\dot{q}_h f(y) + \dot{q}_\alpha g(y)x)^2 dxdydz \\
=& \iiint \rho\rho(\dot{q}_h^2\{f(y)\}^2 + 2\dot{q}_h\dot{q}_\alpha f(y)g(y)x + \dot{q}_\alpha^2\{g(y)\}^2x^2)dxdydz \\
=& \frac{1}{2}\Big[\dot{q}_h^2\iiint \rho\{f(y)\}^2 dxdydz + 2\dot{q}_h\dot{q}_\alpha\iiint \rho f(y)g(y)x\ dxdydz \\
& \qquad + \dot{q}_\alpha^2\iiint \{g(y)\}^2x^2 dxdydz\Big] \\
=& \frac{1}{2}(\dot{q}_h^2 M_{hh} + 2\dot{q}_h\dot{q}_\alpha M_{h\alpha} + \dot{q}_\alpha^2 M_{\alpha\alpha})
\end{aligned}
\tag{B.25}
$$

where

$$
\begin{aligned}
M_{hh} &\equiv \iiint \rho\{f(y)\}^2 dxdydz \\
M_{h\alpha} &\equiv \iiint \rho f(y)g(y)x\ dxdydz \\
M_{\alpha\alpha} &\equiv \iiint \rho\{g(y)\}^2x^2 dxdydz
\end{aligned}
\tag{B.26}
$$

For $w = q_h(t)f(y) + q_\alpha(t)g(y)x$ the potential energy is given as follows:

$$
\begin{aligned}
&' \equiv \frac{d}{dy} \\
&\left(\frac{\partial^2 h}{\partial y^2}\right) = q_h f''(y),\ \frac{\partial\alpha}{\partial y} = q_\alpha g'(y),\ \frac{\partial^2\alpha}{\partial y^2} = q_\alpha g''(y) \text{ into (II.24)}
\end{aligned}
$$

$$
\begin{aligned}
U =& \frac{1}{2}\iint D[\{q_h f''(y)\}^2 + 2q_h f''(y)q_\alpha g''(y)x + \{q_\alpha g''(y)\}^2x^2 \\
& + 2(1-\nu)\{q_\alpha g'(y)\}^2]dxdy \\
=& \frac{1}{2}\iint D[q_h^2\{f''(y)\}^2 + 2q_h q_\alpha f''(y)g''(y)x + q_\alpha^2[\{g''(y)\}^2y^2 \\
& + 2(1-\nu)\{g'(y)\}62]]dxdy \\
=& \frac{1}{2}\Big[q_h^2\iint D\{f''(y)\}^2 dxdy + 2q_h q_\alpha\iint Df''(y)g''(y)x\ dxdy \\
& + q_\alpha^2\iint D\{g''(y)\}^2x^2 + 2(1-\nu)\{g'(y)\}^2\Big]dxdy \\
=& \frac{1}{2}[q_h^2 K_{hh} + 2q_h q_\alpha K_{h\alpha} + q_\alpha^2 K_{\alpha\alpha}]
\end{aligned}
\tag{B.27}
$$

where

$$
\begin{aligned}
K_{hh} &\equiv \iint D\{f''(y)\}^2 dxdy \\
K_{h\alpha} &\equiv \iint Df''(y)g''(y)x\, dxdy \\
K_{\alpha\alpha} &\equiv \iint D[\{g''(y)\}^2 x^2 + 2(1-\nu)\{g'(y)\}^2] dxdy
\end{aligned}
\tag{B.28}
$$

Virtual work

$$
\delta W = \iint p\delta w\, dxdy
$$

where

$$
\begin{aligned}
\delta w = \delta h + \delta\alpha x &= f(y)\delta q_h + g(y)x\delta q_\alpha \\
\text{Therefore } \delta W &= \iint p(f(y)\delta q_h + g(y)x\delta q_\alpha) dxdy \\
&= \delta q_h \iint pf(y) dxdy + \delta q_\alpha \iint pg(y)x\, dxdy \\
&= Q_h \delta q_h + Q_\alpha \delta q_\alpha
\end{aligned}
$$

where

$$
\begin{aligned}
Q_h &\equiv \iint pf(y) dxdy \\
Q_\alpha &\equiv \iint pg(y) \cdot x\, dxdy
\end{aligned}
\tag{B.29}
$$

The Lagrangian, $L \equiv T - U$, may be written

$$
= \frac{1}{2}(\dot{q}_h^2 M_{hh} + 2\dot{q}_h\dot{q}_\alpha M_{h\alpha} + \dot{q}_\alpha^2 M_{\alpha\alpha})
$$

$$
-\frac{1}{2}(q_h^2 K_{hh} + 2q_h q_\alpha K_{h\alpha} + q_\alpha^2 K_{\alpha\alpha})
$$

$$
\frac{\partial L}{\partial \dot{q}_h} = \dot{q}_h M_{hh} + \dot{q}_\alpha M_{h\alpha}, \frac{\partial L}{\partial q_h} = -q_h \cdot K_{hh} - q_\alpha K_{h\alpha}
$$

Therefore

$$
\frac{\partial L}{\partial \dot{q}_\alpha} = \dot{q}_h M_{h\alpha} + \dot{q}_\alpha M_{\alpha\alpha}, \frac{\partial L}{\partial q_\alpha} = -q_h K_{h\alpha} - q_\alpha K_{\alpha\alpha}
$$

Then Lagrange's equations of motion are

$$\begin{aligned}\frac{d}{dt}\left(\frac{\partial L}{\partial \dot{q}_h}\right)-\frac{\partial L}{\partial q_h}&=Q_h \rightarrow M_{hh}\ddot{q}_h+M_{h\alpha}\ddot{q}_\alpha+K_{hh}q_h+K_{h\alpha}\cdot q_\alpha=Q_h\\ \frac{d}{dt}\left(\frac{\partial L}{\partial \dot{q}_\alpha}\right)-\frac{\partial L}{\partial q_\alpha}&=Q_\alpha \rightarrow M_{h\alpha}\ddot{q}_h+M_{\alpha\alpha}\ddot{q}_\alpha+K_{h\alpha}q_h+K_{\alpha\alpha}q_\alpha=Q_\alpha\end{aligned} \tag{B.30}$$

where M_{hh}, $M_{h\alpha}$, $M_{\alpha\alpha}$, K_{hh}, $K_{h\alpha}$, $K_{\alpha\alpha}$, Q_h and Q_α are given in (B.26), (B.28) and (B.29).

5. When

$$w(x,y,t)=\sum_m q_m(t)\psi_m(x,y)$$

$$\begin{aligned}\frac{\partial^2 w}{\partial x^2}&=\sum_m q_m\frac{\partial^2\psi_m}{\partial x^2}\\ \frac{\partial^2 w}{\partial y^2}&=\sum_m q_m\frac{\partial^2\psi_m}{\partial y^2}\\ \frac{\partial^2 w}{\partial x\partial y}&=\sum_m q_m\frac{\partial^2\psi_m}{\partial x\partial y}\end{aligned}$$

$$\begin{aligned}\left(\frac{\partial^2 w^2}{\partial x^2}\right)&=\sum_m\sum_n q_m q_n\frac{\partial^2\psi_m}{\partial x^2}\frac{\partial^2\psi_n}{\partial x^2}\\ \left(\frac{\partial^2 w^2}{\partial y^2}\right)&=\sum_m\sum_n q_m q_n\frac{\partial^2\psi_m}{\partial y^2}\frac{\partial^2\psi_n}{\partial y^2}\\ \left(\frac{\partial^2 w^2}{\partial x^2}\right)\left(\frac{\partial^2 w}{\partial y^2}\right)&=\sum_m\sum_n q_m q_n\frac{\partial^2\psi_m}{\partial x^2}\frac{\partial^2\psi_n}{\partial y^2}\\ \left(\frac{\partial^2 w^2}{\partial x\partial y}\right)&=\sum_m\sum_n q_m q_n\frac{\partial^2\psi_m}{\partial x^\partial y}\frac{\partial^2\psi_n}{\partial x\partial y}\end{aligned}$$

Then from (B.23) the potential energy is

$$
\begin{aligned}
U =& \frac{1}{2}\iint D\Big[\sum_m\sum_n q_m q_n \frac{\partial^2\psi_m}{\partial x^2}\frac{\partial^2\psi_n}{\partial x^2} + \sum_m\sum_n q_m q_n \frac{\partial^2\psi_m}{\partial y^2}\frac{\partial^2\psi_n}{\partial y^2} \\
&+2\nu\sum_m\sum_n q_m q_n \frac{\partial^2\psi_m}{\partial x^2}\frac{\partial^2\psi_n}{\partial y^2} + 2(1-\nu)\sum_m\sum_n q_m q_n \frac{\partial^2\psi_m}{\partial x\partial y}\frac{\partial^2\psi_n}{\partial x\partial y}\Big]dxdy \\
=& \frac{1}{2}\sum_m\sum_n q_m q_n \iint D\Big[\frac{\partial^2\psi_m}{\partial x^2}\frac{\partial^2\psi_n}{\partial x^2} + \frac{\partial^2\psi_m}{\partial y^2}\frac{\partial^2\psi_n}{\partial y^2} + 2\nu\frac{\partial^2\psi_m}{\partial x^2}\frac{\partial^2\psi_n}{\partial y^2} \\
&+2(1-\nu)\frac{\partial^2\psi_m}{\partial x\partial y}\frac{\partial^2\psi_n}{\partial x\partial y}\Big]dxdy \\
=& \frac{1}{2}\sum_m\sum_n q_m q_n \cdot K_{mn}
\end{aligned}
\tag{B.31}
$$

where

$$
\begin{aligned}
K_{mn} \equiv \iint D\Big[&\frac{\partial^2\psi_m}{\partial x^2}\frac{\partial^2\psi_n}{\partial x^2} + \frac{\partial^2\psi_m}{\partial y^2}\frac{\partial^2\psi_n}{\partial y^2} + 2\nu\frac{\partial^2\psi_m}{\partial x^2}\frac{\partial^2\psi_n}{\partial y^2} \\
&+ 2(1-\nu)\frac{\partial^2\psi_m}{\partial x\partial y}\frac{\partial^2\psi_n}{\partial x\partial y}\Big]dxdy
\end{aligned}
$$

Note $K_{mn} \neq K_{nm}$!

Kinetic energy

$$
\frac{\partial w}{\partial t} = \sum_m \dot{q}_m \psi_m(x, y)
$$

$$
\text{therefore} \quad \left(\frac{\partial w}{\partial t}\right)^2 = \sum_m\sum_n \dot{q}_m\dot{q}_n\psi_m\psi_n
$$

$$
\begin{aligned}
T &= \frac{1}{2}\iiint \rho\left(\sum_m\sum_n \dot{q}_m\dot{q}_n\psi_m\psi_n\right)dxdydz \\
&= \frac{1}{2}\sum_m\sum_n \dot{q}_m\dot{q}_n \iiint \rho\psi_m\psi_n\, dxdxdz \\
&= \frac{1}{2}\sum_m\sum_n \dot{q}_m\dot{q}_n M_{mn}
\end{aligned}
\tag{B.32}
$$

where

$$
M_{mn} \equiv \iiint \rho\psi_m\psi_n\, dxdydz
$$

Virtual work

$$\begin{aligned}\delta W &= \iint p w \, dx dy \\ &= \iint p \left(\sum_m \delta q_m \psi_m \right) dx dy \\ \delta W &= \sum_m \delta q_m \iint p \psi_m dx dy \\ &= \sum_m Q_m \delta q_m\end{aligned} \tag{B.33}$$

where

$$Q_m \equiv \iint p \psi_m dx dy$$

Lagrangian:

$$\begin{aligned}L &= T - U = \frac{1}{2} \sum_m \sum_n \dot{q}_m \dot{q}_n M_{mn} - \frac{1}{2} \sum_m \sum_n q_m q_n K_{mn} \\ \frac{\partial L}{\partial \dot{q}_j} &= \frac{1}{2} \sum_n \dot{q}_n M_{jn} + \frac{1}{2} \sum_m \dot{q}_m M_{mj} = \frac{1}{2} \sum_m \dot{q}_m (M_{jm} + M_{mj}) \\ &= \sum_m \dot{q}_m M_{mj} \qquad (M_{mj} = M_{jm}) \\ \frac{\partial L}{\partial q_j} &= -\frac{1}{2} \left(\sum_n q_n K_{jn} + \sum_m q_m K_{mj} \right) = -\frac{1}{2} \sum_m (K_{mj} + K_{jm})\end{aligned}$$

Lagrange's equations of motion

$$\frac{d}{dt} \left(\frac{\partial L}{\partial \dot{q}_j} \right) - \frac{\partial L}{\partial q_j} = \sum_m \ddot{q}_m M_{mj} + \frac{1}{2} \sum_m q_m (K_{mj} + K_{jm}) = Q_j \quad (j = 1, 2 \ldots) \tag{B.34}$$

Note: $K_{mj} + K_{jm} = K_{jm} + K_{mj}$, i.e., coefficient symmetry is preserved in final equations.

B.3 For Sect. 3.3

Question.

Use the vertical translation of and angular rotation about the center of mass of the typical section, see Fig. B.7, as generalized coordinates.

Fig. B.7

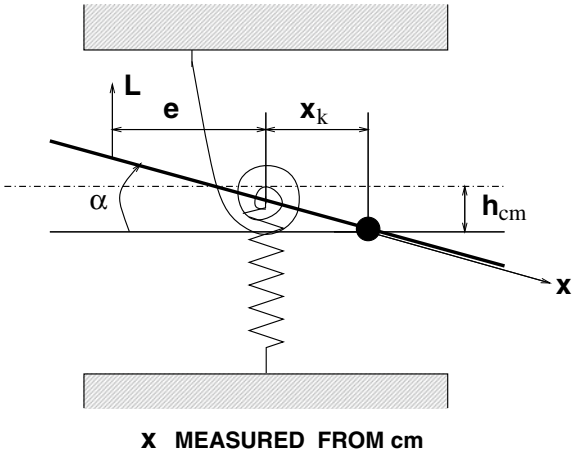

a. Derive the equations of motion.
b. Determine the flutter dynamic pressure and show that it is the same as discussed in text. Use steady or quasi-steady aerodynamic theory.

Answer

$$T = \frac{m}{2}\dot{h}_{cm}^2 + \frac{I_{cm}}{2}\dot{\alpha}^2$$
$$U = \frac{1}{2}K_h(h_{cm} - \alpha x_k)^2 + \frac{1}{2}K_\alpha \alpha^2$$
$$\delta W = \int p\delta w\, dx \qquad \text{where} \qquad w = -h_{cm} - x\alpha$$

is the vertical displacement of a point on airfoil. Thus

$$\begin{aligned}\delta W &= \int p(-\delta h_{cm} - x\delta\alpha)dx \\ &= \delta h_{cm}\left(-\int p dx\right) + \delta\alpha\left(-\int pxdx\right) \\ &= \delta h_{cm}(-L) + \delta\alpha(M_y)\end{aligned}$$

where M_y is the moment about c.m and

$$
\begin{aligned}
{}^{M}Q_{h_{cm}} &= -L \equiv -\int pdx \\
{}^{M}\quad Q_{\alpha} &= M_y \equiv -\int pxdx \\
T - U &= \frac{m}{2}\dot{h}_{cm}^2 + \frac{I_{cm}}{2}\dot{\alpha}^2 - \frac{K_h}{2}(h_{cm} - \alpha x_k)^2 - \frac{K_\alpha}{2}\alpha^2
\end{aligned}
$$

From Lagrange's equations,

$$
\begin{aligned}
&-m\ddot{h}_{cm} - K_h(h_{cm} - \alpha x_K) - \int pdx = 0 \\
&-I_{cm}\ddot{\alpha} + K_h x_K(h_{cm} - \alpha x_K) - K_\alpha \alpha - \int pxdx = 0
\end{aligned}
\tag{B.35}
$$

Substituting

$$
\int pdx = qS\frac{\partial C_L}{\partial \alpha}, \qquad \int pxdx = -qS(e + x_k)\frac{\partial C_L}{\partial \alpha}\alpha, \qquad h = \bar{h}e^{pt}
$$

and $\alpha = \bar{\alpha}e^{pt}$ into the above equations, we obtain

$$
\begin{bmatrix} (mp^2 + K_h) & -K_h x_k + qS\frac{\partial C_L}{\partial \alpha} \\ -K_h x_K & I_{cm}p^2 + K_h x_k^2 + K_\alpha - qS\left(e + x_k\frac{\partial C_L}{\partial \alpha}\right) \end{bmatrix} \begin{Bmatrix} \bar{h}e^{pt} \\ \bar{\alpha}e^{pt} \end{Bmatrix} = \begin{Bmatrix} 0 \\ 0 \end{Bmatrix}
$$

The condition that the determinant of the coefficient matrix is zero gives

$$
Ap^4 + Bp^2 + C = 0 \tag{B.36}
$$

where

$$
\begin{aligned}
A &= mI_{cm} = mI_\alpha - S_\alpha^2 \qquad (I_{cm} = I_\alpha - mx_k^2, \quad S_\alpha = mx_k) \\
B &= m\left[K_h x_k^2 + K_\alpha - qS(e + x_k)\frac{\partial C_L}{\partial \alpha}\right] + K_h I_{cm} \\
&= m\left[K_\alpha - qSc\frac{\partial C_L}{\partial \alpha}\right] + K_h\alpha - S_\alpha qS\frac{\partial C_L}{\partial \alpha} \\
C &= K_h\left[\cancel{K_h x_k^2 + K_\alpha} - qS(\cancel{e + x_k})\frac{\partial C_L}{\partial \alpha}\right] + K_h x_k\left(\cancel{-K_h x_k} + \cancel{qS\frac{\partial C_L}{\partial \alpha}}\right) \\
&= K_h\left[K_\alpha - qSe\frac{\partial C_L}{\partial \alpha}\right]
\end{aligned}
$$

These A, B, and C are the same as in equation (3.3.51), Sect. 3.3, in the text. Thus we have the same flutter boundary.

$$p^2 = \frac{-B + [B^2 - 4AC]^{\frac{1}{2}}}{2A}$$

(a) $B > 0$ ($A > 0,\ C > 0 \leftarrow$ divergence free.) If p^2 is complex (not real), then instability occurs.

Therefore $B^2 - 4AC = 0$ gives the flutter boundary, i.e.,

$$Dq_F^2 + Eq_F + F = 0$$

or

$$q_f = \frac{-E \pm [E^2 - 4DF]}{2D}$$

where

$$D \equiv \left\{(me + S_\alpha)S\frac{\partial C_L}{\partial \alpha}\right\}^2$$

$$E \equiv \left\{-2(me + S_\alpha)[mK_\alpha + K_h I_\alpha] + 4[mI_\alpha - S_\alpha^2]eKS\frac{\partial C_L}{\partial \alpha}\right\}$$

$$F \equiv [mK_\alpha + K_h I_\alpha]^2 - 4[mI_\alpha - S_\alpha^2]K_h K_\alpha$$

The smaller, real, and positive q_f is the flutter dynamic pressure.
(b) $B < 0$. Note that $B = 2\sqrt{AC}$ before $B = 0$ as q increases. Hence flutter always occurs for $B > 0$.

Question

Prove that
1.

$$\phi_{hF}(\tau) = \phi_{Fh}(-\tau)$$

and
2.

$$\Phi_{hF}(\omega) = H_{hF}(-\omega)\Phi_{FF}(\omega)$$

This is a useful exercise to confirm one's facility with the concepts of correlation function and power spectral density.

Answer

1. Prove that $\phi_{hF}(\tau) = \phi_{Fh}(-\tau)$. We start with the definition of the cross-correlation function[2]:

$$\phi_{hF}(\tau) = \lim_{T\to\infty} \frac{1}{2T} \int_{-T}^{+T} h(t)F(t+\tau)dt \tag{B.37}$$

The response $h(t)$ is given by

$$h(t) = \int_0^t I_{hF}(t-\tau_1)F(\tau_1)d\tau_1 \tag{B.38}$$

Here we have taken $h(t)$ in dimensional form and $I_{hF}(t)$ represents the response to an impulse. Substituting (B.38) into (B.37),

$$\phi_{hF}(\tau) = \lim_{T\to\infty} \frac{1}{2T} \int_{-T}^{+T} \int_{-\infty}^{+\infty} I_{hF}(t-\tau_1)F(\tau_1)F(t+\tau)d\tau_1 dt$$

(One may change the limit $(0, t)$ in the inner integral to $(-\infty, +\infty)$ since the impulse will be zero for $(t-\tau_1) < 0$.) Let $t' \equiv t - \tau_1 \Rightarrow \tau_1 = t - t'$ and interchange the order of integration. Then $d\tau_1 = -dt'$ and

$$\begin{aligned}\phi_{hF}(\tau) &= -\int_{+\infty}^{-\infty} I_{hF}(t') \lim_{T\to\infty} \frac{1}{2T} \int_{-T}^{+T} F(t-t')F(t+\tau)dtdt' \\ &= -\int_{+\infty}^{-\infty} I_{hF}(t')\phi_{FF}(\tau+t')dt'\end{aligned}$$

Thus

$$\phi_{hF}(\tau) = +\int_{-\infty}^{+\infty} I_{hF}(\lambda)\phi_{FF}(\tau+\lambda)d\lambda \tag{B.39}$$

where $\lambda \equiv t' =$ dummy variable.

We follow the same procedure for $\phi_{Fh}(\tau)$.

$$\begin{aligned}\phi_{Fh}(\tau) &= \lim_{T\to\infty} \frac{1}{2T} \int_{-T}^{+T} F(t)h(t+\tau)dt \\ &= \lim_{T\to\infty} \frac{1}{2T} \int_{-T}^{+T} F(t) \left\{ \int_{-\infty}^{+\infty} I_{hF}(t+\tau-t_2)F(t_2)dt_2 \right\} dt\end{aligned}$$

let $t'' = t + \tau - \tau_2$. $\Rightarrow dt'' = -d\tau_2$, $\tau_2 = \tau + t - t''$

[2] A short proof goes as follows. Define $\eta \equiv t - \tau$. Then $d\eta = dt$ and $t = \eta - \tau$; using these and (B.37) the proof follows by inspection.

$$\begin{aligned}\phi_{Fh}(\tau) &= -\int_{+\infty}^{-\infty} I_{hF}(t'')\left\{\lim_{T\to\infty}\frac{1}{2T}\int_{-T}^{+T} F(t-t''+\tau)F(t)dt\right\}dt'' \\ &= -\int_{+\infty}^{-\infty} I_{hF}(t'')\phi_{FF}(\tau-t'')dt'' \\ &= -\int_{-\infty}^{+\infty} I_{hF}(\lambda)\phi_{FF}(\tau-\lambda)d\lambda\end{aligned}$$

Let $\tau \to -\tau$:

$$\phi_{Fh}(-\tau) = +\int_{-\infty}^{+\infty} I_{hF}(\lambda)\phi_{FF}(-\tau-\lambda)d\lambda$$

but $\phi_{FF}(\tau) = \phi_{FF}(-\tau)$ and hence

$$\phi_{Fh}(-\tau) = +\int_{-\infty}^{+\infty} I_{hF}(\lambda)\phi_{FF}(+\tau+\lambda)d\lambda \tag{B.40}$$

Comparing (B.39) and (B.40) we see that

$$\phi_{hF}(\tau) = \phi_{Fh}(-\tau)$$

2. Prove that $\Phi_{hF}(\omega) = H_{hF}(-\omega)\Phi_{FF}$. By definition, the spectral density function is the Fourier transform of the correlation function.
Transforming the cross correlation function defined by (B.39).

$$\begin{aligned}\Phi_{hF}(\omega) &\equiv \frac{1}{\pi}\int_{-\infty}^{+\infty}\phi_{hF}(\tau)e^{-i\omega\tau}d\tau \\ \Phi_{hF}(\omega) &= \frac{1}{\pi}\int_{-\infty}^{+\infty}\int_{-\infty}^{+\infty} I_{hF}(t)\phi_{FF}(\tau+t)e^{i\omega\tau}dtd\tau \\ &= \frac{1}{\pi}\int_{-\infty}^{+\infty}\int_{-\infty}^{+\infty} I_{hF}(t)e^{+i\omega\tau}\phi_{FF}(\tau+t)e^{-i\omega\tau-i\omega t}dtd\tau \\ &= \int_{-\infty}^{+\infty} I_{hF}(t)\left\{\frac{1}{\pi}\int_{-\infty}^{+\infty}\phi_{FF}(\tau+t)e^{-i\omega(\tau+t)}d\tau\right\}e^{+i\omega t}dt\end{aligned}$$

By definition

$$\frac{1}{\pi}\int_{-\infty}^{+\infty}\phi_{FF}(\tau')e^{-i\omega\tau'}d\tau' = \Phi_{FF}(\omega)$$

Let $\tau' \equiv \tau + t$, and substitute in RHS of equation for Φ_{hF}. Then

$$\Phi_{hF}(\omega) = \int_{-\infty}^{+\infty} I_{hF}(t)e^{+i\omega t}\Phi_{FF}(\omega)dt$$

Now, since

$$H_{hF}(\omega) = \int_{-\infty}^{+\infty} I_{hF}(t) e^{-i\omega t} dt \quad \text{it follows that}$$
$$\Phi_{hF}(\omega) = H_{hF}(-\omega)\Phi_{FF}(\omega)$$

B.4 For Sect. 3.6

Typical section flutter analysis using piston theory aerodynamics

Pressure: $p = \rho a \left[\frac{\partial z_a}{\partial t} + \frac{\partial z_a}{\partial x}\right]$
Motion: $z_a = -h - \alpha(x - x_{EA})$[3]
Upper surface: $p_U = \rho a \left[-\dot{h} - \dot{\alpha}(x - x_{EA}) - U_\alpha\right]$
Lower surface: $p_L = -\rho a \left[-\dot{h} - \dot{\alpha}(x - x_{EA}) - U\alpha\right]$
Net pressure: $p_L - p_U = \frac{4\rho U^2}{2M}\left[\frac{\dot{h}}{U} + \frac{\dot{\alpha}}{U}(x - x_{EA}) + \alpha\right]$
Lift: $L \equiv \int_0^{2b}(p_L - p_U)dx = \frac{4\rho U^2}{2M}\left\{\left[\frac{\dot{h}}{U} - \frac{\dot{\alpha} x_{EA}}{U} + \alpha\right]2b + \frac{\dot{\alpha}}{U}\frac{(2b)^2}{2}\right\}$
Moment: $M_y = -\int_0^{2b}(p_L - p_U)(x - x_{EA})dx = x_{EA}L - \frac{4\rho U^2}{2M}\left[\frac{\dot{h}}{U} - \dot{\alpha}\frac{x_{EA}}{U} + \alpha\right]\frac{(2b)^2}{2}$

$$- \frac{4\rho U^2}{2M}\frac{\dot{\alpha}}{U}\frac{(2b)^2}{3} \tag{B.41}$$

Assume simple harmonic motion,

$$\begin{aligned}
h &= \bar{h} e^{i\omega t} \\
\alpha &= \bar{\alpha} e^{1\omega t} \\
L &= \bar{L} e^{i\omega t} \\
M_y &= \bar{M}_y e^{1\omega t} \\
\bar{L} &= \frac{4\rho U^2}{2M}\left\{\frac{i\omega}{U} 2b\bar{h}\right. \\
&\quad \left. + \left[\frac{-i\omega x_{EA}}{U} + 1 + \frac{i\omega}{U}\frac{(2b)}{2}\right]2b\bar{\alpha}\right\} \\
&\equiv 2\rho b^2\omega^2(2b)\left\{(L_1 + iL_2)\frac{\bar{h}}{b} + [L_3 + iL_4]\bar{\alpha}\right\}
\end{aligned}$$

Thus from Eq. (3.6.3) in Sect. 3.6,

$$L_1 + iL_2 = \frac{\frac{2\rho U^2}{M}\frac{i\omega\rho 2b}{U}}{2\rho b^2\omega^2(2b)\frac{1}{b}} = \frac{i}{M}\frac{U}{\omega b} \tag{B.42}$$

[3] x is measured from airfoil leading edge: b is half-chord of airfoil.

and

$$\begin{aligned} L_3 + iL_4 &= \frac{\frac{2\rho U^2}{M}\left[\frac{-i\omega x_{EA}}{U} + 1 + \frac{i\omega(2b)}{U^2}\right]2b}{2\rho b^2\omega^2(2b)} \\ &= \frac{1}{M}\left(\frac{U}{b\omega}\right)^2\left[\frac{-i\omega b}{U}\frac{x_{EA}}{b} + 1 + \frac{i\omega b}{U}\right] \end{aligned} \tag{B.43}$$

Questions

(1) Derive a similar equation for

$$M_1 + iM_2 \quad \text{and} \quad M_3 + iM_4$$

(2) Fix $\frac{\omega_h}{\omega_\alpha} = 0.5,\ r_\alpha = 0.5,\ x_\alpha = 0.05$

$$\frac{x_{ea}}{b} = 1.4,\ M = 2$$

Choose several k, say $k = 0.1,\ 0.2,\ 0.5$, and solve for

$$\left(\frac{\omega}{\omega_\alpha}\right)^2 \quad \text{and} \quad \frac{m}{2\rho_\infty bS} \equiv \mu \qquad (S \equiv 2b)$$

from (3.6.4) using the method described on pp. 107 and 108. Plot k verses μ and ω/ω_αvs μ.

Finally plot $\frac{U}{b\omega_\alpha} \equiv \frac{\omega/\omega_\alpha}{k}$ vs μ. This is the flutter velocity as a function of mass ratio.

Answers

Recall Eq. (3.6.3) and again from Sect. 3.6,

$$\bar{M}_y = -2\rho b^3\omega^2(2b)\left\{[M_1 + iM_2]\frac{\bar{h}}{b} + [M_3 + iM_4]\bar{\alpha}\right\}$$

Comparing the above and (B.41), one can identify

$$\begin{aligned} M_1 + iM_2 &= \frac{iU}{Mb\omega}\left[1 - \frac{x_{ea}}{b}\right] \\ M_3 + iM_4 &= \frac{1}{M}\left(\frac{U}{b\omega}\right)^2\left[-\frac{x_{ea}}{b}\right] + i\frac{1}{M}\frac{U}{b\omega}\left\{\left[1 - \frac{x_{ea}}{b}\right]^2 + \frac{1}{3}\right\} \end{aligned} \tag{B.44}$$

Recall the method described in Sect. 3.6 for determining the flutter boundary.

1. Evaluate real and imaginary parts of equation (3.6.4) and set each individually to zero.
2. Solve for $(\omega_\alpha/\omega)^2$ in terms of the mass ratio,μ, from the imaginary part of the equation.
3. Substituting this result into the real part of the equation, obtain a quadratic in μ. Solve for possible values of μ for various k. To be physically meaningful, μ must be positive and real.
4. Return to 2. To evaluate ω/ω_α
5. Finally determine $\frac{U}{b\omega_\alpha} = \frac{U}{b\omega}\frac{\omega}{\omega_\alpha} = \frac{1}{k}\frac{\omega}{\omega_\alpha}$.
In detail these steps are given below.

1. *Real part*

$$\begin{aligned}&\mu^2\left\{\left[1-\left(\frac{\omega_\alpha}{\omega}\right)^2\left(\frac{\omega_h}{\omega_\alpha}\right)^2\right]r_\alpha^2\left[1-\left(\frac{\omega_\alpha}{\omega}\right)^2\right]-x_\alpha^2\right\}\\&+\mu\left\{\frac{-1}{k^2M}\left(1-\frac{x_{ea}}{b}\right)\left[1-\left(\frac{\omega_\alpha}{\omega}\right)^2\left(\frac{\omega_h}{\omega_\alpha}\right)^2\right]+\frac{x_\alpha}{k^2M}\right\}-\frac{1}{3k^2M^2}=0\end{aligned}\tag{B.45}$$

Imaginary part

$$\begin{aligned}&\mu r_\alpha^2\left[1-\left(\frac{\omega_\alpha}{\omega}\right)^2\right]-\frac{1}{k^2M}\left(1-\frac{x_{ea}}{b}\right)\\&+\left[\left(1-\frac{x_{ea}}{b}\right)^2+\frac{1}{3}\right]\left[1-\left(\frac{\omega_\alpha}{\omega}\right)^2\left(\frac{\omega_h}{\omega_\alpha}\right)^2\right]\mu\\&-\left[1-\frac{x_{ea}}{b}\right]\mu x_\alpha-\left[1-\frac{x_{ea}}{b}\right]\left[\mu x_\alpha-\frac{1}{k^2M}\right]=0\end{aligned}\tag{B.46}$$

2. Solving for $(\omega_\alpha/\omega)^2$ from (B.46),

$$\left(\frac{\omega_\alpha}{\omega}\right)^2=\frac{r_\alpha^2+\left(1-\frac{x_{ea}}{b}\right)^2+\frac{1}{3}-2x_\alpha\left(1-\frac{x_{ea}}{b}\right)}{r_\alpha^2+\left(\frac{\omega_h}{\omega_\alpha}\right)^2\left[\left(1-\frac{x_{ea}}{b}\right)^2+\frac{1}{3}\right]}\tag{B.47}$$

Note (B.47) is independent of μ and k; this is a consequence of using piston theory aerodynamics and would not be true, in general, for a more elaborate (and hopefully more accurate) aerodynamic theory.

Substituting the various numerical parameters previously specified into (B.47) gives

$$\left(\frac{\omega_\alpha}{\omega}\right)^2=2.099\quad\text{or}\quad\frac{\omega}{\omega_\alpha}=0.69\tag{B.48}$$

3. Using (B.48) in (B.45) along with the other numerical parameters gives

$$-0.133\mu^2 + \frac{0.121}{k^2}\mu - \frac{1}{12k^2} = 0 \tag{B.49}$$

Solving for μ,

$$\mu_{1,2} = \frac{0.45}{k^2} \pm \frac{1}{k}\left[\frac{0.21}{k^2} - 0.63\right]^{\frac{1}{2}} \tag{B.50}$$

Note that there is a maximum values of k possible, $k_{MAX} = [0.21/0.63]^{\frac{1}{2}}$. Larger k gives complex μ which are physically meaningless. Also note that $\mu \to 0.67,\ \infty$ as $k \to 0$.
4. ω/ω_α is evaluated in (B.48) and for these simple aerodynamics does not vary with μ or k.
5. From (B.48) and a knowledge of k, $U/b\omega_\alpha$ is known.

The above results are tabulated below.

k	μ_1	μ_2	$U/b\omega_\alpha$
0.0	0.67	∞	∞
0.1	0.69	89.6	6.9
0.2	0.72	22	3.45
0.3	0.75	9.28	2.3
0.4	0.81	4.3	1.73
0.5	0.937	2.66	1.38
0.57	1.39	1.39	1.21

From the above table (as well as Eq. (B.50)) one sees that for $4\mu < 0.67$, no flutter is possible. This is similar to the flutter behavior of the typical section at incompressible speeds. At these low speeds mass ratios of this magnitude may occur in hydrofoil applications. Although no such applications exist at high supersonic speeds, it is of interest at least from a fundamental point of view that this somewhat surprising behavior at small μ occurs there as well.

B.5 For Sect. 4.1

Question

1. Starting from Bermoulli's equation, show that

$$\frac{\hat{a}}{a_\infty} \sim M_\infty^2 \frac{\hat{u}}{U_\infty}$$

2. Previously we had shown that the boundary condition on a moving body is (within a linear approximation)

$$\frac{\partial \hat{\phi}}{\partial z}\Big|_{z=0} = \frac{\partial z_a}{\partial t} + U_\infty \frac{\partial z_a}{\partial x}$$

What is the corresponding boundary condition in terms of $\hat{p}$?

3. Derive approximate formulae for the perturbation pressure over a two-dimensional airfoil at supersonic speeds for very low and very high frequencies.

Answer

1. Bernoulli's equation is

$$\frac{\partial \phi}{\partial t} + \frac{\nabla\phi \cdot \nabla\phi}{2} + \int_{p_\infty}^{p} \frac{dp_1}{\rho^1(p^1)} = \frac{U_\infty^2}{2}$$

Since

$$a^2 \equiv \frac{\partial p}{\partial \rho} \quad \text{and} \quad \frac{p}{\rho^\gamma} = \text{ constant}$$

we may evaluate integral in the above to obtain

$$\frac{U_\infty^2}{2}\frac{\partial \phi}{\partial t} + \frac{u^2}{2} = \frac{a^2 - a_\infty^2}{\gamma - 1}, \qquad u \equiv |\nabla\phi|$$

Assume

$$\begin{aligned} a &= a_\infty + \hat{a} \\ u &= U_\infty + \hat{u} \\ \phi &= U_\infty x + \hat{\phi} \end{aligned}$$

where $\hat{a} \ll a_\infty$, etc. To first order

$$-M_\infty^2 \frac{\hat{u}}{U_\infty} - \frac{1}{a_\infty^2}\frac{\partial \hat{\phi}}{\partial t} = \frac{2}{\gamma - 1}\frac{\hat{a}}{a_\infty} + \text{ terms } (\hat{a}^2, \text{ etc.})$$

This means that $M_\infty^2(\hat{u}/U_\infty)$ and $\hat{a}/a_\infty$ are quantities of the same order, at least for steady flow where $\partial\hat{\phi}/\partial t \equiv 0$.

2.

$$\frac{\partial \hat{\phi}}{\partial z}\Big|_{z=0} = Dz_a; \qquad D \equiv \frac{\partial}{\partial t} + U_\infty \frac{\partial}{\partial x} \tag{B.51}$$

By the linearized momentum equation

$$-\frac{\partial \hat{p}}{\partial x} = \rho_\infty D\hat{u}$$

but

$$\hat{u} = \frac{\partial \hat{\phi}}{\partial x}$$

$$\text{therefore} \quad \hat{p} = -\rho_\infty D\hat{\phi}$$

$$\text{therefore} \quad -\frac{\partial \hat{p}}{\partial z} = \rho_\infty \frac{\partial}{\partial z}(D\hat{\phi})$$

$$= \rho_\infty \frac{\partial}{\partial z}(D(\hat{\phi})) = \rho_\infty D\left(\frac{\partial}{\partial z}\hat{\phi}\right)$$

From (B.51) and the above

$$-\frac{\partial \hat{p}}{\partial z}\Big|_{z=0} = \rho_\infty D^2 z_a$$

$$\frac{\partial p}{\partial z} = -\rho_\infty D^2 z_a \quad \text{at} \quad z = 0 \tag{B.52}$$

3.

$$\nabla^2\phi - \frac{1}{a_\infty^2}\left[\frac{\partial}{\partial t} + U_\infty \frac{\partial}{\partial x}\right]^2 \phi = 0$$

where

$$\frac{\partial \phi}{\partial z}\Big|_{z=0} = \frac{\partial}{\partial t} z_a + U_\infty \frac{\partial}{\partial x} z_a \equiv w$$

off wing

$$\frac{\partial \phi}{\partial z}\Big|_{z=0} = 0 \qquad \text{thickness case}$$

This does not matter here, because there are no disturbances ahead of wing in supersonic flow.

$$\phi\Big|_{z=0} = 0 \qquad \text{lifting case,}$$

For a two dimensional solution, let $\phi(x, z, t) = \bar{\phi}(x, z)e^{i\omega t}$ and $w = \bar{w}e^{i\omega t}$. Thus

$$\frac{\partial^2 \bar{\phi}}{\partial x^2} + \frac{\partial^2 \bar{\phi}}{\partial z^2} - \frac{1}{a_\infty^2}\left[-\omega^2 \bar{\phi} + 2i\omega U_\infty \frac{\partial \bar{\phi}}{\partial x} + U_\infty^2 \frac{\partial^2 \bar{\phi}}{\partial x^2}\right] = 0$$

Recall $u, v, w = 0$ for $x \leq 0$ (leading edge) in supersonic flow. Taking a Laplace transform (quiescent condition at $x = 0$)

$$\Phi \equiv \int_0^\infty \bar{\phi} e^{-px} dx$$

then

$$p^2\Phi + \frac{\partial^2\Phi}{\partial z^2} - \frac{1}{a_\infty^2}[-\omega^2\Phi + 2i\omega pU_\infty\Phi + p^2U_\infty^2\Phi]$$

or

$$\frac{d^2\Phi}{dz}\left[-p^2 - \frac{\omega^2}{a_\infty^2} + \frac{2i\omega pM}{a_\infty} + p^2M^2\right]\Phi \equiv \mu^2\Phi$$

Thus

$$\Phi = Be^{-\mu z}$$

Now

$$\frac{d\Phi}{dz}\Big|_{z=0} = W, \quad W \equiv \int_0^\infty \bar{w}e^{-px}dx$$

Thus

$$\frac{d\Phi}{dz}\Big|_{z=0} = -\mu B, \quad B = -\frac{W}{\mu}$$

Hence

$$\Phi = -\frac{w}{\mu}e^{-\mu z}$$

so

$$\bar{\phi}|_{z=0} = \int \mathcal{L}^{-1}\left\{-\frac{1}{\mu}\right\}\bar{w}(\xi,\omega)d\xi$$

For low frequencies , we can ignore the ω^2 terms so

$$\mu^2 \cong (M^2-1)\left\{p + \frac{iM\omega}{a_\infty(M^2-1)}\right\}^2$$

$$-\frac{1}{\mu} = \frac{-1}{\sqrt{M^2-1}}\left(\frac{1}{p + \frac{iM\omega}{a_\infty(M^2-1)}}\right)$$

$$\mathcal{L}^{-1}\left(\frac{-1}{\mu}\right) = \frac{-1}{\sqrt{M^2-1}}\exp[-iM\omega x/a_\infty(M^2-1)]$$

and

$$\bar{\phi}|_{z=0} = \frac{-1}{\sqrt{M^2-1}}\int_0^x \exp[-iM\omega(x-\xi)/a_\infty(M^2-1)]\bar{w}(\xi,\omega)d\xi$$

and if we select our coordinate system such that $w(0) = 0$, for low frequencies the perturbation pressure, $\hat{p}$, is from Bernoulli's equation

$$\hat{p} = \frac{\rho_\infty e^{i\omega t}}{\sqrt{M^2-1}}\Big[- \frac{i\omega \exp[i\omega(t - Mx/a_\infty(M^2-1))]}{(M^2-1)} \times \int \exp[iM\omega\xi/a_\infty(M^2-1)]\bar{w}(\xi,\omega)d\xi + U_\infty \bar{w}(x,\omega)\Big] \qquad \text{(B.53)}$$

$$\cong \frac{\rho_\infty e^{i\omega t}}{\sqrt{M^2-1}} U_\infty \bar{w}(x)$$

For high frequencies,

$$\frac{d^2\Phi}{dx^2} = \left[\frac{-\omega^2}{a_\infty^2} + \frac{2i\omega pM}{a_\infty} + (M^2-1)p^2\right]\Phi \cong \left[\frac{i\omega}{a_\infty} + pM\right]^2 \Phi$$

when we ignore the $(-p^2)$ term compared to those involving ω. Then,

$$\frac{-1}{\mu} \cong \frac{-1}{pM + \frac{i\omega}{a_\infty}}$$

and

$$\bar{\phi}|_{z=0} = \int \mathcal{L}^{-1}\left(\frac{-1}{\mu}\right)\Big|_{x-\xi} \bar{w}(\xi,\omega)d\xi$$

by the convolution theorem. Now

$$\mathcal{L}^{-1}\left[\frac{-1}{pM + \frac{i\omega}{a}}\right] = \frac{-1}{M}\exp(-i\omega x/a_\infty M)$$

so

$$\bar{\phi}|_{z=0} = -\frac{1}{M}\int_0^x \exp[-i\omega(x-\xi)/a_\infty M]\bar{w}(\xi,x)d\xi$$

and from Bernoulli's equation therefore

$$\hat{p} = \cancel{\frac{\rho_\infty}{M}} i\omega \exp[i\omega(x - x/a_\infty M)]\int_0^x \exp(i\omega\xi/a_\infty M)\bar{w}(\xi,\omega)d\xi + \frac{\rho_\infty U_\infty}{M}\exp[i\omega(t - x/a_\infty M)]\exp(i\omega x/a_\infty M)\bar{w}(x,\omega) - \cancel{\frac{\rho_\infty U_\infty}{M}\frac{i\omega}{a_\infty M}}\exp[i\omega(t - x/a_\infty M)]\int_0^x \exp(i\omega\xi/a_\infty M)\bar{w}(\xi,\omega)d\xi$$

$$\hat{p} \cong \frac{\rho_\infty U_\infty}{M}\bar{w}(x,\omega)e^{i\omega t} \qquad for high frequencies$$

This is known as the (linearized, small perturbation) piston theory approximation. It is a useful and interesting exercise to determine pressure distributions, lift and moment for translation and rotation of a flate plate using the piston theory.[4] The low frequency approximation considered earlier is also useful in this respect.

[4] Ashley, H. and Zartarian, G., 'Piston Theory - A New Aerodynamic Tool for the Aeroelastician', *J. Aero. Sciences, 23* (December 1956) pp. 1109–1118.

Appendix C
Shock Wave Boundary Layer Interaction in Hypersonic Flow—A Fluid Structures Thermal Dynamics Interaction (FSTDI) Perspective

The field of fluid dynamics has had many successes over the years in providing a rigorous and practical framework for developing basic understanding of complex physical phenomena of great interest. Yet some phenomena are still not well understood fundamentally or in practice. Perhaps foremost of these is turbulence, but surely not far behind in terms of importance and lack of understanding is shock wave/boundary layer interaction in high speed flows. Here a discussion of proposed work to study the linear and nonlinear dynamics of shock wave/boundary interaction is provided for a canonical geometry to test the hypothesis that the dangerous shock oscillations and enhanced heating that has been observed in wind tunnel experiments and in flight are due to a global instability arising from a bifurcation of the steady flow field when key parameters are changed including geometry, Mach number and Reynolds number.

C.1 Shock Wave Boundary Layer Interaction in Hypersonic Flow—A Brief Review of the Literature and a Proposed Research Approach

Shock Wave Boundary Layer Interaction (SWBLI) has been studied for many years and several excellent reviews of this challenging and still not well understood topic have been published [1–4]. The first of these was published in 2001 by David Dolling with the title "Fifty Years of Shock-Wave Boundary Layer Interaction Research: What Next?" That is still the question nearly 20 years later. More recent reviews by Clemens and Narayanaswamy [2] and Gaitone [3] and Girannelis, Vio and Levinski [4] are informative, but the source of the basic physical mechanism that leads to shock oscillations and hence enhanced heating and strong excitation of a flexible structure underneath the shock is still in question.

One hypothesis is that the shock oscillations arise from the pressure fluctuations in a turbulent boundary layer forcing the shock in a resonant fluid mode [5]. Yet

E. H. Dowell (ed.), *A Modern Course in Aeroelasticity*, Solid Mechanics and Its Applications 264, https://doi.org/10.1007/978-3-030-74236-2

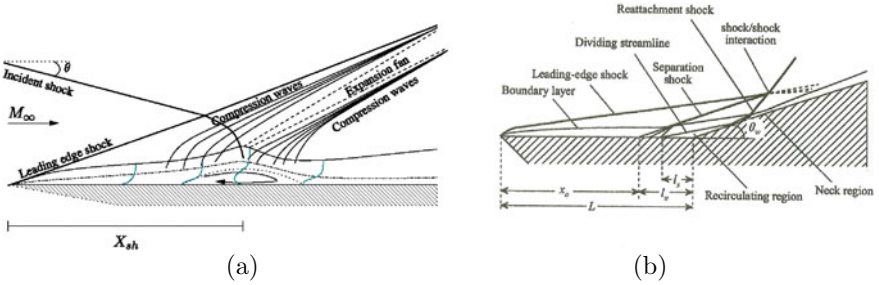

Fig. C.1 **a** Incident impinging shock, after Robinet and **b** ramp, after Mallinson, Gai, and Mudford

a different hypothesis is that there is a global instability of the flow field. Recent work in transonic flow supports the latter hypothesis [4,6–8], but little has been done in the hypersonic regime except for the study by Robinet [9]. Robinet has studied a laminar boundary layer on flat surface with an incident shock impinging on the surface from above and found that indeed a global dynamic instability may occur in his computational model. See Fig. C.1. Moreover in the flow geometry that he studied there is a leading edge and the flow separation that occurs is a significant fraction of the distance from the leading edge to the point of shock impingement. And using this same characteristic length the reduced frequency, i.e. frequency (in radians per unit time) multiplied by the characteristic length and divided by the flow speed, is of order 1. This is consistent with a scaling analysis of the Navier-Stokes equations, e.g. see [10].

It would be especially valuable and timely to study the possibility of a dynamic global instability at hypersonic speeds for two geometries, a two-dimensional flow over a flat plate with a leading edge and (1) an impinging shock [9] or (2) followed by a ramp [11]. The three-dimensional counterpart of the ramp configuration would be an axi-symmetric flow over cone followed by a flare. Note that even though the geometry is axi-symmetric, the bifurcation to a global instability may lead to an oscillating flow that is three-dimensional and no longer axi-symmetric.

C.2 Proposed Approach

The proposed work is mathematical and computational, but with a close eye on creating a computational base that can be evaluated and validated by experiment. Indeed one of the goals of the research is to inspire and help guide a new approach to experimental studies. The incident impinging shock, ramp and cone/flare geometries have been often studied in experiments, but not yet from a dynamical bifurcation global instability perspective.

There are basically two approaches that can be taken in computational studies. One is to do time simulations and that is the approached suggested here. However an eigenvalue and frequency domain, harmonic balance approach is currently being undertaken by Professor Kenneth Hall. The two approaches are complementary and mutually supporting and will provide greater confidence in the results of each study.

C.2.1 Flat Plate with a Leading Edge Followed by a Ramp

For definiteness and brevity the two dimensional flow over a flat (splitter) plate with a leading edge followed by a ramp will be discussed here. See Fig. C.1.

To begin the study we plan to do time simulations with various levels of fluid modeling, i.e. Euler, RANS and Direct Navier-Stokes using the well-known ANSYS/Fluent CFD code. It will be an advantage to use the same code for all three fluid models. Note this code has been used successfully recently to do transonic buffet computations where the buffet arises due to shock wave boundary layer interactions [8]. It is now established that buffet in transonic flow is a limit cycle oscillation due to a global dynamic instability of the flow. Some investigators claim that the onset of buffet (the onset of shock oscillations) can be approximately determined using a Euler code, though this assertion remains controversial. We will explore that possibility. However it is clear that to determine the flow separation and the consequent (limit cycle) oscillations of the shock require at least a RANS and possibly a DNS computational model.

C.2.2 Computational Protocol

The ramp will be allowed to move. It will be given a motion that may include a step change in ramp angle or an oscillating ramp angle about a mean ramp angle. The purpose of the ramp motion is to excite the flow field including of course the shock and the separated flow region. By varying the motion of the ramp the dynamics of flow may be determined even in the absence of flow separation as well as with flow separation. Specifically the frequency and damping of the dominant fluid modes well be determined. More particularly the damping in the fluid mode that leads to a bifurcation as the mean ramp angle is increased will be tracked as the damping of the dominant modes tends to a zero as a parameter is changed, e.g. mean ramp angle, Mach number or Reynolds number. Then once the dynamic instability occurs when the damping goes to zero and then changes sign, the amplitude of the shock motion and separation length (and other flow variables that may prove to be of interest) will be tracked with systematic variations in ramp angle, Mach number and/or Reynolds number. Also the amplitude of the oscillating ramp can be varied to examine whether there is hysteresis in the bifurcation (global dynamic instability)

boundary and subsequent limit cycle oscillations. A similar protocol may be used for an incident shock with the shock angle allowed to move.

C.2.3 Expected Outcomes

A reduced frequency (2π times the Strouhal number) will be computed based upon various length scales in the configuration to see if it indeed is of order 1 when based upon the length from the leading edge to the beginning of the ramp or location of the incident shock.

A theoretical scaling analysis will be done [10] to provide a qualitative check on the computational results with respect to reduced frequency and amplitude of the shock oscillations.

Perhaps most importantly the basic physical mechanism for shock oscillations due to a global instability will be established and the dependence of this physical mechanism on key physical parameters such as geometrical lengths, Mach number and Reynolds will be explored.

Also this work will naturally lead to a consideration of axi-symmetric conical flows and other geometries of interest in the future.

And finally and importantly, the computational/theoretical results will provide a foundation for new and creative experiments.

References

1 Dolling DS (2001) Fifty years of shock-wave boundary layer interaction research: what next? AIAA J 39:1517–1531
2 Clemens NT, Narayanaswamy V (2014) Low-frequency unsteadiness of shock wave/turbulent boundary layer interactions. Ann Rev Fluid Mech 46:469–492
3 Gaitone DV (2015) Progress in shock wave/boundary layer interactions. Prog Aerosp Sci 71:80–99
4 Giannelis NF, Vio GA, Levinski O (2017) A review of recent developments in the understanding of transonic buffet. Prog Aerosp Sci 92:39–84
5 Touber E, Sandham ND (2011) Low-order stochastic modelling of low-frequency motion in reflected shock-wave/boundary -layer interaction. J Fluid Mech 671:417–465
6 Crouch JD, Barbarak A, Magidor D, Travin A (2009) Origin of transonic buffet on airfoils. J Fluid Mech 628:357–369.
7 Raveh D, Dowell EH (2011) Frequency lock-in phenomenon for oscillating airfoils in buffeting flows. J Fluids Struct 27:89–104
8 Bastos K, Dowell EH (2019) Computation of buffet oscillations at high Reynolds numbers over an airfoil. In: Presented at the international forum on aeroelasticity and structural dynamics, Savannah, Georgia.
9 Robinet J-Ch (2007) Bifurcations in shock-wave/laminar-boundary-layer interaction: global instability approach. J Fluid Mech 579:85–113

10 Jaworski JW, Dowell EH (2012) Scaling analysis for aeroelastic phenomena using the Navier-stokes fluid model. AIAA J 50:2622–2626
11 Mallinson SG, Gai SL, Mudford NR (1997) The interaction of a shock wave with a laminar boundary layer at a compression corner in high-enthalpy flows including real gas effects. J Fluid Mech 342:1–35

Index

E. H. Dowell (ed.), *A Modern Course in Aeroelasticity*, Solid Mechanics and Its Applications 264, https://doi.org/10.1007/978-3-030-74236-2

F

G

H

I